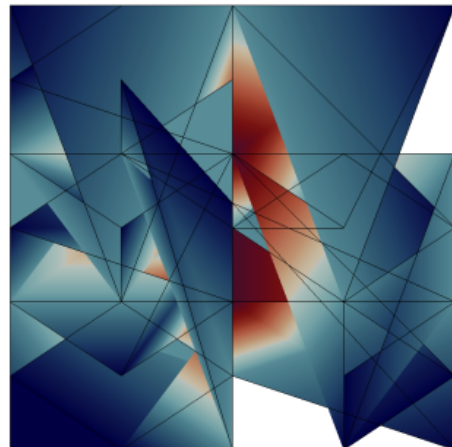


# FieldStone

[Finite Elements (duh!) applied to Stones]



C. Thieulot

With (direct or indirect) contributions from: Wolfgang Bangerth, Eric van den Hoogen, Jort Jansen, Job Mos, Taka Shinohara, Thomas Theunissen, Erik van der Wiel, Lukas van de Wiel, Alraune Zech, Wim Spakman.

If you find anything in this document useful for your research please cite it as follows (*please* include the doi!):

```
@article{Thieulot2019,  
author = "C.A.P. (Cedric) Thieulot",  
title = "{Fieldstone: The Finite Element Method in Computational Geodynamics}",  
year = "2019",  
month = "8",  
url = "https://uu.figshare.com/articles/manual_pdf/9209393",  
doi = "10.23644/uu.9209393.v1"}
```

*Why do I have to promise where I am going while I am not there yet?*

*You can't google something you don't know exists.*

*You can be correct or you can get stuff done.*

# Computational Geodynamics

C. Thieulot

January 16, 2020

## Contents

<b>1</b>	<b>Introduction</b>	<b>14</b>
1.1	Philosophy . . . . .	14
1.2	ambition & motivation . . . . .	14
1.3	Acknowledgements . . . . .	14
1.4	About the author . . . . .	14
1.5	Essential/relevant literature . . . . .	15
1.6	Installation . . . . .	15
1.7	What is a (real) fieldstone? . . . . .	15
1.8	Why the Finite Element method? . . . . .	16
1.9	Oldies but goodies . . . . .	16
1.10	Notations . . . . .	19
1.11	Colour maps for visualisation . . . . .	19
1.12	How my bibliography works . . . . .	19
<b>2</b>	<b>List of stones</b>	<b>21</b>
2.1	Velocity based stones . . . . .	21
2.2	Displacement based stones . . . . .	23
2.3	Stream function based stones . . . . .	23
2.4	Other stones . . . . .	23
<b>3</b>	<b>The physical equations</b>	<b>26</b>
3.1	Coordinate systems . . . . .	26
3.1.1	Cartesian coordinates . . . . .	26
3.1.2	Cylindrical coordinates . . . . .	26
3.1.3	Spherical coordinates . . . . .	26
3.2	A continuum mechanics primer . . . . .	28
3.2.1	Forces . . . . .	28
3.2.2	Stress tensor and tractions . . . . .	29
3.2.3	Strain rate and spin tensor . . . . .	30
3.3	Viscous Newtonian rheology . . . . .	30
3.4	The heat transport equation - energy conservation equation . . . . .	31
3.5	The momentum conservation equations . . . . .	32
3.6	The mass conservation equations . . . . .	32
3.7	The equations in ASPECT manual . . . . .	32
3.8	Equations for thermal convection in an anelastic, compressible, selfgravitating spherical mantle . . . . .	33
3.9	The Navier-Stokes equations in cylindrical coordinates . . . . .	36
3.10	The Navier-Stokes equations in spherical coordinates . . . . .	36
3.11	The equations for axisymmetric geometries . . . . .	37
3.12	The Boussinesq approximation . . . . .	39
3.13	The Extended Boussinesq approximation . . . . .	39
3.14	Stokes equation for elastic medium . . . . .	40
3.15	The strain rate tensor in all coordinate systems . . . . .	41

3.15.1	Cartesian coordinates . . . . .	41
3.15.2	Polar coordinates . . . . .	41
3.15.3	Cylindrical coordinates . . . . .	41
3.15.4	Spherical coordinates . . . . .	42
3.16	Boundary conditions . . . . .	43
3.16.1	The Stokes equations . . . . .	43
3.16.2	The heat transport equation . . . . .	43
3.17	Meaningful physical quantities . . . . .	44
3.18	Principal stress and principal invariants . . . . .	46
3.18.1	In two dimensions . . . . .	47
3.18.2	In three dimensions . . . . .	49
3.19	Tensor (moment) invariants . . . . .	52
3.20	Stress & strain rate invariants . . . . .	53
3.21	Alternative principal stresses notations . . . . .	55
3.22	Rheology in geodynamics . . . . .	57
3.22.1	Linear viscous aka Newtonian . . . . .	57
3.22.2	Power-law model . . . . .	58
3.22.3	Carreau model . . . . .	58
3.22.4	Bingham model . . . . .	59
3.22.5	Herschel-Bulkley visco-plastic model . . . . .	59
3.22.6	The Casson model . . . . .	60
3.22.7	The Ellis model . . . . .	60
3.22.8	One model to rule them all? . . . . .	60
3.22.9	Dislocation and Diffusion creep . . . . .	61
3.22.10	Combining diffusion and dislocation creep . . . . .	63
3.22.11	The von Mises failure criterion . . . . .	65
3.22.12	The Tresca failure criterion . . . . .	68
3.22.13	The Mohr-Coulomb failure criterion . . . . .	69
3.22.14	The Drucker-Prager failure criterion . . . . .	70
3.22.15	The Griffith-Murrell failure criterion . . . . .	73
3.22.16	The Cam-clay failure criterion . . . . .	73
3.22.17	The failure envelope, or yield surface . . . . .	73
3.22.18	Peierls creep . . . . .	76
3.22.19	Stress limiting rheology . . . . .	76
3.22.20	Arrhenius law . . . . .	76
3.22.21	Simple parametrisation of the mantle . . . . .	77
3.22.22	Glen's law for ice . . . . .	77
3.22.23	Viscoelasticity . . . . .	78
3.22.24	Elasto+Visco+Plasticity ? . . . . .	78
3.22.25	Anisotropic viscosity . . . . .	82
3.22.26	Rheology of the lithosphere . . . . .	82
3.23	Moment of inertia . . . . .	83
3.24	The need for numerical modelling . . . . .	84
<b>4</b>	<b>The building blocks of the Finite Element Method</b>	<b>85</b>
4.1	Numerical integration . . . . .	85
4.1.1	in 1D - theory . . . . .	85
4.1.2	in 1D - examples . . . . .	88
4.1.3	in 2D/3D - theory . . . . .	88
4.1.4	quadrature on triangles . . . . .	89
4.1.5	quadrature on tetrahedra . . . . .	89
4.1.6	The Gauss-Lobatto approach . . . . .	90
4.2	The mesh . . . . .	91
4.3	A bit of FE terminology . . . . .	91
4.4	Elements and basis functions in 1D . . . . .	92
4.4.1	Linear basis functions ( $Q_1$ ) . . . . .	92

4.4.2	Quadratic basis functions ( $Q_2$ ) . . . . .	93
4.4.3	Cubic basis functions ( $Q_3$ ) . . . . .	93
4.4.4	Quartic basis functions ( $Q_4$ ) . . . . .	96
4.5	Elements and basis functions in 2D . . . . .	98
4.5.1	Bilinear basis functions in 2D ( $Q_1$ ) . . . . .	99
4.5.2	Biquadratic basis functions in 2D ( $Q_2$ ) . . . . .	101
4.5.3	Eight node serendipity basis functions in 2D ( $Q_2^{(8)}$ ) . . . . .	102
4.5.4	Bicubic basis functions in 2D ( $Q_3$ ) . . . . .	104
4.5.5	Biquartic basis functions in 2D ( $Q_4$ ) . . . . .	105
4.5.6	Linear basis functions for triangles in 2D ( $P_1$ ) . . . . .	105
4.5.7	Linear basis functions for quadrilaterals in 2D ( $P_1$ ) . . . . .	107
4.5.8	Enriched linear basis functions in triangles ( $P_1^+$ ) . . . . .	108
4.5.9	Quadratic basis functions for triangles in 2D ( $P_2$ ) . . . . .	110
4.5.10	Enriched quadratic basis functions in triangles ( $P_2^+$ ) . . . . .	111
4.5.11	Cubic basis functions for triangles ( $P_3$ ) . . . . .	113
4.6	Elements and basis functions in 3D . . . . .	113
4.6.1	Linear basis functions in tetrahedra ( $P_1$ ) . . . . .	113
4.6.2	Enriched linear in tetrahedra( $P_1^+$ ) . . . . .	114
4.6.3	Triquadratic basis functions in 3D ( $Q_2$ ) . . . . .	116
4.6.4	Enriched quadratic basis functions in tetrahedra ( $P_2^+$ ) . . . . .	117
4.6.5	Linear basis functions for tetrahedra ( $P_1$ ) . . . . .	117
4.6.6	20-node serendipity basis functions in 3D ( $Q_2^{(20)}$ ) . . . . .	118
<b>5</b>	<b>Solving the heat transport equation with linear Finite Elements</b>	<b>119</b>
5.1	The diffusion equation in 1D . . . . .	119
5.2	The advection-diffusion equation in 1D . . . . .	126
5.3	The advection-diffusion equation in 2D . . . . .	128
5.3.1	Dealing with the time discretisation . . . . .	129
5.3.2	On steady states . . . . .	131
5.3.3	Anisotropic heat conduction . . . . .	131
5.3.4	About the assembly . . . . .	131
<b>6</b>	<b>Solving the flow equations with the FEM</b>	<b>133</b>
6.1	Strong and weak forms . . . . .	133
6.2	Which velocity-pressure pair for Stokes? . . . . .	133
6.2.1	The compatibility condition (or LBB condition) . . . . .	133
6.2.2	Families . . . . .	133
6.2.3	The bi/tri-linear velocity - constant pressure element ( $Q_1 \times P_0$ ) . . . . .	134
6.2.4	The bi/tri-quadratic velocity - discontinuous linear pressure element ( $Q_2 \times P_{-1}$ ) . . . . .	134
6.2.5	The bi/tri-quadratic velocity - bi/tri-linear pressure element ( $Q_2 \times Q_1$ ) . . . . .	134
6.2.6	The stabilised bi/tri-linear velocity - constant pressure element ( $Q_1 \times P_0\text{-stab}$ ) . . . . .	135
6.2.7	The stabilised bi/tri-linear velocity - bi/tri-linear pressure element ( $Q_1 \times Q_1\text{-stab}$ ) . . . . .	135
6.2.8	The MINI triangular element ( $P_1^+ \times P_1$ ) in 2D . . . . .	135
6.2.9	The quadratic velocity - linear pressure triangle ( $P_2 \times P_1$ ) . . . . .	136
6.2.10	The Crouzeix-Raviart triangle ( $P_2^+ \times P_{-1}$ ) . . . . .	136
6.2.11	The Rannacher-Turek element - rotated $Q_1 \times P_0$ . . . . .	137
6.2.12	Other elements . . . . .	137
6.2.13	A note about incompressibility and standard mixed methods . . . . .	137
6.3	The penalty approach for viscous flow . . . . .	137
6.4	The mixed FEM for viscous flow . . . . .	141
6.4.1	in three dimensions . . . . .	141
6.4.2	Going from 3D to 2D . . . . .	147
6.5	Solving the elastic equations . . . . .	149
6.6	A quick tour of similar literature . . . . .	149
6.7	The case against the $Q_1 \times P_0$ element . . . . .	149
6.8	Isoviscous Stokes for incompressible flow . . . . .	150

<b>7</b>	<b>The Discontinuous Galerkin Finite Element Method (DG-FEM)</b>	<b>152</b>
7.1	First-order advection ODE in 1D . . . . .	152
7.2	Steady state diffusion in 1D . . . . .	153
7.3	Time-dependent diffusion PDE in 1D . . . . .	159
7.4	Time-dependent advection PDE in 1D . . . . .	161
7.5	Steady-state diffusion in 2D . . . . .	163
7.6	Time-dependent diffusion PDE in 2D . . . . .	164
7.7	Stokes equations . . . . .	165
<b>8</b>	<b>Additional techniques, features, measurements</b>	<b>166</b>
8.1	Dealing with a free surface (and mesh deformation) . . . . .	167
8.1.1	The fully Lagrangian approach . . . . .	167
8.1.2	The Eulerian approach: using sticky air . . . . .	168
8.1.3	The Arbitrary Lagrangian Eulerian (ALE) approach . . . . .	170
8.1.4	On the topic of moving internal nodes . . . . .	175
8.2	Convergence criterion for nonlinear iterations . . . . .	177
8.3	Strain weakening . . . . .	178
8.4	The gravity vector . . . . .	180
8.5	The SUPG formulation for the energy equation . . . . .	181
8.5.1	Linear elements . . . . .	181
8.6	The method of manufactured solutions . . . . .	183
8.6.1	Analytical benchmark I - "DH" . . . . .	183
8.6.2	Analytical benchmark II - "DB2D" . . . . .	185
8.6.3	Analytical benchmark III - "DB3D" . . . . .	185
8.6.4	Analytical benchmark IV - "Bercovier & Engelman" . . . . .	186
8.6.5	Analytical benchmark V - "VJ1" . . . . .	186
8.6.6	Analytical benchmark VI - "Ilinca & Pelletier" . . . . .	187
8.6.7	Analytical benchmark VII - "grooves" . . . . .	187
8.6.8	Analytical benchmark VIII - "Kovasznay" . . . . .	190
8.6.9	Analytical benchmark IX - "VJ2" . . . . .	191
8.6.10	Analytical benchmark X - "VJ3" . . . . .	191
8.6.11	Analytical benchmark XI - "PPC1" . . . . .	193
8.6.12	Analytical benchmark XII - "PPC2" . . . . .	193
8.6.13	Annulus with kinematical b.c. . . . .	193
8.6.14	Viscous beam under extension . . . . .	195
8.6.15	Channel flow with Herschel-Bulkley rheology . . . . .	196
8.7	Geodynamical benchmarks . . . . .	203
8.7.1	Relaxation of sinusoidal topography . . . . .	205
8.7.2	the plastic brick . . . . .	206
8.7.3	Infinite plate with a circular hole [2094] . . . . .	209
8.7.4	Slope stability for elasto-plastic materials a la [2094] . . . . .	210
8.7.5	Time-dependent benchmark in an annulus . . . . .	210
8.7.6	Convection in 2D-box . . . . .	211
8.7.7	The sinker problem . . . . .	212
8.7.8	The hot blob problem . . . . .	213
8.7.9	The punch/indentor problem in 2D . . . . .	213
8.7.10	Lid driven cavity with analytical solution . . . . .	215
8.7.11	Flow around a cylinder . . . . .	216
8.7.12	Thin layer entrainment . . . . .	216
8.7.13	Heat flow around a cylinder . . . . .	219
8.7.14	Thermal diffusion of half-cooling space . . . . .	219
8.7.15	Laplace equation on a semi infinite plate . . . . .	220
8.7.16	Slab detachment benchmark . . . . .	222
8.7.17	Layered flow with viscosity contrast . . . . .	222
8.7.18	Elastic material in simple shear . . . . .	225
8.7.19	Elastic material in pure shear . . . . .	225

8.7.20	Uniform strip load on elastic material . . . . .	226
8.8	Assigning values to quadrature points . . . . .	227
8.9	Matrix (Sparse) storage . . . . .	230
8.9.1	2D domain - One degree of freedom per node . . . . .	230
8.9.2	2D domain - Two degrees of freedom per node . . . . .	231
8.9.3	Matrix Storage in fieldstone . . . . .	232
8.9.4	Sparse Matrix-Vector multiplication . . . . .	233
8.10	Mesh generation . . . . .	234
8.10.1	Quadrilateral-based meshes . . . . .	234
8.10.2	Delaunay triangulation and Voronoi cells, and triangle-based meshes . . . . .	236
8.10.3	Tetrahedra . . . . .	239
8.10.4	Hexahedra . . . . .	239
8.10.5	Adaptive Mesh Refinement . . . . .	239
8.10.6	Conformal Mesh Refinement . . . . .	243
8.10.7	Meshes in an annulus . . . . .	244
8.10.8	Meshes in a hollow sphere . . . . .	244
8.11	Visco-Plasticity . . . . .	248
8.11.1	Scalar viscoplasticity . . . . .	248
8.12	Pressure smoothing . . . . .	249
8.13	Pressure scaling . . . . .	251
8.14	Pressure normalisation . . . . .	252
8.14.1	Basic idea and naive implementation . . . . .	252
8.14.2	Implementation – the real deal . . . . .	252
8.15	Solving the Stokes system . . . . .	253
8.15.1	when using the penalty formulation . . . . .	253
8.15.2	Conjugate gradient and the Schur complement approach . . . . .	254
8.15.3	Conjugate gradient and the Schur complement approach . . . . .	255
8.15.4	The Augmented Lagrangian approach . . . . .	259
8.15.5	The GMRES approach . . . . .	260
8.16	The consistent boundary flux (CBF) . . . . .	261
8.16.1	The CBF applied to the Stokes equation . . . . .	261
8.16.2	The CBF applied to the heat transport equation . . . . .	262
8.16.3	Some implementation details for the Stokes equation . . . . .	262
8.17	The value of the timestep . . . . .	265
8.18	Mappings . . . . .	266
8.18.1	Linear mapping on a triangle . . . . .	266
8.18.2	Bilinear mapping on a linear quadrilateral . . . . .	266
8.18.3	biquadratic mapping of a straight-line face $Q_2$ element . . . . .	270
8.18.4	biquadratic mapping of a not-so straight-line face $Q_2$ element . . . . .	271
8.18.5	bilinear, biquadratic and bicubic mapping in an annulus . . . . .	271
8.19	Exporting data to vtk format . . . . .	274
8.20	Runge-Kutta methods . . . . .	276
8.20.1	Using RK methods to advect particles/markers . . . . .	277
8.21	Am I in or not? - finding reduced coordinates . . . . .	279
8.21.1	Two-dimensional space . . . . .	279
8.21.2	Three-dimensional space . . . . .	279
8.22	Error measurements and convergence rates . . . . .	282
8.22.1	About extrapolation . . . . .	283
8.23	The initial temperature field . . . . .	284
8.23.1	Single layer with imposed temperature b.c. . . . .	284
8.23.2	Single layer with imposed heat flux b.c. . . . .	285
8.23.3	Single layer with imposed heat flux and temperature b.c. . . . .	285
8.23.4	Half cooling space . . . . .	285
8.23.5	Plate model . . . . .	285
8.23.6	McKenzie slab . . . . .	285
8.23.7	Initial temperature for global mantle convection models . . . . .	287

8.24	Kinematic boundary conditions . . . . .	288
8.24.1	In-out flux boundary conditions for lithospheric models . . . . .	288
8.25	Computing gradients - the recovery process . . . . .	289
8.25.1	Global recovery . . . . .	289
8.25.2	Local recovery - centroid average over patch . . . . .	289
8.25.3	Local recovery - nodal average over patch . . . . .	289
8.25.4	Local recovery - least squares over patch . . . . .	289
8.25.5	Link to pressure smoothing . . . . .	289
8.26	Tracking materials and/or interfaces . . . . .	290
8.26.1	The Particle-in-cell technique . . . . .	291
8.26.2	The level set function technique . . . . .	294
8.26.3	The field/composition technique . . . . .	294
8.26.4	The Volume-of-Fluid method . . . . .	295
8.26.5	The method of characteristics . . . . .	296
8.26.6	The Marker Chain method . . . . .	296
8.26.7	Hybrid methods . . . . .	296
8.26.8	Boundary fitted mesh . . . . .	297
8.27	Static condensation . . . . .	298
8.28	Measuring incompressibility . . . . .	299
8.29	Periodic boundary conditions . . . . .	300
8.30	Removing rotational nullspace . . . . .	301
8.30.1	Three dimensions . . . . .	301
8.30.2	Two dimensions . . . . .	302
8.31	Picard and Newton . . . . .	304
8.31.1	Picard iterations . . . . .	304
8.32	Defect correction formulation . . . . .	305
8.33	Parallel or not? . . . . .	306
8.34	Stream function . . . . .	307
8.34.1	In Cartesian coordinates . . . . .	307
8.34.2	In Cylindrical coordinates . . . . .	307
8.35	Corner flow . . . . .	308
8.36	Surface processes . . . . .	310
8.36.1	In 1D - simple nonlinear diffusion a la [365] . . . . .	310
8.36.2	In 1D - not so simple, a la [42] . . . . .	310
8.37	Geometric multigrid . . . . .	312
8.38	Algebraic multigrid . . . . .	314
8.39	Computing depth . . . . .	315
8.40	Imposing boundary conditions . . . . .	316
8.41	The Geoid . . . . .	317
8.41.1	What is the geoid? . . . . .	317
8.41.2	How to compute it? . . . . .	317
8.41.3	Interesting modelling . . . . .	317
8.42	The Lyapunov time/exponent, mixing stirring . . . . .	318
8.43	Phase transitions . . . . .	320
<b>9</b>	<b>Geodynamics GEO3-1313 - Utrecht University</b>	<b>322</b>
9.1	Introduction . . . . .	322
9.2	Global internal structure and temperature of the Earth . . . . .	323
9.2.1	Early models of the Earth's density . . . . .	325
9.2.2	The moment of inertia of a spherically symmetric density distribution . . . . .	325
9.2.3	Density, gravity and pressure in the Earth . . . . .	327
9.2.4	Gravity field of a mass distribution . . . . .	328
9.2.5	The gravity and pressure field for parameterized density models with self-gravitation	331
9.2.6	The pressure effect on density . . . . .	333
9.2.7	Adiabatic density distribution . . . . .	338
9.2.8	Current density models . . . . .	340

9.2.9	Earth's chemical composition . . . . .	340
9.2.10	Phase transitions as anchor points of the geotherm . . . . .	342
9.3	Programming exercises - February 2020 . . . . .	346
9.3.1	Background . . . . .	346
9.4	WORK in PROGRESS. DUH. . . . .	348
	<b>Stone 01: simple analytical solution (D&amp;H)</b>	<b>351</b>
	<b>Stone 02: Stokes sphere</b>	<b>353</b>
	<b>Stone 03: Convection in a 2D box</b>	<b>354</b>
	<b>Stone 04: The lid driven cavity</b>	<b>359</b>
	<b>Stone 05: SolCx benchmark</b>	<b>361</b>
	<b>Stone 06: SolKz benchmark</b>	<b>363</b>
	<b>Stone 07: SolVi benchmark</b>	<b>364</b>
	<b>Stone 08: the indentor benchmark</b>	<b>366</b>
	<b>Stone 09: the annulus benchmark</b>	<b>371</b>
	<b>Stone 10: Stokes sphere (3D) - penalty</b>	<b>373</b>
	<b>Stone 11: stokes sphere (3D) - mixed formulation</b>	<b>375</b>
	<b>Stone 12: consistent pressure recovery</b>	<b>377</b>
	<b>Stone 13: the Particle in Cell technique (1) - the effect of averaging</b>	<b>383</b>
	<b>Stone 14: solving the full saddle point problem</b>	<b>387</b>
	<b>Stone 15: saddle point problem with Schur complement approach - benchmark</b>	<b>389</b>
	<b>Stone 16: saddle point problem with Schur complement approach - Stokes sphere</b>	<b>391</b>
	<b>Stone 17: solving the full saddle point problem in 3D</b>	<b>393</b>
	<b>Stone 18: solving the full saddle point problem with <math>Q_2 \times Q_1</math> elements</b>	<b>398</b>
	<b>Stone 19: solving the full saddle point problem with <math>Q_3 \times Q_2</math> elements</b>	<b>399</b>
	<b>Stone 20: the Busse benchmark</b>	<b>401</b>
	<b>Stone 22: The stabilised <math>Q_1 \times Q_1</math> element</b>	<b>406</b>
	<b>Stone 23: compressible flow (1) - analytical benchmark</b>	<b>410</b>
	<b>Stone 24: compressible flow (2) - convection box</b>	<b>412</b>
	<b>Stone 25: Rayleigh-Taylor instability (1) - instantaneous</b>	<b>427</b>
	<b>Stone 26: Slab detachment benchmark (1) - instantaneous</b>	<b>429</b>
	<b>Stone 27: Consistent Boundary Flux</b>	<b>431</b>
	<b>Stone 28: convection 2D box - Tosi et al, 2015</b>	<b>435</b>

Stone 29: open boundary conditions	447
Stone 30: conservative velocity interpolation	450
Stone 31: conservative velocity interpolation 3D	451
Stone 32: 2D analytical sol. from stream function	452
Stone 33: Convection in an annulus	456
Stone 34: the Cartesian geometry elastic aquarium	461
Stone 35: 2D analytical sol. in annulus from stream function	463
Stone 36: the annulus geometry elastic aquarium	469
Stone 37: marker advection and population control	472
Stone 38: Critical Rayleigh number	473
Stone 39: chpe15	475
Stone 40: Rayleigh-Taylor instability	485
Stone 42: 1D diffusion	487
Stone 43: the rotating cone	488
Stone 44: the flat slab	491
Stone 45: the corner flow	493
Stone 46: MMS1 with Crouzeix-Raviart ( $P_2^+ \times P_{-1}$ ) elements	497
Stone 47: MMS1 with MINI ( $P_1^+ \times P_1$ ) elements	498
Stone 48: D&H with $Q_1 \times P_0$ , $Q_2 \times Q_1$ , $Q_3 \times Q_2$ and $Q_4 \times Q_3$ elements	500
Stone 49: Consistent Boundary Flux method on D&H benchmark with 4 elements	506
Stone 50: Lithosphere extension	507
Stone 51: Triangular domain benchmark with MINI element	508
Stone 52: Serendipity element in 2D	512
Stone 53: the sinking block benchmark	514
Stone 54: ALEs	515
Stone 55: Subduction as a thin-sheet problem	525
Stone 56: Dynamics of the Salt Water - Fresh Water Interface	529
Stone 57: 1D steady state diffusion with DG-FEM	530
Stone 58: Elastic disk under compression	532
Stone 59: Flow Down an Inclined Plane	539
Stone 60: 1D advection with DG-FEM	546

<b>10 fieldstone: Gravity: buried sphere</b>	<b>547</b>
<b>11 Problems, to do list and projects for students</b>	<b>549</b>
<b>A Three-dimensional applications</b>	<b>552</b>
<b>B Codes in geodynamics</b>	<b>553</b>
<b>C Matrix properties</b>	<b>562</b>
C.1 Symmetric matrices . . . . .	562
C.2 Eigenvalues of positive definite matrix . . . . .	562
C.3 Schur complement . . . . .	562
<b>D Dont be a hero - unless you have to</b>	<b>564</b>
<b>E A FANTOM, an ELEFANT and a GHOST</b>	<b>566</b>
<b>F Some useful Python commands</b>	<b>571</b>
F.1 Sparse matrices . . . . .	571
F.2 condition number . . . . .	571
<b>G Some useful maths</b>	<b>572</b>
G.1 Inverse of a 3x3 matrix . . . . .	572
G.2 Inverse of a 3x3 matrix . . . . .	572
<b>H Topics in (computational) geodynamics literature</b>	<b>573</b>
H.1 Big review papers - very good for students . . . . .	573
H.2 Analogue modelling . . . . .	575
H.3 Archean tectonics, early Earth . . . . .	576
H.4 Anisotropy, Lattice/Crystal preferred orientation, SKS splitting . . . . .	576
H.5 Benchmark, analytical solutions, code comparisons, methodology, num. methods, theory . . . . .	576
H.6 Core dynamics, core formation, CMB temperature/heat flux . . . . .	577
H.7 Computational Structural geology . . . . .	577
H.8 Channel flow model . . . . .	577
H.9 Core complexes . . . . .	577
H.10 Dataset (gravity, goce, grace, tomography, gps, heat flow) and/or their calculations/use . . . . .	577
H.11 Discontinuous Galerkin (DG) . . . . .	578
H.12 Dynamo . . . . .	578
H.13 (role of) Elasticity in geodynamics modelling . . . . .	578
H.14 (Geodynamics+) surface processes, erosion, sedimentation, topography evolution . . . . .	578
H.15 Geotechnics . . . . .	579
H.16 Glacier dynamics, ice sheets, ice flow, ice rheology . . . . .	579
H.17 (use of) Inverse methods, inversion, adjoint methods, assimilation . . . . .	579
H.18 Large scale mantle-plate interaction, whole Earth models . . . . .	579
H.19 Crust/Lithosphere modelling, plate motion, plate stress . . . . .	580
H.20 Delamination, edge driven convection, gravitational instability, mantle unrooting . . . . .	580
H.21 Detachment faults . . . . .	580
H.22 Dynamic topography . . . . .	580
H.23 Lithospheric stress, intraplate stress . . . . .	581
H.24 Passive margins . . . . .	581
H.25 Folding, buckling . . . . .	581
H.26 Geoid . . . . .	582
H.27 Geothermal Energy . . . . .	582
H.28 Grain size (evolution) & influence on geodynamics . . . . .	582
H.29 LLSVP, ULVZ, CMB layer, thermo-chemical piles, D" layer . . . . .	582
H.30 Magma ocean . . . . .	583

H.31 Magma transport / melting / two phase flow/ (intra-plate) volcanism / lava flow/ continental flood basalt . . . . .	583
H.32 Mantle convection/dynamics, whole Earth models, plate interaction . . . . .	583
H.33 Mantle rheology, phase transitions, stratification, (temperature) profile . . . . .	584
H.34 Mantle wedge . . . . .	585
H.35 Mixing, stirring, degassing . . . . .	585
H.36 Obduction, ophiolites . . . . .	585
H.37 Plate motion and mantle, plate tectonic reconstruction . . . . .	585
H.38 Plume dynamics . . . . .	585
H.39 Plume-Lithosphere interaction, LIP, hotspots . . . . .	586
H.40 Porous media . . . . .	586
H.41 Preconditioner business . . . . .	586
H.42 Reservoir modeling . . . . .	586
H.43 Regenauer-Lieb . . . . .	586
H.44 Rheology, material parameters, rock mechanics . . . . .	587
H.45 Rifting, seafloor spreading, mid-ocean ridges, pull-apart basins, extension . . . . .	587
H.46 Salt tectonics, Shale tectonics . . . . .	588
H.47 Sea Level evolution . . . . .	588
H.48 Segregated methods to solve the Stokes system . . . . .	588
H.49 Seismo-tectonics, subduction earthquakes . . . . .	588
H.50 Subduction . . . . .	589
H.51 Subduction - slab detachment, break-off . . . . .	589
H.52 Subduction + water (fluids) . . . . .	590
H.53 Subduction/plate tectonics initiation . . . . .	590
H.54 Subduction - flat/low angle/horizontal subduction . . . . .	590
H.55 Teaching . . . . .	590
H.56 Tectonics, small deformation, rock mechanics . . . . .	591
H.57 Wilson cycle, supercontinent cycles . . . . .	591
H.58 Meshless methods (SPH, RKPM, DEM, FPM, ...) . . . . .	591
H.59 Element Free Galerkin Method . . . . .	591
H.60 Planetary accretion, exoplanets, planet formation, segregation . . . . .	591
H.61 Accretionary wedges, nappes, thrust wedges, orogenic wedge, fold-thrust belt . . . . .	591
H.62 Thrust-wrench fault . . . . .	591
H.63 Transpressional systems . . . . .	591
H.64 Urey ratio . . . . .	591
H.65 Intrusions, diapirism, Rayleigh-Taylor instability . . . . .	591
H.66 Visualization, rendering . . . . .	592
H.67 Solving Stokes Saddle Point problem . . . . .	592
H.68 Celestial bodies . . . . .	592
H.69 Locations . . . . .	593
<b>I Elemental mass matrices for simple geometries</b> . . . . .	<b>595</b>
I.1 1D segments . . . . .	595
I.1.1 Linear basis functions . . . . .	595
I.1.2 Quadratic basis functions . . . . .	595
I.1.3 Cubic basis functions . . . . .	596
I.1.4 Quartic basis functions . . . . .	598
I.2 Quadrilaterals: rectangular elements . . . . .	599
I.3 Hexahedra: cuboid elements . . . . .	599
<b>J Finite element terminology in various languages</b> . . . . .	<b>600</b>
<b>K Fun modelling</b> . . . . .	<b>601</b>
<b>L Beautiful/interesting images from computational geodynamics</b> . . . . .	<b>603</b>
<b>M People</b> . . . . .	<b>605</b>

<b>N Working with Git</b>	<b>606</b>
<b>General Index</b>	<b>736</b>
<b>Contributors</b>	<b>739</b>
<b>Topics in the literature</b>	<b>740</b>

# WARNING: this is work in progress

## 1 Introduction

### 1.1 Philosophy

This document was written with my students in mind, i.e. 3rd and 4th year Geology/Geophysics students at Utrecht University. I have chosen to use as little jargon as possible unless it is a term that is commonly found in the geodynamics literature (methods paper as well as application papers). There is no mathematical proof of any theorem that may be mentioned but I will try to refer to the appropriate sources, i.e. generic Numerical Analysis, Finite Element and Linear Algebra books. If you find that this book lacks references to Sobolev spaces, Hilbert spaces, and other spaces, this book is just not for you.

The codes I provide here are by no means optimised as I have chosen code readability over code efficiency. I have also chosen to avoid resorting to multiple code files or even functions in order to favour a sequential reading of the codes. These codes are not designed to form the basis of a real life application: Existing open source highly optimised codes should be preferred, such as ASPECT [1507, 1169], CITCOM [2909, 2905], LAMEM [1402], PTATIN [1746, 1743], PYLITH[1], ... (see Section B).

All kinds of feedback is welcome on the text (grammar, typos, ...), on the text, the equations or on the code(s). You will have my eternal gratitude if you wish to contribute an example, a benchmark, a cookbook.

All the python scripts and this document are freely available at

<https://github.com/cedrict/fieldstone>

### 1.2 ambition & motivation

I wish to provide the community with:

- an enormous bibliography data base - simply search the pdf for keywords. The  $\text{\LaTeX}$  file is also available next to the manual.tex file on github;
- a go-to document for anybody who wants to know more about a particular topic in computational geodynamics;
- a useful teaching tool for researchers, teachers, students and PhD students alike;
- small, readable, educative codes.

### 1.3 Acknowledgements

I have benefitted from many discussions, lectures, tutorials, coffee machine discussions, debugging sessions, conference poster sessions, etc ... over the years. I wish to name these instrumental people in particular and in alphabetic order: Wolfgang Bangerth, Jean Braun, Rens Elbertsen, Philippe Fullsack, Menno Fraters, Anne Glerum, Timo Heister, Dave May, Robert Myhill, John Naliboff, E. Gerry Puckett, Melchior Schuh-Senlis, Michael Tetley, Lukas van de Wiel, Arie van den Berg, Eric van den Hoogen, Tom Weir, and the whole ASPECT family/team.

### 1.4 About the author

I have BSc in mathematics, and an MSc diploma in physics (with a specialization in musical acoustics [678]). I did my PhD at the university of Groningen (The Netherlands) title *Thermodynamically consistent fluid particle modelling of phase separating mixtures*<sup>1</sup>. Although half of the thesis deals with the re-derivation of the Navier-Stokes equations for such systems[796], the second half is concerned with the implementation of these equations with the Smoothed Particle Hydrodynamics method [2536, 2537, 2535].

I then taught physics and programming at the University of Rennes (France) for a year, after which I did a 2-year post-doc with Prof. J. Braun<sup>2</sup> in the Geosciences department. I then did a 4-year post-doc

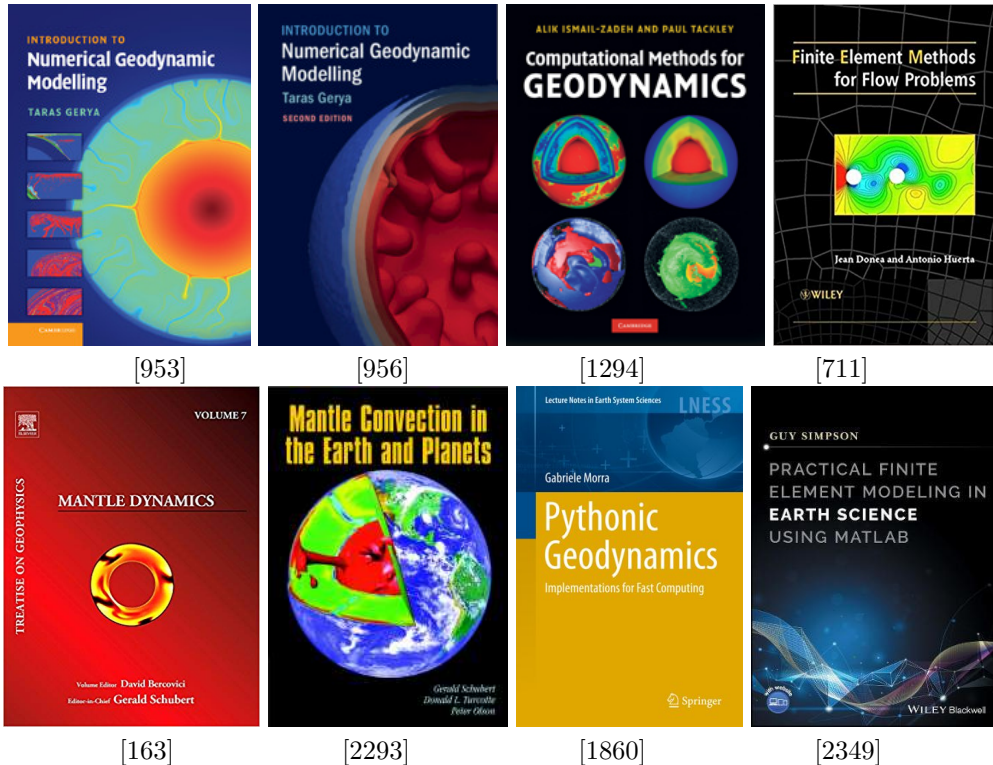
---

<sup>1</sup><http://cedrictchielot.net/thesis.html>

<sup>2</sup><https://www.gfz-potsdam.de/en/staff/jean-braun/>

with prof. R. Huismans<sup>3</sup> at the University of Bergen (Norway), followed by a 3-year post-doc with profs. T. Torsvik and W. Spakman at the Utrecht University (The Netherlands). Since June 2015 I am assistant professor there in the geophysics group.

## 1.5 Essential/relevant literature



- *Numerical modeling of Earth Systems* by Thorsten W. Becker and Boris J. P. Kaus, <http://www-udc.ig.utexas.edu/external/becker/teaching-557.html>
- *Myths & Methods in Modeling* by M. Spiegelman, <https://www.ldeo.columbia.edu/~mspieg/mmm/>
- *Computational Science I* by Matthew G. Knepley, <https://cse.buffalo.edu/~knepley/classes/caam519/Syllabus.html>
- *Introduction to Numerical Methods for Variational Problems* by Hans Petter Langtangen and Kent-Andre Mardal, <https://hplgit.github.io/fem-book/doc/pub/book/pdf/fem-book-4print.pdf>

## 1.6 Installation

If numpy, scipy or matplotlib are not installed on your machine, here is how you can install them:

```
python3.6 -m pip install --user numpy scipy matplotlib
```

To install the umfpack solver:

```
pip install --upgrade scikit-umfpack --user
```

## 1.7 What is a (real) fieldstone?

Simply put, it is stone collected from the surface of fields where it occurs naturally. It also stands for the bad acronym: *finite element deformation of stones* which echoes the primary application of these codes: geodynamic modelling.

---

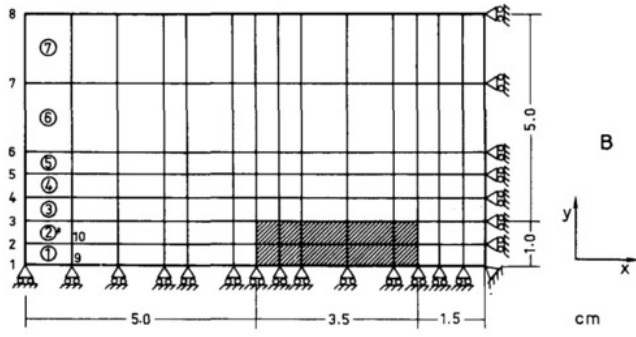
<sup>3</sup><https://folk.uib.no/huismans/>

## 1.8 Why the Finite Element method?

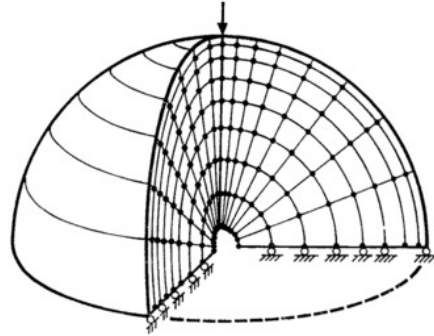
The Finite Element Method (FEM) is by no means the only method to solve PDEs in geodynamics, nor is it necessarily the best one. Other methods are employed very successfully, such as the Finite Difference Method (FDM), the Finite Volume Method (FVM), and to a lesser extent the Discrete Element Method (DEM) [2503, 758, 759, 908], the Lattice-Boltzmann method [1241], the Rigid Element Method [1532], or the Element Free Galerkin Method (EFGM) [1134]. I have been using FEM since 2008 and I do not have real experience to speak of in FVM or FDM so I concentrate in this book on what I know best.

## 1.9 Oldies but goodies

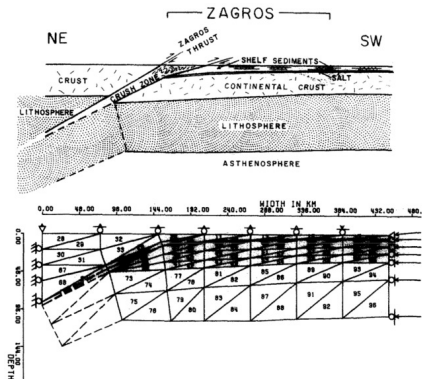
The first papers I could find showcasing the FEM in geodynamics are listed hereafter [922], [37][1773][288] [782] [2522][2294] [783][1857] [2949] [239] [273] [276]. I hereunder show a few plots taken from early geodynamics papers.



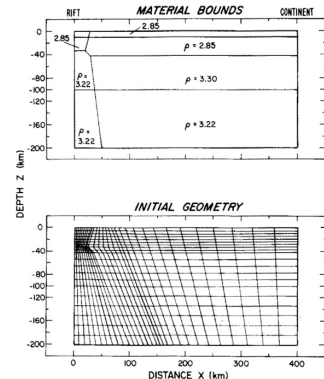
1971: Model a boudinage structure [2431]



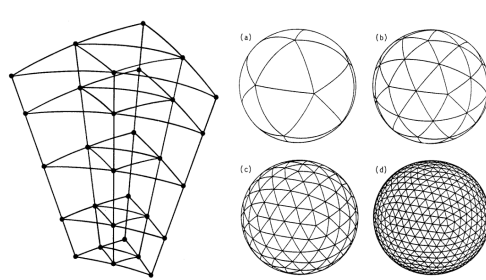
1972: Crustal Structure from Surface Load Tilts [128]



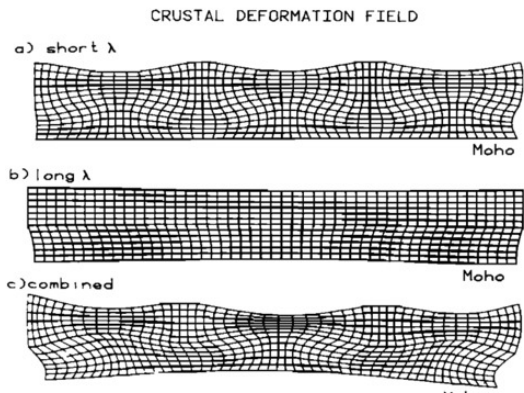
1978: Finite element modelling of lithosphere deformation: the Zagros collision orogeny [201]



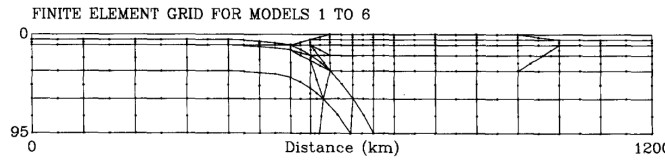
1981: Thermal regimes, mantle diapirs and crustal stresses of continental rifts [289]



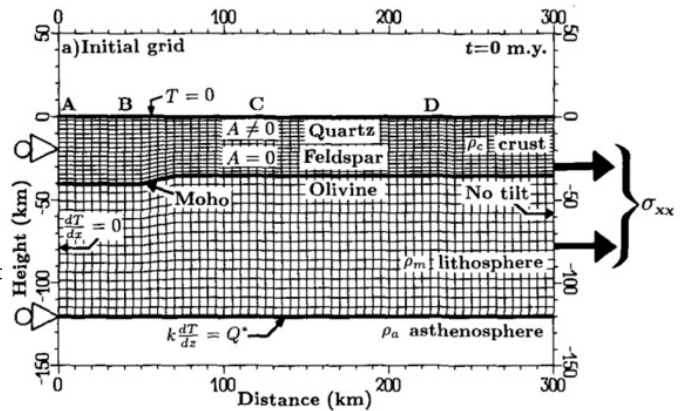
1985: Three-Dimensional Treatment of Convective Flow in the Earth's Mantle. [109]



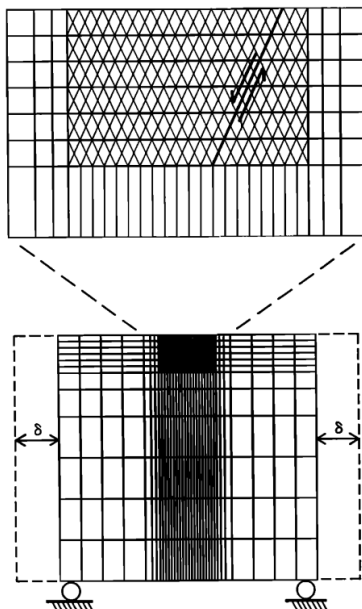
1986: Lithospheric necking: a dynamic model for rift morphology [2950]



1989: Plate boundary forces at subduction zones and trench-arc compression [239]

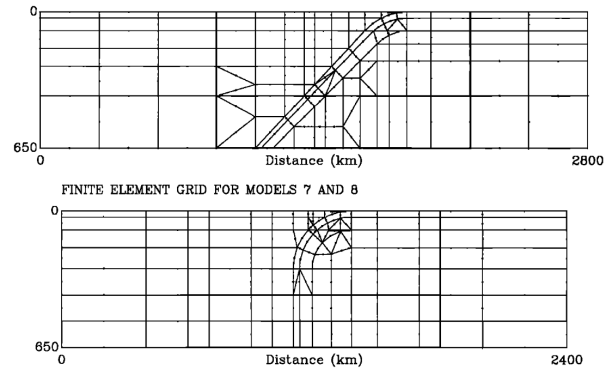


1989: Relation between flank uplifts and the breakup unconformity at rifted continental margins [275]

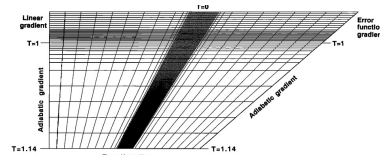


1989: Mechanics of graben formation in crustal rocks [1774]

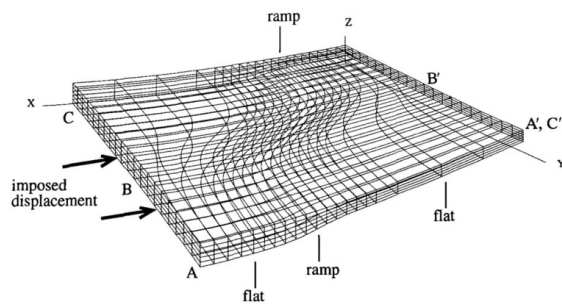
FINITE ELEMENT GRID FOR MODELS 3 AND 4



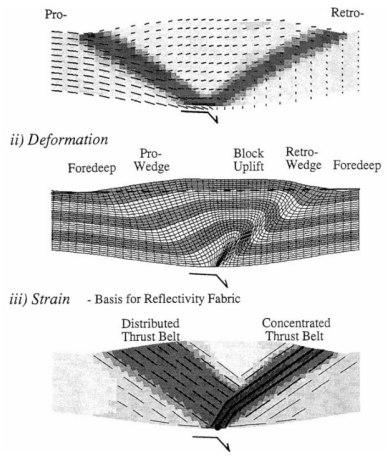
1992: Stresses and plate boundary forces associated with subduction plate margins [2780]



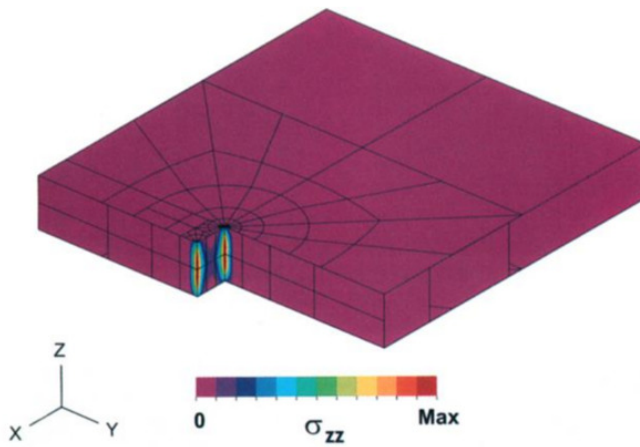
1992: Temperature field in subduction zones [641]



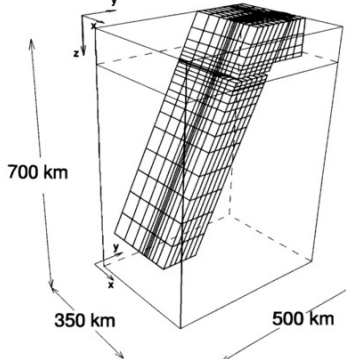
1993: 3D numerical modeling of compressional orogenies: Thrust geometry and oblique convergence [272]



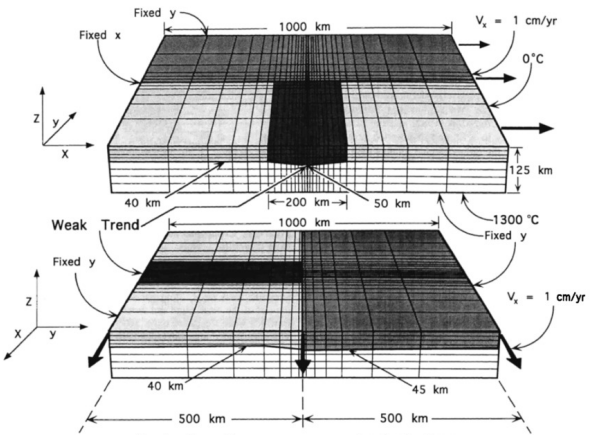
1994: Crustal-scale compressional orogens [129]



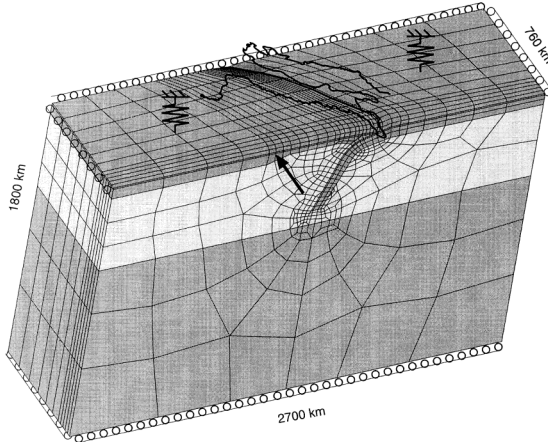
1995: modeling of pull-apart basins [1393]



1995: 3D numerical modeling of detachment of subducted lithosphere [2854]



1996: 3D dynamical model of continental rift propagation and margin plateau formation [731]



1989: Model geometry, boundary conditions and 3-D finite element mesh used in the calculations. The circles denote a free-slip condition. The arrow denotes the velocity applied in some calculations to the southern boundary of the Tyrrhenian domain to simulate the motion of the African plate. The springs represent the buoyant restoring force applied at the surface. [1926]

## 1.10 Notations

Scalars such as temperature, density, pressure, etc ... are simply obtained in L<sup>A</sup>T<sub>E</sub>X by using the math mode, e.g.  $T$ ,  $\rho$ ,  $p$ . Although it is common to lump vectors and matrices/tensors together by using bold fonts, I have decided in the interest of clarity to distinguish between those: vectors are denoted by an arrow atop the quantity, e.g.  $\vec{v}$ ,  $\vec{g}$ , while matrices and tensors are in bold  $M$ ,  $\sigma$ , etc ...

Also I use the  $\cdot$  notation between two vectors to denote a dot product  $\vec{u} \cdot \vec{v} = u_i v_i$  or a matrix-vector multiplication  $M \cdot \vec{a} = M_{ij} a_j$ . If there is no  $\cdot$  between vectors, it means that the result  $\vec{a}\vec{b} = a_i b_j$  is a matrix (it is a dyadic product<sup>4</sup>). Case in point,  $\vec{\nabla} \cdot \vec{v}$  is the velocity divergence while  $\vec{\nabla} \vec{v}$  is the velocity gradient tensor.

## 1.11 Colour maps for visualisation

In an attempt to homogenise the figures obtained with ParaView, I have decided to use a fixed colour scale for each field throughout this document. These colour scales were obtained from <https://peterkovesi.com/projects/colourmaps> and are Perceptually Uniform Colour Maps [1500].

Field	colour code
Velocity/displacement	CET-D1A
Pressure	CET-L17
Velocity divergence	CET-L1
Density	CET-D3
Strain rate	CET-R2
Viscosity	CET-R3
Temperature	CET-D9

## 1.12 How my bibliography works

There is a single (large) bibliography file for this document:

<sup>4</sup><https://en.wikipedia.org/wiki/Dyadics>

**biblio\_geosciences.bib**

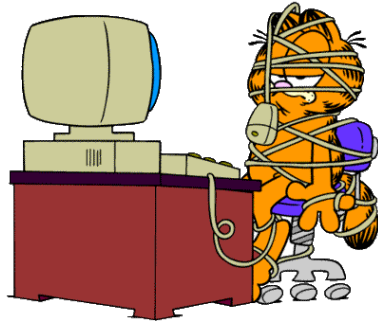
If the paper is a single-author paper, say by Garfield<sup>5</sup>, published in 1978<sup>6</sup>, its code in my bibliography file is *garf78* (i.e. the first four letters of the name, followed by the two digits of the publication year).

If the paper was written by two authors, say Garfield and Odie, in 1987, its code will be *gaod87*, i.e. the first two letters of the first author followed by the two first letters of the second author followed by two digits.

If the paper was written by three or more authors, say Garfield, Odie, John and Irene in 2003, its code will be *gaoj03*, i.e. the first two letters of the first author followed by the first letter of the second author, the first letter of the third author and the year.

If multiple papers are published the same year by the same authors, I simply append a,b,c... to the above rules.

**Remark.** Dutch names such as '*van Hunen*' or '*van den Berg*' are classified under letter '*v*', not '*h*' or '*d*' nor '*b*'.



---

<sup>5</sup>This is just an example

<sup>6</sup>May be not, after all, since Garfield the cat was born in 1978

## 2 List of stones

### 2.1 Velocity based stones

feature	1	2	3	4	5	6	7	8
geometry	Box	Box	Box	Box	Box	Box	Box	
element type	$Q_1 \times P_0$	$Q_1 \times P_0$	$Q_1 \times P_0$	$Q_1 \times P_0$	$Q_1 \times P_0$	$Q_1 \times P_0$	$Q_1 \times P_0$	$Q_1 \times P_0$
mixed or penalty	penalty	penalty	penalty	penalty	penalty	penalty	penalty	
matrix storage	full	full	full	full	full	full	full	
outer solver	N.A.	N.A.	N.A.	N.A.	N.A.	N.A.	N.A.	
3 dimensions	.	.	.	.	.	.	.	.
compressible (Y/N)	.	.	.	.	.	.	.	.
analytical benchmark (Y/N)	Y	.	.	.	Y	Y	Y	Y
numerical benchmark (Y/N)	.	.	Y	.	.	.	.	.
error convergence (Y/N)	.	.	.	Y	.	.	.	.
thermo-mechanically coupled (Y/N)	.	.	.	Y	.	.	.	.
time-stepping (Y/N)	.	.	Y	.	.	.	.	.
external mesher (Y/N)	.	.	.	.	.	.	.	.
non-linear (Y/N)	.	.	.	.	.	.	.	Y
plasticity (Y/N)	.	.	.	.	.	.	.	Y
Buoyancy driven flow	.	.	Y	Y	.	.	.	.
Vrms	.	.	Y	.	.	.	.	.
Nusselt nb	.	.	Y	.	.	.	.	.
Pressure norm.	.	.	.	.	.	.	.	.
Pressure smoothing	.	.	.	Y	.	.	Y	Y
Computing residual(s)	.	.	.	.	.	.	.	.
Paraview output	.	.	Y	Y	.	.	.	.
Add. feature	.	.	.	.	.	.	.	.
Description	"Donea & Huerta" mms 8.6.1	Stokes sphere	"Blankenbach" benchmark	Lid driven cavity	SolCx	SolKz	SolVi	Indentor
Status	better matplotlib interface?	OK	OK	OK	OK	OK	OK	OK

21

feature	9	10	11	12	13	14	15	16
geometry	Annulus	Box	Box	Box				
element type	$Q_1 \times P_0$	$Q_1 \times P_0$	$Q_1 \times P_0$	$Q_1 \times P_0$				
mixed or penalty	penalty	penalty	penalty	penalty				
matrix storage	'lil'	'lil'	mixed					
outer solver (N.A., direct, SchurComp)	N.A.	N.A.	full					
3 dimensions	.	Y	Y	.				
compressible (Y/N)	.	.	.	.				
analytical benchmark (Y/N)	Y	.	.	Y				
numerical benchmark (Y/N)	.	.	.	.				
error convergence (Y/N)	Y	.	.	Y				
thermo-mechanically coupled (Y/N)	.	.	.	.				
time-stepping (Y/N)	.	.	.	.				
external mesher (Y/N)	.	.	.	.				
non-linear (Y/N)	.	.	.	.				
plasticity (Y/N)	.	.	.	.				
Buoyancy driven flow	.	Y	Y	.				
Vrms	.	.	.	.				
Nusselt nb	.	.	.	.				
Pressure norm.	.	.	Y	.				
Pressure smoothing	.	.	.	.				
Computing residual(s)	.	.	.	.				
Paraview output	Y	Y	Y	.				
Add. feature	.	.	Lagrange multiplier	Consistent press. recovery				
Description	Annulus bench- mark	3D Stokes sphere	3D Stokes sphere	"Donea & Huerta" mms 8.6.1				
Status	OK	OK	OK	OK				

feature	17	18	19	20	21	22	23	24
geometry	Box			Box	?	Box		
element type	$Q_2 \times Q_1$			$Q_1 \times P_0 - Q_1$	?	$Q_1 \times Q_1\text{-stab}$		
mixed or penalty	mixed			mixed				
matrix storage	full			lil				
outer solver (N.A., direct, SchurComp)	N.A.			N.A.				
3 dimensions	Y			Y				
compressible (Y/N)	N			.				
analytical benchmark (Y/N)	Y			Y				
numerical benchmark (Y/N)	.			Y				
error convergence (Y/N)	Y			.				
thermo-mechanically coupled (Y/N)	.			Y				
time-stepping (Y/N)	.			Y				
external mesher (Y/N)	.			.				
non-linear (Y/N)	.			.				
plasticity (Y/N)	.			.				
Buoyancy driven flow	.			Y				
Vrms	.			Y				
Nusselt nb	.			Y				
Pressure norm.	Y			.				
Pressure smoothing	.			.				
Computing residual(s)	.			Y				
Paraview output	Y			.				
Add. feature								
Description	Burstedde benchmark 8.6.3			Busse				
Status	OK			?				

feature	25	26	27	28	29	30	31	32
geometry	Box							
element type	$Q_1 \times P_0 \& Q_2 \times Q_1$							
mixed or penalty	mixed							
matrix storage	full							
outer solver (N.A., direct, SchurComp)	N.A.							
3 dimensions	.							
compressible (Y/N)	.							
analytical benchmark (Y/N)	.							
numerical benchmark (Y/N)	Y							
error convergence (Y/N)	.							
thermo-mech. coupled (Y/N)	.							
time-stepping (Y/N)	.							
external mesher (Y/N)	.							
non-linear (Y/N)	.							
plasticity (Y/N)	.							
Buoyancy driven flow	Y							
Vrms	Y							
Nusselt nb	.							
Pressure norm.	Y							
Pressure smoothing	Y							
Computing residual(s)	.							
Paraview output	Y							
Add. feature	Boundary fitted mesh							
Description	T-R instability [2659]							
Status	OK							

feature	33				
geometry	Annulus				
element type	$Q_1 \times P_0$ mixed or penalty	penalty			
matrix storage					
outer solver (N.A., direct, SchurComp)					
3 dimensions	.				
compressible (Y/N)	.				
analytical benchmark (Y/N)	.				
numerical benchmark (Y/N)	.				
error convergence (Y/N)	.				
thermo-mech. coupled (Y/N)	Y				
time-stepping (Y/N)	Y				
external meshers (Y/N)	.				
non-linear (Y/N)	Y				
plasticity (Y/N)	.				
Buoyancy driven flow	Y				
Vrms	Y				
Nusselt nb	Y				
Pressure norm.	.				
Pressure smoothing	Y				
Computing residual(s)	Y				
Paraview output	Y				
Add. feature					
Description	Convection in annulus				
Status					

## 2.2 Displacement based stones

### 2.3 Stream function based stones

## 2.4 Other stones

stone number	element	outer solver	formulation	physical problem	3D	temperature	time stepping	nonlinear	compressible	analytical benchmark	numerical benchmark	elastomechanics
12	$Q_1 \times P_0$		penalty	analytical benchmark + consistent press recovery								
13	$Q_1 \times P_0$		penalty	Stokes sphere + markers averaging								
14	$Q_1 \times P_0$	full matrix	mixed	analytical benchmark								
15	$Q_1 \times P_0$	Schur comp. CG	mixed	analytical benchmark								
16	$Q_1 \times P_0$	Schur comp. PCG	mixed	Stokes sphere								
17	$Q_2 \times Q_1$	full matrix	mixed	Burstedde benchmark	†							
18	$Q_2 \times Q_1$	full matrix	mixed	analytical benchmark								
19	$Q_3 \times Q_2$	full matrix	mixed	analytical benchmark								
20	$Q_1 \times P_0$		penalty	Busse et al., 1993	†	†	†					
21	$Q_1 \times P_0$ R-T		penalty	analytical benchmark								
22	$Q_1 \times Q_1$ -stab	full matrix	mixed	analytical benchmark								
23	$Q_1 \times P_0$		mixed	analytical benchmark				†				
24	$Q_1 \times P_0$		mixed	convection box	†	†	†	†				

stone number	element	outer solver	formulation	physical problem	3D	temperature	time stepping	nonlinear	compressible	analytical benchmark	numerical benchmark	elastomechanics
25	$Q_1 \times P_0$	full matrix	mixed	Rayleigh-Taylor instability								
26	$Q_1 \times P_0$	full matrix	mixed	Slab detachment				†				
27	$Q_1 \times P_0$	full matrix	mixed	CBF benchmarks				†		†		
28	$Q_1 \times P_0$	full matrix	mixed	Tosi et al, 2015		†	†	†			†	
29	$Q_1 \times P_0$	full matrix	mixed	Open Boundary conditions						†		
30	$Q_1, Q_2$	X	X	Cons. Vel. Interp (cv1)			†			†		
31	$Q_1, Q_2$	X	X	Cons. Vel. Interp (cv1)	†	†				†		
32	$Q_1 \times P_0$	full matrix	mixed	analytical benchmark						†		
33	$Q_1 \times P_0$		penalty	convection in annulus		†	†	†				
34	$Q_1$			elastic Cartesian aquarium					†	†	†	
35												
36	$Q_1$			elastic annulus aquarium				†	†		†	
37	$Q_1, Q_2$	X	X	population control, bmw test	†					†		
38				Critical Rayleigh number								
39	$Q_2 \times Q_1$	full matrix	mixed									
40				Inst. Rayleigh-Taylor instability								
41												
42				1D diffusion								
43				Rotating cone								
44	$P_2^+ \times P_{-1}$		mixed	flat slab Melanie								
45	$P_2^-$			Slab temp corner [2655]								
46	$P_2^+ \times P_{-1}$			analytical benchmark MMS1								
47												
48												
49												
50												
51												
52												
53												
XX												

Analytical benchmark means that an analytical solution exists while numerical benchmark means that a comparison with other code(s) has been carried out.

### 3 The physical equations

Symbol	meaning	unit
$t$	Time	s
$x, y, z$	Cartesian coordinates	m
$r, \theta$	Polar coordinates	m,-
$r, \theta, z$	Cylindrical coordinates	m,-,m
$r, \theta, \phi$	Spherical coordinates	m,-,-
$\vec{v} = (u, v, w)$	velocity vector	$\text{m} \cdot \text{s}^{-1}$
$\vec{u}$	displacement vector	m
$\rho$	mass density	$\text{kg}/\text{m}^3$
$\eta$	dynamic viscosity	$\text{Pa} \cdot \text{s}$
$\lambda$	penalty parameter	$\text{Pa} \cdot \text{s}$
$T$	temperature	K
$\vec{\nabla}$	gradient operator	$\text{m}^{-1}$
$\vec{\nabla} \cdot$	divergence operator	$\text{m}^{-1}$
$p$	pressure	Pa
$\dot{\varepsilon}(\vec{v})$	strain rate tensor	$\text{s}^{-1}$
$\alpha$	thermal expansion coefficient	$\text{K}^{-1}$
$k$	thermal conductivity	$\text{W}/(\text{m} \cdot \text{K})$
$C_p$	Heat capacity	J/K
$H$	intrinsic specific heat production	$\text{W}/\text{kg}$
$\beta_T$	isothermal compressibility	$\text{Pa}^{-1}$
$\tau$	deviatoric stress tensor	Pa
$\sigma$	full stress tensor	Pa

#### 3.1 Coordinate systems

##### 3.1.1 Cartesian coordinates

The unit vectors along the  $x$ ,  $y$  and  $z$  axis are  $\vec{e}_x$ ,  $\vec{e}_y$  and  $\vec{e}_z$  respectively.

##### 3.1.2 Cylindrical coordinates

We have  $r > 0$  and  $\theta = [0, 2\pi[$ , defined in the  $(x, y)$ -plane.

The relation between the unit vector in Cartesian and Polar/Cylindrical coordinates is given by:

$$\begin{pmatrix} \vec{e}_r \\ \vec{e}_\theta \end{pmatrix} = \begin{pmatrix} \cos \theta & \sin \theta \\ -\sin \theta & \cos \theta \end{pmatrix} \cdot \begin{pmatrix} \vec{e}_x \\ \vec{e}_y \end{pmatrix}$$

which yields

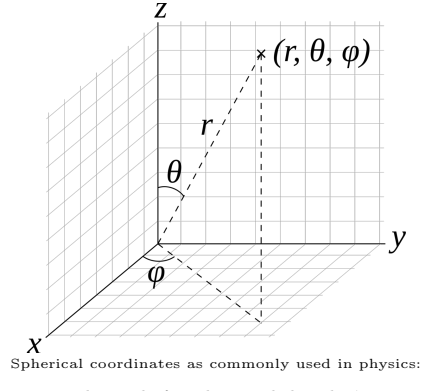
$$\begin{pmatrix} \vec{e}_x \\ \vec{e}_y \end{pmatrix} = \begin{pmatrix} \cos \theta & -\sin \theta \\ \sin \theta & \cos \theta \end{pmatrix} \cdot \begin{pmatrix} \vec{e}_r \\ \vec{e}_\theta \end{pmatrix}$$

so that for any vector  $\vec{V}$

$$\begin{aligned} \vec{V} &= V_x \vec{e}_x + V_y \vec{e}_y \\ &= V_x[(\cos \theta) \vec{e}_r - (\sin \theta) \vec{e}_\theta] + V_y[(\sin \theta) \vec{e}_r + (\cos \theta) \vec{e}_\theta] \\ &= [V_x(\cos \theta) + V_y(\sin \theta)] \vec{e}_r + [-V_x(\sin \theta) + V_y(\cos \theta)] \vec{e}_\theta \end{aligned} \tag{1}$$

##### 3.1.3 Spherical coordinates

On the following figure are represented the three cartesian axis, a point and its spherical coordinates  $r, \theta, \phi$ :



In this case  $\theta \in [0 : \pi]$  and  $\phi \in ] -\pi : \pi ]$  and we have the following relationships:

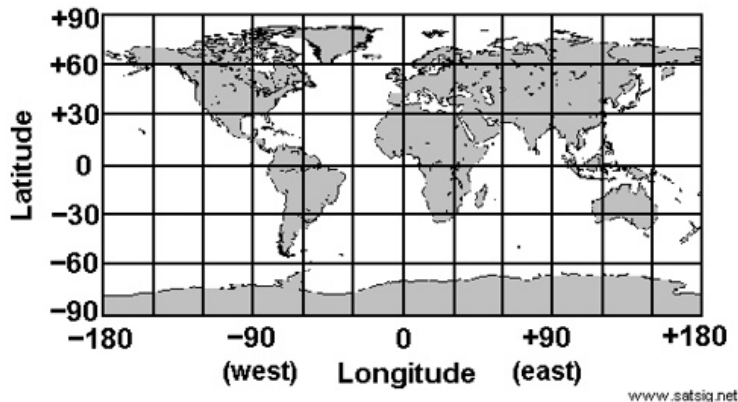
$$r = \sqrt{x^2 + y^2 + z^2} \quad (2)$$

$$\theta = \arccos(z/r) \quad (3)$$

$$\phi = \arctan(y/x) \quad (4)$$

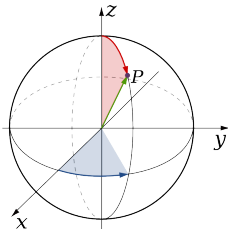
The inverse tangent used to compute  $\phi$  must be suitably defined, taking into account the correct quadrant of  $(x, y)$ , which is why the atan2 intrinsic function is used in fortran for example.

In geography one uses latitude and longitude, represented hereunder:



- Latitude  $\in [-90 : 90]$ , or  $\in [-\pi/2 : \pi/2]$
- Longitude  $\in ] -180 : 180 ]$ , or  $\in ] -\pi : \pi ]$

Since the colatitude is the complementary angle of the latitude, i.e. the difference between 90 and the latitude, where southern latitudes are denoted with a minus sign,  $\theta$  as shown above is actually the colatitude. The co-latitude is shown in red on the following figure:



The volume of a sphere of radius  $R$  is easily obtained by computing

$$\begin{aligned}
V &= \int dV \\
&= \int_0^R r^2 dr \int_0^\pi \sin \theta d\theta \int_0^{2\pi} d\phi \\
&= \frac{1}{3} R^3 \cdot 2 \cdot 2\pi \\
&= \frac{4}{3}\pi R^3
\end{aligned} \tag{5}$$

The spherical unit vectors are related to the cartesian unit vectors by:

$$\begin{pmatrix} \vec{e}_r \\ \vec{e}_\theta \\ \vec{e}_\phi \end{pmatrix} = \begin{pmatrix} \sin \theta \cos \phi & \sin \theta \sin \phi & \cos \theta \\ \cos \theta \cos \phi & \cos \theta \sin \phi & -\sin \theta \\ -\sin \phi & \cos \phi & 0 \end{pmatrix} \begin{pmatrix} \vec{e}_x \\ \vec{e}_y \\ \vec{e}_z \end{pmatrix}$$

and the cartesian unit vectors are related to the spherical unit vectors by

$$\begin{pmatrix} \vec{e}_x \\ \vec{e}_y \\ \vec{e}_z \end{pmatrix} = \begin{pmatrix} \sin \theta \cos \phi & \cos \theta \cos \phi & -\sin \phi \\ \sin \theta \sin \phi & \cos \theta \sin \phi & \cos \phi \\ \cos \theta & -\sin \theta & 0 \end{pmatrix} \begin{pmatrix} \vec{e}_r \\ \vec{e}_\theta \\ \vec{e}_\phi \end{pmatrix}$$

$$\vec{v} = u\vec{e}_x + v\vec{e}_y + w\vec{e}_z \tag{6}$$

$$= u(\sin \theta \cos \phi \vec{e}_r + \cos \theta \cos \phi \vec{e}_\theta - \sin \phi \vec{e}_\phi) \tag{7}$$

$$+ v(\sin \theta \sin \phi \vec{e}_r + \cos \theta \sin \phi \vec{e}_\theta + \cos \phi \vec{e}_\phi) \tag{8}$$

$$+ w(\cos \theta \vec{e}_r - \sin \theta \vec{e}_\theta) \tag{9}$$

$$= v_r \vec{e}_r + v_\theta \vec{e}_\theta + v_\phi \vec{e}_\phi \tag{10}$$

with

$$v_r = u \sin \theta \cos \phi + v \sin \theta \sin \phi + w \cos \theta \tag{11}$$

$$v_\theta = u \cos \theta \cos \phi + v \cos \theta \sin \phi - w \sin \theta \tag{12}$$

$$v_\phi = -u \sin \phi + v \cos \phi \tag{13}$$

## 3.2 A continuum mechanics primer

*Contains contributions by W. Spakman*

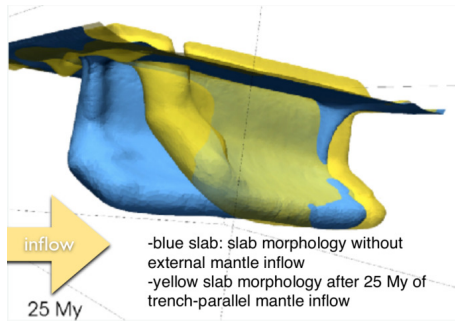
### 3.2.1 Forces

In continuum mechanics we make a distinction between two broad classes of forces:

- Body forces defined as force per unit volume ( $\text{N}/\text{m}^3$ ): gravity, electro-magnetic forces
- Tractions: Surface forces defined as force per unit surface area ( $\text{N}/\text{m}^2$ ): Contact forces, elastic forces per unit area, internal flow friction, pressure, ...

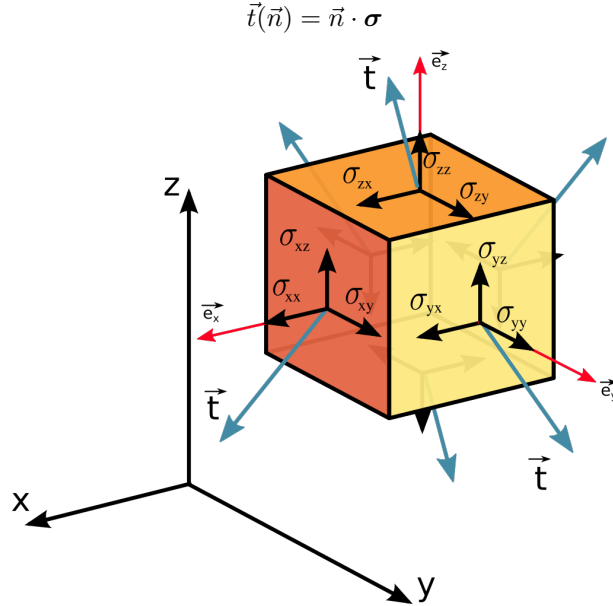
A traction is the surface average of all atomic forces exerted by atoms on the one side on atoms on the other side of the surface. For real-Earth processes, internal tractions are ultimately caused by the body forces, usually gravity.

Existing mantle flow(i.e. flow that is forced elsewhere) can exert tractions (shear stresses) on the subducting slab or for instance at the base of lithosphere plates. In HPT-laboratory experiments external tractions (pressure, shear traction) are applied to a rock sample, which cause internal tractions to balance the exerted forces.



### 3.2.2 Stress tensor and tractions

The Cauchy tensor<sup>7</sup> consists of nine components  $\sigma_{ij}$  that completely define the state of stress at a point inside a material. The tensor relates a unit-length direction vector  $\vec{n}$  to the so-called 'stress vector' (most commonly called 'traction')  $\vec{t}(\vec{n})$  across an imaginary surface perpendicular to  $\vec{n}$ :



Modified from original file on Wikipedia<sup>8</sup>

With respect to an orthonormal basis  $\{\vec{e}_x, \vec{e}_y, \vec{e}_z\}$ , the Cauchy stress tensor is given by:

$$\boldsymbol{\sigma} = \begin{pmatrix} \sigma_{xx} & \sigma_{xy} & \sigma_{xz} \\ \sigma_{yx} & \sigma_{yy} & \sigma_{yz} \\ \sigma_{zx} & \sigma_{zy} & \sigma_{zz} \end{pmatrix} \quad (14)$$

The three diagonal elements are called normal stresses while the off-diagonal terms are called shear stresses.

One can easily prove (see for instance Section 3.3.6 of [1067]) that the balance of angular momentum leads reduces to the statement that the Cauchy stress tensor is symmetric, i.e.  $\boldsymbol{\sigma} = \boldsymbol{\sigma}^T$ . Therefore, the stress state of the medium at any point and instant can be specified by only six independent parameters, rather than nine:

$$\boldsymbol{\sigma} = \begin{pmatrix} \sigma_{xx} & \sigma_{xy} & \sigma_{xz} \\ \sigma_{xy} & \sigma_{yy} & \sigma_{yz} \\ \sigma_{xz} & \sigma_{yz} & \sigma_{zz} \end{pmatrix} \quad \text{or sometimes} \quad \boldsymbol{\sigma} = \begin{pmatrix} \sigma_x & \tau_{xy} & \tau_{xz} \\ \tau_{xy} & \sigma_y & \tau_{yz} \\ \tau_{xz} & \tau_{yz} & \sigma_z \end{pmatrix} \quad (15)$$

where the elements  $\sigma_x, \sigma_y, \sigma_z$  are called the orthogonal normal stresses (relative to the chosen coordinate system), and  $\tau_{xy}, \tau_{xz}, \tau_{yz}$  the orthogonal shear stresses.

As seen above, the SI units of both stress tensor and traction are N/m<sup>2</sup>.

<sup>7</sup>[https://en.wikipedia.org/wiki/Cauchy\\_stress\\_tensor](https://en.wikipedia.org/wiki/Cauchy_stress_tensor)

<sup>8</sup>[https://commons.wikimedia.org/wiki/File:Components\\_stress\\_tensor\\_cartesian.svg](https://commons.wikimedia.org/wiki/File:Components_stress_tensor_cartesian.svg)

### 3.2.3 Strain rate and spin tensor

The velocity gradient is given in Cartesian coordinates by:

$$\vec{\nabla}\vec{v} = \begin{pmatrix} \frac{\partial u}{\partial x} & \frac{\partial v}{\partial x} & \frac{\partial w}{\partial x} \\ \frac{\partial u}{\partial y} & \frac{\partial v}{\partial y} & \frac{\partial w}{\partial y} \\ \frac{\partial u}{\partial z} & \frac{\partial v}{\partial z} & \frac{\partial w}{\partial z} \end{pmatrix} \quad (16)$$

It can be decomposed into its symmetric and skew-symmetric parts according to:

$$\vec{\nabla}\vec{v} = \vec{\nabla}^s\vec{v} + \vec{\nabla}^w\vec{v} = \dot{\epsilon}(\vec{v}) + \dot{\omega}(\vec{v}) \quad (17)$$

The symmetric part is called the strain rate (or rate of deformation):

$$\dot{\epsilon}(\vec{v}) = \frac{1}{2} \left( \vec{\nabla}\vec{v} + (\vec{\nabla}\vec{v})^T \right) \quad (18)$$

The skew-symmetric tensor is called spin tensor (or vorticity tensor):

$$\dot{\omega}(\vec{v}) = \frac{1}{2} \left( \vec{\nabla}\vec{v} - (\vec{\nabla}\vec{v})^T \right) \quad (19)$$

**Remark.** In the mathematical literature a different notation for the strain rate tensor is often used, i.e.  $D(\vec{v})$ , such as for instance in Fullsack (1995) [901].

## 3.3 Viscous Newtonian rheology

The relationship between velocity-related stresses and velocity derivatives is such that the total stress tensor has the form [163]

$$\boldsymbol{\sigma} = -p\mathbf{1} + \mathbf{A} : \dot{\epsilon} \quad (20)$$

where  $p$  is the thermodynamic pressure which is a function of the density  $\rho$  and the temperature  $T$  (an equation of state is then needed) and  $\mathbf{A}$  is the fourth-rank stiffness tensor.

Since both the stress and the strain tensors are symmetric and for isotropic fluids we have [1699]

$$\mathbf{A} : \dot{\epsilon} = \lambda(\vec{\nabla} \cdot \vec{v})\mathbf{1} + 2\eta\dot{\epsilon} \quad (21)$$

where  $\lambda$  is the bulk viscosity and  $\eta$  is the dynamic viscosity<sup>9</sup>. The stress tensor is then

$$\boldsymbol{\sigma} = (-p + \lambda(\vec{\nabla} \cdot \vec{v}))\mathbf{1} + 2\eta\dot{\epsilon} \quad (22)$$

By writing

$$\dot{\epsilon} = \frac{1}{3}\text{tr}(\dot{\epsilon})\mathbf{1} + \dot{\epsilon}^d = \frac{1}{3}(\vec{\nabla} \cdot \vec{v})\mathbf{1} + \dot{\epsilon}^d$$

where  $\dot{\epsilon}^d$  is the deviatoric strain rate tensor and (in Cartesian coordinates)

$$\vec{\nabla} \cdot \vec{v} = \text{div}(\vec{v}) = \text{tr}(\dot{\epsilon}) = \frac{\partial u}{\partial x} + \frac{\partial v}{\partial y} + \frac{\partial w}{\partial z} \quad (23)$$

where  $\text{tr}$  is the trace operator, we arrive at

$$\boldsymbol{\sigma} = (-p + \lambda(\vec{\nabla} \cdot \vec{v}))\mathbf{1} + 2\eta \left[ \frac{1}{3}(\vec{\nabla} \cdot \vec{v})\mathbf{1} + \dot{\epsilon}^d \right] \quad (24)$$

$$= \left[ -p + \left( \lambda + \frac{2}{3}\eta \right) (\vec{\nabla} \cdot \vec{v}) \right] \mathbf{1} + 2\eta\dot{\epsilon}^d \quad (25)$$

---

<sup>9</sup>also sometimes called shear viscosity

Introducing the second viscosity  $\zeta = \lambda + \frac{2}{3}\eta$ :

$$\boldsymbol{\sigma} = [-p + \zeta(\vec{\nabla} \cdot \vec{v})] \mathbf{1} + 2\eta\dot{\epsilon}^d \quad (26)$$

$$= -\bar{p}\mathbf{1} + 2\eta\dot{\epsilon}^d \quad (27)$$

The effect of the volume viscosity  $\zeta$  is that the mechanical pressure  $\bar{p}$  is not equivalent to the thermodynamic pressure  $p$

$$\bar{p} = p - \zeta(\vec{\nabla} \cdot \vec{v}) \quad (28)$$

In other words: the isotropic average of the total stress is *not* the pressure term! This difference is usually neglected (and it is safe to do so, see [163, section 7.02.3.2.2]) by explicitly assuming  $\zeta = 0$  (also called the Stokes assumption [2293, p256]), so that one can then refer to pressure as a single well-defined value. Note that in the case of an incompressible Newtonian Fluid, the strain rate tensor is deviatoric ( $\text{tr}(\dot{\epsilon}) = \text{div}(\vec{v}) = 0$ ) and the above considerations vanish.

Finally, for both compressible and incompressible flow, the stress tensor becomes simply

$$\boldsymbol{\sigma} = -p\mathbf{1} + 2\eta\dot{\epsilon}^d = -p\mathbf{1} + \boldsymbol{\tau} \quad (29)$$

where  $\boldsymbol{\tau} = 2\eta\dot{\epsilon}^d$  is the deviatoric stress tensor.

**Remark.** On page 256 of Schubert, Turcotte and Olson [2293], equation 6.5.3, the authors write  $\tau_{ii}/3 = k_B e_{ii}$  while stating that  $\boldsymbol{\tau}$  is deviatoric in equation 6.4.2. This is an obvious conflict of notations.

### 3.4 The heat transport equation - energy conservation equation

Let us start from the heat transport equation as shown in Schubert, Turcotte and Olson [2293]:

$$\rho C_p \frac{DT}{Dt} - \alpha T \frac{Dp}{Dt} = \vec{\nabla} \cdot k \vec{\nabla} T + \Phi + \rho H \quad (30)$$

with  $D/Dt$  being the total derivatives, i.e.

$$\frac{DT}{Dt} = \frac{\partial T}{\partial t} + \vec{v} \cdot \vec{\nabla} T \quad \text{and} \quad \frac{Dp}{Dt} = \frac{\partial p}{\partial t} + \vec{v} \cdot \vec{\nabla} p \quad (31)$$

Solving for temperature, this equation is often rewritten as follows:

$$\rho C_p \frac{DT}{Dt} - \vec{\nabla} \cdot k \vec{\nabla} T = \alpha T \frac{Dp}{Dt} + \Phi + \rho H \quad (32)$$

where  $\Phi$  is the shear heating [2118, p287]. In many publications,  $\Phi$  is given by  $\Phi = \tau_{ij} \partial_j v_i = \boldsymbol{\tau} : \vec{\nabla} \vec{v}$ .

In what follows I use the index notation as it makes for easier derivations:

$$\begin{aligned} \Phi &= \tau_{ij} \partial_j v_i \\ &= 2\eta \dot{\epsilon}_{ij}^d \partial_j v_i \\ &= 2\eta \frac{1}{2} (\dot{\epsilon}_{ij}^d \partial_j v_i + \dot{\epsilon}_{ji}^d \partial_i v_j) \\ &= 2\eta \frac{1}{2} (\dot{\epsilon}_{ij}^d \partial_j v_i + \dot{\epsilon}_{ij}^d \partial_i v_j) \\ &= 2\eta \dot{\epsilon}_{ij}^d \frac{1}{2} (\partial_j v_i + \partial_i v_j) \\ &= 2\eta \dot{\epsilon}_{ij}^d \dot{\epsilon}_{ij} \\ &= 2\eta \dot{\epsilon}^d : \dot{\epsilon} \\ &= 2\eta \dot{\epsilon}^d : \left( \dot{\epsilon}^d + \frac{1}{3} (\vec{\nabla} \cdot \vec{v}) \mathbf{1} \right) \\ &= 2\eta \dot{\epsilon}^d : \dot{\epsilon}^d + 2\eta \dot{\epsilon}^d : \mathbf{1} (\vec{\nabla} \cdot \vec{v}) \\ &= 2\eta \dot{\epsilon}^d : \dot{\epsilon}^d \end{aligned} \quad (33)$$

Finally

$$\Phi = \boldsymbol{\tau} : \vec{\nabla} \vec{v} = 2\eta \dot{\epsilon}^d : \dot{\epsilon}^d = 2\eta ((\dot{\epsilon}_{xx}^d)^2 + (\dot{\epsilon}_{yy}^d)^2 + 2(\dot{\epsilon}_{xy}^d)^2) \quad (34)$$

### 3.5 The momentum conservation equations

Because the Prandlt number is virtually zero in Earth science applications the Navier Stokes equations reduce to the Stokes equation:

$$\vec{\nabla} \cdot \boldsymbol{\sigma} + \rho \vec{g} = \vec{0} \quad (35)$$

Since

$$\boldsymbol{\sigma} = -p\mathbf{1} + \boldsymbol{\tau} \quad (36)$$

it also writes

$$-\vec{\nabla}p + \vec{\nabla} \cdot \boldsymbol{\tau} + \rho \vec{g} = \vec{0} \quad (37)$$

Using the relationship  $\boldsymbol{\tau} = 2\eta \dot{\boldsymbol{\varepsilon}}^d$  we arrive at

$$-\vec{\nabla}p + \vec{\nabla} \cdot (2\eta \dot{\boldsymbol{\varepsilon}}^d) + \rho \vec{g} = \vec{0} \quad (38)$$

### 3.6 The mass conservation equations

The mass conservation equation is given by

$$\frac{D\rho}{Dt} + \rho \vec{\nabla} \cdot \vec{v} = 0$$

or, since

$$\frac{D\rho}{Dt} = \frac{\partial \rho}{\partial t} + \vec{v} \cdot \vec{\nabla} \rho$$

then

$$\frac{D\rho}{Dt} + \rho \vec{\nabla} \cdot \vec{v} = \frac{\partial \rho}{\partial t} + \vec{v} \cdot \vec{\nabla} \rho + \rho \vec{\nabla} \cdot \vec{v} = 0$$

and finally:

$$\frac{\partial \rho}{\partial t} + \vec{\nabla} \cdot (\rho \vec{v}) = 0$$

In the case of an incompressible flow, then  $\partial \rho / \partial t = 0$  and  $\vec{\nabla} \rho = 0$ , i.e.  $D\rho/Dt = 0$  and the remaining equation is simply:

$$\vec{\nabla} \cdot \vec{v} = 0$$

A vector field that is divergence-free is also called solenoidal<sup>10</sup>.

### 3.7 The equations in ASPECT manual

The following is lifted off the ASPECT manual. We focus on the system of equations in a  $d = 2$ - or  $d = 3$ -dimensional domain  $\Omega$  that describes the motion of a highly viscous fluid driven by differences in the gravitational force due to a density that depends on the temperature. In the following, we largely follow the exposition of this material in Schubert, Turcotte and Olson [2293].

Specifically, we consider the following set of equations for velocity  $\mathbf{u}$ , pressure  $p$  and temperature  $T$ :

$$-\vec{\nabla} \cdot \left[ 2\eta \left( \dot{\boldsymbol{\varepsilon}}(\vec{v}) - \frac{1}{3}(\vec{\nabla} \cdot \vec{v})\mathbf{1} \right) \right] + \vec{\nabla}p = \rho \vec{g} \quad \text{in } \Omega, \quad (39)$$

$$\vec{\nabla} \cdot (\rho \vec{v}) = 0 \quad \text{in } \Omega, \quad (40)$$

$$\begin{aligned} \rho C_p \left( \frac{\partial T}{\partial t} + \vec{v} \cdot \vec{\nabla} T \right) - \vec{\nabla} \cdot k \vec{\nabla} T &= \rho H \\ &+ 2\eta \left( \dot{\boldsymbol{\varepsilon}}(\mathbf{v}) - \frac{1}{3}(\vec{\nabla} \cdot \vec{v})\mathbf{1} \right) : \left( \dot{\boldsymbol{\varepsilon}}(\mathbf{v}) - \frac{1}{3}(\vec{\nabla} \cdot \vec{v})\mathbf{1} \right) \\ &+ \alpha T (\mathbf{v} \cdot \vec{\nabla} p) \end{aligned} \quad (41)$$

in  $\Omega$ ,

---

<sup>10</sup>[https://en.wikipedia.org/wiki/Solenoidal\\_vector\\_field](https://en.wikipedia.org/wiki/Solenoidal_vector_field)

where  $\dot{\epsilon}(\vec{v}) = \frac{1}{2}(\vec{\nabla}\vec{v} + \vec{\nabla}\vec{v}^T)$  is the symmetric gradient of the velocity (often called the *strain rate*).

In this set of equations, (69) and (70) represent the compressible Stokes equations in which  $\mathbf{v} = \mathbf{v}(\mathbf{x}, t)$  is the velocity field and  $p = p(\mathbf{x}, t)$  the pressure field. Both fields depend on space  $\mathbf{x}$  and time  $t$ . Fluid flow is driven by the gravity force that acts on the fluid and that is proportional to both the density of the fluid and the strength of the gravitational pull.

Coupled to this Stokes system is equation (932) for the temperature field  $T = T(\mathbf{x}, t)$  that contains heat conduction terms as well as advection with the flow velocity  $\mathbf{v}$ . The right hand side terms of this equation correspond to

- internal heat production for example due to radioactive decay;
- friction (shear) heating;
- adiabatic compression of material;

In order to arrive at the set of equations that ASPECT solves, we need to

- neglect the  $\partial p / \partial t$
- neglect the  $\partial \rho / \partial t$

from equations above. A partial answer is given in the next section.

Also, their definition of the shear heating term  $\Phi$  is:

$$\Phi = k_B(\nabla \cdot \mathbf{v})^2 + 2\eta\dot{\epsilon}^d : \dot{\epsilon}^d$$

For many fluids the bulk viscosity  $k_B$  is very small and is often taken to be zero, an assumption known as the Stokes assumption:  $k_B = \lambda + 2\eta/3 = 0$ . Note that  $\eta$  is the dynamic viscosity and  $\lambda$  the second viscosity. Also,

$$\boldsymbol{\tau} = 2\eta\dot{\epsilon} + \lambda(\nabla \cdot \mathbf{v})\mathbf{1}$$

but since  $k_B = \lambda + 2\eta/3 = 0$ , then  $\lambda = -2\eta/3$  so

$$\boldsymbol{\tau} = 2\eta\dot{\epsilon} - \frac{2}{3}\eta(\nabla \cdot \mathbf{v})\mathbf{1} = 2\eta\dot{\epsilon}^d$$

### 3.8 Equations for thermal convection in an anelastic, compressible, selfgravitating spherical mantle

What follows is borrowed from Section 2.1 of Glišović et al (2012) [1003]. We start from the conservation mass, momentum and energy equations (the full Navier-Stokes equations):

$$\frac{\partial \rho}{\partial t} + \vec{\nabla} \cdot (\rho \vec{v}) = \vec{0} \quad (42)$$

$$\rho \frac{D\vec{v}}{Dt} = \vec{\nabla} \cdot \boldsymbol{\sigma} \quad (43)$$

$$\rho C_p \frac{DT}{Dt} = \vec{\nabla} \cdot k \vec{\nabla} T + \alpha T \frac{Dp}{Dt} + \Phi + Q \quad (44)$$

In solving for the mantle flow field that satisfies the equation of momentum conservation, we incorporate all effects arising from self-gravitation and we must therefore explicitly consider the 3-D variation of gravity throughout Earths interior. The gravitational acceleration is written as

$$\vec{g} = \vec{\nabla}\phi$$

where  $\phi$  is Earths gravitational potential which satisfies Poisson's equation

$$\Delta\phi = -4\pi G\rho$$

The gravitational potential is expressed as

$$\phi = \phi_0(r) + \phi_1(r, \theta, \phi)$$

where the subscript 0 denotes a hydrostatic reference state, in which the structure of the mantle (density, gravity, pressure, temperature) varies with radius alone and the subscript 1 denotes all 3D perturbations arising from the thermal convection process. This decomposition makes sense in the context of a perfect sphere.

The total perturbed density and pressure fields in the mantle may similarly be expressed as

$$\rho = \rho_0(r) + \rho_1(r, \theta, \phi)$$

$$p = p_0(r) + p_1(r, \theta, \phi)$$

The equation of state relates the density perturbations to the temperature and pressure perturbations as follows

$$\rho_1 = \rho_0[1 - \alpha(T - T_0(r)) + K^{-1}(p - p_0(r))]$$

where  $K$  is the bulk modulus and the term  $T_0(r)$  represents the horizontally averaged temperature (i.e. the geotherm) which varies with radius only. The effects of compressibility on the density are found to be at least two orders of magnitude smaller than the effects of temperature variations. Therefore, the last term of this equation is often neglected.

Important simplifications are made assuming the anelastic-liquid approximation (e.g. [1339] Jarvis & McKenzie (1980) [1339], Solheim & Peltier (1990) [2371]). This approximation is justified because the velocities associated with mantle convection are very slow compared to the local sound speed and hence acoustic waves cannot be generated by the slow changes in the mantle pressure field. We therefore neglect the time derivative of density, thereby eliminating sound waves:

$$\frac{\partial \rho}{\partial t} \simeq 0$$

For the same reason, the pressure distribution may be considered (to first-order accuracy) as the pressure of a fluid in hydrostatic equilibrium which yields

$$\frac{Dp}{Dt} = \frac{\partial p}{\partial t} + \vec{v} \cdot \vec{\nabla} p \simeq -u_r \rho_0(r) g_0(r)$$

The equations are then rewritten in terms of dimensionless variables according to the relations:

$$r' = \frac{r}{d} \quad (45)$$

$$\mathbf{v}' = \frac{\mathbf{v}}{U} \quad (46)$$

$$t' = \frac{U}{d/t} \quad (47)$$

$$T' = \frac{T}{\Delta T} \quad (48)$$

$$\rho' = \frac{\rho}{\rho_{0s}} \quad (49)$$

$$g' = \frac{g}{g_{0s}} \quad (50)$$

$$\phi' = \frac{\phi}{g_{0s}d} \quad (51)$$

$$\alpha' = \frac{\alpha}{\alpha_s} \quad (52)$$

$$p' = \frac{p}{\alpha_s \Delta T \rho_{0s} g_{0s} d} \quad (53)$$

$$\tau_{ij} = \frac{\tau_{ij}}{\alpha_s \Delta T \rho_{0s} g_{0s} d} \quad (54)$$

$$\eta' = \frac{\eta}{\eta_s} \quad (55)$$

$$k' = \frac{k}{k_s} \quad (56)$$

$$Q' = \frac{Qd^2}{k_s \Delta T} \quad (57)$$

$$U = \frac{\rho_{0s} g_{0s} \alpha_s \Delta T d^2}{\eta_s} \quad (58)$$

in which the primes represent the dimensionless variables, the subscript  $s$  means that we consider the surface value of the variable to which it is applied. The length scale  $d$  and temperature scale  $\Delta T$  are respectively the depth of the mantle and the difference of temperature between the bottom and the top of the mantle.

Often one deals with dimensionless variables and the primes are dropped for notational convenience (this is the case in what follows).

It is a tedious but trivial exercise to show that the dimensionless equation of conservation of momentum is then written as follows:

$$\rho \frac{Ra_s}{Pr_s} \frac{D\vec{v}}{Dt} = \frac{\rho}{\alpha_s \Delta T} \vec{\nabla} \phi - \vec{\nabla} p + \vec{\nabla} \cdot \boldsymbol{\tau}$$

in which we introduce the surface Rayleigh  $Ra_s$  and Prandtl  $Pr_s$  numbers defined, respectively, by

$$Ra_s = \frac{\rho_{0s}^2 C_p g_{0s} \alpha_s \Delta T d^3}{k_s \eta_s} \quad Pr_s = \frac{\eta_s C_p}{k_s}$$

Because of the very high viscosity of mantle rocks, the left-hand term is smaller than the other terms by several orders of magnitude and may therefore be neglected. This important simplification is called the infinite Prandtl number approximation.

The equation of energy conservation may also be rewritten in terms of the surface Rayleigh number, as follows

$$\frac{DT}{Dt} = \frac{1}{\rho Ra_s} \left( \vec{\nabla} \cdot k \vec{\nabla} T + Q \right) + \frac{Di}{\rho} \left( -\alpha T \frac{Dp}{Dt} + \Phi \right)$$

where  $Di$  is the dissipation number (see Peltier (1972) [2001]) which measures the importance of compression work and frictional heating, and it is defined as

$$Di = \frac{\alpha_s g_{0s} d}{C_p}$$

$Di$  also measures the ratio of the depth of mantle convection ( $d$ ) to the adiabatic scale height ( $C_p/\alpha g_0$ ) and for whole-mantle convection is close to order 1 (see Jarvis & McKenzie (1980) [1339]).

After simplifications, the dimensionless system of governing equations is written as

$$\vec{\nabla} \cdot (\rho_0 \vec{v}) = 0 \quad (59)$$

$$\frac{\rho}{\alpha_s \Delta T} \vec{\nabla} \phi - \vec{\nabla} p + \vec{\nabla} \cdot \boldsymbol{\tau} = \vec{0} \quad (60)$$

$$\frac{\partial T}{\partial t} + \vec{v} \cdot \vec{\nabla} T = \frac{1}{\rho_0 Ra_s} \left( \vec{\nabla} \cdot k \vec{\nabla} T + Q \right) + \frac{Di}{\rho_0} (-\alpha T \rho_0 g_0 u_r + \Phi) \quad (61)$$

with

$$\Delta \phi = -4\pi G\rho$$

$$\rho_1 = \rho_0 (1 - \alpha(T - T_0(r)))$$

VERIFY all this !

### 3.9 The Navier-Stokes equations in cylindrical coordinates

In cylindrical coordinates,  $(r, \theta, z)$ , the continuity equation for an incompressible fluid is

$$\frac{1}{r} \frac{\partial}{\partial r} (r v_r) + \frac{1}{r} \frac{\partial}{\partial \theta} (v_\theta) + \frac{\partial v_z}{\partial z} = 0 \quad (62)$$

The Navier-Stokes equations of motion for an incompressible fluid with uniform viscosity are:

$$\begin{aligned} \rho \left( \frac{D v_r}{Dt} - \frac{v_\theta^2}{r} \right) &= -\frac{\partial p}{\partial r} + f_r + \eta \left( \Delta v_r - \frac{v_r}{r^2} - \frac{2}{r^2} \frac{\partial v_\theta}{\partial \theta} \right) \\ \rho \left( \frac{D v_\theta}{Dt} + \frac{v_\theta v_r}{r} \right) &= -\frac{1}{r} \frac{\partial p}{\partial \theta} + f_\theta + \eta \left( \Delta v_\theta - \frac{v_\theta}{r^2} + \frac{2}{r^2} \frac{\partial v_r}{\partial \theta} \right) \\ \rho \frac{D v_z}{Dt} &= -\frac{\partial p}{\partial z} + f_z + \eta \Delta v_z \end{aligned} \quad (63)$$

where The Lagrangian or material derivative is

$$\frac{D}{Dt} = \frac{\partial}{\partial t} + v_r \frac{\partial}{\partial r} + \frac{v_\theta}{r} \frac{\partial}{\partial \theta} + v_z \frac{\partial}{\partial z}$$

and the Laplacian operator is

$$\Delta = \frac{\partial^2}{\partial r^2} + \frac{1}{r} \frac{\partial}{\partial r} + \frac{1}{r^2} \frac{\partial^2}{\partial \theta^2} + \frac{\partial^2}{\partial z^2} \quad (64)$$

### 3.10 The Navier-Stokes equations in spherical coordinates

In spherical coordinates,  $(r, \theta, \phi)$ , the continuity equation for an incompressible fluid is

$$\frac{1}{r^2} \frac{\partial}{\partial r} (r^2 v_r) + \frac{1}{r \sin \theta} \frac{\partial}{\partial \theta} (v_\theta \sin \theta) + \frac{1}{r \sin \theta} \frac{\partial v_\phi}{\partial \phi} = 0 \quad (65)$$

The Navier-Stokes equations of motion for an incompressible fluid with uniform viscosity are:

$$\begin{aligned} \rho \left( \frac{D v_r}{Dt} - \frac{v_\theta^2 + v_\phi^2}{r} \right) &= -\frac{\partial p}{\partial r} + f_r + \eta \left( \Delta v_r - \frac{2v_r}{r^2} - \frac{2}{r^2} \frac{\partial v_\theta}{\partial \theta} - \frac{2v_\theta \cot \theta}{r^2} - \frac{2}{r^2 \sin \theta} \frac{\partial v_\phi}{\partial \phi} \right) \\ \rho \left( \frac{D v_\theta}{Dt} + \frac{v_\theta v_r}{r} - \frac{v_\phi^2 \cot \theta}{r} \right) &= -\frac{1}{r} \frac{\partial p}{\partial \theta} + f_\theta + \eta \left( \Delta v_\theta + \frac{2}{r^2} \frac{\partial v_r}{\partial \theta} - \frac{v_\theta}{r^2 \sin^2 \theta} - \frac{2 \cot \theta}{r^2 \sin \theta} \frac{\partial v_\phi}{\partial \phi} \right) \\ \rho \left( \frac{D v_\phi}{Dt} + \frac{v_\phi v_r}{r} - \frac{v_\theta v_\phi \cot \theta}{r} \right) &= -\frac{1}{r \sin \theta} \frac{\partial p}{\partial \phi} + f_\phi + \eta \left( \Delta v_\phi + \frac{2}{r^2 \sin \theta} \frac{\partial v_r}{\partial \phi} - \frac{v_\phi}{r^2 \sin^2 \theta} + \frac{2 \cot \theta}{r^2 \sin \theta} \frac{\partial v_\theta}{\partial \phi} \right) \end{aligned} \quad (66)$$

where The Lagrangian or material derivative is

$$\frac{D}{Dt} = \frac{\partial}{\partial t} + v_r \frac{\partial}{\partial r} + \frac{v_\theta}{r} \frac{\partial}{\partial \theta} + \frac{v_\phi}{r \sin \theta} \frac{\partial}{\partial \phi}$$

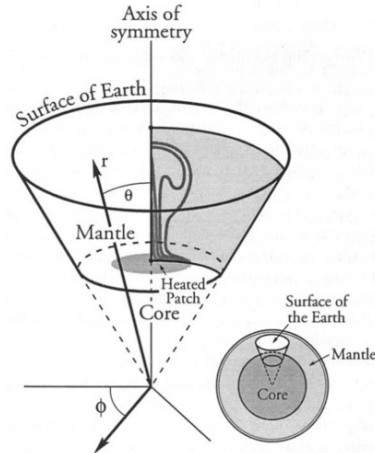
and the Laplacian operator is

$$\Delta = \frac{1}{r^2} \frac{\partial}{\partial r} \left( r^2 \frac{\partial}{\partial r} \right) + \frac{1}{r^2 \sin \theta} \frac{\partial}{\partial \theta} \left( \sin \theta \frac{\partial}{\partial \theta} \right) + \frac{1}{r^2 \sin^2 \theta} \frac{\partial^2}{\partial \phi^2}$$

THESE EQUATIONS SHOULD BE CHECKED and RE-CHECKED !!

### 3.11 The equations for axisymmetric geometries

In some cases the assumption can be made that the object we wish to study has an axisymmetric geometry, for example a plume:



Taken from Kellogg & King (1997) [1419].

Assuming the flow velocity does not depend on  $\phi$  ( $\partial_\phi = 0$ ) and therefore also that  $v_\phi = 0$

$$0 = -\frac{\partial p}{\partial r} + f_r + \eta \left( \Delta v_r - \frac{2v_r}{r^2} - \frac{2}{r^2} \frac{\partial v_\theta}{\partial \theta} - \frac{2v_\theta \cot \theta}{r^2} \right)$$

$$0 = -\frac{1}{r} \frac{\partial p}{\partial \theta} + \eta \left( \Delta v_\theta + \frac{2}{r^2} \frac{\partial v_r}{\partial \theta} - \frac{v_\theta}{r^2 \sin^2 \theta} \right)$$

with

$$\Delta = \frac{1}{r^2} \frac{\partial}{\partial r} \left( r^2 \frac{\partial}{\partial r} \right) + \frac{1}{r^2 \sin \theta} \frac{\partial}{\partial \theta} \left( \sin \theta \frac{\partial}{\partial \theta} \right)$$

THESE EQUATIONS SHOULD BE CHECKED and RE-CHECKED !!

$$\Delta = \frac{1}{r^2} \frac{\partial}{\partial r} \left( r^2 \frac{\partial}{\partial r} \right) + \frac{1}{r^2 \sin \theta} \frac{\partial}{\partial \theta} \left( \sin \theta \frac{\partial}{\partial \theta} \right) + \frac{1}{r^2 \sin^2 \theta} \frac{\partial^2}{\partial \phi^2}$$

THESE EQUATIONS SHOULD BE CHECKED and RE-CHECKED !!

From [2870]:

$$\frac{1}{r^2} \frac{\partial}{\partial r} (r^2 v_r) + \frac{1}{r \sin \theta} \frac{\partial}{\partial \theta} (v_\theta \sin \theta) + \frac{1}{r \sin \theta} \frac{\partial v_\phi}{\partial \phi} = 0 \quad (67)$$

Pb with  $1/r^2$  ??

$$0 = -\frac{\partial p}{\partial r} + (1 - \zeta) Ra r T + \frac{1}{r^2} \frac{\partial}{\partial r} \left( 2\eta r^2 \frac{\partial v_r}{\partial r} \right) + \frac{1}{r^2 \sin \theta} \frac{\partial}{\partial \theta} \left( \eta \sin \theta \frac{\partial v_r}{\partial \theta} \right) + \frac{\partial}{\partial \theta} \left( \eta \frac{\partial v_\theta}{\partial r} \frac{v_r}{r} \right) \quad (68)$$

where  $\zeta = R_i/R_o$

The dimensional form of the energy equation in a spherical axisymmetric geometry is given by (assuming the conductivity  $k$  to be constant):

$$\rho C_p \left( \frac{\partial T}{\partial t} + v_r \frac{\partial T}{\partial r} + \frac{v_\theta}{r} \frac{\partial T}{\partial \theta} \right) = k \frac{1}{r^2} \frac{\partial}{\partial r} \left( r^2 \frac{\partial T}{\partial r} \right) + k \frac{1}{r^2 \sin \theta} \frac{\partial}{\partial \theta} \left( \sin \theta \frac{\partial T}{\partial \theta} \right) \dots$$

THESE EQUATIONS SHOULD BE CHECKED and RE-CHECKED !!

### 3.12 The Boussinesq approximation

As nicely explained in Spiegel & Veronis [2395]: "In the study of problems of thermal convection it is a frequent practice to simplify the basic equations by introducing certain approximations which are attributed to Boussinesq (1903). The Boussinesq approximations can best be summarized by two statements:

1. The fluctuations in density which appear with the advent of motion result principally from thermal (as opposed to pressure) effects.
2. In the equations for the rate of change of momentum and mass, density variations may be neglected except when they are coupled to the gravitational acceleration in the buoyancy force."

Note that their paper examines the Boussinesq approximation for compressible fluids.

[from ASPECT manual] The Boussinesq approximation assumes that the density can be considered constant in all occurrences in the equations with the exception of the buoyancy term on the right hand side of (69). The primary result of this assumption is that the continuity equation (70) will now read

$$\nabla \cdot \mathbf{v} = 0$$

This implies that the strain rate tensor is deviatoric. Under the Boussinesq approximation, the equations are much simplified:

$$-\nabla \cdot [2\eta\dot{\varepsilon}(\mathbf{v})] + \nabla p = \rho\mathbf{g} \quad \text{in } \Omega, \quad (69)$$

$$\nabla \cdot (\rho\mathbf{v}) = 0 \quad \text{in } \Omega, \quad (70)$$

$$\rho_0 C_p \left( \frac{\partial T}{\partial t} + \mathbf{v} \cdot \nabla T \right) - \nabla \cdot k \nabla T = \rho H \quad \text{in } \Omega \quad (71)$$

Note that all terms on the rhs of the temperature equations have disappeared, with the exception of the source term.

### 3.13 The Extended Boussinesq approximation

Yuen et al (2007) [2863] state that "the background of the extended Boussinesq equations can be found described in Christensen and Yuen (1985) [488] and more completely in Matyska and Yuen (2007) [1737].

### 3.14 Stokes equation for elastic medium

What follows is mostly borrowed from Becker & Kaus lecture notes.

The strong form of the PDE that governs force balance in a medium is given by

$$\vec{\nabla} \cdot \boldsymbol{\sigma} + \vec{f} = \vec{0}$$

where  $\boldsymbol{\sigma}$  is the stress tensor and  $\vec{f}$  is a body force.

The stress tensor is related to the strain tensor through the generalised Hooke's law<sup>11</sup>:

$$\sigma_{ij} = \sum_{kl} C_{ijkl} \varepsilon_{kl} \quad \text{or} \quad \boldsymbol{\sigma} = \mathbf{C} : \boldsymbol{\varepsilon} \quad (72)$$

where  $\mathbf{C}$  is the fourth-order elastic tensor.

Due to the inherent symmetries of  $\boldsymbol{\sigma}$ ,  $\boldsymbol{\varepsilon}$ , and  $\mathbf{C}$ , only 21 elastic coefficients of the latter are independent. For isotropic media (which have the same physical properties in any direction),  $\mathbf{C}$  can be reduced to only two independent numbers (for example the bulk modulus  $K$  and the shear modulus  $G$  that quantify the material's resistance to changes in volume and to shearing deformations, respectively).

One often then write Eq. (72) as follows:

$$\boldsymbol{\sigma} = \lambda(\vec{\nabla} \cdot \vec{u})\mathbf{1} + 2\mu\boldsymbol{\varepsilon} \quad (73)$$

where  $\lambda$  is the Lamé parameter and  $\mu$  is the shear modulus<sup>12</sup>. The term  $\vec{\nabla} \cdot \vec{u}$  is the isotropic dilation.

The strain tensor is related to the displacement as follows:

$$\boldsymbol{\varepsilon} = \frac{1}{2}(\vec{\nabla}\vec{u} + (\vec{\nabla}\vec{u})^T)$$

The incompressibility (or bulk modulus)  $K$  is defined as  $p = -K\vec{\nabla} \cdot \vec{u}$  where  $p$  is the pressure with

$$\begin{aligned} p &= -\frac{1}{3}\text{tr}(\boldsymbol{\sigma}) \\ &= -\frac{1}{3}[\lambda(\vec{\nabla} \cdot \vec{u})\text{tr}[\mathbf{1}] + 2\mu\text{tr}[\boldsymbol{\varepsilon}]] \\ &= -\frac{1}{3}[\lambda(\vec{\nabla} \cdot \vec{u})3 + 2\mu(\vec{\nabla} \cdot \vec{u})] \\ &= -\left[\lambda + \frac{2}{3}\mu\right](\vec{\nabla} \cdot \vec{u}) \end{aligned} \quad (74)$$

so that

$$p = -K\vec{\nabla} \cdot \vec{u} \quad \text{with} \quad K = \lambda + \frac{2}{3}\mu$$

**Remark.** Eq. (72) and (73) are analogous to the ones that one has to solve in the context of viscous flow using the penalty method. In this case  $\lambda$  is the penalty coefficient,  $\mathbf{u}$  is the velocity, and  $\mu$  is then the dynamic viscosity.

The Lamé parameter and the shear modulus are also linked to  $\nu$  the poisson ratio, and  $E$ , Young's modulus:

$$\lambda = \mu \frac{2\nu}{1-2\nu} = \frac{\nu E}{(1+\nu)(1-2\nu)} \quad \text{with} \quad E = 2\mu(1+\nu)$$

The shear modulus, expressed often in GPa, describes the material's response to shear stress. The poisson ratio describes the response in the direction orthogonal to uniaxial stress. The Young modulus, expressed in GPa, describes the material's strain response to uniaxial stress in the direction of this stress.

<sup>11</sup>[https://en.wikipedia.org/wiki/Hooke's\\_law](https://en.wikipedia.org/wiki/Hooke%27s_law)

<sup>12</sup>It is also sometimes written  $G$

### 3.15 The strain rate tensor in all coordinate systems

The strain rate tensor  $\dot{\varepsilon}$  is given by

$$\dot{\varepsilon}(\vec{v}) = \frac{1}{2}(\vec{\nabla}\vec{v} + (\vec{\nabla}\vec{v})^T) \quad (75)$$

#### 3.15.1 Cartesian coordinates

$$\dot{\varepsilon}_{xx} = \frac{\partial u}{\partial x} \quad (76)$$

$$\dot{\varepsilon}_{yy} = \frac{\partial v}{\partial y} \quad (77)$$

$$\dot{\varepsilon}_{zz} = \frac{\partial w}{\partial z} \quad (78)$$

$$\dot{\varepsilon}_{yx} = \dot{\varepsilon}_{xy} = \frac{1}{2} \left( \frac{\partial u}{\partial y} + \frac{\partial v}{\partial x} \right) \quad (79)$$

$$\dot{\varepsilon}_{zx} = \dot{\varepsilon}_{xz} = \frac{1}{2} \left( \frac{\partial u}{\partial z} + \frac{\partial w}{\partial x} \right) \quad (80)$$

$$\dot{\varepsilon}_{zy} = \dot{\varepsilon}_{yz} = \frac{1}{2} \left( \frac{\partial v}{\partial z} + \frac{\partial w}{\partial y} \right) \quad (81)$$

#### 3.15.2 Polar coordinates

$$\dot{\varepsilon}_{rr} = \frac{\partial \mathbf{v}_r}{\partial r} \quad (82)$$

$$\dot{\varepsilon}_{\theta\theta} = \frac{\mathbf{v}_r}{r} + \frac{1}{r} \frac{\partial \mathbf{v}_\theta}{\partial \theta} \quad (83)$$

$$\dot{\varepsilon}_{\theta r} = \dot{\varepsilon}_{r\theta} = \frac{1}{2} \left( \frac{\partial \mathbf{v}_\theta}{\partial r} - \frac{\mathbf{v}_\theta}{r} + \frac{1}{r} \frac{\partial \mathbf{v}_r}{\partial \theta} \right) \quad (84)$$

#### 3.15.3 Cylindrical coordinates

$$\dot{\varepsilon}_{rr} = \frac{\partial \mathbf{v}_r}{\partial r} \quad (85)$$

$$\dot{\varepsilon}_{\theta\theta} = \frac{\mathbf{v}_r}{r} + \frac{1}{r} \frac{\partial \mathbf{v}_\theta}{\partial \theta} \quad (86)$$

$$\dot{\varepsilon}_{\theta r} = \dot{\varepsilon}_{r\theta} = \frac{1}{2} \left( \frac{\partial \mathbf{v}_\theta}{\partial r} - \frac{\mathbf{v}_\theta}{r} + \frac{1}{r} \frac{\partial \mathbf{v}_r}{\partial \theta} \right) \quad (87)$$

$$\dot{\varepsilon}_{zz} = \frac{\partial \mathbf{v}_z}{\partial z} \quad (88)$$

$$\dot{\varepsilon}_{rz} = \dot{\varepsilon}_{zr} = \frac{1}{2} \left( \frac{\partial \mathbf{v}_r}{\partial z} + \frac{\partial \mathbf{v}_z}{\partial r} \right) \quad (89)$$

$$\dot{\varepsilon}_{\theta z} = \dot{\varepsilon}_{z\theta} = \frac{1}{2} \left( \frac{1}{r} \frac{\partial \mathbf{v}_z}{\partial \theta} + \frac{\partial \mathbf{v}_\theta}{\partial z} \right) \quad (90)$$

### 3.15.4 Spherical coordinates

$$\dot{\varepsilon}_{rr} = \frac{\partial \mathbf{v}_r}{\partial r} \quad (91)$$

$$\dot{\varepsilon}_{\theta\theta} = \frac{\mathbf{v}_r}{r} + \frac{1}{r} \frac{\partial \mathbf{v}_\theta}{\partial \theta} \quad (92)$$

$$\dot{\varepsilon}_{\phi\phi} = \frac{1}{r \sin \theta} \frac{\partial \mathbf{v}_\phi}{\partial \phi} + \frac{\mathbf{v}_r}{r} + \frac{\mathbf{v}_\theta \cot \theta}{r} \quad (93)$$

$$\dot{\varepsilon}_{\theta r} = \dot{\varepsilon}_{r\theta} = \frac{1}{2} \left( r \frac{\partial}{\partial r} \left( \frac{\mathbf{v}_\theta}{r} \right) + \frac{1}{r} \frac{\partial \mathbf{v}_r}{\partial \theta} \right) \quad (94)$$

$$\dot{\varepsilon}_{\phi r} = \dot{\varepsilon}_{r\phi} = \frac{1}{2} \left( \frac{1}{r \sin \theta} \frac{\partial \mathbf{v}_r}{\partial \phi} + r \frac{\partial}{\partial r} \left( \frac{\mathbf{v}_\phi}{r} \right) \right) \quad (95)$$

$$\dot{\varepsilon}_{\phi\theta} = \dot{\varepsilon}_{\theta\phi} = \frac{1}{2} \left( \frac{\sin \theta}{r} \frac{\partial}{\partial \theta} \left( \frac{\mathbf{v}_\phi}{\sin \theta} \right) + \frac{1}{r \sin \theta} \frac{\partial \mathbf{v}_\theta}{\partial \phi} \right) \quad (96)$$

## 3.16 Boundary conditions

In mathematics, the Dirichlet (or first-type) boundary condition is a type of boundary condition, named after Peter Gustav Lejeune Dirichlet. When imposed on an ODE or PDE, it specifies the values that a solution needs to take along the boundary of the domain. Note that a Dirichlet boundary condition may also be referred to as a fixed boundary condition.

The Neumann (or second-type) boundary condition is a type of boundary condition, named after Carl Neumann. When imposed on an ordinary or a partial differential equation, the condition specifies the values in which the derivative of a solution is applied within the boundary of the domain.

It is possible to describe the problem using other boundary conditions: a Dirichlet boundary condition specifies the values of the solution itself (as opposed to its derivative) on the boundary, whereas the Cauchy boundary condition, mixed boundary condition and Robin boundary condition are all different types of combinations of the Neumann and Dirichlet boundary conditions.

### 3.16.1 The Stokes equations

You may find the following terms in the computational geodynamics literature:

- free surface: this means that no force is acting on the surface, i.e.  $\sigma \cdot \vec{n} = \vec{0}$ . It is usually used on the top boundary of the domain and allows for topography evolution.
- free slip:  $\vec{v} \cdot \vec{n} = 0$  and  $(\sigma \cdot \vec{n}) \times \vec{n} = \vec{0}$ . This condition ensures a frictionless flow parallel to the boundary where it is prescribed.
- no slip: this means that the velocity (or displacement) is exactly zero on the boundary, i.e.  $\vec{v} = \vec{0}$ .
- prescribed velocity:  $\vec{v} = \vec{v}_{bc}$
- stress b.c.:
- open .b.c.: see fieldstone 29.

### 3.16.2 The heat transport equation

There are two types of boundary conditions for this equation: temperature boundary conditions (Dirichlet boundary conditions) and heat flux boundary conditions (Neumann boundary conditions).

### 3.17 Meaningful physical quantities

- Velocity  $\vec{v}$ (m/s): This is a vector quantity and both magnitude and direction are needed to define it. It is the rate of change of position with respect to a frame of reference.
- Root mean square velocity  $v_{rms}$ (m/s):

$$v_{rms} = \left( \frac{\int_{\Omega} |\vec{v}|^2 d\Omega}{\int_{\Omega} d\Omega} \right)^{1/2} = \left( \frac{1}{V_{\Omega}} \int_{\Omega} |\vec{v}|^2 d\Omega \right)^{1/2} \quad (97)$$

**Remark.**  $V_{\Omega}$  is usually computed numerically at the same time  $v_{rms}$  is computed.

In Cartesian coordinates, for a cuboid domain of size  $L_x \times L_y \times L_z$ , the  $v_{rms}$  is simply given by:

$$v_{rms} = \left( \frac{1}{L_x L_y L_z} \int_0^{L_x} \int_0^{L_y} \int_0^{L_z} (u^2 + v^2 + w^2) dx dy dz \right)^{1/2} \quad (98)$$

In the case of an annulus domain, although calculations are carried out in Cartesian coordinates, it makes sense to look at the radial velocity component  $v_r$  and the tangential velocity component  $v_{\theta}$ , and their respective root mean square averages:

$$v_r|_{rms} = \left( \frac{1}{V_{\Omega}} \int_{\Omega} v_r^2 d\Omega \right)^{1/2} \quad (99)$$

$$v_{\theta}|_{rms} = \left( \frac{1}{V_{\Omega}} \int_{\Omega} v_{\theta}^2 d\Omega \right)^{1/2} \quad (100)$$

- Pressure  $p$ (Pa):
- Stress tensor  $\sigma$  (Pa):
- Strain tensor  $\epsilon$  (dimensionless):
- Strain rate tensor  $\dot{\epsilon}$ (s<sup>-1</sup>):
- Rayleigh number  $Ra$  (X): It is a dimensionless number that expresses the ratio of the driving forces to the opposing forces. The buoyancy force comes from the volumetric thermal expansion while the viscous forces and the heat diffusivity oppose convection (the latter one smoothes out thermal gradients).

The Rayleigh number for convection driven by a constant temperature hot base and a cold surface in a domain of thickness  $D$  is:

$$Ra = \frac{\rho_0 g \alpha D^3}{\eta \kappa} \cdot \Delta T = \frac{\rho_0^2 C_p g \alpha D^3 \Delta T}{\eta k}$$

The Rayleigh number for convection driven by a hot base (constant basal heat flow  $q_b$ ) and a colder surface is:

$$Ra = \frac{\rho_0 g \alpha D^3}{\eta \kappa} \cdot \frac{q_b D}{k}$$

The Rayleigh number for convection driven by internal heating  $H$  (production per cubic meter) is:

$$Ra = \frac{\rho_0 g \alpha D^3}{\eta \kappa} \cdot \frac{H D^2}{k}$$

The Rayleigh number for convection driven by both basal heat flow and internal heating is:

$$Ra = \frac{\rho_0 g \alpha D^3}{\eta \kappa} \cdot \frac{q_b D + H D^2}{k}$$

For convection to occur, the Rayleigh number must be larger than the so-called critical Rayleigh number, which ranges from 600 to 3000 (it depends on the boundary conditions and the geometry).

- Prandtl number  $Pr$  (X): It is named after the German physicist Ludwig Prandtl and is defined as the ratio of momentum diffusivity to thermal diffusivity. It is given as:

$$Pr = \frac{\text{momentum diffusivity}}{\text{thermal diffusivity}} = \frac{\eta/\rho}{k/(\rho C_p)} = \frac{\eta C_p}{k}$$

For Earth materials, we have  $Pr \sim (10^{21} 1000)/3 \gg 1$ , which means that momentum diffusivity dominates.

- Nusselt number  $Nu$  (X): the Nusselt number ( $Nu$ ) is the ratio of convective to conductive heat transfer across (normal to) the boundary. The conductive component is measured under the same conditions as the heat convection but with a (hypothetically) stagnant (or motionless) fluid.

In practice the Nusselt number  $Nu$  of a layer (typically the mantle of a planet) is defined as follows:

$$Nu = \frac{q}{q_c} \quad (101)$$

where  $q$  is the heat transferred by convection while  $q_c = k\Delta T/D$  is the amount of heat that would be conducted through a layer of thickness  $D$  with a temperature difference  $\Delta T$  across it with  $k$  being the thermal conductivity.

For 2D Cartesian systems of size  $(L_x, L_y)$  the  $Nu$  is computed [209]

$$Nu = \frac{\frac{1}{L_x} \int_0^{L_x} k \frac{\partial T}{\partial y}(x, y = L_y) dx}{-\frac{1}{L_x} \int_0^{L_x} k T(x, y = 0) / L_y dx} = -L_y \frac{\int_0^{L_x} \frac{\partial T}{\partial y}(x, y = L_y) dx}{\int_0^{L_x} T(x, y = 0) dx}$$

i.e. it is the mean surface temperature gradient over the mean bottom temperature.

finish, not happy with definition. Look at literature

Note that in the case when no convection takes place then the measured heat flux at the top is the one obtained from a purely conductive profile which yields  $Nu=1$ .

Note that a relationship  $Ra \propto Nu^\alpha$  exists between the Rayleigh number  $Ra$  and the Nusselt number  $Nu$  in convective systems, see [2806] and references therein.

Turning now to cylindrical geometries with inner radius  $R_1$  and outer radius  $R_2$ , we define  $f = R_1/R_2$ . A small value of  $f$  corresponds to a high degree of curvature. We assume now that  $R_2 - R_1 = 1$ , so that  $R_2 = 1/(1-f)$  and  $R_1 = f/(1-f)$ . Following [1343], the Nusselt number at the inner and outer boundaries are:

$$Nu_{inner} = \frac{f \ln f}{1-f} \frac{1}{2\pi} \int_0^{2\pi} \left( \frac{\partial T}{\partial r} \right)_{r=R_1} d\theta \quad (102)$$

$$Nu_{outer} = \frac{\ln f}{1-f} \frac{1}{2\pi} \int_0^{2\pi} \left( \frac{\partial T}{\partial r} \right)_{r=R_2} d\theta \quad (103)$$

Note that a conductive geotherm in such an annulus between temperatures  $T_1$  and  $T_2$  is given by

$$T_c(r) = \frac{\ln(r/R_2)}{\ln(R_1/R_2)} = \frac{\ln(r(1-f))}{\ln f}$$

so that

$$\frac{\partial T_c}{\partial r} = \frac{1}{r \ln f}$$

We then find:

$$Nu_{inner} = \frac{f \ln f}{1-f} \frac{1}{2\pi} \int_0^{2\pi} \left( \frac{\partial T_c}{\partial r} \right)_{r=R_1} d\theta = \frac{f \ln f}{1-f} \frac{1}{R_1 \ln f} = 1 \quad (104)$$

$$Nu_{outer} = \frac{\ln f}{1-f} \frac{1}{2\pi} \int_0^{2\pi} \left( \frac{\partial T_c}{\partial r} \right)_{r=R_2} d\theta = \frac{\ln f}{1-f} \frac{1}{R_2 \ln f} = 1 \quad (105)$$

As expected, the recovered Nusselt number at both boundaries is exactly 1 when the temperature field is given by a steady state conductive geotherm.

[derive formula for Earth size R1 and R2](#)

### Relevant Literature[1207]

- Temperature (K):
- (Dynamic) Viscosity (Pa.s): For air it is roughly  $10^{-5}$  Pa.s, about  $10^{-3}$  Pa.s for water, about  $10^{10}$  Pa.s for ice and about  $10^{17}$  Pa.s for salt.
- Density ( $\text{kg}/\text{m}^3$ ):
- Heat capacity  $C_p$  ( $\text{J}\cdot\text{K}^{-1}$ ): It is the measure of the heat/energy required to increase the temperature of a unit quantity of a substance by unit degree. Note that the specific heat capacity  $c_p$  of a substance is the heat capacity of a sample of the substance divided by the mass of the sample, with units  $\text{J}\cdot\text{K}\cdot\text{kg}^{-1}$ .
- Heat conductivity, or thermal conductivity  $k$  ( $\text{W}\cdot\text{m}^{-1}\cdot\text{K}^{-1}$ ). It is the property of a material that indicates its ability to conduct heat. It appears primarily in Fourier's Law for heat conduction. Note that it is a function of temperature, especially in mantle convection settings [1809]. See also [229] and refs therein. Note also that it can be a tensorial quantity in anisotropic context.
- Heat diffusivity:  $\kappa = k/(\rho C_p)$  ( $\text{m}^2\cdot\text{s}^{-1}$ ). Substances with high thermal diffusivity rapidly adjust their temperature to that of their surroundings, because they conduct heat quickly in comparison to their volumetric heat capacity or 'thermal bulk'.
- thermal expansion  $\alpha$  ( $\text{K}^{-1}$ ): it is the tendency of a matter to change in volume in response to a change in temperature. Note that it is a function of temperature, especially in mantle convection settings [1809].
- Urey Ratio: mantle heat production divided by heat loss) is a key constraint for thermal history models. Recent Urey ratio estimates are in the range of 0.210.49. [1575]
- Shear modulus: modulus of rigidity, usually expressed in GPa. It describes the material response to shear stress.
- Poisson ratio: response in the direction orthogonal to uniaxial stress.
- Young's modulus: describes the material strain response to uniaxial stress in the direction of this stress, usually expressed in GPa.
- Average viscosity: following Christensen (1983) [479], one can compute the averaged viscosity in a domain as follows:

$$\langle \eta \rangle = \frac{\int_V \eta \dot{\varepsilon}_e^2 dV}{\int_V \dot{\varepsilon}_e^2 dV} \quad (106)$$

[check aspect manual The 2D cylindrical shell benchmarks by Davies et al. 5.4.12](#)

## 3.18 Principal stress and principal invariants

As seen before (see Section 3.2.2) the stress tensor is a symmetric  $3 \times 3$  real matrix, and linear algebra tells us that it therefore has three mutually orthogonal unit-length eigenvectors  $\vec{n}_1, \vec{n}_2, \vec{n}_3$  and three real eigenvalues  $\lambda_1, \lambda_2, \lambda_3$  such that  $\sigma \cdot \vec{n}_i = \lambda_i \vec{n}_i$ .

As a consequence, in a coordinate system with axes  $\vec{n}_1, \vec{n}_2, \vec{n}_3$ , the stress tensor is a diagonal matrix, and has only the three normal components  $\lambda_1, \lambda_2, \lambda_3$  i.e. the principal stresses. If the three eigenvalues are equal, the stress is an isotropic compression or tension, always perpendicular to any surface, there is no shear stress, and the tensor is a diagonal matrix in any coordinate frame.

### 3.18.1 In two dimensions

We are looking for the stress tensor eigenvector vector  $\vec{n} = (n_x, n_y)$  associated to the eigenvalue  $\lambda$  such that

$$\begin{pmatrix} \sigma_{xx} & \sigma_{xy} \\ \sigma_{xy} & \sigma_{yy} \end{pmatrix} \cdot \begin{pmatrix} n_x \\ n_y \end{pmatrix} = \lambda \begin{pmatrix} n_x \\ n_y \end{pmatrix}$$

or,

$$\begin{pmatrix} \sigma_{xx} & \sigma_{xy} \\ \sigma_{xy} & \sigma_{yy} \end{pmatrix} \cdot \begin{pmatrix} n_x \\ n_y \end{pmatrix} - \begin{pmatrix} \lambda & 0 \\ 0 & \lambda \end{pmatrix} \cdot \begin{pmatrix} n_x \\ n_y \end{pmatrix} = \vec{0}$$

i.e.,

$$\begin{pmatrix} \sigma_{xx} - \lambda & \sigma_{xy} \\ \sigma_{xy} & \sigma_{yy} - \lambda \end{pmatrix} \cdot \begin{pmatrix} n_x \\ n_y \end{pmatrix} = \vec{0}$$

which yields

$$(\sigma_{xx} - \lambda)(\sigma_{yy} - \lambda) - \sigma_{xy}^2 = 0$$

or,

$$\lambda^2 - (\sigma_{xx} + \sigma_{yy})\lambda + (\sigma_{xx}\sigma_{yy} - \sigma_{xy}^2) = 0$$

The discriminant  $\Delta$  is

$$\begin{aligned} \Delta &= (\sigma_{xx} + \sigma_{yy})^2 - 4(\sigma_{xx}\sigma_{yy} - \sigma_{xy}^2) \\ &= (\sigma_{xx} - \sigma_{yy})^2 + 4\sigma_{xy}^2 \end{aligned}$$

The roots are given by:

$$\begin{aligned} \lambda_{\pm} &= \frac{(\sigma_{xx} + \sigma_{yy}) \pm \sqrt{(\sigma_{xx} - \sigma_{yy})^2 + 4\sigma_{xy}^2}}{2} \\ &= \frac{\sigma_{xx} + \sigma_{yy}}{2} \pm \sqrt{\left(\frac{\sigma_{xx} - \sigma_{yy}}{2}\right)^2 + \sigma_{xy}^2} \end{aligned}$$

The two principal stresses are then:

$$\begin{aligned} \sigma_1 &= \frac{\sigma_{xx} + \sigma_{yy}}{2} + \sqrt{\left(\frac{\sigma_{xx} - \sigma_{yy}}{2}\right)^2 + \sigma_{xy}^2} \\ \sigma_2 &= \frac{\sigma_{xx} + \sigma_{yy}}{2} - \sqrt{\left(\frac{\sigma_{xx} - \sigma_{yy}}{2}\right)^2 + \sigma_{xy}^2} \end{aligned}$$

with the convention  $\sigma_1 > \sigma_2$ . The maximum shear stress is defined as one-half the difference between the two principal stresses

$$\tau_{max} = \frac{\sigma_1 - \sigma_2}{2} = \sqrt{\left(\frac{\sigma_{xx} - \sigma_{yy}}{2}\right)^2 + \sigma_{xy}^2}$$

The eigenvector  $\vec{n}_1$  corresponding to  $\sigma_1$  is obtained by solving

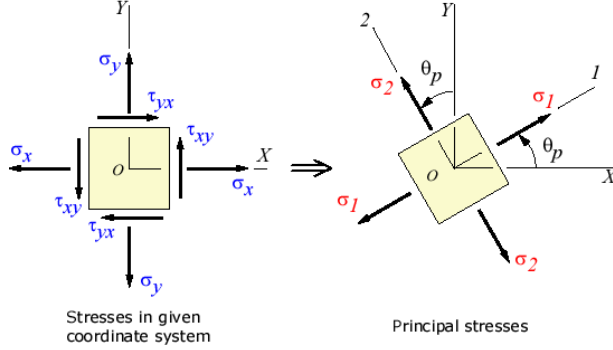
$$\boldsymbol{\sigma} \cdot \vec{n}_1 = \sigma_1 \vec{n}_1$$

and same for the other eigenvalue/vector:

$$\boldsymbol{\sigma} \cdot \vec{n}_2 = \sigma_2 \vec{n}_2$$

Each is a system of two equations with two unknowns. These are not difficult to solve, but can prove cumbersome. Note that linear algebra tells us that  $\vec{n}_1 \cdot \vec{n}_2 = 0$ , i.e. the eigenvectors form a basis of  $\mathbb{R}^2$ .

This is the reason why often people go another route. One can ask the question: what is the value of the angle  $\theta_p$  which, if used to perform a rotation of the axis system, yields a stress tensor that is diagonal, with the principal stresses on the diagonal?



Taken from [https://www.efunda.com/formulae/solid\\_mechanics/mat\\_mechanics/plane\\_stress\\_principal.cfm](https://www.efunda.com/formulae/solid_mechanics/mat_mechanics/plane_stress_principal.cfm)

The rotation matrix is

$$\mathbf{R} = \begin{pmatrix} \cos \theta_p & -\sin \theta_p \\ \sin \theta_p & \cos \theta_p \end{pmatrix}$$

and the image of  $\boldsymbol{\sigma}$  by means of the axis rotation is  $\boldsymbol{\sigma}' = \mathbf{R} \cdot \boldsymbol{\sigma} \cdot \mathbf{R}^{-1}$ , i.e.

$$\begin{aligned} \boldsymbol{\sigma}' &= \begin{pmatrix} \cos \theta_p & -\sin \theta_p \\ \sin \theta_p & \cos \theta_p \end{pmatrix} \cdot \begin{pmatrix} \sigma_{xx} & \sigma_{xy} \\ \sigma_{xy} & \sigma_{yy} \end{pmatrix} \cdot \begin{pmatrix} \cos \theta_p & \sin \theta_p \\ -\sin \theta_p & \cos \theta_p \end{pmatrix} \\ &= \begin{pmatrix} \cos \theta_p & -\sin \theta_p \\ \sin \theta_p & \cos \theta_p \end{pmatrix} \cdot \begin{pmatrix} \sigma_{xx} \cos \theta_p - \sigma_{xy} \sin \theta_p & \sigma_{xx} \sin \theta_p + \sigma_{xy} \cos \theta_p \\ \sigma_{xy} \cos \theta_p - \sigma_{yy} \sin \theta_p & \sigma_{xy} \sin \theta_p + \sigma_{yy} \cos \theta_p \end{pmatrix} \\ &= \begin{pmatrix} \dots & \cos \theta_p (\sigma_{xx} \sin \theta_p + \sigma_{xy} \cos \theta_p) - \sin \theta_p (\sigma_{xy} \sin \theta_p + \sigma_{yy} \cos \theta_p) \\ \dots & \dots \end{pmatrix} \end{aligned}$$

In the matrix above I have only computed the off diagonal term since we are actually looking for  $\theta_p$  such that  $\sigma'_{xy} = 0$ , or

$$\begin{aligned} \cos \theta_p (\sigma_{xx} \sin \theta_p + \sigma_{xy} \cos \theta_p) - \sin \theta_p (\sigma_{xy} \sin \theta_p + \sigma_{yy} \cos \theta_p) &= 0 \\ \sin \theta_p \cos \theta_p (\sigma_{xx} - \sigma_{yy}) + (\cos^2 \theta_p - \sin^2 \theta_p) \sigma_{xy} &= 0 \end{aligned}$$

and then

$$\frac{\sin \theta_p \cos \theta_p}{\cos^2 \theta_p - \sin^2 \theta_p} = \frac{\sigma_{xy}}{\sigma_{xx} - \sigma_{yy}}$$

The left hand term is actually a trigonometric identity<sup>13</sup>:

$$\frac{\sin \theta_p \cos \theta_p}{\cos^2 \theta_p - \sin^2 \theta_p} = \frac{1}{2} \tan 2\theta_p$$

and finally:

$$\tan 2\theta_p = \frac{2\sigma_{xy}}{\sigma_{xx} - \sigma_{yy}} \quad \text{or} \quad \theta_p = \frac{1}{2} \tan^{-1} \frac{2\sigma_{xy}}{\sigma_{xx} - \sigma_{yy}}$$

Once  $\theta_p$  has been found the other direction is given by  $\theta_p + \pi/2$ .

Example: Let us assume a diagonal stress tensor of the form

$$\boldsymbol{\sigma} = \begin{pmatrix} a & 0 \\ 0 & b \end{pmatrix}$$

then  $\tan 2\theta_p = 0$ , and then  $\theta_p = 0$ . The principal directions are the horizontal and vertical directions, i.e. the Cartesian axis system, which is consistent.

<sup>13</sup>[https://en.wikipedia.org/wiki/List\\_of\\_trigonometric\\_identities](https://en.wikipedia.org/wiki/List_of_trigonometric_identities)

### 3.18.2 In three dimensions

We are looking for the stress tensor eigenvector vector  $\vec{n} = (n_x, n_y, n_z)$  associated to the eigenvalue  $\lambda$  such that

$$\begin{pmatrix} \sigma_{xx} & \sigma_{xy} & \sigma_{xz} \\ \sigma_{xy} & \sigma_{yy} & \sigma_{yz} \\ \sigma_{xz} & \sigma_{yz} & \sigma_{zz} \end{pmatrix} \cdot \begin{pmatrix} n_x \\ n_y \\ n_z \end{pmatrix} = \lambda \begin{pmatrix} n_x \\ n_y \\ n_z \end{pmatrix}$$

or,

$$\begin{pmatrix} \sigma_{xx} & \sigma_{xy} & \sigma_{xz} \\ \sigma_{xy} & \sigma_{yy} & \sigma_{yz} \\ \sigma_{xz} & \sigma_{yz} & \sigma_{zz} \end{pmatrix} \cdot \begin{pmatrix} n_x \\ n_y \\ n_z \end{pmatrix} - \begin{pmatrix} \lambda & 0 & 0 \\ 0 & \lambda & 0 \\ 0 & 0 & \lambda \end{pmatrix} \cdot \begin{pmatrix} n_x \\ n_y \\ n_z \end{pmatrix} = \vec{0}$$

$$\begin{pmatrix} \sigma_{xx} - \lambda & \sigma_{xy} & \sigma_{xz} \\ \sigma_{xy} & \sigma_{yy} - \lambda & \sigma_{yz} \\ \sigma_{xz} & \sigma_{yz} & \sigma_{zz} - \lambda \end{pmatrix} \cdot \begin{pmatrix} n_x \\ n_y \\ n_z \end{pmatrix} = \vec{0}$$

Non-trivial solutions of this equation require

$$\begin{vmatrix} \sigma_{xx} - \lambda & \sigma_{xy} & \sigma_{xz} \\ \sigma_{xy} & \sigma_{yy} - \lambda & \sigma_{yz} \\ \sigma_{xz} & \sigma_{yz} & \sigma_{zz} - \lambda \end{vmatrix} = 0$$

Expanding the determinant results in the following cubic equation:

$$\begin{aligned} 0 &= (\sigma_{xx} - \lambda)[(\sigma_{yy} - \lambda)(\sigma_{zz} - \lambda) - \sigma_{yz}^2] - \sigma_{xy}[\sigma_{xy}(\sigma_{zz} - \lambda) - \sigma_{yz}\sigma_{xz}] + \sigma_{xz}[\sigma_{xy}\sigma_{yz} - (\sigma_{yy} - \lambda)\sigma_{xz}] \\ &= (\sigma_{xx} - \lambda)[\sigma_{yy}\sigma_{zz} - \lambda(\sigma_{yy} + \sigma_{zz}) + \lambda^2 - \sigma_{yz}^2] - \sigma_{xy}[\sigma_{xy}(\sigma_{zz} - \lambda) - \sigma_{yz}\sigma_{xz}] + \sigma_{xz}[\sigma_{xy}\sigma_{yz} - (\sigma_{yy} - \lambda)\sigma_{xz}] \\ &= -\lambda^3 + (\sigma_{xx} + \sigma_{yy} + \sigma_{zz})\lambda^2 + (-\sigma_{yy}\sigma_{zz} - \sigma_{xx}\sigma_{yy} - \sigma_{xx}\sigma_{zz} + \sigma_{yz}^2 + \sigma_{xy}^2 + \sigma_{xz}^2)\lambda + \det(\boldsymbol{\sigma}) \end{aligned}$$

or, after multiplying the last line by -1,

$$\lambda^3 - K_1(\boldsymbol{\sigma})\lambda^2 + K_2(\boldsymbol{\sigma})\lambda - K_3(\boldsymbol{\sigma}) = 0 \quad (107)$$

with:

$$\begin{aligned} K_1(\boldsymbol{\sigma}) &= \sigma_{xx} + \sigma_{yy} + \sigma_{zz} \\ K_2(\boldsymbol{\sigma}) &= \sigma_{xx}\sigma_{yy} + \sigma_{yy}\sigma_{zz} + \sigma_{xx}\sigma_{zz} - \sigma_{xy}^2 - \sigma_{xz}^2 - \sigma_{yz}^2 \\ K_3(\boldsymbol{\sigma}) &= \det(\boldsymbol{\sigma}) \\ &= \sigma_{xx}\sigma_{yy}\sigma_{zz} - \sigma_{xx}\sigma_{yz}^2 - \sigma_{xy}^2\sigma_{zz} + \sigma_{xy}\sigma_{yz}\sigma_{xz} + \sigma_{xz}\sigma_{xy}\sigma_{yz} - \sigma_{xz}^2\sigma_{yy} \\ &= \sigma_{xx}\sigma_{yy}\sigma_{zz} + 2\sigma_{xy}\sigma_{yz}\sigma_{xz} - (\sigma_{xx}\sigma_{yz}^2 + \sigma_{zz}\sigma_{xy}^2 + \sigma_{yy}\sigma_{xz}^2) \end{aligned} \quad (108)$$

$K_1$ ,  $K_2$  and  $K_3$  are called **principal** invariants<sup>14</sup> (see also Appendix A.1 of Zienkiewicz & Taylor [2941]). These invariants can be written in a coordinate-free manner:

$$\begin{aligned} K_1(\boldsymbol{\sigma}) &= \text{tr}(\boldsymbol{\sigma}) \\ K_2(\boldsymbol{\sigma}) &= \frac{1}{2}(\text{tr}(\boldsymbol{\sigma})^2 - \text{tr}(\boldsymbol{\sigma}^2)) \\ K_3(\boldsymbol{\sigma}) &= \det(\boldsymbol{\sigma}) \end{aligned}$$

and if the stress tensor is diagonal, we have

$$\begin{aligned} K_1(\boldsymbol{\sigma}) &= \sigma_1 + \sigma_2 + \sigma_3 \\ K_2(\boldsymbol{\sigma}) &= \sigma_1\sigma_2 + \sigma_2\sigma_3 + \sigma_1\sigma_3 \\ K_3(\boldsymbol{\sigma}) &= \sigma_1\sigma_2\sigma_3 \end{aligned}$$

---

<sup>14</sup>[https://en.wikipedia.org/wiki/Invariants\\_of\\_tensors](https://en.wikipedia.org/wiki/Invariants_of_tensors)

The principal invariants  $K_{\{1,2,3\}}$  are related to the **moment** invariants  $\mathcal{I}_{\{1,2,3\}}$  (see Section 3.19) as follows (Appendix A.2 of Zienkiewicz & Taylor [2941]):

$$\mathcal{I}_1(\boldsymbol{\sigma}) = K_1(\boldsymbol{\sigma}) \quad (109)$$

$$\mathcal{I}_2(\boldsymbol{\sigma}) = \frac{1}{2}K_1(\boldsymbol{\sigma})^2 - K_2(\boldsymbol{\sigma}) \quad (110)$$

$$\mathcal{I}_3(\boldsymbol{\sigma}) = \frac{1}{6}K_1(\boldsymbol{\sigma})^3 - K_1(\boldsymbol{\sigma})K_2(\boldsymbol{\sigma}) + K_3(\boldsymbol{\sigma}) \quad (111)$$

Very often we will find ourselves interested in the principal components of the deviatoric stress tensor  $\boldsymbol{\tau}$  so that we now have the following determinant to compute:

$$\begin{vmatrix} \tau_{xx} - \lambda & \tau_{xy} & \tau_{xz} \\ \tau_{xy} & \tau_{yy} - \lambda & \tau_{yz} \\ \tau_{xz} & \tau_{yz} & \tau_{zz} - \lambda \end{vmatrix} = 0$$

and therefore obtain the following cubic equation

$$\lambda^3 - K_1(\boldsymbol{\tau})\lambda^2 + K_2(\boldsymbol{\tau})\lambda - K_3(\boldsymbol{\tau}) = 0 \quad (112)$$

By definition of a deviatoric tensor we have  $K_1(\boldsymbol{\tau}) = 0$  and then Eqs. (110) and (111) become

$$\mathcal{I}_2(\boldsymbol{\tau}) = -K_2(\boldsymbol{\tau}) \quad (113)$$

$$\mathcal{I}_3(\boldsymbol{\tau}) = K_3(\boldsymbol{\tau}) \quad (114)$$

so that the cubic equation becomes

$$\lambda^3 - \mathcal{I}_2(\boldsymbol{\tau})\lambda - \mathcal{I}_3(\boldsymbol{\tau}) = 0 \quad (115)$$

Noting the trigonometric identity<sup>15</sup>

$$\sin 3\theta = 3 \sin \theta - 4 \sin^3 \theta \quad \text{or,} \quad \sin^3 \theta - \frac{3}{4} \sin \theta + \frac{1}{4} \sin 3\theta = 0 \quad (116)$$

and substituting  $\lambda = r \sin \theta$  into (115) we have<sup>16</sup>

$$\sin^3 \theta - \frac{\mathcal{I}_2(\boldsymbol{\tau})}{r^2} \sin \theta - \frac{\mathcal{I}_3(\boldsymbol{\tau})}{r^3} = 0 \quad (117)$$

Comparing (116) and (117) gives

$$r = \frac{2}{\sqrt{3}} \sqrt{\mathcal{I}_2(\boldsymbol{\tau})} \quad (118)$$

$$\sin 3\theta = -\frac{4\mathcal{I}_3(\boldsymbol{\tau})}{r^3} = -\frac{3\sqrt{3}}{2} \frac{\mathcal{I}_3(\boldsymbol{\tau})}{\mathcal{I}_2(\boldsymbol{\tau})^{3/2}} \quad (119)$$

The so-called Lode angle [2933] is then given by

$$\theta = \frac{1}{3} \sin^{-1} \left( -\frac{3\sqrt{3}}{2} \frac{\mathcal{I}_3(\boldsymbol{\tau})}{\mathcal{I}_2(\boldsymbol{\tau})^{3/2}} \right) \quad (120)$$

with  $-\pi/6 < \theta < \pi/6$ . The very same equation is also found in Willett (1992) [2786] for instance.

The first root of (119) with  $\theta$  determined for  $3\theta$  in the range  $\pm\pi/2$  is a convenient alternative to the third invariant,  $\mathcal{I}_3(\boldsymbol{\tau})$ . By noting the cyclic nature of  $\sin(3\theta + 2n\pi)$  we have immediately the three (and only three) possible values of  $\sin \theta$  which define the three principal stresses. The deviatoric principal stresses are given by  $\lambda = r \sin \theta$  on substitution of the three values of  $\sin \theta$  in turn.

<sup>15</sup>see section 7.4 of Owen & Hinton [1983]

<sup>16</sup>Note that  $r$  and  $\theta$  have nothing to do with polar, cylindrical or spherical coordinates.

We then obtain

$$\begin{Bmatrix} \tau_1 \\ \tau_2 \\ \tau_3 \end{Bmatrix} = \frac{2}{\sqrt{3}} \sqrt{\mathcal{I}_2(\boldsymbol{\tau})} \begin{Bmatrix} \sin(\theta + 2\pi/3) \\ \sin \theta \\ \sin(\theta + 4\pi/3) \end{Bmatrix} \quad (121)$$

with  $\tau_1 > \tau_2 > \tau_3$  and  $-\pi/6 \leq \theta \leq \pi/6$ . It is indeed easy to verify that for  $-\pi/6 \leq \theta \leq \pi/6$  we have  $\sin(\theta + 2\pi/3) > \sin \theta > \sin(\theta + 4\pi/3)$ .

Finally, we wish to compute the principal stresses of the full stress tensor  $\boldsymbol{\sigma}$ . In the right coordinate system both stress and deviatoric stress tensors are diagonal and  $\boldsymbol{\sigma} = -p\mathbf{1} + \boldsymbol{\tau}$  writes:

$$\begin{pmatrix} \sigma_1 & 0 & 0 \\ 0 & \sigma_2 & 0 \\ 0 & 0 & \sigma_3 \end{pmatrix} = \begin{pmatrix} -p & 0 & 0 \\ 0 & -p & 0 \\ 0 & 0 & -p \end{pmatrix} + \begin{pmatrix} \tau_1 & 0 & 0 \\ 0 & \tau_2 & 0 \\ 0 & 0 & \tau_3 \end{pmatrix}$$

so that (since  $p = -\frac{1}{3}\text{tr}(\boldsymbol{\sigma}) = -\frac{1}{3}\mathcal{I}_1(\boldsymbol{\sigma})$ )

$$\sigma_1 = \tau_1 - p = \tau_1 + \frac{1}{3}\mathcal{I}_1(\boldsymbol{\sigma}) \quad (122)$$

$$\sigma_2 = \tau_2 - p = \tau_2 + \frac{1}{3}\mathcal{I}_1(\boldsymbol{\sigma}) \quad (123)$$

$$\sigma_3 = \tau_3 - p = \tau_3 + \frac{1}{3}\mathcal{I}_1(\boldsymbol{\sigma}) \quad (124)$$

and finally the total principal stresses are

$$\begin{Bmatrix} \sigma_1 \\ \sigma_2 \\ \sigma_3 \end{Bmatrix} = \frac{2}{\sqrt{3}} \sqrt{\mathcal{I}_2(\boldsymbol{\tau})} \begin{Bmatrix} \sin(\theta + 2\pi/3) \\ \sin \theta \\ \sin(\theta + 4\pi/3) \end{Bmatrix} + \frac{\mathcal{I}_1(\boldsymbol{\sigma})}{3} \begin{Bmatrix} 1 \\ 1 \\ 1 \end{Bmatrix} \quad (125)$$

with  $\sigma_1 > \sigma_2 > \sigma_3$  and  $-\pi/6 \leq \theta \leq \pi/6$ . We have

$$\begin{aligned} \sin(\theta + 2\pi/3) &= \sin \theta \cos 2\pi/3 + \cos \theta \sin 2\pi/3 \\ &= -\frac{1}{2} \sin \theta + \cos \theta \frac{\sqrt{3}}{2} \end{aligned} \quad (126)$$

$$\begin{aligned} \sin(\theta + 4\pi/3) &= \sin \theta \cos 4\pi/3 + \cos \theta \sin 4\pi/3 \\ &= -\frac{1}{2} \sin \theta - \cos \theta \frac{\sqrt{3}}{2} \end{aligned} \quad (127)$$

so that

$$\begin{Bmatrix} \sigma_1 \\ \sigma_2 \\ \sigma_3 \end{Bmatrix} = \frac{2}{\sqrt{3}} \sqrt{\mathcal{I}_2(\boldsymbol{\tau})} \begin{Bmatrix} -\frac{1}{2} \sin \theta + \cos \theta \frac{\sqrt{3}}{2} \\ \sin \theta \\ -\frac{1}{2} \sin \theta - \cos \theta \frac{\sqrt{3}}{2} \end{Bmatrix} + \frac{\mathcal{I}_1(\boldsymbol{\sigma})}{3} \begin{Bmatrix} 1 \\ 1 \\ 1 \end{Bmatrix} \quad (128)$$

$$= \sqrt{\mathcal{I}_2(\boldsymbol{\tau})} \begin{Bmatrix} -\frac{1}{\sqrt{3}} \sin \theta + \cos \theta \\ \frac{2}{\sqrt{3}} \sin \theta \\ -\frac{1}{\sqrt{3}} \sin \theta - \cos \theta \end{Bmatrix} + \frac{\mathcal{I}_1(\boldsymbol{\sigma})}{3} \begin{Bmatrix} 1 \\ 1 \\ 1 \end{Bmatrix} \quad (129)$$

**Remark.** The Lode angle is one of the Lode coordinates<sup>17</sup>, or Haigh-Westergaard coordinates.

---

<sup>17</sup>[https://en.wikipedia.org/wiki/Lode\\_coordinates](https://en.wikipedia.org/wiki/Lode_coordinates)

**Remark.** The Lode angle  $\theta$  is essentially similar to the Lode parameter defined by  $-\sqrt{3} \tan \theta$  [1983].

**Remark.** There are 3 different Lode angles, as explained online<sup>18</sup>:

$$\sin 3\theta_s = -\sin 3\bar{\theta}_s = \cos 3\theta_c = \frac{3\sqrt{3}}{2} \frac{\mathcal{I}_3(\boldsymbol{\tau})}{(\mathcal{I}_2(\boldsymbol{\tau}))^{3/2}}$$

and they are related by  $\theta_s = \frac{\pi}{6} - \theta_c$  and  $\theta_s = -\bar{\theta}_s$ . The one used in fieldstone is in fact the  $\bar{\theta}_s$  above.

To recap:

$$\sigma_1 = \frac{\mathcal{I}_1(\boldsymbol{\sigma})}{3} + \sqrt{\mathcal{I}_2(\boldsymbol{\tau})} \left( -\frac{1}{\sqrt{3}} \sin \theta + \cos \theta \right) \quad (130)$$

$$\sigma_2 = \frac{\mathcal{I}_1(\boldsymbol{\sigma})}{3} + \sqrt{\mathcal{I}_2(\boldsymbol{\tau})} \left( \frac{2}{\sqrt{3}} \sin \theta \right) \quad (131)$$

$$\sigma_3 = \frac{\mathcal{I}_1(\boldsymbol{\sigma})}{3} + \sqrt{\mathcal{I}_2(\boldsymbol{\tau})} \left( -\frac{1}{\sqrt{3}} \sin \theta - \cos \theta \right) \quad (132)$$

We will later need  $\sigma_1 - \sigma_3$  and  $\sigma_1 + \sigma_3$  so we compute these quantities hereafter:

$$\begin{aligned} \sigma_1 - \sigma_3 &= \sqrt{\mathcal{I}_2(\boldsymbol{\tau})} \left( -\frac{1}{\sqrt{3}} \sin \theta + \cos \theta + \frac{1}{\sqrt{3}} \sin \theta + \cos \theta \right) \\ &= 2 \cos \theta \sqrt{\mathcal{I}_2(\boldsymbol{\tau})} \end{aligned} \quad (133)$$

$$\begin{aligned} \sigma_1 + \sigma_3 &= \frac{\mathcal{I}_1(\boldsymbol{\sigma})}{3} + \sqrt{\mathcal{I}_2(\boldsymbol{\tau})} \left( -\frac{1}{\sqrt{3}} \sin \theta + \cos \theta \right) + \frac{\mathcal{I}_1(\boldsymbol{\sigma})}{3} + \sqrt{\mathcal{I}_2(\boldsymbol{\tau})} \left( -\frac{1}{\sqrt{3}} \sin \theta - \cos \theta \right) \\ &= \frac{2}{3} \mathcal{I}_1(\boldsymbol{\sigma}) - \sqrt{\mathcal{I}_2(\boldsymbol{\tau})} \frac{2}{\sqrt{3}} \sin \theta \end{aligned} \quad (134)$$

or,

$$\frac{\sigma_1 - \sigma_3}{2} = \cos \theta \sqrt{\mathcal{I}_2(\boldsymbol{\tau})} \quad (135)$$

$$\frac{\sigma_1 + \sigma_3}{2} = \frac{1}{3} \mathcal{I}_1(\boldsymbol{\sigma}) - \sqrt{\mathcal{I}_2(\boldsymbol{\tau})} \frac{1}{\sqrt{3}} \sin \theta \quad (136)$$

**Remark.** The expression for the Lode angle is different in [2942, p101] than in [2933] or [2941, p62]. They all look suspiciously wrong too.

### 3.19 Tensor (moment) invariants

There are many different notations used in the literature for invariants and these can prove to be confusing<sup>19</sup>. Note that we only consider symmetric tensors in what follows. Given a tensor  $\mathbf{T}$ , one can compute its (moment) invariants as follows (see [2118, p.339], or Appendix A.2 of [2941])

<sup>18</sup>[https://en.wikipedia.org/wiki/Lode\\_coordinates](https://en.wikipedia.org/wiki/Lode_coordinates)

<sup>19</sup>No kidding, true story.

$$\mathcal{I}_1(\mathbf{T}) = \text{tr}[\mathbf{T}] \quad (137)$$

$$= T_{xx} + T_{yy} + T_{zz} \quad (138)$$

$$\mathcal{I}_2(\mathbf{T}) = \frac{1}{2} \text{tr}[\mathbf{T} \cdot \mathbf{T}] \quad (139)$$

$$= \frac{1}{2} \sum_{ij} T_{ij} T_{ji} \quad (140)$$

$$= \frac{1}{2} (T_{xx}^2 + T_{yy}^2 + T_{zz}^2) + T_{xy}^2 + T_{xz}^2 + T_{yz}^2 \quad (141)$$

$$\mathcal{I}_3(\mathbf{T}) = \frac{1}{3} \text{tr}[\mathbf{T} \cdot \mathbf{T} \cdot \mathbf{T}] \quad (142)$$

$$= \frac{1}{3} \sum_i \sum_j \sum_k T_{ij} T_{jk} T_{ki} \quad (143)$$

$$= \frac{1}{3} (T_{xx}(T_{xx} T_{xx} + T_{xy} T_{xy} + T_{xz} T_{xz})) \quad (i = j = x, k = x, y, z)$$

$$+ \frac{1}{3} (T_{yy}(T_{yx} T_{yx} + T_{yy} T_{yy} + T_{yz} T_{yz})) \quad (i = j = y, k = x, y, z)$$

$$+ \frac{1}{3} (T_{zz}(T_{zx} T_{zx} + T_{zy} T_{zy} + T_{zz} T_{zz})) \quad (i = j = z, k = x, y, z)$$

$$+ \frac{2}{3} (T_{xy}(T_{xx} T_{yx} + T_{xy} T_{yy} + T_{xz} T_{yz})) \quad (i = x, j = y, k = x, y, z)$$

$$+ \frac{2}{3} (T_{xz}(T_{xx} T_{zx} + T_{xy} T_{zy} + T_{xz} T_{zz})) \quad (i = x, j = z, k = x, y, z)$$

$$+ \frac{2}{3} (T_{yz}(T_{yx} T_{zx} + T_{yy} T_{zy} + T_{yz} T_{zz})) \quad (i = y, j = z, k = x, y, z)$$

$$= \frac{1}{3} T_{xx}(T_{xx}^2 + 3T_{xy}^2 + 3T_{xz}^2)$$

$$+ \frac{1}{3} T_{yy}(3T_{xy}^2 + T_{yy}^2 + 3T_{yz}^2)$$

$$+ \frac{1}{3} T_{zz}(3T_{xz}^2 + 3T_{yz}^2 + T_{zz}^2)$$

$$+ 2T_{xy} T_{xz} T_{yz} \quad (144)$$

### 3.20 Stress & strain rate invariants

The implementation of the plasticity criterions relies essentially on the invariants of the (deviatoric) stress  $\boldsymbol{\tau}$  and the (deviatoric) strainrate tensors  $\dot{\boldsymbol{\epsilon}}$ :

$$\mathcal{I}_1(\boldsymbol{\sigma}) = \sigma_{xx} + \sigma_{yy} + \sigma_{zz} \quad (145)$$

$$\mathcal{I}_2(\boldsymbol{\tau}) = \frac{1}{2} (\tau_{xx}^2 + \tau_{yy}^2 + \tau_{zz}^2) + \tau_{xy}^2 + \tau_{xz}^2 + \tau_{yz}^2 \quad (146)$$

$$= \frac{1}{6} [(\sigma_{xx} - \sigma_{yy})^2 + (\sigma_{yy} - \sigma_{zz})^2 + (\sigma_{xx} - \sigma_{zz})^2] + \sigma_{xy}^2 + \sigma_{xz}^2 + \sigma_{yz}^2 \quad (147)$$

$$\begin{aligned} \mathcal{I}_3(\boldsymbol{\tau}) = & \frac{1}{3} \tau_{xx} (\tau_{xx}^2 + 3\tau_{xy}^2 + 3\tau_{xz}^2) \\ & + \frac{1}{3} \tau_{yy} (3\tau_{xy}^2 + \tau_{yy}^2 + 3\tau_{yz}^2) \\ & + \frac{1}{3} \tau_{zz} (3\tau_{xz}^2 + 3\tau_{yz}^2 + \tau_{zz}^2) \\ & + 2\tau_{xy} \tau_{xz} \tau_{yz} \end{aligned} \quad (148)$$

and also the second invariant of the deviatoric strain rate is:

$$\mathcal{I}_2(\dot{\varepsilon}^d) = \frac{1}{2} [(\dot{\varepsilon}_{xx}^d)^2 + (\dot{\varepsilon}_{yy}^d)^2 + (\dot{\varepsilon}_{zz}^d)^2] + (\dot{\varepsilon}_{xy}^d)^2 + (\dot{\varepsilon}_{xz}^d)^2 + (\dot{\varepsilon}_{yz}^d)^2 \quad (149)$$

$$= \frac{1}{6} [(\dot{\varepsilon}_{xx} - \dot{\varepsilon}_{yy})^2 + (\dot{\varepsilon}_{yy} - \dot{\varepsilon}_{zz})^2 + (\dot{\varepsilon}_{xx} - \dot{\varepsilon}_{zz})^2] + \dot{\varepsilon}_{xy}^2 + \dot{\varepsilon}_{xz}^2 + \dot{\varepsilon}_{yz}^2 \quad (150)$$

**Remark.**  $\mathcal{I}_2(\boldsymbol{\tau})$  is often called  $J_2$  or  $J'_2$  so that one sometimes speaks of  $J_2$ -plasticity.

These (second) invariants are almost always used under a square root so we define:

$$\tau_e = \sqrt{\mathcal{I}_2(\boldsymbol{\tau})} \quad \dot{\varepsilon}_e = \sqrt{\mathcal{I}_2(\dot{\varepsilon}^d)}$$

Note that these quantities have the same dimensions as their tensor counterparts, i.e. Pa for stresses and  $\text{s}^{-1}$  for strain rates.

If the stress tensor is such that it is diagonal, i.e.

$$\boldsymbol{\sigma} = \begin{pmatrix} \sigma_1 & 0 & 0 \\ 0 & \sigma_2 & 0 \\ 0 & 0 & \sigma_3 \end{pmatrix} \quad \text{and} \quad \boldsymbol{\tau} = \begin{pmatrix} \tau_1 & 0 & 0 \\ 0 & \tau_2 & 0 \\ 0 & 0 & \tau_3 \end{pmatrix}$$

then the invariants are

$$\begin{aligned} \mathcal{I}_1(\boldsymbol{\sigma}) &= \sigma_1 + \sigma_2 + \sigma_3 \\ \mathcal{I}_2(\boldsymbol{\tau}) &= \frac{1}{6} [(\sigma_1 - \sigma_2)^2 + (\sigma_2 - \sigma_3)^2 + (\sigma_1 - \sigma_3)^2] \end{aligned} \quad (151)$$

$$\begin{aligned} \mathcal{I}_3(\boldsymbol{\tau}) &= \frac{1}{3} \text{tr}[\boldsymbol{\tau} \cdot \boldsymbol{\tau} \cdot \boldsymbol{\tau}] \\ &= \frac{1}{3} \text{tr} \left[ \begin{pmatrix} \tau_1 & 0 & 0 \\ 0 & \tau_2 & 0 \\ 0 & 0 & \tau_3 \end{pmatrix} \cdot \begin{pmatrix} \tau_1 & 0 & 0 \\ 0 & \tau_2 & 0 \\ 0 & 0 & \tau_3 \end{pmatrix} \cdot \begin{pmatrix} \tau_1 & 0 & 0 \\ 0 & \tau_2 & 0 \\ 0 & 0 & \tau_3 \end{pmatrix} \right] \\ &= \frac{1}{3} \text{tr} \begin{pmatrix} \tau_1^3 & 0 & 0 \\ 0 & \tau_2^3 & 0 \\ 0 & 0 & \tau_3^3 \end{pmatrix} \\ &= \frac{1}{3} (\tau_1^3 + \tau_2^3 + \tau_3^3) \\ &= \frac{1}{3} [(\sigma_1 - \mathcal{I}_1(\boldsymbol{\sigma})/3)^3 + (\sigma_2 - \mathcal{I}_1(\boldsymbol{\sigma})/3)^3 + (\sigma_3 - \mathcal{I}_1(\boldsymbol{\sigma})/3)^3] \\ &= \frac{1}{3 \cdot 27} [(3\sigma_1 - \mathcal{I}_1(\boldsymbol{\sigma}))^3 + (3\sigma_2 - \mathcal{I}_1(\boldsymbol{\sigma}))^3 + (3\sigma_3 - \mathcal{I}_1(\boldsymbol{\sigma}))^3] \\ &= \frac{1}{81} [(2\sigma_1 - \sigma_2 - \sigma_3)^3 + (2\sigma_2 - \sigma_1 - \sigma_3)^3 + (2\sigma_3 - \sigma_1 - \sigma_2)^3] \end{aligned} \quad (152)$$

The formulation of the third invariant of  $\boldsymbol{\tau}$  in Eq. 152 is used in Wojciechowski [2802].

NOT SURE AT ALL. One can prove that (REF?)<sup>20</sup>

$$\begin{aligned} \mathcal{I}_3(\boldsymbol{\tau}) &= \frac{1}{27} (2\mathcal{I}_1(\boldsymbol{\sigma})^3 + 9\mathcal{I}_1(\boldsymbol{\sigma})\mathcal{I}_2(\boldsymbol{\sigma}) + 27\mathcal{I}_3(\boldsymbol{\sigma})) \\ &= \det(\boldsymbol{\tau}) \\ &= \tau_1 \tau_2 \tau_3 \end{aligned} \quad (153)$$

---

<sup>20</sup>Near identical equations are to be found at [https://en.wikipedia.org/wiki/Cauchy\\_stress\\_tensor](https://en.wikipedia.org/wiki/Cauchy_stress_tensor)

**Two-dimensional plane strain calculations** The plane strain assumption is such that the problem at hand is assumed to be infinite in a given direction. In the case of computational geodynamics, most 2D modelling is a vertical section of the crust-lithosphere-mantle and the underlying implicit assumption is then that the orogen/rift/subduction/etc ... is infinite in the direction perpendicular to the screen/paper.

For example, let us assume that the deformation takes place in the  $x, y$ -plane. We then have  $\dot{\varepsilon}_{zz} = 0$  as well as  $\dot{\varepsilon}_{xz} = 0$  and  $\dot{\varepsilon}_{yz} = 0$ , so that the strain rate tensor is

$$\dot{\varepsilon} = \begin{pmatrix} \dot{\varepsilon}_{xx} & \dot{\varepsilon}_{xy} & 0 \\ \dot{\varepsilon}_{xy} & \dot{\varepsilon}_{yy} & 0 \\ 0 & 0 & 0 \end{pmatrix}$$

However, very importantly, this does not mean that the stress is zero in the  $z$ -direction! Pressure is isotropic and the stress tensor is then

$$\sigma = -p\mathbf{1} + \tau = \begin{pmatrix} \sigma_{xx} & \sigma_{xy} & 0 \\ \sigma_{xy} & \sigma_{yy} & 0 \\ 0 & 0 & -p \end{pmatrix}$$

However, it is important to keep in mind that the invariants we need to implement the rheologies are  $\mathcal{I}_1(\sigma)$ ,  $\mathcal{I}_2(\tau)$  and  $\mathcal{I}_3(\tau)$ . By formulating our yield surfaces with pressure  $p = -\mathcal{I}_1(\sigma)/3$  we can then avoid confusion, and since the other two invariants are functions of  $\tau$  the pressure term does not pose any problem: simply set  $\tau_{xz}$ ,  $\tau_{yz}$  and  $\tau_{zz}$  to zero in the equations of Section 3.20 and we obtain:

$$\mathcal{I}_2(\tau) = \frac{1}{2}(\tau_{xx}^2 + \tau_{yy}^2) + \tau_{xy}^2 \quad (154)$$

$$\begin{aligned} \mathcal{I}_3(\tau) &= \frac{1}{3}\tau_{xx}(\tau_{xx}^2 + 3\tau_{xy}^2) + \frac{1}{3}\tau_{yy}(3\tau_{xy}^2 + \tau_{yy}^2) \\ &= \frac{1}{3}(\tau_{xx}^3 + 3\tau_{xx}\tau_{xy}^2 + 3\tau_{yy}\tau_{xy}^2 + \tau_{yy}^3) \\ &= \frac{1}{3}(\tau_{xx}^3 + 3(\tau_{xx} + \tau_{yy})\tau_{xy}^2 + \tau_{yy}^3) \\ &= \frac{1}{3}(\tau_{xx}^3 + \tau_{yy}^3) \quad \text{since } \tau_{ii} = 0 \end{aligned} \quad (155)$$

What of all this if the flow is compressible?

### 3.21 Alternative principal stresses notations

The principal stress of the stress tensor  $\sigma$  are  $\sigma_1$ ,  $\sigma_2$  and  $\sigma_3$  with  $\sigma_1 \geq \sigma_2 \geq \sigma_3$ . Following Wojciechowski [2802], we start by stating that the intermediate principal stress can always be represented as a linear combination of two other stresses:

$$\sigma_2 = (1 - b)\sigma_1 + b\sigma_3 \quad \text{where} \quad b = \frac{\sigma_1 - \sigma_2}{\sigma_1 - \sigma_3} \in [0, 1] \quad (156)$$

The quantity  $b$  is called the principal stress ratio. Let us now introduce the maximum shear plane stresses  $\sigma_m$  and  $\tau_m$  such that<sup>21</sup>

$$\sigma_m = \frac{\sigma_1 + \sigma_3}{2} \quad \tau_m = \frac{\sigma_1 - \sigma_3}{2} \quad (157)$$

so that we have

$$\sigma_1 = \sigma_m + \tau_m \quad (158)$$

$$\sigma_2 = \sigma_m - a\tau_m \quad (159)$$

$$\sigma_3 = \sigma_m - \tau_m \quad (160)$$

<sup>21</sup>Although most of this section is inspired by Wojciechowski [2802], I have decided not to use his notations which are very confusing since he denotes  $\sigma_m$  by  $p$

The quantity  $a \in [-1, 1]$  is an equivalent measure of the principal stress ratio and is defined as

$$a = 2b - 1 = 2\frac{\sigma_1 - \sigma_2}{\sigma_1 - \sigma_3} - 1 = \frac{\sigma_1 - 2\sigma_2 + \sigma_3}{\sigma_1 - \sigma_3} \quad (161)$$

We can introduce  $a, p, q$  in the invariants above:

$$\begin{aligned} \mathcal{I}_1(\boldsymbol{\sigma}) &= \sigma_1 + \sigma_2 + \sigma_3 \\ &= (\sigma_m + \tau_m) + (\sigma_m - a\tau_m) + (\sigma_m - \tau_m) \\ &= 3\sigma_m - a\tau_m \end{aligned} \quad (162)$$

$$\begin{aligned} \mathcal{I}_2(\boldsymbol{\tau}) &= \frac{1}{6} [(\sigma_1 - \sigma_2)^2 + (\sigma_2 - \sigma_3)^2 + (\sigma_1 - \sigma_3)^2] \\ &= \frac{1}{6} [(\sigma_m + \tau_m - \sigma_m + a\tau_m)^2 + (\sigma_m - a\tau_m - \sigma_m + \tau_m)^2 + (\sigma_m + \tau_m - \sigma_m + \tau_m)^2] \\ &= \frac{1}{6} [(\tau_m + a\tau_m)^2 + (-a\tau_m + \tau_m)^2 + (\tau_m + \tau_m)^2] \\ &= \frac{\tau_m^2}{6} [(1+a)^2 + (-a+1)^2 + 4] \\ &= \frac{\tau_m^2}{6} [1 + 2a + a^2 + 1 - 2a + a^2 + 4] \\ &= \frac{\tau_m^2}{3} (a^2 + 3) \end{aligned} \quad (163)$$

Using the definition of the third invariant of Eq. (152):

$$\begin{aligned} \mathcal{I}_3(\boldsymbol{\tau}) &= \frac{1}{81} [(2\sigma_1 - \sigma_2 - \sigma_3)^3 + (2\sigma_2 - \sigma_1 - \sigma_3)^3 + (2\sigma_3 - \sigma_1 - \sigma_2)^3] \\ &= \frac{1}{81} [(2\sigma_m + 2\tau_m - \sigma_m + a\tau_m - \sigma_m + \tau_m)^3 + (2\sigma_m - 2a\tau_m - \sigma_m - \tau_m - \sigma_m + \tau_m)^3 + (2\sigma_m - 2\tau_m - \sigma_m - \tau_m)^3] \\ &= \frac{1}{81} [(2\tau_m + a\tau_m + \tau_m)^3 + (-2a\tau_m - \tau_m + \tau_m)^3 + (-2\tau_m - \tau_m + a\tau_m)^3] \\ &= \frac{\tau_m^3}{81} [(3+a)^3 + (-2a)^3 + (-3+a)^3] \\ &= \frac{\tau_m^3}{81} [27 + 9a + 3a^2 + a^3 - 8a^3 - 27 + 9a - 3a^2 + a^3] \\ &= \frac{\tau_m^3}{81} (18a - 6a^3) \\ &= \frac{2a\tau_m^3}{27} (3 - a^2) \end{aligned}$$

which is different than Eq. (14) of Wojciechowski [2802]!!

To recap:

$\mathcal{I}_1(\boldsymbol{\sigma}) = 3\sigma_m - a\tau_m$	$\mathcal{I}_2(\boldsymbol{\tau}) = \frac{\tau_m^2}{3} (a^2 + 3)$	$\mathcal{I}_3(\boldsymbol{\tau}) = \frac{2a\tau_m^3}{27} (3 - a^2)$
--	---	--

(165)

**Remark.** Wojciechowski [2802] defines the Lode angle as being the opposite of my definition in Eq. 120.

Finally, we can show using Eqs. (130,131,132) that

$$\begin{aligned}
a &= \frac{\sigma_1 - 2\sigma_2 + \sigma_3}{\sigma_1 - \sigma_3} \\
&= \frac{\sqrt{\mathcal{I}_2(\boldsymbol{\tau})} \left( -\frac{1}{\sqrt{3}} \sin \theta + \cos \theta \right) - 2\sqrt{\mathcal{I}_2(\boldsymbol{\tau})} \left( \frac{2}{\sqrt{3}} \sin \theta \right) + \sqrt{\mathcal{I}_2(\boldsymbol{\tau})} \left( -\frac{1}{\sqrt{3}} \sin \theta - \cos \theta \right)}{\sqrt{\mathcal{I}_2(\boldsymbol{\tau})} \left( -\frac{1}{\sqrt{3}} \sin \theta + \cos \theta \right) - \sqrt{\mathcal{I}_2(\boldsymbol{\tau})} \left( -\frac{1}{\sqrt{3}} \sin \theta - \cos \theta \right)} \\
&= \frac{\left( -\frac{1}{\sqrt{3}} \sin \theta + \cos \theta \right) - 2 \left( \frac{2}{\sqrt{3}} \sin \theta \right) + \left( -\frac{1}{\sqrt{3}} \sin \theta - \cos \theta \right)}{\left( -\frac{1}{\sqrt{3}} \sin \theta + \cos \theta \right) - \left( -\frac{1}{\sqrt{3}} \sin \theta - \cos \theta \right)} \\
&= \frac{-\frac{6}{\sqrt{3}} \sin \theta}{2 \cos \theta} \\
&= -\frac{3}{\sqrt{3}} \frac{\sin \theta}{\cos \theta} \\
&= -\sqrt{3} \tan \theta
\end{aligned} \tag{166}$$

Here again we arrive at the opposite of Eq. (16) of Wojciechowski [2802].

## 3.22 Rheology in geodynamics

The reader is referred to Barnes [93] for a discussion and review of non-linear viscous rheologies and to Coussot [583] for a review of experimental data for yield stress fluid flows. See also Tanner & Tanner [2504] for a summary of Heinrich Hencky's scientific work on rheology.

Here is a quick recap of notations:

$\boldsymbol{\sigma}$	(full) stress tensor
$\sigma_1, \sigma_2, \sigma_3$	principal stresses
$\boldsymbol{\tau}$	deviatoric stress tensor
$\tau_1, \tau_2, \tau_3$	principal stresses
$\mathcal{I}_1(\boldsymbol{T})$	first invariant of tensor $\boldsymbol{T}$
$\mathcal{I}_2(\boldsymbol{T})$	first invariant of tensor $\boldsymbol{T}$
$\mathcal{I}_3(\boldsymbol{T})$	first invariant of tensor $\boldsymbol{T}$
$\tau_e = \sqrt{\mathcal{I}_2(\boldsymbol{\tau})}$	effective deviatoric stress
$\dot{\varepsilon}_e = \sqrt{\mathcal{I}_2(\dot{\boldsymbol{\varepsilon}}^d)}$	effective deviatoric strain rate

Note that for incompressible flow, the stress tensor is given by  $\boldsymbol{\sigma} = -p\mathbf{1} + \boldsymbol{\tau}$  so that  $\mathcal{I}_1(\boldsymbol{\sigma}) = -p\mathcal{I}_1(\mathbf{1}) + \mathcal{I}_1(\boldsymbol{\tau})$ . Since  $\boldsymbol{\tau}$  is deviatoric, its first invariant is zero. We then have  $\mathcal{I}_1(\boldsymbol{\sigma}) = -pn_D$  where  $n_D$  is the number of dimensions.

### 3.22.1 Linear viscous aka Newtonian

Simply put, a Newtonian fluid is a fluid in which the viscous stresses at every point are linearly proportional to the local strain rate. Mathematically speaking, this means that the fourth-order tensor  $\mathbf{C}$  relating the viscous stress tensor to the strain rate tensor does not depend on the stress state and velocity of the flow.

$$\boldsymbol{\tau} = \mathbf{C} : \dot{\boldsymbol{\varepsilon}}$$

One very often make sthe assumption that the fluid is isotropic, i.e. its mechanical properties are the same along any direction. As a consequence the fourth order viscosity tensor  $\mathbf{C}$  is symmetric and will have only two independent real parameters: a bulk viscosity coefficient, that defines the resistance of the medium to gradual uniform compression; and a dynamic viscosity coefficient  $\eta$  that expresses its resistance to gradual shearing, (we here neglect the so-called rotational viscosity coefficient which results from a coupling between the fluid flow and the rotation of the individual particles).

Rather logically we denote by non-Newtonian fluids with are not Newtonian, i.e. their viscosity (tensor) depends on stress. Such fluids are part of our daily life, e.g. honey, toothpaste, paint, blood, and shampoo. They are also sometimes denoted as Generalized Newtonian Fluid .

### 3.22.2 Power-law model

One of the simplest non-Newtonian viscosity model is the power-law model:

$$\eta = K \dot{\varepsilon}_e^{(n-1)/2} \quad (167)$$

where  $n$  and  $K$  are parameters.  $n$  is called the power-law index.

Note that a Newtonian viscosity is recovered when  $n = 1$ . Also  $n$  and  $K$  may depend on temperature [2118, p339].

 Relevant Literature[786]

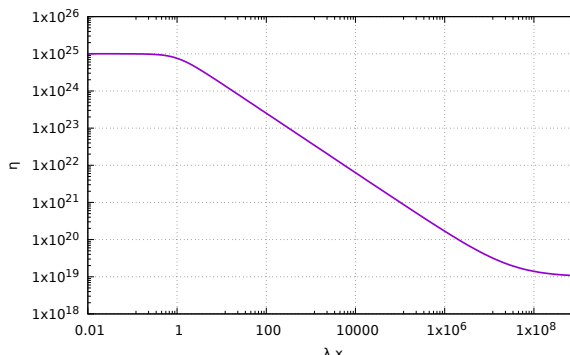
### 3.22.3 Carreau model

Note that this model is sometimes called Bird-Carreau in the literature. As explained in [2118], the power-law model poses no restriction on how small or large the viscosity may become, which may prove problematic once implemented as it can lead to runaway effects (strain rate becomes large  $\rightarrow$  viscosity becomes smaller  $\rightarrow$  strain rate becomes larger, etc ...). This problem is alleviated in the so-called Carreau<sup>22</sup> model [2945]. The viscosity is then given by

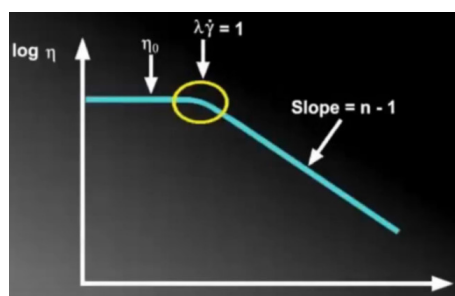
$$\eta = \eta_\infty + (\eta_0 - \eta_\infty) (1 + (\lambda \dot{\varepsilon}_e)^2)^{(n-1)/2} \quad (168)$$

where  $\eta_0$ ,  $\eta_\infty$ ,  $\lambda$  and  $n \in [0, 1]$  are material parameters.  $\lambda$  is called the relaxation time: it is the inverse of the shear rate at which the fluid changes from Newtonian to power-law behavior.

At low strain rate a Carreau fluid behaves as a Newtonian fluid with viscosity  $\eta_0$ . At intermediate strain rates  $\dot{\varepsilon}_e \lambda \sim 1$  a Carreau fluid behaves as a Power-law fluid. At high strain rate, a Carreau fluid behaves as a Newtonian fluid again with viscosity  $\eta_\infty$ .



Carreau model effective viscosity as a function of the product  $\lambda \dot{\varepsilon}_e$



<https://youtu.be/qErs5zZV4BQ>

Note that the (Bird)-Carreau-Yasuda model [1981] is very similar to the standard (Bird)-Carreau:

$$\eta = \eta_\infty + (\eta_0 - \eta_\infty) (1 + (\lambda \dot{\varepsilon}_e)^a)^{(n-1)/a} \quad (169)$$

It is for instance used in [2599].

 Relevant Literature[168, 1713]

<sup>22</sup>[https://en.wikipedia.org/wiki/Carreau\\_fluid](https://en.wikipedia.org/wiki/Carreau_fluid)

### 3.22.4 Bingham model

Bingham fluids can sustain an applied stress without any motion occurring. Only when the applied stress exceeds a yield stress  $\tau_0$  then the fluid flows. This translates as follows [2118]:

$$\boldsymbol{\tau} = \left( \frac{\tau_0}{\dot{\varepsilon}} + 2\eta_0 \right) \dot{\varepsilon}^d \quad \text{if } \tau_e > \tau_0 \quad (170)$$

$$\boldsymbol{\tau} = \mathbf{0} \quad \text{if } \tau_e \leq \tau_0 \quad (171)$$

When flow occurs, the effective viscosity is then given by:

$$\eta_{eff} = \frac{\tau_0}{\dot{\varepsilon}_e} + 2\eta_0$$

and when the strain rate is large we recover a Newtonian behaviour. Typical Bingham fluids are mud, slurry, toothpaste.

When using a velocity-based FEM code, the implementation of this rheological behaviour is complicated by the no-flow condition under a given stress. However, our codes require a relationship between stress and strain rate in the form of an effective viscosity which cannot be zero. This difficulty can be circumvented by implementing Bingham fluids as follows [2118]:

$$\boldsymbol{\tau} = \left( \frac{\tau_0(1 - \eta/\eta_r)}{\dot{\varepsilon}_e} + 2\eta_0 \right) \dot{\varepsilon} \quad \text{if } \tau_e > \tau_0 \quad (172)$$

$$\boldsymbol{\tau} = 2\eta_r \dot{\varepsilon} \quad \text{if } \tau_e \leq \tau_0 \quad (173)$$

where  $\eta_r$  is a pre-yield viscosity and  $\eta/\eta_r \ll 1$  (typically 1% or less). This is a form of regularisation, and we will see a similar one in the next section.

Note the interesting paper by Barnes and Walter (1985) [94] who argue that "the yield stress concept is an idealization, and that, given accurate measurements, no yield stress exists. The simple Cross model is shown to be a useful empiricism for many non-Newtonian fluids, including those which have hitherto been thought to possess a yield stress." The Cross model is presented in Section 3.22.8.

 Relevant Literature: [1992, 207, 1807, 1636, 1689, 2459, 198, 88, 176, 2457]

### 3.22.5 Herschel-Bulkley visco-plastic model

The Herschel-Bulkley model is effectively a combination of the power-law model and a simple plastic model:

$$\boldsymbol{s} = 2 \left( K \dot{\varepsilon}_e^{n-1} + \frac{\tau_0}{\dot{\varepsilon}} \right) \dot{\varepsilon} \quad \text{if } \tau_e > \tau_0 \quad (174)$$

$$\dot{\varepsilon} = \mathbf{0} \quad \text{if } \tau_e \leq \tau_0 \quad (175)$$

in which  $\tau_0$  is the yield stress,  $K$  the consistency, and  $n$  is the flow index general [653]. The flow index measures the degree to which the fluid is shear-thinning ( $n < 1$ ) or shear-thickening ( $n > 1$ ). If  $n = 1$  and  $\tau_0 = 0$  the model reduces to the Newtonian model.

The term between parenthesis above is the nonlinear effective viscosity. Concretely, the implementation goes as follows<sup>23</sup>:

$$\eta_{eff} = \begin{cases} \eta_0 & \dot{\varepsilon}_e \leq \dot{\varepsilon}_0 \\ K \dot{\varepsilon}_e^{n-1} + \frac{\tau_0}{\dot{\varepsilon}_e} & \dot{\varepsilon}_e \geq \dot{\varepsilon}_0 \end{cases}$$

The limiting viscosity  $\eta_0$  is chosen such that  $\eta_0 = K \dot{\varepsilon}_0^{n-1} + \frac{\tau_0}{\dot{\varepsilon}_0}$

A large limiting viscosity means that the fluid will only flow in response to a large applied force. This feature captures the Bingham-type behaviour of the fluid. Note that when strain rates are large, the power-law behavior dominates.

As we have seen for Bingham fluids, the equations above are not easily amenable to implementation so that one usually resorts to regularisation, which is a modification of the equations by introducing a

<sup>23</sup>[https://en.wikipedia.org/wiki/Herschel-Bulkley\\_fluid](https://en.wikipedia.org/wiki/Herschel-Bulkley_fluid)

new material parameter which controls the exponential growth of stress. This way the equation is valid for both yielded and unyielded areas [207, 1992, 2945, 2457]:

$$\eta_{eff} = K\dot{\varepsilon}_e^{n-1} + \frac{\tau_0}{\dot{\varepsilon}_e} [1 - \exp(-m\dot{\varepsilon}_e)] \quad (176)$$

When the strain rate becomes (very) small a Taylor expansion of the regularisation term yields  $1 - \exp(-m\dot{\varepsilon}) \sim m\dot{\varepsilon}$  so that  $\eta_{eff} \rightarrow m\tau_0$ . However, it seems more physically meaningful to replace  $m$  by a reference strain rate value  $\dot{\varepsilon}_0$  so that

$$\eta_{eff} = K\dot{\varepsilon}_e^{n-1} + \frac{\tau_0}{\dot{\varepsilon}_e} \left[ 1 - \exp \left( -\frac{\dot{\varepsilon}_e}{\dot{\varepsilon}_0} \right) \right] \quad (177)$$

In this case, when strain rate becomes (very) small a Taylor expansion of the regularisation term yields

$$\frac{\tau_0}{\dot{\varepsilon}_e} \left[ 1 - \exp \left( -\frac{\dot{\varepsilon}_e}{\dot{\varepsilon}_0} \right) \right] \simeq \frac{\tau_0 \dot{\varepsilon}_e}{\dot{\varepsilon}_e \dot{\varepsilon}_0} = \frac{\tau_0}{\dot{\varepsilon}_0} \quad (178)$$

This has the dimensions of a viscosity and this is effectively the definition of a maximum viscosity  $\eta_{max}$ .

 **Relevant Literature:** [1733, 1679]. Check dam break problem of [34, 519, 87, 2497, 1806]. Also flow through a sudden axisymmetric expansion [1345]. H-B Yield surface [359]. Carbopol, used in analogue models is also a H-B fluid [694].

**(MSc Thesis):** redo the sinking sphere in Bingham or herschel-Bulkley fluid experiment [653, 929].

### 3.22.6 The Casson model

It is described by [93]

$$\sqrt{\sigma} = \sqrt{\sigma_y} + \sqrt{\eta_p \dot{\varepsilon}_e}$$

or, when squaring it:

$$\sigma = \sigma_y + \eta_p \dot{\varepsilon}_e + 2\sqrt{\sigma_y \eta_p \dot{\varepsilon}_e}$$

This modelled has been found to accurately describe the behaviour of synthetic based muds [5].

### 3.22.7 The Ellis model

An Ellis equation would be of the form [2169]

$$\frac{\eta - \eta_\infty}{\eta_0 - \eta_\infty} = \frac{1}{1 + (\sigma/\sigma_c)^m}$$

where  $\sigma$  is the shear stress,  $\sigma_c$  is a critical shear stress and  $m$  is a large number.

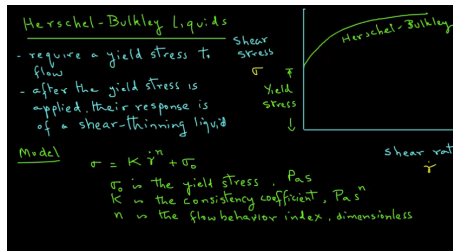
### 3.22.8 One model to rule them all?

Let us consider the base equation

$$\frac{\eta - \eta_\infty}{\eta_0 - \eta_\infty} = [1 + (K\dot{\varepsilon}_e)^a]^{-(1-n)/a}$$

This equation is purposefully generic and specific parameter combination choices allow to recover any of the above models (and more) [1981]. See also an early paper by Cross [597] for a somewhat similar equation.

Similar conclusions are reached in the following video:



<https://youtu.be/dVCbi1dZR7Y>

### 3.22.9 Dislocation and Diffusion creep

The standard dislocation creep effective viscosity is given by:

$$\eta_{eff}^{ds} = \frac{1}{2} f A^{-1/n} \dot{\varepsilon}_e^{(1-n)/n} \exp\left(\frac{Q + pV}{nRT}\right)$$

where  $A$  is the pre-exponential scaling factor,  $f$  is a scaling factor representing viscous weakening or strengthening,  $Q$  is the activation energy,  $V$  is the activation volume,  $T$  is the absolute temperature,  $n$  is the power-law exponent,  $R$  is the universal gas constant.

The coefficients  $A, n, Q, V$  are material parameters and are obtained in the laboratory by means of high pressure/temperature experiments[1383]. Unfortunately these experiments cannot be run at Earth-like strain rate values ( $\sim 10^{-15} \text{s}^{-1}$ ) so that extrapolations must be carried out over several orders of magnitude to arrive at values we can use in our numerical models. The 1/2 factor arises from the relationship between deviatoric stress and strain rate which involves a factor 2.

The factor  $f$  is in fact a tuning parameter used to explore end members (e.g. 'weak crust' vs 'strong crust'), see discussion in the supplementary material in [1256]. This approach has been extensively used by the SOPALE users community, see for instance [2744, 2745, 2746, 1058].

Furthermore, we know that several other factors will strongly affect the rheology:

- water content, or as often mentioned: 'dry' vs 'wet'. Following [1383], dry means water-free and wet means water-saturated conditions.

Mechanism	Dry	Wet
<i>Dislocation creep</i>		
$A (\text{s}^{-1})$	$3.5 \times 10^{22}$	$2.0 \times 10^{18}$
$n$	3.5	3.0
$m$	0	0
$E^* (\text{kJ mol}^{-1})$	540	430
$V^* (\text{cm}^3 \text{mol}^{-1})$	15 to 25†	10 to 20†
<i>Diffusion creep</i>		
$A (\text{s}^{-1})$	$8.7 \times 10^{15}$	$5.3 \times 10^{15}$
$n$	1.0	1.0
$m$	2.5‡	2.5‡
$E^* (\text{kJ mol}^{-1})$	300	240
$V^* (\text{cm}^3 \text{mol}^{-1})$	6§	5§

†The activation volume for dislocation creep is not well constrained. Values from  $13 \text{ cm}^3 \text{mol}^{-1}$  at wet conditions to  $27 \text{ cm}^3 \text{mol}^{-1}$  at nearly dry conditions have been reported (33). Considering this uncertainty, we used a range of activation volumes, 15 to  $25 \text{ cm}^3 \text{mol}^{-1}$  for dry olivine and 10 to  $20 \text{ cm}^3 \text{mol}^{-1}$  for wet olivine. The grain-size exponent is reported as 2 for dry olivine and 3 for wet olivine (16). However, extrapolation to a large grain size, the grain-size exponent may change from 2 to 3 or from 3 to 2 (16). Taking this uncertainty into account, we chose a grain-size exponent of 2.5, and the preexponential factors were modified accordingly. §The activation volume for diffusion is determined as  $6 \text{ cm}^3 \text{mol}^{-1}$  at dry conditions (26). No data are available for the activation volume for diffusion at wet conditions; we assumed that this value is ~80% of the activation volume at dry conditions.

Taken from Karato and Wu [1383].

 Relevant Literature: [2088] and refs therein for the effects of water migration on models of subduction dynamics.

- composition: while one typically assigns olivine properties to the mantle in models, the mineral olivine<sup>24</sup> is actually a magnesium iron silicate with the formula  $(\text{Mg}^{2+}, \text{Fe}^{2+})_2\text{SiO}_4$ . and the ratio of magnesium to iron varies between the two endmembers of the solid solution series: forsterite (Mg-endmember:  $\text{Mg}_2\text{SiO}_4$ ) and fayalite (Fe-endmember:  $\text{Fe}_2\text{SiO}_4$ ).
- grain size: this only affects diffusion creep mechanisms [1383]. Grain size varies over several orders of magnitude and also evolves over time and its evolution is affected by the ambient deformation and the deformation history. Dannberg et al [618] then used a diffusion creep effective viscosity given by:

$$\eta_{eff}^{df} = \frac{1}{2} A_{df}^{-1} d^m \exp\left(\frac{Q_{df} + pV_{df}}{RT}\right)$$

where  $d$  is the (variable) grain size and  $m$  the grain size exponent. Grain growth/evolution is usually approximated using semi-empirical expressions [618, section 2.2]. Smaller grains facilitating faster creep.

Relevant literature on this topic is in Section H.28.

- anisotropy, LPO: see relevant literature in Section H.4.

<sup>24</sup><https://en.wikipedia.org/wiki/Olivine>

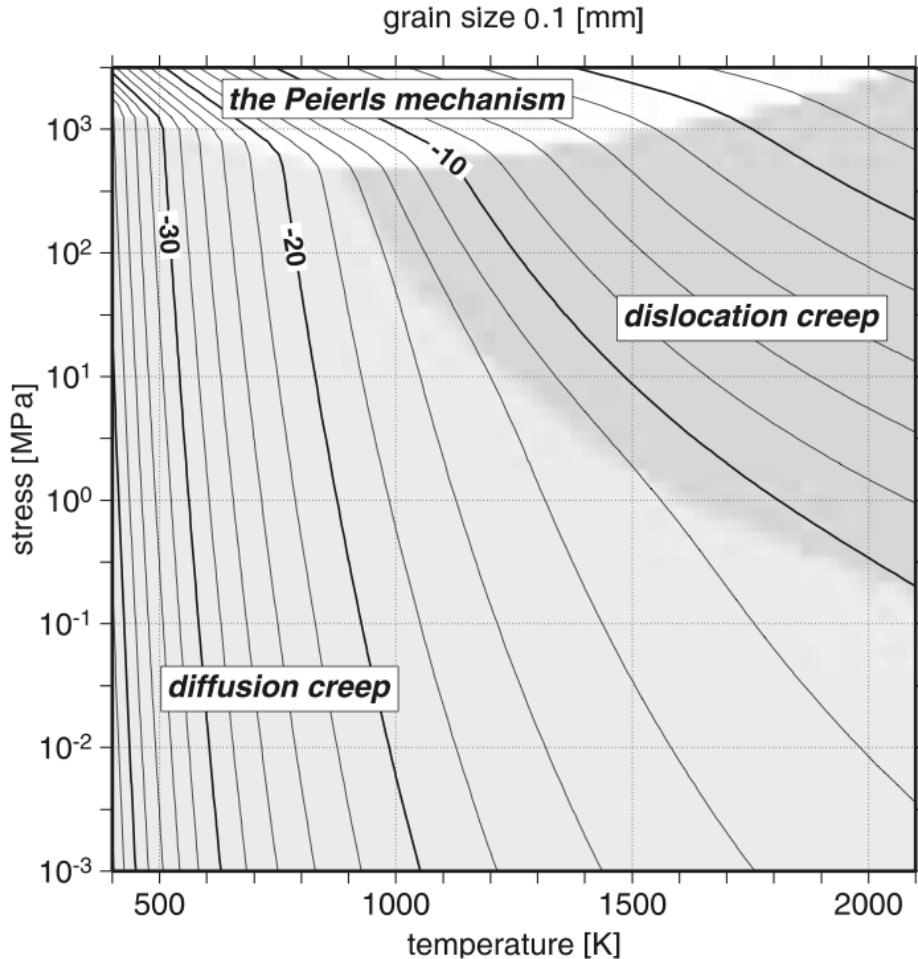
- phase changes:

**Remark.** It is not uncommon to find in the literature effective viscosity formulations written as a function of  $B$  with  $B = A^{-1/n}$  [2744, 2745, 2746]. Also, this  $B$  coefficient often contains the conversion factor of the next remark.

**Remark.** uniaxial stuff An additional coefficient is added to the effective viscosity formula(s ??) [1058, 1060].

$$3^{-(1+n)/2n} 2^{(1-n)/n}$$

[2103]



Deformation mechanism map calculated for grain size  $a = 0.1\text{ mm}$ . The lightly shaded area indicates that deformation mainly occurs by diffusion creep. The densely shaded area indicates that deformation mainly occurs by power-law creep. The white region indicates that deformation mainly occurs by the Peierls mechanism. The solid curves are lines of constant strain rate. The numbers attached to each contour indicate the logarithm of the strain rate in the unit of  $\text{s}^{-1}$  [1374].

**A closer look at the diffusion creep of Karato & Wu (1993)** In the article, the following equation is used:

$$\dot{\varepsilon} = A \left( \frac{\tau}{\mu} \right) \left( \frac{b}{d} \right)^m \exp \left( -\frac{Q + pV}{RT} \right)$$

where  $\mu$  is the shear modulus ( $\sim 80\text{ GPa}$ ),  $b$  is the length of the Burgers vector ( $\sim 0.5\text{ nm}$ ) and  $d$  is the grain size. One can express the above equation in terms of second invariants (see Section 3.19):

$$\dot{\varepsilon}_e = A \left( \frac{\tau_e}{\mu} \right) \left( \frac{b}{d} \right)^m \exp \left( -\frac{Q + pV}{RT} \right)$$

and assuming a Newtonian linearisation/relation between deviatoric stress and strain rate  $\underline{\tau}_e = 2\eta_{df}\dot{\underline{\epsilon}}_e$ , one arrive at

$$\eta_{df} = \frac{1}{2} \left( \frac{A}{\mu} \right)^{-1} \left( \frac{b}{d} \right)^{-m} \exp \left( \frac{Q + pV}{RT} \right)$$

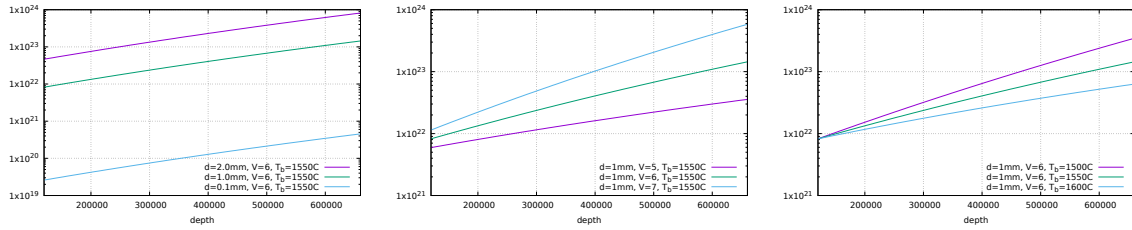
or,

$$\eta_{df} = \frac{1}{2} \left[ \frac{A}{\mu} \left( \frac{b}{d} \right)^m \right]^{-1} \exp \left( \frac{Q + pV}{RT} \right)$$

The effective diffusion creep viscosity is independent of strain-rate so that one could substitute the total pressure for lithostatic pressure in the equation, assume a geotherm and easily compute the predicted viscosity as a function of grain size  $d$ .

Let us assume that the 1D profile starts from the base of the lithosphere (say 120km depth) and ends at the 660 boundary. Assume the temperature to increase linearly from 1300°C to  $T_{bottom}$ . At the bottom of the lithosphere, the lithostatic pressure is of the order of  $\rho \cdot g \cdot L \simeq 3000 \cdot 10 \cdot 120e3 \simeq 4\text{GPa}$ . At the bottom of the domain, the pressure has increased by  $3300 \cdot 10 \cdot 630e3 \simeq 21\text{GPa}$ .

The viscosity profile is plotted hereunder for three different grain sizes, bottom temperature and activation volumes (4,5,6 cm<sup>3</sup>/mol).



Although this exercise only provides us with first-order results, we can conclude that one can essentially change the diffusion creep effective viscosity by up to 2 orders of magnitude simply by choosing key parameters within acceptable ranges.

### 3.22.10 Combining diffusion and dislocation creep

It is rather common in the computational geodynamics to combine both viscosities into one so-called 'effective viscous viscosity' (as opposed to the so-called 'effective plastic viscosity'). The harmonic average is then used:

$$\eta_{eff} = \frac{\eta_{df}\eta_{ds}}{\eta_{df} + \eta_{ds}} = \left( \frac{1}{\eta_{df}} + \frac{1}{\eta_{ds}} \right)^{-1} \quad (179)$$

See for instance [1445].

However, although this formula seems simple enough, it hides an important fact: strain rates are supposed to be additive, i.e. the total strain rate  $\dot{\epsilon}_T$  of the deformation is the sum of the dislocation strain rate  $\dot{\epsilon}_{ds}$  and the diffusion strain rate  $\dot{\epsilon}_{df}$ :

$$\dot{\epsilon}_T = \dot{\epsilon}_{df} + \dot{\epsilon}_{ds}$$

and so are the effective strain rates (the underscore e has been dropped for convenience - see section 3.19 for definitions):

$$\dot{\epsilon}_T = \dot{\epsilon}_{df} + \dot{\epsilon}_{ds}$$

i.e.,

$$\dot{\epsilon}_T = A_{df}\tau \exp \left( -\frac{Q_{df} + pV_{df}}{RT} \right) + A_{ds}\tau^n \exp \left( -\frac{Q_{ds} + pV_{ds}}{RT} \right)$$

where  $\tau$  is the effective shear stress.

We know all the coefficients in this equation with the exception of the scalar  $\tau$  (the total strain rate is obtained from the previous nonlinear iteration velocity or previous time-step velocity) so that it can be cast under the form  $f(\tau) = 0$

$$f(\tau) = \dot{\epsilon}_T - A_{df}\tau \exp \left( -\frac{Q_{df} + pV_{df}}{RT} \right) - A_{ds}\tau^n \exp \left( -\frac{Q_{ds} + pV_{ds}}{RT} \right)$$

A Newton method can be used where the iterations will be of the form:

$$\tau_{n+1} = \tau_n - \frac{f(\tau_n)}{f'(\tau_n)}$$

where the derivative of the function  $f$  with respect to  $\tau$  reads:

$$f'(\tau) = \frac{\partial f}{\partial \tau} = -A_{df} \exp\left(-\frac{Q_{df} + pV_{df}}{RT}\right) - A_{ds} n \tau^{n-1} \exp\left(-\frac{Q_{ds} + pV_{ds}}{RT}\right)$$

Also, from the additivity of strain rates follows the harmonic averaging of viscosities:

$$\dot{\varepsilon}_T = \dot{\varepsilon}_{df} + \dot{\varepsilon}_{ds} \quad \Rightarrow \quad \frac{\tau}{2\eta_{eff}} = \frac{\tau}{2\eta_{df}} + \frac{\tau}{2\eta_{ds}} \quad \Rightarrow \quad \frac{1}{\eta_{eff}} = \frac{1}{\eta_{df}} + \frac{1}{\eta_{ds}}$$

so that the algorithm simply writes:

1. compute  $\tau$  iteratively
2. compute  $\dot{\varepsilon}_{df}$ ,  $\dot{\varepsilon}_{ds}$
3. compute  $\eta_{ds} = \tau/(2\dot{\varepsilon}_{ds})$ ,  $\eta_{df} = \tau/(2\dot{\varepsilon}_{df})$
4. compute  $\eta_{eff}$

Note that one can also directly compute  $\eta_{eff}$  as  $\eta_{eff} = \frac{\tau}{2\dot{\varepsilon}_T}$  since

$$\eta_{eff} = \frac{\tau}{2\dot{\varepsilon}_T} = \frac{\tau}{2\dot{\varepsilon}_{ds} + 2\dot{\varepsilon}_{df}} = \frac{1}{2\dot{\varepsilon}_{ds}/\tau + 2\dot{\varepsilon}_{df}/\tau} = \frac{1}{1/\eta_{ds} + 1/\eta_{df}}$$

In the case where many deformation mechanisms are present, the total strain rate is seen as the sum of the strain rates associated to each mechanism:

$$\dot{\varepsilon}_T = \dot{\varepsilon}_1 + \dot{\varepsilon}_2 + \dot{\varepsilon}_3 + \dots$$

and then

$$\dot{\varepsilon}_T = \dot{\varepsilon}_1 + \dot{\varepsilon}_2 + \dot{\varepsilon}_3 + \dots \quad \Rightarrow \quad \frac{\tau}{2\eta_{eff}} = \frac{\tau}{2\eta_1} + \frac{\tau}{2\eta_2} + \frac{\tau}{2\eta_3} + \dots \quad \Rightarrow \quad \frac{1}{\eta_{eff}} = \frac{1}{\eta_1} + \frac{1}{\eta_2} + \frac{1}{\eta_3} + \dots$$

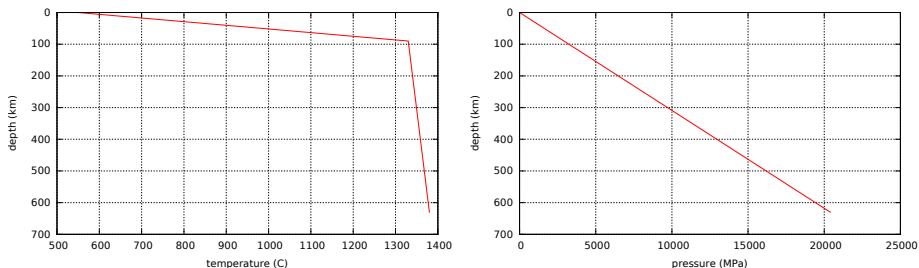
Rather importantly, as we will see hereafter, the following variant is implemented in some codes (e.g. DOUAR, FANTOM, SOPALE) so as to bypass the costly Newton iterations:

1. compute  $\eta_{ds}$  and  $\eta_{df}$  with the *same* strainrate, pressure and temperature values
2. average them by means of an harmonic average

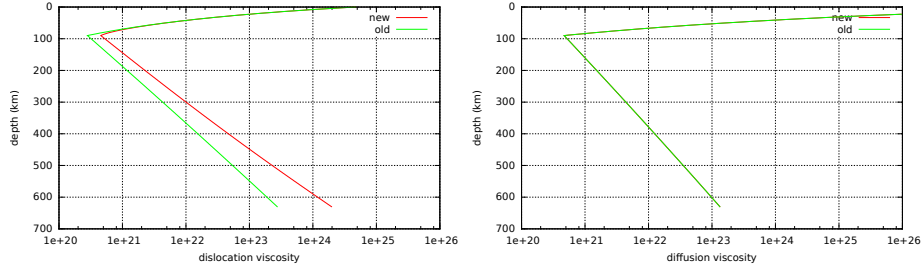
In this case, we have

$$\dot{\varepsilon}_T = A_{df} \tau_{df} \exp\left(-\frac{Q_{df} + pV_{df}}{RT}\right) \quad \dot{\varepsilon}_T = A_{ds} \tau_{ds}^n \exp\left(-\frac{Q_{ds} + pV_{ds}}{RT}\right)$$

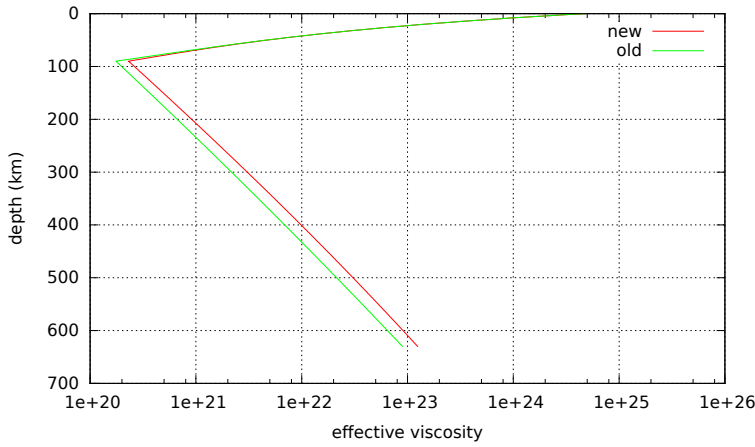
**A concrete example** Let us consider a vertical section of upper mantle, from 660km depth to 30km depth. The lithosphere is assumed to be 90km thick. The temperature at the moho (the top of the domain) is set to 550C, 1330C at the LMB and 1380C at the bottom. A constant strainrate  $\dot{\varepsilon}$  is assumed. The density is set to a constant 3300kg/m<sup>3</sup> and we assume a lithostatic pressure. The temperature and pressure fields are shown hereunder:



In what follows, the values obtained with Newton iterations are coined 'new' and those obtained without are coined 'old'. The diffusion and dislocation creep viscosities can be computed for both old and new algorithms and are shown hereunder (the diffusion creep viscosity is independent of strain rate so is the same for both):



Using the algorithm highlighted hereabove we can compute the composite effective viscosity and compare it with the 'standard' effective viscosity:



look at folder, codes, clean up, change labels new and old

### 3.22.11 The von Mises failure criterion

The von Mises yield criterion suggests that the yielding of materials begins when the second deviatoric stress invariant  $\mathcal{I}_2(\boldsymbol{\tau})$  reaches a critical value. For this reason, it is sometimes called the  $J_2$ -plasticity or  $J_2$  flow theory<sup>25</sup>. It is part of a plasticity theory that applies best to ductile materials, such as metals.

In material science and engineering the von Mises yield criterion can be also formulated in terms of the von Mises stress or equivalent tensile stress,  $\sigma_v$ , a scalar stress value that can be computed from the stress tensor. In this case, a material is said to start yielding when its von Mises stress reaches a critical value known as the yield strength,  $\sigma_Y$ . The von Mises stress is used to predict yielding of materials under any loading condition from results of simple uniaxial tensile tests. The von Mises stress satisfies the property that two stress states with equal distortion energy have equal von Mises stress.

Because the von Mises yield criterion is independent of the first stress invariant,  $\mathcal{I}_1(\boldsymbol{\sigma})$ , it is applicable for the analysis of plastic deformation for ductile materials such as metals, as the onset of yield for these materials does not depend on the hydrostatic component of the stress tensor.

Although formulated by Maxwell in 1865, it is generally attributed to von Mises [2713]. Huber (1904), in a paper in Polish, anticipated to some extent this criterion. Heinrich Hencky formulated the same criterion as von Mises independently in 1924 [1172, 2504]. This criterion is also referred to as the Maxwell-Huber-Hencky-von Mises theory.

The von Mises yield criterion (also known as Prandtl-Reuss yield criterion) is expressed in the principal stresses as

$$\sqrt{\mathcal{I}_2(\boldsymbol{\tau})} = c \quad \text{or,} \quad \frac{1}{6}[(\sigma_1 - \sigma_2)^2 + (\sigma_2 - \sigma_3)^2 + (\sigma_3 - \sigma_1)^2] = c^2$$

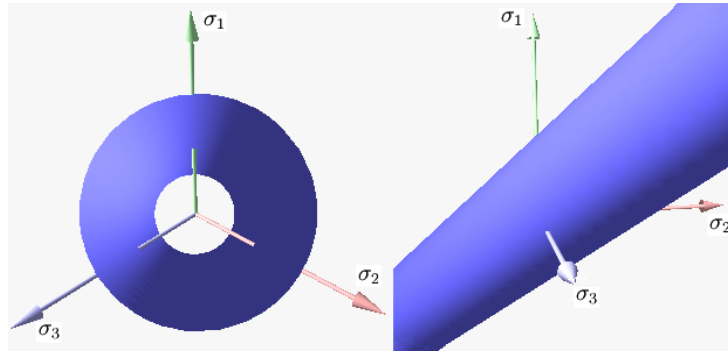
<sup>25</sup> $J_2$  is the common notation for  $\mathcal{I}_2(\boldsymbol{\tau})$

where  $c$  is the yield stress in uniaxial tension. The von Mises yield criterion writes:

$$F^{\text{VM}} = \sqrt{\mathcal{I}_2(\boldsymbol{\tau})} - c \quad (180)$$

which is the Drucker-Prager criterion with  $\phi = 0$ .

The following figure shows the von Mises yield surface in the three-dimensional space of principal stresses.



It is a circular cylinder of infinite length with its axis inclined at equal angles to the three principal stresses.

Relevant Literature: [1992, 2542]

**The yield surface** Let us try to draw the yield function in the space  $\sigma_1, \sigma_2, \sigma_3$ . It is given by

$$\sqrt{\mathcal{I}_2(\boldsymbol{\tau})} = c \quad (181)$$

$$\Rightarrow \mathcal{I}_2(\boldsymbol{\tau}) = c^2 \quad (182)$$

$$\Rightarrow \frac{1}{6} [(\sigma_1 - \sigma_2)^2 + (\sigma_2 - \sigma_3)^2 + (\sigma_1 - \sigma_3)^2] = c^2 \quad (183)$$

$$\Rightarrow (\sigma_1 - \sigma_2)^2 + (\sigma_2 - \sigma_3)^2 + (\sigma_1 - \sigma_3)^2 = 6c^2 \quad (184)$$

or, temporarily setting  $x = \sigma_1$ ,  $y = \sigma_2$  and  $z = \sigma_3$ :

$$(x - y)^2 + (y - z)^2 + (x - z)^2 = 6c^2 \quad (185)$$

$$(x - y)^2 + y^2 - 2yz + z^2 + x^2 - 2xz + z^2 = 6c^2 \quad (186)$$

$$2z^2 - 2(x + y)z + (x - y)^2 + x^2 + y^2 - 6c^2 = 0 \quad (187)$$

This is a second order polynomial in  $z$ . Its discriminant  $\Delta$  is

$$\begin{aligned} \Delta &= 4(x + y)^2 - 4 \cdot 2 \cdot [(x - y)^2 + x^2 + y^2 - 6c^2] \\ &= 4x^2 + 8xy + 4y^2 - 8[x^2 - 2xy + y^2 + x^2 + y^2 - 6c^2] \\ &= 4x^2 + 8xy + 4y^2 - 8[2x^2 - 2xy + 2y^2 - 6c^2] \\ &= 4x^2 + 8xy + 4y^2 - 16x^2 + 16xy - 16y^2 + 48c^2 \\ &= -12x^2 + 24xy - 12y^2 + 48c^2 \\ &= -12(x^2 - 2xy + y^2) + 48c^2 \\ &= -12(x - y)^2 + 48c^2 \end{aligned}$$

Since I am looking for  $z(x, y) \in \mathbb{R}$  then  $\Delta > 0$  and this imposes a restriction on admissible  $x, y$  pairs:

$$-12(x - y)^2 + 48c^2 > 0$$

$$(x - y)^2 < 4c^2$$

$$x - y < 2c \quad \text{or,} \quad y - x < 2c$$

$$y > x - 2c \quad \text{or,} \quad y < x + 2c$$

So the discriminant is positive in the band given by  $y > x - 2c$  and  $y < x + 2c$  in the  $x, y$ -plane, which is a band centered around the line  $y = x$ . When  $\Delta > 0$  we have then

$$z = \frac{2(x+y) \pm \sqrt{\Delta}}{4}$$

which means that for each pair  $x, y$  there are 2  $z$  values. The middle of this surface is given by the line  $z = (x+y)/2$ . The plane normal to this line is given by  $z = -2(x+y)$ .

This approach is reasonably simple for the von Mises criterion but quickly becomes untractable for other criteria.

### 3.22.12 The Tresca failure criterion

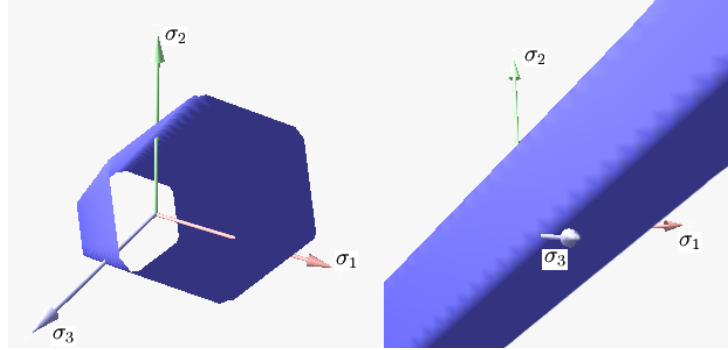
The Tresca or maximum shear stress yield criterion is taken to be the work of Henri Tresca. It is also referred as the Tresca-Guest (TG) criterion. The functional form of this yield criterion is

$$f(\sigma_1, \sigma_2, \sigma_3) = 0$$

In terms of the principal stresses the Tresca criterion is expressed as

$$\max(|\sigma_1 - \sigma_2|, |\sigma_2 - \sigma_3|, |\sigma_3 - \sigma_1|) = c$$

The following figure shows the Tresca-Guest yield surface in the three-dimensional space of principal stresses.



It is a prism of six sides and having infinite length. This means that the material remains viscous when all three principal stresses are roughly equivalent (a hydrostatic pressure), no matter how much it is compressed or stretched. However, when one of principal stresses becomes smaller (or larger) than the others the material is subject to shearing. In such situations, if the shear stress reaches the yield limit then the material enters the plastic domain.

**Remark.** *The yield function presents sharp corners, making its numerical implementation more difficult (directional derivatives are needed)*

We have already established in Eq. 135:

$$\sigma_1 - \sigma_3 = 2\sqrt{I_2(\boldsymbol{\tau})} \cos \theta$$

with  $\sigma_1 > \sigma_2 > \sigma_3$ , so that the failure criterion is given by

$$F^{\text{TR}} = 2\sqrt{I_2(\boldsymbol{\tau})} \cos \theta - c$$

Relevant Literature: [2542]

### 3.22.13 The Mohr-Coulomb failure criterion

Mohr-Coulomb theory is a model describing the response of a material such as rubble piles or concrete to shear stress as well as normal stress. Most of the classical engineering materials somehow follow this rule in at least a portion of their shear failure envelope. In geology it is used to define shear strength of soils at different effective stresses [1133].

In structural engineering it is used to determine failure load as well as the angle of fracture of a displacement fracture in concrete and similar materials. Coulomb's friction hypothesis is used to determine the combination of shear and normal stress that will cause a fracture of the material. Mohr's circle is used to determine which principal stresses that will produce this combination of shear and normal stress, and the angle of the plane in which this will occur. According to the principle of normality the stress introduced at failure will be perpendicular to the line describing the fracture condition.

The Mohr-Coulomb failure criterion represents the linear envelope that is obtained from a plot of the shear strength of a material versus the applied normal stress. This relation is expressed as [1983, p219]

$$\tau_m = -\sigma_m \sin \phi + c \cos \phi \quad (188)$$

where  $\tau_m$  is the magnitude of the shear stress,  $\sigma_m$  is the normal stress,  $c$  is the intercept of the failure envelope with the  $\tau$  axis, and  $\phi$  is the slope of the failure envelope. The quantity  $c$  is often called the cohesion and the angle  $\phi$  is called the angle of internal friction.

We have

$$\tau_m = \frac{\sigma_1 - \sigma_3}{2} \quad \sigma_m = \frac{\sigma_1 + \sigma_3}{2}$$

with  $\sigma_1$  is the maximum principal stress and  $\sigma_3$  is the minimum principal stress, or

$$\frac{\sigma_1 - \sigma_3}{2} = -\frac{\sigma_1 + \sigma_3}{2} \sin \phi + c \cos \phi$$

Using Eqs. (135) and (136) for  $(\sigma_1 - \sigma_3)/2$  and  $(\sigma_1 + \sigma_3)/2$ :

$$\begin{aligned} \frac{\sigma_1 - \sigma_3}{2} &= -\frac{\sigma_1 + \sigma_3}{2} \sin \phi + c \cos \phi \\ \Rightarrow \sqrt{\mathcal{I}_2(\boldsymbol{\tau})} \cos \theta &= -\left(\frac{1}{3}\mathcal{I}_1(\boldsymbol{\sigma}) - \sqrt{\mathcal{I}_2(\boldsymbol{\tau})}\frac{1}{\sqrt{3}} \sin \theta\right) \sin \phi + c \cos \phi \\ \Rightarrow \frac{1}{3}\mathcal{I}_1(\boldsymbol{\sigma}) \sin \phi + \sqrt{\mathcal{I}_2(\boldsymbol{\tau})} \left(\cos \theta - \frac{1}{\sqrt{3}} \sin \theta \sin \phi\right) &- c \cos \phi = 0 \end{aligned}$$

$$F^{\text{MC}} = \frac{1}{3}\mathcal{I}_1(\boldsymbol{\sigma}) \sin \phi + \sqrt{\mathcal{I}_2(\boldsymbol{\tau})} \left(\cos \theta - \frac{1}{\sqrt{3}} \sin \theta \sin \phi\right) - c \cos \phi \quad (189)$$

This formula (without the cohesion) is used in [2786]. Since  $p = -\frac{1}{3}\mathcal{I}_1(\boldsymbol{\sigma})$ , we also have:

$$F^{\text{MC}} = \sqrt{\mathcal{I}_2(\boldsymbol{\tau})} \left(\cos \theta - \frac{1}{\sqrt{3}} \sin \theta \sin \phi\right) - (p \sin \phi + c \cos \phi) \quad (190)$$

**Remark.** The expression for  $F$  in the Mohr-Coulomb case in [2933] contains errors which is later corrected in [2942, p102].



Relevant Literature: this criterion is also used in computer graphics animation [2928]

### 3.22.14 The Drucker-Prager failure criterion

The von Mises yield criterion is not suitable for modelling the yielding of frictional material as it does not include the effect of mean stress as observed in experiments. To overcome this limitation, Drucker and Prager [720] proposed a revised function for frictional materials.

The Drucker-Prager yield criterion has the function form

$$F^{DP}(\boldsymbol{\sigma}) = F(\mathcal{I}_1(\boldsymbol{\sigma}), \mathcal{I}_2(\boldsymbol{\tau})) = 0 \quad (191)$$

This criterion is most often used for concrete where both normal and shear stresses can determine failure. The Drucker-Prager yield criterion may be expressed as

$$F^{DP} = \sqrt{\mathcal{I}_2(\boldsymbol{\tau})} + \alpha \mathcal{I}_1(\boldsymbol{\sigma}) + k = 0 \quad (192)$$

Using the parameters  $\sigma_m$ ,  $\tau_m$ ,  $a = -\sqrt{3} \tan \theta$ ,  $\mathcal{I}_1(\boldsymbol{\sigma})$  and  $\mathcal{I}_2(\boldsymbol{\tau})$  of Section 3.21 we have

$$\begin{aligned} F^{DP} &= \sqrt{\mathcal{I}_2(\boldsymbol{\tau})} + \alpha \mathcal{I}_1(\boldsymbol{\sigma}) + k \\ &= \sqrt{\frac{\tau_m^2}{3}(a^2 + 3)} + \alpha(3\sigma_m - a\tau_m) + k \\ &= \tau_m \sqrt{(a^2/3 + 1)} + \alpha(3\sigma_m + \tau_m \sqrt{3} \tan \theta) + k \quad (\text{since } \tau_m > 0) \\ &= \tau_m \sqrt{\tan^2 \theta + 1} + \alpha(3\sigma_m + \tau_m \sqrt{3} \tan \theta) + k \\ &= \tau_m \sqrt{\frac{1}{\cos^2 \theta}} + \alpha(3\sigma_m + \tau_m \sqrt{3} \tan \theta) + k \\ &= \tau_m \frac{1}{\cos \theta} + \alpha(3\sigma_m + \tau_m \sqrt{3} \tan \theta) + k \quad (\text{since } \cos \theta > 0) \end{aligned}$$

$F = 0$  then leads to write

$$\begin{aligned} \tau_m + (3\alpha\sigma_m + k) \cos \theta + \tau_m \alpha \sqrt{3} \sin \theta &= 0 \\ \Rightarrow \tau_m(1 + \alpha \sqrt{3} \sin \theta) + (3\alpha\sigma_m + k) \cos \theta &= 0 \end{aligned}$$

and finally

$$\tau_m = -\frac{(3\alpha\sigma_m + k) \cos \theta}{1 + \alpha \sqrt{3} \sin \theta} = -\frac{3\alpha \cos \theta}{1 + \alpha \sqrt{3} \sin \theta} \sigma_m - \frac{k \cos \theta}{1 + \alpha \sqrt{3} \sin \theta}$$

**Remark.** This is the same equation as Eq. 19 of Wojciechowski [2802] but with  $\theta \rightarrow -\theta$ .

The Mohr-Coulomb yield criterion writes (see Eq. (188))

$$\tau_m = -\sigma_m \sin \phi + c \cos \phi$$

so that equating both expressions of  $\tau_m$  for the Drucker-Prager and Mohr-Coulomb criteria leads to:

$$-\frac{3\alpha \cos \theta}{1 + \alpha \sqrt{3} \sin \theta} = -\sin \phi \quad (193)$$

$$-\frac{k \cos \theta}{1 + \alpha \sqrt{3} \sin \theta} = c \cos \phi \quad (194)$$

Eq. (193) yields

$$\begin{aligned} 3\alpha \cos \theta &= \sin \phi(1 + \alpha \sqrt{3} \sin \theta) \\ \Rightarrow 3\alpha \cos \theta - \alpha \sqrt{3} \sin \theta \sin \phi &= \sin \phi \end{aligned}$$

and finally

$$\alpha(\phi) = \frac{\sin \phi}{3 \cos \theta - \sqrt{3} \sin \theta \sin \phi}$$

Inserting this into Eq. (194):

$$\begin{aligned}
-k \cos \theta &= c \cos \phi \left( 1 + \alpha \sqrt{3} \sin \theta \right) \\
&= c \cos \phi \left( 1 + \frac{\sin \phi}{3 \cos \theta - \sqrt{3} \sin \theta \sin \phi} \sqrt{3} \sin \theta \right) \\
&= c \cos \phi \left( 1 + \frac{\sqrt{3} \sin \phi \sin \theta}{3 \cos \theta - \sqrt{3} \sin \theta \sin \phi} \right) \\
&= c \cos \phi \left( \frac{3 \cos \theta - \sqrt{3} \sin \theta \sin \phi}{3 \cos \theta - \sqrt{3} \sin \theta \sin \phi} + \frac{\sqrt{3} \sin \phi \sin \theta}{3 \cos \theta - \sqrt{3} \sin \theta \sin \phi} \right) \\
&= c \cos \phi \left( \frac{3 \cos \theta}{3 \cos \theta - \sqrt{3} \sin \theta \sin \phi} \right)
\end{aligned}$$

so that

$$k(c, \phi) = -\frac{3 c \cos \phi}{3 \cos \theta - \sqrt{3} \sin \theta \sin \phi}$$

The Drucker-Prager yield criterion which for a given  $\theta$  is equal to the Mohr-Coulomb yield is then:

$$\begin{aligned}
F^{\text{DP}} &= \sqrt{\mathcal{I}_2(\boldsymbol{\tau})} + \alpha(\phi) \mathcal{I}_1(\boldsymbol{\sigma}) + k(c, \phi) \\
&= \sqrt{\mathcal{I}_2(\boldsymbol{\tau})} + \frac{\sin \phi}{3 \cos \theta - \sqrt{3} \sin \theta \sin \phi} \mathcal{I}_1(\boldsymbol{\sigma}) - \frac{3 c \cos \phi}{3 \cos \theta - \sqrt{3} \sin \theta \sin \phi} \\
&= \sqrt{\mathcal{I}_2(\boldsymbol{\tau})} - \left[ -\frac{3 \sin \phi}{3 \cos \theta - \sqrt{3} \sin \theta \sin \phi} \frac{\mathcal{I}_1(\boldsymbol{\sigma})}{3} + \frac{3 c \cos \phi}{3 \cos \theta - \sqrt{3} \sin \theta \sin \phi} \right] \quad (195) \\
&= \sqrt{\mathcal{I}_2(\boldsymbol{\tau})} - \left[ \frac{3 p \sin \phi}{3 \cos \theta - \sqrt{3} \sin \theta \sin \phi} + \frac{3 c \cos \phi}{3 \cos \theta - \sqrt{3} \sin \theta \sin \phi} \right] \\
&= \sqrt{\mathcal{I}_2(\boldsymbol{\tau})} - \frac{3 p \sin \phi + 3 c \cos \phi}{3 \cos \theta - \sqrt{3} \sin \theta \sin \phi} \\
&= \sqrt{\mathcal{I}_2(\boldsymbol{\tau})} - \frac{p \sin \phi + c \cos \phi}{\cos \theta - \frac{1}{\sqrt{3}} \sin \theta \sin \phi} \quad (196)
\end{aligned}$$

which, when multiplied by  $\cos \theta - \frac{1}{\sqrt{3}} \sin \theta \sin \phi$ , gives the Mohr-Coulomb criterion of Eq. (189).

For  $\theta = \pi/6$ , the DP yield surface **circumscribes** the MC yield surface and Eq. (195) writes:

$$\begin{aligned}
F^{\text{DP}} &= \sqrt{\mathcal{I}_2(\boldsymbol{\tau})} - \left[ -\frac{3 \sin \phi}{3\sqrt{3}/2 - \sqrt{3}/2 \sin \phi} \frac{\mathcal{I}_1(\boldsymbol{\sigma})}{3} + \frac{3 c \cos \phi}{3\sqrt{3}/2 - \sqrt{3}/2 \sin \phi} \right] \\
&= \sqrt{\mathcal{I}_2(\boldsymbol{\tau})} - \left[ -\frac{6 \sin \phi}{\sqrt{3}(3 - \sin \phi)} \frac{\mathcal{I}_1(\boldsymbol{\sigma})}{3} + \frac{6 c \cos \phi}{\sqrt{3}(3 - \sin \phi)} \right] \\
&= \sqrt{\mathcal{I}_2(\boldsymbol{\tau})} - \frac{6 p \sin \phi + 6 c \cos \phi}{\sqrt{3}(3 - \sin \phi)} \quad (197)
\end{aligned}$$

which is the formula used in Glerum et al (2018) [1002].

For  $\theta = -\pi/6$ , the DP yield surface **middle circumscribes** the MC yield surface and Eq. (195) writes:

$$\begin{aligned}
F^{\text{DP}} &= \sqrt{\mathcal{I}_2(\boldsymbol{\tau})} - \left[ -\frac{3 \sin \phi}{3\sqrt{3}/2 + \sqrt{3}/2 \sin \phi} \frac{\mathcal{I}_1(\boldsymbol{\sigma})}{3} + \frac{3 c \cos \phi}{3\sqrt{3}/2 + \sqrt{3}/2 \sin \phi} \right] \\
&= \sqrt{\mathcal{I}_2(\boldsymbol{\tau})} - \left[ -\frac{6 \sin \phi}{\sqrt{3}(3 + \sin \phi)} \frac{\mathcal{I}_1(\boldsymbol{\sigma})}{3} + \frac{6 c \cos \phi}{\sqrt{3}(3 + \sin \phi)} \right] \\
&= \sqrt{\mathcal{I}_2(\boldsymbol{\tau})} - \frac{6 p \sin \phi + 6 c \cos \phi}{\sqrt{3}(3 + \sin \phi)} \quad (198)
\end{aligned}$$

Another DP formulation which **incribes** the MC yield surface is found on the wikipedia page of the Drucker-Prager yield criterion<sup>26</sup> (but I have no idea how it is arrived at):

$$F^{\text{DP}} = \sqrt{\mathcal{I}_2(\boldsymbol{\tau})} - \left[ -\frac{3 \sin \phi}{\sqrt{9 + 3 \sin^2 \phi}} \frac{\mathcal{I}_1(\boldsymbol{\sigma})}{3} + \frac{3 c \cos \phi}{\sqrt{9 + 3 \sin^2 \phi}} \right] \quad (199)$$

The yield surfaces of these three Drucker-Prager formulations are plotted against the Mohr-Coulomb yield surface in Section 3.22.17.

**Remark.** Leroy & Ortiz [1589] use the Drucker-Prager plasticity model also and match it to the Mohr-Coulomb model in the triaxial test and formulate it as follows (Their definition of the second invariant of stress contains a 3/2 term):

$$\begin{aligned} F &= \tau_e \sqrt{3} + \frac{6 \sin \phi}{3 - \sin \phi} \left( -p - \frac{c}{\tan \phi} \right) \\ &= \tau_e \sqrt{3} - \left( \frac{6 \sin \phi}{3 - \sin \phi} p + c \frac{6 \cos \phi}{3 - \sin \phi} \right) \\ &= \sqrt{3} \left[ \tau_e - \left( \frac{6 \sin \phi}{\sqrt{3}(3 - \sin \phi)} p + c \frac{6 \cos \phi}{\sqrt{3}(3 - \sin \phi)} \right) \right] \end{aligned} \quad (200)$$

Except for the  $\sqrt{3}$  this is identical to Eq. (197).

**Remark.** Bui et al (2008) [322] use yet again another formulation:

$$\begin{aligned} F &= \sqrt{\mathcal{I}_2(\boldsymbol{\tau})} + \frac{\tan \phi}{\sqrt{9 + 12 \tan^2 \phi}} \mathcal{I}_1(\boldsymbol{\sigma}) - \frac{3c}{\sqrt{9 + 12 \tan^2 \phi}} \\ &= \sqrt{\mathcal{I}_2(\boldsymbol{\tau})} + \frac{\sin \phi}{\sqrt{9 \cos^2 \phi + 12 \sin^2 \phi}} \mathcal{I}_1(\boldsymbol{\sigma}) - \frac{3c \cos \phi}{\sqrt{9 \cos^2 \phi + 12 \sin^2 \phi}} \\ &= \sqrt{\mathcal{I}_2(\boldsymbol{\tau})} + \frac{\sin \phi}{\sqrt{9 + 3 \sin^2 \phi}} \mathcal{I}_1(\boldsymbol{\sigma}) - \frac{3c \cos \phi}{\sqrt{9 + 3 \sin^2 \phi}} \end{aligned}$$

which is identical to (199).

**Remark.** Cacace & Jacquay (2017) [400] replace  $\sqrt{\mathcal{I}_2(\boldsymbol{\tau})}$  by  $\sqrt{\mathcal{I}_2(\boldsymbol{\tau}) + \epsilon_0^2}$  where  $\epsilon_0$  is a small non-hardening parameter here introduced to relax the singularity at the cones tip of the Drucker-Prager yield envelope.

---

<sup>26</sup>[https://en.wikipedia.org/wiki/Drucker-Prager\\_yield\\_criterion](https://en.wikipedia.org/wiki/Drucker-Prager_yield_criterion)

### 3.22.15 The Griffith-Murrell failure criterion

The Griffith-Murrell yield criterion [273, 276, 102] is not often used. Extending the work of Griffith (1921) to three dimensional stress distributions, Murrell (1963) suggested the following criterion for rock failure expressed in terms of the principal stresses:

$$(\sigma_1 - \sigma_2)^2 + (\sigma_2 - \sigma_3)^2 + (\sigma_3 - \sigma_1)^2 + 24T_0(\sigma_1 + \sigma_2 + \sigma_3) = 0$$

where  $T_0$  is a material property called the tensile strength. In principal stress space, this criterion is represented by a paraboloid of revolution around the pressure (or hydrostatic) axis.

Using the definition of  $\mathcal{I}_2(\boldsymbol{\tau})$  and  $\mathcal{I}_1(\boldsymbol{\sigma})$ , it also writes:

$$\mathcal{I}_2(\boldsymbol{\tau}) - 12T_0 p = 0$$

which is the formulation used in Hansen et al (2000) [1137], although the authors use the lithostatic pressure instead of the full pressure. They also use a tensile strength parameter  $T_0^e$  and a compressive strength parameter  $T_0^c$ , both around a few tens of MPas.

### 3.22.16 The Cam-clay failure criterion

The Original Cam-Clay model is based on the assumption that the soil is isotropic, elasto-plastic, deforms as a continuum, and it is not affected by creep.

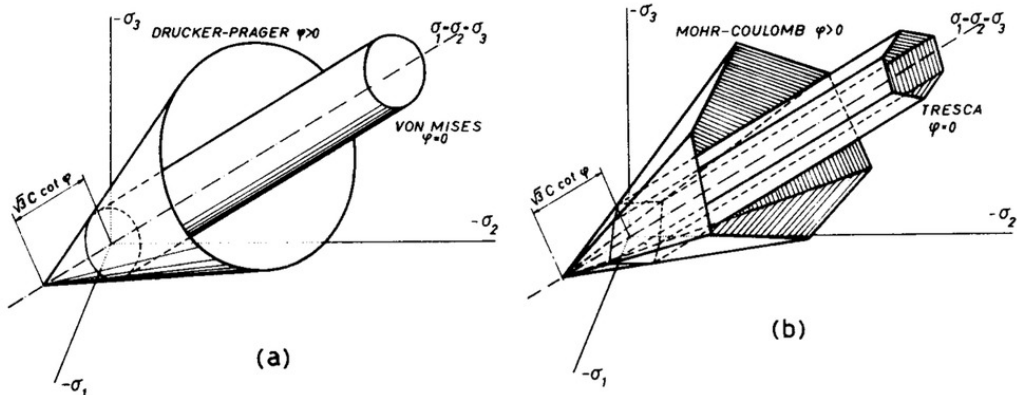
 Relevant Literature: [2011]

### 3.22.17 The failure envelope, or yield surface

 Relevant Literature: Schöpfer et al (2013) [2283].

A yield surface is a five-dimensional surface in the six-dimensional space of stresses. The state of stress of inside the yield surface is elastic. When the stress state lies on the surface the material is said to have reached its yield point and the material is said to have become plastic. Further deformation of the material causes the stress state to remain on the yield surface, even though the surface itself may change shape and size as the plastic deformation evolves, this is because stress states that lie outside the yield surface are non-permissible.

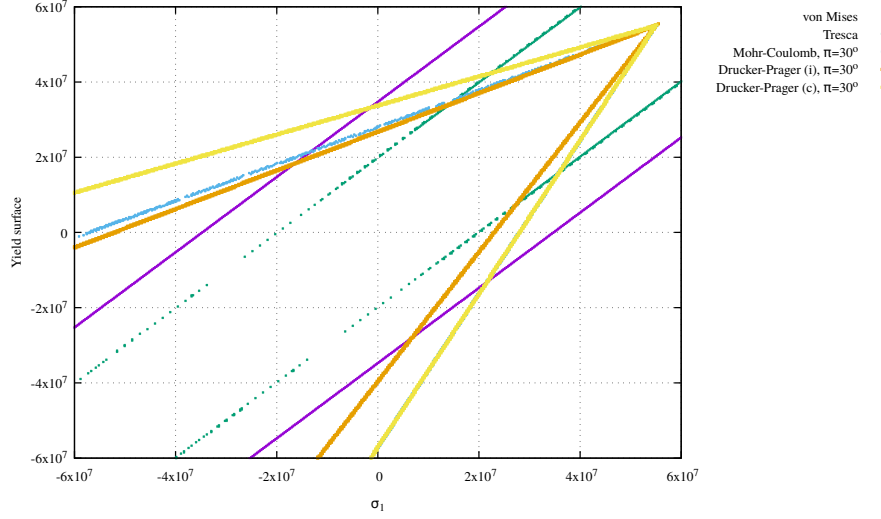
The yield surface is usually expressed in terms of (and visualized in) a three-dimensional principal stress space  $(\sigma_1, \sigma_2, \sigma_3)$ , a two- or three-dimensional space spanned by stress invariants or a version of the three-dimensional Haigh-Westergaard space.



Having obtained the equations for the yield functions in the previous sections, we can easily test them as follows: in the  $(\sigma_1, \sigma_2, \sigma_3)$  space we can look for stress states that fulfill the yield equations. I set  $c = 20\text{MPa}$  and  $\phi = 20^\circ$  and restrain the search to the space  $[-100\text{MPa}:100\text{Mpa}]^3$ . The python code and the gnuplot script used to generate the plots hereafter are in `images/rheology/surfaces`. The

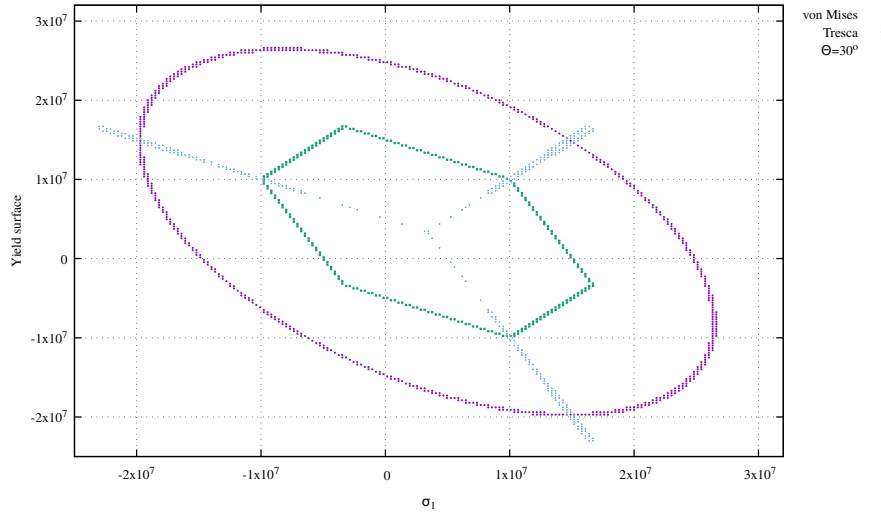
implemented algorithm is somewhat naive and quite inefficient: discretise the space in  $N^3$  points and for each point check whether any of the von Mises, Tresca, Mohr-Coulomb and (the three variants of) Drucker-Prager is satisfied and when the point is in the space  $\sigma_1 + \sigma_2 + \sigma_3 = 10\text{Mpa}$  (perpendicular to the  $x = y = z$  line) write it to the corresponding file.

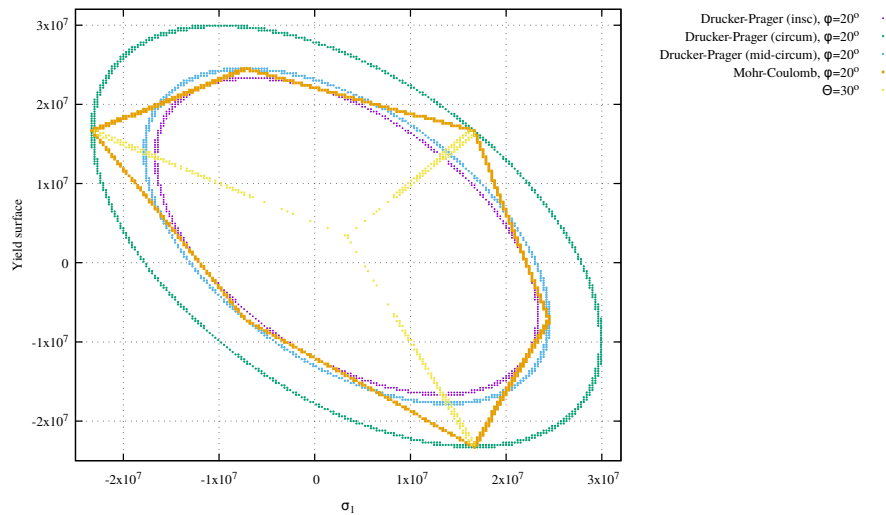
The recovered surfaces are similar to those of the figure above but their plot in a 3D space is difficult. I have therefore isolated two sub-plots. The first one is for  $\sigma_1 = \sigma_2$ :



We see that the von Mises and Tresca envelopes are parallel to the line  $\sigma_1 = \sigma_2 = \sigma_3$  (which is expected since they do not depend on pressure).

The second plot is in the plane  $\sigma_1 + \sigma_2 + \sigma_3 = 0$  which is perpendicular to the middle line  $\sigma_1 = \sigma_2 = \sigma_3 = 0$ . To facilitate plotting the envelopes are plotted as a function of  $\sigma_1$  only (so that even though they are circles in the chosen plane they appear here as ellipses):





We see that we indeed recover that the three Drucker-Prager formulations inscribe (purple), middle-circumscribe (blue) and circumscribe (green) the Mohr-Coulomb one.

### 3.22.18 Peierls creep

Looking at the literature, there seems to be many formulations for the Peierls creep deformation mechanism but it appears that a standard formulation for the Peierls creep writes:

$$\dot{\epsilon} = A\sigma^n \exp \left[ -\frac{Q+pV}{RT} \left( 1 - \left( \frac{\sigma}{\sigma_P} \right)^k \right)^q \right]$$

and it seems common to take  $k = 1$ , and  $n = 2$  [953, 1389]

$$\dot{\epsilon} = A\sigma^2 \exp \left[ -\frac{Q+pV}{RT} \left( 1 - \frac{\sigma}{\sigma_P} \right)^q \right]$$

In Chenin et al. (2019) [456] the authors state that their Peierls creep implementation relies on parameters from Evans and Goetze (1979) [798] using the approach of Kameyama et al (1999) [1374]:

$$\eta^{pe} = \frac{2}{3} \frac{(1-s)/s}{(1+s)/2s} A (\varepsilon_e^{ds})^{\frac{1}{n}-1}$$

with  $A$  for this formulation:

$$A = \left[ A_p \exp \left( -\frac{Q(1-\gamma)^2}{RT} \right) \right]^{-1/s} \gamma \sigma_p$$

where  $s$  is an effective stress exponent that depends on the temperature:

$$s = 2\gamma \frac{Q}{RT} (1-\gamma)$$

where  $\gamma$  is a fitting parameter.

 Relevant Literature[69, 377, 824, 918, 953, 1014, 1389, 1407, 1379, 1771, 2906, 455, 2331] Review article from 1966: Guyot & Dorn [1108]

### 3.22.19 Stress limiting rheology

Taken from [2646]:

$$\eta_y = \tau_y \dot{\epsilon}_y^{-1/n_y} \dot{\epsilon}^{(1/n_y)-1}$$

where the yield stress  $\tau_y$ , the yield strain rate  $\dot{\epsilon}_y$  and the yield exponent  $n_y$  are prescribed parameters. In this article,  $n_y = 10$ ,  $\dot{\epsilon}_y = 10^{-15} s^{-1}$ . When  $n_y = 1$  the viscosity is constant and given by  $\tau_y \dot{\epsilon}_y^{-1/n_y}$ .

### 3.22.20 Arrhenius law

A purely temperature-dependent dimensional Arrhenius law that emulates the temperature dependence of viscosity in silicate rock is often employed for mantle rocks [15, 2882, 2635, 251, 1910, 2411, 211, 1080]:

$$\eta(T) = \eta_0 \exp \left( \frac{Q}{R} \left( \frac{1}{T} - \frac{1}{T_0} \right) \right) \quad \text{or} \quad \eta(T) = \eta_0 \exp \left( \frac{Q}{RT} \right) \quad (201)$$

where  $\eta_0$  is a reference viscosity and  $T_0$  its corresponding reference temperature.

It can also account for pressure effects as in [1668] where the diffusion creep viscosity (under the assumption of homogeneous grain size) is temperature- and pressure-dependent:

$$\eta(T) = \eta_0 \exp \left( \frac{1}{R} \left( \frac{Q-pV}{T} - \frac{Q}{T_0} \right) \right)$$

(I find the minus sign rather suspicious)

### 3.22.21 Simple parametrisation of the mantle

Many CITCOMs-based publications [340, 339] have used the following (dimensionless) viscosity for the mantle:

$$\eta(T, z) = \eta_r(r) \exp(A(0.5 - T))$$

where  $\eta_r$  is a depth dependent viscosity profile (usually defined as discontinuous linear profiles for various shells)

The non-dimensional activation coefficient is chosen to be  $A = 9.2103$  in [339] which leads to a temperature-induced viscosity contrast of  $10^4$  (for  $T \in [0, 1]$ ).

This is also called the Frank-Kamenetskii flow rule, as used in [2411, 1543]:

$$\eta' = \eta_0 \exp(-\theta T)$$

where the parameters  $\eta_0, \theta$  account for the local chemical composition of the rock.

Another temperature-dependent common expression is as follows [843]:

$$\eta(T) = \eta_\infty \exp\left(\frac{Q}{R}\left(\frac{1}{T} - \frac{1}{T_\infty}\right)\right)$$

Also, following [843]: For studying transient convection in a non-Newtonian rheological fluid, it is expedient from a computational point of view to employ a law which behaves linearly for low stresses initially and becomes gradually non-Newtonian only after a certain threshold stress level has been surpassed [481, 489]:

$$\eta(T, p, \tau_2) = \eta(T, p) \frac{1}{A_2 + A_3 \tau_2^2}$$

where  $A_2$  is a parameter describing the linear creep at low stress levels and  $A_3$  governs the transition stress between Newtonian and non-Newtonian rheologies.

Coltice and Sheppard (2018) [551] use a depth- and temperature-dependent viscosity formulation:

$$\eta(z, T) = \eta_0(z) \exp \frac{Q}{RT}$$

Note that this expression is supplemented with a pseudo-plastic formulation [2187].

 Relevant Literature: [1445]

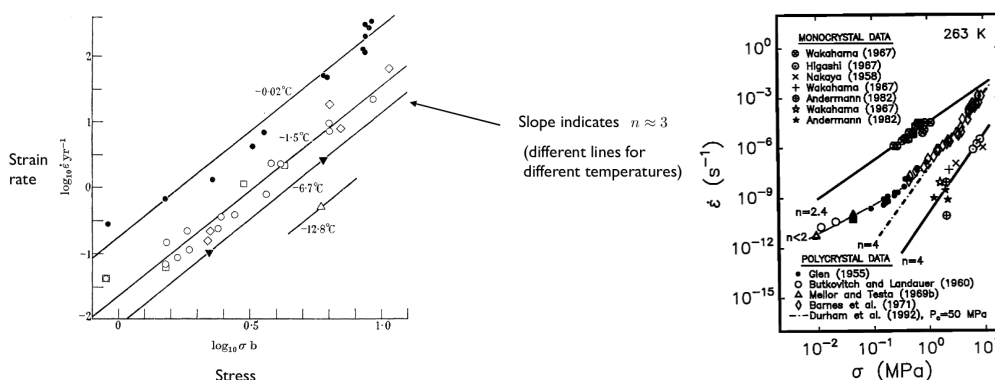
### 3.22.22 Glen's law for ice

As it turns out, ice and rocks share similarities in terms of rheology. Glens law is the most commonly used flow law for ice in glaciers and ice sheets [1001] and it is actually a power-law type rheology:

$$\dot{\varepsilon} = A \tau^n$$

with  $n \sim 3$  and  $A \sim 2.4 \cdot 10^{-24} \text{ Pa}^{-3} \cdot \text{s}^{-1}$  at  $0^\circ\text{C}$ . The effective viscosity is then given by

$$\eta = \frac{1}{2A\tau_e^{n-1}}$$



Left: Taken from Glen [1001]; Right: taken from [1023].

Most of these studies suggest values of the power-law exponent  $n \sim 2 - 4$ , and there seems to be a general indication that the exponent is lower at lower stresses.

The  $A$  coefficient above has been found to depend on temperature and is reasonably described with an Arrhenius law:

$$A(T) = A_0 \exp\left(-\frac{Q}{RT}\right)$$

A standard formulation is the Paterson-Budd law with a fixed Glen exponent  $n = 3$  and a split Arrhenius term [1995]:

$$A = 3.615 \cdot 10^{-13} \text{ Pa}^{-3} \cdot \text{s}^{-1}, \quad Q = 60 \text{ kJ/mol}, \quad \text{if } T < 263\text{K}$$

$$A = 1.733 \cdot 10^3 \text{ Pa}^{-3} \cdot \text{s}^{-1}, \quad Q = 139 \text{ kJ/mol}, \quad \text{if } T > 263\text{K}$$

Be careful that in these two equations the temperature  $T$  is the pressure-adjusted temperature [1995].

Note that  $A$  is also affected by the water content and the presence of impurities.

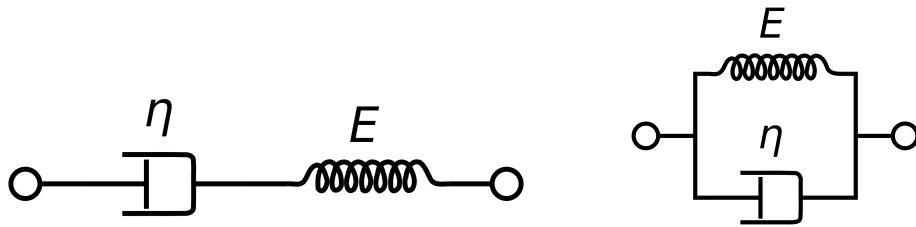
Finally, Glen's law is the standard rheology used for ice-sheet modelling but it does not account for the complex evolution of fabric and resulting anisotropy.

 Relevant Literature[1066, 1502, 1067, 1287, 1170]

### 3.22.23 Viscoelasticity

It is the property of materials that exhibit both viscous and elastic characteristics when undergoing deformation. Two main models prevail: the Maxwell model and the Kelvin-Voigt model.

The Maxwell model can be represented by a purely viscous damper and a purely elastic spring connected in series, as shown in the following figure.



Left: Maxwell mode. Right: Kelvin-Voigt mode.

Images taken from <https://en.wikipedia.org/wiki/Viscoelasticity>

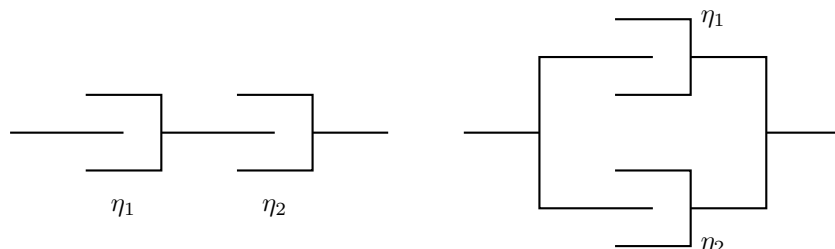
The Kelvin-Voigt model, also known as the Voigt model, consists of a Newtonian damper and Hookean elastic spring connected in parallel

 Relevant Literature: [222]

### 3.22.24 Elasto+Visco+Plasticity ?

When multiple viscous deformation mechanisms are present, one needs more dashpots, and more complicated element diagrams than the ones above occur (also when adding plastic deformation). Two important rules are to be remembered:

- for parallel components, stresses are additive, strain rates are equal in each.
- for components in series, stresses are equal in each and strain rates are additive.



- two viscous dampers in series: each is subjected to the same stress  $\tau$  but deforms with its own strain rate  $\dot{\varepsilon}_1$  and  $\dot{\varepsilon}_2$  and we have

$$\dot{\varepsilon}_T = \dot{\varepsilon}_1 + \dot{\varepsilon}_2 = \frac{\tau}{2\eta_1} + \frac{\tau}{2\eta_2} \quad (202)$$

The effective viscosity of this combination is denoted  $\eta_{eff}$  and is such that  $\eta_{eff} = \tau/2\dot{\varepsilon}_T$ , which means that

$$\frac{\tau}{2\dot{\varepsilon}_T} = \frac{\tau}{2\eta_1} + \frac{\tau}{2\eta_2}$$

or,

$$\eta_{eff} = \left( \frac{1}{\eta_1} + \frac{1}{\eta_2} \right)^{-1}$$

i.e. it follows that the effective viscosity of two or more viscous dampers in series is the harmonic average of the individual viscosities of the dampers.

In general, for  $n$  dampers in series:

$$\eta_{eff} = \left( \sum_{i=1}^n \frac{1}{\eta_i} \right)^{-1}$$

- two viscous dampers in parallel: each is deforms with the same strain rate  $\dot{\varepsilon}_T$  and their stresses add up:

$$\tau = \tau_1 + \tau_2 = 2\eta_1\dot{\varepsilon}_T + 2\eta_2\dot{\varepsilon}_T$$

and since we define the effective viscosity as  $\tau = 2\eta_{eff}\dot{\varepsilon}_T$  then it follows:

$$2\eta_{eff}\dot{\varepsilon}_T = 2\eta_1\dot{\varepsilon}_T + 2\eta_2\dot{\varepsilon}_T$$

or,

$$\eta_{eff} = \eta_1 + \eta_2$$

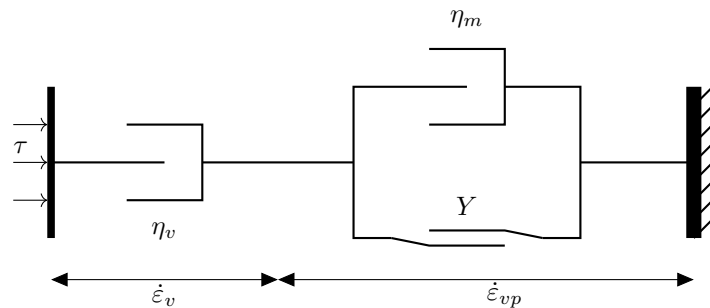
i.e., the effective viscosity of two or more viscous dampers is the sum of their viscosities (*but not their arithmetic mean!*).

- one viscous damper and a plastic element in parallel: the effective viscosity is then

$$\eta_{eff} = \frac{Y}{2\dot{\varepsilon}_T} + \eta_m$$

which is the viscosity of a Bingham fluid (see Section 3.22.4).

- two viscous dampers and a plastic element arranged as follows:



This rheology would be called visco-viscoplastic. The algorithm goes then as follows:

1. Assume we know  $\eta_v$  and  $\dot{\varepsilon}_T$  (from previous iteration), as well as the plasticity parameters  $Y$  and  $\eta_m$ .
2. if  $2\eta_v\dot{\varepsilon}_T < Y$  the stress is below the yield stress value and plasticity is not active. Use  $\eta_v$  in the material model and  $\dot{\varepsilon}_v = \dot{\varepsilon}_T$ .

3. if  $2\eta_v\dot{\varepsilon}_T > Y$  the stress is above the yield value, which is not allowed. In this case the plastic element is 'switched on'. In that case the viscous damper is in series with the (visco)plastic element. The former deforms with a strain rate  $\dot{\varepsilon}_v$  while the latter with  $\dot{\varepsilon}_{vp}$  (both under the same stress  $\tau$ ) and we have  $\dot{\varepsilon}_T = \dot{\varepsilon}_v + \dot{\varepsilon}_{vp}$ .

$$\begin{aligned}
\dot{\varepsilon}_T &= \dot{\varepsilon}_v + \dot{\varepsilon}_{vp} \\
&= \dot{\varepsilon}_v + \frac{\tau}{2\eta_{vp}} \\
&= \dot{\varepsilon}_v + \frac{\tau}{2\left(\frac{Y}{2\dot{\varepsilon}_{vp}} + \eta_m\right)} \\
&= \dot{\varepsilon}_v + \frac{\tau}{2\left(\frac{Y}{2(\dot{\varepsilon}_T - \dot{\varepsilon}_v)} + \eta_m\right)} \\
\dot{\varepsilon}_T - \dot{\varepsilon}_v &= \frac{\tau}{2\left(\frac{Y}{2(\dot{\varepsilon}_T - \dot{\varepsilon}_v)} + \eta_m\right)} \\
2(\dot{\varepsilon}_T - \dot{\varepsilon}_v)\left(\frac{Y}{2(\dot{\varepsilon}_T - \dot{\varepsilon}_v)} + \eta_m\right) &= \tau \\
Y + 2(\dot{\varepsilon}_T - \dot{\varepsilon}_v)\eta_m &= \tau \\
Y + 2(\dot{\varepsilon}_T - \frac{\tau}{2\eta_v})\eta_m &= \tau \\
Y + (2\eta_v\dot{\varepsilon}_T - \tau)\frac{\eta_m}{\eta_v} &= \tau \\
Y + 2\eta_m\dot{\varepsilon}_T &= \tau(1 + \frac{\eta_m}{\eta_v})
\end{aligned}$$

and finally

$$\tau = \frac{Y + 2\eta_m\dot{\varepsilon}_T}{1 + \frac{\eta_m}{\eta_v}} \quad (203)$$

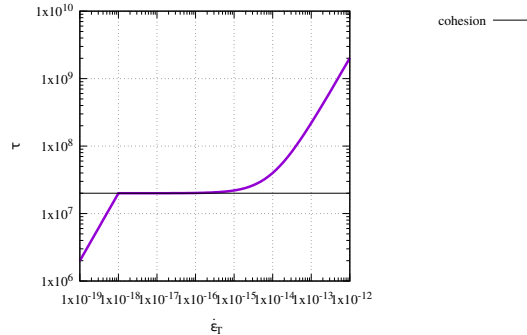
Note that this solution exists even when  $\eta_m = 0$ , and then rather logically  $\tau = Y$ .

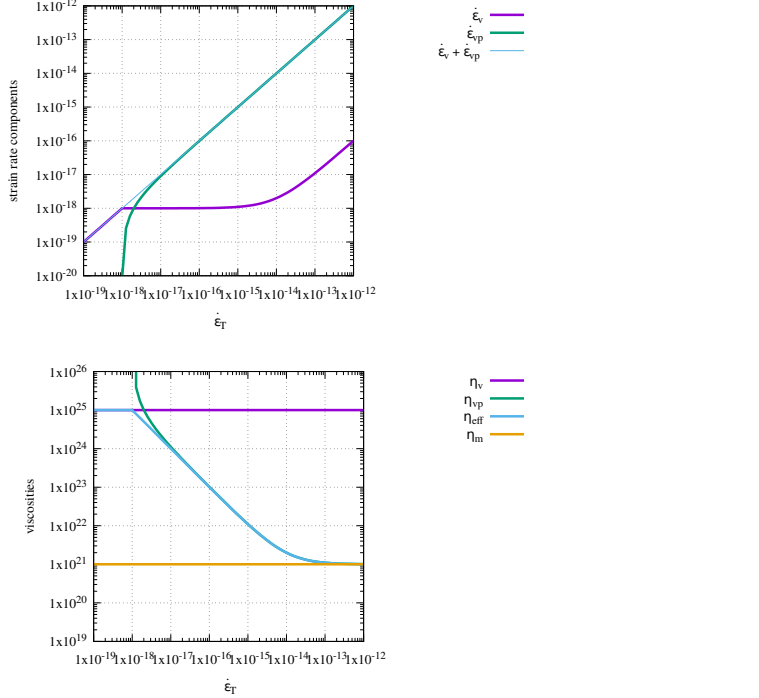
4. Once we have  $\tau$ , we can easily compute  $\dot{\varepsilon}_v = \frac{\tau}{2\eta_v}$
5. We then compute  $\dot{\varepsilon}_{vp} = \dot{\varepsilon}_T - \dot{\varepsilon}_v$  which we use to compute  $\eta_{vp} = Y/2\dot{\varepsilon}_{vp} + \eta_m$
6. Having obtained  $\eta_{vp}$  we can compute the final effective viscosity

$$\eta_{eff} = \left( \frac{1}{\eta_v} + \frac{1}{\eta_{vp}} \right)^{-1}$$

images/rheology/vvp

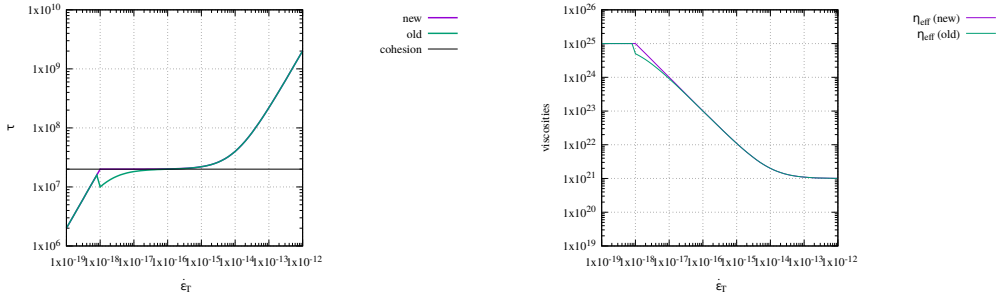
On the following plots are shown  $\tau$ ,  $\dot{\varepsilon}_{vp}$ ,  $\dot{\varepsilon}_v$ ,  $\eta_{vp}$ , and  $\eta_{eff}$  as a function of  $\dot{\varepsilon}_T$ :





Obtained for  $\eta_m = 10^{21}$ ,  $Y = 20\text{MPa}$  and  $\eta_v = 10^{25}$ . Python code in images/rheology/vvp/

In the following plots the resulting stress  $\tau$  and effective viscosities  $\eta_{eff}$  are compared between the above approach ('new') and the simpler (and naive) approach where  $\dot{\epsilon}_T$  is used in  $\eta_{vp}$  instead of  $\dot{\epsilon}$  ('old'). In this particular case we see that it makes a difference at low strain rates close to the brittle-ductile transition.



Obtained for  $\eta_m = 10^{21}$ ,  $Y = 20\text{MPa}$  and  $\eta_v = 10^{25}$ . Python code in images/rheology/vvp/

**Remark.** *The introduction of the damper  $\eta_m$  in parallel with the plastic element has an unavoidable effect: the stress  $\tau$  becomes larger than  $Y$  at high strain rate values! Since the vp block is akin to a bingham fluid, this is no surprise.*

Following Chenin et al (2019) [456], one can base the rheological model on the additive decomposition of the deviatoric strain rate tensor  $\boldsymbol{\epsilon}^d$ :

$$\boldsymbol{\epsilon}^d = \boldsymbol{\epsilon}^{el} + \boldsymbol{\epsilon}^{pl} + \boldsymbol{\epsilon}^{ds} + \boldsymbol{\epsilon}^{df} + \boldsymbol{\epsilon}^{pe}$$

where the five strain rate terms correspond respectively to the elastic, plastic, and viscous creep (dislocation, diffusion, peierls) contributions. This implies that all these elements are in series and the associated viscosities are then averaged with an harmonic mean. Rather interestingly, it is then stated that "this strain rate equation is nonlinear and solved locally on cell centroids and vertices in order to define the current effective viscosity and stress [2054]."

Relevant Literature: [1209, 1666, 1208, 2262, 1660, 42, 764]

### 3.22.25 Anisotropic viscosity

Following the paper by Lev and Hager (2008) [1592], the anisotropic viscosity enters the equation of momentum through a 'correction' term added to the isotropic part of the constitutive equation relating stress and strain rate [1877]:

$$\sigma_{ij} = -p\delta_{ij} + 2\eta_N \dot{\varepsilon}_{ij} - 2(\eta_N - \eta_S)\Lambda_{ijkl}\dot{\varepsilon}_{kl}$$

where  $\eta_N$  is the normal viscosity and  $\eta_S$  is the shear viscosity. The fourth order tensor  $\Lambda$  reflects the orientation of the directors in space, denoted by  $\vec{n}$ :

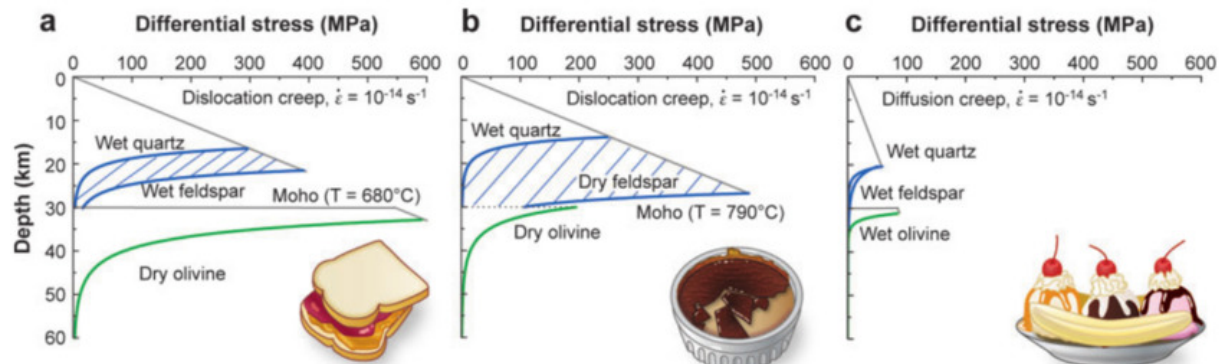
$$\Lambda_{ijkl} = \frac{1}{2}(n_i n_k \delta_{lj} + n_j n_k \delta_{il} + n_i n_l \delta_{kj} n_j n_l \delta_{ik}) - 2n_i n_j n_k n_l$$

Following [1842, 1877], the 'directors' are advected through the model and are analogous to particles. The directors are vector-particles pointing normal to the easy-glide plane or layer, thus defining the directions associated with  $\eta_N$  and  $\eta_S$ . In each time step of the calculation, the directors are advected and rotated by the flow, and in return determine the viscosity structure for the next time step [1876].

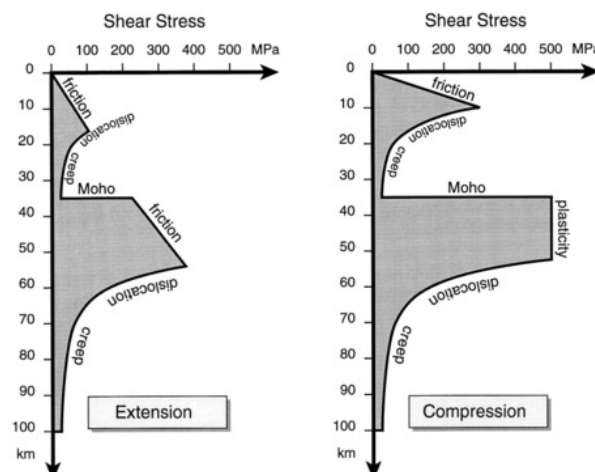
(MSc Thesis): redo the Rayleigh-Taylor instabilities with anisotropic lithospheric viscosity. experiments of Lev & Hager (2008) [1592].

 Relevant Literature: [1877, 2688, 1876, 1877, 1787, 2159, 2219]

### 3.22.26 Rheology of the lithosphere



Schematic view of the three most common first order rheological models of the continental lithosphere under a strain rate of  $10^{-14} \text{ s}^{-1}$ . In all three models the upper crust has its frictional strength increased with pressure and depth. (a) The jelly sandwich model has a weak mid-lower crust and a strong mantle composed of dry olivine. (b) The crème brûlée model assumes that the mantle is weak, due to the presence of water and high temperature deformation, and the dry and brittle crust determines the strength of the lithosphere. (c) The banana split model assumes that the lithosphere as a whole has its strength greatly reduced due to various strain weakening and feedback processes [358]



Taken from [203]. Typical vertical distribution of maximum shear stress in continental lithosphere undergoing compressional (right) or extensional (left) strain at  $10^{-15}$ s. Friction controls level of shear stress in upper part of crust and sometimes in mantle lithosphere; then, below brittle/ductile transition, shear stress is controlled by thermally-activated dislocation creep.

### Relevant Literature[375, 358, 2106, 2104]

I need to talk about Byerlee's law. [398]

## 3.23 Moment of inertia

Consider a rigid body rotating with fixed angular velocity  $\omega$  about an axis which passes through the origin. Let  $\mathbf{r}_i$  be the position vector of the  $i$ th mass element, whose mass is  $m_i$ . We expect this position vector to precess about the axis of rotation (which is parallel to  $\omega$ ) with angular velocity  $\omega$ .

$$\frac{d\mathbf{r}_i}{dt} = \boldsymbol{\omega} \times \mathbf{r}_i.$$

Thus, the above equation specifies the velocity,  $\mathbf{v}_i = d\mathbf{r}_i/dt$ , of each mass element as the body rotates with fixed angular velocity  $\omega$  about an axis passing through the origin.

The total angular momentum of the body (about the origin) is written

$$\mathbf{L} = \sum_{i=1,N} m_i \mathbf{r}_i \times \frac{d\mathbf{r}_i}{dt} = \sum_{i=1,N} m_i \mathbf{r}_i \times (\boldsymbol{\omega} \times \mathbf{r}_i) = \sum_{i=1,N} m_i [r_i^2 \boldsymbol{\omega} - (\mathbf{r}_i \cdot \boldsymbol{\omega}) \mathbf{r}_i]$$

The above formula can be written as a matrix equation of the form

$$\begin{pmatrix} L_x \\ L_y \\ L_z \end{pmatrix} = \begin{pmatrix} I_{xx} & I_{xy} & I_{xz} \\ I_{yx} & I_{yy} & I_{yz} \\ I_{zx} & I_{zy} & I_{zz} \end{pmatrix} \begin{pmatrix} \omega_x \\ \omega_y \\ \omega_z \end{pmatrix}$$

where

$$\begin{aligned} I_{xx} &= + \sum_{i=1,N} (y_i^2 + z_i^2) m_i = \int (y^2 + z^2) dm = \int_V (y^2 + z^2) \rho(x, y, z) dV \\ I_{yy} &= + \sum_{i=1,N} (x_i^2 + z_i^2) m_i = \int (x^2 + z^2) dm = \int_V (x^2 + z^2) \rho(x, y, z) dV \\ I_{zz} &= + \sum_{i=1,N} (x_i^2 + y_i^2) m_i = \int (x^2 + y^2) dm = \int_V (x^2 + y^2) \rho(x, y, z) dV \\ I_{xy} = I_{yx} &= - \sum_{i=1,N} x_i y_i m_i = - \int x y dm = - \int x y \rho(x, y, z) dV \\ I_{yz} = I_{zy} &= - \sum_{i=1,N} y_i z_i m_i = - \int y z dm = - \int y z \rho(x, y, z) dV \\ I_{xz} = I_{zx} &= - \sum_{i=1,N} x_i z_i m_i = - \int x z dm = - \int x z \rho(x, y, z) dV \end{aligned}$$

Here,  $I_{xx}$  is called the moment of inertia about the  $x$ -axis,  $I_{yy}$  the moment of inertia about the  $y$ -axis,  $I_{xy}$  the  $xy$  product of inertia,  $I_{yz}$  the  $yz$  product of inertia, etc. The matrix of the  $I_{ij}$  values is known as the moment of inertia tensor.

In general, the angular momentum vector,  $\mathbf{L}$  points in a different direction to the angular velocity vector,  $\boldsymbol{\omega}$ . In other words,  $\mathbf{L}$  is generally not parallel to  $\boldsymbol{\omega}$ .

Finally, although the above results were obtained assuming a fixed angular velocity, they remain valid at each instant in time if the angular velocity varies.

In the simplified case of a spherically symmetric planet, it is easy to see that  $I_{xx} = I_{yy} = I_{zz}$  so that  $I = \frac{1}{3}(I_{xx} + I_{yy} + I_{zz})$ , and  $\rho = \rho(r)$  with  $dV = 4\pi r^2 dr$ , leading to

$$I = \frac{8\pi}{3} \int_0^R \rho(r) r^4 dr$$

Assuming further that the planet has a constant density  $\rho_0$ , we obtain

$$I = \frac{8\pi}{3}\rho_0 \int_0^R r^4 dr = \frac{8\pi}{3}\rho_0 \frac{R^5}{5} = \frac{2}{5}MR^2$$

where  $M$  is the mass of the planet and  $R$  is its radius.

Assuming now that the planet is composed of a core of radius  $R_c$  and density  $\rho_c$  surrounded by a mantle of density  $\rho_m$ , we have

$$I = \frac{8\pi}{3} \int_0^R \rho(r)r^4 dr = \frac{8\pi}{3} \left( \int_0^{R_c} \rho_c r^4 dr + \int_{R_c}^R \rho_m r^4 dr \right) = \frac{8\pi}{15} (\rho_c R_c^5 + \rho_m (R^5 - R_c^5))$$

The moment of inertia of the core is given in Table 2 of "Core Dynamics", Treatise on Geophysics, edited by Peter Olson:  $I_{core} = 9.2 \times 10^{36} kg.m^2$ . The total moment of inertia for the Earth is then given by  $I = I_{core} + I_{mantle}$ .

### 3.24 The need for numerical modelling

The governing equations we have seen in this chapter require the use of numerical solution techniques for three main reasons:

- the advection term in the energy equation couples velocity and temperature;
- the constitutive law (the relationship between stress and strain rate) often depends on velocity (or rather, strain rate), temperature, pressure, ...
- Even when the coefficients of the PDE's are linear, often their spatial variability, coupled to potentially complex domain geometries prevent arriving at the analytical solution.

Note that in CFD one makes a distinction between verification and validation. Simply put [2168]:

- verification: "solving the equations right"
- validation: "solving the right equations"

## 4 The building blocks of the Finite Element Method

### 4.1 Numerical integration

As we will see later, using the Finite Element method to solve problems involves computing integrals which are more often than not too complex to be computed analytically/exactly. We will then need to compute them numerically.

[wiki] In essence, the basic problem in numerical integration is to compute an approximate solution to a definite integral

$$\int_a^b f(x)dx$$

to a given degree of accuracy. This problem has been widely studied and we know that if  $f(x)$  is a smooth function, and the domain of integration is bounded, there are many methods for approximating the integral to the desired precision.

There are several reasons for carrying out numerical integration.

- The integrand  $f(x)$  may be known only at certain points, such as obtained by sampling. Some embedded systems and other computer applications may need numerical integration for this reason.
- A formula for the integrand may be known, but it may be difficult or impossible to find an antiderivative that is an elementary function. An example of such an integrand is  $f(x) = \exp(-x^2)$ , the antiderivative of which (the error function, times a constant) cannot be written in elementary form.
- It may be possible to find an antiderivative symbolically, but it may be easier to compute a numerical approximation than to compute the antiderivative. That may be the case if the antiderivative is given as an infinite series or product, or if its evaluation requires a special function that is not available.

#### 4.1.1 in 1D - theory

The simplest method of this type is to let the interpolating function be a constant function (a polynomial of degree zero) that passes through the point  $((a+b)/2, f((a+b)/2))$ .

This is called the midpoint rule or rectangle rule.

$$\int_a^b f(x)dx \simeq (b-a)f\left(\frac{a+b}{2}\right)$$

insert here figure

The interpolating function may be a straight line (an affine function, i.e. a polynomial of degree 1) passing through the points  $(a, f(a))$  and  $(b, f(b))$ .

This is called the trapezoidal rule.

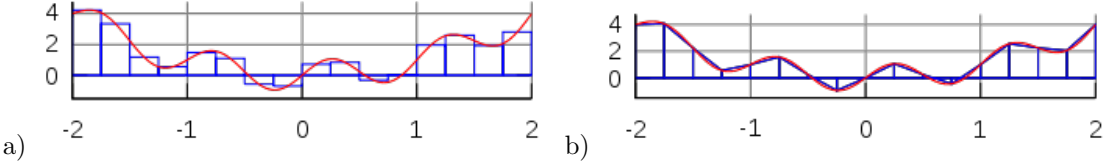
$$\int_a^b f(x)dx \simeq (b-a)\frac{f(a) + f(b)}{2}$$

insert here figure

For either one of these rules, we can make a more accurate approximation by breaking up the interval  $[a, b]$  into some number  $n$  of subintervals, computing an approximation for each subinterval, then adding up all the results. This is called a composite rule, extended rule, or iterated rule. For example, the composite trapezoidal rule can be stated as

$$\int_a^b f(x)dx \simeq \frac{b-a}{n} \left( \frac{f(a)}{2} + \sum_{k=1}^{n-1} f(a + k \frac{b-a}{n}) + \frac{f(b)}{2} \right)$$

where the subintervals have the form  $[kh, (k+1)h]$ , with  $h = (b-a)/n$  and  $k = 0, 1, 2, \dots, n-1$ .



The interval  $[-2, 2]$  is broken into 16 sub-intervals. The blue lines correspond to the approximation of the red curve by means of a) the midpoint rule, b) the trapezoidal rule.

There are several algorithms for numerical integration (also commonly called 'numerical quadrature', or simply 'quadrature'). Interpolation with polynomials evaluated at equally spaced points in  $[a, b]$  yields the Newton-Cotes formulas, of which the rectangle rule and the trapezoidal rule are examples. If we allow the intervals between interpolation points to vary, we find another group of quadrature formulas, such as the Gauss(ian) quadrature formulas. A Gaussian quadrature rule is typically more accurate than a Newton-Cotes rule, which requires the same number of function evaluations, if the integrand is smooth (i.e., if it is sufficiently differentiable).

An  $n$ -point Gaussian quadrature rule, named after Carl Friedrich Gauss, is a quadrature rule constructed to yield an exact result for polynomials of degree  $2n - 1$  or less by a suitable choice of the points  $x_i$  and weights  $w_i$  for  $i = 1, \dots, n$ .

The domain of integration for such a rule is conventionally taken as  $[-1, 1]$ , so the rule is stated as

$$\int_{-1}^{+1} f(x) dx = \sum_{i_q=1}^n w_{i_q} f(x_{i_q})$$

In this formula the  $x_{i_q}$  coordinate is the  $i$ -th root of the Legendre polynomial  $P_n(x)$ .

It is important to note that a Gaussian quadrature will only produce good results if the function  $f(x)$  is well approximated by a polynomial function within the range  $[-1, 1]$ . As a consequence, the method is not, for example, suitable for functions with singularities.

Number of points, $n$	Points, $x_i$	Weights, $w_i$
1	0	2
2	$\pm\sqrt{\frac{1}{3}}$	1
3	0	$\frac{8}{9}$
	$\pm\sqrt{\frac{3}{5}}$	$\frac{5}{9}$
4	$\pm\sqrt{\frac{3}{7} - \frac{2}{7}\sqrt{\frac{6}{5}}}$	$\frac{18+\sqrt{30}}{36}$
	$\pm\sqrt{\frac{3}{7} + \frac{2}{7}\sqrt{\frac{6}{5}}}$	$\frac{18-\sqrt{30}}{36}$
5	0	$\frac{128}{225}$
	$\pm\frac{1}{3}\sqrt{5 - 2\sqrt{\frac{10}{7}}}$	$\frac{322+13\sqrt{70}}{900}$
	$\pm\frac{1}{3}\sqrt{5 + 2\sqrt{\frac{10}{7}}}$	$\frac{322-13\sqrt{70}}{900}$

Gauss-Legendre points and their weights.

n	$x_{iq}$	$w_{iq}$	$x_{iq}$ (approx)	$w_{iq}$ (approx)
1	0	2	0	2
2	$\pm\sqrt{1/3}$	1	$\pm 0.577\ 350\ 269\ 189\ 626$	1
3	0	$8/9$	0	0.888 888 888 888 888
	$\pm\sqrt{3/5}$	$5/9$	$\pm 0.774\ 596\ 669\ 241\ 483$	0.555 555 555 555 555
4	$\pm\sqrt{\frac{3}{7} - \frac{2}{7}\sqrt{6/5}}$	$\frac{18+\sqrt{30}}{36}$	$\pm 0.339\ 981\ 043\ 584\ 856$	0.652 145 154 862 546
	$\pm\sqrt{\frac{3}{7} + \frac{2}{7}\sqrt{6/5}}$	$\frac{18-\sqrt{30}}{36}$	$\pm 0.861\ 136\ 311\ 594\ 953$	0.347 854 845 137 454
5	0	$128/225$	0	0.568 888 888 888 889
	$\pm\frac{1}{3}\sqrt{5 - 2\sqrt{\frac{10}{7}}}$	$\frac{322+13\sqrt{70}}{900}$	$\pm 0.538\ 469\ 310\ 105\ 683$	0.478 628 670 499 366
	$\pm\frac{1}{3}\sqrt{5 + 2\sqrt{\frac{10}{7}}}$	$\frac{322-13\sqrt{70}}{900}$	$\pm 0.906\ 179\ 845\ 938\ 664$	0.236 926 885 056 189
6	?	?	$\pm 0.238\ 619\ 186\ 083\ 197$ $\pm 0.661\ 209\ 386\ 466\ 265$ $\pm 0.932\ 469\ 514\ 203\ 152$	0.467 913 934 572 691 0.360 761 573 048 139 0.171 324 492 379 170
7			$\pm 0.946\ 107\ 912\ 342\ 759$ $\pm 0.741\ 531\ 185\ 599\ 394$ $\pm 0.405\ 845\ 151\ 377\ 397$ 0.000 000 000 000 000	0.129 484 966 168 870 0.279 705 391 489 277 0.381 830 050 505 119 0.417 959 183 673 469
8			$\pm 0.960\ 289\ 856\ 497\ 536$ $\pm 0.796\ 666\ 477\ 413\ 627$ $\pm 0.525\ 532\ 409\ 916\ 329$ $\pm 0.183\ 434\ 642\ 495\ 650$	0.101 228 536 290 376 0.222 381 034 453 374 0.313 706 645 877 887 0.362 683 783 378 362
9			$\pm 0.968\ 160\ 239\ 507\ 626$ $\pm 0.836\ 031\ 107\ 326\ 636$ $\pm 0.613\ 371\ 432\ 700\ 590$ $\pm 0.324\ 253\ 423\ 403\ 809$ 0.000 000 000 000 000	0.081 274 388 361 574 0.180 648 160 694 857 0.260 610 696 402 935 0.312 347 077 040 003 0.330 239 355 001 260
10			$\pm 0.973\ 906\ 528\ 517\ 172$ $\pm 0.865\ 063\ 366\ 688\ 985$ $\pm 0.679\ 409\ 568\ 299\ 024$ $\pm 0.433\ 395\ 394\ 129\ 247$ $\pm 0.148\ 874\ 338\ 981\ 631$	0.066 671 344 308 688 0.149 451 349 150 581 0.219 086 362 515 982 0.269 266 719 309 996 0.295 524 224 714 753

Abscissae and weights for Gauss quadratures up to  $n = 10$ . See [1596, p89]

As shown in the above table, it can be shown that the weight values must fulfill the following condition:

$$\sum_{iq} w_{iq} = 2 \quad (204)$$

and it is worth noting that all quadrature point coordinates are symmetrical around the origin.

Since most quadrature formula are only valid on a specific interval, we now must address the problem of their use outside of such intervals. The solution turns out to be quite simple: one must carry out a change of variables from the interval  $[a, b]$  to  $[-1, 1]$ .

We then consider the reduced coordinate  $r \in [-1, 1]$  such that

$$r = \frac{2}{b-a}(x-a) - 1$$

This relationship can be reversed such that when  $r$  is known, its equivalent coordinate  $x \in [a, b]$  can be computed:

$$x = \frac{b-a}{2}(1+r) + a$$

From this it follows that

$$dx = \frac{b-a}{2}dr$$

and then

$$\int_a^b f(x)dx = \frac{b-a}{2} \int_{-1}^{+1} f(r)dr \simeq \frac{b-a}{2} \sum_{i_q=1}^n w_{i_q} f(r_{i_q})$$

#### 4.1.2 in 1D - examples

**example 1** Since we know how to carry out any required change of variables, we choose for simplicity  $a = -1$ ,  $b = +1$ . Let us take for example  $f(x) = \pi$ . Then we can compute the integral of this function over the interval  $[a, b]$  exactly:

$$I = \int_{-1}^{+1} f(x)dx = \pi \int_{-1}^{+1} dx = 2\pi$$

We can now use a Gauss-Legendre formula to compute this same integral:

$$I_{gq} = \int_{-1}^{+1} f(x)dx = \sum_{i_q=1}^{n_q} w_{i_q} f(x_{i_q}) = \sum_{i_q=1}^{n_q} w_{i_q} \pi = \pi \underbrace{\sum_{i_q=1}^{n_q} w_{i_q}}_{=2} = 2\pi$$

where we have used the property of the weight values of Eq.(204). Since the actual number of points was never specified, this result is valid for all quadrature rules.

**example 2** Let us now take  $f(x) = mx + p$  and repeat the same exercise:

$$I = \int_{-1}^{+1} f(x)dx = \int_{-1}^{+1} (mx + p)dx = [\frac{1}{2}mx^2 + px]_{-1}^{+1} = 2p$$

$$I_{gq} = \int_{-1}^{+1} f(x)dx = \sum_{i_q=1}^{n_q} w_{i_q} f(x_{i_q}) = \sum_{i_q=1}^{n_q} w_{i_q} (mx_{i_q} + p) = m \underbrace{\sum_{i_q=1}^{n_q} w_{i_q} x_{i_q}}_{=0} + p \underbrace{\sum_{i_q=1}^{n_q} w_{i_q}}_{=2} = 2p$$

since the quadrature points are symmetric w.r.t. to zero on the x-axis. Once again the quadrature is able to compute the exact value of this integral: this makes sense since an  $n$ -point rule exactly integrates a  $2n - 1$  order polynomial such that a 1 point quadrature exactly integrates a first order polynomial like the one above.

**example 3** Let us now take  $f(x) = x^2$ . We have

$$I = \int_{-1}^{+1} f(x)dx = \int_{-1}^{+1} x^2 dx = [\frac{1}{3}x^3]_{-1}^{+1} = \frac{2}{3}$$

and

$$I_{gq} = \int_{-1}^{+1} f(x)dx = \sum_{i_q=1}^{n_q} w_{i_q} f(x_{i_q}) = \sum_{i_q=1}^{n_q} w_{i_q} x_{i_q}^2$$

- $n_q = 1$ :  $x_{i_q}^{(1)} = 0$ ,  $w_{i_q} = 2$ .  $I_{gq} = 0$
- $n_q = 2$ :  $x_q^{(1)} = -1/\sqrt{3}$ ,  $x_q^{(2)} = 1/\sqrt{3}$ ,  $w_q^{(1)} = w_q^{(2)} = 1$ .  $I_{gq} = \frac{2}{3}$
- It also works  $\forall n_q > 2$  !

#### 4.1.3 in 2D/3D - theory

Let us now turn to a two-dimensional integral of the form

$$I = \int_{-1}^{+1} \int_{-1}^{+1} f(x, y) dxdy$$

The equivalent Gaussian quadrature writes:

$$I_{gq} \simeq \sum_{i_q=1}^{n_q} \sum_{j_q=1}^{n_q} f(x_{i_q}, y_{j_q}) w_{i_q} w_{j_q}$$

#### 4.1.4 quadrature on triangles

Quadrature rules for triangles can be found in Dunavant, 1985 [730]. The following ones are identical to those in *ip\_triangle.m* file of the MILAMIN code [614].

	$r_q$	$s_q$	$w_q$	
$iq = 1$	1/3	1/3	1/2	
$iq = 1$	1/6	1/6	1/6	
$iq = 2$	2/3	1/6	1/6	
$iq = 3$	1/6	2/3	1/6	
$iq = 1$	1/3	1/3	-27/96	
$iq = 2$	0.6	0.2	25/96	
$iq = 3$	0.2	0.6	25/96	
$iq = 4$	0.2	0.2	25/96	
$iq = 1$	$1 - 2g_1$	$g_1$	$w_1/2$	0.108103018168070
$iq = 2$	$g_1$	$1 - 2g_1$	$w_1/2$	0.445948490915965
$iq = 3$	$g_1$	$g_1$	$w_1/2$	0.445948490915965
$iq = 4$	$1 - 2g_2$	$g_2$	$w_2/2$	0.816847572980459
$iq = 5$	$g_2$	$1 - 2g_2$	$w_2/2$	0.091576213509771
$iq = 6$	$g_2$	$g_2$	$w_2/2$	0.091576213509771
$iq = 1$				0.091576213509771
$iq = 2$				0.816847572980459
$iq = 3$				0.091576213509771
$iq = 4$				0.445948490915965
$iq = 5$				0.108103018168070
$iq = 6$				0.445948490915965
$iq = 1$				0.091576213509771
$iq = 2$				0.091576213509771
$iq = 3$				0.816847572980459
$iq = 4$				0.091576213509771
$iq = 5$				0.445948490915965
$iq = 6$				0.108103018168070
$iq = 7$				0.223381589678011/2.0
$iq = 1$				0.091576213509771
$iq = 2$				0.091576213509771
$iq = 3$				0.091576213509771
$iq = 4$				0.091576213509771
$iq = 5$				0.091576213509771
$iq = 6$				0.091576213509771
$iq = 7$				0.091576213509771
$iq = 1$				0.1012865073235
$iq = 2$				0.7974269853531
$iq = 3$				0.1012865073235
$iq = 4$				0.4701420641051
$iq = 5$				0.4701420641051
$iq = 6$				0.0597158717898
$iq = 7$				0.3333333333333
$iq = 1$				0.1012865073235
$iq = 2$				0.7974269853531
$iq = 3$				0.1012865073235
$iq = 4$				0.4701420641051
$iq = 5$				0.4701420641051
$iq = 6$				0.0597158717898
$iq = 7$				0.3333333333333
$iq = 1$				0.3333333333333
$iq = 1$				5.01426509658179E - 01
$iq = 2$				2.49286745170910E - 01
$iq = 3$				2.49286745170910E - 01
$iq = 4$				8.73821971016996E - 01
$iq = 5$				6.30890144915020E - 02
$iq = 6$				6.30890144915020E - 02
$iq = 7$				5.31450498448170E - 02
$iq = 8$				6.36502499121399E - 01
$iq = 9$				3.10352451033784E - 01
$iq = 10$				5.31450498448170E - 02
$iq = 11$				6.36502499121399E - 01
$iq = 12$				3.10352451033784E - 01
$iq = 1$				5.83931378631895E - 02
$iq = 2$				5.83931378631895E - 02
$iq = 3$				5.83931378631895E - 02
$iq = 4$				2.54224531851035E - 02
$iq = 5$				2.54224531851035E - 02
$iq = 6$				2.54224531851035E - 02
$iq = 7$				2.54224531851035E - 02
$iq = 8$				2.54224531851035E - 02
$iq = 9$				2.54224531851035E - 02
$iq = 10$				2.54224531851035E - 02
$iq = 11$				2.54224531851035E - 02
$iq = 12$				2.54224531851035E - 02
$iq = 1$				5.83931378631895E - 02
$iq = 2$				5.83931378631895E - 02
$iq = 3$				5.83931378631895E - 02
$iq = 4$				0.109951743655322/2.0
$iq = 5$				0.109951743655322/2.0
$iq = 6$				0.109951743655322/2.0
$iq = 7$				0.109951743655322/2.0
$iq = 8$				0.109951743655322/2.0
$iq = 9$				0.109951743655322/2.0
$iq = 10$				0.109951743655322/2.0
$iq = 11$				0.109951743655322/2.0
$iq = 12$				0.109951743655322/2.0

where

$$g_1 = \left( 8 - \sqrt{10} + \sqrt{38 - 44\sqrt{2/5}} \right) / 18 \quad g_2 = \left( 8 - \sqrt{10} - \sqrt{38 - 44\sqrt{2/5}} \right) / 18$$

$$w_1 = \left( 620 + \sqrt{213125 - 53320\sqrt{10}} \right) / 3720 \quad w_2 = \left( 620 - \sqrt{213125 - 53320\sqrt{10}} \right) / 3720$$

#### 4.1.5 quadrature on tetrahedra

**Remark.** In what follows the coefficients in the tables are not the reduced coordinates of the quadrature points but the coefficients corresponding to the 4 nodes.

Quadrature rules on tetrahedra take the form:

$$\int \int \int_{el} f(x, y, z) dx dy dz = V_{el} \sum_{iq=1}^{nqel} w_{iq} f(\xi_1^{iq}, \xi_2^{iq}, \xi_3^{iq}, \xi_4^{iq})$$

or, that is to say:

$$\int \int \int_{el} f(x, y, z) dx dy dz = \sum_{iq=1}^{nqel} (w_{iq} V_{el}) f(\xi_1^{iq}, \xi_2^{iq}, \xi_3^{iq}, \xi_4^{iq})$$

with in our case  $V_{el} = 1/6$ .

In the literature it can be found that a one point quadrature is characterised by

$$w_{iq} = 1 \quad \xi_1^{iq} = \xi_2^{iq} = \xi_3^{iq} = \xi_4^{iq} = 0.25$$

i.e, the coordinates of the single point are given by:

$$x_{iq} = \sum_{i=1}^4 \xi_i^{iq} x_i = \frac{1}{4}(x_1 + x_2 + x_3 + x_4)$$

Same for  $y$  and  $z$  coordinates.

A four-point quadrature rule is characterised by  $w_{iq} = V_{el} * 0.25 = 1/24 \simeq 04166666666666667$  and

	$\xi_1$	$\xi_2$	$\xi_3$	$\xi_4$
$iq=1$	0.585410196624969	0.138196601125011	0.138196601125011	0.138196601125011
$iq=2$	0.138196601125011	0.585410196624969	0.138196601125011	0.138196601125011
$iq=3$	0.138196601125011	0.138196601125011	0.585410196624969	0.138196601125011
$iq=4$	0.138196601125011	0.138196601125011	0.138196601125011	0.585410196624969

We then have:

$$r_{iq} = \sum_{i=1}^4 \xi_i^{iq} x_i = (\xi_1^{iq}, \xi_2^{iq}, \xi_3^{iq}, \xi_4^{iq}) \cdot (r_1, r_2, r_3, r_4) = (\xi_1^{iq}, \xi_2^{iq}, \xi_3^{iq}, \xi_4^{iq}) \cdot (0, 1, 0, 0) = \xi_2^{iq}$$

$$s_{iq} = \sum_{i=1}^4 \xi_i^{iq} y_i = (\xi_1^{iq}, \xi_2^{iq}, \xi_3^{iq}, \xi_4^{iq}) \cdot (s_1, s_2, s_3, s_4) = (\xi_1^{iq}, \xi_2^{iq}, \xi_3^{iq}, \xi_4^{iq}) \cdot (0, 0, 1, 0) = \xi_3^{iq}$$

$$t_{iq} = \sum_{i=1}^4 \xi_i^{iq} z_i = (\xi_1^{iq}, \xi_2^{iq}, \xi_3^{iq}, \xi_4^{iq}) \cdot (t_1, t_2, t_3, t_4) = (\xi_1^{iq}, \xi_2^{iq}, \xi_3^{iq}, \xi_4^{iq}) \cdot (0, 0, 0, 1) = \xi_4^{iq}$$

Finally:

	$r_q$	$s_q$	$t_q$	$w_q$
$iq = 1$	0.138196601125011	0.138196601125011	0.138196601125011	0.04166666666666667
$iq = 2$	0.585410196624969	0.138196601125011	0.138196601125011	0.04166666666666667
$iq = 3$	0.138196601125011	0.585410196624969	0.138196601125011	0.04166666666666667
$iq = 4$	0.138196601125011	0.138196601125011	0.585410196624969	0.04166666666666667

#### 4.1.6 The Gauss-Lobatto approach

All what we have seen above falls under the Gauss-Legendre quadrature method. There is however another somewhat common quadrature method: the Gauss-Lobatto quadrature. . It is similar to Gaussian quadrature with the following important differences: 1) There are integration points in the interval but they also always include the end points of the integration interval; 2) It is accurate for polynomials up to degree  $2n - 3$ , where  $n$  is the number of integration points.

In 1D, it reads:

$$\int_{-1}^{+1} f(x) dx = \frac{2}{n(n-1)} [f(-1) + f(1)] + \sum_{i=2}^{n-1} w_i f(x_i)$$

The locations and weights of the integration points are as follows:

n	$x_{iq}$	$w_{iq}$	$x_{iq}$ (approx)	$w_{iq}$ (approx)
3	0	4/3	4/3	1/3
	$\pm 1$	1/3		
4	$\pm \sqrt{\frac{1}{5}}$	5/6	5/6	1/6
	$\pm 1$	1/6		
5	0	32/45	32/45	1/10
	$\pm \sqrt{\frac{3}{7}}$	49/90		
	$\pm 1$	1/10		
6	$\pm \sqrt{\frac{1}{3} - \frac{2\sqrt{7}}{21}}$	$\frac{14+\sqrt{7}}{30}$	$\frac{14+\sqrt{7}}{30}$	$\frac{14-\sqrt{7}}{30}$
	$\pm \sqrt{\frac{1}{3} + \frac{2\sqrt{7}}{21}}$	$\frac{14-\sqrt{7}}{30}$		
	$\pm 1$	1/15		

## 4.2 The mesh

## 4.3 A bit of FE terminology

We introduce here some terminology for efficient element descriptions [1065]:

- For triangles/tetrahedra, the designation  $P_m \times P_n$  means that each component of the velocity is approximated by continuous piecewise complete Polynomials of degree  $m$  and pressure by continuous piecewise complete Polynomials of degree  $n$ . For example  $P_2 \times P_1$  means

$$u \sim a_1 + a_2x + a_3y + a_4xy + a_5x^2 + a_6y^2$$

with similar approximations for  $v$ , and

$$p \sim b_1 + b_2x + b_3y$$

Both velocity and pressure are continuous across element boundaries, and each triangular element contains 6 velocity nodes and three pressure nodes.

- For the same families,  $P_m \times P_{-n}$  is as above, except that pressure is approximated via piecewise discontinuous polynomials of degree  $n$ . For instance,  $P_2 \times P_{-1}$  is the same as  $P_2P_1$  except that pressure is now an independent linear function in each element and therefore discontinuous at element boundaries.
- For quadrilaterals/hexahedra, the designation  $Q_m \times Q_n$  means that each component of the velocity is approximated by a continuous piecewise polynomial of degree  $m$  in each direction on the quadrilateral and likewise for pressure, except that the polynomial is of degree  $n$ . For instance,  $Q_2 \times Q_1$  means

$$u \sim a_1 + a_2x + a_3y + a_4xy + a_5x^2 + a_6y^2 + a_7x^2y + a_8xy^2 + a_9x^2y^2$$

and

$$p \sim b_1 + b_2x + b_3y + b_4xy$$

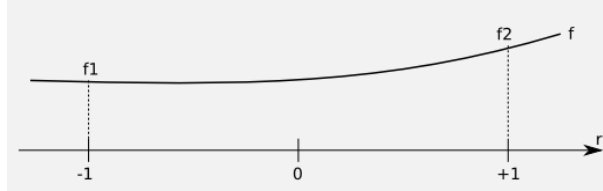
- For these same families,  $Q_m \times Q_{-n}$  is as above, except that the pressure approximation is not continuous at element boundaries.
- Again for the same families,  $Q_m \times P_{-n}$  indicates the same velocity approximation with a pressure approximation that is a discontinuous complete piecewise polynomial of degree  $n$  (not of degree  $n$  in each direction !)
- The designation  $P_m^+$  or  $Q_m^+$  means that some sort of bubble function was added to the polynomial approximation for the velocity. You may also find the term 'enriched element' in the literature.
- Finally, for  $n = 0$ , we have piecewise-constant pressure, and we omit the minus sign for simplicity.

Another point which needs to be clarified is the use of so-called 'conforming elements' (or 'non-conforming elements'). Following again [1065], conforming velocity elements are those for which the basis functions for a subset of  $H^1$  for the continuous problem (the first derivatives and their squares are integrable in  $\Omega$ ). For instance, the rotated  $Q_1 \times P_0$  element of Rannacher and Turek (see section ??) is such that the velocity is discontinuous across element edges, so that the derivative does not exist there. Another typical example of non-conforming element is the Crouzeix-Raviart element [601].

## 4.4 Elements and basis functions in 1D

### 4.4.1 Linear basis functions ( $Q_1$ )

Let  $f(r)$  be a  $C^1$  function on the interval  $[-1 : 1]$  with  $f(-1) = f_1$  and  $f(1) = f_2$ .



Let us assume that the function  $f(r)$  is to be approximated on  $[-1, 1]$  by the first order polynomial

$$f(r) = a + br \quad (205)$$

Then it must fulfill

$$\begin{aligned} f(r = -1) &= a - b = f_1 \\ f(r = +1) &= a + b = f_2 \end{aligned}$$

This leads to

$$a = \frac{1}{2}(f_1 + f_2) \quad b = \frac{1}{2}(-f_1 + f_2)$$

and then replacing  $a, b$  in Eq. (205) by the above values on gets

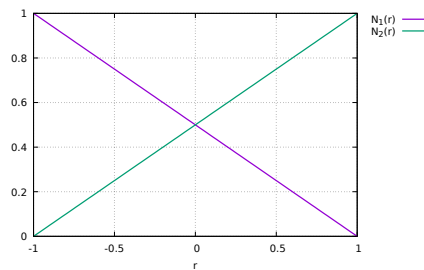
$$f(r) = \left[ \frac{1}{2}(1 - r) \right] f_1 + \left[ \frac{1}{2}(1 + r) \right] f_2$$

or

$$f(r) = \sum_{i=1}^2 N_i(r) f_i$$

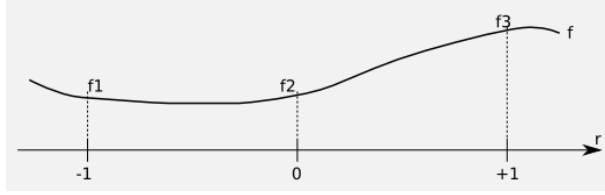
with

$N_1(r) = \frac{1}{2}(1 - r)$ $N_2(r) = \frac{1}{2}(1 + r)$	(206)
--	-------



#### 4.4.2 Quadratic basis functions ( $Q_2$ )

Let  $f(r)$  be a  $C^1$  function on the interval  $[-1 : 1]$  with  $f(-1) = f_1$ ,  $f(0) = f_2$  and  $f(1) = f_3$ .



Let us assume that the function  $f(r)$  is to be approximated on  $[-1, 1]$  by the second order polynomial

$$f(r) = a + br + cr^2 \quad (207)$$

Then it must fulfill

$$\begin{aligned} f(r = -1) &= a - b + c = f_1 \\ f(r = 0) &= a = f_2 \\ f(r = +1) &= a + b + c = f_3 \end{aligned}$$

This leads to

$$a = f_2 \quad b = \frac{1}{2}(-f_1 + f_3) \quad c = \frac{1}{2}(f_1 + f_3 - 2f_2)$$

and then replacing  $a, b, c$  in Eq. (207) by the above values one gets

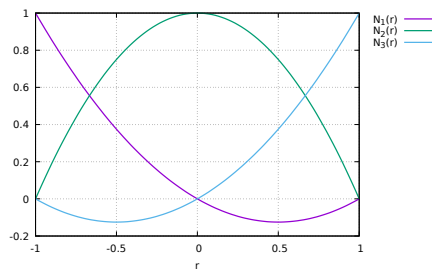
$$f(r) = \left[ \frac{1}{2}r(r-1) \right] f_1 + (1-r^2)f_2 + \left[ \frac{1}{2}r(r+1) \right] f_3$$

or,

$$f(r) = \sum_{i=1}^3 N_i(r) f_i$$

with

$\begin{aligned} N_1(r) &= \frac{1}{2}r(r-1) \\ N_2(r) &= (1-r^2) \\ N_3(r) &= \frac{1}{2}r(r+1) \end{aligned} \quad (208)$
---



#### 4.4.3 Cubic basis functions ( $Q_3$ )

The 1D basis polynomial is given by

$$f(r) = a + br + cr^2 + dr^3$$

with the nodes at position  $-1, -1/3, +1/3$  and  $+1$ .

$$\begin{aligned}
f(-1) &= a - b + c - d = f_1 \\
f(-1/3) &= a - \frac{b}{3} + \frac{c}{9} - \frac{d}{27} = f_2 \\
f(+1/3) &= a - \frac{b}{3} + \frac{c}{9} - \frac{d}{27} = f_3 \\
f(+1) &= a + b + c + d = f_4
\end{aligned}$$

Adding the first and fourth equation and the second and third, one arrives at

$$f_1 + f_4 = 2a + 2c \quad f_2 + f_3 = 2a + \frac{2c}{9}$$

and finally:

$$\begin{aligned}
a &= \frac{1}{16}(-f_1 + 9f_2 + 9f_3 - f_4) \\
c &= \frac{9}{16}(f_1 - f_2 - f_3 + f_4)
\end{aligned}$$

Combining the original 4 equations in a different way yields

$$2b + 2d = f_4 - f_1 \quad \frac{2b}{3} + \frac{2d}{27} = f_3 - f_2$$

so that

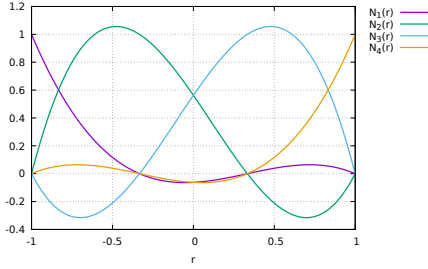
$$\begin{aligned}
b &= \frac{1}{16}(f_1 - 27f_2 + 27f_3 - f_4) \\
d &= \frac{9}{16}(-f_1 + 3f_2 - 3f_3 + f_4)
\end{aligned}$$

Finally,

$$\begin{aligned}
f(r) &= a + b + cr^2 + dr^3 \\
&= \frac{1}{16}(-1 + r + 9r^2 - 9r^3)f_1 \\
&\quad + \frac{1}{16}(9 - 27r - 9r^2 + 27r^3)f_2 \\
&\quad + \frac{1}{16}(9 + 27r - 9r^2 - 27r^3)f_3 \\
&\quad + \frac{1}{16}(-1 - r + 9r^2 + 9r^3)f_4 \\
&= \sum_{i=1}^4 N_i(r)f_i
\end{aligned}$$

where

$ \begin{aligned} N_1 &= \frac{1}{16}(-1 + r + 9r^2 - 9r^3) \\ N_2 &= \frac{1}{16}(9 - 27r - 9r^2 + 27r^3) \\ N_3 &= \frac{1}{16}(9 + 27r - 9r^2 - 27r^3) \\ N_4 &= \frac{1}{16}(-1 - r + 9r^2 + 9r^3) \end{aligned} $
--



These are identical to [1596, p49]

Verification:

- Let us assume  $f(r) = C$ , then

$$\hat{f}(r) = \sum_i N_i(r) f_i = \sum_i N_i C = C \sum_i N_i = C$$

so that a constant function is exactly reproduced, as expected.

- Let us assume  $f(r) = r$ , then  $f_1 = -1$ ,  $f_2 = -1/3$ ,  $f_3 = 1/3$  and  $f_4 = +1$ . We then have

$$\begin{aligned}
\hat{f}(r) &= \sum_i N_i(r) f_i \\
&= -N_1(r) - \frac{1}{3}N_2(r) + \frac{1}{3}N_3(r) + N_4(r) \\
&= [-(-1 + r + 9r^2 - 9r^3) \\
&\quad - \frac{1}{3}(9 - 27r - 9r^2 - 27r^3) \\
&\quad + \frac{1}{3}(9 + 27r - 9r^2 + 27r^3) \\
&\quad + (-1 - r + 9r^2 + 9r^3)]/16 \\
&= [-r + 9r + 9r - r]/16 + \dots 0\dots \\
&= r
\end{aligned} \tag{209}$$

The basis functions derivative are given by

$\frac{\partial N_1}{\partial r}$	$=$	$\frac{1}{16}(1 + 18r - 27r^2)$
$\frac{\partial N_2}{\partial r}$	$=$	$\frac{1}{16}(-27 - 18r + 81r^2)$
$\frac{\partial N_3}{\partial r}$	$=$	$\frac{1}{16}(+27 - 18r - 81r^2)$
$\frac{\partial N_4}{\partial r}$	$=$	$\frac{1}{16}(-1 + 18r + 27r^2)$

Verification:

- Let us assume  $f(r) = C$ , then

$$\begin{aligned}
\frac{\partial \hat{f}}{\partial r} &= \sum_i \frac{\partial N_i}{\partial r} f_i \\
&= C \sum_i \frac{\partial N_i}{\partial r} \\
&= \frac{C}{16} [(1 + 18r - 27r^2) \\
&\quad + (-27 - 18r + 81r^2) \\
&\quad + (+27 - 18r - 81r^2) \\
&\quad + (-1 + 18r + 27r^2)] \\
&= 0
\end{aligned}$$

- Let us assume  $f(r) = r$ , then  $f_1 = -1$ ,  $f_2 = -1/3$ ,  $f_3 = 1/3$  and  $f_4 = +1$ . We then have

$$\begin{aligned}
\frac{\partial \hat{f}}{\partial r} &= \sum_i \frac{\partial N_i}{\partial r} f_i \\
&= \frac{1}{16} [-(1 + 18r - 27r^2) \\
&\quad - \frac{1}{3}(-27 - 18r + 81r^2) \\
&\quad + \frac{1}{3}(+27 - 18r - 81r^2) \\
&\quad + (-1 + 18r + 27r^2)] \\
&= \frac{1}{16} [-2 + 18 + 54r^2 - 54r^2] \\
&= 1
\end{aligned}$$

#### 4.4.4 Quartic basis functions ( $Q_4$ )

The 1D basis polynomial is given by

$$f(r) = a + br + cr^2 + dr^3 + er^4$$

with the nodes at position -1,-1/2, 0, +1/2 and +1.

$$\begin{aligned}
f(-1) &= a - b + c - d + e = f_1 \\
f(-1/2) &= a - \frac{b}{2} + \frac{c}{4} - \frac{d}{8} + \frac{e}{16} = f_2 \\
f(0) &= a = f_3 \\
f(+1/2) &= a - \frac{b}{2} + \frac{c}{4} - \frac{d}{8} + \frac{e}{16} = f_4 \\
f(+1) &= a + b + c + d + e = f_5
\end{aligned}$$

or,

$$\begin{pmatrix} 1 & -1 & 1 & -1 & 1 \\ 1 & -1/2 & 1/4 & -1/8 & 1/16 \\ 1 & 0 & 0 & 0 & 0 \\ 1 & 1/2 & 1/4 & 1/8 & 1/16 \\ 1 & 1 & 1 & 1 & 1 \end{pmatrix} \begin{pmatrix} a \\ b \\ c \\ d \\ e \end{pmatrix} = \begin{pmatrix} f_1 \\ f_2 \\ f_3 \\ f_4 \\ f_5 \end{pmatrix} \quad (210)$$

The third line gives  $a = f_3$  so that

$$\underbrace{\begin{pmatrix} -1 & 1 & -1 & 1 \\ -1/2 & 1/4 & -1/8 & 1/16 \\ 1/2 & 1/4 & 1/8 & 1/16 \\ 1 & 1 & 1 & 1 \end{pmatrix}}_A \begin{pmatrix} b \\ c \\ d \\ e \end{pmatrix} = \begin{pmatrix} f_1 - f_3 \\ f_2 - f_3 \\ f_4 - f_3 \\ f_5 - f_3 \end{pmatrix} \quad (211)$$

The inverse of the matrix  $A$  is:

$$A^{-1} = \frac{1}{6} \begin{pmatrix} 1 & -8 & 8 & -1 \\ -1 & 16 & 16 & -1 \\ -4 & 8 & -8 & 4 \\ 4 & -16 & -16 & 4 \end{pmatrix}$$

so that

$$\begin{pmatrix} b \\ c \\ d \\ e \end{pmatrix} = \frac{1}{6} \begin{pmatrix} 1 & -8 & 8 & -1 \\ -1 & 16 & 16 & -1 \\ -4 & 8 & -8 & 4 \\ 4 & -16 & -16 & 4 \end{pmatrix} \cdot \begin{pmatrix} f_1 - f_3 \\ f_2 - f_3 \\ f_4 - f_3 \\ f_5 - f_3 \end{pmatrix}$$

and then

$$b = \frac{1}{6} (f_1 - 8f_2 + 8f_4 - f_5) \quad (212)$$

$$c = \frac{1}{6} (-f_1 + 16f_2 - 30f_3 + 16f_4 - f_5) \quad (213)$$

$$d = \frac{1}{6} (-4f_1 + 8f_2 - 8f_4 + 4f_5) \quad (214)$$

$$e = \frac{1}{6} (4f_1 - 16f_2 + 24f_3 - 16f_4 + 4f_5) \quad (215)$$

$$f(r) = a + br + cr^2 + dr^3 + er^4 \quad (216)$$

$$= f_3 + \frac{1}{6} (f_1 - 8f_2 + 8f_4 - f_5) r + \frac{1}{6} (-f_1 + 16f_2 - 30f_3 + 16f_4 - f_5) r^2 + \quad (217)$$

$$+ \frac{1}{6} (-4f_1 + 8f_2 - 8f_4 + 4f_5) r^3 + \frac{1}{6} (4f_1 - 16f_2 + 24f_3 - 16f_4 + 4f_5) r^4 \quad (218)$$

$$= \frac{1}{6} (r - r^2 - 4r^3 + 4r^4) f_1 \quad (219)$$

$$+ \frac{1}{6} (-8r + 16r^2 + 8r^3 - 16r^4) f_2 \quad (220)$$

$$+ (1 - 5r^2 + 4r^4) f_3 \quad (221)$$

$$+ \frac{1}{6} (8r + 16r^2 - 8r^3 - 16r^4) f_4 \quad (222)$$

$$+ \frac{1}{6} (-r - r^2 + 4r^3 + 4r^4) f_5 \quad (223)$$

Finally

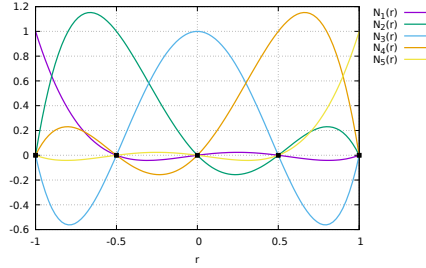
$$N_1(r) = \frac{1}{6} (r - r^2 - 4r^3 + 4r^4) \quad (224)$$

$$N_2(r) = \frac{1}{6} (-8r + 16r^2 + 8r^3 - 16r^4) \quad (225)$$

$$N_3(r) = (1 - 5r^2 + 4r^4) \quad (226)$$

$$N_4(r) = \frac{1}{6} (8r + 16r^2 - 8r^3 - 16r^4) \quad (227)$$

$$N_5(r) = \frac{1}{6} (-r - r^2 + 4r^3 + 4r^4) \quad (228)$$



The basis functions derivative are given by

$$\frac{\partial N_1}{\partial r} = \frac{1}{6} (1 - 2r - 12r^2 + 16r^3) \quad (229)$$

$$\frac{\partial N_2}{\partial r} = \frac{1}{6} (-8 + 32r + 24r^2 - 64r^3) \quad (230)$$

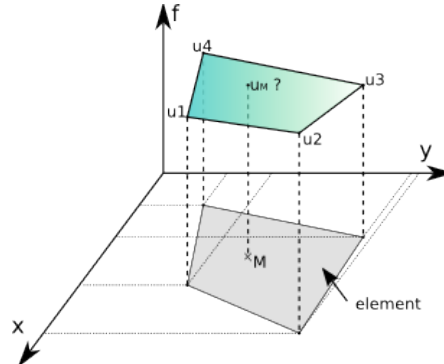
$$\frac{\partial N_3}{\partial r} = -10r + 16r^3 \quad (231)$$

$$\frac{\partial N_4}{\partial r} = \frac{1}{6} (8 + 32r - 24r^2 - 64r^3) \quad (232)$$

$$\frac{\partial N_5}{\partial r} = \frac{1}{6} (-1 - 2r + 12r^2 + 16r^3) \quad (233)$$

## 4.5 Elements and basis functions in 2D

Let us for a moment consider a single quadrilateral element in the  $xy$ -plane, as shown on the following figure:



Let us assume that we know the values of a given field  $u$  at the vertices. For a given point  $M$  inside the element in the plane, what is the value of the field  $u$  at this point? It makes sense to postulate that  $u_M = u(x_M, y_M)$  will be given by

$$u_M = \phi(u_1, u_2, u_3, u_4, x_M, y_M)$$

where  $\phi$  is a function to be determined. Although  $\phi$  is not unique, we can decide to express the value  $u_M$  as a weighed sum of the values at the vertices  $u_i$ . One option could be to assign all four vertices the same weight, say  $1/4$  so that  $u_M = (u_1 + u_2 + u_3 + u_4)/4$ , i.e.  $u_M$  is simply given by the arithmetic mean of the vertices values. This approach suffers from a major drawback as it does not use the location of point  $M$  inside the element. For instance, when  $(x_M, y_M) \rightarrow (x_2, y_2)$  we expect  $u_M \rightarrow u_2$ .

In light of this, we could now assume that the weights would depend on the position of  $M$  in a continuous fashion:

$$u(x_M, y_M) = \sum_{i=1}^4 N_i(x_M, y_M) u_i$$

where the  $N_i$  are continuous ("well behaved") functions which have the property:

$$N_i(x_j, y_j) = \delta_{ij}$$

or, in other words:

$$N_3(x_1, y_1) = 0 \quad (234)$$

$$N_3(x_2, y_2) = 0 \quad (235)$$

$$N_3(x_3, y_3) = 1 \quad (236)$$

$$N_3(x_4, y_4) = 0 \quad (237)$$

The functions  $N_i$  are commonly called basis functions.

Omitting the  $M$  subscripts for any point inside the element, the velocity components  $u$  and  $v$  are given by:

$$\hat{u}(x, y) = \sum_{i=1}^4 N_i(x, y) u_i \quad (238)$$

$$\hat{v}(x, y) = \sum_{i=1}^4 N_i(x, y) v_i \quad (239)$$

Rather interestingly, one can now easily compute velocity gradients (and therefore the strain rate tensor) since we have assumed the basis functions to be "well behaved" (in this case differentiable):

$$\dot{\epsilon}_{xx}(x, y) = \frac{\partial u}{\partial x} = \sum_{i=1}^4 \frac{\partial N_i}{\partial x} u_i \quad (240)$$

$$\dot{\epsilon}_{yy}(x, y) = \frac{\partial v}{\partial y} = \sum_{i=1}^4 \frac{\partial N_i}{\partial y} v_i \quad (241)$$

$$\dot{\epsilon}_{xy}(x, y) = \frac{1}{2} \frac{\partial u}{\partial y} + \frac{1}{2} \frac{\partial v}{\partial x} = \frac{1}{2} \sum_{i=1}^4 \frac{\partial N_i}{\partial y} u_i + \frac{1}{2} \sum_{i=1}^4 \frac{\partial N_i}{\partial x} v_i \quad (242)$$

How we actually obtain the exact form of the basis functions is explained in the coming section.

#### 4.5.1 Bilinear basis functions in 2D ( $Q_1$ )

In this section, we place ourselves in the most favorable case, i.e. the element is a square defined by  $-1 < r < 1$ ,  $-1 < s < 1$  in the Cartesian coordinates system  $(r, s)$ :

```
3=====2
|           |   (r_0,s_0)=(-1,-1)
|           |   (r_1,s_1)=(+1,-1)
|           |   (r_2,s_2)=(+1,+1)
|           |   (r_3,s_3)=(-1,+1)
|
0=====1
```

This element is commonly called the reference element. How we go from the  $(x, y)$  coordinate system to the  $(r, s)$  once and vice versa will be dealt later on. For now, the basis functions in the above reference element and in the reduced coordinates system  $(r, s)$  are given by:

$$\begin{aligned} N_1(r, s) &= 0.25(1 - r)(1 - s) \\ N_2(r, s) &= 0.25(1 + r)(1 - s) \\ N_3(r, s) &= 0.25(1 + r)(1 + s) \\ N_4(r, s) &= 0.25(1 - r)(1 + s) \end{aligned}$$

The partial derivatives of these functions with respect to  $r$  and  $s$  automatically follow:

$$\begin{aligned} \frac{\partial N_1}{\partial r}(r, s) &= -0.25(1 - s) & \frac{\partial N_1}{\partial s}(r, s) &= -0.25(1 - r) \\ \frac{\partial N_2}{\partial r}(r, s) &= +0.25(1 - s) & \frac{\partial N_2}{\partial s}(r, s) &= -0.25(1 + r) \\ \frac{\partial N_3}{\partial r}(r, s) &= +0.25(1 + s) & \frac{\partial N_3}{\partial s}(r, s) &= +0.25(1 + r) \\ \frac{\partial N_4}{\partial r}(r, s) &= -0.25(1 + s) & \frac{\partial N_4}{\partial s}(r, s) &= +0.25(1 - r) \end{aligned}$$

Let us go back to Eq.(239). And let us assume that the function  $v(r, s) = C$  so that  $v_i = C$  for  $i = 1, 2, 3, 4$ . It then follows that

$$\hat{v}(r, s) = \sum_{i=1}^4 N_i(r, s) v_i = C \sum_{i=1}^4 N_i(r, s) = C[N_1(r, s) + N_2(r, s) + N_3(r, s) + N_4(r, s)] = C$$

This is a very important property: if the  $v$  function used to assign values at the vertices is constant, then the value of  $\hat{v}$  *anywhere* in the element is exactly  $C$ . If we now turn to the derivatives of  $v$  with respect to  $r$  and  $s$ :

$$\frac{\partial \hat{v}}{\partial r}(r, s) = \sum_{i=1}^4 \frac{\partial N_i}{\partial r}(r, s) v_i = C \sum_{i=1}^4 \frac{\partial N_i}{\partial r}(r, s) = C[-0.25(1 - s) + 0.25(1 - s) + 0.25(1 + s) - 0.25(1 + s)] = 0$$

$$\frac{\partial \hat{v}}{\partial s}(r, s) = \sum_{i=1}^4 \frac{\partial N_i}{\partial s}(r, s) v_i = C \sum_{i=1}^4 \frac{\partial N_i}{\partial s}(r, s) = C[-0.25(1 - r) - 0.25(1 + r) + 0.25(1 + r) + 0.25(1 - r)] = 0$$

We reassuringly find that the derivative of a constant field anywhere in the element is exactly zero.

If we now choose  $v(r, s) = ar + bs$  with  $a$  and  $b$  two constant scalars, we find:

$$\hat{v}(r, s) = \sum_{i=1}^4 N_i(r, s) v_i \tag{243}$$

$$= \sum_{i=1}^4 N_i(r, s)(ar_i + bs_i) \tag{244}$$

$$= \underbrace{a \sum_{i=1}^4 N_i(r, s)r_i}_{r} + \underbrace{b \sum_{i=1}^4 N_i(r, s)s_i}_{s} \tag{245}$$

$$\begin{aligned} &= a[0.25(1 - r)(1 - s)(-1) + 0.25(1 + r)(1 - s)(+1) + 0.25(1 + r)(1 + s)(+1) + 0.25(1 - r)(1 + s)(-1)] \\ &+ b[0.25(1 - r)(1 - s)(-1) + 0.25(1 + r)(1 - s)(-1) + 0.25(1 + r)(1 + s)(+1) + 0.25(1 - r)(1 + s)(+1)] \\ &= a[-0.25(1 - r)(1 - s) + 0.25(1 + r)(1 - s) + 0.25(1 + r)(1 + s) - 0.25(1 - r)(1 + s)] \\ &+ b[-0.25(1 - r)(1 - s) - 0.25(1 + r)(1 - s) + 0.25(1 + r)(1 + s) + 0.25(1 - r)(1 + s)] \\ &= ar + bs \end{aligned} \tag{246}$$

**verify above eq.** This set of bilinear shape functions is therefore capable of exactly representing a bilinear field. The derivatives are:

$$\frac{\partial \hat{v}}{\partial r}(r, s) = \sum_{i=1}^4 \frac{\partial N_i}{\partial r}(r, s) v_i \quad (247)$$

$$= a \sum_{i=1}^4 \frac{\partial N_i}{\partial r}(r, s) r_i + b \sum_{i=1}^4 \frac{\partial N_i}{\partial r}(r, s) s_i \quad (248)$$

$$= a [-0.25(1-s)(-1) + 0.25(1-s)(+1) + 0.25(1+s)(+1) - 0.25(1+s)(-1)]$$

$$+ b [-0.25(1-s)(-1) + 0.25(1-s)(-1) + 0.25(1+s)(+1) - 0.25(1+s)(+1)]$$

$$= \frac{a}{4} [(1-s) + (1-s) + (1+s) + (1+s)]$$

$$+ \frac{b}{4} [(1-s) - (1-s) + (1+s) - (1+s)]$$

$$= a \quad (249)$$

Here again, we find that the derivative of the bilinear field inside the element is exact:  $\frac{\partial \hat{v}}{\partial r} = \frac{\partial v}{\partial r}$ .

However, following the same methodology as above, one can easily prove that this is no more true for polynomials of degree strivtly higher than 1. This fact has serious consequences: if the solution to the problem at hand is for instance a parabola, the  $Q_1$  shape functions cannot represent the solution properly, but only by approximating the parabola in each element by a line. As we will see later,  $Q_2$  basis functions can remedy this problem by containing themselves quadratic terms.

#### 4.5.2 Biquadratic basis functions in 2D ( $Q_2$ )

This element is part of the so-called LAgrange family.

citation needed

Inside an element the local numbering of the nodes is as follows:

```

3=====6=====2
|       |       |   (r_0,s_0)=(-1,-1)   (r_4,s_4)=( 0,-1)
|       |       |   (r_1,s_1)=(+1,-1)   (r_5,s_5)=(+1, 0)
7=====8=====5   (r_2,s_2)=(+1,+1)   (r_6,s_6)=( 0,+1)
|       |       |   (r_3,s_3)=(-1,+1)   (r_7,s_7)=(-1, 0)
|       |       |                           (r_8,s_8)=( 0, 0)
0=====4=====1

```

Note that this numbering is also employed in [1596, 56]. The basis polynomial is then

$$f(r, s) = a + br + cs + drs + er^2 + fs^2 + gr^2s + hrs^2 + ir^2s^2$$

The velocity shape functions are given by:

$N_0(r, s) = \frac{1}{2}r(r-1)\frac{1}{2}s(s-1)$
$N_1(r, s) = \frac{1}{2}r(r+1)\frac{1}{2}s(s-1)$
$N_2(r, s) = \frac{1}{2}r(r+1)\frac{1}{2}s(s+1)$
$N_3(r, s) = \frac{1}{2}r(r-1)\frac{1}{2}s(s+1)$
$N_4(r, s) = (1-r^2)\frac{1}{2}s(s-1)$
$N_5(r, s) = \frac{1}{2}r(r+1)(1-s^2)$
$N_6(r, s) = (1-r^2)\frac{1}{2}s(s+1)$
$N_7(r, s) = \frac{1}{2}r(r-1)(1-s^2)$
$N_8(r, s) = (1-r^2)(1-s^2)$

These are identical to [1596, p57]. Their derivatives are given by:

$\frac{\partial N_0}{\partial r} = \frac{1}{2}(2r-1)\frac{1}{2}s(s-1)$	$\frac{\partial N_0}{\partial s} = \frac{1}{2}r(r-1)\frac{1}{2}(2s-1)$
$\frac{\partial N_1}{\partial r} = \frac{1}{2}(2r+1)\frac{1}{2}s(s-1)$	$\frac{\partial N_1}{\partial s} = \frac{1}{2}r(r+1)\frac{1}{2}(2s-1)$
$\frac{\partial N_2}{\partial r} = \frac{1}{2}(2r+1)\frac{1}{2}s(s+1)$	$\frac{\partial N_2}{\partial s} = \frac{1}{2}r(r+1)\frac{1}{2}(2s+1)$
$\frac{\partial N_3}{\partial r} = \frac{1}{2}(2r-1)\frac{1}{2}s(s+1)$	$\frac{\partial N_3}{\partial s} = \frac{1}{2}r(r-1)\frac{1}{2}(2s+1)$
$\frac{\partial N_4}{\partial r} = (-2r)\frac{1}{2}s(s-1)$	$\frac{\partial N_4}{\partial s} = (1-r^2)\frac{1}{2}(2s-1)$
$\frac{\partial N_5}{\partial r} = \frac{1}{2}(2r+1)(1-s^2)$	$\frac{\partial N_5}{\partial s} = \frac{1}{2}r(r+1)(-2s)$
$\frac{\partial N_6}{\partial r} = (-2r)\frac{1}{2}s(s+1)$	$\frac{\partial N_6}{\partial s} = (1-r^2)\frac{1}{2}(2s+1)$
$\frac{\partial N_7}{\partial r} = \frac{1}{2}(2r-1)(1-s^2)$	$\frac{\partial N_7}{\partial s} = \frac{1}{2}r(r-1)(-2s)$
$\frac{\partial N_8}{\partial r} = (-2r)(1-s^2)$	$\frac{\partial N_8}{\partial s} = (1-r^2)(-2s)$

#### 4.5.3 Eight node serendipity basis functions in 2D ( $Q_2^{(8)}$ )

The serendipity elements are those rectangular elements which have no interior nodes [2118, p65].

Inside an element the local numbering of the nodes is as follows:

```
3=====6=====2
|       |       |   (r_0,s_0)=(-1,-1)   (r_4,s_4)=( 0,-1)
|       |       |   (r_1,s_1)=(+1,-1)   (r_5,s_5)=(+1, 0)
7=====+=====5   (r_2,s_2)=(+1,+1)   (r_6,s_6)=( 0,+1)
|       |       |   (r_3,s_3)=(-1,+1)   (r_7,s_7)=(-1, 0)
|       |       |
0=====4=====1
```

The main difference with the  $Q_2$  element resides in the fact that there is no node in the middle of the element. The basis polynomial is then

$$f(r, s) = a + br + cs + drs + er^2 + fs^2 + gr^2s + hrs^2$$

Note that absence of the  $r^2s^2$  term which was previously associated to the center node. We find that

$$N_0(r, s) = \frac{1}{4}(1-r)(1-s)(-r-s-1) \quad (250)$$

$$N_1(r, s) = \frac{1}{4}(1+r)(1-s)(r-s-1) \quad (251)$$

$$N_2(r, s) = \frac{1}{4}(1+r)(1+s)(r+s-1) \quad (252)$$

$$N_3(r, s) = \frac{1}{4}(1-r)(1+s)(-r+s-1) \quad (253)$$

$$N_4(r, s) = \frac{1}{2}(1-r^2)(1-s) \quad (254)$$

$$N_5(r, s) = \frac{1}{2}(1+r)(1-s^2) \quad (255)$$

$$N_6(r, s) = \frac{1}{2}(1-r^2)(1+s) \quad (256)$$

$$N_7(r, s) = \frac{1}{2}(1-r)(1-s^2) \quad (257)$$

The shape functions at the mid side nodes are products of a second order polynomial parallel to side and a linear function perpendicular to the side while shape functions for corner nodes are modifications of the bilinear quadrilateral element.

$$\frac{\partial N_0}{\partial r}(r, s) = -\frac{1}{4}(s-1)(2r+s) \quad (258)$$

$$\frac{\partial N_1}{\partial r}(r, s) = -\frac{1}{4}(s-1)(2r-s) \quad (259)$$

$$\frac{\partial N_2}{\partial r}(r, s) = \frac{1}{4}(s+1)(2r+s) \quad (260)$$

$$\frac{\partial N_3}{\partial r}(r, s) = \frac{1}{4}(s+1)(2r-s) \quad (261)$$

$$\frac{\partial N_4}{\partial r}(r, s) = r(s-1) \quad (262)$$

$$\frac{\partial N_5}{\partial r}(r, s) = \frac{1}{2}(1-s^2) \quad (263)$$

$$\frac{\partial N_6}{\partial r}(r, s) = -r(s+1) \quad (264)$$

$$\frac{\partial N_7}{\partial r}(r, s) = -\frac{1}{2}(1-s^2) \quad (265)$$

$$\frac{\partial N_0}{\partial s}(r, s) = -\frac{1}{4}(r-1)(r+2s) \quad (266)$$

$$\frac{\partial N_1}{\partial s}(r, s) = -\frac{1}{4}(r+1)(r-2s) \quad (267)$$

$$\frac{\partial N_2}{\partial s}(r, s) = \frac{1}{4}(r+1)(r+2s) \quad (268)$$

$$\frac{\partial N_3}{\partial s}(r, s) = \frac{1}{4}(r-1)(r-2s) \quad (269)$$

$$\frac{\partial N_4}{\partial s}(r, s) = -\frac{1}{2}(1-r^2) \quad (270)$$

$$\frac{\partial N_5}{\partial s}(r, s) = -(r+1)s \quad (271)$$

$$\frac{\partial N_6}{\partial s}(r, s) = \frac{1}{2}(1-r^2) \quad (272)$$

$$\frac{\partial N_7}{\partial s}(r, s) = (r-1)s \quad (273)$$

#### 4.5.4 Bicubic basis functions in 2D ( $Q_3$ )

Inside an element the local numbering of the nodes is as follows:

12==13==14==15	$(r,s)_{\{00\}}=(-1,-1)$	$(r,s)_{\{08\}}=(-1,+1/3)$
	$(r,s)_{\{01\}}=(-1/3,-1)$	$(r,s)_{\{09\}}=(-1/3,+1/3)$
08==09==10==11	$(r,s)_{\{02\}}=(+1/3,-1)$	$(r,s)_{\{10\}}=(+1/3,+1/3)$
	$(r,s)_{\{03\}}=(+1,-1)$	$(r,s)_{\{11\}}=(+1,+1/3)$
04==05==06==07	$(r,s)_{\{04\}}=(-1,-1/3)$	$(r,s)_{\{12\}}=(-1,+1)$
	$(r,s)_{\{05\}}=(-1/3,-1/3)$	$(r,s)_{\{13\}}=(-1/3,+1)$
00==01==02==03	$(r,s)_{\{06\}}=(+1/3,-1/3)$	$(r,s)_{\{14\}}=(+1/3,+1)$
	$(r,s)_{\{07\}}=(+1,-1/3)$	$(r,s)_{\{15\}}=(+1,+1)$

The velocity shape functions are given by:

$$N_1(r) = (-1 + r + 9r^2 - 9r^3)/16$$

$$N_1(t) = (-1 + t + 9t^2 - 9t^3)/16$$

$$N_2(r) = (+9 - 27r - 9r^2 + 27r^3)/16$$

$$N_2(t) = (+9 - 27t - 9t^2 + 27t^3)/16$$

$$N_3(r) = (+9 + 27r - 9r^2 - 27r^3)/16$$

$$N_3(t) = (+9 + 27t - 9t^2 - 27t^3)/16$$

$$N_4(r) = (-1 - r + 9r^2 + 9r^3)/16$$

$$N_4(t) = (-1 - t + 9t^2 + 9t^3)/16$$

$$\begin{aligned}
N_{01}(r, s) &= N_1(r)N_1(s) = (-1 + r + 9r^2 - 9r^3)/16 * (-1 + t + 9s^2 - 9s^3)/16 \\
N_{02}(r, s) &= N_2(r)N_1(s) = (+9 - 27r - 9r^2 + 27r^3)/16 * (-1 + t + 9s^2 - 9s^3)/16 \\
N_{03}(r, s) &= N_3(r)N_1(s) = (+9 + 27r - 9r^2 - 27r^3)/16 * (-1 + t + 9s^2 - 9s^3)/16 \\
N_{04}(r, s) &= N_4(r)N_1(s) = (-1 - r + 9r^2 + 9r^3)/16 * (-1 + t + 9s^2 - 9s^3)/16 \\
N_{05}(r, s) &= N_1(r)N_2(s) = (-1 + r + 9r^2 - 9r^3)/16 * (9 - 27s - 9s^2 + 27s^3)/16 \\
N_{06}(r, s) &= N_2(r)N_2(s) = (+9 - 27r - 9r^2 + 27r^3)/16 * (9 - 27s - 9s^2 + 27s^3)/16 \\
N_{07}(r, s) &= N_3(r)N_2(s) = (+9 + 27r - 9r^2 - 27r^3)/16 * (9 - 27s - 9s^2 + 27s^3)/16 \\
N_{08}(r, s) &= N_4(r)N_2(s) = (-1 - r + 9r^2 + 9r^3)/16 * (9 - 27s - 9s^2 + 27s^3)/16
\end{aligned} \tag{274}$$

$$N_{09}(r, s) = N_1(r)N_3(s) = \dots \tag{274}$$

$$N_{10}(r, s) = N_2(r)N_3(s) = \dots \tag{275}$$

$$N_{11}(r, s) = N_3(r)N_3(s) = \dots \tag{276}$$

$$N_{12}(r, s) = N_4(r)N_3(s) = \dots \tag{277}$$

$$N_{13}(r, s) = N_1(r)N_4(s) = \dots \tag{278}$$

$$N_{14}(r, s) = N_2(r)N_4(s) = \dots \tag{279}$$

$$N_{15}(r, s) = N_3(r)N_4(s) = \dots \tag{280}$$

$$N_{16}(r, s) = N_4(r)N_4(s) = \dots \tag{281}$$

#### 4.5.5 Biquartic basis functions in 2D ( $Q_4$ )

Inside an element the local numbering of the nodes is as follows:

```

20====21====22====23====24
||    ||    ||    ||
15====16====17====18====19
||    ||    ||    ||
10====11====12====13====14
||    ||    ||    ||
05====06====07====08====09
||    ||    ||    ||
00====01====02====03====04

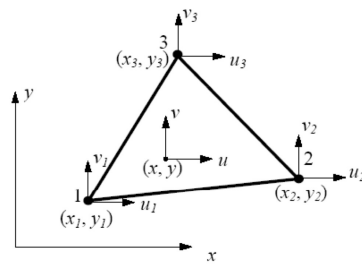
```

#### 4.5.6 Linear basis functions for triangles in 2D ( $P_1$ )

Velocities (or displacements)  $(u, v)$  in a plane element are interpolated from nodal velocities  $(u_i, v_i)$  using shape functions  $N_i$  as follows,

$$\begin{pmatrix} u \\ v \end{pmatrix} = \begin{pmatrix} N_1 & 0 & N_2 & 0 & N_3 & 0 \\ 0 & N_1 & 0 & N_2 & 0 & N_3 \end{pmatrix} \cdot \begin{pmatrix} u_1 \\ v_1 \\ u_2 \\ v_2 \\ u_3 \\ v_3 \end{pmatrix}$$

This is the simplest 2D element, which is also called linear triangular element.



For this element, we have three nodes at the vertices of the triangle, which are numbered around the element in the counterclockwise direction. Each node has two degrees of freedom (can move in the  $x$  and  $y$  directions). The velocities  $u$  and  $v$  are assumed to be linear functions within the element, that is,

$$u = b_1 + b_2x + b_3y \quad v = b_4 + b_5x + b_6y$$

where  $b_i$  are constants to be determined and which depend on the triangle shape. Note that the strain rate components are then given by

$$\dot{\varepsilon}_{xx} = b_2 \quad \dot{\varepsilon}_{yy} = b_6 \quad \dot{\varepsilon}_{xy} = (b_3 + b_5)/2$$

and are constant throughout the element.

The velocities should satisfy the following six equations:

$$\begin{aligned} u_1 &= b_1 + b_2x_1 + b_3y_1 \\ u_2 &= b_1 + b_2x_2 + b_3y_2 \\ u_3 &= b_1 + b_2x_3 + b_3y_3 \\ v_1 &= b_4 + b_5x_1 + b_6y_1 \\ v_2 &= b_4 + b_5x_2 + b_6y_2 \\ v_3 &= b_4 + b_5x_3 + b_6y_3 \end{aligned}$$

This can be re-written:

$$\begin{pmatrix} u_1 \\ u_2 \\ u_3 \end{pmatrix} = \begin{pmatrix} 1 & x_1 & y_1 \\ 1 & x_2 & y_2 \\ 1 & x_3 & y_3 \end{pmatrix} \cdot \begin{pmatrix} b_1 \\ b_2 \\ b_3 \end{pmatrix}$$

In order to obtain  $b_1, b_2, b_3$  we need to solve this system, or simply to compute the inverse of the  $3 \times 3$   $\mathbf{M}$  matrix, as explained in G.2.

We define  $D = \det(\mathbf{M})$  and we get

$$\begin{aligned} \begin{pmatrix} b_1 \\ b_2 \\ b_3 \end{pmatrix} &= \frac{1}{D} \tilde{\mathbf{M}} \cdot \begin{pmatrix} u_1 \\ u_2 \\ u_3 \end{pmatrix} \\ \begin{pmatrix} b_4 \\ b_5 \\ b_6 \end{pmatrix} &= \frac{1}{D} \tilde{\mathbf{M}} \cdot \begin{pmatrix} v_1 \\ v_2 \\ v_3 \end{pmatrix} \end{aligned}$$

The matrix  $\tilde{\mathbf{M}}$  writes:

$$\tilde{\mathbf{M}} = \begin{pmatrix} x_2y_3 - x_3y_2 & -(y_3 - y_2) & x_3 - x_2 \\ -(x_1y_3 - x_3y_1) & y_3 - y_1 & -(x_3 - x_1) \\ x_1y_2 - x_2y_1 & -(y_2 - y_1) & x_2 - x_1 \end{pmatrix}$$

ie,

$$\tilde{\mathbf{M}} = \begin{pmatrix} x_2y_3 - x_3y_2 & y_2 - y_3 & x_3 - x_2 \\ x_3y_1 - x_1y_3 & y_3 - y_1 & x_1 - x_3 \\ x_1y_2 - x_2y_1 & y_1 - y_2 & x_2 - x_1 \end{pmatrix}$$

and finally the linear shape functions are given by:

$$\begin{aligned} N_1(x, y) &= \frac{1}{D}[(x_2y_3 - x_3y_2) + (y_2 - y_3)x + (x_3 - x_2)y] \\ N_2(x, y) &= \frac{1}{D}[(x_3y_1 - x_1y_3) + (y_3 - y_1)x + (x_1 - x_3)y] \\ N_3(x, y) &= \frac{1}{D}[(x_1y_2 - x_2y_1) + (y_1 - y_2)x + (x_2 - x_1)y] \end{aligned}$$

Note that the area  $A$  of the triangle is given by:

$$A = \frac{1}{2}D = \frac{1}{2} \begin{vmatrix} 1 & x_1 & y_1 \\ 1 & x_2 & y_2 \\ 1 & x_3 & y_3 \end{vmatrix}$$

If we now consider the reference element in the reduced coordinates space  $(r, s)$ :

```

2
|\ \
|   \   (r_0,s_0)=(0,0)
|     \ (r_1,s_1)=(1,0)
|       \ (r_2,s_2)=(0,2)
0=====1

```

The basis polynomial is then

$$f(r,s) = a + br + cs$$

and the shape functions:

$$N_0(r,s) = 1 - r - s \quad (282)$$

$$N_1(r,s) = r \quad (283)$$

$$N_2(r,s) = s \quad (284)$$

#### 4.5.7 Linear basis functions for quadrilaterals in 2D ( $P_1$ )

```

.=====.
|      |      |
|      3      | (r_1,s_1)=(0,0)
|      |      | (r_2,s_2)=(1/2,0)
.=====1==2==. (r_3,s_3)=(0,1/2)
|      |      |
|      |      |
|      |      |
.=====.

```

Let us assume that the function  $f(r,s)$  is to be approximated on  $[-1,1] \times [-1,1]$  by

$$f(r,s) = a + br + cs$$

The function  $f$  then must fulfil:

$$\begin{aligned} f(r_1, s_1) &= a = f_1 \\ f(r_2, s_2) &= a + \frac{b}{2} = f_2 \\ f(r_3, s_3) &= a + \frac{c}{2} = f_3 \end{aligned} \quad (285)$$

This leads to :

$$a = f_1 \quad b = 2(f_2 - f_1) \quad c = 2(f_3 - f_1)$$

Then

$$f(r,s) = f_1 + 2(f_2 - f_1)r + 2(f_3 - f_1)s$$

or,

$$f(r) = \sum_{i=1}^3 N_i(r,s) f_i$$

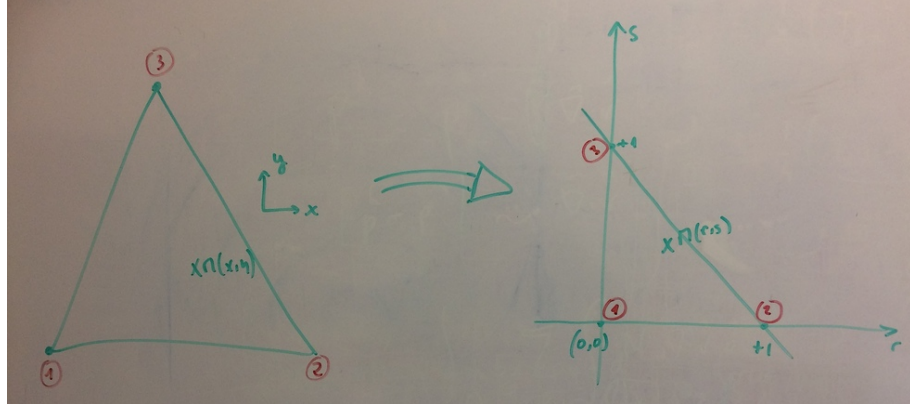
with

$$\begin{aligned} N_1(r) &= 1 - 2(r+s) \\ N_2(r) &= 2r \\ N_3(r) &= 2s \end{aligned} \quad (286)$$

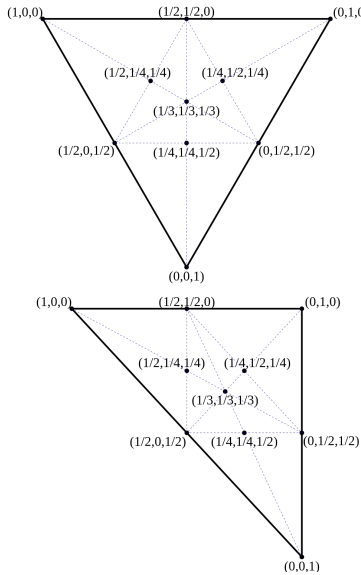
#### 4.5.8 Enriched linear basis functions in triangles ( $P_1^+$ )

As we will see in Section 6.2.8 the above  $P_1$  can be enriched with a so-called bubble function. The bubble function of the MINI element is described in [52] as being  $\lambda_1\lambda_2\lambda_3$  where  $\lambda_i$  are the so-called barycentric coordinates<sup>27</sup>.

$$\begin{aligned}\lambda_1 &= \frac{(y_2 - y_3)(x - x_3) + (x_3 - x_2)(y - y_3)}{(y_2 - y_3)(x_1 - x_3) + (x_3 - x_2)(y_1 - y_3)} \\ \lambda_2 &= \frac{(y_3 - y_1)(x - x_3) + (x_1 - x_3)(y - y_3)}{(y_2 - y_3)(x_1 - x_3) + (x_3 - x_2)(y_1 - y_3)} \\ \lambda_3 &= 1 - \lambda_1 - \lambda_2\end{aligned}$$



representation of the element in the real coordinate system  $(x, y)$  and in the reduced coordinate system  $(r, s)$



Barycentric coordinates  $(\lambda_1, \lambda_2, \lambda_3)$  on an equilateral triangle and on a right triangle.

In the reference triangle, the barycentric coordinates write

$$\begin{aligned}\lambda_1 &= \frac{(s_2 - s_3)(r - r_3) + (r_3 - r_2)(s - s_3)}{(s_2 - s_3)(r_1 - r_3) + (r_3 - r_2)(s_1 - s_3)} = \frac{(-1)(r) + (-1)(s - 1)}{(-1)(0) + (-1)(-1)} = -r - s + 1 \\ \lambda_2 &= \frac{(s_3 - s_1)(r - r_3) + (r_1 - r_3)(s - s_3)}{(s_2 - s_3)(r_1 - r_3) + (r_3 - r_2)(s_1 - s_3)} = \frac{(1)(r) + (0)(s - 1)}{(-1)(0) + (-1)(-1)} = r \\ \lambda_3 &= 1 - \lambda_1 - \lambda_2 = 1 - (-r - s + 1) - r = s\end{aligned}$$

<sup>27</sup>[https://en.wikipedia.org/wiki/Barycentric\\_coordinate\\_system](https://en.wikipedia.org/wiki/Barycentric_coordinate_system)

As we have seen before the bubble function is given by  $\lambda_1\lambda_2\lambda_3 = (1 - r - s)rs$  and the polynomial form for the shape functions is given by:

$$f(r, s) = a + br + cs + d(1 - r - s)rs$$

Setting the location of the bubble at  $r = s = 1/3$ , i.e.  $\lambda_1\lambda_2\lambda_3 = 1/3$ , we then have

$$\begin{aligned} f(r_1, s_1) &= f_1 = a + br_1 + cs_1 + d(1 - r_1 - s_1)r_1s_1 = a \\ f(r_2, s_2) &= f_2 = a + br_2 + cs_2 + d(1 - r_2 - s_2)r_2s_2 = a + b \\ f(r_3, s_3) &= f_3 = a + br_3 + cs_3 + d(1 - r_3 - s_3)r_3s_3 = a + c \\ f(r_4, s_4) &= f_4 = a + br_4 + cs_4 + d(1 - r_4 - s_4)r_4s_4 = a + \frac{b}{3} + \frac{c}{3} + \frac{1}{27} \end{aligned}$$

where point 4 is the location of the bubble. This yields

$$a = f_1 \quad b = f_2 - a = f_2 - f_1 \quad c = f_3 - a = f_3 - f_1$$

and

$$d = 27(f_4 - a - \frac{b}{3} - \frac{c}{3}) = 27(f_4 - f_1 - \frac{f_2 - f_1}{3} - \frac{f_3 - f_1}{3}) = 27(f_4 - \frac{f_1}{3} - \frac{f_2}{3} - \frac{f_3}{3})$$

Finally

$$\begin{aligned} f(r, s) &= a + br + cs + d(1 - r - s)rs \\ &= f_1 + (f_2 - f_1)r + (f_3 - f_1)s + 27(f_4 - \frac{f_1}{3} - \frac{f_2}{3} - \frac{f_3}{3})(1 - r - s)rs \\ &= [1 - r - s - 9(1 - r - s)rs]f_1 + [r - 9(1 - r - s)rs]f_2 + [s - 9(1 - r - s)rs]f_3 + [27(1 - r - s)rs]f_4 \end{aligned}$$

so that

$$f(r, s) = \sum_{i=1}^4 N_i(r, s)f_i$$

with

$$\begin{aligned} N_1(r, s) &= 1 - r - s - 9(1 - r - s)rs \\ N_2(r, s) &= r - 9(1 - r - s)rs \\ N_3(r, s) &= s - 9(1 - r - s)rs \\ N_4(r, s) &= 27(1 - r - s)rs \end{aligned}$$

It is trivial to verify that  $\sum_i N_i = 1$  for all values of  $r, s$  and the gradients of the shape functions are:

$$\frac{\partial N_1}{\partial r}(r, s) = -1 - 9(1 - 2r - s)s \quad (287)$$

$$\frac{\partial N_2}{\partial r}(r, s) = +1 - 9(1 - 2r - s)s \quad (288)$$

$$\frac{\partial N_3}{\partial r}(r, s) = -9(1 - 2r - s)s \quad (289)$$

$$\frac{\partial N_4}{\partial r}(r, s) = 27(1 - 2r - s)s \quad (290)$$

(291)

$$\frac{\partial N_1}{\partial s}(r, s) = -1 - 9(1 - r - 2s)r \quad (292)$$

$$\frac{\partial N_2}{\partial s}(r, s) = -9(1 - r - 2s)r \quad (293)$$

$$\frac{\partial N_3}{\partial s}(r, s) = +1 - 9(1 - r - 2s)r \quad (294)$$

$$\frac{\partial N_4}{\partial s}(r, s) = 27(1 - r - 2s)r \quad (295)$$

We have two coordinate systems for the element: the global coordinates  $(x, y)$  and the natural coordinates  $(r, s)$ . Inside the element, the relation between the two is given by

$$\begin{aligned} x &= N_1x_1 + N_2x_2 + N_3x_3 + N_4x_4 = \sum_i N_i(r, s)x_i \\ y &= N_1y_1 + N_2y_2 + N_3y_3 + N_4y_4 = \sum_i N_i(r, s)y_i \end{aligned} \quad (296)$$

or,

$$\begin{aligned} x &= [1 - r - s - 9(1 - r - s)rs]x_1 + [r - 9(1 - r - s)rs]x_2 + [s - 9(1 - r - s)rs]x_3 + [27(1 - r - s)rs]x_4 \\ &= x_1 - r(x_1 - x_2) - s(x_1 - x_3) + (1 - r - s)rs(-9x_1 - 9x_2 - 9x_3 + 27x_4) \\ &= x_1 - r(x_1 - x_2) - s(x_1 - x_3) + (1 - r - s)rs(-9x_1 - 9x_2 - 9x_3 + 27(x_1 + x_2 + x_3)/3) \\ &= x_1 - r(x_1 - x_2) - s(x_1 - x_3) \\ &= x_1 - rx_{12} - sx_{13} \\ y &= [1 - r - s - 9(1 - r - s)rs]y_1 + [r - 9(1 - r - s)rs]y_2 + [s - 9(1 - r - s)rs]y_3 + [27(1 - r - s)rs]y_4 \\ &= y_1 - r(y_1 - y_2) - s(y_1 - y_3) + (1 - r - s)rs(-9y_1 - 9y_2 - 9y_3 + 27y_4) \\ &= y_1 - r(y_1 - y_2) - s(y_1 - y_3) + (1 - r - s)rs(-9y_1 - 9y_2 - 9y_3 + 27(y_1 + y_2 + y_3)/3) \\ &= y_1 - r(y_1 - y_2) - s(y_1 - y_3) \\ &= y_1 - ry_{12} - sy_{13} \end{aligned}$$

#### 4.5.9 Quadratic basis functions for triangles in 2D ( $P_2$ )

```

2
|\ \
|  \      (r_0,s_0)=(0,0)  (r_3,s_3)=(1/2,0)
5   4      (r_1,s_1)=(1,0)  (r_4,s_4)=(1/2,1/2)
|     \    (r_2,s_2)=(0,1)  (r_5,s_5)=(0,1/2)
|       \
0====3====1

```

The basis polynomial is then

$$f(r, s) = c_1 + c_2r + c_3s + c_4r^2 + c_5rs + c_6s^2$$

We have

$$\begin{aligned} f_1 = f(r_1, s_1) &= c_1 \\ f_2 = f(r_2, s_2) &= c_1 + c_2 + c_4 \\ f_3 = f(r_3, s_3) &= c_1 + c_3 + c_6 \\ f_4 = f(r_4, s_4) &= c_1 + c_2/2 + c_4/4 \\ f_5 = f(r_5, s_5) &= c_1 + c_2/2 + c_3/2 \\ &\quad + c_4/4 + c_5/4 + c_6/4 \\ f_6 = f(r_6, s_6) &= c_1 + c_3/2 + c_6/4 \end{aligned}$$

This can be cast as  $\mathbf{f} = \mathbf{A} \cdot \mathbf{c}$  where  $\mathbf{A}$  is a 6x6 matrix:

$$\mathbf{A} = \begin{pmatrix} 1 & 0 & 0 & 0 & 0 & 0 \\ 1 & 1 & 0 & 1 & 0 & 0 \\ 1 & 0 & 1 & 0 & 0 & 1 \\ 1 & 1/2 & 0 & 1/4 & 0 & 0 \\ 1 & 1/2 & 1/2 & 1/4 & 1/4 & 1/4 \\ 1 & 0 & 1/2 & 0 & 0 & 1/4 \end{pmatrix}$$

It is rather trivial to compute the inverse of this matrix:

$$\mathbf{A}^{-1} = \begin{pmatrix} 1 & 0 & 0 & 0 & 0 & 0 \\ -3 & -1 & 0 & 4 & 0 & 0 \\ -3 & 0 & -1 & 0 & 0 & 4 \\ 2 & 2 & 0 & -4 & 0 & 0 \\ 4 & 0 & 0 & -4 & 4 & -4 \\ 2 & 0 & 2 & 0 & 0 & -4 \end{pmatrix}$$

In the end, one obtains:

$$\begin{aligned} f(r, s) &= f_1 + (-3f_1 - f_2 + 4f_4)r + (-3f_1 - f_3 + 4f_6)s \\ &\quad + (2f_1 + 2f_2 - 4f_4)r^2 + (4f_1 - 4f_4 + 4f_5 - 4f_6)rs \\ &\quad + (2f_1 + 2f_3 - 4f_6)s^2 \\ &= \sum_{i=1}^6 N_i(r, s)f_i \end{aligned} \tag{297}$$

with

$N_1(r, s)$	$=$	$1 - 3r - 3s + 2r^2 + 4rs + 2s^2$
$N_2(r, s)$	$=$	$-r + 2r^2$
$N_3(r, s)$	$=$	$-s + 2s^2$
$N_4(r, s)$	$=$	$4r - 4r^2 - 4rs$
$N_5(r, s)$	$=$	$4rs$
$N_6(r, s)$	$=$	$4s - 4rs - 4s^2$

#### 4.5.10 Enriched quadratic basis functions in triangles ( $P_2^+$ )

This is used by the Crouzeix-Raviart element, see Section 6.2.10.

```

03      (r_1,s_1)=(0,0)
|| \\
||  \\
||  \\
06  05  (r_5,s_5)=(1/2,1/2)
|| 07  \\
||    \\
01==04==02

```

The shape functions are given by:

[find reference](#)

$$N_1(r, s) = (1 - r - s)(1 - 2r - 2s + 3rs) \tag{298}$$

$$N_2(r, s) = r(2r - 1 + 3s - 3rs - 3s^2) \tag{299}$$

$$N_3(r, s) = s(2s - 1 + 3r - 3r^2 - 3rs) \tag{300}$$

$$N_4(r, s) = 4(1 - r - s)r(1 - 3s) \tag{301}$$

$$N_5(r, s) = 4rs[-2 + 3r + 3s] \tag{302}$$

$$N_6(r, s) = 4(1 - r - s)s(1 - 3r) \tag{303}$$

$$N_7(r, s) = 27(1 - r - s)rs \tag{304}$$

It is then easy to verify that for all shape functions we have  $N_i(r_j, s_j) = \delta_{ij}$  where  $j$  denotes one of the seven nodes.

The derivatives are as follows:

$$\frac{\partial N_1}{\partial r}(r, s) = r(4 - 6s) - 3s^2 + 7s - 3 \quad (305)$$

$$\frac{\partial N_2}{\partial r}(r, s) = r(4 - 6s) - 3s^2 + 3s - 1 \quad (306)$$

$$\frac{\partial N_3}{\partial r}(r, s) = -3s(2r + s - 1) \quad (307)$$

$$\frac{\partial N_4}{\partial r}(r, s) = 4(3s - 1)(2r + s - 1) \quad (308)$$

$$\frac{\partial N_5}{\partial r}(r, s) = 4s(6r + 3s - 2) \quad (309)$$

$$\frac{\partial N_6}{\partial r}(r, s) = 4s(6r + 3s - 4) \quad (310)$$

$$\frac{\partial N_7}{\partial r}(r, s) = -27s(2r + s - 1) \quad (311)$$

$$\frac{\partial N_1}{\partial s}(r, s) = -3r^2 + r(7 - 6s) + 4s - 3 \quad (312)$$

$$\frac{\partial N_2}{\partial s}(r, s) = -3r(r + 2s - 1) \quad (313)$$

$$\frac{\partial N_3}{\partial s}(r, s) = -3r^2 + r(3 - 6s) + 4s - 1 \quad (314)$$

$$\frac{\partial N_4}{\partial s}(r, s) = 4r(3r + 6s - 4) \quad (315)$$

$$\frac{\partial N_5}{\partial s}(r, s) = 4r(3r + 6s - 2) \quad (316)$$

$$\frac{\partial N_6}{\partial s}(r, s) = 4(3r - 1)(r + 2s - 1) \quad (317)$$

$$\frac{\partial N_7}{\partial s}(r, s) = -27r(r + 2s - 1) \quad (318)$$

Note that the shape functions can also be expressed as a function of the barycentric coordinates, as in the MILAMIN code [614] or in Cuvelier et al, 1986 [613]<sup>28</sup>

```

03
|| \\
|| \\
||  \\
05  04
|| 07 \\
||      \\
01==06==02

```

$$N_1(\lambda_1, \lambda_2, \lambda_3) = \eta_1(2\eta_1 - 1) + 3\eta_1\eta_2\eta_3 \quad (319)$$

$$N_2(\lambda_1, \lambda_2, \lambda_3) = \eta_2(2\eta_2 - 1) + 3\eta_1\eta_2\eta_3 \quad (320)$$

$$N_3(\lambda_1, \lambda_2, \lambda_3) = \eta_3(2\eta_3 - 1) + 3\eta_1\eta_2\eta_3 \quad (321)$$

$$N_4(\lambda_1, \lambda_2, \lambda_3) = 4\eta_2\eta_3 - 12\eta_1\eta_2\eta_3 \quad (322)$$

$$N_5(\lambda_1, \lambda_2, \lambda_3) = 4\eta_1\eta_3 - 12\eta_1\eta_2\eta_3 \quad (323)$$

$$N_6(\lambda_1, \lambda_2, \lambda_3) = 4\eta_1\eta_2 - 12\eta_1\eta_2\eta_3 \quad (324)$$

$$N_7(\lambda_1, \lambda_2, \lambda_3) = 27\eta_1\eta_2\eta_3 \quad (325)$$

---

<sup>28</sup>Note that the numbering of the nodes in the book is different with respect to the one above.

VERIFY that when  $\eta_1 = 1 - r - s$ ,  $\eta_2 = r$  and  $\eta_3 = s$  we find the above  $r, s$  shape functions

#### 4.5.11 Cubic basis functions for triangles ( $P_3$ )

```

2
|\          (r_0,s_0)=(0,0)   (r_5,s_5)=(2/3,1/3)
| \        (r_1,s_1)=(1,0)   (r_6,s_6)=(1/3,2/3)
7   6      (r_2,s_2)=(0,1)   (r_7,s_7)=(0,2/3)
|   \
8   9   5    (r_3,s_3)=(1/3,0) (r_8,s_8)=(0,1/3)
|       \
0==3==4==1

```

The basis polynomial is then

$$f(r, s) = c_1 + c_2r + c_3s + c_4r^2 + c_5rs + c_6s^2 + c_7r^3 + c_8r^2s + c_9rs^2 + c_{10}s^3$$

$$N_0(r, s) = \frac{9}{2}(1 - r - s)(1/3 - r - s)(2/3 - r - s) \quad (326)$$

$$N_1(r, s) = \frac{9}{2}r(r - 1/3)(r - 2/3) \quad (327)$$

$$N_2(r, s) = \frac{9}{2}s(s - 1/3)(s - 2/3) \quad (328)$$

$$N_3(r, s) = \frac{27}{2}(1 - r - s)r(2/3 - r - s) \quad (329)$$

$$N_4(r, s) = \frac{27}{2}(1 - r - s)r(r - 1/3) \quad (330)$$

$$N_5(r, s) = \frac{27}{2}rs(r - 1/3) \quad (331)$$

$$N_6(r, s) = \frac{27}{2}rs(r - 2/3) \quad (332)$$

$$N_7(r, s) = \frac{27}{2}(1 - r - s)s(s - 1/3) \quad (333)$$

$$N_8(r, s) = \frac{27}{2}(1 - r - s)s(2/3 - r - s) \quad (334)$$

$$N_9(r, s) = 27rs(1 - r - s) \quad (335)$$

verify those

## 4.6 Elements and basis functions in 3D

#### 4.6.1 Linear basis functions in tetrahedra ( $P_1$ )

$$(r_0, s_0) = (0, 0, 0)$$

$$(r_1, s_1) = (1, 0, 0)$$

$$(r_2, s_2) = (0, 2, 0)$$

$$(r_3, s_3) = (0, 0, 1)$$

The basis polynomial is given by

$$f(r, s, t) = c_0 + c_1r + c_2s + c_3t$$

$$f_1 = f(r_1, s_1, t_1) = c_0 \quad (336)$$

$$f_2 = f(r_2, s_2, t_2) = c_0 + c_1 \quad (337)$$

$$f_3 = f(r_3, s_3, t_3) = c_0 + c_2 \quad (338)$$

$$f_4 = f(r_4, s_4, t_4) = c_0 + c_3 \quad (339)$$

which yields:

$$c_0 = f_1 \quad c_1 = f_2 - f_1 \quad c_2 = f_3 - f_1 \quad c_3 = f_4 - f_1$$

$$\begin{aligned} f(r, s, t) &= c_0 + c_1 r + c_2 s + c_3 t \\ &= f_1 + (f_2 - f_1)r + (f_3 - f_1)s + (f_4 - f_1)t \\ &= f_1(1 - r - s - t) + f_2 r + f_3 s + f_4 t \\ &= \sum_i N_i(r, s, t) f_i \end{aligned}$$

Finally,

$N_1(r, s, t) = 1 - r - s - t$
$N_2(r, s, t) = r$
$N_3(r, s, t) = s$
$N_4(r, s, t) = t$

#### 4.6.2 Enriched linear in tetrahedra( $P_1^+$ )

These shape functions would be used in the MINI element, see Section 6.2.8.

In 3D the bubble function looks like  $rst(1 - r - s - t)$  so that

$$f(r, s, t) = a + b r + c s + d t + e rst(1 - r - s - t)$$

We have node 1 at location  $(r, s, t) = (0, 0, 0)$ , node 2 at  $(r, s, t) = (1, 0, 0)$ , node 3 at  $(r, s, t) = (0, 1, 0)$ , node 4 at  $(r, s, t) = (0, 0, 1)$  and we set the location of the bubble (node 5) at  $r = s = t = 1/4$  so that

$$f(r_1, s_1, t_1) = f_1 = a + b r_1 + c s_1 + d t_1 + e r_1 s_1 t_1 (1 - r_1 - s_1 - t_1) \quad (340)$$

$$f(r_2, s_2, t_2) = f_2 = a + b r_2 + c s_2 + d t_2 + e r_2 s_2 t_2 (1 - r_2 - s_2 - t_2) \quad (341)$$

$$f(r_3, s_3, t_3) = f_3 = a + b r_3 + c s_3 + d t_3 + e r_3 s_3 t_3 (1 - r_3 - s_3 - t_3) \quad (342)$$

$$f(r_4, s_4, t_4) = f_4 = a + b r_4 + c s_4 + d t_4 + e r_4 s_4 t_4 (1 - r_4 - s_4 - t_4) \quad (343)$$

$$f(r_5, s_5, t_5) = f_5 = a + b r_5 + c s_5 + d t_5 + e r_5 s_5 t_5 (1 - r_5 - s_5 - t_5) \quad (344)$$

i.e.,

$$f_1 = a \quad (345)$$

$$f_2 = a + b \quad (346)$$

$$f_3 = a + c \quad (347)$$

$$f_4 = a + d \quad (348)$$

$$f_5 = a + b/4 + c/4 + d/4 + e/64(1 - 1/4 - 1/4 - 1/4) \quad (349)$$

$$= a + b/4 + c/4 + d/4 + e/256 \quad (350)$$

Then

$$a = f_1 \quad (351)$$

$$b = f_2 - f_1 \quad (352)$$

$$c = f_3 - f_1 \quad (353)$$

$$d = f_4 - f_1 \quad (354)$$

$$e = 256(f_5 - a - b/4 - c/4 - d/4) \quad (355)$$

$$= 256(f_5 - f_1 - (f_2 - f_1)/4 - (f_3 - f_1)/4 - (f_4 - f_1)/4) \quad (356)$$

$$= 256(-f_1/4 - f_2/4 - f_3/4 - f_4/4 + f_5) \quad (357)$$

$$= 64(-f_1 - f_2 - f_3 - f_4 + 4f_5) \quad (358)$$

Finally:

$$\begin{aligned}
f(r, s, t) &= a + br + cs + dt + erst(1 - r - s - t) \\
&= f_1 + (f_2 - f_1)r + (f_3 - f_1)s + (f_4 - f_1)t + 64(-f_1 - f_2 - f_3 - f_4 + 4f_5)rst(1 - r - s - t) \\
&= f_1[1 - r - s - t - 64rst(1 - r - s - t)] \\
&\quad + f_2[r - 64rst(1 - r - s - t)] \\
&\quad + f_3[s - 64rst(1 - r - s - t)] \\
&\quad + f_4[t - 64rst(1 - r - s - t)] \\
&\quad + f_5[256rst(1 - r - s - t)] \\
&= \sum_{i=1}^5 N_i(r, s, t) f_i
\end{aligned} \tag{359}$$

with

$$N_1(r, s, t) = 1 - r - s - t - 64rst(1 - r - s - t) \tag{360}$$

$$N_2(r, s, t) = r - 64rst(1 - r - s - t) \tag{361}$$

$$N_3(r, s, t) = s - 64rst(1 - r - s - t) \tag{362}$$

$$N_4(r, s, t) = t - 64rst(1 - r - s - t) \tag{363}$$

$$N_5(r, s, t) = +256rst(1 - r - s - t) \tag{364}$$

The derivatives are given by:

$$\frac{\partial N_1}{\partial r}(r, s, t) = -1 - 64st(1 - 2r - s - t)$$

$$\frac{\partial N_2}{\partial r}(r, s, t) = +1 - 64st(1 - 2r - s - t)$$

$$\frac{\partial N_3}{\partial r}(r, s, t) = -64st(1 - 2r - s - t)$$

$$\frac{\partial N_4}{\partial r}(r, s, t) = -64st(1 - 2r - s - t)$$

$$\frac{\partial N_5}{\partial r}(r, s, t) = 256st(1 - 2r - s - t)$$

$$\frac{\partial N_1}{\partial s}(r, s, t) = -1 - 64rt(1 - r - 2s - t)$$

$$\frac{\partial N_2}{\partial s}(r, s, t) = -64rt(1 - r - 2s - t)$$

$$\frac{\partial N_3}{\partial s}(r, s, t) = +1 - 64rt(1 - r - 2s - t)$$

$$\frac{\partial N_4}{\partial s}(r, s, t) = -64rt(1 - r - 2s - t)$$

$$\frac{\partial N_5}{\partial s}(r, s, t) = 256rt(1 - r - 2s - t)$$

$$\frac{\partial N_1}{\partial t}(r, s, t) = -1 - 64rs(1 - r - s - 2t)$$

$$\frac{\partial N_2}{\partial t}(r, s, t) = -64rs(1 - r - s - 2t)$$

$$\frac{\partial N_3}{\partial t}(r, s, t) = -64rs(1 - r - s - 2t)$$

$$\frac{\partial N_4}{\partial t}(r, s, t) = +1 - 64rs(1 - r - s - 2t)$$

$$\frac{\partial N_5}{\partial t}(r, s, t) = 256rs(1 - r - s - 2t)$$

### 4.6.3 Triquadratic basis functions in 3D ( $Q_2$ )

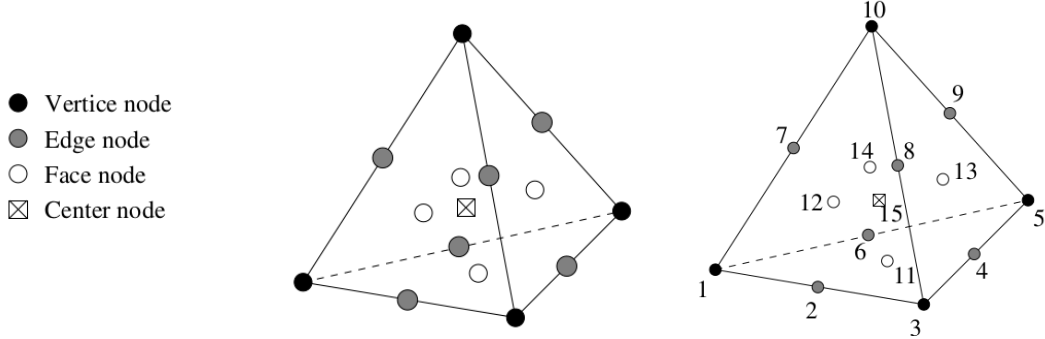
```

t
|
. --s
/
r
          05=====16=====08
          |       |       |
          |       |       |
13=====26=====15  17=====25=====20
          |       |       |
          |       |       |
06=====14=====07  22=====27=====24  01=====12=====04 @ r=-1
          |       |       |
          |       |       |
18=====23=====14  09=====21=====11 @ r=0
          |       |       |
          |       |       |
02=====10=====03 @ r=+1

```

$$\begin{aligned}
N_1 &= 0.5r(r-1) 0.5s(s-1) 0.5t(t-1) \\
N_2 &= 0.5r(r+1) 0.5s(s-1) 0.5t(t-1) \\
N_3 &= 0.5r(r+1) 0.5s(s+1) 0.5t(t-1) \\
N_4 &= 0.5r(r-1) 0.5s(s+1) 0.5t(t-1) \\
N_5 &= 0.5r(r-1) 0.5s(s-1) 0.5t(t+1) \\
N_6 &= 0.5r(r+1) 0.5s(s-1) 0.5t(t+1) \\
N_7 &= 0.5r(r+1) 0.5s(s+1) 0.5t(t+1) \\
N_8 &= 0.5r(r-1) 0.5s(s+1) 0.5t(t+1) \\
N_9 &= (1 - r^2) 0.5s(s-1) 0.5t(t-1) \\
N_{10} &= 0.5r(r+1) (1 - s^2) 0.5t(t-1) \\
N_{11} &= (1 - r^2) 0.5s(s+1) 0.5t(t-1) \\
N_{12} &= 0.5r(r-1) (1 - s^2) 0.5t(t-1) \\
N_{13} &= (1 - r^2) 0.5s(s-1) 0.5t(t+1) \\
N_{14} &= 0.5r(r+1) (1 - s^2) 0.5t(t+1) \\
N_{15} &= (1 - r^2) 0.5s(s+1) 0.5t(t+1) \\
N_{16} &= 0.5r(r-1) (1 - s^2) 0.5t(t+1) \\
N_{17} &= 0.5r(r-1) 0.5s(s-1) (1 - t^2) \\
N_{18} &= 0.5r(r+1) 0.5s(s-1) (1 - t^2) \\
N_{19} &= 0.5r(r+1) 0.5s(s+1) (1 - t^2) \\
N_{20} &= 0.5r(r-1) 0.5s(s+1) (1 - t^2) \\
N_{21} &= (1 - r^2) (1 - s^2) 0.5t(t-1) \\
N_{22} &= (1 - r^2) 0.5s(s-1) (1 - t^2) \\
N_{23} &= 0.5r(r+1) (1 - s^2) (1 - t^2) \\
N_{24} &= (1 - r^2) 0.5s(s+1) (1 - t^2) \\
N_{25} &= 0.5r(r-1) (1 - s^2) (1 - t^2) \\
N_{26} &= (1 - r^2) (1 - s^2) 0.5t(t+1) \\
N_{27} &= (1 - r^2) (1 - s^2) (1 - t^2)
\end{aligned}$$

#### 4.6.4 Enriched quadratic basis functions in tetrahedra ( $P_2^+$ )



The velocity shape functions are:

$$\phi_i = \lambda_i(2\lambda_i - 1) + 3(\lambda_i\lambda_j\lambda_k + \lambda_i\lambda_j\lambda_l + \lambda_i\lambda_k\lambda_l) - 4\lambda_i\lambda_j\lambda_k\lambda_l \quad (365)$$

$$\phi_{ij} = 4\lambda_i\lambda_j - 12(\lambda_i\lambda_j\lambda_k + \lambda_i\lambda_j\lambda_l) + 32\lambda_i\lambda_j\lambda_k\lambda_l \quad (366)$$

$$\phi_{ijk} = 27\lambda_i\lambda_j\lambda_k - 108\lambda_i\lambda_j\lambda_k\lambda_l \quad (367)$$

$$\phi_c = 256\lambda_i\lambda_j\lambda_k\lambda_l \quad (368)$$

REFS ??? better definition of functions !

#### 4.6.5 Linear basis functions for tetrahedra ( $P_1$ )

This is essentially in the  $Q_2 \times P_{-1}$  element.

I choose the reduced coordinates of the pressure nodes to be :

point	r	s	t
1	1/2	-1/2	-1/2
2	-1/2	1/2	-1/2
3	-1/2	-1/2	1/2
4	1/2	1/2	1/2

Inside the element the pressure is given as a linear function of the reduced coordinates  $r, s, t$ :

$$p(r, s, t) = a + br + cs + dt$$

This expression must exactly interpolate the pressure at all four pressure nodes:

$$\begin{aligned} p_1 &= p(r_1, s_1, t_1) = a + br_1 + cs_1 + dt_1 = a + b/2 - c/2 - d/2 \\ p_2 &= p(r_2, s_2, t_2) = a + br_2 + cs_2 + dt_2 = a - b/2 + c/2 - d/2 \\ p_3 &= p(r_3, s_3, t_3) = a + br_3 + cs_3 + dt_3 = a - b/2 - c/2 + d/2 \\ p_4 &= p(r_4, s_4, t_4) = a + br_4 + cs_4 + dt_4 = a + b/2 + c/2 + d/2 \end{aligned}$$

or,

$$\begin{pmatrix} 1 & 1/2 & -1/2 & -1/2 \\ 1 & -1/2 & +1/2 & -1/2 \\ 1 & -1/2 & -1/2 & +1/2 \\ 1 & 1/2 & +1/2 & +1/2 \end{pmatrix} \begin{pmatrix} a \\ b \\ c \\ d \end{pmatrix} = \begin{pmatrix} p_1 \\ p_2 \\ p_3 \\ p_4 \end{pmatrix}$$

The matrix is invertible and we get:

$$\begin{pmatrix} a \\ b \\ c \\ d \end{pmatrix} = \begin{pmatrix} 1/4 & 1/4 & 1/4 & 1/4 \\ 1/2 & -1/2 & -1/2 & 1/2 \\ -1/2 & 1/2 & -1/2 & 1/2 \\ -1/2 & -1/2 & 1/2 & 1/2 \end{pmatrix} \begin{pmatrix} p_1 \\ p_2 \\ p_3 \\ p_4 \end{pmatrix}$$

so

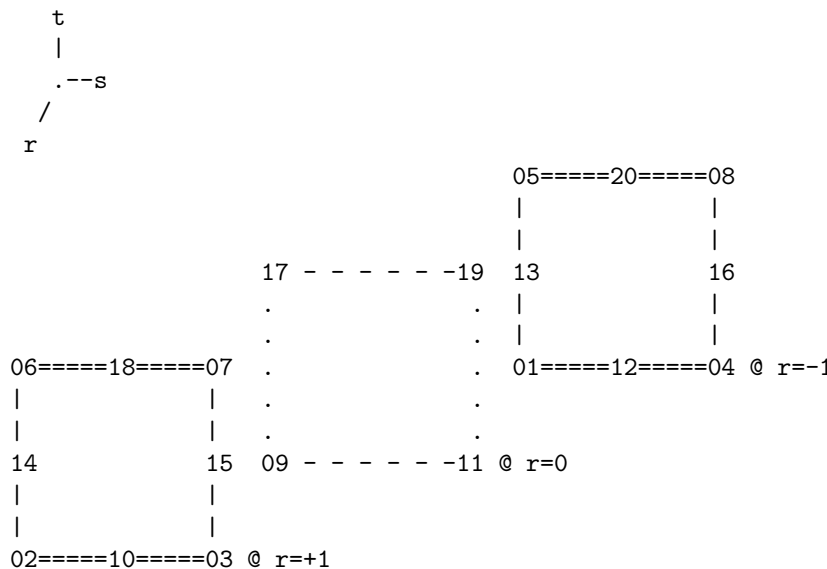
$$\begin{aligned}
 p(r, s, t) &= a + br + cs + dt \\
 &= \frac{1}{4}(p_1 + p_2 + p_3 + p_4) + \frac{1}{2}(p_1 - p_2 - p_3 + p_4)r + \frac{1}{2}(-p_1 + p_2 - p_3 + p_4)s + \frac{1}{2}(-p_1 - p_2 + p_3 + p_4)t \\
 &= \frac{1}{4}(1 + 2r - 2s - 2t)p_1 + \frac{1}{4}(1 - 2r + 2s - 2t)p_2 + \frac{1}{4}(1 - 2r - 2s + 2t)p_3 + \frac{1}{4}(1 + 2r + 2s + 2t)p_4 \\
 &= \sum_{i=1}^4 N_i(r, s, t)p_i
 \end{aligned} \tag{369}$$

with

$$\begin{aligned}
 N_1(r, s, t) &= \frac{1}{4}(1 + 2r - 2s - 2t) \\
 N_2(r, s, t) &= \frac{1}{4}(1 - 2r + 2s - 2t) \\
 N_3(r, s, t) &= \frac{1}{4}(1 - 2r - 2s + 2t) \\
 N_4(r, s, t) &= \frac{1}{4}(1 + 2r + 2s + 2t)
 \end{aligned}$$

#### 4.6.6 20-node serendipity basis functions in 3D ( $Q_2^{(20)}$ )

The serendipity elements are those rectangular elements which have no interior nodes [2118, p91].

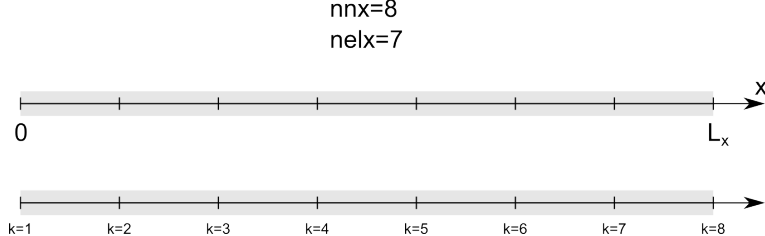


find/build shape functions!

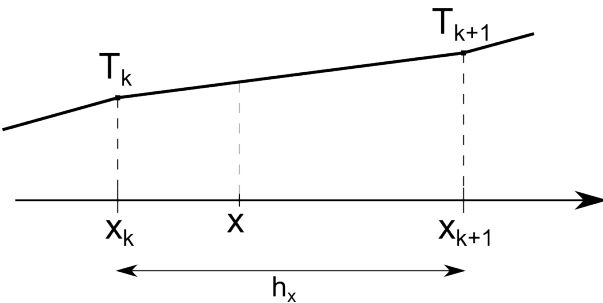
## 5 Solving the heat transport equation with linear Finite Elements

### 5.1 The diffusion equation in 1D

Let us consider the following one-dimensional grid:



Its spans the domain  $\Omega$  of length  $L_x$ . It is discretised by means of  $nnx$  nodes and  $nelx = nnx - 1$  elements. Zooming in on element which is bounded by two nodes  $k$  and  $k + 1$ , its size (also sometimes called diameter) is  $h_x = x_{k+1} - x_k$ , and the temperature field we wish to compute is located on those nodes so that they are logically called  $T_k$  and  $T_{k+1}$ :



We focus here on the 1D diffusion equation (no advection, no heat sources):

$$\rho C_p \frac{\partial T}{\partial t} = \frac{\partial}{\partial x} \left( k \frac{\partial T}{\partial x} \right) \quad (370)$$

This is the **strong form** of the ODE to solve. I can multiply this equation by a function<sup>29</sup>  $f(x)$  and integrate it over  $\Omega$ :

$$\int_{\Omega} f(x) \rho C_p \frac{\partial T}{\partial t} dx = \int_{\Omega} f(x) \frac{\partial}{\partial x} \left( k \frac{\partial T}{\partial x} \right) dx \quad (371)$$

Looking at the right hand side, it is of the form  $\int uv'$  so that I naturally integrate it by parts:

$$\int_{\Omega} f(x) \frac{\partial}{\partial x} \left( k \frac{\partial T}{\partial x} \right) dx = \left[ f(x) k \frac{\partial T}{\partial x} \right]_{\partial\Omega} - \int_{\Omega} \frac{\partial f}{\partial x} k \frac{\partial T}{\partial x} dx \quad (372)$$

Assuming there is no heat flux prescribed on the boundary (i.e.  $q_x = -k \partial T / \partial x = 0$ ),

NOT happy with this statement!!

then:

$$\int_{\Omega} f(x) \frac{\partial}{\partial x} \left( k \frac{\partial T}{\partial x} \right) dx = - \int_{\Omega} \frac{\partial f}{\partial x} k \frac{\partial T}{\partial x} dx \quad (373)$$

We then obtain the **weak form** of the diffusion equation in 1D:

$$\int_{\Omega} f(x) \rho C_p \frac{\partial T}{\partial t} dx + \int_{\Omega} \frac{\partial f}{\partial x} k \frac{\partial T}{\partial x} dx = 0$$

(374)

<sup>29</sup>This function should be well-behaved with special properties, but we here assume it is a polynomial function.

We then use the additive property of the integral  $\int_{\Omega} \dots = \sum_{elts} \int_{\Omega_e} \dots$  so that

$$\sum_{elts} \left( \underbrace{\int_{\Omega_e} f(x) \rho C_p \frac{\partial T}{\partial t} dx}_{\Lambda_f^e} + \underbrace{\int_{\Omega_e} \frac{\partial f}{\partial x} k \frac{\partial T}{\partial x} dx}_{\Upsilon_f^e} \right) = 0 \quad (375)$$

In order to compute these integrals (analytically or by means of a numerical quadrature), we will need to evaluate  $T$  inside the element. However, inside the element, the temperature is not known: all we have is the temperature at the nodes. For  $x \in [x_k, x_{k+1}]$  we need to come up with a way to compute the temperature at this location. It makes sense to think that  $T(x)$  will then be a function of the temperature at the nodes, i.e.  $T(x) = \alpha T_k + \beta T_{k+1}$  where  $\alpha$  and  $\beta$  are coefficients. One over-simplified approach would be to assign  $T(x) = (T_k + T_{k+1})/2$  but this would make the temperature discontinuous from element to element. The rather logical solution to this problem is a linear temperature field between  $T_k$  and  $T_{k+1}$ :

$$T(x) = \underbrace{\frac{x_{k+1} - x}{h_x} T_k}_{N_k^\theta(x)} + \underbrace{\frac{x - x_k}{h_x} T_{k+1}}_{N_{k+1}^\theta(x)}$$

where  $N_k^\theta(x)$  is the (temperature) shape function associated to node  $k$  and  $N_{k+1}^\theta(x)$  is the shape function associated to node  $k+1$ .

Rather reassuringly, we have:

- $x = x_k$  yields  $T(x) = T_k$
- $x = x_{k+1}$  yields  $T(x) = T_{k+1}$
- $x = (x_k + x_{k+1})/2$  yields  $T(x) = (T_k + T_{k+1})/2$

In what follows we abbreviate  $\partial T / \partial x$  by  $\dot{T}$ . Let us compute  $\Lambda_f^e$  and  $\Upsilon_f^e$  separately.

$$\begin{aligned} \Lambda_f^e &= \int_{x_k}^{x_{k+1}} f(x) \rho C_p \dot{T}(x) dx \\ &= \int_{x_k}^{x_{k+1}} f(x) \rho C_p [N_k^\theta(x) \dot{T}_k + N_{k+1}^\theta(x) \dot{T}_{k+1}] dx \\ &= \int_{x_k}^{x_{k+1}} f(x) \rho C_p N_k^\theta(x) \dot{T}_k dx + \int_{x_k}^{x_{k+1}} f(x) \rho C_p N_{k+1}^\theta(x) \dot{T}_{k+1} dx \\ &= \left( \int_{x_k}^{x_{k+1}} f(x) \rho C_p N_k^\theta(x) dx \right) \dot{T}_k + \left( \int_{x_k}^{x_{k+1}} f(x) \rho C_p N_{k+1}^\theta(x) dx \right) \dot{T}_{k+1} \end{aligned}$$

Taking  $f(x) = N_k^\theta(x)$  and omitting ' $(x)$ ' in the rhs:

$$\Lambda_{N_k^\theta}^e = \left( \int_{x_k}^{x_{k+1}} \rho C_p N_k^\theta N_k^\theta dx \right) \dot{T}_k + \left( \int_{x_k}^{x_{k+1}} \rho C_p N_k^\theta N_{k+1}^\theta dx \right) \dot{T}_{k+1}$$

Taking  $f(x) = N_{k+1}^\theta(x)$  and omitting ' $(x)$ ' in the rhs:

$$\Lambda_{N_{k+1}^\theta}^e = \left( \int_{x_k}^{x_{k+1}} \rho C_p N_{k+1}^\theta N_k^\theta dx \right) \dot{T}_k + \left( \int_{x_k}^{x_{k+1}} \rho C_p N_{k+1}^\theta N_{k+1}^\theta dx \right) \dot{T}_{k+1}$$

We can rearrange these last two equations as follows:

$$\begin{pmatrix} \Lambda_{N_k^\theta}^e \\ \Lambda_{N_{k+1}^\theta}^e \end{pmatrix} = \begin{pmatrix} \int_{x_k}^{x_{k+1}} N_k^\theta \rho C_p N_k^\theta dx & \int_{x_k}^{x_{k+1}} N_k^\theta \rho C_p N_{k+1}^\theta dx \\ \int_{x_k}^{x_{k+1}} N_{k+1}^\theta \rho C_p N_k^\theta dx & \int_{x_k}^{x_{k+1}} N_{k+1}^\theta \rho C_p N_{k+1}^\theta dx \end{pmatrix} \cdot \begin{pmatrix} \dot{T}_k \\ \dot{T}_{k+1} \end{pmatrix}$$

and we can take the integrals outside of the matrix:

$$\begin{pmatrix} \Lambda_{N_k^\theta}^e \\ \Lambda_{N_{k+1}^\theta}^e \end{pmatrix} = \left[ \int_{x_k}^{x_{k+1}} \rho C_p \begin{pmatrix} N_k^\theta N_k^\theta & N_k^\theta N_{k+1}^\theta \\ N_{k+1}^\theta N_k^\theta & N_{k+1}^\theta N_{k+1}^\theta \end{pmatrix} dx \right] \cdot \begin{pmatrix} \dot{T}_k \\ \dot{T}_{k+1} \end{pmatrix}$$

Finally, we can define the vectors

$$\vec{N}^T = \begin{pmatrix} N_k^\theta(x) \\ N_{k+1}^\theta(x) \end{pmatrix}$$

and

$$\vec{T}^e = \begin{pmatrix} T_k \\ T_{k+1} \end{pmatrix} \quad \dot{\vec{T}}^e = \begin{pmatrix} \dot{T}_k \\ \dot{T}_{k+1} \end{pmatrix}$$

so that

$$\begin{pmatrix} \Lambda_{N_k^\theta}^e \\ \Lambda_{N_{k+1}^\theta}^e \end{pmatrix} = \left( \int_{x_k}^{x_{k+1}} \vec{N}^T \rho C_p \vec{N} dx \right) \cdot \dot{\vec{T}}^e$$

Back to the diffusion term:

$$\begin{aligned} \Upsilon_f^e &= \int_{x_k}^{x^{k+1}} \frac{\partial f}{\partial x} k \frac{\partial T}{\partial x} dx \\ &= \int_{x_k}^{x^{k+1}} \frac{\partial f}{\partial x} k \frac{\partial (N_k^\theta(x) T_k + N_{k+1}^\theta(x) T_{k+1})}{\partial x} dx \\ &= \left( \int_{x_k}^{x^{k+1}} \frac{\partial f}{\partial x} k \frac{\partial N_k^\theta}{\partial x} dx \right) T_k + \left( \int_{x_k}^{x^{k+1}} \frac{\partial f}{\partial x} k \frac{\partial N_{k+1}^\theta}{\partial x} dx \right) T_{k+1} \end{aligned}$$

Taking  $f(x) = N_k^\theta(x)$

$$\Upsilon_{N_k^\theta}^e = \left( \int_{x_k}^{x^{k+1}} k \frac{\partial N_k^\theta}{\partial x} \frac{\partial N_k^\theta}{\partial x} dx \right) T_k + \left( \int_{x_k}^{x^{k+1}} k \frac{\partial N_k^\theta}{\partial x} \frac{\partial N_{k+1}^\theta}{\partial x} dx \right) T_{k+1}$$

Taking  $f(x) = N_{k+1}^\theta(x)$

$$\begin{aligned} \Upsilon_{N_{k+1}^\theta}^e &= \left( \int_{x_k}^{x^{k+1}} k \frac{\partial N_{k+1}^\theta}{\partial x} \frac{\partial N_k^\theta}{\partial x} dx \right) T_k + \left( \int_{x_k}^{x^{k+1}} k \frac{\partial N_{k+1}^\theta}{\partial x} \frac{\partial N_{k+1}^\theta}{\partial x} dx \right) T_{k+1} \\ \begin{pmatrix} \Upsilon_{N_k^\theta}^e \\ \Upsilon_{N_{k+1}^\theta}^e \end{pmatrix} &= \begin{pmatrix} \int_{x_k}^{x^{k+1}} \frac{\partial N_k^\theta}{\partial x} k \frac{\partial N_k^\theta}{\partial x} dx & \int_{x_k}^{x^{k+1}} \frac{\partial N_k^\theta}{\partial x} k \frac{\partial N_{k+1}^\theta}{\partial x} dx \\ \int_{x_k}^{x^{k+1}} \frac{\partial N_{k+1}^\theta}{\partial x} k \frac{\partial N_k^\theta}{\partial x} dx & \int_{x_k}^{x^{k+1}} \frac{\partial N_{k+1}^\theta}{\partial x} k \frac{\partial N_{k+1}^\theta}{\partial x} dx \end{pmatrix} \cdot \begin{pmatrix} T_k \\ T_{k+1} \end{pmatrix} \end{aligned}$$

or,

$$\begin{pmatrix} \Upsilon_{N_k^\theta}^e \\ \Upsilon_{N_{k+1}^\theta}^e \end{pmatrix} = \left[ \int_{x_k}^{x^{k+1}} k \begin{pmatrix} \frac{\partial N_k^\theta}{\partial x} \frac{\partial N_k^\theta}{\partial x} & \frac{\partial N_k^\theta}{\partial x} \frac{\partial N_{k+1}^\theta}{\partial x} \\ \frac{\partial N_{k+1}^\theta}{\partial x} \frac{\partial N_k^\theta}{\partial x} & \frac{\partial N_{k+1}^\theta}{\partial x} \frac{\partial N_{k+1}^\theta}{\partial x} \end{pmatrix} dx \right] \cdot \begin{pmatrix} T_k \\ T_{k+1} \end{pmatrix}$$

Finally, we can define the vector

$$\vec{B}^T = \begin{pmatrix} \frac{\partial N_k^\theta}{\partial x} \\ \frac{\partial N_{k+1}^\theta}{\partial x} \end{pmatrix}$$

so that

$$\begin{pmatrix} \Upsilon_{N_k^\theta}^e \\ \Upsilon_{N_{k+1}^\theta}^e \end{pmatrix} = \left( \int_{x_k}^{x_{k+1}} \vec{B}^T k \vec{B} dx \right) \cdot \vec{T}^e$$

The weak form discretised over 1 element becomes

$$\underbrace{\left( \int_{x_k}^{x_{k+1}} \vec{N}^T \rho C_p \vec{N} dx \right)}_{\mathbf{M}^e} \cdot \dot{\vec{T}}^e + \underbrace{\left( \int_{x_k}^{x_{k+1}} \vec{B}^T k \vec{B} dx \right)}_{\mathbf{K}_d^e} \cdot \vec{T}^e = 0$$

or,

$$\boxed{\mathbf{M}^e \cdot \dot{\vec{T}}^e + \mathbf{K}_d^e \cdot \vec{T}^e = 0}$$

or,

$$\boxed{\mathbf{M}^e \cdot \frac{\partial \vec{T}^e}{\partial t} + \mathbf{K}_d^e \cdot \vec{T}^e = 0}$$

$\mathbf{M}^e$  is commonly called the mass matrix, or capacitance matrix [2118, p103].

Using a backward first order in time discretisation for the time derivative:

$$\dot{\vec{T}} = \frac{\partial \vec{T}}{\partial t} = \frac{\vec{T}^{new} - \vec{T}^{old}}{\delta t}$$

we get

$$\mathbf{M}^e \cdot \frac{\vec{T}^{new} - \vec{T}^{old}}{\delta t} + \mathbf{K}_d^e \cdot \vec{T}^{new} = 0$$

or,

$$\boxed{(\mathbf{M}^e + \mathbf{K}_d^e \delta t) \cdot \vec{T}^{new} = \mathbf{M}^e \cdot \vec{T}^{old}}$$

with

$$\mathbf{M}^e = \int_{x_k}^{x_{k+1}} \vec{N}^T \rho C_p \vec{N} dx \quad \mathbf{K}_d^e = \int_{x_k}^{x_{k+1}} \vec{B}^T k \vec{B} dx$$

Let us compute  $\mathbf{M}$  for an element:

$$\mathbf{M}^e = \int_{x_k}^{x_{k+1}} \vec{N}^T \rho C_p \vec{N} dx$$

with

$$\vec{N}^T = \begin{pmatrix} N_k(x) \\ N_{k+1}(x) \end{pmatrix} = \begin{pmatrix} \frac{x_{k+1}-x}{h_x} \\ \frac{x-x_k}{h_x} \end{pmatrix}$$

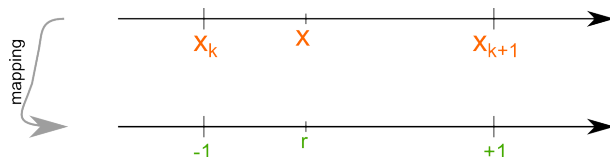
Then

$$\mathbf{M}^e = \begin{pmatrix} M_{11} & M_{12} \\ M_{21} & M_{22} \end{pmatrix} = \begin{pmatrix} \int_{x_k}^{x_{k+1}} \rho C_p N_k^\theta N_k^\theta dx & \int_{x_k}^{x_{k+1}} \rho C_p N_k^\theta N_{k+1}^\theta dx \\ \int_{x_k}^{x_{k+1}} \rho C_p N_{k+1}^\theta N_k^\theta dx & \int_{x_k}^{x_{k+1}} \rho C_p N_{k+1}^\theta N_{k+1}^\theta dx \end{pmatrix}$$

I only need to compute 3 integrals since  $M_{12} = M_{21}$ . Let us start with  $M_{11}$ :

$$M_{11} = \int_{x_k}^{x_{k+1}} \rho C_p N_k^\theta(x) N_k^\theta(x) dx = \int_{x_k}^{x_{k+1}} \rho C_p \frac{x_{k+1}-x}{h_x} \frac{x_{k+1}-x}{h_x} dx$$

It is then customary to carry out the change of variable  $x \rightarrow r$  where  $r \in [-1 : 1]$  as shown hereunder:



The relationships between  $x$  and  $r$  are:

$$r = \frac{2}{h_x}(x - x_k) - 1 \quad x = \frac{h_x}{2}(1 + r) + x_k$$

In what follows we assume for simplicity that  $\rho$  and  $C_p$  are constant within each element.

$$M_{11} = \rho C_p \int_{x_k}^{x_{k+1}} \frac{x_{k+1} - x}{h_x} \frac{x_{k+1} - x}{h_x} dx = \frac{\rho C_p h_x}{8} \int_{-1}^{+1} (1 - r)(1 - r) dr = \frac{h_x}{3} \rho C_p$$

Similarly we arrive at

$$M_{12} = \rho C_p \int_{x_k}^{x_{k+1}} \frac{x_{k+1} - x}{h_x} \frac{x - x_k}{h_x} dx = \frac{\rho C_p h_x}{8} \int_{-1}^{+1} (1 - r)(1 + r) dr = \frac{h_x}{6} \rho C_p$$

and

$$M_{22} = \rho C_p \int_{x_k}^{x_{k+1}} \frac{x - x_k}{h_x} \frac{x - x_k}{h_x} dx = \frac{\rho C_p h_x}{8} \int_{-1}^{+1} (1 + r)(1 + r) dr = \frac{h_x}{3} \rho C_p$$

Finally

$$\boxed{\mathbf{M}^e = \frac{h_x}{3} \rho C_p \begin{pmatrix} 1 & 1/2 \\ 1/2 & 1 \end{pmatrix}}$$

In the new coordinate system, the shape functions

$$N_k^\theta(x) = \frac{x_{k+1} - x}{h_x} \quad N_{k+1}^\theta(x) = \frac{x - x_k}{h_x}$$

become

$$N_k^\theta(r) = \frac{1}{2}(1 - r) \quad N_{k+1}^\theta(r) = \frac{1}{2}(1 + r)$$

Also,

$$\frac{\partial N_k^\theta}{\partial x} = -\frac{1}{h_x} \quad \frac{\partial N_{k+1}^\theta}{\partial x} = \frac{1}{h_x}$$

so that

$$\vec{B}^T = \begin{pmatrix} \frac{\partial N_k^\theta}{\partial x} \\ \frac{\partial N_{k+1}^\theta}{\partial x} \end{pmatrix} = \begin{pmatrix} -\frac{1}{h_x} \\ \frac{1}{h_x} \end{pmatrix}$$

We here also assume that  $k$  is constant within the element:

$$\mathbf{K}_d = \int_{x_k}^{x_{k+1}} \vec{B}^T k \vec{B} dx = k \int_{x_k}^{x_{k+1}} \vec{B}^T \vec{B} dx$$

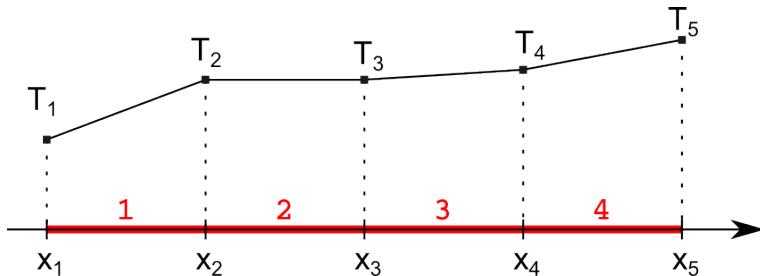
simply becomes

$$\mathbf{K}_d = k \int_{x_k}^{x_{k+1}} \frac{1}{h_x^2} \begin{pmatrix} 1 & -1 \\ -1 & 1 \end{pmatrix} dx$$

and then

$$\boxed{\mathbf{K}_d = \frac{k}{h_x} \begin{pmatrix} 1 & -1 \\ -1 & 1 \end{pmatrix}}$$

Let us consider this very simple grid consisting of 4 elements/5 nodes:



For each element we have

$$\underbrace{(\mathbf{M}^e + \mathbf{K}_d^e \delta t)}_{\mathbf{A}^e} \cdot \vec{\mathbf{T}}^{new} = \underbrace{\mathbf{M}^e \cdot \vec{\mathbf{T}}^{old}}_{\vec{\mathbf{b}}^e}$$

We can write this equation very explicitly for each element:

- element 1

$$\mathbf{A}^1 \cdot \begin{pmatrix} T_1 \\ T_2 \end{pmatrix} = \vec{\mathbf{b}}^1$$

$$\begin{cases} A_{11}^1 T_1 + A_{12}^1 T_2 = b_x^1 \\ A_{21}^1 T_1 + A_{22}^1 T_2 = b_y^1 \end{cases}$$

- element 2

$$\mathbf{A}^2 \cdot \begin{pmatrix} T_2 \\ T_3 \end{pmatrix} = \vec{\mathbf{b}}^2$$

$$\begin{cases} A_{11}^2 T_2 + A_{12}^2 T_3 = b_1^2 \\ A_{21}^2 T_2 + A_{22}^2 T_3 = b_2^2 \end{cases}$$

- element 3

$$\mathbf{A}^3 \cdot \begin{pmatrix} T_3 \\ T_4 \end{pmatrix} = \vec{\mathbf{b}}^3$$

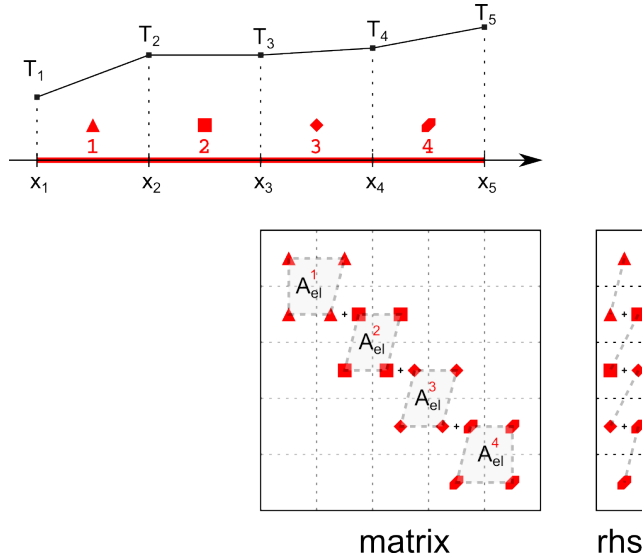
$$\begin{cases} A_{11}^3 T_3 + A_{12}^3 T_4 = b_1^3 \\ A_{21}^3 T_3 + A_{22}^3 T_4 = b_2^3 \end{cases}$$

- element 4

$$\mathbf{A}^4 \cdot \begin{pmatrix} T_4 \\ T_5 \end{pmatrix} = \vec{\mathbf{b}}^4$$

$$\begin{cases} A_{11}^4 T_4 + A_{12}^4 T_5 = b_1^4 \\ A_{21}^4 T_4 + A_{22}^4 T_5 = b_2^4 \end{cases}$$

All equations can be cast into a single linear system: this is the **assembly** phase. The process can also be visualised as shown hereunder. Because nodes 2,3,4 belong to two elements elemental contributions will be summed in the matrix and the rhs:



The assembled matrix and rhs are then:

$$\begin{pmatrix} A_{11}^1 & A_{12}^1 & 0 & 0 & 0 \\ A_{21}^1 & A_{22}^1 + A_{11}^2 & A_{12}^2 & 0 & 0 \\ 0 & A_{21}^2 & A_{22}^2 + A_{11}^3 & A_{12}^3 & 0 \\ 0 & 0 & A_{21}^3 & A_{22}^3 + A_{11}^4 & A_{12}^4 \\ 0 & 0 & 0 & A_{21}^4 & A_{22}^4 \end{pmatrix} \begin{pmatrix} T_1 \\ T_2 \\ T_3 \\ T_4 \\ T_5 \end{pmatrix} = \begin{pmatrix} b_1^1 \\ b_2^1 + b_1^2 \\ b_2^2 + b_1^3 \\ b_2^3 + b_1^4 \\ b_2^4 \end{pmatrix}$$

Ultimately the assembled matrix system also takes the form

$$\begin{pmatrix} A_{11} & A_{12} & 0 & 0 & 0 \\ A_{21} & A_{22} & A_{23} & 0 & 0 \\ 0 & A_{32} & A_{33} & A_{34} & 0 \\ 0 & 0 & A_{43} & A_{44} & A_{45} \\ 0 & 0 & 0 & A_{54} & A_{55} \end{pmatrix} \begin{pmatrix} T_1 \\ T_2 \\ T_3 \\ T_4 \\ T_5 \end{pmatrix} = \begin{pmatrix} b_1 \\ b_2 \\ b_3 \\ b_4 \\ b_5 \end{pmatrix}$$

and we see that it is sparse. Its sparsity structure is easy to derive: each row corresponds to a dof, and since nodes 1 and 2 'see' each other (they belong to the same element) there will be non-zero entries in the first and second column. Likewise, node 2 'sees' node 1 (in other words, there is an edge linking nodes 1 and 2), itself, and node 3, so that there are non-zero entries in the second row at columns 1, 2, and 3.

Before we solve the system, we need to take care of boundary conditions. Let us assume that we wish to fix the temperature at node 2, or in other words we wish to set

$$T_2 = T^{bc}$$

This equation can be cast as

$$(0 \ 1 \ 0 \ 0 \ 0) \begin{pmatrix} T_1 \\ T_2 \\ T_3 \\ T_4 \\ T_5 \end{pmatrix} = \begin{pmatrix} 0 \\ T^{bc} \\ 0 \\ 0 \\ 0 \end{pmatrix}$$

This replaces the second line in the previous matrix equation:

$$\begin{pmatrix} A_{11} & A_{12} & 0 & 0 & 0 \\ 0 & 1 & 0 & 0 & 0 \\ 0 & A_{32} & A_{33} & A_{34} & 0 \\ 0 & 0 & A_{43} & A_{44} & A_{45} \\ 0 & 0 & 0 & A_{54} & A_{55} \end{pmatrix} \begin{pmatrix} T_1 \\ T_2 \\ T_3 \\ T_4 \\ T_5 \end{pmatrix} = \begin{pmatrix} b_1 \\ T^{bc} \\ b_3 \\ b_4 \\ b_5 \end{pmatrix}$$

That's it, we have a linear system of equations which can be solved!

## 5.2 The advection-diffusion equation in 1D

We start with the 1D advection-diffusion equation

$$\rho C_p \left( \frac{\partial T}{\partial t} + u \frac{\partial T}{\partial x} \right) = \frac{\partial}{\partial x} \left( k \frac{\partial T}{\partial x} \right) + H \quad (376)$$

This is the **strong form** of the ODE to solve. As in the previous section, I multiply this equation by a function  $f(x)$  and integrate it over the domain  $\Omega$ :

$$\int_{\Omega} f(x) \rho C_p \frac{\partial T}{\partial t} dx + \int_{\Omega} f(x) \rho C_p u \frac{\partial T}{\partial x} dx = \int_{\Omega} f(x) \frac{\partial}{\partial x} \left( k \frac{\partial T}{\partial x} \right) dx + \int_{\Omega} f(x) H dx$$

As in the previous section I integrate the r.h.s. by parts:

$$\int_{\Omega} f(x) \frac{\partial}{\partial x} \left( k \frac{\partial T}{\partial x} \right) dx = \left[ f(x) k \frac{\partial T}{\partial x} \right]_{\partial\Omega} - \int_{\Omega} \frac{\partial f}{\partial x} k \frac{\partial T}{\partial x} dx$$

Disregarding the boundary term for now, we then obtain the **weak form** of the diffusion equation in 1D:

$$\boxed{\int_{\Omega} f(x) \rho C_p \frac{\partial T}{\partial t} dx + \int_{\Omega} f(x) \rho C_p u \frac{\partial T}{\partial x} dx + \int_{\Omega} \frac{\partial f}{\partial x} k \frac{\partial T}{\partial x} dx = \int_{\Omega} f(x) H dx}$$

We then use the additive property of the integral  $\int_{\Omega} \cdots = \sum_{elts} \int_{\Omega_e} \cdots$

$$\sum_{elts} \left( \underbrace{\int_{\Omega_e} f(x) \rho C_p \frac{\partial T}{\partial t} dx}_{\Lambda_f^e} + \underbrace{\int_{\Omega_e} f(x) \rho C_p u \frac{\partial T}{\partial x} dx}_{\Sigma_f^e} + \underbrace{\int_{\Omega_e} \frac{\partial f}{\partial x} k \frac{\partial T}{\partial x} dx}_{\Upsilon_f^e} - \underbrace{\int_{\Omega_e} f(x) H dx}_{\Omega_f^e} \right) = 0$$

In the element, we have seen that the temperature can be written:

$$T(x) = N_k^\theta(x) T_k + N_{k+1}^\theta(x) T_{k+1}$$

In the previous presentation we have computed  $\Lambda_f^e$  and  $\Upsilon_f^e$ . Let us now turn to  $\Sigma_f^e$  and  $\Omega_f^e$ .

$$\begin{aligned} \Sigma_f^e &= \int_{x_k}^{x_{k+1}} f(x) \rho C_p u \frac{\partial T}{\partial x} dx \\ &= \int_{x_k}^{x_{k+1}} f(x) \rho C_p u \frac{\partial [N_k^\theta(x) T_k + N_{k+1}^\theta(x) T_{k+1}]}{\partial x} dx \\ &= \int_{x_k}^{x_{k+1}} f(x) \rho C_p u \frac{\partial N_k^\theta}{\partial x} T_k dx + \int_{x_k}^{x_{k+1}} f(x) \rho C_p u \frac{\partial N_{k+1}^\theta}{\partial x} T_{k+1} dx \\ &= \left( \int_{x_k}^{x_{k+1}} f(x) \rho C_p u \frac{\partial N_k^\theta}{\partial x} dx \right) T_k + \left( \int_{x_k}^{x_{k+1}} f(x) \rho C_p u \frac{\partial N_{k+1}^\theta}{\partial x} dx \right) T_{k+1} \end{aligned}$$

Taking  $f(x) = N_k^\theta(x)$  and omitting '(x)' in the rhs:

$$\Sigma_{N_k^\theta}^e = \left( \int_{x_k}^{x_{k+1}} \rho C_p u N_k^\theta \frac{\partial N_k^\theta}{\partial x} dx \right) T_k + \left( \int_{x_k}^{x_{k+1}} \rho C_p u N_{k+1}^\theta \frac{\partial N_{k+1}^\theta}{\partial x} dx \right) T_{k+1}$$

Taking  $f(x) = N_{k+1}^\theta(x)$  and omitting '(x)' in the rhs:

$$\Sigma_{N_{k+1}^\theta}^e = \left( \int_{x_k}^{x_{k+1}} \rho C_p u N_{k+1}^\theta \frac{\partial N_k^\theta}{\partial x} dx \right) T_k + \left( \int_{x_k}^{x_{k+1}} \rho C_p u N_{k+1}^\theta \frac{\partial N_{k+1}^\theta}{\partial x} dx \right) T_{k+1}$$

$$\begin{pmatrix} \Sigma_{N_k^\theta} \\ \Sigma_{N_{k+1}^\theta} \end{pmatrix} = \begin{pmatrix} \int_{x_k}^{x_{k+1}} \rho C_p u N_k^\theta \frac{\partial N_k^\theta}{\partial x} dx & \int_{x_k}^{x_{k+1}} \rho C_p u N_k^\theta \frac{\partial N_{k+1}^\theta}{\partial x} dx \\ \int_{x_k}^{x_{k+1}} \rho C_p u N_{k+1}^\theta \frac{\partial N_k^\theta}{\partial x} dx & \int_{x_k}^{x_{k+1}} \rho C_p u N_{k+1}^\theta \frac{\partial N_{k+1}^\theta}{\partial x} dx \end{pmatrix} \cdot \begin{pmatrix} T_k \\ T_{k+1} \end{pmatrix}$$

or,

$$\begin{pmatrix} \Sigma_{N_k^\theta} \\ \Sigma_{N_{k+1}^\theta} \end{pmatrix} = \left[ \int_{x_k}^{x_{k+1}} \rho C_p u \begin{pmatrix} N_k^\theta \frac{\partial N_k^\theta}{\partial x} & N_k^\theta \frac{\partial N_{k+1}^\theta}{\partial x} \\ N_{k+1}^\theta \frac{\partial N_k^\theta}{\partial x} & N_{k+1}^\theta \frac{\partial N_{k+1}^\theta}{\partial x} \end{pmatrix} dx \right] \cdot \begin{pmatrix} T_k \\ T_{k+1} \end{pmatrix}$$

Finally, we have already defined the vectors

$$\vec{N}^T = \begin{pmatrix} N_k^\theta(x) \\ N_{k+1}^\theta(x) \end{pmatrix} \quad \vec{B}^T = \begin{pmatrix} \frac{\partial N_k^\theta}{\partial x} \\ \frac{\partial N_{k+1}^\theta}{\partial x} \end{pmatrix} \quad \vec{T}^e = \begin{pmatrix} T_k \\ T_{k+1} \end{pmatrix}$$

so that

$$\begin{pmatrix} \Sigma_{N_k^\theta} \\ \Sigma_{N_{k+1}^\theta} \end{pmatrix} = \left( \int_{x_k}^{x_{k+1}} \vec{N}^T \rho C_p u \vec{B} dx \right) \cdot \vec{T}^e = \mathbf{K}_a \cdot \vec{T}^e$$

One can easily show that

$$\mathbf{K}_a^e = \rho C_p u \begin{pmatrix} -1/2 & 1/2 \\ -1/2 & 1/2 \end{pmatrix}$$

Note that the matrix  $\mathbf{K}_a^e$  is not symmetric.

Let us now look at the source term:

$$\Omega_f^e = \int_{x_k}^{x_{k+1}} f(x) H(x) dx$$

Taking  $f(x) = N_k^\theta(x)$ :

$$\Omega_{N_k^\theta} = \int_{x_k}^{x_{k+1}} N_k^\theta(x) H(x) dx$$

Taking  $f(x) = N_{k+1}^\theta(x)$ :

$$\Omega_{N_{k+1}^\theta} = \int_{x_k}^{x_{k+1}} N_{k+1}^\theta(x) H(x) dx$$

We can rearrange both equations as follows:

$$\begin{pmatrix} \Omega_{N_k^\theta} \\ \Omega_{N_{k+1}^\theta} \end{pmatrix} = \begin{pmatrix} \int_{x_k}^{x_{k+1}} N_k^\theta(x) H(x) dx \\ \int_{x_k}^{x_{k+1}} N_{k+1}^\theta(x) H(x) dx \end{pmatrix}$$

or,

$$\begin{pmatrix} \Omega_{N_k^\theta} \\ \Omega_{N_{k+1}^\theta} \end{pmatrix} = \left[ \int_{x_k}^{x_{k+1}} \begin{pmatrix} N_k^\theta(x) H(x) \\ N_{k+1}^\theta(x) H(x) \end{pmatrix} dx \right]$$

so that

$$\begin{pmatrix} \Omega_{N_k^\theta} \\ \Omega_{N_{k+1}^\theta} \end{pmatrix} = \left( \int_{x_k}^{x_{k+1}} \vec{N}^T H(x) dx \right)$$

The weak form discretised over 1 element becomes

$$\underbrace{\left( \int_{x_k}^{x_{k+1}} \vec{N}^T \rho C_p \mathbf{N} dx \right)}_{\mathbf{M}^e} \cdot \dot{\vec{T}}^e + \underbrace{\left( \int_{x_k}^{x_{k+1}} \vec{N}^T \rho C_p u \mathbf{B} dx \right)}_{\mathbf{K}_a^e} \cdot \vec{T}^e + \underbrace{\left( \int_{x_k}^{x_{k+1}} \vec{B}^T k \mathbf{B} dx \right)}_{\mathbf{K}_d^e} \cdot \vec{T}^e = \underbrace{\left( \int_{x_k}^{x_{k+1}} \vec{N}^T H(x) dx \right)}_{\vec{F}^e}$$

or,

$$\mathbf{M}^e \cdot \dot{\vec{T}}^e + (\mathbf{K}_a^e + \mathbf{K}_d^e) \cdot \vec{T}^e = \vec{F}^e$$

or,

$$\mathbf{M}^e \cdot \frac{\partial \vec{T}^e}{\partial t} + (\mathbf{K}_a^e + \mathbf{K}_d^e) \cdot \vec{T}^e = \vec{F}^e$$

### 5.3 The advection-diffusion equation in 2D

We start from the 'bare-bones' heat transport equation (source terms are omitted):

$$\rho C_p \left( \frac{\partial T}{\partial t} + \vec{v} \cdot \vec{\nabla} T \right) = \vec{\nabla} \cdot k \vec{\nabla} T \quad (377)$$

In what follows we assume that the velocity field  $\vec{v}$  is known so that temperature is the only unknown. Let  $N^\theta$  be the temperature basis functions so that the temperature inside an element is given by<sup>30</sup>:

$$T^h(\vec{r}) = \sum_{i=1}^{m_T} N_i^\theta(\vec{r}) T_i = \vec{N}^\theta \cdot \vec{T} \quad (378)$$

where  $\vec{T}$  is a vector of length  $m_T$ . The weak form is then

$$\begin{aligned} \int_{\Omega} N_i^\theta \left[ \rho C_p \left( \frac{\partial T}{\partial t} + \vec{v} \cdot \vec{\nabla} T \right) \right] d\Omega &= \int_{\Omega} N_i^\theta \vec{\nabla} \cdot k \vec{\nabla} T d\Omega \\ \underbrace{\int_{\Omega} N_i^\theta \rho C_p \frac{\partial T}{\partial t} d\Omega}_{I} + \underbrace{\int_{\Omega} N_i^\theta \rho C_p \vec{v} \cdot \vec{\nabla} T d\Omega}_{II} &= \underbrace{\int_{\Omega} N_i^\theta \vec{\nabla} \cdot k \vec{\nabla} T d\Omega}_{III} \quad i = 1, m_T \end{aligned} \quad (379)$$

Looking at the first term:

$$\int_{\Omega} N_i^\theta \rho C_p \frac{\partial T}{\partial t} d\Omega = \int_{\Omega} N_i^\theta \rho C_p \vec{N}^\theta \cdot \dot{\vec{T}} d\Omega \quad (380)$$

$$(381)$$

so that when we assemble all contributions for  $i = 1, m_T$  we get:

$$I = \int_{\Omega} \vec{N}^\theta \rho C_p \vec{N}^\theta \cdot \dot{\vec{T}} d\Omega = \left( \int_{\Omega} \rho C_p \vec{N}^\theta \vec{N}^\theta d\Omega \right) \cdot \dot{\vec{T}} = \mathbf{M}^T \cdot \dot{\vec{T}}$$

where  $\mathbf{M}^T$  is the mass matrix of the system of size  $(m_T \times m_T)$  with

$$M_{ij}^T = \int_{\Omega} \rho C_p N_i^\theta N_j^\theta d\Omega$$

Turning now to the second term:

$$\int_{\Omega} N_i^\theta \rho C_p \vec{v} \cdot \vec{\nabla} T d\Omega = \int_{\Omega} N_i^\theta \rho C_p (u \frac{\partial T}{\partial x} + v \frac{\partial T}{\partial y}) d\Omega \quad (382)$$

$$= \int_{\Omega} N_i^\theta \rho C_p (u \frac{\partial \vec{N}^\theta}{\partial x} + v \frac{\partial \vec{N}^\theta}{\partial y}) \cdot \vec{T} d\Omega \quad (383)$$

$$(384)$$

---

<sup>30</sup>the  $\theta$  superscript has been chosen to denote temperature so as to avoid confusion with the transpose operator

so that when we assemble all contributions for  $i = 1, m_T$  we get:

$$II = \left( \int_{\Omega} \rho C_p \vec{N}^{\theta} (u \frac{\partial \vec{N}^{\theta}}{\partial x} + v \frac{\partial \vec{N}^{\theta}}{\partial y}) d\Omega \right) \cdot \vec{T} = \mathbf{K}_a \cdot \vec{T}$$

where  $\mathbf{K}_a$  is the advection term matrix of size  $(m_T \times m_T)$  with

$$(K_a)_{ij} = \int_{\Omega} \rho C_p N_i^{\theta} \left( u \frac{\partial N_j^{\theta}}{\partial x} + v \frac{\partial N_j^{\theta}}{\partial y} \right) d\Omega$$

Now looking at the third term, we carry out an integration by part and neglect the surface term for now, so that

$$\int_{\Omega} N_i^{\theta} \vec{\nabla} \cdot k \vec{\nabla} T d\Omega = - \int_{\Omega} k \vec{\nabla} N_i^{\theta} \cdot \vec{\nabla} T d\Omega \quad (385)$$

$$= - \int_{\Omega} k \vec{\nabla} N_i^{\theta} \cdot \vec{\nabla} (\vec{N}^{\theta} \cdot \vec{T}) d\Omega \quad (386)$$

(387)

with

$$\vec{\nabla} \vec{N}^{\theta} = \begin{pmatrix} \partial_x N_1^{\theta} & \partial_x N_2^{\theta} & \dots & \partial_x N_{m_T}^{\theta} \\ \partial_y N_1^{\theta} & \partial_y N_2^{\theta} & \dots & \partial_y N_{m_T}^{\theta} \end{pmatrix}$$

so that finally:

$$III = - \left( \int_{\Omega} k (\vec{\nabla} \vec{N}^{\theta})^T \cdot \vec{\nabla} \vec{N}^{\theta} d\Omega \right) \cdot \vec{T} = - \mathbf{K}_d \cdot \vec{T}$$

where  $\mathbf{K}_d$  is the diffusion term matrix:

$$\mathbf{K}_d = \int_{\Omega} k (\vec{\nabla} \vec{N}^{\theta})^T \cdot \vec{\nabla} \vec{N}^{\theta} d\Omega$$

Ultimately terms  $I, II, III$  together yield:

$$\boxed{\mathbf{M}^{\theta} \cdot \dot{\vec{T}} + (\mathbf{K}_a + \mathbf{K}_d) \cdot \vec{T} = \vec{0}}$$

add source term!!

### 5.3.1 Dealing with the time discretisation

??

Essentially we have to solve a PDE of the type:

$$\frac{\partial T}{\partial t} = \mathcal{F}(\vec{v}, T, \vec{\nabla} T, \Delta T)$$

with  $\mathcal{F} = \frac{1}{\rho C_p} (-\vec{v} \cdot \vec{\nabla} T + \vec{\nabla} \cdot k \vec{\nabla} T)$ .

The (explicit) forward Euler method is:

$$\frac{T^{n+1} - T^n}{\delta t} = \mathcal{F}^n(T, \vec{\nabla} T, \Delta T)$$

The (implicit) backward Euler method is:

$$\frac{T^{n+1} - T^n}{\delta t} = \mathcal{F}^{n+1}(T, \vec{\nabla} T, \Delta T)$$

and the (implicit) Crank-Nicolson algorithm is:

$$\frac{T^{n+1} - T^n}{\delta t} = \frac{1}{2} [\mathcal{F}^n(T, \vec{\nabla} T, \Delta T) + \mathcal{F}^{n+1}(T, \vec{\nabla} T, \Delta T)]$$

where the superscript  $n$  indicates the time step. The Crank-Nicolson is obviously based on the trapezoidal rule, with second-order convergence in time.

In what follows, I omit the superscript on the mass matrix to simplify notations:  $\mathbf{M}^\theta = \mathbf{M}$ . In terms of Finite Elements, these become:

- Explicit Forward euler:

$$\frac{1}{\delta t}(\mathbf{M}^{n+1} \cdot \vec{T}^{n+1} - \mathbf{M}^n \cdot \vec{T}^n) = -(\mathbf{K}_a^n + \mathbf{K}_d^n) \cdot \vec{T}^n$$

or,

$$\boxed{\mathbf{M}^{n+1} \cdot \vec{T}^{n+1} = (\mathbf{M}^n + (\mathbf{K}_a^n + \mathbf{K}_d^n)\delta t) \cdot \vec{T}^n}$$

- Implicit Backward euler:

$$\frac{1}{\delta t}(\mathbf{M}^{n+1} \cdot \vec{T}^{n+1} - \mathbf{M}^n \cdot \vec{T}^n) = -(\mathbf{K}_a^{n+1} + \mathbf{K}_d^{n+1}) \cdot \vec{T}^{n+1}$$

or,

$$\boxed{(\mathbf{M}^{n+1} + (\mathbf{K}_a^{n+1} + \mathbf{K}_d^{n+1})\delta t) \cdot \vec{T}^{n+1} = \mathbf{M}^n \cdot \vec{T}^n}$$

- Crank-Nicolson

$$\frac{1}{\delta t}(\mathbf{M}^{n+1} \cdot \vec{T}^{n+1} - \mathbf{M}^n \cdot \vec{T}^n) = \frac{1}{2} [-(\mathbf{K}_a^{n+1} + \mathbf{K}_d^{n+1}) \cdot \vec{T}^{n+1} - (\mathbf{K}_a^n + \mathbf{K}_d^n) \cdot \vec{T}^n]$$

or,

$$\boxed{\left( \mathbf{M}^{n+1} + (\mathbf{K}_a^{n+1} + \mathbf{K}_d^{n+1}) \frac{\delta t}{2} \right) \cdot \vec{T}^{n+1} = \left( \mathbf{M}^n + (\mathbf{K}_a^n + \mathbf{K}_d^n) \frac{\delta t}{2} \right) \cdot \vec{T}^n}$$

Note that in benchmarks where the domain/grid does not deform, the coefficients do not change in space and the velocity field is constant in time, or in practice out of convenience, the  $\mathbf{K}$  and  $\mathbf{M}$  matrices do not change and the r.h.s. can be constructed with the same matrices as the FE matrix.

**The Backward differentiation formula** (see for instance [1119] or Wikipedia<sup>31</sup>. The second-order BDF (or BDF-2) as shown in [1507] is as follows: it is a finite-difference quadratic interpolation approximation of the  $\partial T / \partial t$  term which involves  $t^n$ ,  $t^{n-1}$  and  $t^{n-2}$ :

$$\frac{\partial T}{\partial t}(t^n) = \frac{1}{\tau_n} \left( \frac{2\tau_n + \tau_{n-1}}{\tau_n + \tau_{n-1}} T(t^n) - \frac{\tau_n + \tau_{n-1}}{\tau_{n-1}} T(t^{n-1}) + \frac{\tau_n^2}{\tau_{n-1}(\tau_n + \tau_{n-1})} T(t^{n-2}) \right) \quad (388)$$

where  $\tau_n = t^n - t^{n-1}$ . Starting again from  $\mathbf{M}^\theta \cdot \dot{\vec{T}} + (\mathbf{K}_a + \mathbf{K}_d) \cdot \vec{T} = \vec{0}$ , we write

$$\mathbf{M}^\theta \cdot \frac{1}{\tau_n} \left( \frac{2\tau_n + \tau_{n-1}}{\tau_n + \tau_{n-1}} \vec{T}^n - \frac{\tau_n + \tau_{n-1}}{\tau_{n-1}} \vec{T}^{n-1} + \frac{\tau_n^2}{\tau_{n-1}(\tau_n + \tau_{n-1})} \vec{T}^{n-2} \right) + (\mathbf{K}_a + \mathbf{K}_d) \cdot \vec{T}^n = \vec{0}$$

and finally:

$$\left[ \frac{2\tau_n + \tau_{n-1}}{\tau_n + \tau_{n-1}} \mathbf{M}^\theta + \tau_n (\mathbf{K}_a + \mathbf{K}_d) \right] \cdot \vec{T}^n = \frac{\tau_n + \tau_{n-1}}{\tau_{n-1}} \mathbf{M}^\theta \cdot \vec{T}^{n-1} - \frac{\tau_n^2}{\tau_{n-1}(\tau_n + \tau_{n-1})} \mathbf{M}^\theta \cdot \vec{T}^{n-2}$$

Note that if all timesteps are equal, i.e.  $\tau_n = \tau_{n-1} = \delta t$ , this equation becomes:

$$\left[ \frac{3}{2} \mathbf{M}^\theta + \delta t (\mathbf{K}_a + \mathbf{K}_d) \right] \cdot \vec{T}^n = \mathbf{M}^\theta \cdot \left( 2\vec{T}^{n-1} - \frac{1}{2}\vec{T}^{n-2} \right)$$

or,

$$\boxed{\left[ \mathbf{M}^\theta + \frac{2}{3} \delta t (\mathbf{K}_a + \mathbf{K}_d) \right] \cdot \vec{T}^n = \mathbf{M}^\theta \cdot \left( \frac{4}{3} \vec{T}^{n-1} - \frac{1}{3} \vec{T}^{n-2} \right)}$$

<sup>31</sup>[https://en.wikipedia.org/wiki/Backward\\_differentiation\\_formula](https://en.wikipedia.org/wiki/Backward_differentiation_formula)

As mentioned before the backward differentiation formula (BDF) is a family of implicit methods for the integration of ODEs. Each BDF- $s$  method achieves order  $s$ . The BDF-1 is simply the backward Euler method as seen above:

$$T^{n+1} - T^n = \delta t \mathcal{F}^{n+1}$$

The BDF-2 is given by

$$T^{n+2} - \frac{4}{3}T^{n+1} + \frac{1}{3}T^n = \frac{2}{3}\delta t \mathcal{F}^{n+2}$$

The BDF-3 is given by

$$T^{n+3} - \frac{18}{11}T^{n+2} + \frac{9}{11}T^{n+1} - \frac{2}{11}T^n = \frac{6}{11}\delta t \mathcal{F}^{n+3}$$

The BDF-4 is given by

$$T^{n+4} - \frac{48}{25}T^{n+1} + \frac{36}{25}T^{n+1} - \frac{16}{25}T^{n+1} + \frac{3}{25}T^n = \frac{12}{25}\delta t \mathcal{F}^{n+4}$$

### 5.3.2 On steady states

It is said that a system is in a steady state if the (state) variables which define the behavior of the system are unchanging in time. In continuous time, this means that the partial derivative with respect to time is zero and remains so:

$$\frac{\partial}{\partial t} = 0 \quad \forall t$$

This is irrelevant for the Stokes equations which do not contain an explicit time dependence but the heat transport equation can reach a steady state. Note that if one is only interested in the steady state solution (and not how the system gets there in time) then the heat transport equation should be solved with  $\partial T / \partial t$  set to zero.

### 5.3.3 Anisotropic heat conduction

It is most often assumed that the heat conductivity is isotropic so that one speaks of heat conductivity as a scalar  $k$ . However many materials are orthotropic and in that case the heat conductivity is a tensor  $\mathbf{k}$  which (in 2D) writes [2118, p121]:

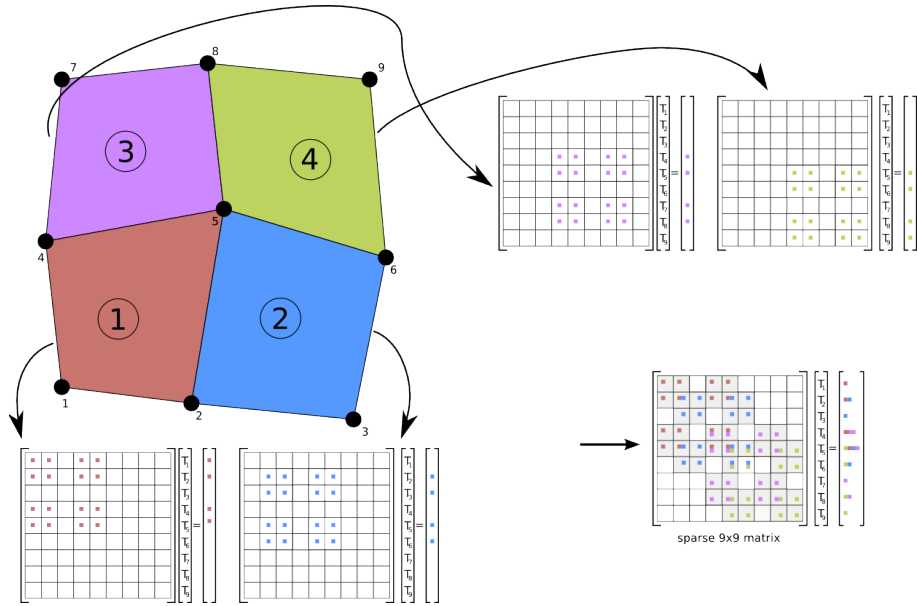
$$\mathbf{k} = \begin{pmatrix} k_{xx} & k_{xy} \\ k_{yx} & k_{yy} \end{pmatrix} = \begin{pmatrix} \cos \theta & \sin \theta \\ -\sin \theta & \cos \theta \end{pmatrix} \cdot \begin{pmatrix} k_1 & 0 \\ 0 & k_2 \end{pmatrix} \cdot \begin{pmatrix} \cos \theta & -\sin \theta \\ \sin \theta & \cos \theta \end{pmatrix}$$

where  $k_1$  and  $k_2$  are the conductivities in the principal axes system and  $\theta$  is the local orientation. In that case the diffusion term in the heat trasport equation becomes  $\vec{\nabla} \cdot (\mathbf{k} \cdot \vec{\nabla} T)$ .

(**MSc Thesis**): [2118, p121], [2118, p143]

### 5.3.4 About the assembly

Let us consider for simplicity the following grid composed of 9 nodes and 4  $Q_1$  elements. Each node carries a single degree of freedom.



There are four elements:

- element 1 is composed of nodes  $(1, 2, 5, 4) = \vec{T}^{el1}$
- element 2 is composed of nodes  $(2, 3, 6, 5) = \vec{T}^{el2}$
- element 3 is composed of nodes  $(4, 5, 8, 7) = \vec{T}^{el3}$
- element 4 is composed of nodes  $(5, 6, 9, 8) = \vec{T}^{el4}$

For each element one has computed an elemental matrix  $\mathbf{A}^{el}$  and a right hand side  $\vec{b}^{el}$ .

$$\mathbf{A}^{el1} \cdot \mathbf{T}^{el1} = \mathbf{b}^{el1}$$

$$\mathbf{A}^{el2} \cdot \mathbf{T}^{el2} = \mathbf{b}^{el2}$$

$$\mathbf{A}^{el3} \cdot \mathbf{T}^{el3} = \mathbf{b}^{el3}$$

$$\mathbf{A}^{el4} \cdot \mathbf{T}^{el4} = \mathbf{b}^{el4}$$

As seen in the 1D case, these four linear systems must be assembled in a single large matrix of size  $9 \times 9$  as shown in the figure above.

## 6 Solving the flow equations with the FEM

In the case of an incompressible flow, we have seen that the continuity (mass conservation) equation takes the simple form  $\vec{\nabla} \cdot \vec{v} = 0$ . In other word flow takes place under the constraint that the divergence of its velocity field is exactly zero everywhere (solenoidal constraint), i.e. it is divergence free.

We see that the pressure in the momentum equation is then a degree of freedom which is needed to satisfy the incompressibility constraint (and it is not related to any constitutive equation) [711]. In other words the pressure is acting as a Lagrange multiplier of the incompressibility constraint.

Various approaches have been proposed in the literature to deal with the incompressibility constraint but we will only focus on the penalty method (section 6.3) and the so-called mixed finite element method 6.4.

### 6.1 Strong and weak forms

The strong form consists of the governing equation and the boundary conditions, i.e. the mass, momentum and energy conservation equations supplemented with Dirichlet and/or Neumann boundary conditions on (parts of) the boundary.

To develop the finite element formulation, the partial differential equations must be restated in an integral form called the weak form. In essence the PDEs are first multiplied by an arbitrary function and integrated over the domain.

### 6.2 Which velocity-pressure pair for Stokes?

The success of a mixed finite element formulation crucially depends on a proper choice of the local interpolations of the velocity and the pressure.

#### 6.2.1 The compatibility condition (or LBB condition)

'LBB stable' elements assure the existence of a unique solution and assure convergence at the optimal rate.

#### 6.2.2 Families

The family of Taylor-Hood finite element spaces on triangular/tetrahedral grids is given by  $P_k \times P_{k-1}$  with  $k \geq 2$ , and on quadrilateral/hexahedral grids by  $Q_k \times Q_{k-1}$  with  $k \geq 2$ . This means that the pressure is then approximated by continuous functions.

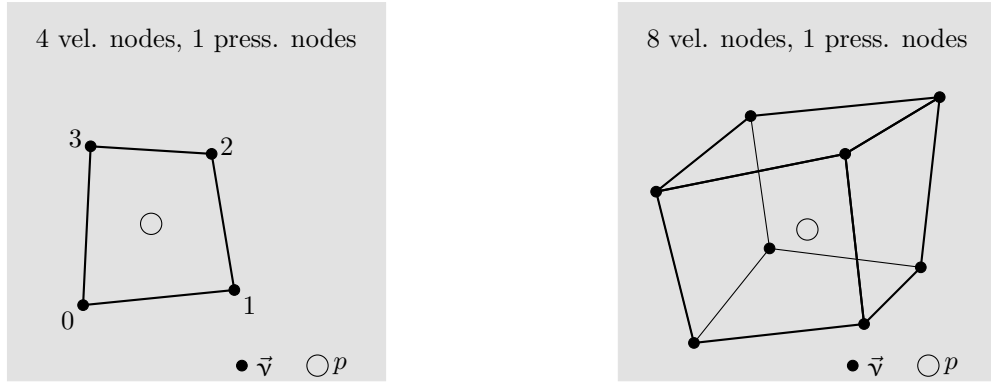
These finite elements are very popular, in particular the pairs for  $k = 2$ , i.e.  $Q_2 \times Q_1$  and  $P_2 \times P_1$ . The reason why  $k \geq 2$  comes from the fact that the  $Q_1 \times Q_0$  (i.e.  $Q_1 \times P_0$ ) and  $P_2 \times P_1$  are not stable elements (they are not inf-sup stable).

**Remark.** Note that a similar element to  $Q_2 \times Q_1$  has been proposed and used successfully used [2511, 1223]: it is denoted by  $Q_2^{(8)} \times Q_1$  since the center node (' $x^2y^2$ ') and its associated degrees of freedom have been removed. It has also been proved to be LBB stable.

The Raviart-Thomas family on triangles and quadrilaterals.

find literature

### 6.2.3 The bi/tri-linear velocity - constant pressure element ( $Q_1 \times P_0$ )



discussed in example 3.71 of [1351]

However simple it may look, the element is one of the hardest elements to analyze and many questions are still open about its properties. The element does not satisfy the inf-sup condition [1251]p211. In [1065] it is qualified as follows: slightly unstable but highly usable.

The  $Q_1 \times P_0$  mixed approximation is the lowest order conforming approximation method defined on a rectangular grid. It also happens to be the most famous example of an unstable mixed approximation method. [776, p235].

This element is discussed in [852], [854] and in [2036] in the context of multigrid use.

This element is plagued by so-called pressure checkerboard modes which have been thoroughly analysed [1069], [443], [2237, 2238]. These can be filtered out [443]. Smoothing techniques are also discussed in [1553].

Relevant Literature[853][1063][1591]

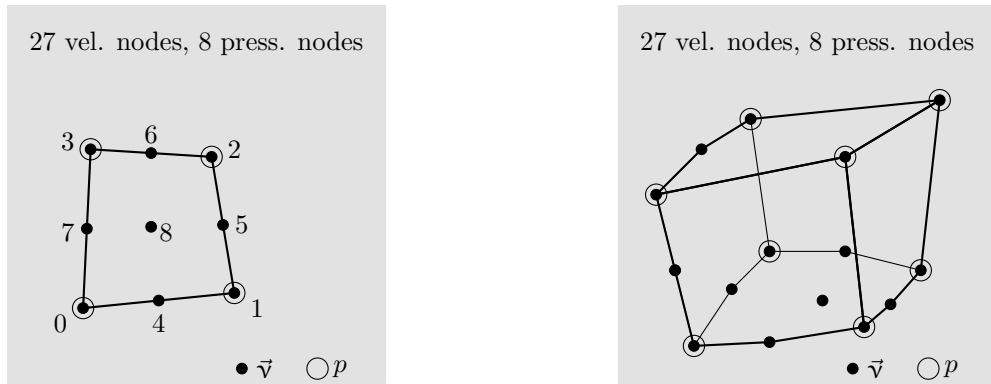
### 6.2.4 The bi/tri-quadratic velocity - discontinuous linear pressure element ( $Q_2 \times P_{-1}$ )

This element is crowned "probably the most accurate 2D element" in [1065].

Piecewise Biquadratic velocities, piecewise linear discontinuous polynomial pressure. The element satisfies the inf-sup condition [1251]p211. It is used in [2600]. See [220] over the two possible choices for the definition of the pressure space.. It is mentioned in [1396], [220], [2000]. It is used in [879] to study 3D fold growth rates (see online supplementary material) and in [2265].

Note that the serendipity version of this pair, i.e.  $Q_2^{(20)} \times P_{-1}$  is also LBB stable [2118, p180].

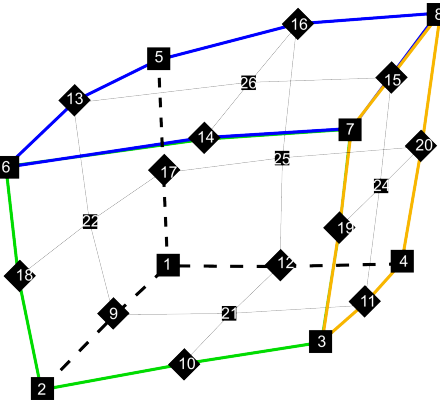
### 6.2.5 The bi/tri-quadratic velocity - bi/tri-linear pressure element ( $Q_2 \times Q_1$ )



In [1065] Gresho & Sani write that in their opinion  $\text{div}(\vec{v}) = 0$  is not strong enough.

This element, implemented in penalised form, is discussed in [175] and the follow-up paper [176].  
CHECK

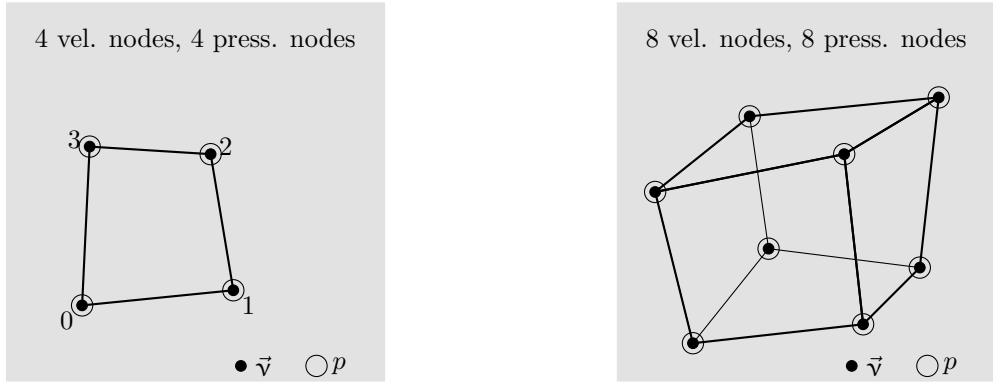
Biquadratic velocities, bilinear pressure. See Hood and Taylor. The element satisfies the inf-sup condition [1251]p215.



### 6.2.6 The stabilised bi/tri-linear velocity - constant pressure element ( $Q_1 \times P_0$ -stab)

Relevant Literature: [2341, 2701, 1410, 2077, 1621, 493, 492]

### 6.2.7 The stabilised bi/tri-linear velocity - bi/tri-linear pressure element ( $Q_1 \times Q_1$ -stab)



See [1955] for a fourier analysis of the normal and stabilised (a la [1253])  $Q_1 - Q_1$  element. This element is used in [381, 382] in conjunction with AMR. Stabilisation is worked out in [705, 215, 216].

$Q_1 \times P_0$ -stab. Pro: stabilisation can be switched off; Con: stabilisation for deformed elements? problem near boundaries: incomplete stencil? choice of parameter  $\beta$ .

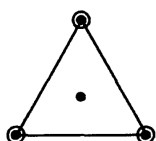
$Q_1 \times Q_1$ -stab. Pro: easier to implement than  $Q_1 \times P_0$ -stab, stabilisation local to element, easier when elements are not rectangular, no free parameter; Con: stabilisation cannot be switched off.

Relevant Literature: [2280, 2519, 2521, 1061, 1280, 1467, 864, 1599]. See Braack & Lube [252] for a review of local projection stabilisation for incompressible flow problems.

This unstable pair is also used in ice sheet modelling [1170, 2875, 2954]

### 6.2.8 The MINI triangular element ( $P_1^+ \times P_1$ ) in 2D

The MINI element was first introduced in Arnold et al, 1984 [52]. It is also discussed in section 3.6.1 of [1351]. It is schematically represented hereunder:



**Mini element:**  
Velocity: continuous linear  
+ cubic bubble function.  
Pressure: continuous linear.  
Satisfies LBB condition,  
Linear convergence.

**Nodes:** • Velocity

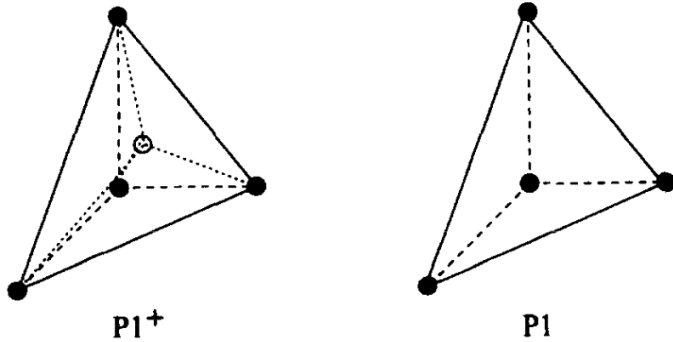
○ Pressure

Figure taken from Donea and Huerta [711]

**Remark.** Note that [863] propose an equal-order-linear-continuous velocity-pressure variables which is enriched with velocity and pressure bubble functions to model the Stokes problem. They show by static condensation that these bubble functions give rise to a stabilized method involving least-squares forms of the momentum and of the continuity equations. In some cases their approach recovers the MINI element. Also check [914].

**Remark.** According to Braess[254], since the support of the bubble is restricted to the element, the associated variable (dofs living on the bubble) can be eliminated from the resulting system of linear equations by static condensation. Also, the MINI element is cheaper than the Taylor-Hood element but it is commonly accepted that it yields a poorer approximation of the pressure.

The 3D MINI element is not very common but it is used for instance in [2028]. It is also said to be LBB stable in [2118, p180].



Velocity and pressure nodes for the 3D MINI element, taken from [2028]

Note that this element is used in [255] in the context of Arbitrary Lagrangian Eulerian finite element analysis of free surface flows. Also used in Zlotnik et al (2007) [2946] for suduction with X-FEM technique.

### 6.2.9 The quadratic velocity - linear pressure triangle ( $P_2 \times P_1$ )

From [2304]: “Taylor-Hood elements [2511] are characterized by the fact that the pressure is continuous in the region  $\Omega$ . A typical example is the quadratic triangle ( $P_2P_1$  element). In this element the velocity is approximated by a quadratic polynomial and the pressure by a linear polynomial. One can easily verify that both approximations are continuous over the element boundaries.” It can be shown, Segal (1979), that this element is admissible if at least 3 elements are used. The quadrilateral counterpart of this triangle is the  $Q_2 \times Q_1$  element. Reddy and Gartling [2118, p179] also report this element to be LBB stable.

Relevant Literature: [2294, 1587]

### 6.2.10 The Crouzeix-Raviart triangle ( $P_2^+ \times P_{-1}$ )

Since the  $P_2 \times P_{-1}$  pair is not LBB stable [2118, p179], it is enhanced by a cubic bubble and is therefore called  $P_2^+ \times P_{-1}$ .

This element was first introduced in [601]. It is the element used in the MILAMIN code [614]. It is a seven-node triangle with quadratic velocity shape functions enhanced by a cubic bubble function and discontinuous linear interpolation for the pressure field [613]. This element is LBB stable and no additional stabilization techniques are required[776]. The '+' in its name stands for the bubble while the '-' stands for the discontinuous character of the pressure field: once again, it is  $P_1$  over the element, but discontinuous across element edges.

**Remark.** Cuvelier et al, 1986 [613] recommend a 6-point or 7-point quadrature rule for this element.

**Remark.** Segal [2304] explains for output purposes (printing, plotting etc.) the discontinuous pressures are averaged in vertices for all the adjoining elements. See also Fig. 7.3 of [613].

**Remark.** The simplest Crouzeix-Raviart element is the non-conforming linear triangle with constant pressure ( $P_1 \times P_0$ ) [613].

It is worth noting that this element has more degrees of freedom than the Taylor-Hood element for the same order of accuracy. However, since the bubble can be eliminated, one can design a modified version of this element.

Check Cuvelier book chapter 8 for modified element

**Remark.** I have once asked the (main) author of MILAMIN why he chose this element, for example over the  $P_2 \times P_1$ . His answer is as follows: "Elements with continuous pressure are incapable of converging in the  $L^\infty$  norm for mechanical problems exhibiting pressure jumps such as the inclusion-host setup. During my MSc and PhD I was focusing on sharp heterogeneities, so this is why I decided to choose  $P_2^+ \times P_{-1}$ . You will see that it is also easy to invert the pressure mass matrix for such elements, which is really useful (both for the augmentation and preconditioning)."

This element is used by Poliakov and Podlachikov [2046] to study the deformation of the surface above a rising diapir. Note that they actually use a "13 point integration formula (Hughes 1987) for calculation of the stiffness matrix was used in order to conserve detailed information from the marker field in the coarse FEM mesh". It is also used in [41] in the context of a new free-surface stabilization scheme. It is the element used in LaCoDe [664].

### 6.2.11 The Rannacher-Turek element - rotated $Q_1 \times P_0$

p. 722 of [1351]  
[2108, 1225, 1466, 1621, 1689, 383]

### 6.2.12 Other elements

- $P_1 \times P_0$ : example 3.70 in [1351], also [1350].
- $P_1 \times P_1$  stabilised [1954, 2462]
- Q2P0: : Quadratic velocities, constant pressure. The element satisfies the inf-sup condition, but the constant pressure assumption may require fine discretisation.
- Q2Q2: This element is never used, probably because a) it is unstable, b) it is very costly. There is one reference to it in [1253].
- P2P2
- the MINI quadrilateral element  $Q_1^+ \times Q_1$ . [75, 1517, 1522]
- Q1P-1 Bilinear velocities, piecewise linear discontinuous polynomial pressure.

### 6.2.13 A note about incompressibility and standard mixed methods

What follows is nicely explained and demonstrated in John et al [1353]. In their example 1.1 they look at the velocity error of benchmark VJ2 (see Section 8.6.9) which analytical solution is a zero velocity field. They show that for the MINI, Taylor-Hood and Crouzeix-Raviart triangular elements the velocity error grows with the magnitude of the rhs. They also make this statement: "there are important applications, e.g., natural convection problems, where the pressure is larger than the velocity by orders of magnitude. In such situations, one cannot expect to compute accurate velocity fields with classical mixed methods, at least for low order methods."

## 6.3 The penalty approach for viscous flow

In order to impose the incompressibility constraint, two widely used procedures are available, namely the Lagrange multiplier method and the penalty method [100, 1251]. The latter is implemented in ELEFANT, which allows for the elimination of the pressure variable from the momentum equation (resulting in a reduction of the matrix size).

Mathematical details on the origin and validity of the penalty approach applied to the Stokes problem can for instance be found in [613], [2117] or [1089].

The penalty formulation of the mass conservation equation is based on a relaxation of the incompressibility constraint and writes

$$\vec{\nabla} \cdot \vec{v} + \frac{p}{\lambda} = 0 \quad (389)$$

where  $\lambda$  is the penalty parameter, that can be interpreted (and has the same dimension) as a bulk viscosity. It is equivalent to say that the material is weakly compressible. It can be shown that if one chooses  $\lambda$  to be a sufficiently large number, the continuity equation  $\vec{\nabla} \cdot \vec{v} = 0$  will be approximately satisfied in the finite element solution. The value of  $\lambda$  is often recommended to be 6 to 7 orders of magnitude larger than the shear viscosity [711, 1254].

Equation (389) can be used to eliminate the pressure in the momentum equation so that the mass and momentum conservation equations fuse to become :

$$\vec{\nabla} \cdot (2\eta \dot{\epsilon}(\vec{v})) + \lambda \vec{\nabla}(\vec{\nabla} \cdot \vec{v}) = \rho g = 0 \quad (390)$$

[1696] have established the equivalence for incompressible problems between the reduced integration of the penalty term and a mixed Finite Element approach if the pressure nodes coincide with the integration points of the reduced rule.

In the end, the elimination of the pressure unknown in the Stokes equations replaces the original saddle-point Stokes problem [159] by an elliptical problem, which leads to a symmetric positive definite (SPD) FEM matrix. This is the major benefit of the penalized approach over the full indefinite solver with the velocity-pressure variables. Indeed, the SPD character of the matrix lends itself to efficient solving strategies and is less memory-demanding since it is sufficient to store only the upper half of the matrix including the diagonal [1025].

list codes which use this approach

Since the penalty formulation is only valid for incompressible flows, then  $\dot{\epsilon} = \dot{\epsilon}^d$  so that the  $d$  superscript is omitted in what follows. Because the stress tensor is symmetric one can also rewrite it the following vector format:

$$\begin{aligned} \begin{pmatrix} \sigma_{xx} \\ \sigma_{yy} \\ \sigma_{zz} \\ \sigma_{xy} \\ \sigma_{xz} \\ \sigma_{yz} \end{pmatrix} &= \begin{pmatrix} -p \\ -p \\ -p \\ 0 \\ 0 \\ 0 \end{pmatrix} + 2\eta \begin{pmatrix} \dot{\epsilon}_{xx} \\ \dot{\epsilon}_{yy} \\ \dot{\epsilon}_{zz} \\ \dot{\epsilon}_{xy} \\ \dot{\epsilon}_{xz} \\ \dot{\epsilon}_{yz} \end{pmatrix} \\ &= \lambda \begin{pmatrix} \dot{\epsilon}_{xx} + \dot{\epsilon}_{yy} + \dot{\epsilon}_{zz} \\ \dot{\epsilon}_{xx} + \dot{\epsilon}_{yy} + \dot{\epsilon}_{zz} \\ \dot{\epsilon}_{xx} + \dot{\epsilon}_{yy} + \dot{\epsilon}_{zz} \\ 0 \\ 0 \\ 0 \end{pmatrix} + 2\eta \begin{pmatrix} \dot{\epsilon}_{xx} \\ \dot{\epsilon}_{yy} \\ \dot{\epsilon}_{zz} \\ \dot{\epsilon}_{xy} \\ \dot{\epsilon}_{xz} \\ \dot{\epsilon}_{yz} \end{pmatrix} \\ &= \underbrace{\lambda \begin{pmatrix} 1 & 1 & 1 & 0 & 0 & 0 \\ 1 & 1 & 1 & 0 & 0 & 0 \\ 1 & 1 & 1 & 0 & 0 & 0 \\ 0 & 0 & 0 & 0 & 0 & 0 \\ 0 & 0 & 0 & 0 & 0 & 0 \\ 0 & 0 & 0 & 0 & 0 & 0 \end{pmatrix}}_{K} + \underbrace{\eta \begin{pmatrix} 2 & 0 & 0 & 0 & 0 & 0 \\ 0 & 2 & 0 & 0 & 0 & 0 \\ 0 & 0 & 2 & 0 & 0 & 0 \\ 0 & 0 & 0 & 1 & 0 & 0 \\ 0 & 0 & 0 & 0 & 1 & 0 \\ 0 & 0 & 0 & 0 & 0 & 1 \end{pmatrix}}_C \cdot \begin{pmatrix} \frac{\partial u}{\partial x} \\ \frac{\partial v}{\partial y} \\ \frac{\partial w}{\partial z} \\ \frac{\partial u}{\partial y} + \frac{\partial v}{\partial x} \\ \frac{\partial u}{\partial z} + \frac{\partial w}{\partial x} \\ \frac{\partial v}{\partial z} + \frac{\partial w}{\partial y} \end{pmatrix} \end{aligned}$$

Remember that

$$\frac{\partial u}{\partial x} = \sum_{i=1}^4 \frac{\partial N_i}{\partial x} u_i \quad \frac{\partial v}{\partial y} = \sum_{i=1}^4 \frac{\partial N_i}{\partial y} v_i \quad \frac{\partial w}{\partial z} = \sum_{i=1}^4 \frac{\partial N_i}{\partial z} w_i$$

and

$$\begin{aligned}\frac{\partial u}{\partial y} + \frac{\partial v}{\partial x} &= \sum_{i=1}^4 \frac{\partial N_i}{\partial y} u_i + \sum_{i=1}^4 \frac{\partial N_i}{\partial x} v_i \\ \frac{\partial u}{\partial z} + \frac{\partial w}{\partial x} &= \sum_{i=1}^4 \frac{\partial N_i}{\partial z} u_i + \sum_{i=1}^4 \frac{\partial N_i}{\partial x} w_i \\ \frac{\partial v}{\partial z} + \frac{\partial w}{\partial y} &= \sum_{i=1}^4 \frac{\partial N_i}{\partial z} v_i + \sum_{i=1}^4 \frac{\partial N_i}{\partial y} w_i\end{aligned}$$

so that

$$\left( \begin{array}{c} \frac{\partial u}{\partial x} \\ \frac{\partial v}{\partial y} \\ \frac{\partial w}{\partial z} \\ \frac{\partial u}{\partial y} + \frac{\partial v}{\partial x} \\ \frac{\partial u}{\partial z} + \frac{\partial w}{\partial x} \\ \frac{\partial v}{\partial z} + \frac{\partial w}{\partial y} \end{array} \right) = \underbrace{\left( \begin{array}{cccccccccccccccc} \frac{\partial N_1}{\partial x} & 0 & 0 & \frac{\partial N_2}{\partial x} & 0 & 0 & \frac{\partial N_3}{\partial x} & 0 & 0 & \dots & \frac{\partial N_4}{\partial x} & 0 & 0 \\ 0 & \frac{\partial N_1}{\partial y} & 0 & 0 & \frac{\partial N_2}{\partial y} & 0 & 0 & \frac{\partial N_3}{\partial y} & 0 & \dots & 0 & \frac{\partial N_4}{\partial y} & 0 \\ 0 & 0 & \frac{\partial N_1}{\partial z} & 0 & 0 & \frac{\partial N_2}{\partial z} & 0 & 0 & \frac{\partial N_3}{\partial z} & \dots & 0 & 0 & \frac{\partial N_4}{\partial z} \\ \frac{\partial N_1}{\partial y} & \frac{\partial N_1}{\partial x} & 0 & \frac{\partial N_2}{\partial y} & \frac{\partial N_2}{\partial x} & 0 & \frac{\partial N_3}{\partial y} & \frac{\partial N_3}{\partial x} & 0 & \dots & \frac{\partial N_4}{\partial y} & \frac{\partial N_4}{\partial x} & 0 \\ \frac{\partial N_1}{\partial z} & 0 & \frac{\partial N_1}{\partial x} & \frac{\partial N_2}{\partial z} & 0 & \frac{\partial N_2}{\partial x} & \frac{\partial N_3}{\partial z} & 0 & \frac{\partial N_3}{\partial x} & \dots & \frac{\partial N_4}{\partial z} & 0 & \frac{\partial N_4}{\partial x} \\ 0 & \frac{\partial N_1}{\partial z} & \frac{\partial N_1}{\partial y} & 0 & \frac{\partial N_2}{\partial z} & \frac{\partial N_2}{\partial y} & 0 & \frac{\partial N_3}{\partial z} & \frac{\partial N_3}{\partial y} & \dots & 0 & \frac{\partial N_4}{\partial z} & \frac{\partial N_4}{\partial y} \end{array} \right)}_{B(6 \times 24)} \cdot \underbrace{\left( \begin{array}{c} u_1 \\ v_1 \\ w_1 \\ u_2 \\ v_2 \\ w_2 \\ u_3 \\ v_3 \\ w_3 \\ \dots \\ u_8 \\ v_8 \\ w_8 \end{array} \right)}_{V(24 \times 1)}.$$

Finally,

$$\vec{\sigma} = \begin{pmatrix} \sigma_{xx} \\ \sigma_{yy} \\ \sigma_{zz} \\ \sigma_{xy} \\ \sigma_{xz} \\ \sigma_{yz} \end{pmatrix} = (\lambda \mathbf{K} + \eta \mathbf{C}) \cdot \mathbf{B} \cdot \vec{V}$$

We will now establish the weak form of the momentum conservation equation. We start again from

$$\vec{\nabla} \cdot \boldsymbol{\sigma} + \vec{b} = \vec{0}$$

For the  $N_i$ 's 'regular enough', we can write:

$$\int_{\Omega_e} N_i \vec{\nabla} \cdot \boldsymbol{\sigma} d\Omega + \int_{\Omega_e} N_i \vec{b} d\Omega = 0$$

We can integrate by parts and drop the surface term<sup>32</sup>:

$$\int_{\Omega_e} \vec{\nabla} N_i \cdot \boldsymbol{\sigma} d\Omega = \int_{\Omega_e} N_i \vec{b} d\Omega$$

or,

$$\int_{\Omega_e} \left( \begin{array}{ccccc} \frac{\partial N_i}{\partial x} & 0 & 0 & \frac{\partial N_i}{\partial y} & \frac{\partial N_i}{\partial z} \\ 0 & \frac{\partial N_i}{\partial y} & 0 & \frac{\partial N_i}{\partial x} & 0 & \frac{\partial N_i}{\partial z} \\ 0 & 0 & \frac{\partial N_i}{\partial z} & 0 & \frac{\partial N_i}{\partial x} & \frac{\partial N_i}{\partial y} \end{array} \right) \cdot \begin{pmatrix} \sigma_{xx} \\ \sigma_{yy} \\ \sigma_{zz} \\ \sigma_{xy} \\ \sigma_{xz} \\ \sigma_{yz} \end{pmatrix} d\Omega = \int_{\Omega_e} N_i \vec{b} d\Omega$$

<sup>32</sup>We will come back to this at a later stage

Let  $i = 1, 2, 3, 4, \dots, 8$  and stack the resulting eight equations on top of one another.

$$\begin{aligned}
\int_{\Omega_e} \begin{pmatrix} \frac{\partial N_i}{\partial x} & 0 & 0 & \frac{\partial N_i}{\partial y} & \frac{\partial N_i}{\partial z} & 0 \\ 0 & \frac{\partial N_i}{\partial y} & 0 & \frac{\partial N_i}{\partial x} & 0 & \frac{\partial N_i}{\partial z} \\ 0 & 0 & \frac{\partial N_i}{\partial z} & 0 & \frac{\partial N_i}{\partial x} & \frac{\partial N_i}{\partial y} \end{pmatrix} \cdot \begin{pmatrix} \sigma_{xx} \\ \sigma_{yy} \\ \sigma_{zz} \\ \sigma_{xy} \\ \sigma_{xz} \\ \sigma_{yz} \end{pmatrix} d\Omega &= \int_{\Omega_e} N_1 \begin{pmatrix} b_x \\ b_y \\ b_z \end{pmatrix} d\Omega \\
\int_{\Omega_e} \begin{pmatrix} \frac{\partial N_i}{\partial x} & 0 & 0 & \frac{\partial N_i}{\partial y} & \frac{\partial N_i}{\partial z} & 0 \\ 0 & \frac{\partial N_i}{\partial y} & 0 & \frac{\partial N_i}{\partial x} & 0 & \frac{\partial N_i}{\partial z} \\ 0 & 0 & \frac{\partial N_i}{\partial z} & 0 & \frac{\partial N_i}{\partial x} & \frac{\partial N_i}{\partial y} \end{pmatrix} \cdot \begin{pmatrix} \sigma_{xx} \\ \sigma_{yy} \\ \sigma_{zz} \\ \sigma_{xy} \\ \sigma_{xz} \\ \sigma_{yz} \end{pmatrix} d\Omega &= \int_{\Omega_e} N_2 \begin{pmatrix} b_x \\ b_y \\ b_z \end{pmatrix} d\Omega \\
&\vdots \\
\int_{\Omega_e} \begin{pmatrix} \frac{\partial N_8}{\partial x} & 0 & 0 & \frac{\partial N_8}{\partial y} & \frac{\partial N_8}{\partial z} & 0 \\ 0 & \frac{\partial N_8}{\partial y} & 0 & \frac{\partial N_8}{\partial x} & 0 & \frac{\partial N_8}{\partial z} \\ 0 & 0 & \frac{\partial N_8}{\partial z} & 0 & \frac{\partial N_8}{\partial x} & \frac{\partial N_8}{\partial y} \end{pmatrix} \cdot \begin{pmatrix} \sigma_{xx} \\ \sigma_{yy} \\ \sigma_{zz} \\ \sigma_{xy} \\ \sigma_{xz} \\ \sigma_{yz} \end{pmatrix} d\Omega &= \int_{\Omega_e} N_8 \begin{pmatrix} b_x \\ b_y \\ b_z \end{pmatrix} d\Omega \quad (391)
\end{aligned}$$

We easily recognize  $\mathbf{B}^T$  inside the integrals! Let us define

$$\vec{N}_b^T = (N_1 b_x, N_1 b_y, N_1 b_z, \dots, N_8 b_x, N_8 b_y, N_8 b_z)$$

then we can write

$$\int_{\Omega_e} \mathbf{B}^T \cdot \begin{pmatrix} \sigma_{xx} \\ \sigma_{yy} \\ \sigma_{zz} \\ \sigma_{xy} \\ \sigma_{xz} \\ \sigma_{yz} \end{pmatrix} d\Omega = \int_{\Omega_e} \vec{N}_b d\Omega$$

and finally:

$$\int_{\Omega_e} \mathbf{B}^T \cdot [\lambda \mathbf{K} + \eta \mathbf{C}] \cdot \mathbf{B} \cdot \vec{V} d\Omega = \int_{\Omega_e} \vec{N}_b d\Omega$$

Since  $\vec{V}$  contains is the vector of unknowns (i.e. the velocities at the corners), it does not depend on the  $x$  or  $y$  coordinates so it can be taking outside of the integral:

$$\underbrace{\left( \int_{\Omega_e} \mathbf{B}^T \cdot [\lambda \mathbf{K} + \eta \mathbf{C}] \cdot \mathbf{B} d\Omega \right)}_{\mathbf{A}_{el}(24 \times 24)} \cdot \underbrace{\vec{V}}_{(24 \times 1)} = \underbrace{\int_{\Omega_e} \vec{N}_b d\Omega}_{\vec{B}_{el}(24 \times 1)}$$

or,

$$\left[ \underbrace{\left( \int_{\Omega_e} \lambda \mathbf{B}^T \cdot \mathbf{K} \cdot \mathbf{B} d\Omega \right)}_{\mathbf{A}_{el}^\lambda(24 \times 24)} + \underbrace{\left( \int_{\Omega_e} \eta \mathbf{B}^T \cdot \mathbf{C} \cdot \mathbf{B} d\Omega \right)}_{\mathbf{A}_{el}^\eta(24 \times 24)} \right] \cdot \underbrace{\vec{V}}_{(24 \times 1)} = \underbrace{\int_{\Omega_e} \vec{N}_b d\Omega}_{\vec{B}_{el}(24 \times 1)}$$



Relevant Literature [1959, 693]

reduced integration [1254]

write about 3D to 2D

## 6.4 The mixed FEM for viscous flow

### 6.4.1 in three dimensions

In what follows the flow is assumed to be incompressible, isoviscous and isothermal.

The methodology to derive the discretised equations of the mixed system is quite similar to the one we have used in the case of the penalty formulation. The big difference comes from the fact that we are now solving for both velocity and pressure at the same time, and that we therefore must solve the mass and momentum conservation equations together. As before, velocity inside an element is given by

$$\vec{v}^h(\vec{r}) = \sum_{i=1}^{m_v} N_i^v(\vec{r}) \vec{v}_i \quad (392)$$

where  $N_i^v$  are the polynomial basis functions for the velocity, and the summation runs over the  $m_v$  nodes composing the element. A similar expression is used for pressure:

$$p^h(\vec{r}) = \sum_{i=1}^{m_p} N_i^p(\vec{r}) p_i \quad (393)$$

Note that the velocity is a vector of size while pressure (and temperature) is a scalar. There are then  $ndof_v$  velocity degrees of freedom per node and  $ndof_p$  pressure degrees of freedom. It is also very important to remember that the numbers of velocity nodes and pressure nodes for a given element are more often than not different and that velocity and pressure nodes need not be colocated. Indeed, unless co-called 'stabilised elements' are used, we have  $m_v > m_p$ , which means that the polynomial order of the velocity field is higher than the polynomial order of the pressure field (usually by value 1).

insert here link(s) to manual and literature

Other notations are sometimes used for Eqs.(392) and (393):

$$u^h(\vec{r}) = \vec{N}^v \cdot \vec{u} \quad v^h(\vec{r}) = \vec{N}^v \cdot \vec{v} \quad w^h(\vec{r}) = \vec{N}^v \cdot \vec{w} \quad p^h(\vec{r}) = \vec{N}^p \cdot \vec{p} \quad (394)$$

where  $\vec{v} = (u, v, w)$  and  $\vec{N}^v$  is the vector containing all basis functions evaluated at location  $\vec{r}$ :

$$\vec{N}^v = (N_1^v(\vec{r}), N_2^v(\vec{r}), N_3^v(\vec{r}), \dots, N_{m_v}^v(\vec{r})) \quad (395)$$

$$\vec{N}^p = (N_1^p(\vec{r}), N_2^p(\vec{r}), N_3^p(\vec{r}), \dots, N_{m_p}^p(\vec{r})) \quad (396)$$

and with

$$\vec{u} = (u_1, u_2, u_3, \dots, u_{m_v}) \quad (397)$$

$$\vec{v} = (v_1, v_2, v_3, \dots, v_{m_v}) \quad (398)$$

$$\vec{w} = (w_1, w_2, w_3, \dots, w_{m_v}) \quad (399)$$

$$\vec{p} = (p_1, p_2, p_3, \dots, p_{m_p}) \quad (400)$$

We will now establish the weak form of the momentum conservation equation. We start again from

$$\vec{\nabla} \cdot \boldsymbol{\sigma} + \vec{b} = \vec{0} \quad (401)$$

$$\vec{\nabla} \cdot \vec{v} = 0 \quad (402)$$

For the  $N_i^v$ 's and  $N_i^p$  'regular enough', we can write:

$$\int_{\Omega_e} N_i^v \vec{\nabla} \cdot \boldsymbol{\sigma} d\Omega + \int_{\Omega_e} N_i^v \vec{b} d\Omega = \vec{0} \quad (403)$$

$$\int_{\Omega_e} N_i^p \vec{\nabla} \cdot \vec{v} d\Omega = 0 \quad (404)$$

We can integrate by parts and drop the surface term<sup>33</sup>:

$$\int_{\Omega_e} \vec{\nabla} N_i^v \cdot \boldsymbol{\sigma} d\Omega = \int_{\Omega_e} N_i^v \vec{b} d\Omega \quad (405)$$

$$\int_{\Omega_e} N_i^p \vec{\nabla} \cdot \vec{v} d\Omega = 0 \quad (406)$$

---

<sup>33</sup>We will come back to this at a later stage

or,

$$\int_{\Omega_e} \begin{pmatrix} \frac{\partial N_i^\gamma}{\partial x} & 0 & 0 & \frac{\partial N_i^\gamma}{\partial y} & \frac{\partial N_i^\gamma}{\partial z} & 0 \\ 0 & \frac{\partial N_i^\gamma}{\partial y} & 0 & \frac{\partial N_i^\gamma}{\partial x} & 0 & \frac{\partial N_i^\gamma}{\partial z} \\ 0 & 0 & \frac{\partial N_i^\gamma}{\partial z} & 0 & \frac{\partial N_i^\gamma}{\partial x} & \frac{\partial N_i^\gamma}{\partial y} \end{pmatrix} \cdot \begin{pmatrix} \sigma_{xx} \\ \sigma_{yy} \\ \sigma_{zz} \\ \sigma_{xy} \\ \sigma_{xz} \\ \sigma_{yz} \end{pmatrix} d\Omega = \int_{\Omega_e} N_i^\gamma \vec{b} d\Omega \quad (407)$$

The above equation can ultimately be written:

$$\int_{\Omega_e} \mathbf{B}^T \cdot \begin{pmatrix} \sigma_{xx} \\ \sigma_{yy} \\ \sigma_{zz} \\ \sigma_{xy} \\ \sigma_{xz} \\ \sigma_{yz} \end{pmatrix} d\Omega = \int_{\Omega_e} \vec{N}_b d\Omega \quad (408)$$

We have previously established that the strain rate vector  $\vec{\varepsilon}$  is:

$$\vec{\varepsilon} = \begin{pmatrix} \frac{\partial u}{\partial x} \\ \frac{\partial v}{\partial y} \\ \frac{\partial w}{\partial z} \\ \frac{\partial u}{\partial y} + \frac{\partial v}{\partial x} \\ \frac{\partial u}{\partial z} + \frac{\partial w}{\partial x} \\ \frac{\partial v}{\partial z} + \frac{\partial w}{\partial y} \end{pmatrix} = \begin{pmatrix} \sum_i \frac{\partial N_i^\gamma}{\partial x} u_i \\ \sum_i \frac{\partial N_i^\gamma}{\partial y} v_i \\ \sum_i \frac{\partial N_i^\gamma}{\partial z} w_i \\ \sum_i \left( \frac{\partial N_i^\gamma}{\partial y} u_i + \frac{\partial N_i^\gamma}{\partial x} v_i \right) \\ \sum_i \left( \frac{\partial N_i^\gamma}{\partial z} u_i + \frac{\partial N_i^\gamma}{\partial x} w_i \right) \\ \sum_i \left( \frac{\partial N_i^\gamma}{\partial z} v_i + \frac{\partial N_i^\gamma}{\partial y} w_i \right) \end{pmatrix} = \underbrace{\begin{pmatrix} \frac{\partial N_1^\gamma}{\partial x} & 0 & 0 & \dots & \frac{\partial N_{m_v}^\gamma}{\partial x} & 0 & 0 \\ 0 & \frac{\partial N_1^\gamma}{\partial y} & 0 & \dots & 0 & \frac{\partial N_{m_v}^\gamma}{\partial y} & 0 \\ 0 & 0 & \frac{\partial N_1^\gamma}{\partial z} & \dots & 0 & 0 & \frac{\partial N_{m_v}^\gamma}{\partial z} \\ \frac{\partial N_1^\gamma}{\partial y} & \frac{\partial N_1^\gamma}{\partial x} & 0 & \dots & \frac{\partial N_{m_v}^\gamma}{\partial x} & \frac{\partial N_{m_v}^\gamma}{\partial x} & 0 \\ \frac{\partial N_1^\gamma}{\partial z} & 0 & \frac{\partial N_1^\gamma}{\partial x} & \dots & \frac{\partial N_{m_v}^\gamma}{\partial z} & 0 & \frac{\partial N_{m_v}^\gamma}{\partial x} \\ 0 & \frac{\partial N_1^\gamma}{\partial z} & \frac{\partial N_1^\gamma}{\partial y} & \dots & 0 & \frac{\partial N_{m_v}^\gamma}{\partial z} & \frac{\partial N_{m_v}^\gamma}{\partial y} \end{pmatrix}}_{\mathbf{B}} \begin{pmatrix} u_1 \\ v_1 \\ w_1 \\ u_2 \\ v_2 \\ w_2 \\ u_3 \\ v_3 \\ \dots \\ u_{m_v} \\ v_{m_v} \\ w_{m_v} \end{pmatrix} \underbrace{\begin{pmatrix} u_1 \\ v_1 \\ w_1 \\ u_2 \\ v_2 \\ w_2 \\ u_3 \\ v_3 \\ \dots \\ u_{m_v} \\ v_{m_v} \\ w_{m_v} \end{pmatrix}}_{\vec{V}} \quad (409)$$

or,  $\vec{\varepsilon} = \mathbf{B} \cdot \vec{V}$  where  $\mathbf{B}$  is the gradient matrix and  $\vec{V}$  is the vector of all vector degrees of freedom for the element. The matrix  $\mathbf{B}$  is then of size  $3 \times m_v \times ndim$  and the vector  $\vec{V}$  is  $m_v * ndof$  long. we have

$$\sigma_{xx} = -p + 2\eta\dot{\varepsilon}_{xx}^d \quad (410)$$

$$\sigma_{yy} = -p + 2\eta\dot{\varepsilon}_{yy}^d \quad (411)$$

$$\sigma_{zz} = -p + 2\eta\dot{\varepsilon}_{zz}^d \quad (412)$$

$$\sigma_{xy} = 2\eta\dot{\varepsilon}_{xy}^d \quad (413)$$

$$\sigma_{xz} = 2\eta\dot{\varepsilon}_{xz}^d \quad (414)$$

$$\sigma_{yz} = 2\eta\dot{\varepsilon}_{yz}^d \quad (415)$$

Since we here only consider incompressible flow, we have  $\dot{\varepsilon}^d = \dot{\varepsilon}$  so

$$\vec{\sigma} = - \begin{pmatrix} 1 \\ 1 \\ 1 \\ 0 \\ 0 \\ 0 \end{pmatrix} p + \mathbf{C} \cdot \vec{\varepsilon} = - \begin{pmatrix} 1 \\ 1 \\ 1 \\ 0 \\ 0 \\ 0 \end{pmatrix} \vec{N}^p \cdot \vec{P} + \mathbf{C} \cdot \mathbf{B} \cdot \vec{V} \quad (416)$$

with

$$\mathbf{C} = \eta \begin{pmatrix} 2 & 0 & 0 & 0 & 0 & 0 \\ 0 & 2 & 0 & 0 & 0 & 0 \\ 0 & 0 & 2 & 0 & 0 & 0 \\ 0 & 0 & 0 & 1 & 0 & 0 \\ 0 & 0 & 0 & 0 & 1 & 0 \\ 0 & 0 & 0 & 0 & 0 & 1 \end{pmatrix} \quad \vec{\varepsilon} = \begin{pmatrix} \dot{\varepsilon}_{xx} \\ \dot{\varepsilon}_{yy} \\ \dot{\varepsilon}_{zz} \\ 2\dot{\varepsilon}_{xy} \\ 2\dot{\varepsilon}_{xz} \\ 2\dot{\varepsilon}_{yz} \end{pmatrix} \quad (417)$$

Let us define matrix  $\mathbf{N}^p$  of size  $6 \times m_p$ :

$$\mathbf{N}^p = \begin{pmatrix} 1 \\ 1 \\ 1 \\ 0 \\ 0 \\ 0 \end{pmatrix} \quad \vec{N}^p = \begin{pmatrix} \vec{N}^p \\ \vec{N}^p \\ \vec{N}^p \\ 0 \\ 0 \\ 0 \end{pmatrix} \quad (418)$$

so that

$$\vec{\sigma} = -\mathbf{N}^p \cdot \vec{P} + \mathbf{C} \cdot \mathbf{B} \cdot \vec{V} \quad (419)$$

finally

$$\int_{\Omega_e} \mathbf{B}^T \cdot [-\mathbf{N}^p \cdot \vec{P} + \mathbf{C} \cdot \mathbf{B} \cdot \vec{V}] d\Omega = \int_{\Omega_e} \mathbf{N}_b d\Omega \quad (420)$$

or,

$$\underbrace{\left( - \int_{\Omega_e} \mathbf{B}^T \cdot \mathbf{N}^p d\Omega \right)}_{\mathbb{G}} \cdot \vec{P} + \underbrace{\left( \int_{\Omega_e} \mathbf{B}^T \cdot \mathbf{C} \cdot \mathbf{B} d\Omega \right)}_{\mathbb{K}} \cdot \vec{V} = \underbrace{\int_{\Omega_e} \vec{N}_b d\Omega}_{\vec{f}} \quad (421)$$

where the matrix  $\mathbb{K}$  is of size  $(m_v * ndof_v \times m_v * ndof_v)$ , and matrix  $\mathbb{G}$  is of size  $(m_v * ndof_v \times m_p * ndof_p)$ .

Turning now to the mass conservation equation:

$$\begin{aligned}
\vec{0} &= \int_{\Omega_e} \vec{N}^p \vec{\nabla} \cdot \vec{v} d\Omega \\
&= \int_{\Omega_e} \vec{N}^p \sum_{i=1}^{m_v} \left( \frac{\partial N_i^v}{\partial x} u_i + \frac{\partial N_i^v}{\partial y} v_i + \frac{\partial N_i^v}{\partial z} w_i \right) d\Omega \\
&= \int_{\Omega_e} \begin{pmatrix} N_1^p \left( \sum_{i=1}^{m_v} \frac{\partial N_i^v}{\partial x} u_i + \sum_{i=1}^{m_v} \frac{\partial N_i^v}{\partial y} v_i + \sum_{i=1}^{m_v} \frac{\partial N_i^v}{\partial z} w_i \right) \\ N_2^p \left( \sum_{i=1}^{m_v} \frac{\partial N_i^v}{\partial x} u_i + \sum_{i=1}^{m_v} \frac{\partial N_i^v}{\partial y} v_i + \sum_{i=1}^{m_v} \frac{\partial N_i^v}{\partial z} w_i \right) \\ N_3^p \left( \sum_{i=1}^{m_v} \frac{\partial N_i^v}{\partial x} u_i + \sum_{i=1}^{m_v} \frac{\partial N_i^v}{\partial y} v_i + \sum_{i=1}^{m_v} \frac{\partial N_i^v}{\partial z} w_i \right) \\ \vdots \\ N_{m_p}^p \left( \sum_{i=1}^{m_v} \frac{\partial N_i^v}{\partial x} u_i + \sum_{i=1}^{m_v} \frac{\partial N_i^v}{\partial y} v_i + \sum_{i=1}^{m_v} \frac{\partial N_i^v}{\partial z} w_i \right) \end{pmatrix} d\Omega \\
&= \int_{\Omega_e} \begin{pmatrix} N_1^p & N_1^p & N_1^p & 0 & 0 & 0 \\ N_2^p & N_2^p & N_2^p & 0 & 0 & 0 \\ N_3^p & N_3^p & N_3^p & 0 & 0 & 0 \\ \vdots & \vdots & \vdots & \vdots & \vdots & \vdots \\ N_{m_p}^p & N_{m_p}^p & N_{m_p}^p & 0 & 0 & 0 \end{pmatrix} \cdot \begin{pmatrix} \sum_i \frac{\partial N_i^v}{\partial x} u_i \\ \sum_i \frac{\partial N_i^v}{\partial y} v_i \\ \sum_i \frac{\partial N_i^v}{\partial z} w_i \\ \sum_i (\frac{\partial N_i^v}{\partial y} u_i + \frac{\partial N_i^v}{\partial x} v_i) \\ \sum_i (\frac{\partial N_i^v}{\partial z} u_i + \frac{\partial N_i^v}{\partial x} w_i) \\ \sum_i (\frac{\partial N_i^v}{\partial z} v_i + \frac{\partial N_i^v}{\partial y} w_i) \end{pmatrix} d\Omega \\
&= \int_{\Omega_e} \underbrace{\begin{pmatrix} N_1^p & N_1^p & N_1^p & 0 & 0 & 0 \\ N_2^p & N_2^p & N_2^p & 0 & 0 & 0 \\ N_3^p & N_3^p & N_3^p & 0 & 0 & 0 \\ \vdots & \vdots & \vdots & \vdots & \vdots & \vdots \\ N_{m_p}^p & N_{m_p}^p & N_{m_p}^p & 0 & 0 & 0 \end{pmatrix}}_{\mathbf{N}^p} \cdot \vec{\varepsilon} d\Omega \\
&= \left( \int \mathbf{N}^p \cdot \mathbf{B} d\Omega \right) \cdot \vec{V} \\
&= -\mathbb{G}_e^T \cdot \vec{V} \tag{422}
\end{aligned}$$

Note that it is common to actually start from  $-\vec{\nabla} \cdot \vec{v} = 0$  (see Eq.(3) in [1746]) so as to arrive at  $\mathbb{G}_e^T \cdot \vec{V} = \vec{0}$

Ultimately we obtain the following system for each element:

$$\begin{pmatrix} \mathbb{K}_e & \mathbb{G}_e \\ -\mathbb{G}_e^T & 0 \end{pmatrix} \cdot \begin{pmatrix} \vec{V} \\ \vec{P} \end{pmatrix} = \begin{pmatrix} \vec{f}_e \\ 0 \end{pmatrix}$$

Such a matrix is then generated for each element and then must be assembled into the global F.E. matrix. Note that in this case the elemental Stokes matrix is antisymmetric. One can also define the following symmetric modified Stokes matrix:

$$\begin{pmatrix} \mathbb{K}_e & \mathbb{G}_e \\ \mathbb{G}_e^T & 0 \end{pmatrix} \cdot \begin{pmatrix} \vec{V} \\ \vec{P} \end{pmatrix} = \begin{pmatrix} \vec{f}_e \\ 0 \end{pmatrix}$$

This matrix is symmetric, but indefinite. It is non-singular if  $\ker(\mathbb{G}^T) = 0$ , which is the case if the compatibility condition holds.

**CHECK:** Matrix  $\mathbb{K}$  is the viscosity matrix. Its size is  $(ndof_v * N_v) \times (ndof_v * N_v)$  where  $ndof_v$  is the number of velocity degrees of freedom per node (typically 1,2 or 3) and  $N_v$  is the number of velocity nodes. The size of matrix  $\mathbb{G}$  is  $(ndof_v * N_v) \times (ndof_p * N_p)$  where  $ndof_p (= 1)$  is the number of velocity degrees of freedom per node and  $N_p$  is the number of pressure nodes. Conversely, the size of matrix  $\mathbb{G}^T$  is  $(ndof_p * N_p) \times (ndof_v * N_v)$ . The size of the global FE matrix is  $N = ndof_v * N_v + ndof_p * N_p$ . Note that matrix  $\mathbb{K}$  is analogous to a discrete Laplacian operator, matrix  $\mathbb{G}$  to a discrete gradient operator, and matrix  $\mathbb{G}^T$  to a discrete divergence operator.

**On the physical dimensions of the Stokes matrix blocks** We start from the Stokes equations:

$$-\vec{\nabla} p + \vec{\nabla} \cdot (2\eta \dot{\boldsymbol{\varepsilon}}) + \rho \mathbf{g} = 0 \quad (423)$$

$$\vec{\nabla} \cdot \vec{v} = 0 \quad (424)$$

The dimensions of the terms in the first equation are:  $ML^{-2}T^{-2}$ . The blocks  $\mathbb{K}$  and  $\mathbb{G}$  stem from the weak form which obtained by multiplying the strong form equations by the (dimensionless) basis functions and integrating over the domain, so that it follows that

$$[\mathbb{K} \cdot \vec{V}] = [\mathbb{G} \cdot \vec{P}] = [\vec{f}] = ML^{-2}T^{-2}L^3 = MLT^{-2}$$

We can then easily deduce:

$$[\mathbb{K}] = MT^{-1} \quad [\mathbb{G}] = L^2$$

**On elemental level mass balance.** Note that in what is above no assumption has been made about whether the pressure basis functions are continuous or discontinuous from one element to another.

Indeed, as mentioned in [1065], since the weak formulation of the momentum equation involves integration by parts of  $\vec{\nabla} p$ , the resulting weak form contains no derivatives of pressure. This introduces the possibility of approximating it by functions (piecewise polynomials, of course) that are not  $C^0$ -continuous, and indeed this has been done and is quite popular/useful.

It is then worth noting that *only* discontinuous pressure elements assure an element-level mass balance [1065]: if for instance  $N_i^p$  is piecewise-constant on element  $e$  (of value 1), the elemental weak form of the mass conservation equation is

$$\int_{\Omega_e} N_i^p \vec{\nabla} \cdot \vec{v} = \int_{\Omega_e} \vec{\nabla} \cdot \vec{v} = \int_{\Gamma_e} \vec{n} \cdot \vec{v} = 0$$

One potentially unwelcome consequence of using discontinuous pressure elements is that they do not possess uniquely defined pressure on the element boundaries; they are dual valued there, and often multi-valued at certain velocity nodes.

**On the  $C$  matrix** The relationship between deviatoric stress and deviatoric strain rate tensor is

$$\boldsymbol{\tau} = 2\eta \dot{\boldsymbol{\varepsilon}}^d \quad (425)$$

$$= 2\eta \left( \dot{\boldsymbol{\varepsilon}} - \frac{1}{3} (\vec{\nabla} \cdot \vec{v}) \mathbf{1} \right) \quad (426)$$

$$= 2\eta \left[ \begin{pmatrix} \dot{\varepsilon}_{xx} & \dot{\varepsilon}_{xy} & \dot{\varepsilon}_{xz} \\ \dot{\varepsilon}_{yx} & \dot{\varepsilon}_{yy} & \dot{\varepsilon}_{yz} \\ \dot{\varepsilon}_{zx} & \dot{\varepsilon}_{zy} & \dot{\varepsilon}_{zz} \end{pmatrix} - \frac{1}{3} (\dot{\varepsilon}_{xx} + \dot{\varepsilon}_{yy} + \dot{\varepsilon}_{zz}) \begin{pmatrix} 1 & 0 & 0 \\ 0 & 1 & 0 \\ 0 & 0 & 1 \end{pmatrix} \right] \quad (427)$$

$$= \frac{2}{3} \eta \begin{pmatrix} 2\dot{\varepsilon}_{xx} - \dot{\varepsilon}_{yy} - \dot{\varepsilon}_{zz} & 3\dot{\varepsilon}_{xy} & 3\dot{\varepsilon}_{xz} \\ 3\dot{\varepsilon}_{yx} & -\dot{\varepsilon}_{yy} + 2\dot{\varepsilon}_{yy} - \dot{\varepsilon}_{yy} & 3\dot{\varepsilon}_{yz} \\ 3\dot{\varepsilon}_{zx} & 3\dot{\varepsilon}_{zy} & -\dot{\varepsilon}_{xx} - \dot{\varepsilon}_{yy} + 2\dot{\varepsilon}_{zz} \end{pmatrix} \quad (428)$$

so that

$$\vec{\tau} = \frac{2}{3}\eta \begin{pmatrix} 2\dot{\varepsilon}_{xx} - \dot{\varepsilon}_{yy} - \dot{\varepsilon}_{zz} \\ -\dot{\varepsilon}_{yy} + 2\dot{\varepsilon}_{yy} - \dot{\varepsilon}_{yy} \\ -\dot{\varepsilon}_{xx} - \dot{\varepsilon}_{yy} + 2\dot{\varepsilon}_{zz} \\ 3\dot{\varepsilon}_{xy} \\ 3\dot{\varepsilon}_{xz} \\ 3\dot{\varepsilon}_{yz} \end{pmatrix} = \underbrace{\frac{\eta}{3} \begin{pmatrix} 4 & -2 & -2 & 0 & 0 & 0 \\ -2 & 4 & -2 & 0 & 0 & 0 \\ -2 & -2 & 4 & 0 & 0 & 0 \\ 0 & 0 & 0 & 3 & 0 & 0 \\ 0 & 0 & 0 & 0 & 3 & 0 \\ 0 & 0 & 0 & 0 & 0 & 3 \end{pmatrix}}_{C^d} \cdot \begin{pmatrix} \dot{\varepsilon}_{xx} \\ \dot{\varepsilon}_{yy} \\ \dot{\varepsilon}_{zz} \\ 2\dot{\varepsilon}_{xy} \\ 2\dot{\varepsilon}_{xz} \\ 2\dot{\varepsilon}_{yz} \end{pmatrix} = \mathbf{C}^d \cdot \vec{\varepsilon} \quad (429)$$

which is identical to the one in the Appendix A of [2265]. In two dimensions, we have

$$\vec{\tau} = \frac{1}{3}\eta \underbrace{\begin{pmatrix} 4 & -2 & 0 \\ -2 & 4 & 0 \\ 0 & 0 & 3 \end{pmatrix}}_{C^d}.$$

see for instance [41].

In the case where we assume incompressible flow from the beginning, i.e.  $\dot{\varepsilon} = \dot{\varepsilon}^d$ , then

$$\vec{\tau} = \eta \underbrace{\begin{pmatrix} 2 & 0 & 0 & 0 & 0 & 0 \\ 0 & 2 & 0 & 0 & 0 & 0 \\ 0 & 0 & 2 & 0 & 0 & 0 \\ 0 & 0 & 0 & 1 & 0 & 0 \\ 0 & 0 & 0 & 0 & 1 & 0 \\ 0 & 0 & 0 & 0 & 0 & 1 \end{pmatrix}}_C \cdot \begin{pmatrix} \dot{\varepsilon}_{xx} \\ \dot{\varepsilon}_{yy} \\ \dot{\varepsilon}_{zz} \\ 2\dot{\varepsilon}_{xy} \\ 2\dot{\varepsilon}_{xz} \\ 2\dot{\varepsilon}_{yz} \end{pmatrix} = \mathbf{C} \cdot \vec{\varepsilon} \quad (430)$$

**Two slightly different formulations** The momentum conservation equation can be written as follows:

$$\vec{\nabla} \cdot (2\eta \vec{\varepsilon}) - \vec{\nabla} p + \vec{b} = \vec{0}$$

When the viscosity  $\eta$  is constant this equation becomes

$$\eta \Delta \vec{v} - \vec{\nabla} p + \vec{b} = \vec{0}$$

In this case the matrix  $\mathbf{B}$  takes a different form [711, Eq. 6.24] and one should be aware that this can have consequences for the Neumann boundary conditions.

In [381] the authors state that when the Laplacian formulation is used it has the computational advantage that the velocity components are coupled only through the incompressibility condition. While the two formulations are equivalent only for constant viscosity, they state that they employ the Laplacian approach formulation as a preconditioner for the viscous term.

Concretely, we apply the same method as above, i.e. we reorganise the terms of the velocity gradient

tensor in a vector:

$$\vec{\nabla} \vec{v} \rightarrow \begin{pmatrix} \partial_x u \\ \partial_y u \\ \partial_z u \\ \partial_x v \\ \partial_y v \\ \partial_z v \\ \partial_x w \\ \partial_y w \\ \partial_z w \end{pmatrix} = \begin{pmatrix} \sum_i \partial_x N_i u_i \\ \sum_i \partial_y N_i u_i \\ \sum_i \partial_z N_i u_i \\ \sum_i \partial_x N_i v_i \\ \sum_i \partial_y N_i v_i \\ \sum_i \partial_z N_i v_i \\ \sum_i \partial_x N_i w_i \\ \sum_i \partial_y N_i w_i \\ \sum_i \partial_z N_i w_i \end{pmatrix}$$

$$= \underbrace{\begin{pmatrix} \partial_x N_1^Y & 0 & 0 & \partial_x N_2^Y & 0 & 0 & \cdots & \partial_x N_{m_v}^Y & 0 & 0 \\ \partial_y N_1^Y & 0 & 0 & \partial_y N_2^Y & 0 & 0 & \cdots & \partial_y N_{m_v}^Y & 0 & 0 \\ \partial_z N_1^Y & 0 & 0 & \partial_z N_2^Y & 0 & 0 & \cdots & \partial_z N_{m_v}^Y & 0 & 0 \\ 0 & \partial_x N_1^Y & 0 & 0 & \partial_x N_2^Y & 0 & \cdots & 0 & \partial_x N_{m_v}^Y & 0 \\ 0 & \partial_y N_1^Y & 0 & 0 & \partial_y N_2^Y & 0 & \cdots & 0 & \partial_y N_{m_v}^Y & 0 \\ 0 & \partial_z N_1^Y & 0 & 0 & \partial_z N_2^Y & 0 & \cdots & 0 & \partial_z N_{m_v}^Y & 0 \\ 0 & 0 & \partial_x N_1^Y & 0 & 0 & \partial_x N_2^Y & \cdots & 0 & 0 & \partial_x N_{m_v}^Y \\ 0 & 0 & \partial_y N_1^Y & 0 & 0 & \partial_y N_2^Y & \cdots & 0 & 0 & \partial_y N_{m_v}^Y \\ 0 & 0 & \partial_z N_1^Y & 0 & 0 & \partial_z N_2^Y & \cdots & 0 & 0 & \partial_z N_{m_v}^Y \end{pmatrix}}_B \cdot \underbrace{\begin{pmatrix} u_1 \\ v_1 \\ w_1 \\ u_2 \\ v_2 \\ w_2 \\ u_3 \\ v_3 \\ \cdots \\ u_{m_v} \\ v_{m_v} \\ w_{m_v} \end{pmatrix}}_{\vec{V}}$$

and in two dimensions:

$$\vec{\nabla} \vec{v} \rightarrow \begin{pmatrix} \partial_x u \\ \partial_y u \\ \partial_x v \\ \partial_y v \end{pmatrix} = \begin{pmatrix} \sum_i \partial_x N_i u_i \\ \sum_i \partial_y N_i u_i \\ \sum_i \partial_x N_i v_i \\ \sum_i \partial_y N_i v_i \end{pmatrix} = \underbrace{\begin{pmatrix} \partial_x N_1^Y & 0 & \partial_x N_2^Y & 0 & \cdots & \partial_x N_{m_v}^Y & 0 \\ \partial_y N_1^Y & 0 & \partial_y N_2^Y & 0 & \cdots & \partial_y N_{m_v}^Y & 0 \\ 0 & \partial_x N_1^Y & 0 & \partial_x N_2^Y & \cdots & 0 & \partial_x N_{m_v}^Y \\ 0 & \partial_y N_1^Y & 0 & \partial_y N_2^Y & \cdots & 0 & \partial_y N_{m_v}^Y \end{pmatrix}}_B \cdot \underbrace{\begin{pmatrix} u_1 \\ v_1 \\ u_2 \\ v_2 \\ u_3 \\ v_3 \\ \cdots \\ u_{m_v} \\ v_{m_v} \end{pmatrix}}_{\vec{V}}$$

### On the 'forgotten' surface terms

#### 6.4.2 Going from 3D to 2D

The world is three-dimensional. However, for many different reasons one may wish to solve problems which are two-dimensional.

Following ASPECT manual, we will think of two-dimensional models in the following way:

- We assume that the domain we want to solve on is a two-dimensional cross section (in the  $x - y$  plane) that extends infinitely far in both negative and positive  $z$  direction.
- We assume that the velocity is zero in the  $z$  direction and that all variables have no variation in the  $z$  direction.

As a consequence, two-dimensional models are three-dimensional ones in which the  $z$  component of the velocity is zero and so are all  $z$  derivatives. This allows to reduce the momentum conservation equations from 3 equations to 2 equations. However, contrarily to what is often seen, the 3D definition of the deviatoric strain rate remains, i.e. in other words:

$$\dot{\epsilon}^d = \dot{\epsilon} - \frac{1}{3}(\vec{\nabla} \cdot \vec{v})\mathbf{1} \quad (431)$$

and not  $1/2$ . In light of all this, the full strain rate tensor and the deviatoric strain rate tensor in 2D are given by:

$$\boldsymbol{\varepsilon} = \begin{pmatrix} \dot{\varepsilon}_{xx} & \dot{\varepsilon}_{xy} & \dot{\varepsilon}_{xz} \\ \dot{\varepsilon}_{yx} & \dot{\varepsilon}_{yy} & \dot{\varepsilon}_{yz} \\ \dot{\varepsilon}_{zx} & \dot{\varepsilon}_{zy} & \dot{\varepsilon}_{zz} \end{pmatrix} = \begin{pmatrix} \frac{\partial u}{\partial x} & \frac{1}{2} \left( \frac{\partial u}{\partial y} + \frac{\partial v}{\partial x} \right) & 0 \\ \frac{1}{2} \left( \frac{\partial u}{\partial y} + \frac{\partial v}{\partial x} \right) & \frac{\partial v}{\partial y} & 0 \\ 0 & 0 & 0 \end{pmatrix} \quad (432)$$

$$\dot{\boldsymbol{\varepsilon}}^d = \frac{1}{3} \begin{pmatrix} 2 \frac{\partial u}{\partial x} - \frac{\partial v}{\partial y} & \frac{1}{2} \left( \frac{\partial u}{\partial y} + \frac{\partial v}{\partial x} \right) & 0 \\ \frac{1}{2} \left( \frac{\partial u}{\partial y} + \frac{\partial v}{\partial x} \right) & -\frac{\partial u}{\partial x} + 2 \frac{\partial v}{\partial y} & 0 \\ 0 & 0 & -\frac{\partial u}{\partial x} - \frac{\partial v}{\partial y} \end{pmatrix} \quad (433)$$

Although the bottom right term may be surprising, it is of no consequence when this expression of the deviatoric strain rate is used in the Stokes equation:

$$\vec{\nabla} \cdot 2\eta \dot{\boldsymbol{\varepsilon}}^d =$$

**FINISH!**

In two dimensions the velocity is then  $\vec{v} = (u, v)$  and the FEM building blocks and matrices are simply:

$$\vec{\dot{\boldsymbol{\varepsilon}}} = \begin{pmatrix} \dot{\varepsilon}_{xx} \\ \dot{\varepsilon}_{yy} \\ 2\dot{\varepsilon}_{xy} \end{pmatrix} = \begin{pmatrix} \frac{\partial u}{\partial x} \\ \frac{\partial v}{\partial y} \\ \frac{\partial u}{\partial y} + \frac{\partial v}{\partial x} \end{pmatrix} = \underbrace{\begin{pmatrix} \frac{\partial N_1^\gamma}{\partial x} & 0 & \frac{\partial N_2^\gamma}{\partial x} & 0 & \frac{\partial N_3^\gamma}{\partial x} & 0 & \dots & \frac{\partial N_{m_v}^\gamma}{\partial x} & 0 \\ 0 & \frac{\partial N_1^\gamma}{\partial y} & 0 & \frac{\partial N_2^\gamma}{\partial y} & 0 & \frac{\partial N_3^\gamma}{\partial y} & \dots & 0 & \frac{\partial N_{m_v}^\gamma}{\partial x} \\ \frac{\partial N_1^\gamma}{\partial y} & \frac{\partial N_1^\gamma}{\partial x} & \frac{\partial N_2^\gamma}{\partial y} & \frac{\partial N_2^\gamma}{\partial x} & \frac{\partial N_3^\gamma}{\partial y} & \frac{\partial N_3^\gamma}{\partial x} & \dots & \frac{\partial N_{m_v}^\gamma}{\partial y} & \frac{\partial N_{m_v}^\gamma}{\partial x} \end{pmatrix}}_B \cdot \underbrace{\begin{pmatrix} u_1 \\ v_1 \\ u_2 \\ v_2 \\ u_3 \\ v_3 \\ \dots \\ u_{m_v} \\ v_{m_v} \end{pmatrix}}_{\vec{V}} \quad (434)$$

we have

$$\sigma_{xx} = -p + 2\eta \dot{\varepsilon}_{xx} \quad (435)$$

$$\sigma_{yy} = -p + 2\eta \dot{\varepsilon}_{yy} \quad (436)$$

$$\sigma_{xy} = +2\eta \dot{\varepsilon}_{xy} \quad (437)$$

so

$$\vec{\sigma} = - \begin{pmatrix} 1 \\ 1 \\ 0 \end{pmatrix} p + \mathbf{C} \cdot \vec{\dot{\boldsymbol{\varepsilon}}} = - \begin{pmatrix} 1 \\ 1 \\ 0 \end{pmatrix} \vec{N}^p \cdot \vec{P} + \mathbf{C} \cdot \mathbf{B} \cdot \vec{V} \quad (438)$$

with

$$\mathbf{C} = \eta \begin{pmatrix} 2 & 0 & 0 \\ 0 & 2 & 0 \\ 0 & 0 & 1 \end{pmatrix} \quad \text{or} \quad \mathbf{C} = \frac{\eta}{3} \begin{pmatrix} 4 & -2 & 0 \\ -2 & 4 & 0 \\ 0 & 0 & 3 \end{pmatrix} \quad (439)$$

**check the right C**

Finally the matrix  $\mathbf{N}^p$  is of size  $3 \times m_p$ :

$$\mathbf{N}^p = \begin{pmatrix} 1 \\ 1 \\ 0 \end{pmatrix} \vec{N}^p = \begin{pmatrix} \vec{N}^p \\ \vec{N}^p \\ 0 \end{pmatrix} \quad (440)$$

## 6.5 Solving the elastic equations

## 6.6 A quick tour of similar literature

- *Treatise on Geophysics*, Volume 7, Edited by D. Bercovici and G. Schubert: "Numerical Methods for Mantle Convection", by S.J. Zhong, D.A. Yuen, L.N. Moresi and M.G. Knepley. Note that it is a revision of the previous edition chapter by S.J. Zhong, D.A. Yuen and L.N. Moresi, Volume 7, pp. 227-252, 2007.
- *Computational Science I*, Lecture Notes for CAAM 519, M.G. Knepley, 2017. <https://cse.buffalo.edu/~knepley/classes/caam519/>
- *Numerical Modeling of Earth Systems - An introduction to computational methods with focus on-solid Earth applications of continuum mechanics*, Th.W. Becker and B.J.P. Kaus, 2018. <http://www-udc.ig.utexas.edu/external/becker/Geodynamics557.pdf>
- *Myths and Methods in Modeling*, M. Spiegelman, 2000. [https://earth.usc.edu/~becker/teaching/557/reading/spiegelman\\_mmm.pdf](https://earth.usc.edu/~becker/teaching/557/reading/spiegelman_mmm.pdf)

## 6.7 The case against the $Q_1 \times P_0$ element

What follows was written by Dave May and sent to me by email in May 2014. It captures so well the problem at hand that I have decided to reproduce it hereunder.

In the case of the incompressible Stokes equations, we would like to solve

$$\begin{pmatrix} \mathbb{K} & \mathbb{G} \\ \mathbb{G}^T & 0 \end{pmatrix} \begin{pmatrix} \vec{\mathcal{V}} \\ \vec{\mathcal{P}} \end{pmatrix} = \begin{pmatrix} \vec{f} \\ 0 \end{pmatrix}$$

with an iterative method which is algorithmically scalable and optimal. Scalable here would mean that the number of iterations doesn't grow as the mesh is refined. Optimal means the solution time varies linearly with the total number of unknowns. When using a stable element, If we right precondition the above system with

$$P = \begin{pmatrix} \mathbb{K} & \mathbb{G} \\ 0 & -\mathbb{S} \end{pmatrix}$$

then convergence will occur in 2 iterations, however this requires an exact solve on  $\mathbb{K}$  and on  $\mathbb{S} = \mathbb{G}^T \cdot \mathbb{K}^{-1} \cdot \mathbb{G}$  ( $\mathbb{S}$  is the pressure schur complement). In practice, people relax the ideal "two iteration" scenario by first replacing  $\mathbb{S}$  via  $\mathbb{S}^* = \int \eta^{-1} \vec{N}^T \vec{N} dv$  (e.g. the pressure mass matrix scaled by the local inverse of viscosity).

$$P^* = \begin{pmatrix} \mathbb{K} & \mathbb{G} \\ 0 & -\mathbb{S}^* \end{pmatrix}$$

Using  $P^*$ , we obtain iteration counts which are larger than 2, but likely less than 10 - *however*, the number of iterations is independent of the mesh size. Replacing the exact  $\mathbb{K}$  solve in  $P^*$  again increases the iterations required to solve Stokes, but it's still independent of the number of elements. When you have this behaviour, we say the preconditioner ( $P^*$ ) is spectrally equivalent to the operator (which here is Stokes)

The problem with  $Q_1 \times P_0$  is that there are no approximations for  $\mathbb{S}$  which can be generated that ensure a spectrally equivalent  $P^*$ . Thus, as you refine the mesh using  $Q_1 \times P_0$  elements, the iteration count ALWAYS grows. I worked on this problem during my thesis, making some improvements to the situation - however the problem still remains, it cannot be completely fixed and stems entirely from using unstable elements.

Citcom solvers works like this:

1. Solve  $\mathbb{S} \cdot \mathcal{P} = \vec{f}'$  for pressure
2. Solve  $\mathbb{K} \cdot \mathcal{V} = \vec{f} - \mathbb{G} \cdot \mathcal{P}$  for velocity

To obtain a scalable method, we need the number of iterations performed in (1) and (2) to be independent of the mesh. This means we need a spectrally equivalent preconditioner for  $\mathbb{S}$  and  $\mathbb{K}$ . Thus, we have the same issue as when you iterate on the full stokes system.

When we don't have a scalable method, it means increasing the resolution requires more cpu time in a manner which cannot be predicted. The increase in iteration counts as the mesh is refined can be dramatic.

If we can bound the number of iterations, AND ensure that the cost per iteration is linearly related to the number of unknowns, then we have a good method which can run on any mesh resolution with a predictable cpu time. Obtaining scalable and optimal preconditioners for  $\mathbb{K}$  is somewhat easier. Multigrid will provide us with this.

The reason citcom doesn't run with  $400^3$  elements is exactly due to this issue. I've added petsc support in citcom (when i was young and naive) - but the root cause of the non-scalable solve is directly caused by the element choice. Note that many of the high resolution citcom jobs are single time step calculations— there is a reason for that.

For many lithosphere dynamics problems, we need a reasonable resolution (at least  $200^3$  and realistically  $400^3$  to  $800^3$ ). Given the increase in cost which occurs when using Q1P0, this is not achievable, as the citcom code has demonstrated. Note that citcom is 20 years old now and for its time, it was great, but we know much more now and we know how to improve on it. As a result of this realization, I dumped all my old Q1P0 codes (and Q1Q1 codes, but for other reasons) in the trash and started from scratch. The only way to make something like  $800^3$  tractable is via iterative, scalable and optimal methods and that mandates stable elements. I can actually run at something like  $1000^3$  (nodal points) these days because of such design choices.

## 6.8 Isoviscous Stokes for incompressible flow

We start from the momentum equation:

$$-\vec{\nabla}p + \vec{\nabla} \cdot (2\eta\dot{\varepsilon}^d(\vec{v})) + \rho\vec{g} = \vec{0} \quad (441)$$

When the viscosity is constant in space, it can be taken out of the divergence operator:

$$-\vec{\nabla}p + 2\eta\vec{\nabla} \cdot \dot{\varepsilon}^d(\vec{v}) + \rho\vec{g} = \vec{0} \quad (442)$$

Let us for simplicity look at a 2D Cartesian formulation of this equation and for incompressible flow:

$$2\vec{\nabla} \cdot \dot{\varepsilon}^d(\vec{v}) = \vec{\nabla} \cdot (\vec{\nabla}\vec{v} + \vec{\nabla}\vec{v}^T) \quad (443)$$

$$= (\partial_x \partial_y) \cdot \begin{pmatrix} \partial_x u & \partial_x v \\ \partial_y u & \partial_y v \end{pmatrix} + (\partial_x \partial_y) \cdot \begin{pmatrix} \partial_x u & \partial_y u \\ \partial_x v & \partial_y v \end{pmatrix} \quad (444)$$

$$= (\partial_x^2 u + \partial_y^2 u, \partial_x^2 v + \partial_y^2 v) + (\partial_x \partial_x u + \partial_y \partial_x v, \partial_x \partial_y u + \partial_y \partial_y v) \quad (445)$$

$$= (\partial_x^2 u + \partial_y^2 u, \partial_x^2 v + \partial_y^2 v) + (\partial_x \underbrace{(\partial_x u + \partial_y v)}_{=0}, \partial_y \underbrace{(\partial_x u + \partial_y v)}_{=0}) \quad (446)$$

$$= (\partial_x^2 u + \partial_y^2 u, \partial_x^2 v + \partial_y^2 v) \quad (447)$$

and then finally the Stokes equation is:

$$-\vec{\nabla}p + \eta\Delta\vec{v} + \rho\vec{g} = \vec{0} \quad (448)$$

The mass conservation equation remains unchanged and so does the pressure gradient term. We shall then focus on the weak form of the previously obtained term. We multiply it by a velocity test function

$N_i^\nu$  and integrate over an element:

$$\begin{aligned}
& \int_{\Omega_e} N_i^\nu \Delta \vec{v}^h dV \\
&= \int_{\Omega_e} \begin{pmatrix} N_i^\nu \Delta u^h \\ N_i^\nu \Delta v^h \end{pmatrix} dV \\
&= \int_{\Omega_e} \begin{pmatrix} N_i^\nu \vec{\nabla} \cdot \vec{\nabla} u^h \\ N_i^\nu \vec{\nabla} \cdot \vec{\nabla} v^h \end{pmatrix} dV \\
&= \int_{\Omega_e} \begin{pmatrix} \vec{\nabla} N_i^\nu \cdot \vec{\nabla} u^h \\ \vec{\nabla} N_i^\nu \cdot \vec{\nabla} v^h \end{pmatrix} dV \\
&= \int_{\Omega_e} \begin{pmatrix} \partial_x N_i^\nu \partial_x u^h + \partial_y N_i^\nu \partial_y u^h \\ \partial_x N_i^\nu \partial_x v^h + \partial_y N_i^\nu \partial_y v^h \end{pmatrix} dV \\
&= \int_{\Omega_e} \begin{pmatrix} \partial_x N_i^\nu & \partial_y N_i^\nu & 0 & 0 \\ 0 & 0 & \partial_x N_i^\nu & \partial_y N_i^\nu \end{pmatrix} \cdot \begin{pmatrix} \partial_x u^h \\ \partial_y u^h \\ \partial_x v^h \\ \partial_y v^h \end{pmatrix} dV \\
&= \int_{\Omega_e} \begin{pmatrix} \partial_x N_i^\nu & \partial_y N_i^\nu & 0 & 0 \\ 0 & 0 & \partial_x N_i^\nu & \partial_y N_i^\nu \end{pmatrix} \cdot \begin{pmatrix} \partial_x N_1^\nu & 0 & \partial_x N_2^\nu & 0 & \cdots & \partial_x N_{m_\nu}^\nu & 0 \\ \partial_y N_1^\nu & 0 & \partial_y N_2^\nu & 0 & \cdots & \partial_y N_{m_\nu}^\nu & 0 \\ 0 & \partial_x N_1^\nu & 0 & \partial_x N_2^\nu & \cdots & 0 & \partial_x N_{m_\nu}^\nu \\ 0 & \partial_y N_1^\nu & 0 & \partial_y N_2^\nu & \cdots & 0 & \partial_y N_{m_\nu}^\nu \end{pmatrix} \cdot \underbrace{\begin{pmatrix} u_1 \\ v_1 \\ u_2 \\ v_2 \\ \vdots \\ u_{m_\nu} \\ v_{m_\nu} \end{pmatrix}}_{\vec{v}} dV
\end{aligned}$$

Writing this equation for  $i = 1, \dots, m_\nu$ , we obtain:

$$\int \underbrace{\begin{pmatrix} \partial_x N_1^\nu & \partial_y N_1^\nu & 0 & 0 \\ 0 & 0 & \partial_x N_1^\nu & \partial_y N_1^\nu \\ \partial_x N_2^\nu & \partial_y N_2^\nu & 0 & 0 \\ 0 & 0 & \partial_x N_2^\nu & \partial_y N_2^\nu \\ \vdots & \vdots & \vdots & \vdots \\ \partial_x N_{m_\nu}^\nu & \partial_y N_{m_\nu}^\nu & 0 & 0 \\ 0 & 0 & \partial_x N_{m_\nu}^\nu & \partial_y N_{m_\nu}^\nu \end{pmatrix}}_{\mathbf{B}} \cdot \underbrace{\begin{pmatrix} \partial_x N_1^\nu & 0 & \partial_x N_2^\nu & 0 & \cdots & \partial_x N_{m_\nu}^\nu & 0 \\ \partial_y N_1^\nu & 0 & \partial_y N_2^\nu & 0 & \cdots & \partial_y N_{m_\nu}^\nu & 0 \\ 0 & \partial_x N_1^\nu & 0 & \partial_x N_2^\nu & \cdots & 0 & \partial_x N_{m_\nu}^\nu \\ 0 & \partial_y N_1^\nu & 0 & \partial_y N_2^\nu & \cdots & 0 & \partial_y N_{m_\nu}^\nu \end{pmatrix}}_{\mathbf{B}^T} \cdot \underbrace{\begin{pmatrix} u_1 \\ v_1 \\ u_2 \\ v_2 \\ \vdots \\ u_{m_\nu} \\ v_{m_\nu} \end{pmatrix}}_{\vec{v}} dV$$

or,

$$\mathbf{K}_\eta = \eta \int_{\Omega_e} \mathbf{B}^T \cdot \mathbf{B} dV$$

where  $\mathbf{B}$  is a  $(ndim * ndim) \times (m_v * ndofV)$  matrix (see also Eq. 6.24 of [711]).

In three dimensions, the matrix  $\mathbf{B}$  is given by

$$\begin{pmatrix} \partial_x N_1^\nu & 0 & \partial_x N_2^\nu & 0 & \cdots & \partial_x N_{m_\nu}^\nu & 0 \\ \partial_y N_1^\nu & 0 & \partial_y N_2^\nu & 0 & \cdots & \partial_y N_{m_\nu}^\nu & 0 \\ \partial_z N_1^\nu & 0 & \partial_z N_2^\nu & 0 & \cdots & \partial_z N_{m_\nu}^\nu & 0 \\ 0 & \partial_x N_1^\nu & 0 & \partial_x N_2^\nu & \cdots & 0 & \partial_x N_{m_\nu}^\nu \\ 0 & \partial_y N_1^\nu & 0 & \partial_y N_2^\nu & \cdots & 0 & \partial_y N_{m_\nu}^\nu \\ 0 & \partial_z N_1^\nu & 0 & \partial_z N_2^\nu & \cdots & 0 & \partial_z N_{m_\nu}^\nu \end{pmatrix}$$

## 7 The Discontinuous Galerkin Finite Element Method (DG-FEM)

Books:

- *Discontinuous Galerkin Methods. Theory, Computation and Applications* by Cockburn, Karniadakis and Shu [531]
- *Mathematical Aspects of Discontinuous Galerkin Methods* by Di Pietro and Ern [696]
- *Discontinuous Galerkin Methods. Analysis and Applications to Compressible Flow* by Dolejsi and Feistauer [707]
- *Discontinuous Galerkin Methods for Solving Elliptic and Parabolic Equations* by Rivière [2166]
- *Discontinuous finite elements in fluid dynamics and heat transfer* by Li [1596]
- *Nodal Discontinuous Galerkin Methods. Algorithms, Analysis, and Applications* by Hesthaven & Warbuton [1189]

There are many different flavours of the Discontinuous Galerkin Finite Element Method:

- **HDG**: Hybridizable DG [532]
- **IIPG**: incomplete interior penalty G [708]
- **LDG**: Local DG [425]

### 7.1 First-order advection ODE in 1D

What follows is borrowed from the book "Discontinuous finite elements in fluid dynamics and heat transfer" by Ben Q. Li [1596].

To illustrate the basic ideas of the discontinuous finite element method, we consider a simple, one-dimensional, first order differential equation with  $u$  specified at one of the boundaries:

$$\frac{du}{dx} + g = 0 \quad x \in [a, b] \quad \text{and} \quad u(x = a) = u_a \quad (449)$$

where  $g$  is a constant (for simplicity). The domain is discretized such that :  $\Omega_j = [x_j, x_{j+1}]$  with  $j = 1, 2, \dots, nel$ . Then, integrating the above equation over the element  $j$  with respect to a weighting function  $f(x)$

$$\int_{x_j}^{x_{j+1}} \left( \frac{du}{dx} + g \right) f(x) dx = 0 \quad (450)$$

Remembering that  $\int_c^d u(x)v'(x)dx = [u(x)v(x)]_c^d - \int_c^d u'(x)v(x)dx$ , we can now perform an integration by parts on the differential operator and we obtain:

$$[u(x)f(x)]_{x_j}^{x_{j+1}} - \int_{x_j}^{x_{j+1}} \left( u \frac{df}{dx} - gf(x) \right) dx = 0 \quad (451)$$

or,

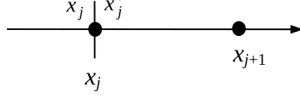
$$u(x_{j+1})f(x_{j+1}) - u(x_j)f(x_j) - \int_{x_j}^{x_{j+1}} \left( u \frac{df}{dx} - gf(x) \right) dx = 0 \quad (452)$$

On  $\Omega_j$   $u$  is approximated by  $u_h \in H$ ,  $H$  being an appropriate function space of finite dimension, and  $f$  by  $f_h$  taken from the same function space as  $u_h$ . Upon substituting  $(u_h, f_h)$  for  $(u, f)$  in the equation above, we have the discontinuous Galerkin finite element formulation:

$$u_h(x_{j+1})f_h(x_{j+1}) - u_h(x_j)f_h(x_j) - \int_{x_j}^{x_{j+1}} \left( u_h \frac{df_h}{dx} - gf_h(x) \right) dx = 0 \quad (453)$$

In the continuous finite element approach, the field variable  $u_h$  is forced to be continuous across the boundary. The essential idea for the discontinuous method is that  $u_h$  is allowed to be discontinuous across the boundary. Therefore, across the element, the following two different values are defined at the two sides of the boundary:

$$u_j^+ = \lim_{x \searrow x_j^+} u_h(x) \quad u_j^- = \lim_{x \nearrow x_j^-} u_h(x) \quad (454)$$



An illustration of the jump across  $x_j$  of element  $j$ :  $x_j$  and  $x_{j+1}$  mark the boundaries of the element

Conversely, we also have:

$$u_{j+1}^+ = \lim_{x \searrow x_{j+1}^+} u_h(x) \quad u_{j+1}^- = \lim_{x \nearrow x_{j+1}^-} u_h(x) \quad (455)$$

It is key to remember that 1)  $u_h$  is discontinuous only at the element boundaries; 2) the solution  $u$  is smooth within (but excluding) the boundary. By this definition, the above equation contains the variables only within the integral limits of  $\Omega_j$ . As a consequence, there is no direct coupling with other intervals or other elements. *The field values at a node, or the interface between two elements, are not unique.* They are calculated using the two limiting values approaching the interface from the two adjacent elements. This feature is certainly desirable for problems with internal discontinuities.

We can now write CHECK CHECK

$$u_{j+1}^- f_h(x_{j+1}) - u_j^+ f_h(x_j) - \int_{x_j}^{x_{j+1}} \left( u_h \frac{df_h}{dx} - g f_h(x) \right) dx = 0 \quad (456)$$

and we can integrate by parts again the term which contains a derivative:

$$\int_{x_j}^{x_{j+1}} u_h(x) \frac{df_h}{dx} dx = [u_h f_h] - \int_{x_j}^{x_{j+1}} f_h(x) \frac{du_h}{dx} dx$$

and then

$$u_{j+1}^- f_h(x_{j+1}) - u_j^+ f_h(x_j) - \int_{x_j}^{x_{j+1}} \left( u_h \frac{df_h}{dx} - g f_h(x) \right) dx = 0 \quad (457)$$

## 7.2 Steady state diffusion in 1D

Let us start simple with the 1D steady state heat conduction problem in 1D, given by the following equation:

$$\frac{d^2T}{dx^2} = 0 \quad T(x=0) = 0 \quad T(x=1) = 1 \quad \text{on } x \in [0, 1] \quad (458)$$

Although this equation is usually solved as is with its second-order derivative, it can also be written in a mixed form, using the heat flux  $q$  (a scalar in 1D):

$$-\frac{dq}{dx} = 0 \quad q - \frac{dT}{dx} = 0 \quad x \in [0, 1]$$

and the boundary conditions remain unchanged.

We apply the standard approach to establish the weak forms of these two first-order ODEs, and we do so on an element  $e$  bound by nodes  $k$  and  $k+1$  with coordinates  $x_k$  and  $x_{k+1}$

$$-\int_{x_k}^{x_{k+1}} \frac{dq}{dx} \tilde{f}(x) dx = -[q\tilde{f}]_{x_k}^{x_{k+1}} + \int_{x_k}^{x_{k+1}} \frac{d\tilde{f}}{dx} q(x) dx = 0 \quad (459)$$

$$\int_{x_k}^{x_{k+1}} \left( q - \frac{dT}{dx} \right) \bar{f}(x) dx = \int_{x_k}^{x_{k+1}} q(x) \bar{f}(x) dx - [T\bar{f}]_{x_k}^{x_{k+1}} + \int_{x_k}^{x_{k+1}} \frac{d\bar{f}}{dx} T(x) dx = 0 \quad (460)$$

where  $\tilde{f}$  and  $\bar{f}$  are test functions. We now must examine the term between square brackets. Inside the element, the test functions  $\tilde{f}$  and  $\bar{f}$  are well defined polynomials and we coin:

$$\tilde{f}_k^+ = \tilde{f}(x_k^+) \quad (461)$$

$$\tilde{f}_{k+1}^- = \tilde{f}(x_{k+1}^-) \quad (462)$$

$$\bar{f}_k^+ = \bar{f}(x_k^+) \quad (463)$$

$$\bar{f}_{k+1}^- = \bar{f}(x_{k+1}^-) \quad (464)$$

Concerning  $q$  and  $T$ , we will for now give them values  $\hat{q}_k$  and  $\hat{T}_k$  at node  $k$  and  $\hat{q}_{k+1}$  and  $\hat{T}_{k+1}$  at node  $k+1$ , and we will specify the hat quantities as follows:

$$\begin{aligned} \hat{T}_k &= \begin{cases} T_k^- & k=1 \\ \frac{1}{2}(T_k^- + T_k^+) + \mathcal{C}(T_k^- - T_k^+) & k=2, \dots, N-1 \\ T_k^+ & k=N \end{cases} \\ \hat{q}_k &= \begin{cases} q_k^+ - \mathcal{E}(T_k^- - T_k^+) & k=1 \\ \frac{1}{2}(q_k^+ + q_k^-) - \mathcal{E}(T_k^- - T_k^+) - \mathcal{C}(q_k^- - q_k^+) & k=2, \dots, N-1 \\ q_k^- - \mathcal{E}(T_k^- - T_k^+) & k=N \end{cases} \end{aligned} \quad (465)$$

where  $N$  is the number of nodes and where  $\mathcal{C}$  and  $\mathcal{E}$  are two constants.

**Discuss the meaning/values of these!**

**Remark.** Note that  $\hat{T}_k = T_1^-$  on the left boundary is consistent with  $\hat{T}_k = \frac{1}{2}(T_k^- + T_k^+) + \mathcal{C}(T_k^- - T_k^+)$  provided  $T_1^- = T_1^+$ . The same goes for the right boundary, and the same reasoning applies for the heat flux terms  $\hat{q}_k$ .

Inside an element bounded by nodes  $k$  and  $k+1$ , the temperature  $T$  and heat flux  $q$  are interpolated over an isoparametric linear element:

$$T_h(x) = N_k(x)T_k^+ + N_{k+1}(x)T_{k+1}^-$$

$$q_h(x) = N_k(x)q_k^+ + N_{k+1}(x)q_{k+1}^-$$

As in the (Continuous) Galerkin case of section 5.1, the test functions are taken to be the shape functions, and in this case for both temperature and flux.

There are four unknowns  $q_k^+$ ,  $q_{k+1}^-$ ,  $T_k^+$  and  $T_{k+1}^-$  per element. All other  $q$  and  $T$  quantities in the above/following equations will need to find their way to the rhs.

- Eq. 484 becomes:

$$\begin{aligned} 0 &= -\hat{q}_{k+1}\tilde{f}(x_{k+1}^-) + \hat{q}_k\tilde{f}(x_k^+) + \int_{x_k}^{x_{k+1}} \frac{d\tilde{f}}{dx}q_h(x)dx \\ &= -\hat{q}_{k+1}\tilde{f}_{k+1}^- + \hat{q}_k\tilde{f}_k^+ + \int_{x_k}^{x_{k+1}} \frac{d\tilde{f}}{dx}(N_k(x)q_k^+ + N_{k+1}(x)q_{k+1}^-)dx \\ &= -\hat{q}_{k+1}\tilde{f}_{k+1}^- + \hat{q}_k\tilde{f}_k^+ + \int_{x_k}^{x_{k+1}} \frac{d\tilde{f}}{dx}N_k(x)dx \cdot q_k^+ + \int_{x_k}^{x_{k+1}} \frac{d\tilde{f}}{dx}N_{k+1}(x)dx \cdot q_{k+1}^- \end{aligned} \quad (466)$$

– We take  $\tilde{f} = N_k$  and by virtue of the properties of shape functions  $N$  we have:

$$\begin{aligned} \tilde{f}_k^+ &= \tilde{f}(x_k^+) = N_k(x_k^+) = 1 \\ \tilde{f}_{k+1}^- &= \tilde{f}(x_{k+1}^-) = N_k(x_{k+1}^-) = 0 \end{aligned}$$

so that

$$\begin{aligned} 0 &= \hat{q}_k + \int_{x_k}^{x_{k+1}} \frac{dN_k}{dx}N_k(x)dx \cdot q_k^+ + \int_{x_k}^{x_{k+1}} \frac{dN_k}{dx}N_{k+1}(x)dx \cdot q_{k+1}^- \\ &= \frac{1}{2}(\textcolor{red}{q_k^+} + q_k^-) - \mathcal{E}(T_k^- - \textcolor{red}{T_k^+}) - \mathcal{C}(q_k^- - \textcolor{red}{q_k^+}) \\ &+ \int_{x_k}^{x_{k+1}} \frac{dN_k}{dx}N_kdx \cdot \textcolor{red}{q_k^+} + \int_{x_k}^{x_{k+1}} \frac{dN_k}{dx}N_{k+1}dx \cdot \textcolor{red}{q_{k+1}^-} \end{aligned} \quad (467)$$

– We take  $\tilde{f} = N_{k+1}$  and likewise:

$$\begin{aligned}\tilde{f}_k^+ &= \tilde{f}(x_k^+) = N_{k+1}(x_k^+) = 0 \\ \tilde{f}_{k+1}^- &= \tilde{f}(x_{k+1}^-) = N_{k+1}(x_{k+1}^-) = 1\end{aligned}$$

so that

$$\begin{aligned}0 &= -\hat{q}_{k+1} + \int_{x_k}^{x_{k+1}} \frac{dN_{k+1}}{dx} N_k(x) dx \cdot q_k^+ + \int_{x_k}^{x_{k+1}} \frac{dN_{k+1}}{dx} N_{k+1}(x) dx \cdot q_{k+1}^- \\ &= -\left[ \frac{1}{2}(q_{k+1}^+ + \textcolor{red}{q}_{k+1}^-) - \mathcal{E}(\textcolor{red}{T}_{k+1}^- - T_{k+1}^+) - \mathcal{C}(\textcolor{red}{q}_{k+1}^- - q_{k+1}^+) \right] \\ &\quad + \int_{x_k}^{x_{k+1}} \frac{dN_{k+1}}{dx} N_k dx \cdot \textcolor{red}{q}_k^+ + \int_{x_k}^{x_{k+1}} \frac{dN_{k+1}}{dx} N_{k+1} dx \cdot \textcolor{red}{q}_{k+1}^-\end{aligned}\tag{468}$$

and finally

$$\begin{aligned}&\int_{x_k}^{x_{k+1}} \left( \begin{array}{cc} \frac{dN_k}{dx} N_k & \frac{dN_k}{dx} N_{k+1} \\ \frac{dN_{k+1}}{dx} N_k & \frac{dN_{k+1}}{dx} N_{k+1} \end{array} \right) dx \cdot \left( \begin{array}{c} q_k^+ \\ q_{k+1}^- \end{array} \right) + \left( \begin{array}{c} (\mathcal{C} + \frac{1}{2})\textcolor{red}{q}_k^+ \\ (\mathcal{C} - \frac{1}{2})\textcolor{red}{q}_{k+1}^- \end{array} \right) + \left( \begin{array}{c} \mathcal{E}\textcolor{red}{T}_k^+ \\ \mathcal{E}\textcolor{red}{T}_{k+1}^- \end{array} \right) \\ &= \left( \begin{array}{c} (\mathcal{C} - \frac{1}{2})q_k^- \\ (\mathcal{C} + \frac{1}{2})q_{k+1}^+ \end{array} \right) + \left( \begin{array}{c} \mathcal{E}T_k^- \\ \mathcal{E}T_{k+1}^+ \end{array} \right)\end{aligned}\tag{469}$$

- Eq. 485 becomes:

$$\begin{aligned} 0 &= -[T\bar{f}]_{x_k}^{x_{k+1}} + \int_{x_k}^{x_{k+1}} q_h(x)\bar{f}(x)dx + \int_{x_k}^{x_{k+1}} \frac{d\bar{f}}{dx} T_h(x)dx \\ &= -\hat{T}_{k+1}\bar{f}_{k+1}^- + \hat{T}_k\bar{f}_k^+ + \int_{x_k}^{x_{k+1}} q_h(x)\bar{f}(x)dx + \int_{x_k}^{x_{k+1}} \frac{d\bar{f}}{dx} T_h(x)dx \end{aligned}$$

– We take  $\bar{f} = N_k$ :

$$\begin{aligned} \bar{f}_k^+ &= \bar{f}(x_k^+) = N_k(x_k^+) = 1 \\ \bar{f}_{k+1}^- &= \bar{f}(x_{k+1}^-) = N_k(x_{k+1}^-) = 0 \end{aligned}$$

so that

$$\begin{aligned} 0 &= \hat{T}_k + \int_{x_k}^{x_{k+1}} q_h(x)N_kdx + \int_{x_k}^{x_{k+1}} \frac{dN_k}{dx} T_h(x)dx \\ &= \frac{1}{2}(T_k^- + \textcolor{red}{T}_k^+) + \mathcal{C}(T_k^- - \textcolor{red}{T}_k^+) \\ &+ \int_{x_k}^{x_{k+1}} (N_k(x)\textcolor{red}{q}_k^+ + N_{k+1}(x)\textcolor{red}{q}_{k+1}^-)N_kdx + \int_{x_k}^{x_{k+1}} \frac{dN_k}{dx} (N_k(x)\textcolor{red}{T}_k^+ + N_{k+1}(x)\textcolor{red}{T}_{k+1}^-) \end{aligned} \quad (470)$$

– We take  $\bar{f} = N_{k+1}$ :

$$\begin{aligned} \bar{f}_k^+ &= \bar{f}(x_k^+) = N_{k+1}(x_k^+) = 0 \\ \bar{f}_{k+1}^- &= \bar{f}(x_{k+1}^-) = N_{k+1}(x_{k+1}^-) = 1 \end{aligned}$$

so that

$$\begin{aligned} 0 &= -\hat{T}_{k+1} + \int_{x_k}^{x_{k+1}} q_h(x)N_{k+1}dx + \int_{x_k}^{x_{k+1}} \frac{dN_{k+1}}{dx} T_h(x)dx \\ &= -\left[\frac{1}{2}(\textcolor{red}{T}_{k+1}^- + T_{k+1}^+) + \mathcal{C}(\textcolor{red}{T}_{k+1}^- - T_{k+1}^+)\right] \\ &+ \int_{x_k}^{x_{k+1}} (N_k(x)\textcolor{red}{q}_k^+ + N_{k+1}(x)\textcolor{red}{q}_{k+1}^-)N_{k+1}dx + \int_{x_k}^{x_{k+1}} \frac{dN_{k+1}}{dx} (N_k(x)\textcolor{red}{T}_k^+ + N_{k+1}(x)\textcolor{red}{T}_{k+1}^-) \end{aligned} \quad (471)$$

and finally

$$\begin{aligned} &\int_{x_k}^{x_{k+1}} \begin{pmatrix} N_k N_k & N_k N_{k+1} \\ N_{k+1} N_k & N_{k+1} N_{k+1} \end{pmatrix} dx \begin{pmatrix} \textcolor{red}{q}_k^+ \\ \textcolor{red}{q}_{k+1}^- \end{pmatrix} + \int_{x_k}^{x_{k+1}} \begin{pmatrix} \frac{dN_k}{dx} N_k & \frac{dN_k}{dx} N_{k+1} \\ \frac{dN_{k+1}}{dx} N_k & \frac{dN_{k+1}}{dx} N_{k+1} \end{pmatrix} dx \begin{pmatrix} \textcolor{red}{T}_k^+ \\ \textcolor{red}{T}_{k+1}^- \end{pmatrix} \\ &+ \begin{pmatrix} (\frac{1}{2} - \mathcal{C})\textcolor{red}{T}_k^+ \\ -(\mathcal{C} + \frac{1}{2})\textcolor{red}{T}_{k+1}^- \end{pmatrix} = \begin{pmatrix} -(\mathcal{C} + \frac{1}{2})T_k^- \\ (\frac{1}{2} - \mathcal{C})T_{k+1}^+ \end{pmatrix} \end{aligned} \quad (473)$$

We will also use the results obtained in Appendix I for 1D linear elements:

$$\mathbf{M}^e = \int_{\Omega_e} \vec{N}^T \vec{N} dV = \int_{\Omega_e} \begin{pmatrix} N_k N_k & N_k N_{k+1} \\ N_{k+1} N_k & N_{k+1} N_{k+1} \end{pmatrix} dV = \frac{h}{2} \frac{1}{3} \begin{pmatrix} 2 & 1 \\ 1 & 2 \end{pmatrix} = \frac{h}{6} \begin{pmatrix} 2 & 1 \\ 1 & 2 \end{pmatrix}$$

and also

$$\mathbf{K}^e = \int_{\Omega_e} \begin{pmatrix} \frac{dN_k}{dx} N_k & \frac{dN_k}{dx} N_{k+1} \\ \frac{dN_{k+1}}{dx} N_k & \frac{dN_{k+1}}{dx} N_{k+1} \end{pmatrix} dV = \frac{1}{2} \begin{pmatrix} -1 & -1 \\ 1 & 1 \end{pmatrix}$$

Filling this into equations (469) and (473), gives

$$\begin{aligned} \mathbf{K}^e \cdot \begin{pmatrix} q_k^+ \\ q_{k+1}^- \end{pmatrix} + \begin{pmatrix} (\mathcal{C} + \frac{1}{2})q_k^+ \\ (\mathcal{C} - \frac{1}{2})q_{k+1}^- \end{pmatrix} + \begin{pmatrix} \mathcal{E} T_k^+ \\ \mathcal{E} T_{k+1}^- \end{pmatrix} &= \begin{pmatrix} (\mathcal{C} - \frac{1}{2})q_k^- \\ (\mathcal{C} + \frac{1}{2})q_{k+1}^+ \end{pmatrix} + \begin{pmatrix} \mathcal{E} T_k^- \\ \mathcal{E} T_{k+1}^+ \end{pmatrix} \\ \mathbf{M}^e \cdot \begin{pmatrix} q_k^+ \\ q_{k+1}^- \end{pmatrix} + \mathbf{K}^e \cdot \begin{pmatrix} T_k^+ \\ T_{k+1}^- \end{pmatrix} + \begin{pmatrix} (\frac{1}{2} - \mathcal{C})T_k^+ \\ -(\mathcal{C} + \frac{1}{2})T_{k+1}^- \end{pmatrix} &= \begin{pmatrix} -(\mathcal{C} + \frac{1}{2})T_k^- \\ (\frac{1}{2} - \mathcal{C})T_{k+1}^+ \end{pmatrix} \end{aligned} \quad (474)$$

which becomes

$$\begin{aligned} \begin{pmatrix} \frac{\mathcal{C}}{2} & -\frac{1}{2} \\ -\mathcal{C} & \end{pmatrix} \begin{pmatrix} q_k^+ \\ q_{k+1}^- \end{pmatrix} + \begin{pmatrix} \mathcal{E} & 0 \\ 0 & \mathcal{E} \end{pmatrix} \begin{pmatrix} T_k^+ \\ T_{k+1}^- \end{pmatrix} &= \begin{pmatrix} (\mathcal{C} - \frac{1}{2})q_k^- + \mathcal{E} T_k^- \\ (\mathcal{C} + \frac{1}{2})q_{k+1}^+ + \mathcal{E} T_{k+1}^+ \end{pmatrix} \\ \frac{h}{6} \begin{pmatrix} 2 & 1 \\ 1 & 2 \end{pmatrix} \begin{pmatrix} q_k^+ \\ q_{k+1}^- \end{pmatrix} + \begin{pmatrix} -\mathcal{C} & -\frac{1}{2} \\ \frac{1}{2} & -\mathcal{C} \end{pmatrix} \begin{pmatrix} T_k^+ \\ T_{k+1}^- \end{pmatrix} &= \begin{pmatrix} -(\frac{1}{2} + \mathcal{C})T_k^- \\ (\frac{1}{2} - \mathcal{C})T_{k+1}^+ \end{pmatrix} \end{aligned}$$

Combining these equations gives the numerical implementation:

$$\boxed{\begin{pmatrix} \frac{h}{3} & \frac{h}{6} & -\mathcal{C} & -\frac{1}{2} \\ \frac{h}{6} & \frac{h}{3} & \frac{1}{2} & -\mathcal{C} \\ \mathcal{C} & -\frac{1}{2} & \mathcal{E} & 0 \\ \frac{1}{2} & \mathcal{C} & 0 & \mathcal{E} \end{pmatrix} \begin{pmatrix} q_k^+ \\ q_{k+1}^- \\ T_k^+ \\ T_{k+1}^- \end{pmatrix} = \begin{pmatrix} -(\frac{1}{2} + \mathcal{C})T_k^- \\ (\frac{1}{2} - \mathcal{C})T_{k+1}^+ \\ -(\frac{1}{2} - \mathcal{C})q_k^- + \mathcal{E} T_k^- \\ (\frac{1}{2} + \mathcal{C})q_{k+1}^+ + \mathcal{E} T_{k+1}^+ \end{pmatrix}} \quad (475)$$

**Left boundary** Special care must be taken for the two elements on the boundaries of the domain. On the left, we have

$$\begin{aligned} \hat{q}_1 &= q_1^+ - \mathcal{E}(T_1^- - T_1^+) \\ \hat{T}_1 &= T_1^- \end{aligned}$$

Eq. (467) becomes:

$$\begin{aligned} 0 &= \hat{q}_k + \int_{x_k}^{x_{k+1}} \frac{dN_k}{dx} N_k(x) dx \cdot q_k^+ + \int_{x_k}^{x_{k+1}} \frac{dN_k}{dx} N_{k+1}(x) dx \cdot q_{k+1}^- \\ &= q_1^+ - \mathcal{E}(T_k^- - T_1^+) + \int_{x_k}^{x_{k+1}} \frac{dN_k}{dx} N_k(x) dx \cdot q_1^+ + \int_{x_k}^{x_{k+1}} \frac{dN_k}{dx} N_{k+1}(x) dx \cdot q_2^- \end{aligned} \quad (476)$$

Eq. (470) becomes:

$$\begin{aligned} 0 &= \hat{T}_1 + \int_{x_k}^{x_{k+1}} q_h(x) N_k(x) dx + \int_{x_k}^{x_{k+1}} \frac{dN_k}{dx} T_h(x) dx \\ &= T_1^- + \int_{x_k}^{x_{k+1}} (N_k(x) q_1^+ + N_{k+1}(x) q_2^-) N_k(x) dx + \int_{x_k}^{x_{k+1}} \frac{dN_k}{dx} (N_k(x) T_1^+ + N_{k+1}(x) T_2^-) dx \end{aligned} \quad (477)$$

Eq. (475) then becomes:

$$\boxed{\begin{pmatrix} \frac{h}{3} & \frac{h}{6} & -\frac{1}{2} & -\frac{1}{2} \\ \frac{h}{6} & \frac{h}{3} & \frac{1}{2} & -\mathcal{C} \\ \frac{1}{2} & -\frac{1}{2} & \mathcal{E} & 0 \\ \frac{1}{2} & \mathcal{C} & 0 & \mathcal{E} \end{pmatrix} \begin{pmatrix} q_1^+ \\ q_2^- \\ T_1^+ \\ T_2^- \end{pmatrix} = \begin{pmatrix} -T_1^- \\ (\frac{1}{2} - \mathcal{C})T_{k+1}^+ \\ \mathcal{E} T_k^- \\ (\frac{1}{2} + \mathcal{C})q_{k+1}^+ + \mathcal{E} T_{k+1}^+ \end{pmatrix}} \quad (478)$$

**Right boundary** The element is composed of nodes  $N - 1$  and  $N$ . The fluxes are

$$\begin{aligned}\hat{q}_N &= q_N^+ - \mathcal{E}(T_N^- - T_N^+) \\ \hat{T}_N &= T_N^-\end{aligned}$$

Eq. (468) becomes:

$$\begin{aligned}0 &= -\hat{q}_N + \int_{x_k}^{x_{k+1}} \frac{dN_{k+1}}{dx} N_k(x) dx \cdot q_{N-1}^+ + \int_{x_k}^{x_{k+1}} \frac{dN_{k+1}}{dx} N_{k+1}(x) dx \cdot q_N^- \\ &= -[q_N^+ - \mathcal{E}(T_N^- - T_N^+)] + \int_{x_k}^{x_{k+1}} \frac{dN_{k+1}}{dx} N_k dx \cdot \textcolor{red}{q}_{N-1}^+ + \int_{x_k}^{x_{k+1}} \frac{dN_{k+1}}{dx} N_{k+1} dx \cdot \textcolor{red}{q}_N^-\end{aligned}\quad (479)$$

Eq. (472) becomes:

$$\begin{aligned}0 &= -\hat{T}_N + \int_{x_k}^{x_{k+1}} q_h(x) N_{k+1} dx + \int_{x_k}^{x_{k+1}} \frac{dN_{k+1}}{dx} T_h(x) dx \\ &= -T_N^- + \int_{x_k}^{x_{k+1}} (N_k(x) \textcolor{red}{q}_{N-1}^+ + N_{k+1}(x) \textcolor{red}{q}_N^-) N_{k+1} dx + \int_{x_k}^{x_{k+1}} \frac{dN_{k+1}}{dx} (N_k(x) \textcolor{red}{T}_{N-1}^+ + N_{k+1}(x) \textcolor{red}{T}_N^-) dx\end{aligned}$$

Eq. (475) then becomes:

$$\begin{pmatrix} \frac{h}{3} & \frac{h}{6} & -\mathcal{C} & -\frac{1}{2} \\ \frac{h}{6} & \frac{h}{3} & \frac{1}{2} & \frac{1}{2} \\ \mathcal{C} & -\frac{1}{2} & \mathcal{E} & 0 \\ \frac{1}{2} & -\frac{1}{2} & 0 & \mathcal{E} \end{pmatrix} \begin{pmatrix} \textcolor{red}{q}_{N-1}^+ \\ \textcolor{red}{q}_N^- \\ \textcolor{red}{T}_{N-1}^+ \\ \textcolor{red}{T}_N^- \end{pmatrix} = \begin{pmatrix} -(\frac{1}{2} + \mathcal{C}) T_{N-1}^- \\ T_N^+ \\ -(\frac{1}{2} - \mathcal{C}) q_{N-1}^- + \mathcal{E} T_{N-1}^- \\ \mathcal{E} T_N^+ \end{pmatrix}\quad (480)$$

**Solving strategies** Following Li [1596], there are three main strategies:

- Successive substitution: all the variables are initialized to zero. Eq. (478) is solved to obtain the data for the first element, where boundary conditions are specified. Then Eq. (475) is used for all interior elements. Finally Eq. (480) is used for the last element. This procedure is carried out until all fields have converged.
- Global assembly: this approach is identical to the one we have taken so far with the continuous Galerkin Finite Element method. We form a large global matrix and then solve the linear system to obtain the solution. The disadvantage of this approach lies in the size of the generated matrix: each node counts 4 dofs so the assembled matrix will be about 4 times as big as in the standard FE case.
- Elimination then assembly: one can first eliminate the variable  $q$  and solve for the temperature  $T$  only. This speeds up the calculations, but also increases the bandwidth of the element matrix. Li [1596] states: "Further comparison shows that the saving in CPU time for solving  $T$  alone is less significant than the  $q - T$  iterative solution, in particular, for 3-D problems."

Eq. (475) can be rewritten:

$$\begin{pmatrix} \mathbf{M}_e & \mathbf{C}_1 \\ \mathbf{C}_2 & \mathbf{E} \end{pmatrix} \cdot \begin{pmatrix} \vec{q} \\ \vec{T} \end{pmatrix} = \begin{pmatrix} \vec{f} \\ \vec{g} \end{pmatrix}\quad (481)$$

The unknown of the original ODE is temperature so this is the quantity we are after. The first line of the matrix can be written

$$\mathbf{M}_e \cdot \vec{q} + \mathbf{C}_1 \cdot \vec{T} = \vec{f}$$

or,

$$\vec{q} = \mathbf{M}_e^{-1} \cdot (\vec{f} - \mathbf{C}_1 \cdot \vec{T})$$

The second line of the matrix is

$$\mathbf{C}_2 \cdot \vec{q} + \mathbf{E} \cdot \vec{T} = \vec{g}$$

and we then replace  $\vec{q}$  by the expression above:

$$\mathbf{C}_2 \cdot [\mathbf{M}_e^{-1} \cdot (\vec{f} - \mathbf{C}_1 \cdot \vec{T})] + \mathbf{E} \cdot \vec{T} = \vec{g}$$

or,

$$-\mathbf{C}_2 \cdot \mathbf{M}_e^{-1} \cdot \mathbf{C}_1 \cdot \vec{T} + \mathbf{E} \cdot \vec{T} = \vec{g} - \mathbf{C}_2 \cdot \mathbf{M}_e^{-1} \cdot \vec{f}$$

and finally

$$[\mathbf{E} - \mathbf{C}_2 \cdot \mathbf{M}_e^{-1} \cdot \mathbf{C}_1] \cdot \vec{T} = \vec{g} - \mathbf{C}_2 \cdot \mathbf{M}_e^{-1} \cdot \vec{f}$$

Note that the matrix will still be twice as big than in the standard FEM case since each node counts two temperature dofs.

**Choice of  $\mathcal{C}$  and  $\mathcal{E}$**  Li [1596] shows satisfying results for  $\mathcal{E} = 4$  and  $\mathcal{C} = -1/2, 0, 1/2$  or  $\mathcal{E} = 0$  and  $\mathcal{C} = 1, 4, 10$ .

### 7.3 Time-dependent diffusion PDE in 1D

Starting from the simple transient 1-D heat conduction problem similar to the steady state heat conduction problem only with added time dependence:

$$\frac{\partial T}{\partial t} = \frac{\partial^2 T}{\partial x^2} \quad T(x=0) = 0 \quad T(x=1) = 1 \quad \text{on } x \in [0, 1] \quad (482)$$

Once again we split this system into two separate first order equations:

$$\frac{\partial T}{\partial t} - \frac{\partial q}{\partial x} = 0 \quad ; \quad \frac{\partial T}{\partial x} - q = 0 \quad (483)$$

We apply the standard approach to establish the weak forms of these two first-order PDEs, and we do so on an element  $e$  bound by nodes  $k$  and  $k+1$  with coordinates  $x_k$  and  $x_{k+1}$

$$-\int_{x_k}^{x_{k+1}} \left( \frac{\partial T}{\partial t} - \frac{\partial q}{\partial x} \right) \tilde{f}(x) dx = \int_{x_k}^{x_{k+1}} \frac{\partial T}{\partial t} \tilde{f}(x) dx - \left[ q \tilde{f} \right]_{x_k}^{x_{k+1}} + \int_{x_k}^{x_{k+1}} \frac{d\tilde{f}}{dx} q(x) dx = 0 \quad (484)$$

$$\int_{x_k}^{x_{k+1}} \left( q - \frac{dT}{dx} \right) \bar{f}(x) dx = \int_{x_k}^{x_{k+1}} q(x) \bar{f}(x) dx - \left[ T \bar{f} \right]_{x_k}^{x_{k+1}} + \int_{x_k}^{x_{k+1}} \frac{d\bar{f}}{dx} T(x) dx = 0 \quad (485)$$

where  $\tilde{f}$  and  $\bar{f}$  are test functions.

In what follows we coin  $\dot{T} = \partial T / \partial t$ . We once again recover Equations (469) and (473), although with an additional time derivative term:

Filling this into equations (469) and (473), gives

$$\begin{aligned} \mathbf{K}^e \cdot \begin{pmatrix} q_k^+ \\ q_{k+1}^- \end{pmatrix} + \mathbf{M}^e \cdot \begin{pmatrix} \dot{T}_k^+ \\ \dot{T}_{k+1}^- \end{pmatrix} + \begin{pmatrix} (\mathcal{C} + \frac{1}{2})q_k^+ \\ (\mathcal{C} - \frac{1}{2})q_{k+1}^- \end{pmatrix} + \begin{pmatrix} \mathcal{E}T_k^+ \\ \mathcal{E}T_{k+1}^- \end{pmatrix} &= \begin{pmatrix} (\mathcal{C} - \frac{1}{2})q_k^- \\ (\mathcal{C} + \frac{1}{2})q_{k+1}^+ \end{pmatrix} + \begin{pmatrix} \mathcal{E}T_k^- \\ \mathcal{E}T_{k+1}^+ \end{pmatrix} \\ \mathbf{M}^e \cdot \begin{pmatrix} q_k^+ \\ q_{k+1}^- \end{pmatrix} + \mathbf{K}^e \cdot \begin{pmatrix} \dot{T}_k^+ \\ \dot{T}_{k+1}^- \end{pmatrix} + \begin{pmatrix} (\frac{1}{2} - \mathcal{C})T_k^+ \\ -(\mathcal{C} + \frac{1}{2})T_{k+1}^- \end{pmatrix} &= \begin{pmatrix} -(\mathcal{C} + \frac{1}{2})T_k^- \\ (\frac{1}{2} - \mathcal{C})T_{k+1}^+ \end{pmatrix} \end{aligned} \quad (486)$$

In what follows we set  $\mathcal{E} = 0$  so that we have

$$\begin{aligned} \mathbf{K}^e \cdot \begin{pmatrix} q_k^+ \\ q_{k+1}^- \end{pmatrix} + \mathbf{M}^e \cdot \begin{pmatrix} \dot{T}_k^+ \\ \dot{T}_{k+1}^- \end{pmatrix} + \begin{pmatrix} (\mathcal{C} + \frac{1}{2})q_k^+ \\ (\mathcal{C} - \frac{1}{2})q_{k+1}^- \end{pmatrix} &= \begin{pmatrix} (\mathcal{C} - \frac{1}{2})q_k^- \\ (\mathcal{C} + \frac{1}{2})q_{k+1}^+ \end{pmatrix} \\ \mathbf{M}^e \cdot \begin{pmatrix} q_k^+ \\ q_{k+1}^- \end{pmatrix} + \mathbf{K}^e \cdot \begin{pmatrix} \dot{T}_k^+ \\ \dot{T}_{k+1}^- \end{pmatrix} + \begin{pmatrix} (\frac{1}{2} - \mathcal{C})T_k^+ \\ -(\mathcal{C} + \frac{1}{2})T_{k+1}^- \end{pmatrix} &= \begin{pmatrix} -(\mathcal{C} + \frac{1}{2})T_k^- \\ (\frac{1}{2} - \mathcal{C})T_{k+1}^+ \end{pmatrix} \end{aligned} \quad (487)$$

Using the expressions for  $\mathbf{M}^e$  and  $\mathbf{K}^e$  obtained in Appendix I for 1D linear elements we arrive at

$$\begin{aligned} \frac{1}{2} \begin{pmatrix} -1 & -1 \\ 1 & 1 \end{pmatrix} \cdot \begin{pmatrix} q_k^+ \\ q_{k+1}^- \end{pmatrix} + \frac{h}{6} \begin{pmatrix} 2 & 1 \\ 1 & 2 \end{pmatrix} \cdot \begin{pmatrix} \dot{T}_k^+ \\ \dot{T}_{k+1}^- \end{pmatrix} + \begin{pmatrix} (\mathcal{C} + \frac{1}{2})q_k^+ \\ (\mathcal{C} - \frac{1}{2})q_{k+1}^- \end{pmatrix} &= \begin{pmatrix} (\mathcal{C} - \frac{1}{2})q_k^- \\ (\mathcal{C} + \frac{1}{2})q_{k+1}^+ \end{pmatrix} \\ \frac{h}{6} \begin{pmatrix} 2 & 1 \\ 1 & 2 \end{pmatrix} \cdot \begin{pmatrix} q_k^+ \\ q_{k+1}^- \end{pmatrix} + \frac{1}{2} \begin{pmatrix} -1 & -1 \\ 1 & 1 \end{pmatrix} \cdot \begin{pmatrix} \dot{T}_k^+ \\ \dot{T}_{k+1}^- \end{pmatrix} + \begin{pmatrix} (\frac{1}{2} - \mathcal{C})T_k^+ \\ -(\mathcal{C} + \frac{1}{2})T_{k+1}^- \end{pmatrix} &= \begin{pmatrix} -(\mathcal{C} + \frac{1}{2})T_k^- \\ (\frac{1}{2} - \mathcal{C})T_{k+1}^+ \end{pmatrix} \end{aligned} \quad (488)$$

which simplifies to

$$\begin{aligned} \begin{pmatrix} C & -1/2 \\ 1/2 & C \end{pmatrix} \cdot \begin{pmatrix} q_k^+ \\ q_{k+1}^- \end{pmatrix} + \begin{pmatrix} h/3 & h/6 \\ h/6 & h/3 \end{pmatrix} \cdot \begin{pmatrix} \dot{T}_k^+ \\ \dot{T}_{k+1}^- \end{pmatrix} &= \begin{pmatrix} (\mathcal{C} - \frac{1}{2})q_k^- \\ (\mathcal{C} + \frac{1}{2})q_{k+1}^+ \end{pmatrix} \\ \begin{pmatrix} h/3 & h/6 \\ h/6 & h/3 \end{pmatrix} \cdot \begin{pmatrix} q_k^+ \\ q_{k+1}^- \end{pmatrix} + \begin{pmatrix} -C & -1/2 \\ 1/2 & -C \end{pmatrix} \cdot \begin{pmatrix} T_k^+ \\ T_{k+1}^- \end{pmatrix} &= \begin{pmatrix} -(\mathcal{C} + \frac{1}{2})T_k^- \\ (\frac{1}{2} - \mathcal{C})T_{k+1}^+ \end{pmatrix} \end{aligned} \quad (489)$$

or,

$$\begin{aligned} \mathbf{C}_1 \vec{q} + \mathbf{M} \vec{T} &= \vec{f} \\ \mathbf{M} \vec{q} + \mathbf{C}_2 \vec{T} &= \vec{g} \end{aligned}$$

so

$$\vec{q} = \mathbf{M}^{-1}(\vec{g} - \mathbf{C}_2 \vec{T})$$

and then

$$\mathbf{C}_1[\mathbf{M}^{-1}(\vec{g} - \mathbf{C}_2 \vec{T})] + \mathbf{M} \vec{T} = \vec{f}$$

## 7.4 Time-dependent advection PDE in 1D

Starting from the 1-D advection equation:

$$\frac{\partial T}{\partial t} + u \frac{\partial T}{\partial x} = 0 \quad (490)$$

where  $T$  is the temperature and  $u$  the velocity. As shown before we start by discretizing the domain into a collection of elements. Then the above equation can be integrated over the element which is bounded by nodes  $x_k$  and  $x_{k+1}$ .

$$\int_{x_k}^{x_{k+1}} \left( \frac{\partial T}{\partial t} + u \frac{\partial T}{\partial x} \right) \tilde{f}(x) dx = \int_{x_k}^{x_{k+1}} \tilde{f}(x) \frac{\partial T}{\partial t} dx + \left[ uT \tilde{f} \right]_{x_k}^{x_{k+1}} - \int_{x_k}^{x_{k+1}} \frac{\partial \tilde{f}}{\partial x} uT dx = 0$$

with the test function  $\tilde{f}$ . Inside the elements the test functions are defined by well defined polynomials. We once again define

$$\begin{aligned} \tilde{f}_k^+ &= \tilde{f}(x_k^+) & \tilde{f}_{k+1}^- &= \tilde{f}(x_{k+1}^-) \\ \int_{x_k}^{x_{k+1}} \left( \tilde{f}(x) \frac{\partial T_h}{\partial t} - \frac{\partial \tilde{f}}{\partial x} uT_h \right) dx + \tilde{f}(x_{k+1}) \widehat{uT}(T_{k+1}^-, T_{k+1}^+) - \tilde{f}(x_k) \widehat{uT}(T_k^-, T_k^+) &= 0 \end{aligned} \quad (491)$$

For a constant  $u$  or a linear problem, an effective numerical flux is the Lax-Friedrichs flux:

$$\widehat{uT}(a, b) = u \frac{(a+b)}{2} - |u| \frac{(b-a)}{2} \quad (492)$$

when  $u > 0$  this flux then simply becomes:

$$uT(a, b) = ua \quad (493)$$

which is in essence an upwinding scheme. Filling this into equation 491 gives:

$$\int_{x_k}^{x_{k+1}} \left( \tilde{f}(x) \frac{\partial T_h}{\partial t} - \frac{\partial \tilde{f}}{\partial x} uT_h \right) dx + \tilde{f}_{k+1}^- uT_{k+1}^- - \tilde{f}_k^- uT_k^- = 0 \quad (494)$$

The function  $T_h$  inside the element can be approximated as follows:

$$T_h(x) = \sum_{i=1}^m N_i(x) T_i = N_k(x) \textcolor{red}{T}_k^+ + N_{k+1}(x) \textcolor{red}{T}_{k+1}^- \quad (495)$$

In what follows we coin  $\dot{T} = \partial T / \partial t$  so

$$\dot{T}_h(x) = \sum_{i=1}^m N_i(x) \dot{T}_i = N_k(x) \textcolor{red}{\dot{T}}_k^+ + N_{k+1}(x) \textcolor{red}{\dot{T}}_{k+1}^- \quad (496)$$

Taking  $\tilde{f}(x) = N_k(x)$  and then  $\tilde{f}(x) = N_{k+1}(x)$  we arrive at

$$\int_{x_k}^{x_{k+1}} \left( N_k(x) \dot{T}_h - \frac{\partial N_k}{\partial x} uT_h \right) dx + \underbrace{N_k(x_{k+1}^-) u \textcolor{red}{T}_{k+1}^-}_{=0} - \underbrace{N_k(x_k^-) uT_k^-}_{=1} = 0 \quad (497)$$

$$\int_{x_k}^{x_{k+1}} \left( N_{k+1}(x) \dot{T}_h - \frac{\partial N_{k+1}}{\partial x} uT_h \right) dx + \underbrace{N_{k+1}(x_{k+1}^-) u \textcolor{red}{T}_{k+1}^-}_{1} - \underbrace{N_{k+1}(x_k^-) uT_k^-}_{=0} = 0 \quad (498)$$

i.e.

$$\int_{x_k}^{x_{k+1}} \left( N_k(x) \dot{T}_h - \frac{\partial N_k}{\partial x} uT_h \right) dx - uT_k^- = 0 \quad (499)$$

$$\int_{x_k}^{x_{k+1}} \left( N_{k+1}(x) \dot{T}_h - \frac{\partial N_{k+1}}{\partial x} uT_h \right) dx + u \textcolor{red}{T}_{k+1}^- = 0 \quad (500)$$

We now use Eqs. (495) and (496)

$$\int_{x_k}^{x_{k+1}} \left( N_k [N_k \dot{T}_k^+ + N_{k+1} \dot{T}_{k+1}^-] - \frac{\partial N_k}{\partial x} u [N_k T_k^+ + N_{k+1} T_{k+1}^-] \right) dx - u T_k^- = 0 \quad (501)$$

$$\int_{x_k}^{x_{k+1}} \left( N_{k+1} [N_k \dot{T}_k^+ + N_{k+1} \dot{T}_{k+1}^-] - \frac{\partial N_{k+1}}{\partial x} u [N_k T_k^+ + N_{k+1} T_{k+1}^-] \right) dx + u T_{k+1}^- = 0 \quad (502)$$

Defining again (see Appendix I)

$$\mathbf{M}_e = \int_{x_k}^{x_{k+1}} \begin{pmatrix} N_k N_k & N_k N_{k+1} \\ N_{k+1} N_k & N_{k+1} N_{k+1} \end{pmatrix} dx = \frac{h}{6} \begin{pmatrix} 2 & 1 \\ 1 & 2 \end{pmatrix}$$

and

$$\mathbf{K}^e = \int_{\Omega_e} \begin{pmatrix} \frac{dN_k}{dx} N_k & \frac{dN_k}{dx} N_{k+1} \\ \frac{dN_{k+1}}{dx} N_k & \frac{dN_{k+1}}{dx} N_{k+1} \end{pmatrix} dV = \frac{1}{2} \begin{pmatrix} -1 & -1 \\ 1 & 1 \end{pmatrix}$$

This results in:

$$\mathbf{M}_e \cdot \begin{pmatrix} \dot{T}_k^+ \\ \dot{T}_{k+1}^- \end{pmatrix} - u \mathbf{K}_e \cdot \begin{pmatrix} T_k^+ \\ T_{k+1}^- \end{pmatrix} + u \begin{pmatrix} 0 & 0 \\ 0 & 1 \end{pmatrix} \cdot \begin{pmatrix} 0 \\ T_{k+1}^- \end{pmatrix} - \begin{pmatrix} u T_k^- \\ 0 \end{pmatrix} = 0 \quad (503)$$

or,

$$\mathbf{M}_e \cdot \begin{pmatrix} \dot{T}_k^+ \\ \dot{T}_{k+1}^- \end{pmatrix} = u \left[ \mathbf{K}_e - \begin{pmatrix} 0 & 0 \\ 0 & 1 \end{pmatrix} \right] \cdot \begin{pmatrix} T_k^+ \\ T_{k+1}^- \end{pmatrix} + u \begin{pmatrix} T_k^- \\ 0 \end{pmatrix} \quad (504)$$

$$\mathbf{M}_e \cdot \begin{pmatrix} \dot{T}_k^+ \\ \dot{T}_{k+1}^- \end{pmatrix} = u \frac{1}{2} \begin{pmatrix} -1 & -1 \\ 1 & -1 \end{pmatrix} \cdot \begin{pmatrix} T_k^+ \\ T_{k+1}^- \end{pmatrix} + u \begin{pmatrix} T_k^- \\ 0 \end{pmatrix} \quad (505)$$

$$\begin{pmatrix} \dot{T}_k^+ \\ \dot{T}_{k+1}^- \end{pmatrix} = u \mathbf{M}_e^{-1} \cdot \frac{1}{2} \begin{pmatrix} -1 & -1 \\ 1 & -1 \end{pmatrix} \cdot \begin{pmatrix} T_k^+ \\ T_{k+1}^- \end{pmatrix} + u \mathbf{M}_e^{-1} \cdot \begin{pmatrix} T_k^- \\ 0 \end{pmatrix} \quad (506)$$

We have already established that

$$\mathbf{M}_e^{-1} = \frac{2}{h} \begin{pmatrix} 2 & -1 \\ -1 & 2 \end{pmatrix}$$

so

$$\boxed{\begin{pmatrix} \dot{T}_k^+ \\ \dot{T}_{k+1}^- \end{pmatrix} = \frac{u}{h} \begin{pmatrix} -3 & -1 \\ 3 & -1 \end{pmatrix} \begin{pmatrix} T_k^+ \\ T_{k+1}^- \end{pmatrix} + \frac{u}{h} \begin{pmatrix} 4 \\ -2 \end{pmatrix} T_k^-} \quad (507)$$

Using the same first order Runge-Kutta method as in the previous section,

$$T^k(t + \delta t) = T_k(t) + \delta t \dot{T}_k \quad (508)$$

we multiply the equation by  $\delta t$  and we obtain

$$\begin{pmatrix} \frac{T_k^+(t + \delta t)}{T_{k+1}^-(t + \delta t)} \\ \frac{T_{k+1}^-(t + \delta t)}{T_{k+1}^-(t)} \end{pmatrix} = \begin{pmatrix} \frac{T_k^+(t)}{T_{k+1}^-(t)} \\ \frac{T_{k+1}^-(t)}{T_{k+1}^-(t)} \end{pmatrix} + \frac{u \delta t}{h} \begin{pmatrix} -3 & -1 \\ 3 & -1 \end{pmatrix} \begin{pmatrix} \frac{T_k^+(t)}{T_{k+1}^-(t)} \\ \frac{T_{k+1}^-(t)}{T_{k+1}^-(t)} \end{pmatrix} + \frac{u \delta t}{h} \begin{pmatrix} 4 \\ -2 \end{pmatrix} T_k^-(t + \delta t) \quad (509)$$

and finally

$$\boxed{\begin{pmatrix} \frac{T_k^+(t + \delta t)}{T_{k+1}^-(t + \delta t)} \\ \frac{T_{k+1}^-(t + \delta t)}{T_{k+1}^-(t)} \end{pmatrix} = \left[ \mathbf{1} + \frac{u \delta t}{h} \begin{pmatrix} -3 & -1 \\ 3 & -1 \end{pmatrix} \right] \cdot \begin{pmatrix} \frac{T_k^+(t)}{T_{k+1}^-(t)} \\ \frac{T_{k+1}^-(t)}{T_{k+1}^-(t)} \end{pmatrix} + \frac{u \delta t}{h} \begin{pmatrix} 4 \\ -2 \end{pmatrix} T_k^-(t + \delta t)} \quad (510)$$

This problem can be solved starting from the left boundary and sweeping through all the elements. The updated values of adjacent elements are used in the calculation of the next element as soon as this element becomes available which is why the last term  $T_k^-$  is taken at  $t + \delta t$ .

## 7.5 Steady-state diffusion in 2D

We start from the steady state (no advection) energy equation:

$$\vec{\nabla} \cdot (k \vec{\nabla} T) + Q = 0$$

where  $Q$  is a source term. As we did in 1D we transform this equation by reintroducing the heat flux <sup>34</sup>  $\vec{q}$

$$\vec{q} = -k \vec{\nabla} T \quad (511)$$

$$\vec{\nabla} \cdot \vec{q} = Q \quad (512)$$

We then multiply these two equations with the test functions  $\vec{N}_q$  (this one is vector valued) and  $N_T$  respectively and integrate over the element  $e$  under consideration:

$$\int_{\Omega_e} \vec{N}_q \cdot \vec{q} dV = - \int_{\Omega_e} \vec{N}_q \cdot k \vec{\nabla} T dV \quad (513)$$

$$\int_{\Omega_e} N_T \vec{\nabla} \cdot \vec{q} dV = \int_{\Omega_e} N_T Q dV \quad (514)$$

We then use integration by parts to make fluxes appear (and assume  $k$  is constant within the element). We have

$$\int_{\Omega_e} \vec{N}_q \cdot k \vec{\nabla} T dV = \int_{\Gamma_e} kT \vec{N}_q \cdot \vec{n} dS - \int_{\Omega_e} kT \vec{\nabla} \cdot \vec{N}_q dV \quad (515)$$

$$\int_{\Omega_e} N_T \vec{\nabla} \cdot \vec{q} dV = \int_{\Gamma_e} N_T \vec{q} \cdot \vec{n} dS - \int_{\Omega_e} \vec{\nabla} N_T \cdot \vec{q} dV \quad (516)$$

We then finally obtain the weak forms that are to be discretised:

$$\int_{\Omega_e} \vec{N}_q \cdot \vec{q} dV = - \int_{\Gamma_e} kT \vec{N}_q \cdot \vec{n} dS + \int_{\Omega_e} kT \vec{\nabla} \cdot \vec{N}_q dV \quad (517)$$

$$\int_{\Gamma_e} N_T \vec{q} \cdot \vec{n} dS - \int_{\Omega_e} \vec{\nabla} N_T \cdot \vec{q} dV = \int_{\Omega_e} N_T Q dV \quad (518)$$

We seek to approximate the exact solution  $(\vec{q}, T)$  with functions  $(\vec{q}_h, T_h)$  inside the element so we now have

$$\int_{\Omega_e} \vec{N}_q \cdot \vec{q}_h dV = - \int_{\Gamma_e} k \hat{T}_h \vec{N}_q \cdot \vec{n} dS + \int_{\Omega_e} kT_h \vec{\nabla} \cdot \vec{N}_q dV \quad (519)$$

$$\int_{\Gamma_e} N_T \hat{q}_h \cdot \vec{n} dS - \int_{\Omega_e} \vec{\nabla} N_T \cdot \vec{q}_h dV = \int_{\Omega_e} N_T Q dV \quad (520)$$

where the numerical fluxes are the approximations to  $(\vec{q}, T)$  on the boundary of element  $e$ . As before we must now specify these fluxes inside the domain and also on the boundaries. These can obviously not be chosen at will since they must at least render the discontinuous formulation stable.

The following table is taken from Li [1596] and lists the numerical fluxes that are considered consistent and stable for the solution of the steady state heat conduction problems [53, 424]:

Method	$\hat{q}_h$	$\hat{T}_h$
LDG [533]	$\{\vec{q}_h\}$	
DG [424]		
Brezzi et al (2000) [287]		
IP [717]		
Bassi-Rebay [98]		
NIPG [2167]		

<sup>34</sup>[https://en.wikipedia.org/wiki/Thermal\\_conduction](https://en.wikipedia.org/wiki/Thermal_conduction)

where the  $C$  coefficients are matrices ?!

I NEED a DRAWING HERE

The average operator and jump operators in the table are defined as follows: let  $\Gamma_{12}$  be an interior edge shared by elements 1 and 2 and let us define the unit normal vectors  $\vec{n}_1$  and  $\vec{n}_2$  on  $\Gamma_{12}$  pointing exterior to element 1 and 2, respectively.

In what follows we adopt the 'DG' formulation (which seems to be the most versatile one since its fluxes can be modified by zeroing some coefficients to obtain other formulations) so that:

$$\int_{\Omega_e} \vec{N}_q \cdot \vec{q}_h dV = - \int_{\Gamma_e} k \llbracket \vec{N}_q \cdot \vec{n} \rrbracket dS + \int_{\Omega_e} k T_h \vec{\nabla} \cdot \vec{N}_q dV \quad (521)$$

$$\int_{\Gamma_e} N_T \llbracket \vec{n} \rrbracket \cdot \vec{n} dS - \int_{\Omega_e} \vec{\nabla} N_T \cdot \vec{q}_h dV = \int_{\Omega_e} N_T Q dV \quad (522)$$

$$\{\vec{q}\} = \frac{1}{2}(\vec{q}_1 + \vec{q}_2) \quad (523)$$

$$\llbracket \vec{q} \rrbracket = \vec{q}_1 \cdot \vec{n}_1 + \vec{q}_2 \cdot \vec{n}_2 \quad (524)$$

$$\{T\} = \frac{1}{2}(T_1 + T_2) \quad (525)$$

$$\llbracket T \rrbracket = T_1 \cdot \vec{n}_1 + T_2 \cdot \vec{n}_2 \quad (526)$$

Note that the jump  $\llbracket \vec{q} \rrbracket$  is a scalar while  $\llbracket T \rrbracket$  is actually a vector.

Inside the element the functions  $T_h$  and  $\vec{q}_h$  are represented by means of the shape functions such that

$$T_h(\vec{r}) = \sum_{k=1}^m N_k(\vec{r}) T_k = \vec{N} \cdot \vec{T}$$

$$\vec{q}_x|_h(\vec{r}) = \sum_{k=1}^m N_k(\vec{r}) q_x|k = \vec{N} \cdot \vec{q}_x$$

$$\vec{q}_y|_h(\vec{r}) = \sum_{k=1}^m N_k(\vec{r}) q_y|k = \vec{N} \cdot \vec{q}_y$$

## 7.6 Time-dependent diffusion PDE in 2D

## 7.7 Stokes equations

Let us start with the dimensionless Stokes system [529]:

$$-\eta \Delta \vec{v} + \vec{\nabla} p = \vec{f} \quad \text{in } \Omega \quad (527)$$

$$\vec{\nabla} \cdot \vec{v} = 0 \quad \text{in } \Omega \quad (528)$$

$$\vec{v} = \vec{v}_D \quad \text{on } \Gamma \quad (529)$$

where  $\Omega$  is a bounded domain of  $\mathbb{R}^d$  and the Dirichlet boundary conditions are such that they satisfy the compatibility condition

$$\int_{\Gamma} \vec{v}_D \cdot \vec{n} = 0$$

where  $\vec{n}$  is the outward unit normal.

In order to obtain the LDG methods we first rewrite this system as the following collection of conservation laws [529]:

$$\mathbf{L} = \vec{\nabla} \vec{v} \quad \text{in } \Omega \quad (530)$$

$$\vec{\nabla} \cdot (-2\eta \mathbf{L} + p \mathbf{1}) = \vec{f} \quad \text{in } \Omega \quad (531)$$

$$\vec{\nabla} \cdot \vec{v} = 0 \quad \text{in } \Omega \quad (532)$$

$$\vec{v} = \vec{v}_D \quad \text{on } \Gamma \quad (533)$$

supplemented by

$$\int_{\Omega} p = 0$$

**Remark.** It may appear counter-intuitive at first to define  $\mathbf{L}$  as being the gradient of the velocity instead of the strain rate tensor but under the assumption of incompressibility  $\partial_x u + \partial_y v = 0$  (and constant viscosity) we can write:

$$\vec{\nabla} \cdot (2\eta \mathbf{L}) = 2\eta \begin{pmatrix} \partial_x^2 u + \frac{1}{2} \partial_x \partial_y v + \frac{1}{2} \partial_y^2 u \\ \frac{1}{2} \partial_x^2 v + \frac{1}{2} \partial_y \partial_x u + \partial_y^2 v \end{pmatrix} = 2\eta \begin{pmatrix} \partial_x^2 u + \frac{1}{2} \partial_x (-\partial_x u) + \frac{1}{2} \partial_y^2 u \\ \frac{1}{2} \partial_x^2 v + \frac{1}{2} \partial_y (-\partial_y v) + \partial_y^2 v \end{pmatrix} = \eta \begin{pmatrix} \partial_x^2 u + \partial_y^2 u \\ \partial_x^2 v + \partial_y^2 v \end{pmatrix} = \eta \Delta \vec{v}$$

RETYPE section 2.1 of [529]

## **8 Additional techniques, features, measurements**

Solving the Stokes equations and the energy equations is one thing. Doing it in a geodynamical context requires a lot of additional techniques.

## 8.1 Dealing with a free surface (and mesh deformation)

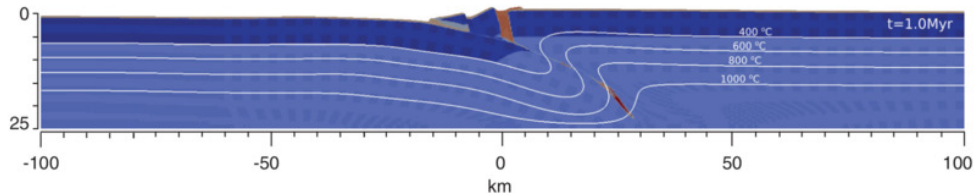
When carrying out global models, typically mantle convection, the effect of the free surface is often neglected/negligible: topography ranges from  $\sim 10\text{km}$  depth to  $\sim 10\text{km}$  height, which is very small compared to the depth of the mantle ( $\sim 3000\text{km}$ ).

However, it has long been recognised that there is a feedback between topography and crust/lithosphere deformation: the surface of the Earth reflects the deeper processes, from orogeny, back-arc basins, rifts, mid-ocean ridges, etc ... (see for instance [274]).

**Remark.** Free surface flows are not unique to Earth sciences, and their modelling has given rise to many studies and textbooks. A typical free-surface flow problem in the CFD literature is the so-called 'dam break' problem [1812, 86, 1623, 1551, 1211, 34]. Other occurrences involve sea waves, flow over structures, flow around ships, mould filling, flow with bubbles [1623].

What distinguishes geodynamics free surface modelling from its engineering counterpart is (i) the absence of surface tension, (ii) the fact that the fluids under consideration are Stokesian, (iii) their rheology is complex (the elastic and plastic components can be dominant at the surface).

The problem of dealing with a free surface can be deceptively simple at first glance: as mentioned before the amplitude of surface movement is often less than 1% of the domain size. Isostacy-driven movements are easy to deal with since the movement is vertical (and often characterised by long wavelength). However, computational problems quickly arise in subduction modelling: the downgoing lithosphere subducts below the overriding plate and the relative convergence of the two is likely to generate a cusp at the trench. The presence of shear bands intersecting the surface accentuates the problem:

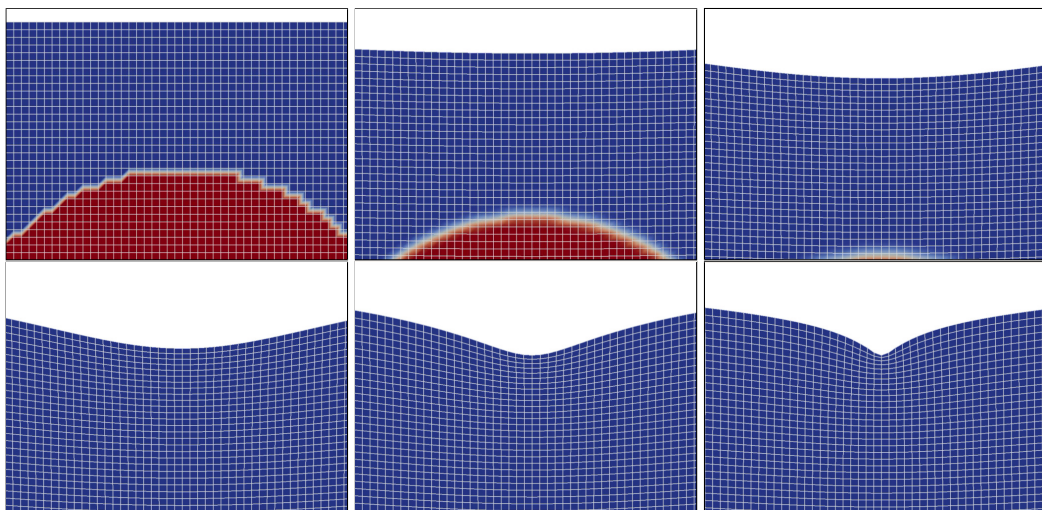


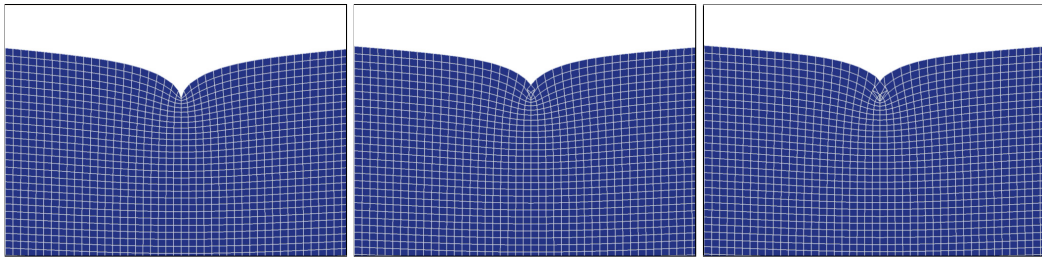
Taken from Maffione et al [1683]. Example of free surface deformation above intra-oceanic subduction initiation

**Remark.** It is difficult to talk about free surface without including the underlying mesh. What follows should be read alongside Section 8.10.

### 8.1.1 The fully Lagrangian approach

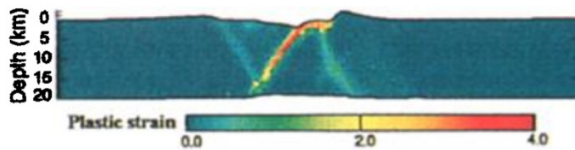
In this case the mesh is deformed with the velocity (or displacement) computed on its nodes. It is sometimes called 'body fitting' [585] or 'boundary fitted'. In the case when large deformation occurs (which is rather frequent in geodynamics - think about subduction or rifting processes where materials end up moving 100's or 1000's of km, horizontally and/or vertically), it leads to highly deformed elements, and in some cases even bow-tied:



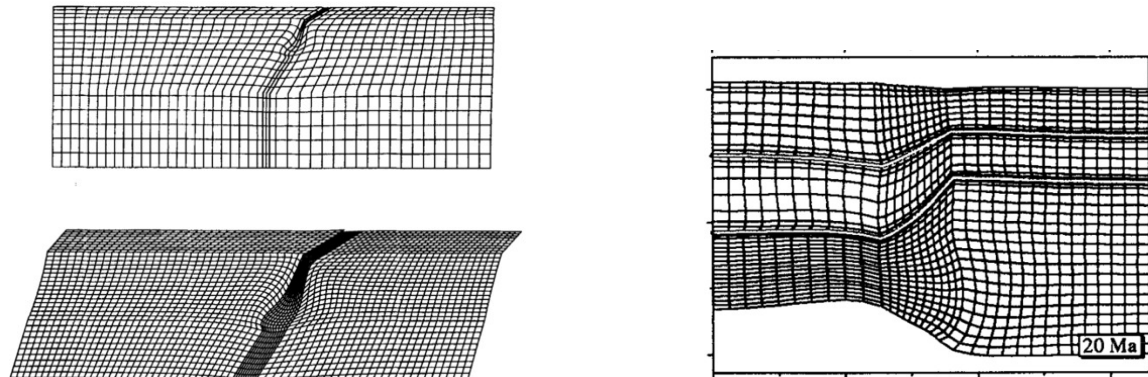


Example of a free surface evolution above a sinking sphere. The isostatic rebound above the sphere generates a cusp which, if no special measure is taken, ultimately leads to a bow-tied element. Once this occurs the simulation stops since the mapping of the bow-tied element to the reference element yields to wrong elemental matrix. Courtesy of M. Fraters

In the mildest cases this does not occur but it has long been established that large mesh deformation yields low accuracy calculations, especially when angles between edges become small or large. One way to overcome this problem is to remesh, i.e. generate a better mesh based on the available information on the deformed one. In 2D this is routinely done, especially when triangular elements are used. In 3D, multiple remeshing are very costly and it is generally avoided. Note also that re-meshing often involves some form of interpolation and therefore some unwanted numerical diffusion. When deformation is reasonably small, fully lagrangian methods work and have been used in geodynamics [1157, 1773, 1537].



Taken from [1537]. Upper-crustal faulting, note that the bottom and the top surface are deformed.



Taken from [1101]. Subduction model, topographic expression is shown without vertical exaggeration.

GET: Crook et al. 2006, and references therein [595]) Beaumont et al. 1994; [119]

### 8.1.2 The Eulerian approach: using sticky air

Sticky air is the default option for numerical methods which mesh cannot be deformed (typically the finite difference method). In this case, the air above the crust/sediments is modelled as a zero-density fluid with very low viscosity (see for instance the early article by Zaleski and Julien [2869]). One problem quickly arises when one realises that the viscosity of the air ( $\sim 18.5 \cdot 10^{-6}$  Pa·s<sup>35</sup>) is almost 25-30 orders of magnitude lower than the (effective) viscosity of Earth materials. Real air viscosity cannot therefore be used because of 1) round-off errors, 2) extremely poorly-conditioned matrices. Low viscosities around  $10^{16} - 10^{19}$  Pa·s are then commonly used as they are still negligible next to those of the (plastic) crust, and the flow of air parallel to Earth materials only generates extremely small shear and normal stress values (thereby approaching the true nature of a free surface). This approach is the one employed in all

<sup>35</sup><https://en.wikipedia.org/wiki/Viscosity>

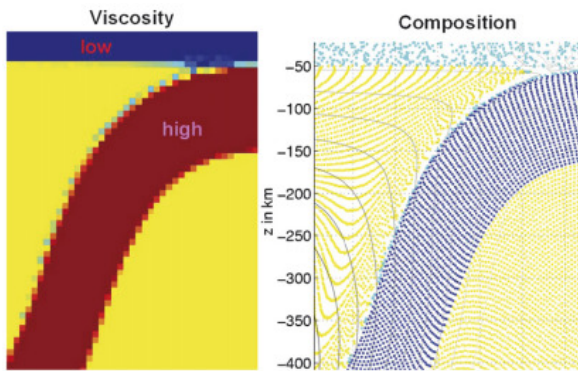
the papers based on the I2/I3(EL)VIS code (see Appendix B) and has been benchmarked in Crameri et al. [585].

This approach has a few advantages:

1. it is simple to implement
2. it is compatible with all the standard numerical methods (FEM, FDM,FVM)
3. it avoids (potentially complicated) remeshing

and quite a few drawbacks:

1. it increases the size of the computational domain, thereby adding more unknowns to the linear system: in [2272] the air layer is set to 50km while the lithospheric domain underneath is 700km thick;
2. it requires the use of averaging all along the free-surface where very large viscosity contrasts are present. Here is what Poliakov and Podlachikov [2046] say about the sticky air method: "Zaleski & Julien [2869] used a top layer with a very low viscosity and density to represent air or water above the surface. This allows a simple representation of the free surface. However, due to the very high viscosity and density contrast and diffusion between the top layer and the underlying layers, calculations sometimes become unstable and give significant errors."
3. it can showcase air entrainment:



Taken from [2272]. Details of the entrainment and lubrication of the soft surface layer. Light blue particles are sticky air particle and are found to greatly alter the viscosity of the subduction channel.

4. it is not clear how thick the air layer must be
5. it often requires to ascribe thermal parameters to the air;
6. it makes the implementation of Dirichlet or Neuman boundary conditions for temperature at the surface less obvious.
7. it makes the coupling with surface processes codes less straightforward.
8. its accuracy depends on the method used to track materials in the rest of the code (markers, level sets, ...). If markers are used, the free surface position is then known up to the average distance between markers.
9. it negatively impacts the condition number of the matrix.

The sticky air approach is employed by various codes in the subduction benchmark study [2272]

The term 'sticky water' is sometimes employed too. The dynamic viscosity of water is about  $10^{-3}$ Pa·s so that it is also negligible compared to the viscosity of Earth materials and the same reasoning as air applies. However, in such a case a density of about  $1000\text{kg/m}^3$  is then assigned to the layer. REF?

In conclusion, as stated in [585]: "the sticky air method is a good way to simulate a free surface for Eulerian approaches, provided that its parameters are chosen carefully."

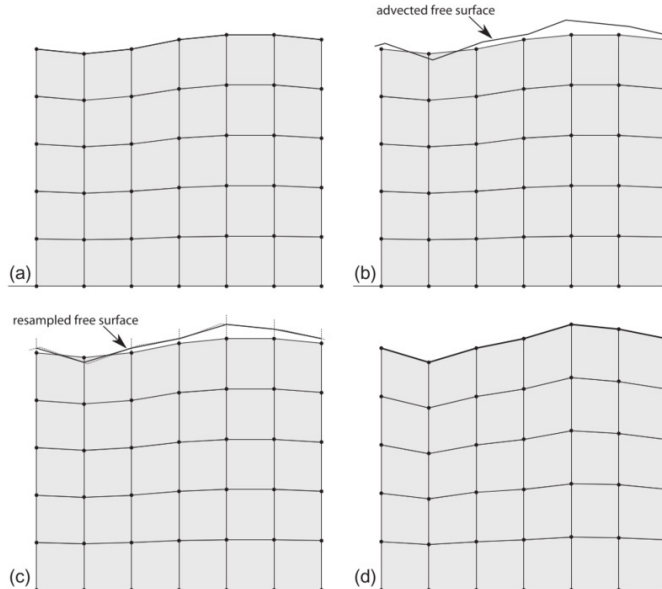
### 8.1.3 The Arbitrary Lagrangian Eulerian (ALE) approach

It is a very widely used approach in FEM-based geodynamics codes but originates in the field of CFD [1201, 1248] and is described at length in [2387, 710, 711]. To put it very simply, the key idea in the ALE formulation is the introduction of a computational mesh which can move and deform with a velocity independent of the velocity carried by the material particles.

**The simple approach in [2528].** What follows is written with a 2D Cartesian model in mind ( $Q_1 \times P_0$  elements are used). The computational domain is a rectangle of size  $L_x \times L_y$  and a  $n_{nx} \times n_{ny}$  rectangular grid spanning the simulation domain is generated. The grid points constituting the top row of the grid define the discrete free surface of the domain. Once the Eulerian velocity field has been computed on these, their position is first updated using a simple Eulerian advection step (see a,b on figure hereunder):

$$\vec{r}_i(t + \delta t) = \vec{r}_i(t) + \vec{v}_i \cdot \delta t \quad i = 1, \dots, n_{nx}$$

The other boundaries of the system remain fixed at locations  $x = 0$ ,  $x = L_x$  and  $y = 0$ . Even though the Eulerian grid must conform to the current domain shape, only vertical motion of grid nodes is allowed. It is therefore necessary to resample the predicted free surface given by  $\vec{r}_i$  at equidistant positions between  $x = 0$  and  $x = L_x$ . The resampling is carried out either with Spline functions or a moving least square algorithm. Finally, the vertical position of all the nodes corresponding to column  $i \in [1, n_{nx}]$  is recalculated so that they are equidistant, as sketched in Figure d. This has the advantage of keeping the mesh distortion to a minimum in the case of large deformation.



The ALE algorithm of [2528] in 2D. (a) Grid and free surface at a given time  $t$ ; (b) advection of the free surface; (c) resampling of the free surface at equidistant abscissae; (d) vertical adjustment of grid nodes in each column at equidistant ordinates.

The ALE method is used in the SOPALE, SULEC, FANTOM, ELEFANT, and ASPECT codes to name a few (see Appendix B).

**The not-so-simple but rather elegant approach of ASPECT** What follows is mostly borrowed from Rose et al [2197]. Their approach has the advantage that it does not presuppose a geometry (Cartesian, Spherical, ...) nor a number of dimensions. It is also designed to work in parallel and on octree-based meshes, and with various combinations of boundary conditions. Note that the authors specify that "for moderate mesh deformation, the mesh stays smooth and well conditioned, though it breaks down for large deformations".

This approach is obtained by simply imposing the obvious condition that no particle (fluid parcel) can cross the free surface (because it is a material surface). This can be imposed in a straightforward

manner by using a Lagrangian description along this surface. However, this condition may be relaxed by imposing only the necessary condition:  $\vec{v}$  equal to zero along the normal to the boundary (ie.  $\vec{n} \cdot \vec{v} = 0$ , where  $\vec{n}$  is the outward unit normal to the fluid domain). The mesh position, normal to the free surface, is determined from the normal component of the particle velocity and remeshing can be performed along the tangent; see, for instance Huerta and Liu, 1989 [1244] or Braess and Wriggers, 2000 [255]

As mentioned above the mesh velocity in normal direction at the free surface (with unit normal  $\vec{n}$ ) has to be consistent with the velocity of the Stokes velocity solution  $\vec{v}(t)$ :

$$\vec{v}_{\text{mesh}}(t) \cdot \vec{n} = \vec{v}(t) \cdot \vec{n} \quad \text{on } \Gamma_F \quad (534)$$

In ALE calculations the internal mesh velocity is usually undetermined, but one wants to smoothly deform the mesh so as to preserve its regularity, avoiding inverted or otherwise poorly conditioned cells. The mesh deformation can be calculated in many different ways, including algebraic (as mentioned in the previous paragraph) and PDE based approaches. The latter is chosen here. The Laplace equation is solved where the unknown is the mesh velocity, i.e. one must solve:

$$\Delta \vec{v}_{\text{mesh}} = 0 \quad (535)$$

subjected to the following boundary conditions:

$$\vec{v}_{\text{mesh}} = \vec{0} \quad \text{on } \Gamma_0 \quad (536)$$

$$\vec{v}_{\text{mesh}} = (\vec{v} \cdot \vec{n})\vec{n} \quad \text{on } \Gamma_F \quad (537)$$

$$\vec{v}_{\text{mesh}} \cdot \vec{n} = 0 \quad \text{on } \Gamma_{FS} \quad (538)$$

where  $\Gamma_{FS}$  is the part of the boundary with free slip boundary conditions,  $\Gamma_0$  is the no-slip part and  $\Gamma_{FS}$  is the free slip part.

Once the mesh velocity has been obtained for all mesh points, these can be moved with said velocity. However, it must be noted that the multiple occurrences of the normal vector in the above equations is not without problem as the normal vectors are not well defined on the mesh vertices, which is where the mesh velocity is defined.

This yields what the author coin the 'quasi-implicit' scheme (we have so far neglected any kind of stabilisation):

1. Solve the Stokes system;
2. Solve for the surface mesh velocity using Equation 539;
3. Solve for the internal mesh velocity using Equations 535, 538;
4. Advect the mesh forward in time using displacements determined by the forward Euler scheme:  
 $\vec{x}(t^{n+1}) = \vec{x}(t^n) + \vec{v}_{\text{mesh}}\delta t$ .

Note that Rose et al (2017) [2197] go further than this, propose a 'nonstandard finite difference scheme' and make a link with the stabilisation presented in Kaus et al (2010) [1398].

The authors list two simple methods of computing the normals:

- one can take  $\vec{n}$  as the direction of the local vertical,
- one could compute  $\vec{n}$  as some weighted average of the cell normals adjacent to a given vertex

but conclude that they have found that these schemes do not necessarily have good mass conservation properties.

A better approach is proposed in the form of an  $L_2$  projection of the normal velocity  $\vec{v} \cdot \vec{n}$  onto the free surface  $\Gamma_F$ . Multiplying the boundary conditions

$$\vec{v}_{\text{mesh}} = (\vec{v} \cdot \vec{n})\vec{n}$$

by a test function  $\vec{w}$  and integrating over the free surface part of the boundary, we find:

$$\int_{\Gamma_F} \vec{w} \cdot \vec{v}_{\text{mesh}} d\Gamma = \int_{\Gamma_F} \vec{w} \cdot (\vec{v} \cdot \vec{n})\vec{n} d\Gamma = \int_{\Gamma_F} (\vec{w} \cdot \vec{n})(\vec{v} \cdot \vec{n}) d\Gamma \quad (539)$$

When discretized, this forms a linear system which can be solved for the mesh velocity  $\vec{v}_{\text{mesh}}$  at the free surface. This system, being nonzero over only the free surface, is relatively computationally inexpensive to solve. The authors unfortunately fail to mention that this approach is particularly interesting since the numerical quadrature used to compute the above integrals require the normal  $\vec{n}$  between the nodes and these normals are well defined over each segment joining two nodes!<sup>36</sup>

In what follows I present in some detail how to carry out the  $L_2$  projection to arrive at the surface velocity for both  $Q_1$  and  $Q_2$  elements.

I start from the following integral over a  $Q_1$  element:

$$\int_{\Gamma_e} N_i \vec{v}_{\text{mesh}} d\Gamma = \int N_i \begin{pmatrix} u_{\text{mesh}} \\ v_{\text{mesh}} \end{pmatrix} d\Gamma \quad (540)$$

$$= \int N_i \begin{pmatrix} N_1 & 0 & N_2 & 0 \\ 0 & N_1 & 0 & N_2 \end{pmatrix} \cdot \begin{pmatrix} u_1 \\ v_1 \\ u_2 \\ v_2 \end{pmatrix} d\Gamma \quad (541)$$

(542)

Writing this equation alternatively for  $N_i = N_1, N_2$  yields:

$$\int_{\Gamma_e} \begin{pmatrix} N_1 N_1 & 0 & N_1 N_2 & 0 \\ 0 & N_1 N_1 & 0 & N_1 N_2 \\ N_2 N_1 & 0 & N_2 N_2 & 0 \\ 0 & N_2 N_1 & 0 & N_2 N_2 \end{pmatrix} \cdot \begin{pmatrix} u_1 \\ v_1 \\ u_2 \\ v_2 \end{pmatrix} d\Gamma = \int_{\Gamma_e} \begin{pmatrix} N_1 N_1 & 0 & N_1 N_2 & 0 \\ 0 & N_1 N_1 & 0 & N_1 N_2 \\ N_2 N_1 & 0 & N_2 N_2 & 0 \\ 0 & N_2 N_1 & 0 & N_2 N_2 \end{pmatrix} d\Gamma \cdot \begin{pmatrix} u_1 \\ v_1 \\ u_2 \\ v_2 \end{pmatrix} \quad (542)$$

Turning now to the right hand side  $\int_{\Gamma_e} N_i (\vec{v} \cdot \vec{n}_e) \vec{n}_e d\Gamma$ , it yields the following rhs:

$$\int_{\Gamma_e} (\vec{v} \cdot \vec{n}_e) \begin{pmatrix} N_1 n_x \\ N_1 n_y \\ N_2 n_x \\ N_2 n_y \end{pmatrix} d\Gamma$$

The elemental matrix and rhs must be built for each element and assembled in a global matrix and rhs. The solution is the mesh velocity vector at all surface nodes. the same approach can be taken for  $Q_2$  elements:

$$\int_{\Gamma_e} N_i \vec{v}_{\text{mesh}} d\Gamma = \int N_i \begin{pmatrix} u_{\text{mesh}} \\ v_{\text{mesh}} \end{pmatrix} d\Gamma \quad (543)$$

$$= \int N_i \begin{pmatrix} N_1 & 0 & N_2 & 0 & N_3 & 0 \\ 0 & N_1 & 0 & N_2 & 0 & N_3 \end{pmatrix} \cdot \begin{pmatrix} u_1 \\ v_1 \\ u_2 \\ v_2 \\ u_3 \\ v_3 \end{pmatrix} d\Gamma \quad (544)$$

Writing this equation alternatively for  $N_i = N_1, N_2, N_3$  yields:

$$\int_{\Gamma_e} \begin{pmatrix} N_1 N_1 & 0 & N_1 N_2 & 0 & N_1 N_3 & 0 \\ 0 & N_1 N_1 & 0 & N_1 N_2 & 0 & N_1 N_3 \\ N_2 N_1 & 0 & N_2 N_2 & 0 & N_2 N_3 & 0 \\ 0 & N_2 N_1 & 0 & N_2 N_2 & 0 & N_2 N_3 \\ N_3 N_1 & 0 & N_3 N_2 & 0 & N_3 N_3 & 0 \\ 0 & N_3 N_1 & 0 & N_3 N_2 & 0 & N_3 N_3 \end{pmatrix} \cdot \begin{pmatrix} u_1 \\ v_1 \\ u_2 \\ v_2 \\ u_3 \\ v_3 \end{pmatrix} d\Gamma$$

$$= \int_{\Gamma_e} \begin{pmatrix} N_1 N_1 & 0 & N_1 N_2 & 0 & N_1 N_3 & 0 \\ 0 & N_1 N_1 & 0 & N_1 N_2 & 0 & N_1 N_3 \\ N_2 N_1 & 0 & N_2 N_2 & 0 & N_2 N_3 & 0 \\ 0 & N_2 N_1 & 0 & N_2 N_2 & 0 & N_2 N_3 \\ N_3 N_1 & 0 & N_3 N_2 & 0 & N_3 N_3 & 0 \\ 0 & N_3 N_1 & 0 & N_3 N_2 & 0 & N_3 N_3 \end{pmatrix} d\Gamma \cdot \begin{pmatrix} u_1 \\ v_1 \\ u_2 \\ v_2 \\ u_3 \\ v_3 \end{pmatrix} \quad (545)$$

<sup>36</sup>what if  $Q_k$  with  $k > 1$  elements are used and nodes on the surface no more form a line?

The right hand side is then

$$\int_{\Gamma_e} (\vec{v} \cdot \vec{n}_e) \begin{pmatrix} N_1 n_x \\ N_1 n_y \\ N_2 n_x \\ N_2 n_y \\ N_3 n_x \\ N_3 n_y \end{pmatrix} d\Gamma$$

Having obtained the boundary condition velocity for the Laplace equation, we can now turn our attention to solving this ODE.

Note that Rose et al (2017) [2197] go further than this and propose a 'nonstandard finite difference scheme' and make a link with the stabilisation presented in Kaus et al (2010) [1398].

In what follows I omit the subscript 'mesh' and focus on the 2D case. The components of the (mesh) velocity are given by

$$u^h = \sum_{i=1}^{m_v} N_i^\gamma u_i \quad v^h = \sum_{i=1}^{m_v} N_i^\gamma v_i \quad \vec{v}^h = \begin{pmatrix} u^h \\ v^h \end{pmatrix}$$

We start from the ODE to solve in its strong form:

$$\Delta \vec{v}^h = \vec{0}$$

We multiply it by a velocity test function  $N_i^\gamma$  and integrate over an element:

$$\begin{aligned} & \vec{0} \\ &= \int_{\Omega_e} N_i^\gamma \Delta \vec{v}^h \\ &= \int_{\Omega_e} N_i^\gamma \Delta \vec{v}^h dV \\ &= \int_{\Omega_e} \begin{pmatrix} N_i^\gamma \Delta u^h \\ N_i^\gamma \Delta v^h \end{pmatrix} dV \\ &= \int_{\Omega_e} \begin{pmatrix} N_i^\gamma \vec{\nabla} \cdot \vec{\nabla} u^h \\ N_i^\gamma \vec{\nabla} \cdot \vec{\nabla} v^h \end{pmatrix} dV \\ &= \int_{\Omega_e} \begin{pmatrix} \vec{\nabla} N_i^\gamma \cdot \vec{\nabla} u^h \\ \vec{\nabla} N_i^\gamma \cdot \vec{\nabla} v^h \end{pmatrix} dV \\ &= \int_{\Omega_e} \begin{pmatrix} \partial_x N_i^\gamma \partial_x u^h + \partial_y N_i^\gamma \partial_y u^h \\ \partial_x N_i^\gamma \partial_x v^h + \partial_y N_i^\gamma \partial_y v^h \end{pmatrix} dV \\ &= \int_{\Omega_e} \begin{pmatrix} \partial_x N_i^\gamma & \partial_y N_i^\gamma & 0 & 0 \\ 0 & 0 & \partial_x N_i^\gamma & \partial_y N_i^\gamma \end{pmatrix} \cdot \begin{pmatrix} \partial_x u^h \\ \partial_y u^h \\ \partial_x v^h \\ \partial_y v^h \end{pmatrix} dV \\ &= \int_{\Omega_e} \begin{pmatrix} \frac{\partial N_i^\gamma}{\partial x} & 0 & \frac{\partial N_1^\gamma}{\partial x} & 0 & \dots & \frac{\partial N_{m_v}^\gamma}{\partial x} & 0 \\ \frac{\partial N_1^\gamma}{\partial y} & 0 & \frac{\partial N_2^\gamma}{\partial y} & 0 & \dots & \frac{\partial N_{m_v}^\gamma}{\partial y} & 0 \\ 0 & \frac{\partial N_1^\gamma}{\partial x} & 0 & \frac{\partial N_2^\gamma}{\partial x} & \dots & 0 & \frac{\partial N_{m_v}^\gamma}{\partial x} \\ 0 & \frac{\partial N_1^\gamma}{\partial y} & 0 & \frac{\partial N_2^\gamma}{\partial y} & \dots & 0 & \frac{\partial N_{m_v}^\gamma}{\partial y} \end{pmatrix} \cdot \begin{pmatrix} u_1 \\ v_1 \\ u_2 \\ v_2 \\ \dots \\ u_{m_v} \\ v_{m_v} \end{pmatrix} dV \end{aligned}$$

Writing this equation for  $i = 1, \dots, m_v$ , we obtain:

$$\int \begin{pmatrix} \frac{\partial N_1^v}{\partial x} & \frac{\partial N_1^v}{\partial y} & 0 & 0 \\ 0 & 0 & \frac{\partial N_2^v}{\partial x} & \frac{\partial N_1^v}{\partial y} \\ \frac{\partial N_2^v}{\partial x} & \frac{\partial N_2^v}{\partial y} & 0 & 0 \\ 0 & 0 & \frac{\partial N_2^v}{\partial x} & \frac{\partial N_2^v}{\partial y} \\ \vdots & \vdots & \vdots & \vdots \\ \vdots & \vdots & \vdots & \vdots \\ \frac{\partial N_{m_v}^v}{\partial x} & \frac{\partial N_{m_v}^v}{\partial y} & 0 & 0 \\ 0 & 0 & \frac{\partial N_{m_v}^v}{\partial x} & \frac{\partial N_{m_v}^v}{\partial y} \end{pmatrix} \cdot \begin{pmatrix} \frac{\partial N_1^v}{\partial x} & 0 & \frac{\partial N_2^v}{\partial x} & 0 & \dots & \frac{\partial N_{m_v}^v}{\partial x} & 0 \\ \frac{\partial N_1^v}{\partial y} & 0 & \frac{\partial N_2^v}{\partial y} & 0 & \dots & \frac{\partial N_{m_v}^v}{\partial y} & 0 \\ 0 & \frac{\partial N_1^v}{\partial x} & 0 & \frac{\partial N_2^v}{\partial x} & \dots & 0 & \frac{\partial N_{m_v}^v}{\partial x} \\ 0 & \frac{\partial N_1^v}{\partial y} & 0 & \frac{\partial N_2^v}{\partial y} & \dots & 0 & \frac{\partial N_{m_v}^v}{\partial y} \end{pmatrix} \cdot \underbrace{\begin{pmatrix} u_1 \\ v_1 \\ u_2 \\ v_2 \\ \dots \\ u_{m_v} \\ v_{m_v} \end{pmatrix}}_{\vec{V}} dV = \vec{0}$$

or,

$$\left( \int_{\Omega_e} \mathbf{B}^T \cdot \mathbf{B} dV \right) \cdot \vec{V} = \vec{0}$$

where  $\mathbf{B}$  is a  $(ndim * ndim) \times (m_v * ndofV)$  matrix. This is implemented in Stone 54.9.4.

**Remark.** The integration by parts should have a minus appear but since the left hand side is 0, it is not taken into account.

surface terms arising from the integration by parts are neglected. EXPLAIN WHY!

**Yet another approach [710]** The unknown position of free surfaces can be computed using the following approach: for the simple case of a single-valued function  $h = h(x, y, t)$ , a hyperbolic equation must be solved,

$$\frac{\partial h}{\partial t} + (\vec{v} \cdot \vec{\nabla}) h = 0 \quad (546)$$

This is the kinematic equation of the surface and has been used, for instance, by Ramaswamy and Kawahara (1987), Huerta and Liu, 1988b, 1990; Souli and Zolesio (2001).

Idea: Eq. (546) is a simple advection equation. One could also add a diffusion operator with a diffusion coefficient  $D$ . Low values of  $D$  could be used to stabilise the surface while higher values (possibly nonlinear ones) could be used to account for simple surface processes.

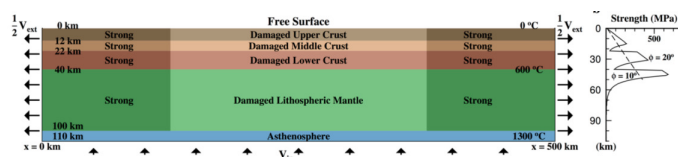
$$\frac{\partial h}{\partial t} + (\vec{v} \cdot \vec{\nabla}) h = D \Delta h \quad (547)$$

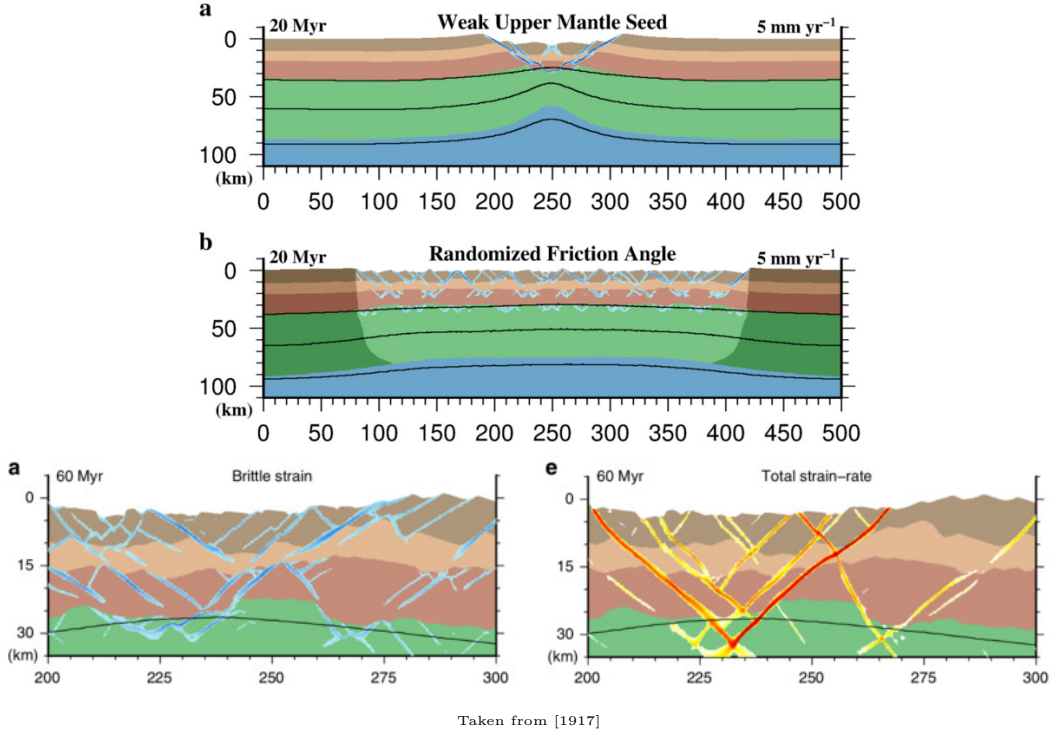
Also, Hansen and Nielsen [1137, 1136] write: During the entire model evolution surface processes act to re-distribute sediments. These processes are modelled by a diffusion equation with a source term enabling the transport of sediments to and from the model profile. The transport equation is written

$$\dot{h} = \nabla \cdot (\kappa \nabla h) + \dot{s}(w)$$

where  $\kappa = 200 \text{ km}^2/\text{Ma}$  is the diffusivity of topography and  $\dot{s}(w)$  is a linear function of water depth.

The following pictures are taken from Naliboff et al [1917] on the topic of how complex fault interaction controls continental rifting. It is a beautiful example (among many) of the importance of free surface geodynamical expression and large deformation:





Taken from [1917]

#### 8.1.4 On the topic of moving internal nodes

Braess & Wriggers [255] propose the following interesting algorithm: "A measure of the quality of a triangular mesh is the quotient of the outer radius  $r_{out}$  and the inner radius  $r_{in}$  of each element. This quotient is important because it plays a certain role in a priori error estimates. If an element degenerates this quotient will approach infinity. Another important feature of good mesh is that no element becomes very large. With these considerations in mind the penalty function  $W$  is defined:

$$W = \sum_{elts} \left( \frac{r_{out}}{r_{in}} \right)^m \left( \frac{r_{out}}{r_0} \right)^n \quad (548)$$

where  $m$ ,  $n$  and  $r_0$  are positive constants. For our calculations we chose  $m = 3$ ,  $n = 1$  and  $r_0 = 1$ , but the results seem to depend only slightly on this choice. Whenever a triangle is distorted or very large, this function becomes very large. A similar penalty function was presented in [1359] for four-node elements. In that case the angles of the elements are used to construct the penalty function. In order to regularize a distorted mesh the coordinates of the internal nodes will be chosen such that  $W$  is minimized. It is not necessary to reach the global minimum, a rough approximation is sufficient. Therefore the minimization of the potential can be done efficiently with standard procedures and will not be discussed in any detail. This algorithm can also be applied to  $h$ -adaptive mesh-generation by choosing appropriate constants  $r_0$  for each triangle."<sup>37</sup>

This is still WORK IN PROGRESS. I Need to look at those papers: [2097] [1244][2053] [157] [2455] [2096] [2518](moving pulse) [739] [745] [41] [1503] [2403] [1690] [1101][2903] [775] [255] [1993] and talk

<sup>37</sup>Indeed, if  $r_0$  is the same for all elements this parameter will not play any role at all in the minimisation process.

about free surface stabilisation [1398, 2087, 739, 2197].

## 8.2 Convergence criterion for nonlinear iterations

MEGA WORK in PROGRESS!!

Following [2396], one can monitor the relative changes in the solution from iteration to iteration. For instance,

$$\frac{\|\Delta \vec{V}\|_{L2}}{\|\vec{V}\|_{L2}} = \left( \frac{\int_{\Omega} (\vec{V}_i - \vec{V}_{i-1}) \cdot (\vec{V}_i - \vec{V}_{i-1}) dV}{\int_{\Omega} \vec{V}_i \cdot \vec{V}_i dV} \right)^{1/2}$$

is a measure of the relative change in the velocity field from iteration  $i - 1$  to  $i$ . The same monitoring can be done for pressure:

$$\frac{\|\Delta \vec{P}\|_{L2}}{\|\vec{P}\|_{L2}} = \left( \frac{\int_{\Omega} (\vec{P}_i - \vec{P}_{i-1}) \cdot (\vec{P}_i - \vec{P}_{i-1}) dV}{\int_{\Omega} \vec{P}_i \cdot \vec{P}_i dV} \right)^{1/2}$$

Convergence is reached when both are below 0.001 [1556] or 0.0001 [1396].

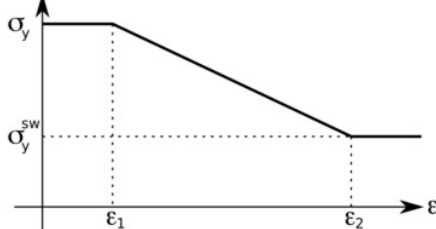
nonlinear residual .. see [2396] p2222.

check correlation of [2528]

### 8.3 Strain weakening

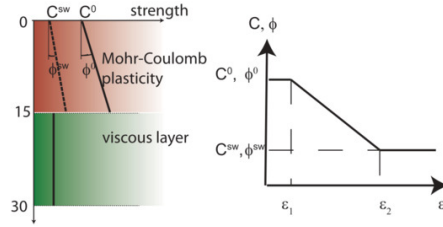
Several mechanisms may contribute to strain or strain rate dependent weakening but their relative and absolute importance is poorly constrained. Furthermore, weakening mechanisms are often crudely parameterised in geodynamical codes with simple mathematical functions and a limited number of parameters.

For example, in [25] the authors use a von Mises plasticity formulation so that the rheology is parameterised by the cohesion  $c$ , or  $c = \sigma_y$  in their notations. The yield strength  $\sigma_y$  starts constant until the strain  $\varepsilon$  reaches the threshold value  $\varepsilon_1$ . It then decreases linearly from  $\sigma_y$  to  $\sigma_y^{sw}$  between  $\varepsilon_1$  and  $\varepsilon_2$ . For strain values  $\varepsilon > \varepsilon_2$ , the yield strength remains constant at  $\sigma_y^{sw}$ .



Taken from [25]

The same authors in a subsequent study use a Drucker-Prager rheology parameterised by cohesion  $c$  and friction angle  $\phi$ . They use the same approach as before but now both parameters are subjected to strain weakening:



Taken from [26], see also [2528]

They further define the factor  $R = C^0/C^{sw} = \phi^0/\phi^{sw} \geq 1$  which is a proxy for the ratio  $\sigma_y/\sigma_y^{sw}$  where  $\sigma_y = p \sin \phi + c \cos \phi$ , and carry out 3D crustal extensional models for  $R$  between 2 and 5.

- In [1543] the authors also define

$$\tau_y = p \sin(\phi(\varepsilon^p)) + c_0 \cos(\phi(\varepsilon^p))$$

but the cohesion is regarded to be constant. The angle of friction  $\phi$  is assumed to decrease as a function of the accumulated plastic strain  $\varepsilon^p$  to

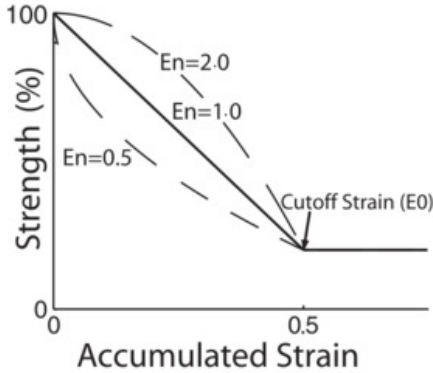
$$\phi(\varepsilon^p) = \max \left( \phi_\infty, \phi_0 - \frac{\varepsilon^p(\phi_0 - \phi_\infty)}{\varepsilon_\infty^p} \right)$$

This equation defines an empirical softening relation which reduces the friction angle linearly with accumulated plastic strain.  $\phi_0$  defines the initial friction angle,  $\varepsilon_\infty^p$  represents the measure of plastic strain after which complete softening is achieved and internal friction angle reaches  $\phi_\infty$ . Plastic strain represents an integrated, tensorial invariant measure of the deformation which has occurred due to plastic yielding. Thus, the quantity  $\varepsilon^p$  can be regarded as a simplified measure of material damage.

- In Dyksterhuis et al [749] a variant of the above formulation is used:

$$f(\varepsilon) = \begin{cases} 1 - (1-a)(\varepsilon/\varepsilon_0)^n & \varepsilon \leq \varepsilon_0 \\ a & \varepsilon \geq \varepsilon_0 \end{cases}$$

where  $\varepsilon$  is the accumulated plastic strain,  $\varepsilon_0$  is the saturation strain beyond which no further weakening takes place,  $n$  is an exponent that controls the shape of the function and  $a$  is a maximum value of strain weakening beyond which no further weakening occurs. This equation leads to the following plot:



Strain-softening behaviour showing strength weakening from 100 to 20% after an accumulated strain of 0.5, after which no further weakening occurs. Dashed lines show the effect of the exponential parameter ( $En$ ) on the curve. Taken from [749]

Although it is not specified in [749] what  $f$  is, other users of the code specify that the yield strength is given by

$$\sigma_y = (B_0 + B_1 p) f(\varepsilon)$$

where  $p$  is the pressure,  $B_0$  is the cohesion, or yield stress at zero pressure, and  $B_p$  is the pressure dependence of the yield stress, equivalent to the friction coefficient in Byerlees law.

In [2841] the authors take a different approach:

$$C = C_0 + C_1 \exp\left(-\frac{\varepsilon_{plast}}{\varepsilon_{ref}}\right)$$

$$\mu = \mu_0 + \mu_1 \exp\left(-\frac{\varepsilon_{plast}}{\varepsilon_{ref}}\right)$$

where  $C_0$  and  $C_0 + C_1$  represent the minimum and maximum cohesions, respectively;  $\mu_0$  and  $\mu_0 + \mu_1$  represent the minimum and maximum frictional coefficients, respectively.  $\varepsilon_{plast}$  and  $\varepsilon_{ref}$  represent accumulated plastic strain and reference strain, respectively.

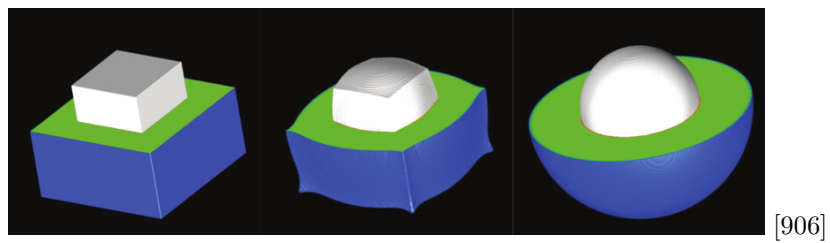
- In [1589] the authors describe another formulation for plastic hardening. The angle of friction changes with the accumulated plastic strain:

$$\sin \phi = \sin \phi_i + \frac{2(\sin \phi_f - \sin \phi_i)\sqrt{\varepsilon_c^p \varepsilon^p}}{\varepsilon^p + \varepsilon_c^p}$$

where  $\phi$  transitions from an initial value  $\phi_i$  to a maximum  $\phi_f$  attained when the effective plastic strain reaches a critical value  $\varepsilon_c^p$ . When  $\varepsilon^p \rightarrow \varepsilon_c^p$  then  $\phi \rightarrow \phi_f$ .

Relevant Literature: [2437, 1942]

#### 8.4 The gravity vector



[906]

## 8.5 The SUPG formulation for the energy equation

As abundantly documented in the literature advection needs to be stabilised as it otherwise showcases non-negligible under- and overshoots. A standard approach is the Streamline Upwind Petrov Galerkin (SUPG) method.

 Relevant Literature[292, 286, 2520, 1249]

### 8.5.1 Linear elements

When using linear elements, its implementation is rather trivial, as shown in the DOUAR paper [269] or the FANTOM paper [2528]. The advection matrix is simply modified and computed as follows:

$$(\mathbf{K}_a^e)_{SUPG} = \int_{x_k}^{x_{k+1}} (\mathbf{N}^*)^T \rho C_p \vec{v} \cdot \mathbf{B} dx \quad \text{with} \quad \mathbf{N}^* = \mathbf{N} + \tau \vec{v} \cdot \mathbf{B}$$

Note that we can also write

$$(\mathbf{K}_a^e)_{SUPG} = \int_{x_k}^{x_{k+1}} \mathbf{N}^T \rho C_p \vec{v} \cdot \mathbf{B} dx + \int_{x_k}^{x_{k+1}} \tau (\vec{v} \cdot \mathbf{B})^T \rho C_p (\vec{v} \cdot \mathbf{B}) dx$$

and we see that the SUPG method introduces an additional term that is akin to a diffusion term in the direction of the flow. This can be seen by looking at the advection matrix a regular grid of 1D elements of size  $h$ :

$$(\mathbf{K}_a^e)_{SUPG} = \mathbf{K}_a^e + \rho C_p \frac{\tau u^2}{h} \begin{pmatrix} 1 & -1 \\ -1 & 1 \end{pmatrix}$$

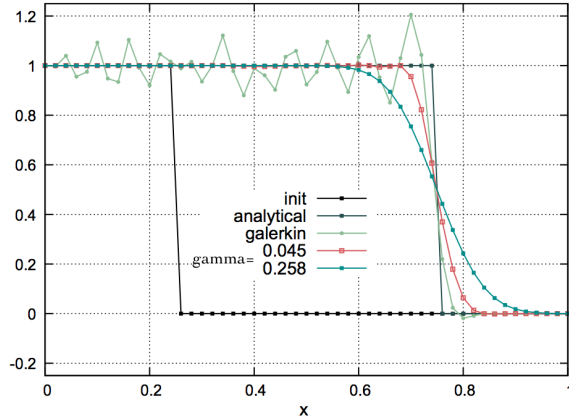
The additional matrix has the same structure as the 1D diffusion matrix matrix in 5.1.

The parameter  $\tau$  is chosen as follows:

$$\tau = \gamma \frac{h}{\nu} \quad (549)$$

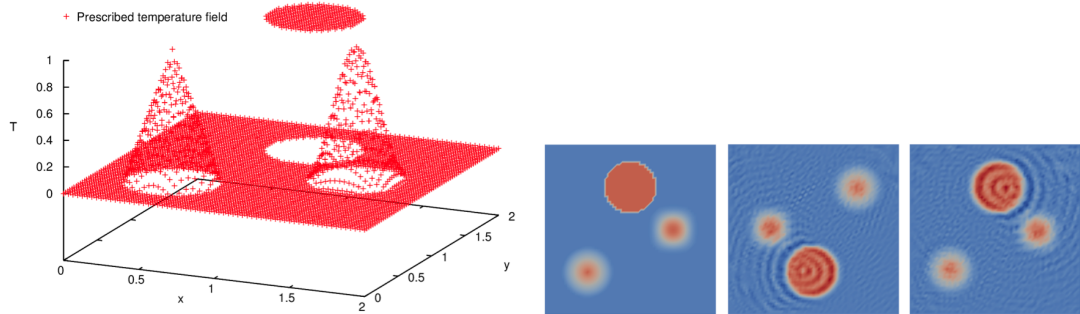
where  $\gamma$  is a user chosen parameter (see Appendix A of [2528]).

A typical test case for testing an advection scheme is the step advection benchmark ( see for instance [711]). At  $t = 0$ , a field  $T(x)$  is prescribed in a 1D domain of unit length. For  $x \leq 1/4$  we have  $T(x) = 1$  and  $T(x) = 0$  everywhere else as shown on the following figure:



The prescribed velocity is  $\nu = 1$ , 50 elements are used and 250 time steps are carried out with  $\delta t = 0.1h/\nu = 0.002$ . As discussed in [2528], using Equation 549, one arrives to  $\gamma = 0.045$ , which leads to a desired removal of the oscillations through a small amount of numerical diffusion. Braun [262] argues for a constant  $\gamma = 1/\sqrt{15} = 0.258$  (after [1252]), which effect is also shown in the figure above. This value is arguably too large and introduces undesirable diffusion.

Another classic example of advection testing is a 2D problem where (for example) a cylinder, a Gaussian and a cone are prescribed and advected with a velocity field (see for instance [711]).



After a  $2\pi$  rotation and in the absence of stabilisation we see that the temperature field showcases clearly visible ripples.

**Remark.** Note that ASPECT originally did not rely on the SUPG formulation to stabilise the advection(-diffusion) equations[1507]. It instead relied on the Entropy Viscosity formulation [1079, 1077]. It is only during the 6th Hackathon in May 2019 that the SUPG was introduced on the code. Note that the ASPECT implementation is based on the deal.II step 63<sup>38</sup>.

---

<sup>38</sup>[https://www.dealii.org/developer/doxygen/deal.II/step\\_63.html](https://www.dealii.org/developer/doxygen/deal.II/step_63.html)

## 8.6 The method of manufactured solutions

The method of manufactured solutions is a relatively simple way of carrying out code verification. In essence, one postulates a solution for the PDE at hand (as well as the proper boundary conditions), inserts it in the PDE and computes the corresponding source term. The same source term and boundary conditions will then be used in a numerical simulation so that the computed solution can be compared with the (postulated) true analytical solution.

Examples of this approach are to be found in [711, 382, 215, 2057, 2055, 1657, 210].

### 8.6.1 Analytical benchmark I - "DH"

Taken from [711]. We consider a two-dimensional problem in the square domain  $\Omega = [0, 1] \times [0, 1]$ , which possesses a closed-form analytical solution. The problem consists of determining the velocity field  $\vec{v} = (u, v)$  and the pressure  $p$  such that

$$\eta \Delta \vec{v} - \vec{\nabla} p + \vec{b} = \vec{0} \quad \text{in } \Omega \quad (550)$$

$$\vec{\nabla} \cdot \vec{v} = 0 \quad \text{in } \Omega \quad (551)$$

$$\vec{v} = \vec{0} \quad \text{on } \Gamma_D \quad (552)$$

where the fluid viscosity is taken as  $\eta = 1$ . The components of the body force  $\vec{b}$  are prescribed as

$$\begin{aligned} b_x &= (12 - 24y)x^4 + (-24 + 48y)x^3 + (-48y + 72y^2 - 48y^3 + 12)x^2 \\ &\quad + (-2 + 24y - 72y^2 + 48y^3)x + 1 - 4y + 12y^2 - 8y^3 \\ b_y &= (8 - 48y + 48y^2)x^3 + (-12 + 72y - 72y^2)x^2 \\ &\quad + (4 - 24y + 48y^2 - 48y^3 + 24y^4)x - 12y^2 + 24y^3 - 12y^4 \end{aligned}$$

With this prescribed body force, the exact solution is

$$\begin{aligned} u(x, y) &= x^2(1-x)^2(2y-6y^2+4y^3) \\ v(x, y) &= -y^2(1-y)^2(2x-6x^2+4x^3) \\ p(x, y) &= x(1-x) - 1/6 \end{aligned}$$

Note that the pressure obeys  $\int_{\Omega} p d\Omega = 0$ . One can turn to the spatial derivatives of the fields:

$$\dot{\varepsilon}_{xx} = \frac{\partial u}{\partial x} = (2x - 6x^2 + 4x^3)(2y - 6y^2 + 4y^3) \quad (553)$$

$$\dot{\varepsilon}_{yy} = \frac{\partial v}{\partial y} = -(2x - 6x^2 + 4x^3)(2y - 6y^2 + 4y^3) \quad (554)$$

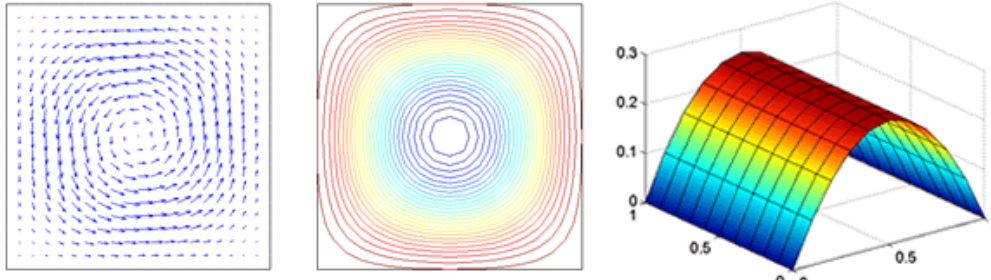
$$\dot{\varepsilon}_{xy} = \frac{1}{2} \left( \frac{\partial u}{\partial y} + \frac{\partial v}{\partial x} \right) = \frac{1}{2} (x^2(1-x)^2(2-12y+12y^2) - y^2(1-y)^2(2-12x+12x^2)) \quad (555)$$

with of course  $\vec{\nabla} \cdot \vec{v} = 0$  and

$$\frac{\partial p}{\partial x} = 1 - 2x \quad (556)$$

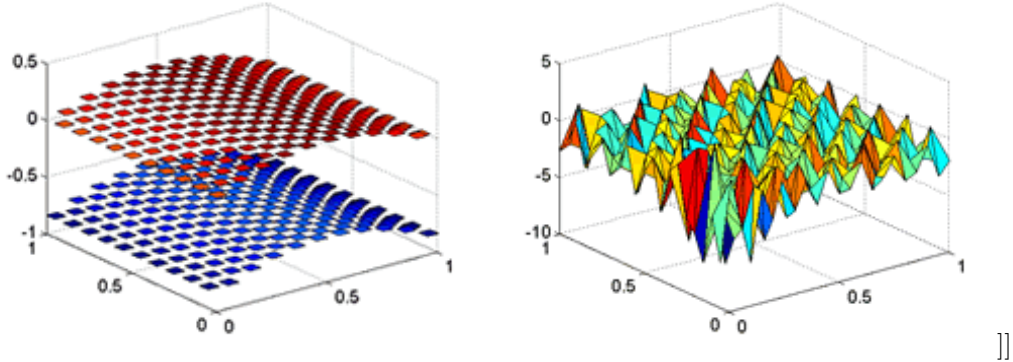
$$\frac{\partial p}{\partial y} = 0 \quad (557)$$

The velocity and pressure fields look like:



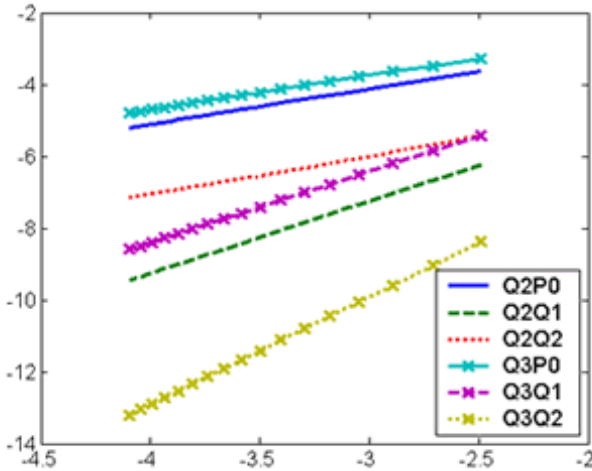
[http://ww2.lacan.upc.edu/huerta/exercises/Incompressible/Incompressible\\_Ex1.htm](http://ww2.lacan.upc.edu/huerta/exercises/Incompressible/Incompressible_Ex1.htm)

As shown in [711], If the LBB condition is not satisfied, spurious oscillations spoil the pressure approximation. Figures below show results obtained with a mesh of 20x20 Q1P0 (left) and P1P1 (right) elements:



[http://ww2.lacan.upc.edu/huerta/exercises/Incompressible/Incompressible\\_Ex1.htm](http://ww2.lacan.upc.edu/huerta/exercises/Incompressible/Incompressible_Ex1.htm)

Taking into account that the proposed problem has got analytical solution, it is easy to analyze convergence of the different pairs of elements:



[http://ww2.lacan.upc.edu/huerta/exercises/Incompressible/Incompressible\\_Ex1.htm](http://ww2.lacan.upc.edu/huerta/exercises/Incompressible/Incompressible_Ex1.htm)

One can also compute the stress components:

$$\sigma_{xx} = 2x^2(2x-2)(4y^3-6y^2+2y) + 4x(-x+1)^2 * (4y^3-6y^2+2y) - x(-x+1) + 1/6 \quad (558)$$

$$\sigma_{xy} = x^2(-x+1)^2 * (12y^2-12y+2) - y^2(-y+1)^2 * (12x^2-12x+2) \quad (559)$$

$$\sigma_{yy} = -x(-x+1) - 2y^2(2y-2)(4x^3-6x^2+2x) - 4y(-y+1)^2(4x^3-6x^2+2x) + 1/6 \quad (560)$$

All the necessary functions to do this benchmark are in `mms/dh.py`:

```
# functions for the Donea & Huerta benchmark (dh)

def u_th(x,y):
    return x**2*(1.-x)**2*(2*y-6*y**2+4*y**3)

def v_th(x,y):
    return -y**2*(1.-y)**2*(2*x-6*x**2+4*x**3)

def p_th(x,y):
    return x*(1-x)-1./6.

def dpdx_th(x,y):
    return 1.-2.*x
```

```

def dpdy_th(x,y):
    return 0.

def exx_th(x,y):
    return x**2*(2*x-2)*(4*y**3-6*y**2+2*y)+2*x*(-x+1)**2*(4*y**3-6*y**2+2*y)

def eyy_th(x,y):
    return (x**2*(-x+1)**2*(12*y**2-12*y+2)-y**2*(-y+1)**2*(12*x**2-12*x+2))/2

def bx(x,y):
    return ((12.-24.*y)*x**4+(-24.+48.*y)*x*x*x +
           (-48.*y+72.*y*y-48.*y*y*y+12.)*x*x +
           (-2.+24.*y-72.*y*y+48.*y*y*y)*x +
           1.-4.*y+12.*y*y-8.*y*y*y)

def by(x,y):
    return ((8.-48.*y+48.*y*y)*x*x*x+
           (-12.+72.*y-72.*y*y)*x*x+
           (4.-24.*y+48.*y*y-48.*y*y*y+24.*y**4)*x -
           12.*y*y+24.*y*y*y-12.*y**4)

```

This benchmark is implemented in ASPECT [91] and in **Stones 01**.

### 8.6.2 Analytical benchmark II - "DB2D"

Taken from [705, 215]. It is for a unit square with  $\nu = \mu/\rho = 1$  and the smooth exact solution is

$$u(x, y) = x + x^2 - 2xy + x^3 - 3xy^2 + x^2y \quad (561)$$

$$v(x, y) = -y - 2xy + y^2 - 3x^2y + y^3 - xy^2 \quad (562)$$

$$p(x, y) = xy + x + y + x^3y^2 - 4/3 \quad (563)$$

Note that the pressure obeys  $\int_{\Omega} p \, d\Omega = 0$

$$b_x = -(1 + y - 3x^2y^2) \quad (564)$$

$$b_y = -(1 - 3x - 2x^3y) \quad (565)$$

This benchmark is also used in [2813].

### 8.6.3 Analytical benchmark III - "DB3D"

This benchmark begins by postulating a polynomial solution to the 3D Stokes equation [705]:

$$\vec{v} = \begin{pmatrix} x + x^2 + xy + x^3y \\ y + xy + y^2 + x^2y^2 \\ -2z - 3xz - 3yz - 5x^2yz \end{pmatrix} \quad (566)$$

and

$$p = xyz + x^3y^3z - 5/32 \quad (567)$$

While it is then trivial to verify that this velocity field is divergence-free (see here under), the corresponding body force of the Stokes equation can be computed by inserting this solution into the momentum equation with a given viscosity  $\eta(x, y, z)$  (constant or position/velocity/strain rate dependent). The domain is a unit cube and velocity boundary conditions simply use Eq. (898). Note that the pressure fulfills

$$\int_{\Omega} p(x, y, z) \, dV = 0.$$

Following [382], the viscosity is given by the smoothly varying function

$$\eta(x, y, z) = \exp(1 - \beta(x(1-x) + y(1-y) + z(1-z))) \quad (568)$$

Choosing  $\beta = 0$  yields a constant velocity  $\eta = e^1$  (and greatly simplifies the right-hand side). One can easily show that the ratio of viscosities  $\eta^*$  in the system follows  $\eta^* = \exp(-3\beta/4)$  so that choosing  $\beta = 10$  yields  $\eta^* \simeq 1808$  and  $\beta = 20$  yields  $\eta^* \simeq 3.269 \times 10^6$ .

The exact form of the rhs is carried out in Stone 9.4.

#### 8.6.4 Analytical benchmark IV - "Bercovier & Engelman"

From [175]. The two-dimensional domain is a unit square. The body forces are:

$$\begin{aligned} f_x &= 128[x^2(x-1)^212(2y-1) + 2(y-1)(2y-1)y(12x^2-12x+2)] \\ f_y &= 128[y^2(y-1)^212(2x-1) + 2(x-1)(2x-1)y(12y^2-12y+2)] \end{aligned} \quad (569)$$

The solution is

$$\begin{aligned} u &= -256x^2(x-1)^2y(y-1)(2y-1) \\ v &= 256y^2(y-1)^2x(x-1)(2x-1) \\ p &= 0 \end{aligned} \quad (570)$$

$$du/dx = 512(1-2x)(-1+x)x(-1+y)y(-1+2y) \quad (571)$$

$$du/dy = -256(-1+x)^2x^2(1-6y+6y^2) \quad (572)$$

$$dv/dx = 256y^2(y-1)^2x(x-1)(2x-1) \quad (573)$$

$$dv/dy = -512(-1+x)x(1-2x)(-1+y)y(-1+2y) \quad (574)$$

$$(575)$$

and we can easily verify that  $\vec{\nabla} \cdot \vec{v} = du/dx + dv/dy = 0$ .

CHECK RHS !

Another choice with a non-zero pressure:

$$\begin{aligned} f_x &= 128[x^2(x-1)^212(2y-1) + 2(y-1)(2y-1)y(12x^2-12x+2)] + y - 1/2 \\ f_y &= 128[y^2(y-1)^212(2x-1) + 2(x-1)(2x-1)y(12y^2-12y+2)] + x - 1/2 \end{aligned} \quad (576)$$

The solution is

$$\begin{aligned} u &= -256x^2(x-1)^2y(y-1)(2y-1) \\ v &= 256y^2(y-1)^2x(x-1)(2x-1) \\ p &= (x-1/2)(y-1/2) \end{aligned} \quad (577)$$

#### 8.6.5 Analytical benchmark V - "VJ1"

This is taken from Appendix D1 of [1351].

The domain  $\Omega$  is a unit square. We consider the stream function

$$\phi(x, y) = 1000x^2(1-x)^4y^3(1-y)^2$$

The velocity field is defined by

$$u(x, y) = \partial_y \phi = 1000(x^2(1-x)^4y^2(1-y)(3-5y)) \quad (578)$$

$$v(x, y) = -\partial_x \phi = 1000(-2x(1-x)^3(1-3x)y^3(1-y)^2) \quad (579)$$

and it is easy to verify that  $\vec{\nabla} \cdot \vec{v} = 0$ .

The pressure is given by:

$$p(x, y) = \pi^2(xy^3 \cos(2\pi x^2 y) - x^2 y \sin(2\pi x y)) + \frac{1}{8}$$

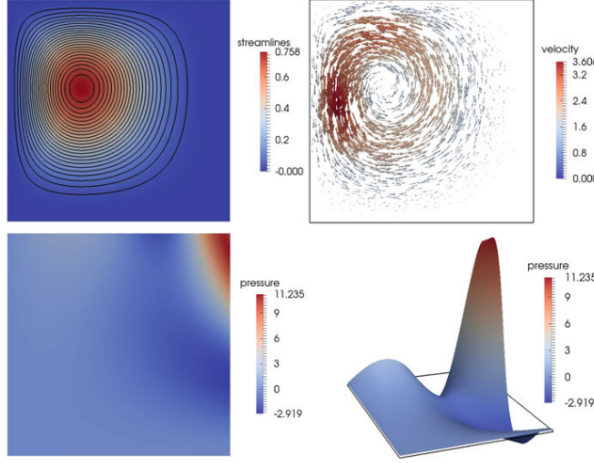


**Fig. D.1** Example D.3. Stream function (top left) velocity (top right) and pressure (bottom). These plots are based on results obtained with numerical simulations

Taken from [1351].

(BSc Thesis)

### 8.6.6 Analytical benchmark VI - "Ilinca & Pelletier"

This is taken from [1284].

Let us consider the Poiseuille flow of a Newtonian fluid. The channel has isothermal flat walls located at  $y = \pm h$ . The velocity distribution is parabolic:

$$u = u_0 \left( 1 - \frac{y^2}{h^2} \right) \quad v = 0$$

where  $u_0$  is the maximum velocity. The (steady state) temperature field is the solution of the advection-diffusion equation:

$$\rho C_p \vec{v} \cdot \vec{\nabla} T = k \Delta T + \Phi$$

where  $\Phi$  is the dissipation function given by

$$\Phi = \eta \left[ 2 \left( \frac{\partial u}{\partial x} \right)^2 + 2 \left( \frac{\partial v}{\partial y} \right)^2 + \left( \frac{\partial v}{\partial x} + \frac{\partial u}{\partial y} \right)^2 \right] = \eta \left( \frac{\partial u}{\partial y} \right)^2 = 4\eta \frac{u_0^2 y^2}{h^4}$$

We logically assume that  $T = T(y)$  so that  $\partial T / \partial x = 0$  and  $\vec{v} \cdot \vec{\nabla} T = 0$ . We then have to solve:

$$k \frac{\partial^2 T}{\partial y^2} + 4\eta \frac{u_0^2 y^2}{h^4} = 0$$

We can integrate twice and use the boundary conditions  $T(y = \pm h) = T_0$  to arrive at:

$$T(y) = T_0 + \frac{1}{3} \frac{\eta u_0^2}{k} \left[ 1 - \left( \frac{y}{h} \right)^4 \right]$$

with a maximum temperature

$$T_M = T(y = 0) = T_0 + \frac{1}{3} \frac{\eta u_0^2}{k}$$

### 8.6.7 Analytical benchmark VII - "grooves"

This benchmark was designed by Dave May. The velocity and pressure fields are given by

$$\begin{aligned} u(x, y) &= x^3 y + x^2 + x y + x \\ v(x, y) &= -\frac{3}{2} x^2 y^2 - 2 x y - \frac{1}{2} y^2 - y \\ p(x, y) &= x^2 y^2 + x y + 5 + p_0 \end{aligned} \tag{580}$$

where  $p_0$  is a constant to be determined based on the type of pressure normalisation. The viscosity is chosen to be

$$\eta(x, y) = -\sin(p) + 1 + \epsilon = -\sin(x^2y^2 + xy + 5) + 1 + \epsilon \quad (581)$$

where  $\epsilon$  actually controls the viscosity contrast. Note that inserting the polynomial expression of the pressure inside the viscosity expression makes the problem linear. We have

$$\begin{aligned} \dot{\varepsilon}_{xx} &= \frac{\partial u}{\partial x} = 3x^2y + 2x + y + 1 \\ \dot{\varepsilon}_{yy} &= \frac{\partial v}{\partial y} = -3x^2y - 2x - y - 1 \\ \dot{\varepsilon}_{xy} &= \frac{1}{2} \left( \frac{\partial u}{\partial y} + \frac{\partial v}{\partial x} \right) = \frac{1}{2} (x^3 + x - 3xy^2 - 2y) \end{aligned} \quad (582)$$

and we can verify that the velocity field is incompressible since  $\vec{\nabla} \cdot \vec{v} = \dot{\varepsilon}_{xx} + \dot{\varepsilon}_{yy} = 0$ . The pressure gradient is given by

$$\begin{aligned} \frac{\partial p}{\partial x} &= 2xy^2 + y \\ \frac{\partial p}{\partial y} &= 2x^2y + x \end{aligned}$$

The right hand side term of the Stokes equation is such that

$$\begin{aligned} -\frac{\partial p}{\partial x} + \frac{\partial s_{xx}}{\partial x} + \frac{\partial s_{yx}}{\partial y} + f_x &= 0 \\ -\frac{\partial p}{\partial y} + \frac{\partial s_{xy}}{\partial x} + \frac{\partial s_{yy}}{\partial y} + f_y &= 0 \end{aligned} \quad (583)$$

with

$$\begin{aligned} \frac{\partial s_{xx}}{\partial x} &= \frac{\partial(2\eta\dot{\varepsilon}_{xx})}{\partial x} = 2\eta \frac{\partial\dot{\varepsilon}_{xx}}{\partial x} + 2\frac{\partial\eta}{\partial x}\dot{\varepsilon}_{xx} \\ \frac{\partial s_{zx}}{\partial z} &= \frac{\partial(2\eta\dot{\varepsilon}_{zx})}{\partial z} = 2\eta \frac{\partial\dot{\varepsilon}_{zx}}{\partial z} + 2\frac{\partial\eta}{\partial z}\dot{\varepsilon}_{zx} \\ \frac{\partial s_{xz}}{\partial x} &= \frac{\partial(2\eta\dot{\varepsilon}_{xz})}{\partial x} = 2\eta \frac{\partial\dot{\varepsilon}_{xz}}{\partial x} + 2\frac{\partial\eta}{\partial x}\dot{\varepsilon}_{xz} \\ \frac{\partial s_{zz}}{\partial z} &= \frac{\partial(2\eta\dot{\varepsilon}_{zz})}{\partial z} = 2\eta \frac{\partial\dot{\varepsilon}_{zz}}{\partial z} + 2\frac{\partial\eta}{\partial z}\dot{\varepsilon}_{zz} \\ \frac{\partial\eta}{\partial x} &= -z(2xz + 1) \cos(x^2z^2 + xz + 5) \\ \frac{\partial\eta}{\partial z} &= -x(2xz + 1) \cos(x^2z^2 + xz + 5) \\ \frac{\partial\dot{\varepsilon}_{xx}}{\partial x} &= 6xz + 2 \\ \frac{\partial\dot{\varepsilon}_{zx}}{\partial z} &= -3xz - 1 \\ \frac{\partial\dot{\varepsilon}_{xz}}{\partial x} &= \frac{1}{2}(3x^2 + 1 - 3z^2) \\ \frac{\partial\dot{\varepsilon}_{zz}}{\partial z} &= -3x^2 - 1 \end{aligned}$$

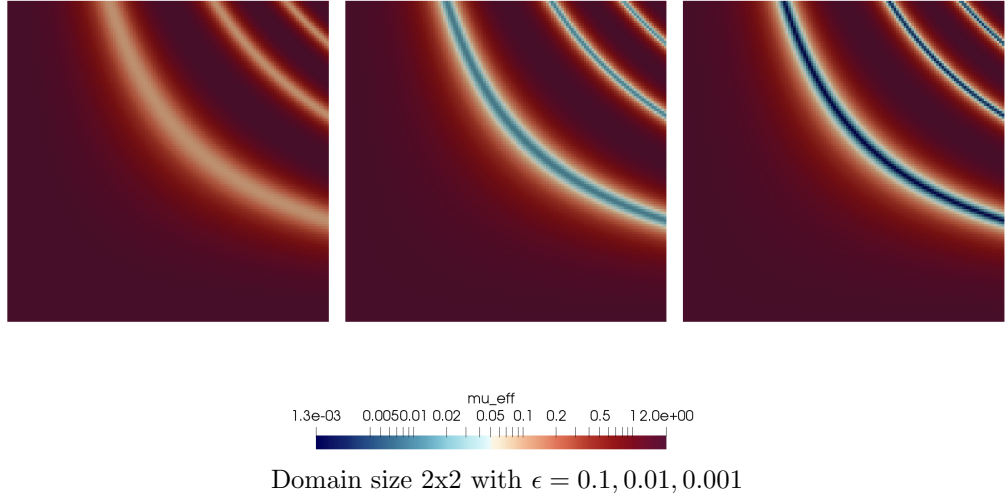
Velocity boundary conditions are prescribed on all four boundaries so that the pressure is known up to a constant (the pressure solution has a nullspace), and the  $p_0$  constant can be determined by requiring that

$$\int_0^L \int_0^L p(x, y) dx dy = \int_0^L \int_0^L (x^2y^2 + xy + 5) dx dy + \int_0^L \int_0^L p_0 dx dy = \int_0^L \int_0^L (x^2y^2 + xy + 5) dx dy + p_0 L^2 = 0$$

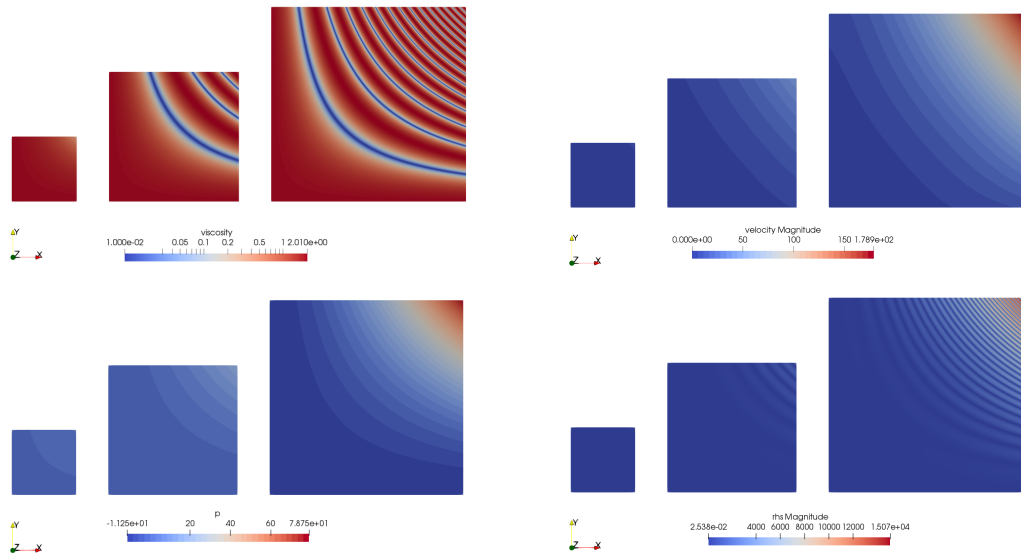
where  $L$  is the size of the square domain. Then

$$p_0 = -\frac{1}{L^2} \int_0^L \int_0^L (x^2y^2 + xy + 5) dx dy = -\frac{L^4}{9} - \frac{L^2}{4} - 5$$

As seen in the following figure, the value of  $\epsilon$  controls the viscosity field amplitude. This is simply explained by the fact that when the sin term of the viscosity takes value 1, the viscosity is then equal to  $\epsilon$ .



Another interesting aspect of this benchmark is the fact that increasing the domain size adds complexity to it as it increases the number of low viscosity zones and the spacing between them also decreases:



Three different domain sizes (1x1, 2x2, 3x3) with  $\epsilon = 0.001$ .

Finally, because the analytical expression for both components of the velocity is a polynomial, we can also compute the root mean square velocity exactly. For instance, for a 2x2 domain:

and we end up with (for  $L = 2$ )

$$v_{rms} = \sqrt{\frac{1}{L^2} \frac{861752}{1575}} = \sqrt{\frac{215438}{1575}} \simeq 11.6955560683$$

(BSc Thesis)

#### 8.6.8 Analytical benchmark VIII - "Kovasznay"

This flow was published by L.I.G. Kovasznay in 1948 [1499]. This paper presents an exact two-dimensional solution of the Navier-Stokes equations with a periodicity in the vertical direction, gives an analytical solution to the steady-state Navier-Stokes equations that is similar which is a flow-field behind a periodic array of cylinders.

$$u(x, y) = 1 - \exp(\lambda x) \cos(2\pi y) \quad (584)$$

$$v(x, y) = \frac{\lambda}{2\pi} \exp(\lambda x) \sin(2\pi y) \quad (585)$$

$$p(x, y) = \frac{1}{2}(1 - \exp(2\lambda x)) \quad (586)$$

$$\lambda = \frac{Re}{2} - \sqrt{\frac{Re^2}{4} + 4\pi^2} \quad (587)$$

Following step-55 of deal.II<sup>39</sup> we have to 'cheat' here since we are not solving the non-linear Navier-Stokes equations, but the linear Stokes system without convective term. Therefore, to recreate the exact same solution we move the convective term into the right-hand side.

The analytical solution is prescribed left and right, while free/no (?) slip is prescribed at top and bottom.

Velocity and pressure solution as implemented in step-55:

```
const double pi2 = pi*pi;

u = -exp(x*(-sqrt(25.0 + 4*pi2) + 5.0))*cos(2*y*pi) + 1

v = (1.0L/2.0L)*(-sqrt(25.0 + 4*pi2) + 5.0)*
    exp(x*(-sqrt(25.0 + 4*pi2) + 5.0))*sin(2*y*pi)/pi

p = -1.0L/2.0L*exp(x*(-2*sqrt(25.0 + 4*pi2) + 10.0)) - 2.0*(-6538034.74494422
    + 0.0134758939981709*exp(4*sqrt(25.0 + 4*pi2)))/(-80.0*exp(3*sqrt(25.0 + 4*pi2)))
    + 16.0*sqrt(25.0 + 4*pi2)*exp(3*sqrt(25.0 + 4*pi2)))
    - 1634508.68623606*exp(-3.0*sqrt(25.0 + 4*pi2))/(-10.0 + 2.0*sqrt(25.0 + 4*pi2))
    + (-0.00673794699908547*exp(sqrt(25.0 + 4*pi2)))
    + 3269017.37247211*exp(-3*sqrt(25.0 + 4*pi2)))/(-8*sqrt(25.0 + 4*pi2) + 40.0)
    + 0.00336897349954273*exp(1.0*sqrt(25.0 + 4*pi2))/(-10.0 + 2.0*sqrt(25.0 + 4*pi2))
```

while the rhs of the PDE is given by

```
const double pi2 = pi * pi;

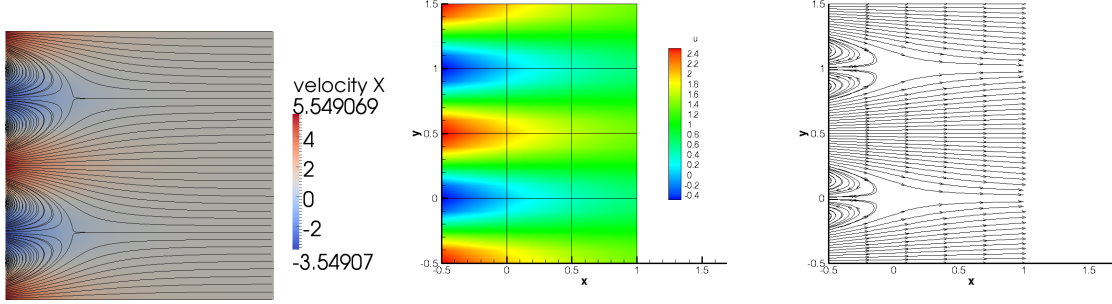
values[0] = -1.0L / 2.0L * (-2 * sqrt(25.0 + 4 * pi2) + 10.0) *
    exp(x*(-2*sqrt(25.0 + 4 * pi2) + 10.0)) -
    0.4 * pi2 * exp(x * (-sqrt(25.0 + 4 * pi2) + 5.0)) * cos(2 * y * pi) +
    0.1 * pow(-sqrt(25.0 + 4 * pi2) + 5.0, 2) *
```

<sup>39</sup>[https://www.dealii.org/current/doxygen/deal.II/step\\_55.html](https://www.dealii.org/current/doxygen/deal.II/step_55.html)

```

exp(x*(-sqrt(25.0 + 4 * pi2) + 5.0)) * cos(2 * y * pi)
values [1] = 0.2 * pi*(-sqrt(25.0 + 4 * pi2) + 5.0) *
exp(x*(-sqrt(25.0 + 4 * pi2) + 5.0)) * sin(2 * y * pi) -
0.05 *pow(-sqrt(25.0 + 4 * pi2) + 5.0, 3) *
exp(x*(-sqrt(25.0 + 4 * pi2) + 5.0)) * sin(2 * y * pi) / pi
values [2] = 0;

```



Left: solution from Step-55. Right: Solution obtained with NekTari++<sup>40</sup>

This benchmark is carried out in many CFD papers: [538], see also Section 7.4.3 of Hesthaven & Warburton [1189].

[Find analytical expression for pressure. Compute expression for rhs. Make stone](#)

(BSc Thesis)

### 8.6.9 Analytical benchmark IX - "VJ2"

It is presented in [1353] and meant to be a peculiar case where the velocity solution is exactly zero. The viscosity is 1, the domain is a unit square, no-slip boundary conditions are prescribed everywhere. The buoyancy force is given by  $\vec{b} = (0, Ra(1 - y + 3y^2))$  where  $Ra > 0$  is a parameter. The flow is incompressible and the analytical pressure solution is given by  $p = Ra(y^3 - y^2/2 + y - 7/12)$ .

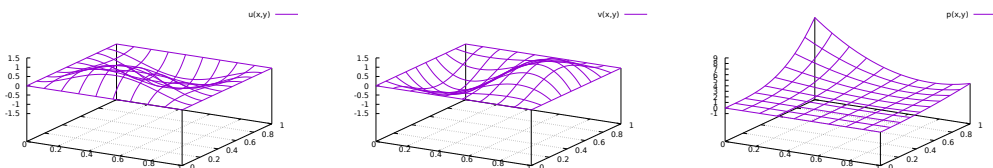
### 8.6.10 Analytical benchmark X - "VJ3"

This benchmark comes from John et al. [1353]. The domain is once again the unit square. The velocity field has the form of a large vortex.

$$u(x, y) = 200x^2(1-x)^2y(1-y)(1-2y) \quad (588)$$

$$v(x, y) = -200x(1-x)(1-2x)y^2(1-y)^2 \quad (589)$$

$$p(x, y) = 10 [(x - 1/2)^3 y^2 + (1 - x)^3 (y - 1/2)^3] \quad (590)$$



<sup>40</sup><http://doc.nektar.info/userguide/4.3.4/user-guidese45.html>

$$\dot{\varepsilon}_{xx} = \frac{\partial u}{\partial x} = -400(1-x)x(2x-1)(y-1)y(2y-1) \quad (591)$$

$$\frac{\partial u}{\partial y} = 200(1-x)^2x^2(6y^2-6y+1) \quad (592)$$

$$\frac{\partial v}{\partial x} = -200(6x^2-6x+1)(1-y)^2y^2 \quad (593)$$

$$\dot{\varepsilon}_{yy} = \frac{\partial v}{\partial y} = 400(x-1)x(2x-1)(1-y)y(2y-1) \quad (594)$$

so that

$$\begin{aligned} \dot{\varepsilon}_{xy} &= \frac{1}{2} [200(1-x)^2x^2(6y^2-6y+1) - 200(6x^2-6x+1)(1-y)^2y^2] \\ &= 100(1-x)^2x^2(6y^2-6y+1) - 100(6x^2-6x+1)(1-y)^2y^2 \end{aligned} \quad (595)$$

Also

$$\begin{aligned} \frac{\partial \dot{\varepsilon}_{xx}}{\partial x} &= 400(6x^2-6x+1)y(2y^2-3y+1) \\ \frac{\partial \dot{\varepsilon}_{xy}}{\partial x} &= 200(-2x^2(1-x)(6y^2-6y+1) + 2x(1-x)^2(6y^2-6y+1) - 6(2x-1)(1-y)^2y^2) \\ &= 100(-2x^2(1-x)(6y^2-6y+1) + 2x(1-x)^2(6y^2-6y+1) - 6(2x-1)(1-y)^2y^2) \\ \frac{\partial \dot{\varepsilon}_{xy}}{\partial y} &= 400(6x^2-6x+1)(1-y)y^2 + 200(1-x)^2x^2(12y-6) - 400(6x^2-6x+1)(1-y)^2y \\ \frac{\partial \dot{\varepsilon}_{yy}}{\partial y} &= -400x(2x^2-3x+1)(6y^2-6y+1) \end{aligned} \quad (596)$$

$$\frac{\partial p}{\partial x} = 30(x-1/2)^2y^2 - 30(1-x)^2(y-1/2)^3 \quad (597)$$

$$\frac{\partial p}{\partial y} = 20(x-1/2)^3y + 30(1-x)^3(y-1/2)^2 \quad (598)$$

From  $\vec{\nabla} \cdot \boldsymbol{\sigma} + \vec{b} = \vec{0}$  we can obtain the rhs as follows:

$$\begin{aligned} \vec{b} &= -\vec{\nabla} \cdot \boldsymbol{\sigma} \\ &= \vec{\nabla} p - \vec{\nabla} \cdot \boldsymbol{s} \\ &= \vec{\nabla} p - \vec{\nabla} \cdot (2\eta \dot{\boldsymbol{\varepsilon}}) \end{aligned} \quad (599)$$

Assuming  $\eta = 1$  we arrive at:

$$b_x = \frac{\partial p}{\partial x} - 2\frac{\partial \dot{\varepsilon}_{xx}}{\partial x} - 2\frac{\partial \dot{\varepsilon}_{xy}}{\partial y} \quad (600)$$

$$b_y = \frac{\partial p}{\partial y} - 2\frac{\partial \dot{\varepsilon}_{xy}}{\partial x} - 2\frac{\partial \dot{\varepsilon}_{yy}}{\partial y} \quad (601)$$

All the necessary functions to do this benchmark are in `mms/vj3.py`:

```
# functions for the Volker John III benchmark (vj3)

def u_th(x,y):
    return 200*x**2*(1-x)**2*y*(1-y)*(1-2*y)

def v_th(x,y):
    return -200*x*(1-x)*(1-2*x)*y**2*(1-y)**2

def p_th(x,y):
    return 10*( (x-1./2.)**3*y**2+(1-x)**3*(y-1./2.)**3 )
```

```

def dpdx_th(x,y):
    return 30*(x-1./2.)**2*y**2-30*(1-x)**2*(y-1./2.)**3

def dpdy_th(x,y):
    return 20*(x-1./2.)**3*y + 30*(1-x)**3*(y-1./2.)**2

def exx_th(x,y):
    return -400*(1-x)*x*(2*x-1)*(y-1)*y*(2*y-1)

def exy_th(x,y):
    return 100*(1-x)**2*x**2*(6*y**2-6*y+1)-100*(6*x**2-6*x+1)*(1-y)**2*y**2

def eyy_th(x,y):
    return 400*(x-1)*x*(2*x-1)*(1-y)*y*(2*y-1)

def dexxdx(x,y):
    return 400*(6*x**2-6*x+1)*y*(2*y**2-3*y+1)

def dexydx(x,y):
    return 100*(-2*x**2*(1-x)*(6*y**2-6*y+1) + 2*x*(1-x)**2*(6*y**2-6*y+1) - 6*(2*x-1)*(1-y)**2*y**2)

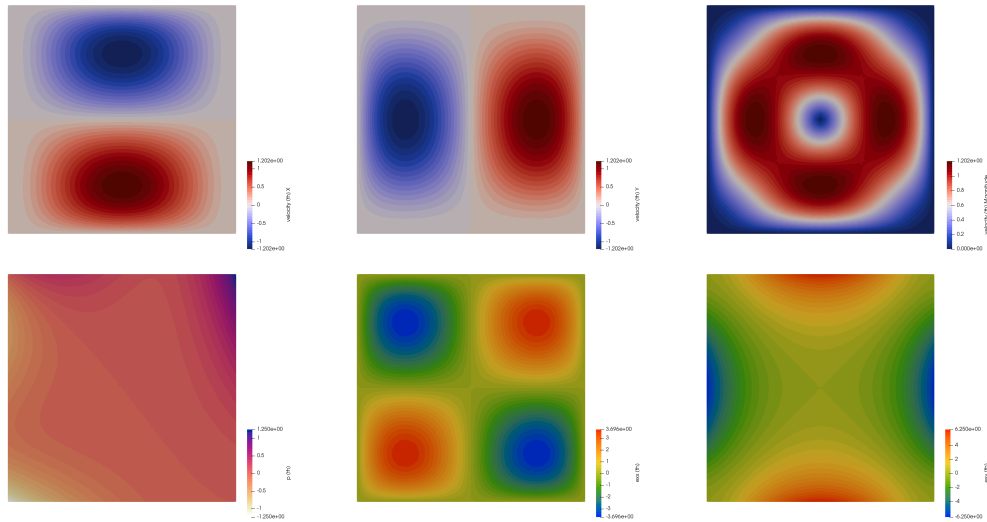
def dexydy(x,y):
    return 200*(6*x**2-6*x+1)*(1-y)*y**2 + 100*(1-x)**2*x**2*(12*y-6) - 200*(6*x**2-6*x+1)*(1-y)**2*y

def deyydy(x,y):
    return -400*x*(2*x**2-3*x+1)*(6*y**2-6*y+1)

def bx(x,y):
    return dpdx_th(x,y)-2*dexxdx(x,y)-2*dexydy(x,y)

def by(x,y):
    return dpdy_th(x,y)-2*dexydx(x,y)-2*deyydy(x,y)

```



### 8.6.11 Analytical benchmark XI - "PPC1"

### 8.6.12 Analytical benchmark XII - "PPC2"

### 8.6.13 Annulus with kinematical b.c.

The domain is a hollow cylinder or inner radius  $R_i = 1$  and outside radius  $R_o = 1$ . Boundary conditions are prescribed both on the inside and the outside with  $\vec{v} = (u, v) = (-y, x)$ , or in polar coordinates  $\vec{v} = r\vec{e}_\theta$ .

The gravity is radial and is set to

$$g_x = -x/r \quad g_z = -y/r$$

where  $r = \sqrt{x^2 + z^2}$ , which in polar coordinates is  $\vec{g} = -\vec{e}_r$ . The viscosity is also set to 1, and the density is given by

$$\rho(r) = r^n$$

where  $n$  is a positive or nul integer. The pressure is set to zero at the outer boundary.

The gradient operator in polar coordinates writes:

$$\vec{\nabla} = \frac{\partial}{\partial r} \vec{e}_r + \frac{1}{r} \frac{\partial}{\partial \theta} \vec{e}_\theta$$

and the Laplacian operator:

$$\Delta = \frac{\partial^2}{\partial r^2} + \frac{1}{r} \frac{\partial}{\partial r} + \frac{1}{r^2} \frac{\partial^2}{\partial \theta^2}$$

Note that in our case we need to take the Laplacian of a vector, and unfortunately the Laplacian of a vector is not the Laplacian of the vector's coordinates in polar coordinates (unlike cartesian coordinates). The Laplacian of a vector is given by<sup>41</sup>

$$\nabla^2 \vec{A} = \nabla(\nabla \cdot \vec{A}) - \nabla \times (\nabla \times \vec{A}) = \begin{pmatrix} \frac{\partial^2 A_r}{\partial r^2} + \frac{1}{r} \frac{\partial A_r}{\partial r} - \frac{1}{r^2} A_r + \frac{1}{r^2} \frac{\partial^2 A_r}{\partial \theta^2} - \frac{2}{r^2} \frac{\partial A_\theta}{\partial \theta} \\ \frac{\partial^2 A_\theta}{\partial r^2} + \frac{1}{r} \frac{\partial A_\theta}{\partial r} - \frac{1}{r^2} A_\theta + \frac{1}{r^2} \frac{\partial^2 A_\theta}{\partial \theta^2} + \frac{2}{r^2} \frac{\partial A_r}{\partial \theta} \end{pmatrix} = \begin{pmatrix} \Delta A_r \\ \Delta A_\theta \end{pmatrix}$$

The Stokes equation writes:

$$\mu \Delta \vec{v} + \rho \vec{g} = \vec{0}$$

The velocity solution is expected to be  $\vec{v} = r \vec{e}_\theta$ . The Stokes equation in polar coordinates then writes:

$$\begin{aligned} -\frac{\partial p}{\partial r} + \Delta v_r + \rho(r)(-1) &= 0 \\ -\frac{1}{r} \frac{\partial p}{\partial \theta} + \Delta v_\theta &= 0 \end{aligned}$$

Since  $\Delta v_\theta = 0$ , then  $\frac{\partial p}{\partial \theta} = 0$  and then the pressure is independent of  $\theta$ , which is what we expect since the density distribution is radial. We then focus on the first equation, and since  $v_r = 0$ , we then obtain:

$$\frac{\partial p}{\partial r} = -\rho(r)$$

- If  $\rho(r) = 1$ , then

$$\frac{\partial p}{\partial r} = -1$$

yields  $p(r) = -r + C$  where  $C$  is a constant determined by means of b.c. ( $p(r=1) = 0$ ) so finally

$$p(r) = 1 - r$$

- If  $\rho(r) = r$ , then

$$\frac{\partial p}{\partial r} = -r$$

so that  $p(r) = -\frac{1}{2}r^2 + C$  and likewise

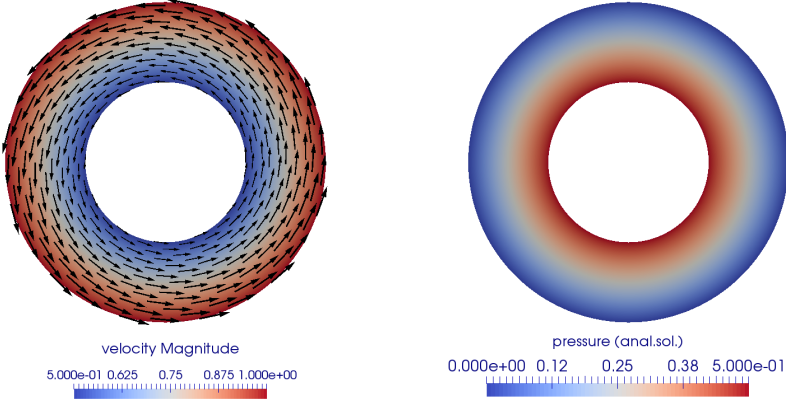
$$p(r) = \frac{1}{2}(1 - r^2)$$

---

<sup>41</sup>[https://en.wikipedia.org/wiki/Vector\\_Laplacian](https://en.wikipedia.org/wiki/Vector_Laplacian)

In general, by taking  $\rho(r) = r^n$  with  $n = 0, 1, \dots$  one arrives to a pressure field given by

$$p(r) = \frac{1}{n+1}(1 - r^{n+1})$$



This benchmark is of course very simple and the fact that the solution is independent of  $\theta$  renders it not so useful. It has successfully been implemented in ELEFANT.

#### 8.6.14 Viscous beam under extension

The domain is a Cartesian box of size  $L_x \times L_y$ . Velocity  $-u_0$  is applied on the left boundary and velocity  $+u_0$  is applied on the right boundary. Bottom and top boundaries are left free. If no vertical velocity is prescribed anywhere there is an obvious nullspace in the solution which is problematic (numerically of course, but also because the solution is then not unique). One might want to set  $v = 0$  at  $y = L_y/2$  on each side for example. The solution to this problem (incompressible Stokes equations) is given by

$$u(x, y) = 2u_0(x/L_x - 1/2) \quad (602)$$

$$v(x, y) = -2u_0L_y/L_x(y/L_y - 1/2) \quad (603)$$

in the absence of gravity. The strain rate tensor is then:

$$\dot{\epsilon} = \begin{pmatrix} \dot{\epsilon}_{xx} & \dot{\epsilon}_{xy} \\ \dot{\epsilon}_{xx} & \dot{\epsilon}_{yy} \end{pmatrix} = \begin{pmatrix} 2u_0/L_x & 0 \\ 0 & -2u_0/L_x \end{pmatrix}$$

and we see that the flow is indeed incompressible as the trace of the strain rate tensor is zero.

The momentum equation is

$$-\vec{\nabla}p + \vec{\nabla} \cdot (2\eta\dot{\epsilon}) = \rho\vec{g}$$

where the viscosity  $\eta$  is constant in space. If gravity is set to zero, we obtain:

$$-\frac{\partial p}{\partial x} = 0 \quad (604)$$

$$-\frac{\partial p}{\partial y} = 0 \quad (605)$$

since the strain rate is constant in space and the divergence operator applied to it returns the zero tensor. We therefore can conclude that pressure should be constant.

Since the top and bottom boundaries are free, we have  $\sigma \cdot \vec{n} = \vec{0}$  on these. The stress tensor is given by  $\sigma = -\mathbf{1} + 2\eta\dot{\epsilon}$  and the normal on the top is  $\vec{n} = (0, +1)$  so that on the top boundary we have

$$-p + 2\eta\dot{\epsilon}_{yy} = 0$$

or,

$$p = 2\eta\dot{\epsilon}_{yy}$$

Note that using the bottom boundary with  $\vec{n} = (0, -1)$  yields the same result.

### 8.6.15 Channel flow with Herschel-Bulkley rheology

We start from the following formulation for the Herschel-Bulkley rheology:

$$\eta_{HB} = \begin{cases} \eta_0 & \dot{\varepsilon}_e \leq \dot{\varepsilon}_0 \\ K\dot{\varepsilon}_e^{n-1} + \frac{\tau_0}{\dot{\varepsilon}_e} & \dot{\varepsilon}_e \geq \dot{\varepsilon}_0 \end{cases}$$

and the limiting viscosity  $\eta_0$  is such that

$$\eta_0 = K\dot{\varepsilon}_0^{n-1} + \frac{\tau_0}{\dot{\varepsilon}_0}$$

We consider a two-dimensional channel in the  $x, y$  plane. The walls are at  $y = 0$  and  $y = H$  with no-slip boundary conditions. In the absence of gravity, the Stokes equation simplify to

$$-\frac{\partial p}{\partial x} + \frac{\partial}{\partial y}(2\eta_{HB}\dot{\varepsilon}_{xy}) = 0 \quad \text{and} \quad \dot{\varepsilon}_{xy} = \frac{1}{2}\frac{\partial u}{\partial y} \quad (606)$$

where we assume the velocity  $\vec{v} = (u(y), 0)$ . It then follows that

$$\dot{\varepsilon}_e = \sqrt{\mathcal{I}_2(\dot{\varepsilon})} = \sqrt{\frac{1}{2}\dot{\varepsilon} : \dot{\varepsilon}} = \sqrt{\frac{1}{2}[(\dot{\varepsilon}_{xx})^2 + (\dot{\varepsilon}_{yy})^2 + (\dot{\varepsilon}_{zz})^2] + (\dot{\varepsilon}_{xy})^2 + (\dot{\varepsilon}_{xz})^2 + (\dot{\varepsilon}_{yz})^2} = \sqrt{\dot{\varepsilon}_{xy}^2} = \left| \frac{1}{2}\frac{\partial u}{\partial y} \right|$$

In the case of a Newtonian fluid, the analytical solution is known and the velocity profile is a parabola with zero velocity on the walls and maximum velocity in the middle. Although the rheology of the fluid is non-linear we assume that a similar velocity profile is expected (although not described by a parabola). We then expect three zones (and we assume that the fluid flows from left to right):

- In the middle, where it is expected that  $\frac{\partial u}{\partial y} = 0$  (at least in one point) because of symmetry. We also therefore expect  $\dot{\varepsilon}_e \leq \dot{\varepsilon}_0$  in this region so that  $\eta_{HB} = \eta_0$ . How thick this region is will be determined later.

Eq. (606) must then be solved

$$\frac{\partial p}{\partial x} = \frac{\partial}{\partial y} \left( 2\eta_{HB} \frac{1}{2} \frac{\partial u}{\partial y} \right) = \eta_0 \frac{\partial^2 u}{\partial y^2} \quad (607)$$

Let us call  $\Pi = \frac{\partial p}{\partial x} < 0$ , then we must solve:

$$\frac{\partial^2 u}{\partial y^2} = \frac{\Pi}{\eta_0}$$

The solution is then of the form

$$u(y)|_{mid} = \frac{1}{2} \frac{\Pi}{\eta_0} y^2 + 2ay + b$$

and

$$\dot{\varepsilon}_{xy}|_{mid} = \frac{1}{2} \frac{\Pi}{\eta_0} y + a$$

We will determine  $a$  and  $b$  later.

- Near the bottom wall, with  $\frac{\partial u}{\partial y} > 0$  so that  $\dot{\varepsilon}_e = +\frac{1}{2} \left( \frac{\partial u}{\partial y} \right)$  and  $\dot{\varepsilon}_e \geq \dot{\varepsilon}_0$ . We solve Eq. (606) again, this time with the non-linear formulation of the viscosity:

$$\begin{aligned} \frac{\partial p}{\partial x} &= \frac{\partial}{\partial y} \left( 2\eta_{HB} \frac{1}{2} \frac{\partial u}{\partial y} \right) \\ &= 2 \frac{\partial}{\partial y} \left[ \left( K\dot{\varepsilon}_e^{n-1} + \frac{\tau_0}{\dot{\varepsilon}_e} \right) \frac{1}{2} \frac{\partial u}{\partial y} \right] \\ &= \frac{\partial}{\partial y} \left[ \left( K \left| \frac{1}{2} \frac{\partial u}{\partial y} \right|^{n-1} + \tau_0 \left| \frac{1}{2} \frac{\partial u}{\partial y} \right|^{-1} \right) \frac{1}{2} \frac{\partial u}{\partial y} \right] \\ &= \frac{\partial}{\partial y} \left[ K \left( \frac{1}{2} \frac{\partial u}{\partial y} \right)^n + \tau_0 \right] \end{aligned} \quad (608)$$

We then must solve:

$$\begin{aligned}\frac{\partial}{\partial y} \left[ K \left( \frac{1}{2} \frac{\partial u}{\partial y} \right)^n + \tau_0 \right] &= \Pi \\ K \left( \frac{1}{2} \frac{\partial u}{\partial y} \right)^n + \tau_0 &= \Pi y + c \\ \left( \frac{1}{2} \frac{\partial u}{\partial y} \right)^n &= \frac{1}{K} (\Pi y + c - \tau_0)\end{aligned}$$

or,

$$\dot{\varepsilon}_{xy}|_{bot} = \frac{1}{2} \frac{\partial u}{\partial y} = \left( \frac{1}{K} (\Pi y + c - \tau_0) \right)^{1/n}$$

so

$$u(y)|_{bot} = 2 \frac{n}{n+1} \frac{K}{\Pi} \left( \frac{1}{K} (\Pi y + c - \tau_0) \right)^{1+1/n} + d$$

- Near the top wall, with  $\frac{\partial u}{\partial y} < 0$  so that  $\dot{\varepsilon}_e = -\frac{1}{2} \left( \frac{\partial u}{\partial y} \right)$  and  $\dot{\varepsilon}_e \geq \dot{\varepsilon}_0$ . We solve yet again Eq. (606):

$$\begin{aligned}\frac{\partial p}{\partial x} &= \frac{\partial}{\partial y} \left( 2\eta_{HB} \frac{1}{2} \frac{\partial u}{\partial y} \right) \\ &= 2 \frac{\partial}{\partial y} \left[ \left( K \dot{\varepsilon}_e^{n-1} + \frac{\tau_0}{\dot{\varepsilon}_e} \right) \frac{1}{2} \frac{\partial u}{\partial y} \right] \\ &= \frac{\partial}{\partial y} \left[ \left( K \left| \frac{1}{2} \frac{\partial u}{\partial y} \right|^{n-1} + \tau_0 \left| \frac{1}{2} \frac{\partial u}{\partial y} \right|^{-1} \right) \frac{1}{2} \frac{\partial u}{\partial y} \right] \\ &= -\frac{\partial}{\partial y} \left[ \left( K \left( -\frac{1}{2} \frac{\partial u}{\partial y} \right)^{n-1} + \tau_0 \left( -\frac{1}{2} \frac{\partial u}{\partial y} \right)^{-1} \right) \left( -\frac{1}{2} \frac{\partial u}{\partial y} \right) \right] \\ &= -\frac{\partial}{\partial y} \left[ K \left( -\frac{1}{2} \frac{\partial u}{\partial y} \right)^n + \tau_0 \right]\end{aligned}\tag{609}$$

We then must solve:

$$\begin{aligned}-\frac{\partial}{\partial y} \left[ K \left( -\frac{1}{2} \frac{\partial u}{\partial y} \right)^n + \tau_0 \right] &= \Pi \\ K \left( -\frac{1}{2} \frac{\partial u}{\partial y} \right)^n + \tau_0 &= -\Pi y + e \\ \left( -\frac{1}{2} \frac{\partial u}{\partial y} \right)^n &= \frac{1}{K} (-\Pi y + e - \tau_0)\end{aligned}$$

which yields

$$\begin{aligned}\dot{\varepsilon}_{xy}|_{top} &= - \left( \frac{1}{K} (-\Pi y + e - \tau_0) \right)^{1/n} \\ u(y)|_{top} &= 2 \frac{n}{n+1} \frac{K}{\Pi} \left( \frac{1}{K} (-\Pi y + e - \tau_0) \right)^{1+1/n} + f\end{aligned}$$

We have 6 integration constants  $a, b, c, d, e, f$  and 6 additional constraints from continuity or boundary conditions:

$$(1) \quad u(0) = 0 \text{ boundary condition} \quad (610)$$

$$(2) \quad u(H) = 0 \text{ boundary condition} \quad (611)$$

$$(3) \quad u(y_1) \text{ must be continuous} \quad (612)$$

$$(4) \quad u(y_2) \text{ must be continuous} \quad (613)$$

$$(5) \quad \dot{\varepsilon}_{xy}(y_1) \text{ must be continuous} \quad (614)$$

$$(6) \quad \dot{\varepsilon}_{xy}(y_2) \text{ must be continuous} \quad (615)$$

**Using symmetry to compute  $a$**  Because of symmetry, we expect  $y_1 = H/2 - \delta$  and  $y_2 = H/2 + \delta$  with  $\delta \neq 0$  (i.e.  $y_1 \neq y_2$ ) and we expect  $u(y_1) = u(y_2)$  so that

$$u(y_1)|_{mid} = \frac{1}{2} \frac{\Pi}{\eta_0} y_1^2 + 2ay_1 + b = \frac{1}{2} \frac{\Pi}{\eta_0} y_2^2 + 2ay_2 + b = u(y_2)|_{mid}$$

or,

$$\frac{1}{2} \frac{\Pi}{\eta_0} (y_1^2 - y_2^2) + 2a(y_1 - y_2) = 0$$

$$\frac{1}{2} \frac{\Pi}{\eta_0} (y_1 - y_2)(y_1 + y_2) + 2a(y_1 - y_2) = 0$$

$$\frac{1}{2} \frac{\Pi}{\eta_0} (y_1 + y_2) + 2a = 0$$

$$\frac{1}{2} \frac{\Pi}{\eta_0} H + 2a = 0$$

and finally we obtain  $a$ :

$$a = -\frac{1}{4} \frac{\Pi}{\eta_0} H$$

Note that we could have obtained the same thing by enforcing that the strain rate at  $y_1$  and  $y_2$  are the opposite of one another. It then follows:

$$u(y)|_{mid} = \frac{1}{2} \frac{\Pi}{\eta_0} y^2 - 2 \frac{1}{4} \frac{\Pi}{\eta_0} Hy + b = \frac{1}{2} \frac{\Pi}{\eta_0} (y^2 - yH) + b$$

and

$$\dot{\varepsilon}_{xy}|_{mid} = \frac{1}{2} \frac{\Pi}{\eta_0} y - \frac{1}{4} \frac{\Pi}{\eta_0} H = \frac{1}{2} \frac{\Pi}{\eta_0} (y - \frac{H}{2})$$

Because of the parabola-like flow profile, we expect the strain rate to be zero in the middle  $y = H/2$ , and positive for  $z_1 < y < H/2$  and negative for  $H/2 < y < z_2$ , which is indeed what we recover ( $\Pi < 0$ ).

**Using bottom boundary condition to obtain  $d$**

$$u(y=0)|_{bot} = 2 \frac{n}{n+1} \frac{K}{\Pi} \left( \frac{1}{K} (c - \tau_0) \right)^{1+1/n} + d = 0$$

so

$$d = -2 \frac{n}{n+1} \frac{K}{\Pi} \left( \frac{1}{K} (c - \tau_0) \right)^{1+1/n}$$

and then

$$u(y)|_{bot} = 2 \frac{n}{n+1} \frac{K}{\Pi} \left[ \left( \frac{1}{K} (\Pi y + c - \tau_0) \right)^{1+1/n} - \left( \frac{1}{K} (c - \tau_0) \right)^{1+1/n} \right]$$

**Using top boundary condition to obtain  $f$**

$$u(y = H)|_{top} = 2 \frac{n}{n+1} \frac{K}{\Pi} \left( \frac{1}{K} (-\Pi H + e - \tau_0) \right)^{1+1/n} + f = 0$$

so

$$f = -2 \frac{n}{n+1} \frac{K}{\Pi} \left( \frac{1}{K} (-\Pi H + e - \tau_0) \right)^{1+1/n}$$

and then

$$u(y)|_{top} = 2 \frac{n}{n+1} \frac{K}{\Pi} \left[ \left( \frac{1}{K} (-\Pi y + e - \tau_0) \right)^{1+1/n} - \left( \frac{1}{K} (-\Pi H + e - \tau_0) \right)^{1+1/n} \right]$$

**computing  $\delta$**  The coordinates of the transitions  $y_1$  and  $y_2$  are the location where the strain rate  $\dot{\varepsilon}_e$  reaches  $\dot{\varepsilon}_0$ . In other words:

$$\dot{\varepsilon}_e|_{mid}(y = y_1) = \dot{\varepsilon}_{xy}|_{mid}(y = y_1) = \frac{1}{2} \frac{\Pi}{\eta_0} \left( y_1 - \frac{H}{2} \right) = \frac{1}{2} \frac{\Pi}{\eta_0} \left( \frac{H}{2} - \delta - \frac{H}{2} \right) = -\frac{1}{2} \frac{\Pi}{\eta_0} \delta = \dot{\varepsilon}_0$$

or,

$$\delta = -\frac{2\dot{\varepsilon}_0 \eta_0}{\Pi}$$

Since  $\Pi < 0$  it adds up and  $\delta > 0$ . We can also write

$$\delta = \frac{2\dot{\varepsilon}_0 \eta_0}{|\Pi|}$$

and we will use throughout what follows:

$$\dot{\varepsilon}_0 = -\frac{1}{2} \frac{\Pi}{\eta_0} \delta$$

**Using strain rate continuity at  $y_1$  to compute  $c$**

$$\begin{aligned} \left( \frac{1}{K} (\Pi y_1 + c - \tau_0) \right)^{1/n} &= \frac{1}{2} \frac{\Pi}{\eta_0} \left( y_1 - \frac{H}{2} \right) = -\frac{1}{2} \frac{\Pi}{\eta_0} \delta \\ \Pi y_1 + c - \tau_0 &= K \left( -\frac{1}{2} \frac{\Pi}{\eta_0} \delta \right)^n \\ c &= K \left( -\frac{1}{2} \frac{\Pi}{\eta_0} \delta \right)^n + \tau_0 - \Pi y_1 \end{aligned}$$

$$c = K \dot{\varepsilon}_0^n + \tau_0 - \Pi y_1$$

$$\begin{aligned} u(y)|_{bot} &= 2 \frac{n}{n+1} \frac{K}{\Pi} \left[ \left( \frac{1}{K} (\Pi y + c - \tau_0) \right)^{1/n+1} - \left( \frac{1}{K} (c - \tau_0) \right)^{1/n+1} \right] \\ &= 2 \frac{n}{n+1} \frac{K}{\Pi} \left[ \left( \frac{1}{K} (\Pi(y - y_1) + K \dot{\varepsilon}_0^n) \right)^{1/n+1} - \left( \frac{1}{K} (K \dot{\varepsilon}_0^n - \Pi y_1) \right)^{1/n+1} \right] \\ &= 2 \frac{n}{n+1} \frac{K}{\Pi} \left[ \left( \frac{\Pi}{K} (y - y_1) + \dot{\varepsilon}_0^n \right)^{1/n+1} - \left( \dot{\varepsilon}_0^n - \frac{\Pi}{K} y_1 \right)^{1/n+1} \right] \\ \dot{\varepsilon}_{xy}|_{bot} &= \left( \frac{1}{K} (\Pi y + c - \tau_0) \right)^{1/n} \\ &= \left( \frac{\Pi}{K} (y - y_1) + \dot{\varepsilon}_0^n \right)^{1/n} \end{aligned}$$

**Using strain rate continuity at  $y_2$  to compute  $e$**

$$\begin{aligned} -\left(\frac{1}{K}(-\Pi y_2 + e - \tau_0)\right)^{1/n} &= \frac{1}{2}\frac{\Pi}{\eta_0}\left(y_2 - \frac{H}{2}\right) = \frac{1}{2}\frac{\Pi}{\eta_0}\delta \\ -\Pi y_2 + e - \tau_0 &= K\left(-\frac{1}{2}\frac{\Pi}{\eta_0}\delta\right)^n \\ e &= K\left(-\frac{1}{2}\frac{\Pi}{\eta_0}\delta\right)^n + \tau_0 + \Pi y_2 \\ \boxed{e = K\dot{\varepsilon}_0^n + \tau_0 + \Pi y_2} \end{aligned}$$

$$\begin{aligned} u(y)|_{top} &= 2\frac{n}{n+1}\frac{K}{\Pi}\left[\left(\frac{1}{K}(-\Pi y + e - \tau_0)\right)^{1/n+1} - \left(\frac{1}{K}(-\Pi H + e - \tau_0)\right)^{1/n+1}\right] \\ &= 2\frac{n}{n+1}\frac{K}{\Pi}\left[\left(-\frac{\Pi}{K}(y - y_2) + \dot{\varepsilon}_0^n\right)^{1/n+1} - \left(-\frac{\Pi}{K}(H - y_2) + \dot{\varepsilon}_0^n\right)^{1/n+1}\right] \\ \dot{\varepsilon}_{xy}|_{top} &= -\left(\frac{1}{K}(-\Pi y + e - \tau_0)\right)^{1/n} \\ &= -\left(-\frac{\Pi}{K}(y - y_2) + \dot{\varepsilon}_0^n\right)^{1/n} \end{aligned}$$

**Using velocity continuity to compute  $b$**  We use  $u(y_1)|_{bot} = u(y_1)|_{mid}$ :

$$\begin{aligned} 2\frac{n}{n+1}\frac{K}{\Pi}\left[\left(\frac{\Pi}{K}(y_1 - y_1) + \dot{\varepsilon}_0^n\right)^{1/n+1} - \left(\dot{\varepsilon}_0^n - \frac{\Pi}{K}y_1\right)^{1/n+1}\right] &= \frac{1}{2}\frac{\Pi}{\eta_0}(y_1^2 - y_1 H) + b \\ 2\frac{n}{n+1}\frac{K}{\Pi}\left[\dot{\varepsilon}_0^{n+1} - \left(\dot{\varepsilon}_0^n - \frac{\Pi}{K}y_1\right)^{1/n+1}\right] &= \frac{1}{2}\frac{\Pi}{\eta_0}y_1(y_1 - H) + b \end{aligned}$$

so

$$b = 2\frac{n}{n+1}\frac{K}{\Pi}\left[\dot{\varepsilon}_0^{n+1} - \left(\dot{\varepsilon}_0^n - \frac{\Pi}{K}y_1\right)^{1/n+1}\right] - \frac{1}{2}\frac{\Pi}{\eta_0}y_1(y_1 - H)$$

**Using velocity continuity to compute  $b$  - AGAIN** This time we use  $u(y_2)|_{top} = u(y_2)|_{mid}$ :

$$\begin{aligned} 2\frac{n}{n+1}\frac{K}{\Pi}\left[\left(-\frac{\Pi}{K}(y_2 - y_2) + \dot{\varepsilon}_0^n\right)^{1/n+1} - \left(-\frac{\Pi}{K}(H - y_2) + \dot{\varepsilon}_0^n\right)^{1/n+1}\right] &= \frac{1}{2}\frac{\Pi}{\eta_0}(y_2^2 - y_2 H) + b \\ 2\frac{n}{n+1}\frac{K}{\Pi}\left[\dot{\varepsilon}_0^{n+1} - \left(-\frac{\Pi}{K}(H - y_2) + \dot{\varepsilon}_0^n\right)^{1/n+1}\right] &= \frac{1}{2}\frac{\Pi}{\eta_0}(y_2^2 - y_2 H) + b \end{aligned}$$

and since  $H - y_2 = H - H/2 - \delta = H/2 - \delta = y_1$  and

$$y_2^2 - y_2 H = y_2(y_2 - H) = (H/2 + \delta)(-y_1) = (-H/2 - \delta)y_1 = (-H + H/2 - \delta)y_1 = (-H + y_1)y_1$$

so that we indeed recover the same  $b$  value as above.

To summarize:

$$\begin{aligned}
u(y)|_{bot} &= 2 \frac{n}{n+1} \frac{K}{\Pi} \left[ \left( \frac{\Pi}{K} (y - y_1) + \dot{\varepsilon}_0^n \right)^{1/n+1} - \left( \dot{\varepsilon}_0^n - \frac{\Pi}{K} y_1 \right)^{1/n+1} \right] \\
u(y)|_{mid} &= \frac{1}{2} \frac{\Pi}{\eta_0} (y^2 - y) + 2 \frac{n}{n+1} \frac{K}{\Pi} \left[ +\dot{\varepsilon}_0^{n+1} - \left( \dot{\varepsilon}_0^n - \frac{\Pi}{K} y_1 \right)^{1/n+1} \right] - \frac{1}{2} \frac{\Pi}{\eta_0} y_1 (y_1 - H) \\
u(y)|_{top} &= 2 \frac{n}{n+1} \frac{K}{\Pi} \left[ \left( -\frac{\Pi}{K} (y + y_2) + \dot{\varepsilon}_0^n \right)^{\frac{1}{n}+1} - \left( -\frac{\Pi}{K} (H + y_2) + \dot{\varepsilon}_0^n \right)^{\frac{1}{n}+1} \right] \\
\dot{\varepsilon}_{xy}|_{bot} &= \left( \frac{\Pi}{K} (y - y_1) + \dot{\varepsilon}_0^n \right)^{1/n} \\
\dot{\varepsilon}_{xy}|_{mid} &= \frac{1}{2} \frac{\Pi}{\eta_0} (y - \frac{H}{2}) \\
\dot{\varepsilon}_{xy}|_{top} &= - \left( -\frac{\Pi}{K} (y + y_2) + \dot{\varepsilon}_0^n \right)^{1/n}
\end{aligned}$$

Rather interestingly we find that  $\tau_0$  does not directly enter the equations above. This can be explained as follows: since we have the relationship

$$\eta_0 = K \dot{\varepsilon}_0^{n-1} + \frac{\tau_0}{\dot{\varepsilon}_0}$$

the parameters  $\eta_0$ ,  $\dot{\varepsilon}_0$ ,  $\tau_0$  and  $K$  cannot be all chosen freely. The viscosity  $\eta_0$  is reached when the strain rate becomes smaller than  $\dot{\varepsilon}_0$ , so these two parameters have a physical meaning. We set  $\eta_0 = 10^{25}$  and  $\dot{\varepsilon}_0 = 10^{-17}$ . When/if  $K$  is zero, then  $\tau_0$  can be interpreted as a yield value for a rigid plastic material so we arbitrarily set it to  $\tau_0 = 10^7$ . Having fixed these parameters we can compute

$$K = \frac{\eta_0 \dot{\varepsilon}_0 - \tau_0}{\dot{\varepsilon}_0^n}$$

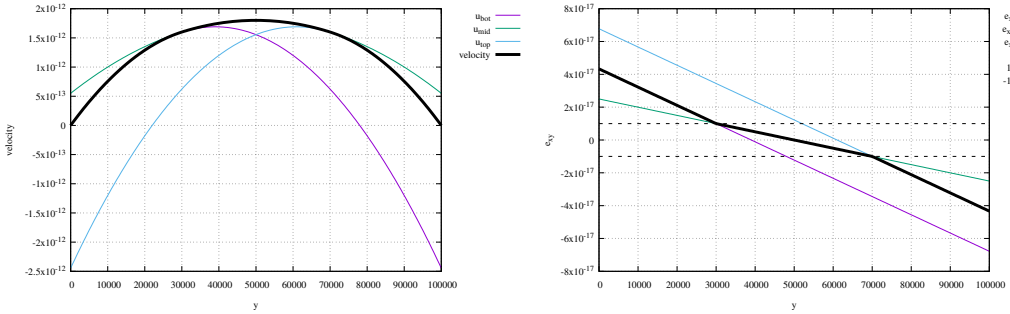
The data used to produce all the following plots is generated by the python program and a gnuplot script to be found in `images/mms/channel_hb/`.

**Let's start simple:**  $n = 1$  In this case the viscosity is given by

$$\eta_{HB} = \begin{cases} \eta_0 & \dot{\varepsilon}_e \leq \dot{\varepsilon}_0 \\ K + \frac{\tau_0}{\dot{\varepsilon}_e} & \dot{\varepsilon}_e \geq \dot{\varepsilon}_0 \end{cases}$$

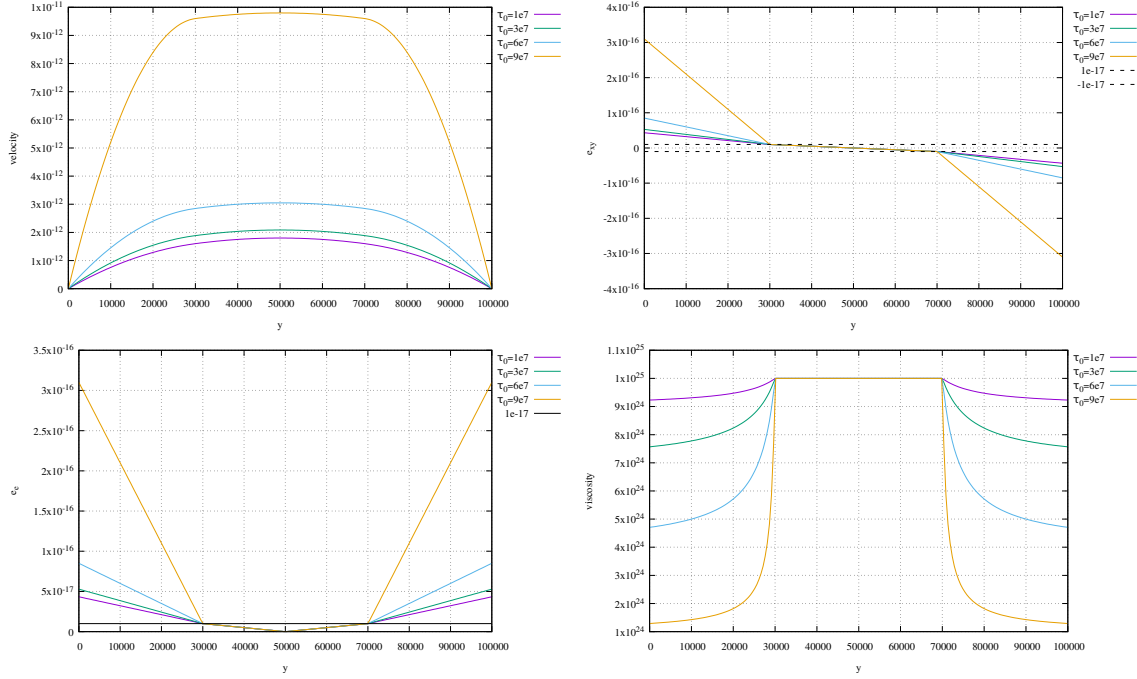
Since  $\dot{\varepsilon}_e = \left| \frac{1}{2} \frac{\partial u}{\partial y} \right|$  then

$$\eta_{HB} = \begin{cases} \eta_0 & \dot{\varepsilon}_e \leq \dot{\varepsilon}_0 \\ K + \frac{2\tau_0}{\left| \frac{\partial u}{\partial y} \right|} & \dot{\varepsilon}_e \geq \dot{\varepsilon}_0 \end{cases}$$



Obtained for  $n = 1$  and  $\tau_0 = 1e7$ . The black lines are the resulting velocity and strain rate profiles obtained by joining the bottom, middle and top functions.

In the following I explore the effect of the  $\tau_0$  value ( $K$  is calculated correspondingly as we have seen before).



## 8.7 Geodynamical benchmarks

Some published numerical experiments have over time become benchmarks for other codes, while some others showcased comparisons between codes. Here is a short list of 'famous' benchmarks' in the computational geodynamics community.

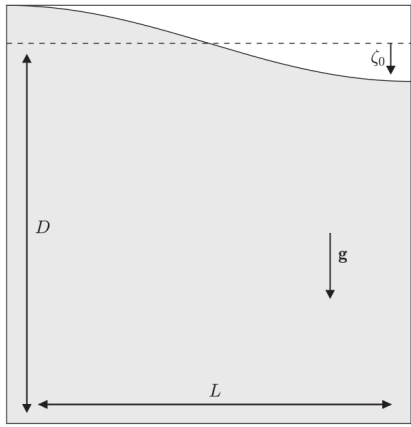
- the plastic brick [1556, 1396, 2089, 1798, 1879, 1690, 2396, 1002, 872]
- 2D Rayleigh-Benard convection (Blankenbach) [209, 2567, 465, 1441, 1584, 2716, 2563, 181, 494] `stone 03`
- 2D Rayleigh-Benard convection, lateral heating, 30+ codes [669]
- 2D Rayleigh-Benard convection with nonlinear rheology [2556, 91]
- 2D Rayleigh-Benard laminar plumes [2687]
- 2D Rayleigh-Taylor convection/instability [2061, 2563, 2762, 2046, 2366, 70, 2492, 243] [104, 2089, 2228, 2451, 562, 1584, 1662, 2716, 2659, 243, 470, 688, 1798] [1690, 893, 666, 633, 664, 91]
- Thin layer entrainment (see Section 8.7.12)
- 3D Rayleigh-Taylor instability [907, 2714]
- subduction problems [2272, 2655, 431]
- numerical sandbox [323, 1690, 332, 1002]
- the Stokes sphere [1523, 91], in visco-plastic fluid [1636, 653]. Finite deformation in and around a fluid sphere [2275, 603].
- the sinking block (sinker) [2528, 431, 953, 974, 1744, 1798, 909, 1690] (see Section 8.7.7)
- multiple sinkers [1746, 1743]
- 1D compression [1841]
- 2D compressible Stokes flow problem [1296, 2499, 1582, 1439, 1652]
- 3D convection at infinite Prandtl number (Busse) [389, 2567, 1969, 1507]
- Free surface evolution [585, 91]
- Love's problem [131]
- Poiseuille flow [851, 897, 2497]
- Couette flow with temperature dependent viscosity [764, 664]
- Couette flow with shear heating [764]
- Poiseuille-Couette flow [893]
- Lid driven cavity [1406, 476, 2280, 855, 983, 238, 1406, 307, 1497, 793]
- Lid driven cavity with analytical solution (see Section 8.7.10)
- Lid driven cavity with nonlinear rheology [176, 2457]
- Wannier flow [2737, 2846, 431]
- bending of elastic plate/beam [431, 225, 2714, 764, 664, 1841, 1640]
- flexure of finite length elastic plate [470]
- thermal diffusion of half-cooling space (see Section 8.7.14)

- thermal diffusion of Gaussian distribution (see compgeo notes, elefant manual)
- stress build-up in Maxwell visco-elastic material [952, 470, 764, 664]
- plastic oedometer test [470]
- SolCx [739, 968, 1744, 664, 91] **Stone** 05
- SolKz [739, 968, 1744, 664, 91] **Stone** 06
- SolVi, inclusion [2279, 1400, 1690, 688, 181, 2451, 2714, 664, 91, 1640] **Stone** 07
- channel flow (nonlinear) [1690, 872, 953, 764] ((**BSc Thesis**))
- indentor, punch problem (see Section 8.7.9). See also [1242, 860, 940] for application. **stone** 08
- relaxation of sinusoidal topography [585, 2197]
- single layer visco-elastic folding [2262, 2714]
- Three-dimensional folding of an embedded viscous layer in pure shear [845]
- dam-break problem [1812, 86, 1623, 1551, 1211, 34, 1068, 1202, 104]
- hot blob problem [381, 909] (see Section 8.7.8)
- viscous(-elastic) flow around a cylinder in a channel (see Section ??)
- Infinite plate with a circular hole [2848, 2094]
- Semi-infinite elastic half plane with a circular hole [2695]
- Slope stability for elasto-plastic materials [2094]
- Time-dependent flow in an annulus [926] (see Section 8.7.5)
- Convection in 2D-box [926] (see Section 8.7.6)
- Onset of convection [91]
- Polydiapirism [2762, 91]
- Slab detachment benchmark (see Section 8.7.16)
- Hollow sphere benchmark [2530]
- Annulus benchmark [91], [2041]
- Viscosity grooves benchmark [91]
- Latent heat benchmark [91]
- Layered flow with viscosity contrast [91] (see Section 8.7.17)
- Brittle thrust wedges benchmark [332, 91]
- 2D linear viscous subduction [2272, 1002]
- mantle convection in 3D spherical shell [2112, 1299, 2909, 2850, 2430, 467, 2905, 1373, 2814, 635, 58, 1650]
- Benchmark of 3D numerical models of subduction against a laboratory experiment [1779]
- 3D subduction [1985]
- heat flow around a cylinder (see Section 8.7.13)
- Laplace equation on a semi infinite plate (see Section 8.7.15)

- 2D Stokes flow over cavity [2056]
- fractal networks of shear bands [2047]
- square plate with a crack subjected to a horizontal tensile traction [1640]
- analytical solution for solitary porosity waves [553]
- analytical solution for solitary wave of magma [620] and refs therein
- Stokes flow caused by the motion of a rigid sphere close to a viscous interface [623]
- Deformation caused by a closed vertical volcanic pipe [223]
- Mantle convection with reversing mobile plates [1471]
- A comparison of mantle convection models featuring plates [2412]
- Elastic material in simple shear (see Section 8.7.18)
- Elastic material in pure shear (see Section 8.7.19)
- Uniform strip load on elastic material (see Section 8.7.20)
- Linear Stability Analysis for Thermal Convections in Spherical Shells [2858]
- Channel flow [1700]
- Visco half-space loading [1155]
- Nakiboglu and Lambeck (1982) has cylindrical load on variety of rheologies [1912]
- Jull and McKenzie (1996) [1362] parabolic load on viscoelastic half-space (and melt fractions)
- Squeezing flow between moving parallel plates [1092]
- generalized half-plane and half-space Cerruti [1957, 2916]
- Analytical Solutions of Displacements Produced by spherically-shaped Internal Overpressure [941]

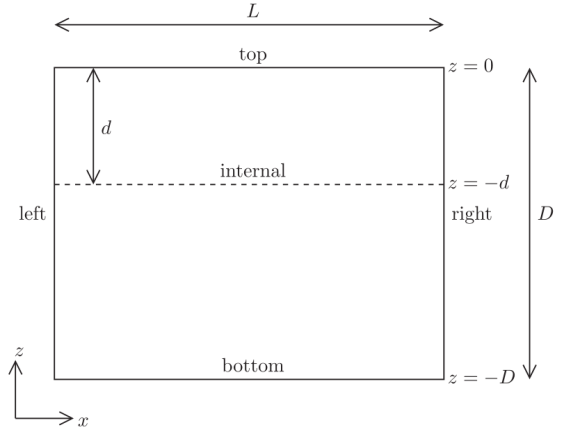
### 8.7.1 Relaxation of sinusoidal topography

Following Kramer et al. [1503, Section 3.1.1] and [2197] the benchmark consists of the relaxation of surface topography in a two-dimensional Cartesian box with an isoviscous fluid. Free slip boundary conditions are imposed on the sides and bottom of the domain. The setup is as follows:



Taken from [2197]. Setup for the free surface relaxation benchmark.

For the tests  $\rho = \eta = g = L = D = 1$  and  $\xi_0 = 0.005$ .



Taken from [1503].  $D = 3 \cdot 10^6$ ,  $\eta = 10^{21}$ ,  $\rho = 4500$ ,  $g = 10$ ,

$\xi_0 = 10^3$ m, and  $L = D/4, D/2, D, 2D, 4D$ .

and the infinitesimal sinusoidal perturbations to the free surface is given by

$$\xi(x, t = 0) = \xi_0 \cos\left(\frac{2\pi nx}{L}\right)$$

where  $n$  is a wavenumber which is an integer multiple of  $1/2$  (taken to be  $1/2$  exactly in both cases).

### 8.7.2 the plastic brick

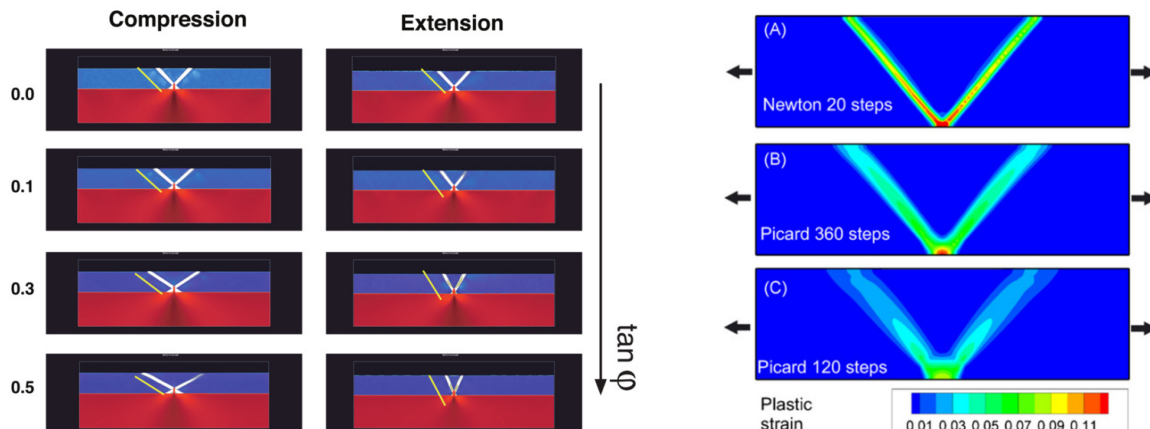


Relevant Literature[1134, 1845, 1556, 1396, 764, 2089, 1798, 1690, 2396, 1002, 872, 91]

Pretty much all of the brick-type (elasto-)visco-plastic experiments in the literature introduce a weak seed at the bottom of the domain to seed deformation (the shear bands will ultimately stem from it). Dimensioned and dimensionless experiments have been carried out, with or without elastic behaviour, with or without adaptive mesh refinement, with first order and second order quadrilateral elements or Taylor-Hood triangles, with or without Newton algorithm, in extension and compression, with or without time-stepping, with or without viscous lower layer.

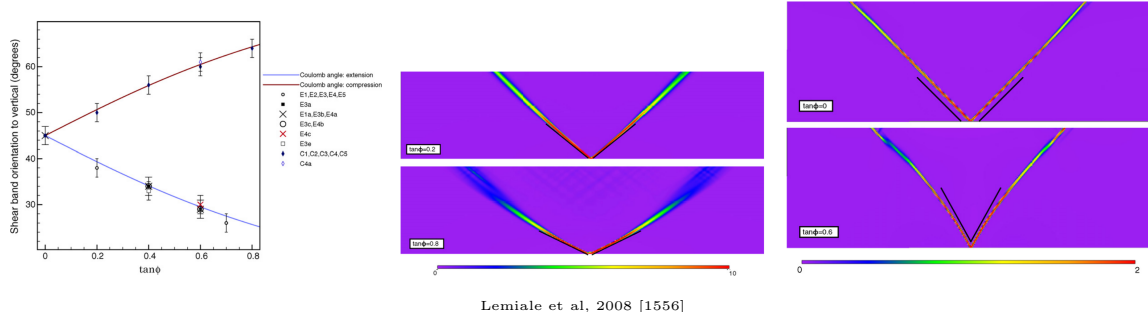


Moresi & Mühlhaus, 2006 [1844]

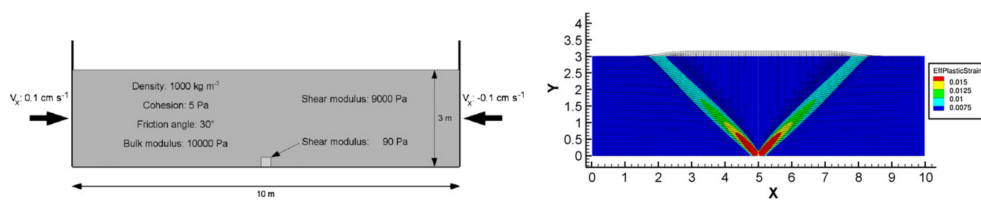


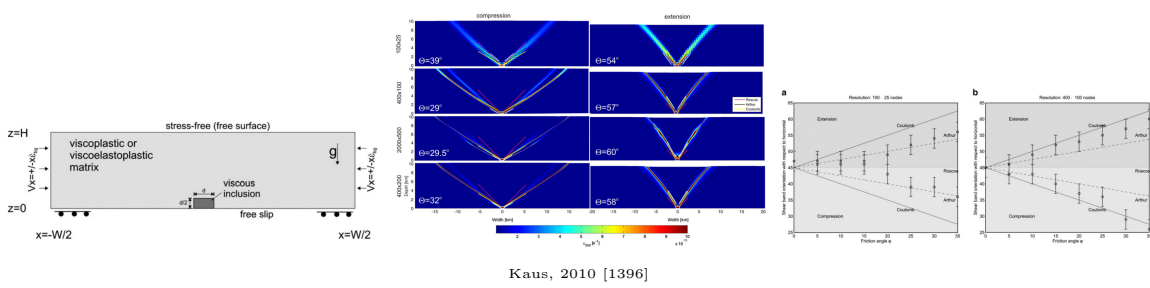
Moresi et al, 2007 [1845]

Popov et al, 2008 [2054]

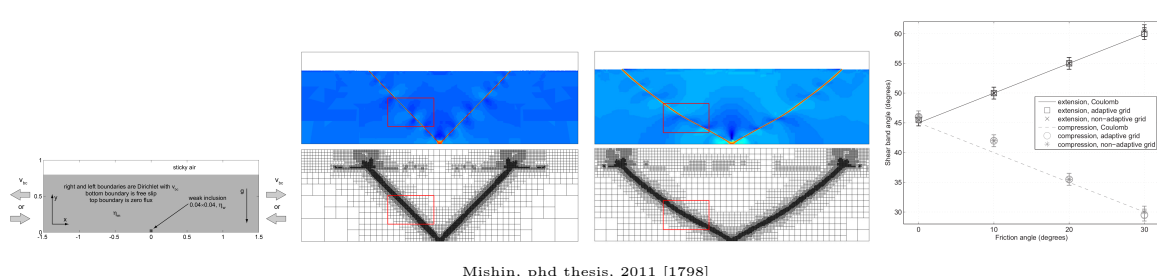


Lemiale et al, 2008 [1556]

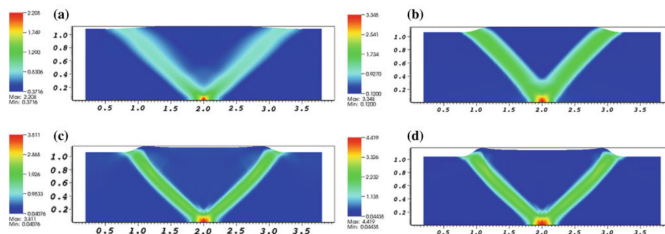




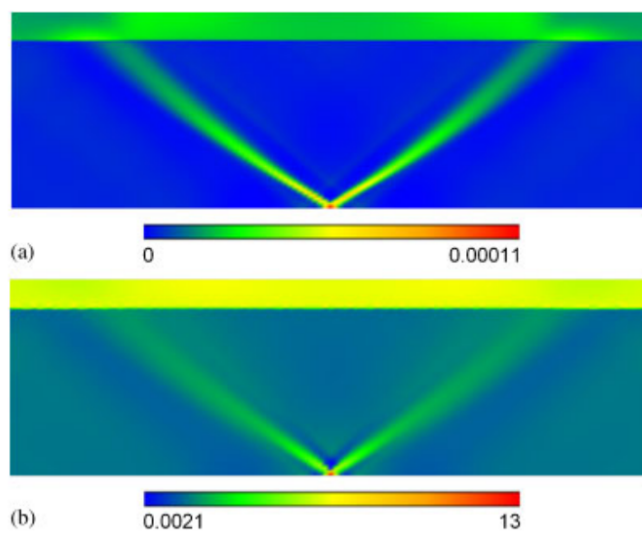
Kaus, 2010 [1396]



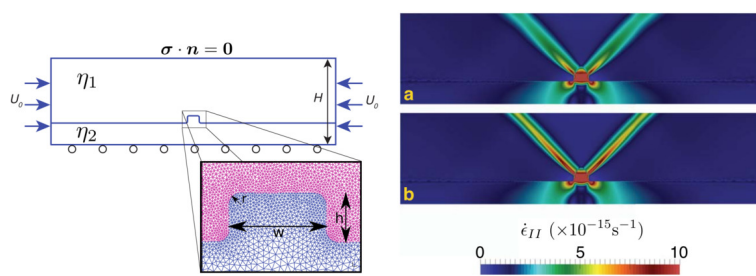
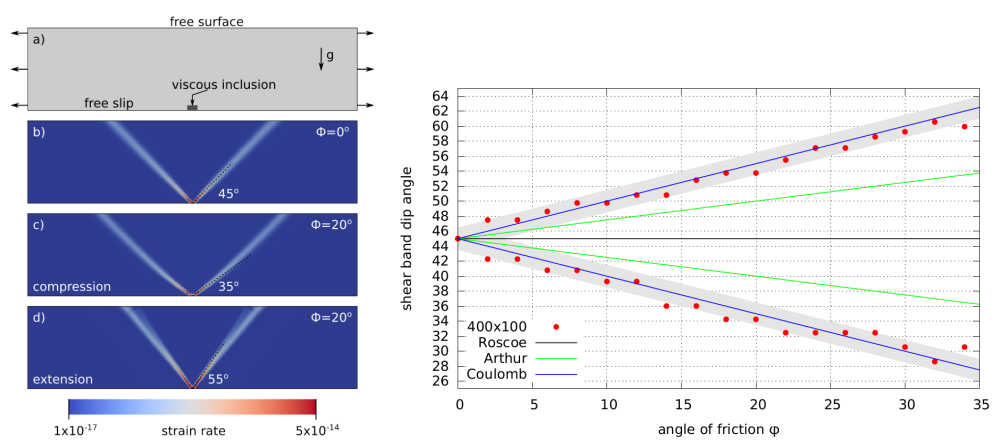
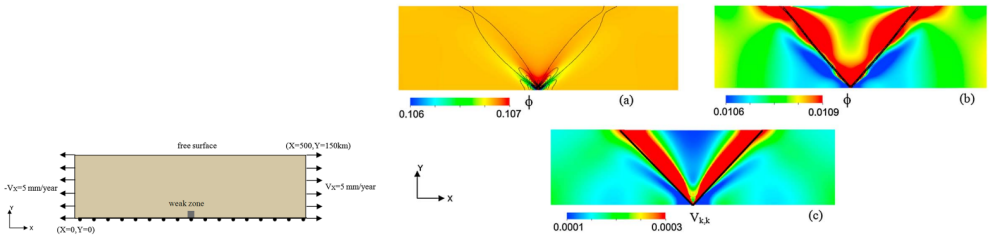
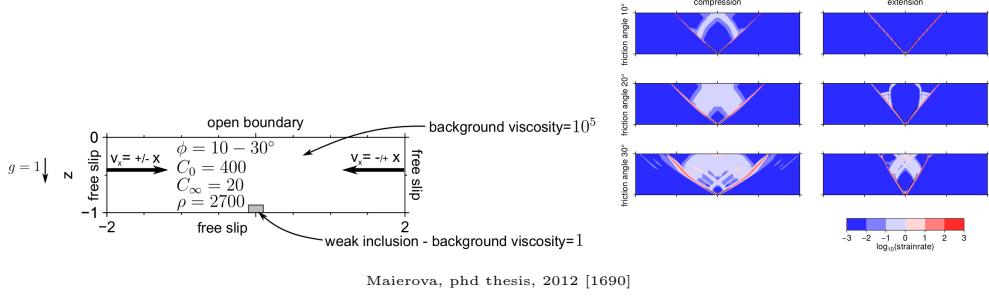
Mishin, phd thesis, 2011 [1798]

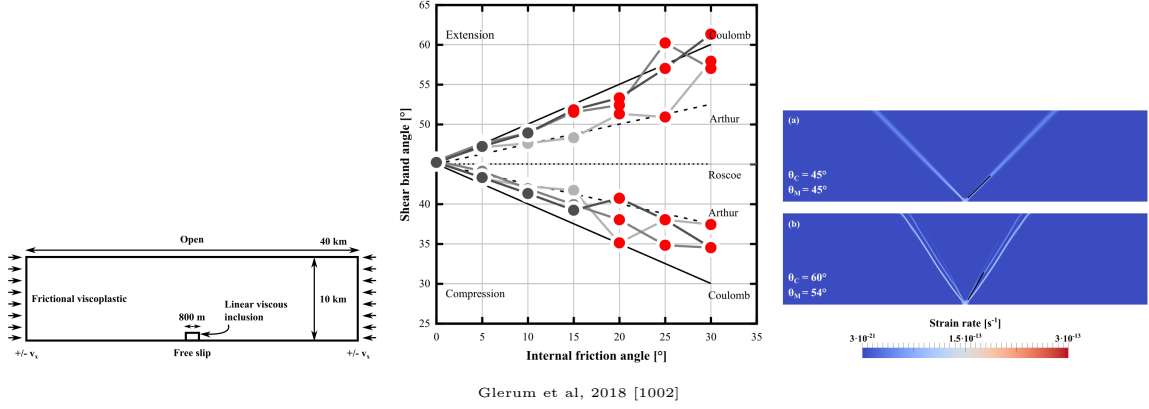


Mühlhaus et al., 2011 [1879].

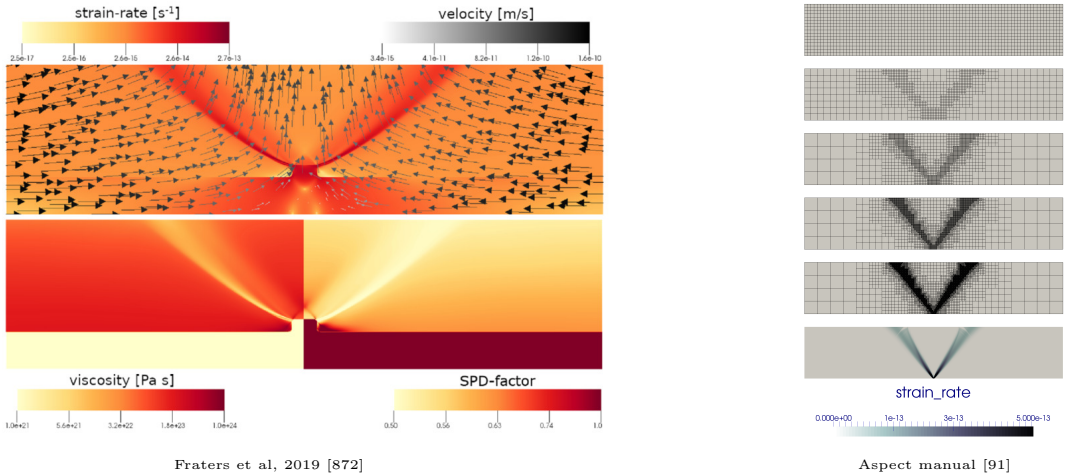


Lemiale et al., 2011 [1558].





Glerum et al, 2018 [1002]



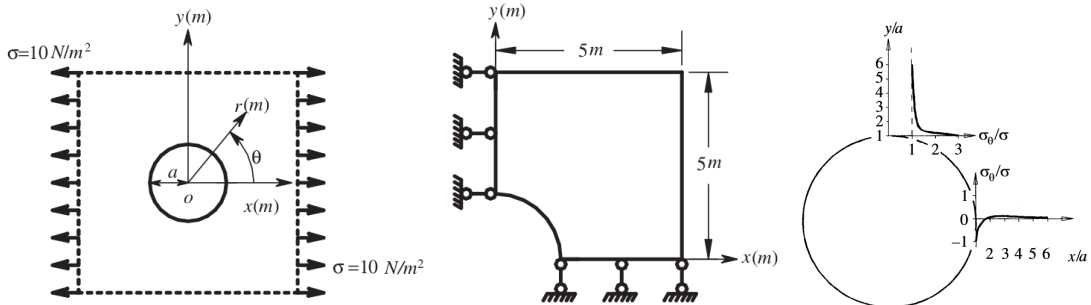
Fraters et al, 2019 [872]

Aspect manual [91]

### 8.7.3 Infinite plate with a circular hole [2094]

(MSc Thesis)

An infinite plate with a circular hole of radius  $a$  is subjected to a unidirectional tensile load of  $\sigma$  in the  $x$  direction as shown in the figure. In this case, only one quarter of the domain is analysed due to symmetry along  $x$  and  $y$  axis.



Left: An infinite plate with a circular hole subjected to unidirectional tension and its quarter model with symmetric conditions imposed on the left and bottom edges. Right: Tangential stress distribution for  $\theta = 0$  and  $\theta = \pi/2$ . [2857]

The inner boundary of the hole is traction free and the right edge was imposed with the tractions based on the analytical solutions. The left edge is constrained in the  $x$  direction and the bottom edge is constrained in the  $y$  direction, respectively. The plane stress condition is considered and the parameters are: Young modulus  $E = 3e7$  MPa, Poisson Ratio  $\nu = 0.3$ , Load  $\sigma = 10 N/m^2$ ,  $a = 1m$ .

The analytical stress components for this problem are

$$\sigma_{xx}(x, y) = \sigma \left( 1 - \frac{a^2}{r^2} \left( \frac{3}{2} \cos 2\theta + \cos 4\theta \right) + \frac{3a^4}{2r^4} \cos 4\theta \right) \quad (616)$$

$$\sigma_{yy}(x, y) = -\sigma \left( \frac{a^2}{r^2} \left( \frac{1}{2} \cos 2\theta - \cos 4\theta \right) - \frac{3a^4}{2r^4} \cos 4\theta \right) \quad (617)$$

$$\sigma_{xy}(x, y) = -\sigma \left( \frac{a^2}{r^2} \left( \frac{1}{2} \sin 2\theta + \sin 4\theta \right) + \frac{3a^4}{2r^4} \sin 4\theta \right) \quad (618)$$

Note that [2094] cites [444] which cites the book [2857, p772] which cites [319] for the solution!

there are discrepancies between [2094] and [444]

Following [2857], it can be shown, from linear elasticity, that the tangential stress throughout the plate is given by

$$\sigma_\theta = \frac{\sigma}{2} \left[ 1 + \frac{a^2}{r^2} - \left( 1 + 3 \frac{a^4}{r^4} \right) \cos 2\theta \right]$$

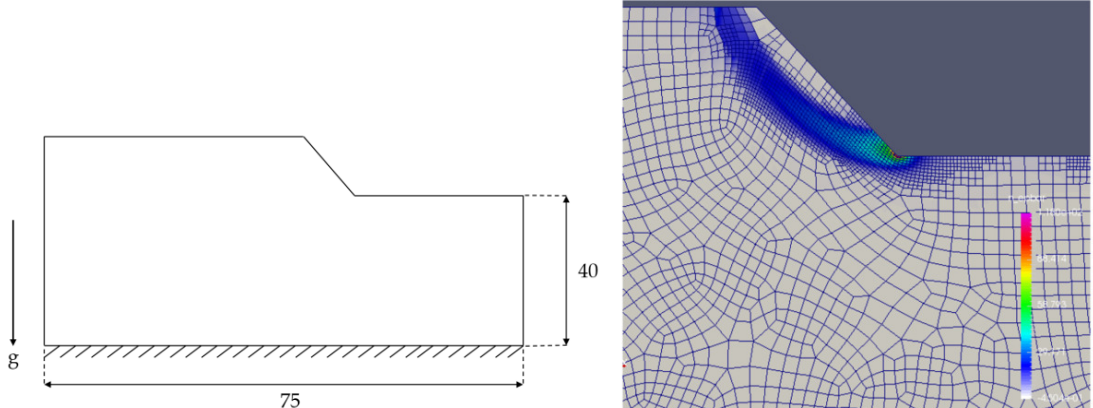
The maximum stress is  $\sigma_\theta = 3\sigma$  at  $r = a$  and  $\theta = \pm\pi/2$ . Along the surface of the hole, the tangential stress is  $-\sigma$  at  $y = 0$  and  $\theta = \pi$ , and increases, as  $\theta$  increases, to  $3\sigma$  at  $\theta = \pi/2$  and  $\theta = 3\pi/2$ .

#### 8.7.4 Slope stability for elasto-plastic materials a la [2094]

(MSc Thesis)

The bottom of the domain is constrained and the model is subjected to gravitational load. The material properties considered are

Young modulus 20e3 MPa, Poisson Ratio 0.49, Constitutive law Mohr-Coulomb (friction angle  $\phi = 20^\circ$ , dilatancy angle  $\phi = 20^\circ$ , cohesion  $c=50$ Mpa).



Left: Slope stability problem setup; Right: Adaptive Refinement based on Plasticity Indicator

#### 8.7.5 Time-dependent benchmark in an annulus

This benchmark is presented in Gassmöller et al [926]. The domain is a 2D annulus with inner and outer radii  $R_1 = 1$  and  $R_2 = 2$ , respectively. In this situation, the incompressible isothermal Stokes equations and their solution can be expressed in a cylindrical coordinate system in terms of the radius  $r$  and the azimuthal angle  $\theta$ . The viscosity is set to  $\eta = 1$ , and the density is given by

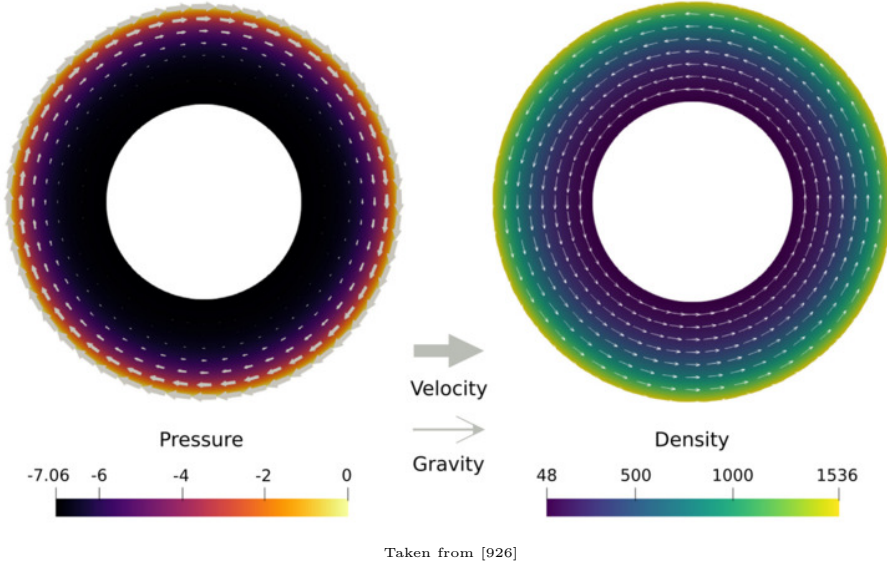
$$\rho(r, \theta) = 48r^5 \quad (619)$$

The gravity vector is set to

$$\vec{g}(r, \theta) = \frac{r^3}{384} \vec{e}_r + \vec{e}_\theta \quad (620)$$

Note that this gravity vector is not the gradient of a gravity potential and consequently not physical. The Stokes system can then be solved using a separation of variables approach and yields

$$\vec{v} = -r^7 \vec{e}_\theta \quad p(r, \theta) = \frac{r^9}{72} - \frac{512}{72} \quad (621)$$



Rather importantly, this benchmark was arrived at by means of a stream function (see Section 8.34)  $\psi(r, \theta) = F(r)G(\theta)$  with  $F(r) = r^8/8$  and  $G(\theta) = 1$ .

### 8.7.6 Convection in 2D-box

We start from the following stream function (see Section 8.34):

$$\psi(x, y) = \frac{1}{\pi} \sin \pi x \sin \pi y \quad (622)$$

which yields:

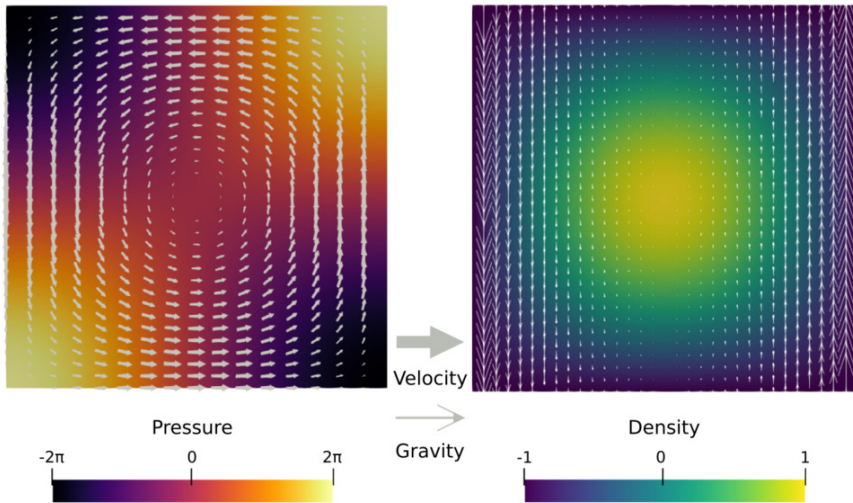
$$\begin{aligned} u(x, y) &= \frac{\partial \psi}{\partial y} = \sin \pi x \cos \pi y \\ v(x, y) &= -\frac{\partial \psi}{\partial x} = -\cos \pi x \sin \pi y \end{aligned} \quad (623)$$

The pressure field is

$$p(x, y) = 2\pi \cos(\pi x) \cos(\pi y) \quad (624)$$

with

$$\rho(x, y) = \sin(\pi x) \sin(\pi y) \quad g_y = -4\pi^2 \frac{\cos(\pi x)}{\sin(\pi x)} \quad (625)$$



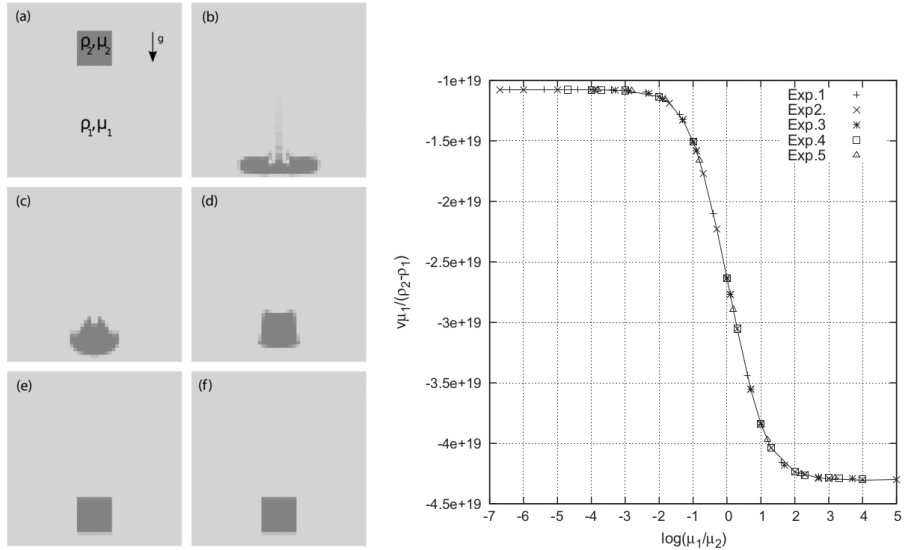
$$\begin{aligned}
v_{rms} &= \sqrt{\frac{1}{L_x L_y} \int_0^1 \int_0^1 (u^2 + v^2) dx dy} \\
&= \sqrt{\int_0^1 \int_0^1 (\sin^2(\pi x) \cos^2(\pi y) + \cos^2(\pi x) \sin^2(\pi y)) dx dy} \\
&= \sqrt{\int_0^1 \sin^2(\pi x) dx \cdot \int_0^1 \cos^2(\pi y) dy + \int_0^1 \cos^2(\pi x) dx \cdot \int \sin^2(\pi y) dy} \\
&= \sqrt{\frac{1}{2} \frac{1}{2} + \frac{1}{2} \frac{1}{2}} \\
&= \frac{\sqrt{2}}{2} \\
&\simeq 0.70711...
\end{aligned} \tag{626}$$

### 8.7.7 The sinker problem

This experiment is not a benchmark stricto sensu since there is no analytical solution. However, it is widely used in the technical literature because of its simple setup and since it allows to test solving strategies. Also, it can conveniently be carried out in both two and three dimensions.

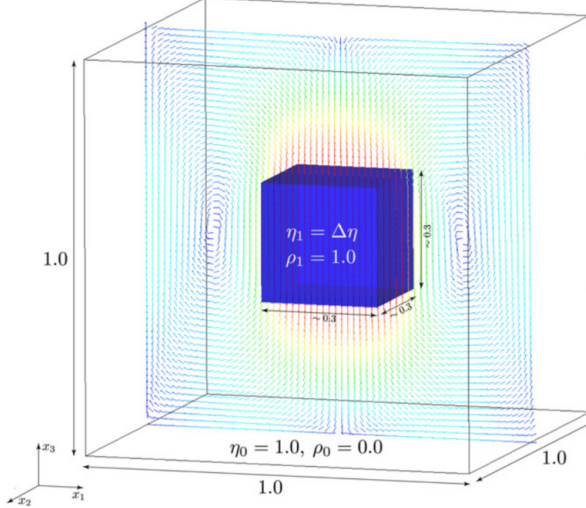
**In two dimensions** The time dependent version of the experiment is for instance to be found in Gerya [953] and the same is repeated in Thieulot [2528].

This simple benchmark provides challenging numerical experiments dealing with large viscosity variations within the simulation domain. It consists of a bulk of fluid 1 ( $\eta_1, \rho_1$ ) in which a block of fluid 2 ( $\eta_2, \rho_2$ ) falls under its own weight. The domain is a square of size  $L_x = L_y = 500$  km and the block is initially centred at point ( $x = 250$  km,  $y = 400$  km) with size  $100 \times 100$  km. Free slip boundary conditions are imposed on all sides of the domain. In [2528] five experiments have been conducted:  $\eta_1 = 10^{20}$  Pa.s,  $\rho_2 = 3220$  kg/m<sup>3</sup>;  $\eta_1 = 10^{21}$  Pa.s,  $\rho_2 = 3300$  kg/m<sup>3</sup>;  $\eta_1 = 10^{22}$  Pa.s,  $\rho_2 = 6600$  kg/m<sup>3</sup>;  $\eta_1 = 10^{23}$  Pa.s,  $\rho_2 = 3300$  kg/m<sup>3</sup>;  $\eta_1 = 10^{24}$  Pa.s,  $\rho_2 = 9900$  kg/m<sup>3</sup>, while in all experiments the density of the surrounding fluid is  $\rho_1 = 3200$  kg/m<sup>3</sup> and the viscosity of the block is varied between  $10^{19}$  and  $5 \cdot 10^{27}$  Pa.s.



Left:  $\eta_1 = 10^{21}$  Pa.s,  $\rho_2 = 3300$  kg/m<sup>3</sup>. (a) Initial setup; (b)  $\eta_1 = 10^{21}$  Pa.s at time  $t = 10$  Myrs; (c)  $\eta_1 = 10^{22}$  Pa.s at time  $t = 20$  Myrs; (d)  $\eta_1 = 10^{23}$  Pa.s at time  $t = 20$  Myrs; (e)  $\eta_1 = 10^{25}$  Pa.s at time  $t = 20$  Myrs; (f)  $\eta_1 = 10^{27}$  Pa.s at time  $t = 20$  Myrs. Right: Velocity measurements as a function of the viscosity contrast between surrounding medium and block for all experiments. Taken from [2528]

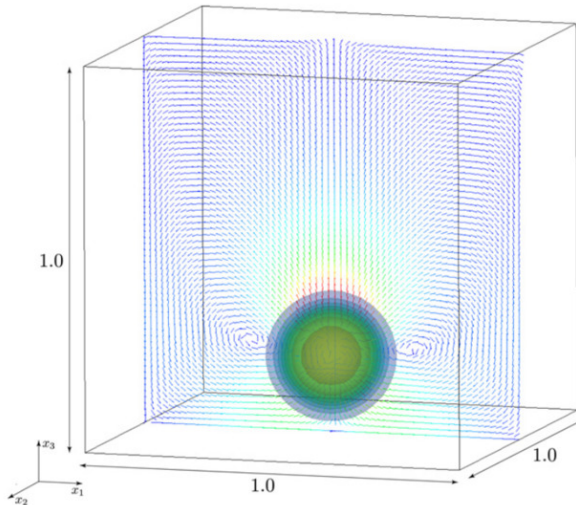
**In three dimensions** Let us look at the sinker experiment from Furuichi et al [909]: The domain is the unit box the origin at the center of the box. A cube with a viscosity  $\eta_1 = \Delta\eta$  and density  $\rho_1 = 1$  was placed at the middle of the domain defined by  $-0.15 \leq x, y, z \leq 0.15$ . The material surrounding the cube has the properties  $\eta_0 = 1$  and  $\rho_0 = 0$ . The body force of the momentum equation was taken as  $(0, 0, -\rho g)$  with  $g = 1$ . Along all walls on the domain, free-slip boundary conditions were employed.



Simulation setup for the 3D falling block (SINKER) problem. The vectors represent computed flow. Taken from [909]

### 8.7.8 The hot blob problem

This is a very similar setup as the 3D sinker from the same authors with higher but more diffusive variation of viscosity. The body force is given by  $(0, 0, \beta T)$  and where the temperature field  $T$  is defined by  $T = \exp(-\gamma(x^2 + y^2 + (z - 0.3)^2))$  with the constant parameters  $\beta = 10^6$  and  $\gamma = 200$ . The temperature-dependent viscosity  $\eta = \exp(-\alpha T)$  is employed with the parameter for viscosity contrast  $\alpha$ .

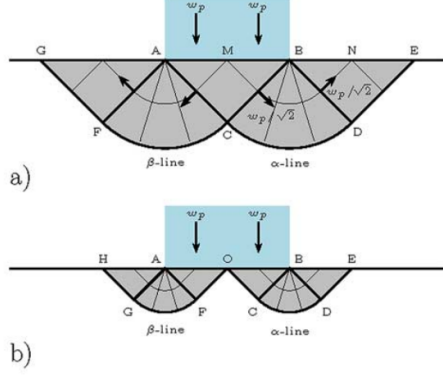


Simulation setting of BLOB problem. Isosurface and vectors represent temperature field and computed flow respectively. Taken from [909]

### 8.7.9 The punch/indentor problem in 2D

The punch benchmark is one of the few boundary value problems involving plastic solids for which there exists an exact solution. Such solutions are usually either for highly simplified geometries (spherical or axial symmetry, for instance) or simplified material models (such as rigid plastic solids) [1366].

In this experiment, a rigid punch indents a rigid plastic half space; the slip line field theory gives exact solutions as shown hereunder:

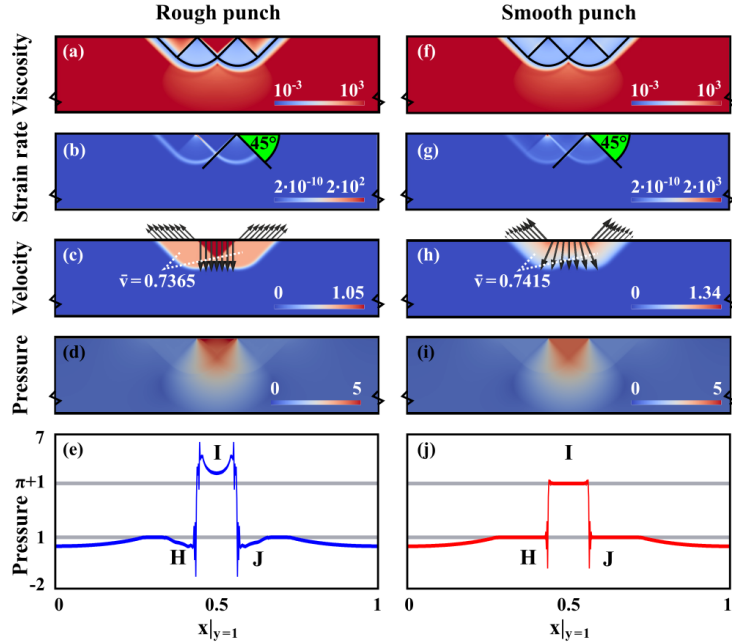


Two-dimensional rigid punch indenting a rigid plastic half space. (a) Prandtl's rigid plastic solution; (b) Hills solution. Taken from [2533]

The plane strain formulation of the equations and the detailed solution to the problem were derived in the Appendix of [2533] and are also presented in [945] and in [246, Chapt.6]. The two dimensional punch problem has been extensively studied numerically for the past 40 years [2938, 2059, 2937, 2940, 491, 490, 1255, 2859, 322, 2091, 1002] and has been used to draw a parallel with the tectonics of eastern China in the context of the India-Eurasia collision [2507, 1816, 782] or the European Alps [2130]. It is also worth noting that it has been carried out in one form or another in series of analogue modelling articles concerning the same region, with a rigid indenter colliding with a rheologically stratified lithosphere [2006, 650, 1355].

Numerically, the one-time step punch experiment is performed on a two-dimensional domain of purely plastic von Mises material. Given that the von Mises rheology yield criterion does not depend on pressure, the density of the material and/or the gravity vector is set to zero. Sides are set to free slip boundary conditions, the bottom to no slip, while a vertical velocity  $(0, -v_p)$  is prescribed at the top boundary for nodes whose  $x$  coordinate is within  $[L_x/2 - \delta/2, L_x/2 + \delta/2]$ .

The analytical solution predicts that the angle of the shear bands stemming from the sides of the punch is  $\pi/4$ , that the pressure right under the punch is  $1 + \pi$ , and that the velocity of the rigid blocks on each side of the punch is  $v_p/\sqrt{2}$  (this is simply explained by invoking conservation of mass).



The punch benchmark results after 500 nonlinear iterations for a rough punch (left column) and a smooth punch (right column). (a,f) Viscosity field with analytical slip lines. (b,g) Strain rate norm  $\dot{\epsilon}_e$  with measured shear band angles. (c,h) Velocity magnitude with velocity vectors along the surface of the domain. (d,i) Pressure field. (e,j) Pressure along the surface of the domain (colored line) and analytical solution values  $\pi + 1$  and 1 (grey lines).

Taken from [1002]

**Remark.** This benchmark is often mentioned or used in the context of bearing capacity, footings, limit state design/analysis [1786, 2919, 1036, 1038, 1552, 2332].

### 8.7.10 Lid driven cavity with analytical solution

This comes from [776](section 3.1.4). The velocity is prescribed to be

$$\vec{v} = (2y(1-x^2); -2x(1-y^2))$$

with a domain given by  $\Omega = [-1 : 1] \times [-1 : 1]$ . The strainrate tensor is then given by:

$$\dot{\epsilon} = \begin{pmatrix} -4xy & -x^2 + y^2 \\ -x^2 + y^2 & 4xy \end{pmatrix}$$

The Stokes equation is then:

$$-\frac{\partial p}{\partial x} + 2\eta(-4y + 2y) = \rho g_x \quad (627)$$

$$-\frac{\partial p}{\partial y} + 2\eta(-2x + 4x) = \rho g_y \quad (628)$$

where we assume the viscosity  $\eta = 1$  to be constant in space. Assuming  $g_x = 0$ , the first equation is

$$\frac{\partial p}{\partial x} = -4y$$

i.e.

$$p(x, y) = -4yx + f(y)$$

Inserting this in the second equation:

$$4x - f'(y) + 4x = \rho g_y$$

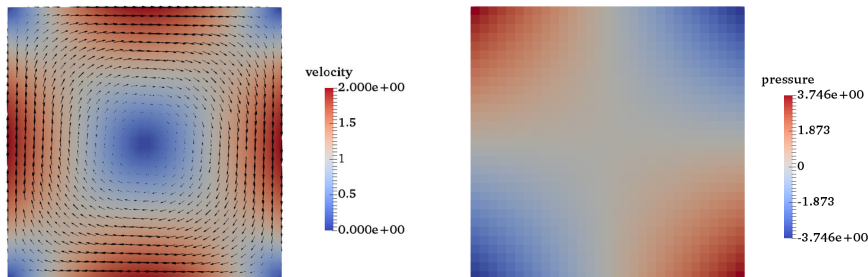
or,

$$-f'(y) + 8x = \rho g_y$$

Assuming  $g_y = -1$ , we get  $\rho = -8x$  and then  $f'(y) = 0$  so  $f(y) = C$  where  $C$  is a constant. Finally the pressure is given by:

$$p(x, y) = -4yx + C$$

We add the following requirement:  $\int_{\Omega} p(x, y) d\Omega = 0$  so that  $C = 0$ .



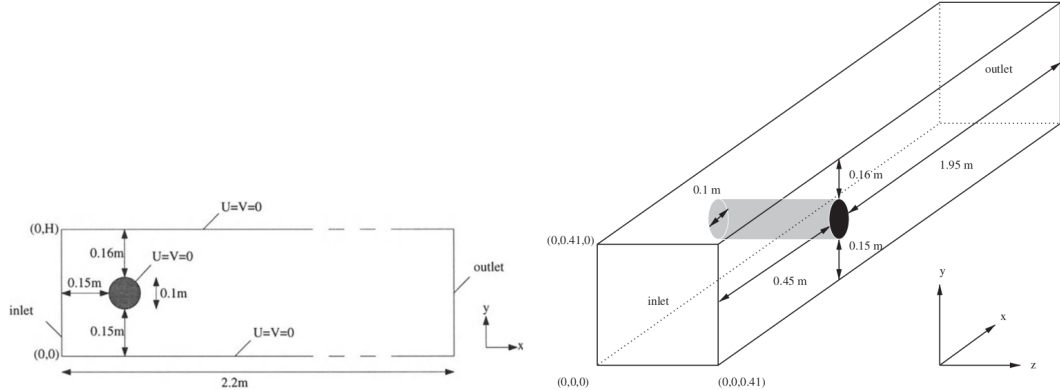
$$\begin{aligned}
 v_{rms}^2 &= \frac{1}{\Omega} \int_{\Omega} (u^2 + v^2) d\Omega \\
 &= \frac{1}{4} \int_{-1}^{+1} \int_{-1}^{+1} (u^2 + v^2) dx dy \\
 &= \frac{1}{4} \int_{-1}^{+1} \int_{-1}^{+1} [4y^2(1-x^2)^2 + 4x^2(1-y^2)^2] dx dy \\
 &=
 \end{aligned} \tag{629}$$

finish vrms calculation of benchmark

### 8.7.11 Flow around a cylinder

??

There are many variants of this problem: 2D [2582], 3D [1352]. Many studies focus on Navier-Stokes flow since the cylinder generates vortices at high Reynolds numbers. Steady state solutions at low Re are shown here<sup>42</sup>. Note the interesting benchmark for 2D visco-elastic flow in [181].



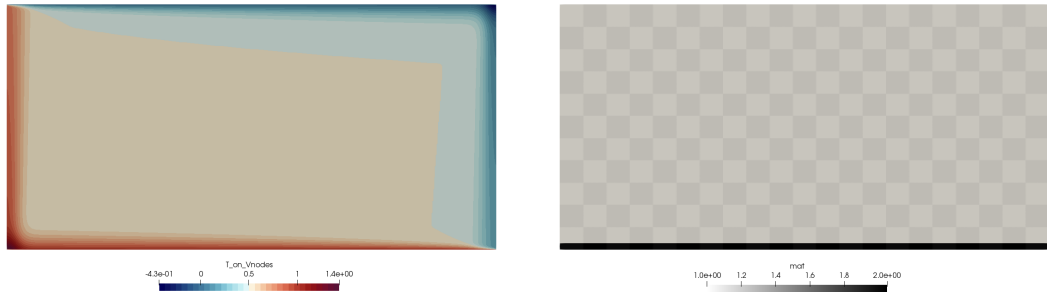
Left: taken from [2582]; Right: taken from [1352]

Relevant Literature: [2465]

### 8.7.12 Thin layer entrainment

) This problem is a simulation to study the amount of entrainment by thermal convection of a dense, thin layer at the bottom of the model [2659]. To the author's knowledge only two other publications [2492, 2672] have presented results pertaining to this benchmark. The results shown here after are obtained with my ELEFANT code using the particle-in-cell technique.

The box is  $2 \times 1$ , and contains two fluids:



Fluid 1 has a density  $\rho_1 = 1$  and a viscosity  $\eta = 1$ . Fluid 2 is heavier ( $\rho_2 = \rho_1 + \Delta\rho$ ) but has the same viscosity. Both fluids have a thermal expansion coefficient  $\alpha = 10^{-10}$ , a thermal conductivity  $k = 1$ , and a heat capacity coefficient  $c_p = 1$ . Fluid 2 is placed at the bottom of the box ( $0 \leq y \leq 0.025$ ).

This experiment is parameterised by the thermal Rayleigh number  $Ra = 300,000$  and the compositional Rayleigh number  $Ra_c = 450,000$  which are defined as follows:

$$Ra_T = \frac{\alpha \rho g \Delta T L_y^3}{\kappa \eta} = \frac{\alpha \rho^2 g \Delta T L_y^3 c_p}{k \eta} = \alpha g \quad (630)$$

$$Ra_c = \frac{\Delta \rho g L_y^3}{\kappa \eta} = \frac{\rho \Delta \rho g L_y^3 c_p}{k \eta} = \Delta \rho g \quad (631)$$

<sup>42</sup>up of the test and data measurement

where I have used the relationship  $\kappa = k/\rho c_p$ .  $B$  is defined as  $B = Ra_T/Ra_c$  so The gravity acceleration is therefore set to  $g = Ra/\alpha$  and this yields  $\Delta\rho = Ra_c/g = BRa_T/g = B \times \alpha$ .

Free-slip boundary conditions are imposed on all sides of the domain. Temperature boundary conditions are  $T(x, y = 0) = 1$  and  $T(x, y = 1) = 0$ . The analytical initial temperature field is given by

$$T(x, y) = T_u(x, y) + T_l(x, y) + T_r(x, y) + T_s(x, y) - \frac{3}{2} \quad (632)$$

where

$$\begin{aligned} T_u(x, y) &= \frac{1}{2} \operatorname{erf} \left( \frac{1-y}{2} \sqrt{\frac{u_0}{x}} \right) \\ T_l(x, y) &= 1 - \frac{1}{2} \operatorname{erf} \left( \frac{y}{2} \sqrt{\frac{u_0}{L_x - x}} \right) \\ T_r(x, y) &= \frac{1}{2} + \frac{Q}{2\sqrt{\pi}} \sqrt{\frac{u_0}{y+1}} \exp \left( -\frac{x^2 u_0}{4y+4} \right) \\ T_s(x, y) &= \frac{1}{2} - \frac{Q}{2\sqrt{\pi}} \sqrt{\frac{u_0}{2-y}} \exp \left( -\frac{(L_x-x)^2 u_0}{8-4y} \right) \end{aligned} \quad (633)$$

with

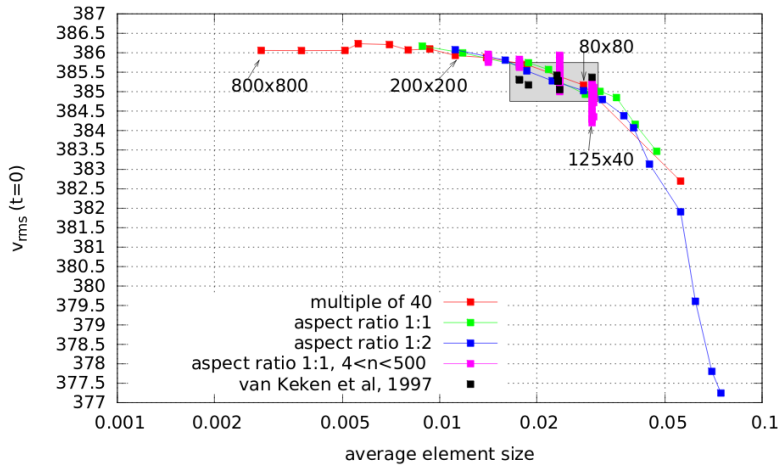
$$u_0 = \frac{L_x^{7/3}}{(1+L_x^4)^{2/3}} \left( \frac{Ra}{2\sqrt{\pi}} \right)^{2/3} \quad Q = 2\sqrt{\frac{L_x}{\pi u_0}} \quad (634)$$

Using  $L_x = 2$ ,  $Ra = 3 \times 10^5$ , one gets  $u_0 \simeq 1469.315$  and  $Q \simeq 0.0416305$ .

Given the small thickness of the bottom layer, it seems quite legitimate to investigate the influence of grid resolution on the simulation. I have therefore looked at the initial root mean square velocity measurement as a function of the element diagonal value (a proxy for the average resolution in the case where elements are not square).

Results are confirm that the element size plays a non negligible role at startup on the dynamics of the system. Superimposed on the figure are the measurements provided by Prof. van Keken (black squares in the gray box). They agree well with my measurements but also indicate that none of the authors in the original study ran the experiment at a high-enough resolution to start with (their results were therefore most likely resolution dependent).

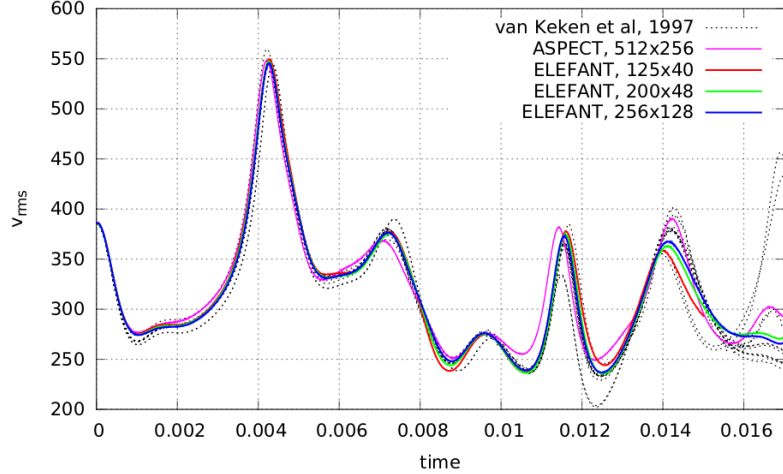
We see that the number of markers per element at startup is critical at (very) low resolution but that it does not lead to significant velocity variations at high resolution.



Thin layer entrainment experiment: root mean square velocity measurements at  $t = 0$  as a function of the element diagonal size. The red square points correspond to resolutions where the number of elements in each direction is a multiple of 40 (i.e.  $L_y/d$ ), so that no element would contain a mix of fluids 1 and 2. Pink points correspond to cases where the number of markers within each element was varied between 4 and 500 (random spatial distribution). Taken from [2529]

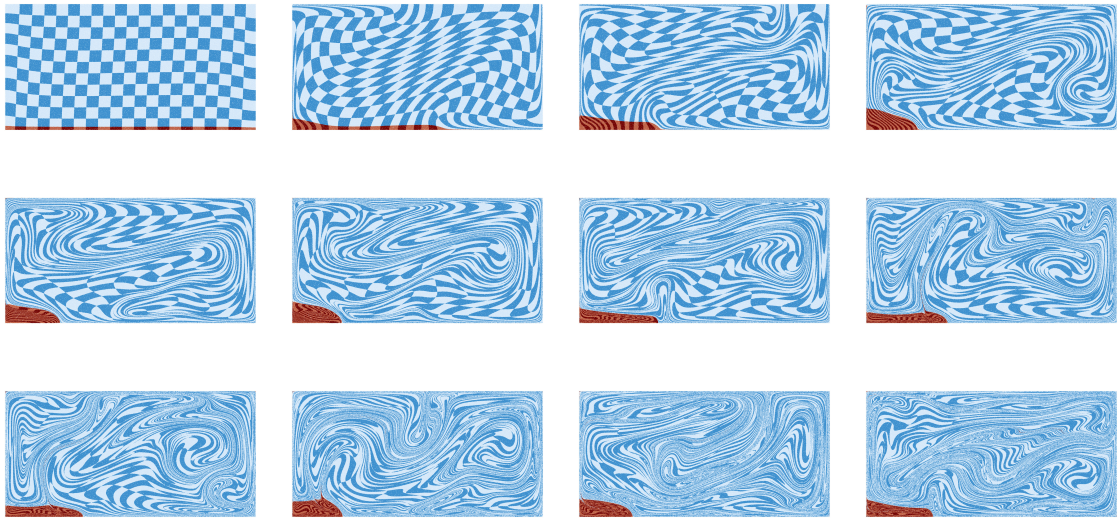
Looking at the root mean square velocity measurements, we see that the measurements done with ELEFANT agree nicely with those presented in [2659]. Past  $t \sim 0.015$ , the curves diverge clearly across

all codes and authors, so I only need to focus the comparison for times  $t < 0.015$ . For the three tested resolutions, measurements agree well and fall within the grey curves representing all results of van Keken et al. Additional tests have been carried out concerning the value of the Courant number (0.1 to 0.25) and the initial number of markers per element (100 or 200) and these parameters led to extremely similar results.



Thin layer entrainment experiment. Root mean square velocity as a function of time. All results presented in van Keken et al. (1997) are collapsed in dashed lines. All simulations were run with an initial marker density of 100 markers per element and with a Courant number of 0.25. Taken from [2529].

As observed in van Keken et al., the dense layer is first swept into the lower left corner. Thermal instabilities then further develop in an asymmetrical way and entrain the dense material. Past  $t \simeq 0.015$  the system becomes more and more chaotic with markers being randomly mixed in the system in a non-orderly fashion.



marker distribution as obtained with ELEFANT for grid 240x120, init\_marker\_density=7, random distribution, CFL=0.25, rkmethod=2, m.to.q=2. Unpublished.

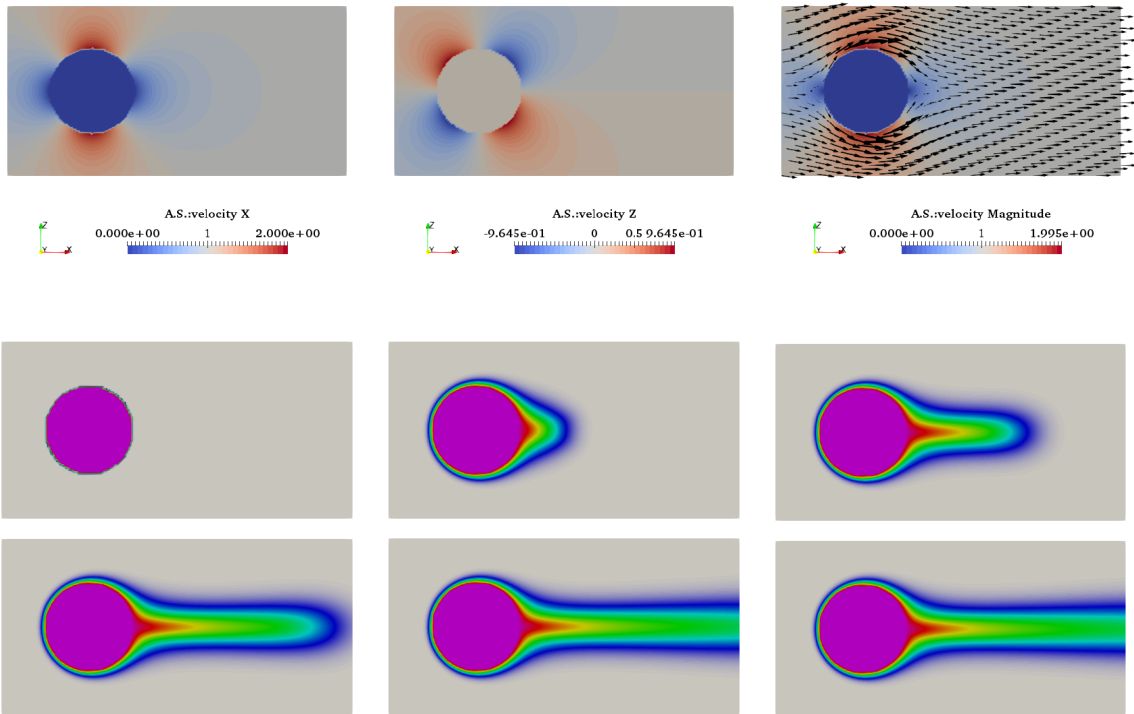
### 8.7.13 Heat flow around a cylinder

The domain is a 2D Cartesian box of size 8x4. The Stokes equations are not solved and the following velocity is prescribed:

$$u(x, y) = U_\infty \left( 1 - \frac{x^2 - y^2}{(x^2 + y^2)^2} \right) \quad (635)$$

$$v(x, y) = -2U_\infty \frac{xy}{(x^2 + y^2)^2} \quad (636)$$

Boundary conditions are as follows:  $T = 0$  is imposed at the top and bottom of the domain.  $T = 1$  is imposed inside a disc centered at (2,2) with radius 1. Further:  $k = 0.01$ ,  $c_p = 1$ ,  $\rho = 1$ , CFL number is 0.1.



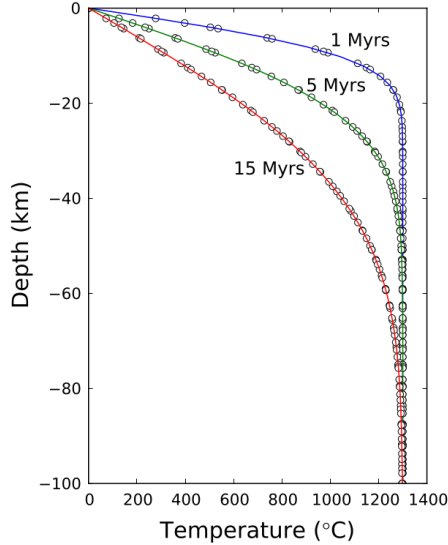
Time evolution of the temperature field. Results obtained with ELEFANT (unpublished)

### 8.7.14 Thermal diffusion of half-cooling space

This is a simple 1D experiment which solution is (for instance) available in Turcotte & Schubert [2581] and is also presented in [470].

The domain is 100km deep.  $T_0 = 0^\circ\text{C}$  is prescribed at the surface and  $T_m = 1300^\circ\text{C}$  is prescribed at the bottom. The initial temperature is  $T(y) = 1300^\circ\text{C}$ . The material is characterised by  $\rho = 1000\text{kg/m}^3$ ,  $C_p = 1000\text{J/kg/K}$ ,  $k = 1\text{J/m/K}$ . The time-dependent solution is given by:

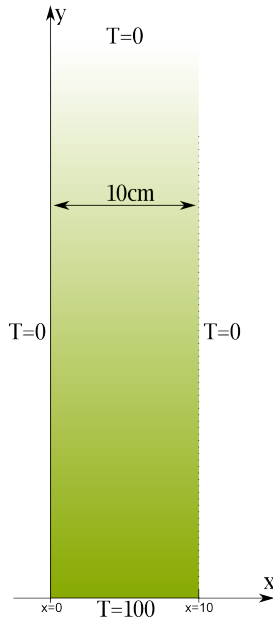
$$T(y, t) = T_0 + (T_0 - T_m) \operatorname{erf} \left( \frac{y}{2\sqrt{kt/\rho C_p}} \right) \quad (637)$$



Thermal diffusion of half space cooling plate. The temperature profiles in the analytical solution at 1, 5, and 15 Myrs are plotted in solid lines. The results from DynEarthSol2D are plotted in circles. Taken from [470]

### 8.7.15 Laplace equation on a semi infinite plate

) This experiment is based on a 2nd year mathematics lecture I give at Utrecht University. One wishes to solve the Laplace equation for temperature on the following plate subject to the indicated boundary conditions:



The temperature satisfies the 2D Laplace equation inside the plate:

$$\frac{\partial^2 T}{\partial x^2} + \frac{\partial^2 T}{\partial y^2} = 0 \quad (638)$$

We could try to solve the equation by using a tentative solution of the form:

$$T(x, y) = \theta(x)\Phi(y) \quad (639)$$

We do not *know* the solution is of this form.

We substitute (2) into (1) and obtain:

$$\Phi \frac{\partial^2 \theta}{\partial x^2} + \theta \frac{\partial^2 \Phi}{\partial y^2} = 0$$

Dividing by  $\theta\Phi$  gives:

$$\frac{1}{\theta} \frac{\partial^2 \theta}{\partial x^2} + \frac{1}{\Phi} \frac{\partial^2 \Phi}{\partial y^2} = 0$$

Separation of variables: we say that each term is a constant because the first term is a function of  $x$  only and the second a function of  $y$  only. We then write

$$\frac{1}{\theta} \frac{\partial^2 \theta}{\partial x^2} = - \frac{1}{\Phi} \frac{\partial^2 \Phi}{\partial y^2} = -k^2$$

where  $k$  is called the separation constant. This leads to

$$\begin{aligned} \frac{\partial^2 \theta}{\partial x^2} + k^2 \theta &= 0 \\ \frac{\partial^2 \Phi}{\partial y^2} - k^2 \Phi &= 0 \end{aligned}$$

- The solution to the first one is  $\theta(x) = \sin kx$  or  $\theta(x) = \cos kx$
- The solution to the second one is  $\Phi(y) = e^{ky}$  or  $\Phi(y) = e^{-ky}$

The general solution writes:

$$T(x, y) = \theta(x)\Phi(y) = \left\{ \begin{array}{l} \sin kx \\ \cos kx \end{array} \right\} \left\{ \begin{array}{l} e^{ky} \\ e^{-ky} \end{array} \right\}$$

We can now use the b.c. to find the solution to the Laplace equation.

- Since  $T \rightarrow 0$  when  $y \rightarrow \infty$  then  $e^{ky}$  unacceptable.
- Since  $T = 0$  when  $x = 0$  then  $\cos kx$  unacceptable.

so

$$T(x, y) = \sin(kx) e^{-ky}$$

We finally use  $T = 0$  at  $x = 10$  which leads to  $10k = n\pi$ , i.e.:

$$T(x, y) = \sin\left(\frac{n\pi x}{10}\right) e^{-n\pi y/10}$$

 Problem: the solution does not satisfy  $T(x, 0) = 100$ . However, a linear combination of solutions is still a solution ! Let's find such a combination which satisfies the b.c. at  $y = 0$  :

$$T(x, y) = \sum_{n=1}^{\infty} b_n \sin\left(\frac{n\pi x}{10}\right) e^{-n\pi y/10}$$

We impose then  $T(x, 0) = 100$ :

$$100 = \sum_{n=1}^{\infty} b_n \sin\left(\frac{n\pi x}{10}\right)$$

This is the Fourier sine series of  $f(x) = 100$  with  $l = 10$  (chapter 7.9 of Boas).

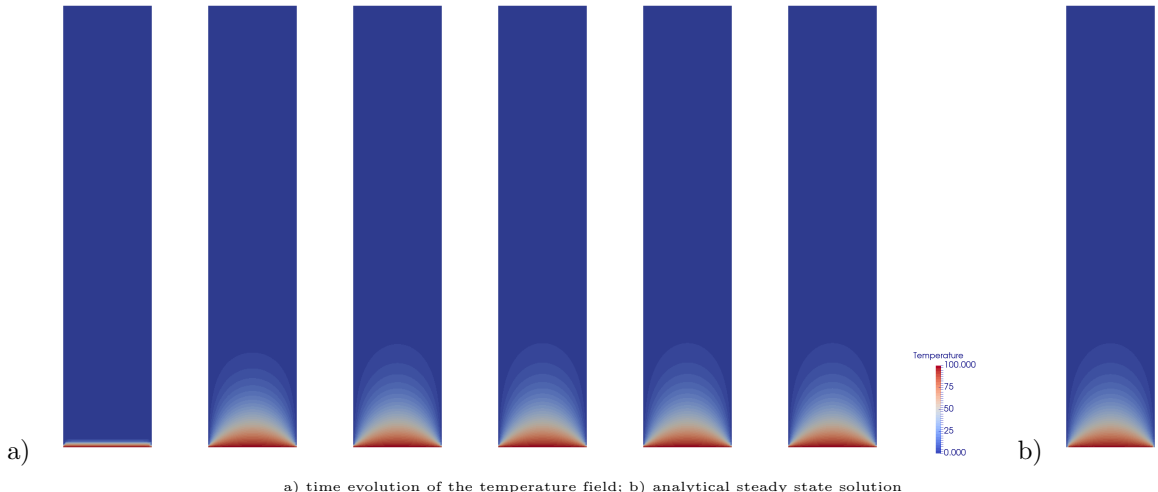
The coefficient  $b_n$  is then given by

$$b_n = \frac{2}{l} \int_0^l f(x) \sin \frac{n\pi x}{l} dx = \frac{2}{10} \int_0^{10} 100 \sin \frac{n\pi x}{10} dx = \begin{cases} 400/n\pi & \text{odd } n \\ 0 & \text{even } n \end{cases}$$

Finally (!):

$$T(x, y) = \frac{400}{\pi} \left( e^{-\pi y/10} \sin\left(\frac{\pi x}{10}\right) + \frac{1}{3} \sin\left(\frac{3\pi x}{10}\right) e^{-3\pi y/10} + \dots \right)$$

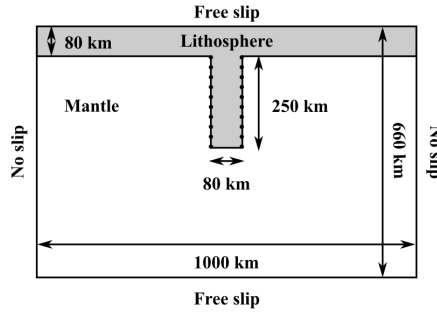
The simulation has been run with a 10x50 domain. All coefficients of the temperature equation are set to 1, and the Stokes equation is not solved. The timestep is fixed to  $dt = 0.1$ . Resolution is 32x160.



a) time evolution of the temperature field; b) analytical steady state solution

### 8.7.16 Slab detachment benchmark

[2258, 91, 1002]



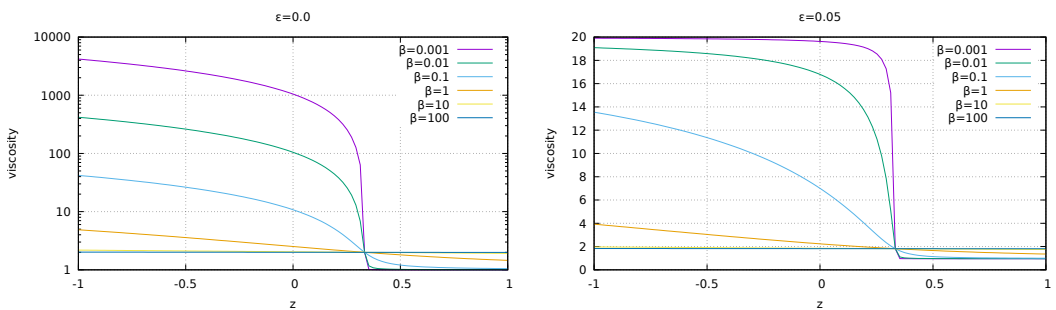
The detachment benchmark model setup of Schmalholz [2258]: a symmetric system of nonlinear viscous lithosphere with a vertical slab extending into a linear viscous mantle. The top and bottom boundaries are free slip, while the vertical boundaries are no slip. Taken from [1002].

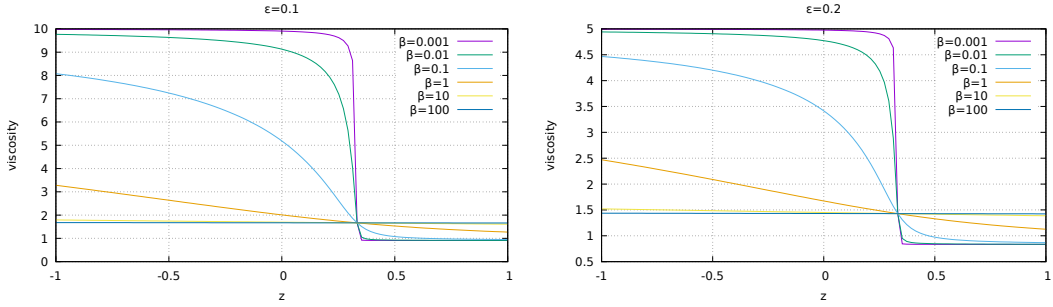
### 8.7.17 Layered flow with viscosity contrast

The idea behind this benchmark is to construct an analytical solution to the incompressible Stokes equation in the case where the viscosity field showcases a viscosity contrast at location  $y = y_0$  whose amplitude and width can be controlled. The viscosity is defined as

$$\eta(y) = \frac{1}{\frac{1}{\pi} \tan^{-1}\left(\frac{y-y_0}{\beta}\right) + 1/2 + \epsilon}$$

where  $\beta$  and  $\epsilon$  are parameters.





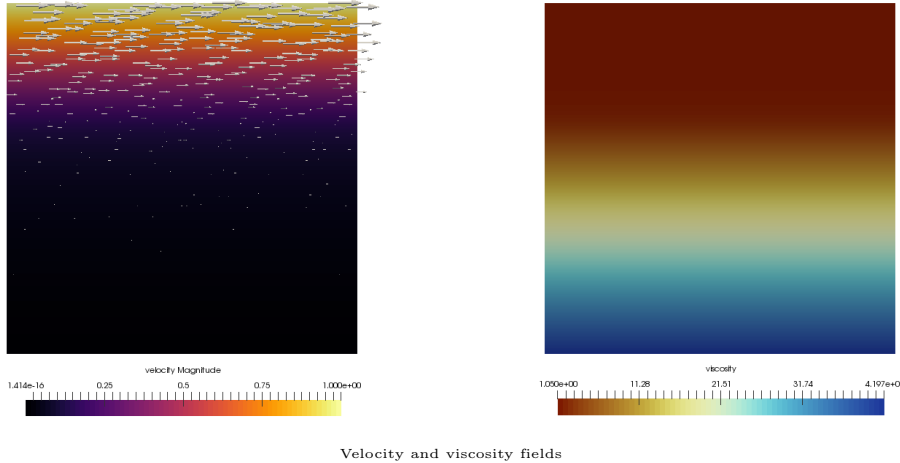
Viscosity profiles for different values of  $\beta$  and  $\epsilon$  for  $y_0 = 1/3$ . When  $\beta$  is very large, the viscosity essentially converges to  $\sim (1/2 + \epsilon)^{-1}$ .  $\beta$  controls the width of the transition while  $\epsilon$  controls the amplitude of the viscosity variation.

The flow is assumed to take place in an infinitely long pipe (in the horizontal direction) and bound by  $y = -1$  and  $y + 1$ . At the bottom we impose  $v_x(y = -1) = 0$  while we impose  $v_x(y = +1) = 1$  at the top. The density is set to 1 while the gravity is set to zero. Under these assumptions, the flow velocity and pressure fields are given by:

$$\begin{aligned} v_x(x, y) &= \frac{1}{2\pi} \left( -\beta C_1 \log[\beta^2 + (z - y_0)^2] + 2(z - y_0)C_1 \tan^{-1} \frac{z - y_0}{\beta} + \pi(1 + 2\epsilon)zC_1 + C_2 \right) \\ v_y(x, y) &= 0 \\ p(x, y) &= 0 \end{aligned} \quad (640)$$

where  $C_1$  and  $C_2$  are integration constants:

$$\begin{aligned} C_1 &= 2\pi \left[ \beta \log[\beta^2 + (1 + y_0)^2] - 2(1 + y_0) \tan^{-1} \frac{1 + y_0}{\beta} - \beta \log[\beta^2 + (1 - y_0)^2] + 2(1 - y_0) \tan^{-1} \frac{1 - y_0}{\beta} + 2\pi(1 + 2\epsilon) \right] \\ C_2 &= \left[ \beta \log[\beta^2 + (1 + y_0)^2] - 2(1 + y_0) \tan^{-1} \frac{1 + y_0}{\beta} + \pi(1 + 2\epsilon) \right] C_1, \end{aligned} \quad (641)$$



**Analytical derivations** The flow takes place in the horizontal direction and is infinite in the this direction too so that:

$$\vec{v} = (u(y), 0)$$

The strain rate tensor is then given by:

$$\dot{\epsilon} = \frac{1}{2} \begin{pmatrix} 0 & du/dy \\ du/dy & 0 \end{pmatrix}$$

The momentum equation then becomes:

$$\vec{\nabla} \cdot (2\eta\dot{\epsilon}) - \vec{\nabla}p = \vec{\nabla} \cdot \left[ \eta(y) \begin{pmatrix} 0 & du/dy \\ du/dy & 0 \end{pmatrix} \right] - \vec{\nabla}p = \rho\vec{g}$$

On the vertical axis, when the gravity is zero, the equation is automatically verified when the pressure is zero. On the horizontal axis:

$$\frac{d}{dy} \left( \eta(y) \frac{du}{dy} \right) = 0$$

Then

$$\eta(y) \frac{du}{dy} = C_1$$

or,

$$\frac{du}{dy} = \frac{C_1}{\eta(y)} = C_1 \left( \frac{1}{\pi} \tan^{-1} \frac{y - y_0}{\beta} + 1/2 + \epsilon \right)$$

so that the velocity is given by:

$$u(y) = \frac{1}{\pi} (y \tan^{-1}((y - y_0)/\beta) - y_0 \tan^{-1}((y - y_0)/\beta) - 0.5 * \beta \log(\beta^2 + y^2 - 2yy_0 + y_0^2) + \pi y(\epsilon + 0.5))$$

$$u(z) = \frac{1}{2\pi} \left( -\beta C_1 \log[\beta^2 + (z - y_0)^2] + 2(z - y_0)C_1 \tan^{-1} \frac{z - y_0}{\beta} + \pi(1 + 2\epsilon)zC_1 + C_2 \right)$$

where  $C_1$  and  $C_2$  are integration constants. I wish to impose  $u(z = -1) = 0$  and  $u(z = +1) = 1$ :

$$\frac{1}{2\pi} \left( -\beta C_1 \log[\beta^2 + (-1 - y_0)^2] + 2(-1 - y_0)C_1 \tan^{-1} \frac{-1 - y_0}{\beta} - \pi(1 + 2\epsilon)C_1 + C_2 \right) = 0$$

$$\frac{1}{2\pi} \left( -\beta C_1 \log[\beta^2 + (1 - y_0)^2] + 2(1 - y_0)C_1 \tan^{-1} \frac{1 - y_0}{\beta} + \pi(1 + 2\epsilon)C_1 + C_2 \right) = 1$$

or,

$$-\beta C_1 \log[\beta^2 + (-1 - y_0)^2] + 2(-1 - y_0)C_1 \tan^{-1} \frac{-1 - y_0}{\beta} - \pi(1 + 2\epsilon)C_1 + C_2 = 0$$

$$-\beta C_1 \log[\beta^2 + (1 - y_0)^2] + 2(1 - y_0)C_1 \tan^{-1} \frac{1 - y_0}{\beta} + \pi(1 + 2\epsilon)C_1 + C_2 = 2\pi$$

or,

$$-\beta C_1 \log[\beta^2 + (-1 - y_0)^2] + 2(1 + y_0)C_1 \tan^{-1} \frac{1 + y_0}{\beta} - \pi(1 + 2\epsilon)C_1 + C_2 = 0$$

$$-\beta C_1 \log[\beta^2 + (1 - y_0)^2] + 2(1 - y_0)C_1 \tan^{-1} \frac{1 - y_0}{\beta} + \pi(1 + 2\epsilon)C_1 + C_2 = 2\pi$$

or,

$$-\beta C_1 \log(\beta^2 + (1 + y_0)^2) + 2(1 + y_0)C_1 \tan^{-1}((1 + y_0)/\beta) - \pi(1 + 2\epsilon)C_1 + C_2 = 0$$

$$-\beta C_1 \log(\beta^2 + (1 - y_0)^2) + 2(1 - y_0)C_1 \tan^{-1}((1 - y_0)/\beta) + \pi(1 + 2\epsilon)C_1 + C_2 = 2\pi$$

I can now subtract the first line from the second line:

$$\beta C_1 \log(\beta^2 + (1 + y_0)^2) - 2(1 + y_0)C_1 \tan^{-1}((1 + y_0)/\beta) - \beta C_1 \log(\beta^2 + (1 - y_0)^2) + 2(1 - y_0)C_1 \tan^{-1}((1 - y_0)/\beta) + 2\pi(1 + 2\epsilon)C_1 =$$

i.e.,

$$C_1 = 2\pi \left[ \beta \log[\beta^2 + (1 + y_0)^2] - 2(1 + y_0) \tan^{-1} \left[ \frac{1 + y_0}{\beta} \right] - \beta \log[\beta^2 + (1 - y_0)^2] + 2(1 - y_0) \tan^{-1} \left[ \frac{1 - y_0}{\beta} \right] + 2\pi(1 + 2\epsilon) \right]$$

and then

$$C_2 = \beta C_1 \log(\beta^2 + (1 + y_0)^2) - 2(1 + y_0)C_1 \tan^{-1}((1 + y_0)/\beta) + \pi(1 + 2\epsilon)C_1$$

### 8.7.18 Elastic material in simple shear

The domain is a Cartesian box of size  $1 \times 1$ . The boundary conditions are as follows:

- bottom:  $u = v = 0$
- top:  $u = 1, v = 0$

The shear modulus  $\mu$  is set to 1, and the Poisson ratio  $\nu$  is set to 0.25. Gravity is set to zero.

The analytical solution for this problem is given by

$$\vec{v} = \begin{pmatrix} y \\ 0 \end{pmatrix}$$

so that

$$\vec{\nabla} \cdot \vec{v} = \begin{pmatrix} 0 & 0 \\ 1 & 0 \end{pmatrix} \quad \varepsilon = \frac{1}{2} \begin{pmatrix} 0 & 1 \\ 1 & 0 \end{pmatrix}$$

The stress tensor then writes:

$$\sigma = \lambda \vec{\nabla} \cdot \vec{v} + 2\mu \varepsilon = \mu \begin{pmatrix} 0 & 1 \\ 1 & 0 \end{pmatrix}$$

since  $\vec{\nabla} \cdot \vec{v} = 0$ .

The principal direction angle  $\theta_p$  defines the principal directions where the only stresses are normal stresses, and is given by the relationship:

$$\tan(2\theta_p) = \frac{2\sigma_{xy}}{\sigma_{xx} - \sigma_{yy}}$$

In our case the rhs is equal to  $\infty$ , which means that  $2\theta_p = \frac{\pi}{2}$  so that  $\theta_p = \frac{\pi}{4}$ .

The principal stresses are found from the original stresses via

$$\sigma_{1,2} = \frac{\sigma_{xx} + \sigma_{yy}}{2} \pm \sqrt{\left(\left(\frac{\sigma_x - \sigma_y}{2}\right)^2 + \sigma_{xy}^2\right)}$$

In our case

$$\sigma_{1,2} = \pm \sigma_{xy} = \pm \mu$$

When plotting the principal stresses on the domain we expect crosses at  $45^\circ$ .

### 8.7.19 Elastic material in pure shear

This is the same material as the previous benchmark but the boundary conditions are now as follows:  $u = -1$  on the left,  $u = 1$  on the right,  $v = 1$  on the bottom and  $v = -1$  on the top.

In this case we have

$$u(x, y) = 2(x - 1/2) \quad v(x, y) = -2(y - 1/2)$$

so

$$\vec{\nabla} \cdot \vec{v} = \begin{pmatrix} 2 & 0 \\ 0 & -2 \end{pmatrix} = \varepsilon$$

and  $\vec{\nabla} \cdot \vec{v} = 0$  so that the stress tensor then writes:

$$\sigma = \lambda \vec{\nabla} \cdot \vec{v} + 2\mu \varepsilon = 2\mu \begin{pmatrix} 2 & 0 \\ 0 & -2 \end{pmatrix}$$

The principal direction angle  $\theta_p$  defines the principal directions where the only stresses are normal stresses, and is given by the relationship:

$$\tan(2\theta_p) = \frac{2\sigma_{xy}}{\sigma_{xx} - \sigma_{yy}} = 0$$

which means that  $\theta_p = 0$ . Then the principal stresses are found from the original stresses via

$$\sigma_{1,2} = \frac{\sigma_{xx} + \sigma_{yy}}{2} \pm \sqrt{\left( \left( \frac{\sigma_x - \sigma_y}{2} \right)^2 + \sigma_{xy}^2 \right)}$$

In our case

$$\sigma_{1,2} = \pm 4\mu$$

When plotting the principal stresses on the domain we expect crosses which align with the axis.

### 8.7.20 Uniform strip load on elastic material

From Davis and Selvadurai [648](section 4.6) we have the components of the stress tensor:

$$\sigma_{xx} = \frac{p_0}{\pi} \left[ \theta - \frac{1}{2} \sin 2\theta \right]_{\theta_1}^{\theta_2} \quad \sigma_{zz} = \frac{p_0}{\pi} \left[ \theta + \frac{1}{2} \sin 2\theta \right]_{\theta_1}^{\theta_2} \quad \sigma_{xz} = \frac{p_0}{\pi} [\sin^2 \theta]_{\theta_1}^{\theta_2}$$

or,

$$\begin{aligned} \tilde{\sigma}_{xx} &= \left[ \theta - \frac{1}{2} \sin 2\theta \right]_{\theta_1}^{\theta_2} = \Theta - \frac{1}{2}(\sin 2\theta_2 - \sin 2\theta_1) \\ \tilde{\sigma}_{zz} &= \left[ \theta + \frac{1}{2} \sin 2\theta \right]_{\theta_1}^{\theta_2} = \Theta + \frac{1}{2}(\sin 2\theta_2 - \sin 2\theta_1) \\ \tilde{\sigma}_{xz} &= [\sin^2 \theta]_{\theta_1}^{\theta_2} = \sin^2 \theta_2 - \sin^2 \theta_1 \end{aligned}$$

with  $\Theta = \theta_2 - \theta_1$  and  $\tilde{\sigma}_{ij} = \sigma_{ij}\pi/p_0$ . The (dimensionless) principal stresses are given by

$$\tilde{\sigma}_{1,2} = \frac{\tilde{\sigma}_{xx} + \tilde{\sigma}_{zz}}{2} \pm \sqrt{\left( \frac{\tilde{\sigma}_{xx} - \tilde{\sigma}_{zz}}{2} \right)^2 + \tilde{\sigma}_{xz}^2}$$

We have

$$\begin{aligned} \frac{\tilde{\sigma}_{xx} + \tilde{\sigma}_{zz}}{2} &= \Theta \\ \frac{\tilde{\sigma}_{xx} - \tilde{\sigma}_{zz}}{2} &= -\frac{1}{2}(\sin 2\theta_2 - \sin 2\theta_1) \\ &= -\frac{1}{2}(2 \cos(\theta_1 + \theta_2) \sin \Theta) \\ &= -\cos(\theta_1 + \theta_2) \sin \Theta \\ \tilde{\sigma}_{xz} &= [\sin^2 \theta]_{\theta_1}^{\theta_2} \\ &= \sin^2 \theta_2 - \sin^2 \theta_1 \\ &= \frac{1}{2}(1 - \cos \theta_2) - \frac{1}{2}(1 - \cos 2\theta_1) \\ &= -\frac{1}{2}(\cos \theta_2 - \cos 2\theta_1) \\ &= -\frac{1}{2}(-2 \sin(\theta_1 + \theta_2) \sin(\theta_2 - \theta_1)) \\ &= \sin(\theta_1 + \theta_2) \sin \Theta \end{aligned}$$

so that the principal stresses are finally given by

$$\sigma_1 = \frac{p_0}{\pi}(\Theta + \sin \Theta) \quad \sigma_3 = \frac{p_0}{\pi}(\Theta - \sin \Theta)$$

The principal stresses will be constant on any circle that passes through the edges of the strip load. It can also be shown that the direction of  $\sigma_1$  points toward the highest point of this circle.

## 8.8 Assigning values to quadrature points

As we have seen in Section 6, the building of the elemental matrix and rhs requires (at least) to assign a density and viscosity value to each quadrature point inside the element. Depending on the type of modelling, this task can prove more complex than one might expect and have large consequences on the solution accuracy.

Here are several options:

- The simplest way (which is often used for benchmarks) consists in computing the 'real' coordinates  $(x_q, y_q, z_q)$  of a given quadrature point based on its reduced coordinates  $(r_q, s_q, t_q)$ , and passing these coordinates to a function which returns density and/or viscosity at this location. For instance, for the Stokes sphere:

```
def rho(x,y):
    if (x-.5)**2+(y-0.5)**2<0.123**2:
        val=2.
    else:
        val=1.
    return val

def mu(x,y):
    if (x-.5)**2+(y-0.5)**2<0.123**2:
        val=1.e2
    else:
        val=1.
    return val
```

This is very simple, but it has been shown to potentially be problematic. In essence, it can introduce very large contrasts inside a single element and perturb the quadrature. Please read section 3.3 of [1169] and/or have a look at the section titled "Averaging material properties" in the ASPECT manual.

- another similar approach consists in assigning a density and viscosity value to the nodes of the FE mesh first, and then using these nodal values to assign values to the quadrature points. Very often ,and quite logically, the shape functions are used to this effect. Indeed we have seen before that for any point  $(r, s, t)$  inside an element we have

$$f_h(r, s, t) = \sum_i^m f_i N_i(r, s, t)$$

where the  $f_i$  are the nodal values and the  $N_i$  the corresponding basis functions.

In the case of linear elements ( $Q_1$  basis functions), this is straightforward. In fact, the basis functions  $N_i$  can be seen as moving weights: the closer the point is to a node, the higher the weight (basis function value).

However, this is quite another story for quadratic elements ( $Q_2$  basis functions). In order to illustrate the problem, let us consider a 1D problem. The basis functions are

$$N_1(r) = \frac{1}{2}r(r-1) \quad N_2(r) = 1 - r^2 \quad N_3(r) = \frac{1}{2}r(r+1)$$

Let us further assign:  $\rho_1 = \rho_2 = 0$  and  $\rho_3 = 1$ . Then

$$\rho_h(r) = \sum_i^m \rho_i N_i(r) = N_3(r)$$

There lies the core of the problem: the  $N_3(r)$  basis function is negative for  $r \in [-1, 0]$ . This means that the quadrature point in this interval will be assigned a negative density, which is nonsensical and numerically problematic!

**use 2X Q1. write about it !**

The above methods work fine as long as the domain contains a single material. As soon as there are multiple fluids in the domain a special technique is needed to track either the fluids themselves or their interfaces. Let us start with markers. We are then confronted to the infernal trio (a *menage à trois*?) which is present for each element, composed of its nodes, its markers and its quadrature points.

Each marker carries the material information (density and viscosity). This information must ultimately be projected onto the quadrature points. Two main options are possible: an algorithm is designed and projects the marker-based fields onto the quadrature points directly or the marker fields are first projected onto the FE nodes and then onto the quadrature points using the techniques above.

---

At a given time, every element  $e$  contains  $n^e$  markers. During the FE matrix building process, viscosity and density values are needed at the quadrature points. One therefore needs to project the values carried by the markers at these locations. Several approaches are currently in use in the community and the topic has been investigated by [688] and [739] for instance.

ELEFANT adopts a simple approach: viscosity and density are considered to be elemental values, i.e. all the markers within a given element contribute to assign a unique constant density and viscosity value to the element by means of an averaging scheme.

While it is common in the literature to treat the so-called arithmetic, geometric and harmonic means as separate averagings, I hereby wish to introduce the notion of generalised mean, which is a family of functions for aggregating sets of numbers that include as special cases the arithmetic, geometric and harmonic means.

If  $p$  is a non-zero real number, we can define the generalised mean (or power mean) with exponent  $p$  of the positive real numbers  $a_1, \dots, a_n$  as:

$$M_p(a_1, \dots, a_n) = \left( \frac{1}{n} \sum_{i=1}^n a_i^p \right)^{1/p} \quad (642)$$

and it is trivial to verify that we then have the special cases:

$$M_{-\infty} = \lim_{p \rightarrow -\infty} M_p = \min(a_1, \dots, a_n) \quad (\text{minimum}) \quad (643)$$

$$M_{-1} = \frac{n}{\frac{1}{a_1} + \frac{1}{a_2} + \dots + \frac{1}{a_n}} \quad (\text{harm. avrg.}) \quad (644)$$

$$M_0 = \lim_{p \rightarrow 0} M_p = \left( \prod_{i=1}^n a_i \right)^{1/n} \quad (\text{geom. avrg.}) \quad (645)$$

$$M_{+1} = \frac{1}{n} \sum_{i=1}^n a_i \quad (\text{arithm. avrg.}) \quad (646)$$

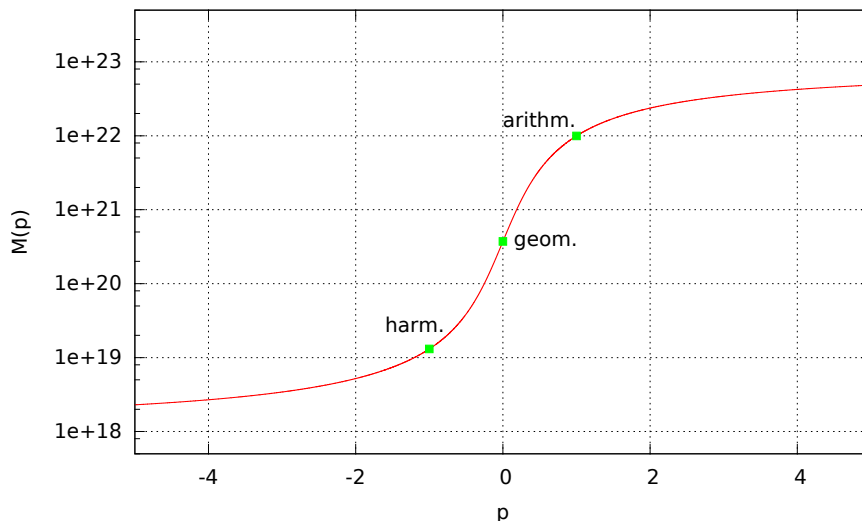
$$M_{+2} = \sqrt{\frac{1}{n} \sum_{i=1}^n a_i^2} \quad (\text{root mean square}) \quad (647)$$

$$M_{+\infty} = \lim_{p \rightarrow +\infty} M_p = \max(a_1, \dots, a_n) \quad (\text{maximum}) \quad (648)$$

Note that the proofs of the limit convergence are given in [342].

An interesting property of the generalised mean is as follows: for two real values  $p$  and  $q$ , if  $p < q$  then  $M_p \leq M_q$ . This property has for instance been illustrated in Fig. 20 of [2272].

One can then for instance look at the generalised mean of a randomly generated set of 1000 viscosity values within  $10^{18} Pa.s$  and  $10^{23} Pa.s$  for  $-5 \leq p \leq 5$ . Results are shown in the figure hereunder and the arithmetic, geometric and harmonic values are indicated too. The function  $M_p$  assumes an arctangent-like shape: very low values of  $p$  will ultimately yield the minimum viscosity in the array while very high values will yield its maximum. In between, the transition is smooth and occurs essentially for  $|p| \leq 5$ .



```
▷ python_codes/fieldstone_markers_avrg
```

## 8.9 Matrix (Sparse) storage

The FE matrix is the result of the assembly process of all elemental matrices. Its size can become quite large when the resolution is being increased (from thousands of lines/columns to tens of millions).

One important property of the matrix is its sparsity. Typically less than 1% of the matrix terms is not zero and this means that the matrix storage can and should be optimised. Clever storage formats were designed early on since the amount of RAM memory in computers was the limiting factor 3 or 4 decades ago. [2215]

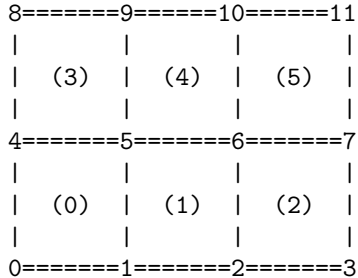
There are several standard formats:

- compressed sparse row (CSR) format
- compressed sparse column format (CSC)
- the Coordinate Format (COO)
- Skyline Storage Format
- ...

I focus on the CSR format in what follows.

### 8.9.1 2D domain - One degree of freedom per node

Let us consider again the  $3 \times 2$  element grid which counts 12 nodes.



In the case there is only a single degree of freedom per node, the assembled FEM matrix will look like this:

$$\left( \begin{array}{cccccc|cc} X & X & & X & X & & & \\ X & X & X & X & X & X & & \\ & X & X & X & X & X & X & \\ & & X & X & & X & X & \\ X & X & & X & X & & X & X \\ X & X & X & X & X & X & X & X \\ & X & X & X & X & X & X & X \\ & & X & X & & X & X & \\ & & & X & X & X & X & X \\ & & & & X & X & X & X \\ & & & & & X & X & X \end{array} \right)$$

where the  $X$  stand for non-zero terms. This matrix structure stems from the fact that

- node 0 sees nodes 0,1,4,5
- node 1 sees nodes 0,1,2,4,5,6
- node 2 sees nodes 1,2,3,5,6,7
- ...

- node 5 sees nodes 0,1,2,4,5,6,8,9,10
- ...
- node 10 sees nodes 5,6,7,9,10,11
- node 11 sees nodes 6,7,10,11

In light thereof, we have

- 4 corner nodes which have 4 neighbours (counting themselves)
- $2(nnx-2)$  nodes which have 6 neighbours
- $2(nny-2)$  nodes which have 6 neighbours
- $(nnx-2) \times (nny-2)$  nodes which have 9 neighbours

In total, the number of non-zero terms in the matrix is then:

$$NZ = 4 \times 4 + 4 \times 6 + 2 \times 6 + 2 \times 9 = 70$$

In general, we would then have:

$$NZ = 4 \times 4 + [2(nnx - 2) + 2(nny - 2)] \times 6 + (nnx - 2)(nny - 2) \times 9$$

Let us temporarily assume  $nnx = nny = n$ . Then the matrix size (total number of unknowns) is  $N = n^2$  and

$$NZ = 16 + 24(n - 2) + 9(n - 2)^2$$

A full matrix array would contain  $N^2 = n^4$  terms. The ratio of  $NZ$  (the actual number of reals to store) to the full matrix size (the number of reals a full matrix contains) is then

$$R = \frac{16 + 24(n - 2) + 9(n - 2)^2}{n^4}$$

It is then obvious that when  $n$  is large enough  $R \sim 1/n^2$ .

CSR stores the nonzeros of the matrix row by row, in a single indexed array A of double precision numbers. Another array COLIND contains the column index of each corresponding entry in the A array. A third integer array RWPTR contains pointers to the beginning of each row, which an additional pointer to the first index following the nonzeros of the matrix A. A and COLIND have length NZ and RWPTR has length N+1.

In the case of the here-above matrix, the arrays COLIND and RWPTR will look like:

$$COLIND = (0, 1, 4, 5, 0, 1, 2, 4, 5, 6, 1, 2, 3, 5, 6, 7, \dots, 6, 7, 10, 11)$$

$$RWPTR = (0, 4, 10, 16, \dots)$$

### 8.9.2 2D domain - Two degrees of freedom per node

When there are now two degrees of freedom per node, such as in the case of the Stokes equation in two-dimensions, the size of the  $\mathbb{K}$  matrix is given by

<code>NfemV=nnp*ndofV</code>
------------------------------

In the case of the small grid above, we have `NfemV=24`. Elemental matrices are now  $8 \times 8$  in size.

We still have

- 4 corner nodes which have 4 neighbours
- $2(nnx-2)$  nodes which have 6 neighbours
- $2(nny-2)$  nodes which have 6 neighbours

- $(nnx-2) \times (nny-2)$  nodes which have 9 neighbours,

but now each degree of freedom from a node sees the other two degrees of freedom of another node too. In that case, the number of nonzeros has been multiplied by four and the assembled FEM matrix looks like:

Note that the degrees of freedom are organised as follows:

$$(u_0, v_0, u_1, v_1, u_2, v_2, \dots, u_{11}, v_{11})$$

In general, we would then have:

$$NZ = 4[4 \times 4 + [2(nnx - 2) + 2(nny - 2)] \times 6 + (nnx - 2)(nny - 2) \times 9]$$

and in the case of the small grid, the number of non-zero terms in the matrix is then:

$$NZ = 4 [4 \times 4 + 4 \times 6 + 2 \times 6 + 2 \times 9] = 280$$

In the case of the here-above matrix, the arrays COLIND and RWPTR will look like:

$$COLIND = (0, 1, 2, 3, 8, 9, 10, 11, 0, 1, 2, 3, 8, 9, 10, 11, \dots)$$

$$RW PTR = (0, 8, 16, 28, \dots)$$

### 8.9.3 Matrix Storage in fieldstone

The majority of the codes have the FE matrix being a full array

```
a_mat = np.zeros((Nfem,Nfem), dtype=np.float64)
```

and it is converted to CSR format on the fly in the solve phase:

```
sol = sps.linalg.spsolve(sps.csr_matrix(a_mat), rhs)
```

Note that linked list storages can be used (`lil_matrix`). Substantial memory savings but much longer compute times.

#### 8.9.4 Sparse Matrix-Vector multiplication

see 9.4 of Kepley's book. [1465]

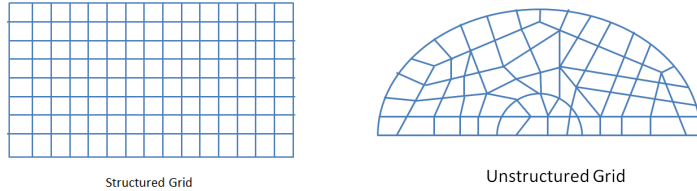
 Relevant Literature[2794, 1509]

## 8.10 Mesh generation

Before basis functions can be defined and PDEs can be discretised and solved we must first tessellate the domain with polygons, e.g. triangles and quadrilaterals in 2D, tetrahedra, prisms and hexahedra in 3D.

When the domain is itself simple (e.g. a rectangle, a sphere, ...) the mesh (or grid) can be (more or less) easily produced and the connectivity array filled with straightforward algorithms [2531]. However, real life applications can involve extremely complex geometries (e.g. a bridge, a human spine, a car chassis and body, etc ...) and dedicated algorithms/softwares must be used (see [2539, 887, 2821]).

We usually distinguish between two broad classes of grids: structured grids (with a regular connectivity) and unstructured grids (with an irregular connectivity).



**Remark.** Various families of so-called meshless methods exist and are commonly employed in Computational Fluid Dynamics [1638, 1603, 1637, 1639]. They are however very rarely used in Computational geodynamics, with a noticeable exception [1134].

### 8.10.1 Quadrilateral-based meshes

Let us now focus on the case of a rectangular computational domain of size  $L_x \times L_y$  with a regular mesh composed of  $\text{nelx} \times \text{nely} = \text{nel}$  quadrilaterals. There are then  $\text{nmx} \times \text{nny} = \text{nnp}$  grid points. The elements are of size  $hx \times hy$  with  $hx = L_x / \text{nelx}$ .

We have no reason to come up with an irregular/illogical node numbering so we can number nodes row by row or column by column as shown on the example hereunder of a  $3 \times 2$  grid:

$\begin{array}{ccccccc}  8 & ===== & 9 & ===== & 10 & ===== & 11 \\    & &   & &   & &   \\    & (3) &   & (4) &   & (5) &   \\    & &   & &   & &   \\  4 & ===== & 5 & ===== & 6 & ===== & 7 \\    & &   & &   & &   \\    & (0) &   & (1) &   & (2) &   \\    & &   & &   & &   \\  0 & ===== & 1 & ===== & 2 & ===== & 3  \end{array}$	$\begin{array}{ccccccc}  2 & ===== & 5 & ===== & 8 & ===== & 11 \\    & &   & &   & &   \\    & (1) &   & (3) &   & (5) &   \\    & &   & &   & &   \\  1 & ===== & 4 & ===== & 7 & ===== & 10 \\    & &   & &   & &   \\    & (0) &   & (2) &   & (4) &   \\    & &   & &   & &   \\  0 & ===== & 3 & ===== & 6 & ===== & 9  \end{array}$
"row by row"	"column by column"

The numbering of the elements themselves could be done in a somewhat chaotic way but we follow the numbering of the nodes for simplicity. The row by row option is the adopted one in **fieldstone** and the coordinates of the points are computed as follows:

```
x = np.empty(nnp, dtype=np.float64)
y = np.empty(nnp, dtype=np.float64)
counter = 0
for j in range(0,nny):
    for i in range(0,nmx):
        x[counter]=i*hx
        y[counter]=j*hy
        counter += 1
```

The inner loop has  $i$  ranging from 0 to  $\text{nmx}-1$  first for  $j=0, 1, \dots$  up to  $\text{nny}-1$  which indeed corresponds to the row by row numbering.

We now turn to the connectivity. As mentioned before, this is a structured mesh so that the so-called connectivity array, named `icon` in our case, can be filled easily. For each element we need to store the node identities of its vertices. Since there are `nel` elements and  $m=4$  corners, this is a  $m \times nel$  array. The algorithm goes as follows:

```
icon = np.zeros((m, nel), dtype=np.int16)
counter = 0
for j in range(0, nely):
    for i in range(0, nelx):
        icon[0, counter] = i + j * nnx
        icon[1, counter] = i + 1 + j * nnx
        icon[2, counter] = i + 1 + (j + 1) * nnx
        icon[3, counter] = i + (j + 1) * nnx
        counter += 1
```

In the case of the  $3 \times 2$  mesh, the `icon` is filled as follows:

	element id→	0	1	2	3	4	5
node id↓							
0		0	1	2	4	5	6
1		1	2	3	5	6	7
2		5	6	7	9	10	11
3		4	5	6	8	9	10

It is to be understood as follows: element #4 is composed of nodes 5, 6, 10 and 9. Note that nodes are always stored in a counter clockwise manner, starting at the bottom left. This is very important since the corresponding basis functions and their derivatives will be labelled accordingly.

In three dimensions things are very similar. The mesh now counts `nelx×nely×nelz=nel` elements which represent a cuboid of size `Lx×Ly×Lz`. The position of the nodes is obtained as follows:

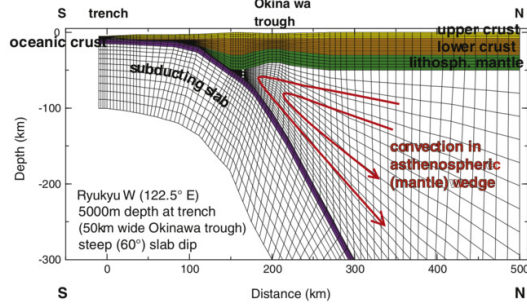
```
x = np.empty(nnp, dtype=np.float64)
y = np.empty(nnp, dtype=np.float64)
z = np.empty(nnp, dtype=np.float64)
counter=0
for i in range(0,nnx):
    for j in range(0,nny):
        for k in range(0,nnz):
            x[counter]=i*hx
            y[counter]=j*hy
            z[counter]=k*hz
            counter += 1
```

The connectivity array is now of size `m×nel` with `m=8`:

```
icon = np.zeros((m, nel), dtype=np.int16)
counter = 0
for i in range(0, nelx):
    for j in range(0, nely):
        for k in range(0, nelz):
            icon[0, counter]=nny*nnz*(i    )+nnz*(j    )+k
            icon[1, counter]=nny*nnz*(i+1)+nnz*(j    )+k
            icon[2, counter]=nny*nnz*(i+1)+nnz*(j+1)+k
            icon[3, counter]=nny*nnz*(i    )+nnz*(j+1)+k
            icon[4, counter]=nny*nnz*(i    )+nnz*(j    )+k+1
            icon[5, counter]=nny*nnz*(i+1)+nnz*(j    )+k+1
            icon[6, counter]=nny*nnz*(i+1)+nnz*(j+1)+k+1
            icon[7, counter]=nny*nnz*(i    )+nnz*(j+1)+k+1
            counter += 1
```

produce drawing of node numbering

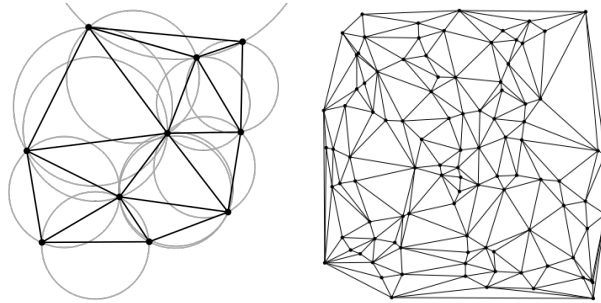
Although it is not very common in geosciences, quadrilateral meshes are sometimes employed in a boundary-fitted way, as shown hereunder:



Relevant Literature: [1359]

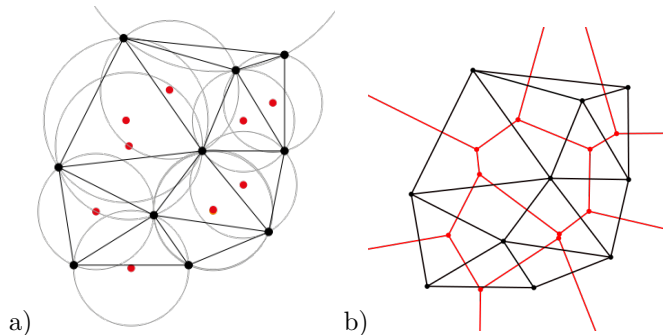
### 8.10.2 Delaunay triangulation and Voronoi cells, and triangle-based meshes

The topic of Delaunay<sup>43</sup> triangulation is vast, but a simple definition can be written as follows: "a Delaunay triangulation for a set  $P$  of points in a plane is a triangulation  $DT(P)$  such that no point in  $P$  is inside the circumcircle of any triangle in  $DT(P)$ ." [wikipedia] Other properties of such triangulations are that they maximize the minimum angle of all the angles of the triangles in the triangulation. Note that for four or more points on the same circle (e.g., the vertices of a rectangle) the Delaunay triangulation is not unique and that points on a line also cannot yield a valid triangulation (for the simple reason that they do not form a triangle).



a) A Delaunay triangulation in the plane with circumcircles shown. b) The Delaunay triangulation of a random set of 100 points in a plane.

The Delaunay triangulation of a discrete point set  $P$  in general corresponds to the dual graph of the Voronoi diagram for  $P$ . A Voronoi diagram is composed of non-overlapping Voronoi cells which make a partition of the plane. For each point there is a corresponding region consisting of all points closer to that point than to any other: this region is the Voronoi cell of that point.



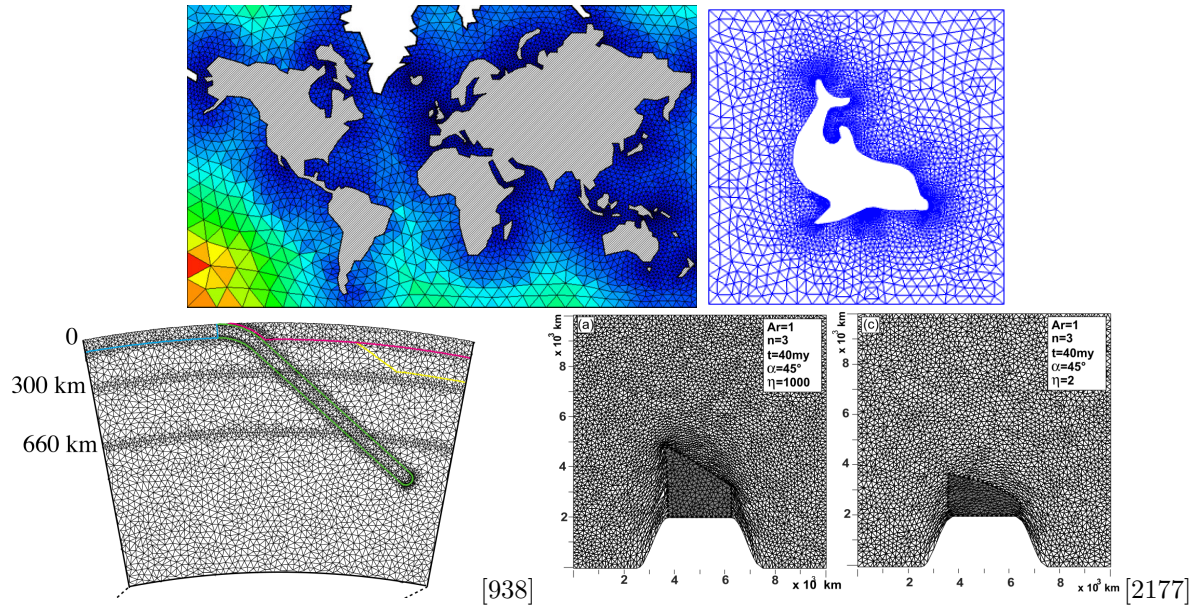
a) The Delaunay triangulation with all the circumcircles and their centers (in red). b) Connecting the centers of the circumcircles produces the Voronoi diagram (in red).

The Delaunay triangulation is used in the DOUAR code which is based on a particle levelset function to track materials. These particles are connected by means of a Delaunay triangulation (usually in a plane at startup, and then in a local Euclidean geometry once the surface is deformed) [269].

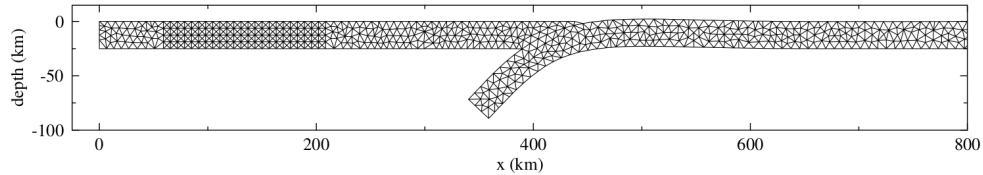
<sup>43</sup>The triangulation is named after Boris Delaunay for his work on this topic from 1934.



Relevant Literature: [935].  
Once a Delaunay triangulation has been obtained it can be used as a FEM mesh. Triangle-based meshes are obviously better suited for simulations of complex geometries:



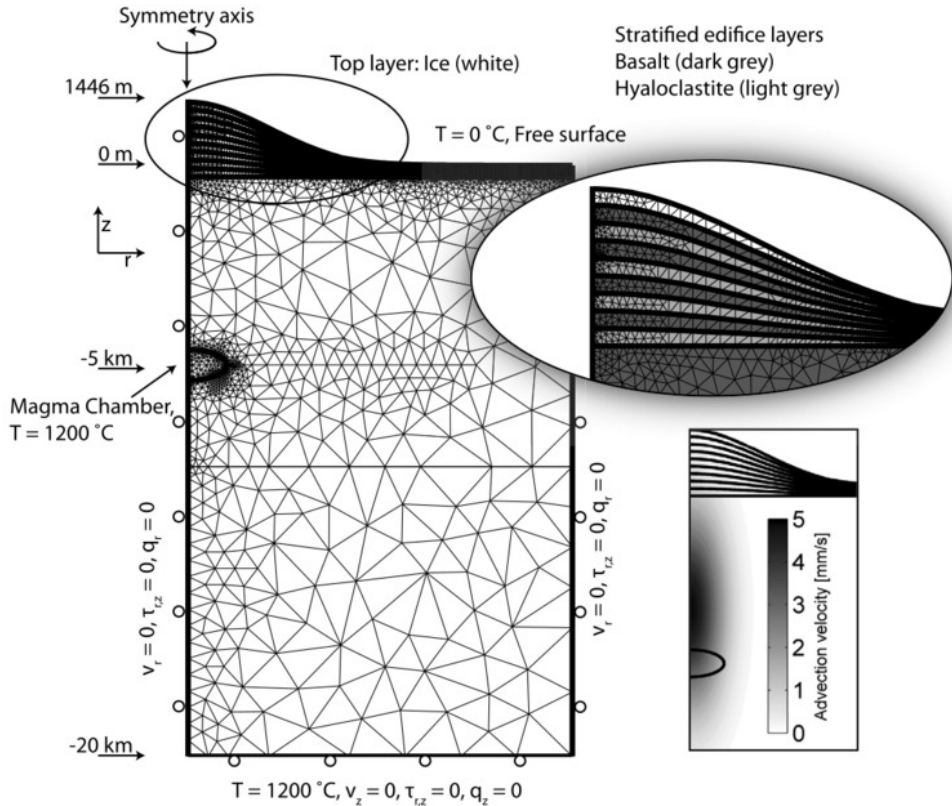
A very practical 2D triangle mesher is the code *Triangle*<sup>44</sup> written by J.R. Shewchuk [2330, 2328, 2329]. *Triangle* is specialized for creating two-dimensional finite element meshes, but can also perform simpler related tasks such as forming Delaunay triangulations under various assumptions.



Taken from Buitier et al [327]. Finite element grid. The subducting plate initially extends to 1226 km in the horizontal direction and is not completely shown here. Discretization in the subducting plate is slightly coarser towards the right edge.

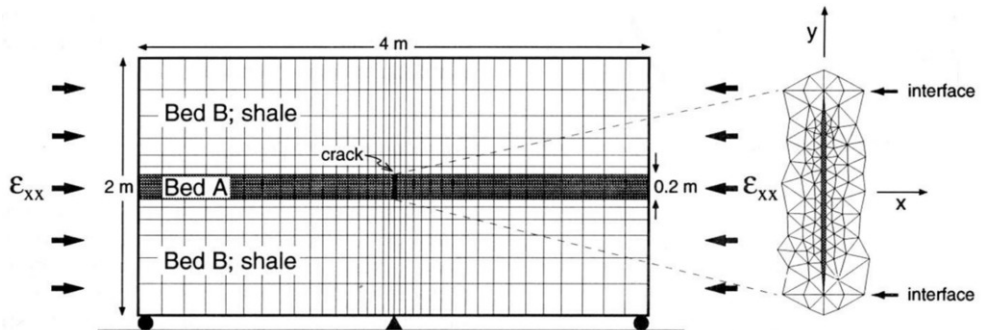
---

<sup>44</sup><https://www.cs.cmu.edu/~quake/triangle.html>



Numerical model setup of the 2D axisymmetric half-space with all applied boundary conditions to study the effects of ice-cap unloading on shallow volcanic systems [78]

Although it is rarely used in practice it is possible to produce meshes which contain both quadrilateral and triangular elements:



Mesh used to analyse the stress distribution around a pressurized crack in a layered elastic medium [839]

Relevant Literature[1886][2689]

**Remark.** The Natural Neighbour Interpolation method [2225, 2226] is based on the Delaunay triangulation.

**Remark.** Moresi & Mather [1854] have released Stripy, a Python module for (constrained) triangulation in Cartesian coordinates and on a sphere, which is based on Stripack [2138, 2139].

[write about gmsh](#)

### 8.10.3 Tetrahedra

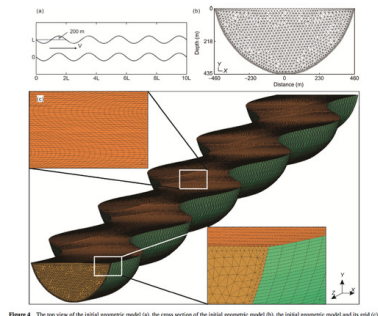
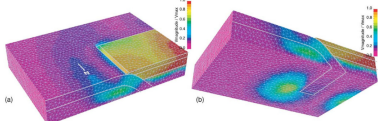


Figure 4 The top view of the initial geometric model (a), the cross section of the initial geometric model (b), the initial geometric model and its grid (c).

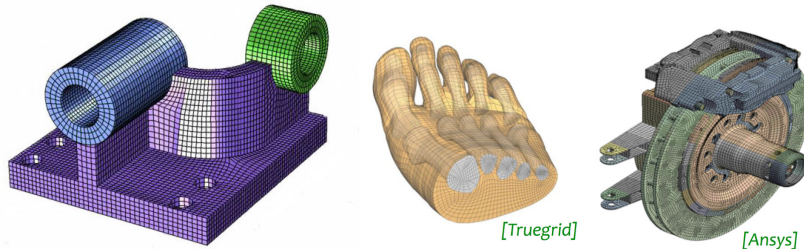
Example of 3D mesh [2834].



Normalized velocities of a STEP subduction model [1042].

### 8.10.4 Hexahedra

A hexahedron is a convex polytope isomorphic to the cube  $[0, 1]^3$ . Edges are line segments, facets are strictly **planar** convex polygons.



Relevant Literature Efficient Volume computation for Three-Dimensional hexahedral Cells [729, 1051]

### 8.10.5 Adaptive Mesh Refinement

Let us do a simple calculation and assume we wish to model mantle convection on Earth. The inner radius is  $R_1 = 3485\text{km}$  and the bottom of the lithosphere is at  $R_2 = 6250\text{km}$ . The volume of fluid is then

$$V = \frac{4}{3}\pi(R_2^3 - R_1^3) \simeq 8.5 \times 10^{11}\text{km}^3$$

Let us further assume that we are satisfied with an average resolution of 10km. Each element/cell is then  $10^3\text{km}^3$  and the total number of elements/cell is then

$$N \simeq 8.5 \times 10^8 \sim \mathcal{O}(10^9)$$

This is a very large number. The resulting linear systems from the discretisation of the equations on such a mesh will be very even larger for the Stokes equations and solving these systems will require very large numbers of CPUs and long compute times.

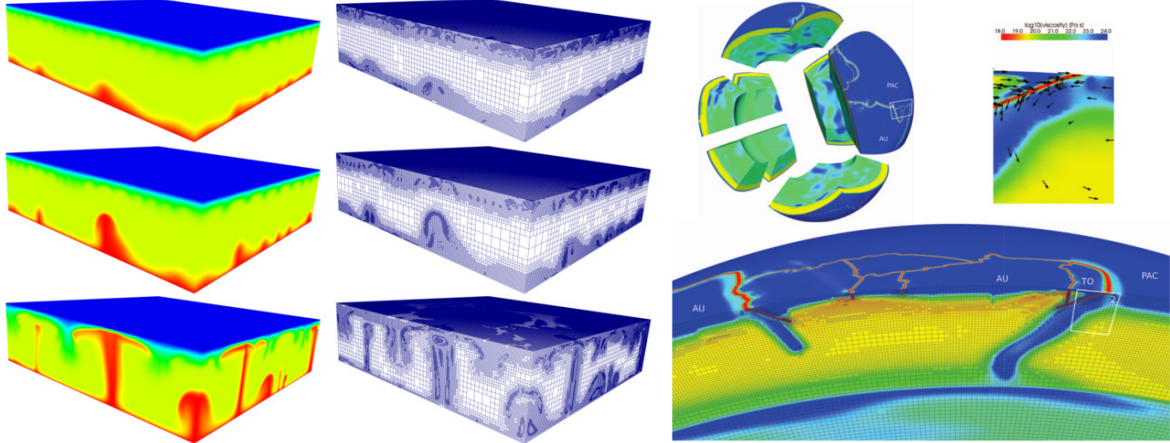
Aside from these considerations it is quite obvious that a high resolution mesh is not needed in parts of the mantle where large scale upwellings and downwellings occur, but probably even higher resolution will be needed in the vicinity of thin plumes and boundary layers. This means that a uniform mesh is a sub-optimal way of discretising space for such problems.

The same reasoning also holds in the lithosphere where for instance narrow plate boundaries need to be adequately resolved while the inside of rigid plates can be modelled with coarser meshes.

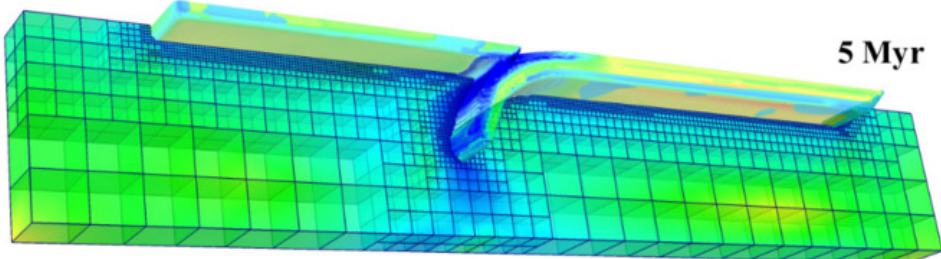
Finally, although one could employ meshing software to arrive at well balanced meshes in space, the dynamic character of the geodynamics modelling renders this approach cumbersome. A subduction zone, a mid-ocean rift or an ascending plume will evolve in time and the mesh will have to evolve in time too.

In light of all this, it was only a matter of time before Adaptive Mesh Refinement was adopted in computational geodynamics. However, since the use and update of such meshes is somewhat complex in terms of numerical algorithms, its introduction came somewhat late (00's and later). The DOUAR code (see Section B) developed originally by J. Braun and Ph. Fullsack is a prime example of an early multi-purpose code relying on a self-written Octree library [269]. More recently the ASPECT code was developed on top of the Octree library p4est [385]

For further reading I suggest you read the review by May, Schellart & Moresi on this topic [1745].



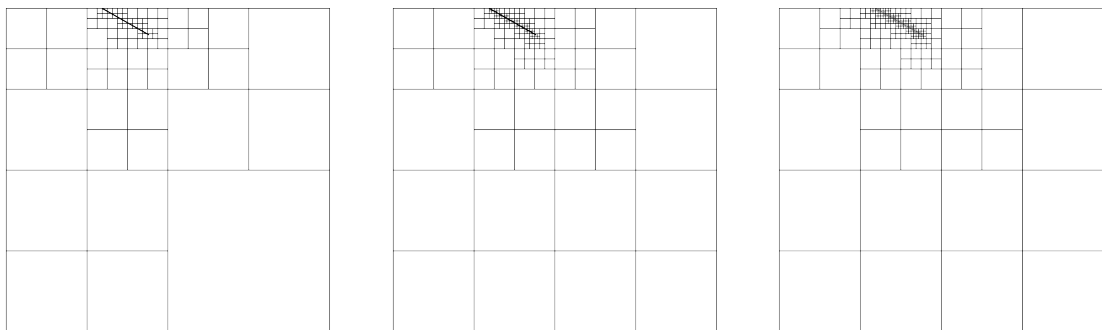
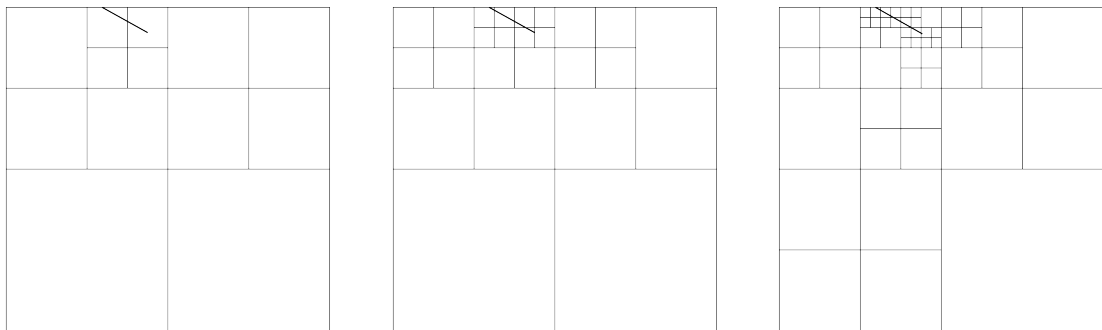
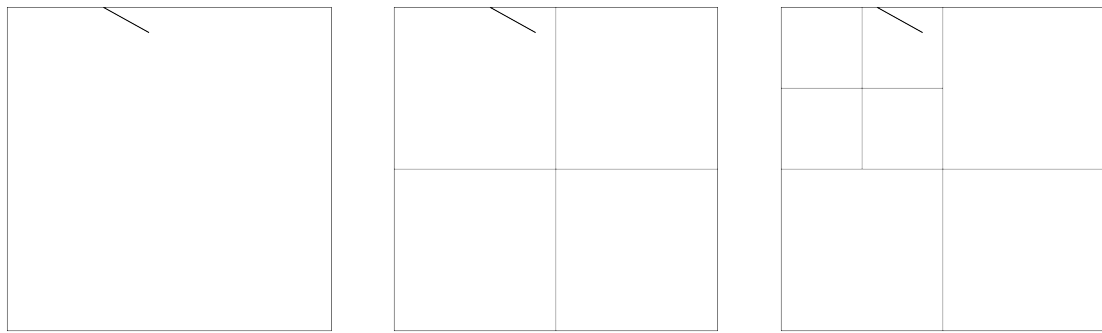
Taken from [380] and [384]



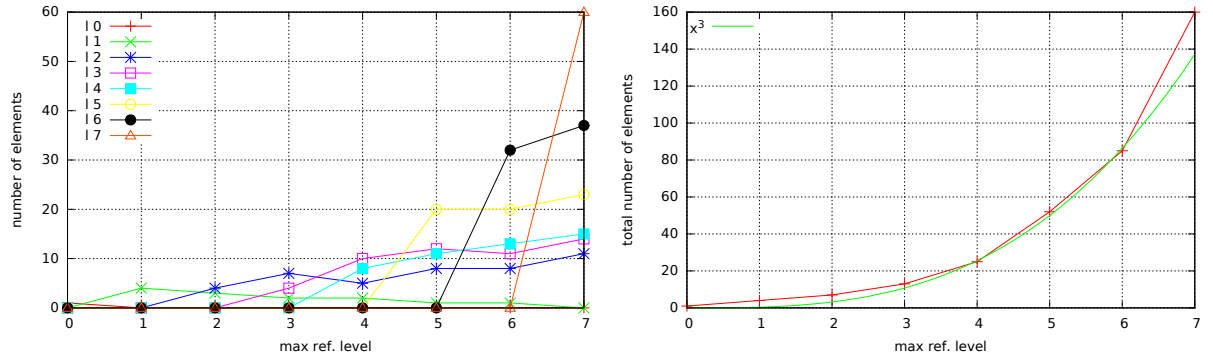
Taken from [1002]

Relevant Literature: [380, 384][1584] [381, sect 3] [633] [2457] [1799]

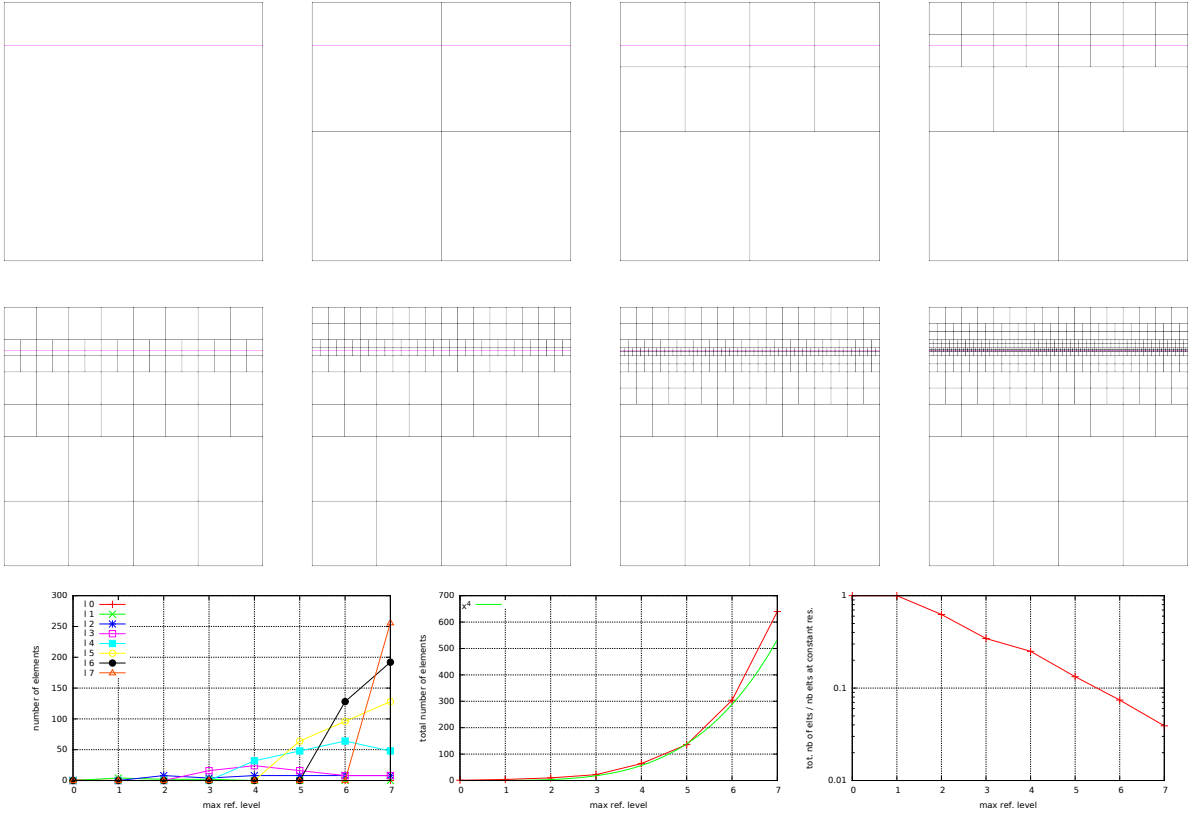
### A short illustrative exercise



	# 10	# 11	# 12	# 13	# 14	# 15	# 16	# 17	# 18
max level= 0	1								
max level= 1	0	4							
max level= 2	0	3	4						
max level= 3	0	2	7	4					
max level= 4	0	2	5	10	8				
max level= 5	0	1	8	12	11	20			
max level= 6	0	1	8	11	13	20	32		
max level= 7	0	0	11	14	15	23	37	60	
max level= 8	0	0	11	13	17	27	43	72	116



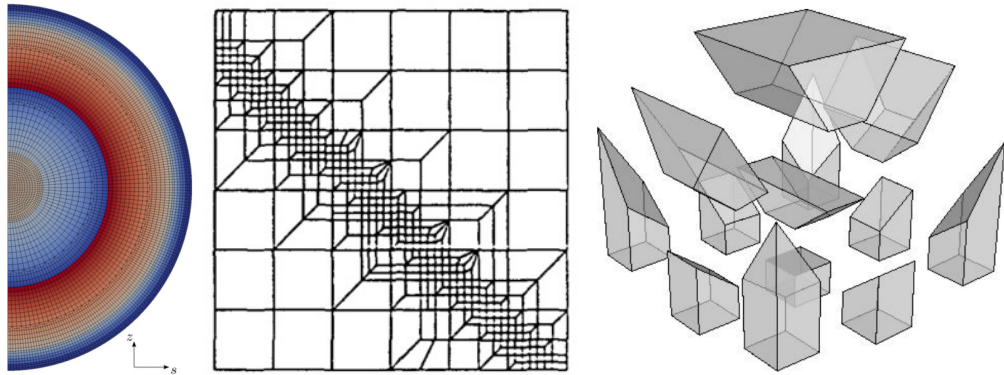
In the particular case presented here, even though the inclusion in a short two-dimensional line, the total number of elements grows faster than the third power of the refinement level. While of course the total number of elements remains much smaller than the constant resolution counterpart, this observation tells us that authorising a unit increase of the maximum refinement level can have a substantial effect on the total number of elements.

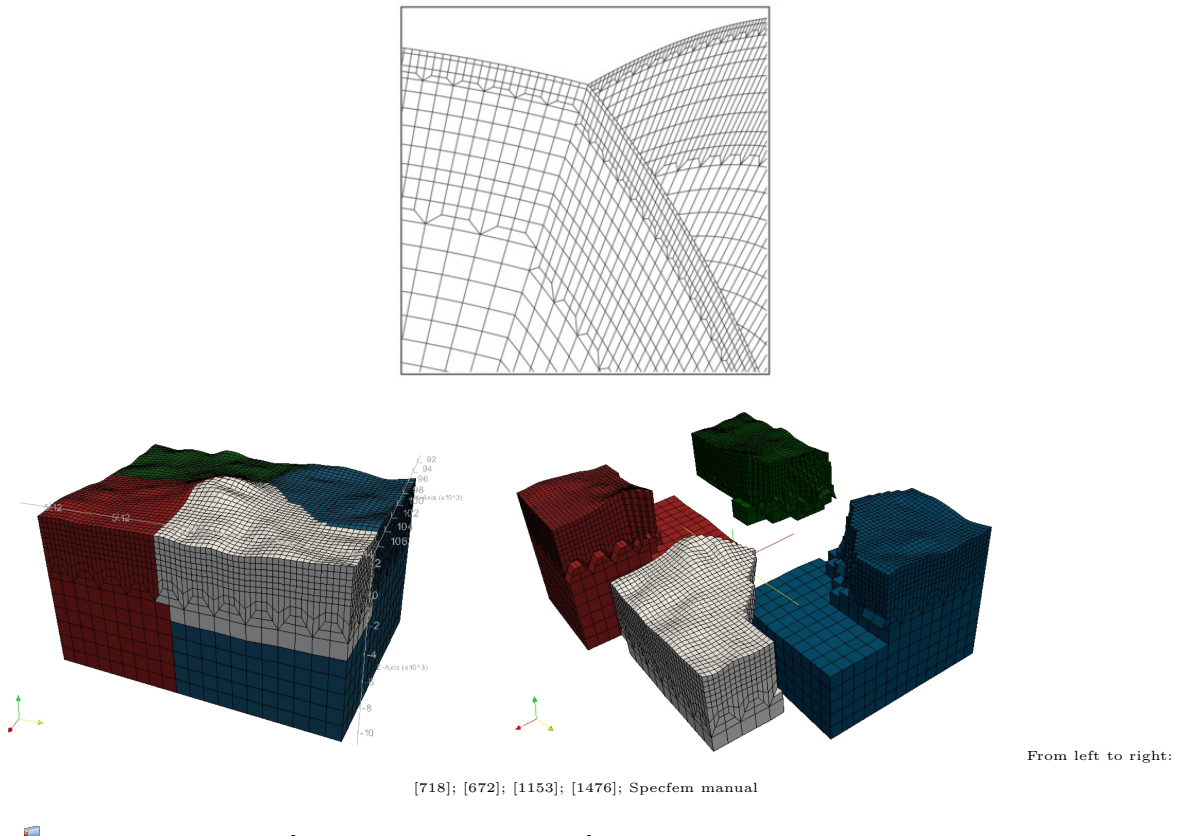


### 8.10.6 Conformal Mesh Refinement

The quadtree/octree mesh refinement presented above is one option when it comes to mesh refinement (or  $h$ -refinement). However their massive drawback is the presence of hanging nodes which require special attention.

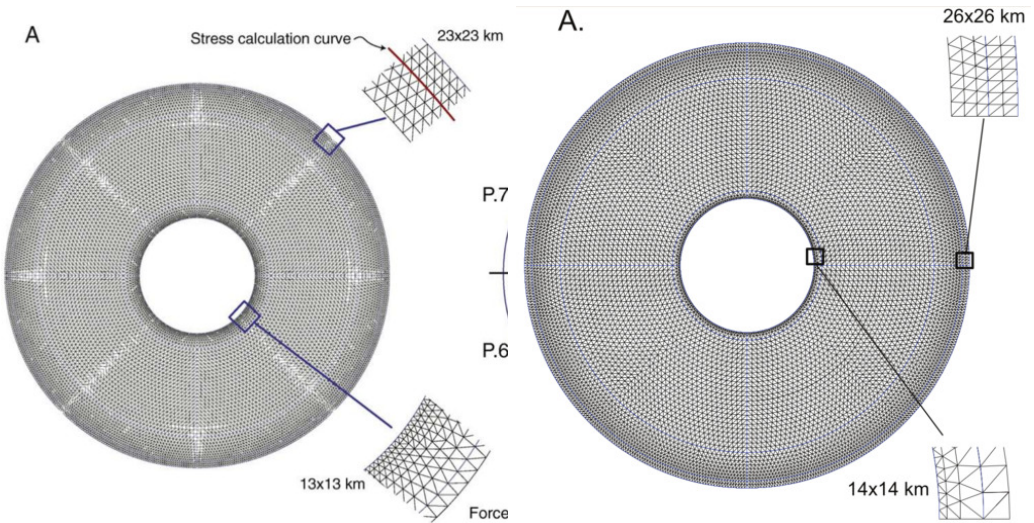
Another approach to mesh refinement is conformal mesh refinement, which





Relevant Literature: [919, 1153, 36, 1941, 1940]

### 8.10.7 Meshes in an annulus



The quadratic finite element mesh as used in [257, 259]

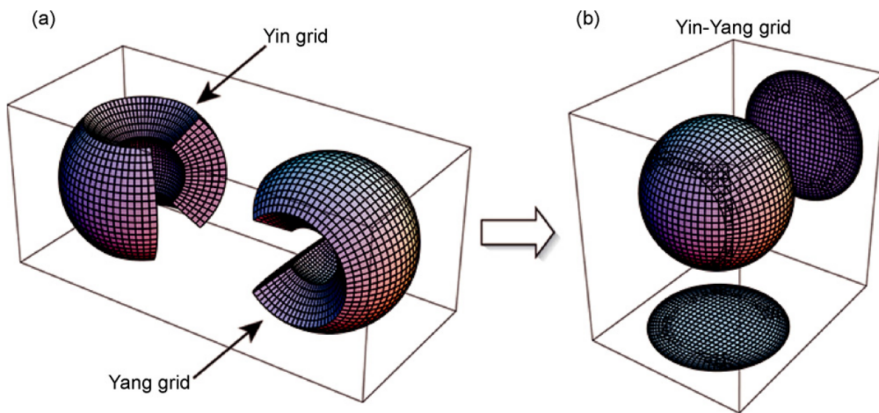
### 8.10.8 Meshes in a hollow sphere

The following is for the most part published in [2531].

To a first approximation the Earth is a sphere: the Earth's polar diameter is about 43 kilometers shorter than its equatorial diameter, a negligible difference of about 0.3%. As a consequence, modelling physical processes which take place in the planet require the discretisation of a sphere. Furthermore, because core dynamics occur on vastly different time scales than mantle dynamics, mantle modelling

usually leaves the core out, thereby requiring simulations to be run on a hollow sphere mesh (with the noticeable exception of [952]).

Although so-called latitude-longitude grids would seem appealing, they suffer from the convergence of meridians at the poles (resulting in over sampling at poles) and the juxtaposition of triangles near the poles and quadrilaterals elsewhere. As a consequence more regular, but more complex, grids have been designed over the years which tessellate the surface of the sphere into triangles or quadrilaterals (sometimes overlapping). There is the 'cubed sphere' [2193, 101, 466, 2430, 467, 284, 2847], the ying-yang grid [1367, 2850, 2853, 1373, 2490, 586, 587], the ying-yang-zhong grid [1160], the spiral grid [1274], an icosahedron-based grid [110, 2463], or a grid composed of 12 blocks further subdivided into quadrilaterals [2909] as used in the CitcomS code. Note that [1961] have also presented a method for generating a numerical grid on a spherical surface which allows the grid to be based on several different regular polyhedrons (including octahedron, cube, icosahedron, and rhombic dodecahedron).



Taken from [1373]

How such meshes are built is often not discussed in the literature. It is a tedious exercise of three-dimensional geometry and it can be time-consuming, especially the connectivity array generation. In [2531] I present an open source mesh generator for three hollow sphere meshes: the 'cubed sphere' mesh, the CitcomS mesh and the icosahedral mesh.

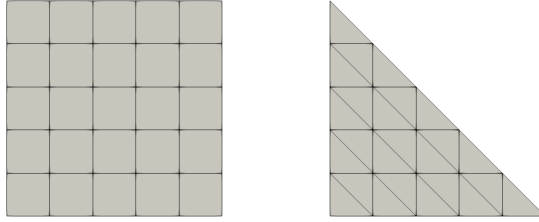
The open source code library GHOST[2531] allows three different types of hollow sphere meshes to be built , i.e. meshes bounded by two concentric spheres:

- The cubed sphere ('HS06'), composed of 6 blocks which are themselves subdivided into  $N_b \times N_b$  quadrilateral shaped cells [2218, 2193, 101, 382]. Four types of cubed spheres meshes have been proposed: the conformal, elliptic, gnomonic and spring types [2068]. However only gnomonic meshes are considered here: these are obtained by inscribing a cube within a sphere and expanding to the surface of the sphere. The cubed sphere has recently been used in large-scale mantle convection simulation in conjunction with Adaptive Mesh Refinement [19, 382].
- The CitcomS mesh ('HS12') composed of 12 blocks also subdivided into  $N_b \times N_b$  quadrilateral shaped cells [2909, 2430, 2905, 58]. Note that ASPECT [1507, 1169], a relatively new code aimed at superseedng CitcomS can generate and use this type of mesh [2530] but is not limited to it.
- The icosahedral mesh ('HS20') composed of 20 triangular blocks [110, 109] subdivided into triangles, which is used in the TERRA code [345, 346, 344, 635].

Given the regularity and symmetry of these meshes determining the location of the mesh nodes in space is a relatively straightforward task. Building the mesh connectivity in an efficient manner is where the difficulty lies.

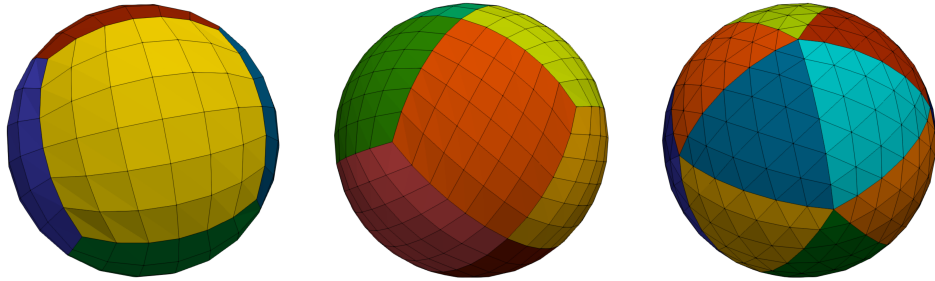
The approach to building all three meshes is identical:

1. A reference square or triangle is populated with cells, parametrised by a level  $l$ : the square is subdivided into  $l \times l$  quadrilaterals while the triangle is subdivided into  $l^2$  triangles.



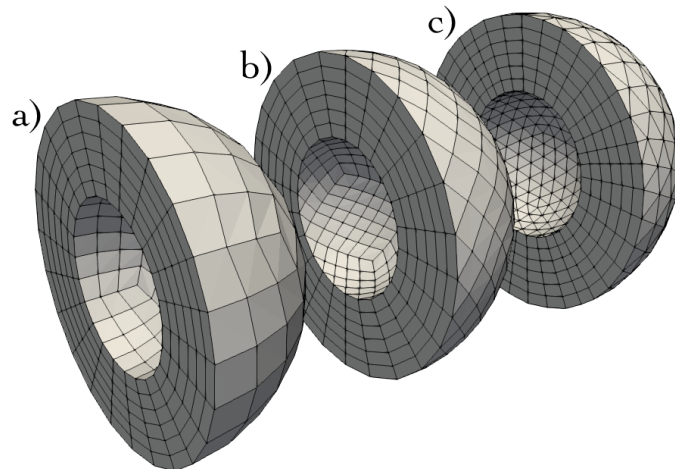
Reference square and triangles meshes at level 5.

2. This reference square or triangle is then replicated  $n_{block}$  times (6, 12 or 20) and mapped onto a portion of a unit sphere. The blocks are such that their union covers a full sphere but they cannot overlap except at the edges:



From left to right: HS06, HS12 and HS20 shells coloured by block number.

3. All block meshes are then merged together to generate a shell mesh. This task is rather complex as duplicate nodes must be removed and all connectivity arrays of the blocks must then be mended accordingly.
4. Shell meshes are replicated  $n_{layer}+1$  times outwards with increasing radii. The  $n_{layer}$  shells are then merged together to form a hollow sphere mesh:



a) HS06 mesh composed of 6 blocks containing each  $6^3$  cells; b) HS12 mesh composed of 12 blocks containing each  $6^3$  cells; e) HS20 mesh composed of 20 blocks containing each  $6^3$  cells.

More information on these steps is available in the manual of the code. In the following table the number of nodes and cells for a variety of resolutions for all three mesh types is reported. Looking at

the CitcomS literature of the past 20 years, we find that the mesh data presented in this table cover the various resolutions used, e.g.  $12 \times 48^3$  [1763, 58],  $12 \times 64^3$  [339]  $12 \times 96^3$  [340],  $12 \times 128^3$  [136, 2768, 2771]. Note that in the case of the HS06 and HS12 meshes the mesh nodes are mapped out to the 6 or 12 blocks following either an equidistant or equiangle approach (see [2068] for details on both approaches).

type	level	$N$	$N_{el}$	structure
HS06	2	78	48	$6 \times 2^3$
HS06	4	490	384	$6 \times 4^3$
HS06	8	3,474	3,072	$6 \times 8^3$
HS06	16	26,146	24,576	$6 \times 16^3$
HS06	32	202,818	196,608	$6 \times 32^3$
HS06	64	1,597,570	1,572,864	$6 \times 64^3$
HS06	128	12,681,474	12,582,912	$6 \times 128^3$
HS06	256	101,057,026	100,663,296	$6 \times 256^3$
HS12	2	150	96	$12 \times 2^3$
HS12	4	970	768	$12 \times 4^3$
HS12	8	6,930	6,144	$12 \times 8^3$
HS12	16	52,258	49,152	$12 \times 16^3$
HS12	32	405,570	393,216	$12 \times 32^3$
HS12	48	1,354,850	1,327,104	$12 \times 48^3$
HS12	64	3,195,010	3,145,728	$12 \times 64^3$
HS12	128	25,362,690	25,165,824	$12 \times 128^3$
HS12	256	202,113,538	201,326,592	$12 \times 256^3$
HS20	2	126	160	$20 \times 2^3$
HS20	4	810	1,280	$20 \times 4^3$
HS20	8	5,778	10,240	$20 \times 8^3$
HS20	16	43,554	81,920	$20 \times 16^3$
HS20	32	337,986	655,360	$20 \times 32^3$
HS20	64	2,662,530	5,242,880	$20 \times 64^3$
HS20	128	21,135,618	41,943,040	$20 \times 128^3$
HS20	256	168,428,034	335,544,320	$20 \times 256^3$

Number of nodes  $N$  and elements/cells  $N_{el}$  for the three types of meshes and for various levels.

HS06: cubed sphere; HS12: CitcomS mesh; HS20: icosahedral mesh.

## 8.11 Visco-Plasticity

 Relevant Literature: [1875, 469, 1844, 1879]  
IMPLEMENTATION of plasticity ... WORK IN PROGRESS

### 8.11.1 Scalar viscoplasticity

This formulation is quite easy to implement. It is widely used, e.g. [2786, 2533, 2396], and relies on the assumption that a scalar quantity  $\eta_p$  (the 'effective plastic viscosity') exists such that the deviatoric stress tensor

$$\tau = 2\eta_p \dot{\epsilon} \quad (649)$$

is bounded by some yield stress value  $Y$ . From Eq. (649) it follows that  $\tau_e = 2\eta_p \dot{\epsilon}_e = Y$  which yields

$$\eta_p = \frac{Y}{2\dot{\epsilon}_e}$$

This approach has also been coined the Viscosity Rescaling Method (VRM) [1366].

insert here the rederivation 2.1.1 of spmw16

It is at this stage important to realise that (i) in areas where the strainrate is low, the resulting effective viscosity will be large, and (ii) in areas where the strainrate is high, the resulting effective viscosity will be low. This is not without consequences since (effective) viscosity contrasts up to 8-10 orders of magnitude have been observed/obtained with this formulation and it makes the FE matrix very stiff, leading to (iterative) solver convergence issues. In order to contain these viscosity contrasts one usually resorts to viscosity limiters  $\eta_{min}$  and  $\eta_{max}$  such that

$$\eta_{min} \leq \eta_p \leq \eta_{max}$$

Caution must be taken when choosing both values as they may influence the final results.

Work in progress

 Relevant Literature [2933, 2935, 2934, 2932, 574, 2936, 2938, 2939, 2698, 2699, 2692, 2943, 2700] [2727, 655, 232, 1166, 183, 1878, 1589, 2283, 656, 658, 657, 2319][742] [1851][113][2360][1539][698][747][743] [1841][2628][1790][1255][1250][889] [1363][1401]

Note that [2698, 2699, 2700, 2943] use the following formulation which they attribute to [2939]:

$$\eta_{eff} = \frac{c + (\dot{\epsilon}_e/\gamma)^{1/n}}{\dot{\epsilon}_e}$$

For a perfectly plastic flow law,  $\gamma \rightarrow \infty$  and then

$$\eta_{eff} = \frac{c}{\dot{\epsilon}_e}$$

and when when  $c = 0$  then the effective viscosity is essentially of the power law type. Also, when  $n = 1$  the formulation becomes identical to the v-vp formulation (when the max viscosity is infinite) and with  $1/\gamma = \eta_{min}$ .

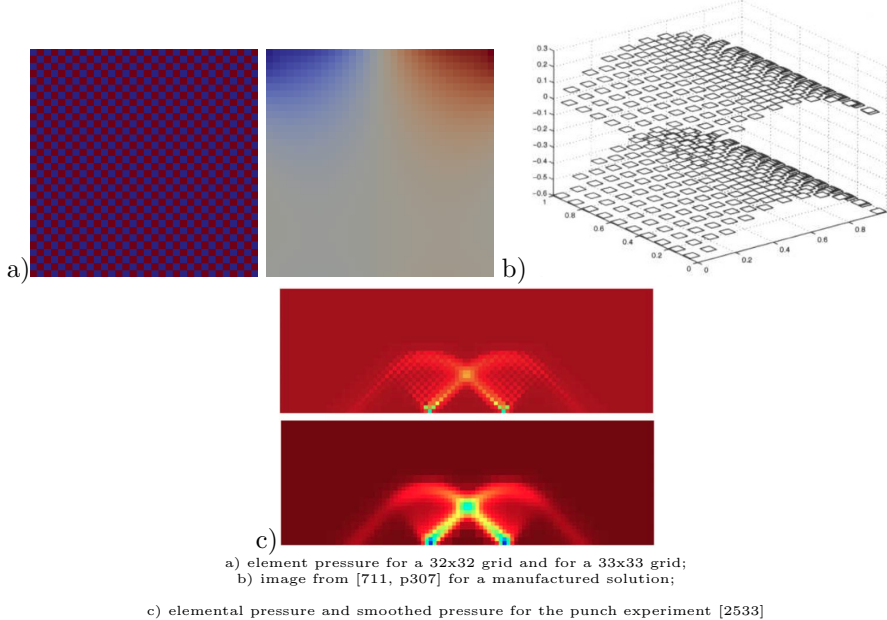
fractal distribution of shear bands in [2048]

## 8.12 Pressure smoothing

It has been widely documented that the use of the  $Q_1 \times P_0$  element is not without problems. Aside from the consequences it has on the FE matrix properties, we will here focus on another unavoidable side effect: the spurious pressure checkerboard modes.

These modes have been thoroughly analysed [1069, 443, 2237, 2238]. They can be filtered out [443] or simply smoothed [1553].

On the following figure (a,b), pressure fields for the lid driven cavity experiment are presented for both an even and un-even number of elements. We see that the amplitude of the modes can sometimes be so large that the 'real' pressure is not visible and that something as simple as the number of elements in the domain can trigger those or not at all.



The easiest post-processing step that can be used (especially when a regular grid is used) is explained in [2533]: "The element-to-node interpolation is performed by averaging the elemental values from elements common to each node; the node-to-element interpolation is performed by averaging the nodal values element-by-element. This method is not only very efficient but produces a smoothing of the pressure that is adapted to the local density of the octree. Note that these two steps can be repeated until a satisfying level of smoothness (and diffusion) of the pressure field is attained."

In the codes which rely on the  $Q_1 \times P_0$  element, the (elemental) pressure is simply defined as

```
p=np.zeros(nel, dtype=np.float64)
```

while the nodal pressure is then defined as

```
q=np.zeros(nnp, dtype=np.float64)
```

The element-to-node algorithm is then simply (in 2D):

```
count=np.zeros(nnp, dtype=np.int16)
for iel in range(0,nel):
    q[icon[0,iel]]+=p[iel]
    q[icon[1,iel]]+=p[iel]
    q[icon[2,iel]]+=p[iel]
    q[icon[3,iel]]+=p[iel]
    count[icon[0,iel]]+=1
    count[icon[1,iel]]+=1
    count[icon[2,iel]]+=1
    count[icon[3,iel]]+=1
q=q/count
```

Pressure smoothing is further discussed in [1254].

[produce figure to explain this](#)

[link to proto paper](#)

[link to least square and nodal derivatives](#)

### 8.13 Pressure scaling

As perfectly explained in the step 32 of deal.ii<sup>45</sup>, we often need to scale the  $\mathbb{G}$  term since it is many orders of magnitude smaller than  $\mathbb{K}$ , which introduces large inaccuracies in the solving process to the point that the solution is nonsensical. This scaling coefficient is  $\eta/L$  where  $\eta$  and  $L$  are representative viscosities and lengths. We start from

$$\begin{pmatrix} \mathbb{K} & \mathbb{G} \\ \mathbb{G}^T & -\mathbb{C} \end{pmatrix} \cdot \begin{pmatrix} \vec{\mathcal{V}} \\ \vec{\mathcal{P}} \end{pmatrix} = \begin{pmatrix} \vec{f} \\ \vec{h} \end{pmatrix}$$

and introduce the scaling coefficient as follows (which in fact does not alter the solution at all):

$$\begin{pmatrix} \mathbb{K} & \frac{\eta}{L}\mathbb{G} \\ \frac{\eta}{L}\mathbb{G}^T & -\frac{\eta^2}{L^2}\mathbb{C} \end{pmatrix} \cdot \begin{pmatrix} \vec{\mathcal{V}} \\ \underline{\mathcal{P}} \end{pmatrix} = \begin{pmatrix} \vec{f} \\ \underline{h} \end{pmatrix}$$

We then end up with the modified Stokes system:

$$\begin{pmatrix} \mathbb{K} & \mathbb{G} \\ \underline{\mathbb{G}}^T & \underline{\mathbb{C}} \end{pmatrix} \cdot \begin{pmatrix} \vec{\mathcal{V}} \\ \underline{\mathcal{P}} \end{pmatrix} = \begin{pmatrix} \vec{f} \\ \underline{h} \end{pmatrix}$$

where

$$\underline{\mathbb{G}} = \frac{\eta}{L}\mathbb{G} \quad \underline{\mathcal{P}} = \frac{L}{\eta}\vec{\mathcal{P}} \quad \underline{\mathbb{C}} = \frac{\eta^2}{L^2}\mathbb{C} \quad \underline{h} = \frac{\eta}{L}\vec{h}$$

After the solve phase, we recover the real pressure with  $\vec{\mathcal{P}} = \frac{\eta}{L}\underline{\mathcal{P}}$ .

---

<sup>45</sup>[https://www.dealii.org/9.0.0/doxygen/deal.II/step\\_32.html](https://www.dealii.org/9.0.0/doxygen/deal.II/step_32.html)

## 8.14 Pressure normalisation

### 8.14.1 Basic idea and naive implementation

When Dirichlet boundary conditions are imposed everywhere on the boundary, pressure is only present by its gradient in the equations. It is thus determined up to an arbitrary constant (one speaks then of a nullspace of size 1). In such a case, one commonly impose the average of the pressure over the whole domain or on a subset of the boundary to have a zero average, i.e.

$$\int_{\Omega} p dV = 0 \quad (650)$$

Another possibility is to impose the pressure value at a single node.

Let us assume for example that we are using  $Q_1 \times P_0$  elements. Then the pressure is constant inside each element. The integral above becomes:

$$\int_{\Omega} p dV = \sum_e \int_{\Omega_e} p dV = \sum_e p_e \int_{\Omega_e} dV = \sum_e p_e A_e = 0 \quad (651)$$

where the sum runs over all elements  $e$  of area  $A_e$ . This can be rewritten

$$\mathbb{L}^T \cdot \vec{\mathcal{P}} = 0$$

and it is a constraint on the pressure solution which couples *all* pressure dofs. We can associate to it a Lagrange multiplier  $\lambda$  so that we must solve the modified Stokes system:

$$\begin{pmatrix} \mathbb{K} & \mathbb{G} & 0 \\ \mathbb{G}^T & 0 & \mathbb{L} \\ 0 & \mathbb{L}^T & 0 \end{pmatrix} \cdot \begin{pmatrix} \vec{\mathcal{V}} \\ \vec{\mathcal{P}} \\ \lambda \end{pmatrix} = \begin{pmatrix} \vec{f} \\ \vec{h} \\ 0 \end{pmatrix}$$

When higher order spaces are used for pressure (continuous or discontinuous) one must then carry out the above integration numerically by means of (usually) a Gauss-Legendre quadrature.

Although valid, this approach has one main disadvantage: it makes the Stokes matrix larger (although marginally so – only one row and column are added), but more importantly it prevents the use of some of the solving strategies of Section 8.15.

### 8.14.2 Implementation – the real deal

The idea is actually quite simple and requires two steps:

1. remove the null space by prescribing the pressure at one location and solve the system;
2. post-process the pressure so as to arrive at a pressure field which fulfills the required normalisation (surface, volume, ...)

The reason why it works is as follows: a constant pressure value lies in the null space, so that one can add or delete any value to the pressure field without consequence. As such I can choose said constant such that the pressure at a given node/element is zero. All other computed pressures are then relative to that one. The post-processing step will redistribute a constant value to all pressures (it will shift them up or down) so that the normalising condition is respected.

## 8.15 Solving the Stokes system

Let us start again from the (full) Stokes system:

$$\begin{pmatrix} \mathbb{K} & \mathbb{G} \\ \mathbb{G}^T & -\mathbb{C} \end{pmatrix} \cdot \begin{pmatrix} \vec{\mathcal{V}} \\ \vec{\mathcal{P}} \end{pmatrix} = \begin{pmatrix} \vec{f} \\ \vec{h} \end{pmatrix} \quad (652)$$

We need to solve this system in order to obtain the solution, i.e. the  $\vec{\mathcal{V}}$  and  $\vec{\mathcal{P}}$  vectors. But how? Unfortunately, this question is not simple to answer and the appropriate method depends on many parameters, but mainly on how big the matrix blocks are and what the condition number of the matrix  $\mathbb{K}$  is.

In what follow I cover:

- solving when the penalty approach is used
- the Schur complement approach
- the FGMRES approach [691]

 Relevant Literature[1988, 1744, 909, 1468, 1469, 1479]

Preconditioners  Relevant Literature: [2306]

### 8.15.1 when using the penalty formulation

In this case we are only solving for velocity since pressure is recovered in a post-processing step:

$$(\mathbb{K}_\eta + \mathbb{K}_\lambda) \cdot \vec{\mathcal{V}} = \vec{f}$$

We also know that the penalty factor is many orders of magnitude higher than the viscosity and in combination with the use of the  $Q_1 \times P_0$  element the resulting matrix condition number is very high so that the use of iterative solvers is precluded. Indeed codes such as SOPALE [901], DOUAR [269], or FANTOM [2528] relying on the penalty formulation all use direct solvers. The most popular are BLK-FCT<sup>46</sup>, MUMPS<sup>47</sup>[30, 32, 31, 33], PasTiX [1173], WSMP<sup>48</sup> [1090, 1091], UMFPACK and CHOLMOD<sup>49</sup> , SuperLU, PARDISO<sup>50</sup> [660, 2691, 1498], or those inside PETSc ??.

Braun et al [269] list the following features of such solvers:

- Robust
- Black-box operation
- Difficult to parallelize
- Memory consumption
- Limited scalability

The main advantage of direct solvers is used in this case: They can solve ill-conditioned matrices. However memory requirements for the storage of number of nonzeros in the Cholesky matrix grow very fast as the number of equations/grid size increases, especially in 3D, to the point that even modern computers with tens of Gb of RAM cannot deal with a  $100^3$  element mesh. This explains why direct solvers are often used for 2D problems and rarely in 3D with noticeable exceptions [2533, 2828, 271, 1663, 25, 26, 27, 2776, 1932].

---

<sup>46</sup><http://dm.unife.it/blkfclt/>

<sup>47</sup><http://mumps.enseeiht.fr/>

<sup>48</sup><http://www.research.ibm.com/projects/wsmp>

<sup>49</sup><http://faculty.cse.tamu.edu/davis/suitesparse.html>

<sup>50</sup><https://www.pardiso-project.org/>

### 8.15.2 Conjugate gradient and the Schur complement approach

Let us write the above system as two equations:

$$\mathbb{K} \cdot \vec{\mathcal{V}} + \mathbb{G} \cdot \vec{\mathcal{P}} = \vec{f} \quad (653)$$

$$\mathbb{G}^T \cdot \vec{\mathcal{V}} = \vec{h} \quad (654)$$

The first line can be re-written  $\vec{\mathcal{V}} = \mathbb{K}^{-1} \cdot (\vec{f} - \mathbb{G} \cdot \vec{\mathcal{P}})$  and can be inserted in the second:

$$\mathbb{G}^T \cdot \vec{\mathcal{V}} = \mathbb{G}^T \cdot [\mathbb{K}^{-1} \cdot (\vec{f} - \mathbb{G} \cdot \vec{\mathcal{P}})] = \vec{h} \quad (655)$$

or,

$$(\mathbb{G}^T \cdot \mathbb{K}^{-1} \cdot \mathbb{G}) \cdot \vec{\mathcal{P}} = \mathbb{G}^T \cdot \mathbb{K}^{-1} \cdot \vec{f} - \vec{h} \quad (656)$$

The matrix  $\mathbb{S} = \mathbb{G}^T \cdot \mathbb{K}^{-1} \cdot \mathbb{G}$  is called the Schur complement. It is Symmetric (since  $\mathbb{K}$  is symmetric) and Positive-Definite<sup>51</sup> (SPD) if  $\text{Ker}(\mathbb{G}) = 0$ . [look in donea-huerta book for details](#) Having solved this equation (we have obtained  $\vec{\mathcal{P}}$ ), the velocity can be recovered by solving  $\mathbb{K} \cdot \vec{\mathcal{V}} = \vec{f} - \mathbb{G} \cdot \vec{\mathcal{P}}$ .

For now, let us assume that we have built the  $\mathbb{S}$  matrix and the right hand side  $\vec{f} = \mathbb{G}^T \cdot \mathbb{K}^{-1} \cdot \vec{f} - \vec{h}$ . We must solve  $\mathbb{S} \cdot \vec{\mathcal{P}} = \vec{f}$ .

One can resort to so-called Richardson iterations, defined as follows (e.g., see [2685], p141): in solving the matrix equation  $\mathbf{A} \cdot \vec{X} = \vec{b}$ , the Richardson iterative method is defined by:

$$\vec{X}_{k+1} = \vec{X}_k + \alpha_k (-\mathbf{A} \cdot \vec{X}_k + \vec{b}) \quad m \geq 0 \quad (657)$$

where the  $\alpha_k$ 's are real scalars. It is easy to see that when the method converges then  $\vec{X}_{k+1} \simeq \vec{X}_k$  and then  $\mathbf{A} \cdot \vec{X} = \vec{b}$  is satisfied. In our case, it writes:

$$\begin{aligned} \vec{\mathcal{P}}_{k+1} &= \vec{\mathcal{P}}_k + \alpha_k (-\mathbb{S} \cdot \vec{\mathcal{P}}_k + \vec{f}) \\ &= \vec{\mathcal{P}}_k + \alpha_k (-\mathbb{G}^T \cdot \mathbb{K}^{-1} \cdot \mathbb{G} \cdot \vec{\mathcal{P}}_k + \mathbb{G}^T \cdot \mathbb{K}^{-1} \cdot \vec{f} - \vec{h}) \\ &= \vec{\mathcal{P}}_k + \alpha_k [\mathbb{G}^T \cdot \mathbb{K}^{-1} \cdot (-\mathbb{G} \cdot \vec{\mathcal{P}}_k + \vec{f}) - \vec{h}] \\ &= \vec{\mathcal{P}}_k + \alpha_k [\mathbb{G}^T \cdot \mathbb{K}^{-1} \cdot (\mathbb{K} \cdot \vec{\mathcal{V}}_k) - \vec{h}] \\ &= \vec{\mathcal{P}}_k + \alpha_k (\mathbb{G}^T \cdot \vec{\mathcal{V}}_k - \vec{h}) \end{aligned} \quad (658)$$

The above iterations are then carried out and for each new pressure field the associated velocity field is computed. The method of using Richardson iterations applied to the Schur complement is commonly called the Uzawa algorithm [254, p221].

Uzawa algorithm (1):

$$\text{solve } \mathbb{K} \cdot \vec{\mathcal{V}}_k = \vec{f} - \mathbb{G} \cdot \vec{\mathcal{P}}_{k-1} \quad (659)$$

$$\vec{\mathcal{P}}_k = \vec{\mathcal{P}}_{k-1} + \alpha (\mathbb{G}^T \cdot \vec{\mathcal{V}}_k - \vec{h}) \quad k = 1, 2, \dots \quad (660)$$

This method is rather simple to implement, although what makes an appropriate set of  $\alpha_k$  values is not straightforward, which is why the conjugate gradient is often preferred, as detailed in the next subsection.

It is known that such iterations will converge for  $0 < \alpha < \rho(\mathbb{S}) = \lambda_{max}(\mathbb{S})$  where  $\rho(\mathbb{S})$  is the spectral radius of the matrix  $\mathbb{S}$  which is essentially the largest, in absolute value, eigenvalue of  $\mathbb{S}$  (neither of which can be computed easily). It can also be proven that the rate of convergence depends on the condition number of the matrix.

Richardson iterations are part of the family of stationary iterative methods, since it can be rewritten

$$\vec{X}_{k+1} = (\mathbf{I} - \alpha_k \mathbf{A}) \cdot \vec{X}_k + \alpha_k \vec{b} \quad (661)$$

<sup>51</sup>  $M$  positive definite  $\iff x^T M x > 0 \forall x \in \mathbb{R}^n \setminus \mathbf{0}$

which is the definition of a stationary method.

Since the  $\alpha$  parameter is the key to a successful Uzawa algorithm, this issue has of course been looked into. What follows is presented in [254, p221]. For the analysis of the Uzawa algorithm, we define the residue

$$\vec{\mathcal{R}}_k = \vec{h} - \mathbb{G}^T \cdot \vec{\mathcal{V}}_k$$

In addition, suppose the solution of the saddle point problem is denoted by  $(\mathcal{V}^*, \mathcal{P}^*)$ . Now substituting the iteration formula for  $\mathcal{V}_k$ , we get

$$\mathcal{R}_k = \mathbb{G}^T \cdot \vec{\mathcal{V}}^* - \mathbb{G}^T \cdot \mathbb{K}^{-1}(\vec{f} - \mathbb{G} \cdot \mathcal{P}_{k-1}) \quad (662)$$

$$= \mathbb{G}^T \cdot \vec{\mathcal{V}}^* - \mathbb{G}^T \cdot \mathbb{K}^{-1}(\mathbb{K} \cdot \vec{\mathcal{V}}^* + \mathbb{G} \cdot \vec{\mathcal{P}}^* - \mathbb{G} \cdot \mathcal{P}_{k-1}) \quad (663)$$

$$= \mathbb{G}^T \cdot \mathbb{K}^{-1} \cdot \mathbb{G} \cdot (\vec{\mathcal{P}}_{k-1} - \vec{\mathcal{P}}^*) \quad (664)$$

From Eq. 660 it follows that:

$$\mathcal{P}_k - \mathcal{P}_{k-1} = \alpha(\mathbb{G}^T \cdot \vec{\mathcal{V}}_k - \vec{h}) \quad (665)$$

$$= -\alpha \vec{\mathcal{R}}_k \quad (666)$$

$$= -\alpha \mathbb{G}^T \cdot \mathbb{K}^{-1} \cdot \mathbb{G} \cdot (\vec{\mathcal{P}}_{k-1} - \vec{\mathcal{P}}^*) \quad (667)$$

$$= \alpha \mathbb{G}^T \cdot \mathbb{K}^{-1} \cdot \mathbb{G} \cdot (\vec{\mathcal{P}}^* - \vec{\mathcal{P}}_{k-1}) \quad (668)$$

Thus the Uzawa algorithm is equivalent to applying the gradient method to the reduced equation using a fixed step size. In particular, the iteration converges for  $\alpha < 2\|\mathbb{G}^T \cdot \mathbb{K}^{-1} \cdot \mathbb{G}\|^{-1}$  and one can show that the good step size  $\alpha_k$  is given by

$$\alpha_k = \frac{\mathcal{R}_k \cdot \mathcal{R}_k}{(\mathbb{G} q_k) \cdot (\mathbb{K}^{-1} \mathbb{G} q_k)} \quad (669)$$

However, if we were to use this rule formally, we would need an additional multiplication by  $\mathbb{K}^{-1}$  in every step of the iteration. This can be avoided by storing an auxiliary vector.

Note that in [1005] it is stated: the convergence of this algorithm is proved for  $\alpha \in (0, 2\mu/d)$  (where  $d$  is the number of dimensions).

check this, and report page number

Note that this algorithm is presented in [2943] in the context of viscoplastic flow.

As mentioned above, there is a way to rework the original Uzawa algorithm to include Eq. (669). It yields a modified Uzawa algorithm [254, p221]:

**Uzawa algorithm (2):** Solve  $\mathbb{K} \cdot \vec{\mathcal{V}}_1 = \vec{f} - \mathbb{G} \cdot \vec{\mathcal{P}}_0$ . For  $k = 1, 2, \dots$ , compute

$$\vec{q}_k = \vec{h} - \mathbb{G}^T \cdot \vec{\mathcal{V}}_k \quad (670)$$

$$\vec{p}_k = \mathbb{G} \cdot q_k \quad (671)$$

$$\vec{H}_k = \mathbb{K}^{-1} \cdot \vec{p}_k \quad (672)$$

$$\alpha_k = \frac{\vec{q}_k \cdot \vec{q}_k}{\vec{p}_k \cdot \vec{H}_k} \quad (673)$$

$$\vec{\mathcal{P}}_k = \vec{\mathcal{P}}_{k-1} - \alpha_k \vec{q}_k \quad (674)$$

$$\vec{\mathcal{V}}_{k+1} = \vec{\mathcal{V}}_k + \alpha_k \vec{H}_k \quad (675)$$

 Relevant Literature[403, 407]

### 8.15.3 Conjugate gradient and the Schur complement approach

Since  $\mathbb{S}$  is SPD, the Conjugate Gradient (CG) method [1188] is very appropriate to solve this system. Indeed, looking at the definition of Wikipedia: "*In mathematics, the conjugate gradient method is an algorithm for the numerical solution of particular systems of linear equations, namely those whose matrix is symmetric and positive-definite. The conjugate gradient method is often implemented as an iterative algorithm, applicable to sparse systems that are too large to be handled by a direct implementation or other*

direct methods such as the Cholesky decomposition. Large sparse systems often arise when numerically solving partial differential equations or optimization problems.”

A simple Google search tells us that the Conjugate Gradient algorithm is as follows:

```

r0 := b − Ax0
if r0 is sufficiently small, then return x0 as the result
p0 := r0
k := 0
repeat
     $\alpha_k := \frac{\mathbf{r}_k^\top \mathbf{r}_k}{\mathbf{p}_k^\top \mathbf{A} \mathbf{p}_k}$ 
    xk+1 := xk +  $\alpha_k \mathbf{p}_k$ 
    rk+1 := rk −  $\alpha_k \mathbf{A} \mathbf{p}_k$ 
    if rk+1 is sufficiently small, then exit loop
     $\beta_k := \frac{\mathbf{r}_{k+1}^\top \mathbf{r}_{k+1}}{\mathbf{r}_k^\top \mathbf{r}_k}$ 
    pk+1 := rk+1 +  $\beta_k \mathbf{p}_k$ 
    k := k + 1
end repeat
return xk+1 as the result

```

Algorithm as obtained from Wikipedia<sup>52</sup>

This algorithm is of course explained in detail in many textbooks such as [2215]

[add biblio](#)

Let us look at this algorithm up close. The parts which may prove to be somewhat tricky are those involving the matrix inverse (in our case the Schur complement). We start the iterations with a guess pressure  $\vec{P}_0$  ( and an initial guess velocity which could be obtained by solving  $\mathbb{K} \cdot \vec{V}_0 = \vec{f} - \mathbb{G} \cdot \vec{P}_0$ ).

$$\vec{r}_0 = \vec{f} - \mathbb{S} \cdot \vec{P}_0 \quad (676)$$

$$= \mathbb{G}^T \cdot \mathbb{K}^{-1} \cdot \vec{f} - \vec{h} - (\mathbb{G}^T \cdot \mathbb{K}^{-1} \cdot \mathbb{G}) \cdot \vec{P}_0 \quad (677)$$

$$= \mathbb{G}^T \cdot \mathbb{K}^{-1} \cdot (\vec{f} - \mathbb{G} \cdot \vec{P}_0) - \vec{h} \quad (678)$$

$$= \mathbb{G}^T \cdot \mathbb{K}^{-1} \cdot \mathbb{K} \cdot \vec{V}_0 - \vec{h} \quad (679)$$

$$= \mathbb{G}^T \cdot \vec{V}_0 - \vec{h} \quad (680)$$

$$(681)$$

We now turn to the  $\alpha_k$  coefficient:

$$\alpha_k = \frac{\vec{r}_k^T \cdot \vec{r}_k}{\vec{p}_k \cdot \mathbb{S} \cdot \vec{p}_k} = \frac{\vec{r}_k^T \cdot \vec{r}_k}{\vec{p}_k \cdot \mathbb{G}^T \cdot \mathbb{K}^{-1} \cdot \mathbb{G} \cdot \vec{p}_k} = \frac{\vec{r}_k^T \cdot \vec{r}_k}{(\mathbb{G} \cdot \vec{p}_k)^T \cdot \mathbb{K}^{-1} \cdot (\mathbb{G} \cdot \vec{p}_k)}$$

We then define  $\tilde{\vec{p}}_k = \mathbb{G} \cdot \vec{p}_k$ , so that  $\alpha_k$  can be computed as follows:

1. compute  $\tilde{\vec{p}}_k = \mathbb{G} \cdot \vec{p}_k$
2. solve  $\mathbb{K} \cdot \vec{d}_k = \tilde{\vec{p}}_k$
3. compute  $\alpha_k = (\vec{r}_k^T \cdot \vec{r}_k) / (\tilde{\vec{p}}_k^T \cdot \vec{d}_k)$

Then we need to look at the term  $\mathbb{S} \cdot \vec{p}_k$ :

$$\mathbb{S} \cdot \vec{p}_k = \mathbb{G}^T \cdot \mathbb{K}^{-1} \cdot \mathbb{G} \cdot \vec{p}_k = \mathbb{G}^T \cdot \mathbb{K}^{-1} \cdot \tilde{\vec{p}}_k = \mathbb{G}^T \cdot \vec{d}_k$$

We can then rewrite the CG algorithm as follows [2914]:

- $\vec{r}_0 = \mathbb{G}^T \cdot \vec{V}_0 - \vec{h}$

---

<sup>52</sup>[https://en.wikipedia.org/wiki/Conjugate\\_gradient\\_method](https://en.wikipedia.org/wiki/Conjugate_gradient_method)

- if  $\vec{r}_0$  is sufficiently small, then return  $(\vec{\mathcal{V}}_0, \vec{\mathcal{P}}_0)$  as the result
- $\vec{p}_0 = \vec{r}_0$
- $k = 0$
- repeat
  - compute  $\tilde{\vec{p}}_k = \mathbb{G} \cdot \vec{p}_k$
  - solve  $\mathbb{K} \cdot \vec{d}_k = \tilde{\vec{p}}_k$
  - compute  $\alpha_k = (\vec{r}_k^T \cdot \vec{r}_k) / (\tilde{\vec{p}}_k^T \cdot \vec{d}_k)$
  - $\vec{\mathcal{P}}_{k+1} = \vec{\mathcal{P}}_k + \alpha_k \vec{p}_k$
  - $\vec{r}_{k+1} = \vec{r}_k - \alpha_k \mathbb{G}^T \cdot \vec{d}_k$
  - if  $\vec{r}_{k+1}$  is sufficiently small, then exit loop
  - $\beta_k = (\vec{r}_{k+1}^T \cdot \vec{r}_{k+1}) / (\vec{r}_k^T \cdot \vec{r}_k)$
  - $\vec{p}_{k+1} = \vec{r}_{k+1} + \beta_k \vec{p}_k$
  - $k = k + 1$
- return  $\vec{\mathcal{P}}_{k+1}$  as result

We see that we have managed to solve the Schur complement equation with the Conjugate Gradient method without ever building the matrix  $\mathbb{S}$ . Having obtained the pressure solution, we can easily recover the corresponding velocity with  $\mathbb{K} \cdot \vec{\mathcal{V}}_{k+1} = \vec{f} - \mathbb{G} \cdot \vec{\mathcal{P}}_{k+1}$ . However, this is rather unfortunate because it requires yet another solve with the  $\mathbb{K}$  matrix. As it turns out, we can slightly alter the above algorithm to have it update the velocity as well so that this last solve is unnecessary.

We have

$$\vec{\mathcal{V}}_{k+1} = \mathbb{K}^{-1} \cdot (\vec{f} - \mathbb{G} \cdot \vec{\mathcal{P}}_{k+1}) \quad (682)$$

$$= \mathbb{K}^{-1} \cdot (\vec{f} - \mathbb{G} \cdot (\vec{\mathcal{P}}_k + \alpha_k \vec{p}_k)) \quad (683)$$

$$= \mathbb{K}^{-1} \cdot (\vec{f} - \mathbb{G} \cdot \vec{\mathcal{P}}_k) - \alpha_k \mathbb{K}^{-1} \cdot \mathbb{G} \cdot \vec{p}_k \quad (684)$$

$$= \vec{\mathcal{V}}_k - \alpha_k \mathbb{K}^{-1} \cdot \tilde{\vec{p}}_k \quad (685)$$

$$= \vec{\mathcal{V}}_k - \alpha_k \vec{d}_k \quad (686)$$

and we can insert this minor extra calculation inside the algorithm and get the velocity solution nearly for free. The final CG algorithm is then

#### solver\_cg:

- compute  $\vec{\mathcal{V}}_0 = \mathbb{K}^{-1} \cdot (\vec{f} - \mathbb{G} \cdot \vec{\mathcal{P}}_0)$
- $\vec{r}_0 = \mathbb{G}^T \cdot \vec{\mathcal{V}}_0 - \vec{h}$
- if  $\vec{r}_0$  is sufficiently small, then return  $(\vec{\mathcal{V}}_0, \vec{\mathcal{P}}_0)$  as the result
- $\vec{p}_0 = \vec{r}_0$
- $k = 0$
- repeat
  - compute  $\tilde{\vec{p}}_k = \mathbb{G} \cdot \vec{p}_k$
  - solve  $\mathbb{K} \cdot \vec{d}_k = \tilde{\vec{p}}_k$
  - compute  $\alpha_k = (\vec{r}_k^T \cdot \vec{r}_k) / (\tilde{\vec{p}}_k^T \cdot \vec{d}_k)$
  - $\vec{\mathcal{P}}_{k+1} = \vec{\mathcal{P}}_k + \alpha_k \vec{p}_k$
  - $\vec{\mathcal{V}}_{k+1} = \vec{\mathcal{V}}_k - \alpha_k \vec{d}_k$
  - $\vec{r}_{k+1} = \vec{r}_k - \alpha_k \mathbb{G}^T \cdot \vec{d}_k$

- if  $\vec{r}_{k+1}$  is sufficiently small ( $\|\vec{r}_{k+1}\|_2 / \|\vec{r}_0\|_2 < tol$ ), then exit loop
- $\beta_k = (r_{k+1}^T r_{k+1}) / (r_k^T r_k)$
- $\vec{p}_{k+1} = \vec{r}_{k+1} + \beta_k \vec{p}_k$
- $k = k + 1$
- return  $\vec{\mathcal{P}}_{k+1}$  as result

This iterative algorithm will converge to the solution with a rate which depends on the condition number of the  $\mathbb{S}$  matrix, which is not easy to compute since  $\mathbb{S}$  is never built. However, it has been established that large viscosity contrasts in the domain will have a negative impact on the convergence.

**Remark.** This algorithm requires one solve with matrix  $\mathbb{K}$  per iteration but says nothing about the method employed to do so (direct solver, iterative solver, ...)

One thing we know improves the convergence of any iterative solver is the use of a preconditioner matrix and therefore now focus on the Preconditioned Conjugate Gradient (PCG) method. Once again a quick Google search yields:

```

r0 := b - Ax0
z0 := M-1r0
p0 := z0
k := 0
repeat
     $\alpha_k := \frac{\mathbf{r}_k^T \mathbf{z}_k}{\mathbf{p}_k^T \mathbf{A} \mathbf{p}_k}$ 
     $\mathbf{x}_{k+1} := \mathbf{x}_k + \alpha_k \mathbf{p}_k$ 
     $\mathbf{r}_{k+1} := \mathbf{r}_k - \alpha_k \mathbf{A} \mathbf{p}_k$ 
    if  $\mathbf{r}_{k+1}$  is sufficiently small then exit loop end if
     $\mathbf{z}_{k+1} := \mathbf{M}^{-1} \mathbf{r}_{k+1}$ 
     $\beta_k := \frac{\mathbf{z}_{k+1}^T \mathbf{r}_{k+1}}{\mathbf{z}_k^T \mathbf{r}_k}$ 
     $\mathbf{p}_{k+1} := \mathbf{z}_{k+1} + \beta_k \mathbf{p}_k$ 
    k := k + 1
end repeat
The result is xk+1

```

Algorithm obtained from Wikipedia<sup>53</sup>.

Note that in the algorithm above the preconditioner matrix  $M$  has to be symmetric positive-definite and fixed, i.e., cannot change from iteration to iteration. We see that this algorithm introduces an additional vector  $\vec{z}$  and a solve with the matrix  $M$  at each iteration, which means that  $M$  must be such that solving  $M \cdot \vec{x} = \vec{f}$  where  $\vec{f}$  is a given rhs vector must be cheap. Ultimately, the PCG algorithm applied to the Schur complement equation takes the form:

#### solver\_pcg:

- compute  $\mathcal{V}_0 = \mathbb{K}^{-1}(f - \mathbb{G}\mathcal{P}_0)$
- $r_0 = \mathbb{G}^T \mathcal{V}_0 - h$
- if  $\vec{r}_0$  is sufficiently small, then return  $(\vec{\mathcal{V}}_0, \vec{\mathcal{P}}_0)$  as the result
- $\vec{z}_0 = M^{-1} \cdot \vec{r}_0$
- $\vec{p}_0 = \vec{z}_0$
- $k = 0$

<sup>53</sup>[https://en.wikipedia.org/wiki/Conjugate\\_gradient\\_method](https://en.wikipedia.org/wiki/Conjugate_gradient_method)

- repeat
  - compute  $\tilde{\vec{p}}_k = \mathbb{G} \cdot \vec{p}_k$
  - solve  $\mathbb{K} \cdot \vec{d}_k = \tilde{\vec{p}}_k$
  - compute  $\alpha_k = (\vec{r}_k^T \cdot \vec{z}_k) / (\tilde{\vec{p}}_k^T \cdot \vec{d}_k)$
  - $\vec{\mathcal{P}}_{k+1} = \mathcal{P}_k + \alpha_k \vec{p}_k$
  - $\vec{\mathcal{V}}_{k+1} = \mathcal{V}_k - \alpha_k \vec{d}_k$
  - $\vec{r}_{k+1} = \vec{r}_k - \alpha_k \mathbb{G}^T \cdot \vec{d}_k$
  - if  $r_{k+1}$  is sufficiently small ( $\|r_{k+1}\|_2 / \|r_0\|_2 < tol$ ), then exit loop
  - $\vec{z}_{k+1} = M^{-1} \cdot r_{k+1}$
  - $\beta_k = (\vec{z}_{k+1}^T \cdot \vec{r}_{k+1}) / (\vec{z}_k^T \cdot \vec{r}_k)$
  - $\vec{p}_{k+1} = \vec{z}_{k+1} + \beta_k \vec{p}_k$
  - $k = k + 1$
- return  $\vec{\mathcal{P}}_{k+1}$  as result

Following [2914] one can define the following matrix as preconditioner:

$$M = \text{diag} [\mathbb{G}^T (\text{diag}[\mathbb{K}])^{-1} \mathbb{G}]$$

which is the preconditioner used for the Citcom codes (see appendix ??). It can be constructed while the FEM matrix is being built/assembled and it is trivial to invert.

how to compute  $M$  for the Schur complement ?

#### 8.15.4 The Augmented Lagrangian approach

see LaCoDe paper [664].

We start from the saddle point Stokes system:

$$\begin{pmatrix} \mathbb{K} & \mathbb{G} \\ \mathbb{G}^T & 0 \end{pmatrix} \cdot \begin{pmatrix} \vec{\mathcal{V}} \\ \vec{\mathcal{P}} \end{pmatrix} = \begin{pmatrix} \vec{f} \\ \vec{h} \end{pmatrix} \quad (687)$$

The AL method consists of subtracting  $\lambda^{-1} \mathbb{M}_p \cdot \vec{\mathcal{P}}$  from the left and right-side of the mass conservation equation (where  $\mathbb{M}_p$  is the pressure mass matrix) and introducing the following iterative scheme:

$$\begin{pmatrix} \mathbb{K} & \mathbb{G} \\ \mathbb{G}^T & -\lambda^{-1} \mathbb{M}_p \end{pmatrix} \cdot \begin{pmatrix} \vec{\mathcal{V}}^{k+1} \\ \vec{\mathcal{P}}^{k+1} \end{pmatrix} = \begin{pmatrix} \vec{f} \\ \vec{h} - \lambda^{-1} \mathbb{M}_p \cdot \vec{\mathcal{P}}^k \end{pmatrix} \quad (688)$$

where  $k$  is the iteration counter and  $\lambda$  is an artificial compressibility term which has the dimensions of dynamic viscosity. The choice of  $\lambda$  can be difficult as too low or too high a value yields either erroneous results and/or terribly ill-conditioned matrices. LaCoDe paper (!! use such a method and report that  $\lambda = \max_{\Omega}(\eta)$ ) works well. Note that at convergence we have  $\|\vec{\mathcal{P}}^{k+1} - \vec{\mathcal{P}}^k\| < \epsilon$  and then Eq.(688) converges to Eq.(687) and the velocity and pressure fields are solution of the unmodified system Eq.(687).

The introduction of this term serves one purpose: allowing us to solve the system in a segregated manner (i.e. computing successive iterates of the velocity and pressure fields until convergence is reached). The second line of Eq. (688) is

$$\mathbb{G}^T \cdot \vec{\mathcal{V}}^{k+1} - \lambda^{-1} \mathbb{M}_p \cdot \vec{\mathcal{P}}^{k+1} = \vec{h} - \lambda^{-1} \mathbb{M}_p \cdot \vec{\mathcal{P}}^k$$

and can therefore be rewritten

$$\vec{\mathcal{P}}^{k+1} = \vec{\mathcal{P}}^k + \lambda \mathbb{M}_p^{-1} \cdot (\mathbb{G}^T \cdot \vec{\mathcal{V}}^{k+1} - \vec{h})$$

We can then substitute this expression of  $\vec{\mathcal{P}}^{k+1}$  in the first equation. This yields:

$$\mathbb{K} \cdot \vec{\mathcal{V}}^{k+1} = \vec{f} - \mathbb{G} \cdot \mathcal{P}^{k+1}) \quad (689)$$

$$\mathbb{K} \cdot \vec{\mathcal{V}}^{k+1} = \vec{f} - \mathbb{G} \cdot (\vec{\mathcal{P}}^k + \lambda \mathbb{M}_p^{-1} \cdot (\mathbb{G}^T \cdot \vec{\mathcal{V}}^{k+1} - \vec{h})) \quad (690)$$

$$\mathbb{K} \cdot \vec{\mathcal{V}}^{k+1} + \lambda \mathbb{G} \cdot \mathbb{M}_p^{-1} \cdot \mathbb{G}^T \cdot \vec{\mathcal{V}}^{k+1} = \vec{f} - \mathbb{G} \cdot (\vec{\mathcal{P}}^k - \lambda \mathbb{M}_p^{-1} \vec{h}) \quad (691)$$

$$\underbrace{(\mathbb{K} + \lambda \mathbb{G} \cdot \mathbb{M}_p^{-1} \cdot \mathbb{G}^T)}_{\tilde{\mathbb{K}}} \cdot \vec{\mathcal{V}}^{k+1} = \underbrace{\vec{f} - \mathbb{G} \cdot (\vec{\mathcal{P}}^k - \lambda \mathbb{M}_p^{-1} \vec{h})}_{\vec{f}^{k+1}} \quad (692)$$

$$(693)$$

The iterative algorithm goes as follows:

1. if it is the first timestep, set  $\vec{\mathcal{P}}^0 = 0$ , otherwise set it to the pressure of the previous timestep.
2. calculate  $\tilde{\mathbb{K}}$
3. calculate  $\vec{f}^{k+1}$
4. solve  $\tilde{\mathbb{K}} \cdot \vec{\mathcal{V}}^{k+1} = \vec{f}^{k+1}$
5. update pressure with  $\vec{\mathcal{P}}^{k+1} = \vec{\mathcal{P}}^k + \lambda \mathbb{M}_p^{-1} \cdot (\mathbb{G}^T \cdot \vec{\mathcal{V}}^{k+1} - \vec{h})$

**Remark.** If discontinuous pressures are used, the pressure mass matrix can be inverted element by element which is cheaper than inverting  $\mathbb{M}_p$  as a whole.

**Remark.** This method has obvious ties with the penalty method.

**Remark.** If  $\lambda >> \max_{\Omega} \eta$  then the matrix  $\tilde{\mathbb{K}}$  is ill-conditioned and an iterative solver must be used.

### 8.15.5 The GMRES approach

The Generalized Minimal Residual method [2216] is an extension of MINRES (which is only applicable to symmetric systems) to unsymmetric systems. Like MINRES, it generates a sequence of orthogonal vectors and combines these through a least-squares solve and update. However, in the absence of symmetry this can no longer be done with short recurrences. As a consequence, all previously computed vectors in the orthogonal sequence have to be retained and for this reason "restarted" versions of the method are used.

It must be said that the (preconditioned) GMRES method is actually much more difficult to implement than the (preconditioned) Conjugate Gradient method. However, since it can deal with unsymmetric matrices, it means that it can be applied directly to the Stokes system matrix (as opposed to the CG method which is used on the Schur complement equation).

 Relevant Literature: [763, p208] [2215, 2214] [96] [65]

finish GMRES algo description, not sure what to do, hard to explain, not easy to code.

## 8.16 The consistent boundary flux (CBF)

The Consistent Boundary Flux technique was devised to alleviate the problem of the accuracy of primary variables derivatives (mainly velocity and temperature) on boundaries. These derivatives are important since they are needed to compute the heat flux (and therefore the Nusselt number) or dynamic topography and geoid.

The idea was first introduced in [1810] and later used in geodynamics [2902]. It was finally implemented in the CitcomS code [2905, 1849] and more recently in the ASPECT code (dynamic topography postprocessor). Note that the CBF should be seen as a post-processor step as it does not alter the primary variables values.

The CBF method is implemented and used in Stone ???. It is also discussed but not explicitly named in [2118, p309]. Also see [1527, 1064, 1727].

### 8.16.1 The CBF applied to the Stokes equation

We start from the strong form:

$$\vec{\nabla} \cdot \boldsymbol{\sigma} + \vec{b} = \vec{0} \quad (694)$$

and then write the weak form on an element  $e$ :

$$\int_{\Omega_e} N_i^y \vec{\nabla} \cdot \boldsymbol{\sigma} d\Omega + \int_{\Omega_e} N_i^y \vec{b} d\Omega = \vec{0} \quad (695)$$

We then use the two equations:

$$\boldsymbol{\nabla} \cdot (N\boldsymbol{\sigma}) = N\boldsymbol{\nabla} \cdot \boldsymbol{\sigma} + \boldsymbol{\nabla}N \cdot \boldsymbol{\sigma} \quad (\text{chain rule})$$

$$\int_{\Omega} (\boldsymbol{\nabla} \cdot \boldsymbol{\sigma}) dV = \int_{\Gamma} \boldsymbol{\sigma} \cdot \mathbf{n} dS \quad (\text{divergence theorem})$$

and integrate by parts in order to obtain:

$$\int_{\Gamma} N_i^y \boldsymbol{\sigma} \cdot \mathbf{n} dS - \int_{\Omega_e} \vec{\nabla} N_i^y \cdot \boldsymbol{\sigma} d\Omega + \int_{\Omega_e} N_i^y \vec{b} d\Omega = \vec{0} \quad (696)$$

and since the traction vector  $\vec{t}$  is given by  $\vec{t} = \boldsymbol{\sigma} \cdot \mathbf{n}$  we have:

$$\int_{\Gamma_e} N_i^y t dS = \int_{\Omega_e} \vec{\nabla} N_i^y \cdot \boldsymbol{\sigma} d\Omega - \int_{\Omega_e} N_i^y \vec{b} d\Omega \quad (697)$$

The core idea of the method lies in considering the traction vector as an unknown living on the nodes on the boundary, and assuming we have already solved the Stokes equation and therefore have obtained the velocity and pressure.

Finally, since the traction vector can be expressed as a function of the velocity shape functions on the edges i.e.

$$\vec{t} = \sum_{i=1}^m N_i^y \vec{t}_i$$

the left hand term yields an edge (1D) mass matrix  $M'$  (see Section I).

**Remark.** In Stone ??? an alternative to equation 697 is used. Although somewhat inefficient, the elemental matrices  $\mathbb{K}$  and  $\mathbb{G}$  and the corresponding body force rhs are built and the rhs of the traction equation is computed as follows:

$$M' \cdot \mathcal{T} = -\mathbb{K}\mathcal{V} - \mathbb{G}\mathcal{P} + f$$

where  $\mathcal{T}$  is the vector of assembled tractions which we want to compute and  $\mathcal{V}$  and  $\mathcal{T}$  are the solutions of the Stokes problem.

**Remark.** The assembled mass matrix is tri-diagonal and can be easily solved with a Conjugate Gradient method.

**Remark.** With a trapezoidal integration rule (i.e. Gauss-Lobatto - see Section 4.1.6) the matrix can even be diagonalised and the resulting matrix is simply diagonal, which results in a very cheap solve [2902].

### 8.16.2 The CBF applied to the heat transport equation

We start from the strong form of the heat transfer equation (without the source terms for simplicity):

$$\rho C_p \left( \frac{\partial T}{\partial t} + \vec{v} \cdot \vec{\nabla} T \right) = \vec{\nabla} \cdot k \vec{\nabla} T$$

The weak form then writes:

$$\int_{\Omega} N^{\theta} \rho C_p \frac{\partial T}{\partial t} dV + \rho C_p \int_{\Omega} N^{\theta} \vec{v} \cdot \vec{\nabla} T dV = \int_{\Omega} N^{\theta} \vec{\nabla} \cdot k \vec{\nabla} T dV$$

Using once again integration by parts and divergence theorem:

$$\int_{\Omega} N \rho C_p \frac{\partial T}{\partial t} dV + \rho C_p \int_{\Omega} N \vec{v} \cdot \nabla T dV = \int_{\Gamma} N k \nabla T \cdot \mathbf{n} d\Gamma - \int_{\Omega} \nabla N \cdot k \nabla T dV$$

On the boundary we are interested in the heat flux  $\mathbf{q} = -k \nabla T$

$$\int_{\Omega} N \rho C_p \frac{\partial T}{\partial t} dV + \rho C_p \int_{\Omega} N \vec{v} \cdot \nabla T dV = - \int_{\Gamma} N \mathbf{q} \cdot \mathbf{n} d\Gamma - \int_{\Omega} \nabla N \cdot k \nabla T dV$$

or,

$$\int_{\Gamma} N \mathbf{q} \cdot \mathbf{n} d\Gamma = - \int_{\Omega} N \rho C_p \frac{\partial T}{\partial t} dV - \rho C_p \int_{\Omega} N \vec{v} \cdot \nabla T dV - \int_{\Omega} \nabla N \cdot k \nabla T dV$$

Considering the normal heat flux  $q_n = \mathbf{q} \cdot \mathbf{n}$  as an unknown living on the nodes on the boundary,

$$q_n = \sum_{i=1}^2 q_{n|i} N_i$$

so that the left hand term becomes a mass matrix for the shape functions living on the boundary. We have already covered the right hand side terms when building the FE system to solve the heat transport equation, so that in the end

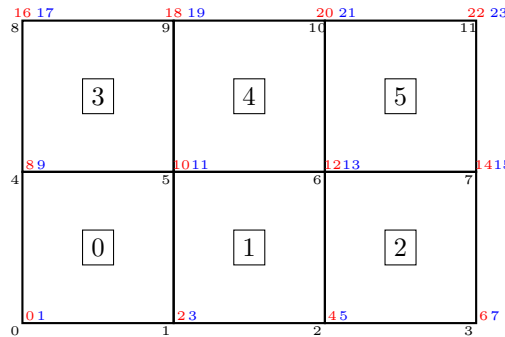
$$M' \cdot \mathcal{Q}_n = -M \cdot \frac{\partial \mathbf{T}}{\partial t} - K_a \cdot \mathbf{T} - K_d \cdot \mathbf{T}$$

where  $\mathcal{Q}_n$  is the assembled vector of normal heat flux components. Note that in all terms the assembly only takes place over the elements along the boundary.

Note that the resulting matrix is symmetric.

### 8.16.3 Some implementation details for the Stokes equation

What follows is relevant for Stone ?? which relies on  $Q_1$  shape functions for the velocity. Let us start with a small example, a 3x2 element FE grid:



Red color corresponds to the dofs in the x direction, blue color indicates a dof in the y direction.

We have nnp=12, nel=6, NfemV=24. Let us assume that free slip boundary conditions are applied. The boundary conditions `fix_bc` array is then:

```
bc_fix=[T T T T T T T T T T T T T T T T T T ]
```

Note that since corners belong to two edges, we effectively prescribed no-slip boundary conditions on those.

[why does array contain only T??](#)

We wish to compute the tractions on the boundaries, and more precisely for the dofs for which a Dirichlet velocity boundary condition has been prescribed. The number of (traction) unknowns NfemTr is then the number of T in the bc\_fix array. In our specific case, we have NfemTr=. This means that we need for each targeted dof to be able to find its identity/number between 0 and NfemTr-1. We therefore create the array bc\_nb which is filled as follows:



This translates as follows in the code:

```
NfemTr=np.sum(bc_fix)
bc_nb=np.zeros(NfemV,dtype=np.int32)
counter=0
for i in range(0,NfemV):
    if (bc_fix[i]):
        bc_nb[i]=counter
        counter+=1
```

The algorithm is then as follows

- A Prepare two arrays to store the matrix  $M_{cbf}$  and its right hand side  $rhs_{cbf}$
- B Loop over all elements
- C For each element touching a boundary, compute the residual vector  $R_{el} = -f_{el} + \mathbb{K}_{el}\mathcal{V}_{el} + \mathbb{G}_{el}\mathcal{P}_{el}$
- D Loop over the four edges of the element using the connectivity array
- E For each edge loop over the number of degrees of freedom (2 in 2D)
- F For each edge assess whether the dofs on both ends are target dofs.
- G If so, compute the mass matrix  $M_{edge}$  for this edge
- H Extract the 2 values off the element residual vector and assemble these in  $rhs_{cbf}$
- I Assemble  $M_{edge}$  into NfemTrxNfemTr matrix using bc\_nb

```
M_cbf = np.zeros((NfemTr,NfemTr),np.float64) # A
rhs_cbf = np.zeros(NfemTr,np.float64)

for iel in range(0,nel): # B
    ... compute elemental residual ... # C

    #boundary 0-1 # D
    for i in range(0,ndofV): # E
        idof0=2*icon[0,iel]+i
        idof1=2*icon[1,iel]+i
        if (bc_fix[idof0] and bc_fix[idof1]): # F
            idofTr0=bc_nb[idof0]
            idofTr1=bc_nb[idof1]
            rhs_cbf[idofTr0]+=res_el[0+i] # H
            rhs_cbf[idofTr1]+=res_el[2+i]
            M_cbf[idofTr0,idofTr0]+=M_edge[0,0] # I
            M_cbf[idofTr0,idofTr1]+=M_edge[0,1]
            M_cbf[idofTr1,idofTr0]+=M_edge[1,0]
            M_cbf[idofTr1,idofTr1]+=M_edge[1,1] # I

    #boundary 1-2 # [D]
```

...	
#boundary 2-3	$\#[D]$
...	
#boundary 3-0	$\#[D]$
...	

## 8.17 The value of the timestep

The chosen time step  $\delta t$  used for time integration is chosen to comply with the Courant-Friedrichs-Lowy condition [40].

$$\delta t = C \min \left( \frac{h}{\max |\mathbf{v}|}, \frac{h^2}{\kappa} \right) \quad (698)$$

where  $h$  is a measure of the element size,  $\kappa = k/\rho C_p$  is the thermal diffusivity and  $C$  is the so-called CFL number chosen in  $[0, 1]$ .

In essence the CFL condition arises when solving hyperbolic PDEs . It limits the time step in many explicit time-marching computer simulations so that the simulation does not produce incorrect results.

This condition is not needed when solving the Stokes equation but it is mandatory when solving the heat transport equation or any kind of advection-diffusion equation. Note that any increase of grid resolution (i.e.  $h$  becomes smaller) yields an automatic decrease of the time step value.

## 8.18 Mappings

The name isoparametric derives from the fact that the same ('iso') functions are used as basis functions and for the mapping to the reference element.

More generally, if  $n_e$  denotes the number of nodes of an element and  $n_g$  denotes the number of nodes describing the geometry of the element, then the element is termed subparametric when  $n_g < n_e$  and superparametric when  $n_g > n_e$ .

### 8.18.1 Linear mapping on a triangle

```

2
|\      s
| \    |_x
|  \
3==1

```

Let us assume that the coordinates of the vertices are  $(x_1, y_1)$ ,  $(x_2, y_2)$ , and  $(x_3, y_3)$ . The coordinates inside the reference element are  $(r, s)$ . We then simply have the following relationship, i.e. any point of the reference element can be mapped to the physical triangle as follows:

$$x = rx_1 + sx_2 + (1 - r - s)x_3 \quad (699)$$

$$y = ry_1 + sy_2 + (1 - r - s)y_3 \quad (700)$$

There is also an inverse map, which is easily computed:

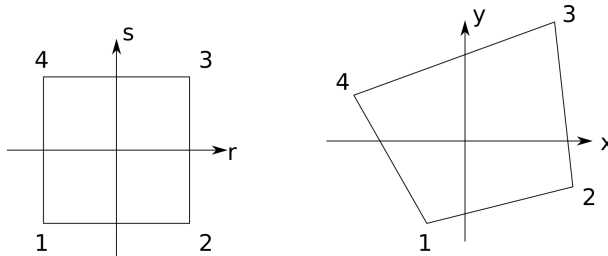
$$r = \frac{(y_2 - y_3)(x - x_3) - (x_2 - x_3)(y - y_3)}{(x_1 - x_3)(y_2 - y_3) - (y_1 - y_3)(x_2 - x_3)} \quad (701)$$

$$s = \frac{-(y_1 - y_3)(x - x_3) + (x_1 - x_3)(y - y_3)}{(x_1 - x_3)(y_2 - y_3) - (y_1 - y_3)(x_2 - x_3)} \quad (702)$$

**Remark.** The denominator will not vanish, because it is a multiple of the area of the triangle.

### 8.18.2 Bilinear mapping on a linear quadrilateral

The is in the  $(r, s)$  space. It is a square of size  $2 \times 2$  centered around the origin. We wish to map it to the quadrilateral in the  $(x, y)$  space:



The coordinates of the vertices are  $(x_1, y_1)$ ,  $(x_2, y_2)$ ,  $(x_3, y_3)$  and  $(x_4, y_4)$ . We then simply have the following relationship, i.e. any point of the reference element can be mapped to the physical quadrilateral as follows:

$$x = N_1(r, s)x_1 + N_2(r, s)x_2 + N_3(r, s)x_3 + N_4(r, s)x_4 \quad (703)$$

$$y = N_1(r, s)y_1 + N_2(r, s)y_2 + N_3(r, s)y_3 + N_4(r, s)y_4 \quad (704)$$

where the shape functions  $N_i(r, s)$  are defined in section 4.4.

In the following example the program randomly generates 10000 points inside the reference element and computes their mapping into the  $(x, y)$  space.

```

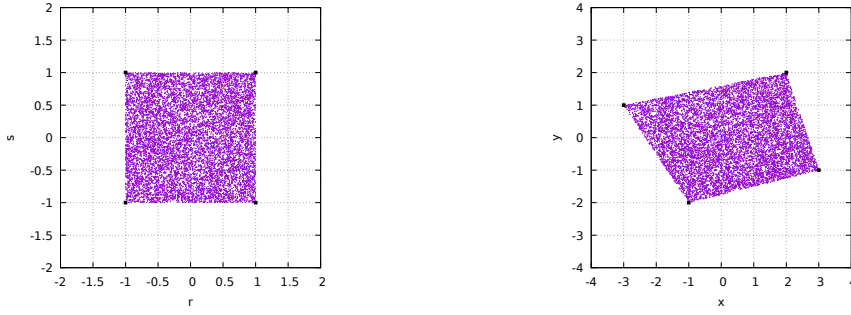
x1=-1 ; y1=-2
x2=3 ; y2=-1
x3=2 ; y3=2
x4=-3 ; y4=1

npts=10000
r=np.zeros(npts,dtype=np.float64)
s=np.zeros(npts,dtype=np.float64)
x=np.zeros(npts,dtype=np.float64)
y=np.zeros(npts,dtype=np.float64)

for i in range(0,npts):
    # compute random r,s coordinates
    r[i]=random.uniform(-1.,+1)
    s[i]=random.uniform(-1.,+1)
    # compute basis function values at r,s
    N1=0.25*(1-r[i])*(1-s[i])
    N2=0.25*(1+r[i])*(1-s[i])
    N3=0.25*(1+r[i])*(1+s[i])
    N4=0.25*(1-r[i])*(1+s[i])
    # compute x,y coordinates
    x[i]=N1*x1+N2*x2+N3*x3+N4*x4
    y[i]=N1*y1+N2*y2+N3*y3+N4*y4

np.savetxt('rs.ascii',np.array([r,s]).T)
np.savetxt('xy.ascii',np.array([x,y]).T)

```



There is also an inverse map, which is not so easily computed (see section 8.21). However, if the quadrilateral in the  $(x, y)$  space is a rectangle of size  $(h_x, h_y)$ , the inverse mapping is trivial:

$$r = \frac{x - x_1}{x_2 - x_1} \quad (705)$$

$$s = \frac{y - y_1}{y_4 - y_1} \quad (706)$$

Also in this case the shape functions can easily be written as functions of  $(x, y)$ :

$$\begin{aligned} N_1(x, y) &= \left( \frac{x_3 - x}{h_x} \right) \left( \frac{y_3 - y}{h_y} \right) \\ N_2(x, y) &= \left( \frac{x - x_1}{h_x} \right) \left( \frac{y_3 - y}{h_y} \right) \\ N_3(x, y) &= \left( \frac{x - x_1}{h_x} \right) \left( \frac{y - y_1}{h_y} \right) \\ N_4(x, y) &= \left( \frac{x_3 - x}{h_x} \right) \left( \frac{y - y_1}{h_y} \right) \end{aligned}$$

On the one hand, any variable defined on the element can be approximated using the shape functions:

$$f_h(r, s) = \sum_i N_i(r, s) f_i. \quad (707)$$

If we treat the coordinate variables  $x$  and  $y$  themselves as functions, then the shape functions can be used to construct the mapping:

$$x(r, s) = \sum_i N_i(r, s)x_i \quad y(r, s) = \sum_i N_i(r, s)y_i, \quad (708)$$

leading to write

$$\frac{\partial x}{\partial r} = \sum_i \frac{\partial N_i}{\partial r} x_i \quad (709)$$

$$\frac{\partial x}{\partial s} = \sum_i \frac{\partial N_i}{\partial s} x_i \quad (710)$$

$$\frac{\partial y}{\partial r} = \sum_i \frac{\partial N_i}{\partial r} y_i \quad (711)$$

$$\frac{\partial y}{\partial s} = \sum_i \frac{\partial N_i}{\partial s} y_i \quad (712)$$

On the other hand we also have

$$\frac{\partial f}{\partial r} = \frac{\partial f}{\partial x} \frac{\partial x}{\partial r} + \frac{\partial f}{\partial y} \frac{\partial y}{\partial r} \quad (713)$$

$$\frac{\partial f}{\partial s} = \frac{\partial f}{\partial x} \frac{\partial x}{\partial s} + \frac{\partial f}{\partial y} \frac{\partial y}{\partial s} \quad (714)$$

or in matrix form:

$$\begin{pmatrix} \frac{\partial f}{\partial r} \\ \frac{\partial f}{\partial s} \end{pmatrix} = \underbrace{\begin{pmatrix} \frac{\partial x}{\partial r} & \frac{\partial y}{\partial r} \\ \frac{\partial x}{\partial s} & \frac{\partial y}{\partial s} \end{pmatrix}}_{J} \cdot \begin{pmatrix} \frac{\partial f}{\partial x} \\ \frac{\partial f}{\partial y} \end{pmatrix}$$

where  $J$  is called the Jacobian of the transformation. By inverting the Jacobian matrix, the desired derivatives with respect to  $x$  and  $y$  can be obtained:

We have:

$$\begin{pmatrix} \frac{\partial f}{\partial x} \\ \frac{\partial f}{\partial y} \end{pmatrix} = J^{-1} \cdot \begin{pmatrix} \frac{\partial f}{\partial r} \\ \frac{\partial f}{\partial s} \end{pmatrix}$$

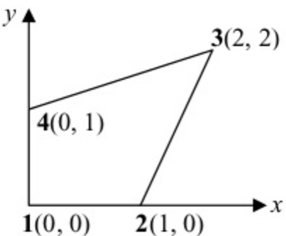
The inverse of the Jacobian matrix can be simply obtained in 2D (Kramer's rule for  $2 \times 2$  matrices):

$$J^{-1} = \frac{1}{|J|} \begin{pmatrix} \frac{\partial y}{\partial s} & -\frac{\partial y}{\partial r} \\ -\frac{\partial x}{\partial s} & \frac{\partial x}{\partial r} \end{pmatrix}$$

The presence of the determinant in the denominator implies that it cannot be zero anywhere, or in other words: the mapping is not valid if  $|J|$  is zero anywhere over the element.

Note that Hua [1237] published analytical inverse transformation for quadrilateral isoparametric elements, i.e. how to compute  $J^{-1}$  as a function of space coordinates and not just at the quadrature points.

Let us look at this by means of a simple example and let us consider the following element:



Then a  $Q_1$  mapping yields:

$$x(r, s) = \sum_i N_i(r, s)x_i = N_2 + 2N_3 = \frac{1}{4}(3 + 3r + s + rt) \quad (715)$$

$$y(r, s) = \sum_i N_i(r, s)y_i = 2N_3 + N_4 = \frac{1}{4}(3 + r + 3s + rt) \quad (716)$$

The Jacobian matrix is then

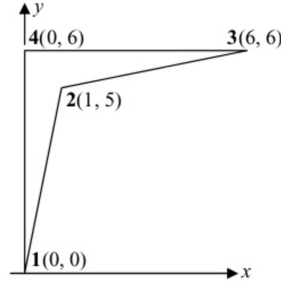
$$\mathbf{J} = \begin{pmatrix} \frac{\partial x}{\partial r} & \frac{\partial x}{\partial s} \\ \frac{\partial y}{\partial r} & \frac{\partial y}{\partial s} \end{pmatrix} = \frac{1}{4} \begin{pmatrix} 3+s & 1+s \\ 1+r & 3+r \end{pmatrix}$$

and its determinant is

$$|\mathbf{J}| = \frac{1}{4}[(3+s)(3+r) - (1+s)(1+r)] = \frac{1}{2} + \frac{1}{8}r + \frac{1}{8}s \quad (717)$$

It is clear that  $|\mathbf{J}| > 0$  for  $-1 \leq r \leq +1$  and  $-1 \leq s \leq +1$ .

Let us now consider another example, the following element:



It follows that

$$x(r, s) = \sum_i N_i(r, s)x_i = \frac{1}{4}(1+r)(7+5s) \quad (718)$$

$$y(r, s) = \sum_i N_i(r, s)y_i = \frac{1}{4}(17+5r+7s-5rs) \quad (719)$$

and the determinant:

$$|\mathbf{J}| = \frac{3}{2} - \frac{15r}{4} + \frac{15s}{4}$$

is zero for  $r - s = 2/5$ . This mapping is invalid!

**Remark.** Problems also arise when the Jacobian matrix is nearly singular due to round-off errors. To avoid problems linked to badly shaped elements, it is recommended that the inside angles of an element are larger than  $15^\circ$  and less than  $165^\circ$ .

From Eq. 708, we can also write:

$$dx = \frac{\partial x}{\partial r}dr + \frac{\partial x}{\partial s}ds \quad (720)$$

$$dy = \frac{\partial y}{\partial r}dr + \frac{\partial y}{\partial s}ds \quad (721)$$

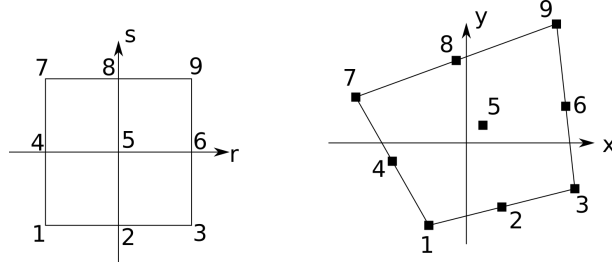
, or,

$$\begin{pmatrix} dx \\ dy \end{pmatrix} = \mathbf{J} \cdot \begin{pmatrix} dr \\ ds \end{pmatrix} \quad (722)$$

This means that

$$\int \int \dots dx dy = \int \int \dots |\mathbf{J}| dr ds \quad (723)$$

### 8.18.3 biquadratic mapping of a straight-line face $Q_2$ element



The reference element now contains 9 nodes: 1,3,7,9 are the corners, nodes 2,4,6,8 are the mid-face points and node 5 is in the middle. The mapping from the  $(r, s)$  space to the  $(x, y)$  space is then as follows:

$$\begin{aligned} \begin{pmatrix} x(r, s) \\ y(r, s) \end{pmatrix} &= N_1(r, s) \begin{pmatrix} x_1 \\ y_1 \end{pmatrix} + N_2(r, s) \begin{pmatrix} x_2 \\ y_2 \end{pmatrix} + N_3(r, s) \begin{pmatrix} x_3 \\ y_3 \end{pmatrix} + N_4(r, s) \begin{pmatrix} x_4 \\ y_4 \end{pmatrix} \\ &+ N_5(r, s) \begin{pmatrix} x_5 \\ y_5 \end{pmatrix} + N_6(r, s) \begin{pmatrix} x_6 \\ y_6 \end{pmatrix} + N_7(r, s) \begin{pmatrix} x_7 \\ y_7 \end{pmatrix} + N_8(r, s) \begin{pmatrix} x_8 \\ y_8 \end{pmatrix} \\ &+ N_9(r, s) \begin{pmatrix} x_9 \\ y_9 \end{pmatrix} \end{aligned}$$

where

$$\begin{aligned} N_1(r, t) &= 0.5r(r-1)0.5t(t-1) \\ N_2(r, t) &= (1-r^2)0.5t(t-1) \\ N_3(r, t) &= 0.5r(r+1)0.5t(t-1) \\ N_4(r, t) &= 0.5r(r-1)(1-t^2) \\ N_5(r, t) &= (1-r^2)(1-t^2) \\ N_6(r, t) &= 0.5r(r+1)(1-t^2) \\ N_7(r, t) &= 0.5r(r-1)0.5t(t+1) \\ N_8(r, t) &= (1-r^2)0.5t(t+1) \\ N_9(r, t) &= 0.5r(r+1)0.5t(t+1) \end{aligned}$$

```

x1=-1 ; y1=-2
x3=3 ; y3=-1
x9=2 ; y9=2
x7=-3 ; y7=1
x2=0.5*(x1+x3) ; y2=0.5*(y1+y3)
x4=0.5*(x1+x7) ; y4=0.5*(y1+y7)
x6=0.5*(x3+x9) ; y6=0.5*(y3+y9)
x8=0.5*(x7+x9) ; y8=0.5*(y7+y9)
x5=0.25*(x1+x3+x7+x9) ; y5=0.25*(y1+y3+y7+y9)

npts=10000
r=np.zeros( npts , dtype=np.float64 )
s=np.zeros( npts , dtype=np.float64 )
xQ1=np.zeros( npts , dtype=np.float64 )
yQ1=np.zeros( npts , dtype=np.float64 )
xQ2=np.zeros( npts , dtype=np.float64 )
yQ2=np.zeros( npts , dtype=np.float64 )

for i in range(0,npts):
    # compute random r, s coordinates
    r[ i ]=random.uniform(-1.,+1)
    s[ i ]=random.uniform(-1.,+1)
    # compute Q2 basis function values at r, s
    N1= 0.5*r[ i ]*( r[ i ]-1. ) * 0.5*s[ i ]*( s[ i ]-1. )

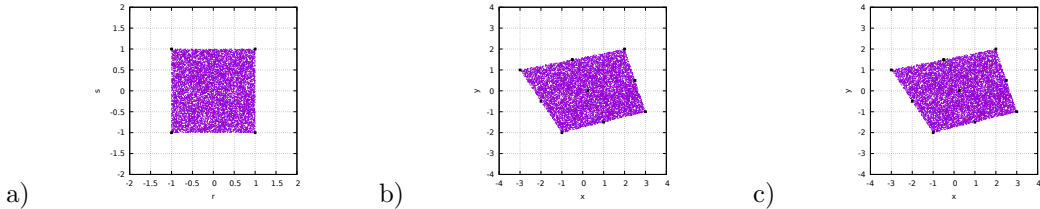
```

```

N2=      (1.-r[i]**2) * 0.5*s[i]*(s[i]-1.)
N3= 0.5*r[i]*(r[i]+1.) * 0.5*s[i]*(s[i]-1.)
N4= 0.5*r[i]*(r[i]-1.) *          (1.-s[i]**2)
N5=      (1.-r[i]**2) *          (1.-s[i]**2)
N6= 0.5*r[i]*(r[i]+1.) *          (1.-s[i]**2)
N7= 0.5*r[i]*(r[i]-1.) * 0.5*s[i]*(s[i]+1.)
N8=      (1.-r[i]**2) * 0.5*s[i]*(s[i]+1.)
N9= 0.5*r[i]*(r[i]+1.) * 0.5*s[i]*(s[i]+1.)
# compute x, y coordinates
xQ2[i]=N1*x1+N2*x2+N3*x3+N4*x4+N5*x5+N6*x6+N7*x7+N8*x8+N9*x9
yQ2[i]=N1*y1+N2*y2+N3*y3+N4*y4+N5*y5+N6*y6+N7*y7+N8*y8+N9*y9
# compute Q1 basis function values at r, s
N1=0.25*(1-r[i])*(1-s[i])
N2=0.25*(1+r[i])*(1-s[i])
N3=0.25*(1+r[i])*(1+s[i])
N4=0.25*(1-r[i])*(1+s[i])
# compute x, y coordinates
xQ1[i]=N1*x1+N2*x3+N3*x9+N4*x7
yQ1[i]=N1*y1+N2*y3+N3*y9+N4*y7

np.savetxt('rs.ascii',np.array([r,s]).T)
np.savetxt('xyQ1.ascii',np.array([xQ1,yQ1]).T)
np.savetxt('xyQ2.ascii',np.array([xQ2,yQ2]).T)

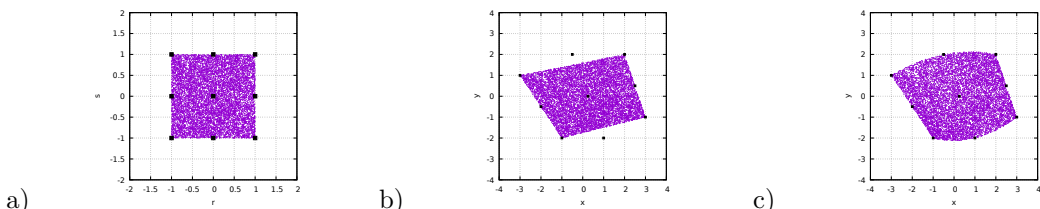
```



a) 10,000 random points in the reference element; b,c) image of these points by means of a bilinear and biquadratic mapping respectively. When the sides of the element are straight we see that a  $Q_1$  mapping is sufficient.

#### 8.18.4 biquadratic mapping of a not-so straight-line face $Q_2$ element

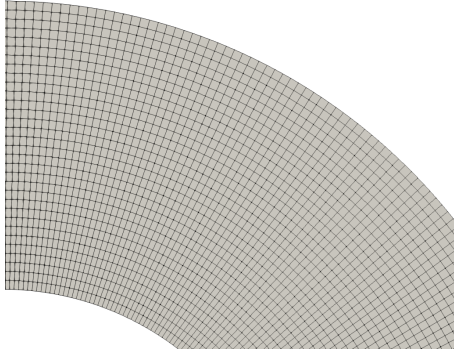
We now carry out the same exercise as before but nodes 2 and 8 are no more in the middle of nodes 1-3 and 7-9 respectively.



a) 10,000 random points in the reference element; b,c) image of these points by means of a bilinear and biquadratic mapping respectively. In this case we see that the  $Q_2$  mapping manages to capture the 'real' shape of the element.

#### 8.18.5 bilinear, biquadratic and bicubic mapping in an annulus

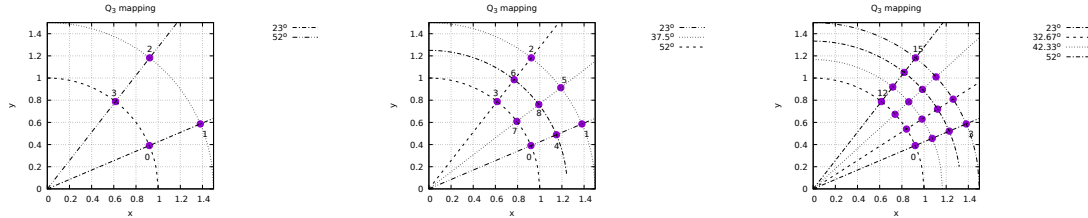
In the light of what precedes, we can now ask ourselves how this translates to a real geodynamic cas. Let us then consider the case of an annular domain, a cross section of a hollow sphere. When using quadrilateral elements, the mesh will look similar to this:



We here focus on  $Q_1$ ,  $Q_2$  and  $Q_3$  mappings. We single out an element, and arbitrarily define it as follows in polar coordinates:

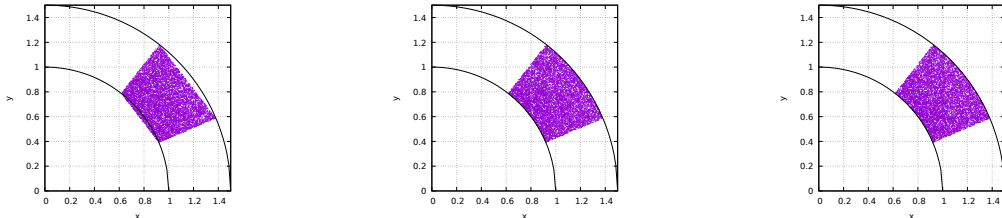
```
theta1=23./180.*np.pi
theta2=52./180.*np.pi
R1=1.
R2=1.5
```

The  $Q_1$  mapping requires four points, the  $Q_2$  nine points and the  $Q_3$  sixteen points. These are placed equidistantly in the  $r, \theta$  coordinate system, as shown hereunder:



Left to right: position of the nodes for the  $Q_1$ ,  $Q_2$  and  $Q_3$  mappings.

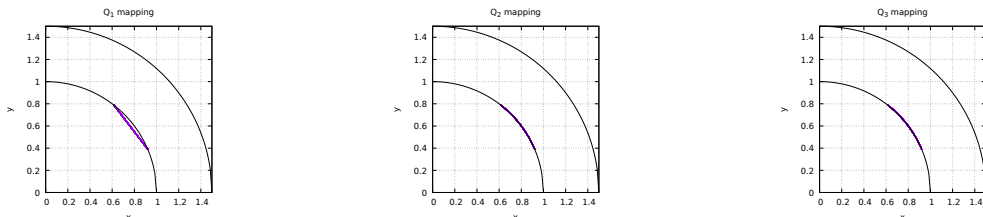
As before, we randomly shoot 10,000 points inside the reference element and map these out in the  $x, y$  space. Resulting swarms of points are shown in the following figures:



Left to right: position of the mapped points for the  $Q_1$ ,  $Q_2$  and  $Q_3$  mappings.

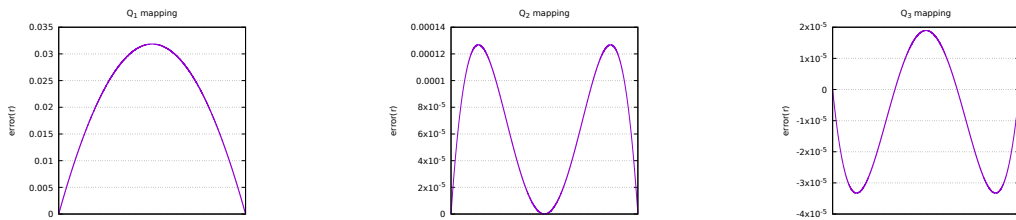
The image of a square with a  $Q_1$  mapping is obviously a quadrilateral so that it looks like quite a few points land outside of the domain  $R_1 \leq r \leq R_2$ . Note that points are well within  $23^\circ \leq \theta \leq 52^\circ$ , which can simply be explained by the fact that the faces of the element are straight lines.

However, it looks like the biquadratic and bicubic mappings are doing a much better job at mapping the region of space  $R_1 \leq r \leq R_2$ . In order to characterise this better, we now place 10,000 points on the bottom face of the reference element (i.e.  $s = -1$ ) and once again compute their coordinates in the the  $x, y$  space:



Left to right: position of the mapped points for the  $Q_1$ ,  $Q_2$  and  $Q_3$  mappings.

For each point  $i$  we now compute ist distance  $r_i$  to the origin, which, if the mapping was perfect, whould be exactly equal to  $R_1 = 1$ . On the following plots are shown the error  $r_i - 1$  for all points, from  $r = -1$  to  $r = +1$ .



Left to right: radius error of the mapped points for the  $Q_1$ ,  $Q_2$  and  $Q_3$  mappings.

We see that the amplitude of the error decreases with the order of the mapping used, which is why for instance ASPECT uses a  $Q_4$  mapping by default. Actually, in this particular case, the equation which describes the cirle is not a polynomial so that no high-order mapping will ever be able to *exactly* represent the curved boundary of the element!

Another interesting point to keep in mind is that the location of the quadrature points in the  $x, y$  space is also determined by the mapping used, which can have consequences on the accuracy of the integration and it will be reflected (for instance) on the error convergence rate.

Finally, the coordinates of the nodes of the element in the  $x, y$  are uniquely determined when they are on the convex hull of the element ( for instance nodes 0-7 for  $Q_2$ ) but we need to choose the position of the last nodes which are inside the element. Unfortunately, this choice is not neutral.

re ask Wolfgang about this - correlate with deal.II



Relevant Literature[2860]

## 8.19 Exporting data to vtk format

This format seems to be the universally accepted format for 2D and 3D visualisation in Computational Geodynamics. Such files can be opened with free softwares such as Paraview<sup>54</sup>, MayaVi<sup>55</sup> or Visit<sup>56</sup>.

Unfortunately it is my experience that no simple tutorial exists about how to build such files. There is an official document which describes the vtk format<sup>57</sup> but it delivers the information in a convoluted way. I therefore describe hereafter how **fieldstone** builds the vtk files.

I hereunder show vtk file corresponding to the 3x2 grid presented earlier ???. In this particular example there are:

- 12 nodes and 6 elements
- 1 elemental field: the pressure  $p$ )
- 2 nodal fields: 1 scalar (the smoothed pressure  $q$ ), 1 vector (the velocity field  $u, v, 0$ )

Note that vtk files are inherently 3D so that even in the case of a 2D simulation the  $z$ -coordinate of the points and for instance their  $z$ -velocity component must be provided. The file, usually called *solution.vtu* starts with a header:

```
<VTKFile type='UnstructuredGrid' version='0.1' byte_order='BigEndian'>
<UnstructuredGrid>
<Piece NumberOfPoints='12' NumberOfCells='6'>
```

We then proceed to write the node coordinates as follows:

```
<Points>
<DataArray type='Float32' NumberOfComponents='3' Format='ascii'>
0.000000e+00 0.000000e+00 0.000000e+00
3.333333e-01 0.000000e+00 0.000000e+00
6.666667e-01 0.000000e+00 0.000000e+00
1.000000e+00 0.000000e+00 0.000000e+00
0.000000e+00 5.000000e-01 0.000000e+00
3.333333e-01 5.000000e-01 0.000000e+00
6.666667e-01 5.000000e-01 0.000000e+00
1.000000e+00 5.000000e-01 0.000000e+00
0.000000e+00 1.000000e+00 0.000000e+00
3.333333e-01 1.000000e+00 0.000000e+00
6.666667e-01 1.000000e+00 0.000000e+00
1.000000e+00 1.000000e+00 0.000000e+00
</DataArray>
</Points>
```

These are followed by the elemental field(s):

```
<CellData Scalars='scalars'>
<DataArray type='Float32' Name='p' Format='ascii'>
-1.333333e+00
-3.104414e-10
1.333333e+00
-1.333333e+00
8.278417e-17
1.333333e+00
</DataArray>
</CellData>
```

Nodal quantities are written next:

```
<PointData Scalars='scalars'>
<DataArray type='Float32' NumberOfComponents='3' Name='velocity' Format='ascii'>
0.000000e+00 0.000000e+00 0.000000e+00
0.000000e+00 0.000000e+00 0.000000e+00
0.000000e+00 0.000000e+00 0.000000e+00
0.000000e+00 0.000000e+00 0.000000e+00
```

<sup>54</sup><https://www.paraview.org/>

<sup>55</sup><https://docs.enthought.com/mayavi/mayavi/>

<sup>56</sup><https://wci.llnl.gov/simulation/computer-codes/visit/>

<sup>57</sup><https://www.vtk.org/wp-content/uploads/2015/04/file-formats.pdf>

```

0.000000e+00 0.000000e+00 0.000000e+00
8.888885e-08 -8.278405e-24 0.000000e+00
8.888885e-08 1.655682e-23 0.000000e+00
0.000000e+00 0.000000e+00 0.000000e+00
1.000000e+00 0.000000e+00 0.000000e+00
</DataArray>
<DataArray type='Float32' NumberOfComponents='1' Name='q' Format='ascii'>
-1.333333e+00
-6.666664e-01
6.666664e-01
1.333333e+00
-1.333333e+00
-6.666664e-01
6.666664e-01
1.333333e+00
-1.333333e+00
-6.666664e-01
6.666664e-01
1.333333e+00
</DataArray>
</PointData>

```

To these informations we must append 3 more datasets. The first one is the connectivity, the second one is the offsets and the third one is the type. The first one is trivial since said connectivity is needed for the Finite Elements. The second must be understood as follows: when reading the connectivity information in a linear manner the offset values indicate the beginning of each element (omitting the zero value). The third simply is the type of element as given in the vtk format document (9 corresponds to a generic quadrilateral with an internal numbering consistent with ours).

```

<Cells>
<DataArray type='Int32' Name='connectivity' Format='ascii'>
0 1 5 4
1 2 6 5
2 3 7 6
4 5 9 8
5 6 10 9
6 7 11 10
</DataArray>
<DataArray type='Int32' Name='offsets' Format='ascii'>
4
8
12
16
20
24
</DataArray>
<DataArray type='Int32' Name='types' Format='ascii'>
9
9
9
9
9
9
</DataArray>
</Cells>

```

The file is then closed with

```

</Piece>
</UnstructuredGrid>
</VTKFile>

```

The *solution.vtu* file can then be opened with ParaView, MayaVi or Visit and the reader is advised to find tutorials online on how to install and use these softwares.

## 8.20 Runge-Kutta methods

These methods were developed around 1900 by the German mathematicians Carl Runge and Martin Kutta. The RK methods are methods for the numerical integration of ODEs<sup>58</sup>. These methods are well documented in any numerical analysis textbook and the reader is referred to [953, 1294]. Any Runge-Kutta method is uniquely identified by its Butcher tableau (REF?) which contains all necessary coefficients to build the algorithm.

The simplest RungeKutta method is the (forward) Euler method. Its tableau is:

missing refs for  
Butcher tableau

0				
	1			

The standard second-order RK method method (also called midpoint method) is:

0				
1/2	1/2			
		0		
			1	

Another second-order RK method, called Heun's method<sup>59</sup> is follows:

0				
1	1			
		1/2		
			1/2	

A third-order RK method is as follows:

0				
1/2	1/2			
1	-1	2		
	1/6	4/6	1/6	

The RK4 method falls in this framework. Its tableau is:

0				
1/2	1/2			
1/2	0	1/2		
1	0	0	1	
	1/6	1/6	1/3	1/6

A slight variation of the standard RK4 method is also due to Kutta in 1901 and is called the 3/8-rule. Almost all of the error coefficients are smaller than in the standard method but it requires slightly more FLOPs per time step. Its Butcher tableau is

0				
1/3	1/3			
2/3	-1/3	1		
1	1	-1	1	
	1/8	3/8	3/8	1/8

The following method is called the Runge-Kutta-Fehlberg method and is commonly abbreviated RKF45<sup>60</sup>. Its Butcher tableau is as follows:

<sup>58</sup>[https://en.wikipedia.org/wiki/Runge-Kutta\\_methods](https://en.wikipedia.org/wiki/Runge-Kutta_methods)

<sup>59</sup>[https://en.wikipedia.org/wiki/Heun%27s\\_method](https://en.wikipedia.org/wiki/Heun%27s_method)

<sup>60</sup>[https://en.wikipedia.org/wiki/Runge-Kutta-Fehlberg\\_method](https://en.wikipedia.org/wiki/Runge-Kutta-Fehlberg_method)

0						
1/4	1/4					
3/8	3/32	9/32				
12/13	1932/2197	-7200/2197	7296/2197			
1	439/216	-8	3680/513	-845/4104		
1/2	-8/27	2	-3544/2565	1859/4104	-11/40	
	16/135	0	6656/12825	28561/56430	-9/50	2/55
	25/216	0	1408/2565	2197/4104	-1/5	0

The first row of coefficients at the bottom of the table gives the fifth-order accurate method, and the second row gives the fourth-order accurate method.

 Relevant Literature[827, 1118, 713, 714, 2060]

### 8.20.1 Using RK methods to advect particles/markers

In the context of geodynamical modelling, one is usually confronted to the following problem: now that I have a velocity field on my FE mesh, how can I use it to advect the Lagrangian markers?

Runge-Kutta methods are used to this effect but only their spatial component is used: the velocity solution is not recomputed at the intermediate fractional timesteps, i.e. only the coefficients of the right hand side of the tableaus is used.

The RK1 method is simple. Carry out a loop over markers and

1. interpolate velocity  $\vec{v}_m$  onto each marker  $m$
2. compute new position as follows:  $\vec{r}_m(t + \delta t) = \vec{r}_m(t) + \vec{v}_m \delta t$

The RK2 method is also simple but requires a bit more work. Carry out a loop over markers and

1. interpolate velocity  $\vec{v}_m$  onto each marker  $m$  at position  $\vec{r}_m$
2. compute new intermediate position as follows:  $\vec{r}_m^{(1)}(t + \delta t) = \vec{r}_m(t) + \vec{v}_m \delta t / 2$
3. compute velocity  $\vec{v}_m^{(1)}$  at position  $\vec{r}_m^{(1)}$
4. compute new position:  $\vec{r}_m(t + \delta t) = \vec{r}_m(t) + \vec{v}_m^{(1)} \delta t$

Note that the intermediate positions could be in a different element of the mesh so extra care must be taken when computing intermediate velocities.

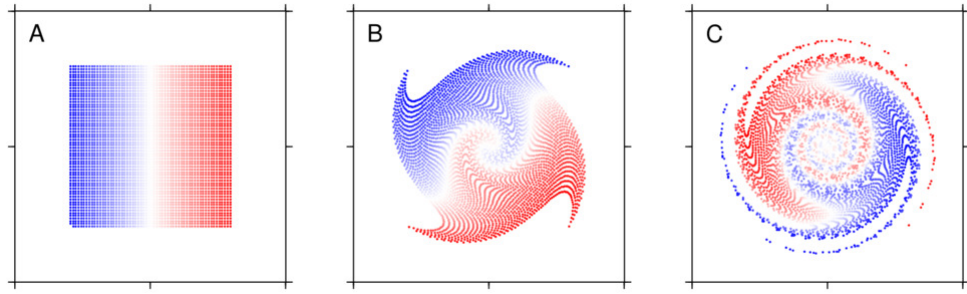
The RK3 method introduces two intermediate steps. Carry out a loop over markers and

1. interpolate velocity  $\vec{v}_m$  onto each marker  $m$  at position  $\vec{r}_m$
2. compute new intermediate position as follows:  $\vec{r}_m^{(1)}(t + \delta t) = \vec{r}_m(t) + \vec{v}_m \delta t / 2$
3. compute velocity  $\vec{v}_m^{(1)}$  at position  $\vec{r}_m^{(1)}$
4. compute new intermediate position as follows:  $\vec{r}_m^{(2)}(t + \delta t) = \vec{r}_m(t) + (2\vec{v}_m^{(1)} - \vec{v}_m) \delta t / 2$
5. compute velocity  $\vec{v}_m^{(2)}$  at position  $\vec{r}_m^{(2)}$
6. compute new position:  $\vec{r}_m(t + \delta t) = \vec{r}_m(t) + (\vec{v}_m + 4\vec{v}_m^{(1)} + \vec{v}_m^{(2)}) \delta t / 6$

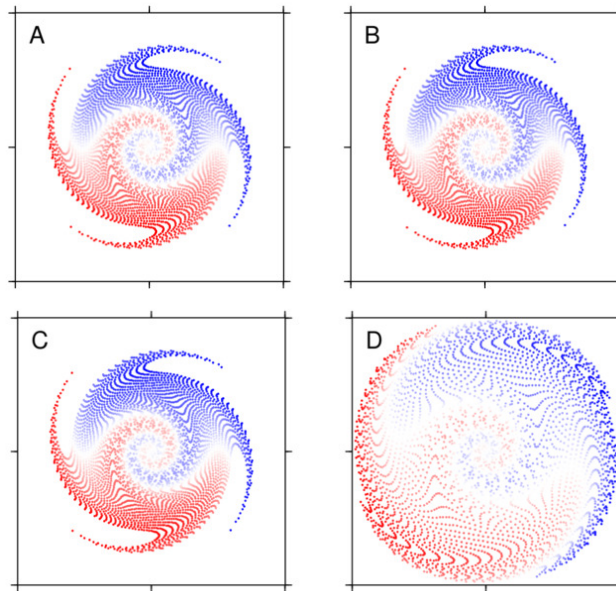
The following example is borrowed from [1690], itself borrowed from Fullsack [901, Section 5.4]. It is a whirl flow [1982], a flow with rotational symmetry in which concentric layers of material rotate around a centre with an angular velocity:

$$\omega(r) = \omega_0 \frac{r}{r_0} \exp\left(-\frac{r}{r_0}\right)$$

The box is  $[-0.5, 0.5] \times [-0.5, 0.5]$ ,  $r_0 = 0.25$ ,  $\omega_0 = 0.3$  and  $\delta t = 1$ .  $60 \times 60$  particles are regularly positioned inside the  $[-0.3, 0.3] \times [-0.3, 0.3]$  square. Maierova [1690] has carried out this experiment for the above Runge-Kutta methods.



Model domain with particles colored at three different time-steps: (A)  $t = 0$  (initial position of particles), (B)  $t = 50$ , and (C)  $t = 200$ . The advection is computed using the fourth-order Runge-Kutta scheme. Taken from [1690]



The same plot as above, but for different advection schemes at  $t = 100$ . Advection was computed using (A) the fourth-order Runge-Kutta scheme, (B) the mid-point method, (C) Heuns method and (D) the explicit Euler method. Taken from [1690]

(BSc Thesis)

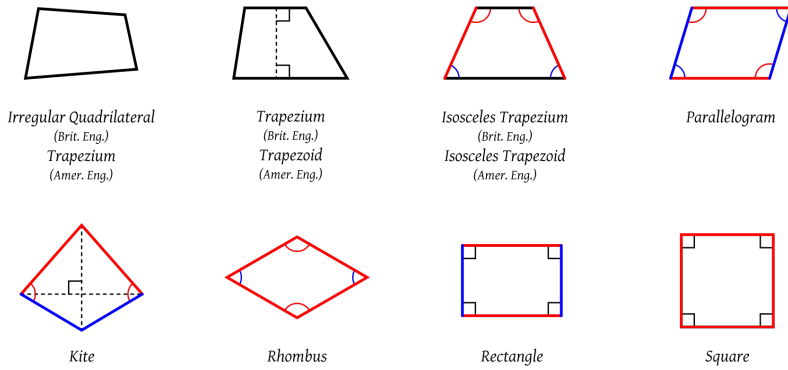
## 8.21 Am I in or not? - finding reduced coordinates

It is quite common that at some point one must answer the question: "Given a mesh and its connectivity on the one hand, and the coordinates of a point on the other, how do I accurately and quickly determine in which element the point resides?"

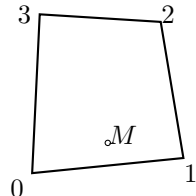
One typical occurrence of such a problem is linked to the use of the Particle-In-Cell technique: particles are advected and move through the mesh, and need to be localised at every time step. This question could arise in the context of a benchmark where certain quantities need to be measured at specific locations inside the domain.

### 8.21.1 Two-dimensional space

We shall first focus on quadrilaterals. There are many kinds of quadrilaterals as shown hereunder:



I wish to arrive at a single algorithm which is applicable to all quadrilaterals and therefore choose an irregular quadrilateral. For simplicity, let us consider a  $Q_1$  element, with a single node at each corner.



Several rather simple options exist:

- we could subdivide the quadrilateral into two triangles and check whether point  $M$  is inside any of them (as it turns out, this problem is rather straightforward for triangles. Simply google it.)
- We could check that point  $M$  is always on the left side of segments  $0 \rightarrow 1$ ,  $1 \rightarrow 2$ ,  $2 \rightarrow 3$ ,  $3 \rightarrow 0$ .
- ...

Any of these approaches will work although some might be faster than others. In three-dimensions all will however become cumbersome to implement and might not even work at all. Fortunately, there is an elegant way to answer the question, as detailed in the following subsection.

### 8.21.2 Three-dimensional space

If point  $M$  is inside the quadrilateral, there exist a set of reduced coordinates  $r, s, t \in [-1 : 1]^3$  such that

$$\sum_{i=1}^4 N_i(r_M, s, t) x_i = x_M \quad \sum_{i=1}^4 N_i(r_M, s, t) y_i = y_M \quad \sum_{i=1}^4 N_i(r_M, s, t) z_i = z_M$$

This can be cast as a system of three equations and three unknowns. Unfortunately, each shape function  $N_i$  contains a term  $rst$  (as well as  $rs$ ,  $rt$ , and  $st$ ) so that it is not a linear system and standard techniques are not applicable. We must then use an iterative technique: the algorithm starts with a guess for values  $r, s, t$  and improves on their value iteration after iteration.

The classical way of solving nonlinear systems of equations is Newton's method. We can rewrite the equations above as  $\mathbf{F}(r, s, t) = 0$ :

$$\begin{aligned} \sum_{i=1}^8 N_i(r, s, t)x_i - x_M &= 0 \\ \sum_{i=1}^8 N_i(r, s, t)y_i - y_M &= 0 \\ \sum_{i=1}^8 N_i(r, s, t)z_i - z_M &= 0 \end{aligned} \quad (724)$$

or,

$$\begin{aligned} F_r(r, s, t) &= 0 \\ F_s(r, s, t) &= 0 \\ F_t(r, s, t) &= 0 \end{aligned}$$

so that we now have to find the zeroes of continuously differentiable functions  $\mathbf{F} : \mathbb{R} \rightarrow \mathbb{R}$ . The recursion is simply:

$$\begin{pmatrix} r_{k+1} \\ s_{k+1} \\ t_{k+1} \end{pmatrix} = \begin{pmatrix} r_k \\ s_k \\ t_k \end{pmatrix} - J_F(r_k, s_k, t_k)^{-1} \begin{pmatrix} F_r(r_k, s_k, t_k) \\ F_s(r_k, s_k, t_k) \\ F_t(r_k, s_k, t_k) \end{pmatrix}$$

where  $J$  the Jacobian matrix:

$$\begin{aligned} J_F(r_k, s_k, t_k) &= \begin{pmatrix} \frac{\partial F_r}{\partial r}(r_k, s_k, t_k) & \frac{\partial F_r}{\partial s}(r_k, s_k, t_k) & \frac{\partial F_r}{\partial t}(r_k, s_k, t_k) \\ \frac{\partial F_s}{\partial r}(r_k, s_k, t_k) & \frac{\partial F_s}{\partial s}(r_k, s_k, t_k) & \frac{\partial F_s}{\partial t}(r_k, s_k, t_k) \\ \frac{\partial F_t}{\partial r}(r_k, s_k, t_k) & \frac{\partial F_t}{\partial s}(r_k, s_k, t_k) & \frac{\partial F_t}{\partial t}(r_k, s_k, t_k) \end{pmatrix} \\ &= \begin{pmatrix} \sum_{i=1}^8 \frac{\partial N_i}{\partial r}(r_k, s_k, t_k)x_i & \sum_{i=1}^8 \frac{\partial N_i}{\partial s}(r_k, s_k, t_k)x_i & \sum_{i=1}^8 \frac{\partial N_i}{\partial t}(r_k, s_k, t_k)x_i \\ \sum_{i=1}^8 \frac{\partial N_i}{\partial r}(r_k, s_k, t_k)y_i & \sum_{i=1}^8 \frac{\partial N_i}{\partial s}(r_k, s_k, t_k)y_i & \sum_{i=1}^8 \frac{\partial N_i}{\partial t}(r_k, s_k, t_k)y_i \\ \sum_{i=1}^8 \frac{\partial N_i}{\partial r}(r_k, s_k, t_k)z_i & \sum_{i=1}^8 \frac{\partial N_i}{\partial s}(r_k, s_k, t_k)z_i & \sum_{i=1}^8 \frac{\partial N_i}{\partial t}(r_k, s_k, t_k)z_i \end{pmatrix} \end{aligned}$$

In practice, we solve the following system:

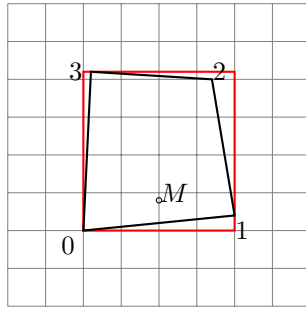
$$J_F(r_k, s_k, t_k) \left[ \begin{pmatrix} r_{k+1} \\ s_{k+1} \\ t_{k+1} \end{pmatrix} - \begin{pmatrix} r_k \\ s_k \\ t_k \end{pmatrix} \right] = - \begin{pmatrix} F_r(r_k, s_k, t_k) \\ F_s(r_k, s_k, t_k) \\ F_t(r_k, s_k, t_k) \end{pmatrix}$$

Finally, the algorithm goes as follows:

- set guess values for  $r, s, t$  (typically 0)
- loop over  $k=0, \dots$
- Compute  $\text{rhs} = -\mathbf{F}(r_k, s_k, t_k)$
- Compute matrix  $J_F(r_k, s_k, t_k)$

- solve system for  $(dr_k, ds_k, dt_k)$
- update  $r_{k+1} = r_k + dr_k$ ,  $s_{k+1} = s_k + ds_k$ ,  $t_{k+1} = t_k + dt_k$
- stop iterations when  $(dr_k, ds_k, dt_k)$  is small
- if  $r_k, s_k, t_k \in [-1, 1]^3$  then  $M$  is inside.

This method converges quickly but involves iterations, and multiple solves of  $3 \times 3$  systems which, when carried out for each marker and at each time step can prove to be expensive. A simple modification can be added to the above algorithm: iterations should be carried out *only* when the point  $M$  is inside of a cuboid of size  $[\min_i x_i : \max_i x_i] \times [\min_i y_i : \max_i y_i] \times [\min_i z_i : \max_i z_i]$  where the sums run over the vertices of the element. In 2D this translates as follows: only carry out Newton iterations when  $M$  is inside the red rectangle!



Note that the algorithm above extends to high degree elements such as  $Q_2$  and higher, even with curved sides.

write about case when element is rectangle/cuboid

## 8.22 Error measurements and convergence rates

What follows is written in the case of a two-dimensional model. Generalisation to 3D is trivial. What follows is mostly borrowed from [2526].

When measuring the order of accuracy of the primitive variables  $\vec{v}$  and  $p$ , it is standard to report errors in both the  $L_1$  and the  $L_2$  norm. For a scalar quantity  $\Psi$ , the  $L_1$  and  $L_2$  norms are computed as

$$\|\Psi\|_1 = \int_V |\Psi| dV \quad \|\Psi\|_2 = \sqrt{\int_V \Psi^2 dV} \quad (725)$$

For a vector quantity  $\vec{k} = (k_x, k_y)$  in a two-dimensional space, the  $L_1$  and  $L_2$  norms are defined as:

$$\|\vec{k}\|_1 = \int_V (|k_x| + |k_y|) dV \quad \|\vec{k}\|_2 = \sqrt{\int_V (k_x^2 + k_y^2) dV} \quad (726)$$

To compute the respective norms the integrals in the above norms can be approximated by splitting them into their element-wise contributions. The element volume integral can then be easily computed by numerical integration using Gauss-Legendre quadrature.

The respective  $L_1$  and  $L_2$  norms for the pressure error can be evaluated via

$$e_p^h|_1 = \sum_{i=1}^{n_e} \sum_{q=1}^{n_q} |e_p^h(\vec{r}_q)| w_q |J_q| \quad e_p^h|_2 = \sqrt{\sum_{i=1}^{n_e} \sum_{q=1}^{n_q} |e_p^h(\vec{r}_q)|^2 w_q |J_q|} \quad (727)$$

where  $e_p^h(\vec{r}_q) = p^h(\vec{r}_q) - p(\vec{r}_q)$  is the pressure error evaluated at the  $q$ -th quadrature associated with the  $i$ th element.  $n_e$  and  $n_q$  refer to the number of elements and the number of quadrature points per element.  $w_q$  and  $J_q$  are the quadrature weight and the Jacobian associated with point  $q$ .

The velocity error  $e_{\vec{v}}^h$  is evaluated using the following two norms

$$e_{\vec{v}}^h|_1 = \sum_{i=1}^{n_e} \sum_{q=1}^{n_q} [|e_u^h(\vec{r}_q)| + |e_v^h(\vec{r}_q)|] w_q |J_q| \quad e_{\vec{v}}^h|_2 = \sqrt{\sum_{i=1}^{n_e} \sum_{q=1}^{n_q} [|e_u^h(\vec{r}_q)|^2 + |e_v^h(\vec{r}_q)|^2] w_q |J_q|} \quad (728)$$

where  $e_u^h(\vec{r}_q) = u^h(\vec{r}_q) - u(\vec{r}_q)$  and  $e_v^h(\vec{r}_q) = v^h(\vec{r}_q) - v(\vec{r}_q)$ .

Another norm is very rarely used in the geodynamics literature but is preferred in the Finite Element literature: the  $H^1$  norm. The mathematical basis for this norm and the nature of the  $H^1(\Omega)$  Hilbert space is to be found in many FE books [711, 1351, 1251]. This norm is expressed as follows for a function  $f$  such that  $f, |\nabla f| \in L^2(\Omega)$ <sup>61</sup>

$$\|f\|_{H^1} = \left( \int_{\Omega} (|f|^2 + |\nabla f|^2) d\Omega \right)^{1/2} \quad (729)$$

We then have

$$e_{\vec{v}}^h|_{H^1} = \|\vec{v}^h - \vec{v}\|_{H^1} = \sqrt{\sum_{i=1}^d \int_{\Omega} [(v_i^h - v_i)^2 + \vec{\nabla}(v_i^h - v_i) \cdot \vec{\nabla}(v_i^h - v_i)] d\Omega} \quad (730)$$

where  $d$  is the number of dimensions. Note that sometimes the following semi-norm is used [705, 215]:

$$e_{\vec{v}}^h|_{H^1} = \|\vec{v}^h - \vec{v}\|_{H^1} = \sqrt{\sum_{i=1}^d \int_{\Omega} [\vec{\nabla}(v_i^h - v_i) \cdot \vec{\nabla}(v_i^h - v_i)] d\Omega} \quad (731)$$

When computing the different error norms for  $e_p$  and  $e_{\vec{v}}$  for a set of numerical experiments with varying resolution  $h$  we expect the error norms to follow the following relationships:

$$e_{\vec{v}}^h|_1 = Ch^{rvL_1} \quad e_{\vec{v}}^h|_2 = Ch^{rvL_2} \quad e_{\vec{v}}^h|_{H^1} = Ch^{rvH^1} \quad (732)$$

---

<sup>61</sup>[https://en.wikipedia.org/wiki/Sobolev\\_space](https://en.wikipedia.org/wiki/Sobolev_space)

$$e_p^h|_1 = Ch^{rpL_1} \quad e_p^h|_2 = Ch^{rpL_2} \quad (733)$$

where  $C$  is a resolution-independent constant and  $rpXX$  and  $rvXX$  are the convergence rates for pressure and velocity in various norms, respectively. Using linear regression on the logarithm of the respective error norm and the resolution  $h$ , one can compute the convergence rates of the numerical solutions.

As mentioned in [705], when finite element solutions converge at the same rates as the interpolants we say that the method is optimal, i.e.:

$$e_v^h|_{L_2} = \mathcal{O}(h^3) \quad e_v^h|_{H^1} = \mathcal{O}(h^2) \quad e_p^h|_{L_2} = \mathcal{O}(h^2) \quad (734)$$

We note that when using discontinuous pressure space (e.g.,  $P_0, P_{-1}$ ), these bounds remain valid even when the viscosity is discontinuous provided that the element boundaries conform to the discontinuity.

### 8.22.1 About extrapolation

*Section contributed by W. Bangerth and part of Thieulot & Bangerth [in prep.]*

In a number of numerical benchmarks we want to estimate the error  $X_h - X^*$  between a quantity  $X_h$  computed from the numerical solution  $\vec{u}_h, p_h$  and the corresponding value  $X$  computed from the exact solution  $\vec{u}, p$ . Examples of such quantities  $X$  are the root mean square velocity  $v_{rms}$ , but it could also be a mass flux across a boundary, an average horizontal velocity at the top boundary, or any other scalar quantity.

If the exact solution is known, then one can of course compute  $X$  from it. On the other hand, we would of course like to assess convergence also in cases where the exact solution is not known. In that case, one can compute an *estimate*  $X^*$  for  $X$  by way of *extrapolation*. To this end, we make the assumption that asymptotically,  $X_h$  converges to  $X$  at a fixed (but unknown) rate  $r$ , so that

$$e_h = |X_h - X| \approx Ch^r. \quad (735)$$

Here,  $X$ ,  $C$  and  $r$  are all unknown constants to be determined, although we are not really interested in  $C$ . We can evaluate  $X_h$  from the numerical solution on successively refined meshes with mesh sizes  $h$ ,  $h/2$ , and  $h/4$ . Then, in addition to (735) we also have

$$e_{h/2} = |X_{h/2} - X| \approx C \left( \frac{h}{2} \right)^r, \quad (736)$$

$$e_{h/4} = |X_{h/4} - X| \approx C \left( \frac{h}{4} \right)^r. \quad (737)$$

Taking ratios of equations (735)–(737), and replacing the unknown  $X$  by an *estimate*  $X^*$ , we then arrive at the following equation:

$$\frac{|X_h - X^*|}{|X_{h/2} - X^*|} = \frac{|X_{h/2} - X^*|}{|X_{h/4} - X^*|} = 2^r.$$

If one assumes that  $X_h$  converges to  $X$  uniformly either from above or below (rather than oscillate around  $X$ ), then this equation allows us to solve for  $X^*$  and  $r$ :

$$X^* = \frac{X_h X_{h/2} - X_{h/2}^2}{X_h - 2X_{h/2} + X_{h/4}}, \quad r = \log_2 \frac{X_{h/2} - X^*}{X_{h/4} - X^*}.$$

In the determination of  $r$ , we could also have used  $X_h$  and  $X_{h/2}$ , but using  $X_{h/2}$  and  $X_{h/4}$  is generally more reliable because the higher order terms we have omitted in (735) are less visible on finer meshes.

## 8.23 The initial temperature field

 Relevant Literature: Thermal gradients in the continental crust [435]

 Relevant Literature: Simple analytical approximation to the temperature structure in subduction zones [787]

### 8.23.1 Single layer with imposed temperature b.c.

Let us take a single layer of material characterised by a heat capacity  $C_p$ , a heat conductivity  $k$  and a heat production term  $H$ .



The Heat transport equation writes

$$\rho C_p \left( \frac{\partial T}{\partial t} + \vec{v} \cdot \vec{\nabla} T \right) = \vec{\nabla} \cdot (k \vec{\nabla} T) + \rho H \quad (738)$$

At steady state and in the absence of a velocity field, assuming that the material properties to be independent of time and space, and assuming that there is no heat production ( $H = 0$ ), this equation simplifies to

$$\Delta T = 0 \quad (739)$$

Assuming the layer to be parallel to the  $x$ -axis, the temperature is  $T(x, y) = T(y) = \alpha T + \beta$ . In order to specify the constants  $\alpha$  and  $\beta$ , we need two constraints.

At the bottom of the layer  $y = y_b$  a temperature  $T_b$  is prescribed while a temperature  $T_t$  is prescribed at the top with  $y = y_t$ . This ultimately yields a temperature field in the layer given by

$$T(y) = \frac{T_t - T_b}{y_t - y_b}(y - y_b) + T_b$$

If now the heat production coefficient is not zero, the differential equation reads

$$k \Delta T + H = 0 \quad (740)$$

The temperature field is then expected to be of the form

$$T(y) = -\frac{H}{2k}y^2 + \alpha y + \beta \quad (741)$$

Supplied again with the same boundary conditions, this leads to

$$\beta = T_b + \frac{H}{2k}y_b^2 - \alpha y_b$$

ie,

$$T(y) = -\frac{H}{2k}(y^2 - y_b^2) + \alpha(y - y_b) + T_b$$

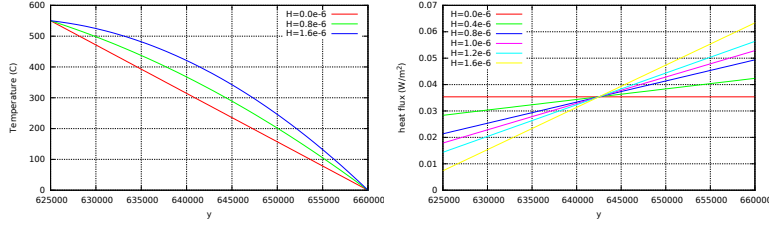
and finally

$$\alpha = \frac{T_t - T_b}{y_t - y_b} + \frac{H}{2k}(y_b + y_t)$$

or,

$$T(y) = -\frac{H}{2k}(y^2 - y_b^2) + \left( \frac{T_t - T_b}{y_t - y_b} + \frac{H}{2k}(y_b + y_t) \right)(y - y_b) + T_b$$

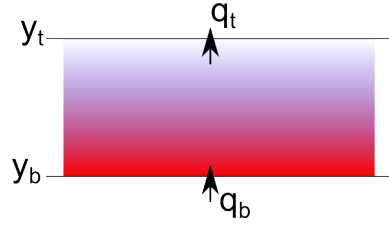
Taking  $H = 0$  in this equation obviously yields the temperature field obtained previously. Taking  $k = 2.25$ ,  $T_t = 0C$ ,  $T_b = 550C$ ,  $y_t = 660km$ ,  $y_b = 630km$  yields the following temperature profiles and heat fluxes when the heat production  $H$  varies:



Looking at the values at the top, which are somewhat estimated to be about  $55 - 65 \text{ mW/m}^2$  [1344, table 8.6], one sees that value  $H = 0.8e-6$  yields a very acceptable heat flux. Looking at the bottom, the heat flux is then about  $0.03 \text{ W/m}^2$  which is somewhat problematic since the heat flux at the Moho is reported to be somewhere between 10 and  $20 \text{ mW/m}^2$  in [1344, table 7.1].

### 8.23.2 Single layer with imposed heat flux b.c.

Let us now assume that heat fluxes are imposed at the top and bottom of the layer:



We start again from the ODE

$$k\Delta T + H = 0$$

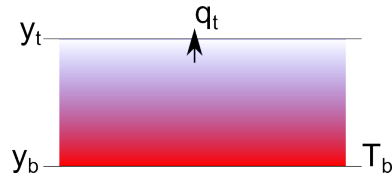
but only integrate it once:

$$k \frac{dT}{dy} + Hy + \alpha = 0$$

At the bottom  $q = k(dT/dy)|_{y=y_b} = q_b$  and at the top  $q = k(dT/dy)|_{y=y_t} = q_t$  so that

[to finish](#)

### 8.23.3 Single layer with imposed heat flux and temperature b.c.



[to finish](#)

### 8.23.4 Half cooling space

TODO.

Relevant Literature[804]

### 8.23.5 Plate model

### 8.23.6 McKenzie slab

When doing thermo-mechanical modelling, the initial temperature field in the domain is of prime importance. This is especially true for the temperature in the slab for subduction modelling as its rheological behaviour is strongly temperature-dependent. One could easily design a simple geometrical initial field but it is unlikely to be close to the field of a slowly subducting slab at an angle in a hot mantle.

McKenzie [1758] derived such approximate initial field from the steady-state energy equation in two dimensions:

$$\rho C_p \vec{v} \cdot \vec{\nabla} T = k \vec{\nabla}^2 T \quad (742)$$

We denote by  $T_l$  the temperature at the base of the lithosphere and  $l$  its thickness (i.e. the thickness of the slab).

Assuming  $\vec{v} = (v_x, 0)$  yields

$$\rho C_p v_x \frac{\partial T}{\partial x} = k \frac{\partial^2 T}{\partial x^2}$$

and substitution of  $T' = T/T_l$ ,  $x' = x/l$  and  $z' = z/l \in [0, 1]$  in this equation leads to

$$\rho C_p v_x \frac{T_l}{l} \frac{\partial T'}{\partial x'} = k \frac{T_l}{l^2} \left( \frac{\partial^2 T'}{\partial x'^2} + \frac{\partial^2 T'}{\partial z'^2} \right)$$

or

$$\frac{\rho C_p v_x l}{k} \frac{\partial T'}{\partial x'} = \frac{\partial^2 T'}{\partial x'^2} + \frac{\partial^2 T'}{\partial z'^2}$$

and finally (see Eq. 2.3 of [1758]):

$$\frac{\partial^2 T'}{\partial x'^2} - 2R \frac{\partial T'}{\partial x'} + \frac{\partial^2 T'}{\partial z'^2} = 0$$

where  $R$  is the thermal Reynolds number

$$R = \frac{\rho C_p v_x l}{2k}$$

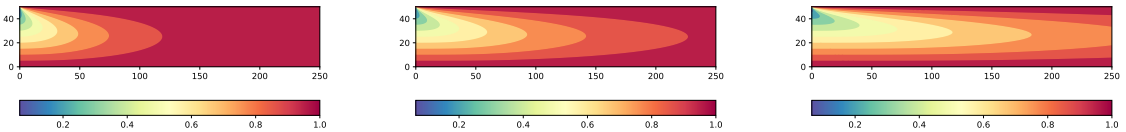
The general solution to this PDE with  $T' = 1$  on the top, left and right boundary is

$$T'(x', z') = 1 + \sum_n C_n \exp \left[ \left( R - (R^2 + n^2 \pi^2)^{1/2} \right) x' \right] \sin(n \pi z')$$

We now must make an assumption about the temperature on the left boundary ( $x' = 0$ ), which is the temperature of the lithosphere. For simplicity McKenzie assumes that  $T'(x' = 0, z') = 1 - z'$  so that  $C_n = 2(-1)^n/n\pi$  and finally

$$T'(x', z') = 1 + 2 \sum_n \frac{(-1)^n}{n\pi} \exp \left[ \left( R - (R^2 + n^2 \pi^2)^{1/2} \right) x' \right] \sin(n \pi z') \quad (743)$$

Let us build a simple temperature model for a  $250\text{km} \times 50\text{km}$  slab, with  $\rho = 3000$ ,  $C_p = 1250$ ,  $k = 3$ . The python code is available in `images/mckenzie/mckenzie1.py`.

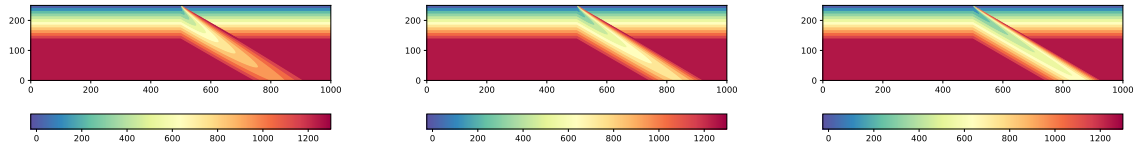


Left to right: Dimensionless temperature  $T'$  in a  $250\text{km} \times 50\text{km}$  slab for  $v_x = 0.5, 1, 2\text{cm/year}$

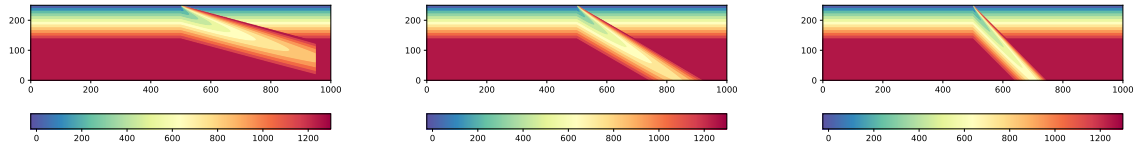
We logically recover the fact that the slower the slab penetrates the mantle the more temperature diffusion dominates over temperature advection. For  $v = 0.5\text{cm/year}$  we see that that the slab assumes a constant temperature  $T' = 1$  at all depths  $0 \leq z' \leq 1$  for  $x' \geq 125\text{km}$ .

Note that this field is a steady-state field, valid for a constant density, heat conductivity and heat capacity, zero heat production, that it implies that the velocity is constant and that the lithosphere temperature is linear.

One can also embed the slab in a more realistic context, a subduction zone, involving a subducting lithosphere, an over-riding plate and a mantle. The domain is  $1000\text{km} \times 250\text{km}$ . The mantle temperature is set to  $1300^\circ$ . The slab dip can be varied and so can the velocity. The python code is available in `images/mckenzie/mckenzie2.py`.



Left to right: temperature  $T$  for  $v_x = 0.5, 1, 2 \text{ cm/year}$  and  $\phi = 30^\circ$ .



Left to right: temperature  $T$  for  $v_x = 1 \text{ cm/year}$  and  $\phi = 15, 30, 45^\circ$ .

### 8.23.7 Initial temperature for global mantle convection models

This is a difficult topic, and Gottschaldt et al [1035] list a few issues or facts to take into account:

- Frequent impacts may have determined the heat structure of the outer layers (Arrhenius and Lepland 2000), leading to an early thermally stable stratification.
- A global magma ocean (Solomatov 2000) or several large scale melting events (Kleine et al. 2004) are also conceivable.
- Fractional crystallisation and subsequent overturn has the potential to result in compositionally or thermally stable layering, too (Elkins-Tanton et al. 2003; Zaranek and Parmentier 2004)

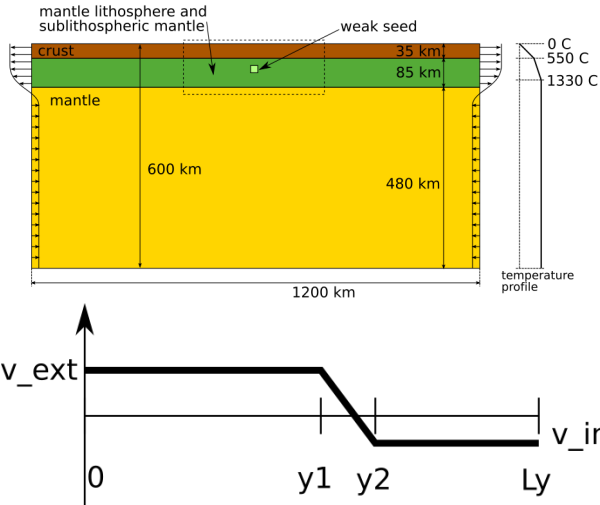
## 8.24 Kinematic boundary conditions

Boundary conditions come in two basic flavors: essential and natural.

- Essential bcs directly affect DOFs, and are imposed on the FEM matrix.
- Natural bcs do not directly affect DOFs and are imposed on the right-hand side vector.

### 8.24.1 In-out flux boundary conditions for lithospheric models

C. Thieulot / Physics of the Earth and Planetary Interiors 188 (2011) 47–68



The velocity on the side is given by

$$\begin{aligned} u(y) &= v_{ext} \quad y < L_1 \\ u(y) &= \frac{v_{in} - v_{ext}}{y_2 - y_1}(y - y_1) + v_{ext} \quad y_1 < y < y_2 \\ u(y) &= v_{in} \quad y > y_2 \end{aligned}$$

The requirement for volume conservation is:

$$\Phi = \int_0^{L_y} u(y) dy = 0$$

Having chosen  $v_{in}$  (the velocity of the plate), one can then compute  $v_{ext}$  as a function of  $y_1$  and  $y_2$ .

$$\begin{aligned} \Phi &= \int_0^{y_1} u(y) dy + \int_{y_1}^{y_2} u(y) dy + \int_{y_2}^{L_y} u(y) dy \\ &= v_{ext}y_1 + \frac{1}{2}(v_{in} + v_{ext})(y_2 - y_1) + (L_y - y_2)v_{in} \\ &= v_{ext}[y_1 + \frac{1}{2}(y_2 - y_1)] + v_{in}[\frac{1}{2}(y_2 - y_1) + (L_y - y_2)] \\ &= v_{ext}\frac{1}{2}(y_1 + y_2) + v_{in}[L_y - \frac{1}{2}(y_1 + y_2)] \end{aligned}$$

and finally

$$v_{ext} = -v_{in} \frac{L_y - \frac{1}{2}(y_1 + y_2)}{\frac{1}{2}(y_1 + y_2)}$$

Relevant Literature[780, 703]

## 8.25 Computing gradients - the recovery process

write about recovering accurate strain rate components and heat flux components on the nodes.

Let  $\vec{g}(\vec{r})$  be the desired nodal field which we want to be the continuous  $Q_1$  representation of the field  $\vec{\nabla}f^h$ . Since the derivative of the shape function does not exist on the nodes we need to design an algorithm do do so. This problem is well known and has been investigated

refs!

. The main standard techniques are listed hereafter.

### 8.25.1 Global recovery

The global recovery approach is rather simple: we wish to find  $\vec{g}^h$  such that it satisfies

$$\int_{\Omega} \phi \vec{g}^h \, d\Omega = \int_{\Omega} \phi \vec{\nabla} f^h \, d\Omega \quad \forall \phi$$

We will then successively replace  $\phi$  by all the shape functions  $N_i$  and since we have  $g^h = \sum_j N_i g_i$  we then obtain

$$\sum_j \int N_i N_j d\Omega g_i = \int N_i \vec{\nabla} f^h \, d\Omega$$

or,

$$\mathbb{M} \cdot \vec{\mathcal{G}} = \vec{f}$$

### 8.25.2 Local recovery - centroid average over patch

### 8.25.3 Local recovery - nodal average over patch

Let  $j$  be the node at which we want to compute  $\vec{g}$ . Then

$$\vec{g}_j = \vec{g}(\vec{r}_j) = \frac{\sum_{e \text{ adj. to } j} |\Omega_e| (\vec{\nabla} f)_e(\vec{r}_j)}{\sum |\Omega_e|}$$

where  $|\Omega_e|$  is the volume of the element and  $(\vec{\nabla} f^h)_e(\vec{r}_j)$  is the gradient of  $f$  as obtained with the shape functions inside element  $e$  and computed at location  $\vec{r}_j$ .

### 8.25.4 Local recovery - least squares over patch

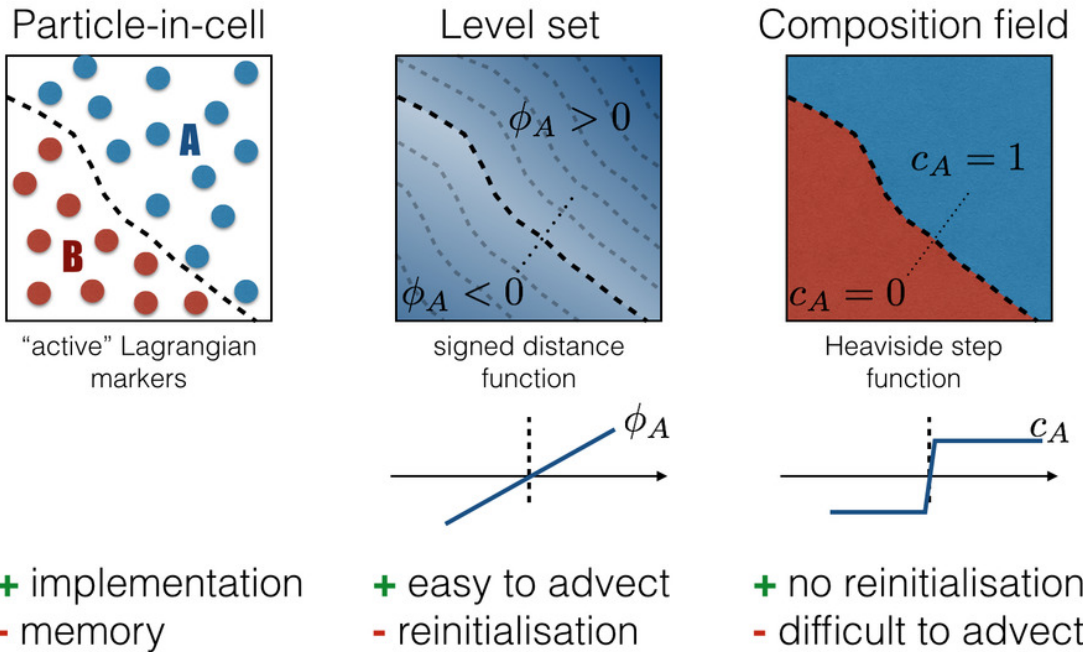
### 8.25.5 Link to pressure smoothing

When the penalty method is used to solve the Stokes equation, the pressure is then given by  $p = -\lambda \vec{\nabla} \cdot \vec{v}$ . As explained in section 6.3, the velocity is first obtained and the pressure is recovered by using this equation as a postprocessing step. Since the divergence cannot be computed easily at the nodes, the pressure is traditionally computed in the middle of the elements, yielding an elemental pressure field (remember, we are talking about  $Q_1 P_0$  elements here – bi/tri-linear velocity, discontinuous constant pressure)

tie to fieldstone 12

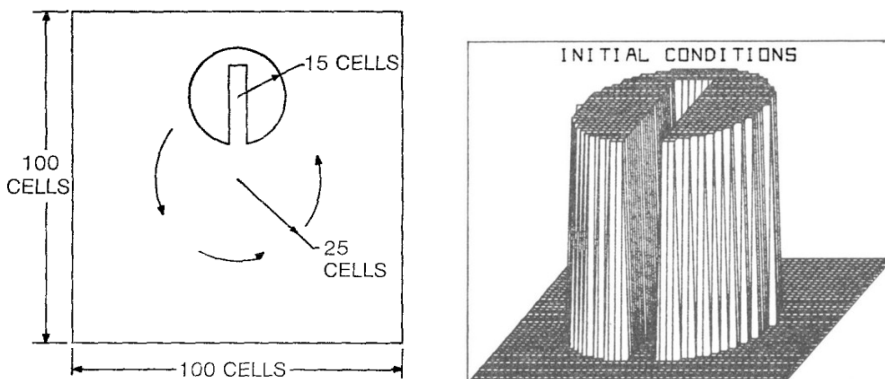
## 8.26 Tracking materials and/or interfaces

Unless using a fully Lagrangian formulation, one needs an additional numerical method to represent/track the various materials present in an undeformable (Eulerian) mesh. The figure below (by B. Hillebrand) illustrates the three main methods used in geodynamics.



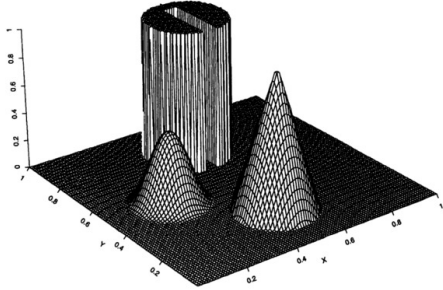
Note that what follows is applicable to FEM, FDM, etc ...

A typical test for advection algorithm is the Zalesak disk [2868]. It is a two dimensional test problem of solid body rotation with a constant angular velocity  $\omega$  (in rad/sec):



Taken from [2868]. Left: Schematic representation of two dimensional solid body rotation problem. The field inside the cut out has value 3 and it is 1 outside. The rotational speed is such that one full revolution is effected in 628 cycles. The width of the gap separating the two halves of the cylinder, as well as the maximum extent of the “bridge” connecting the two halves, is 5 cells. Right: Perspective view of initial conditions for the two dimensional solid body rotation problem. Note that only a  $50 \times 50$  portion of the mesh centered on the cylinder is displayed.

This benchmark is widely used in the literature [2456, 2626, 2030, 104, 2892]. Note that the Zalesak disc is often supplemented with a cone and a Gaussian features:



Taken from [1594]. Initial data for solid rotation tests

### 8.26.1 The Particle-in-cell technique

**Remark.** The terms 'particle' and 'marker' are commonly (and unfortunately) interchangeably used in the literature in the context of the particle-in-cell technique. However, one should be aware that the marker-and-cell (MAC) technique is something different: it was invented in the early 60's at the Los Alamos Laboratories by Harlow and Welch [1149]. For more information on MAC see the review paper by McKee et al [1751].

The Particle-in-cell method is by far the most widely used in computational geodynamics. In its most basic form it is a rather simple method to implement and this probably owes to its success and early adoption [2046] in non-parallel codes such as SOPALE [901], I2VIS [974] or CITCOM [1763] (Appendix B). It has been implemented in ASPECT [925] and the inherent load balancing issues arising from the parallel implementation as well as from the use of Adaptive Mesh Refinement are discussed. It has also been implemented in the MILAMIN code [614] to study LLSVPs [1886].

The basic methodology goes as follows:

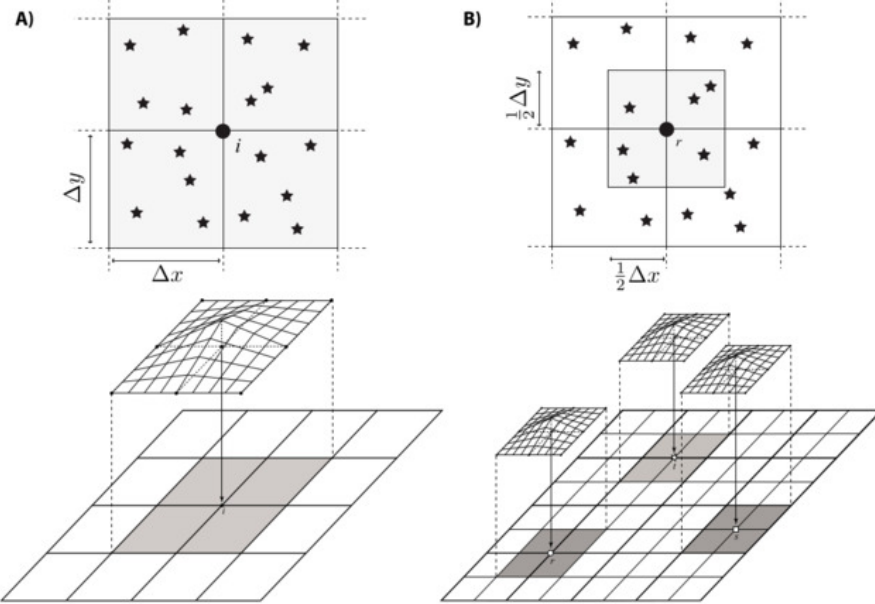
1. distribute particles in the domain
2. assign a material identity (and/or any other quantity) to each of them
3. project particle quantities of the Eulerian nodes of the mesh
4. solve the Stokes equations for a new velocity field
5. interpolate the velocity onto the particles
6. move the particles with their respective velocities
7. go back to step 3

As it turns out each step above needs to be carefully executed and is more difficult than it first looks.

**Distributing particles in the domain**. Let us assume we wish to distribute  $N_p$  particles in the domain. How large must  $N_p$  be? To simplify, one end member could be 'as many particles as possible that fit in memory' while the other end member could be 'one per element/cell on average'. While the former does not necessarily guarantee a desired accuracy while being CPU and memory intensive, the latter will certainly lead to zones in the domain void of particles which will be problematic since the projection onto the mesh might yield zero values or very inaccurate values. How many particles (per element/cell) will be enough? Also, should the particles be randomly distributed in the domain or on some kind of regular grid? See fieldstone 13 (Section 9.4).

**Averaging and projection**. This is a very critical step. Unfortunately, there is no community-wide agreed-upon method. The problem at hand boils down to: at a given location ( $\vec{r}$ ) in space I need a quantity which is carried by the particles. The first step is to find the particle(s) close to this point. If done naively, this is a very costly affair, and begs the question what 'close' means. Finding all particles within a radius  $R$  of point  $\vec{r}$  can be done very efficiently (e.g. with linked lists, Verlet lists, ...) but the choice of  $R$  proves to be critical: if too small, there may not be any particle inside the circle, and if too

large there may be many particles inside the circle and the averaging over so many particles in space will prove to be over diffusive. In practice, the FD or FE mesh is used to provide an indication of  $R$ . In FDM, the four cells (or quarter cells) around a node represent the volume of space containing the particles whose properties are to be averaged [739] as illustrated in the following figure:



Taken from [739]. The "4-cell" and "1-cell" schemes for projecting properties defined on the markers (denoted by stars) onto a node (denoted by the solid circle). (A) The 4-cell scheme. The support of the interpolating function  $N_i$  associated with node  $i$  is indicated by the shaded region. Only markers within the support of node  $i$  contribute to the projection operation used to define the nodal value at  $i$ . The shape of the bilinear interpolation function for node  $i$  is indicated in the lower frame. (B) The 1-cell scheme. The thick lines in the lower frame indicate the grid used to discretize the Stokes equations, while the thin lines indicate the grid onto which marker properties are projected. The 1-cell scheme utilizes a compact support of size  $\Delta x \times \Delta y$ . The support for nodes  $r$ ,  $s$ ,  $t$  are indicated by the shaded regions. Only markers within the nodal support contribute to the projection operation for that node.

Given that the FEM requires to compute integrals over each element, only the particles inside the element will contribute to the average values assigned to the quadrature points. However, one could also decide to first average the properties onto the nodes before using these nodal values to assign values to the quadrature points. In this case the FDM approach applies.

Finally, in both FDM and FEM bi/trilinear shape functions are used for the interpolation as they can be interpreted as weighing functions. Higher order shape functions could also be used but the standard  $Q_2$  shape functions (Section 4.5) are 2-nd order polynomials which can take negative values (as opposed to the  $Q_1$  shape functions which are strictly positive) and this can pose problems: in some cases, although all values to be averaged are positive, their weighed average can be negative.

#### Q1 projection PUCKETT

it would be nice to have a Q1 and Q2 drawing of a 1D element and show that indeed negative values arise

Assuming that we have established a list of particles, all tracking a field  $f(\vec{r})$  and that each particle has an associated weight  $N_i$  (function of the location where the average is to be computed or not), we must now compute their average value  $\langle f \rangle$ . The simplest approach which comes to mind is the (weighed) arithmetic mean (*am*):

$$\langle f \rangle_{am} = \frac{\sum_{i=1}^n N_i f_i}{\sum_{i=1}^n N_i}$$

In the case where  $f$  is the (mass) density  $\rho$ , it is indeed what should be used. However, turning now to viscosity  $\eta$ , we know that its value can vary by many orders of magnitude over very short distances. It is then likely that the average runs over values spanning values between  $10^{18}\text{Pa s}$  and  $10^{25}\text{Pa s}$ . As explained in [2272] the arithmetic averaging tends to 'favour' large values: if the sum runs over 10

particles, 9 carrying the value  $10^{25}$  and 1 carrying the value  $10^{19}$ , the average value (assuming  $N_i = 1$  for simplicity) is then

$$\langle \eta \rangle = \frac{9 \cdot 10^{25} + 1 \cdot 10^{19}}{10} \simeq 0.9 \cdot 10^{25}$$

which is much closer to  $10^{25}$  than to  $10^{19}$ . Other averagings are then commonly used, namely the geometric mean ( $gm$ ) and the harmonic mean ( $hm$ ), defined as follows:

$$\langle f \rangle_{gm} = \left( \prod_i f_i^{N_i} \right)^{1/\sum_i N_i} \quad \text{or,} \quad \log_{10} \langle f \rangle_{gm} = \frac{\sum_i N_i \log_{10} f_i}{\sum_i N_i}$$

and

$$\langle f \rangle_{hm} = \left( \frac{\sum_{i=1}^n N_i \frac{1}{f_i}}{\sum_i N_i} \right)^{-1} \quad \text{or,} \quad \frac{1}{\langle f \rangle_{hm}} = \frac{\sum_{i=1}^n N_i \frac{1}{f_i}}{\sum_i N_i}$$

The geometric mean can be seen as a form of arithmetic mean of  $\log_{10}$  values, while the harmonic mean can be seen as a form of arithmetic mean of the inverse values.

Looking back at the above example, the geometric mean of the viscosities is given by

$$\log \langle \eta \rangle_{gm} = \frac{9 \cdot 25 + 1 \cdot 19}{10} = 24.4 \quad \text{or,} \quad \langle \eta \rangle_{gm} \simeq 2.5 \cdot 10^{24}$$

and the harmonic mean:

$$\langle \eta \rangle_{hm} \simeq \left( \frac{1}{10 \cdot 10^{19}} \right)^{-1} = 10^{20}$$

We see that the harmonic mean tends to favour the small values. Also we recover the known property:

$$\langle f \rangle_{am} \geq \langle f \rangle_{gm} \geq \langle f \rangle_{hm} \tag{744}$$

When all  $f_i$  are equal to  $f_0$  their computed average should also be equal to  $f_0$ . As a consequence the weights  $N_i$  should fulfill the condition  $\sum_{i=1}^n N_i = 1$ . If all weights are equal, then  $N_i = 1/n$  and the averagings become:

$$\langle f \rangle_{am} = \frac{1}{n} \sum_{i=1}^n f_i \quad \langle f \rangle_{gm} = \prod_i f_i^{1/n} \quad \langle f \rangle_{hm} = \left( \frac{1}{n} \sum_i \frac{1}{f_i} \right)^{-1} \tag{745}$$

There are many papers which have looked at particle averagings and projections. I will for now simply point to the following ones: [2272] [688] [739] [1842] [2054] [2526] [925][2232] [926]. Also check the multiscale PIC in [60]

[write more about particle averaging and projection](#)



Relevant Literature: [2492]

### Interpolation of the velocity onto particles .

Once the particle  $i$  has been localised inside a given element (Section 8.21) and its reduced coordinates  $(r, s, t)$  determined, the velocity at this location can be computed through the shape functions:

$$\vec{v}_i = \sum_{k=1}^m N_k(r, s, t) \vec{v}_k$$

This approach is not without problem: while the nodal velocities  $\vec{v}_k$  are such that<sup>62</sup>  $\vec{\nabla} \cdot \vec{v} = 0$  (in the weak sense), the computed velocity  $\vec{v}_i$  is not necessarily divergence-free! In order to remedy this, a Conservative Velocity Interpolation (CVI) has been proposed in [2719].

**Moving the particles** This is discussed in the context of the Runge-Kutta Methods, see Section 8.20.1.

---

<sup>62</sup>for incompressible flows, of course

### 8.26.2 The level set function technique

This method was developed in the 80's by Stanley Osher and James Sethian [1667]

The Level-set Method (LSM), as it is commonly used in Computational Fluid Dynamics – and especially in Computational Geodynamics – represents a close curve  $\Gamma$  (say, in our case, the interface between two fluids or layers) by means of a function  $\phi$  (called the level-set function, or LSF).  $\Gamma$  is then the zero level-set of  $\phi$ :

$$\Gamma = \{(x, y) \mid \phi(x, y) = 0\} \quad (746)$$

The convention is that  $\phi > 0$  inside the region delimited by  $\Gamma$  and  $\phi < 0$  outside. The function value indicates on which side of the interface a point is located (negative or positive) and this is used to identify materials.

Furthermore, if the curve  $\Gamma$  moves with a velocity  $\vec{v}$ , then it satisfies the following equation:

$$\frac{\partial \phi}{\partial t} + \vec{v} \cdot \vec{\nabla} \phi = 0 \quad (747)$$

The level set function is generally chosen to be a signed distance function, i.e.  $|\vec{\nabla} \phi| = 1$  everywhere and its value is also the distance to the interface.

As explained in [1195], the level-set function  $\phi$  is advected with the velocity  $\vec{v}$  which is obtained by solving the Stokes equations. This velocity does not guarantee that after an advection step the signed distance quality of the LSF is preserved. The LSF then needs to be corrected, which is also called reinitialisation. Finally, solving the advection equation must be done in an accurate manner both in time and space, so that so-called ENO (essentially non-oscillatory) schemes are often employed for the space derivative [1980, 2228].

The level set method has not often been used in the geodynamics community with some notable exceptions [243, 244, 1120, 1075, 2947, 1121, 2451, 2450, 1195] An overview of the method and applications can be found in [1979].

Several improvements upon the original LSM have been proposed, such as for instance the conservative level set of [2892]. The most notable difference between CLS method originally proposed by Olsson et al. [1966, 1967] and standard LS method lies in the choice of LS function. Instead of the signed distance function, the CLS methods employ the Heaviside function  $H(\phi)$

$$H(\phi) = \begin{cases} 1 & \phi > 0 \\ 1/2 & \phi = 0 \\ 0 & \phi < 0 \end{cases}$$

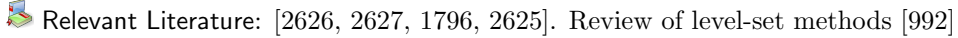
where  $\phi$  is the signed distance function as in the LSM. In practice, a hyperbolic tangent function is used:

$$H(\phi) = \frac{1}{2}(1 + \tanh(\phi/2\epsilon))$$

where  $\epsilon$  defines the spreading width of  $H$ . In the case where there are only two fluids (i.e. a single level set is sufficient), the material properties such as density and viscosity are computed as follows:

$$\rho = \rho_1 + (\rho_2 - \rho_1)H(\phi)$$

$$\eta = \eta_1 + (\eta_2 - \eta_1)H(\phi)$$



Relevant Literature: [2626, 2627, 1796, 2625]. Review of level-set methods [992]

### 8.26.3 The field/composition technique

This is the approach taken by the ASPECT developers [1507, 1169]. Each material  $i$  is represented by a compositional field  $c_i$ , which takes values between 0 and 1. Each compositional field is then advected with the (prescribed or computed) Stokes velocity [478]:

$$\frac{\partial c_i}{\partial t} + \mathbf{v} \cdot \nabla c_i = 0 \quad (748)$$

The value at a point (Finite element node or quadrature point) is 1 if it is in the domain covered by the material  $i$ , and 0 otherwise. In one dimension, each compositional field is a Heavyside function. This approach is somewhat similar to the LSM but the field is essentially discontinuous across the interface, which makes it very difficult to advect. On the plus side, compositional fields need not be reinitialised, as opposed to LSF's.

Accurate numerical advection is a notoriously difficult problem. Unless very specialised techniques are used it often yields undershoot ( $c_i < 0$ ) and overshoot ( $c_i > 0$ ), which ultimately yields mass conservation issues. Also, unless special care is taken, compositional fields tend to become more and more diffuse over time: the SUPG method (Section 8.5) and the entropy viscosity method add small amounts of diffusion to dampen the under- and overshoots. This means that at a given point two or more compositions may have values, which require some form of averaging. If under- and overshoots are present, these averagings can become very problematic and even yield meaningless quantities (e.g. negative viscosities).

One rather old and popular filtering approach is the so-called Lenardic and Kaula filter [1561]:

The filtering algorithm for two-component flow is as follows. An initial step distribution in  $C$  is assumed with  $C = 0$  and  $C = 1$  used to distinguish distinct materials. A high-order upwind solution scheme is applied to equation (2), with prescribed initial conditions, resulting in an uncorrected  $C$  field. The field is corrected via the following filtering algorithm:

1. The initial sum of all nodal  $C$  values is calculated and is assigned to the variable  $C_{sum0}$ .
2. Nodal  $C$  values below 0 are set to 0 and the peak value below 0 is assigned to the variable  $C_{min}$ .
3. Nodal  $C$  values above 1 are set to 1 and the peak value above 1 is assigned to the variable  $C_{max}$ .
4. Nodal  $C$  values less than or equal to the absolute value of  $C_{min}$  are set to 0.
5. Nodal  $C$  values greater than or equal to  $2 - C_{max}$  are set to 1.
6. The sum of all nodal  $C$  values is calculated and assigned to the variable  $C_{sum1}$ .
7. The number of nodal  $C$  values not 1 or 0 is assigned to the variable NUM.
8. The variable DIST is defined as  $(C_{sum0} - C_{sum1})/NUM$  and is added to all  $C$  values not 1 or 0.

Taken from Lenardic and Kaula [1561]

The basic idea of the filtering algorithm is to ensure that  $\phi$  remains within the bounds  $0 \leq \phi \leq 1$ , and to minimize dispersion error. We refer the reader to Lenardic and Kaula (1993) for the detailed explanation and here give the outline of the algorithm for a discrete property field  $\phi = \{\phi_i\}$ .

---

#### Algorithm 10 A property filtering algorithm

---

- (1) Compute the initial sum  $S_0$  of all values of  $\phi$ .
  - (2) Find the minimal value  $\phi_{min}$  below 0.
  - (3) Find the maximal value  $\phi_{max}$  above 1.
  - (4) Set  $\phi_i = 0$  if  $\phi_i \leq |\phi_{min}|$ .
  - (5) Set  $\phi_i = 1$  if  $\phi_i \geq 2 - \phi_{max}$ .
  - (6) Compute the sum  $S_1$  of all values of  $\phi$ .
  - (7) Compute the number num of  $0 < \phi_i < 1$ .
  - (8) Add  $dist = (S_1 - S_0)/num$  to all  $0 < \phi_i < 1$ .
- 

From FENICS book

 Relevant Literature: [2716]  
Entropy viscosity method [1078]

write about DG approach

#### 8.26.4 The Volume-of-Fluid method

[1202]

### 8.26.5 The method of characteristics

ask Arie to write something

[666]

### 8.26.6 The Marker Chain method

In two dimensions, the idea is quite simple: each interface is discretised by means of a number of Lagrangian points (which may or may not vary in time). The points are numbered and connected (think of the connectivity array of a 1D FEM code). In the case of small deformations, and in the absence of in/out-flow boundaries, the method is reasonably trivial to implement, and each couple of point defines a segment (and therefore its normal vector too) which can then be used to answer the question: "at this location, am I above or below this interface" or "am I this domain our outside this domain" (in the case that the interface does not reach any of the boundaries).

This method becomes somewhat impractical when large deformation occurs or, for example, when a domain splits into two (think: slab break off). One interface must then become two, and it requires an algorithm capable of detecting the breakup of the surface and capable of rebuilding/patching the new ones so that they can still be used further. Note that in case of large deformation some markers may get further and further apart from each other which makes for a poor representation of the surface. New markers should then be added but the question of when and where must then be addressed.

Also, switching to three dimensions can prove to be very difficult or simply very costly: the generation of the initial marker position is trivial but their connectivity can be complicated to establish at startup: for instance, a Stokes sphere will require a mesh made of triangles which maps exactly the surface of the sphere (see [2531, 1854] for methods on how to efficiently produce such meshes). In the case of more complex 3D geometries this may prove nearly impossible to do. So will the problem of splitting a surface into two (or merging two domains).

This method is usually coupled to Eulerian meshes (typically with FDM, but not only). It was used in [2801] in the context of salt domes analysis and later in [483, 489]. It is also used in [2659] but little details are given about the algorithms used to track and update the chain in the presence of such large deformation. It is also used (although coupled to level set functions) in the DOUAR code[269] (see Section B). Having worked myself on this code and having had to produce complex initial triangulated surfaces for simulations (see for example [1663]) it is easy to understand why later users of this code did implement the marker-in-cell technique. More recently, it is used to track the free surface position in a FDM code [745, 456].

Finally, Christensen [478] makes the following interesting comment: "One might assume that different methods of representing the discontinuity, for example, by a tracer chain [489] or a cloud of tracers, would solve these problems. However, the difficulties arise not only from the way in which material boundaries are represented. Physically, the rate of shear strain parallel to a rheological boundary is discontinuous. Within the finite element scheme such jump can only be realized at an element boundary. In an Eulerian scheme, where the discontinuity will crosscut the elements, the jump in strain rate must be approximated by a continuous variation, and effectively, the rheological properties on both sides of the discontinuity will be averaged in some way within the element."

I still have  
pics from the  
old days using  
DOUAR- in-  
clude

### 8.26.7 Hybrid methods

In Braun et al. [269] a level set method is presented which is based on a 3-D set of triangulated points, which makes it a hybrid between tracers and level set functions: in the DOUAR code (Appendix B) the interface is then explicitly tracked by means of the tracers while the LSF is computed on the FE nodes. Although very promising in theory, this method proved to be difficult to use in practice since it requires a) a triangulation of the interfaces at  $t = 0$  which is not trivial if the geometries are complex (think about a slab in 3D); b) the addition or removal of tracers because of the interface deformation and the patching of the triangulation; c) the calculation of the distance to the interfaces for each FE node based on the triangle normal vectors. This probably explains why the Particle-In-Cell method was later implemented in this code (pers. comm.). Note that another very similar approach is used in [2228].

#### 8.26.8 Boundary fitted mesh

This method is rather simple to implement and works well for small deformations. It is for instance used by Frehner [879] (see online supplementary material) in which it is stated: "The numerical grid is set up in such a way that the interface between different material phases (two layers in this case) coincides with element boundaries. Hence, each element belongs to a unique material phase and no interpolation is necessary." With such a method, each element is initially attributed a material phase/number and its material properties do not change.



Relevant Literature: three-dimensional front tracking method using a triangular mesh [2270].

## 8.27 Static condensation

The idea behind static condensation is quite simple: in some cases, there are dofs belonging to an element which only belong to that element. For instance, the so-called MINI element ( $P_1^+ \times P_1$ ) showcases a bubble function in the middle (see section ??). In the following,  $\vec{V}^*$  corresponds to the list of such dofs inside an element. The discretised Stokes equations on any element looks like:

$$\begin{pmatrix} \mathbb{K} & L & \mathbb{G} \\ L^T & \mathbb{K}^* & H \\ \mathbb{G}^T & H^T & 0 \end{pmatrix}_e \begin{pmatrix} \vec{\mathcal{V}} \\ \vec{V}^* \\ \vec{\mathcal{P}} \end{pmatrix}_e = \begin{pmatrix} \vec{f} \\ \vec{f}^* \\ \vec{h} \end{pmatrix}_e \quad (749)$$

This is only a re-writing of the elemental Stokes matrix where the matrix  $\mathbb{K}$  has been split in four parts. Note that the matrix  $\mathbb{K}^*$  is diagonal.

This can also be re-written in non-matrix form:

$$\mathbb{K} \cdot \vec{\mathcal{V}} + L \cdot \vec{V}^* + \mathbb{G} \cdot \vec{\mathcal{P}} = \vec{f} \quad (750)$$

$$L^T V + K^* \cdot \vec{V}^* + H \cdot \vec{\mathcal{P}} = \vec{f}^* \quad (751)$$

$$\mathbb{G}^T \cdot \vec{\mathcal{V}} + H^T \vec{V}^* = \vec{h} \quad (752)$$

The  $V^*$  in the second equation can be isolated:

$$\vec{V}^* = \mathbb{K}^{-*} \cdot (\vec{f}^* - L^T \cdot \vec{\mathcal{V}} - H \cdot \vec{\mathcal{P}})$$

and inserted in the first and third equations:

$$\mathbb{K} \cdot \vec{\mathcal{V}} + L \left[ \mathbb{K}^{-*} (\vec{f}^* - L^T \cdot \vec{\mathcal{V}} - H \cdot \vec{\mathcal{P}}) \right] + \mathbb{G} \cdot \vec{\mathcal{P}} = \vec{f} \quad (753)$$

$$\mathbb{G}^T \cdot \vec{\mathcal{V}} + H^T \left[ \mathbb{K}^{-*} (\vec{f}^* - L^T \cdot \vec{\mathcal{V}} - H \cdot \vec{\mathcal{P}}) \right] = \vec{h} \quad (754)$$

or,

$$(\mathbb{K} - L \cdot \mathbb{K}^{-*} \cdot L^T) \cdot \vec{\mathcal{V}} + (G - L \cdot \mathbb{K}^{-*} \cdot H) \cdot \vec{\mathcal{P}} = \vec{f} - L \cdot \mathbb{K}^{-*} \cdot \vec{f}^* \quad (755)$$

$$(G^T - H^T \cdot \mathbb{K}^{-*} \cdot L^T) \cdot \vec{\mathcal{V}} - (H^T \cdot \mathbb{K}^{-*} \cdot H) \cdot \vec{\mathcal{P}} = \vec{h} - H^T \cdot \mathbb{K}^{-*} \cdot \vec{f}^* \quad (756)$$

i.e.

$$\underline{\mathbb{K}} \cdot \vec{\mathcal{V}} + \underline{\mathbb{G}} \cdot \vec{\mathcal{P}} = \vec{f} \quad (757)$$

$$\underline{\mathbb{G}}^T \cdot \vec{\mathcal{V}} - \underline{\mathbb{C}} \cdot \vec{\mathcal{P}} = \vec{h} \quad (758)$$

with

$$\underline{\mathbb{K}} = K - L \cdot \mathbb{K}^{-*} \cdot L^T \quad (759)$$

$$\underline{\mathbb{G}} = G - L \cdot \mathbb{K}^{-*} \cdot H \quad (760)$$

$$\underline{\mathbb{C}} = H^T \cdot \mathbb{K}^{-*} \cdot H \quad (761)$$

$$\underline{\vec{f}} = \vec{f} - L \cdot \mathbb{K}^{-*} \cdot \vec{f}^* \quad (762)$$

$$\underline{\vec{h}} = \vec{h} - H^T \cdot \mathbb{K}^{-*} \cdot \vec{f}^* \quad (763)$$

Note that  $\underline{\mathbb{K}}$  is symmetric, and so is the Stokes matrix.

For instance, in the case of the MINI element, the dofs corresponding to the bubble could be eliminated at the elemental level, which would make the Stokes matrix smaller. However, it is then important to note that static condensation introduces a pressure-pressure term which was not there in the original formulation.

## 8.28 Measuring incompressibility

The velocity divergence error integrated over the whole element is given by

$$e_{div} = \int_{\Omega} (\vec{\nabla} \cdot \vec{v}^h - \underbrace{\vec{\nabla} \cdot \vec{v}}_{=0}) d\Omega = \int_{\Omega} (\vec{\nabla} \cdot \vec{v}^h) d\Omega \quad (764)$$

where  $\Gamma_e$  is the boundary of element  $e$  and  $\vec{n}$  is the unit outward normal of  $\Gamma_e$ .

Furthermore, one can show that [705]:

$$e_{div} = \int_{\Gamma_e} \vec{v}^h \cdot \vec{n} d\Gamma$$

The reason is as follows and is called the divergence theorem<sup>63</sup>: suppose a volume  $V$  subset of  $\mathbb{R}^d$  which is compact and has a piecewise smooth boundary  $S$ , and if  $\vec{F}$  is a continuously differentiable vector field then

$$\int_V (\vec{\nabla} \cdot \vec{F}) dV = \int_S (\vec{F} \cdot \vec{n}) dS$$

The left side is a volume integral while the right side is a surface integral. Note that sometimes the notation  $d\vec{S} = \vec{n} dS$  is used so that  $\vec{F} \cdot \vec{n} dS = \vec{F} \cdot d\vec{S}$ .

The average velocity divergence over an element can be defined as

$$\langle \vec{\nabla} \cdot \vec{v} \rangle_e = \frac{1}{V_e} \int_{\Omega_e} (\vec{\nabla} \cdot \vec{v}) d\Omega = \frac{1}{V_e} \int_{\Gamma_e} \vec{v} \cdot \vec{n} d\Gamma$$

Note that for elements using discontinuous pressures we shall recover a zero divergence element per element (local mass conservation) while for continuous pressure elements the mass conservation is guaranteed only globally (i.e. over the whole domain), see section 3.13.2 of [1065].

Note that one could instead compute  $\langle |\vec{\nabla} \cdot \vec{v}| \rangle_e$ . Either volume or surface integral can be computed by means of an appropriate Gauss-Legendre quadrature algorithm.

[implement and report](#)

---

<sup>63</sup>[https://en.wikipedia.org/wiki/Divergence\\_theorem](https://en.wikipedia.org/wiki/Divergence_theorem)

## 8.29 Periodic boundary conditions

This type of boundary conditions can be handy in some specific cases such as infinite domains. The idea is simple: when material leaves the domain through a boundary it comes back in through the opposite boundary (which of course presupposes a certain topology of the domain).

For instance, if one wants to model a gas at the molecular level and wishes to avoid interactions of the molecules with the walls of the container, such boundary conditions can be used, mimicking an infinite domain in all directions.

Let us consider the small mesh depicted hereunder:

missing picture

We wish to implement horizontal boundary conditions so that

$$u_5 = u_1 \quad u_{10} = u_6 \quad u_{15} = u_{11} \quad u_{20} = u_{16}$$

One could of course rewrite these conditions as constraints and extend the Stokes matrix but this approach turns out to be not practical at all.

Instead, the method is rather simple: replace in the connectivity array the dofs on the right side (nodes 5, 10, 15, 20) by the dofs on the left side. In essence, we wrap the system upon itself in the horizontal direction so that elements 4, 8 and 12 'see' and are 'made of' the nodes 1, 6, 11 and 16. In fact, this is only necessary during the assembly. Everywhere in the loops nodes 5, 10, 15 and 20 appear one must replace them by their left pendants 1, 6, 11 and 16. This automatically generates a matrix with lines and columns corresponding to the  $u_5$ ,  $u_{10}$ ,  $u_{15}$  and  $u_{20}$  being exactly zero. The Stokes matrix is the same size, the blocks are the same size and the symmetric character of the matrix is respected. However, there remains a problem. There are zeros on the diagonal of the above mentioned lines and columns. One must then place there 1 or a more appropriate value.

Another way of seeing this is as follows: let us assume we have built and assembled the Stokes matrix, and we want to impose periodic b.c. so that dof  $j$  and  $i$  are the same. The algorithm is composed of four steps:

1. add col  $j$  to col  $i$
2. add row  $j$  to row  $i$  (including rhs)
3. zero out row  $j$ , col  $j$
4. put average diagonal value on diagonal  $(j, j)$

**Remark.** *Unfortunately the non-zero pattern of the matrix with periodic b.c. is not the same as the matrix without periodic b.c.*

## 8.30 Removing rotational nullspace

When free slip boundary conditions are prescribed in an annulus or hollow sphere geometry there exists a rotational nullspace, or in other words there exists a tangential velocity field ('pure rotation') which, if added or subtracted to the solution, generates a solution which is still the solution of the PDEs.

As in the pressure normalisation case (see section 8.14), the solution is simple:

1. fix the tangential velocity at *one* node on a boundary, and solve the system (the nullspace has been removed)<sup>64</sup>
2. post-process the solution to have the velocity field fulfill the required conditions, i.e. either a zero net angular momentum or a zero net angular velocity of the domain.

**Remark.** In ASPECT this is available under the option "Remove nullspace = angular momentum" and "Remove nullspace = net rotation". The "angular momentum" option removes a rotation such that the net angular momentum is zero. The "net rotation" option removes the net rotation of the domain.

**Angular momentum approach** In order to remove the angular momentum, we search for a rotation vector  $\vec{\omega}$  such that

$$\int_{\Omega} \rho[\vec{r} \times (\vec{v} - \vec{\omega} \times \vec{r})] dV = \vec{0} \quad (765)$$

The angular momentum of a rigid body can be obtained from the sum of the angular momentums of the particles forming the body<sup>65</sup>:

$$\vec{H} = \sum_i \vec{L}_i \quad (766)$$

$$= \sum_i \vec{r}_i \times m_i \vec{v}_i \quad (767)$$

$$= \sum_i \vec{r}_i \times m_i (\vec{\omega}_i \times \vec{r}_i) \quad (768)$$

$$= \sum_i m_i \begin{pmatrix} \sum_i m_i(y_i^2 + z_i^2) & -\sum_i m_i x_i y_i & -\sum_i m_i x_i z_i \\ -\sum_i m_i x_i y_i & \sum_i m_i(x_i^2 + z_i^2) & -\sum_i m_i y_i z_i \\ -\sum_i m_i x_i z_i & -\sum_i m_i y_i z_i & \sum_i m_i(x_i^2 + y_i^2) \end{pmatrix} \cdot \begin{pmatrix} \omega_x \\ \omega_y \\ \omega_z \end{pmatrix} \quad (769)$$

In the continuum limit, we have:

$$\vec{H} = \int_{\Omega} \rho(\vec{r}) \vec{r} \times \vec{v} dV \quad (770)$$

and the  $3 \times 3$  moment of inertia tensor  $\mathbf{I}$  (also called inertia tensor) is given by<sup>66</sup>

$$\mathbf{I} = \int_{\Omega} \rho(\vec{r}) [\vec{r} \cdot \vec{r} \mathbf{1} - \vec{r} \times \vec{r}] dV \quad (771)$$

so that the above equation writes:  $\vec{H} = \mathbf{I} \cdot \vec{\omega}$  and then  $\vec{\omega} = \mathbf{I}^{-1} \cdot \vec{H}$ .

Ultimately, at each velocity node a rotation about the rotation vector  $\vec{\omega}$  is then subtracted from the velocity solution [2905, eq. 26]:

$$\vec{v}_{new} = \vec{v}_{old} - \vec{\omega} \times \vec{r} \quad (772)$$

### 8.30.1 Three dimensions

The angular momentum vector is given by:

$$\vec{H} = \int_{\Omega} \rho(\vec{r}) \begin{pmatrix} yw - zv \\ zu - xw \\ xv - yu \end{pmatrix} d\vec{r} = \begin{pmatrix} \int_{\Omega} \rho(\vec{r})(yw - zv) d\vec{r} \\ \int_{\Omega} \rho(\vec{r})(zu - xw) d\vec{r} \\ \int_{\Omega} \rho(\vec{r})(xv - yu) d\vec{r} \end{pmatrix} = \begin{pmatrix} H_x \\ H_y \\ H_z \end{pmatrix} \quad (773)$$

---

<sup>64</sup><https://scicomp.stackexchange.com/questions/3531/how-to-remove-rigid-body-motions-in-linear-elasticity>

<sup>65</sup><http://www.kwon3d.com/theory/moi/iten.html>

<sup>66</sup>[https://en.wikipedia.org/wiki/Moment\\_of\\_inertia](https://en.wikipedia.org/wiki/Moment_of_inertia)

while the inertia tensor for a continuous body is given by

$$\mathbf{I} = \int_{\Omega} \rho(\vec{r}) [\vec{r} \cdot \vec{r} \mathbf{1} - \vec{r} \times \vec{r}] d\vec{r} \quad (774)$$

$$= \int_{\Omega} \rho(\vec{r}) \left[ \begin{pmatrix} x^2 + y^2 + z^2 & 0 & 0 \\ 0 & x^2 + y^2 + z^2 & 0 \\ 0 & 0 & x^2 + y^2 + z^2 \end{pmatrix} - \begin{pmatrix} xx & xy & xz \\ yx & yy & yz \\ zx & zy & zz \end{pmatrix} \right] d\vec{r} \quad (775)$$

$$= \int_{\Omega} \rho(\vec{r}) \begin{pmatrix} y^2 + z^2 & -xy & -xz \\ -yx & x^2 + z^2 & -yz \\ -zx & -zy & x^2 + y^2 \end{pmatrix} d\vec{r} \quad (776)$$

$$= \begin{pmatrix} \int_{\Omega} \rho(\vec{r})(y^2 + z^2) d\vec{r} & -\int_{\Omega} \rho(\vec{r})xy d\vec{r} & -\int_{\Omega} \rho(\vec{r})xz d\vec{r} \\ -\int_{\Omega} \rho(\vec{r})yx d\vec{r} & \int_{\Omega} \rho(\vec{r})(x^2 + z^2) d\vec{r} & -\int_{\Omega} \rho(\vec{r})yz d\vec{r} \\ -\int_{\Omega} \rho(\vec{r})zx d\vec{r} & -\int_{\Omega} \rho(\vec{r})zy d\vec{r} & \int_{\Omega} \rho(\vec{r})(x^2 + y^2) d\vec{r} \end{pmatrix} \quad (777)$$

$$= \begin{pmatrix} I_{xx} & I_{xy} & I_{xz} \\ I_{yx} & I_{yy} & I_{yz} \\ I_{zx} & I_{zy} & I_{zz} \end{pmatrix} \quad (778)$$

### 8.30.2 Two dimensions

In two dimensions, flow is taking place in the  $(x, y)$  plane. This means that  $\vec{r} = (x, y, 0)$  and  $\vec{v} = (u, v, 0)$  are coplanar, and therefore that  $\vec{\omega}$  is perpendicular to the plane. We have then

$$\vec{H} = \int_{\Omega} \rho(\vec{r}) \begin{pmatrix} 0 \\ 0 \\ xv - yu \end{pmatrix} d\vec{r} = \begin{pmatrix} 0 \\ 0 \\ \int_{\Omega} \rho(\vec{r})(xv - yu) d\vec{r} \end{pmatrix} \quad (779)$$

and

$$\mathbf{I} = \begin{pmatrix} I_{xx} & I_{xy} & I_{xz} \\ I_{yx} & I_{yy} & I_{yz} \\ I_{zx} & I_{zy} & I_{zz} \end{pmatrix} = \begin{pmatrix} I_{xx} & I_{xy} & 0 \\ I_{yx} & I_{yy} & 0 \\ 0 & 0 & I_{zz} \end{pmatrix} \quad (780)$$

since  $I_{xz} = I_{yz} = 0$  as  $z = 0$ , and with  $I_{xx} = \int_{\Omega} \rho(\vec{r})y^2 d\vec{r}$  and  $I_{yy} = \int_{\Omega} \rho(\vec{r})x^2 d\vec{r}$ . The solution to  $\mathbf{I} \cdot \vec{\omega} = \vec{H}$  can be easily obtained (see Appendix G.2):

$$\omega_x = \frac{1}{\det(\mathbf{I})} \begin{vmatrix} 0 & I_{xy} & 0 \\ 0 & I_{yy} & 0 \\ H_3 & 0 & I_{zz} \end{vmatrix} = 0 \quad (781)$$

$$\omega_y = \frac{1}{\det(\mathbf{I})} \begin{vmatrix} I_{xx} & 0 & 0 \\ I_{yx} & 0 & 0 \\ 0 & H_z & I_{zz} \end{vmatrix} = 0 \quad (782)$$

$$\omega_z = \frac{1}{\det(\mathbf{I})} \begin{vmatrix} I_{xx} & I_{xy} & 0 \\ I_{yx} & I_{yy} & 0 \\ 0 & 0 & H_z \end{vmatrix} \quad (783)$$

$$= \frac{1}{\det(\mathbf{I})} (I_{xx}I_{yy}H_z - I_{yx}I_{xy}H_z) \quad (784)$$

$$= \frac{1}{\det(\mathbf{I})} (I_{xx}I_{yy} - I_{yx}I_{xy}) H_z \quad (785)$$

with  $\det(\mathbf{I}) = I_{xx}I_{yy}I_{zz} - I_{yx}I_{xy}I_{zz} = (I_{xx}I_{yy} - I_{yx}I_{xy})I_{zz}$  and then

$$\omega_z = \frac{(I_{xx}I_{yy} - I_{yx}I_{xy})H_z}{(I_{xx}I_{yy} - I_{yx}I_{xy})I_{zz}} = \frac{H_z}{I_{zz}} = \frac{\int_{\Omega} \rho(\vec{r})(xv - yu) d\vec{r}}{\int_{\Omega} \rho(\vec{r})(x^2 + y^2) d\vec{r}}$$

Concretely, this means that in 2D one does not need to solve the system  $\mathbf{I} \cdot \vec{\omega} = \vec{H}$  since only  $\omega_z$  is not zero.

Then, since  $\vec{r} = (x, y, z)$  and  $\vec{\omega} = (0, 0, \omega_z)$ :

$$\vec{v}_{new}(\vec{r}) = \vec{v}_{old} - \vec{\omega} \times \vec{r} = \begin{pmatrix} u_{old} - (-\omega_z y) \\ v_{old} - (\omega_z x) \\ 0 \end{pmatrix} \quad (786)$$

## 8.31 Picard and Newton

explain why our eqs are nonlinear



Relevant Literature Quasi Newton methods [781]

### 8.31.1 Picard iterations

Let us consider the following system of nonlinear algebraic equations:

$$\mathbb{A}(\vec{X}) \cdot \vec{X} = \vec{b}(\vec{X})$$

Both matrix and right hand side depend on the solution vector  $\vec{X}$ .

For many mildly nonlinear problems, a simple successive substitution iteration scheme (also called Picard method) will converge to the solution and it is given by the simple relationship:

$$\mathbb{A}(\vec{X}^n) \cdot \vec{X}^{n+1} = \vec{b}(\vec{X}^n)$$

where  $n$  is the iteration number. It is easy to implement:

1. guess  $\vec{X}^0$  or use the solution from previous time step
2. compute  $\mathbb{A}$  and  $\vec{b}$  with current solution vector  $\vec{X}^{old}$
3. solve system, obtain  $\vec{T}^{new}$
4. check for convergence (are  $\vec{X}^{old}$  and  $\vec{X}^{new}$  close enough?)
5.  $\vec{X}^{old} \leftarrow \vec{X}^{new}$
6. go back to 2.

There are various ways to test whether iterations have converged. The simplest one is to look at  $\|\vec{X}^{old} - \vec{X}^{new}\|$  (in the  $L_1$ ,  $L_2$  or maximum norm) and assess whether this term is smaller than a given tolerance  $\epsilon$ . However this approach poses a problem: in geodynamics, if two consecutively obtained temperatures do not change by more than a thousandth of a Kelvin (say  $\epsilon = 10^{-3}\text{K}$ ) we could consider that iterations have converged but looking now at velocities which are of the order of a cm/year (i.e.  $\sim 3 \cdot 10^{-11}\text{m/s}$ ) we would need a tolerance probably less than  $10^{-13}\text{m/s}$ . We see that using absolute values for a convergence criterion is a potentially dangerous affair, which is why one uses a relative formulation (thereby making  $\epsilon$  a dimensionless parameter):

$$\frac{\|\vec{X}^{old} - \vec{X}^{new}\|}{\|\vec{X}^{new}\|} < \epsilon$$

Another convergence criterion is proposed by Reddy (section 3.7.2) [2118]:

$$\left( \frac{(\vec{X}^{old} - \vec{X}^{new}) \cdot (\vec{X}^{old} - \vec{X}^{new})}{\vec{X}^{new} \cdot \vec{X}^{new}} \right)^{1/2} < \epsilon$$

Yet another convergence criterion is used in [2528]: the means  $\langle \vec{X}^{old} \rangle$ ,  $\langle \vec{X}^{new} \rangle$  as well as the variances  $\sigma^{old}$  and  $\sigma^{new}$  are computed, followed by the correlation factor  $R$ :

$$R = \frac{\langle (\vec{X}^{old} - \langle \vec{X}^{old} \rangle) \cdot (\vec{X}^{new} - \langle \vec{X}^{new} \rangle) \rangle}{\sqrt{\sigma^{old} \sigma^{new}}}$$

Since the correlation is normalised, it takes values between 0 (very dissimilar velocity fields) and 1 (very similar fields). The following convergence criterion is then used:  $1 - R < \epsilon$ .

write about nonlinear residual

Note that in some instances and improvement in convergence rate can be obtained by use of a relaxation formula where one first solves

$$\mathbb{A}(\vec{X}^n) \cdot \vec{X}^* = \vec{b}(\vec{X}^n)$$

and then updates  $\vec{X}^n$  as follows:

$$\vec{X}^n = \gamma \vec{X}^n + (1 - \gamma) \vec{X}^* \quad 0 < \gamma \leq 1$$

When  $\gamma = 1$  we recover the standard Picard iterations formula above.

### 8.32 Defect correction formulation

Work in progress.

We start from the system to solve:

$$\mathbf{A}(\vec{X}) \cdot \vec{X} = \vec{b}(\vec{X})$$

with the associated residual vector  $\vec{F}$

$$\vec{F}(\vec{X}) = \mathbf{A}(\vec{X}) \cdot \vec{X} - \vec{b}(\vec{X})$$

The Newton-Raphson algorithm consists of two steps:

1. solve  $\mathbf{J}_k \cdot \delta \vec{X}_k = -\vec{F}(\vec{X}_k)$ , or in the case of the incompressible Stokes equation FEM system:

$$\begin{pmatrix} \mathbf{J}_k^{\mathcal{V}\mathcal{V}} & \mathbf{J}_k^{\mathcal{V}\mathcal{P}} \\ \mathbf{J}_k^{\mathcal{P}\mathcal{V}} & 0 \end{pmatrix} \cdot \begin{pmatrix} \delta \vec{\mathcal{V}}_k \\ \delta \vec{\mathcal{P}}_k \end{pmatrix} = \begin{pmatrix} -\vec{F}_k^{\mathcal{V}} \\ -\vec{F}_k^{\mathcal{P}} \end{pmatrix}$$

2. update  $\vec{X}_{k+1} = \vec{X}_k + \alpha_k \delta \vec{X}_k$

The defect correction Picard approach consists of neglecting the derivative terms present in the  $J$  terms (Eqs. 16,17,18 of [872]) so that

$$\mathbf{J}_k^{\mathcal{V}\mathcal{V}} \simeq \mathbb{K}_k \quad \mathbf{J}_k^{\mathcal{V}\mathcal{P}} \simeq \mathbb{G} \quad \mathbf{J}_k^{\mathcal{P}\mathcal{V}} \simeq \mathbb{G}^T$$

and step 1 of the above iterations become:

$$\begin{pmatrix} \mathbb{K}_k & \mathbb{G} \\ \mathbb{G}^T & 0 \end{pmatrix} \cdot \begin{pmatrix} \delta \vec{\mathcal{V}}_k \\ \delta \vec{\mathcal{P}}_k \end{pmatrix} = \begin{pmatrix} -\vec{F}_k^{\mathcal{V}} \\ -\vec{F}_k^{\mathcal{P}} \end{pmatrix}$$

**(MSc Thesis):** implement a simple Newton solver and apply it to a few nonlinear benchmarks.

### 8.33 Parallel or not?

Let us assume that we want to run a simulation of the whole Earth mantle with a constant resolution of 5km. The volume of the mantle is

$$V_{mantle} = \frac{4}{3}\pi(R_{out}^3 - R_{in}^3) \simeq 10^{12} km^3$$

while the volume of an element is  $V_e = 125 km^3$  (this is only an average since the tessellation of a hollow sphere with hexahedra yields elements which are not all similar [2531]). Consequently, the number of cells needed to discretise the mantle is

$$N_{el} = \frac{V_{mantle}}{V_e} \simeq 8 \times 10^9$$

We know that the matrix size is approx. 4 times the number of elements in 3D:

$$N \simeq 25 \times 10^9$$

Using between 9 and 125 particles per element (a very conservative number), the total number of particles is then

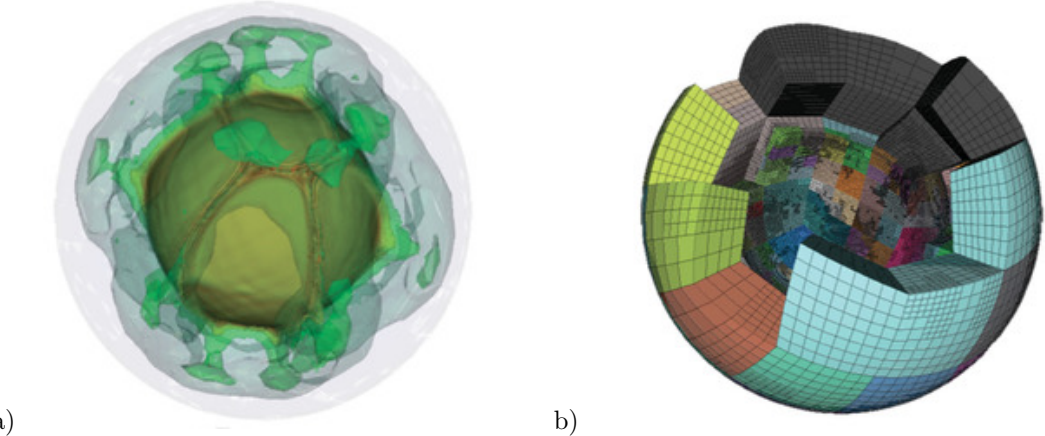
$$N_{particles} \geq 10^{10}$$

The unescapable conclusion is that high-resolution 3D calculations have a very large memory footprint and require extremely long computational times.

The only way to overcome this problem is by resorting to using supercomputers with many processors and large memory capacities.

The idea behind parallel programming is to have each processor carry out only a subset of the total number of operations required. In order to reduce the memory footprint on each processor, only a subset of the computational mesh is known by each: one speaks then of domain decomposition.

An example of such a large parallel calculation of 3D convection with domain decomposition in a spherical shell can be found in [1507]:



a) Isocontours of the temperature field; b) Partitioning of the domain onto 512 proc. The mesh counts 1,424,176 cells. The solution has approximately 54 million unknowns (39 million vel., 1.7 million press., and 13 million temp.)

## 8.34 Stream function

 Relevant Literature[993][2273][489][481][1140][1960]

### 8.34.1 In Cartesian coordinates

The Stream function (commonly denoted by  $\Phi$  or  $\Psi$ ) approach is a useful approach in fluid dynamics as it can provide relatively quick solutions to 2D incompressible flow problems. Lines of constant  $\Phi$  are called stream lines and give a useful representation of the flow. The definition of the stream function is such that

$$u = -\frac{\partial \Phi}{\partial y} \quad (787)$$

$$v = \frac{\partial \Phi}{\partial x} \quad (788)$$

It then follows that the velocity field based on the above equations automatically fulfills the continuity equation:

$$\vec{\nabla} \cdot \vec{v} = \frac{\partial u}{\partial x} + \frac{\partial v}{\partial y} = -\frac{\partial^2 \Phi}{\partial x \partial y} + \frac{\partial^2 \Phi}{\partial y \partial x} = 0$$

The stream function can also be substituted into the (constant viscosity) Stokes equation  $-\vec{\nabla} p + \eta \Delta \vec{v} = \vec{0}$ :

$$-\frac{\partial p}{\partial x} - \eta \left( \frac{\partial^3 \Phi}{\partial^2 x \partial y} + \frac{\partial^3 \Phi}{\partial^3 y} \right) = 0 \quad (789)$$

$$-\frac{\partial p}{\partial y} - \eta \left( \frac{\partial^3 \Phi}{\partial^3 x} + \frac{\partial^3 \Phi}{\partial x \partial^2 y} \right) = 0 \quad (790)$$

We can now eliminate the pressure term by taking the partial derivative of the first equation with respect to  $y$  and the partial derivative of the second one with respect to  $x$ , and subtracting both. We get:

$$\frac{\partial^4 \Phi}{\partial x^4} + \frac{\partial^4 \Phi}{\partial x^2 \partial y^2} + \frac{\partial^4 \Phi}{\partial y^4} = 0 \quad (791)$$

or,

$$\left( \frac{\partial^2}{\partial x^2} + \frac{\partial^2}{\partial y^2} \right) \left( \frac{\partial^2}{\partial x^2} + \frac{\partial^2}{\partial y^2} \right) \Phi = 0 \quad (792)$$

or,

$$\vec{\nabla}^2 \vec{\nabla}^2 \Phi = \vec{\nabla}^4 \Phi = 0$$

which is known as the Biharmonic operator.

### 8.34.2 In Cylindrical coordinates

TODO

VERIFY THOSE! minus signs ?

$$\mathbf{v}_r = \frac{1}{r} \frac{\partial \Phi}{\partial \theta}$$

$$\mathbf{v}_\theta = -\frac{\partial \Phi}{\partial r}$$

### 8.35 Corner flow

The mantle wedge comprised between the downgoing slab and the overriding plate has been extensively studied since very important geodynamical processes take place in it or right above it (slab dehydration and water transport, melting, over-riding plate deformation, vulcanism, ...).

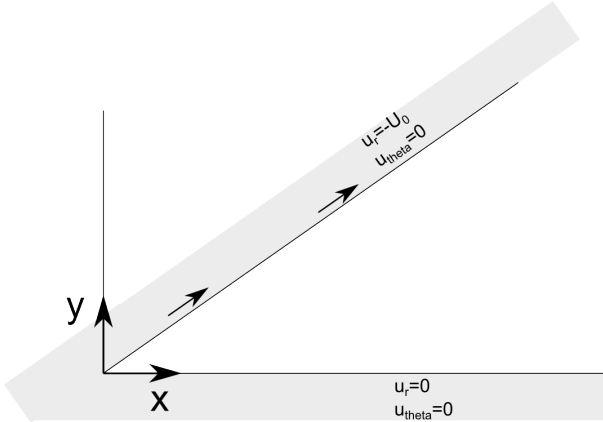
To first approximation one can approach the problem and simplify it greatly by assuming that both plates kinematic behaviour are independent of what happens in the wedge, that the wedge geometry does not change over time, that the problem is essentially 2D, and that the mantle extends very far away from the actual wedge (plates are infinite).

Under such assumptions, it is possible to derive an analytical solution for incompressible Stokes flow in the wedge as documented at p. 224 in Batchelor [99].

Literature: [2562]

FIND refs. check new version of Vol7 theoretical geophys

A corner flow setup is shown hereunder:



The solution to this problem is arrived at by means of the stream function  $\Phi$ , defined as  $u = -\partial\Phi/\partial y$  and  $v = \partial\Phi/\partial x$ , so that we automatically have  $\vec{\nabla} \cdot \vec{v} = 0$ . As shown in Section 8.34, the stream function  $\Phi$  is then the solution to the biharmonic equation

$$\vec{\nabla}^2 \vec{\nabla}^2 \Phi = \vec{\nabla}^4 \Phi = 0$$

Considering the geometry of the problem has plates of infinite extent with constant relative velocity, the solution for velocity everywhere is expected to be independent of  $r$ . This means the equation is separable and we will use a solution of the form

$$\Phi(r, \theta) = R(r)f(\theta)$$

However, given the infinite extent of the domain, the velocity is expected to be independent of  $r$ , so we postulate  $R(r) = r$  (look at the relationship between velocity components and stream function), or:

$$\Phi(r, \theta) = rf(\theta)$$

and we then have to solve

$$\Delta \left( \frac{1}{r}(f + f'') \right) = \frac{1}{r^3}(f + 2f'' + f''') = 0.$$

The solution of this equation for  $f$  is:

$$\begin{aligned} f(\theta) &= A \sin \theta + B \cos \theta + C \theta \sin \theta + D \theta \cos \theta \\ f'(\theta) &= A \cos \theta - B \sin \theta + C(\sin \theta + \theta \cos \theta) + D(\cos \theta - \theta \sin \theta) \end{aligned}$$

with

$$\begin{aligned} v_r &= \frac{1}{r} \frac{\partial \Phi}{\partial \theta} = f'(\theta) \\ v_\theta &= -\frac{\partial \Phi}{\partial r} = -f(\theta) \end{aligned}$$

$A, B, C$  and  $D$  are four constants to be determined by means of the boundary conditions which are as follows:

$$\begin{aligned}\mathbf{v}_r(\theta = 0) &= 0 \\ \mathbf{v}_\theta(\theta = 0) &= 0 \\ \mathbf{v}_r(\theta = \theta_0) &= -U_0 \\ \mathbf{v}_\theta(\theta = \theta_0) &= 0\end{aligned}$$

or,

$$f'(0) = A + D = 0 \quad (793)$$

$$f(0) = B = 0 \quad (794)$$

$$f'(\theta_0) = -U_0 \quad (795)$$

$$f(\theta_0) = 0 \quad (796)$$

From the second equation it is trivial to see that  $B = 0$ , so that:

$$f(\theta) = A \sin \theta + C\theta \sin \theta + D\theta \cos \theta$$

$$f'(\theta) = A \cos \theta + C(\sin \theta + \theta \cos \theta) + D(\cos \theta - \theta \sin \theta)$$

From the first one we obtain  $D = -A$  so that

$$f(\theta) = A(\sin \theta - \theta \cos \theta) + C\theta \sin \theta$$

$$f'(\theta) = A(\theta \sin \theta) + C(\sin \theta + \theta \cos \theta)$$

The last two boundary conditions yield:

$$0 = A(\sin \theta_0 - \theta_0 \cos \theta_0) + C\theta_0 \sin \theta_0$$

$$-U_0 = A(\theta_0 \sin \theta_0) + C(\sin \theta_0 + \theta_0 \cos \theta_0)$$

or,

$$A = -U_0 \frac{\theta_0 \sin \theta_0}{\theta_0^2 - \sin^2 \theta_0} \quad C = U_0 \frac{\sin \theta_0 - \theta_0 \cos \theta_0}{\theta_0^2 - \sin^2 \theta_0}$$

Finally:

$$(A, B, C, D) = (-\theta_0 \sin \theta_0, 0, \sin \theta_0 - \theta_0 \cos \theta_0, \theta_0 \sin \theta_0) \frac{U_0}{\theta_0^2 - \sin^2 \theta_0}$$

We have

$$\mathbf{e}_r = \cos \theta \mathbf{e}_x + \sin \theta \mathbf{e}_y \quad (797)$$

$$\mathbf{e}_\theta = -\sin \theta \mathbf{e}_x + \cos \theta \mathbf{e}_y \quad (798)$$

so that the velocity field can be expressed in cartesian coordinates:

$$\begin{aligned}\mathbf{v} &= \mathbf{v}_r \mathbf{e}_r + \mathbf{v}_\theta \mathbf{e}_\theta \\ &= \mathbf{v}_r (\cos \theta \mathbf{u}_x + \sin \theta \mathbf{u}_y) + \mathbf{v}_\theta (-\sin \theta \mathbf{u}_x + \cos \theta \mathbf{u}_y) \\ &= (\mathbf{v}_r \cos \theta - \mathbf{v}_\theta \sin \theta) \mathbf{e}_x + (\mathbf{v}_r \sin \theta + \mathbf{v}_\theta \cos \theta) \mathbf{e}_y\end{aligned} \quad (799)$$

## 8.36 Surface processes

### 8.36.1 In 1D - simple nonlinear diffusion a la [365]

The tectonic-scale transport equations describe long term changes in topography  $h(x, y, t)$  as a result of simultaneous short- and long-range mass transport processes [118, 1480].

The short-range surface processes are represented by cumulative effects of hillslope processes (soil creep, rainsplash, slides) that remove material from uplifted areas down to the valleys. It is then assumed that the horizontal material flux  $\vec{q}_s$  is related to local slope  $\vec{\nabla}h$  by  $\vec{q}_s = -K_s \vec{\nabla}h$  where  $K_s$  is the effective diffusivity. Assumption of conservation of mass volume leads to the linear diffusion equation for erosion:

$$\frac{\partial h}{\partial t} = K_s \Delta h$$

This equation can be solved with constant-elevation (fixed  $h$  value) boundary conditions simulating local base levels of erosion.

Note that in practice the coefficient  $K_s$  might depend on slope and curvature, i.e.

$$\frac{\partial h}{\partial t} = K_s(x, y, h, \vec{\nabla}h) \Delta h$$

Following [1032], Burov & Cloetingh use an empirical non linear expression  $K_s = k_s(x)(\vec{\nabla}h)^n$ .

### 8.36.2 In 1D - not so simple, a la [42]

The change in surface elevation rate due to surface processes is equal to the divergence of the sediment flux (assuming there is no density difference between the bedrock and sediment and ignoring the effects of compaction):

$$\frac{\partial h}{\partial t} = -\frac{\partial q_s}{\partial x}$$

where  $h$  is the topography,  $t$  is the time,  $q_s$  represents the sediment flux, and  $x$  is the horizontal coordinate.

The next step consists in a formulation for the sediment flux. Still following [42], in the subaerial environment, it is possible to define the sediment transport flux  $q_s$  in terms of the water flux  $q_w$  as

$$q_s = -(K + cq_w^n) \frac{\partial h}{\partial x}$$

where  $K$  is the slope diffusivity,  $c$  is the transport coefficient, and  $n \geq 1$  is the power law that defines the type of relationship between the sediment transport and the water flux (Simpson & Schlunegger, 2003; Smith & Bretherton, 1972).

[get these papers](#)

This model accounts for hillslope diffusion processes where the topography will tend to a dispersive diffusion (Culling, 1960) and fluvial transport processes that result in concentrative diffusion due to water run off (Graf, 1984). For a simple parameterization we choose a linear relationship between sediment transport and water flux ( $n = 1$ ).

The water flux can be related to the water discharge/effective rainfall  $\alpha$  as

$$\frac{\partial}{\partial x}(\vec{n}q_w) = -\alpha$$

where  $\vec{n}$  is a unit vector directed down the surface gradient (Smith & Bretherton, 1972). By assuming a constant  $\alpha$  and integrating equation (12) over the surface in the downstream direction, we obtain

$$q_w = \alpha x_d$$

where  $x_d$  is the downstream distance from the drainage divide. By substituting equations (11) and (13) into (10) we obtain the 1-D sediment mass conservation equation for combined hillslope and discharge-dependent fluvial transport

$$\frac{\partial h}{\partial t} = \frac{\partial}{\partial x} \left( (K + k\alpha x_d) \frac{\partial h}{\partial x} \right)$$

where the downstream distance  $x_d$  is calculated at each time step as the distance from the topographic highs to the valley floors. Because  $q_w$  is dependent on the length of the drainage, the model mimics 1-D landscapes similar to river profiles in which fluvial processes are dominant.

### 8.37 Geometric multigrid

The following is mostly borrowed from the Wikipedia page on multigrid methods<sup>67</sup>.

There are many types of (geometric) multigrid algorithms, but the common features are that a hierarchy of grids is considered. The important steps are:

- *Smoothing*: reducing high frequency errors, for example using a few iterations of the Gauss-Seidel method.
- *Residual Computation*: computing residual error after the smoothing operation(s).
- *Restriction*: downsampling the residual error to a coarser grid.
- *Interpolation or prolongation*: interpolating a correction computed on a coarser grid into a finer grid.
- *Correction*: Adding prolonged coarser grid solution onto the finer grid.

There are many choices of multigrid methods with varying trade-offs between speed of solving a single iteration and the rate of convergence with said iteration. The 3 main types are V-Cycle, F-Cycle, and W-Cycle.

Any geometric multigrid cycle iteration is performed on a hierarchy of grids and hence it can be coded using recursion. Since the function calls itself with smaller sized (coarser) parameters, the coarsest grid is where the recursion stops.

Note that the ratio of the number of nodes between two consecutive levels has to be constant between all the levels. Often powers of 2 are used (especially if the grids are based on quad/octrees) but it is not a requirement.

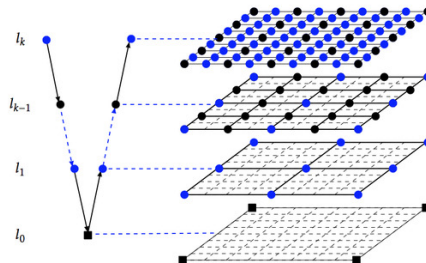


Image from <http://web.utk.edu/~wfeng1/research.html>

What follows is a pseudo-code example of a recursive V-Cycle Multigrid for solving the Poisson equation ( $\nabla^2\phi = f$ ) on a uniform grid of spacing  $h$ :

```
function phi = V_Cycle(phi,f,h)
% Pre-Smoothing
phi = smoothing(phi,f,h);
% Compute Residual Errors
r = residual(phi,f,h);
% Restriction
rhs = restriction(r);
eps = zeros(size(rhs));
% stop recursion at smallest grid size
if smallest_grid_size_is_achieved
    eps = smoothing(eps,rhs,2*h);
else
    eps = V_Cycle(eps,rhs,2*h);
end
% Prolongation and Correction
```

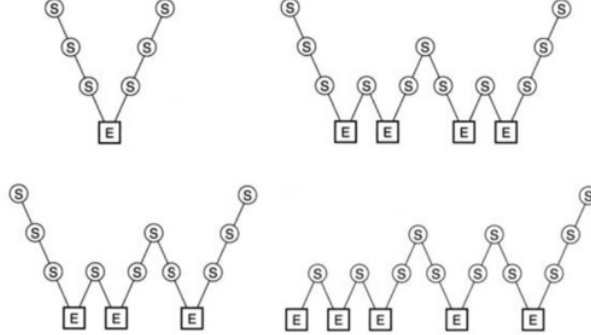
<sup>67</sup>[https://en.wikipedia.org/wiki/Multigrid\\_method](https://en.wikipedia.org/wiki/Multigrid_method)

```

phi = phi + prolongation(eps);
% Post-Smoothing
phi = smoothing(phi,f,h);
end

```

A multigrid method with an intentionally reduced tolerance can be used as an efficient preconditioner for an external iterative solver. The solution may still be obtained in  $\mathcal{O}(N)$  time as well as in the case where the multigrid method is used as a solver. Multigrid preconditioning is used in practice even for linear systems, typically with one cycle per iteration.



Taken from [1294]: Different types of multigrid cycle with four grid levels: (top left) V-cycle, (top right) W-cycle, (bottom left) F-cycle and (bottom right) full multigrid. S denotes smoothing while E denotes exact coarse-grid solution.

Check Kaus BEcker syllabus!

Relevant Literature: [2036, 1631, 1294, 953, 1743, 1657, 2569, 1868, 2843, 2774, 2517, 2845, 507] Book [290]

### 8.38 Algebraic multigrid



Relevant Literature: [1923][1956]

### 8.39 Computing depth

In the case of a perfectly rectangular, cylindrical or spherical domain, computing the depth of any given point inside the domain is trivial. However, when the free surface becomes somewhat distorted, the concept of depth needs to be refined. What follows is an attempt at bringing clarity as to how to compute depth in all cases.

The depth  $d(\mathbf{r})$  satisfies the equation:

$$\frac{\mathbf{g}}{|\mathbf{g}|} \cdot \nabla d = 1$$

with  $d = 0$  at the surface.

This is a form of steady-state advection equation (the time derivative is zero, there is no diffusion, nor any source term).

Given the boundary conditions, one could solve this equation over the whole domain.

Note that in the case of a cartesian box,  $\mathbf{g} = -g\mathbf{u}_z$ , we need to solve

$$-\frac{\partial}{\partial z} d = 1$$

For a flat top surface at  $d(z = L_z) = 0$  so that in the end

$$d(z) = L_z - z$$

## 8.40 Imposing boundary conditions

Let us consider a quadrilateral element with one degree of freedom per node and let us assume that we are solving the temperature equation. The local matrix and right-hand side vector are given by

$$A_{el}(4 \times 4) \quad \text{and} \quad B_{el}(4)$$

Let us assume that we want to impose  $\tilde{T} = 10$  on the third node (local coordinates numbering). For instance, having built  $A_{el}$  and  $B_{el}$ , the system looks like :

$$\begin{pmatrix} 3 & 1 & 6 & 9 \\ 5 & 2 & 2 & 8 \\ 7 & 4 & 11 & 2 \\ 9 & 6 & 4 & 3 \end{pmatrix} \begin{pmatrix} T_1 \\ T_2 \\ T_3 \\ T_4 \end{pmatrix} = \begin{pmatrix} 4 \\ 3 \\ 1 \\ 2 \end{pmatrix}$$

which can be rewritten

$$3T_1 + T_2 + 6T_3 + 9T_4 = 4$$

$$5T_1 + 2T_2 + 2T_3 + 8T_4 = 3$$

$$7T_1 + 4T_2 + 11T_3 + 2T_4 = 1$$

$$9T_1 + 6T_2 + 4T_3 + 3T_4 = 2$$

or,

$$3T_1 + T_2 + +9T_4 = 4 - 6T_3$$

$$5T_1 + 2T_2 + +8T_4 = 3 - 2T_3$$

$$7T_1 + 4T_2 + 11T_3 + 2T_4 = 1$$

$$9T_1 + 6T_2 + +3T_4 = 2 - 4T_3$$

- Technique 1: Replace the hereabove system by

$$\begin{pmatrix} 3 & 1 & 6 & 9 \\ 5 & 2 & 2 & 8 \\ 7 & 4 & 11 + 10^{12} & 2 \\ 9 & 6 & 4 & 3 \end{pmatrix} \begin{pmatrix} T_1 \\ T_2 \\ T_3 \\ T_4 \end{pmatrix} = \begin{pmatrix} 4 \\ 3 \\ \tilde{T} \times (11 + 10^{12}) \\ 2 \end{pmatrix}$$

- Technique 2: One can choose not to solve for  $T_3$  anymore, i.e. not to consider it as a degree of freedom and therefore write:

$$3T_1 + T_2 + 9T_4 = 4 - 6T_3$$

$$5T_1 + 2T_2 + 8T_4 = 3 - 2T_3$$

$$9T_1 + 6T_2 + 3T_4 = 2 - 4T_3$$

- Technique 3: Since we want to impose  $T_3 = 10$ , then we can write

$$3T_1 + T_2 + +9T_4 = 4 - 6T_3$$

$$5T_1 + 2T_2 + +8T_4 = 3 - 2T_3$$

$$0 + 0 + T_3 + 0 = 10$$

$$9T_1 + 6T_2 + +3T_4 = 2 - 4T_3$$

and in matrix form :

$$\begin{pmatrix} 3 & 1 & 0 & 9 \\ 5 & 2 & 0 & 8 \\ 0 & 0 & 1 & 0 \\ 9 & 6 & 0 & 3 \end{pmatrix} \begin{pmatrix} T_1 \\ T_2 \\ T_3 \\ T_4 \end{pmatrix} = \begin{pmatrix} 4 - A_{13}T_3 \\ 3 - A_{23}T_3 \\ 10 \\ 2 - A_{43}T_3 \end{pmatrix}$$

The first technique is not a good idea in practice as it introduces very large values and will likely derail the solver. The second option is somewhat difficult to implement as it means that elemental matrix and rhs sizes will change from element to element and it therefore requires more book-keeping. The third technique is the one adopted throughout this document.

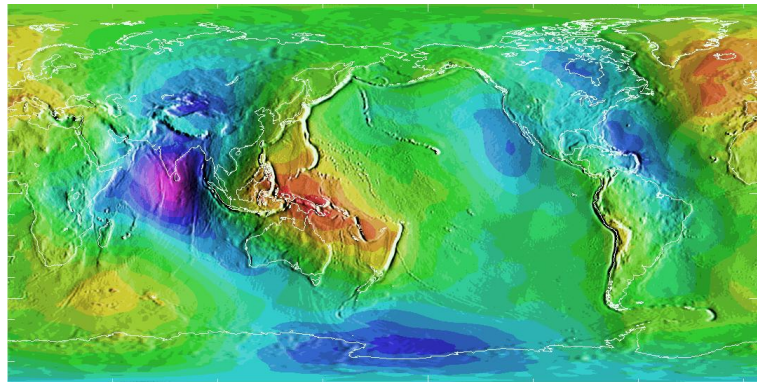
As shown in [2815], it is better to replace the 1 on the diagonal by the former diagonal term as it reduces the condition number of the matrix. The rhs must then be modified accordingly.

## 8.41 The Geoid

### 8.41.1 What is the geoid?

The geoid is usually defined in two ways:

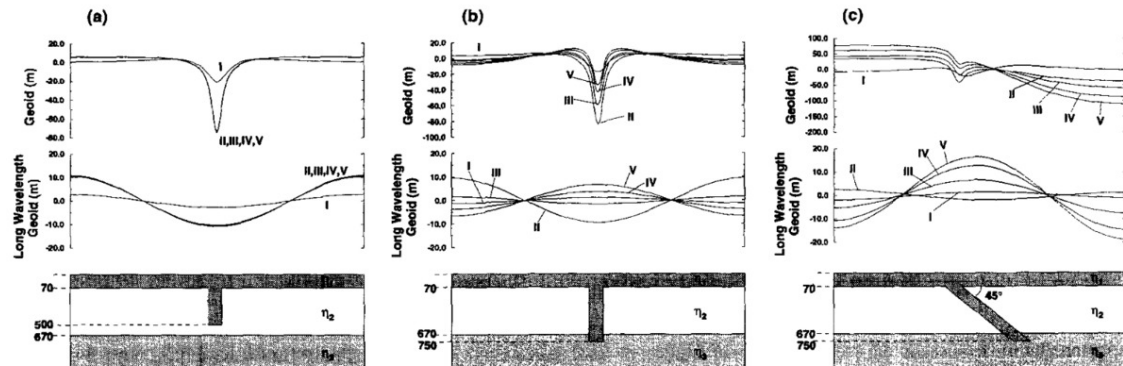
- Mean sea level (easy to define in the oceans, but harder on land)
- A gravitational equipotential surface. This means that everywhere at sea level experiences the same value of gravity potential, so there is no tendency for water to flow downhill since all points in the vicinity have the same value of gravity potential, pointed toward the center of the earth.



Data Max value: 85.4 meters, east of New Guinea. Data Min value:-107.0 meters, south of India. This image shows 15'x15' geoid undulations covering the planet Earth from the NIMA/GSFC WGS-84 EGM96 15' Geoid Height File. The undulations refer to the differences from the WGS-84(G873) reference ellipsoid. Map and description from National Geodetic Survey.

### 8.41.2 How to compute it?

### 8.41.3 Interesting modelling



Idealized 2D slab calculations for each viscosity model: geoid and geoid filtered to pass only the longest wavelengths ( $\sim 4000$  km). (a) Cold slab extends to 500 km depth in the upper mantle, (b) Slab extends to 750 km so that it is partly supported by the high viscosity lower mantle at 670 km. (c) Slab tilted at  $45^\circ$  to the vertical extending to the top of the lower mantle. Taken from [1843]

## 8.42 The Lyapunov time/exponent, mixing stirring

Simply put, the Lyapunov time is the characteristic timescale on which a dynamical system is chaotic. It is defined as the inverse of a system's largest Lyapunov exponent.

The Lyapunov time mirrors the limits of the predictability of the system. By convention, it is defined as the time for the distance between nearby trajectories of the system to increase by a factor of  $e$ . However, measures in terms of 2-foldings and 10-foldings are sometimes found, since they correspond to the loss of one bit of information or one digit of precision respectively.

The Lyapunov exponent or Lyapunov characteristic exponent of a dynamical system is a quantity that characterizes the rate of separation of infinitesimally close trajectories. Quantitatively, two trajectories in phase space with initial separation  $\delta\mathbf{Z}_0$  diverge (provided that the divergence can be treated within the linearized approximation) at a rate given by

$$|\delta\mathbf{Z}(t)| \approx e^{\lambda t} |\delta\mathbf{Z}_0|$$

where  $\lambda$  is the Lyapunov exponent.

Measuring the Lyapunov exponent or time (or related quantities) is relevant in the context of mantle stirring. On the one hand it is argued that the mantle is convecting and very efficient at mixing resulting in a somewhat homogenous composition. On the other hand, there are modeling studies that suggest that whole-mantle convection can preserve heterogeneity in the presence of well-mixed mantle.

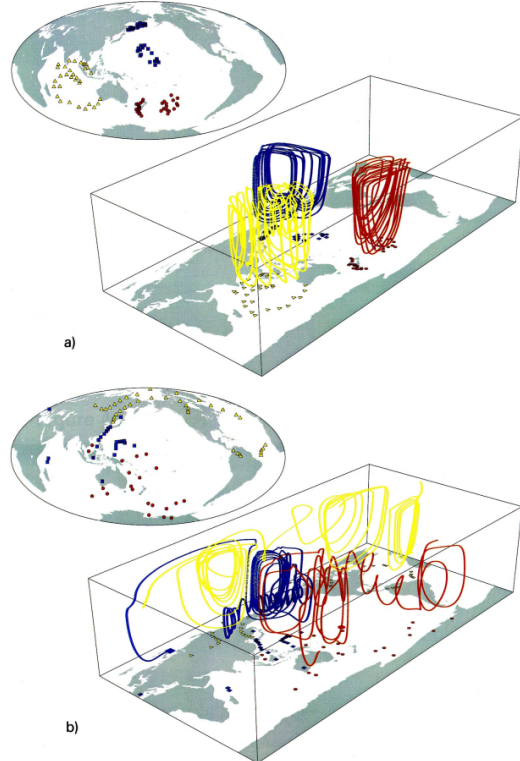
Mixing takes place by the repeated stretching and folding of interfaces. A measure of the mixing efficiency is the time evolution of the area of the mixing surface. Maximum efficiency of mixing is reached with turbulent mixing behavior where one can formally show whether mixing is laminar or turbulent by evaluating the Luyaponov exponents  $\sigma$ . These are of the form:

$$\sigma = \lim_{t \rightarrow \infty} \lim_{X \rightarrow 0} \left[ \frac{1}{t} \ln \left( \frac{X(t)}{X(t=0)} \right) \right]$$

where  $X(t)$  is the length of this segment at time  $t$ . Non-zero Luyaponov exponents indicate that stretching is exponential and the larger the exponent, the more efficient mixing is. However, the limits in the above equation are difficult to evaluate and the interpretation of the 'finite-time' Luyaponov exponent, where both limits are truncated, is difficult to formalize.

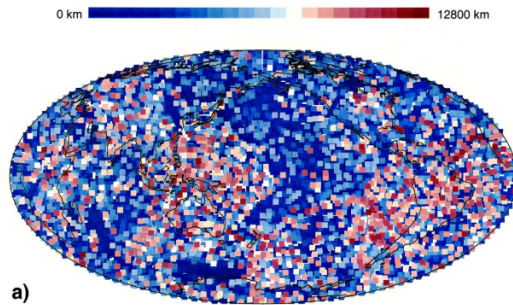
Two approaches are taken in the literature when it comes to studying mixing/stirring and/or measuring Lyapunov quantities::

- using marker advection: in van Keken and Zhong [2652] the authors use a steady state velocity pattern obtained for a model of present-day mantle convection. The velocity model is based on the solution of the Stokes equations in a 3D spherical model with variable rheology. To study mixing, they release particles in the velocity model and follow these by numerical integration.



a) The three particles in this plot were selected for their relatively regular pattern. b) Three other particles that traverse a large portion of the model. These particles feel the strong toroidal motion and their paths form corkscrew-like patterns. They indicate that certain parts of the model can exhibit strong mixing. Taken from [2652].

Rather than calculating the exponents explicitly, the authors use an approximation to the finite-time, finite-length Luyapponov exponent by evaluating the distance between two points that are closely spaced at time  $t = 0$ . For this they compute the advection of a large number of 10 km long line segments that were originally at 1500 km depth. The length of these segments is approximated by the distance between the endpoints and the results are summarized in the following figure:



Length of the line segment after 4 billion years. Approximately 14,000 line segments were released with regular spacing at 1500 km depth. The length of the segment is indicated by the colored symbols that are plotted at the initial position. The results indicate that there is a strong diversity in mixing behavior. In some regions (north Pacific, parts under the Indian/Australian plate) stretching is very limited, indicating laminar and consequently inefficient mixing. Regions that are under strong toroidal surface motion (western Pacific, Nazca and South America) show very efficient stretching of up to the maximum length of the diameter of the Earth. Taken from [2652].

- twin experiments [143]

Talk about configurational entropy [1024, 1915].

Relevant Literature[2652, 820, 821, 2227, 2233, 143]

## 8.43 Phase transitions

The topic of phase transitions and their implementation in computational geodynamics is a very vast topic. It requires input from thermodynamics, geochemistry and petrology, and also requires dedicated algorithms which are quite complex.

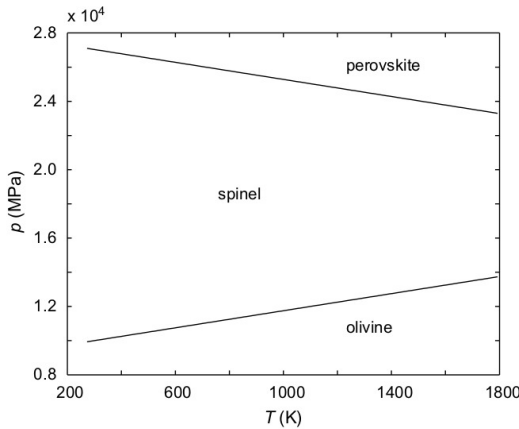
Let us start with simple examples from the literature:

- Zlotnik et al, 2007 [2946]. The equations used in this work are the standard incompressible Stokes equations by the authors chose to represent the density as a function of temperature and pressure by the following expression:

$$\rho(T, p) = \rho_0[1 - \alpha(T - T_0)][1 + \beta(p - p_0)]$$

where  $\alpha$  and  $\beta$  are, respectively, the thermal expansion and compressibility coefficients, and  $T_0$  and  $p_0$  are reference values at surface.

The authors then proceed to divide the phase diagram into three regions corresponding to three minerals: olivine, spinel-structured olivine, and perovskite:



Phase diagram indicating stable mineral phases in the temperature-pressure plane. The phase diagram is divided into three regions corresponding to three distinct minerals: olivine, spinel and perovskite. Taken from [2946].

They state that two major mineralogical phase transitions occur, one at 410 km depth and other at 660 km depth (other deeper transitions run outside the domain under study because their domain is 1000km deep). The density increases discontinuously across these phase transitions. In order to take into account the effect of these discontinuities, the density  $\rho_0$  above is taken as a reference density plus an increment  $\Delta\rho$ :

$$\rho_0 = \rho_{\text{olivine}} + \Delta\rho$$

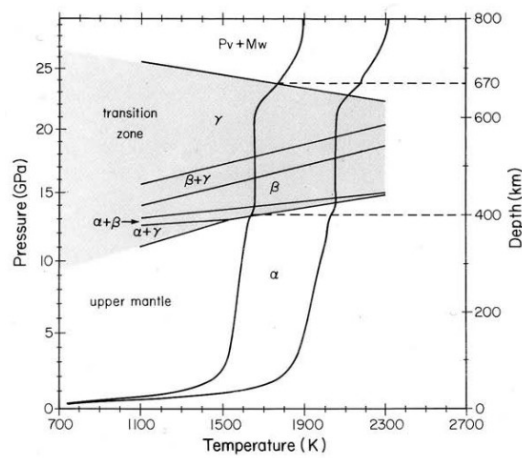
where

$$\Delta\rho = \begin{cases} 0 & \text{if } (T, p) \text{ is in the olivine region} \\ \Delta\rho_{es} & \text{if } (T, p) \text{ is in the spinel region} \\ \Delta\rho_{per} & \text{if } (T, p) \text{ is in the perovskite region} \end{cases}$$

The authors unfortunately fail to report how the phase transitions affect the viscosity.

The obvious problem with this otherwise simple approach is that density varies in the domain but is not accompanied by a volume change so that it violates mass conservation.

- the following phase diagram is taken from Peltier et al (1997) [2004].



Phase boundary for the  $\alpha \rightarrow \beta \rightarrow \gamma$  transitions of Olivine

## 9 Geodynamics GEO3-1313 - Utrecht University

What follows was written by Arie van den Berg and was used as the syllabus for the 3rd year geodynamics course at Utrecht University. It is reproduced with Arie's permission and has been slightly modified by me.

### 9.1 Introduction

The internal constitution of the Earth has been investigated systematically from the nineteenth century on. With the advent of seismological instrumentation for the registration of tele-seismic events, by the end of that century, the main tool for obtaining direct information about distribution of the material properties controlling seismic wave propagation became available. Before this, mainly global properties could be determined from gravity and magnetic field observations, astronomical data and indications about the heatflow from the Earth's interior. As a result of the early seismological investigations the main internal structure of the Earth was revealed within the first few decades of the twentieth century with the discovery of the earth's core in 1906 by Oldham and Gutenberg (1912) and the solid inner core in 1936 by Lehmann.

From the radial distribution of the seismic velocity profile, obtained by processing the tables of traveltimes versus epicentral distance, Williamson and Adams (1923) [2795] made a first estimate of the density profile for a compressible homogeneous mantle model, consistent with the total mass of the Earth and obtained at the same time strong indication for a high density core, compositionally distinct from the mantle. They concluded that "It is therefore impossible to explain the high density of the Earth on the basis of compression alone. The dense interior cannot consist of ordinary rocks compressed to a small volume; we must therefore fall back on the only reasonable alternative, namely, the presence of a heavier material, presumably some metal, which, to judge from its abundance in the Earth's crust, in meteorites and in the Sun, is probably iron."

Bullen<sup>68</sup> (1975) [341] further refined the analysis and showed the assumption of a homogeneous mantle to be inconsistent with the known moment of inertia of the Earth. In the 1940s and 1950s he introduced a global division of the Earth in concentric shells, labelled A through G, ranging from the Earth's crust (A), bounded by the moho discontinuity, to the inner core (G). Region C between, roughly 400km and 900km, characterized by rapid increase of the seismic velocities, was identified by Bullen as a transition region between the upper mantle region B and a homogeneous lower mantle, region D. The deduced inhomogeneity of the mantle was projected by Bullen in this C region. E through G were used to label subdivisions of the core. Region E indicated the liquid, adiabatic outer core, F a transition region between inner and outer core and G the solid inner core. Birch (1952) [199] published improved equations of state, based on finite-strain theory, thereby giving a more firm physical basis to interpretation of available data in terms of a compressible medium.

In the second half of the twentieth century the resolution and accuracy of the models were further improved using continuously improved seismological observations and a growing data set. It also became possible to obtain independent information about the radial density distribution from spectral analysis of radial eigen-vibrations of the Earth after very large earthquakes. This development resulted in the publication of the Preliminary Reference Earth Model (PREM) by Dziewonski and Anderson (1981) [751] which still serves as a global reference.

The improved seismological models indicated that the continuous rapid velocity increase in the transition zone (C) was actually a succession of several abrupt changes, confirming radial inhomogeneity in mineral phase and possibly in chemical composition of the mantle.

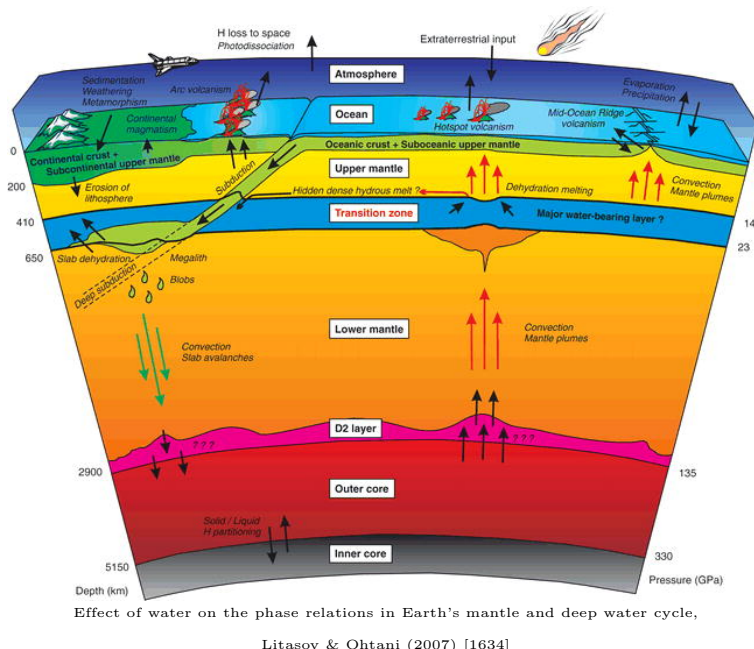
From geological and cosmochemical arguments a probable composition of the Earth had been derived consisting of a mantle with major element composition dominated by magnesium-iron silicates and an iron-nickel core with a small amount of lighter elements mixed in, most likely including mainly sulphur. In the 1960s this resulted in the definition of a so-called pyrolytic composition of the mantle by Ringwood which could explain the main mantle petrological observations regarding the complementary nature of basalts and ultra mafic mantle rocks found in ophiolites, kimberlites and mantle peridotite bodies (Ringwood, 1975 [2161]).

<sup>68</sup>Keith Edward Bullen (29 June 1906 – 23 September 1976) was a New Zealand-born mathematician and geophysicist. He is noted for his seismological interpretation of the deep structure of the Earth's mantle and core.

In experimental high-pressure and temperature work on the candidate mantle materials a series of phase transitions were found at pressure and temperature values relevant for the Earth's mantle which could be related to the seismic discontinuities revealed by the seismological data. From these the most prominent at approximately 410 and 660 km depth were identified as the phase transition of the olivine component  $(\text{Mg}, \text{Fe})_2\text{SiO}_4$  of the pyrolytic mantle to a denser wadsleyite crystal structure and, at 660 km, a transition (dissociation) from a  $\gamma$ -spinel (known as ringwoodite) structure to a two-phase assemblage, post-spinel, i.e. magnesium-iron perovskite,  $(\text{Mg}, \text{Fe})\text{SiO}_3$  and wüstite  $(\text{Mg}, \text{Fe})\text{O}$ .

It was also found that the 660 km boundary corresponds to an endothermic phase transition which would have implications for large scale circulation in the mantle, leading to long-standing speculations about the degree of layering in mantle convection (Christensen & Yuen (1985) [488] Albarede & van der Hilst (2002) [14]), <http://www.mantleplumes.org>.

A more recent development in this area is the discovery of a new phase transition of magnesium-perovskite to a denser form for pressure temperature conditions, approximately 125 GPa 2500 K, relevant for the D'' layer close to the core-mantle boundary (Lay et al., 2005, van der Hilst et al., 2007).



In the following sections the density distribution in the Earth's interior is treated in relation to the gravity field and internal pressure distribution of a self-gravitating compressible planet model and the link is shown with results from theoretical mineral physics and high pressure-temperature experimental data for mantle materials.

## 9.2 Global internal structure and temperature of the Earth

To understand the Earth's internal dynamics and evolution we need to know its internal structure and material properties. What do we know about Earth's global internal structure?

For a substance of given chemical composition, the material properties are determined by temperature and pressure. A full understanding of the Earth's internal dynamics therefore requires that we know the internal distribution of composition, temperature and pressure as illustrated in the following figure:

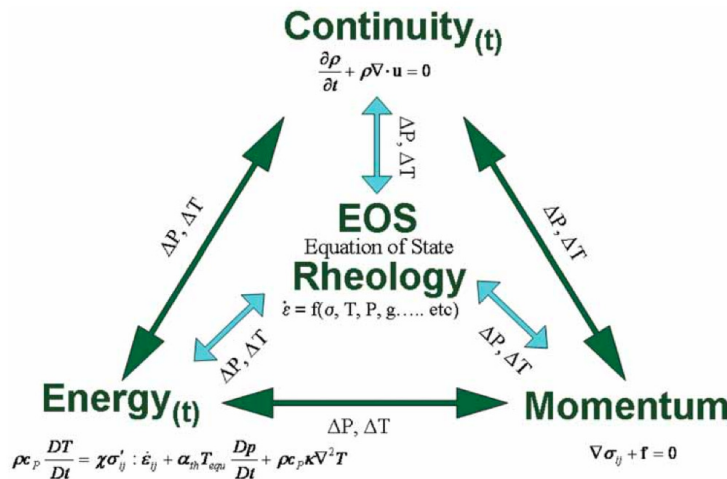
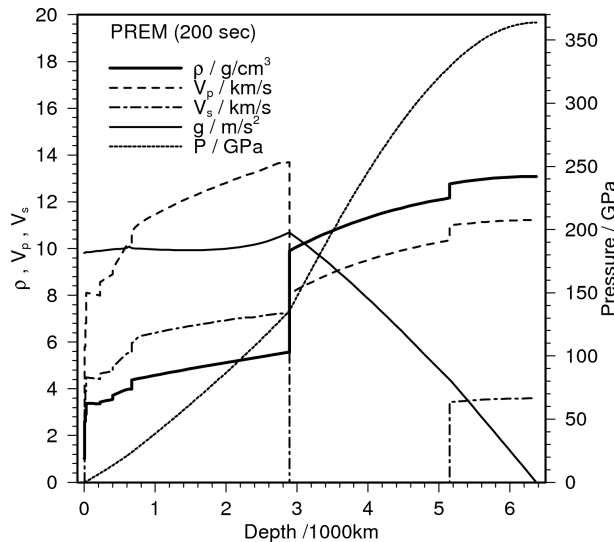


Illustration of the central roles that pressure, temperature and density play in geophysics. Taken from Regenauer-Lieb et al., Phil. Mag., 2006 [2129].

The internal pressure distribution is directly linked with the Earth's own internal gravity field and density distribution because the local pressure gradient equals the local gravity acceleration times the density (see problem 6). In section 9.2.3 density, gravity and pressure are treated together in a consistent way.

If the internal pressure distribution is known we can relate sharp transitions in the physical parameters as shown in the PREM model, illustrated in the following figure to phase transitions, solid-solid or solid-liquid, in the Earth's deep interior.



Radial (depth)distribution of density  $\rho$ , seismic velocities  $v_p$  and  $v_s$ , gravity acceleration  $g$  and pressure  $P$   
in the PREM model (Dziewonski and Anderson (1981) [751]).

Phase transitions in 'candidate' materials for the Earth's interior are investigated under high pressure and temperature conditions in HPT laboratory experiments<sup>69</sup>. Using theoretical mineral physics models the complete mineral phase diagram of mantle silicates can, in principle, be constructed from a limited set of experimental data (Stixrude & Lithgow-Bertelloni (2005) [2439, 2438] Jacobs & de Jong (2007) [1308]). To constrain the possible candidate materials we also need to know the internal distribution of the Earth's chemical composition. Such composition models are derived from geological evidence and cosmochemical considerations.

<sup>69</sup> Deep Earth pressure and temperature conditions can be produced in a Diamond Anvil Cell (DAC), see [http://en.wikipedia.org/wiki/Diamond\\_anvil\\_cell](http://en.wikipedia.org/wiki/Diamond_anvil_cell).

### 9.2.1 Early models of the Earth's density

The total Earth mass  $M_{\oplus}$  and average density  $\langle \rho \rangle$  were not known before independent measurement of Newton's gravitational constant by Cavendish, (see section 9.2.3). When the average density had been determined as approximately  $5.5 \cdot 10^3 \text{ kg} \cdot \text{m}^{-3}$  it became clear, from the lower density of surface rocks of around  $2.7 \cdot 10^3 \text{ kg} \cdot \text{m}^{-3}$ , that the Earth's interior must consist of higher density material.

Besides the mass or average density the (average) moment of inertia  $I$  (defined in section 9.2.2) provides a constraint on the radial distribution of density.

These two integral parameter values have been applied in several two-parameter models for the radial density distribution of the Earth. At the end of the nineteenth century Wiechert<sup>70</sup> assumed that the compressibility of Earth materials would be negligible to first approximation and that Earth's high mean density was due to a dense, probably metallic, core. He assumed an iron core based on astronomical evidence of high iron content of the sun's outer layers (see also section 9.2.9).

Wiechert considered in particular layered spherically symmetric models consisting of two uniform layers, core and mantle. Since the radius of the Earth's core had not yet been determined by seismology, Wiechert used the core radius  $R_c$  and density  $\rho_c$  as unknown parameters to be determined from the known data. Wiechert assumed the density of the mantle to be  $\rho_m = 3.2 \cdot 10^3 \text{ kg} \cdot \text{m}^{-3}$  and using known values for  $M$  and  $I$  he derived for the radius of the core  $R_c/R = 0.779$  corresponding to a mantle depth of about 1400 km and a core density  $\rho_c = 8.2 \cdot 10^3 \text{ kg} \cdot \text{m}^{-3}$ . This model is investigated in problem 3.

Later, after  $R_c/R = 0.545$  had been determined using seismic data, Jeffreys substituted the known value of the core radius and derived for the mantle and core densities  $\rho_c = 12.6 \cdot 10^3 \text{ kg} \cdot \text{m}^{-3}$  and  $\rho_m = 4.14 \cdot 10^3 \text{ kg} \cdot \text{m}^{-3}$  (Bullen (1975) [341]). This model is investigated in problem 4.

The (radially averaged) density distribution in the Earth remains a topic of research [1424].

### 9.2.2 The moment of inertia of a spherically symmetric density distribution

The moment of inertia  $I$  of a point mass of mass  $m$ , with respect to a given rotation axis is defined as  $I = md^2$  where  $d$  is the distance from the point mass to the axis. This quantity relates the angular velocity  $\omega$ , about the rotation axis, to the angular momentum  $J$ , of the point mass, in  $J = I\omega$ . This is an analogous relation as the one between the linear momentum  $p$  and the linear velocity  $v$ ,  $p = mv$ . For an extended mass distribution in a volume  $V$ , a moment of inertia tensor,  $I_{ij}$ , relating the angular momentum vector  $\mathbf{J}$  to the rotation vector  $\boldsymbol{\Omega}$  can be defined as  $J_i = I_{ij}\Omega_j$ , where the summation convention for repeated indices is implied. This tensor is described by a  $3 \times 3$  matrix defined by volume integration over point masses in the volume. Here we only consider spherically symmetric mass distributions where the moment tensor is isotropic,  $I_{ij} = I\delta_{ij}$ , with scalar coefficient  $I$ .<sup>71</sup> In simple terms, the moment of inertia is the same for any rotation axis through the centre of the spherically symmetric body.

The moment of inertia  $I$  can be determined from Earth's global gravity field and the precession rate of the rotation axis determined from astronomical data, see Bullen, *The Earth's density*, 1975.

For a *spherically symmetric* body of finite volume, the scalar moment of inertia is defined as a volume integral over point masses,  $I = \int_V \rho d^2 dV$ . It is often expressed in terms of the total mass  $M$ , the outer radius  $R$  and a prefactor  $f$  as,

$$I = fMR^2 \quad (800)$$

We have seen that the planetary mass and surface density were used to constrain models for the interior density distribution. These models are further constrained by the planets moment of inertia  $I$  that can be determined from (satellite) geodetic and astronomical observations. For Earth the following values for the total mass and moment of inertia prefactor have been found,

$$\begin{aligned} M &= 5.97 \cdot 10^{24} \text{ kg} \\ I &= 0.3307MR^2 \end{aligned}$$

where  $R = 6371 \text{ km}$  is the mean radius. The observed moment of inertia prefactor  $f = 0.3307$  is smaller than the value 0.4 for a homogeneous sphere (see problem 2), another indication of mass concentration towards the earth's centre.

<sup>70</sup>Emil Johann Wiechert (26 December 1861 – 19 March 1928) was a German physicist and geophysicist who made many contributions to both fields, including presenting the first verifiable model of a layered structure of the Earth and being among the first to discover the electron

<sup>71</sup> $\delta_{ij}$  is the Kronecker delta, i.e.  $\delta_{ij} = 1$  for  $i = j$  and zero otherwise.

**problem: 1.** Derive the following expression for the moment of inertia of a spherically symmetric Earth model with outer radius  $R$ ,

$$I = \frac{8\pi}{3} \int_0^R \rho(r) r^4 dr \quad (801)$$

Hint: use the symmetry and compute  $I = \frac{1}{3}(I_x + I_y + I_z)$ , where  $I_x$  is the moment of inertia with respect to a rotation axis coinciding with the  $x$ -axis.

**problem: 2.** Derive from (801) the value of the prefactor  $f$  of the moment of inertia for a uniform sphere. answer:  $f = 2/5$ .

In general the moment of inertia prefactor  $f$  is an indicator of the degree of mass concentration towards the centre of a spherically symmetric mass distribution. Endmembers of mass concentration are a) a concentrated central point mass and b) all mass concentrated on a spherical surface of zero thickness.

Verify that the moment of inertia of the point mass endmember equals zero and that for the prefactor for a spherical shell of vanishing thickness we have  $f = \frac{2}{3}$ .

Wiechert's two-layer model with a distinct core is constrained by the moment of inertia prefactor  $f$ , the mantle radius  $R$  and density  $\rho_m$  and the total mass  $M$  or, equivalently, the mean density  $\langle \rho \rangle$ . Expressions for the core radius  $R_c$  and density  $\rho_c$  can be formulated for this model as specified in the following exercise (Bullen, 1975).

**problem: 3.** Derive a 2-parameter model for the earth's 1-D radial density distribution  $\rho(r)$  consisting of two uniform layers (core and mantle) of radius  $R_c$  and  $R$  respectively and with contrasting uniform densities  $\rho_c$  and  $\rho_m$  for core and mantle respectively. Assume  $\rho_m$  to be known, leaving  $\rho_c$  and  $R_c$  as unknown parameters that can be determined from the known moment of inertia prefactor  $f$  and the average density  $\langle \rho \rangle$ .

Compute the total mass  $M$

Compute the average density and arrive at:

$$\langle \rho \rangle = \frac{3}{R^3} \int_0^R \rho r^2 dr \quad (802)$$

Use  $I = fMR^2$  and the total mass to arrive at:

$$fR^5 \langle \rho \rangle = 2 \int_0^R \rho r^4 dr \quad (803)$$

Derive the following expressions for  $R_c$  and  $\rho_c$ ,

$$\frac{R_c}{R} = \left( \frac{\frac{5}{2}f\frac{\langle \rho \rangle}{\rho_m} - 1}{\frac{\langle \rho \rangle}{\rho_m} - 1} \right)^{1/2}, \quad \rho_c = \rho_m \left\{ 1 + \left( \frac{R}{R_c} \right)^3 \left( \frac{\langle \rho \rangle}{\rho_m} - 1 \right) \right\} \quad (804)$$

In Bullen's two-layer model the core radius is assumed to be known from seismology. For this model the mantle and core densities can be expressed in the known parameters in the following problem.

**problem: 4.** Assume the core radius  $R_c$  to be a known parameter in the following. Derive a 2-parameter model for the earth's 1-D radial density distribution  $\rho(r)$  consisting of two uniform layers (core and mantle), with a core and mantle radius  $R_c$  and  $R$  and different uniform densities  $\rho_m$  and  $\rho_c$  for mantle and core. Express the parameters  $\rho_m$  and  $\rho_c$  in terms of the mass and moment of inertia. Hint: compute  $M$  first, then  $I$ , as a function of all other parameters. Establish a relationship of the form  $(M, I)^T = A \cdot (\rho_c, \rho_m)^T$  where  $A$  is a  $2 \times 2$  matrix.

Solution: in matrix-vector format,

$$\begin{pmatrix} \rho_c \\ \rho_m \end{pmatrix} = \frac{4\pi}{3\Delta} \begin{pmatrix} \frac{2}{5}(R^5 - R_c^5) & -(R^3 - R_c^3) \\ -\frac{2}{5}R_c^5 & R_c^3 \end{pmatrix} \begin{pmatrix} M \\ I \end{pmatrix} \quad (805)$$

where the determinant  $\Delta = \frac{32\pi^2}{45} (R_c^3(R^5 - R_c^5) - R_c^5(R^3 - R_c^3))$ .

**problem: 5.** The numerical value of the interim expressions in (805) exceeds the magnitude of single precision real type variables in computer programs, that are limited to approximately  $1.7 \cdot 10^{38}$ . A work around for this problem may be to use double precision real variables that have a higher maximum magnitude of about  $10^{308}$ .

An alternative solution is to switch to using non-dimensional parameters, denoted by primes, in the following way: define  $R'_c = R_c/R$ ,  $M_0 = 4/3 \cdot \pi R^3 \rho_0$  and  $M = M_0 \cdot M/M_0 = M_0 \cdot M'$ ,  $\rho_c = \rho_0 \rho'_c$ ,  $\rho_m = \rho_0 \rho'_m$  and express the moment of inertia in the reference density  $\rho_0$  and outer radius as,  $I = fMR^2 = f4/3 \cdot \pi R^5 \rho_0$ . With these definitions rewrite (805) into the non-dimensional form,

$$\begin{pmatrix} \rho'_c \\ \rho'_m \end{pmatrix} = \frac{16\pi^2}{9\Delta'} \begin{pmatrix} \frac{2}{5}(1-R'_c)^5 & -(1-R'_c)^3 \\ -\frac{2}{5}R'_c^5 & R'_c^3 \end{pmatrix} \begin{pmatrix} M' \\ f \end{pmatrix} \quad (806)$$

where the determinant  $\Delta' = \frac{32\pi^2}{45} (R'_c^3(1-R'_c)^5 - R'_c^5(1-R'_c)^3)$ .

### 9.2.3 Density, gravity and pressure in the Earth

In the Earth's mantle major solid state phase transitions occur in the silicate material which constitutes the planetary mantle outside the metallic iron/nickle core. These phase transitions are induced by the increase in the static pressure from a 1 bar ( $10^5$  Pa) atmospheric value at the Earth's surface to  $136 \cdot 10^9$  Pa at the core mantle boundary at a depth of approximately 2900 km. Phase transitions in the Earth's interior are associated with changes in the elastic wave velocities that can be deduced from seismological observations. In high pressure experiments, phase transitions in candidate mantle silicates can be studied and correlated with the seismological data to constrain the mineralogy and pressure/temperature distribution in the mantle. Knowledge of the internal material constitution of the Earth, such as the mineral phase, is a requirement for understanding the main geodynamical processes that determine Earth's evolution.

Density and pressure inside the Earth are linked with self-gravitation. This means that the hydrostatic or lithostatic pressure is a direct result of the gravity field generated by the Earth's own mass distribution. The lithostatic pressure can be expressed as the weight of a column of unit cross-sectional area extending from zero depth, at the Earth's surface, to the depth  $z$  of the evaluation point,

$$P(z) = \int_0^z \rho(z')g(z')dz' \quad (807)$$

where  $\rho$  is the mass density and  $g$  is the magnitude of the gravitational acceleration.

The gravity field defining  $g$  is generated by the Earth's own density distribution. Weak periodic gravity 'perturbations' are generated by celestial bodies, expressed in the external tides, both ocean tides and solid earth tides. The main tides are generated by the Earth's moon and by the Sun.

In the following section expressions for the gravity field in terms of the density distribution are given, based on Newton's law of gravitation.

In the description of the density distribution we will first neglect the role of self-compression and consider a number of one-dimensional (1-D), spherically symmetric, parameterized density distributions. Self-compression and compressibility are then treated in section 9.2.6. Self-compression and finite compressibility result in a continuous increase of density with pressure in agreement with several geophysical observations.

**problem: 6.** Derive the expression (807) (where the depth  $z$  is not to be confused with a cartesian coordinate) for the lithostatic pressure in a spherically symmetric planet from the elastostatic equation for a static medium,

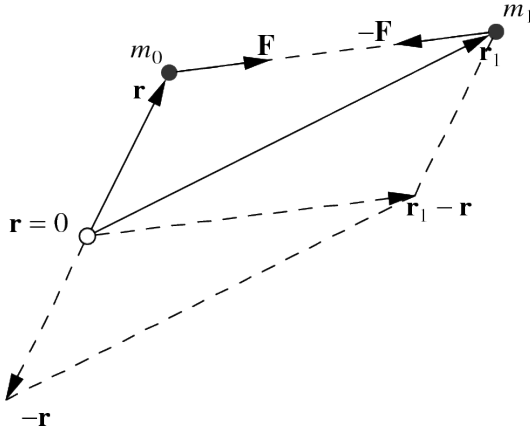
$$\partial_j \sigma_{ij} + \rho g_i = 0 \quad (808)$$

*Hint:* Assume hydrostatic conditions where the stress tensor can be written as  $\sigma_{ij} = -P\delta_{ij}$ , with  $\delta_{ij}$  the Kronecker delta, and derive from equation (808) for the pressure gradient,  $\nabla P = \rho g$ .

#### 9.2.4 Gravity field of a mass distribution

Newton formulated the attraction force acting on a point mass  $m_0$ , located in a point with position vector  $\mathbf{r} = (x, y, z)$ , with  $x, y, z$  the cartesian coordinates, from a second point mass  $m_1$  located at  $\mathbf{r}_1 = (x_1, y_1, z_1)$ , illustrated in the following figure as,

$$\mathbf{F}(\mathbf{r}) = \frac{Gm_0m_1}{|\mathbf{r}_1 - \mathbf{r}|^2} \mathbf{e}_{\mathbf{rr}_1} \quad (809)$$



Vector diagram of the gravitational forces acting on the two point masses  $m_0, m_1$  in vector locations  $\mathbf{r}$  and  $\mathbf{r}_1$  respectively. From the expression for the gravity field (809) it follows that the forces on both masses are of equal magnitude and in opposite direction.

Where  $\mathbf{e}_{\mathbf{rr}_1}$  is the unit vector in  $\mathbf{r}$  pointing towards  $\mathbf{r}_1$  and  $\mathbf{F}(\mathbf{r}_1) = -\mathbf{F}(\mathbf{r})$ .  $\mathbf{r}, \mathbf{r}_1$  are the position vectors of the two point masses and  $|\mathbf{r}_1 - \mathbf{r}| = \sqrt{(x_1 - x)^2 + (y_1 - y)^2 + (z_1 - z)^2}$  is the distance between the points  $\mathbf{r}$  and  $\mathbf{r}_1$ .  $G$  is the gravitational constant  $G = 6.6732 \times 10^{-11} \text{ Nm}^2\text{kg}^{-2}$ ,  $m_0, m_1$  the mass of the respective pointmasses.

This gravitation effect is usually specified as a gravitation force per unit mass or acceleration vector  $\mathbf{g}$ ,

$$\mathbf{g}(\mathbf{r}) = \frac{Gm_1}{|\mathbf{r}_1 - \mathbf{r}|^2} \mathbf{e}_{\mathbf{rr}_1} \quad (810)$$

It can be verified by inspection that the acceleration vector field can be written as the gradient of a scalar potential field  $U(\mathbf{r})$  with  $\mathbf{g} = -\nabla U = (-\frac{\partial U}{\partial x}, -\frac{\partial U}{\partial y}, -\frac{\partial U}{\partial z})$ , (see problem 9),

$$U(\mathbf{r}) = -\frac{Gm_1}{|\mathbf{r}_1 - \mathbf{r}|} \quad (811)$$

The gravity acceleration and corresponding potential field are additive such that the total force or potential of a collection of  $N$  point masses is obtained by summation over individual point contributions,

$$\mathbf{g}(\mathbf{r}) = \sum_j^N \frac{Gm_j}{|\mathbf{r}_j - \mathbf{r}|^2} \mathbf{e}_{\mathbf{rr}_j}, \quad U(\mathbf{r}) = -\sum_j^N \frac{Gm_j}{|\mathbf{r}_j - \mathbf{r}|} \quad (812)$$

With this definition and sign convention the potential field of a point source in the origin is represented by a potential well ( $U(\mathbf{r}) < 0$ ). This is known as Coulomb's law and the equivalent form for a continuous mass distribution of density  $\rho$  (mass per unit volume) contained in a volume  $V$  is,

$$\mathbf{g}(\mathbf{r}) = \int_V \frac{G\rho(\mathbf{r}')}{|\mathbf{r}' - \mathbf{r}|^2} \mathbf{e}_{\mathbf{rr}'} dV(\mathbf{r}'), \quad U(\mathbf{r}) = - \int_V \frac{G\rho(\mathbf{r}')}{|\mathbf{r}' - \mathbf{r}|} dV(\mathbf{r}') \quad (813)$$

Besides the integral expression for the gravity field defined in (813) there is also the differential form using the second order partial differential equations of Laplace and Poisson. It can be shown by verification that  $U$  in (813) satisfies Poisson's equation,

$$\nabla^2 U = 4\pi G\rho \quad (814)$$

which reduces to Laplace's equation  $\nabla^2 U = 0$  outside the mass distribution in  $V$  (where  $\rho = 0$ ). <sup>72</sup>

In Newton's time the numerical value of  $G$  had not been determined yet. As a result it was not possible to determine the mass of the Earth  $M_{\oplus}$  by measuring the gravitation force of the Earth on a known 'test mass'. This way only the value of  $GM_{\oplus}$  could be determined. Only with the experiment named after Cavendish (1798) <sup>73</sup> it became possible to measure  $G$  directly, in a torsion balance experiment, by determining the gravitational attraction of two closely spaced test masses.

**problem: 7.** Verify that the familiar surface value of the Earth's gravity acceleration  $g_0 = 9.8 \text{ m/s}^2$  corresponds to the value of a point mass at the Earth's centre with the same mass as the Earth (see Table).

	Radius km	Mass kg	Density $\text{kg/m}^3$
Earth	$6371$	$5.97 \cdot 10^{24}$	$5.515 \times 10^3$
Moon	$1738$	$7.34 \cdot 10^{22}$	$3.34 \times 10^3$
Mars	$3394$	$6.42 \cdot 10^{23}$	$3.93 \times 10^3$
Jupiter	$71492$	$1.9 \cdot 10^{27}$	$1.326 \times 10^3$
Sun	$6.96 \cdot 10^5$	$1.99 \cdot 10^{30}$	-

Radius-mass parameters of Earth moon and planets.

**problem: 8.** Fig. ?? suggests that the magnitude of the gravity acceleration is approximately constant throughout the Earth's mantle. Assume an approximate uniform value of  $g$  in the Earth's mantle, equal to the surface value  $g_0 \sim 9.8 \text{ m/s}^2$  and use an approximate average mantle density  $\rho_m \sim 4.5 \times 10^3 \text{ kg/m}^3$  to obtain from Eq. (807) an approximation of the static pressure at the core-mantle boundary at a depth of  $2891 \text{ km}$ .

**problem: 9.** Verify the consistency of the expression for the gravity acceleration and potential of a point mass in (810) and (811), i.e. prove from these expressions by explicit calculation of the gradient vector from the scalar potential field that  $\mathbf{g} = -\nabla U$ .

*Hint:* specify the potential in cartesian coordinates and differentiate the result with respect to the coordinates  $x, y, z$ .

<sup>72</sup> To show that  $U$  in (813) satisfies Poisson's equation integrate the normal component of the acceleration field over an arbitrary closed surface  $S$  enclosing  $V$  and change the order of integration for the volume and surface integral.

$$\int_S \nabla U(\mathbf{r}) \cdot \mathbf{n} \, dA(\mathbf{r}) = - \int_V G\rho(\mathbf{r}') \left\{ \int_S \nabla \left( \frac{1}{|\mathbf{r}' - \mathbf{r}|} \right) \cdot \mathbf{n} \, dA(\mathbf{r}) \right\} dV(\mathbf{r}') \quad (815)$$

The surface integral on the right is independent of the choice of the surface  $S$  as long as it contains  $\mathbf{r}'$ . We therefore replace this surface by a sphere of radius  $R$  centered at  $\mathbf{r}'$  and find for the surface integral the value  $-4\pi$ . Next we apply the Gauss divergence theorem to the left hand surface integral to obtain,

$$\int_V \nabla^2 U \, dV = \int_V 4\pi G\rho \, dV \quad (816)$$

Note that the surface has been contracted on the volume  $V$  to obtain (816). Since the surface and enclosed volume are arbitrary we obtain the Poisson equation,

$$\nabla^2 U = 4\pi G\rho \quad (817)$$

<sup>73</sup> [http://en.wikipedia.org/wiki/Cavendish\\_experiment](http://en.wikipedia.org/wiki/Cavendish_experiment)

**problem: 10.** Apply the Poisson equation (814) to obtain the gravity field of a point-mass distribution with mass  $M$ , described by a Dirac delta function,  $\rho(\mathbf{r}) = M\delta(\mathbf{r} - \mathbf{r}_0)$ . Where the following property holds for the delta function,

$$\int_V \delta(\mathbf{r} - \mathbf{r}_0) dV = \begin{cases} 1, & \mathbf{r}_0 \in V \\ 0, & \mathbf{r}_0 \notin V \end{cases} \quad \text{or, more general } \int_V f(\mathbf{r}) \delta(\mathbf{r} - \mathbf{r}_0) dV = \begin{cases} f(\mathbf{r}_0), & \mathbf{r}_0 \in V \\ 0, & \mathbf{r}_0 \notin V \end{cases} \quad (818)$$

*Hint: integrate (814) over a spherical volume, centered at  $\mathbf{r}_0$  and apply the Gauss divergence theorem: for a vector field  $\mathbf{A} = (A_1, A_2, A_3)$  with divergence  $\nabla \cdot \mathbf{A} = \frac{\partial A_1}{\partial x} + \frac{\partial A_2}{\partial y} + \frac{\partial A_3}{\partial z}$*

$$\int_V \nabla \cdot \mathbf{A} dV = \int_{\partial V} \mathbf{A} \cdot \mathbf{n} dS \quad (819)$$

where  $\partial V$  is the closed boundary surface of  $V$ .

**problem: 11.** Check the dimensional units in (814) and verify that the gravitational potential has the dimension of energy per unit mass. This is in agreement with the identification of the gravity potential with the potential (gravitational) energy of a unit mass in the gravity field. <sup>a</sup>

<sup>a</sup> The local potential field value  $U(\mathbf{r}_1)$  equals the negative of the (gravitational) potential energy  $W(\mathbf{r}_1)$  of a unit point mass positioned at  $\mathbf{r}_1$ . It can be shown that the change in potential energy  $\Delta W$  that results from moving a unit mass from  $\mathbf{r}_1$  to  $\mathbf{r}_2$  follows directly from the potential field values  $U(\mathbf{r}_1)$ ,  $U(\mathbf{r}_2)$  and is independent of the path taken between  $\mathbf{r}_1$  and  $\mathbf{r}_2$ . This property defines a so called conservative field  $U$ .

To derive this result we compute the potential energy difference as the path (line) integral of the work done by the gravity force field on a unit mass and apply the gradient property  $\mathbf{g} = -\nabla U$ . The work done by moving a unit point mass from a location  $\mathbf{r}_1$  to  $\mathbf{r}_2$  is defined by the line integral,

$$\Delta W = \int_{\mathbf{r}_1}^{\mathbf{r}_2} \mathbf{F} \cdot d\mathbf{r} = \int_{\mathbf{r}_1}^{\mathbf{r}_2} \mathbf{g} \cdot d\mathbf{r} = \int_{\mathbf{r}_1}^{\mathbf{r}_2} -\nabla U \cdot d\mathbf{r} = \int_{U(\mathbf{r}_1)}^{U(\mathbf{r}_2)} -dU = -(U(\mathbf{r}_2) - U(\mathbf{r}_1)) = -\Delta U \quad (820)$$

Here the following gradient property has been used, relating the gradient vector to the differential of the scalar potential field,

$$dU = \frac{\partial U}{\partial x} dx + \frac{\partial U}{\partial y} dy + \frac{\partial U}{\partial z} dz = \nabla U \cdot d\mathbf{r} \quad (821)$$

The gravitational potential field can thus be defined in terms of the work done by the gravity field to move a unit mass from infinity to the evaluation point.

$$W(\mathbf{r}_1) = \int_{\mathbf{r}_\infty}^{\mathbf{r}_1} \mathbf{g} \cdot d\mathbf{r} = \int_{\mathbf{r}_\infty}^{\mathbf{r}_1} -\nabla U \cdot d\mathbf{r} = \int_{U(\mathbf{r}_\infty)}^{U(\mathbf{r}_1)} -dU = -U(\mathbf{r}_1) + U(\mathbf{r}_\infty) = -U(\mathbf{r}_1) \quad (822)$$

Where  $U(\mathbf{r}_\infty) = 0$  has been used.

The above can be applied in the determination of the escape velocity from the surface of a planet. This is the minimum launch velocity to escape from the planet's gravity field. For a spherically symmetric planet the external gravity potential is given by (829). Moving an object from the surface, the gravity potential changes by  $\Delta U = U(r) - U(R) = GM(-\frac{1}{r} + \frac{1}{R})$ . Applying an energy conservation argument we require the change in total (potential plus kinetic) energy per unit mass to be:  $\Delta E = \Delta U + \Delta K = 0$ . With  $\Delta K = -v_{ex}^2/2$  we get  $v_{esc} = \sqrt{2GM/R}$ .

**problem: 12.** Compute the surface escape velocities for different celestial bodies using the parameters given in Table ??

**problem: 13.** The potential energy of a self-gravitating planet in its own gravity field is defined in terms of the volume density  $\rho U$  as,

$$E = - \int_V \rho U dV \quad (823)$$

Derive the following expression for the potential energy of a spherically symmetric, uniform density model, using the expression for the internal gravity potential defined in (828)

$$E = \frac{8\pi}{5} G \rho_0 M R^2 \quad (824)$$

Compute the potential energy value  $E$ , assuming a density  $\rho_0 = 5.5 \cdot 10^3 \text{ kg/m}^3$  and planetary radius  $R = 6371 \text{ km}$ .

answer:  $4.4 \cdot 10^{32} \text{ J}$

The gravitational energy considered above plays an important role in major compositional differentiation processes that occurred in the early Earth and are still occurring today.

- A so called ‘core catastrophe’ occurred when the iron/nickel core of the Earth differentiated from the silicate mantle in the first few million years after the formation of the Earth in the early solar system. This event has probably freed enough potential energy to melt the mantle completely, resulting in a global magma ocean <sup>74</sup>.
- Crystallization of the solid inner core from the liquid outer core, as a result of core cooling, is accompanied by compositional differentiation. The liquid outer core contains a lighter fraction, possibly sulfur, which stays behind in the liquid during freezing of the inner core. The enriched residual liquid near the inner core boundary is less dense than the average liquid of the outer core and this results in a gravitationally unstable layering that induces ‘chemically driven’ convective flow in the outer core. The potential energy released in this chemical convection is probably an important energy source in powering the geodynamo that generates the Earth’s present day magnetic field.

### 9.2.5 The gravity and pressure field for parameterized density models with self-gravitation

In the following problems a number of simple density distributions are investigated that will serve as a reference for models more constrained by geophysical observations to be introduced in later sections. The gravity field can be determined by solving the governing Poisson equation (814) using suitable boundary conditions. For the special case of spherically symmetric mass distributions simple 1-D integral expressions can be used to derive the corresponding radial pressure distribution.

---

<sup>74</sup>[https://en.wikipedia.org/wiki/Iron\\_catastrophe](https://en.wikipedia.org/wiki/Iron_catastrophe)

**problem: 14.** The internal and external gravity field for a simple model of a planet can be derived by solving the Poisson equation (814), and applying appropriate boundary conditions to the general solution. Consider a spherically symmetric planet of radius  $R$  and uniform density  $\rho_0$ .

- Derive expressions for the gravity potential field  $U$  and the gravity force field  $g = |\mathbf{g}|$  inside and outside the planet.

*Hints:* Solve Poisson's equation in spherical coordinates for the interior ( $r \leq R$ ) and exterior domain  $r \geq R$  separately. The separate solutions for the interior  $U_{int}, g_{int}$  and exterior  $U_{ext}, g_{ext}$  domain each contain two integration constants which can be determined by applying the following boundary conditions,

$$\lim_{r \rightarrow \infty} U_{ext}(r) = 0, \quad \lim_{r \rightarrow 0} g_{int}(r) < \infty \quad (825)$$

Continuity of the gravity acceleration  $g$  at the surface  $r = R$ ,

$$g_{int}(R) = g_{ext}(R) \quad (826)$$

Continuity of the gravity potential  $U$  at the surface  $r = R$ ,

$$U_{int}(R) = U_{ext}(R) \quad (827)$$

*Answers*

$$g_{int} = \frac{4\pi}{3} G \rho_0 r, \quad U_{int} = \frac{2\pi}{3} G \rho_0 r^2 - \frac{3}{2} \frac{GM}{R} \quad (828)$$

where  $M = \frac{4\pi}{3} R^3 \rho_0$  is the planet mass and  $G$  is the gravitational constant.

$$g_{ext} = \frac{GM}{r^2}, \quad U_{ext} = -\frac{GM}{r} \quad (829)$$

- Verify that the external gravity force field is identical to the field of a concentrated point mass at  $r = 0$ .

- Derive an expression for the radial distribution of the pressure in the planetary interior and compute the central pressure for a case with  $\rho_0 = 5.5 \cdot 10^3 \text{ kg m}^{-3}$  and  $R = 6.371 \times 10^6 \text{ m}$ .

*Solution:*  $P(r) = \frac{2\pi}{3} \rho_0^2 G (R^2 - r^2)$

The gravity field of a spherically symmetric density distribution is identical to the field of an equivalent point-mass. (see problem 14 for the spatial case of a uniform density distribution). This can be formulated as follows,

$$g(r) = \frac{Gm(r)}{r^2}, \quad (830)$$

with

$$m(r) = \int_{V(r)} \rho dV = \int_0^r \rho(r') 4\pi r'^2 dr' \quad (831)$$

Here  $m(r)$  is the mass inside a sphere of radius  $r$  and  $g(r)$  is the corresponding magnitude of the gravity acceleration. For the corresponding gravity potential this implies, with  $\int_r^\infty \frac{dU}{dr'} dr' = U(\infty) - U(r) = -U(r)$ ,

$$U(r) = - \int_r^\infty \frac{dU}{dr'} dr' = \int_r^\infty g_r(r') dr' = \int_r^\infty -g(r') dr' = - \int_r^\infty \frac{Gm(r')}{r'^2} dr' \quad (832)$$

where the radial vector component  $g_r$  has been expressed in the vector length  $g$  as  $g_r = \mathbf{g} \cdot \mathbf{e}_r = -g$ .

To derive (830), the potential field at the radial coordinate  $r$  can be split in contributions originating from an internal- and external density distribution  $U(r) = U_i(r) + U_e(r)$ . With corresponding pairs,  $U_i \leftrightarrow \rho_i$ , and  $U_e \leftrightarrow \rho_e$ , where  $\rho_e(r') = 0$ ,  $r' \leq r$ , and  $\rho_e(r') = \rho(r')$ ,  $r' > r$ . This follows from the linearity of the governing Poisson equation.

The field generated by the internal mass distribution is obtained by integrating the corresponding Poisson equation in spherical coordinates,

$$\frac{1}{r'^2} \frac{d}{dr'} r'^2 \frac{dU_i}{dr'} = 4\pi G \rho_i \quad (833)$$

$$\int_0^r \frac{d}{dr'} \left( r'^2 \frac{dU_i}{dr'} \right) dr' = \int_0^r 4\pi G \rho_i r'^2 dr' \quad (834)$$

The radial component of the gravity acceleration becomes,

$$g_r(r) = -\frac{dU_i}{dr} = -\frac{1}{r^2} \int_0^r 4\pi G \rho_i r'^2 dr' = -\frac{Gm(r)}{r^2} \quad (835)$$

Furthermore the acceleration field  $g_e$  from the external mass distribution  $\rho_e$  for internal evaluation points  $r' < r$  is zero. The corresponding gravity potential  $U_e$  is uniform, which follows from the relevant Poisson equation, in spherical coordinates for a spherically symmetric mass distribution,

$$\frac{1}{r'^2} \frac{d}{dr'} r'^2 \frac{dU_e}{dr'} = 4\pi G \rho_e = 0 \rightarrow r'^2 \frac{dU_e}{dr} = A \rightarrow g_e(r') = -\frac{dU_e}{dr'} = -\frac{A}{r'^2} \quad (836)$$

A non-singular field requires  $A = 0$ ,  $g_e(r') = 0$ ,  $r' \leq 0$  and,

$$\frac{dU_e}{dr'} = 0 \rightarrow U_e(r') = B, \quad r' \leq r \quad (837)$$

**problem: 15.** Verify that (830) and (832), applied to the special case of a homogeneous sphere of density  $\rho_0$ , lead to the same expression for the internal and external potential and acceleration field as given in problem 14.

For a two-parameter spherically symmetric planet model consisting of a uniform core and mantle with radius  $R_c$  and  $R_m$  and contrasting densities  $\rho_c$  and  $\rho_m$ , the gravity field can also be determined by solving the Poisson equation for the particular density distribution and determination of the integration constants from the boundary conditions. However in this case the formula (830) are more convenient to obtain expressions for the gravity field.

**problem: 16.** Derive expressions for the gravity acceleration and internal pressure distribution for the two-parameter model

$$\rho(r) = \begin{cases} \rho_c, & r < R_c \\ \rho_m, & R_c < r \leq R \\ \rho_e = 0, & r > R \end{cases}, \quad g(r) = \begin{cases} g_c, & r < R_c \\ g_m, & R_c < r \leq R \\ g_e, & r > R \end{cases}, \quad P(r) = \begin{cases} P_c, & r < R_c \\ P_m, & r \geq R_c \end{cases} \quad (838)$$

using (830) and (807). See also (844).

**Answer:**

$$g_c(r) = \frac{4\pi}{3} G \rho_c r, \quad g_m(r) = \frac{G}{r^2} \left\{ \frac{4\pi}{3} \rho_m (r^3 - R_c^3) + M_c \right\}, \quad g_e(r) = \frac{G}{r^2} (M_m + M_c) \quad (839)$$

$$M_c = \frac{4\pi}{3} R_c^3 \rho_c, \quad M_m = \frac{4\pi}{3} \rho_m (R^3 - R_c^3) \quad (840)$$

$$P_c(r) = P_m(R_c) + \frac{2\pi}{3} G \rho_c^2 (R_c^2 - r^2) \quad (841)$$

$$P_m(r) = \frac{2\pi}{3} G \rho_m^2 \left\{ R_m^2 - r^2 + 2 \left( \frac{\rho_c}{\rho_m} - 1 \right) R_c^3 \left( \frac{1}{r} - \frac{1}{R_m} \right) \right\} \quad (842)$$

## 9.2.6 The pressure effect on density

In the previous sections we considered the gravity field of a given mass distribution. For self-gravitating planets of sufficient size **the local density depends on the pressure, through selfcompression** i.e. the compression of the material caused by the planets own gravity field. As we have seen in previous sections the lithostatic pressure depends on the gravity field and the density distribution. It follows that the determination of the density, gravity and pressure are coupled problems that must be solved simultaneously and can not be solved separately. Here we will consider the solution of such coupled problems.

From observations of the average density of surface rocks of some  $2.7 \cdot 10^3 \text{ kg/m}^3$  and the known mean density of the Earth  $5.5 \cdot 10^3 \text{ kg/m}^3$ , it follows that the surface density is less than half the mean Earth

value. The difference between both density values suggests a density increase in the interior which could be related either to different composition at depth, for example corresponding to a dense metallic core, and/or the effect of selfcompression in an otherwise homogeneous planet. Solid state phase transitions of mantle material due to increasing pressure can also explain part of the high mean density value.

From the nineteenth century on, models of the internal density distribution of the earth have been investigated. These models have in common that the radial density distribution is parameterized in a simple way with a small number of parameters, typically two, which are then adjusted to the known data such as the surface density and the Earth's total mass or moment of inertia.

In the following the relation between density, gravity and pressure in a self-gravitating planet will be investigated in a more self consistent way.

For a spherically symmetric density distribution the corresponding magnitude of the gravity acceleration vector is given by (835),

$$g(r) = |\mathbf{g}(\mathbf{r})| = |g_r(r)| = \frac{4\pi G}{r^2} \int_0^r \rho(r') r'^2 dr' = \frac{Gm(r)}{r^2} \quad (843)$$

where  $m(r)$  is the mass of a sphere of radius  $r$  and  $\rho(r)$  is the corresponding radial density profile.

**problem: 17.** Use (843) to show that it is not possible to derive a unique radial mass distribution of a spherically symmetric planet from the observed surface value of the gravity field alone. This can be verified by showing that multiple density profiles exist that produce the same surface gravity. To illustrate this sketch a schematic internal radial profile of the gravity acceleration in a comparison of two spherically symmetric planets of identical mass  $M$  and radius  $R$ . The first one is a homogeneous planet with density  $\rho_0$  and the second one is a differentiated planet with a uniform high density core  $\rho_c = \rho_0 + \delta\rho$  and less dense mantle  $\rho_m = \rho_0 - \delta\rho$ . Verify that these assumptions correspond to this special case with volume fraction of the core  $\phi_c = 1/2$ .

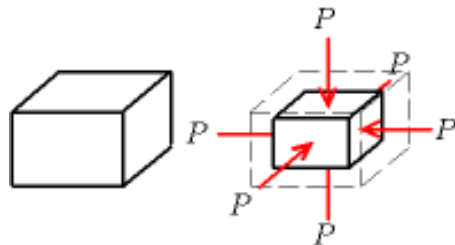
From the above results the lithostatic pressure distribution can be obtained by substitution for the gravity acceleration and integrating the pressure gradient  $dP/dr = -\rho g$ . Assuming a zero pressure value at the surface this results in,

$$P(r) = \int_r^R \rho(r') g(r') dr' = 4\pi G \int_r^R \rho(r') \left\{ \frac{1}{r'^2} \int_0^{r'} \rho(r'') r''^2 dr'' \right\} dr' \quad (844)$$

The pressure in the Earth's interior reaches values over 350 GPa as shown in Fig. ???. For such high pressure values the effect of self-compression on the density is significant. In the following this effect is further explored.

**The bulkmodulus** An isotropic linear elastic solid can be described by two independent elasticity parameters, for instance the Lamé parameters  $\lambda$  and  $\mu$ <sup>75</sup>. The bulkmodulus can be expressed in the Lamé parameters as,  $K = \lambda + \frac{2}{3}\mu$ . The bulkmodulus  $K$  and the shearmodulus  $\mu$  are the most commonly used parameters to specify the elastic parameters of Earth materials.

The bulk modulus  $K$  of a substance measures the substance's resistance to uniform compression. It is defined as the ratio of the infinitesimal pressure increase to the resulting relative decrease of the volume. Its SI unit is the Pascal, and its dimensional form is  $M^1 L^{-1} T^{-2}$ .



<sup>75</sup>[https://en.wikipedia.org/wiki/Elastic\\_modulus](https://en.wikipedia.org/wiki/Elastic_modulus)

The incompressibility  $K$ , or bulkmodulus, is defined as,

$$\frac{1}{K} = \frac{1}{\rho} \frac{d\rho}{dP} \quad (845)$$

By substitution of  $dP = -\rho g dr$  in (845) we derive a differential equation for the density profile of a compressible planet model,

$$\frac{1}{K} = \frac{-1}{\rho^2 g} \frac{d\rho}{dr} \Rightarrow \frac{d\rho}{dr} = -\frac{\rho^2 g}{K} \quad (846)$$

**Parameterization of the bulkmodulus** The radial density distribution for a selfcompressing planet can be obtained from (846) once the bulkmodulus  $K$  is known. We will first consider simple cases where  $K$  is either a uniform constant or it is parameterized in terms of the density.

**problem: 18.** Assume both  $K$  and  $g$  in (846) to be uniform in the mantle and derive the following density profile,

$$\rho(z) = \frac{\rho_0}{1 - \frac{\rho_0 g z}{K}} \quad (847)$$

where  $z = R - r$  is the depth coordinate and  $\rho_0 = \rho(0)$  is the surface density value.

- Compute the depth  $z_1$  where the expression (847) becomes singular, i.e.  $\rho \rightarrow \infty$ , suggesting infinite compression of the material. To do this assume Earth(mantle)-like values of the incompressibility,  $K = 400\text{GPa}$  (see Fig. ??) and the surface density  $\rho_0 = 3 \cdot 10^3 \text{ kg/m}^3$ .
- Now consider a simplified model of a large rocky exoplanet of Earth-like composition with  $M = 8M_\oplus$  and  $R = 1.5R_\oplus$ . Assume uniform gravity (adapted for the given  $M, R$ ) and uniform incompressibility  $K$ . Do you now find the singular depth  $z_1$  within the depth range of the planet? Comment on the assumption of a uniform gravity field in view of the models presented in section 9.2.5.

**problem: 19.** The result of problem 18 gives the density depth distribution for the model with constant properties. The resulting expression (847) also contains the uniform gravity acceleration. A more fundamental relation between density and pressure, not including gravity, can be derived for this model with constant material property  $K$  as an equation of state (EOS) for the density.

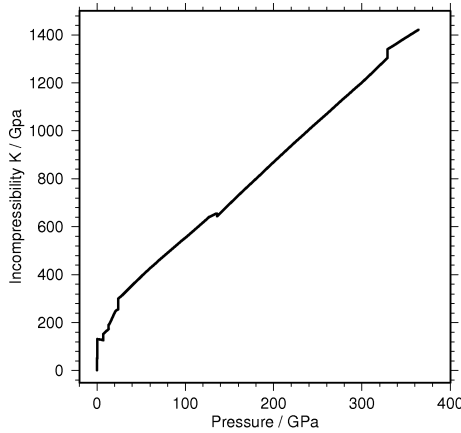
Derive from the definition of the bulkmodulus (845) the following logarithmic EOS for the density in terms of the static pressure,

$$P = \ln \left( \left( \frac{\rho}{\rho_0} \right)^K \right) \quad (848)$$

Show that the above EOS (848) can be inverted to obtain an explicit expression for density as a function of pressure.

The singular behavior in the density model of problem 18 is a result of the assumed uniform  $g$  and  $K$  in (846). While  $g$  is reasonably constant with depth in the mantle, as illustrated in Fig. ??,  $K$  is not. The incompressibility increases with increasing depth/pressure and as a result the compression remains finite for earth-like conditions. The incompressibility can be expressed in the density and the seismic wave velocities,  $v_p = \sqrt{(\lambda + 2\mu)/\rho}$ ,  $v_s = \sqrt{\mu/\rho}$ . With  $K = \lambda + \frac{2}{3}\mu$  this becomes  $K = \rho(v_p^2 - 4/3v_s^2)$ . A radial profile  $K(P(r))$  can therefore be derived, from the seismic velocities determined from inversion of traveltimes tables of longitudinal and shearwave seismic arrivals.

The  $K(P(r))$  profile derived from the PREM model of Dziewonski and Anderson (1981) appears to be roughly linear as shown in the following figure:



Incompressibility profile derived from the PREM model.

A linear relation between bulk modulus and pressure as suggested by this figure is also obtained using the following power law parameterization for the bulk modulus in terms of the density  $K(\rho)$ .

$$K = C\rho^n \Rightarrow \ln(K) = \ln(C) + n\ln(\rho) \Rightarrow n = \frac{d\ln(K)}{d\ln(\rho)} = \frac{dK}{dP} = K'_0 \quad (849)$$

where  $C$  is a constant. The constant pressure derivative in this model implies a linear pressure relation  $K(P) = K_0 + K'_0 P$ . This appears to approximate the distribution of  $K$  in particular in the lower mantle as determined from seismological data in the PREM model.  $K'_0 \approx 4$  for the magnesium-iron silicates  $(\text{Mg}, \text{Fe})\text{SiO}_3$  (perovskite) and dense oxides  $(\text{Mg}, \text{Fe})\text{O}$  (wüstite), representative for the earth's deep mantle.

**The Murnaghan e.o.s.** An equation of state directly relating the density or specific volume,  $V = 1/\rho$ , to pressure can be derived from such an ‘ansatz’ of a linear pressure dependence  $K = K_0 + K'_0 P$  as shown in the following,

$$\frac{1}{\rho} \frac{d\rho}{dP} = \frac{1}{K} \rightarrow \frac{1}{V} \frac{dV}{dP} = -\frac{1}{K} \rightarrow dP = -(K_0 + K'_0 P) \frac{1}{V} dV \quad (850)$$

$$\int_0^P \frac{dP'}{K_0 + K'_0 P'} = - \int_{V_0}^V \frac{1}{V'} dV' = \int_V^{V_0} \frac{1}{V'} dV' = \ln\left(\frac{V_0}{V}\right) \quad (851)$$

Substitution in the integral over pressure of  $K_0 + K'_0 P' = x$ ,  $dx = K'_0 dP'$  gives,

$$\int_{x_0=K_0}^{x_P=K_0+K'_0 P} \frac{1}{K'_0} \frac{dx}{x} = \frac{1}{K'_0} \ln\left(\frac{K_0 + K'_0 P}{K_0}\right) = \ln\left(\frac{V_0}{V}\right) \quad (852)$$

$$1 + \frac{K'_0 P}{K_0} = \left(\frac{V_0}{V}\right)^{K'_0} \rightarrow P = \frac{K_0}{K'_0} \left( \left(\frac{V_0}{V}\right)^{K'_0} - 1 \right) \quad (853)$$

This relation is known as the Murnaghan equation of state (EOS).

The Murnaghan equation of state is a relationship between the volume of a body and the pressure to which it is subjected. This is one of many state equations that have been used in earth sciences and shock physics to model the behavior of matter under conditions of high pressure. It owes its name to Francis D. Murnaghan who proposed it in 1944 to reflect material behavior under a pressure range as wide as possible to reflect an experimentally established fact: **the more a solid is compressed, the more difficult it is to compress further**.

The Murnaghan equation is derived, under certain assumptions, from the equations of continuum mechanics. It involves two adjustable parameters: the modulus of incompressibility  $K_0$  and its first derivative with respect to the pressure,  $K'_0$ , both measured at ambient pressure. In general, these coefficients are determined by a regression on experimentally obtained values of volume  $V$  as a function of the pressure  $P$ . These experimental data can be obtained by X-ray diffraction or by shock tests. Regression can also be performed on the values of the energy as a function of the volume obtained from ab-initio and molecular dynamics calculations.

**problem: 20.** Derive an explicit expression for the pressure dependent density from the Murnaghan equation of state (853).

Answer:

$$\rho(P) = \rho_0 \left( \frac{K'_0 P}{K_0} + 1 \right)^{1/K'_0} \quad (854)$$

**problem: 21.** In problem 18 we have seen that a simple model with uniform incompressibility and gravity  $K = K_0$  and  $g = g_0$  leads to physically impossible solutions. In a refined version of this model, applied to the Earth's mantle,  $g = g_0$  is maintained (compare Fig.??), and  $K$  is parameterized using the powerlaw relation (849).

Derive the following density profile for the model corresponding to (849).

$$\rho(r) = \rho_0 \left( 1 + (n - 1) \frac{\rho_0 g_0 z}{K_0} \right)^{\frac{1}{n-1}} \quad (855)$$

where  $z = R - r$  is the depth coordinate and the 0 subscript refers to zero pressure conditions. Note that the singularity for  $\rho_0 g_0 z / K_0 = 1$  in problem 18 is absent in this model.

A more widely used and more accurate EOS for a higher pressure range is the equation derived by Birch (1952) from a consideration of elastic strain energy, known as the Birch-Murnaghan EOS (Poirier, 2000).

In other cases than the special simplified cases discussed above, in particular in problems 18 and 21, the gravity acceleration varies also with depth. Also more accurate equations of state may be necessary for very high pressure, encountered in the deep interior of large (exo)planets, that result in large compression. Such models can be formulated in a more general way by the following coupled set of equations for pressure, gravity and density.

$$\frac{dP}{dr} = -\rho g \quad (856)$$

$$g(r) = \frac{Gm(r)}{r^2} \quad (857)$$

$$F(\rho, P, T) = 0 \quad (858)$$

where the radial mass distribution  $m(r)$  is defined as in (??). A model based on (856), (857), and (858) can be constructed for the internal structure (density, gravity, pressure) of a planet of given mass  $M$  and composition, i.e. with given parameters of the EOS (858) such as  $\rho_0, K_0, K'_0$  in the Murnaghan EOS (853). Consider the application of such a model to a planet for which only the planet mass  $M$  is known.<sup>76</sup> Assume a homogeneous terrestrial (rocky) planet without a distinct metallic core. Assuming an earth-mantle like composition, representative values of the EOS parameters can be used, to solve the coupled model equations in the following iterative scheme.

1. Define a grid along the radial coordinate  $r_i, i = 1, \dots, N, r_1 = 0$ . This grid defines a subdivision of the interior in  $N - 1$  concentric layers and must be chosen large enough, i.e.  $r_N > R$ .
2. Choose an initial estimate of the central pressure  $P^{(1)}(0)$ .
3. In a loop over the internal layers, starting upward from the centre, first compute the pressure decrement over the layer from (856). This is then used to obtain the pressure at the next grid point and corresponding density from the EOS (858). From the computed density the corresponding mass distribution  $m(r_i)$  and gravity  $g(r_i)$  (857) follow.
4. The layer iteration in the previous item is stopped when a zero pressure value has been reached. The radial level reached this way now defines the next approximation of the planetary radius  $R^{(j)}$  and  $M^{(j)} = m(R^{(j)})$  is a new approximation of the planet mass  $M$ .

<sup>76</sup> Such models can be applied to exoplanets that are recently being discovered [https://en.wikipedia.org/wiki/Methods\\_of\\_detecting\\_exoplanets](https://en.wikipedia.org/wiki/Methods_of_detecting_exoplanets). For some of these planets, detected from radial velocity variations of the star, only the planet mass  $M$  is known.

5. From the total mass defect  $\Delta M^{(j)} = M^{(j)} - M$  a correction to the central pressure is computed as  $\Delta P^{(j)}$ , (problem 22). In the next iteration the radial integration is repeated from item 3 with an updated central pressure  $P^{(j+1)}(0) = P^{(j)}(0) + \Delta P^{(j)}$  and this iterative procedure is repeated until convergence is reached, i.e. until  $|\Delta M^{(j)}|/M$  drops below a specified tolerance value.

**problem: 22.** A correction for the central pressure in item 4 can be estimated by distributing the mass defect  $\Delta M^{(j)}$  over a spherical shell of thickness  $\Delta R^{(j)}$ , positioned at the surface, and computing an approximate pressure  $\Delta P^{(j)}$  at the bottom of this shell.

Derive the following expression for the thickness of this spherical shell,

$$\frac{\Delta R^{(j)}}{R^{(j)}} = \left( \frac{\Delta M^{(j)}}{M^{*(j)}} + 1 \right)^{1/3} - 1 \quad (859)$$

Where  $M^{*(j)} = \frac{4\pi}{3} \rho(R^{(j)}) R^{(j)3}$ .

The correction for the central pressure is then defined as,  $\Delta P^{(j)} = \rho(R^{(j)}) g(R^{(j)}) \Delta R^{(j)}$ .

### 9.2.7 Adiabatic density distribution

In the previous section density models were based on assumptions about the parameterization of the bulkmodulus  $K$ . The density model of Williamson and Adams (1923), (Hemley, 2006) does not depend on a parameterized  $K$ . Instead it is defined in terms of the seismic wave velocities  $v_p$  and  $v_s$  that can be determined from inversion of seismological traveltimes as  $K/\rho = v_p^2 - 4/3v_s^2$ .

The W-A model can be derived from thermodynamic principles for a homogeneous self-compressing layer which is in an adiabatic state. The bulkmodulus applied in this model is expressed in the seismic wave velocities which in turn depend on the elasticity parameters and the density. The elastic deformation process in seismic wave propagation occurs on a relatively short time scale (seconds-minutes) compared to the characteristic time scale of conductive heat transport in solids (see ??). Therefore (diffusive) heat exchange can be neglected and adiabatic conditions apply in seismic wave propagation. This implies that the elasticity parameters determined from seismic data, including the bulkmodulus  $K$  pertain to adiabatic conditions (see also Appendix ??).

Other processes such as convective mantle flow that occur on a much longer time scale may take place under more general (non-adiabatic) conditions.

In section ?? on the thermal state of the Earth it is shown that adiabatic conditions hold for the interior of a fluid layer when heat transport is dominated by advection and heat diffusion by conduction/radiation plays a minor role. Assuming the Earth's mantle to be in a state of vigorous thermal convection it also follows that the average temperature profile, the geotherm, corresponds to an adiabatic distribution.

In general the density differential can be written as,

$$d\rho = \left( \frac{\partial \rho}{\partial P} \right)_S dP + \left( \frac{\partial \rho}{\partial S} \right)_P dS \quad (860)$$

where the differential of the entropy  $S$  is dropped in case of adiabatic conditions and the pressure derivative is written in terms of the adiabatic bulkmodulus  $K_S$  defined in (845),  $1/K_S = (\partial \rho / \partial P)_S / \rho$ .

**problem: 23.** Derive the Williamson-Adams equation for a homogeneous adiabatic layer from the density differential (860) and assumption of isentropic (adiabatic) conditions with  $dS \equiv 0$ ,

$$\frac{d\rho}{dr} = -\frac{\rho^2 g}{K_S} \quad (861)$$

The density solution of the W-A equation can be expressed in terms of the seismic parameter  $\Phi = K_S / \rho$  which in turn can be obtained from seismic velocity models:  $\Phi = v_p^2 - \frac{4}{3}v_s^2$  for  $P$  and  $S$  waves.  $\sqrt{\Phi} = \sqrt{K_S / \rho}$  is known as the bulkvelocity. For a given bulkvelocity profile, obtained from seismic observations, the W-A density profile is derived from (861) as,

$$\ln \left( \frac{\rho(r)}{\rho(R)} \right) = \int_r^R \Phi^{-1}(r') g(r') dr' \quad (862)$$

**problem: 24.** Derive (862) by integration of the W-A equation (861).

In (862) the gravity acceleration  $g$  depends on the density distribution  $\rho(r)$  in the lefthand side. Therefore the density profile can not be simply obtained from a seismologically determined  $\Phi(r)$  profile and a single evaluation of the integral in (862). The expression represents an integral equation that can be solved iteratively as specified in problem 25.

**problem: 25.** Assume that a seismic parameter profile for the mantle  $\Phi(r)$ , obtained from seismic travel times, is available. Investigate how (862) can be used to compute a sequence of mantle density profiles  $\rho^{(j)}(r), j = 1, 2, \dots$  in an iterative procedure, by successive substitution. How would you define a starting profile  $\rho^{(1)}(r)$  for this iterative procedure?

*Hint:* Substitute the density profile for iteration number  $j$  in the gravity acceleration in the righthand side of (862) for the computation of an updated profile  $j + 1$ . This is an example of a general solution strategy for non-linear problems known as ‘successive substitution’ or Picard iteration.

Williamson and Adams (1923) [2795] used the iterative scheme in problem 25 to test the hypothesis that the mass concentration towards the Earth’s centre is completely explained by compression of a homogeneous self-gravitating sphere. They showed that integrating (862) from a surface value of  $3.3 \cdot 10^3 \text{ kg/m}^3$  results in unrealistically high density values for depths greater than the core-mantle boundary. This way they concluded that an inhomogeneous earth with a dense, compositionally distinct core, probably iron-nickel, was required by the observations. The necessary multiple integrals in the evaluation of (862) had to be computed by means of graphical approximation methods in 1923, several decades before the advent of electronic computers.

In a later analysis Bullen (1936) showed that the assumption of a homogeneous selfcompressing mantle described by the W-A equation, and a chemically distinct dense core, leads to unrealistically high values of the moment of inertia for the core  $I_c = f M_c R_c^2$ , with a prefactor value  $f \sim 0.57$  greater than the value of a core with uniform density, 0.4. Since this would imply a density decrease towards the centre Bullen concluded that the applicability of the W-A model for the whole mantle can not be maintained and that instead a distinct mantle transition layer, labeled C-layer, must be included between the upper and lower mantle proper, related to transitions in mineral phase and/or composition (Bullen, 1975).

**problem: 26.**

1. Derive the following equation for the temperature distribution of a W-A layer (see Appendix ??),

$$\frac{dT}{dr} = -\frac{\alpha g}{c_P} T \quad (863)$$

where  $\alpha$  and  $c_P$  are the thermal expansion coefficient and the specific heat at constant pressure.

*Hint:* Use the differential for the entropy,

$$dS = \left( \frac{\partial S}{\partial T} \right)_P dT + \left( \frac{\partial S}{\partial P} \right)_T dP \quad (864)$$

and the thermodynamic relations:  $(\partial S/\partial T)_P = c_P/T$  and  $(\partial S/\partial P)_T = -\alpha/\rho$ .

2. Derive the expression for the temperature profile for an adiabatic layer, sometimes referred to as the ‘adiabat’, by solving equation (863),

$$T(r) = T(R) \exp \left( \int_r^R \frac{\alpha g}{c_P} dr' \right) \quad (865)$$

The temperature extrapolated to the surface,  $T_P = T(R)$  is known as the potential temperature of the layer. The quantity  $H_T = (\alpha g/c_P)^{-1}$  is known as the thermal scale height of the layer.

3. Derive an expression from (865) for the special case with a constant value of the scale height parameter.

The W-A equation for the density of an adiabatic layer can be generalized introducing the Bullen

parameter  $\eta$  which is used as a measure of the departure of the actual density/temperature profile from an adiabat. This is done by writing,

$$\eta(r) = -\frac{\Phi}{\rho g} \frac{d\rho}{dr} \quad (866)$$

where  $\eta(r)$  has been substituted for the constant value ( $\equiv 1$ ) in the W-A equation.

### 9.2.8 Current density models

The concept of an adiabatic layer was essential when no independent determinations for the density distribution were available and the W-A equation was used to compute  $\rho(r)$  for given values of the seismic parameter  $\Phi(r)$  determined from seismological observations (Bullen, 1975).

During the 1970s a radial density distribution has been obtained for the Earth from inversion of seismological observations, incorporating spectral analysis of the Earth's eigen vibrations, under the constraints of the given values for  $M$  and  $I$ . This, together with seismic velocities determined from bodywave traveltimes and surface wave dispersion, has resulted in the Preliminary Reference Earth Model (PREM), (Dziewonski and Anderson, 1981 [751]).

Since  $\rho(r)$  can be determined from analysis of the earth's normal modes (radial eigen vibrations) the 'adiabaticity' of the mantle is no longer assumed.

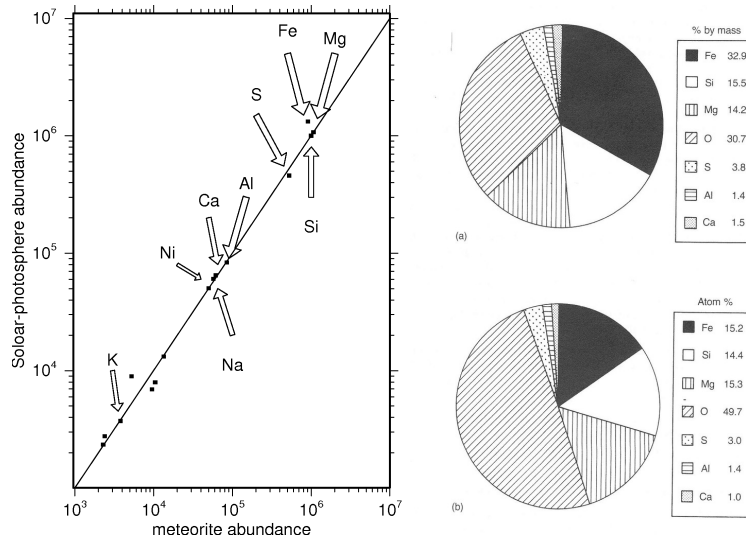
The degree of 'adiabaticity' is used in numerical modelling experiments as a diagnostic for the dynamic state - where a high degree of adiabaticity indicates vigorous thermal convection and predominantly convective heat transport (van den Berg and Yuen, 1998, [2609] Matyska and Yuen, 2000, [1736] Bunge et al., 2001).

Usually the outcome of such experiments shows that the upper and lower mantle separately are approximately adiabatic - away from boundary layers conductive transport dominates. In recent years models of the deep lower mantle have become popular where a compositionally distinct dense layer occupies the bottom 30% (roughly) of the lower mantle (Kellogg et al. (1999) [1421], Albarede and van der Hilst (2002) [14]).

### 9.2.9 Earth's chemical composition

For a complete description of the Earth's interior we need to know its chemical composition, temperature and pressure. In section 9.2.3 the pressure is expressed in the density distribution and the related internal gravity field. Once the internal pressure distribution is known, sharp transitions or discontinuities in the material properties, like the seismic velocities  $v_p, v_s$  and the density in the PREM model, can be identified with mineral phase transitions and as such they can be related to the mineral ( $P, T$ ) phase diagram of candidate mantle silicate materials in order to estimate the temperature in the Earth's interior. Such phase diagrams are determined from experimental (HPT) and theoretical work in mineral physics.

What do we know about Earth's bulk chemical composition? Candidate mantle materials have been defined based on cosmochemical and petrological considerations. Models of the chemical composition of the Earth are commonly based on the hypothesis that the planet was formed in a multi-stage accretion process from material that condensed from the original solar nebula approximately 4.6 billion years ago at the time of formation of the solar system. The chemical composition of chondritic meteorites, in particular the carbonaceous chondrites (CI type) (McBride and Gilmour (2003) [1748]) show a strong correlation with the composition of the outer layer of the sun (photosphere), determined from spectral analysis of the solar light, as illustrated in the following figure:



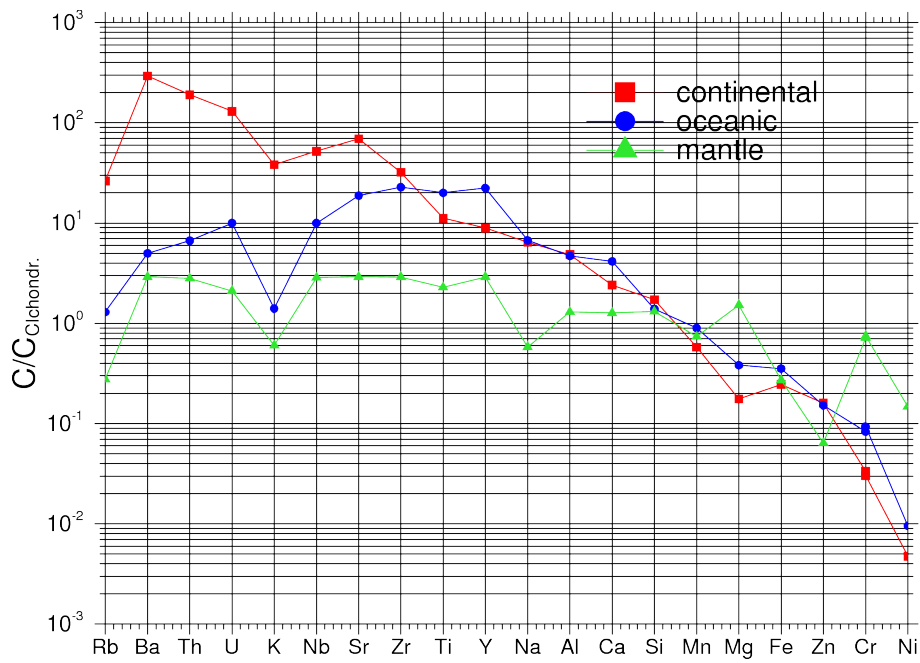
Left: Element abundance (normalized with  $Si = 10^6$ ), of the solar shallow photosphere compared to chondritic meteorites (Anders & Grevesse (1989) [35]). Right: amounts of Earth's major elements assuming a chondritic composition (Brown & Mussett (1993) [293]).

The solar-chondritic data in the lefthand frame show that Mg, Fe and Si are by far the most abundant (non-volatile) elements. According to the chondritic Earth hypothesis a similar abundance can be expected for the bulk-earth. This is illustrated in the righthand pie diagrams. Note the large proportion of oxygen, bound in oxides. In most crust-mantle rocks S is less abundant than Al or Ca. This is usually explained by assuming that S is relatively volatile and also ‘siderophile’, meaning that a significant fraction may have ended up in the iron-nickel core during an early core-mantle differentiation.

The chondritic meteorites are thought to be representative of the undifferentiated material condensed from the solar nebula.

Around 1960 a model chemical composition for the bulk of the Earth’s mantle, coined pyrolite, was introduced by Ringwood (see (Ringwood, 1975) and original references therein). This is still used as a reference model. The pyrolytic composition is associated with the main upper mantle rock type peridotite that is brought to the Earth’s surface in small fragments included in volcanic rocks (xenoliths) and also in larger, kilometer sized, fragments in so called peridotite bodies (Spengler et al., 2006). The pyrolytic composition of the upper mantle rocks is also strongly correlated with the composition of chondritic meteorites, in agreement with the hypothesis of a chondritic origin of the Earth.

Mantle peridotites are found with different degrees of depletion (mass fraction lost) by partial melting. More depleted material is denoted as harzburgite and the relatively undepleted peridotite is known as lherzolite. During progressive partial melting the mineral composition of the residual rock material, a mineral assemblage consisting of olivine, pyroxene and garnet, shifts towards the olivine composition. The olivine enriched harzburgitic residue appears to be the chemical complement of the basaltic melt product, with respect to the original lherzolitic mantle source rock. This depletion relation, between oceanic and continental crust on the one hand and peridotitic mantle rock on the other, is reflected in the element abundance of crust and mantle rocks, illustrated in the following figure:



Chemical abundance of crustal and mantle rocks, normalized with respect to CI chondritic values. Data from (McBride and Gilmour, 2003 [1748]).

This figure shows abundance ratio's relative to the CI-chondritic composition. The curve for mantle rock appears to be relatively close to the chondritic composition, whereas the crustal material is enriched with respect to the mantle in most elements shown.

A notable exception to this crustal enrichment is found for magnesium which appears to be enriched in average mantle peridotite. This is in agreement with the previous observation that the olivine/pyroxene content ratio of the residual increases with the degree of partial melting. Magnesium content increases with the olivine (forsterite  $Mg_2SiO_4$ )/pyroxene  $MgSiO_3$  ratio.

An other observation that can be made from the figure above is the apparent depletion of the siderophile elements Fe and Ni, both in crust and mantle material, with respect to the chondritic composition. This is usually explained by the formation of a liquid Fe, Ni rich metal core of the Earth during the first few million years of the accretion proces, in the early solar system. During this event the molten liquid metal would have differentiated from the silicate mantle, leaving the mantle depleted in siderophile (iron loving) elements.

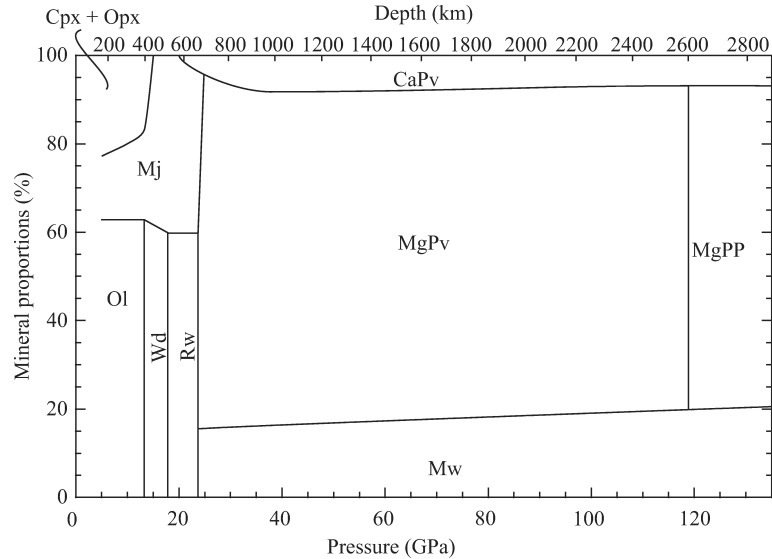
Core formation is also sometimes used as an explanation of the apparent K (potassium) depletion of both mantle and crust with respect to chondrites. In this explanation K is dissolved in liquid iron in significant quantity at high pressure and temperature (Rama Murthy et al., 2003). An alternative explanation for the Earth's K depletion is an escape of K due to significant volatilization during the planetary accretion proces.

**problem: 27.** From Figure ?? it can be concluded that the Earth's mantle and crust lost roughly 2/3 of its original iron content corresponding to a chondritic composition. Verify how this iron-depletion of crust and mantle could be explained by differentiation of the Earth's mostly-iron core. Use the following data in your argument: a) The mass fraction of the core  $X_c = M_c/M_\oplus = 0.315$ . b) The Fe mass fraction  $X_{mFe} \sim 10\%$  of the pyrolytic mantle, c) The mass fraction of lighter elements in the core - (S, Si, O) amounts to about 20%. d) The Fe mass fraction of the bulk Earth  $X_{\oplus Fe} \sim 33\%$  (Fig. ??)

### 9.2.10 Phase transitions as anchor points of the geotherm

Major phase boundaries in the Earth's mantle and core have been identified with sharp transitions in the seismic wave velocities and the density distribution of the PREM model.

The depth distribution of the mineral composition for a pyrolytic mantle model is shown in the following figure:



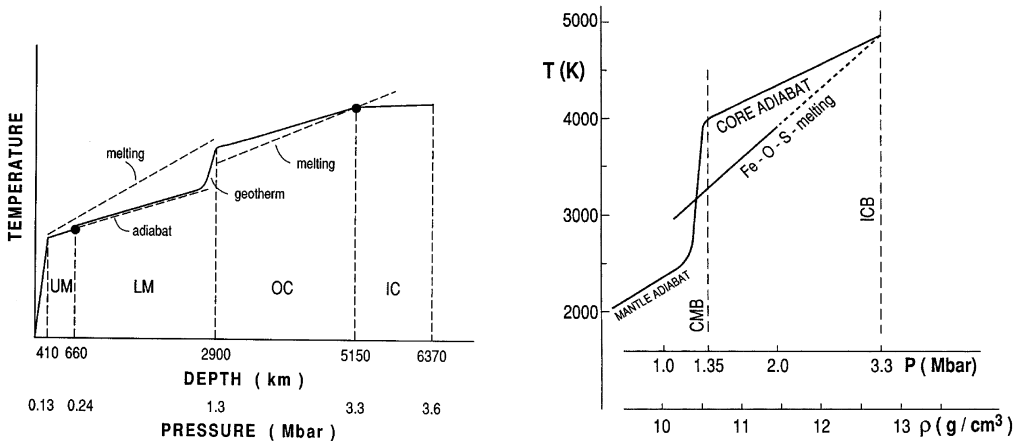
Pressure/depth distribution of mineral assemblage for a pyrolytic mantle model. Cpx: clinopyroxene, Opx: orthopyroxene, Mj: majorite garnet, Ol: olivine, Wd: wadsleyite, Rw: ringwoodite, CaPv:  $\text{CaSiO}_3$  perovskite MgPv:  $\text{MgSiO}_3$ -rich perovskite, MgPP:  $\text{MgSiO}_3$ -rich post-perovskite, Mw: magnesiowüstite. (From: (Hirose, 2007))

This figure clearly illustrates the different mineral composition of the upper and lower mantle regions separated by the major phase boundary near 660 km depth ( $\sim 24$  GPa), where the ringwoodite polymorph of olivine,  $(\text{Mg}, \text{Fe})_2\text{SiO}_4$ , transforms (dissociates) into a mineral assemblage of perovskite,  $(\text{Mg}, \text{Fe})\text{SiO}_3$  and magnesiowüstite,  $(\text{Mg}, \text{Fe})\text{O}$ .

For a given mantle composition, for instance for a pyrolytic mantle, the pressure-temperature mineral phase diagram can be determined for the relevant  $P, T$  range of the Earth's mantle by HPT experiments and mineral physics theory. A sharp transition at a pressure  $P_t$  in the PREM model can then be located at the corresponding pressure in the phase diagram by the intersection of the  $P_t$  isobar with the diagram phase boundaries. The (possibly multiple) intersection points define the corresponding transition temperature  $T_t$ . The pressure-temperature point located in the phase diagram defines an 'anchor point' that constrains the geotherm. In this procedure the phase transition is used as a mantle/core thermometer.

This way several  $(P, T)$  'anchor points' of the geotherm have been determined, related to the solid state phase transition near 660 km depth and the solid/liquid inner/outer core boundary at 1220 km from the Earth's centre.

The following figure from Boehler (1996) [219] illustrates the determination of anchor points of the geotherm at the phase boundary near 660 km depth ( $P_{660} = 24$  GPa,  $T_{660} = 1900 \pm 100$  K) and at the boundary between the outer and inner core at 5150 km depth, ( $P_{ICB} = 330$  GPa,  $T_{ICB} = 4850 \pm 200$  K).



Schematic radial temperature distribution in the mantle and core, constrained by major phase transitions (Boehler, 1996), (UM-upper mantle, LM lower mantle, OC outer core, IC inner core). The temperature of the upper/lower mantle boundary is constrained by the  $\gamma$ -spinel to postspinel phase

transition at 660 km depth. The temperature at the inner/outer core boundary at 5150 km depth (radius 1220 km) is constrained by the melting temperature of the hypothetical core ‘Fe-O-S’ alloy. The right hand frame shows a schematic core temperature distribution (geotherm) labeled ‘CORE ADIABAT’ in the liquid outer core versus pressure and the melting curve (liquidus) of the core ‘Fe-O-S’ alloy. (CMB core-mantle boundary, ICB inner core boundary). The ICB is determined by the intersection of the liquidus and the geotherm. During core cooling the ICB moves outward as the inner core grows by crystallisation.

Starting from these anchor points the temperature is then extrapolated from both sides to the core mantle boundary at 2900 km depth. For this temperature extrapolation assumptions have to be made about the dominant heat transport mechanism and in this case it is assumed that heat transport operates mainly through thermal convection. This will be further investigated in later sections dealing with heat transport in the Earth’s mantle.

**problem: 28.** Estimate the temperature near the bottom of the mantle by adiabatic extrapolation of the temperature  $T_{660} \sim 1900\text{K}$  of the phase transition near 660 km depth, to the depth of the core mantle boundary, using the general expression for the adiabat in a homogeneous layer.

Hints: apply the result of problem 26 and assume uniform values of the ‘scale height parameter’  $H_T = (\alpha g/c_P)^{-1}$ , with  $\alpha = 2 \cdot 10^{-5}\text{K}^{-1}$ ,  $g = 10\text{ms}^{-2}$ ,  $c_P = 1250\text{Jkg}^{-1}\text{K}^{-1}$ . Further: approximate the adiabat by a linear depth function, in agreement with the schematic diagram of Boehler (1996) - see figure above - to obtain a uniform adiabatic temperature gradient.

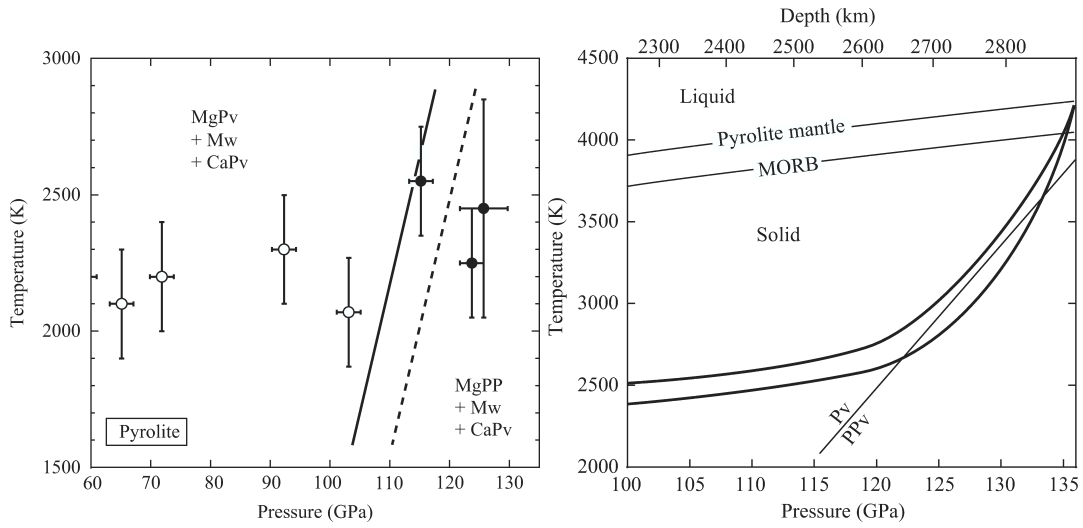
The ‘head’ of the extrapolated outer core adiabat is at a temperature of approximately 4000 K and the ‘foot’ of the lower mantle adiabat at approximately 2700 K. This result indicates a large temperature contrast of about 1300 K across the CMB.

How can such a large contrast be explained physically? As we will see later, this can be explained by interpreting the CMB as a boundary between two separately convecting fluid layers, each with a thermal boundary layer where the main heat transport mechanism shifts from convection in the interior of the fluid layers, to conduction near the boundary interface, where vertical convective transport vanishes with the flow velocity component normal to the boundary. Separately convecting layers are in agreement with the large density contrast across the CMB where the density almost doubles, as illustrated in the PREM profile. The resulting strong temperature contrast across the CMB is consistent with a lower mantle in a state of vigorous thermal convection.

**problem: 29.** Explain why we can not turn this argument around and conclude from these indications for a strong temperature contrast at CMB that the mantle convects vigorously.

Hint: Check Appendix ?? for the assumptions made for an adiabatic geotherm in the lower mantle.

More recent developments, providing independent information, shed new light on the temperature distribution in the bottom layer of the lower mantle. A previously unknown mantle phase transition has been identified, in the main constituent magnesium-perovskite, to a ( $\sim 1.5\%$ ) denser phase (post-perovskite) both in experimental HPT and theoretical (mineral physics) work at temperatures and pressure conditions corresponding to a region in the lowermost mantle close to the core-mantle boundary. This is illustrated in the figure hereafter showing experimental data points delineating the phase boundary.



Left: phase relations near the bottom of the mantle for pyrolytic material (Hirose, 2007). The solid- and dashed line correspond to different pressure calibration of the HPT experiments. The Clapeyron slope of the phase boundary is assumed  $11.5 \text{ MPa/K}$ . CaPv:  $\text{CaSiO}_3$  perovskite MgPv:  $\text{MgSiO}_3$ -rich perovskite, MgPP:  $\text{MgSiO}_3$ -rich post-perovskite, Mw: magnesiowüstite. Right: schematic temperature profiles in the lower mantle in relation to the perovskite (PV) to postperovskite (PPV) phase transition and the melting curve for pyrolytic mantle material and subducted basaltic crust (MORB) (Hirose et al (2007) [1199]).

This phase transition has a high valued positive slope of the phase boundary (Clapeyron parameter)  $dP_t/dT \sim 10 \text{ MPa K}^{-1}$ . The intercept of the phase boundary with the core-mantle boundary at  $\sim 136 \text{ GPa}$  appears to be at a temperature several hundred Kelvin below the temperature of the liquid metal outer core as illustrated in the right part of the above figure. As a consequence the geotherm may intersect the phase boundary at multiple depth's, depending on the local mantle temperature, a phenomenon known as 'double crossing' (Hernlund et al., 2005). When a double crossing of the geotherm occurs, a thin layer exists directly bordering the core, where perovskite is the stable phase while on top of this bottom PV layer, a postperovskite layer exists with a variable thickness of up to several hundred kilometers.

A further implication of the phase diagram illustrated in is that the PPV layer will be absent in hot regions where the geotherm is completely above the PV-PPV phase boundary. This post-perovskite phase boundary has also been associated with the top of the D'' layer at variable height  $\sim 100 - 300 \text{ km}$  above the CMB (Lay et al., 2005).

These seismological interpretations of the postperovskite phase boundary have been based on limited resolution methods applying 1-D radial velocity models. In a more recent development, techniques related to seismic wave migration methods, used in the oil and gas exploration industry, are applied to delineate reflecting interfaces in 2-D and 3-D models in seismic stratigraphy of the CMB region (van der Hilst et al., 2007). This way the spatial resolution has been brought down to about 20 km, allowing mapping of detailed structures in the lowermost mantle. An important target of these high resolution seismic methods is the bottom interface of a postperovskite layer, associated with the 'double crossing', where mantle material transforms back from postperovskite into perovskite due to the steep increase in temperature in the bottom thermal boundary layer, illustrated in the figure above, related to the temperature contrast across the CMB.

In a similar way as for the spinel-postspinel phase transition the temperature at the seismic interfaces can then be estimated from the given depth(pressure) and the experimentally determined parameters of the postperovskite phase transition. This way a mantle adiabatic geotherm and boundary layer structure (error function) have been estimated with a CMB temperature  $T_{cmb} \sim 4000 \text{ K}$  (van der Hilst et al., 2007). The 'foot' of the adiabatic mantle geotherm derived from this lies at a temperature of approximately 2500 K. Both the estimated CMB temperature and the foot of the adiabat seem to confirm independent earlier findings based on adiabatic temperature extrapolation over large depth ranges (Boehler, 1996 [219]).

The temperature contrast of about 1500 K across the core-mantle boundary resulting from these interpretations identify the bottom of the mantle as a thermal boundary layer, characteristic of a vigorously convecting layer where the boundary interface has a fixed or slowly varying temperature, as we will see in the section on heat transport in the mantle. As such these results from mineral physics and seismology have produced new evidence for strong mantle convective flow near the core-mantle boundary.

### 9.3 Programming exercises - February 2020

#### 9.3.1 Background

We have seen that the calculation of the gravity vector and/or the gravity potential for a mass distribution in 3D space is of the form

$$\xi(\vec{r}) = \mathcal{G} \int_V f(\vec{r}, \vec{r}') \rho(\vec{r}') d\vec{r}'$$

where  $\xi$  is either  $g_x$ ,  $g_y$ ,  $g_z$  or  $U$  and  $f$  is a function of the coordinates  $\vec{r}$  and  $\vec{r}'$ .

Let us now assume that the body under consideration can be subdivided into  $N_e$  smaller blocks/elements. But virtue of the linearity of the integral, we have

$$\xi(\vec{r}) = \mathcal{G} \sum_{e=1}^{N_e} \int_{V_e} f(\vec{r}, \vec{r}') \rho(\vec{r}') d\vec{r}'$$

We can further assume that inside each element the density is constant so that

$$\xi(\vec{r}) = \mathcal{G} \sum_{e=1}^{N_e} \rho_e \int_{V_e} f(\vec{r}, \vec{r}') d\vec{r}'$$

We will now make a strong assumption which is only valid when elements are (very) small: we will assume that we can replace  $f(\vec{r}, \vec{r}')$  by  $f(\vec{r}, \vec{r}_e)$  where  $\vec{r}_e$  is the location of the 'center' of the element. We then get:

$$\xi(\vec{r}) = \mathcal{G} \sum_{e=1}^{N_e} \rho_e f(\vec{r}, \vec{r}_e) \int_{V_e} d\vec{r}'$$

And finally the integral term is simply the volume of the element  $V_e$ :

$$\xi(\vec{r}) = \mathcal{G} \sum_{e=1}^{N_e} \rho_e f(\vec{r}, \vec{r}_e) V_e$$

In the end, assuming that the body of interest can be split into many small elements of constant density, the gravity fields at a location  $\vec{r} = (x, y, z)$  can be computed as follows:

$$\begin{aligned} g_x(x, y, z) &= \mathcal{G} \sum_{e=1}^{N_e} \rho_e V_e \frac{x - x_e}{|\vec{r} - \vec{r}_e|^3} \\ g_y(x, y, z) &= \mathcal{G} \sum_{e=1}^{N_e} \rho_e V_e \frac{y - y_e}{|\vec{r} - \vec{r}_e|^3} \\ g_z(x, y, z) &= \mathcal{G} \sum_{e=1}^{N_e} \rho_e V_e \frac{z - z_e}{|\vec{r} - \vec{r}_e|^3} \\ U(x, y, z) &= -\mathcal{G} \sum_{e=1}^{N_e} \rho_e V_e \frac{1}{|\vec{r} - \vec{r}_e|} \end{aligned}$$

where

$$|\vec{r} - \vec{r}_e| = \sqrt{(x - x_e)^2 + (y - y_e)^2 + (z - z_e)^2}$$

The following exercises are designed to test this approach which lends itself to numerical implementation. The basic idea is rather simple: generate a cloud of points in a regular manner such that we can assign them a corresponding volume and a density when they are in the geometry of interest, and then use the formula above to compute the gravity vector and potential, and finally compare these values with the analytical solutions we derived for simple spherical bodies.

INSERT HERE FIGURE

### Exercise 1: Full sphere

- In a domain of size  $2R \times 2R \times 2R$  centered on the origin compute and store the coordinates of  $N^3$  points (use  $R = 6371\text{km}$ ). Please use arrays `x`, `y` and `z` to store the coordinates. These arrays are  $N^3$  long.
- Compute the associated volume  $dV$  of a point as a function of  $R$  and  $N$ .
- For points inside a sphere of radius  $R$  assign a density  $\rho_0 = 3000\text{kg/m}^3$  and zero otherwise, store these values in the `rho` array.
- Compute the mass of the system
- Compute the moment of inertia of the system (use Eq. 801).
- Compute the gravity potential and vector components  $H = 10^m$  meters above the north pole with  $m = 0, 1, 2, 3, ..8$ . Compute first the position of these points and store them in arrays `xm`, `ym` `zm` before using these for gravity calculations.
- Plot the computed quantities as a function of  $H$  and plot on the same graphic the analytical values.
- Repeat the exercise with different values of  $N \in (10, 20, 30, 40, 50)$ . For the mass and moment of inertia, plot the relative error as a function of  $h$ . Discuss.
- Fix  $m = 4$ . Progressively increase  $N$  and record the absolute error on the gravity vector norm as a function of  $dV^{1/3}$ . Plot this in log-log scale. Discuss.
- Use the `prem_density` function to assign the density to the points. Compute the mass of the planet with this new density distribution and compare it with the mass of the Earth. Compute the gravity at the surface.

### Exercise 2: Hollow sphere

This is based on the previous exercise.

- For points with radius  $r$  such that  $R/2 \leq r \leq R$  assign a density  $\rho_0 = 3000\text{kg/m}^3$  and zero otherwise.
- Compute the gravity potential and vector components on the  $x$  axis between  $r = 0$  and  $r = 3R$  with steps of  $R/100$ .
- Plot the results and the analytical solution on the same plot as a function of  $r$ .
- Repeat the exercise with different values of  $N$ . Discuss.

### Exercise 3: Full sphere - revisited

We are now going to re-do the first exercise but this time we do not want any point outside of the sphere. We shall therefore use the spherical coordinates (see Section 3.1.3). We will use three for loops, one over  $r \in [0, R]$  values, one over  $\theta \in [0, \pi]$  values and one over  $\phi \in [-\pi, \pi]$  values. The number of points in each direction in this space is still  $N$  so that the total number of points is still  $N^3$ .

- Compute and store the coordinates of the points in the  $r, \theta, \phi$  space. Store these in arrays `r`, `theta`, `phi`.
- Use these coordinates to compute and store the Cartesian coordinates of these points.
- Plot this cloud of points in 3D. Discuss.
- Repeat the calculations of the first exercise.
- The cost of the calculation is the same as in exercise 1, but what about accuracy?

## 9.4 WORK in PROGRESS. DUH.

We start from the Poisson equation for the gravity potential:

$$\Delta U = 4\pi\rho\mathcal{G} \quad (867)$$

As a consequence, inside a domain where  $\rho = 0$ , the equation becomes  $\Delta U = 0$ .

Let us assume that the spherical coordinates are appropriate for the problem at hand, and that the potential can be decomposed as follows:

$$U(r, \theta, \phi) = U_r(r)U_\perp(\theta, \phi)$$

The full Laplacian operator in spherical coordinates is given by<sup>77</sup>:

$$\Delta U = \underbrace{\frac{1}{r^2} \frac{\partial}{\partial r} \left( r^2 \frac{\partial U}{\partial r} \right)}_{\Delta_r} + \underbrace{\frac{1}{r^2 \sin \theta} \frac{\partial}{\partial \theta} \left( \sin \theta \frac{\partial U}{\partial \theta} \right)}_{\Delta_\perp} + \frac{1}{r^2 \sin^2 \theta} \frac{\partial^2 U}{\partial \phi^2}$$

we then have:

$$(\Delta_r + \Delta_\perp)(U_r U_\perp) = 0$$

i.e.,

$$U_\perp \Delta_r U_r + U_r \Delta_\perp U_\perp = 0$$

Assuming  $U_\perp = \sum_l \sum_m U_{lm} Y_{lm}$ , knowing that spherical harmonics functions verify

$$r^2 \Delta_\perp Y_l^m(\theta, \phi) = -l(l+1)Y_l^m(\theta, \phi)$$

and assuming for now that the problem at hand is 1st degree ( $l=1$ ), then

$$\Delta_\perp Y_l^m(\theta, \phi) = -\frac{2}{r^2} Y_l^m(\theta, \phi)$$

and then

$$\Delta_r U_r - U_r \frac{2}{r^2} = 0$$

make a link with my 2018 paper.

---

<sup>77</sup>[https://en.wikipedia.org/wiki/Laplace\\_operator](https://en.wikipedia.org/wiki/Laplace_operator)

In spherical coordinates, the Laplacian is given by

$$\Delta = \frac{1}{r^2} \frac{\partial}{\partial r} \left( r^2 \frac{\partial}{\partial r} \right) + \frac{1}{r^2 \sin^2 \theta} \frac{\partial}{\partial \theta} \left( \sin \theta \frac{\partial}{\partial \theta} \right) + \frac{1}{r^2 \sin^2 \theta} \frac{\partial^2}{\partial \phi^2}$$

We wish to solve Laplace's equation  $\Delta T(r, \theta, \phi) = 0$  using the method of separation of variables:

$$T(r, \theta, \phi) = R(r)\Theta(\theta)\Phi(\phi)$$

We can insert this decomposition into the Laplace equation and multiply it by  $r^2/R\Theta\Phi$  to obtain

$$\frac{1}{R} \frac{d}{dr} \left( r^2 \frac{dR}{dr} \right) + \frac{1}{\Theta} \frac{1}{\sin \theta} \frac{d}{d\theta} \left( \sin \theta \frac{d\Theta}{d\theta} \right) + \frac{1}{\Phi} \frac{1}{\sin^2 \theta} \frac{d^2\Phi}{d\phi^2} = 0$$

For reasons that will become clear later, the separation constant is taken to be  $-m^2$ :

$$\frac{1}{\Phi} \frac{d^2\Phi}{d\phi^2} = -m^2 \quad (868)$$

and

$$-\frac{\sin \theta}{\Theta} \frac{d}{d\theta} \left( \sin \theta \frac{d\Theta}{d\theta} \right) - \frac{\sin^2 \theta}{R} \frac{d}{dr} \left( r^2 \frac{dR}{dr} \right) = -m^2 \quad (869)$$

The first equation yields

$$\Phi(\phi) = \begin{cases} e^{im\phi} \\ e^{-im\phi} \end{cases} \quad \text{for } m = 0, 1, 2, 3, \dots$$

Note that  $m$  must be an integer since  $\phi$  is a periodic variable and  $\Phi(\phi + 2\pi) = \Phi(\phi)$ . In the case of  $m = 0$ , the general solution is  $\Phi(\phi) = a\phi + b$ , but we must choose  $a = 0$  to be consistent with  $\Phi(\phi + 2\pi) = \Phi(\phi)$ . Hence in the case of  $m = 0$ , only one solution is allowed.

Equation 869 can now be recast in the following form:

$$\frac{1}{R} \frac{d}{dr} \left( r^2 \frac{dR}{dr} \right) = -\frac{1}{\Theta} \frac{1}{\sin \theta} \frac{d}{d\theta} \left( \sin \theta \frac{d\Theta}{d\theta} \right) + \frac{m^2}{\sin^2 \theta} = l(l+1) \quad (870)$$

where the separation variable at this step is denoted by  $l(l+1)$  for reasons that will shortly become clear. The resulting radial equation is

$$\frac{1}{R} \frac{d}{dr} \left( r^2 \frac{dR}{dr} \right) = l(l+1)$$

or,

$$r^2 \frac{d^2R}{dr^2} + 2r \frac{dR}{dr} - l(l+1)R = 0$$

The solution is of the form  $R = r^s$ . To determine the exponent  $s$ , we insert this solution back into the above ODE. The end result is

$$s(s+1) = l(l+1) \quad \Rightarrow \quad s = l \text{ or } s = -l-1$$

or,

$$R(r) = \begin{cases} r^l \\ r^{-(l+1)} \end{cases}$$

Eq. (870) also yields:

$$\frac{1}{\sin \theta} \frac{d}{d\theta} \left( \sin \theta \frac{d\Theta}{d\theta} \right) + \left[ l(l+1) - \frac{m^2}{\sin^2 \theta} \right] \Theta = 0$$

One can then carry out the following change of variables  $x = \cos \theta$  and  $y = \Theta(\theta)$  so that the above equation reduces to:

$$(1-x^2) \frac{d^2y}{dx^2} - 2x \frac{dy}{dx} + \left[ l(l+1) - \frac{m^2}{\sin^2 \theta} \right] y = 0$$

This equation is the differential equation for associated Legendre polynomials<sup>78</sup>. We then have

$$y = P_l^m(x) \quad \text{for } l = 0, 1, 2, 3, \dots \quad \text{and } m = -l, -l+1, \dots, 0, \dots, l = 1, l$$

and

$$P_l^m(x) = \frac{(-1)^m}{2^l l!} (1-x^2)^{m/2} \frac{d^{l+m}}{dx^{l+m}} (x^2 - 1)^l$$

with  $m \geq 0$  and  $l \geq 0$ .

In our case the differential equation for the associated Legendre polynomials, given above, depends on  $m^2$  and is therefore not sensitive to the sign of  $m$ . Consequently,  $P_l^m(x)$  and  $P_l^{-m}(x)$  must be equivalent solutions and hence proportional to each other, and one can show that

$$P_l^{-m}(\cos \theta) = (-1)^m \frac{(l-m)!}{(l+m)!} P_l^m(\cos \theta) \quad (871)$$

Combining all the results obtained above, we have found that the general solution to Laplaces equation is of the form

$$T(r, \theta, \phi) = \left\{ \begin{array}{c} r^l \\ r^{-(l+1)} \end{array} \right\} P_l^m(\cos \theta) \left\{ \begin{array}{c} e^{im\phi} \\ e^{-im\phi} \end{array} \right\}$$

where  $l = 0, 1, 2, 3, \dots$  and  $m = -l, -l+1, \dots, l-1, l$ .

When solving the Laplaces equation in spherical coordinates, it is traditional to introduce the spherical harmonics,  $Y_l^m(\theta, \phi)$ :

$$Y_l^m(\theta, \phi) = (-1)^m \sqrt{\frac{2l+1}{4\pi} \frac{(l-m)!}{(l+m)!}} P_l^m(\cos \theta) e^{im\phi} \quad \text{for } l = 0, 1, 2, 3, \dots \text{ and } m = -l, -l+1, \dots, l-1, l \quad (872)$$

The phase factor (1), introduced originally by Condon and Shortley, is convenient for applications in quantum mechanics. Note that eq. (871) implies that

$$Y_l^m(\theta, \phi) = (1)^m Y_l^m(\theta, \phi)$$

where the star means complex conjugation.

The normalization factor in eq. (872) has been chosen such that the spherical harmonics are normalized to one. In particular, these functions are orthonormal and complete. The orthonormality relation is given by:

$$\int Y_l^m(\theta, \phi) Y_{l'}^{m'}(\theta, \phi) d\Omega = \delta_{ll'} \delta_{mm'}$$

where  $d\Omega = \sin \theta d\theta d\phi$  is the differential solid angle in spherical coordinates.

**Remark.** In [2905] the authors use a normalized associated Legendre polynomial that is related to the associated Legendre polynomial  $P_l^m$  as:

$$p_{lm}(\theta, \phi) = \sqrt{\frac{2l+1}{2\pi(1+\delta_{m0})} \frac{(l-m)!}{(l+m)!}} P_l^m(\cos \theta)$$

Note the absence of the  $(-1)^m$  term and the presence of the kronecker delta in the denominator.

 Relevant Literature[596]

---

<sup>78</sup>[https://en.wikipedia.org/wiki/Associated\\_Legendre\\_polynomials](https://en.wikipedia.org/wiki/Associated_Legendre_polynomials)

## Stone 01: simple analytical solution (D&H)

This fieldstone was developed in collaboration with Job Mos.

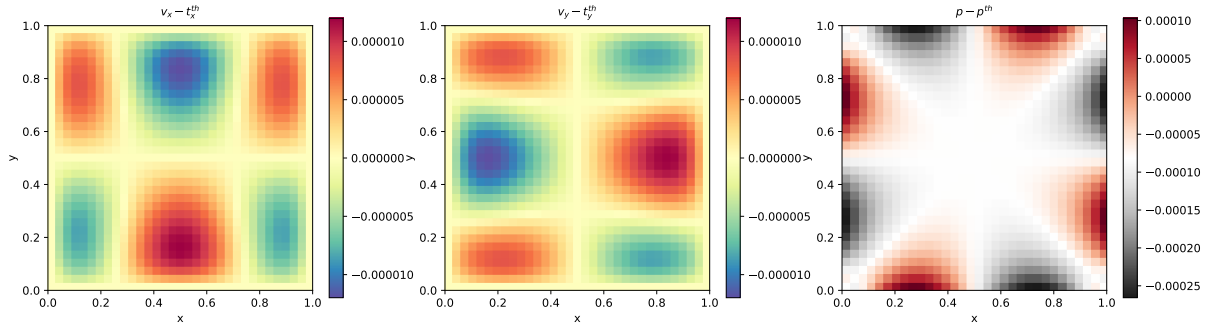
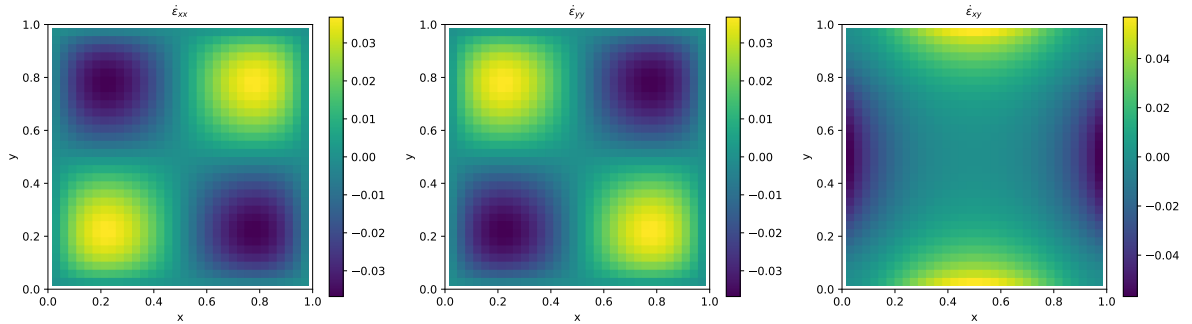
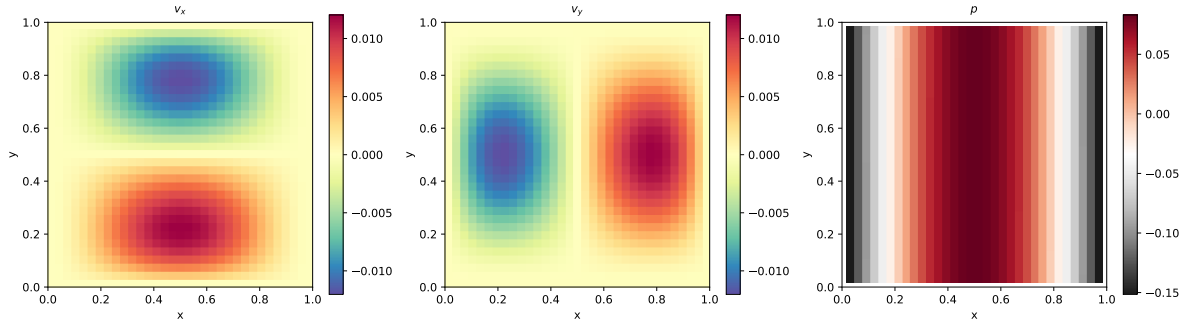
This benchmark is taken from [711] and is described fully in section 8.6. In order to illustrate the behavior of selected mixed finite elements in the solution of stationary Stokes flow, we consider a two-dimensional problem in the square domain  $\Omega = [0, 1] \times [0, 1]$ , which possesses a closed-form analytical solution. The problem consists of determining the velocity field  $\mathbf{v} = (u, v)$  and the pressure  $p$  such that

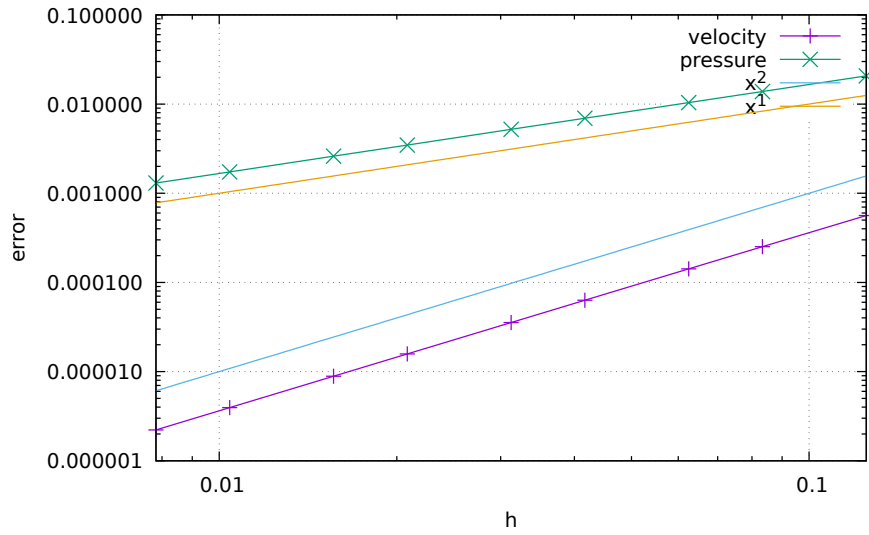
$$\eta \Delta \vec{v} - \vec{\nabla} p + \vec{b} = \vec{0} \quad \text{in } \Omega$$

$$\vec{\nabla} \cdot \vec{v} = 0 \quad \text{in } \Omega$$

$$\vec{v} = \vec{0} \quad \text{on } \Gamma_D$$

where the fluid viscosity is taken as  $\eta = 1$ .

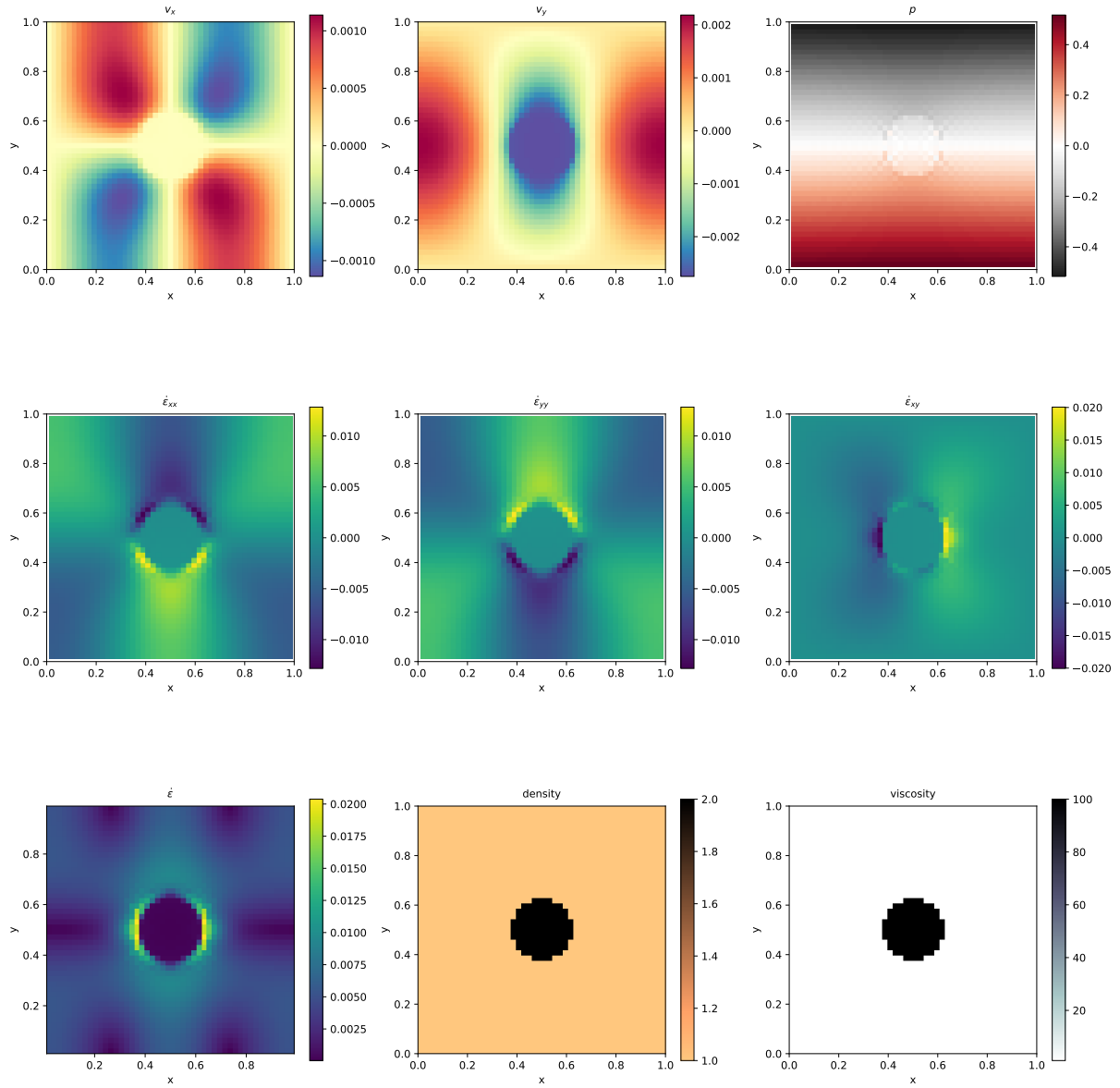




Quadratic convergence for velocity error, linear convergence for pressure error, as expected.

## Stone 02: Stokes sphere

The domain is a unit square. The fluid is characterised by  $\rho = 1$  and  $\eta = 1$  while the sphere is characterised by  $\rho = 2$  and  $\eta = 1000$ . The gravity vector is  $\vec{g} = (0, -1)$ . Boundary conditions are free slip on all sides. Viscosity and density directly computed at the quadrature points.



## Stone 03: Convection in a 2D box

This benchmark deals with the 2-D thermal convection of a fluid of infinite Prandtl number in a rectangular closed cell. In what follows, I carry out the case 1a, 1b, and 1c experiments as shown in [209]: steady convection with constant viscosity in a square box.

The temperature is fixed to zero on top and to  $\Delta T$  at the bottom, with reflecting symmetry at the sidewalls (i.e.  $\partial_x T = 0$ ) and there are no internal heat sources. Free-slip conditions are implemented on all boundaries.

The Rayleigh number is given by

$$Ra = \frac{\alpha g_y \Delta T h^3}{\kappa \nu} = \frac{\alpha g_y \Delta T h^3 \rho^2 C_p}{k \mu} \quad (873)$$

In what follows, I use the following parameter values:  $L_x = L_y = 1, \rho_0 = c_P = k = \mu = 1, T_0 = 0, \alpha = 10^{-2}, g = 10^2 Ra$  and I run the model with  $Ra = 10^4, 10^5$  and  $10^6$ .

The initial temperature field is given by

$$T(x, y) = (1 - y) - 0.01 \cos(\pi x) \sin(\pi y) \quad (874)$$

The perturbation in the initial temperature fields leads to a perturbation of the density field and sets the fluid in motion.

Depending on the initial Rayleigh number, the system ultimately reaches a steady state after some time.

The Nusselt number (i.e. the mean surface temperature gradient over mean bottom temperature) is computed as follows [209]:

$$Nu = L_y \frac{\int_0^{L_x} \frac{\partial T}{\partial y} (y = L_y) dx}{\int_0^{L_x} T(y = 0) dx} \quad (875)$$

Note that in our case the denominator is equal to 1 since  $L_x = 1$  and the temperature at the bottom is prescribed to be 1.

The steady state root mean square velocity and Nusselt number measurements are indicated in the following Table alongside those of [209] and [2466]. (Note that this benchmark was also carried out and published in other publications [2567, 15, 953, 181, 637, 1584] but since they did not provide a complete set of measurement values, they are not included in the table.)

		Blankenbach et al	Tackley [2466]
$Ra = 10^4$	$V_{rms}$	$42.864947 \pm 0.000020$	42.775
	$Nu$	$4.884409 \pm 0.000010$	4.878
$Ra = 10^5$	$V_{rms}$	$193.21454 \pm 0.00010$	193.11
	$Nu$	$10.534095 \pm 0.000010$	10.531
$Ra = 10^6$	$V_{rms}$	$833.98977 \pm 0.00020$	833.55
	$Nu$	$21.972465 \pm 0.000020$	21.998

Steady state Nusselt number  $Nu$  and  $V_{rms}$  measurements as reported in the literature.

Food for thought: Looking at the mass, momentum and energy conservation equations, we see that that they are coupled: the temperature enters the rhs of the momentum equation since the density depends on the temperature (Boussinesq approximation) while the velocity is present in the advection term of the energy equation. One should then solve all three equations with  $u, v, p, T$  as unknowns. However this is rarely done in practice and often the system is solved in a segregated way: first solve for  $u, v, p$  assuming  $T$  known, then solving for  $T$  assuming  $u, v, p$  known. If small time steps are used this is a reasonable approach, or, like in this case, when one wishes to compute the steady state of the system rather than an accurate time-evolution of the system. Better schemes are available and one example thereof is explained in Kronbichler et al (2012) [1507].

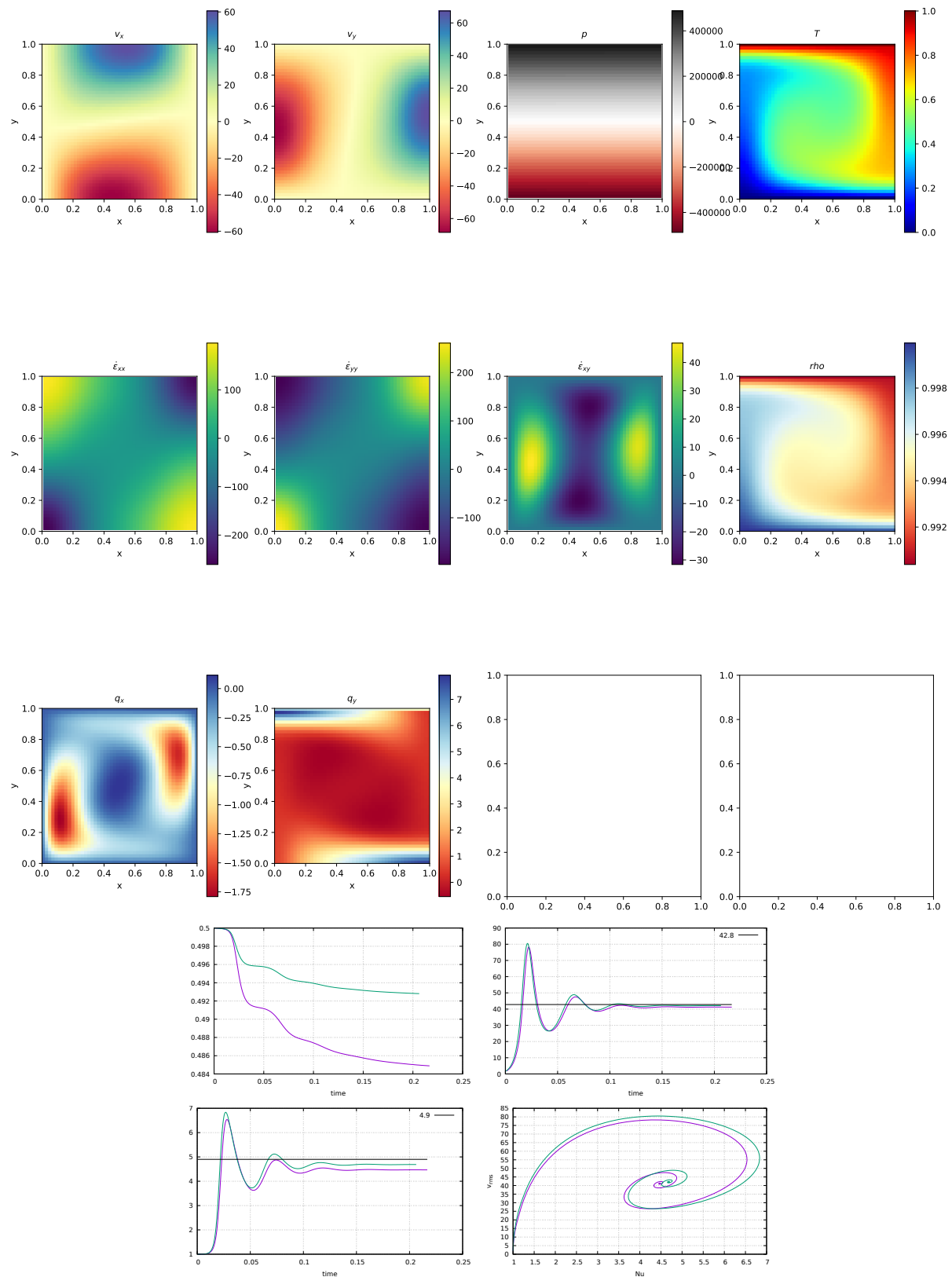
Also, the current version of this stone uses a simple time discretisation of the  $\partial T / \partial t$  term as explained in Section 5.1. A Crank-Nicolson algorithm could easily be implemented as explained in Section ??.

Something must be said about how the Nusselt number is computed. Its calculation requires the integral of the temperature gradient along an edge. Because it is much simpler to compute the temperature gradient in the middle of the element alongside other quantities such as pressure, this (elemental)

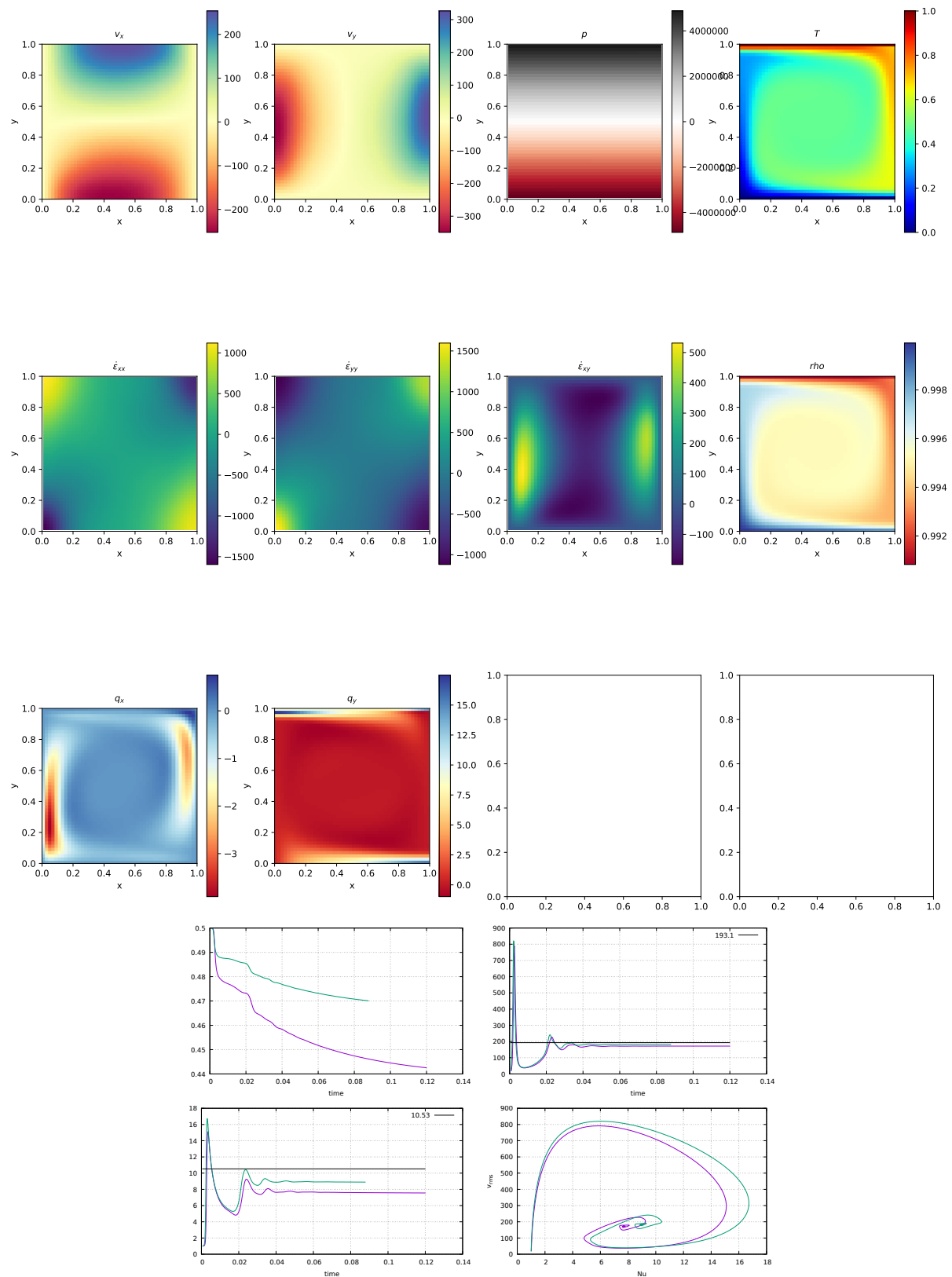
quantity is used in the Nusselt number calculations, which makes it inaccurate and therefore explains the discrepancy between the computed values and those of other publications.

Finally, it is expected that the thickness of the boundary layers decreases with higher Rayleigh number values. As a consequence, in order to appropriately capture those, one needs a higher resolution than at low Ra numbers. This explains why acceptable results are obtained for  $Ra = 10^4$  at low resolution 32x32.

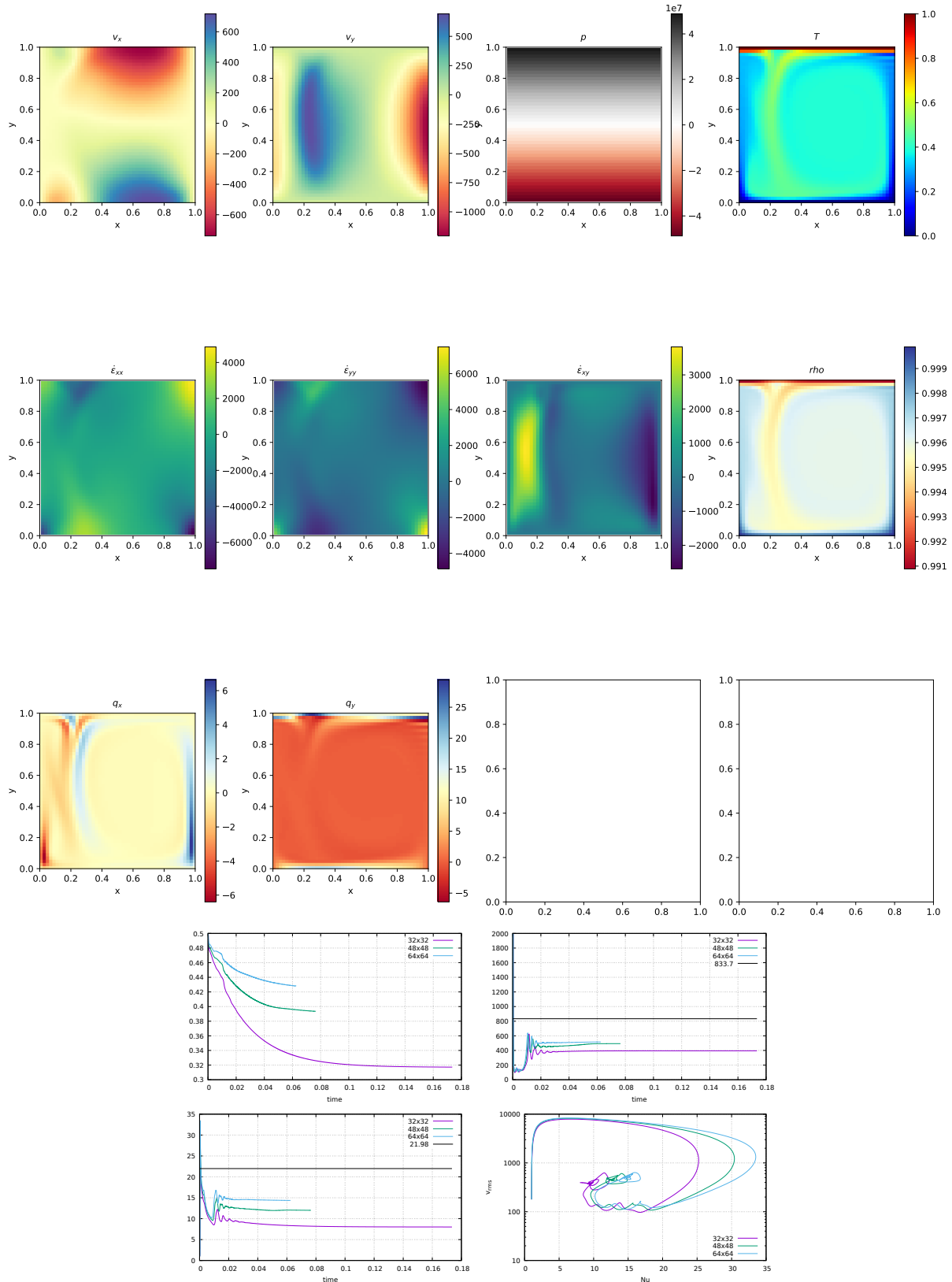
**Results for  $Ra = 10^4$**



**Results for  $Ra = 10^5$**



## Results for $Ra = 10^6$ .



I have tested the influence of the CFL number (0.5 instead of 1) and it does not change much at all.

## Stone 04: The lid driven cavity

The lid driven cavity is a famous Computational Fluid Dynamics test case [1406, 983, 1989, 238, 307, 1068, 2314] and has been studied in countless publications with a wealth of numerical techniques (see [793] for a succinct review) and also in the laboratory [1497].

It models a plane flow of an isothermal isoviscous fluid in a rectangular (usually square) lid-driven cavity. The boundary conditions are no slip on left, right and bottom. The gravity is set to zero as the flow is entirely driven by the moving lid.

### The lid driven cavity problem (`ldc=0`)

In the standard case, the upper side of the cavity moves in its own plane at unit speed, while the other sides are fixed. This thereby introduces a discontinuity in the boundary conditions at the two upper corners of the cavity and yields an uncertainty as to which boundary (side or top) the corner points belong to. In this version of the code the top corner nodes are considered to be part of the lid. If these are excluded the recovered pressure showcases an extremely large checkboard pattern.

This benchmark is usually discussed in the context of low to very high Reynolds number with the full Navier-Stokes equations being solved (with the noticeable exception of [2237, 2238, 443, 762] which focus on the Stokes equation). In the case of the incompressible Stokes flow, the absence of inertia renders this problem instantaneous so that only one time step/Stokes solve is needed.

### The lid driven cavity problem - regularisation I (`ldc=1`)

We avoid the top corner nodes issue altogether by prescribing the horizontal velocity of the lid as follows:

$$u(x) = x^2(1-x)^2. \quad (876)$$

In this case the velocity and its first derivative is continuous at the corners. This is the so-called regularised lid-driven cavity problem [2031].

### The lid driven cavity problem - regularisation II (`ldc=2`)

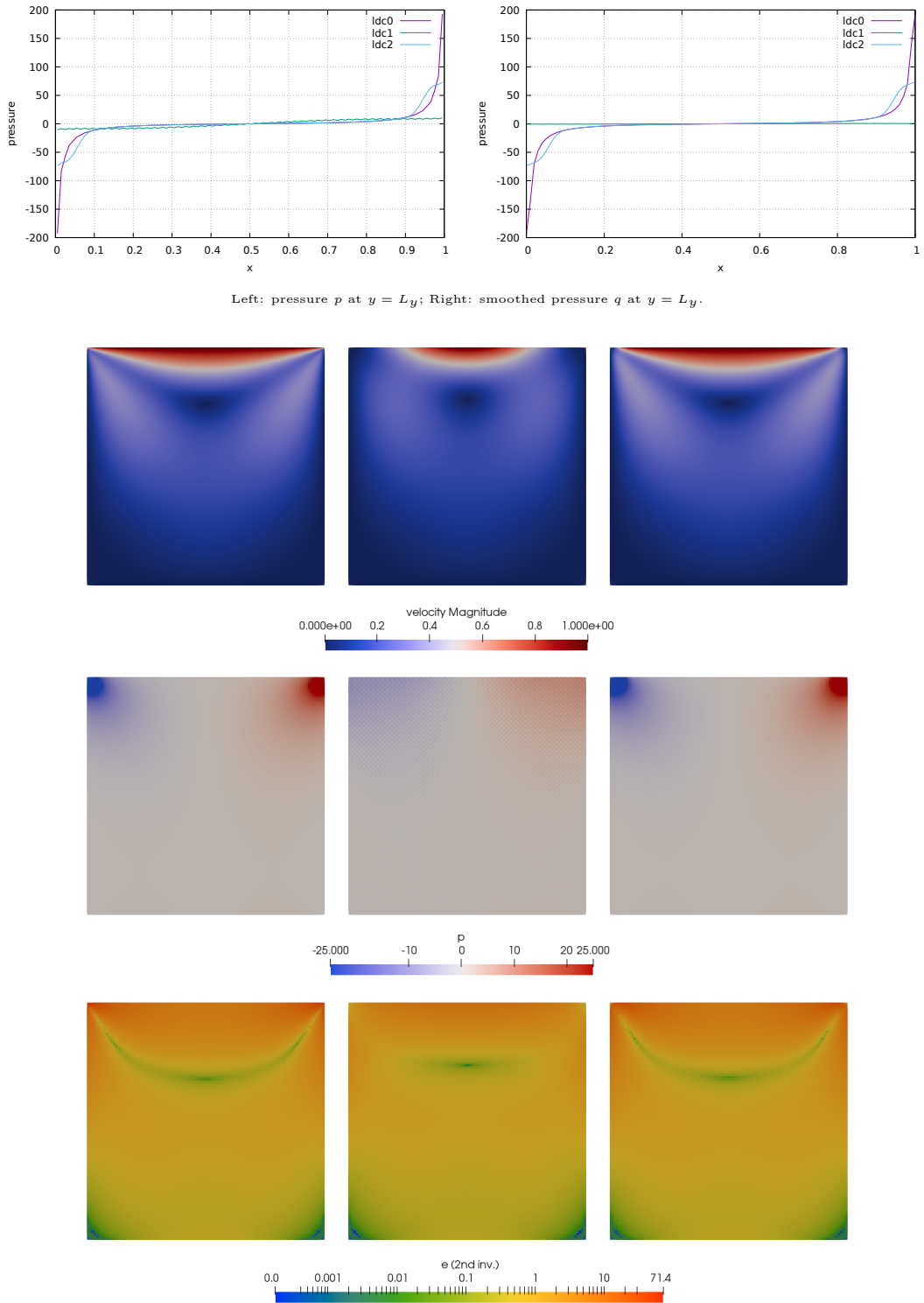
Another regularisation was presented in [663]. Also in Appendix D.4 of [1351]. Here, a regularized lid driven cavity is studied which is consistent in the sense that  $\nabla \cdot \mathbf{v} = 0$  holds also at the corners of the domain. There are no-slip conditions at the boundaries  $x = 0$ ,  $x = 1$ , and  $y = 0$ .

The velocity at  $y = 1$  is given by

$$\begin{aligned} u(x) &= 1 - \frac{1}{4} \left( 1 - \cos\left(\frac{x_1 - x}{x_1}\pi\right) \right)^2 & x \in [0, x_1] \\ u(x) &= 1 & x \in [x_1, 1 - x_1] \\ u(x) &= 1 - \frac{1}{4} \left( 1 - \cos\left(\frac{x - (1 - x_1)}{x_1}\pi\right) \right)^2 & x \in [1 - x_1, 1] \end{aligned} \quad (877)$$

Results are obtained with  $x_1 = 0.1$ .

A 100x100 element grid is used. A zero vertical velocity is prescribed at the top and the exact form of the prescribed horizontal velocity is controlled by the `ldc` parameter.



## Stone 05: SolCx benchmark

The SolCx benchmark is intended to test the accuracy of the solution to a problem that has a large jump in the viscosity along a line through the domain. Such situations are common in geophysics: for example, the viscosity in a cold, subducting slab is much larger than in the surrounding, relatively hot mantle material.

The SolCx benchmark computes the Stokes flow field of a fluid driven by spatial density variations, subject to a spatially variable viscosity. Specifically, the domain is  $\Omega = [0, 1]^2$ , gravity is  $\mathbf{g} = (0, -1)^T$  and the density is given by

$$\rho(x, y) = \sin(\pi y) \cos(\pi x) \quad (878)$$

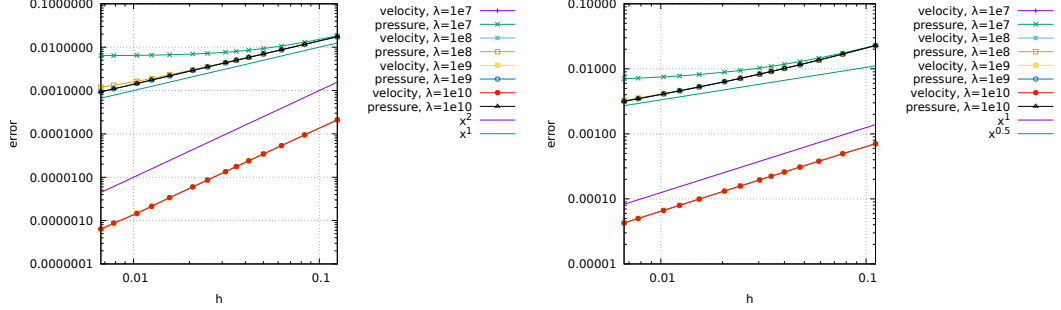
Boundary conditions are free slip on all of the sides of the domain and the temperature plays no role in this benchmark. The viscosity is prescribed as follows:

$$\mu(x, y) = \begin{cases} 1 & \text{for } x < 0.5 \\ 10^6 & \text{for } x > 0.5 \end{cases} \quad (879)$$

Note the strongly discontinuous viscosity field yields a stagnant flow in the right half of the domain and thereby yields a pressure discontinuity along the interface.

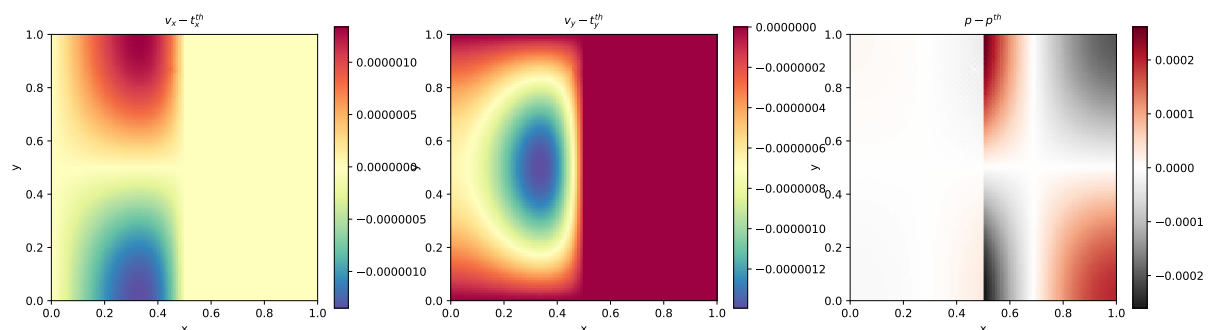
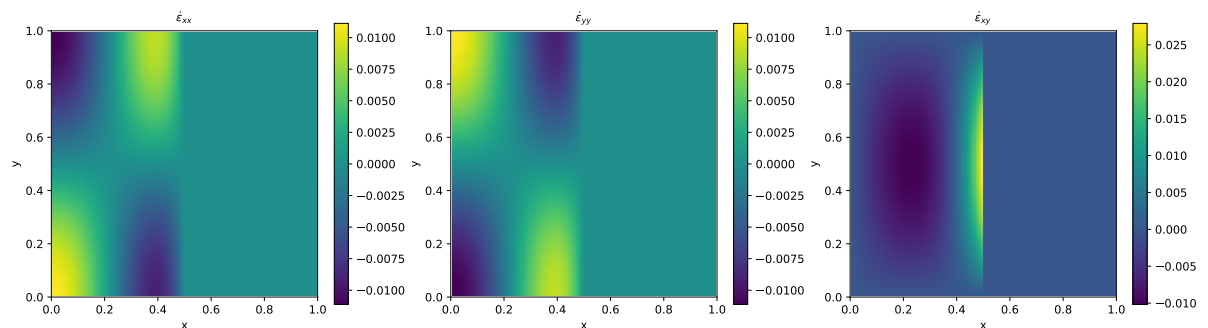
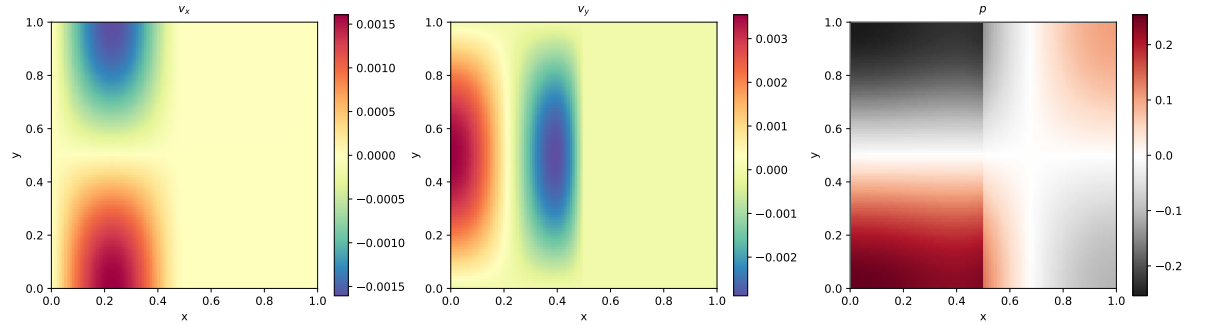
The SolCx benchmark was previously showcased in Duretz et al (2011) [739] (references to earlier uses of the benchmark are available there) and its analytic solution is given in [2912]. It has been carried out in Kronbichler et al (2012) [1507] and Gerya et al (2013) [968]. Note that the source code which evaluates the velocity and pressure fields for both SolCx and SolKz is distributed as part of the open source package Underworld (Moresi et al, 2007 [1846], <http://underworldproject.org>).

In this particular example, the viscosity is computed analytically at the quadrature points (i.e. tracers are not used to attribute a viscosity to the element). If the number of elements is even in any direction, all elements (and their associated quadrature points) have a constant viscosity (1 or  $10^6$ ). If it is odd, then the elements situated at the viscosity jump have half their integration points with  $\mu = 1$  and half with  $\mu = 10^6$  (which is a pathological case since the used quadrature rule inside elements cannot represent accurately such a jump).



Velocity and pressure error convergence as a function of mesh size and for various values of the penalty parameter. Left: even number of elements in each direction; Right: odd numbers.

Because of the high viscosity in the right part of the domain, the penalty parameter should be high enough to insure an incompressible flow and thereby recover the expected convergence rate (at least for the even case). Note that values higher than  $\lambda = 10^{10}$  yield erroneous solutions due to round-off errors.



Various fields for 100x100 mesh

## Stone 06: SolKz benchmark

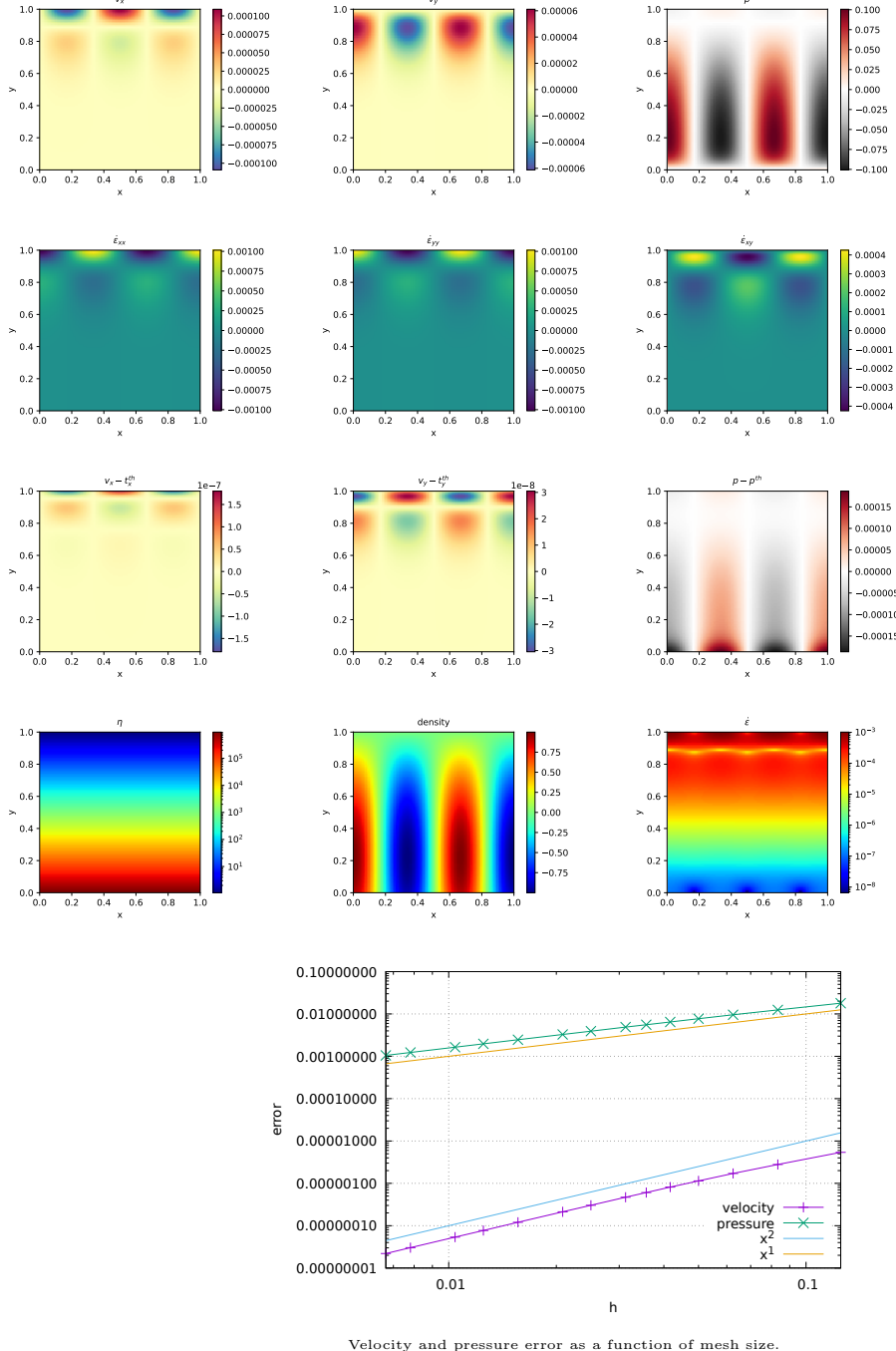
The SolKz benchmark [2143] is similar to the SolCx benchmark, but the viscosity is now a function of the space coordinates:

$$\mu(y) = \exp(By) \quad \text{with} \quad B = 13.8155 \quad (880)$$

It is however not a discontinuous function but grows exponentially with the vertical coordinate so that its overall variation is again  $10^6$ . The forcing is again chosen by imposing a spatially variable density variation as follows:

$$\rho(x, y) = \sin(2y) \cos(3\pi x) \quad (881)$$

Free slip boundary conditions are imposed on all sides of the domain. This benchmark is presented in [2912] as well and is studied in [739] and [968].



Velocity and pressure error as a function of mesh size.

## Stone 07: SolVi benchmark

Following SolCx and SolKz, the SolVi inclusion benchmark solves a problem with a discontinuous viscosity field, but in this case the viscosity field is chosen in such a way that the discontinuity is along a circle. Given the regular nature of the grid used by a majority of codes and the present one, this ensures that the discontinuity in the viscosity never aligns to cell boundaries. This in turns leads to almost discontinuous pressures along the interface which are difficult to represent accurately. Schmid & Podlachikov (2003) [2279] derived a simple analytic solution for the pressure and velocity fields for a circular inclusion under simple shear and it was used in [688, 2451, 739, 1507, 968].

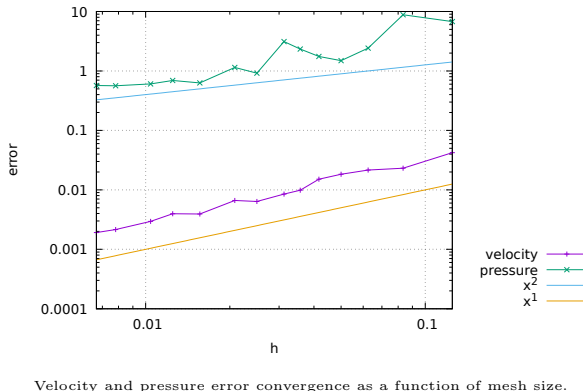
Because of the symmetry of the problem, we only have to solve over the top right quarter of the domain. The analytical solution requires a strain rate boundary condition (e.g., pure shear) to be applied far away from the inclusion. In order to avoid using very large domains and/or dealing with this type of boundary condition altogether, the analytical solution is evaluated and imposed on the boundaries of the domain. By doing so, the truncation error introduced while discretizing the strain rate boundary condition is removed.

A characteristic of the analytic solution is that the pressure is zero inside the inclusion, while outside it follows the relation

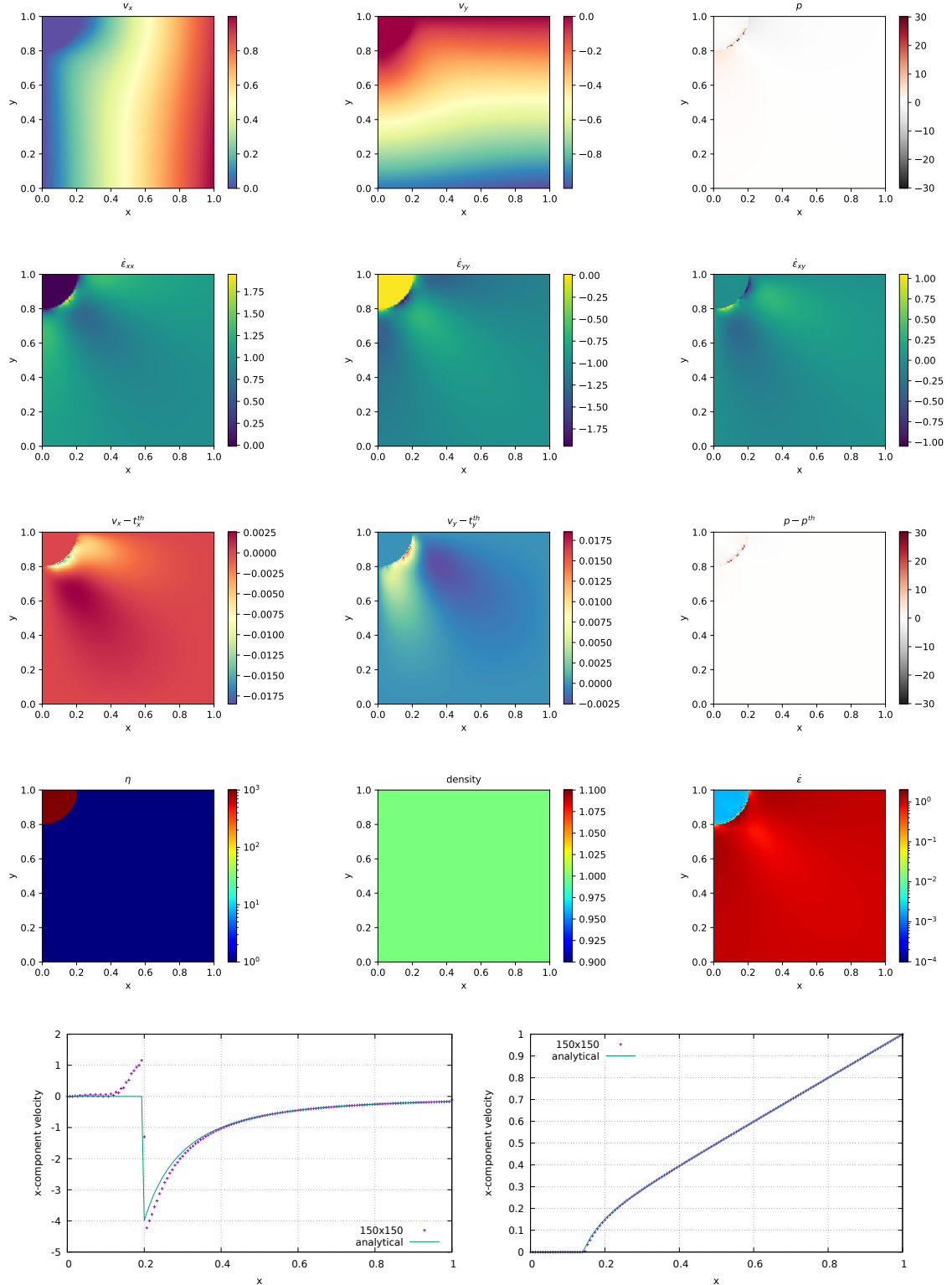
$$p_m = 4\dot{\epsilon} \frac{\mu_m(\mu_i - \mu_m)}{\mu_i + \mu_m} \frac{r_i^2}{r^2} \cos(2\theta) \quad (882)$$

where  $\mu_i = 10^3$  is the viscosity of the inclusion and  $\mu_m = 1$  is the viscosity of the background media,  $\theta = \tan^{-1}(y/x)$ , and  $\dot{\epsilon} = 1$  is the applied strain rate.

Deubelbeiss & Kauss (2008) [688] thoroughly investigated this problem with various numerical methods (FEM, FDM), with and without tracers, and conclusively showed how various averagings lead to different results. Duretz et al (2011) [739] obtained a first order convergence for both pressure and velocity, while Kronbichler et al (2012) [1507] and Gerya et al (2013) [968] showed that the use of adaptive mesh refinement in respectively the FEM and FDM yields convergence rates which depend on refinement strategies.



Velocity and pressure error convergence as a function of mesh size.



Left: Pressure at the bottom of the domain. Right:  $u$  on the diagonal  $x = y$ .

## Stone 08: the indentor benchmark

The punch benchmark is one of the few boundary value problems involving plastic solids for which there exists an exact solution. Such solutions are usually either for highly simplified geometries (spherical or axial symmetry, for instance) or simplified material models (such as rigid plastic solids) [1366].

In this experiment, a rigid punch indents a rigid plastic half space; the slip line field theory gives exact solutions as shown in section 8.7.9. The plane strain formulation of the equations and the detailed solution to the problem were derived in the Appendix of [2533] and are also presented in [945].

The two dimensional punch problem has been extensively studied numerically for the past 40 years [2938, 2937, 491, 490, 1255, 2859, 322, 2091] and has been used to draw a parallel with the tectonics of eastern China in the context of the India-Eurasia collision [2507, 1816]. It is also worth noting that it has been carried out in one form or another in series of analogue modelling articles concerning the same region, with a rigid indenter colliding with a rheologically stratified lithosphere [2006, 650, 1355].

Numerically, the one-time step punch experiment is performed on a two-dimensional domain of purely plastic von Mises material. Given that the von Mises rheology yield criterion does not depend on pressure (see Section 3.22.11), the density of the material and/or the gravity vector is set to zero. Sides are set to free slip boundary conditions, the bottom to no slip, while a vertical velocity  $(0, -v_p)$  is prescribed at the top boundary for nodes whose  $x$  coordinate is within  $[L_x/2 - \delta/2, L_x/2 + \delta/2]$ .

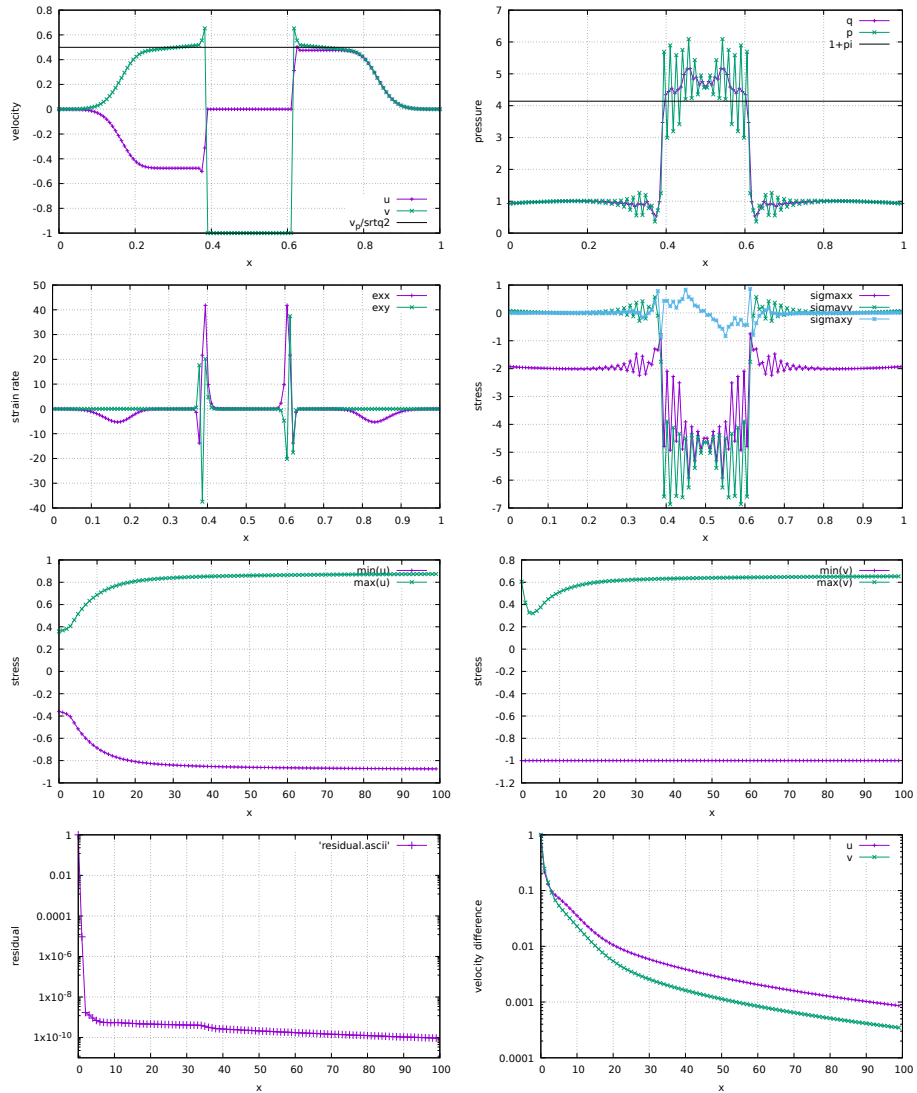
The following parameters are used:  $L_x = 1$ ,  $L_y = 0.5$ ,  $\mu_{min} = 10^{-3}$ ,  $\mu_{max} = 10^3$ ,  $v_p = 1$ ,  $\delta = 0.11111$  and the yield value of the material is set to  $\sigma_Y = 1$ .

The analytical solution predicts that the angle of the shear bands stemming from the sides of the punch is  $\pi/4$ , that the pressure right under the punch is  $1 + \pi$ , and that the velocity of the rigid blocks on each side of the punch is  $v_p/\sqrt{2}$  (this is simply explained by invoking conservation of mass).

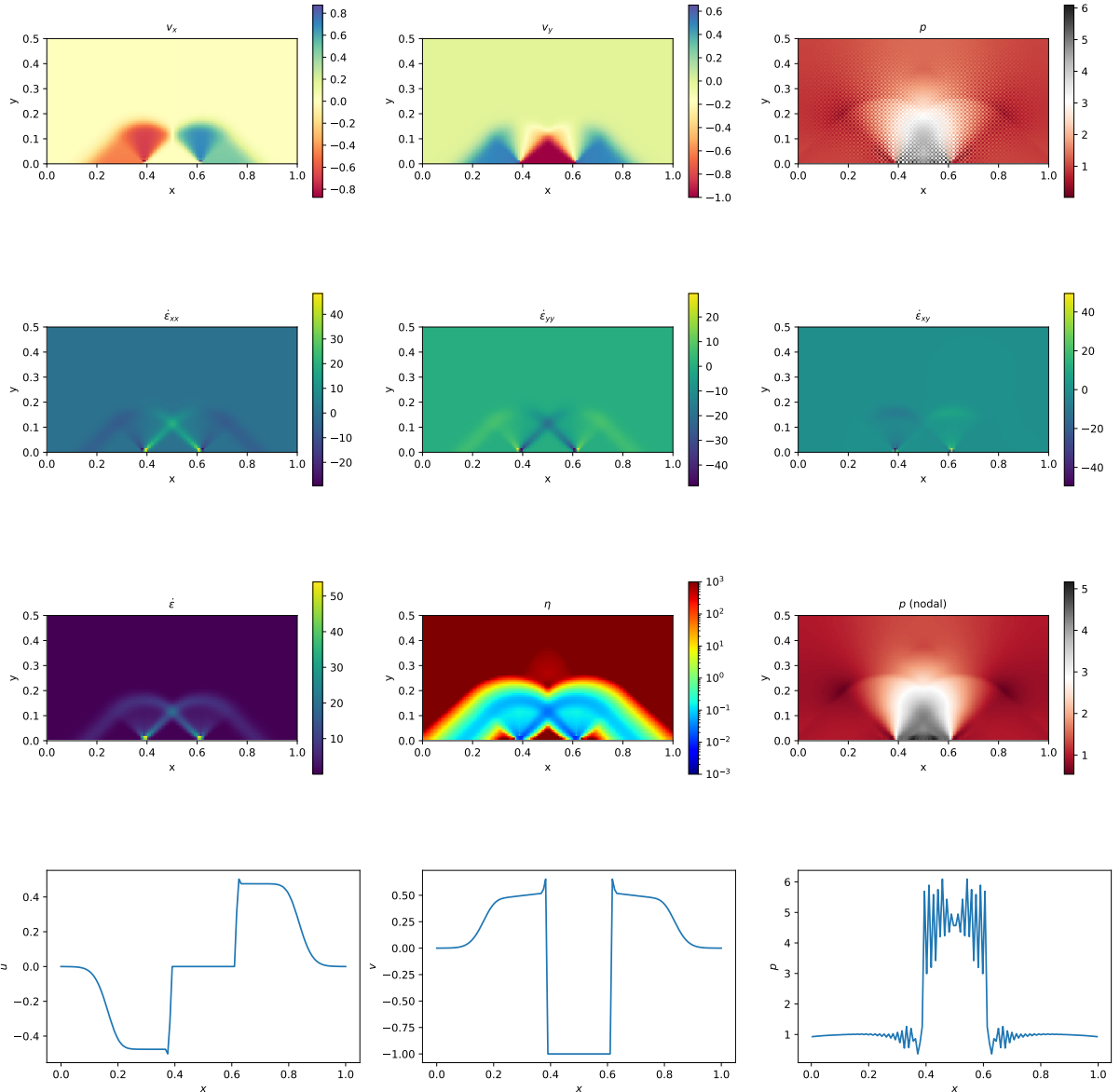
In what follows I show results of the rough and smooth punch for a 124x68 grid. The difference between the two lies in the nature of the kinematic boundary conditions under the punched area. 'rough' means that the indentor also fixes the horizontal velocity component to zero while it is free in the smooth case.

We see that the smooth punch does not trigger the checkerboard pressure modes as much as the rough case and we recover nicely the analytical pressure under the punch [2533, 1002].

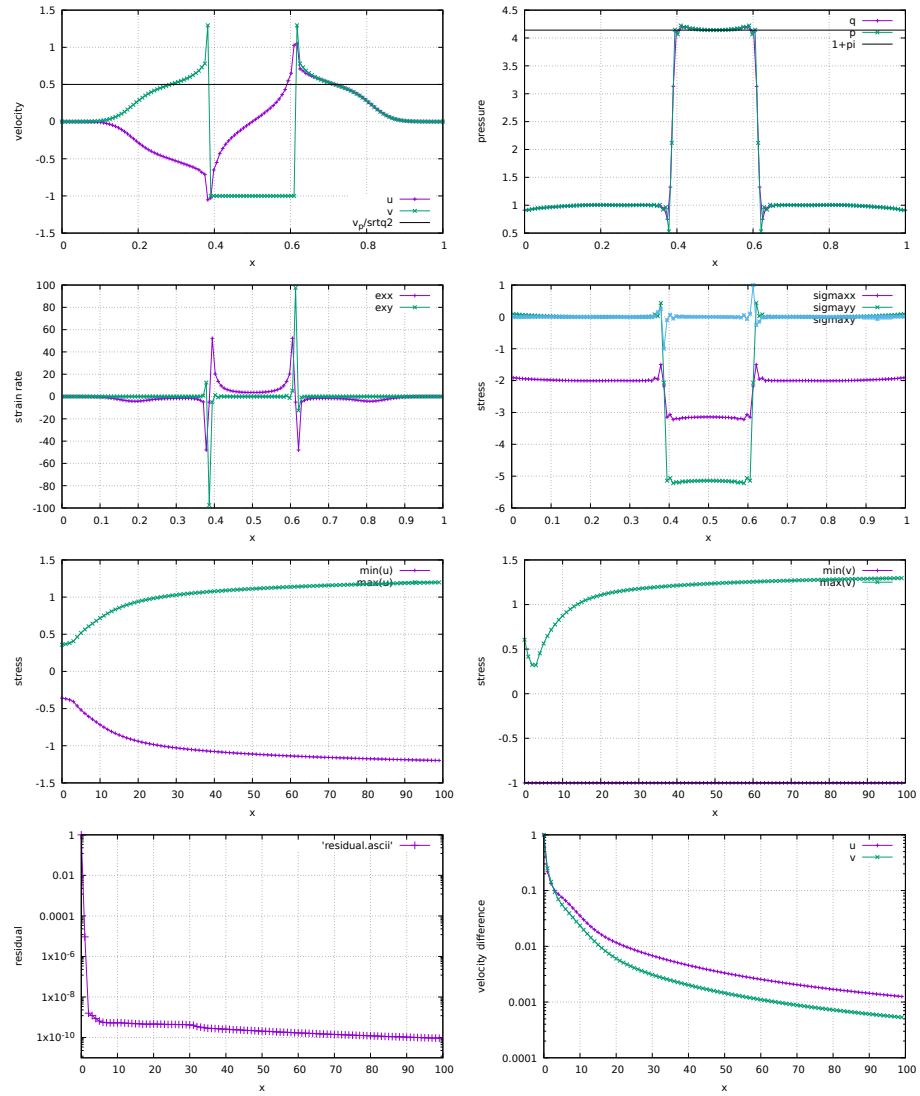
## Rough punch



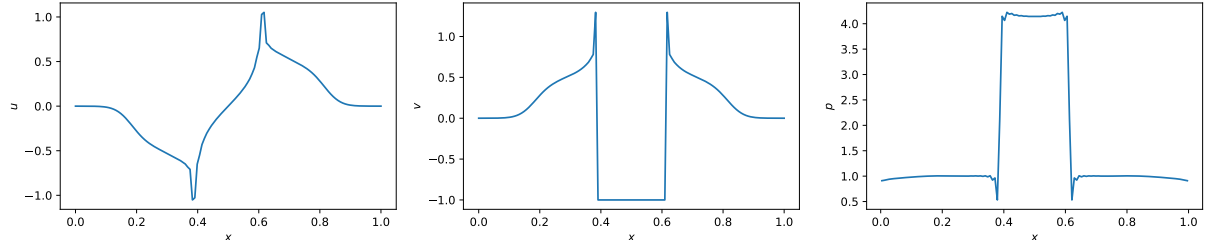
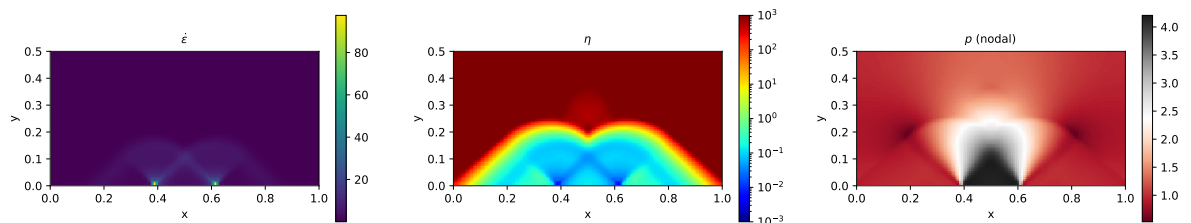
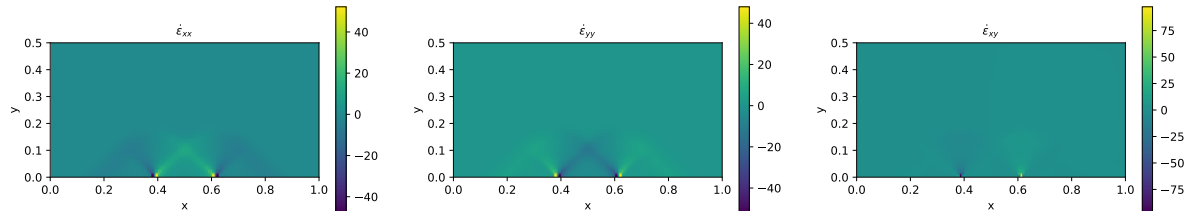
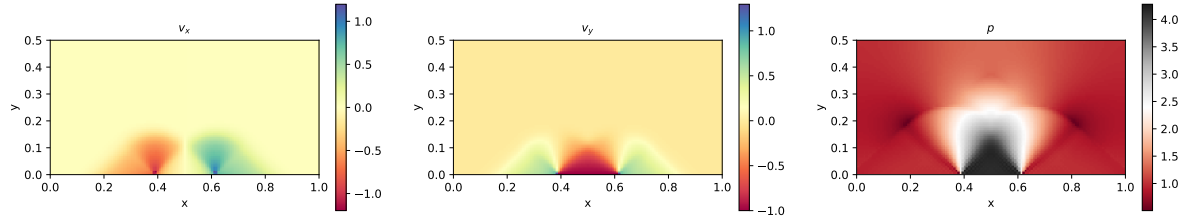
a,b,c,d) velocity, pressure, strainrate and stress at the top of the domain; e,f) min/max value of  $u$  and  $v$ ; g,h) residual and normalised velocity difference.



## Smooth punch



a,b,c,d) velocity, pressure, strainrate and stress at the top of the domain; e,f) min/max value of  $u$  and  $v$ ; g,h) residual and normalised velocity difference.



## Stone 09: the annulus benchmark

This fieldstone was developed in collaboration with Prof. E.G.P. Puckett.

An analytical solution to the isoviscous incompressible Stokes equations is derived in an annulus geometry. The velocity and pressure fields are as follows:

$$v_r(r, \theta) = g(r)k \sin(k\theta), \quad (883)$$

$$v_\theta(r, \theta) = f(r) \cos(k\theta), \quad (884)$$

$$p(r, \theta) = kh(r) \sin(k\theta), \quad (885)$$

$$\rho(r, \theta) = \aleph(r)k \sin(k\theta), \quad (886)$$

with

$$f(r) = Ar + B/r, \quad (887)$$

$$g(r) = \frac{A}{2}r + \frac{B}{r} \ln r + \frac{C}{r}, \quad (888)$$

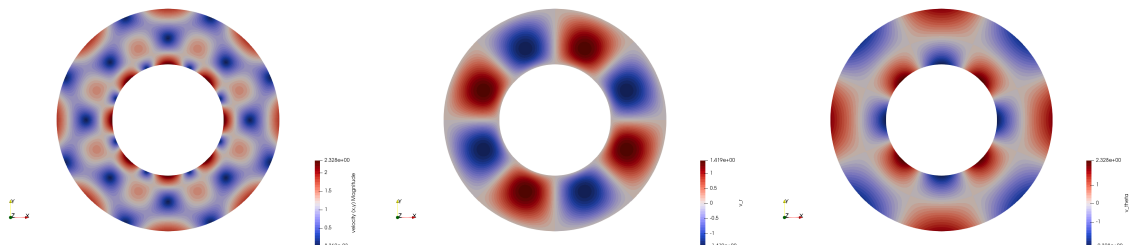
$$h(r) = \frac{2g(r) - f(r)}{r}, \quad (889)$$

$$\aleph(r) = g'' - \frac{g'}{r} - \frac{g}{r^2}(k^2 - 1) + \frac{f}{r^2} + \frac{f'}{r}, \quad (890)$$

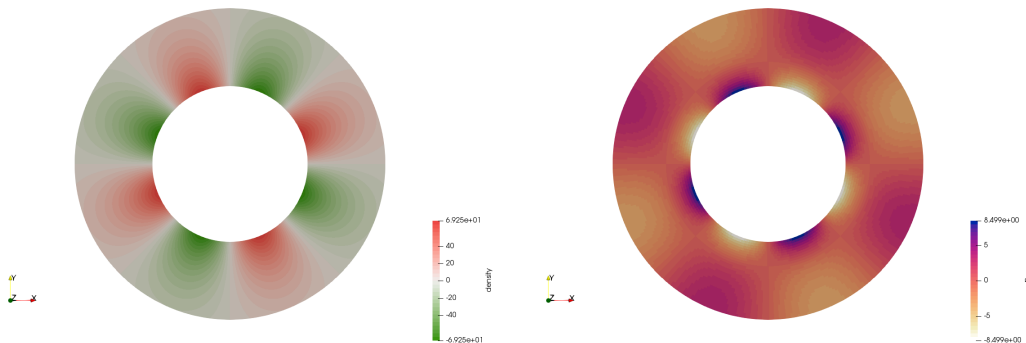
$$A = -C \frac{2(\ln R_1 - \ln R_2)}{R_2^2 \ln R_1 - R_1^2 \ln R_2}, \quad (891)$$

$$B = -C \frac{R_2^2 - R_1^2}{R_2^2 \ln R_1 - R_1^2 \ln R_2}. \quad (892)$$

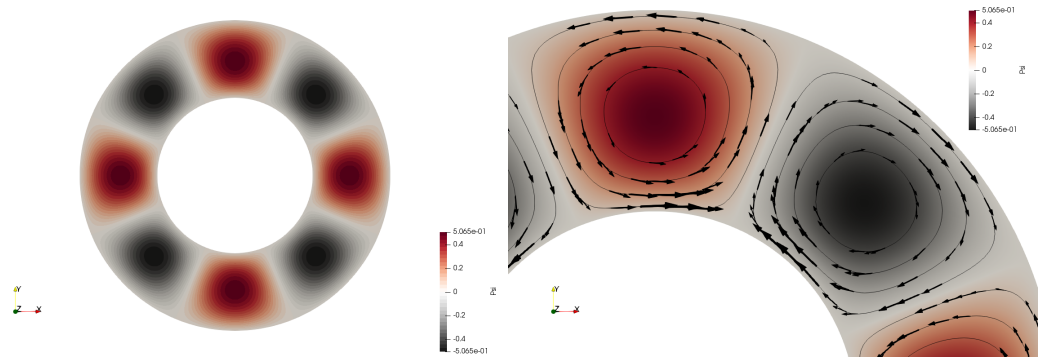
The parameters  $A$  and  $B$  are chosen so that  $v_r(R_1) = v_r(R_2) = 0$ , i.e. the velocity is tangential to both inner and outer surfaces. The gravity vector is radial and of unit length. In the present case, we set  $R_1 = 1$ ,  $R_2 = 2$  and  $C = -1$ .



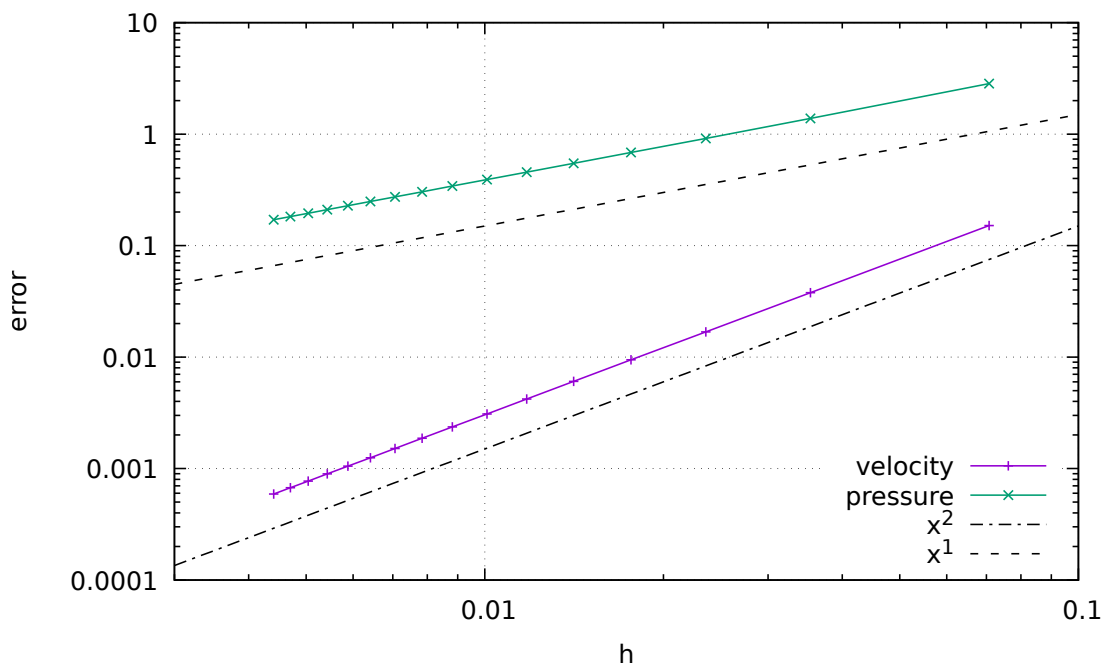
Left to right: velocity norm,  $r$  component,  $\theta$  component



Left: density field; right: pressure field.



Left:  $\psi$  field; right:  $\psi$  isolines with velocity arrows.



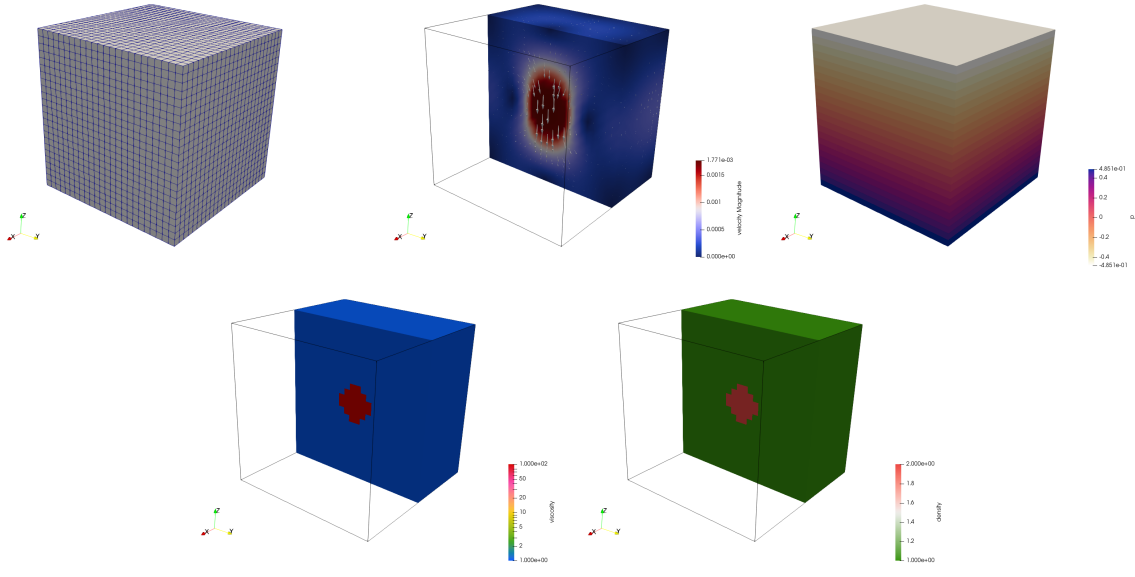
## Stone 10: Stokes sphere (3D) - penalty

The domain is a unit cube. Free slip boundary conditions are imposed on all sides. The mesh counts  $\text{nelx} \times \text{nely} \times \text{nelz} = \text{nel}$  elements and  $\text{nnx} \times \text{nny} \times \text{nnz} = \text{NV}$  nodes. The density and the viscosity are prescribed in the domain by means of two functions: the density is set to 2 inside a sphere of radius 0.123 centered at (0.5, 0.5, 0.5) and 1 outside. The viscosity is 100 inside the sphere and 1 outside. The gravity vector is set to  $\vec{g} = (0, 0, -1)$ .

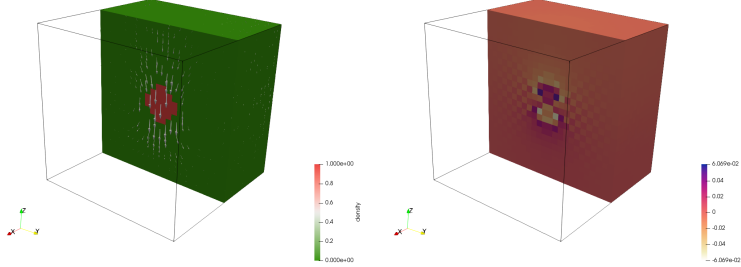
The FE matrix size grows even faster now than in the previous 2D case so choosing the right matrix storage is of paramount importance.

Three experiments are carried out:

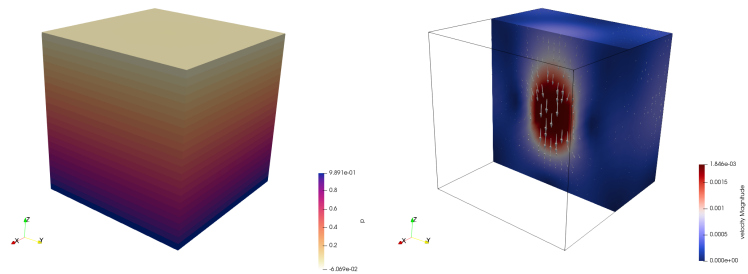
1. the one described above. We see that the pressure field is dominated by the lithostatic signal.
2. same as experiment 1, but a reference density of 1 is subtracted to all densities, so that the sphere density is 1 and the density of the surrounding fluid is now 0. In essence, we remove a 'background' density which does not participate in the flow generation, and thereby get rid of the lithostatic signal of the pressure.
3. same as experiment 2, but the top boundary is now open (free surface)



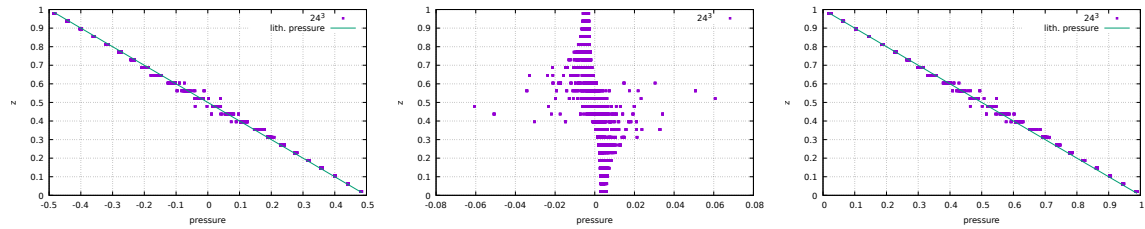
Experiment 1: resolution 24x24x24



Experiment 2: Density and pressure fields. Resolution 24x24x24



Experiment 3: pressure and velocity fields. Resolution 24x24x24



Elemental pressure for all elements as a function of their vertical (middle) coordinate for (from left to right) experiments 1, 2 and 3.

## Stone 11: stokes sphere (3D) - mixed formulation

The setup is identical to the one of the Stone 9.4.

The difference lies in how we solve the Stokes equation. This stone does not rely on the penalty method (Section 6.3) but instead used a mixed formulation, i.e. we solve for both velocity and pressure at the same time (see Section 6.4).

In the case when free slip boundary conditions are applied on all 6 faces of the cube we know that there is a pressure nullspace, i.e. that the pressure can be computed up to a constant. In order to remove this nullspace one must add an additional constraint. We here choose to (somewhat arbitrarily) enforce that the average pressure over the whole domain is zero:

$$\langle p \rangle = \frac{1}{|\Omega|} \int_{\Omega} pdV = 0$$

Since the code relies of discontinuous zero-th order polynomial shape functions for pressure this condition simply writes (and since  $|\Omega| = 1$ ):

$$\langle p \rangle = \frac{1}{|\Omega|} \int_{\Omega} pdV = \sum_e \int_{\Omega_e} pdV = \sum_e p_e V_e = h^3 \sum_e p_e = 0$$

Dividing all by  $h^3$ , the condition becomes simply:

$$p_1 + p_2 + p_3 + \dots + p_{nel} = 0$$

How this constraint is incorporated in the Stokes matrix is explained in Section 8.14.

It is also important to remember that if one now switches to a free surface at the top then the null space is absent from the equations and the constraint should be removed/switched off.

The pressure normalisation is controled by the boolean `pnormalise` in the code. Since the pressure constraint adds a line to the global FE, we then logically have:

```
if pnormalise:
    a_mat = np.zeros((Nfem+1,Nfem+1), dtype=np.float64)
    rhs   = np.zeros(Nfem+1, dtype=np.float64)
else:
    a_mat = np.zeros((Nfem,Nfem), dtype=np.float64)
    rhs   = np.zeros(Nfem, dtype=np.float64)
```

Once the solve has been done, we retrieve the separate velocity and pressure fields as follows:

```
u,v,w=np.reshape(sol[0:NfemV],(nnp,3)).T
p=sol[NfemV:Nfem]
```

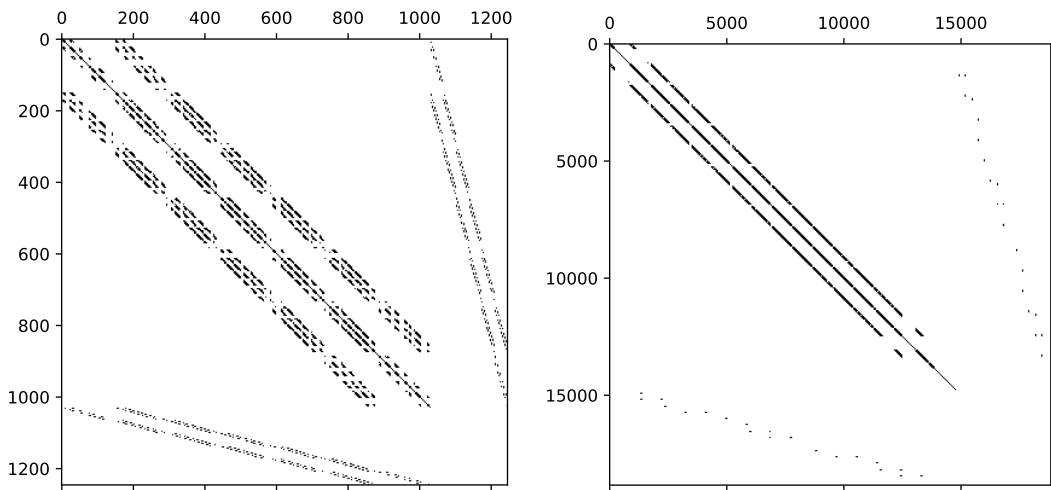
and the Lagrange multiplier is a scalar at the bottom of the array:

```
if pnormalise:
    print("----->Lagrange_multiplier: %.4e" % sol[Nfem])
```

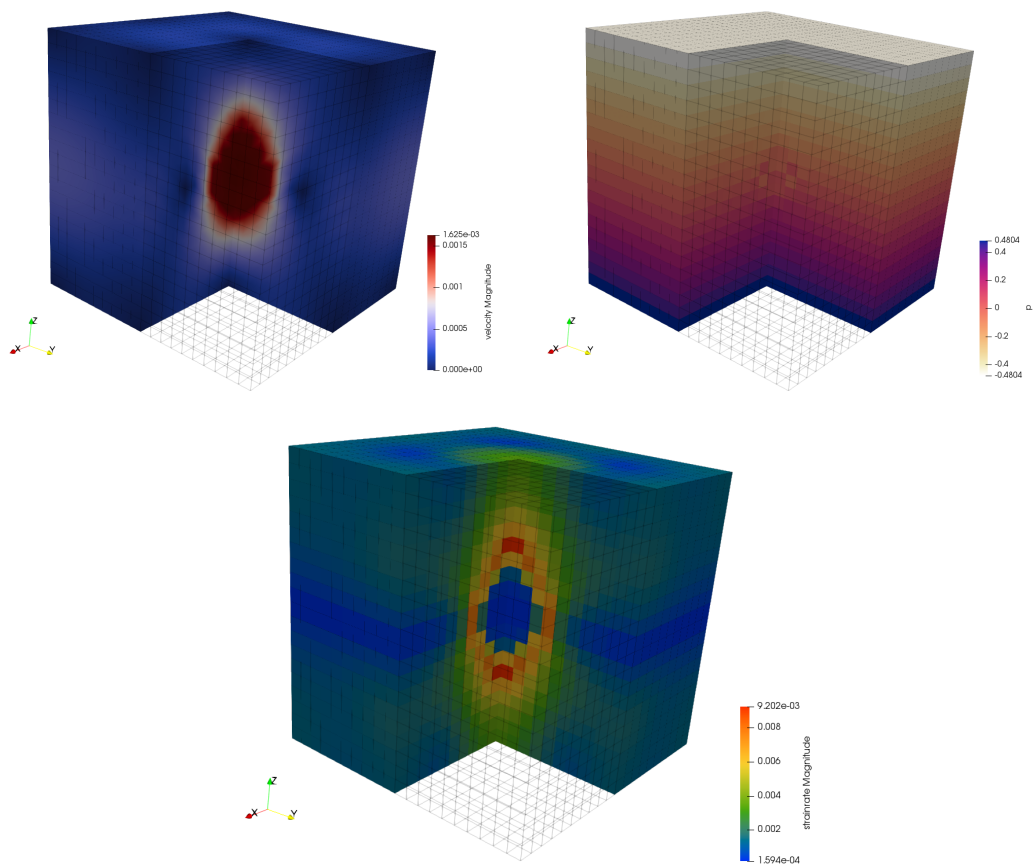
It is quite easy in python to visualise the matrix structure with the `spy` function:

```
plt.spy(a_mat)
```

and we see that we indeed recover the block structure with a zero block for the pressure-pressure entries.



Sparsity pattern of the Stokes matrix for a  $6 \times 6 \times 6$  mesh (left) and a  $16 \times 16 \times 16$  mesh (right).



Velocity, pressure and effective strain rate fields for a  $20 \times 20 \times 20$  mesh.

## Stone 12: consistent pressure recovery

We start from the analytical benchmark of Section 8.6.1 and we use  $Q_1 \times P_0$  elements with a penalty formulation. We have seen in the first stone how to recover the elemental pressure as a postprocessing step. However, the discontinuous nature of the pressure field (and the presence of a parasitic checkerboard mode) can be problematic for many reasons (pressure enters the rheology, plotting , ...) . We then wish to project the elemental pressure onto the nodes of the mesh.

Terminology: in general, when a discontinuous elemental pressure is used in a stone, it is called  $p$  while its projection onto the nodes is coined  $q$ . In this case we compute several nodal pressures:

- $q_1$  is smoothed pressure obtained with the center-to-node approach. We loop over elements and each element adds its pressure to its corner nodes. Interior nodes 'receive' 4 values, edge nodes 2 values and corner nodes only 1. An average per node is then computed. This is a very simple and cost-effective method and it is used in papers based on DOUAR or FANTOM [269, 2533, 2528].

```
q1=np.zeros(NV,dtype=np.float64)
count=np.zeros(NV,dtype=np.float64)
for iel in range(0,nel):
    q1[icon[0,iel]]+=p[iel]
    q1[icon[1,iel]]+=p[iel]
    q1[icon[2,iel]]+=p[iel]
    q1[icon[3,iel]]+=p[iel]
    count[icon[0,iel]]+=1
    count[icon[1,iel]]+=1
    count[icon[2,iel]]+=1
    count[icon[3,iel]]+=1
```

- $q_2$  is recovered pressure obtained with the method presented in Zienkiewicz & Nakazawa (1982) [2931]. In the second part of this publication the authors wish to establish a simple and effective numerical method to calculate variables eliminated by the penalisation process. The method involves an additional finite element solution for the nodal pressures using the same finite element basis and numerical quadrature as used for the velocity.

Let us start with:

$$p = -\lambda \vec{\nabla} \cdot \vec{v}$$

which lead to

$$(q, p) = -\lambda(q, \vec{\nabla} \cdot \vec{v})$$

and then

$$\left( \int \mathbf{N} \mathbf{N} d\Omega \right) \cdot \mathbf{P} = - \left( \lambda \int \mathbf{N} \nabla \mathbf{N} d\Omega \right) \cdot \mathbf{V}$$

or,

$$\mathbf{M} \cdot \mathbf{P} = -\mathbf{D} \cdot \mathbf{V}$$

and finally

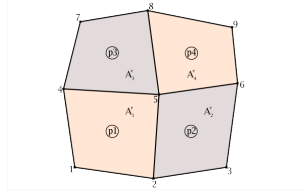
$$\mathbf{P} = -\mathbf{M}^{-1} \cdot \mathbf{D} \cdot \mathbf{V}$$

with  $\mathbf{M}$  of size  $(np \times np)$ ,  $\mathbf{D}$  of size  $(np * ndof \times np * ndof)$  and  $\mathbf{V}$  of size  $(np * ndof)$ . The vector  $\mathbf{P}$  contains the  $np$  nodal pressure values directly, with no need for a smoothing scheme. The mass matrix  $\mathbf{M}$  is to be evaluated at the full integration points, while the constraint part (the right hand side of the equation) is to be evaluated at the reduced integration point.

As noted by [2931], it is interesting to note that when linear elements are used and the lumped matrices are used for the  $\mathbf{M}$  the resulting algebraic equation is identical to the smoothing scheme based on the averaging method only if the uniform square finite element mesh is used. In this respect this method is expected to yield different results when elements are not square or even rectangular.

- $q_3$  is recovered pressure obtained with [2931] but with lumped mass matrix. In this case the assembled mass matrix is diagonal.

- $q_4$  is smoothed pressure obtained with the center-to-node approach with element area weighing.  
This filtering scheme is presented in [2237]. Let us consider a subset of four elements of the system:

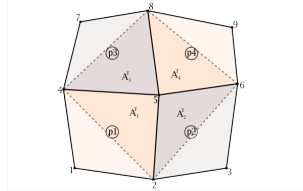


The pressure at the central node 5 is given by

$$p_5 = \frac{\sum_{j=1}^4 p_j^e A_j^e}{\sum_{j=1}^4 A_j^e} = \frac{p_1^e A_1^e + p_2^e A_2^e + p_3^e A_3^e + p_4^e A_4^e}{A_1^e + A_2^e + A_3^e + A_4^e}$$

where  $A_j^e$  is the area of element  $j$ . The implementation is rather trivial (although one must compute the area/volume of elements before hand) and the recovered nodal pressure is equivalent to  $q_1$  if all elements have the same area.

- $q_6$  is smoothed pressure obtained with a similar approach as for  $q_4$  but with triangular area weighing.  
This filtering scheme is also presented in [2237]. The weighing of the pressures is done this time using the areas of the triangles as shown on the following figure:



The pressure at the central node 5 is then given by

$$p_5 = \frac{\sum_{j=1}^4 p_j^e A_j^T}{\sum_{j=1}^4 A_j^T} = \frac{p_1^e A_1^T + p_2^e A_2^T + p_3^e A_3^T + p_4^e A_4^T}{A_1^T + A_2^T + A_3^T + A_4^T}$$

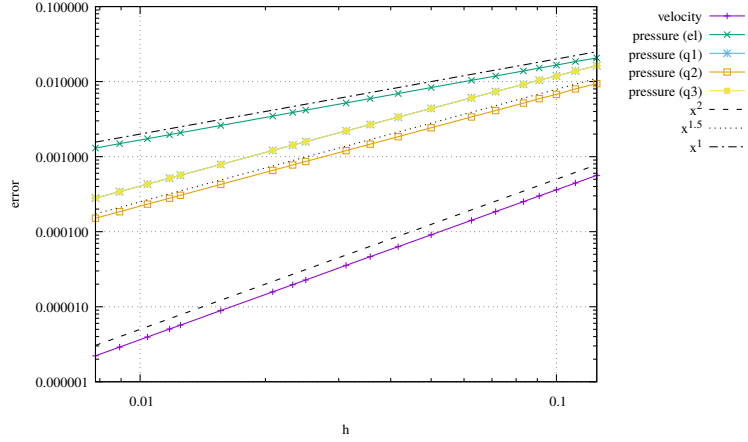
Here too, if all elements have the same area and shape, we will have  $q_6 = q_1$ .

- $q_5$  is smoothed pressure obtained with the center-to-node approach with inverse element area weighing.

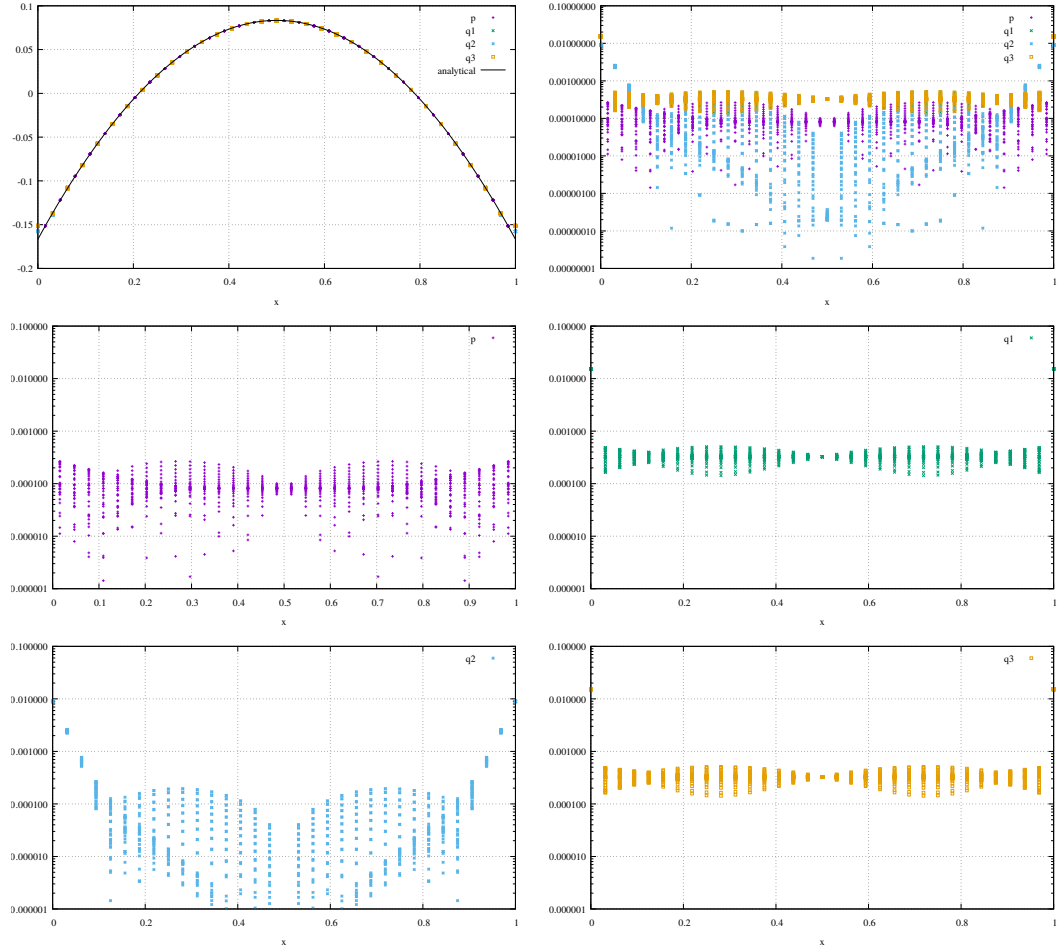
All nodal pressures are filtered so that they fulfill the zero average condition:  $\int pd\Omega = 0$ .

TODO: nodes on edges and corners may need special treatment as documented in [2237], which is not done here.

**Regular mesh made of square elements** We compute the error convergence for  $p$ ,  $q_1$ ,  $q_2$  and  $q_3$ :



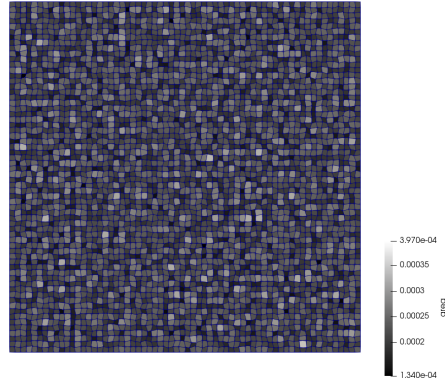
We find that  $q_1$  and  $q_2$  are more accurate than elemental ( $h^{1.5}$  vs.  $h^1$ ), and we see that  $q_2$  is more accurate than  $q_1$ .



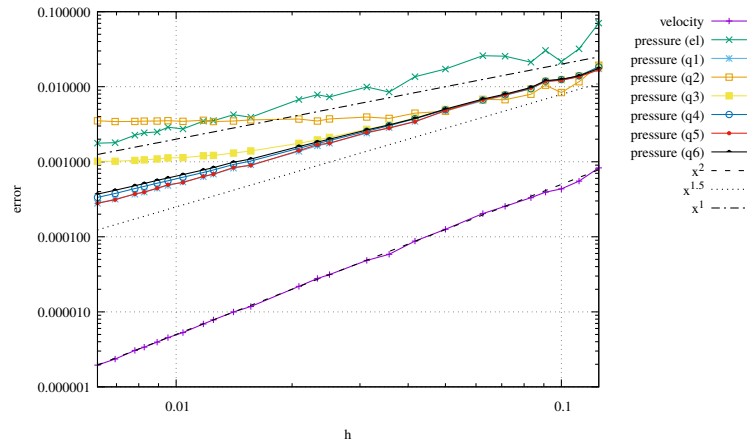
Left: pressure fields as a function of the  $x$ -coordinate. Right: absolute error with regards to the analytical solution. All on 32x32 mesh.

We see that  $q_2$  is substantially more accurate than  $p$  or  $q_1$  in the middle of the domain but both nodal pressures exhibit substantial overshoot near the boundaries.  $q_3$  does as good as  $q_1$  which is not surprising since in this case (regular square mesh) it is identical to the algorithm for  $q_1$ .

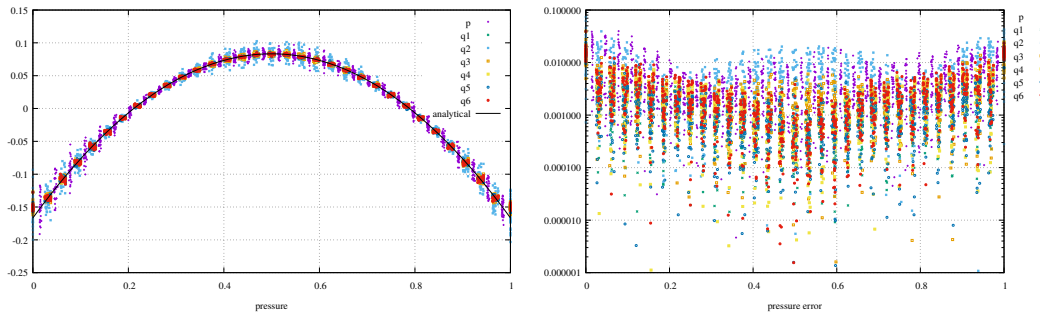
**Adding randomness to internal node positions** We now add a random value  $\xi h$  to the location of all nodes which are not on the boundary where  $h=L_x/\text{nelx}$  and we set  $\xi = 20\%$ . In this case a 64x64 mesh looks as follows:

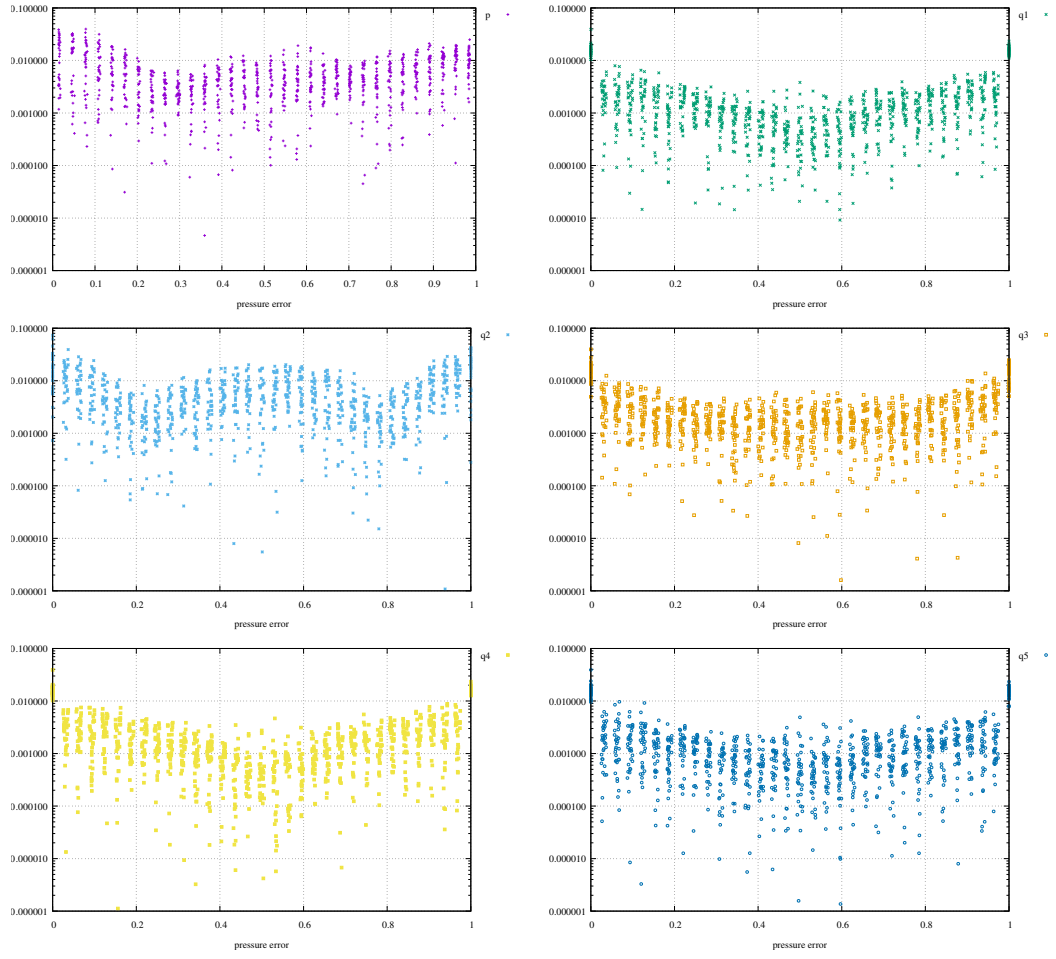


We repeat the same exercise as before on such a mesh and look at the errors

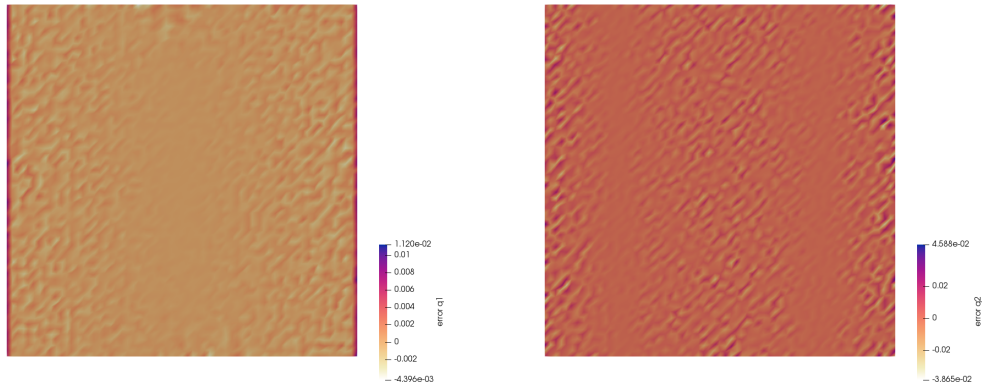


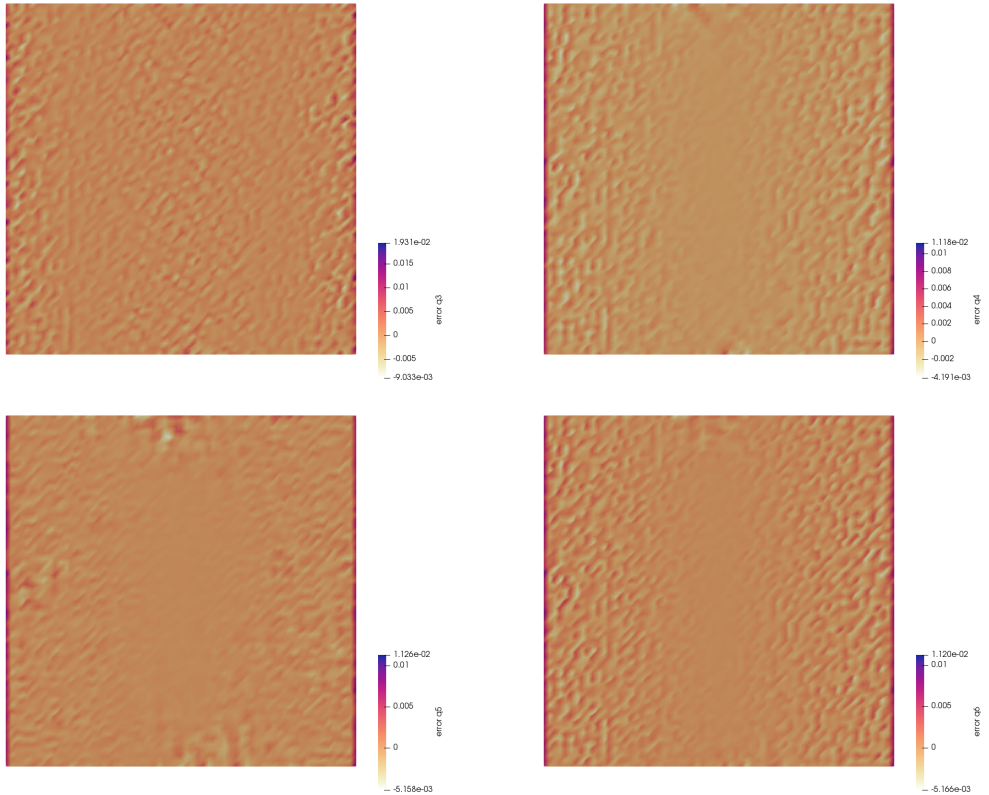
Rather surprisingly we find that  $q_1$  proves to be the most accurate of all pressures and it converges with  $h^{1.5}$  as before. Because checkerboard modes are triggered the convergence of the elemental pressure is more chaotic but on average linear. The  $q_2$  and  $q_3$  fields seem to unexpectedly stop converging above a given resolution.





Left: pressure fields as a function of the  $x$ -coordinate.



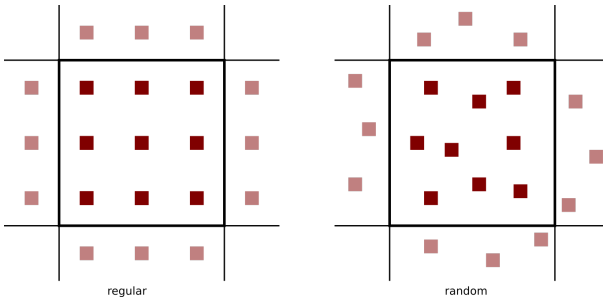


## Stone 13: the Particle in Cell technique (1) - the effect of averaging

This fieldstone was developed in collaboration with BSc student Eric Hoogen.

After the initial setup of the grid, markers can then be generated and placed in the domain. One could simply randomly generate the marker positions in the whole domain but unless a *very* large number of markers is used, the chance that an element does not contain any marker exists and this will prove problematic. In order to get a better control over the markers spatial distribution, one usually generates the marker per element, so that the total number of markers in the domain is the product of the number of elements times the user-chosen initial number of markers per element.

Our next concern is how to actually place the markers inside an element. Two methods come to mind: on a regular grid, or in a random manner, as shown on the following figure:



In both cases we make use of the basis shape functions: we generate the positions of the markers (random or regular) in the reference element first ( $r_{im}, s_{im}$ ), and then map those out to the real element as follows:

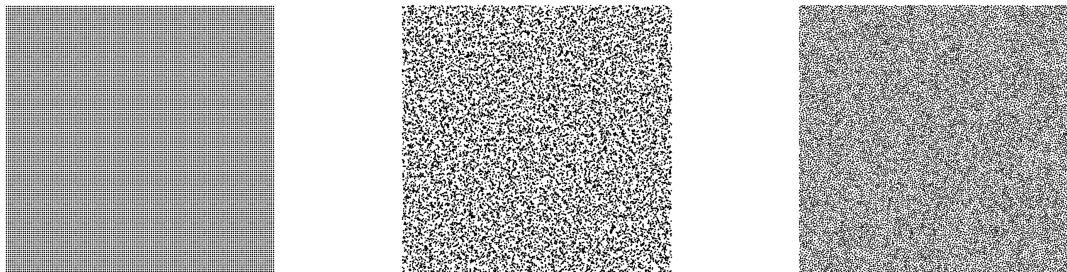
$$x_{im} = \sum_i^m N_i(r_{im}, s_{im}) x_i \quad y_{im} = \sum_i^m N_i(r_{im}, s_{im}) y_i \quad (893)$$

where  $x_i, y_i$  are the coordinates of the vertices of the element.

A third option consists in the use of the so-called Poisson-disc sampling which produces points that are tightly-packed, but no closer to each other than a specified minimum distance, resulting in a more natural pattern<sup>79</sup>. Note that the Poisson-disc algorithm fills the whole domain at once, not element after element.

say smthg about avrg dist

insert here theory and link about Poisson disc



Left: regular distribution, middle: random, right: Poisson disc.  
16384 markers (32x32 grid, 16 markers per element).

When using *active* markers, one is faced with the problem of transferring the properties they carry to the mesh on which the PDEs are to be solved. As we have seen, building the FE matrix involves a loop over all elements, so one simple approach consists of assigning each element a single property computed as

<sup>79</sup><https://en.wikipedia.org/wiki/Supersampling>

the average of the values carried by the markers in that element. Often in colloquial language "average" refers to the arithmetic mean:

$$\langle \phi \rangle_{am} = \frac{1}{n} \sum_k^n \phi_i \quad (894)$$

where  $\langle \phi \rangle_{am}$  is the arithmetic average of the  $n$  numbers  $\phi_i$ . However, in mathematics other means are commonly used, such as the geometric mean:

$$\langle \phi \rangle_{gm} = \left( \prod_i^n \phi_i \right) \quad (895)$$

PROBLEM with this formula!!!! and the harmonic mean:

$$\langle \phi \rangle_{hm} = \left( \frac{1}{n} \sum_i^n \frac{1}{\phi_i} \right)^{-1} \quad (896)$$

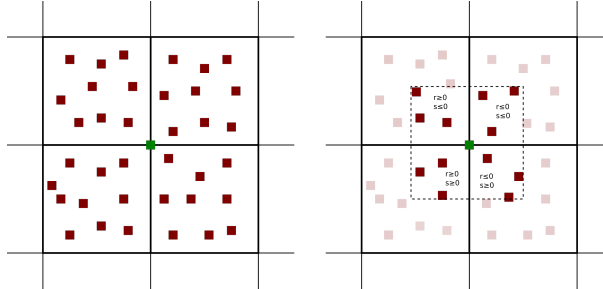
Furthermore, there is a well known inequality for any set of positive numbers,

$$\langle \phi \rangle_{am} \geq \langle \phi \rangle_{gm} \geq \langle \phi \rangle_{hm} \quad (897)$$

which will prove to be important later on.

Let us now turn to a simple concrete example: the 2D Stokes sphere. There are two materials in the domain, so that markers carry the label "mat=1" or "mat=2". For each element an average density and viscosity need to be computed. The majority of elements contains markers with a single material label so that the choice of averaging does not matter (it is trivial to verify that if  $\phi_i = \phi_0$  then  $\langle \phi \rangle_{am} = \langle \phi \rangle_{gm} = \langle \phi \rangle_{hm} = \phi_0$ ). Remain the elements crossed by the interface between the two materials: they contain markers of both materials and the average density and viscosity inside those depends on 1) the total number of markers inside the element, 2) the ratio of markers 1 to markers 2, 3) the type of averaging.

This averaging problem has been studied and documented in the literature [2272, 688, 2526, 2064]



Nodal projection. Left: all markers inside elements to which the green node belongs to are taken into account.

Right: only the markers closest to the green node count.

Let  $k$  be the green node of the figures above. Let  $(r, s)$  denote the coordinates of a marker inside its element. For clarity, we define the follow three nodal averaging schemes:

- nodal type A:

$$f_k = \frac{\text{sum of values carried by markers in 4 neighbour elements}}{\text{number of markers in 4 neighbour elements}}$$

- nodal type B:

$$f_k = \frac{\text{sum of values carried by markers inside dashed line}}{\text{number of markers in area delimited by the dashed line}}$$

- nodal type C

$$f_k = \frac{\text{sum of values carried by markers in 4 neighbour elements} * N_p(r, s)}{\text{sum of } N_p(r, s)}$$

where  $N_p$  is the  $Q_1$  basis function corresponding to node  $p$  defined on each element. Since these functions are 1 on node  $k$  and then linearly decrease and become zero on the neighbouring nodes, this effectively gives more weight to those markers closest to node  $k$ .

This strategy is adopted in [1746, 1743] (although it is used to interpolate onto the nodes of  $Q_2P_{-1}$  elements. It is formulated as follows:

"We assume that an arbitrary material point property  $f$ , is discretized via  $f(\mathbf{x}) \simeq \delta(\mathbf{x} - \mathbf{x}_p)f_p$ . We then utilize an approximate local  $L_2$  projection of  $f_p$  onto a continuous  $Q_1$  finite element space. The corner vertices of each  $Q_2$  finite element define the mesh  $f_p$  is projected onto. The local reconstruction for a node  $i$  is defined by

$$\hat{f}_i = \frac{\int_{\Omega_i} N_i(\mathbf{x}) f(\mathbf{x})}{\int_{\Omega_i} N_i(\mathbf{x})} \simeq \frac{\sum_p N_i(\mathbf{x}_p) f_p}{\sum_p N_i(\mathbf{x}_p)}$$

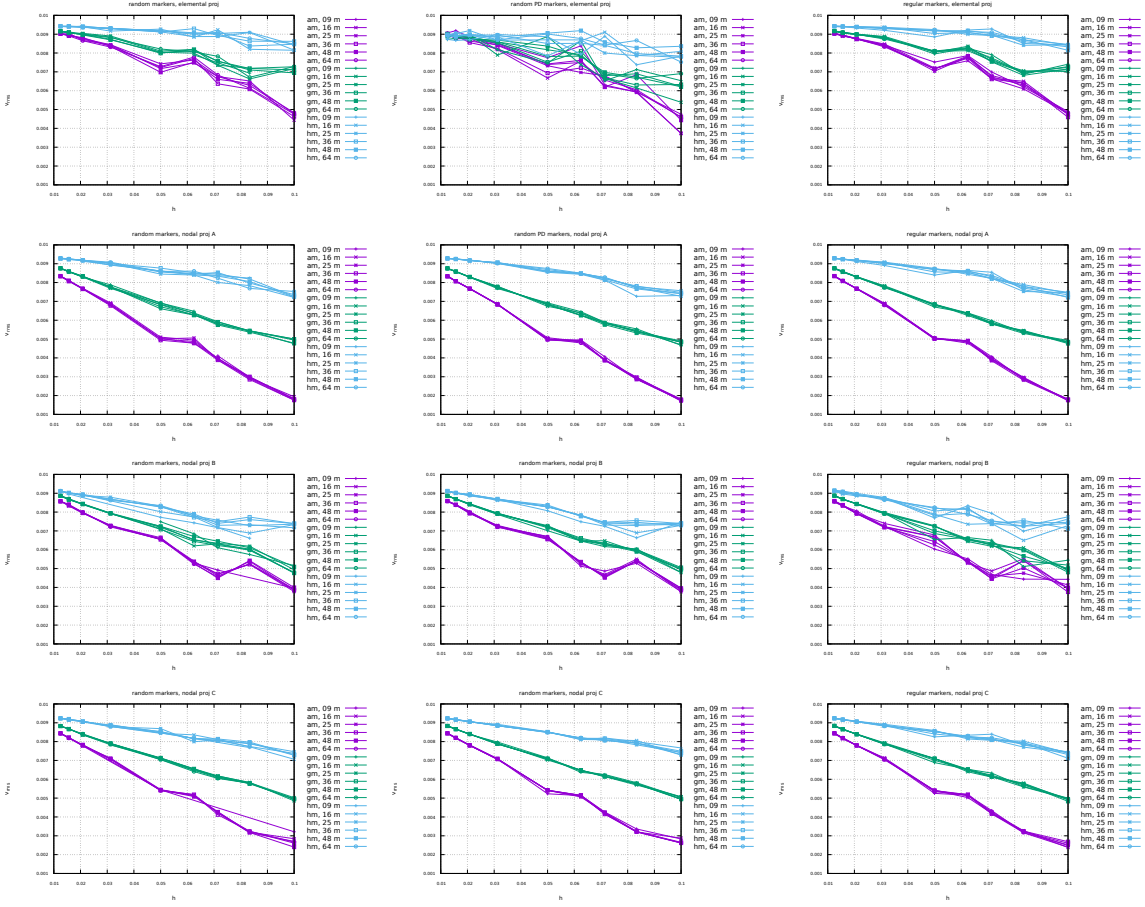
where the summation over  $p$  includes all material points contained within the support  $\Omega_i$  of the trilinear interpolant  $N_i$ ".

The setup is identical to the Stokes sphere experiment. The bash script `script_runall` runs the code for many resolutions, both initial marker distribution and all four averaging types. The viscosity of the sphere has been set to  $10^3$  while the viscosity of the surrounding fluid is 1. The average density is always computed with an arithmetic mean.

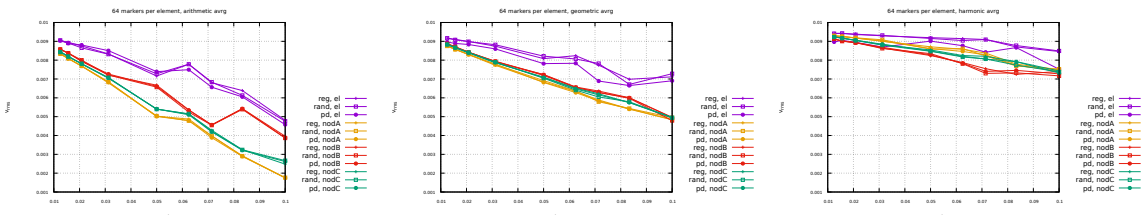
Conclusions:

- With increasing resolution ( $h \rightarrow 0$ ) vrms values seem to converge towards a single value, irrespective of the number of markers.
- At low resolution, say 32x32 (i.e.  $h=0.03125$ ), vrms values for the three averagings differ by about 10%. At higher resolution, say 128x128, vrms values are still not converged.
- The number of markers per element plays a role at low resolution, but less and less with increasing resolution.
- Results for random and regular marker distributions are not identical but follow a similar trend and seem to converge to the same value.
- elemental values yield better results (espccially at low resolutions)
- harmonic mean yields overal the best results

Root mean square velocity results are shown hereunder:



Left column: random markers, middle column: Poisson disc, right column: regular markers. First row: elemental projection, second row: nodal 1 projection, third row: nodal 2 projection, fourth row: nodal 3 projection.



Left to right: arithmetic, geometric, harmonic averaging for viscosity.

## Stone 14: solving the full saddle point problem

The details of the numerical setup are presented in Section ??.

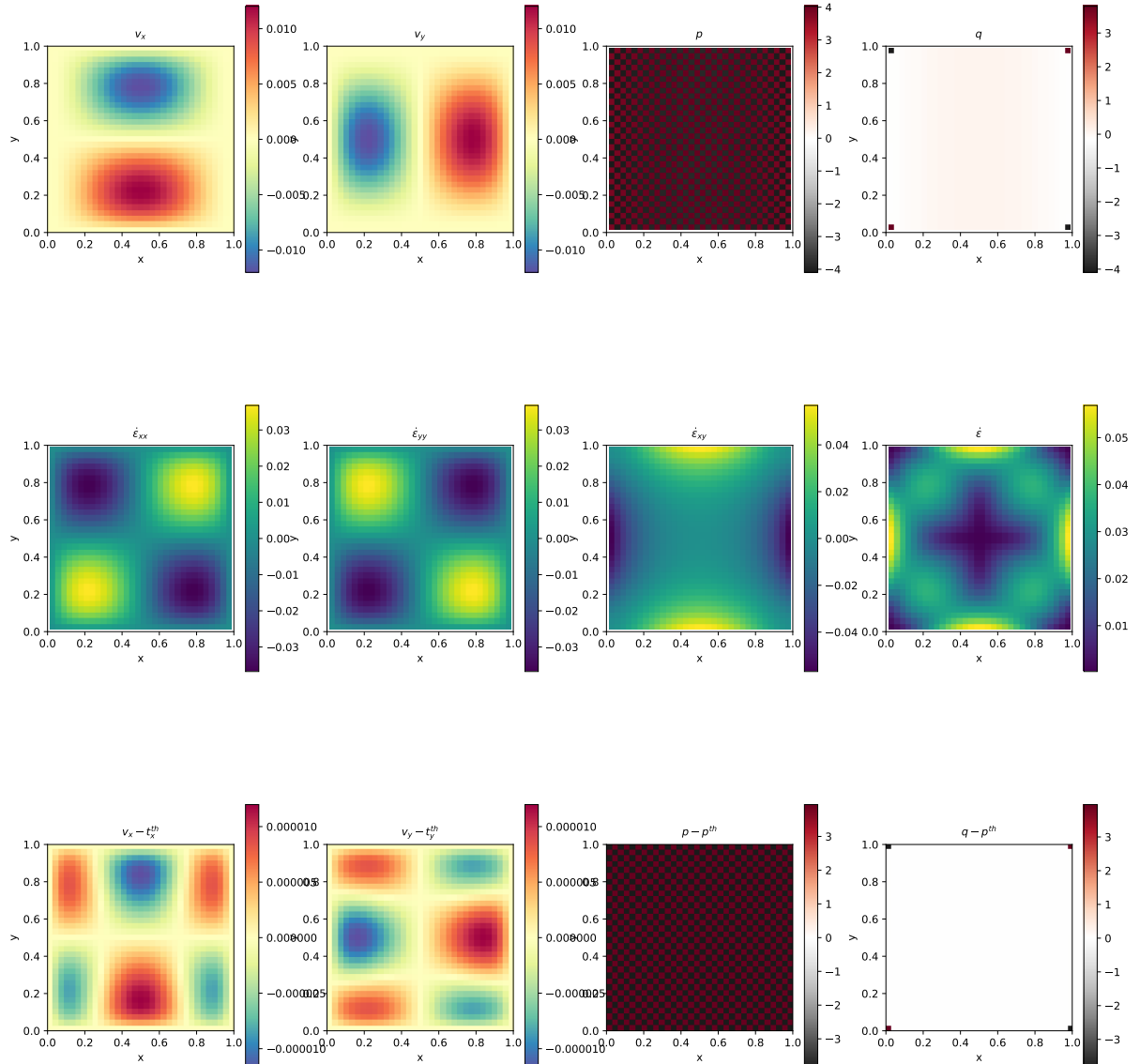
The main difference is that we no longer use the penalty formulation and therefore keep both velocity and pressure as unknowns. Therefore we end up having to solve the following system:

$$\begin{pmatrix} \mathbb{K} & \mathbb{G} \\ \mathbb{G}^T & 0 \end{pmatrix} \cdot \begin{pmatrix} V \\ P \end{pmatrix} = \begin{pmatrix} f \\ h \end{pmatrix} \quad \text{or,} \quad \mathbb{A} \cdot X = rhs$$

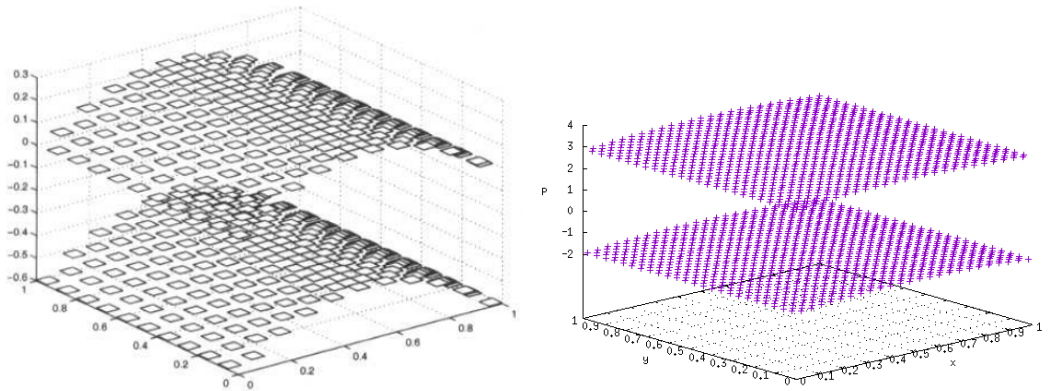
Each block  $\mathbb{K}$ ,  $\mathbb{G}$  and vector  $f$ ,  $h$  are built separately in the code and assembled into the matrix  $\mathbb{A}$  and vector  $rhs$  afterwards.  $\mathbb{A}$  and  $rhs$  are then passed to the solver. We will see later that there are alternatives to solve this approach which do not require to build the full Stokes matrix  $\mathbb{A}$ .

Each element has  $m = 4$  vertices so in total  $ndofV \times m = 8$  velocity dofs and a single pressure dof, commonly situated in the center of the element. The total number of velocity dofs is therefore  $NfemV = nnp \times ndofV$  while the total number of pressure dofs is  $NfemP = nel$ . The total number of dofs is then  $Nfem = NfemV + NfemP$ .

As a consequence, matrix  $\mathbb{K}$  has size  $NfemV, NfemV$  and matrix  $\mathbb{G}$  has size  $NfemV, NfemP$ . Vector  $f$  is of size  $NfemV$  and vector  $h$  is of size  $NfemP$ .



Unlike the results obtained with the penalty formulation (see Section ??), the pressure showcases a very strong checkerboard pattern, similar to the one in [711].



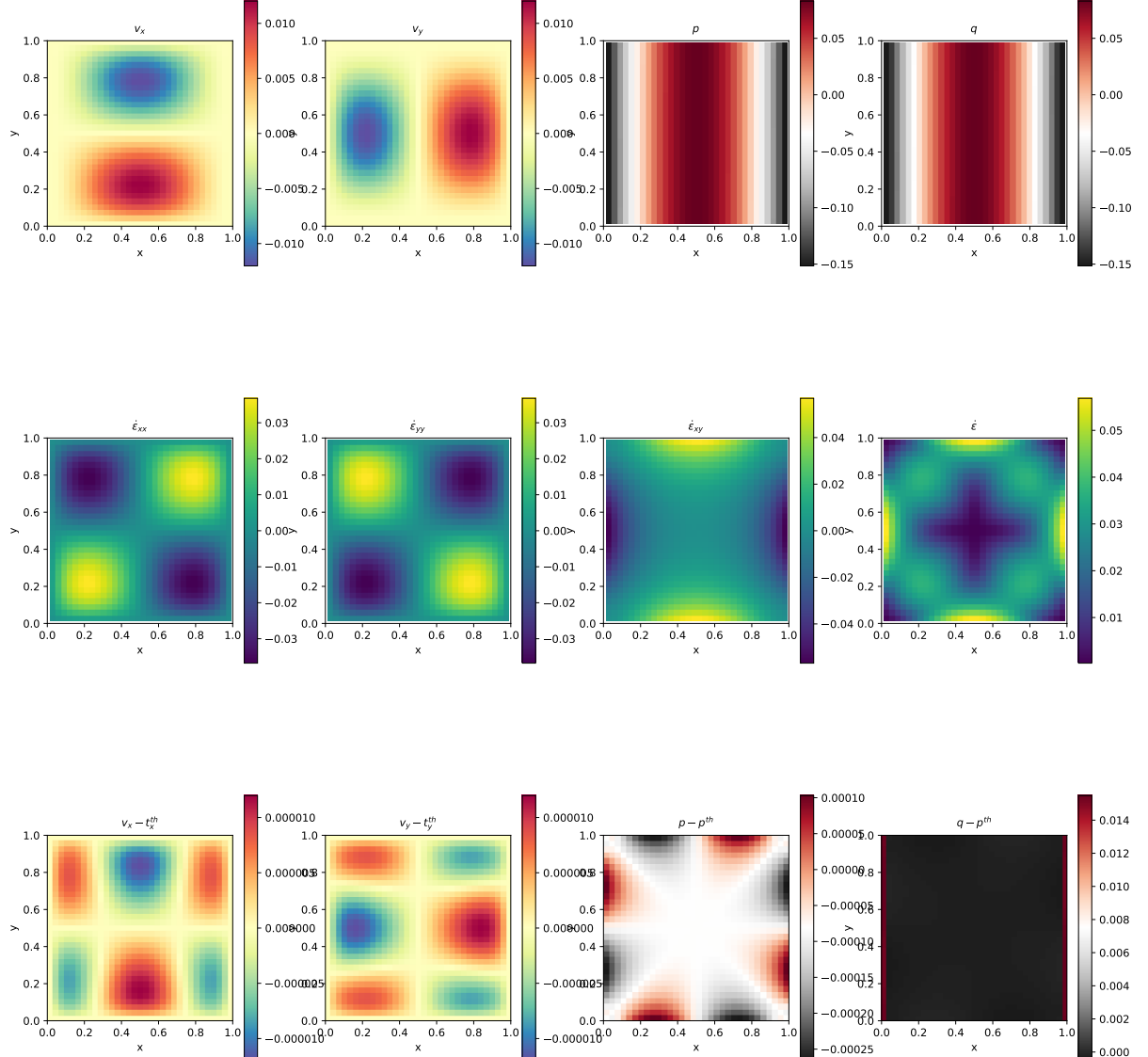
Left: pressure solution as shown in [711]; Right: pressure solution obtained with fieldstone.

Rather interestingly, the nodal pressure (obtained with a simple center-to-node algorithm) fails to recover a correct pressure at the four corners.

Note that the umfpack solver complains a lot about the matrix condition number, even at (very) low resolutions. I believe it does not like the zeros on the (2,2) block of the assembled Stokes matrix.

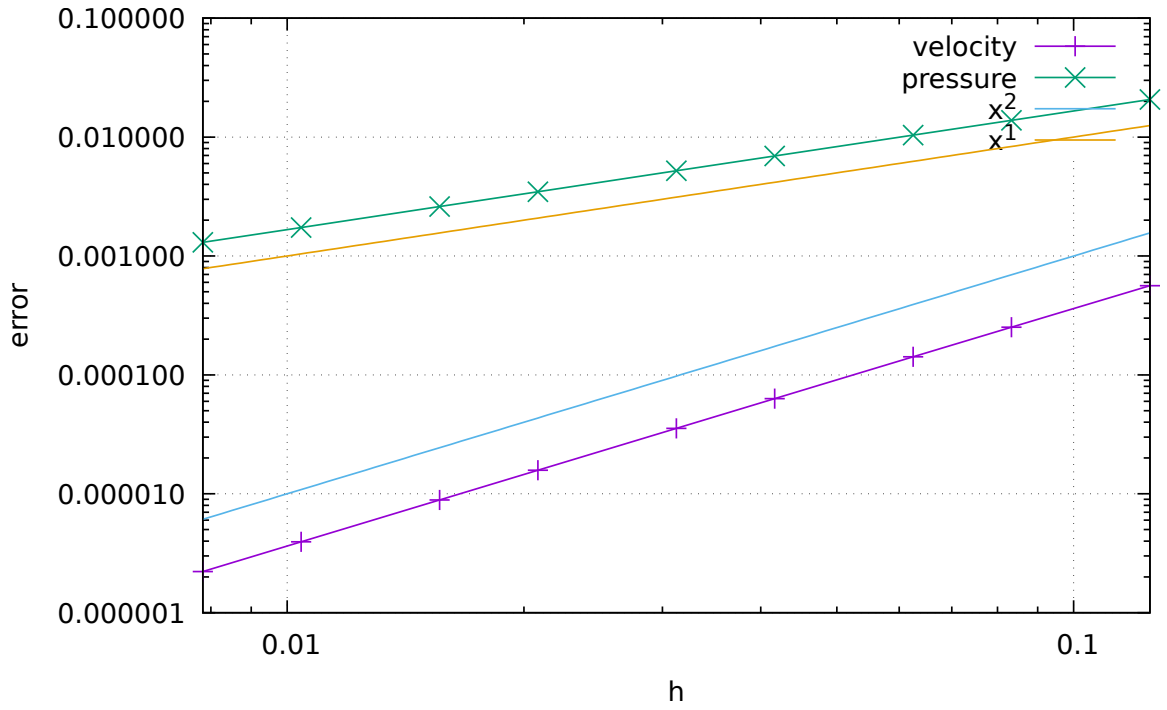
## Stone 15: saddle point problem with Schur complement approach - benchmark

The details of the numerical setup are presented in Section ???. The main difference resides in the Schur complement approach to solve the Stokes system, as presented in Section ??? (see `solver_cg`). This iterative solver is very easy to implement once the blocks  $\mathbb{K}$  and  $\mathbb{G}$ , as well as the rhs vectors  $f$  and  $h$  have been built.

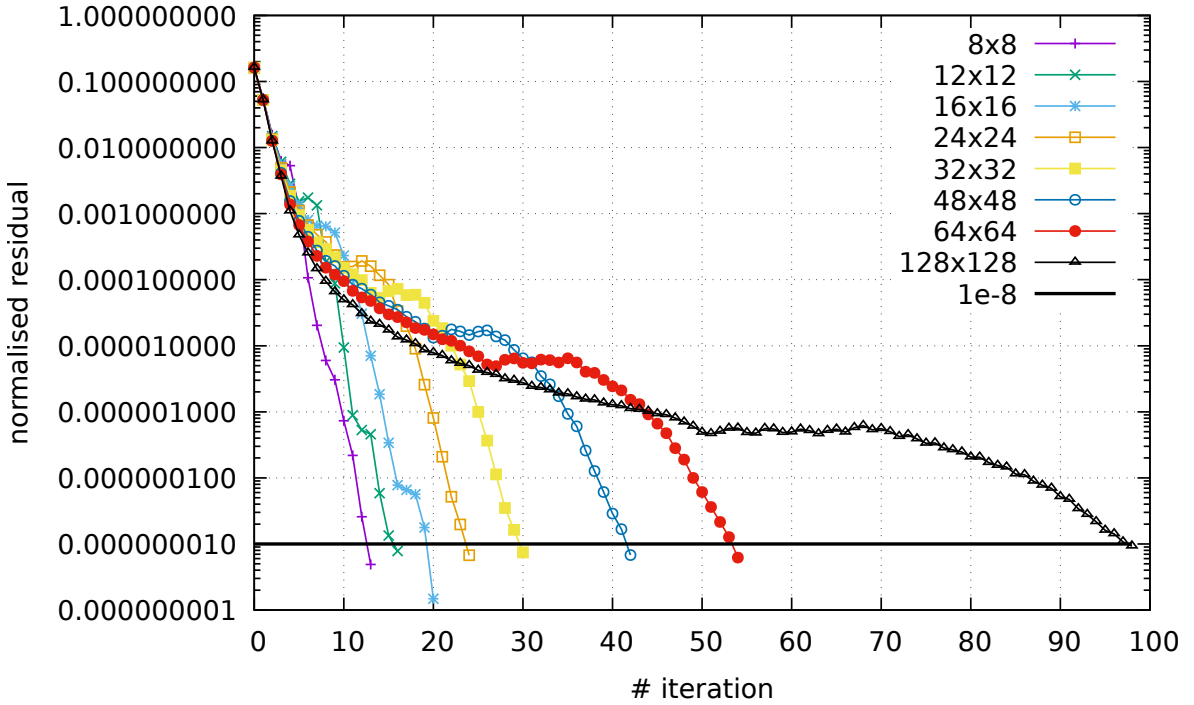


Rather interestingly the pressure checkerboard modes are not nearly as present as in Section ??? which uses a full matrix approach.

Looking at the discretisation errors for velocity and pressure, we of course recover the same rates and values as in the full matrix case.



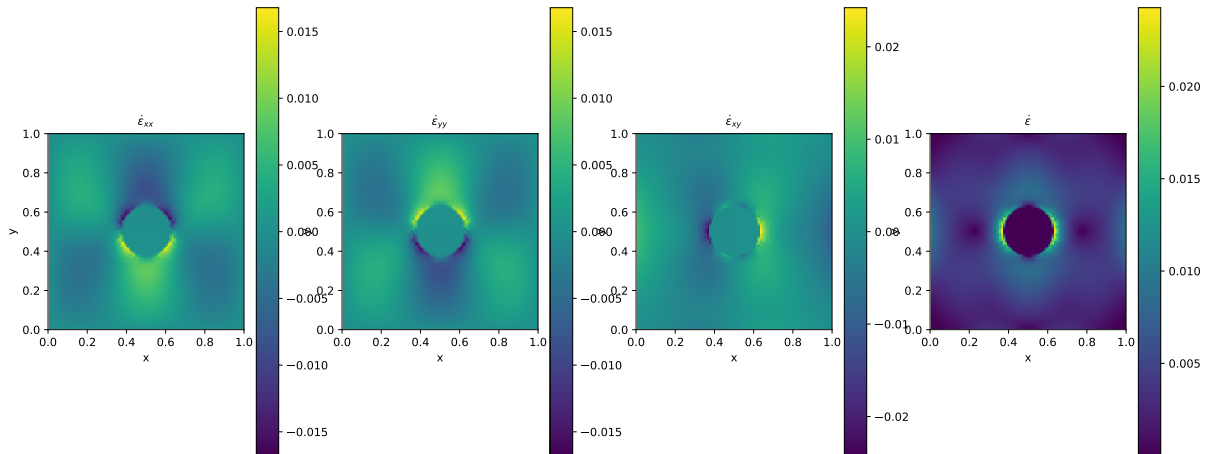
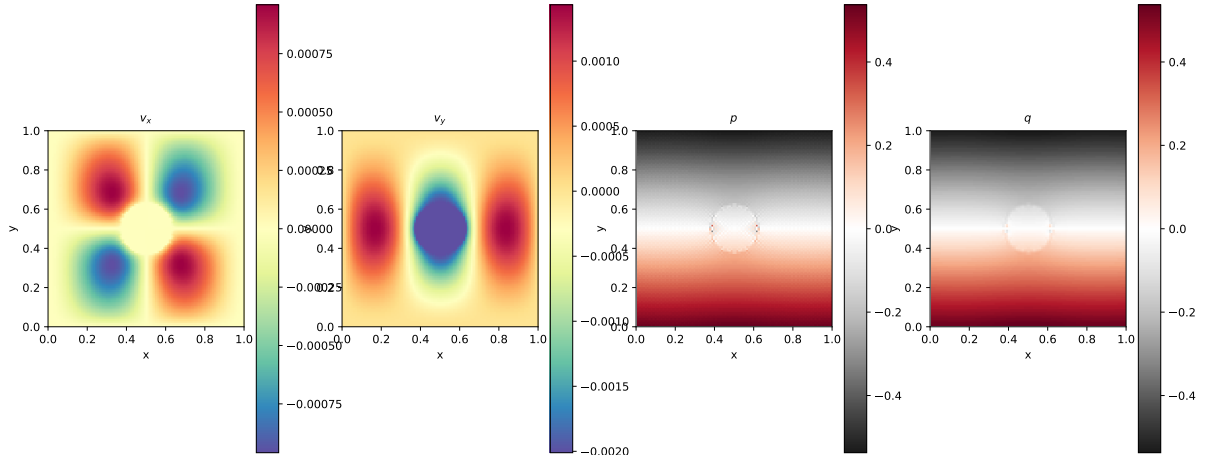
Finally, for each experiment the normalised residual (see `solver_cg`) was recorded. We see that all things equal the resolution has a strong influence on the number of iterations the solver must perform to reach the required tolerance. This is one of the manifestations of the fact that the  $Q_1 \times P_0$  element is not a stable element: the condition number of the matrix increases with resolution. We will see that this is not the case of stable elements such as  $Q_2 \times Q_1$ .



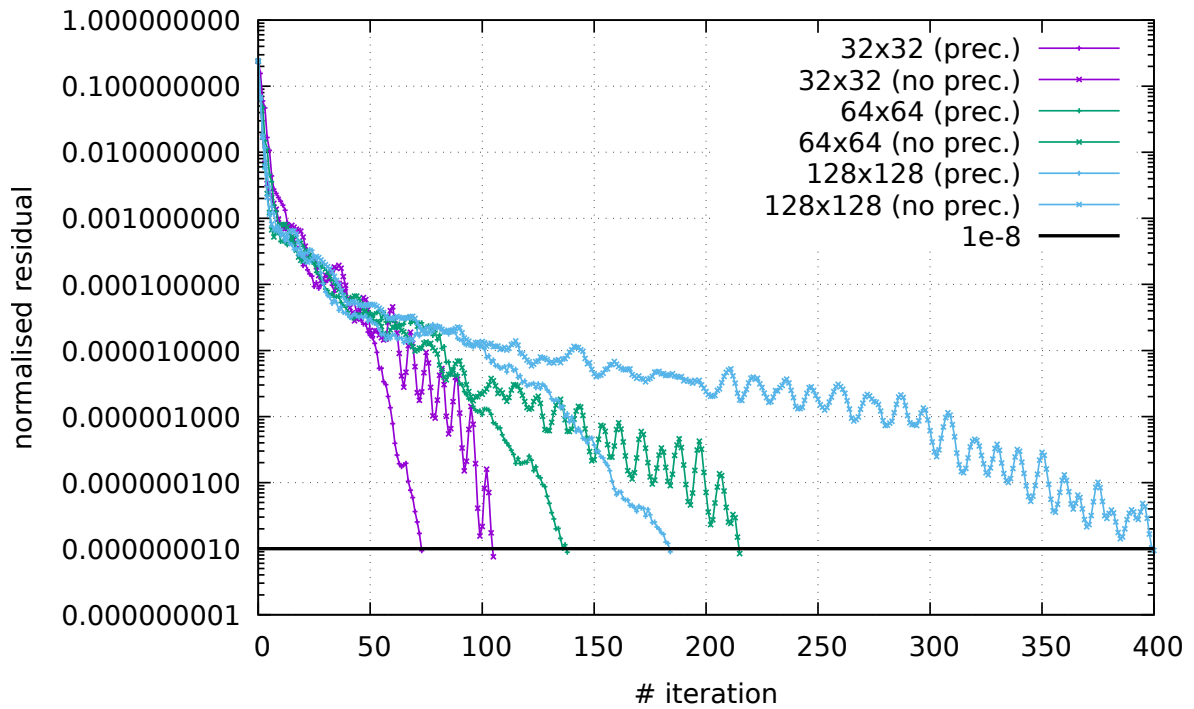
build S and have python compute its smallest and largest eigenvalues as a function of resolution?

## Stone 16: saddle point problem with Schur complement approach - Stokes sphere

We are revisiting the 2D Stokes sphere problem, but this time we use the Schur complement approach to solve the Stokes system. Because there are viscosity contrasts in the domain, it is advisable to use the Preconditioned Conjugate Gradient as presented in Section ?? (see `solver_pcg`).



The normalised residual (see `solver_pcg`) was recorded. We see that all things equal the resolution has a strong influence on the number of iterations the solver must perform to reach the required tolerance. However, we see that the use of the preconditioner can substantially reduce the number of iterations inside the Stokes solver. At resolution 128x128, this number is halved.



## Stone 17: solving the full saddle point problem in 3D

When using  $Q_1 \times P_0$  elements, this benchmark fails because of the Dirichlet b.c. on all 6 sides and all three components. However, as we will see, it does work well with  $Q_2 \times Q_1$  elements.

This benchmark begins by postulating a polynomial solution to the 3D Stokes equation [705]:

$$\vec{v} = \begin{pmatrix} x + x^2 + xy + x^3y \\ y + xy + y^2 + x^2y^2 \\ -2z - 3xz - 3yz - 5x^2yz \end{pmatrix} \quad (898)$$

and

$$p = xyz + x^3y^3z - 5/32 \quad (899)$$

While it is then trivial to verify that this velocity field is divergence-free, the corresponding body force of the Stokes equation can be computed by inserting this solution into the momentum equation with a given viscosity  $\eta$  (constant or position/velocity/strain rate dependent). The domain is a unit cube and velocity boundary conditions simply use Eq. (898). Following [382], the viscosity is given by the smoothly varying function

$$\eta = \exp(1 - \beta(x(1-x) + y(1-y) + z(1-z))) \quad (900)$$

One can easily show that the ratio of viscosities  $\eta^*$  in the system follows  $\eta^* = \exp(-3\beta/4)$  so that choosing  $\beta = 10$  yields  $\eta^* \simeq 1808$  and  $\beta = 20$  yields  $\eta^* \simeq 3.269 \times 10^6$ .

We start from the momentum conservation equation:

$$-\vec{\nabla}p + \vec{\nabla} \cdot (2\eta\dot{\epsilon}) = \vec{f}$$

The  $x$ -component of this equation writes

$$f_x = -\frac{\partial p}{\partial x} + \frac{\partial}{\partial x}(2\eta\dot{\epsilon}_{xx}) + \frac{\partial}{\partial y}(2\eta\dot{\epsilon}_{xy}) + \frac{\partial}{\partial z}(2\eta\dot{\epsilon}_{xz}) \quad (901)$$

$$= -\frac{\partial p}{\partial x} + 2\eta\frac{\partial}{\partial x}\dot{\epsilon}_{xx} + 2\eta\frac{\partial}{\partial y}\dot{\epsilon}_{xy} + 2\eta\frac{\partial}{\partial z}\dot{\epsilon}_{xz} + 2\frac{\partial\eta}{\partial x}\dot{\epsilon}_{xx} + 2\frac{\partial\eta}{\partial y}\dot{\epsilon}_{xy} + 2\frac{\partial\eta}{\partial z}\dot{\epsilon}_{xz} \quad (902)$$

Let us compute all the block separately:

$$\begin{aligned} \dot{\epsilon}_{xx} &= 1 + 2x + y + 3x^2y \\ \dot{\epsilon}_{yy} &= 1 + x + 2y + 2x^2y \\ \dot{\epsilon}_{zz} &= -2 - 3x - 3y - 5x^2y \\ 2\dot{\epsilon}_{xy} &= (x + x^3) + (y + 2xy^2) = x + y + 2xy^2 + x^3 \\ 2\dot{\epsilon}_{xz} &= (0) + (-3z - 10xyz) = -3z - 10xyz \\ 2\dot{\epsilon}_{yz} &= (0) + (-3z - 5x^2z) = -3z - 5x^2z \end{aligned}$$

In passing, one can verify that  $\dot{\epsilon}_{xx} + \dot{\epsilon}_{yy} + \dot{\epsilon}_{zz} = 0$ . We further have

$$\begin{aligned}\frac{\partial}{\partial x} 2\dot{\epsilon}_{xx} &= 2(2 + 6xy) \\ \frac{\partial}{\partial y} 2\dot{\epsilon}_{xy} &= 1 + 4xy \\ \frac{\partial}{\partial z} 2\dot{\epsilon}_{xz} &= -3 - 10xy \\ \frac{\partial}{\partial x} 2\dot{\epsilon}_{xy} &= 1 + 2y^2 + 3x^2 \\ \frac{\partial}{\partial y} 2\dot{\epsilon}_{yy} &= 2(2 + 2x^2) \\ \frac{\partial}{\partial z} 2\dot{\epsilon}_{yz} &= -3 - 5x^2 \\ \frac{\partial}{\partial x} 2\dot{\epsilon}_{xz} &= -10yz \\ \frac{\partial}{\partial y} 2\dot{\epsilon}_{yz} &= 0 \\ \frac{\partial}{\partial z} 2\dot{\epsilon}_{zz} &= 2(0)\end{aligned}\tag{903}$$

$$\begin{aligned}\frac{\partial p}{\partial x} &= yz + 3x^2y^3z \\ \frac{\partial p}{\partial y} &= xz + 3x^3y^2z\end{aligned}\tag{904}$$

$$\frac{\partial p}{\partial z} = xy + x^3y^3\tag{905}$$

**Pressure normalisation** Here again, because Dirichlet boundary conditions are prescribed on all sides the pressure is known up to an arbitrary constant. This constant can be determined by (arbitrarily) choosing to normalised the pressure field as follows:

$$\int_{\Omega} p \, d\Omega = 0\tag{906}$$

This is a single constraint associated to a single Lagrange multiplier  $\lambda$  and the global Stokes system takes the form

$$\begin{pmatrix} \mathbb{K} & \mathbb{G} & 0 \\ \mathbb{G}^T & 0 & \mathcal{C} \\ 0 & \mathcal{C}^T & 0 \end{pmatrix} \begin{pmatrix} V \\ P \\ \lambda \end{pmatrix}$$

In this particular case the constraint matrix  $\mathcal{C}$  is a vector and it only acts on the pressure degrees of freedom because of Eq.(906). Its exact expression is as follows:

$$\int_{\Omega} p \, d\Omega = \sum_e \int_{\Omega_e} p \, d\Omega = \sum_e \int_{\Omega_e} \sum_i N_i^p p_i \, d\Omega = \sum_e \sum_i \left( \int_{\Omega_e} N_i^p \, d\Omega \right) p_i = \sum_e \mathcal{C}_e \cdot \mathbf{p}_e$$

where  $\mathbf{p}_e$  is the list of pressure dofs of element  $e$ . The elemental constraint vector contains the corresponding pressure basis functions integrated over the element. These elemental constraints are then assembled into the vector  $\mathcal{C}$ .

## Constant viscosity

Choosing  $\beta = 0$  yields a constant velocity  $\eta(x, y, z) = \exp(1) \simeq 2.718$  (and greatly simplifies the right-hand side) so that

$$\frac{\partial}{\partial x} \eta(x, y, z) = 0 \quad (907)$$

$$\frac{\partial}{\partial y} \eta(x, y, z) = 0 \quad (908)$$

$$\frac{\partial}{\partial z} \eta(x, y, z) = 0 \quad (909)$$

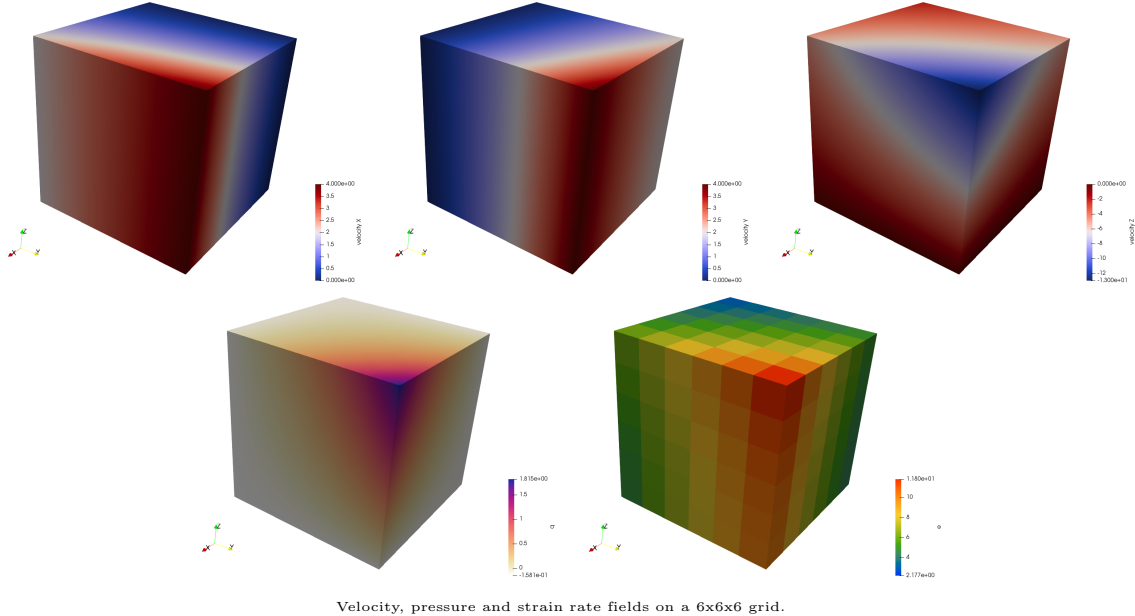
and

$$\begin{aligned} f_x &= -\frac{\partial p}{\partial x} + 2\eta \frac{\partial}{\partial x} \dot{\epsilon}_{xx} + 2\eta \frac{\partial}{\partial y} \dot{\epsilon}_{xy} + 2\eta \frac{\partial}{\partial z} \dot{\epsilon}_{xz} \\ &= -(yz + 3x^2y^3z) + 2(2 + 6xy) + (1 + 4xy) + (-3 - 10xy) \\ &= -(yz + 3x^2y^3z) + \eta(2 + 6xy) \\ f_y &= -\frac{\partial p}{\partial y} + 2\eta \frac{\partial}{\partial x} \dot{\epsilon}_{xy} + 2\eta \frac{\partial}{\partial y} \dot{\epsilon}_{yy} + 2\eta \frac{\partial}{\partial z} \dot{\epsilon}_{yz} \\ &= -(xz + 3x^3y^2z) + \eta(1 + 2y^2 + 3x^2) + \eta(2(2 + 2x^2) + \eta(-3 - 5x^2)) \\ &= -(xz + 3x^3y^2z) + \eta(2 + 2x^2 + 2y^2) \\ f_z &= -\frac{\partial p}{\partial z} + 2\eta \frac{\partial}{\partial x} \dot{\epsilon}_{xz} + 2\eta \frac{\partial}{\partial y} \dot{\epsilon}_{yz} + 2\eta \frac{\partial}{\partial z} \dot{\epsilon}_{zz} \\ &= -(xy + x^3y^3) + \eta(-10yz) + 0 + 0 \\ &= -(xy + x^3y^3) + \eta(-10yz) \end{aligned}$$

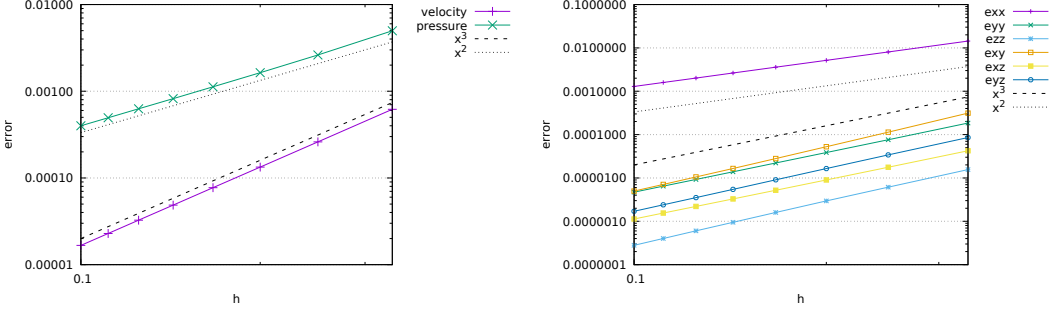
Finally

$$\vec{f} = - \begin{pmatrix} yz + 3x^2y^3z \\ xz + 3x^3y^2z \\ xy + x^3y^3 \end{pmatrix} + \eta \begin{pmatrix} 2 + 6xy \\ 2 + 2x^2 + 2y^2 \\ -10yz \end{pmatrix} \quad (910)$$

**Remark.** There seems to be a sign problem with Eq.(26) in [382].



Velocity, pressure and strain rate fields on a  $6 \times 6 \times 6$  grid.



Since the strain rate is the spatial derivative of the velocity field we should find that it converges like  $h^2$  as expected. However I am quite puzzled as to why the convergence of  $\dot{\epsilon}_{xx}$  is quadratic but at the same time almost 2 orders of magnitude higher than the other 5 components which in turn converge abnormally fast like  $h^3$ .

### Variable viscosity

The spatial derivatives of the viscosity are then given by

$$\begin{aligned}\frac{\partial}{\partial x}\eta(x, y, z) &= -(1 - 2x)\beta\eta(x, y, z) \\ \frac{\partial}{\partial y}\eta(x, y, z) &= -(1 - 2y)\beta\eta(x, y, z) \\ \frac{\partial}{\partial z}\eta(x, y, z) &= -(1 - 2z)\beta\eta(x, y, z)\end{aligned}$$

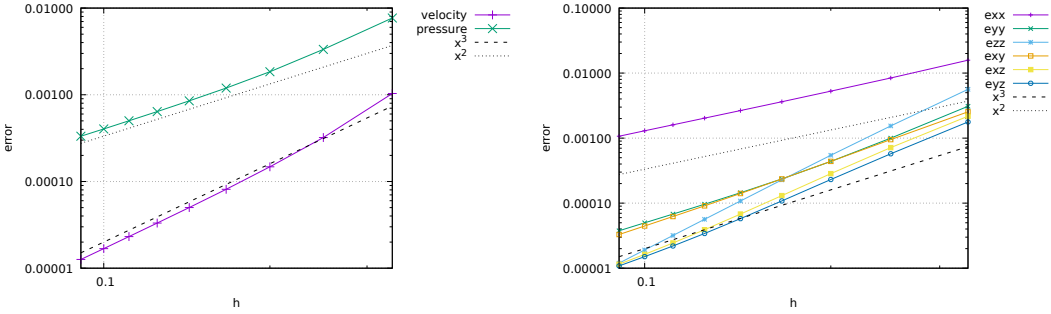
and the right-hand side by

$$\begin{aligned}\vec{f} &= - \begin{pmatrix} yz + 3x^2y^3z \\ xz + 3x^3y^2z \\ xy + x^3y^3 \end{pmatrix} + \eta \begin{pmatrix} 2 + 6xy \\ 2 + 2x^2 + 2y^2 \\ -10yz \end{pmatrix} - (1 - 2x)\beta\eta(x, y, z) \begin{pmatrix} 2\dot{\epsilon}_{xx} \\ 2\dot{\epsilon}_{xy} \\ 2\dot{\epsilon}_{xz} \end{pmatrix} \\ &\quad - (1 - 2y)\beta\eta(x, y, z) \begin{pmatrix} 2\dot{\epsilon}_{xy} \\ 2\dot{\epsilon}_{yy} \\ 2\dot{\epsilon}_{yz} \end{pmatrix} - (1 - 2z)\beta\eta(x, y, z) \begin{pmatrix} 2\dot{\epsilon}_{xz} \\ 2\dot{\epsilon}_{yz} \\ 2\dot{\epsilon}_{zz} \end{pmatrix} \\ &= - \begin{pmatrix} yz + 3x^2y^3z \\ xz + 3x^3y^2z \\ xy + x^3y^3 \end{pmatrix} + \eta \begin{pmatrix} 2 + 6xy \\ 2 + 2x^2 + 2y^2 \\ -10yz \end{pmatrix} - (1 - 2x)\beta\eta \begin{pmatrix} 2 + 4x + 2y + 6x^2y \\ x + y + 2xy^2 + x^3 \\ -3z - 10xyz \end{pmatrix} \\ &\quad - (1 - 2y)\beta\eta \begin{pmatrix} x + y + 2xy^2 + x^3 \\ 2 + 2x + 4y + 4x^2y \\ -3z - 5x^2z \end{pmatrix} - (1 - 2z)\beta\eta \begin{pmatrix} -3z - 10xyz \\ -3z - 5x^2z \\ -4 - 6x - 6y - 10x^2y \end{pmatrix}\end{aligned}\tag{911}$$

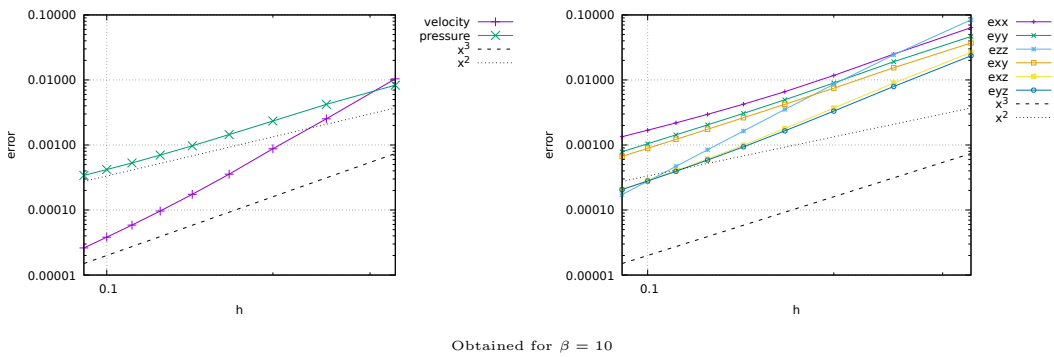
Note that at  $(x, y, z) = (0, 0, 0)$ ,  $\eta = \exp(1)$ , and at  $(x, y, z) = (0.5, 0.5, 0.5)$ ,  $\eta = \exp(1 - 3\beta/4)$  so that the maximum viscosity ratio is given by

$$\eta^* = \frac{\exp(1 - 3\beta/4)}{\exp(1)} = \exp(-3\beta/4)$$

By varying  $\beta$  between 1 and 22 we can get up to 7 orders of magnitude viscosity difference.

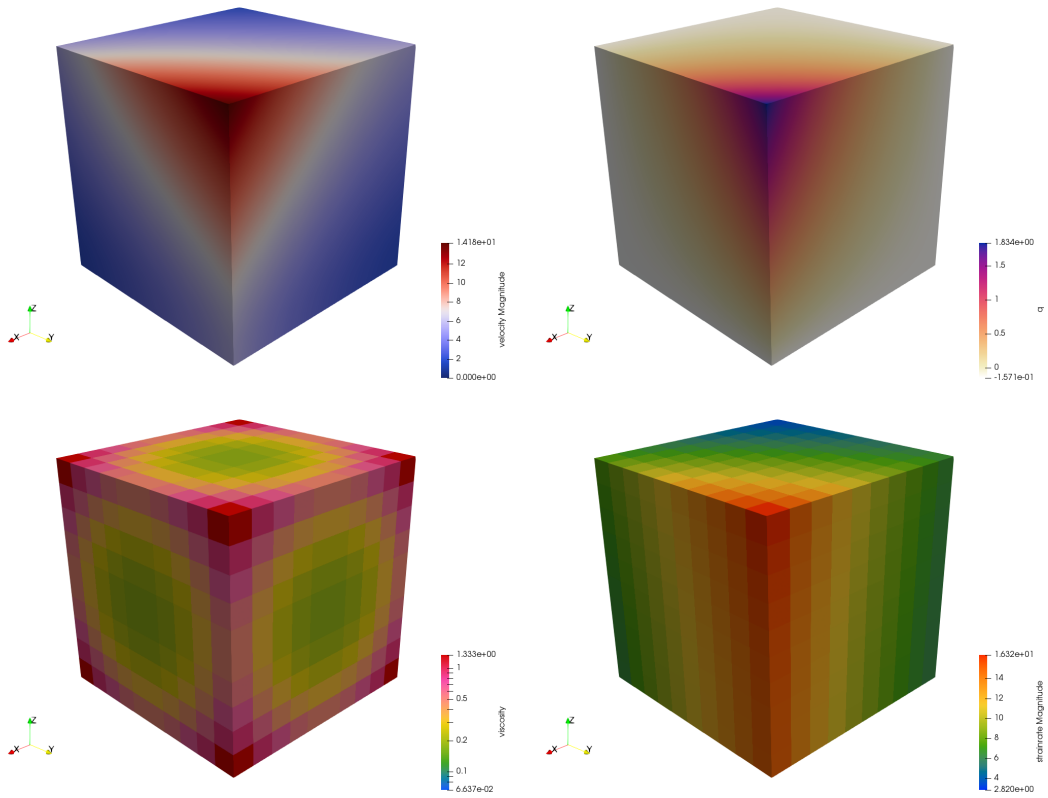


Obtained for  $\beta = 5$



We see that with increasing viscosity contrasts higher and higher resolutions are needed to attain the expected convergence rates for velocity and pressure. As for strain rate convergence, as puzzled as before

...

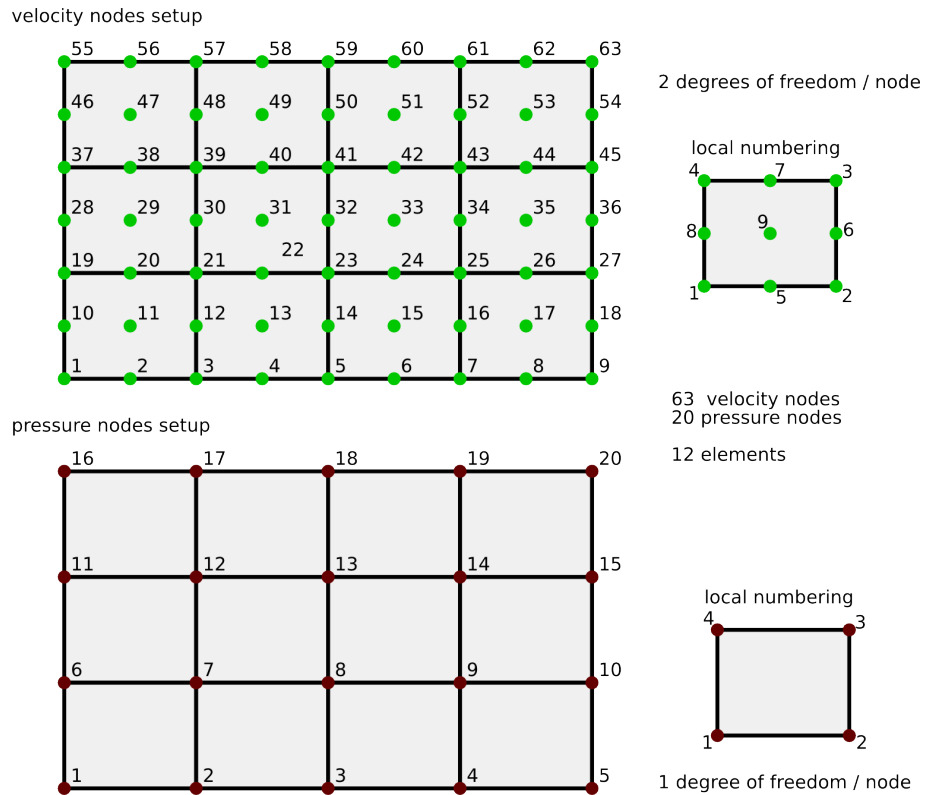


## Stone 18: solving the full saddle point problem with $Q_2 \times Q_1$ elements

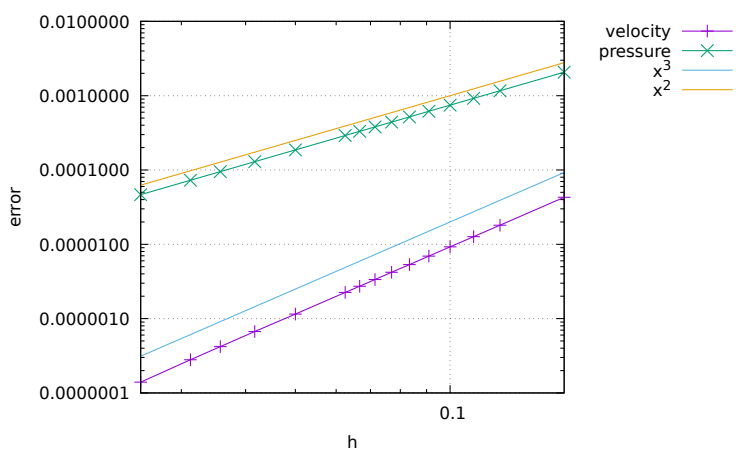
The details of the numerical setup are presented in Section ??.

Each element has  $m_V = 9$  vertices so in total  $ndof_V \times m_V = 18$  velocity dofs and  $ndof_P \times m_P = 4$  pressure dofs. The total number of velocity dofs is therefore  $NfemV = nnp \times ndofV$  while the total number of pressure dofs is  $NfemP = nel$ . The total number of dofs is then  $Nfem = NfemV + NfemP$ .

As a consequence, matrix  $\mathbb{K}$  has size  $NfemV, NfemV$  and matrix  $\mathbb{G}$  has size  $NfemV, NfemP$ . Vector  $f$  is of size  $NfemV$  and vector  $h$  is of size  $NfemP$ .



renumber all nodes to start at zero!! Also internal numbering does not work here



## Stone 19: solving the full saddle point problem with $Q_3 \times Q_2$ elements

The details of the numerical setup are presented in Section ??.

Each element has  $m_V = 16$  vertices so in total  $ndof_V \times m_V = 32$  velocity dofs and  $ndof_P \times m_P = 9$  pressure dofs. The total number of velocity dofs is therefore  $NfemV = nnp \times ndofV$  while the total number of pressure dofs is  $NfemP = nel$ . The total number of dofs is then  $Nfem = NfemV + NfemP$ .

As a consequence, matrix  $\mathbb{K}$  has size  $NfemV, NfemV$  and matrix  $\mathbb{G}$  has size  $NfemV, NfemP$ . Vector  $f$  is of size  $NfemV$  and vector  $h$  is of size  $NfemP$ .

```

60====61====62====63====64====65====66====67====68====70
||          ||          ||          ||
50    51    52    53    54    55    56    57    58    59
||          ||          ||          ||
40    41    42    43    44    45    46    47    48    49
||          ||          ||          ||
30====31====32====33====34====35====36====37====38====39
||          ||          ||          ||
20    21    22    23    24    25    26    27    28    29
||          ||          ||          ||
10    11    12    13    14    15    16    17    18    19
||          ||          ||          ||
00====01====02====03====04====05====06====07====08====09

```

Example of 3x2 mesh.  $n_{nx}=10$ ,  $n_{ny}=7$ ,  $nnp=70$ ,  $nelx=3$ ,  $nely=2$ ,  $nel=6$

```

12====13====14====15          06=====07=====08
||  ||  ||  ||          ||  ||  ||  ||
08====09====10====11          ||  ||  ||  ||
||  ||  ||  ||          03=====04=====05
04====05====06====07          ||  ||  ||  ||
||  ||  ||  ||          00=====01=====02
00====01====02====03

```

Velocity (Q3)

```

(r,s)_{00}=(-1,-1)          (r,s)_{00}=(-1,-1)
(r,s)_{01}=(-1/3,-1)         (r,s)_{01}=(0,-1)
(r,s)_{02}=(+1/3,-1)         (r,s)_{02}=(+1,-1)
(r,s)_{03}=(+1,-1)           (r,s)_{03}=(-1,0)
(r,s)_{04}=(-1,-1/3)         (r,s)_{04}=(0,0)
(r,s)_{05}=(-1/3,-1/3)       (r,s)_{05}=(+1,0)
(r,s)_{06}=(+1/3,-1/3)       (r,s)_{06}=(-1,+1)
(r,s)_{07}=(+1,-1/3)          (r,s)_{07}=(0,+1)
(r,s)_{08}=(-1,+1/3)          (r,s)_{08}=(+1,+1)
(r,s)_{09}=(-1/3,+1/3)
(r,s)_{10}=(+1/3,+1/3)
(r,s)_{11}=(+1,+1/3)
(r,s)_{12}=(-1,+1)
(r,s)_{13}=(-1/3,+1)
(r,s)_{14}=(+1/3,+1)
(r,s)_{15}=(+1,+1)

```

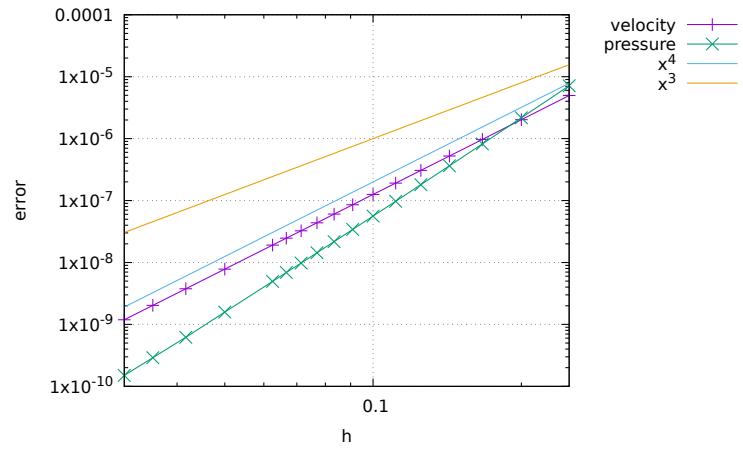
Pressure (Q2)

```

(r,s)_{00}=(-1,-1)
(r,s)_{01}=(0,-1)
(r,s)_{02}=(+1,-1)
(r,s)_{03}=(-1,0)
(r,s)_{04}=(0,0)
(r,s)_{05}=(+1,0)
(r,s)_{06}=(-1,+1)
(r,s)_{07}=(0,+1)
(r,s)_{08}=(+1,+1)

```

Write about 4 point quadrature.



velocity error rate is cubic, pressure superconvergent since the pressure field is quadratic and therefore lies into the Q2 space.

## Stone 20: the Busse benchmark

This three-dimensional benchmark was first proposed by Busse et al (1993) [389]. It has been subsequently carried out in [2466, 2567, 15, 1969, 637, 1507]. We here focus on Case 1 of [389]: an isoviscous bimodal convection experiment at  $Ra = 3 \cdot 10^5$ .

The domain is of size  $a \times b \times h$  with  $a = 1.0079h$ ,  $b = 0.6283h$  with  $h = 2700\text{km}$ . It is filled with a Newtonian fluid characterised by  $\rho_0 = 3300\text{kg.m}^{-3}$ ,  $\alpha = 10^{-5}\text{K}^{-1}$ ,  $\mu = 8.0198 \times 10^{23}\text{Pa.s}$ ,  $k = 3.564\text{W.m}^{-1}\text{.K}^{-1}$ ,  $C_p = 1080\text{J.K}^{-1}\text{.kg}^{-1}$ . The gravity vector is set to  $\mathbf{g} = (0, 0, -10)^T$ . The temperature is imposed at the bottom ( $T = 3700^\circ\text{C}$ ) and at the top ( $T = 0^\circ\text{C}$ ).

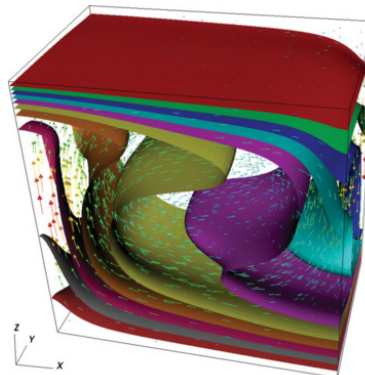
Note that using these numbers (as provided in the original paper), we arrive at  $\text{Ra}=29967.01$ , which is not exactly  $3 \cdot 10^5$  as announced. Also, the heat diffusivity  $\kappa = k/\rho_0 C_p$  is *exactly*  $10^{-6}$ .

The various measurements presented in [389] are listed hereafter:

- The Nusselt number  $Nu$  computed at the top surface following Eq. (875):

$$Nu = L_z \frac{\int \int_{z=L_z} \frac{\partial T}{\partial y} dx dy}{\int \int_{z=0} T dx dy}$$

- the root mean square velocity  $v_{rms}$  and the temperature mean square velocity  $T_{rms}$
- The vertical velocity  $w$  and temperature  $T$  at points  $\mathbf{x}_1 = (0, 0, L_z/2)$ ,  $\mathbf{x}_2 = (L_x, 0, L_z/2)$ ,  $\mathbf{x}_3 = (0, L_y, L_z/2)$  and  $\mathbf{x}_4 = (L_x, L_y, L_z/2)$ ;
- the vertical component of the heat flux  $Q$  at the top surface at all four corners.



Velocity field and isosurfaces of the temperature at steady state obtained with ASPECT.

Taken from Kronbichler et al (2012) [1507].

Given the dimensions of the domain, here are resolutions that would yield (roughly) cubic elements:

$1.0079 \times 2700\text{km}$	$\text{nelx}=$	16	20	24	28	32	36	40
$0.6283 \times 2700\text{km}$	$\text{nely}=$	10	13	15	18	20	23	25
$1.0000 \times 2700\text{km}$	$\text{nelz}=$	16	20	24	28	32	36	40

### Methodology

In what follows I highlight a few important points which are key to understanding how the code is put together and works.

```

load needed modules and functions
define parameters
build V grid (xV,yV,zV)
build V connectivity (iconV)
define b.c. for velocity (bc_fixV,bc_valV)
build T grid (xT,yT,zT)
build T connectivity (iconT)

```

```

define b.c. for temperature (bc_fixT,bc_valT)
initial temperature field
.-----> istep -----
| build K,G,f,h
| assemble them in A,rhs
| solve
| split solution vector in u,v,w,p
| {u,v,w}=relax*{u,v,w}+(1-relax)*{u,v,w}
| compute vrms
| build A, rhs for temperature
| solve for temperature T
| T=relax*T+(1-relax)*T
| compute elemental strainrate
| compute nodal strainrate
| compute nodal pressure
| measure V and T at mid side edges, Nu ...
| export to vtu and ascii files
.-----<-----

```

I fist load the shape functions which are in two separate files:

```

from shape_functionsV import NNV,dNNVdr,dNNVds,dNNVdt
from shape_functionsT import NNT,dNNTdr,dNNTds,dNNTdt

```

There are NV=nnx\*nny\*nnz velocity nodes and NT=NV temperature nodes.

The velocity grid is built: xV, yV, zV, iconV, and these are copied in xT, yT, zT and iconT for the temperature grid.

The initial temperature field is built as follows:

```

for i in range(0,NT):
    T[i] = (Temperature2-Temperature1)/Lz*zT[i]+Temperature1 \
        + 100*(np.cos(np.pi*xT[i]/Lx) + np.cos(np.pi*yT[i]/Ly))*np.sin(np.pi*zT[i]/Lz)

```

The  $\mathbf{C}$  matrix of Eq. 417 is then built:

```

c_mat = np.array([[2,0,0,0,0,0], \
                  [0,2,0,0,0,0], \
                  [0,0,2,0,0,0], \
                  [0,0,0,1,0,0], \
                  [0,0,0,0,1,0], \
                  [0,0,0,0,0,1]], dtype=np.float64)

```

**Getting to steady state** In this case we are not so much interested in the path to steady state since the published values/measurements are *at* steady state. The mass and momentum conservation equations for incompressible Stokes flow do not contain a time derivative but the energy conservation equation does. At steady state the terms  $\partial_t T$  is zero by definition so we must solve the following equation<sup>80</sup> (see Section 3.4):

$$\vec{\nabla} \cdot \vec{\nabla} T - \vec{\nabla} \cdot k \vec{\nabla} T = 0 \quad (912)$$

The Finite Element discretisation of this equation yields

$$(\mathbf{K}_a + \mathbf{K}_d) \cdot \vec{T} = \vec{0}$$

which is much simpler than the time-dependent one and avoids to carefully consider the time-discretisation altogether.

We now have to solve three coupled equations:

$$-\vec{\nabla} p + \vec{\nabla} \cdot (2\eta \dot{\varepsilon}^d) + \rho(T) \vec{g} = \vec{0} \quad (913)$$

$$\vec{\nabla} \cdot \vec{v} = 0 \quad (914)$$

$$\vec{\nabla} \cdot \vec{\nabla} T - \vec{\nabla} \cdot k \vec{\nabla} T = 0 \quad (915)$$

---

<sup>80</sup>Adiabatic heating, shear heating and internal heating are not considered in the benchmark

We could then proceed to write the weak forms of these equations and cast these as we have done before, but this time considering velocity, pressure and temperature as unknowns of a (very) large system:

$$\begin{pmatrix} \mathbb{K} & \mathbb{G} & \cdot \\ \mathbb{G}^T & 0 & \cdot \\ \cdot & \cdot & \cdot \end{pmatrix} \cdot \begin{pmatrix} V \\ P \\ T \end{pmatrix} = \begin{pmatrix} \cdot \\ \cdot \\ \cdot \end{pmatrix}$$

Once this matrix is filled a single solve will yield the steady state velocity, pressure and temperature fields!

The term  $\rho(T)$  will naturally end up in the (1,3) block of the assembled matrix as matrix  $\mathbf{L}$ . The mass conservation equation in this form is independent of temperature so the (2,3) block will be zero. The diffusion term  $\mathbf{K}_d$  naturally finds its way to the (3,3) block and since there is not occurrence of pressure in the energy equation the (3,2) block will be zero. We then obtain:

$$\begin{pmatrix} \mathbb{K} & \mathbb{G} & \mathbf{L} \\ \mathbb{G}^T & 0 & 0 \\ \cdot & 0 & \mathbf{K}_d \end{pmatrix} \cdot \begin{pmatrix} V \\ P \\ T \end{pmatrix} = \begin{pmatrix} \cdot \\ \cdot \\ \cdot \end{pmatrix}$$

The last remaining term is the advection term of the energy equation and it is a problematic one: it features the product of the velocity by the temperature. As such it is nonlinear and one cannot either put it in the (3,1) block nor in the (3,3) block.

This approach fails, which is why the problem is solved iteratively. The idea is simple: when solving the coupled mass and momentum equations, assume temperature known, and when solving the energy equation assume velocity known. We can then alternatively solve one system and then the other, constantly updating the fields when re-building the matrices or right hand sides.

However, it is well known that a straightforward implementation of this algorithm does not work in practice, i.e. it fails to converge, which is why a relaxation scheme is often implemented.

1. Solve for velocity and pressure

2. relax velocity

```
u=relax*u+(1-relax)*u_old
v=relax*v+(1-relax)*v_old
w=relax*w+(1-relax)*w_old
```

3. Solve for temperature

4. relax temperature

```
T=relax*T+(1-relax)*T_old
```

5. check for convergence:

```
if np.abs(Nu-Nu_old)<1.e-5:
    break
```

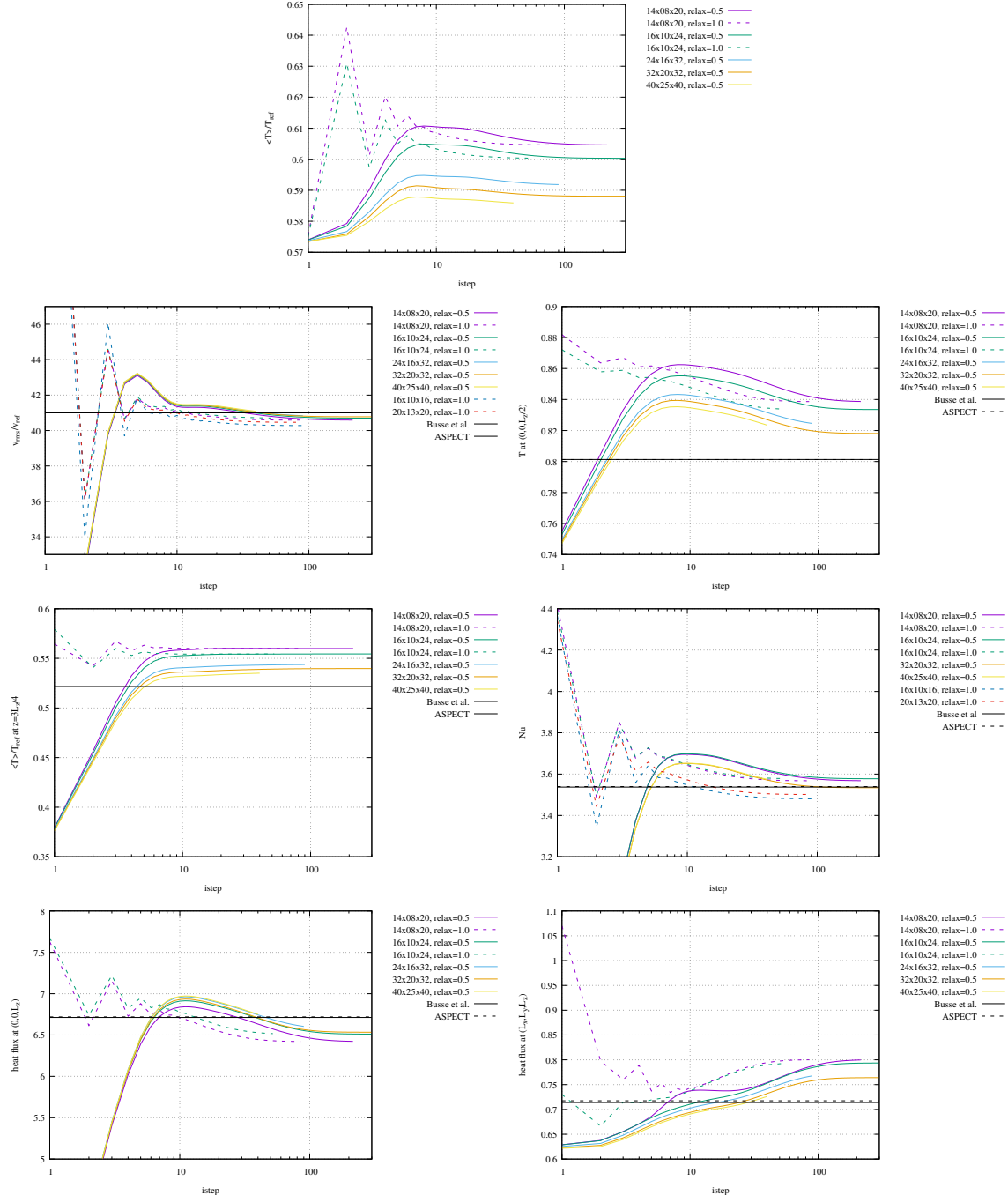
6. store old fields

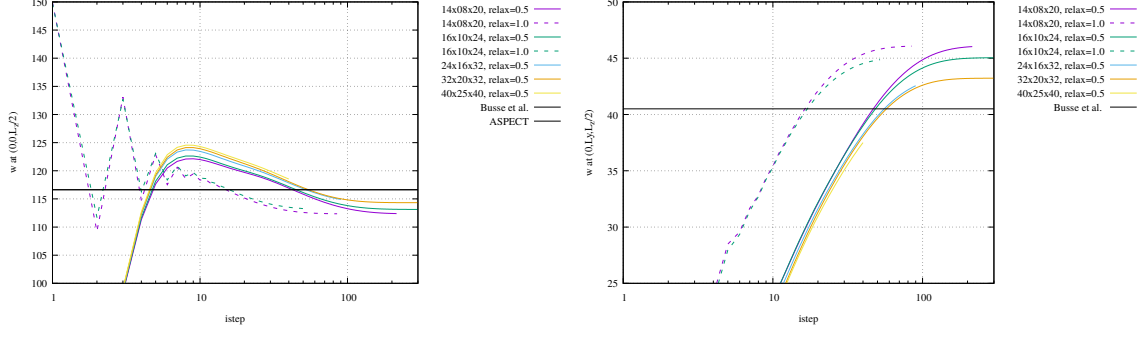
```
u_old=u
v_old=v
w_old=w
T_old=T
```

**Computing nodal derivatives** Another interesting approach here is how the strain rate is computed on the nodes as well as the temperature gradient. The strain rate is not needed for the required measurements of this benchmark but the Nusselt number calculations require  $\partial T / \partial z$  at the top boundary. The idea is simple: loop over all elements, and for each element loop over its support nodes (in this case the 2x2x2 nodes of the  $Q_1$ ), compute the required derivative there and add its contribution to the nodal field. Finally divide the obtained field by the number of elements each node is part of.

## Results

Given how the code is written and how costly 3D simulations are in general, high resolution runs take a *very* long time to run, even using relaxation instead of time stepping.





The reported values for Busse et al. in the following table are taken from Table 3 of [389]. The reported values for fieldstone are adimensionalised by means of a reference temperature (3700K), a reference lengthscale 2700km, and a reference time  $L_z^2/\kappa \sim 7.29e + 18s$ .

Mesh size	ASPECT			Busse et al [389]
	$L_z/24$	$L_z/32$	$L_z/48$	
Nu	3.5539	3.5447	3.5397	$3.5374 \pm 0.0005$
$v_{rms}$	40.997	40.999	40.999	$40.999 \pm 0.004$
$\langle T \rangle$ at $0.75 * L_z$	0.52148	0.52148	0.52148	$0.52148 \pm 0.00003$
$w(0,0,L_z/2)$	116.605	116.618	116.623	$116.625 \pm 0.030$
$w(L_x,0,L_z/2)$	-	-	-	-
$w(L_x,L_y,L_z/2)$	-	-	-	-
$w(0,L_y,L_z/2)$				$40.500 \pm 0.030$
$T(0,0,L_z/2)$	0.80126	0.80128	0.80129	$0.80130 \pm 0.00005$
$T(L_x,0,L_z/2)$	-	-	-	-
$T(L_x,L_y,L_z/2)$	-	-	-	-
$T(0,L_y,L_z/2)$				$0.61876 \pm 0.00005$
$dTdz(0,0,L_z)$	6.7679	6.7357	6.7189	$6.7127 \pm 0.0500$
$dTdz(L_x,0,L_z)$				$1.5080 \pm 0.0500$
$dTdz(L_x,L_y,L_z)$	0.7237	0.7205	0.7174	$0.7140 \pm 0.0500$
$dTdz(0,L_y,L_z)$				$3.1740 \pm 0.0500$

THIS IS NOT FINISHED: I need to run the model at higher resolutions, which will take a few days.

## Stone 22: The stabilised $Q_1 \times Q_1$ element

The details of the numerical setup are presented in Section 8.6.

We wish to use  $Q_1 \times Q_1$  element, which, unless stabilised, violates the LBB stability condition and therefore is unusable. Stabilisation can be of two types: least-squares [711, 2519, 1434, 217], or by means of an additional term in the weak form as first introduced in [705, 215], which is appealing since there is no explicit stabilisation parameter. It is further analysed in [1955, 1599, 1253, 2280, 1061]. Note that an equal-order velocity-pressure formulation that does not exhibit spurious pressure modes (without stabilisation) has been presented in [2153].

This element corresponds to bilinear velocities, bilinear pressure (equal order interpolation for both velocity and pressure) which is very convenient in terms of data structures since all dofs are colocated.

In geodynamics, it is used in the Rhea code [2402, 382] and in Gale [57]. It is also used in [1584] in its stabilised form, in conjunction with AMR. This element is quickly discussed at page 217 of Volker John's book [1351].

The stabilisation term  $\mathbb{C}$  enters the Stokes matrix in the (2,2) position:

$$\begin{pmatrix} \mathbb{K} & \mathbb{G} \\ \mathbb{G}^T & -\mathbb{C} \end{pmatrix} \cdot \begin{pmatrix} \mathcal{V} \\ \mathcal{P} \end{pmatrix} = \begin{pmatrix} f \\ h \end{pmatrix}$$

The purpose of the  $\mathbb{C}$  term is to stabilise the linear system. It is given by:

$$\mathbb{C}(p, q) = \sum_e \int_{\Omega_e} \frac{1}{\eta} (p - \Pi p)(q - \Pi q) d\Omega$$

where  $\Pi$  is the  $L^2$ -projection onto the space of element-wise constant functions:

$$\Pi p = \frac{1}{|\Omega_e|} \int_{\Omega_e} p d\Omega$$

Because of the stabilisation matrix  $\mathbb{C}$ , the numerical solution satisfies the incompressibility condition only approximately. Local mesh refinement helps to control these unwanted effects [381, 382]. Since  $\mathbb{K}$  and  $\mathbb{C}$  are symmetric matrices, the Stokes system is then an indefinite symmetric system. The Schur complement matrix  $\mathbb{S}$  is then given by

$$\mathbb{S} = \mathbb{G}^T \cdot \mathbb{K}^{-1} \cdot \mathbb{G} + \mathbb{C}$$

One can further expand the above expression for the  $\mathbb{C}$  term:

$$\begin{aligned} \mathbb{C}(p, q) &= \sum_e \int_{\Omega_e} \frac{1}{\eta} (p - \Pi p)(q - \Pi q) d\Omega \\ &= \sum_e \int_{\Omega_e} \frac{1}{\eta} [pq - (\Pi p)q - (\Pi q)p + (\Pi p)(\Pi q)] d\Omega \\ &= \sum_e \frac{1}{\eta_e} \left[ \int_{\Omega_e} pq d\Omega - \int_{\Omega_e} (\Pi p)qd\Omega - \int_{\Omega_e} (\Pi q)pd\Omega + \int_{\Omega_e} (\Pi p)(\Pi q)d\Omega \right] \\ &= \sum_e \frac{1}{\eta_e} \left[ \int_{\Omega_e} pq d\Omega - (\Pi p) \int_{\Omega_e} q d\Omega - (\Pi q) \int_{\Omega_e} p d\Omega + (\Pi p)(\Pi q) \int_{\Omega_e} d\Omega \right] \\ &= \sum_e \frac{1}{\eta_e} \left[ \int_{\Omega_e} pq d\Omega - (\Pi p)|\Omega_e|(\Pi q) - (\Pi q)|\Omega_e|(\Pi p) + (\Pi p)(\Pi q)|\Omega_e| \right] \\ &= \sum_e \frac{1}{\eta_e} \left[ \int_{\Omega_e} pq d\Omega - |\Omega_e|(\Pi p)(\Pi q) \right] \end{aligned} \tag{916}$$

where we have used the fact that on each element  $\Pi p^h$  is constant. The left term will obviously yield a  $Q_1$  mass matrix (scaled by the elemental viscosities). Note that this approach is not used in practice as we'll see hereafter.

The pressure inside an element is given by

$$p^h(\vec{x}) = \sum_k N_k^p(\vec{x}) p_k$$

so that

$$\Pi p^h = \frac{1}{|\Omega_e|} \int_{\Omega_e} \sum_k N_k^p p_k d\Omega = \sum_k \left( \underbrace{\frac{1}{|\Omega_e|} \int_{\Omega_e} N_k^p d\Omega}_{\tilde{N}_k^p} \right) p_k \quad (917)$$

and then

$$p^h - \Pi p^h = \sum_k N_k^p(\vec{x}) p_k - \sum_k \tilde{N}_k^p p_k = \sum_k (N_k^p(\vec{x}) - \tilde{N}_k^p) p_k$$

The algorithm is straightforward and as follows: In the loop over elements, a) Compute the average of each shape function  $N_k^p(\vec{x})$  over the element; b) Subtract this average to the shape function; c) Build mass matrix with modified/offset shape functions (taking in account the viscosity).

In the case of rectangular elements of size  $(h_x, h_y)$ ,  $\tilde{N}_k^p$  simplifies even more:

$$\tilde{N}_k^p = \frac{1}{|\Omega_e|} \int_{\Omega_e} N_k^p(\vec{x}) d\Omega = \frac{1}{h_x h_y} \frac{h_x h_y}{4} \int_{-1}^{+1} \int_{-1}^{+1} N_k^p(r, s) dr ds = \frac{1}{4} \int_{-1}^{+1} \int_{-1}^{+1} N_k^p(r, s) dr ds \quad (918)$$

It is easy to show that the average of the  $Q_1$  shape functions over the reference element is 1, so that  $\tilde{N}_k^p = 1/4$ . This explains why in the code we have:

```
Navrg = np.zeros(m, dtype=np.float64)
Navrg[0]=0.25
Navrg[1]=0.25
Navrg[2]=0.25
Navrg[3]=0.25
```

This also means that  $\Pi p^h = (p_1 + p_2 + p_3 + p_4)/4$ , i.e. the projected pressure is the mean of the vertex values. It follows, as shown on p.244 of [776] that the elemental  $\mathbb{C}$  matrix is (omitting the viscosity term)

$$\mathbb{C}_{el} = \mathbb{M}_{el} - \vec{q}^T \vec{q} |\Omega_e| \quad \vec{q} = \left( \frac{1}{4}, \frac{1}{4}, \frac{1}{4}, \frac{1}{4} \right)$$

The nullspace of  $\mathbb{C}$  consists of constant vectors, i.e.  $\vec{1} \in \text{null}(\mathbb{C})$  which means that the assembled stabilisation operator is consistent.

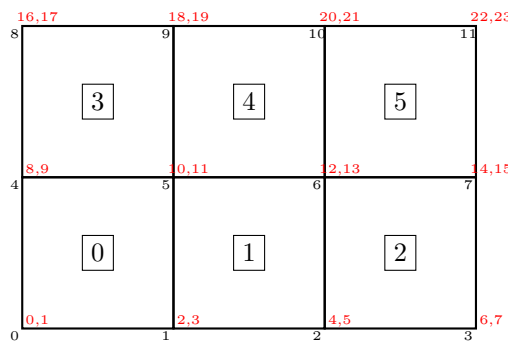
The elemental  $\mathbb{C}_{el}$  matrix is then computed like a mass matrix, although with modified shape function vectors. Inside the loop over quadrature points, we do:

```
Nvect[0:0:m]=N[0:m]-Navrg[0:m]
C_el+=Nvect.T.dot(Nvect)*jacob*weightq/viscosity(xq,yq,case)
```

It is then assembled inside the big FEM matrix

```
for k1 in range(0,m):
    for k2 in range(0,m):
        C_mat[icon[k1, ie1], icon[k2, ie1]]+=C_el[k1, k2]
```

Non-zero pattern of the  $\mathbb{G}$  matrix: Let us take a simple example: a 3x2 element grid.



The  $\mathbb{K}$  matrix is of size  $NfemV \times NfemV$  with  $NfemV = ndofV \times nnp = 2 \times 12 = 24$ . The  $\mathbb{G}$  matrix is of size  $NfemV \times NfemP$  with  $NfemP = ndofP \times nnp = 1 \times 12 = 12$ . The  $\mathbb{C}$  matrix is of size  $NfemP \times NfemP$ .

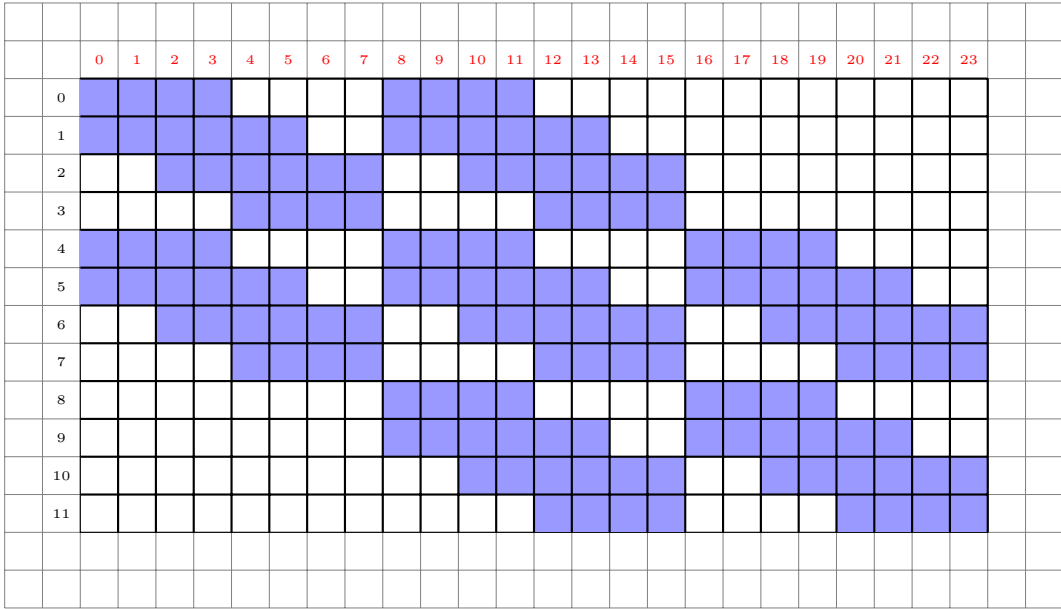
A corner pdof sees 4 vdofs, a side pdof sees 12 vdofs and an inside pdof sees 18 vdofs, so that the total number of nonzeros in  $\mathbb{G}$  can be computed as follows:

$$NZ_{\mathbb{G}} = \underbrace{4}_{\text{corners}} + \underbrace{2(nnx - 2) * 12}_{\text{2hor.sides}} + \underbrace{2(nny - 2) * 12}_{\text{2vert.sides}} + \underbrace{(nnx - 2)(nny - 2) * 18}_{\text{insidenodes}}$$

Concretely,

- pdof #0 sees vdofs 0,1,2,3,8,9,10,11
- pdof #1 sees vdofs 0,1,2,3,4,5,8,9,10,11,12,13
- pdof #5 sees vdofs 0,1,2,3,4,5,8,9,10,11,12,13,16,17,18,19,20,21

so that the  $\mathbb{G}^T$  matrix non-zero structure then is as follows:



Non-zero pattern of the  $\mathbb{C}$  matrix: Let us take a simple example: a 3x2 element grid.

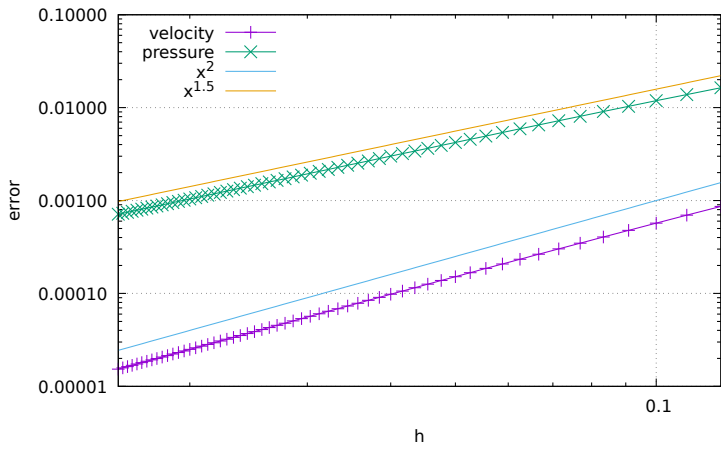
`finish structure of C matrix for q1q1`

We impose  $\int pdV = 0$  which means that the following constraint is added to the Stokes matrix:

$$\begin{pmatrix} \mathbb{K} & \mathbb{G} & 0 \\ \mathbb{G}^T & \mathbb{C} & \mathbb{L} \\ 0 & \mathbb{L}^T & 0 \end{pmatrix} \cdot \begin{pmatrix} \mathcal{V} \\ \mathcal{P} \\ \lambda \end{pmatrix} = \begin{pmatrix} f \\ h \\ 0 \end{pmatrix}$$

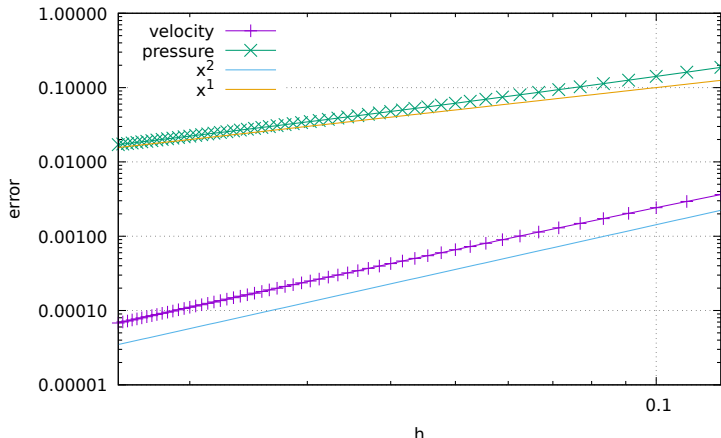
## The Donea & Huerta benchmark

As in [711] we solve the benchmark problem presented in section 8.6.1.



## The Dohrmann & Bochev benchmark

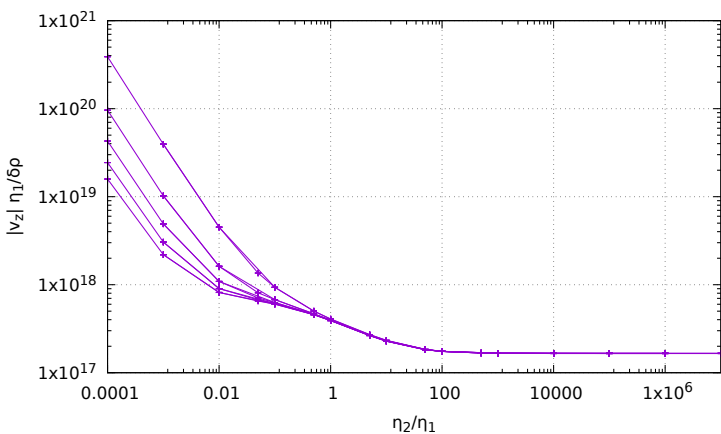
As in [705] we solve the benchmark problem presented in section 8.6.2.



compare my rates with original paper!

## The falling block experiment

The setup is described in [2532].



## Stone 23: compressible flow (1) - analytical benchmark

This work is part of the MSc thesis of T. Weir (2018).

We first start with an isothermal Stokes flow, so that we disregard the heat transport equation and the equations we wish to solve are simply:

$$-\nabla \cdot \left[ 2\eta \left( \dot{\epsilon}(\mathbf{v}) - \frac{1}{3}(\nabla \cdot \mathbf{v})\mathbf{1} \right) \right] + \nabla p = \rho \mathbf{g} \quad \text{in } \Omega, \quad (919)$$

$$\nabla \cdot (\rho \mathbf{v}) = 0 \quad \text{in } \Omega \quad (920)$$

The second equation can be rewritten  $\nabla \cdot (\rho \mathbf{v}) = \rho \nabla \cdot \mathbf{v} + \mathbf{v} \cdot \nabla \rho = 0$  or,

$$\nabla \cdot \mathbf{v} + \frac{1}{\rho} \mathbf{v} \cdot \nabla \rho = 0$$

Note that this presupposes that the density is not zero anywhere in the domain.

We use a mixed formulation and therefore keep both velocity and pressure as unknowns. We end up having to solve the following system:

$$\begin{pmatrix} \mathbb{K} & \mathbb{G} \\ \mathbb{G}^T + \mathbb{Z} & 0 \end{pmatrix} \cdot \begin{pmatrix} \mathcal{V} \\ \mathcal{P} \end{pmatrix} = \begin{pmatrix} f \\ h \end{pmatrix} \quad \text{or,} \quad \mathbb{A} \cdot X = rhs$$

Where  $\mathbb{K}$  is the stiffness matrix,  $\mathbb{G}$  is the discrete gradient operator,  $\mathbb{G}^T$  is the discrete divergence operator,  $\mathcal{V}$  the velocity vector,  $\mathcal{P}$  the pressure vector. Note that the term  $\mathbb{Z}\mathcal{V}$  derives from term  $\mathbf{v} \cdot \nabla \rho$  in the continuity equation.

Each block  $\mathbb{K}$ ,  $\mathbb{G}$ ,  $\mathbb{Z}$  and vectors  $f$  and  $h$  are built separately in the code and assembled into the matrix  $\mathbb{A}$  and vector  $rhs$  afterwards.  $\mathbb{A}$  and  $rhs$  are then passed to the solver. We will see later that there are alternatives to solve this approach which do not require to build the full Stokes matrix  $\mathbb{A}$ .

**Remark:** the term  $\mathbb{Z}\mathcal{V}$  is often put in the rhs (i.e. added to  $h$ ) so that the matrix  $\mathbb{A}$  retains the same structure as in the incompressible case. This is indeed how it is implemented in ASPECT. This however requires more work since the rhs depends on the solution and some form of iterations is needed.

In the case of a compressible flow the strain rate tensor and the deviatoric strain rate tensor are no more equal (since  $\nabla \cdot \mathbf{v} \neq 0$ ). The deviatoric strainrate tensor is given by<sup>81</sup>

$$\dot{\epsilon}^d(\mathbf{v}) = \dot{\epsilon}(\mathbf{v}) - \frac{1}{3} Tr(\dot{\epsilon})\mathbf{1} = \dot{\epsilon}(\mathbf{v}) - \frac{1}{3}(\nabla \cdot \mathbf{v})\mathbf{1}$$

In that case:

$$\dot{\epsilon}_{xx}^d = \frac{\partial u}{\partial x} - \frac{1}{3} \left( \frac{\partial u}{\partial x} + \frac{\partial v}{\partial y} \right) = \frac{2}{3} \frac{\partial u}{\partial x} - \frac{1}{3} \frac{\partial v}{\partial y} \quad (921)$$

$$\dot{\epsilon}_{yy}^d = \frac{\partial v}{\partial y} - \frac{1}{3} \left( \frac{\partial u}{\partial x} + \frac{\partial v}{\partial y} \right) = -\frac{1}{3} \frac{\partial u}{\partial x} + \frac{2}{3} \frac{\partial v}{\partial y} \quad (922)$$

$$2\dot{\epsilon}_{xy}^d = \frac{\partial u}{\partial y} + \frac{\partial v}{\partial x} \quad (923)$$

and then

$$\dot{\epsilon}^d(\mathbf{v}) = \begin{pmatrix} \frac{2}{3} \frac{\partial u}{\partial x} - \frac{1}{3} \frac{\partial v}{\partial y} & \frac{1}{2} \frac{\partial u}{\partial y} + \frac{1}{2} \frac{\partial v}{\partial x} \\ \frac{1}{2} \frac{\partial u}{\partial y} + \frac{1}{2} \frac{\partial v}{\partial x} & -\frac{1}{3} \frac{\partial u}{\partial x} + \frac{2}{3} \frac{\partial v}{\partial y} \end{pmatrix}$$

From  $\vec{\tau} = 2\eta \vec{\epsilon}^d$  we arrive at:

$$\begin{pmatrix} \tau_{xx} \\ \tau_{yy} \\ \tau_{xy} \end{pmatrix} = 2\eta \begin{pmatrix} \dot{\epsilon}_{xx}^d \\ \dot{\epsilon}_{yy}^d \\ \dot{\epsilon}_{xy}^d \end{pmatrix} = 2\eta \begin{pmatrix} 2/3 & -1/3 & 0 \\ -1/3 & 2/3 & 0 \\ 0 & 0 & 1/2 \end{pmatrix} \cdot \begin{pmatrix} \frac{\partial u}{\partial x} \\ \frac{\partial v}{\partial y} \\ \frac{\partial u}{\partial y} + \frac{\partial v}{\partial x} \end{pmatrix} = \eta \begin{pmatrix} 4/3 & -2/3 & 0 \\ -2/3 & 4/3 & 0 \\ 0 & 0 & 1 \end{pmatrix} \cdot \begin{pmatrix} \frac{\partial u}{\partial x} \\ \frac{\partial v}{\partial y} \\ \frac{\partial u}{\partial y} + \frac{\partial v}{\partial x} \end{pmatrix}$$

or,

$$\vec{\tau} = \mathbf{C}_\eta \mathbf{B} \mathbf{V}$$

---

<sup>81</sup>See the ASPECT manual for a justification of the 3 value in the denominator in 2D and 3D.

In order to test our implementation we have created a few manufactured solutions:

- benchmark #1 (ibench=1): Starting from a density profile of:

$$\rho(x, y) = xy \quad (924)$$

We derive a velocity given by:

$$v_x(x, y) = \frac{C_x}{x}, v_y(x, y) = \frac{C_y}{y} \quad (925)$$

With  $g_x(x, y) = \frac{1}{x}$  and  $g_y(x, y) = \frac{1}{y}$ , this leads us to a pressure profile:

$$p = -\eta \left( \frac{4C_x}{3x^2} + \frac{4C_y}{3y^2} \right) + xy + C_0 \quad (926)$$

This gives us a strain rate:

$$\dot{\epsilon}_{xx} = \frac{-C_x}{x^2} \quad \dot{\epsilon}_{yy} = \frac{-C_y}{y^2} \quad \dot{\epsilon}_{xy} = 0$$

In what follows, we choose  $\eta = 1$  and  $C_x = C_y = 1$  and for a unit square domain  $[1 : 2] \times [1 : 2]$  we compute  $C_0$  so that the pressure is normalised to zero over the whole domain and obtain  $C_0 = -1$ .

- benchmark #2 (ibench=2): Starting from a density profile of:

$$\rho = \cos(x) \cos(y) \quad (927)$$

We derive a velocity given by:

$$v_x = \frac{C_x}{\cos(x)}, v_y = \frac{C_y}{\cos(y)} \quad (928)$$

With  $g_x = \frac{1}{\cos(y)}$  and  $g_y = \frac{1}{\cos(x)}$ , this leads us to a pressure profile:

$$p = \eta \left( \frac{4C_x \sin(x)}{3 \cos^2(x)} + \frac{4C_y \sin(y)}{3 \cos^2(y)} \right) + (\sin(x) + \sin(y)) + C_0 \quad (929)$$

$$\dot{\epsilon}_{xx} = C_x \frac{\sin(x)}{\cos^2(x)} \quad \dot{\epsilon}_{yy} = C_y \frac{\sin(y)}{\cos^2(y)} \quad \dot{\epsilon}_{xy} = 0$$

We choose  $\eta = 1$  and  $C_x = C_y = 1$ . The domain is the unit square  $[0 : 1] \times [0 : 1]$  and we obtain  $C_0$  as before and obtain

$$C_0 = 2 - 2 \cos(1) + 8/3(\frac{1}{\cos(1)} - 1) \simeq 3.18823730$$

(thank you WolframAlpha)

- benchmark #3 (ibench=3)
- benchmark #4 (ibench=4)
- benchmark #5 (ibench=5)

ToDo:

- pbs with odd vs even number of elements
- q is 'fine' everywhere except in the corners - revisit pressure smoothing paper?
- redo A v d Berg benchmark (see Tom Weir thesis)

## Stone 24: compressible flow (2) - convection box

This work is part of the MSc thesis of T. Weir (2018).



Relevant Literature[1296, 2499, 1582, 1439, 1584, 1652, 1169, 495]

### The physics

Let us start with some thermodynamics. Every material has an equation of state. The equilibrium thermodynamic state of any material can be constrained if any two state variables are specified. Examples of state variables include the pressure  $p$  and specific volume  $\nu = 1/\rho$ , as well as the temperature  $T$ .

After linearisation, the density depends on temperature and pressure as follows:

$$\rho(T, p) = \rho_0 ((1 - \alpha(T - T_0) + \beta_T p)$$

where  $\alpha$  is the coefficient of thermal expansion, also called thermal expansivity:

$$\alpha = -\frac{1}{\rho} \left( \frac{\partial \rho}{\partial T} \right)_p$$

$\alpha$  is the percentage increase in volume of a material per degree of temperature increase; the subscript  $p$  means that the pressure is held fixed.

$\beta_T$  is the isothermal compressibility of the fluid, which is given by

$$\beta_T = \frac{1}{K} = \frac{1}{\rho} \left( \frac{\partial \rho}{\partial P} \right)_T$$

with  $K$  the bulk modulus. Values of  $\beta_T = 10^{-12} - 10^{-11} \text{ Pa}^{-1}$  are reasonable for Earth's mantle, with values decreasing by about a factor of 5 between the shallow lithosphere and core-mantle boundary. This is the percentage increase in density per unit change in pressure at constant temperature. Both the coefficient of thermal expansion and the isothermal compressibility can be obtained from the equation of state.

The full set of equations we wish to solve is given by

$$-\nabla \cdot [2\eta \dot{\epsilon}^d(\mathbf{v})] + \nabla p = \rho_0 ((1 - \alpha(T - T_0) + \beta_T p) \mathbf{g} \quad \text{in } \Omega \quad (930)$$

$$\nabla \cdot \mathbf{v} + \frac{1}{\rho} \mathbf{v} \cdot \nabla \rho = 0 \quad \text{in } \Omega \quad (931)$$

$$\rho C_p \left( \frac{\partial T}{\partial t} + \mathbf{v} \cdot \nabla T \right) - \nabla \cdot k \nabla T = \rho H + 2\eta \dot{\epsilon}^d : \dot{\epsilon}^d + \alpha T \left( \frac{\partial p}{\partial t} + \mathbf{v} \cdot \nabla p \right) \quad \text{in } \Omega, \quad (932)$$

Note that this presupposes that the density is not zero anywhere in the domain.

### The numerics

We use a mixed formulation and therefore keep both velocity and pressure as unknowns. We end up having to solve the following system:

$$\begin{pmatrix} \mathbb{K} & \mathbb{G} + \mathbb{W} \\ \mathbb{G}^T + \mathbb{Z} & 0 \end{pmatrix} \cdot \begin{pmatrix} \mathcal{V} \\ \mathcal{P} \end{pmatrix} = \begin{pmatrix} f \\ h \end{pmatrix} \quad \text{or,} \quad \mathbb{A} \cdot X = rhs$$

Where  $\mathbb{K}$  is the stiffness matrix,  $\mathbb{G}$  is the discrete gradient operator,  $\mathbb{G}^T$  is the discrete divergence operator,  $\mathcal{V}$  the velocity vector,  $\mathcal{P}$  the pressure vector. Note that the term  $\mathbb{Z}\mathcal{V}$  derives from term  $\mathbf{v} \cdot \nabla \rho$  in the continuity equation.

As perfectly explained in the step 32 of deal.II<sup>82</sup>, we need to scale the  $\mathbb{G}$  term since it is many orders of magnitude smaller than  $\mathbb{K}$ , which introduces large inaccuracies in the solving process to the point that

<sup>82</sup>[https://www.dealii.org/9.0.0/doxygen/deal.II/step\\_32.html](https://www.dealii.org/9.0.0/doxygen/deal.II/step_32.html)

the solution is nonsensical. This scaling coefficient is  $\eta/L$ . After building the  $\mathbb{G}$  block, it is then scaled as follows:  $\mathbb{G}' = \frac{\eta}{L}\mathbb{G}$  so that we now solve

$$\begin{pmatrix} \mathbb{K} & \mathbb{G}' + \mathbb{W} \\ \mathbb{G}'^T + \mathbb{Z} & 0 \end{pmatrix} \cdot \begin{pmatrix} \mathcal{V} \\ \mathcal{P}' \end{pmatrix} = \begin{pmatrix} f \\ h \end{pmatrix}$$

After the solve phase, we recover the real pressure with  $\mathcal{P} = \frac{\eta}{L}\mathcal{P}'$ .

adapt notes since I should scale  $\mathbb{W}$  and  $\mathbb{Z}$  too.  $h$  should be scaled too !!!!!!!!

Each block  $\mathbb{K}$ ,  $\mathbb{G}$ ,  $\mathbb{Z}$  and vectors  $f$  and  $h$  are built separately in the code and assembled into the matrix  $\mathbb{A}$  and vector  $rhs$  afterwards.  $\mathbb{A}$  and  $rhs$  are then passed to the solver. We will see later that there are alternatives to solve this approach which do not require to build the full Stokes matrix  $\mathbb{A}$ .

**Remark 1:** the terms  $\mathbb{Z}\mathcal{V}$  and  $\mathbb{W}\mathcal{P}$  are often put in the rhs (i.e. added to  $h$ ) so that the matrix  $\mathbb{A}$  retains the same structure as in the incompressible case. This is indeed how it is implemented in ASPECT, see also appendix A of [1582]. This however requires more work since the rhs depends on the solution and some form of iterations is needed.

**Remark 2:** Very often the adiabatic heating term  $\alpha T(\mathbf{v} \cdot \nabla p)$  is simplified as follows: If you assume the vertical component of the gradient of the dynamic pressure to be small compared to the gradient of the total pressure (in other words, the gradient is dominated by the gradient of the hydrostatic pressure), then  $-\rho\mathbf{g} \simeq \nabla p$  and then  $\alpha T(\mathbf{v} \cdot \nabla p) \simeq -\alpha\rho T\mathbf{v} \cdot \mathbf{g}$ . We will however not be using this approximation in what follows.

We have already established that

$$\vec{\tau} = \mathbf{C}_\eta \mathbf{B} \mathbf{V}$$

The following measurements are carried out:

- The root mean square velocity (**vrms**):

$$v_{rms} = \sqrt{\frac{1}{V} \int_V v^2 dV}$$

- The average temperature (**Tavrg**):

$$\langle T \rangle = \frac{1}{V} \int_V T dV$$

- The total mass (**mass**):

$$M = \int_V \rho dV$$

- The Nusselt number (**Nu**):

$$Nu = -\frac{1}{Lx} \frac{1}{\Delta T} \int_0^{Lx} \frac{\partial T(x, y = L_y)}{\partial y} dx$$

- The kinetic energy (**EK**):

$$E_K = \int_V \frac{1}{2} \rho v^2 dV$$

- The work done against gravity

$$\langle W \rangle = - \int_V \rho g_y v_y dV$$

- The total viscous dissipation (**visc\_diss**)

$$\langle \Phi \rangle = \int \Phi dV = \frac{1}{V} \int 2\eta \dot{\epsilon} : \dot{\epsilon} dV$$

- The gravitational potential energy (**EG**)

$$E_G = \int_V \rho g_y (L_y - y) dV$$

- The internal thermal energy (ET)

$$E_T = \int_V \rho_{(0)} C_p T dV$$

**Remark 3:** Measuring the total mass can be misleading: indeed because  $\rho = \rho_0(1 - \alpha T)$ , then measuring the total mass amounts to measuring a constant minus the volume-integrated temperature, and there is no reason why the latter should be zero, so that there is no reason why the total mass should be zero...!

## The experimental setup

The setup is as follows: the domain is  $Lx = Ly = 3000\text{km}$ . Free slip boundary conditions are imposed on all four sides. The initial temperature is given by:

$$T(x, y) = \left( \frac{L_y - y}{L_y} - 0.01 \cos\left(\frac{\pi x}{L_x}\right) \sin\left(\frac{\pi y}{L_y}\right) \right) \Delta T + T_{surf}$$

with  $\Delta T = 4000\text{K}$ ,  $T_{surf} = T_0 = 273.15\text{K}$ . The temperature is set to  $\Delta T + T_{surf}$  at the bottom and  $T_{surf}$  at the top. We also set  $k = 3$ ,  $C_p = 1250$ ,  $|g| = 10$ ,  $\rho_0 = 3000$  and we keep the Rayleigh number  $Ra$  and dissipation number  $Di$  as input parameters:

$$Ra = \frac{\alpha g \Delta T L^3 \rho_0^2 C_p}{\eta k} \quad Di = \frac{\alpha g L}{C_p}$$

From the second equation we get  $\alpha = \frac{Di C_p}{gL}$ , which we can insert in the first one:

$$Ra = \frac{Di C_p^2 \Delta T L^2 \rho_0^2}{\eta k} \quad \text{or}, \quad \eta = \frac{Di C_p^2 \Delta T L^2 \rho_0^2}{Ra k}$$

For instance, for  $Ra = 10^4$  and  $Di = 0.75$ , we obtain  $\alpha \simeq 3 \cdot 10^{-5}$  and  $\eta \simeq 10^{25}$  which are quite reasonable values.

## Scaling

Following [1439], we non-dimensionalize the equations using the reference values for density  $\rho_r$ , thermal expansivity  $\alpha_r$ , temperature contrast  $\Delta T_r$  (`refTemp`), thermal conductivity  $k_r$ , heat capacity  $C_p$ , depth of the fluid layer  $L$  and viscosity  $\eta_r$ . The non-dimensionalization for velocity,  $u_r$ , pressure  $p_r$  and time,  $t_r$  become

$$u_r = \frac{k_r}{\rho_r C_p L} \quad (\text{refvel})$$

$$p_r = \frac{\eta_r k_r}{\rho_r C_p L^2} \quad (\text{refpress})$$

$$t_r = \frac{\rho_r C_p L^2}{k_r} \quad (\text{reftime})$$

In the case of the setup described hereabove, and when choosing  $Ra = 10^4$  and  $Di = 0.5$ , we get:

```
alphaT 2.08333e-05
eta 8.437500e+24
reftime 1.125000e+19
refvel 2.666667e-13
refPress 7.500000e+05
```

## Conservation of energy 1

### under BA and EBA approximations

Following [1582], we take the dot product of the momentum equation with the velocity  $\mathbf{v}$  and integrate over the whole volume<sup>83</sup>:

$$\int_V [-\nabla \cdot \boldsymbol{\tau} + \nabla p] \cdot \mathbf{v} dV = \int_V \rho \mathbf{g} \cdot \mathbf{v} dV$$

or,

$$-\int_V (\nabla \cdot \boldsymbol{\tau}) \cdot \mathbf{v} dV + \int_V \nabla p \cdot \mathbf{v} dV = \int_V \rho \mathbf{g} \cdot \mathbf{v} dV$$

Let us look at each block separately:

$$-\int_V (\nabla \cdot \boldsymbol{\tau}) \cdot \mathbf{v} dV = -\int_S \boldsymbol{\tau} \underbrace{\mathbf{v} \cdot \mathbf{n}}_{=0 \text{ (b.c.)}} dS + \int_V \boldsymbol{\tau} : \nabla \mathbf{v} dV = \int_V \boldsymbol{\tau} : \dot{\boldsymbol{\varepsilon}} dV = \int_V \Phi dV$$

which is the volume integral of the shear heating. Then,

$$\int_V \nabla p \cdot \mathbf{v} dV = \int_S p \underbrace{\mathbf{v} \cdot \mathbf{n}}_{=0 \text{ (b.c.)}} dS - \int_V \underbrace{\nabla \cdot \mathbf{v}}_{=0 \text{ (incomp.)}} pdV = 0$$

which is then zero in the case of an incompressible flow. And finally

$$\int_V \rho \mathbf{g} \cdot \mathbf{v} dV = W$$

which is the work against gravity.

Conclusion for an *incompressible* fluid: we should have

$$\int_V \Phi dV = \int_V \rho \mathbf{g} \cdot \mathbf{v} dV \quad (933)$$

This formula is hugely problematic: indeed, the term  $\rho$  in the rhs is the full density. We know that to the value of  $\rho_0$  corresponds a lithostatic pressure gradient  $p_L = \rho_0 gy$ . In this case one can write  $\rho = \rho_0 + \rho'$  and  $p = p_L + p'$  so that we also have

$$\int_V [-\nabla \cdot \boldsymbol{\tau} + \nabla p'] \cdot \mathbf{v} dV = \int_V \rho' \mathbf{g} \cdot \mathbf{v} dV$$

which will ultimately yield

$$\int_V \Phi dV = \int_V \rho' \mathbf{g} \cdot \mathbf{v} dV = \int_V (\rho - \rho_0) \mathbf{g} \cdot \mathbf{v} dV \quad (934)$$

Obviously Eqs.(933) and (934) cannot be true at the same time. The problem comes from the nature of the (E)BA approximation:  $\rho = \rho_0$  in the mass conservation equation but it is not constant in the momentum conservation equation, which is of course inconsistent. Since the mass conservation equation is  $\nabla \cdot \mathbf{v} = 0$  under this approximation then the term  $\int_V \nabla p \cdot \mathbf{v} dV$  is always zero for any pressure (full pressure  $p$ , or overpressure  $p - p_L$ ), hence the paradox. This paradox will be lifted when a consistent set of equations will be used (compressible formulation). On a practical note, Eqs.(933) is not verified by the code, while (934) is.

In the end:

$$\boxed{\int_V \Phi dV = \underbrace{\int_V (\rho - \rho_0) \mathbf{g} \cdot \mathbf{v} dV}_{\text{visc.diss}} + \underbrace{\int_V (\rho - \rho_0) \mathbf{g} \cdot \mathbf{v} dV}_{\text{work_grav}}} \quad (935)$$

<sup>83</sup>Check: this is akin to looking at the power, force\*velocity, says Arie

**under no approximation at all**

$$\int_V \nabla p \cdot \mathbf{v} dV = \int_S p \underbrace{\mathbf{v} \cdot \mathbf{n}}_{=0 \text{ (b.c.)}} dS - \int_V \nabla \cdot \mathbf{v} pdV = 0 \quad (936)$$

$$= \int_V \frac{1}{\rho} \mathbf{v} \cdot \nabla \rho pdV = 0 \quad (937)$$

(938)

**ToDo:** see section 3 of [1582] where this is carried out with the Adams-Williamson eos.

## Conservation of energy 2

Also, following the Reynold's transport theorem [1699], p210, we have for a property  $A$  (per unit mass)

$$\frac{d}{dt} \int_V A \rho dV = \int_V \frac{\partial}{\partial t} (A \rho) dV + \int_S A \rho \mathbf{v} \cdot \mathbf{n} dS$$

Let us apply to this to  $A = C_p T$  and compute the time derivative of the internal energy:

$$\frac{d}{dt} \int_V \rho C_p T dV = \int_V \frac{\partial}{\partial t} (\rho C_p T) dV + \int_S \rho \underbrace{\mathbf{v} \cdot \mathbf{n}}_{=0 \text{ (b.c.)}} dS = \underbrace{\int_V C_p T \frac{\partial \rho}{\partial t} dV}_I + \underbrace{\int_V \rho C_p \frac{\partial T}{\partial t} dV}_{II} \quad (939)$$

In order to expand  $I$ , the mass conservation equation will be used, while the heat transport equation will be used for  $II$ :

$$I = \int_V C_p T \frac{\partial \rho}{\partial t} dV = - \int_V C_p T \nabla \cdot (\rho \mathbf{v}) dV = - \int_V C_p T \rho \underbrace{\mathbf{v} \cdot \mathbf{n}}_{=0 \text{ (b.c.)}} dS + \int_V \rho C_p \nabla T \cdot \mathbf{v} dV \quad (940)$$

$$II = \int_V \rho C_p \frac{\partial T}{\partial t} dV = \int_V \left[ -\rho C_p \mathbf{v} \cdot \nabla T + \nabla \cdot k \nabla T + \rho H + \Phi + \alpha T \left( \frac{\partial p}{\partial t} + \mathbf{v} \cdot \nabla p \right) \right] dV \quad (941)$$

$$= \int_V \left[ -\rho C_p \mathbf{v} \cdot \nabla T + \rho H + \Phi + \alpha T \left( \frac{\partial p}{\partial t} + \mathbf{v} \cdot \nabla p \right) \right] dV + \int_V \nabla \cdot k \nabla T dV \quad (942)$$

$$= \int_V \left[ -\rho C_p \mathbf{v} \cdot \nabla T + \rho H + \Phi + \alpha T \left( \frac{\partial p}{\partial t} + \mathbf{v} \cdot \nabla p \right) \right] dV + \int_S k \nabla T \cdot \mathbf{n} dS \quad (943)$$

$$= \int_V \left[ -\rho C_p \mathbf{v} \cdot \nabla T + \rho H + \Phi + \alpha T \left( \frac{\partial p}{\partial t} + \mathbf{v} \cdot \nabla p \right) \right] dV - \int_S \mathbf{q} \cdot \mathbf{n} dS \quad (944)$$

Finally:

$$I + II = \underbrace{\frac{d}{dt} \int_V \rho C_p T dV}_{ET} = \int_V \left[ \rho H + \Phi + \alpha T \left( \frac{\partial p}{\partial t} + \mathbf{v} \cdot \nabla p \right) \right] dV - \int_S \mathbf{q} \cdot \mathbf{n} dS \quad (945)$$

$$= \int_V \rho H dV + \underbrace{\int_V \Phi dV}_{visc\_diss} + \underbrace{\int_V \alpha T \frac{\partial p}{\partial t} dV}_{extra} + \underbrace{\int_V \alpha T \mathbf{v} \cdot \nabla p dV}_{adiab\_heating} - \underbrace{\int_S \mathbf{q} \cdot \mathbf{n} dS}_{heatflux\_boundary} \quad (946)$$

This was of course needlessly complicated as the term  $\partial \rho / \partial t$  is always taken to be zero, so that  $I = 0$  automatically. The mass conservation equation is then simply  $\nabla \cdot (\rho \mathbf{v}) = 0$ . Then it follows that

$$0 = \int_V C_p T \nabla \cdot (\rho \mathbf{v}) dV = - \int_V C_p T \rho \underbrace{\mathbf{v} \cdot \mathbf{n}}_{=0 \text{ (b.c.)}} dS + \int_V \rho C_p \nabla T \cdot \mathbf{v} dV \quad (947)$$

$$= \int_V \rho C_p \nabla T \cdot \mathbf{v} dV \quad (948)$$

so that the same term in Eq.(944) vanishes too, and then Eq.(946) is always valid, although one should be careful when computing  $E_T$  in the BA and EBA cases as it should use  $\rho_0$  and not  $\rho$ .

## The problem of the onset of convection

[wiki] In geophysics, the Rayleigh number is of fundamental importance: it indicates the presence and strength of convection within a fluid body such as the Earth's mantle. The mantle is a solid that behaves as a fluid over geological time scales.

The Rayleigh number essentially is an indicator of the type of heat transport mechanism. At low Rayleigh numbers conduction processes dominate over convection ones. At high Rayleigh numbers it is the other way around. There is a so-called critical value of the number with delineates the transition from one regime to the other.

This problem has been studied and approached both theoretically and numerically [2581, e.g.] and it was found that the critical Rayleigh number  $Ra_c$  is

$$Ra_c = (27/4)\pi^4 \simeq 657.5$$

in setups similar to ours.

### VERY BIG PROBLEM

The temperature setup is built as follows:  $T_{surf}$  is prescribed at the top,  $T_{surf} + \Delta T$  is prescribed at the bottom. The initial temperature profile is linear between these two values. In the case of BA, the actual value of  $T_{surf}$  is of no consequence. However, for the EBA the full temperature is present in the adiabatic heating term on the rhs of the hte, and the value of  $T_{surf}$  will therefore influence the solution greatly. This is very problematic as there is no real way to arrive at the surface temperature from the King paper. On top of this, the density uses a reference temperature  $T_0$  which too will influence the solution without being present in the controlling  $Ra$  and  $Di$  numbers!!

In light thereof, it will be very difficult to recover the values of King et al for EBA!

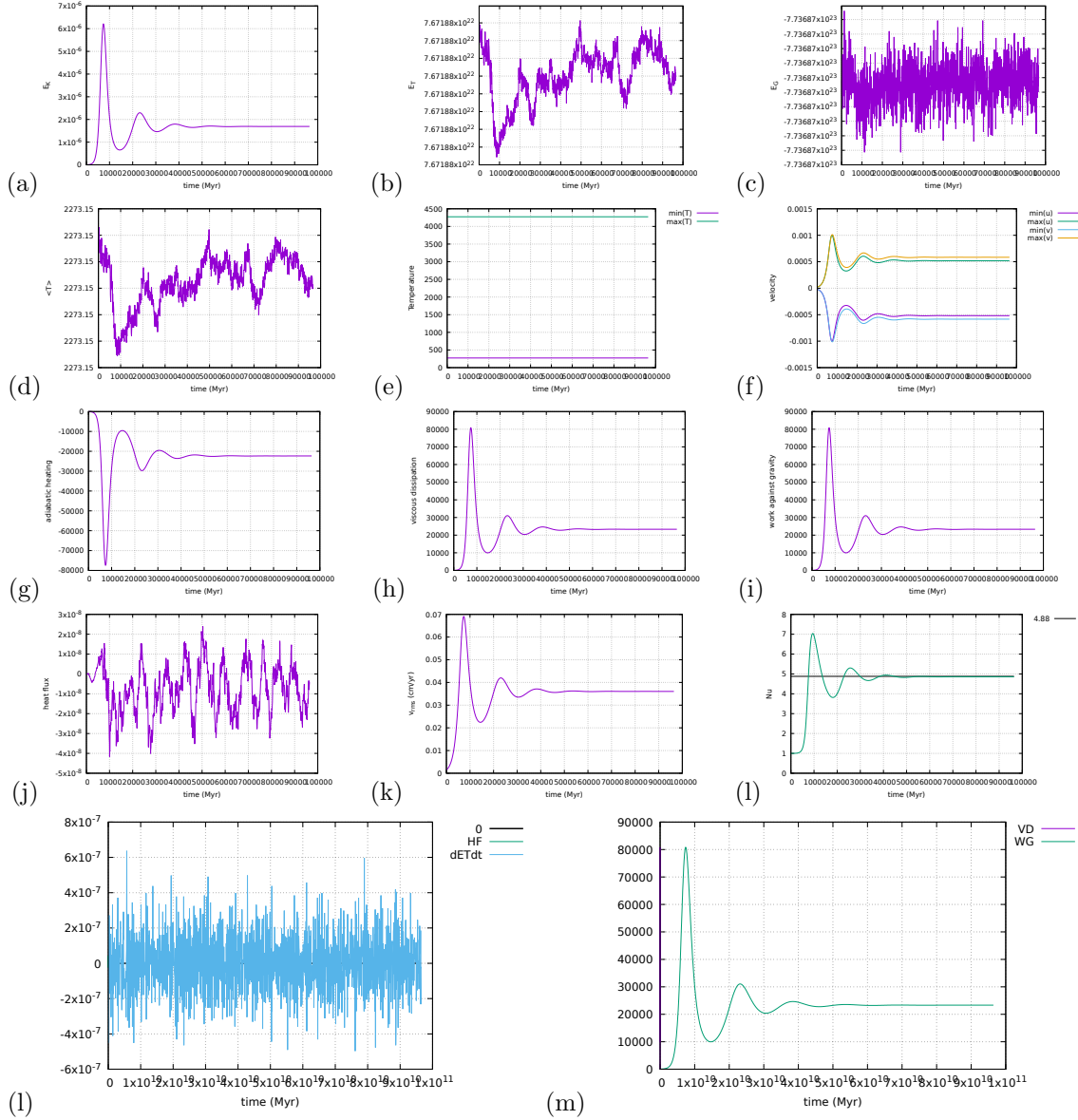
Relevant literature: [164, 1296, 2499, 1582, 1439, 1584, 1652, 1169]

ToDo:

- heat flux is at the moment elemental, so Nusselt and heat flux on boundaries measurements not as accurate as could be.
- implement steady state detection
- do  $Ra = 10^5$  and  $Ra = 10^6$
- velocity average at surface
- non dimensional heat flux at corners [209]
- depth-dependent viscosity (case 2 of [209])

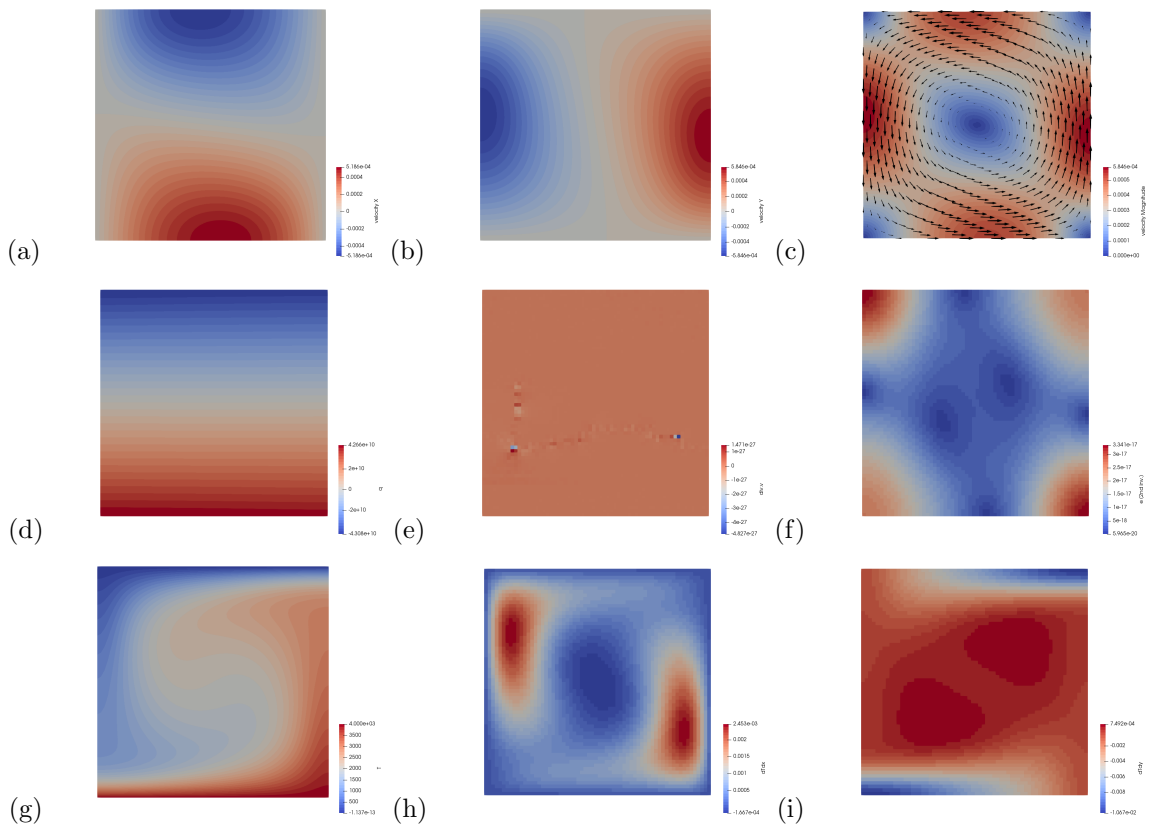
## results - BA - $Ra = 10^4$

These results were obtained with a 64x64 resolution, and CFL number of 1. Steady state was reached after about 1250 timesteps.



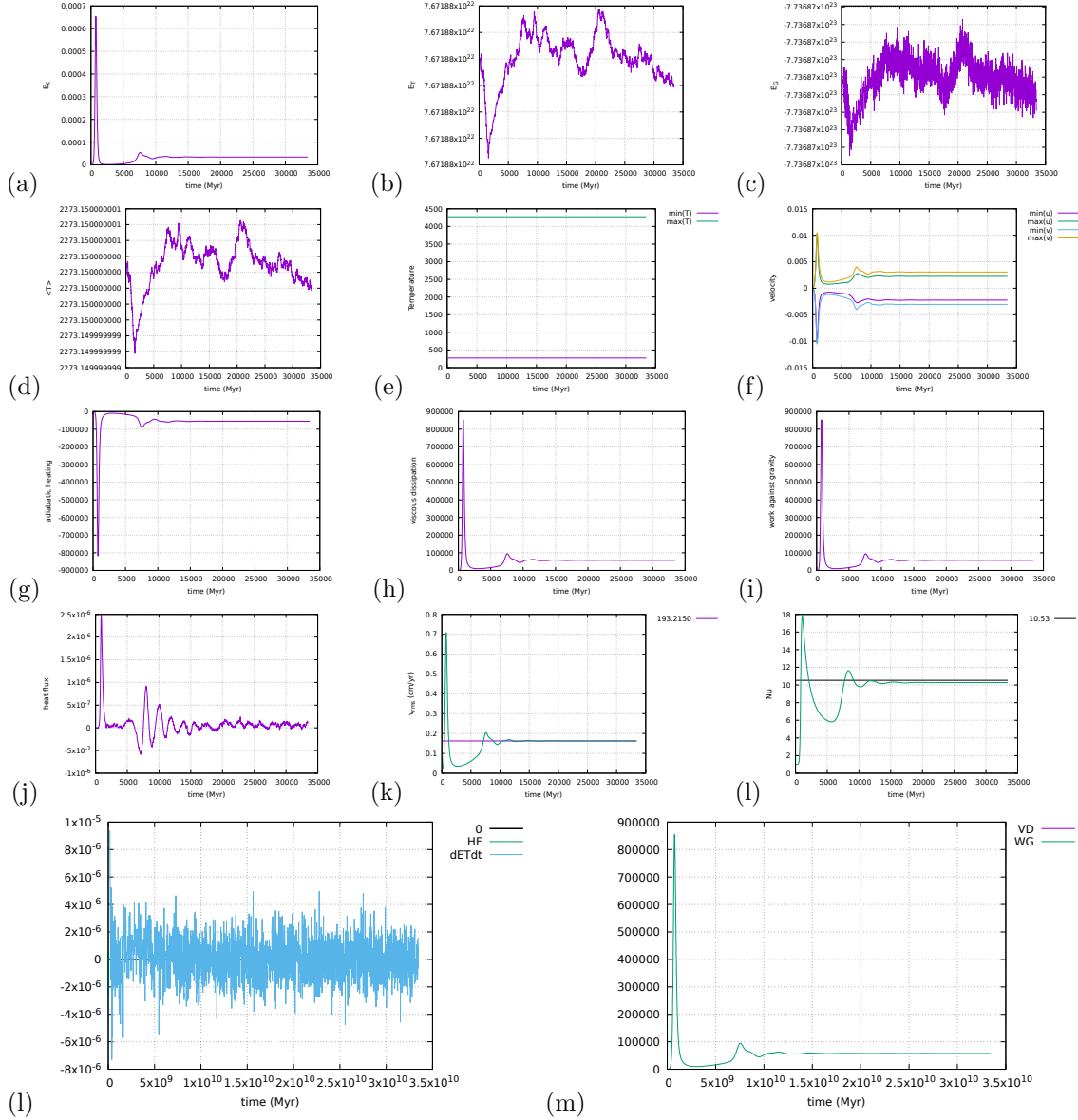
AH: adiabatic heating, VD: viscous dissipation, HF: heat flux, WG: work against gravity

Eq.(946) is verified by (l) and Eq.(935) is verified by (m).



## results - BA - $Ra = 10^5$

These results were obtained with a 64x64 resolution, and CFL number of 1. Steady state was reached after about 1250 timesteps.



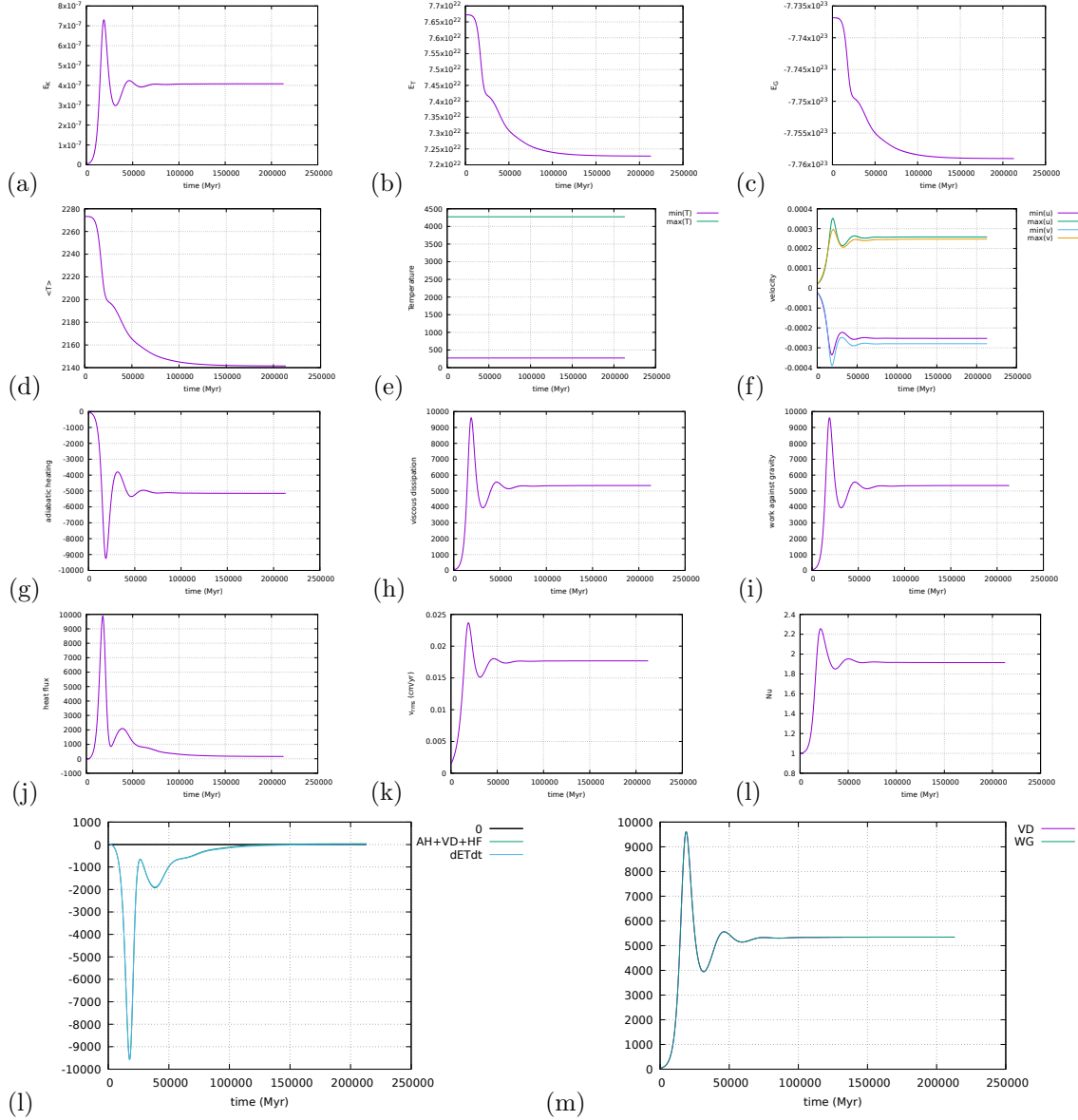
AH: adiabatic heating, VD: viscous dissipation, HF: heat flux, WG: work against gravity

Eq.(946) is verified by (l) and Eq.(935) is verified by (m).

**results - BA -  $Ra = 10^6$**

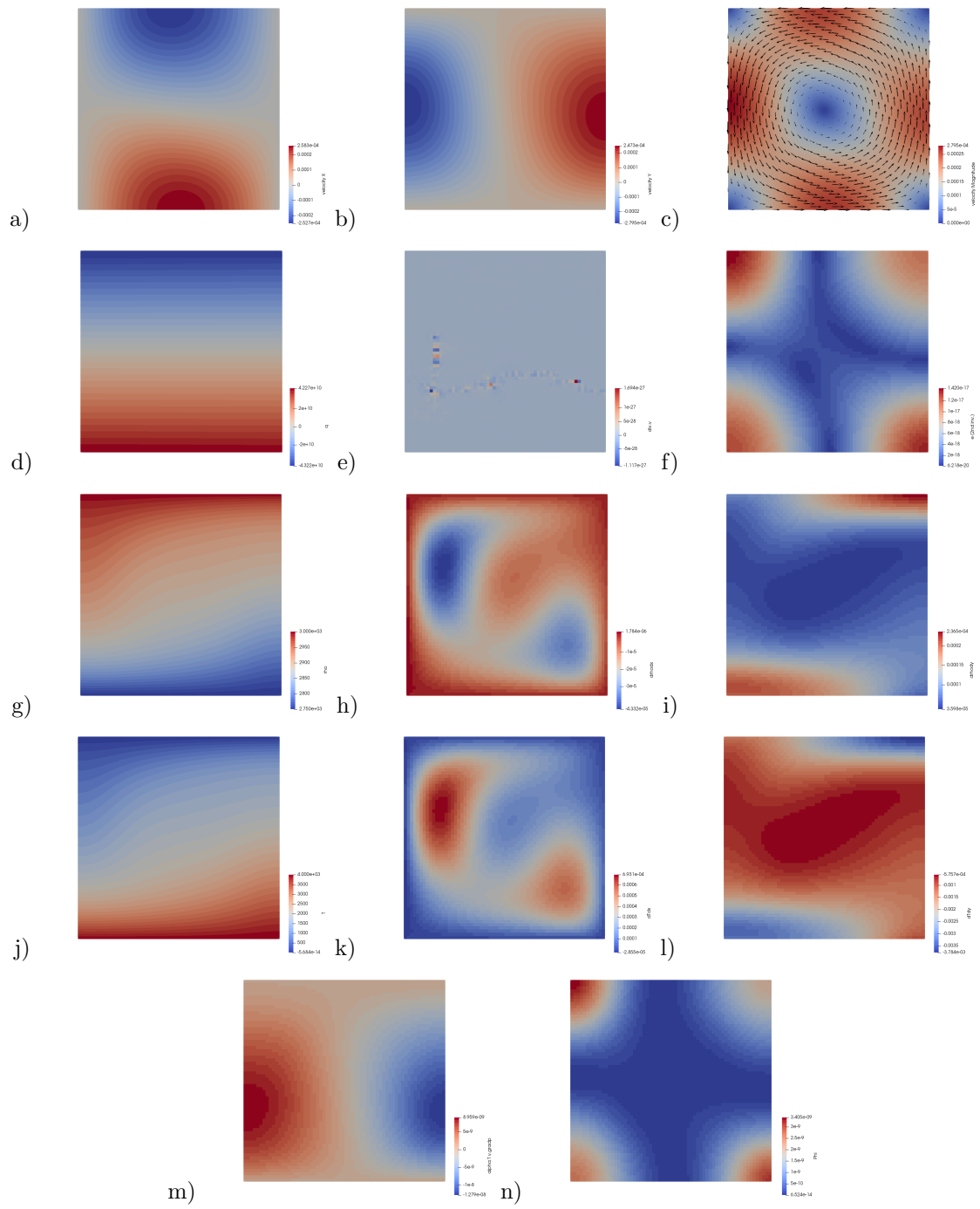
## results - EBA - $Ra = 10^4$

These results were obtained with a 64x64 resolution, and CFL number of 1. Steady state was reached after about 2500 timesteps



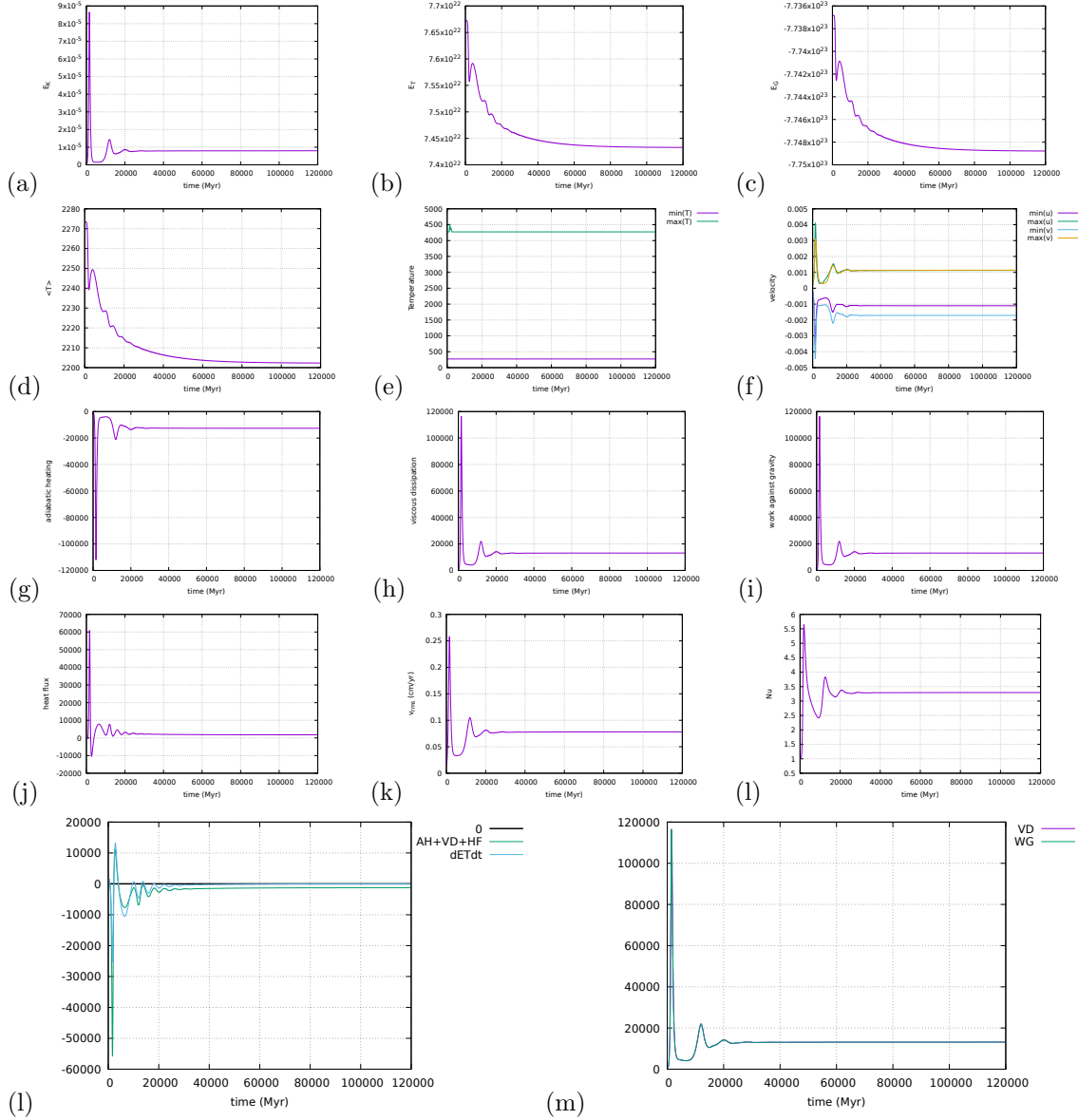
AH: adiabatic heating, VD: viscous dissipation, HF: heat flux, WG: work against gravity

Eq.(946) is verified by (l) and Eq.(935) is verified by (m).



## results - EBA - $Ra = 10^5$

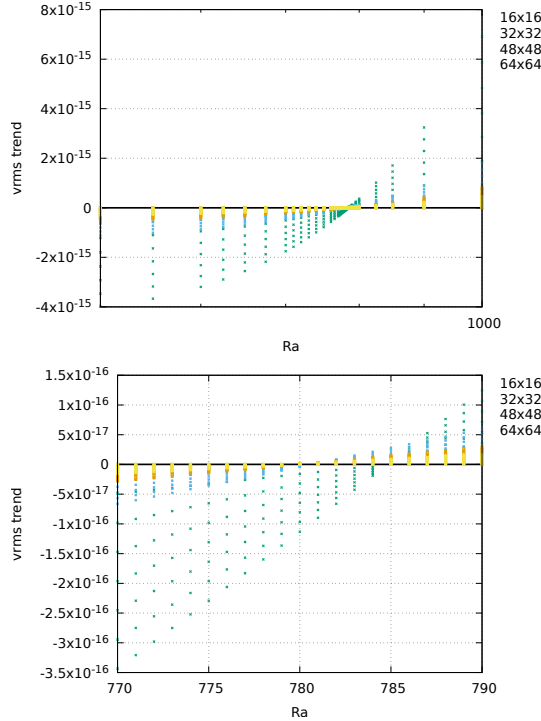
These results were obtained with a 64x64 resolution, and CFL number of 1. Simulation was stopped after about 4300 timesteps.



AH: adiabatic heating, VD: viscous dissipation, HF: heat flux, WG: work against gravity

## Onset of convection

The code can be run for values of  $\text{Ra}$  between 500 and 1000, at various resolutions for the BA formulation. The value  $v_{rms}(t) - v_{rms}(0)$  is plotted as a function of  $\text{Ra}$  and for the 10 first timesteps. If the  $v_{rms}$  is found to decrease, then the Rayleigh number is not high enough to allow for convection and the initial temperature perturbation relaxes by diffusion (and then  $v_{rms}(t) - v_{rms}(0) < 0$ ). If the  $v_{rms}$  is found to increase, then  $v_{rms}(t) - v_{rms}(0) > 0$  and the system is going to showcase convection. The zero value of  $v_{rms}(t) - v_{rms}(0)$  gives us the critical Rayleigh number, which is found between 775 and 790.

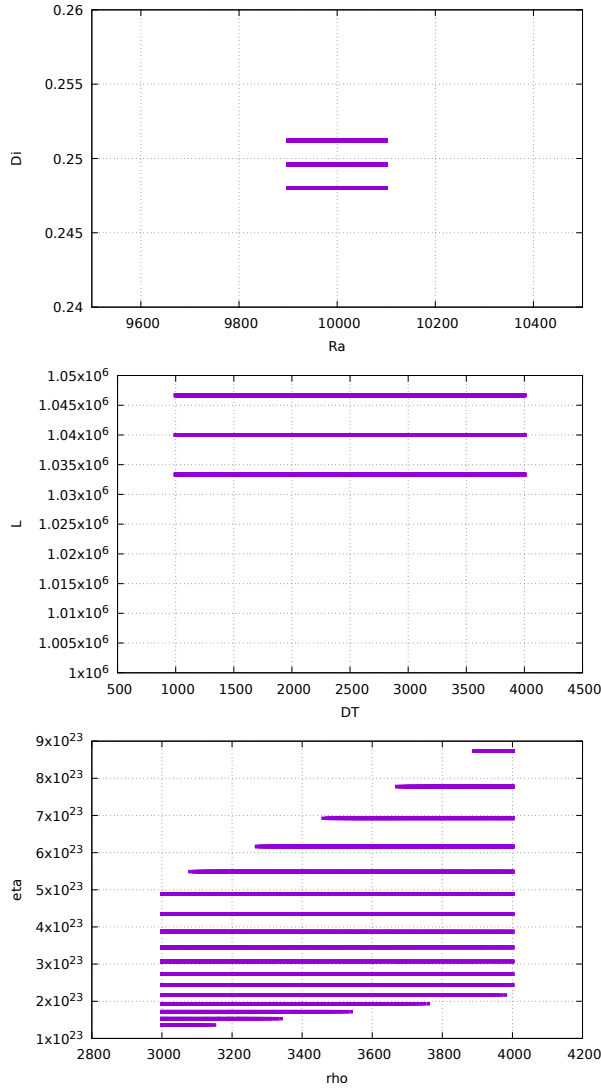


**Appendix:** Looking for the right combination of parameters for the King benchmark.

I run a quadruple do loop over  $L$ ,  $\Delta T$ ,  $\rho_0$  and  $\eta_0$  between plausible values (see code targets.py) and write in a file only the combination which yields the required Rayleigh and Dissipation number values (down to 1% accuracy).

```
alpha=3e-5
g=10
hcapa=1250
hcond=3
DTmin=1000 ; DTmax=4000 ; DTnpts=251
Lmin=1e6 ; Lmax=3e6 ; Lnpts=251
rhomin=3000 ; rhomax=3500 ; rhonpts=41
etamin=19 ; etamax=25 ; etanpts=100
```

On the following plots the 'winning' combinations of these four parameters are shown:



We see that:

- the parameter  $L$  (being to the 3rd power in the  $Ra$  number) cannot vary too much. Although it is varied between 1000 and 3000km there seems to be a 'right' value at about 1040 km. (why?)
- viscosities are within  $10^{23}$  and  $10^{24}$  which are plausible values (although a bit high?).
- densities can be chosen freely between 3000 and 3500
- $\Delta T$  seems to be the most problematic value since it can range from 1000 to 4000K ...

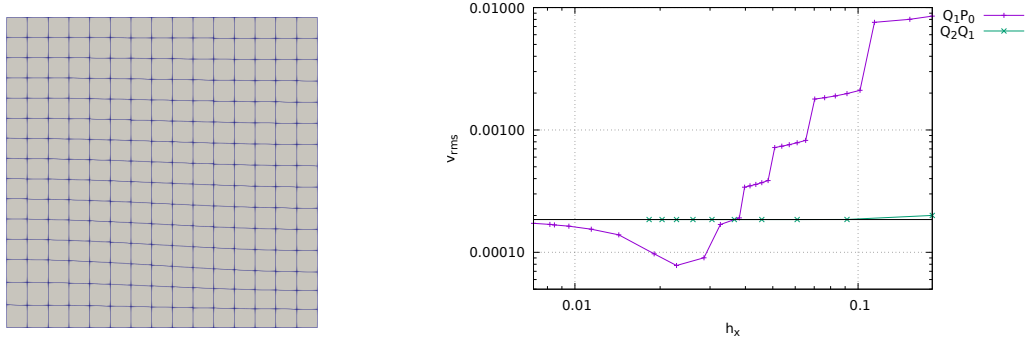
## Stone 25: Rayleigh-Taylor instability (1) - instantaneous

This numerical experiment was first presented in [2659]. It consists of an isothermal Rayleigh-Taylor instability in a two-dimensional box of size  $L_x = 0.9142$  and  $L_y = 1$ . Two Newtonian fluids are present in the system: the buoyant layer is placed at the bottom of the box and the interface between both fluids is given by  $y(x) = 0.2 + 0.02 \cos\left(\frac{\pi x}{L_x}\right)$ . The bottom fluid is parametrised by its mass density  $\rho_1$  and its viscosity  $\mu_1$ , while the layer above is parametrised by  $\rho_2$  and  $\mu_2$ .

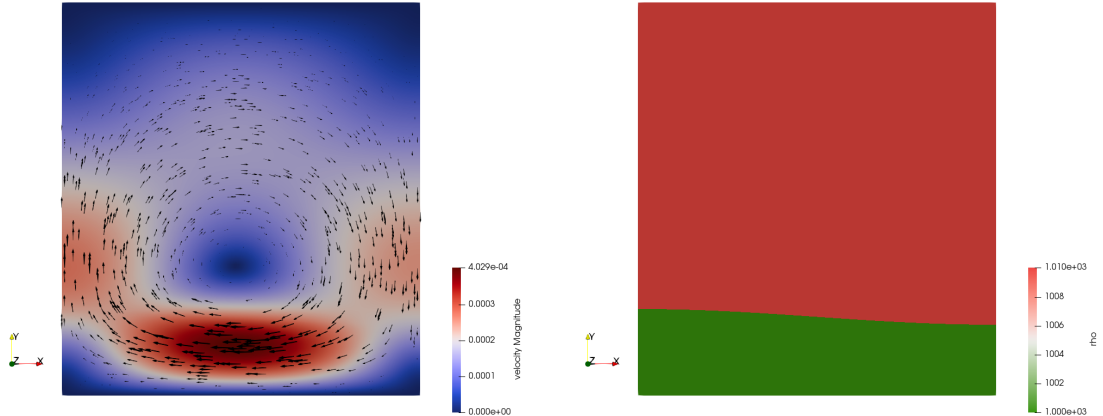
No-slip boundary conditions are applied at the bottom and at the top of the box while free-slip boundary conditions are applied on the sides.

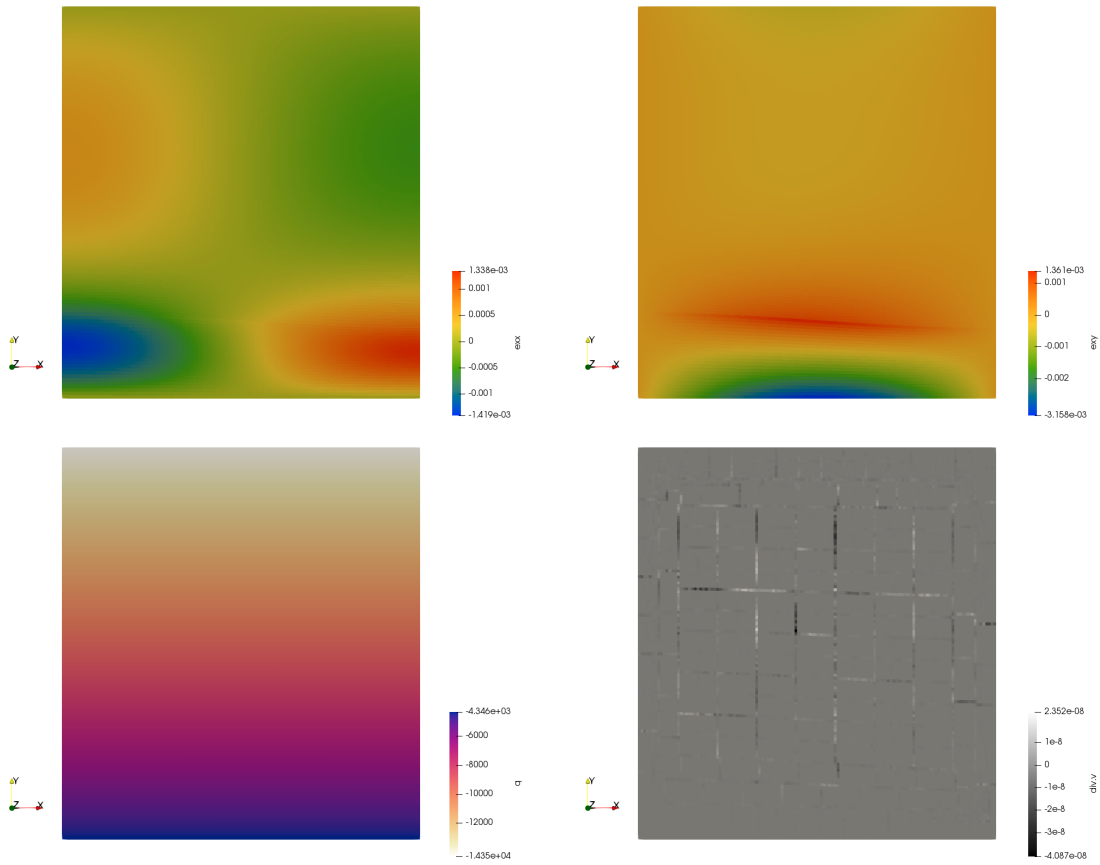
In the original benchmark the system is run over 2000 units of dimensionless time and the timing and position of various upwellings/downwellings is monitored. In this present experiment only the root mean square velocity is measured at  $t = 0$ : the code is indeed not yet foreseen of any algorithm capable of tracking deformation.

Another approach than the ones presented in the extensive literature which showcases results of this benchmark is taken. The mesh is initially fitted to the fluids interface and the resolution is progressively increased. This results in the following figure:



The green line indicates results obtained with my code ELEFANT with grids up to 2000x2000 with the exact same methodology.





Results obtained with  $Q_1 \times P_0$  elements.

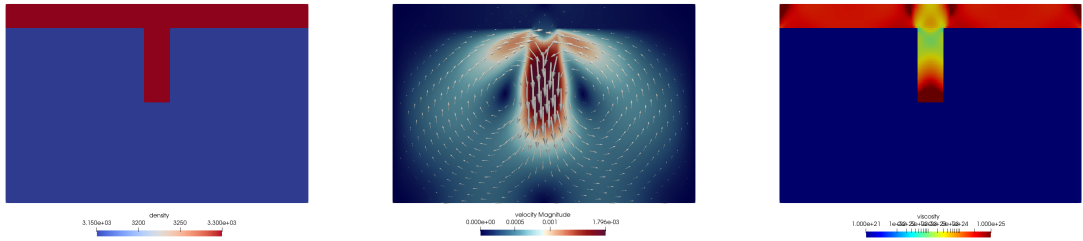
## Stone 26: Slab detachment benchmark (1) - instantaneous

As in [2258], the computational domain is  $1000\text{km} \times 660\text{km}$ . No-slip boundary conditions are imposed on the sides of the system while free-slip boundary conditions are imposed at the top and bottom. Two materials are present in the domain: the lithosphere (mat.1) and the mantle (mat.2). The overriding plate (mat.1) is  $80\text{km}$  thick and is placed at the top of the domain. An already subducted slab (mat.1) of  $250\text{km}$  length hangs vertically under this plate. The mantle occupies the rest of the domain.

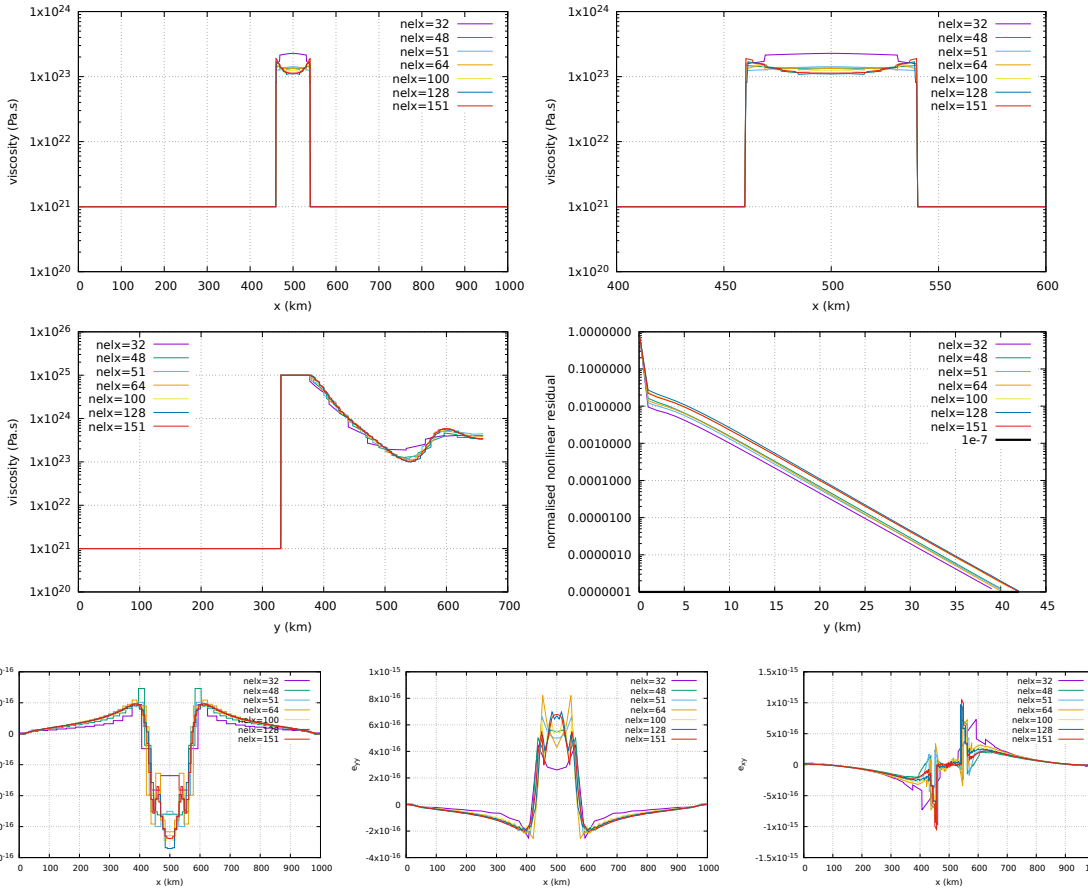
The mantle has a constant viscosity  $\eta_0 = 10^{21}\text{Pa.s}$  and a density  $\rho = 3150\text{kg/m}^3$ . The slab has a density  $\rho = 3300\text{kg/m}^3$  and is characterised by a power-law flow law so that its effective viscosity depends on the second invariant of the strainrate  $I_2$  as follows:

$$\eta_{eff} = \frac{1}{2}A^{-1/n_s}I_2^{1/n_s-1} = \frac{1}{2}[(2 \times 4.75 \times 10^{11})^{-n_s}]^{-1/n_s}I_2^{1/n_s-1} = 4.75 \times 10^{11}I_2^{1/n_s-1} = \eta_0 I_2^{1/n_s-1} \quad (949)$$

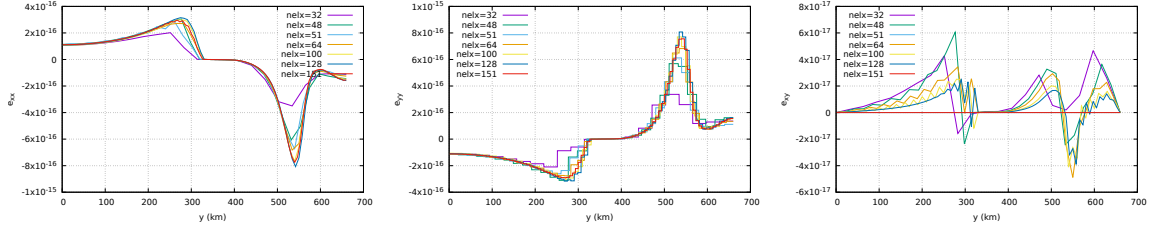
with  $n_s = 4$  and  $A = (2 \times 4.75 \times 10^{11})^{-n_s}$ , or  $\eta_0 = 4.75 \times 10^{11}$ .



Fields at convergence for 151x99 grid.



Along the horizontal line



Along the vertical line

Todo: nonlinear mantle, pressure normalisation

Also check Bellas et al, 2018 [142].

## Stone 27: Consistent Boundary Flux

In what follows we will be re-doing the numerical experiments presented in Zhong et al. [2902].

The first benchmark showcases a unit square domain with free slip boundary conditions prescribed on all sides. The resolution is fixed to  $64 \times 64 Q_1 \times P_0$  elements. The flow is isoviscous and the buoyancy force  $\mathbf{f}$  is given by

$$\begin{aligned} f_x &= 0 \\ f_y &= \rho_0 \alpha T(x, y) \end{aligned}$$

with the temperature field given by

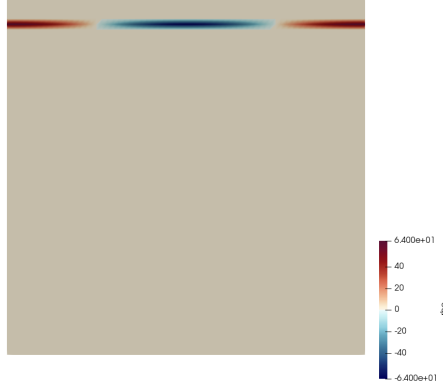
$$T(x, y) = \cos(kx)\delta(y - y_0)$$

where  $k = 2\pi/\lambda$  and  $\lambda$  is a wavelength, and  $y_0$  represents the location of the buoyancy strip. We set  $g_y = -1$  and prescribe  $\rho(x, y) = \rho_0 \alpha \cos(kx)\delta(y - y_0)$  on the nodes of the mesh.

One can prove ([2902] and refs. therein) that there is an analytic solution for the surface stress  $\sigma_{zz}$ <sup>84</sup>

$$\frac{\sigma_{yy}}{\rho \alpha g h} = \frac{\cos(kx)}{\sinh^2(k)} [k(1 - y_0) \sinh(k) \cosh(ky_0) - k \sinh(k(1 - y_0)) + \sinh(k) \sinh(ky_0)]$$

We choose  $\rho_0 \alpha = 64$ ,  $\eta = 1$  (note that in this case the normalising coefficient of the stress is exactly 1 (since  $h = L_x/nelx = 1/64$ ) so it is not implemented in the code).  $\lambda = 1$  is set to 1 and we explore  $y_0 = \frac{63}{64}, \frac{62}{64}, \frac{59}{64}$  and  $y_0 = 32/64$ . Under these assumptions the density field for  $y_0 = 59/64$  is:

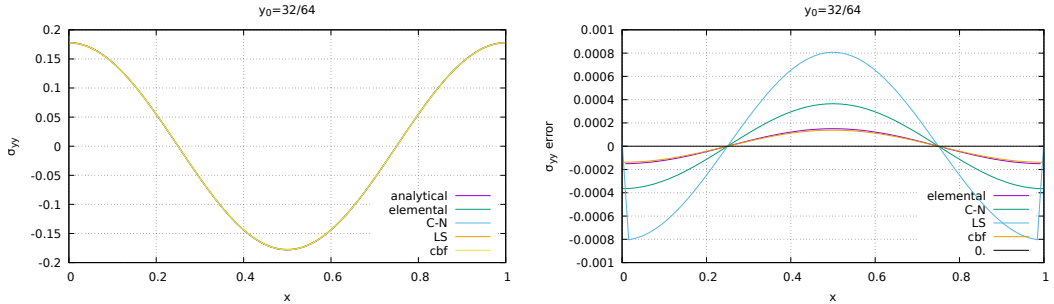


We can recover the stress at the boundary by computing the  $yy$  component of the stress tensor in the top row of elements:

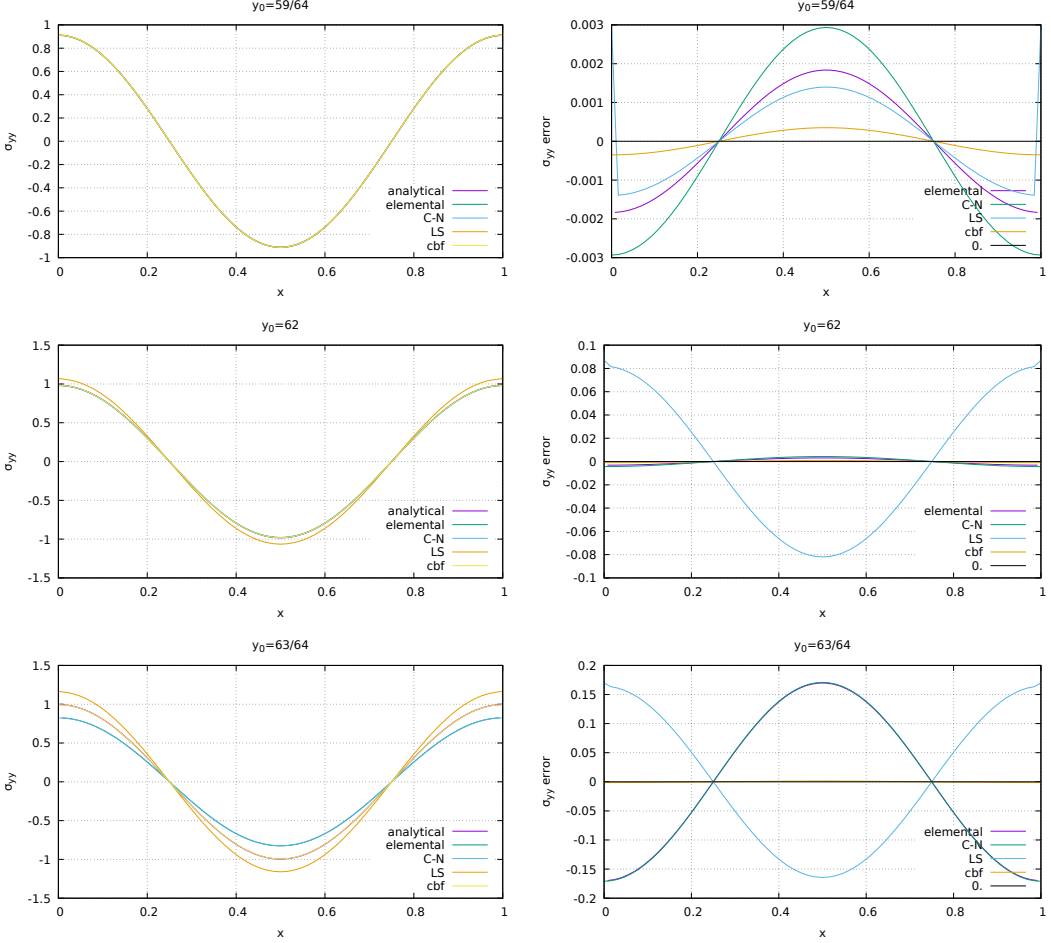
$$\sigma_{yy} = -p + 2\eta\dot{\epsilon}_{yy}$$

Note that pressure is by definition elemental, and that strain rate components are then also computed in the middle of each element.

These elemental quantities can be projected onto the nodes (see section ??) by means of the C→N algorithm or a least square algorithm (LS).



<sup>84</sup>Note that in the paper the authors use  $\rho \alpha g$  which does not have the dimensions of a stress



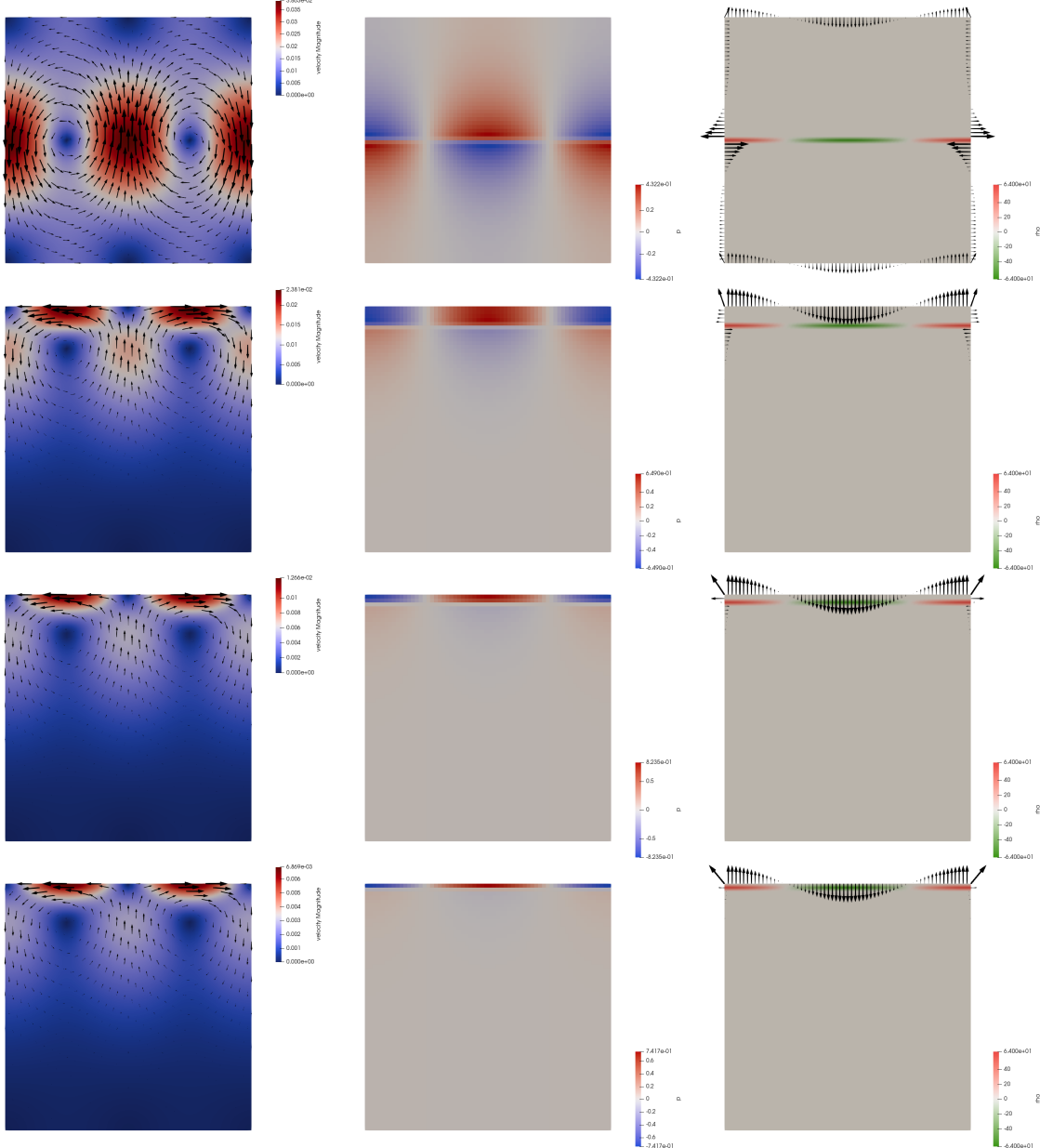
The consistent boundary flux (CBF) method allows us to compute traction vectors  $\mathbf{t} = \boldsymbol{\sigma} \cdot \mathbf{n}$  on the boundary of the domain. On the top boundary,  $\mathbf{n} = (0, 1)$  so that  $\mathbf{t} = (\sigma_{xy}, \sigma_{yy})^T$  and  $t_y$  is the quantity we need to consider and compare to other results.

In the following table are shown the results presented in [2902] alongside the results obtained with Fieldstone:

Method	$y_0 = 63/64$	$y_0 = 62/64$	$y_0 = 59/64$ <sup>85</sup>	$y_0 = 32/64$
Analytic solution	0.995476	0.983053	0.912506	0.178136
Pressure smoothing [2902]	1.15974	1.06498	0.911109	n.a.
CBF [2902]	0.994236	0.982116	0.912157	n.a.
fieldstone: elemental	0.824554 (-17.17 %)	0.978744 (-0.44%)	0.909574 (-0.32 %)	0.177771 (-0.20 %)
fieldstone: nodal (C→N)	0.824554 (-17.17 %)	0.978744 (-0.44%)	0.909574 (-0.32 %)	0.177771 (-0.20 %)
fieldstone: LS	1.165321 ( 17.06 %)	1.070105 ( 8.86%)	0.915496 ( 0.33 %)	0.178182 ( 0.03 %)
fieldstone: CBF	0.994236 ( -0.13 %)	0.982116 (-0.10%)	0.912157 (-0.04 %)	0.177998 (-0.08 %)

We see that we recover the published results with the same exact accuracy, thereby validating our implementation. Also rather fascinating is the fact that the original paper carries out the whole study without showing any image of the 2D domain ever.

On the following figures are shown the velocity, pressure and traction fields for two cases  $y_0 = 32/64$  and  $y_0 = 63/64$ .



Here lies the superiority of our approach over the one presented in the original article: our code computes all traction vectors on all boundaries at once.

[explain how Medge is arrived at!](#)

[compare with ASPECT ???](#)

[pressure average on surface instead of volume ?](#)

**Remark.** The original article on the CBF [2902] uses a penalty-based formulation (see Section 6.3) so that they do not have to worry about pressure normalisation. However, since constant pressure fields lie in the nullspace of  $\mathbb{G}$  the pressure normalisation constant does not play a role.

As shown in Appendix I, the  $Q_1$  mass matrix for the reference cell/element is given by:

$$\mathbf{M}^e = \frac{1}{3} \begin{pmatrix} 2 & 1 \\ 1 & 2 \end{pmatrix}$$

This matrix needs to be multiplied by  $h/2$  for an element of size  $h$ . Following the methodology presented in [2902], one can also use the Gauss-Lobatto quadrature method to arrive at the mass matrix, and in

this case the simple trapezoidal integration rule variant thereof (see Section 4.1.1). We then have:

$$\mathbf{M}_e = \int_{\Omega_e} \vec{N}^T \vec{N} dV = \int_{-1}^{+1} \vec{N}^T \vec{N} dr \quad (950)$$

on the reference element, with

$$\vec{N}^T = \begin{pmatrix} N_1(r) \\ N_2(r) \end{pmatrix} = \frac{1}{2} \begin{pmatrix} 1-r \\ 1+r \end{pmatrix}$$

We know compute the following integrals with the trapezoidal rule:

$$\int_{-1}^{+1} N_1(r) N_1(r) dr = (1 - -1) \frac{N_1(-1) N_1(-1) + N_1(+1) N_1(+1)}{2} = 1 \quad (951)$$

$$\int_{-1}^{+1} N_1(r) N_2(r) dr = (1 - -1) \frac{N_1(-1) N_2(-1) + N_1(+1) N_2(+1)}{2} = 0 \quad (952)$$

$$\int_{-1}^{+1} N_2(r) N_2(r) dr = (1 - -1) \frac{N_2(-1) N_2(-1) + N_2(+1) N_2(+1)}{2} = 1 \quad (953)$$

and finally

$$\mathbf{M}^e = \begin{pmatrix} 1 & 0 \\ 0 & 1 \end{pmatrix}$$

The resulting matrix is diagonal and it is simply the lumped version of the exact mass matrix.

## Stone 28: convection 2D box - Tosi et al, 2015

This fieldstone was developed in collaboration with Rens Elbertsen.

The viscosity field  $\mu$  is calculated as the harmonic average between a linear part  $\mu_{lin}$  that depends on temperature only or on temperature and depth  $d$ , and a non-linear, plastic part  $\mu_{plast}$  dependent on the strain rate:

$$\mu(T, z, \dot{\epsilon}) = 2 \left( \frac{1}{\mu_{lin}(T, z)} + \frac{1}{\mu_{plast}(\dot{\epsilon})} \right)^{-1}. \quad (954)$$

The linear part is given by the linearized Arrhenius law (the so-called Frank-Kamenetskii approximation [869]):

$$\mu_{lin}(T, z) = \exp(-\gamma_T T + \gamma_z z), \quad (955)$$

where  $\gamma_T = \ln(\Delta\mu_T)$  and  $\gamma_z = \ln(\Delta\mu_z)$  are parameters controlling the total viscosity contrast due to temperature ( $\Delta\mu_T$ ) and pressure ( $\Delta\mu_z$ ). The non-linear part is given by [2567, 2566]:

$$\mu_{plast}(\dot{\epsilon}) = \mu^* + \frac{\sigma_Y}{\sqrt{\dot{\epsilon} : \dot{\epsilon}}}, \quad (956)$$

where  $\mu^*$  is a constant representing the effective viscosity at high stresses [2412] and  $\sigma_Y$  is the yield stress, also assumed to be constant. In 2-D, the denominator in the second term of equation (956) is given explicitly by

$$\sqrt{\dot{\epsilon} : \dot{\epsilon}} = \sqrt{\dot{\epsilon}_{ij}\dot{\epsilon}_{ij}} = \sqrt{\left(\frac{\partial u_x}{\partial x}\right)^2 + \frac{1}{2} \left(\frac{\partial u_x}{\partial y} + \frac{\partial u_y}{\partial x}\right)^2 + \left(\frac{\partial u_y}{\partial y}\right)^2}. \quad (957)$$

The viscoplastic flow law (equation 954) leads to linear viscous deformation at low stresses (equation (955)) and to plastic deformation for stresses that exceed  $\sigma_Y$  (equation (956)), with the decrease in viscosity limited by the choice of  $\mu^*$  [2412].

In all cases that we present, the domain is a two-dimensional square box. The mechanical boundary conditions are for all boundaries free-slip with no flux across, i.e.  $\tau_{xy} = \tau_{yx} = 0$  and  $\mathbf{u} \cdot \mathbf{n} = 0$ , where  $\mathbf{n}$  denotes the outward normal to the boundary. Concerning the energy equation, the bottom and top boundaries are isothermal, with the temperature  $T$  set to 1 and 0, respectively, while side-walls are assumed to be insulating, i.e.  $\partial T / \partial x = 0$ . The initial distribution of the temperature field is prescribed as follows:

$$T(x, y) = (1 - y) + A \cos(\pi x) \sin(\pi y), \quad (958)$$

where  $A = 0.01$  is the amplitude of the initial perturbation.

In the following Table, we list the benchmark cases according to the parameters used.

Case	$Ra$	$\Delta\mu_T$	$\Delta\mu_y$	$\mu^*$	$\sigma_Y$	Convective regime
1	$10^2$	$10^5$	1	—	—	Stagnant lid
2	$10^2$	$10^5$	1	$10^{-3}$	1	Mobile lid
3	$10^2$	$10^5$	10	—	—	Stagnant lid
4	$10^2$	$10^5$	10	$10^{-3}$	1	Mobile lid
5a	$10^2$	$10^5$	10	$10^{-3}$	4	Periodic
5b	$10^2$	$10^5$	10	$10^{-3}$	3 – 5	Mobile lid – Periodic – Stagnant lid

Benchmark cases and corresponding parameters.

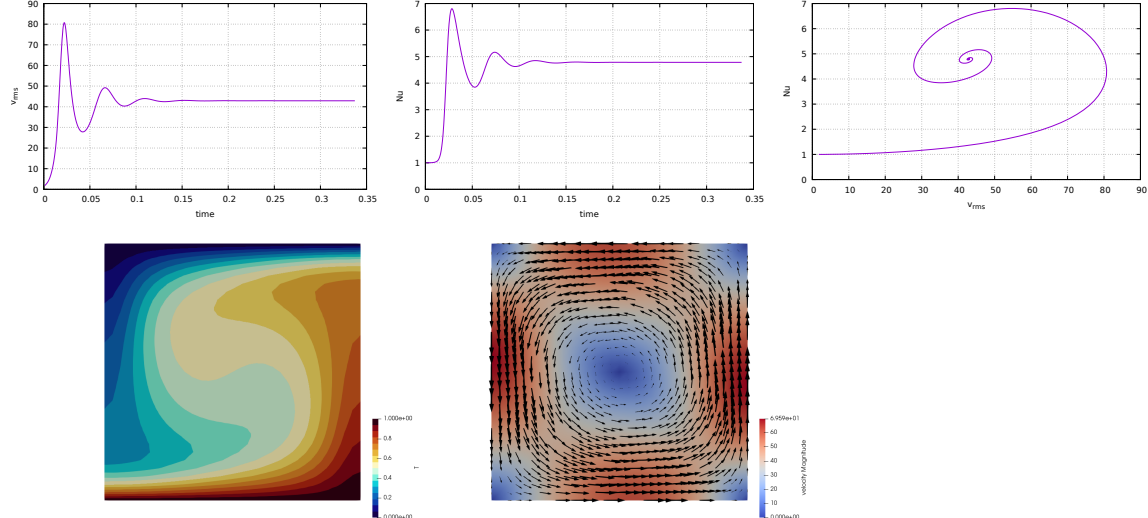
In Cases 1 and 3 the viscosity is directly calculated from equation (955), while for Cases 2, 4, 5a, and 5b, we used equation (954). For a given mesh resolution, Case 5b requires running simulations with yield stress varying between 3 and 5

In all tests, the reference Rayleigh number is set at the surface ( $y = 1$ ) to  $10^2$ , and the viscosity contrast due to temperature  $\Delta\mu_T$  is  $10^5$ , implying therefore a maximum effective Rayleigh number of  $10^7$  for  $T = 1$ . Cases 3, 4, 5a, and 5b employ in addition a depth-dependent rheology with viscosity contrast  $\Delta\mu_z = 10$ . Cases 1 and 3 assume a linear viscous rheology that leads to a stagnant lid regime. Cases 2 and 4 assume a viscoplastic rheology that leads instead to a mobile lid regime. Case 5a also

assumes a viscoplastic rheology but a higher yield stress, which ultimately causes the emergence of a strictly periodic regime. The setup of Case 5b is identical to that of Case 5a but the test consists in running several simulations using different yield stresses. Specifically, we varied  $\sigma_Y$  between 3 and 5 in increments of 0.1 in order to identify the values of the yield stress corresponding to the transition from mobile to periodic and from periodic to stagnant lid regime.

NOTE: no crank-nicolson scheme for temperature !!

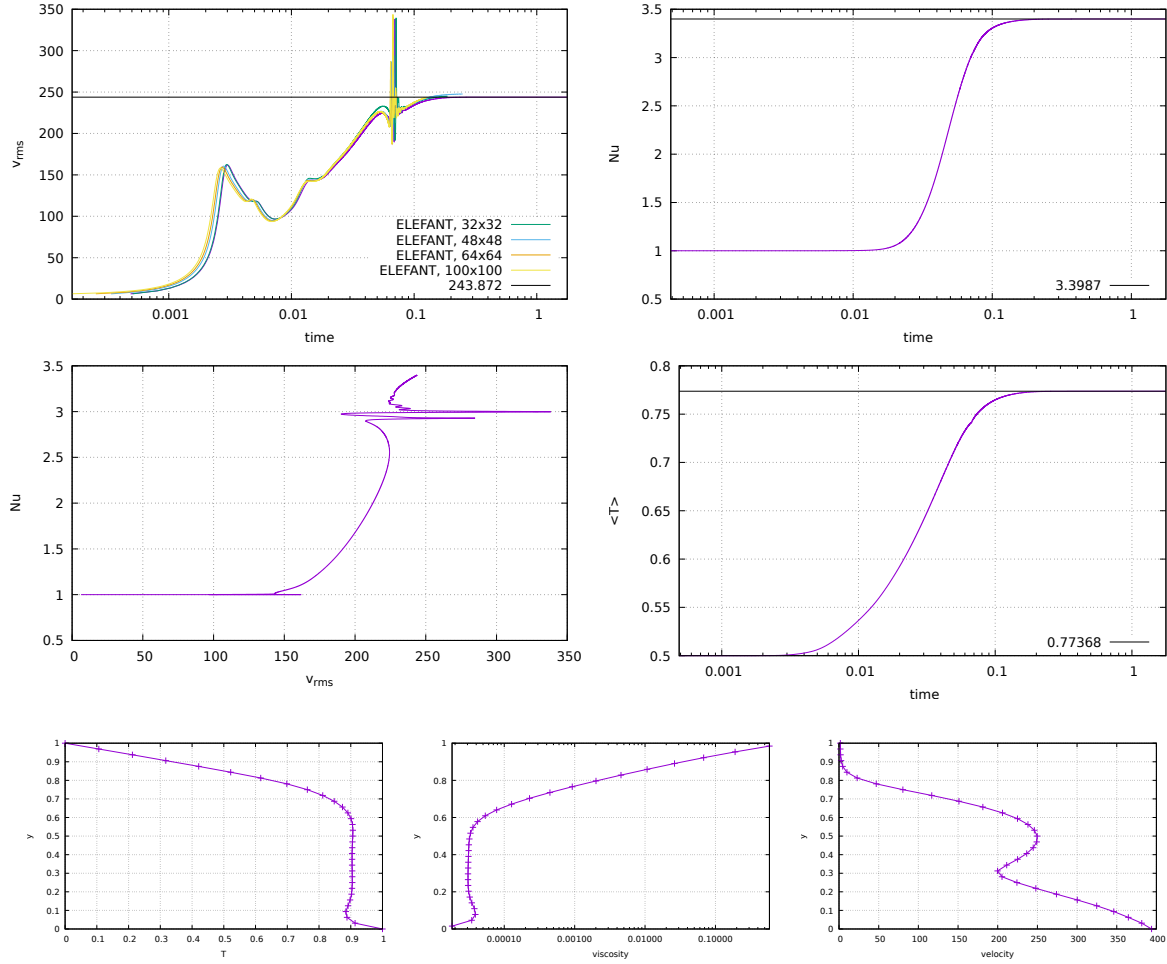
#### Case 0: Newtonian case, a la Blankenbach et al., 1989

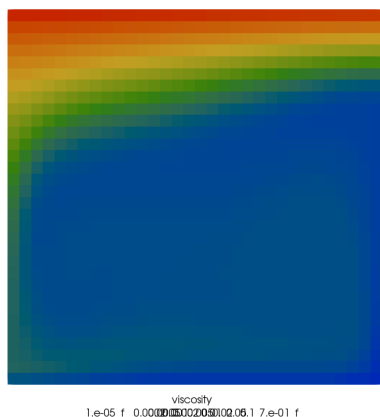
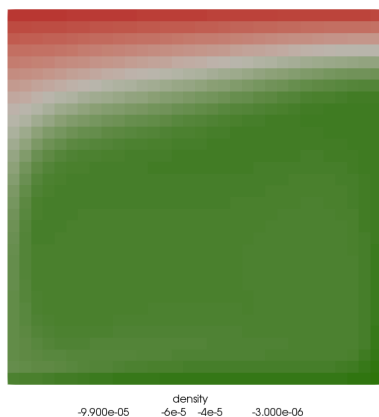
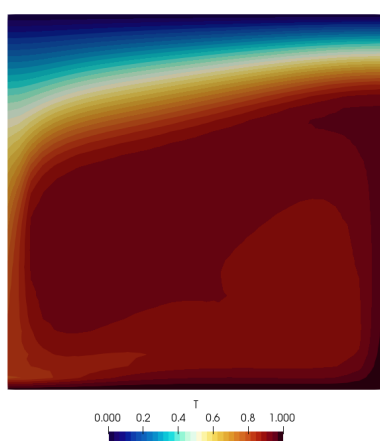
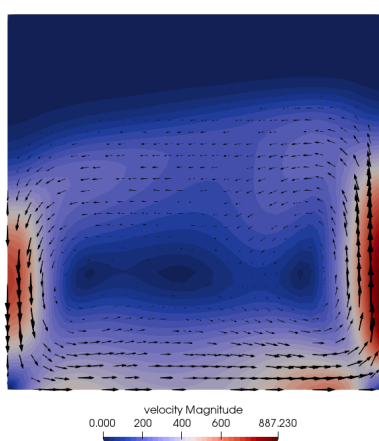
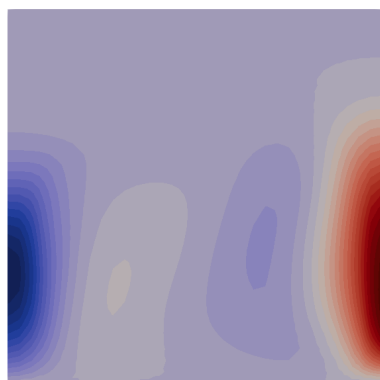
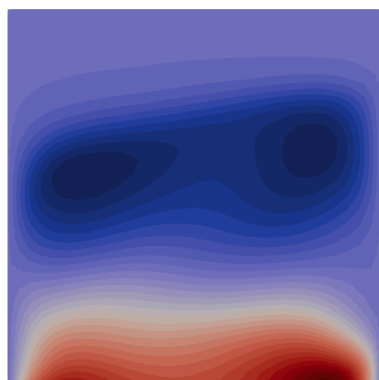


## Case 1

In this case  $\mu^* = 0$  and  $\sigma_Y = 0$  so that  $\mu_{plast}$  can be discarded. The CFL number is set to 0.5 and the viscosity is given by  $\mu(T, z, \dot{\epsilon}) = \mu_{lin}(T, z)$ . And since  $\Delta\mu_z = 1$  then  $\gamma_z = 0$  so that  $\mu_{lin}(T, z) = \exp(-\gamma_T T)$

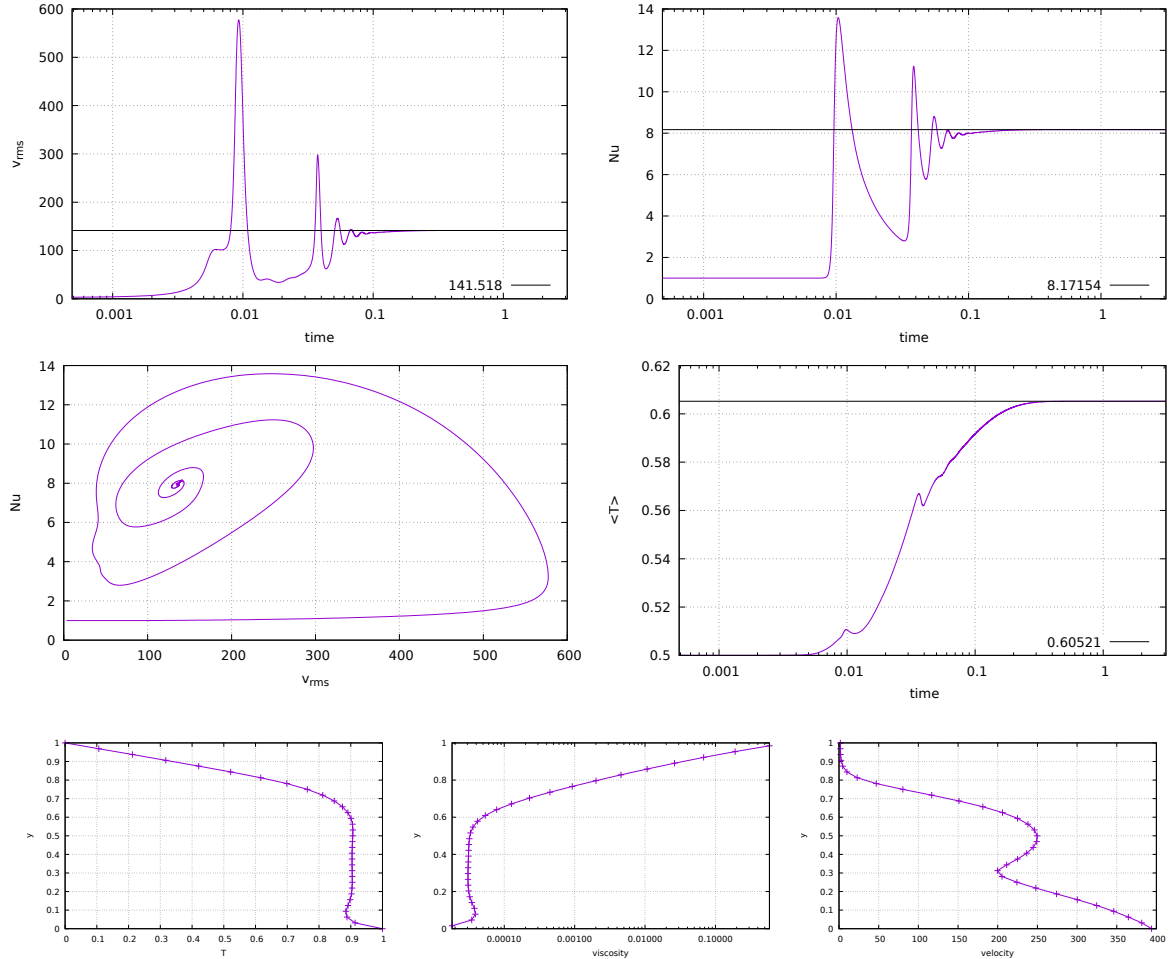
Code	YACC 100 × 100	Plaatjes 128×128r	CHIC 80 × 80	GAIA 100r×100r	StreamV 80 × 80	StagYY 128×128r	FEniCS 80 × 80	Fluidity 128 × 128	ELEFANT 100 × 100	ASPECT 64 × 64	MC3D 100 × 100
<i>Case 1</i>											
$\langle T \rangle$	0.7767	0.7759	0.7758	0.7759	0.776	0.776	0.7759	0.7758	0.7758	0.7768	0.779
$Nu_{top}$	3.4298	3.4159	3.4260	3.4213	3.4091	3.419	3.5889	3.4253	3.4214	3.4305	3.3129
$Nu_{bot}$	3.3143	3.4159	3.4259	3.4213	3.4091	3.419	3.4231	3.3795	3.313	3.4142	3.3139
$u_{rms}$	251.7997	249.54	249.2985	250.0738	252.0906	249.541	249.5730	248.9252	249.134	251.3069	296.6156
$u_{surf}^{rms}$	1.8298	1.878	1.8999	1.8836	1.8823	1.8723	1.8698	1.8474	1.8642	1.8695	1.1114
$u_{surf}^{max}$	2.5516	2.618	2.6477	2.6254	2.64	2.6104	2.6066	2.5761	2.6119	2.6064	1.5329
$\langle W \rangle$	2.4583	2.369	2.431	2.4121	2.4071	2.4189	2.4246	2.4148	2.4316	2.4282	2.5548
$\langle \Phi \rangle / Ra$	2.4333	2.4119	2.4189	2.4165	2.392	2.4182	2.4246	2.4148	2.4276	2.4281	2.31916
$\delta$	1.02%	1.78%	0.50%	0.18%	0.63%	0.03%	< 0.01%	< 0.01%	0.16%	< 0.01%	9.22%

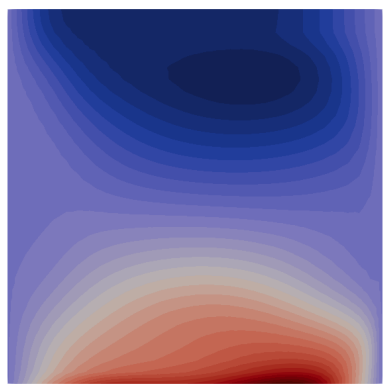




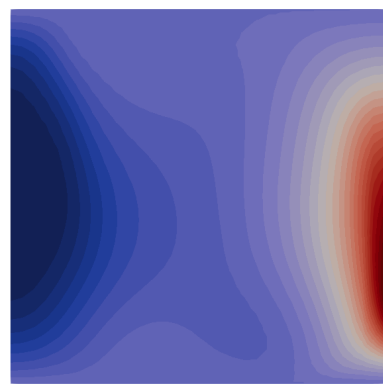
## Case 2

$\langle T \rangle$	0.5289	0.5276	0.5276	0.5289	0.5283	0.527304	0.527521	0.5274	0.5277	0.5278	0.5364
$Nu_{top}$	6.5572	6.6156	6.6074	6.5913	6.6356	6.61082	6.68224	6.6401	6.5912	6.6249	7.4376
$Nu_{bot}$	6.5243	6.6158	6.6073	6.5913	6.6356	6.61082	6.66899	6.6326	6.5834	6.6267	7.4376
$U_{RMS}$	79.6202	79.1358	79.0181	78.6652	79.4334	78.9903	79.0684	79.0318	79.1105	79.1996	98.8912
$U_{RMS}^{\text{surf}}$	75.4814	75.1727	75.0434	74.1719	74.8587	75.0606	75.0975	75.0827	74.7596	75.1903	93.5057
$U_{\max}^{\text{surf}}$	89.2940	88.9715	88.8130	87.6118	89.1444	88.823	88.8753	88.85	88.9146	88.9848	123.046
$\eta_{\min}$	$1.9174 \times 10^{-4}$	$1.9220 \times 10^{-4}$	$1.9448 \times 10^{-4}$	$1.9204 \times 10^{-4}$	$1.9900 \times 10^{-4}$	$1.9574 \times 10^{-4}$	$1.9167 \times 10^{-4}$	$1.9200 \times 10^{-4}$	$1.9860 \times 10^{-4}$	$1.9178 \times 10^{-4}$	$1.93 \times 10^{-4}$
$\eta_{\max}$	1.6773	1.9834	1.6508	1.9670	1.1800	1.6665	1.7446	1.8891	1.5200	1.8831	$5.67 \times 10^{-3}$
$\langle W \rangle$	5.6512	5.6251	5.6076	5.5903	5.629	5.61012	5.61425	5.6136	5.6216	5.6235	6.751
$\langle \Phi \rangle / \text{Ra}$	5.6463	5.6174	5.6024	5.5434	5.6325	5.60152	5.61425	5.6136	5.6182	5.6235	7.786
$\delta$	0.09%	0.14%	0.09%	0.84%	0.06%	0.15%	<0.01%	<0.01%	0.06%	<0.01%	13.29%

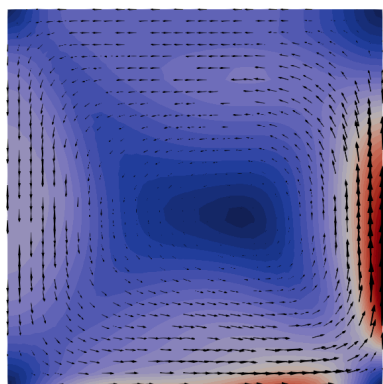




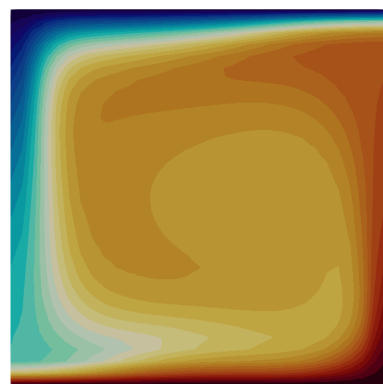
velocity X  
-1.437e+02 0 100 200 3.247e+02



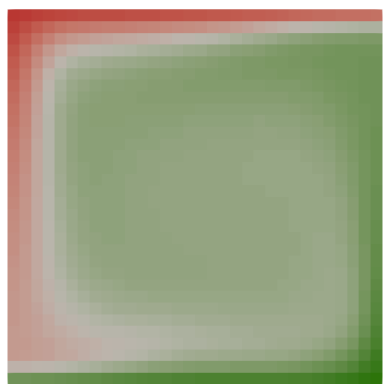
velocity Y  
-1.764e+02 0 200 4.549e+02



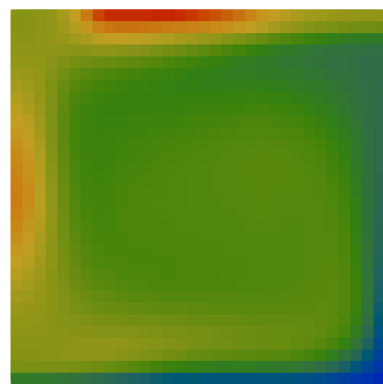
velocity Magnitude  
0.000e+00 100 200 300 4.549e+02



T  
0.000 0.2 0.4 0.6 0.8 1.000



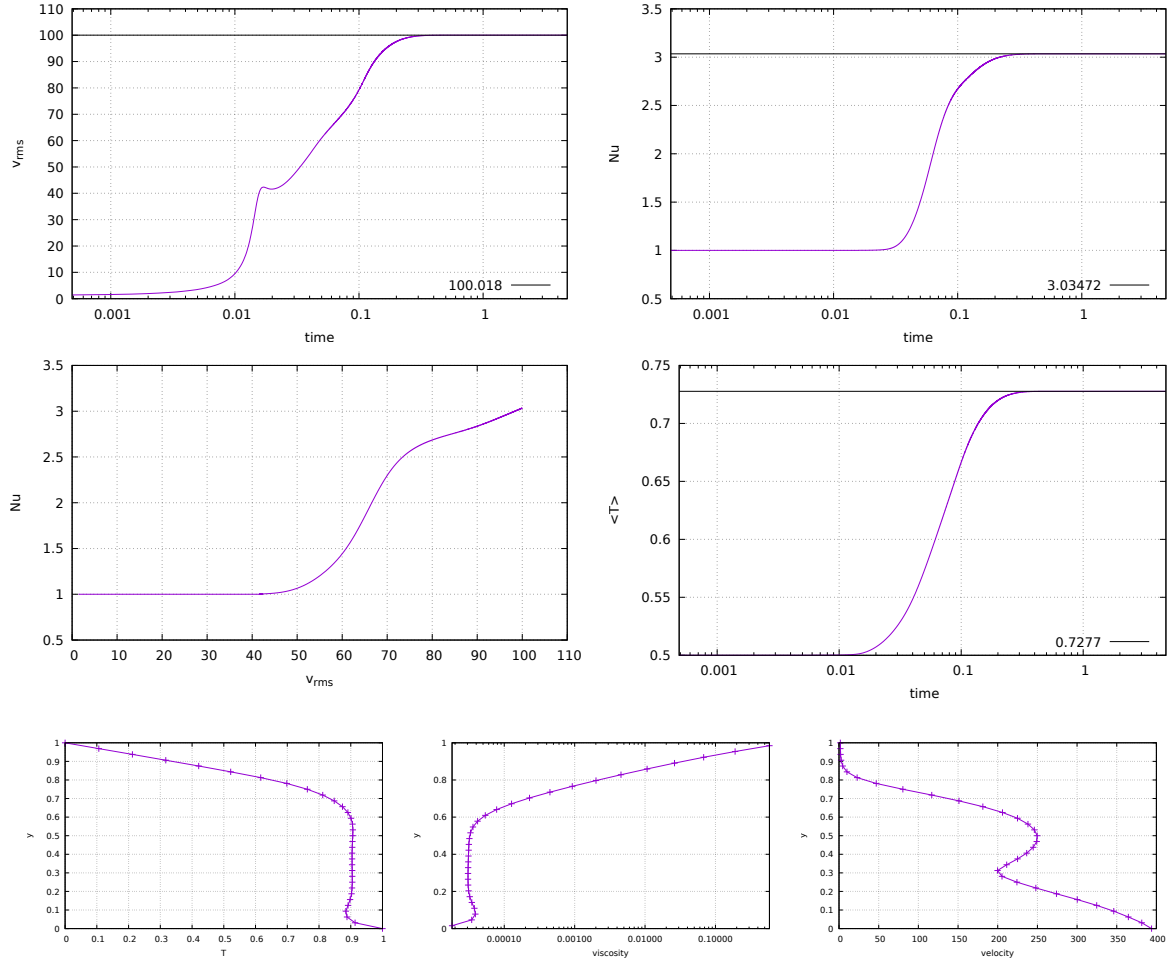
density  
-9.900e-05 -6e-5 -4e-5 -2.000e-06

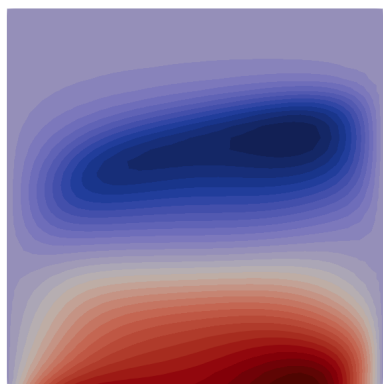


viscosity  
2.300e-05 0.000002030102.05 6.326e-01

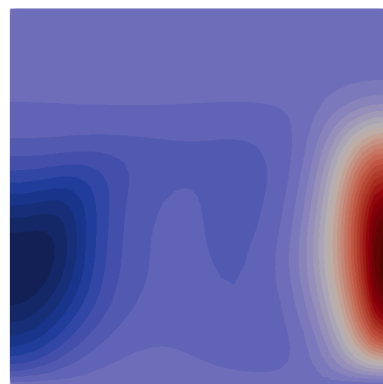
### Case 3

$\langle T \rangle$	0.7286	0.7275	0.7271	0.7272	0.7241	0.7274	0.727464	0.7275	0.7275	0.7278	0.7305
$Nu_{top}$	3.0374	3.0298	3.0324	3.0314	3.0253	3.03025	3.0918	3.0399	3.0347	3.0371	2.9311
$Nu_{bot}$	2.9628	3.0298	3.0323	3.0314	3.0253	3.03025	3.03487	3.0376	2.9908	3.0410	2.9311
$u_{RMS}$	100.9467	100.024	99.8701	99.9917	100.197	100.018	100.127	100.0396	100.1208	100.3368	111.6121
$u_{surf}^{surf}$	2.0374	2.0785	2.0916	2.0835	2.0789	2.07299	2.07301	2.0569	2.0652	2.0727	1.356
$u_{max}$	2.8458	2.9029	2.9201	2.9094	2.9207	2.89495	2.89501	2.873	2.9019	2.8946	1.8806
$\eta_{min}$	$4.7907 \times 10^{-5}$	$4.8140 \times 10^{-5}$	$4.8014 \times 10^{-5}$	$4.8047 \times 10^{-5}$	$4.8400 \times 10^{-5}$	$4.7951 \times 10^{-5}$	$4.8081 \times 10^{-5}$	$4.8000 \times 10^{-5}$	$4.8080 \times 10^{-5}$	$4.7972 \times 10^{-5}$	$10^{-4}$
$\eta_{max}$	1	0.9987	0.9857	0.9988	0.9010	0.9637	0.9999	1	0.9023	1	1
$\langle W \rangle$	2.0400	2.0028	2.0340	2.0269	2.0235	2.03002	2.03482	2.0298	2.0384	2.0362	2.056
$\langle \Phi \rangle / Ra$	2.0335	2.0277	2.0304	2.0286	2.0164	2.0302	2.03482	2.0298	2.037	2.0362	1.865
$\delta$	0.32%	1.23%	0.18%	0.08%	0.35%	0.01%	<0.01%	<0.01%	0.07%	<0.01%	9.29%

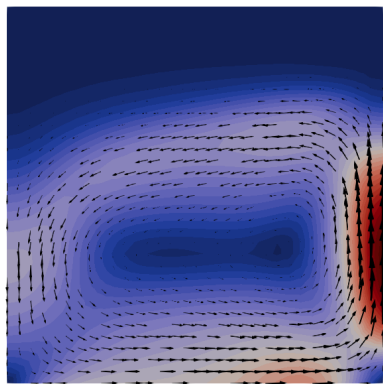




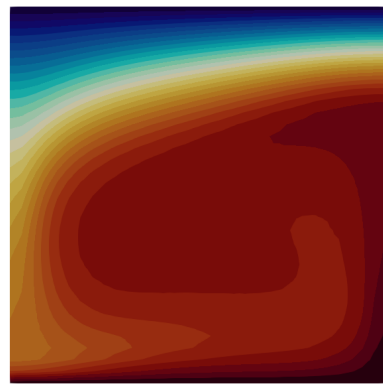
-133.934      0      100      204.210  
velocity X



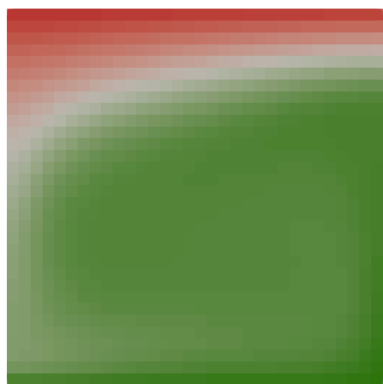
-137.969      0      100      200      330.512  
velocity Y



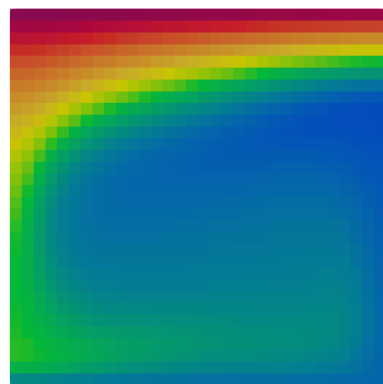
0.000      100      200      330.512  
velocity Magnitude



0.000      0.2      0.4      0.6      0.8      1.000  
T



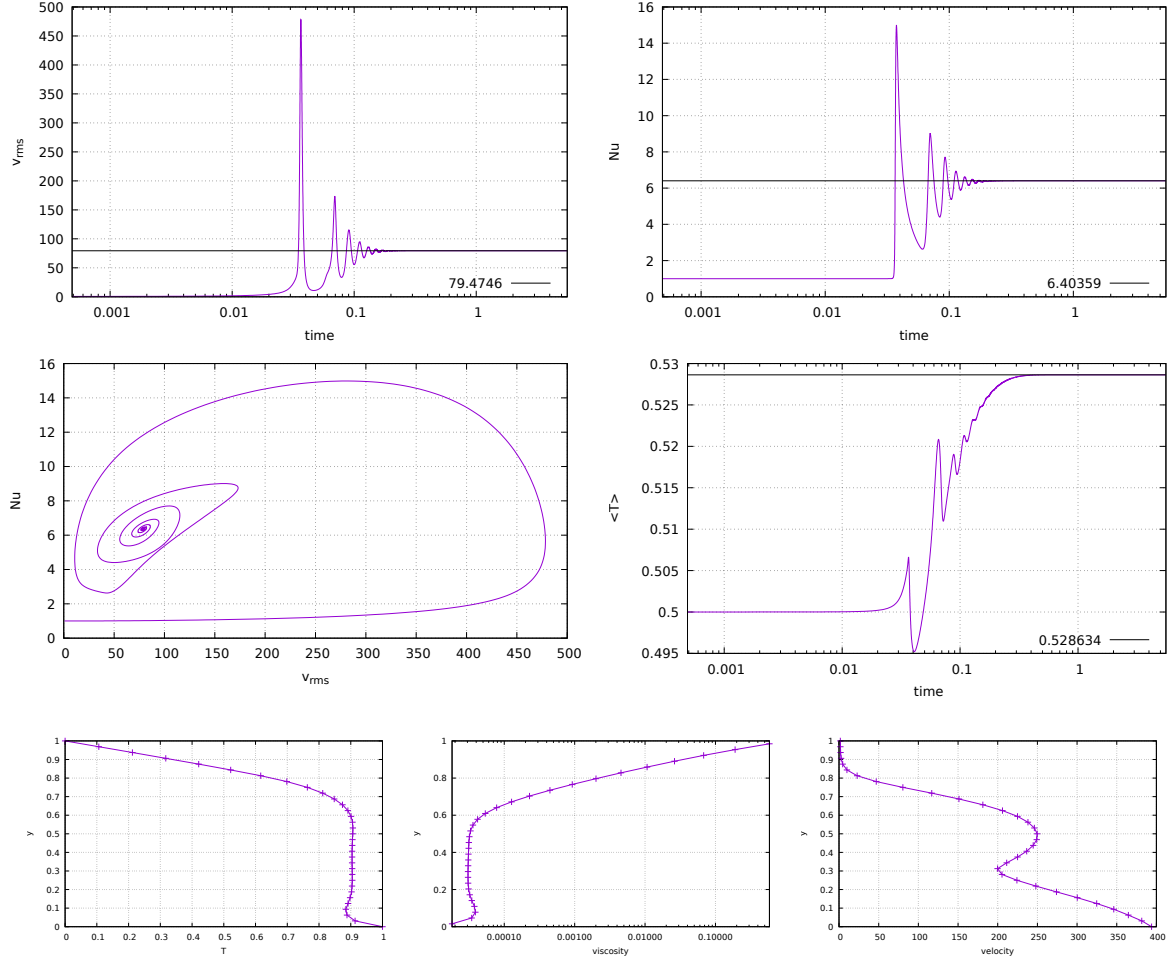
-1.000e-04      -6e-5      -4e-5      -3.000e-06  
density

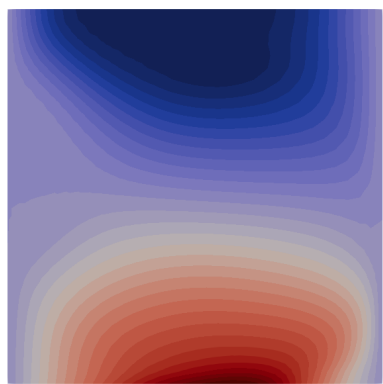


4.800e-05      0.000020000020.001      7.802e-01  
viscosity

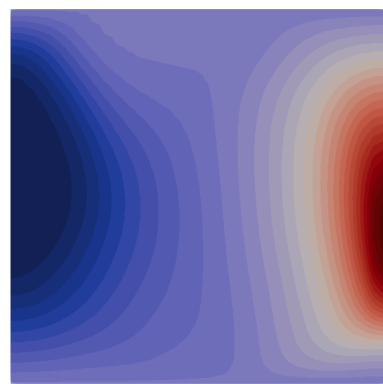
## Case 4

$\langle T \rangle$	0.5289	0.5276	0.5276	0.5289	0.5283	0.527304	0.527521	0.5274	0.5277	0.5278	0.5364
$Nu_{top}$	6.5572	6.6156	6.6074	6.5913	6.6356	6.61082	6.68224	6.6401	6.5912	6.6249	7.4376
$Nu_{bot}$	6.5243	6.6158	6.6073	6.5913	6.6356	6.61082	6.66899	6.6326	6.5834	6.6267	7.4376
$U_{RMS}$	79.6202	79.1358	79.0181	78.6652	79.4334	78.9903	79.0684	79.0318	79.1105	79.1996	98.8912
$U_{RMS}^{surf}$	75.4814	75.1727	75.0434	74.1719	74.8587	75.0606	75.0975	75.0827	74.7596	75.1903	93.5057
$U_{max}^{surf}$	89.2940	88.9715	88.8130	87.6118	89.1444	88.823	88.8753	88.85	88.9146	88.9848	123.046
$\eta_{min}$	$1.9174 \times 10^{-4}$	$1.9220 \times 10^{-4}$	$1.9448 \times 10^{-4}$	$1.9204 \times 10^{-4}$	$1.9900 \times 10^{-4}$	$1.9574 \times 10^{-4}$	$1.9167 \times 10^{-4}$	$1.9200 \times 10^{-4}$	$1.9860 \times 10^{-4}$	$1.9178 \times 10^{-4}$	$1.93 \times 10^{-4}$
$\eta_{max}$	1.6773	1.9834	1.6508	1.9670	1.1800	1.6665	1.7446	1.8891	1.5200	1.8831	$5.67 \times 10^{-3}$
$\langle W \rangle$	5.6512	5.6251	5.6076	5.5903	5.629	5.61012	5.61425	5.6136	5.6216	5.6235	6.751
$\langle \Phi \rangle / Ra$	5.6463	5.6174	5.6024	5.5434	5.6325	5.60152	5.61425	5.6136	5.6182	5.6235	7.786
$\delta$	0.09%	0.14%	0.09%	0.84%	0.06%	0.15%	<0.01%	<0.01%	0.06%	<0.01%	13.29%

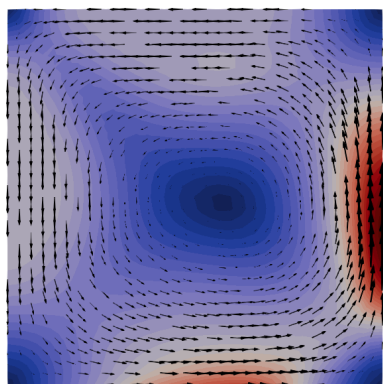




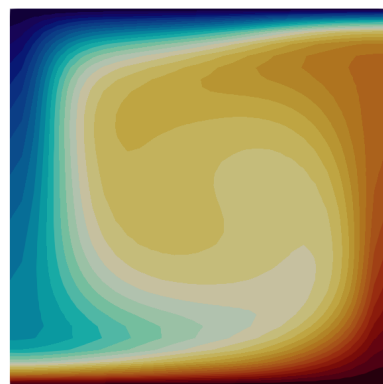
velocity X  
-92.305 -50 0 50 100 153.873



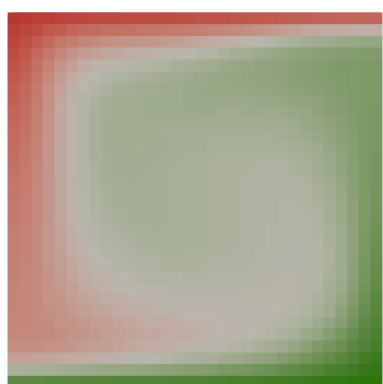
velocity Y  
-97.677 0 100 209.053



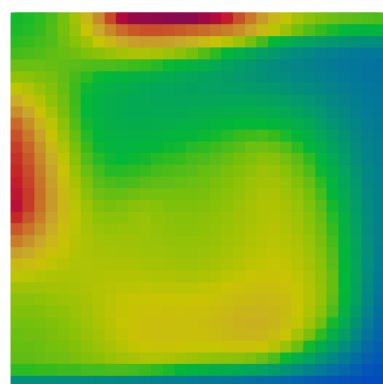
velocity Magnitude  
0.000 50 100 150 209.053



T  
0.000 0.2 0.4 0.6 0.8 1.000

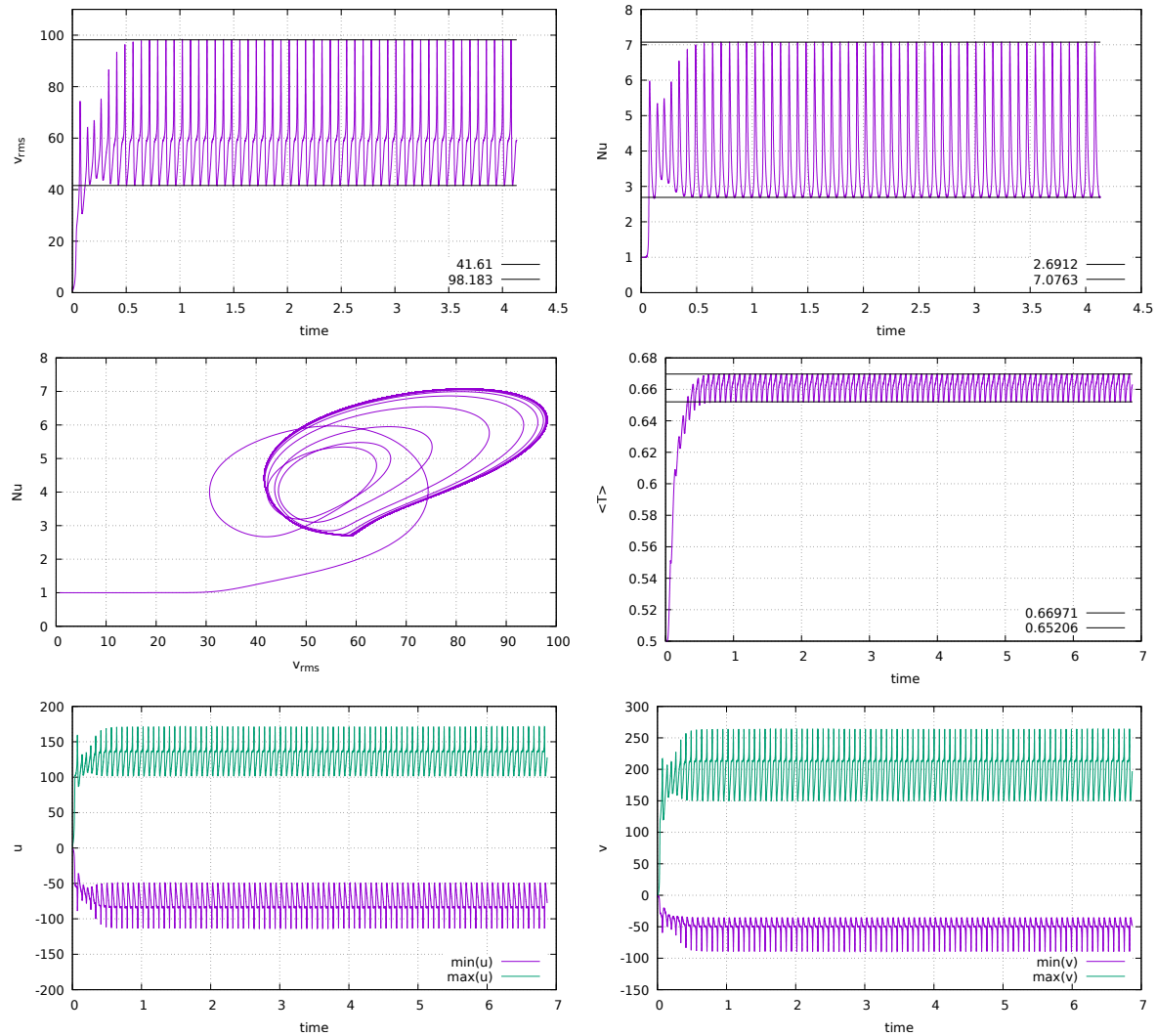


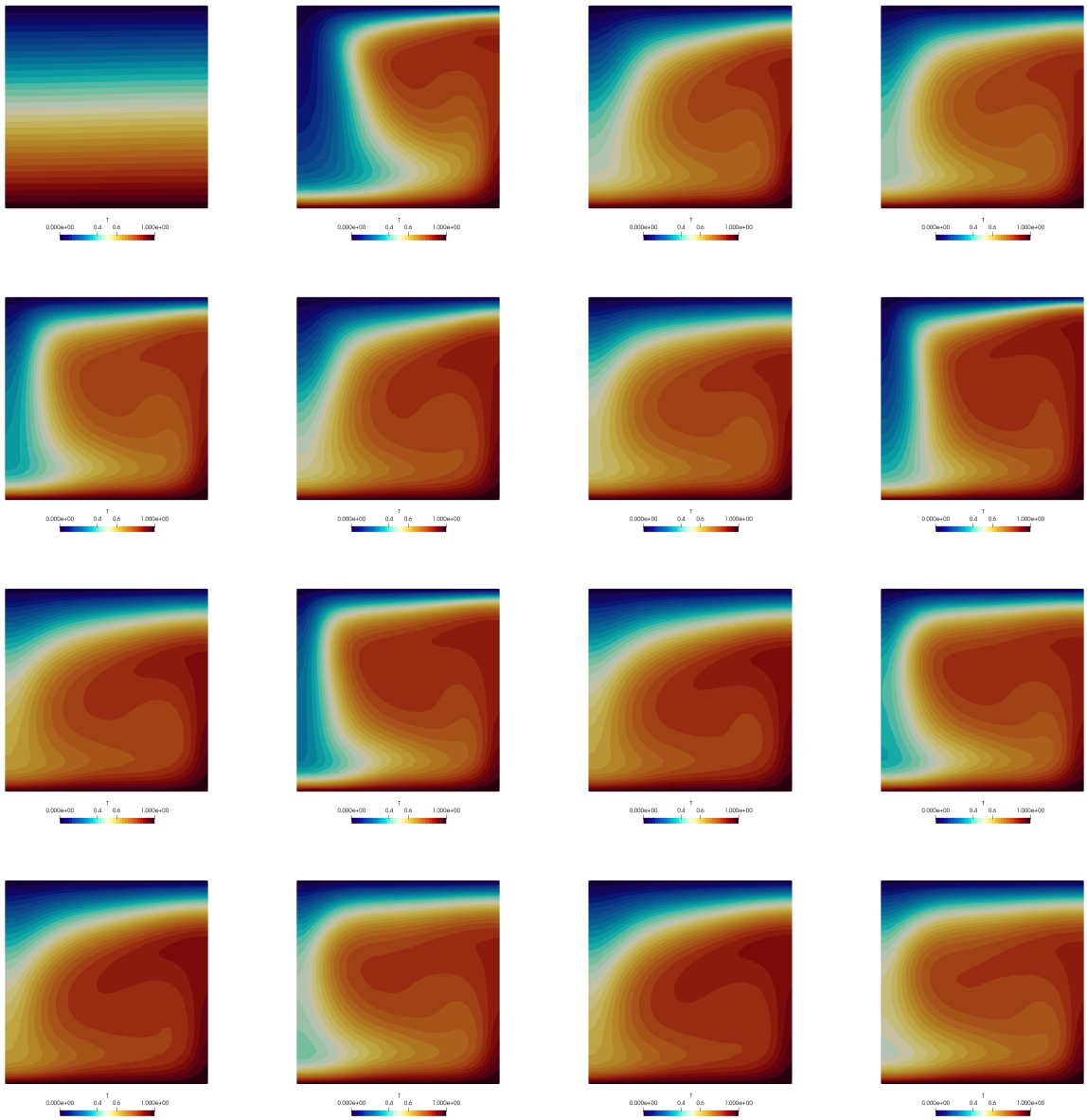
density  
-9.900e-05 -4e-5 -1.000e-06



viscosity  
0.00021 0.00203 0.020.05.1 0.75499

## Case 5





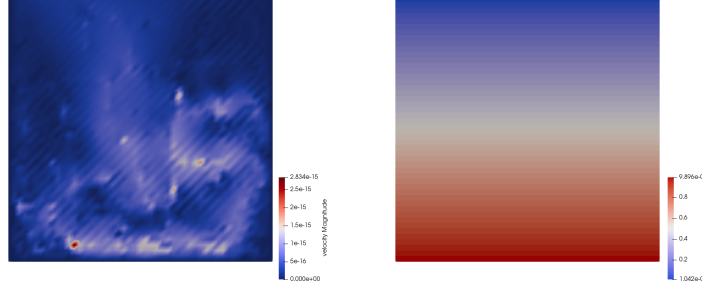
## Stone 29: open boundary conditions



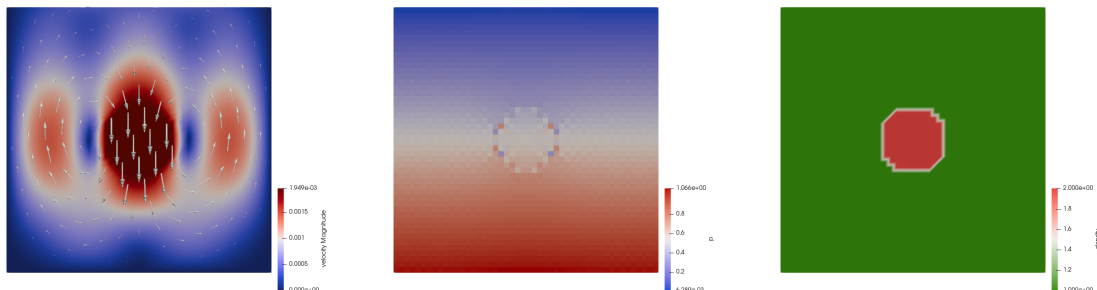
Relevant Literature[457]

In what follows we will investigate the use of the so-called open boundary conditions in the very simple context of a 2D Stokes sphere experiment.

We start with a domain without the sphere. Essentially, it is what people would call an aquarium. Free slip boundary conditions are prescribed on the sides and no-slip conditions at the bottom. The top surface is left free. The fluid has a density  $\rho_0 = 1$  and a viscosity  $\eta_0 = 1$ . In the absence of any density difference in the domain there is no active buoyancy force so that we expect a zero velocity field and a lithostatic pressure field. This is indeed what we recover:



If we now implement a sphere parametrised by its density  $\rho_s = \rho_0 + 1$ , its viscosity  $\eta_s = 10^3$  and its radius  $R_s = 0.123$  in the middle of the domain, we see clear velocity field which logically shows the sphere falling downward and a symmetric return flow of the fluid on each side:

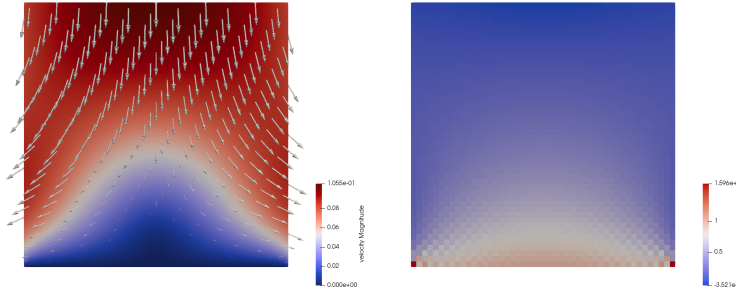


Unfortunately it has been widely documented that the presence of free-slip boundary conditions affects the evolution of subduction [457], even when these are placed rather far from the subduction zone. A proposed solution to this problem is the use of 'open boundary conditions' which are in fact stress boundary conditions. The main idea is to prescribe a stress on the lateral boundaries (instead of free slip) so that it balances out exactly the existing lithostatic pressure inside the domain along the side walls. Only pressure deviations with respect to the lithostatic are responsible for flow and such boundary conditions allow flow across the boundaries.

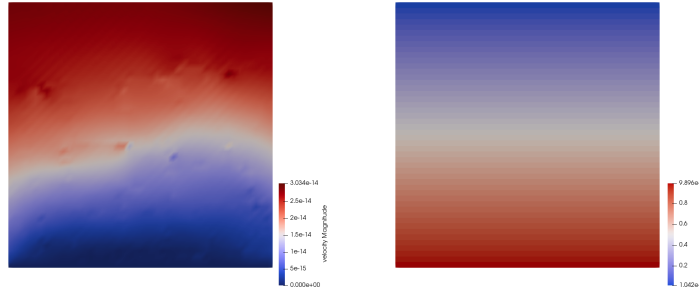
We need the lithostatic pressure and compute it before hand (which is trivial in our case but can prove to be a bit more tedious in real life situations when for instance density varies in the domain as a function of temperature and/or pressure).

```
plith = np.zeros(nnp, dtype=np.float64)
for i in range(0, nnp):
    plith[i] = (Ly - y[i]) * rho0 * abs(gy)
```

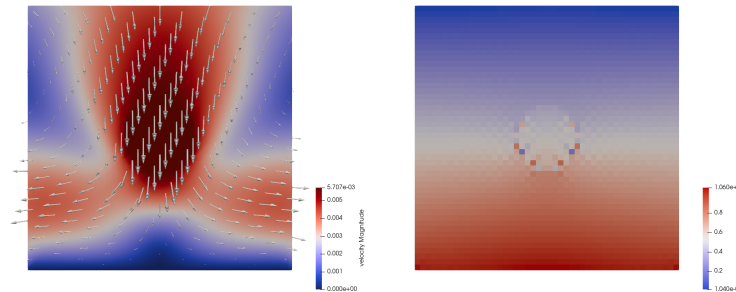
Let us start with a somewhat pathological case: even in the absence of the sphere, what happens when no boundary conditions are prescribed on the sides? The answer is simple: think about an aquarium without side walls, or a broken dam. The velocity field indeed shows a complete collapse of the fluid left and right of the bottom.



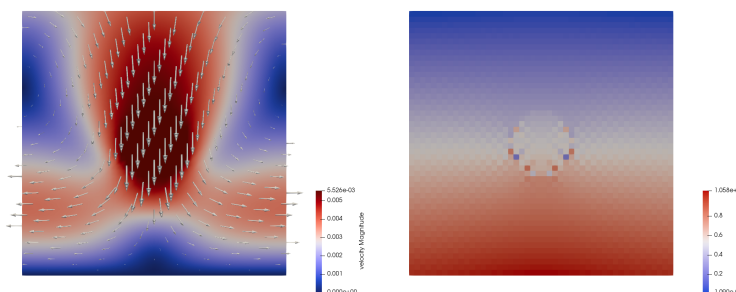
Let us then continue (still with no sphere) but let us now switch on the open boundary conditions. Since the side boundary conditions match the lithostatic pressure we expect no flow at all in the absence of any density perturbation in the system. This is indeed what is recovered:



Finally, let us reintroduce the sphere. This time flow is allowed through the left and right side boundaries:



Finally, although horizontal velocity Dirichlet boundary conditions and open boundary conditions are not compatible, the same is not true for the vertical component of the velocity: the open b.c. implementation acts on the horizontal velocity dofs only, so that one can fix the vertical component to zero, as is shown hereunder:



We indeed see that the in/outflow on the sides is perpendicular to the boundaries.

Turning now to the actual implementation, we see that it is quite trivial, since all element edges are vertical, and all have the same vertical dimension  $h_x$ . Since we use a  $Q_0$  approximation for the pressure

we need to prescribe a single pressure value in the middle of the element. Finally because of the sign of the normal vector projection onto the  $x$ -axis, we obtain:

```

if open_bc_left and x[icon[0,iel]]<eps: # left side
    pmid=0.5*(plith[icon[0,iel]]+plith[icon[3,iel]])
    f_el[0]+=0.5*hy*pmid
    f_el[6]+=0.5*hy*pmid
if open_bc_right and x[icon[1,iel]]>Lx-eps: # right side
    pmid=0.5*(plith[icon[1,iel]]+plith[icon[2,iel]])
    f_el[2]-=0.5*hy*pmid
    f_el[4]-=0.5*hy*pmid

```

These few lines of code are added after the elemental matrices and rhs are built, and before the application of other Dirichlet boundary conditions, and assembly.

## Stone 30: conservative velocity interpolation

In this the Stokes equations are not solved. It is a 2D implementation of the cvi algorithm as introduced in [2719] which deals with the advection of markers.  $Q_1$  and  $Q_2$  basis functions are used and in both cases the cvi algorithm can be toggled on/off. Markers can be distributed regularly or randomly at startup.

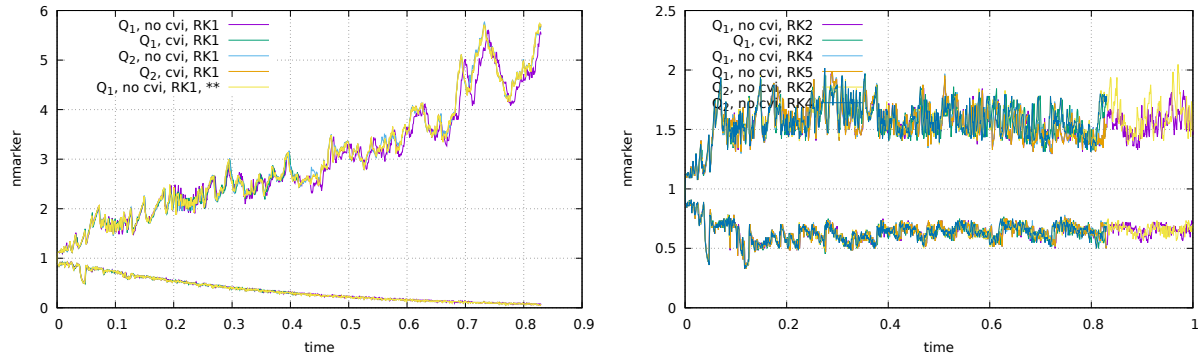
Three velocity fields are prescribed on the mesh:

- the so-called Couette flow of [2719]
- the SolCx solution
- a flow created by means of a stream line function (see fieldstone 32)

### Couette flow

#### SolCx

#### Streamline flow



In this case RK order seems to be more important than cvi.

Explore why ?!

## **Stone 31: conservative velocity interpolation 3D**

## Stone 32: 2D analytical sol. from stream function

### Background theory

The stream function is a function of coordinates and time of an inviscid liquid. It allows to determine the components of velocity by differentiating the stream function with respect to the space coordinates. A family of curves  $\Psi = \text{const}$  represent *streamlines*, i.e. the stream function remains constant along a streamline. Although also valid in 3D, this approach is mostly used in 2D because of its relative simplicity

#### REFERENCES.

In two dimensions the velocity is obtained as follows:

$$\mathbf{v} = \left( \frac{\partial \Psi}{\partial y}, -\frac{\partial \Psi}{\partial x} \right) \quad (959)$$

Provided the function  $\Psi$  is a smooth enough function, this automatically insures that the flow is incompressible:

$$\nabla \cdot \mathbf{v} = \frac{\partial u}{\partial x} + \frac{\partial v}{\partial y} = \frac{\partial^2 \Psi}{\partial x \partial y} - \frac{\partial^2 \Psi}{\partial y \partial x} = 0 \quad (960)$$

Assuming constant viscosity, the Stokes equation writes:

$$-\nabla p + \mu \Delta \mathbf{v} = \rho \mathbf{g} \quad (961)$$

Let us introduce the vector  $\mathbf{W}$  for convenience such that in each dimension:

$$W_x = -\frac{\partial p}{\partial x} + \mu \left( \frac{\partial^2 u}{\partial x^2} + \frac{\partial^2 u}{\partial x \partial y} \right) = \rho g_x \quad (962)$$

$$W_y = -\frac{\partial p}{\partial y} + \mu \left( \frac{\partial^2 v}{\partial x^2} + \frac{\partial^2 v}{\partial x \partial y} \right) = \rho g_y \quad (963)$$

Taking the curl of the vector  $\mathbf{W}$  and only considering the component perpendicular to the  $xy$ -plane:

$$\frac{\partial V_y}{\partial x} - \frac{\partial V_x}{\partial y} = \frac{\partial \rho g_y}{\partial x} - \frac{\partial \rho g_x}{\partial y} \quad (964)$$

The advantage of this approach is that the pressure terms cancel out (the curl of a gradient is always zero), so that:

$$\frac{\partial}{\partial x} \mu \left( \left( \frac{\partial^2 v}{\partial x^2} + \frac{\partial^2 v}{\partial x \partial y} \right) - \frac{\partial}{\partial y} \mu \left( \frac{\partial^2 u}{\partial x^2} + \frac{\partial^2 u}{\partial x \partial y} \right) \right) = \frac{\partial \rho g_y}{\partial x} - \frac{\partial \rho g_x}{\partial y} \quad (965)$$

and then replacing  $u, v$  by their stream function derivatives yields (for a constant viscosity):

$$\mu \left( \frac{\partial^4 \Psi}{\partial x^4} + \frac{\partial^4 \Psi}{\partial y^4} + 2 \frac{\partial^4 \Psi}{\partial x^2 \partial y^2} \right) = \frac{\partial \rho g_y}{\partial x} - \frac{\partial \rho g_x}{\partial y} \quad (966)$$

or,

$$\nabla^4 \Psi = \left( \frac{\partial^2}{\partial x^2} + \frac{\partial^2}{\partial y^2} \right) \left( \frac{\partial^2}{\partial x^2} + \frac{\partial^2}{\partial y^2} \right) \Psi = \frac{\partial \rho g_y}{\partial x} - \frac{\partial \rho g_x}{\partial y} \quad (967)$$

These equations are also to be found in the geodynamics literature, eee Eq. 1.43 of Tackley book, p 70-71 of Gerya book.

### A simple application

I wish to arrive at an analytical formulation for a 2D incompressible flow in the square domain  $[-1 : 1] \times [-1 : 1]$ . The fluid has constant viscosity  $\mu = 1$  and is subject to free slip boundary conditions on all sides. For reasons that will become clear in what follows I postulate the following stream function:

$$\Psi(x, y) = \sin(m\pi x) \sin(n\pi y) \quad (968)$$

We have the velocity being defined as:

$$\mathbf{v} = (u, v) = \left( \frac{\partial \Psi}{\partial y}, -\frac{\partial \Psi}{\partial x} \right) = (n\pi \sin(m\pi x) \cos(n\pi y), -m\pi \cos(m\pi x) \sin(n\pi y)) \quad (969)$$

The strain rate components are then:

$$\dot{\varepsilon}_{xx} = \frac{\partial u}{\partial x} = mn\pi^2 \cos(m\pi x) \cos(n\pi y) \quad (970)$$

$$\dot{\varepsilon}_{yy} = \frac{\partial v}{\partial y} = -mn\pi^2 \cos(m\pi x) \cos(n\pi y) \quad (971)$$

$$2\dot{\varepsilon}_{xy} = \frac{\partial u}{\partial y} + \frac{\partial v}{\partial x} \quad (972)$$

$$= \frac{\partial^2 \Psi}{\partial y^2} - \frac{\partial^2 \Psi}{\partial x^2} \quad (973)$$

$$= -n^2\pi^2\Psi + m^2\pi^2\Psi \quad (974)$$

$$= (m^2 - n^2)\pi^2 \sin(m\pi x) \sin(n\pi y) \quad (975)$$

Note that if  $m = n$  the last term is identically zero, which is not desirable (flow is too 'simple') so in what follows we will prefer  $m \neq n$ .

It is also easy to verify that  $u = 0$  on the sides and  $v = 0$  at the top and bottom and that the term  $\dot{\varepsilon}_{xy}$  is null on all four sides, thereby guaranteeing free slip.

Our choice of stream function yields:

$$\nabla^4 \Psi = \frac{\partial^4 \Psi}{\partial x^4} + \frac{\partial^4 \Psi}{\partial y^4} + 2 \frac{\partial^2 \Psi}{\partial x^2 \partial y^2} = \pi^4 (m^4 \Psi + n^4 \Psi + 2m^2 n^2 \Psi) = (m^4 + n^4 + 2m^2 n^2) \pi^4 \Psi$$

We assume  $g_x = 0$  and  $g_y = -1$  so that we simply have

$$(m^4 + n^4 + 2m^2 n^2) \pi^4 \Psi = -\frac{\partial \rho}{\partial x} \quad (976)$$

so that (assuming the integration constant to be zero):

$$\rho(x, y) = \frac{m^4 + n^4 + 2m^2 n^2}{m} \pi^3 \cos(m\pi x) \sin(n\pi y)$$

The  $x$ -component of the momentum equation is

$$-\frac{\partial p}{\partial x} + \frac{\partial^2 u}{\partial x^2} + \frac{\partial^2 u}{\partial y^2} = -\frac{\partial p}{\partial x} - m^2 n \pi^3 \sin(m\pi x) \cos(n\pi y) - n^3 \pi^3 \sin(m\pi x) \cos(n\pi y) = 0$$

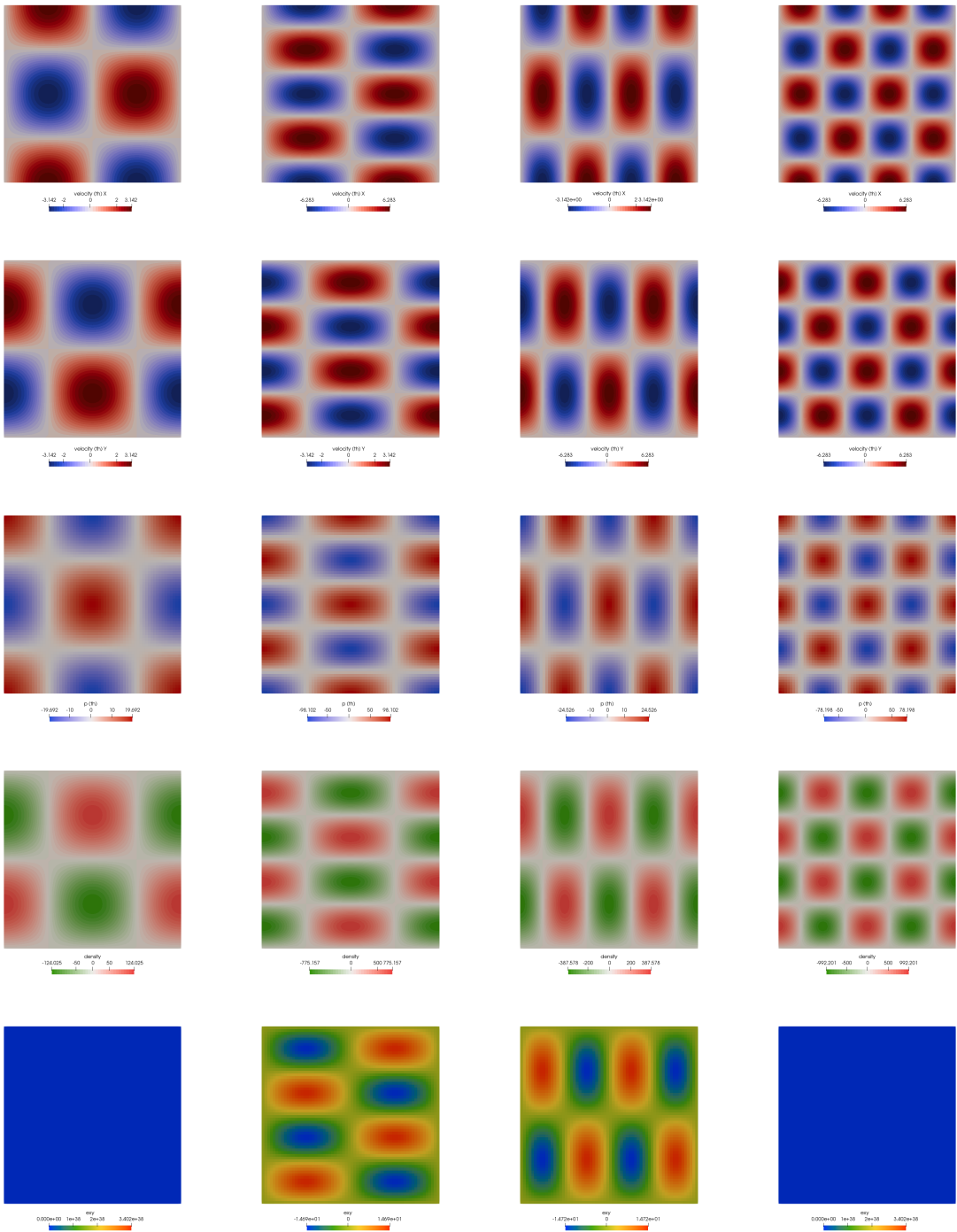
so

$$\frac{\partial p}{\partial x} = -(m^2 n + n^3) \pi^3 \sin(m\pi x) \cos(n\pi y)$$

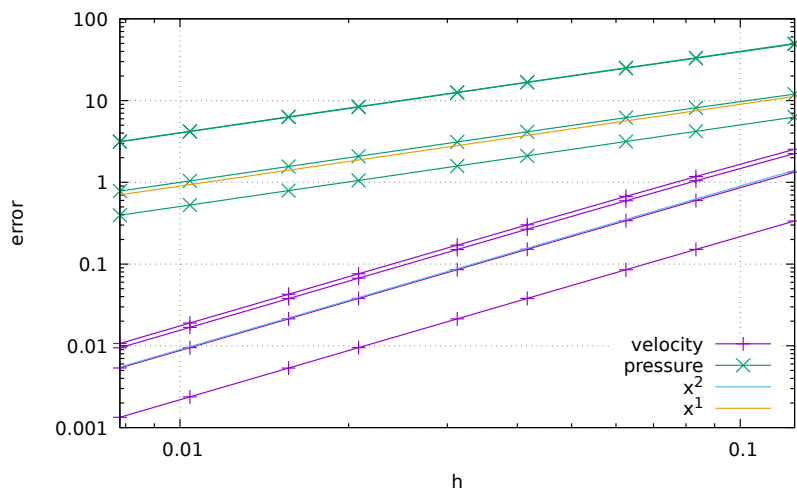
and the pressure field is then (once again neglecting the integration constant):

$$p(x, y) = \frac{m^2 n + n^3}{m} \pi^2 \cos(\pi x) \cos(\pi y)$$

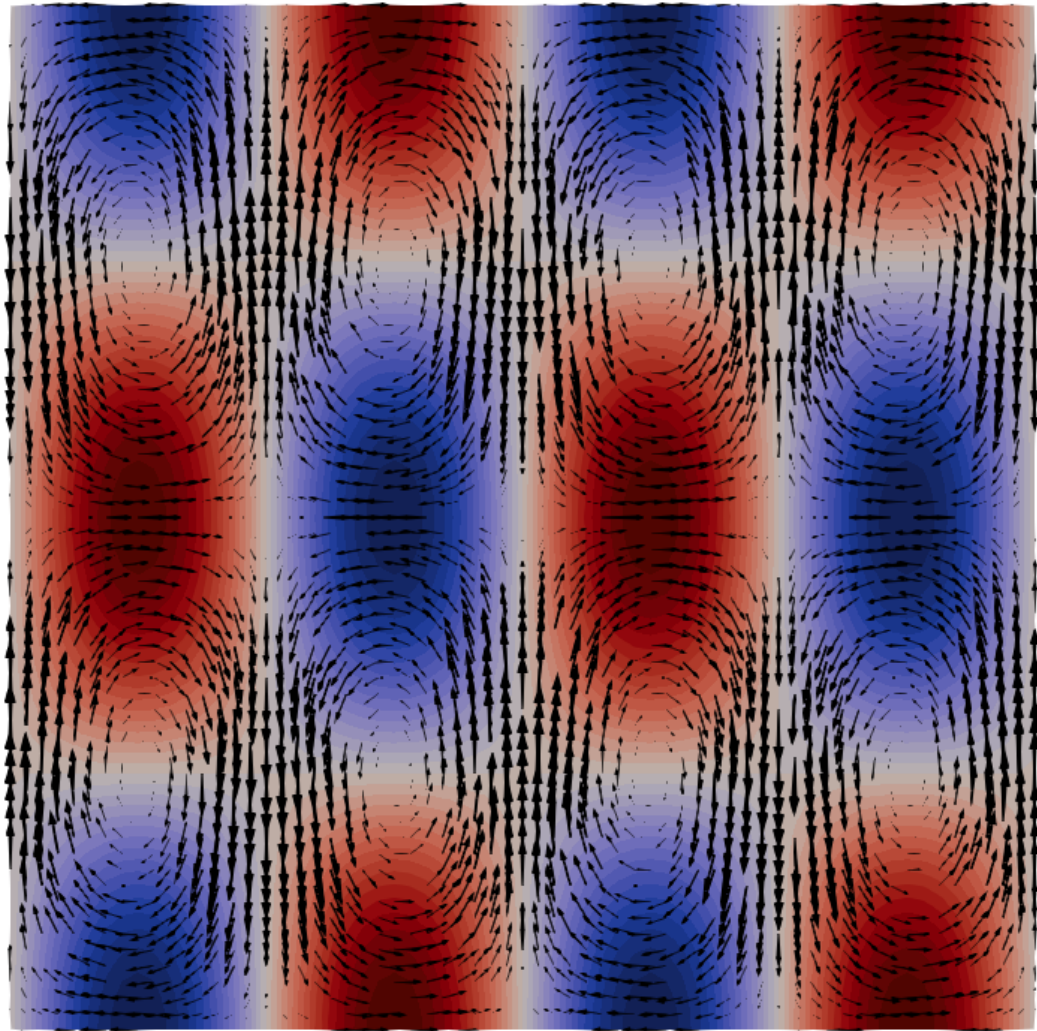
Note that in this case  $\int p dV = 0$  so that volume normalisation of the pressure is turned on (when free slip boundary conditions are prescribed on all sides the pressure is known up to a constant and this undeterminacy can be lifted by adding an additional constraint to the pressure field).



Top to bottom: Velocity components  $u$  and  $v$ , pressure  $p$ , density  $\rho$  and strain rate  $\dot{\epsilon}_{xy}$ . From left to right:  
 $(m, n) = (1, 1)$ ,  $(m, n) = (1, 2)$ ,  $(m, n) = (2, 1)$ ,  $(m, n) = (2, 2)$



Errors for velocity and pressure for  $(m, n) = (1, 1), (1, 2), (2, 1), (2, 2)$



Velocity arrows for  $(m, n) = (2, 1)$

## Stone 33: Convection in an annulus

This fieldstone was developed in collaboration with Rens Elbertsen.

This is based on the community benchmark for viscoplastic thermal convection in a 2D square box (Tosi et al (2015) [2556]) as already carried out in ??.

In this experiment the geometry is an annulus of inner radius  $R_1 = 1.22$  and outer radius  $R_2 = 2.22$ . The rheology and buoyancy forces are identical to those of the box experiment. The initial temperature is now given by:

$$T(r, \theta) = T_c(r) + A s(1 - s) \cos(N_0 \theta) \quad s = \frac{R_2 - r}{R_2 - R_1} \in [0, 1]$$

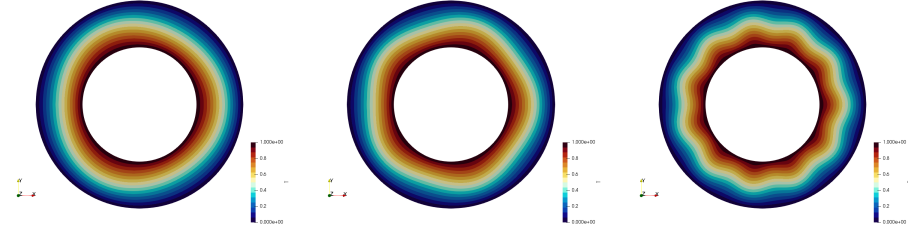
where  $s$  is the normalised depth,  $A$  is the amplitude of the perturbation and  $N_0$  the number of lobes. In this equation  $T_c(r)$  stands for the steady state purely conductive temperature solution which is obtained by solving the Laplace's equation in polar coordinates (all terms in  $\theta$  are dropped because of radial symmetry) supplemented with two boundary conditions:

$$\Delta T_c = \frac{1}{r} \frac{\partial}{\partial r} \left( r \frac{\partial T}{\partial r} \right) = 0 \quad T(r = R_1) = T_1 = 1 \quad T(r = R_2) = T_2 = 0$$

We obtain

$$T_c(r) = \frac{\log(r/R_2)}{\log(R_1/R_2)}$$

Note that this profile differs from the straight line that is used in Tosi et al (2015) [2556] and in section 9.4.



Examples of initial temperature fields for  $N_0 = 3, 5, 11$

Boundary conditions can be either no-slip or free-slip on both inner and outer boundary. However, when free-slip is used on both a velocity null space exists and must be filtered out. In other words, the solver may be able to come up with a solution to the Stokes operator, but that solution plus an arbitrary rotation is also an equally valid solution. This additional velocity field can be problematic since it is used for advecting temperature (and/or compositions) and it also essentially determines the time step value for a chosen mesh size (CFL condition).

**About the nullspace** For these reasons the nullspace must be removed from the obtained solution after every timestep. There are two types of nullspace removal: removing net angular momentum, and removing net rotations. The technique that we use here is simple:

1. pin the first node which is at position ( $x = R_1, y = 0$ ) and set its vertical velocity to zero. This eliminates the nullspace completely.
2. compute the angular momentum and correct the velocity field so that it is zero as explained in section 8.30.

The corrected velocity field  $\vec{v}'$  is then given by

$$\vec{v}' = \vec{v} - \langle \vec{\omega} \rangle \times \vec{r}$$

and it is easy to verify that

$$\begin{aligned}
\langle \vec{\omega}' \rangle &= \frac{1}{V} \int_V \frac{\vec{r} \times \vec{\nabla}'}{r^2} dV \\
&= \frac{1}{V} \int_V \frac{\vec{r} \times (\vec{\nabla} - \langle \vec{\omega} \rangle \times \vec{r})}{r^2} dV \\
&= \frac{1}{V} \int_V \frac{\vec{r} \times \vec{\nabla}}{r^2} dV - \frac{1}{V} \int_V \frac{\vec{r} \times \langle \vec{\omega} \rangle \times \vec{r}}{r^2} dV \\
&= \langle \vec{\omega} \rangle - \langle \vec{\omega} \rangle \frac{1}{V} \int_V dV = 0
\end{aligned} \tag{977}$$

**Measurements** We calculate and monitor the following quantities:

- the average temperature  $\langle T \rangle$

$$\langle T \rangle = \frac{\int_{\Omega} T d\Omega}{\int_{\Omega} d\Omega} = \frac{1}{V_{\Omega}} \int_{\Omega} T d\Omega \tag{978}$$

- the root mean square velocity  $v_{rms}$  as given by equation (97).
- the root mean square of the radial and tangential velocity components as given by equations (99) and (100).
- the heat transfer through both boundaries  $Q$ :

$$Q_{inner,outer} = \int_{\Gamma_{i,o}} \mathbf{q} \cdot \mathbf{n} d\Gamma \tag{979}$$

- the Nusselt number at both boundaries  $Nu$  as given by equations (102) and (103).
- the power spectrum of the temperature field:

$$PS_n(T) = \left| \int_{\Omega} T(r, \theta) e^{in\theta} d\Omega \right|^2. \tag{980}$$

- the average viscosity  $\langle \eta \rangle$  (see Eq. 106)

**Cases and rheologies** In the following Table, we list the benchmark cases according to the parameters used.

Case	$Ra$	$\Delta\mu_T$	$\Delta\mu_y$	$\mu^*$	$\sigma_Y$	Convective regime
1	$10^2$	$10^5$	1	—	—	Stagnant lid
2	$10^2$	$10^5$	1	$10^{-3}$	1	Mobile lid
3	$10^2$	$10^5$	10	—	—	Stagnant lid
4	$10^2$	$10^5$	10	$10^{-3}$	1	Mobile lid
5a	$10^2$	$10^5$	10	$10^{-3}$	4	Periodic
5b	$10^2$	$10^5$	10	$10^{-3}$	3 – 5	Mobile lid – Periodic – Stagnant lid

Benchmark cases and corresponding parameters.

**Steady state** As explained in 9.4 we use a relaxation technique in combination with an energy equation stripped from its time derivative term. The use of this technique is controlled by the `find_ss` parameter.

The termination criterion is based on the Nusselt number also.

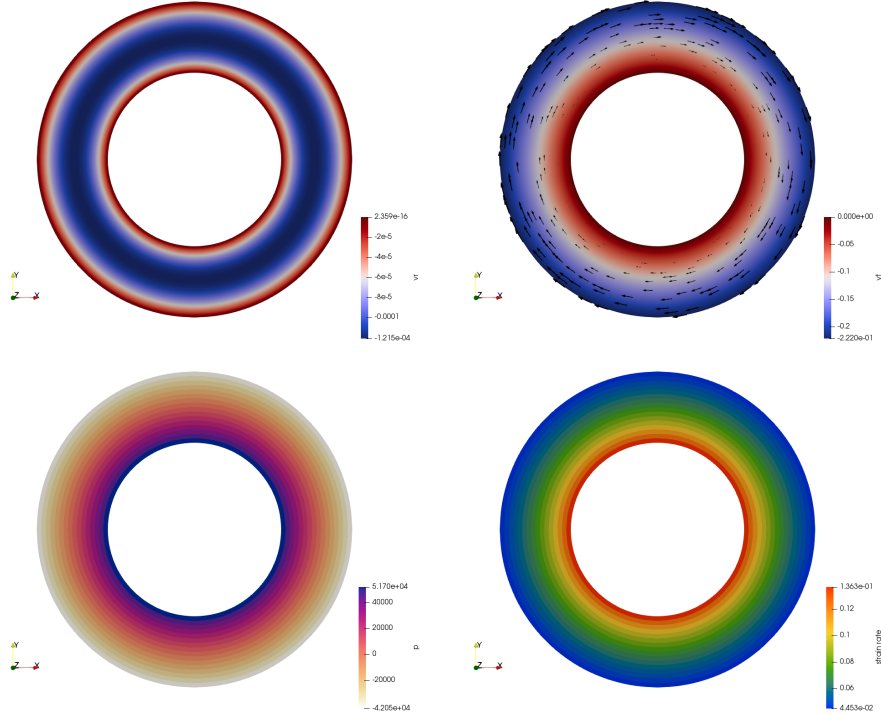
```

if np.abs(Nu_boundary1-Nu_boundary1_old) and \
np.abs(Nu_boundary2-Nu_boundary2_old) < 1.e-5:
    print("Nu_converged_to_1e-5")
    break

```

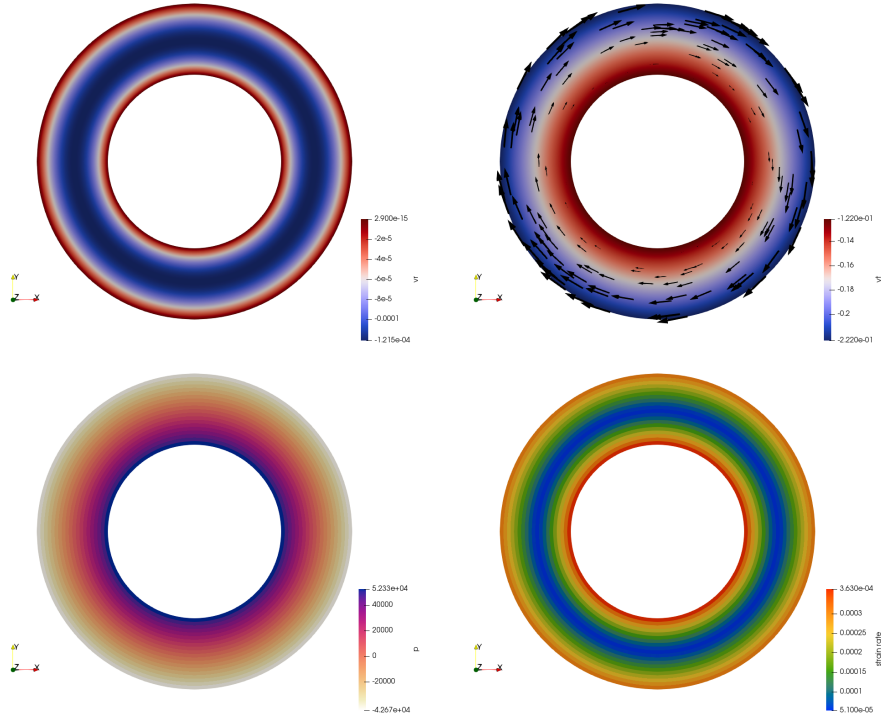
**Spectral analysis/power spectrum** CHECK [283] for power spectrum of Nusselt nb. check [349, 1764, 2065, 2174, 2295, 2755]

**test 1** We here wish to test the boundary conditions. We set  $\vec{v} = (y, -x)$  on the outside boundary, and  $\vec{v} = (0, 0)$  on the inside boundary, set the temperature to zero, and run a single time step (note that the no net rotation/angular momentum algorithm must be turned off then).



The radial velocity is not zero (or machine precision zero) because of the use of the penalty method.

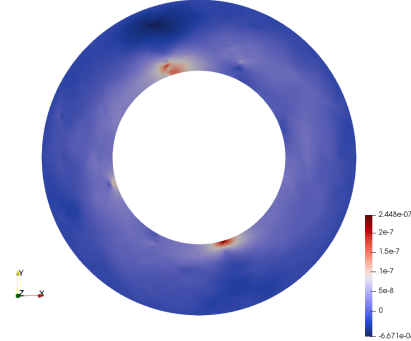
**test 2a** This is the same experiment as above but now the inner boundary is free slip. We then expect a constant angular velocity (measured by the code as  $-9.999999e-01$ ) and also a velocity on the inner boundary equal (in magnitude) to  $R_1 = 1.22$  which is indeed what we recover:



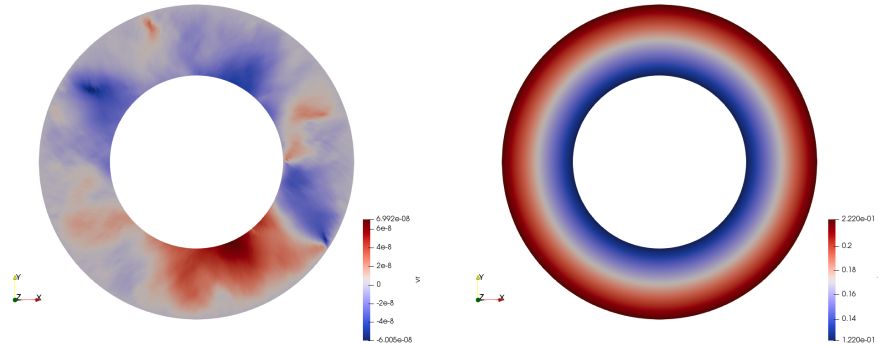
Unsurprisingly the pressure and radial velocity fields are unaffected by this change of boundary conditions.

**test 3** Same experiment as exp.2, but boundary conditions are switched (free slip outside, prescribed inside). Results are not shown but the angular velocity has the right value, and so does the velocity field.

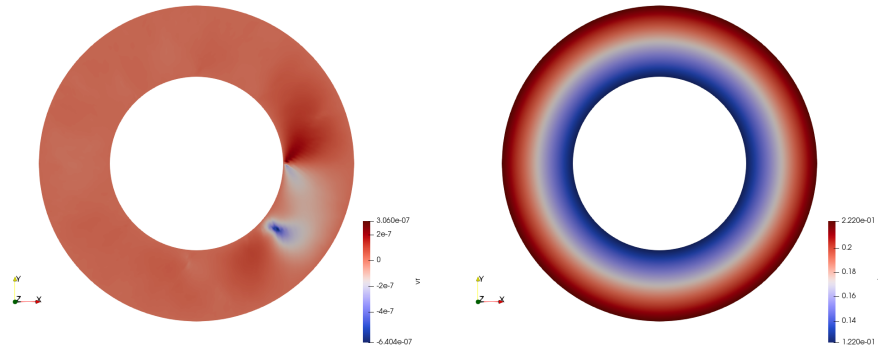
**test 2b** Same as exp.2 but now the net rotation algorithm is switched on. Since the boundary conditions are such that a constant angular rotation is expected, then the algorithm should yield a tangential velocity that is null, and this is indeed what we recover (at least 8 orders of magnitude smaller than before removal):



**test 4** We now set free slip boundary conditions on the outside boundary and only a single node at position  $(R_1, 0)$  is prescribed a velocity  $(0, R_1)$ . Gravity is set to zero and no net angular velocity removal is applied. We recover a (near) zero radial velocity component and a the expected angular velocity  $9.999984e - 01$ .

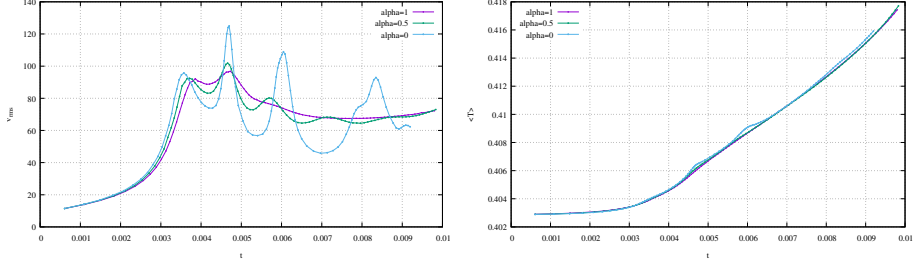


**test 4b** Same as test 4, but now free slip boundary conditions are imposed on both the inner and outer boundaries at the exception of a single node as above. We expect identical results as in test 4 (same physics) and we indeed do recover the same  $v_t$  velocity field and a similarly negligible  $v_r$  field:



These tests are convincing: the free-slip and no-slip boundary conditions work as expected and the single node velocity b.c. to remove the nullspace in conjunction with free-slip also works. Let us now turn to resolution and time-discretisation.

### Influence of time discretisation of energy equation .



## Stone 34: the Cartesian geometry elastic aquarium

This fieldstone was developed in collaboration with Lukas van de Wiel.

The setup is as follows: a 2D square of elastic material of size  $L$  is subjected to the following boundary conditions: free slip on the sides, no slip at the bottom and free at the top. It has a density  $\rho$  and is placed in a gravity field  $\mathbf{g} = -ge_y$ . For an isotropic elastic medium the stress tensor is given by:

$$\boldsymbol{\sigma} = \lambda(\nabla \cdot \mathbf{u})\mathbf{1} + 2\mu\boldsymbol{\varepsilon}$$

where  $\lambda$  is the Lamé parameter and  $\mu$  is the shear modulus. The displacement field is  $\mathbf{u} = (0, u_y(y))$  because of symmetry reasons (we do not expect any of the dynamic quantities to depend on the  $x$  coordinate and also expect the horizontal displacement to be exactly zero). The velocity divergence is then  $\nabla \cdot \mathbf{u} = \partial u_y / \partial y$  and the strain tensor:

$$\boldsymbol{\varepsilon} = \begin{pmatrix} 0 & 0 \\ 0 & \frac{\partial u_y}{\partial y} \end{pmatrix}$$

so that the stress tensor is:

$$\begin{aligned} \boldsymbol{\sigma} &= \begin{pmatrix} \lambda \frac{\partial u_y}{\partial y} & 0 \\ 0 & (\lambda + 2\mu) \frac{\partial u_y}{\partial y} \end{pmatrix} \\ \nabla \cdot \boldsymbol{\sigma} &= (\partial_x \quad \partial_y) \cdot \begin{pmatrix} \lambda \frac{\partial u_y}{\partial y} & 0 \\ 0 & (\lambda + 2\mu) \frac{\partial u_y}{\partial y} \end{pmatrix} = \begin{pmatrix} 0 \\ (\lambda + 2\mu) \frac{\partial^2 u_y}{\partial y^2} \end{pmatrix} = \begin{pmatrix} 0 \\ \rho g \end{pmatrix} \end{aligned}$$

so that the vertical displacement is then given by:

$$u_y(y) = \frac{1}{2} \frac{\rho g}{\lambda + 2\mu} y^2 + \alpha y + \beta$$

where  $\alpha$  and  $\beta$  are two integration constants. We need now to use the two boundary conditions: the first one states that the displacement is zero at the bottom, i.e.  $u_y(y=0) = 0$  which immediately implies  $\beta = 0$ . The second states that the stress at the top is zero (free surface), which implies that  $\partial u_y / \partial y(y=L) = 0$  which allows us to compute  $\alpha$ . Finally:

$$u_y(y) = \frac{\rho g}{\lambda + 2\mu} \left( \frac{y^2}{2} - Ly \right)$$

The pressure is given by

$$p = -(\lambda + \frac{2}{3}\mu)\nabla \cdot \mathbf{u} = (\lambda + \frac{2}{3}\mu) \frac{\rho g}{\lambda + 2\mu} (L - y) = \frac{\lambda + \frac{2}{3}\mu}{\lambda + 2\mu} \rho g (L - y) = \frac{1 + \frac{2\mu}{3\lambda}}{1 + 2\mu/\lambda} \rho g (L - y)$$

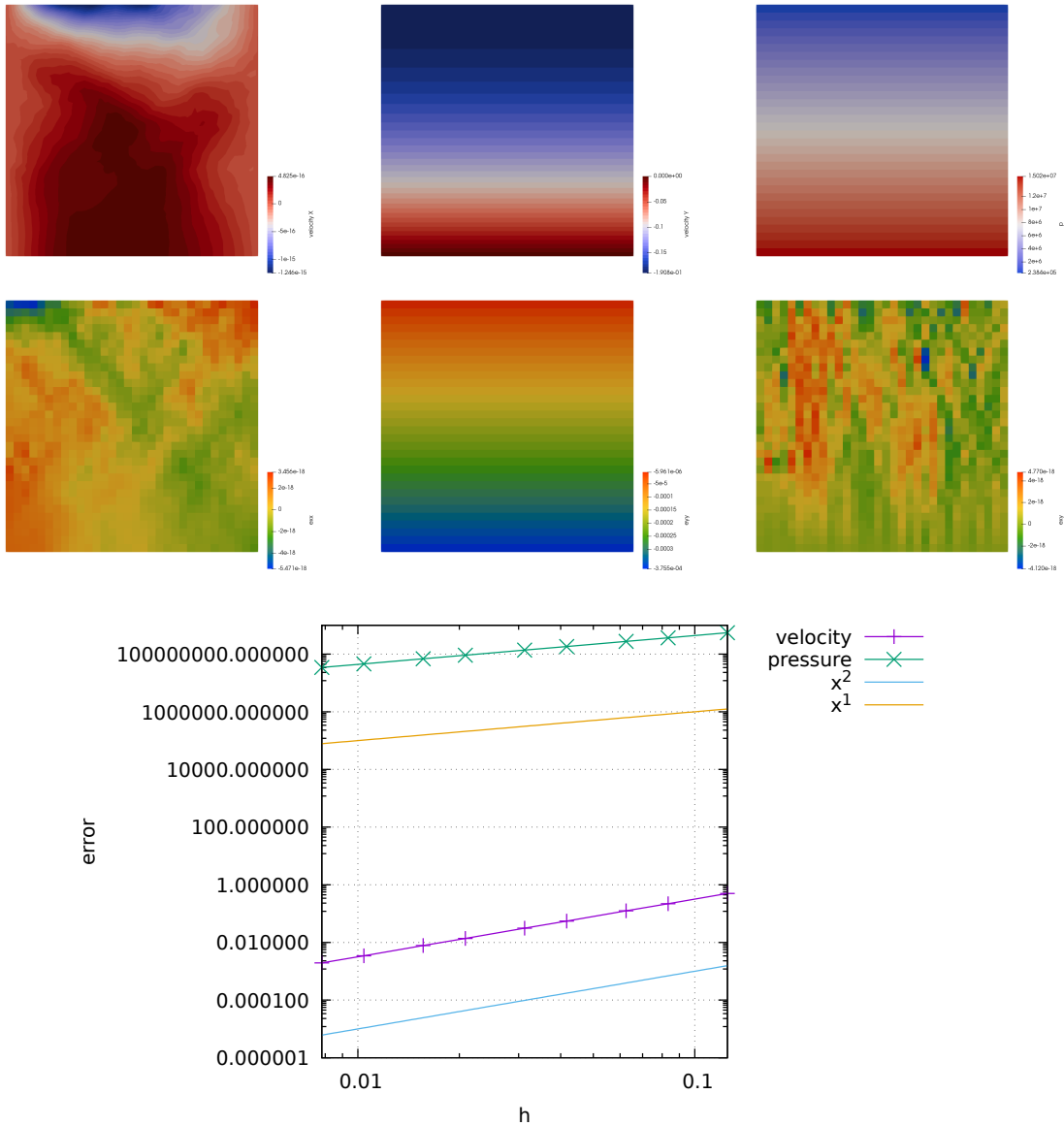
In the incompressible limit, the poisson ratio is  $\nu \sim 0.5$ . Materials are characterised by a finite Young's modulus  $E$ , which is related to  $\nu$  and  $\lambda$ :

$$\lambda = \frac{E\nu}{(1+\nu)(1-2\nu)} \quad \mu = \frac{E}{2(1+\nu)}$$

It is then clear that for incompressible parameters  $\lambda$  becomes infinite while  $\mu$  remains finite. In that case the pressure then logically converges to the well known formula:

$$p = \rho g(L - y)$$

In what follows we set  $L = 1000\text{m}$ ,  $\rho = 2800$ ,  $\nu = 0.25$ ,  $E = 6 \cdot 10^{10}$ ,  $g = 9.81$ .



## Stone 35: 2D analytical sol. in annulus from stream function



We seek an exact solution to the incompressible Stokes equations for an isoviscous, isothermal fluid in an annulus. Given the geometry of the problem, we work in polar coordinates. We denote the orthonormal basis vectors by  $\mathbf{e}_r$  and  $\mathbf{e}_\theta$ , the inner radius of the annulus by  $R_1$  and the outer radius by  $R_2$ . Further, we assume that the viscosity  $\mu$  is constant, which we set to  $\mu = 1$  we set the gravity vector to  $\mathbf{g} = -g_r \mathbf{e}_r$  with  $g_r = 1$ .

Given these assumptions, the incompressible Stokes equations in the annulus are [2293]

$$A_r = \frac{\partial^2 v_r}{\partial r^2} + \frac{1}{r} \frac{\partial v_r}{\partial r} + \frac{1}{r^2} \frac{\partial^2 v_r}{\partial \theta^2} - \frac{v_r}{r^2} - \frac{2}{r^2} \frac{\partial u_\theta}{\partial \theta} - \frac{\partial p}{\partial r} = \rho g_r \quad (981)$$

$$A_\theta = \frac{\partial^2 v_\theta}{\partial r^2} + \frac{1}{r} \frac{\partial v_\theta}{\partial r} + \frac{1}{r^2} \frac{\partial^2 v_\theta}{\partial \theta^2} + \frac{2}{r^2} \frac{\partial v_r}{\partial \theta} - \frac{v_\theta}{r^2} - \frac{1}{r} \frac{\partial p}{\partial \theta} = 0 \quad (982)$$

$$\frac{1}{r} \frac{\partial(rv_r)}{\partial r} + \frac{1}{r} \frac{\partial v_\theta}{\partial \theta} = 0 \quad (983)$$

Equations (981) and (982) are the momentum equations in polar coordinates while Equation (983) is the incompressibility constraint. The components of the velocity are obtained from the stream function as follows:

$$v_r = \frac{1}{r} \frac{\partial \Psi}{\partial \theta} \quad v_\theta = - \frac{\partial \Psi}{\partial r}$$

where  $v_r$  is the radial component and  $v_\theta$  is the tangential component of the velocity vector.

The stream function is defined for incompressible (divergence-free) flows in 2D (as well as in 3D with axisymmetry). The stream function can be used to plot streamlines, which represent the trajectories of particles in a steady flow. From calculus it is known that the gradient vector  $\nabla \Psi$  is normal to the curve  $\Psi = C$ . It can be shown that everywhere  $\mathbf{u} \cdot \nabla \Psi = 0$  using the formula for  $\mathbf{u}$  in terms of  $\Psi$  which proves that level curves of  $\Psi$  are streamlines:

$$\mathbf{u} \cdot \nabla \Psi = v_r \frac{\partial \Psi}{\partial r} + v_\theta \frac{1}{r} \frac{\partial \Psi}{\partial \theta} = \frac{1}{r} \frac{\partial \Psi}{\partial \theta} \frac{\partial \Psi}{\partial r} - \frac{\partial \Psi}{\partial r} \frac{1}{r} \frac{\partial \Psi}{\partial \theta} = 0$$

In polar coordinates the curl of a vector  $\mathbf{A}$  is:

$$\nabla \times \mathbf{A} = \frac{1}{r} \left( \frac{\partial(rA_\theta)}{\partial r} - \frac{\partial A_r}{\partial \theta} \right)$$

Taking the curl of vector  $\mathbf{A}$  yields:

$$\frac{1}{r} \left( \frac{\partial(rA_\theta)}{\partial r} - \frac{\partial A_r}{\partial \theta} \right) = \frac{1}{r} \left( - \frac{\partial(\rho g_r)}{\partial \theta} \right)$$

Multiplying on each side by  $r$

$$\frac{\partial(rA_\theta)}{\partial r} - \frac{\partial A_r}{\partial \theta} = - \frac{\partial(\rho g_r)}{\partial \theta}$$

If we now replace  $A_r$  and  $A_\theta$  by their expressions as a function of velocity and pressure, we see that the pressure terms cancel out and assuming the viscosity and the gravity vector to be constant we get: Let us assume the following separation of variables  $\boxed{\Psi(r, \theta) = \phi(r)\xi(\theta)}$ . Then

$$v_r = \frac{1}{r} \frac{\partial \Psi}{\partial \theta} = \frac{\phi \xi'}{r} \quad v_\theta = - \frac{\partial \Psi}{\partial r} = -\phi' \xi$$

Let us first express  $A_r$  and  $A_\theta$  as functions of  $\Psi$  and

$$A_r = \frac{\partial^2 v_r}{\partial r^2} + \frac{1}{r} \frac{\partial v_r}{\partial r} + \frac{1}{r^2} \frac{\partial^2 v_r}{\partial \theta^2} - \frac{v_r}{r^2} - \frac{2}{r^2} \frac{\partial u_\theta}{\partial \theta} \quad (984)$$

$$= \frac{\partial^2}{\partial r^2} \left( \frac{\phi \xi'}{r} \right) + \frac{1}{r} \frac{\partial}{\partial r} \left( \frac{\phi \xi'}{r} \right) + \frac{1}{r^2} \frac{\partial^2}{\partial \theta^2} \left( \frac{\phi \xi'}{r} \right) - \frac{1}{r^2} \left( \frac{\phi \xi'}{r} \right) - \frac{2}{r^2} \frac{\partial}{\partial \theta} (-\phi' \xi) \quad (985)$$

$$= \left( \frac{\phi''}{r} - 2 \frac{\phi'}{r^2} + 2 \frac{\phi}{r^3} \right) \xi' + \left( \frac{\phi'}{r^2} - \frac{\phi}{r^3} \right) \xi' + \frac{\phi}{r^3} \xi''' - \frac{\phi \xi'}{r^3} + \frac{2}{r^2} \phi' \xi' \quad (986)$$

$$= \frac{\phi'' \xi'}{r} + \frac{\phi' \xi'}{r^2} + \frac{\phi \xi'''}{r^3} \quad (987)$$

$$\frac{\partial A_r}{\partial \theta} = \frac{\phi'' \xi''}{r} + \frac{\phi' \xi''}{r^2} + \frac{\phi \xi''''}{r^3} \quad (988)$$

(989)

$$A_\theta = \frac{\partial^2 v_\theta}{\partial r^2} + \frac{1}{r} \frac{\partial v_\theta}{\partial r} + \frac{1}{r^2} \frac{\partial^2 v_\theta}{\partial \theta^2} + \frac{2}{r^2} \frac{\partial v_r}{\partial \theta} - \frac{v_\theta}{r^2} \quad (990)$$

$$= \frac{\partial^2}{\partial r^2} (-\phi' \xi) + \frac{1}{r} \frac{\partial}{\partial r} (-\phi' \xi) + \frac{1}{r^2} \frac{\partial^2}{\partial \theta^2} (-\phi' \xi) + \frac{2}{r^2} \frac{\partial}{\partial \theta} \left( \frac{\phi \xi'}{r} \right) - \frac{1}{r^2} (-\phi' \xi) \quad (991)$$

$$= -\phi''' \xi - \frac{\phi'' \xi}{r} - \frac{\phi' \xi''}{r^2} + \frac{2\phi \xi''}{r^2} + \frac{\phi' \xi}{r^2} \quad (992)$$

$$\frac{\partial(rA_\theta)}{\partial r} = \quad (993)$$

WRONG:

$$\frac{\partial(r\Delta v)}{\partial r} = \frac{\partial}{\partial r} \left( \frac{\partial}{\partial r} \left( r \frac{\partial v}{\partial r} \right) + \frac{1}{r} \frac{\partial^2 v}{\partial \theta^2} \right) \quad (994)$$

$$= \frac{\partial^2}{\partial r^2} \left( r \frac{\partial v}{\partial r} \right) + \frac{\partial}{\partial r} \left( \frac{1}{r} \frac{\partial^2 v}{\partial \theta^2} \right) \quad (995)$$

$$= \frac{\partial^2}{\partial r^2} \left( r \frac{\partial}{\partial r} \left( -\frac{\partial \Psi}{\partial r} \right) \right) + \frac{\partial}{\partial r} \left( \frac{1}{r} \frac{\partial^2}{\partial \theta^2} \left( -\frac{\partial \Psi}{\partial r} \right) \right) \quad (996)$$

$$= -\frac{\partial^2}{\partial r^2} \left( r \frac{\partial^2 \Psi}{\partial r^2} \right) - \frac{\partial}{\partial r} \left( \frac{1}{r} \frac{\partial^3 \Psi}{\partial \theta^2 \partial r} \right) \quad (997)$$

$$= -2 \frac{\partial^3 \Psi}{\partial r^3} - r \frac{\partial^4 \Psi}{\partial r^4} + \frac{1}{r^2} \frac{\partial^3 \Psi}{\partial \theta^2 \partial r} - \frac{1}{r} \frac{\partial^4 \Psi}{\partial \theta^2 \partial r^2} \quad (998)$$

$$\frac{\partial \Delta u}{\partial \theta} = \frac{\partial}{\partial \theta} \left( \frac{1}{r} \frac{\partial}{\partial r} \left( r \frac{\partial u}{\partial r} \right) + \frac{1}{r^2} \frac{\partial^2 u}{\partial \theta^2} \right) \quad (999)$$

$$= \frac{\partial}{\partial \theta} \left( \frac{1}{r} \frac{\partial}{\partial r} \left( r \frac{\partial u}{\partial r} \right) \right) + \frac{1}{r^2} \frac{\partial^3 u}{\partial \theta^3} \quad (1000)$$

$$= \frac{\partial}{\partial \theta} \left( \frac{1}{r} \frac{\partial}{\partial r} \left( r \frac{\partial}{\partial r} \left( \frac{1}{r} \frac{\partial \Psi}{\partial \theta} \right) \right) \right) + \frac{1}{r^2} \frac{\partial^3}{\partial \theta^3} \left( \frac{1}{r} \frac{\partial \Psi}{\partial \theta} \right) \quad (1001)$$

$$= \frac{1}{r^3} \frac{\partial^2 \Psi}{\partial \theta^2} - \frac{1}{r^2} \frac{\partial^3 \Psi}{\partial r \partial \theta^2} + \frac{1}{r} \frac{\partial^4 \Psi}{\partial r^2 \partial \theta^2} + \frac{1}{r^3} \frac{\partial^4 \Psi}{\partial \theta^4} \quad (1002)$$

Assuming the following separation of variables  $\boxed{\Psi(r, \theta) = \phi(r)\xi(\theta)}$ :

$$\frac{\partial(r\Delta v)}{\partial r} = -2\phi'''\xi - r\phi''''\xi + \frac{1}{r^2}\phi'\xi'' - \frac{1}{r}\phi''\xi'' \quad (1003)$$

$$\frac{\partial \Delta u}{\partial \theta} = \frac{1}{r^3}\phi\xi'' - \frac{1}{r^2}\phi'\xi'' + \frac{1}{r}\phi''\xi'' + \frac{1}{r^3}\phi\xi''' \quad (1004)$$

so that

$$\frac{\partial(r\Delta v)}{\partial r} - \frac{\partial \Delta u}{\partial \theta} = -2\phi'''\xi - r\phi''''\xi + \frac{1}{r^2}\phi'\xi'' - \frac{1}{r}\phi''\xi'' - \frac{1}{r^3}\phi\xi'' + \frac{1}{r^2}\phi'\xi'' - \frac{1}{r}\phi''\xi'' - \frac{1}{r^3}\phi\xi'''$$

Further assuming  $\boxed{\xi(\theta) = \cos(k\theta)}$ , then  $\xi'' = -k^2\xi$  and  $\xi''' = k^4\xi$  then

$$\frac{\partial(r\Delta v)}{\partial r} - \frac{\partial \Delta u}{\partial \theta} = -2\phi'''\xi - r\phi''''\xi - k^2 \frac{1}{r^2} \phi' \xi + k^2 \frac{1}{r} \phi'' \xi + k^2 \frac{1}{r^3} \phi \xi - k^2 \frac{1}{r^2} \phi' \xi + k^2 \frac{1}{r} \phi'' \xi - k^4 \frac{1}{r^3} \phi \xi$$

By choosing  $\rho$  such that  $\rho = \lambda(r)\Upsilon(\theta)$  and such that  $\partial_\theta \Upsilon = \xi = \cos(k\theta)$  then we have

$$-2\phi'''\xi - r\phi''''\xi - k^2 \frac{1}{r^2} \phi' \xi + k^2 \frac{1}{r} \phi'' \xi + k^2 \frac{1}{r^3} \phi \xi - k^2 \frac{1}{r^2} \phi' \xi + k^2 \frac{1}{r} \phi'' \xi - k^4 \frac{1}{r^3} \phi \xi = -\frac{1}{\eta} \lambda \xi g_r$$

and then dividing by  $\xi$ : (IS THIS OK ?)

$$-2\phi'''' - r\phi''''' - k^2 \frac{1}{r^2} \phi' + k^2 \frac{1}{r} \phi'' + k^2 \frac{1}{r^3} \phi - k^2 \frac{1}{r^2} \phi' + k^2 \frac{1}{r} \phi'' - k^4 \frac{1}{r^3} \phi = -\frac{1}{\eta} \lambda g_r$$

$$-2\phi'''' - r\phi''''' - 2k^2 \frac{1}{r^2} \phi' + 2k^2 \frac{1}{r} \phi'' + (k^2 - k^4) \frac{1}{r^3} \phi = -\frac{1}{\eta} \lambda g_r$$

so

$$\lambda(r) = \frac{\eta}{g_r} \left( 2\phi'''' + r\phi''''' + 2k^2 \frac{1}{r^2} \phi' - 2k^2 \frac{1}{r} \phi'' - (k^2 - k^4) \frac{1}{r^3} \phi \right)$$

Also not forget  $\Upsilon = \frac{1}{k} \sin(k\theta)$

## Linking with our paper

We have

$$\phi(r) = -rg(r) \quad (1005)$$

$$\phi'(r) = -g(r) - rg'(r) = -f(r) \quad (1006)$$

$$\phi''(r) = -f'(r) \quad (1007)$$

$$\phi'''(r) = -f''(r) \quad (1008)$$

$$\phi''''(r) = -f'''(r) \quad (1009)$$

$$f(r) = \frac{\eta_0}{g_0} \left( 2f''(r) + rf'''(r) + 2k^2 \frac{1}{r^2} f(r) - 2k^2 \frac{1}{r} f'(r) + (k^2 - k^4) \frac{1}{r^2} g(r) \right)$$

## No slip boundary conditions

No-slip boundary conditions inside and outside impose that all components of the velocity must be zero on both boundaries, i.e.

$$\mathbf{v}(r = R_1) = \mathbf{v}(r = R_2) = \mathbf{0}$$

Due to the separation of variables, and since  $\xi(\theta) = \cos(k\theta)$  we have

$$u(r, \theta) = \frac{1}{r} \frac{\partial \Psi}{\partial \theta} = \frac{1}{r} \phi \xi' = -\frac{1}{r} \phi(r) k \sin(k\theta) \quad v(r, \theta) = -\frac{\partial \Psi}{\partial r} = -\phi'(r) \xi = -\phi'(r) \cos(k\theta)$$

It is obvious that the only way to insure no-slip boundary conditions is to have

$$\phi(R_1) = \phi(R_2) = \phi'(R_1) = \phi'(R_2) = 0$$

We could then choose

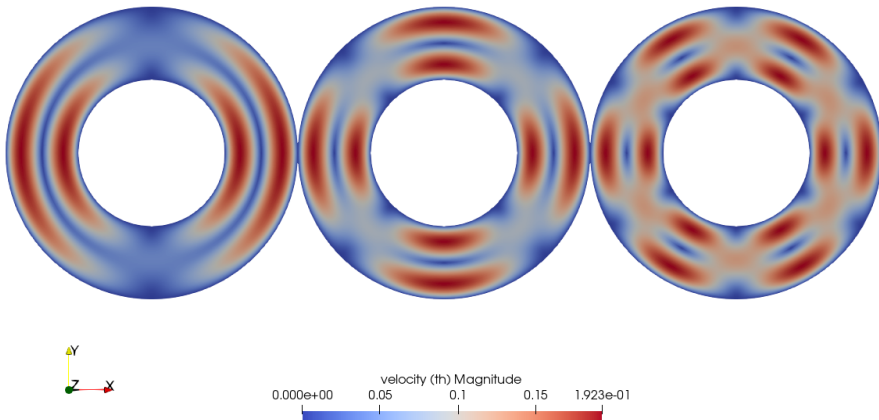
$$\phi(r) = (r - R_1)^2 (r - R_2)^2 \mathcal{F}(r) \quad (1010)$$

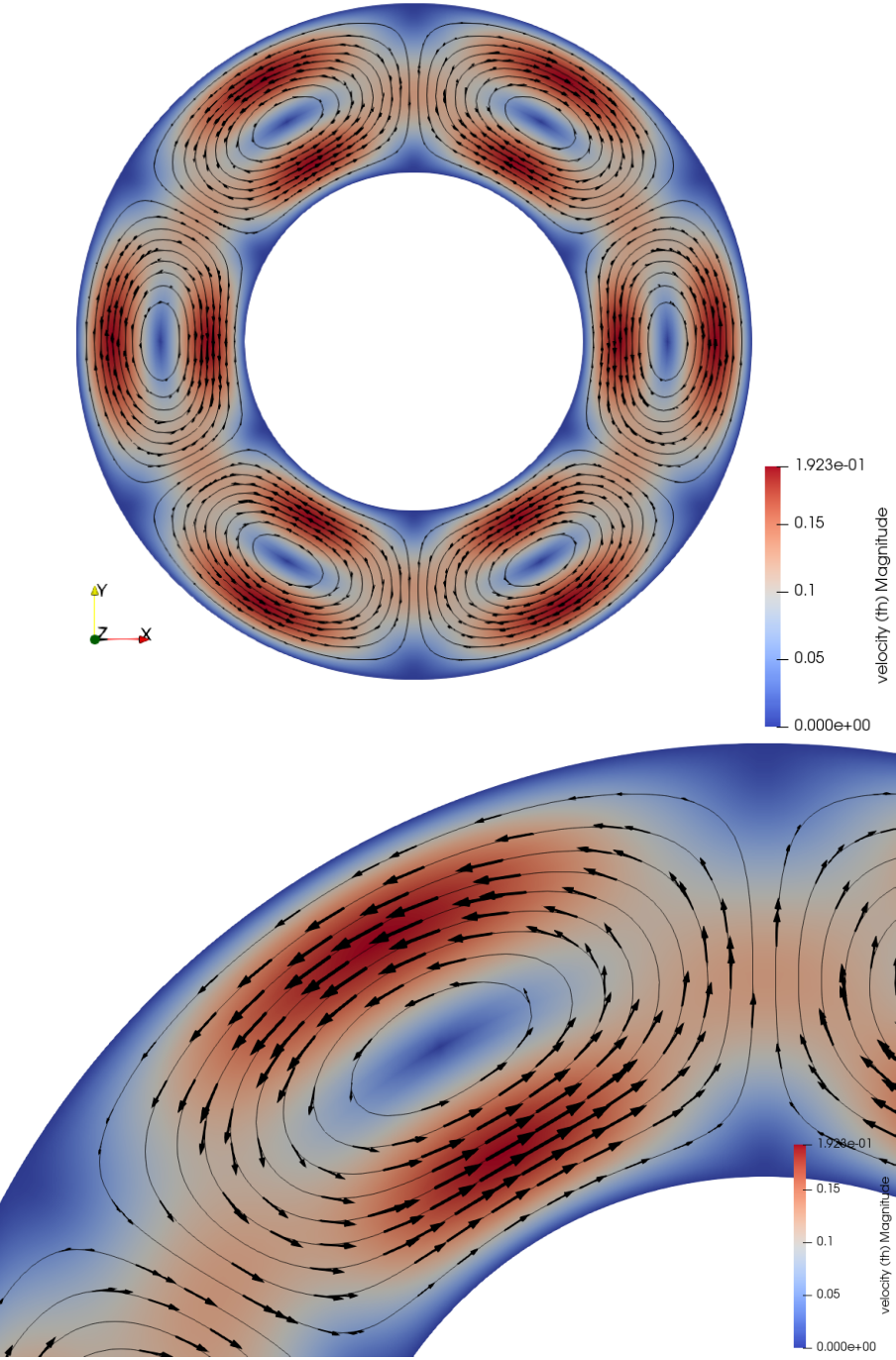
$$\phi'(r) = 2(r - R_1)(r - R_2)^2 \mathcal{F}(r) + 2(r - R_1)^2(r - R_2) \mathcal{F}(r) + (r - R_1)^2(r - R_2)^2 \mathcal{F}'(r) \quad (1011)$$

which are indeed identically zero on both boundaries. Here  $\mathcal{F}(r)$  is any (smooth enough) function of  $r$ . We would then have

$$\boxed{\Psi(r, \theta) = (r - R_1)^2 (r - R_2)^2 \mathcal{F}(r) \cos(k\theta)}$$

In what follows we will take  $\mathcal{F}(r) = 1$  for simplicity.





COMPUTE  $f$  from  $\phi$  and then the pressure.

### Free slip boundary conditions

Before postulating the form of  $\phi(r)$ , let us now turn to the boundary conditions that the flow must fulfill, i.e. free-slip on both boundaries. Two conditions must be met:

- $\mathbf{v} \cdot \mathbf{n} = 0$  (no flow through the boundaries) which yields  $u(r = R_1) = 0$  and  $u(r = R_2) = 0$  :

$$\frac{1}{r} \frac{\partial \Psi}{\partial \theta}(r = R_1, R_2) = 0 \quad \forall \theta$$

which gives us the first constraint since  $\Psi(r, \theta) = \phi(r)\xi(\theta)$ :

$$\phi(r = R_1) = \phi(r = R_2) = 0$$

- $(\sigma \cdot n) \times n = \mathbf{0}$  (the tangential stress at the boundary is zero) which imposes:  $\sigma_{\theta r} = 0$ , with

$$\sigma_{\theta r} = 2\eta \cdot \frac{1}{2} \left( \frac{\partial v}{\partial r} - \frac{v}{r} + \frac{1}{r} \frac{\partial u}{\partial \theta} \right) = \eta \left( \frac{\partial}{\partial r} \left( -\frac{\partial \Psi}{\partial r} \right) - \frac{1}{r} \left( -\frac{\partial \Psi}{\partial r} \right) + \frac{1}{r} \frac{\partial}{\partial \theta} \left( \frac{1}{r} \frac{\partial \Psi}{\partial \theta} \right) \right)$$

Finally  $\Psi$  must fulfill (on the boundaries!):

$$-\frac{\partial^2 \Psi}{\partial r^2} + \frac{1}{r} \frac{\partial \Psi}{\partial r} + \frac{1}{r^2} \frac{\partial^2 \Psi}{\partial \theta^2} = 0$$

$$-\phi''\xi + \frac{1}{r}\phi'\xi + \frac{1}{r^2}\phi\xi'' = 0$$

or,

$$-\phi'' + \frac{1}{r}\phi' - k^2 \frac{1}{r^2}\phi = 0$$

Note that this equation is a so-called Euler Differential Equation<sup>86</sup>. Since we are looking for a solution  $\phi$  such that  $\phi(R_1) = \phi(R_2) = 0$  then the 3rd term of the equation above is by definition zero on the boundaries. We have to ensure the following equality on the boundary:

$$-\phi'' + \frac{1}{r}\phi' = 0 \quad \text{for } r = R_1, R_2$$

The solution of this ODE is of the form  $\phi(r) = ar^2 + b$  and it becomes evident that it cannot satisfy  $\phi(r = R_1) = \phi(r = R_2) = 0$ .

Separation of variables leads to solutions which cannot fulfill the free slip boundary conditions

---

<sup>86</sup><http://mathworld.wolfram.com/EulerDifferentialEquation.html>

## Stone 36: the annulus geometry elastic aquarium

This fieldstone was developed in collaboration with Lukas van de Wiel.

The domain is an annulus with inner radius  $R_1$  and outer radius  $R_2$ . It is filled with a single elastic material characterised by a Young's modulus  $E$  and a Poisson ratio  $\nu$ , a density  $\rho_0$ . The gravity  $\mathbf{g} = -g_0 \mathbf{e}_r$  is pointing towards the center of the domain.

The problem at hand is axisymmetric so that the tangential component of the displacement vector  $v_\theta$  is assumed to be zero as well as all terms containing  $\partial_\theta$ . The components of the strain tensor are

$$\varepsilon_{rr} = \frac{\partial v_r}{\partial r} \quad (1012)$$

$$\varepsilon_{\theta\theta} = \frac{v_r}{r} + \frac{1}{r} \frac{\partial v_\theta}{\partial \theta} = \frac{v_r}{r} \quad (1013)$$

$$\varepsilon_{r\theta} = \frac{1}{2} \left( \frac{\partial v_\theta}{\partial r} - \frac{v_\theta}{r} + \frac{1}{r} \frac{\partial v_r}{\partial \theta} \right) = 0 \quad (1014)$$

so that the tensor simply is

$$\boldsymbol{\varepsilon} = \begin{pmatrix} \varepsilon_{rr} & \varepsilon_{r\theta} \\ \varepsilon_{r\theta} & \varepsilon_{\theta\theta} \end{pmatrix} = \begin{pmatrix} \frac{\partial v_r}{\partial r} & 0 \\ 0 & \frac{v_r}{r} \end{pmatrix} \quad (1015)$$

The pressure is

$$p = -\lambda \nabla \cdot \mathbf{v} = -\lambda \left( \frac{1}{r} \frac{\partial(rv_r)}{\partial r} \right) \quad (1016)$$

and finally the stress tensor:

$$\boldsymbol{\sigma} = -p \mathbf{1} + 2\mu \boldsymbol{\varepsilon} = \begin{pmatrix} \lambda \frac{1}{r} \frac{\partial(rv_r)}{\partial r} + 2\mu \frac{\partial v_r}{\partial r} & 0 \\ 0 & \lambda \frac{1}{r} \frac{\partial(rv_r)}{\partial r} + 2\mu \frac{v_r}{r} \end{pmatrix} \quad (1017)$$

The divergence of the stress tensor is given by [2293]:

$$\nabla \cdot \boldsymbol{\sigma} = \begin{pmatrix} \frac{\partial \sigma_{rr}}{\partial r} + \frac{\sigma_{rr} - \sigma_{\theta\theta}}{r} + \frac{1}{r} \frac{\partial \sigma_{\theta r}}{\partial \theta} \\ \frac{\partial \sigma_{r\theta}}{\partial r} + \frac{1}{r} \frac{\sigma_{\theta\theta}}{\partial \theta} + \frac{\sigma_{r\theta} + \sigma_{\theta r}}{r} \end{pmatrix} \quad (1018)$$

Given the diagonal nature of the stress tensor this simplifies to (also remember that  $\partial_\theta = 0$ ):

$$\nabla \cdot \boldsymbol{\sigma} = \begin{pmatrix} \frac{\partial \sigma_{rr}}{\partial r} + \frac{\sigma_{rr} - \sigma_{\theta\theta}}{r} \\ 0 \end{pmatrix} \quad (1019)$$

Focusing on the  $r$ -component of the stress divergence:

$$(\nabla \cdot \boldsymbol{\sigma})_r = \frac{\partial \sigma_{rr}}{\partial r} + \frac{\sigma_{rr} - \sigma_{\theta\theta}}{r} \quad (1020)$$

$$= \frac{\partial}{\partial r} \left[ \lambda \frac{1}{r} \frac{\partial(rv_r)}{\partial r} + 2\mu \frac{\partial v_r}{\partial r} \right] + \frac{1}{r} \left[ \lambda \frac{1}{r} \frac{\partial(rv_r)}{\partial r} + 2\mu \frac{\partial v_r}{\partial r} - \lambda \frac{1}{r} \frac{\partial(rv_r)}{\partial r} - 2\mu \frac{v_r}{r} \right] \quad (1021)$$

$$= \lambda \frac{\partial}{\partial r} \frac{1}{r} \frac{\partial(rv_r)}{\partial r} + 2\mu \frac{\partial^2 v_r}{\partial r^2} + \lambda \frac{1}{r^2} \frac{\partial(rv_r)}{\partial r} + \frac{2\mu}{r} \frac{\partial v_r}{\partial r} - \lambda \frac{1}{r^2} \frac{\partial(rv_r)}{\partial r} - \frac{2\mu v_r}{r^2} \quad (1022)$$

$$= \lambda \left( -\frac{v_r}{r^2} + \frac{1}{r} \frac{\partial v_r}{\partial r} + \frac{\partial^2 v_r}{\partial r^2} \right) + 2\mu \frac{\partial^2 v_r}{\partial r^2} + \frac{2\mu}{r} \frac{\partial v_r}{\partial r} - \frac{2\mu v_r}{r^2} \quad (1023)$$

$$= -(2\mu + \lambda) \frac{v_r}{r^2} + (2\mu + \lambda) \frac{1}{r} \frac{\partial v_r}{\partial r} + (2\mu + \lambda) \frac{\partial^2 v_r}{\partial r^2} \quad (1024)$$

So the momentum conservation in the  $r$  direction is

$$(\nabla \cdot \boldsymbol{\sigma} + \rho_0 \mathbf{g})_r = -(2\mu + \lambda) \frac{v_r}{r^2} + (2\mu + \lambda) \frac{1}{r} \frac{\partial v_r}{\partial r} + (2\mu + \lambda) \frac{\partial^2 v_r}{\partial r^2} - \rho_0 g_0 = 0 \quad (1025)$$

or,

$$\frac{\partial^2 v_r}{\partial r^2} + \frac{1}{r} \frac{\partial v_r}{\partial r} - \frac{v_r}{r^2} = \frac{\rho_0 g_0}{\lambda + 2\mu} \quad (1026)$$

We now look at the boundary conditions. On the inner boundary we prescribe  $v_r(r = R_1) = 0$  while free surface boundary conditions are prescribed on the outer boundary, i.e.  $\boldsymbol{\sigma} \cdot \mathbf{n} = 0$  (i.e. there is no force applied on the surface).

The general form of the solution can then be obtained:

$$v_r(r) = C_1 r^2 + C_2 r + \frac{C_3}{r} \quad (1027)$$

with

$$C_1 = \frac{\rho_0 g_0}{3(\lambda + 2\mu)} \quad C_2 = -C_1 R_1 - \frac{C_3}{R_1^2} \quad C_3 = \frac{k_1 + k_2}{(R_1^2 + R_2^2)(2\mu + \lambda) + (R_2^2 - R_1^2)\lambda} \quad (1028)$$

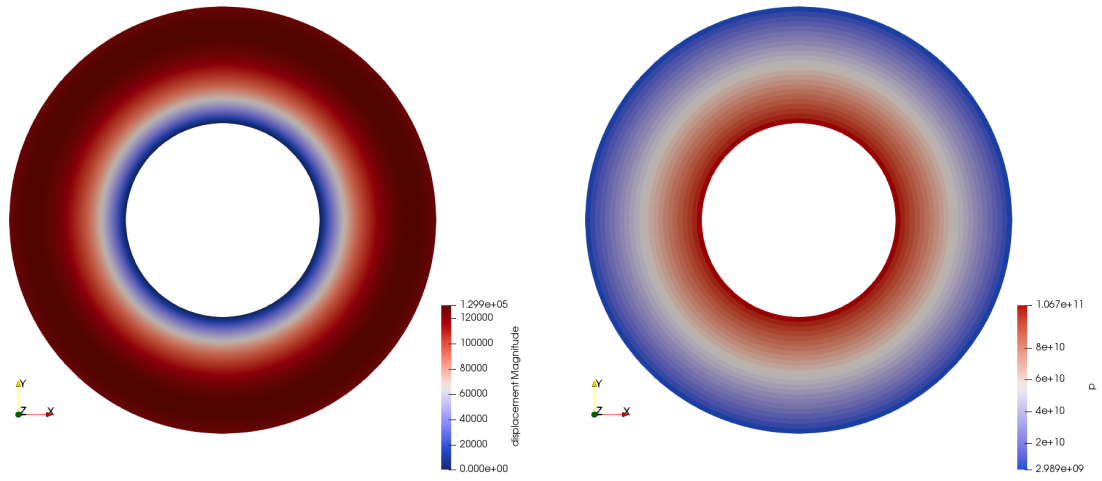
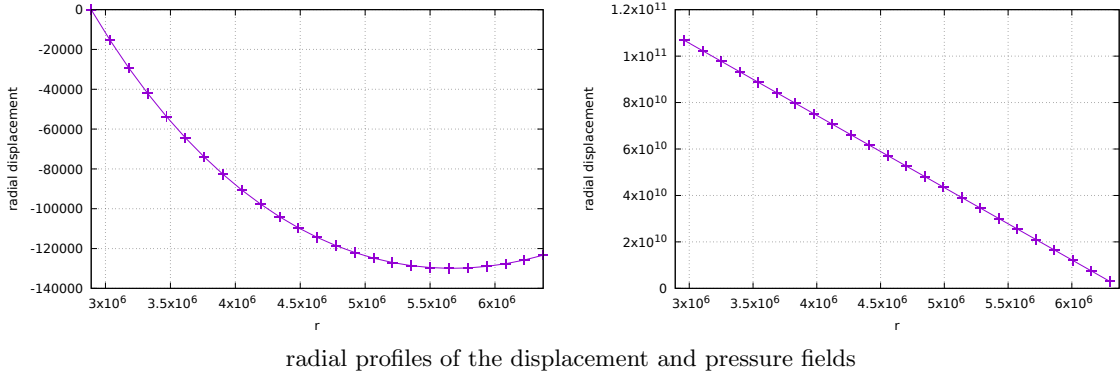
and

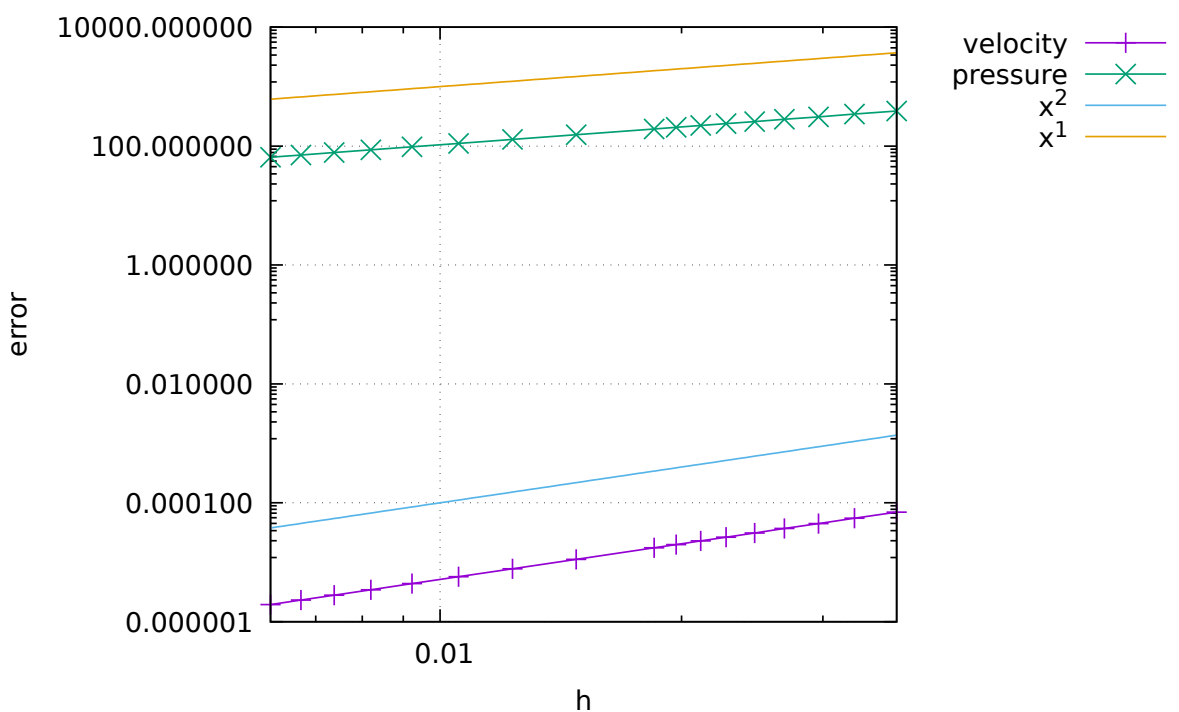
$$k_1 = (2\mu + \lambda)C_1(2R_1^2 R_2^3 - R_1^3 R_2^2) \quad k_2 = \lambda C_1(R_1^2 R_2^3 - R_1^3 R_2^2) \quad (1029)$$

Pressure can then be computed as follows:

$$p = -\lambda \nabla \cdot \mathbf{v} = -\lambda \left( \frac{1}{r} \frac{\partial(r v_r)}{\partial r} \right) = -\lambda \left( \frac{1}{r} (3C_1 r^2 + 2C_2 r) \right) = -\lambda (3C_1 r + 2C_2) \quad (1030)$$

We choose  $R_1 = 2890\text{km}$ ,  $R_2 = 6371\text{km}$ ,  $g_0 = 9.81\text{ms}^{-2}$ ,  $\rho_0 = 3300$ ,  $E = 6 \cdot 10^{10}$ ,  $\nu = 0.49$ .





## Stone 37: marker advection and population control



The domain is a unit square. The Stokes equations are not solved, the velocity is prescribed everywhere in the domain as follows:

$$u = -(z - 0.5) \quad (1031)$$

$$v = 0 \quad (1032)$$

$$w = (x - 0.5) \quad (1033)$$

At the moment, velocity is computed on the marker itself (rk0 algorithm). When markers are advected outside, they are arbitrarily placed at location (-0.0123,-0.0123).

in construction.

## Stone 38: Critical Rayleigh number

This fieldstone was developed in collaboration with Arie van den Berg.

The system is a layer of fluid between  $y = 0$  and  $y = 1$ , with boundary conditions  $T(x, y = 0) = 1$  and  $T(x, y = 1) = 0$ , characterized by  $\rho$ ,  $C_p$ ,  $k$ ,  $\eta_0$ . The Rayleigh number of the system is

$$\text{Ra} = \frac{\rho_0 g_0 \alpha \Delta T h^3}{\eta_0 \kappa}$$

We have  $\Delta T = 1$ ,  $h = 1$  and choose  $\kappa = 1$  so that the Rayleigh number simplifies to  $\text{Ra} = \rho_0 g_0 \alpha / \eta_0$ .

The Stokes equation is  $\vec{\nabla} \cdot \boldsymbol{\sigma} + \vec{b} = \vec{0}$  with  $\vec{b} = \rho \vec{g}$ . Then the components of this equation on the  $x$ - and  $y$ -axis are:

$$(\vec{\nabla} \cdot \boldsymbol{\sigma})_x = -\rho \vec{g} \cdot \vec{e}_x = 0 \quad (1034)$$

$$(\vec{\nabla} \cdot \boldsymbol{\sigma})_y = -\rho \vec{g} \cdot \vec{e}_y = \rho g_0 \quad (1035)$$

since  $\vec{g}$  and  $\vec{e}_y$  are in opposite directions ( $\vec{g} = -g_0 \vec{e}_y$ , with  $g_0 > 0$ ). The stream function formulation of the incompressible isoviscous Stokes equation is then

$$\nabla^4 \Psi = \frac{g_0}{\eta_0} \frac{\partial \rho}{\partial x}$$

Assuming a linearised density field with regards to temperature  $\rho(T) = \rho_0(1 - \alpha T)$  we have

$$\frac{\partial \rho}{\partial x} = -\rho_0 \alpha \frac{\partial T}{\partial x}$$

and then

$$\boxed{\nabla^4 \Psi = -\frac{\rho_0 g_0 \alpha}{\eta_0} g \frac{\partial T}{\partial x} = -Ra \frac{\partial T}{\partial x}} \quad (1036)$$

For small perturbations of the conductive state  $T_0(y) = 1 - y$  we define the temperature perturbation  $T_1(x, y)$  such that

$$T(x, y) = T_0(y) + T_1(x, y)$$

The temperature perturbation  $T_1$  satisfies the homogeneous boundary conditions  $T_1(x, y = 0) = 0$  and  $T_1(x, y = 1) = 0$ . The temperature equation is

$$\rho C_p \frac{DT}{Dt} = \rho C_p \left( \frac{\partial T}{\partial t} + \vec{v} \cdot \vec{\nabla} T \right) = \rho C_p \left( \frac{\partial T_0 + T_1}{\partial t} + \vec{v} \cdot \vec{\nabla}(T_0 + T_1) \right) = k \Delta (T_0 + T_1)$$

and can be simplified as follows:

$$\rho C_p \left( \frac{\partial T_1}{\partial t} + \vec{v} \cdot \vec{\nabla} T_0 \right) = k \Delta T_1$$

since  $T_0$  does not depend on time,  $\Delta T_0 = 0$  and we assume the nonlinear term  $\vec{v} \cdot \vec{\nabla} T_1$  to be second order (temperature perturbations and coupled velocity changes are assumed to be small). Using the relationship between velocity and stream function  $v_y = -\partial_x \Psi$  we have  $\vec{v} \cdot \vec{\nabla} T_0 = -v_y = \partial_x \Psi$  and since  $\kappa = k/\rho C_p = 1$  we get

$$\boxed{\frac{\partial T_1}{\partial t} - \kappa \Delta T_1 = -\frac{\partial \Psi}{\partial x}} \quad (1037)$$

Looking at these equations, we immediately think about a separation of variables approach to solve these equations. Both equations showcase the Laplace operator  $\Delta$ , and the eigenfunctions of the biharmonic operator and the Laplace operator are the same. We then pose that  $\Psi$  and  $T_1$  can be written:

$$\Psi(x, y, t) = A_\Psi \exp(pt) \exp(\pm i k_x x) \exp(\pm i k_y y) = A_\Psi E_\psi(x, y, t) \quad (1038)$$

$$T_1(x, y, t) = A_T \exp(pt) \exp(\pm i k_x x) \exp(\pm i k_y y) = A_T E_T(x, y, t) \quad (1039)$$

where  $k_x$  and  $k_y$  are the horizontal and vertical wave number respectively. Note that we then have

$$\nabla^2 \Psi = -(k_x^2 + k_y^2) \Psi \quad \nabla^2 T_1 = -(k_x^2 + k_y^2) T_1$$

The boundary conditions on  $T_1$ , coupled with a choice of a real function for the  $x$  dependence yields:

$$E_T(x, y, t) = \exp(pt) \cos(k_x x) \sin(n\pi y).$$

**from here onwards check for minus signs!**

The velocity boundary conditions are  $v_y(x, y=0) = 0$  and  $v_y(x, y=1) = 0$  which imposes conditions on  $\partial\Psi/\partial x$  and we find that we can use the same  $y$  dependence as for  $T_1$ . Choosing again for a real function for the  $x$  dependence yields:

$$E_\Psi(x, y, t) = \exp(pt) \sin(k_x x) \sin(n\pi z)$$

We then have

$$\Psi(x, y, t) = A_\Psi \exp(pt) \sin(k_x x) \sin(n\pi z) = A_\Psi E_\Psi(x, y, t) \quad (1040)$$

$$T_1(x, y, t) = A_T \exp(pt) \cos(k_x x) \sin(n\pi z) = A_T E_T(x, y, t) \quad (1041)$$

In what follows we simplify notations:  $k = k_x$ . Then the two PDEs become:

$$pT_1 + \kappa(k^2 + n^2\pi^2) - kA_\Psi \exp(pt) \cos(k_x x) \sin(n\pi z) = kA_\Psi E_\theta \quad (1042)$$

$$-RaA_T \cos(kx) \sin(n\pi z) + \kappa(k^2 + n^2\pi^2)^2 A_\Psi = -RaA_T E_\Psi + \kappa(k^2 + n^2\pi^2)^2 A_\Psi = 0 \quad (1043)$$

These equations must then be verified for all ... which leads to write:

$$\begin{pmatrix} p + (k^2 + n^2\pi^2) & -k \\ -Ra k & (k^2 + n^2\pi^2)^2 \end{pmatrix} \begin{pmatrix} A_\theta \\ A_\Psi \end{pmatrix} = \begin{pmatrix} 0 \\ 0 \end{pmatrix}$$

The determinant of such system must be nul otherwise there is only a trivial solution to the problem, i.e.  $A_\theta = 0$  and  $A_\Psi = 0$  which is not helpful. CHECK/REPHRASE

$$D = [p + (k^2 + n^2\pi^2)](k^2 + n^2\pi^2)^2 - Ra k^2 = 0$$

or,

$$p = \frac{Ra k^2 - (k^2 + n^2\pi^2)^3}{(k^2 + n^2\pi^2)^2}$$

The coefficient  $p$  determines the stability of the system: if it is negative, the system is stable and both  $\Psi$  and  $T_1$  will decay to zero (return to conductive state). If  $p = 0$ , then the system is meta-stable, and if  $p > 0$  then the system is unstable and the perturbations will grow. The threshold is then  $p = 0$  and the solution of the above system is

## Stone 39: chpe15

The Drucker-Prager yield function is given by the function  $f$ :

$$f = p \sin \phi + c \cos \phi - \tau_e$$

where  $\tau_e$  is the square root of the second invariant of the deviatoric stress (the 'effective' deviatoric stress). We have

$$p = \frac{1}{2}(\sigma_1 + \sigma_3)$$

and

$$\tau = \frac{1}{2}(\sigma_1 - \sigma_3)$$

Inserting these into  $f$  yields:

$$f = \frac{1}{2}(\sigma_1 + \sigma_3) \sin \phi + c \cos \phi - \frac{1}{2}(\sigma_1 - \sigma_3)$$

The yield condition  $f = 0$  can be reworked as follows:

$$\sigma_1 - \frac{1 + \sin \phi}{1 - \sin \phi} \sigma_3 - 2 \frac{\cos \phi}{1 - \sin \phi} c = 0$$

The third term can further be modified as follows:

$$\frac{\cos \phi}{1 - \sin \phi} = \frac{\sqrt{1 - \sin^2 \phi}}{\sqrt{(1 - \sin \phi)^2}} = \frac{\sqrt{(1 - \sin \phi)(1 + \sin \phi)}}{\sqrt{(1 - \sin \phi)^2}} = \sqrt{\frac{1 + \sin \phi}{1 - \sin \phi}}$$

Finally, we define  $N_\phi$  as follows

$$N_\phi = \frac{1 + \sin \phi}{1 - \sin \phi}$$

so that the yield condition becomes:

$$\sigma_1 - N_\phi \sigma_3 - 2\sqrt{N_\phi} c = 0$$

which is Eq. 3 of the article by Choi & Petersen [469].

This paper offers a solution to the problem of the angle of shear bands in geodynamic models. The underlying idea is based on simple modifications brought to existing incompressible flow codes. Note that the codes featured in that paper also implemented elastic behaviour but this can be easily switched off by setting  $Z = 1$  in their equations.

Their plasticity implementation starts with a modification of the continuity equation:

$$\vec{\nabla} \cdot \vec{v} = R = 2 \sin \psi \dot{\varepsilon}_p$$

where  $R$  is the dilation rate,  $\Psi$  is the dilation angle and  $\dot{\varepsilon}_p$  is the square root of the second invariant of the plastic strain rate.

Under this assumption, the deviatoric strain rate tensor is given by

$$\dot{\varepsilon}^d(\vec{v}) = \dot{\varepsilon}(\vec{v}) - \frac{1}{3} \text{Tr}[\dot{\varepsilon}(\vec{v})] \mathbf{1} = \dot{\varepsilon}(\vec{v}) - \frac{1}{3} \vec{\nabla} \cdot \vec{v} \mathbf{1} = \dot{\varepsilon}(\vec{v}) - \frac{1}{3} R \mathbf{1} \quad (1044)$$

Turning now to the momentum conservation equation:

$$\begin{aligned} -\vec{\nabla} p + \vec{\nabla} \cdot \boldsymbol{\tau} &= -\vec{\nabla} p + \vec{\nabla} \cdot (2\eta \dot{\varepsilon}^d(\vec{v})) \\ &= -\vec{\nabla} p + \vec{\nabla} \cdot \left[ 2\eta \left( \dot{\varepsilon}(\vec{v}) - \frac{1}{3} R \mathbf{1} \right) \right] \\ &= -\vec{\nabla} p + \vec{\nabla} \cdot (2\eta \dot{\varepsilon}(\vec{v})) - \frac{2}{3} \vec{\nabla} (\eta R) \end{aligned} \quad (1045)$$

The last term is then an addition to the right hand side of the momentum equation and its weak form is as follows:

$$\vec{f}' = \int_{\Omega} N_v \frac{2}{3} \vec{\nabla}(\eta R) dV = \frac{4}{3} \sin \Psi \int_{\Omega} N_v \vec{\nabla}(\eta \dot{\epsilon}_p) dV \quad (1046)$$

This formulation proves to be problematic since in order to compute the gradient, we would need the viscosity and the plastic strain rate on the mesh nodes and both these quantities are effectively computed on the quadrature points. One option could be to project those quadrature values onto the nodes, which may introduce interpolation errors/artefacts and/or smoothing. Another option is to resort to integration by parts:

$$\int_{\Omega} N_v \vec{\nabla}(\eta \dot{\epsilon}_p) dV = [N_v \eta \dot{\epsilon}_p]_{\Gamma} - \int_{\Omega} \vec{\nabla} N_v (\eta \dot{\epsilon}_p) dV \quad (1047)$$

The last term is now trivial to compute since the shape function derivatives, the viscosity and the plastic strain rate are known at the quadrature points. Remains the surface term. We will neglect it for now to simplify our implementation and note that a) it will not directly affect what happens inside the domain, b) it could be somewhat important when shear bands intersect with the free surface.

$$\vec{f}' = -\frac{4}{3} \sin \psi \int_{\Omega} \vec{\nabla} N_v (\eta \dot{\epsilon}_p) dV = -\frac{2}{3} \int_{\Omega} \vec{\nabla} N_v (\eta R) dV \quad (1048)$$

Although the authors do indicate that they add a term in each rhs, it is not very clear how they deal with the implementation issue above. We then propose an alternative: instead of explicitly removing the deviatoric part of the strain rate as in Eq. 1045 and replace the trace of the tensor by  $R$ , one could leave the term inside the matrix, thereby using a compressible form of the viscous block of the Stokes matrix. We will recover the same converged solution as before, but the path to convergence will be different than the first approach. In what follows, we denote the original approach by Choi & Petersen 'method 1' and the latter 'method 2'.

Finally, we need to define what the plastic strain rate tensor is. When using a rigid plastic rheology, the only deformation mechanism *is* plasticity so that the plastic strain rate *is* the strain rate. When using a visco-plastic rheology, the plastic strain rate is the strain rate of the zones above/at yield (the shear bands, where the vrm is active).

**Remark.** *The rhs of the continuity equation is formulated as a function of the (effective) plastic strain rate so that in the case of multiple deformation mechanisms one should be careful about this term.*

## The 2010 brick

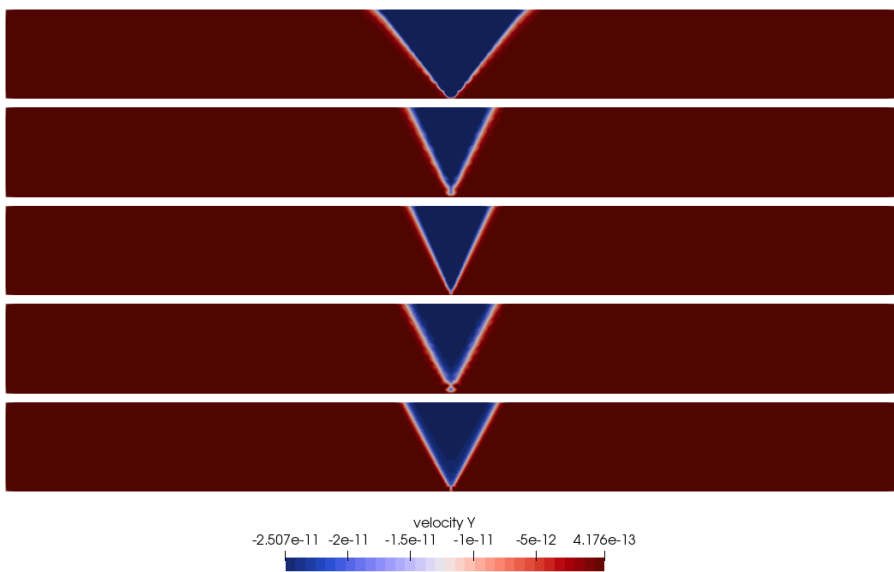
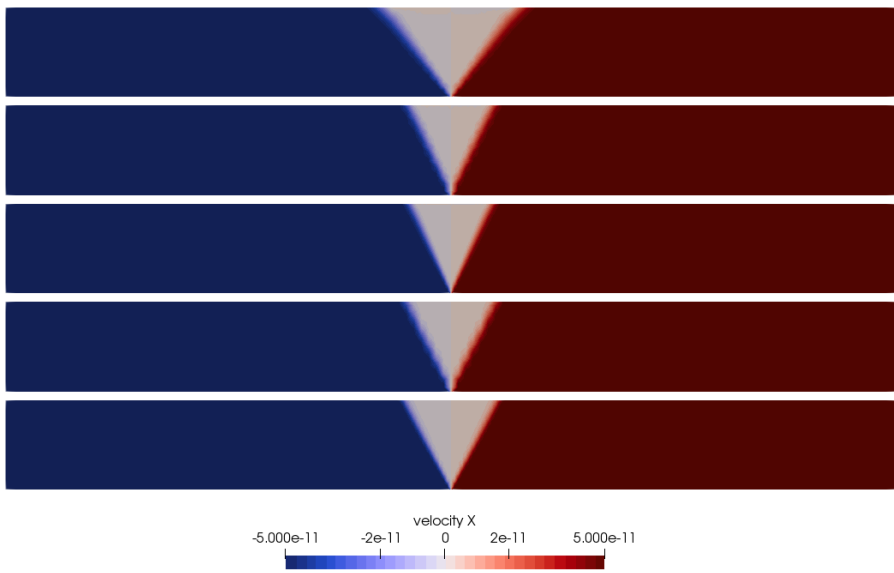
The setup is similar to the one in [1396]. It is a 2D Cartesian domain filled with a single rigid-plastic material characterised by a cohesion  $c = 10\text{MPa}$ , an angle of friction  $\phi$ , a dilation angle  $\psi$  and a density  $\rho = 2800\text{kg/m}^3$ . Extensional boundary conditions are as follows:

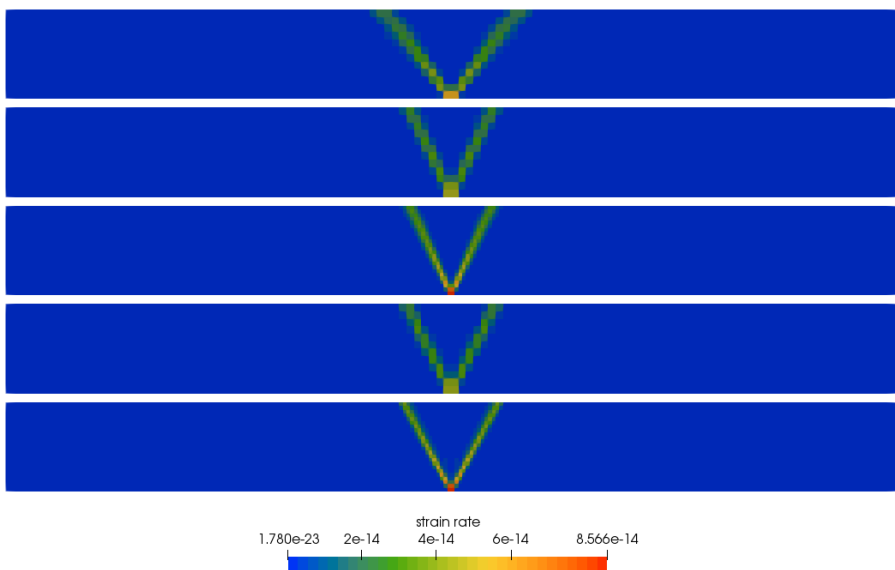
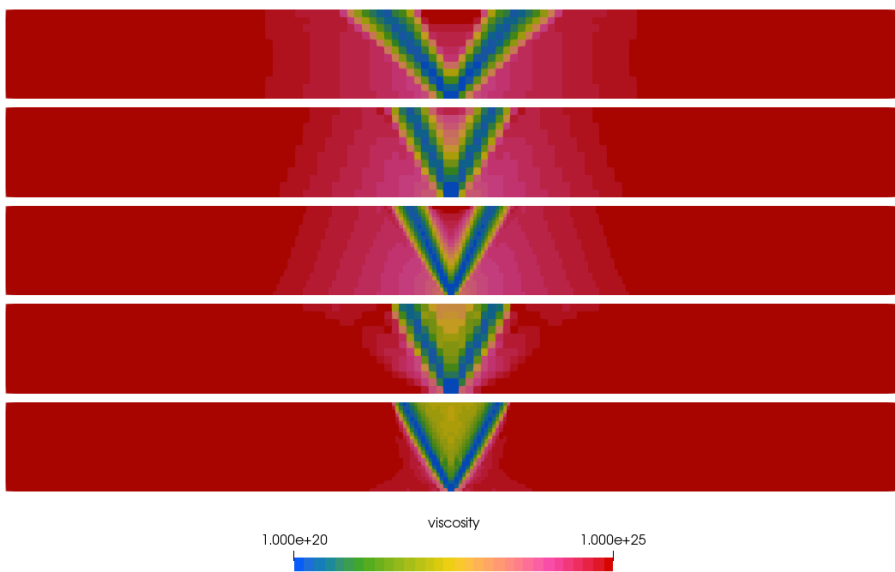
- left boundary:  $u = -v_{bc}$ ;
- right boundary:  $u = +v_{bc}$ ;
- bottom boundary:  $v = 0$ ,  $u = -v_{bc}$  for  $x < L_x/2$ ,  $u = +v_{bc}$  for  $x > L_x/2$ , and  $u = 0$  if  $x = L_x/2$ ;
- top boundary: zero traction.

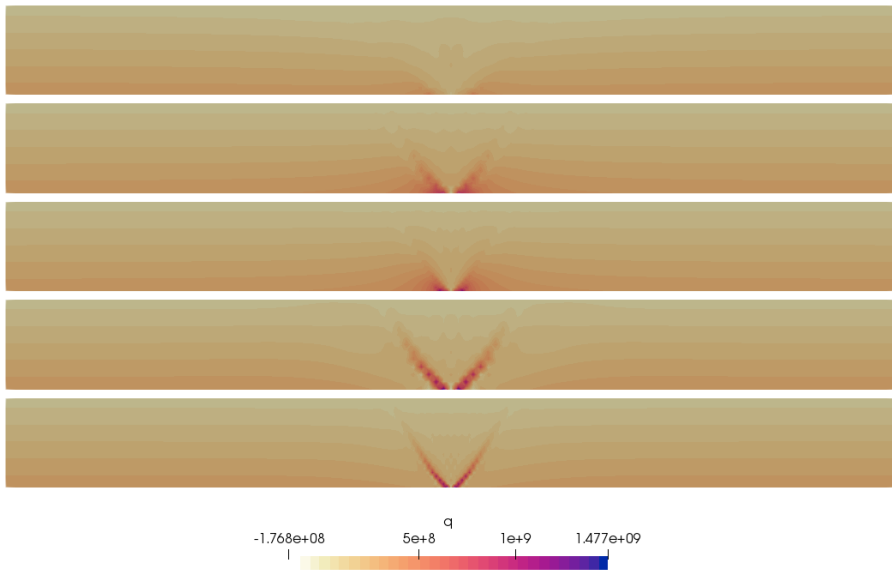
For compressional boundary conditions the signs of all horizontal velocities should be reversed. The nonlinear tolerance is set to  $\text{tol} = 10^{-6}$ . Nonlinear iterations stop when maximum of the normalised nonlinear residual reaches the desired tolerance.

Following Choi & Petersen [469], we run the experiment with an associative ( $\phi = \psi$ ) plasticity and a non associative one ( $\psi = 0$ , i.e.  $R = 0$ ). This second approach is essentially what many codes do.

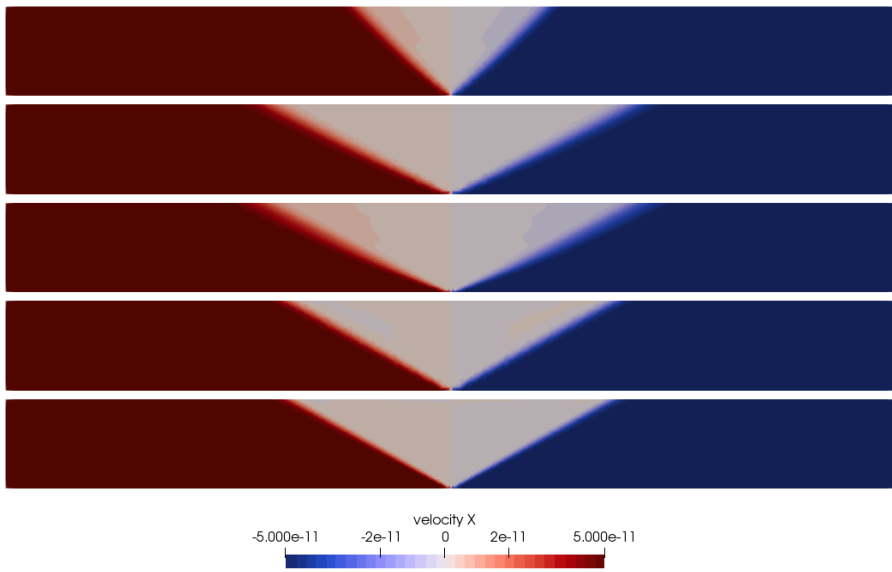
The velocity, pressure, strain rate, dilation rate, and velocity divergence are shown hereunder both in extension and compression.

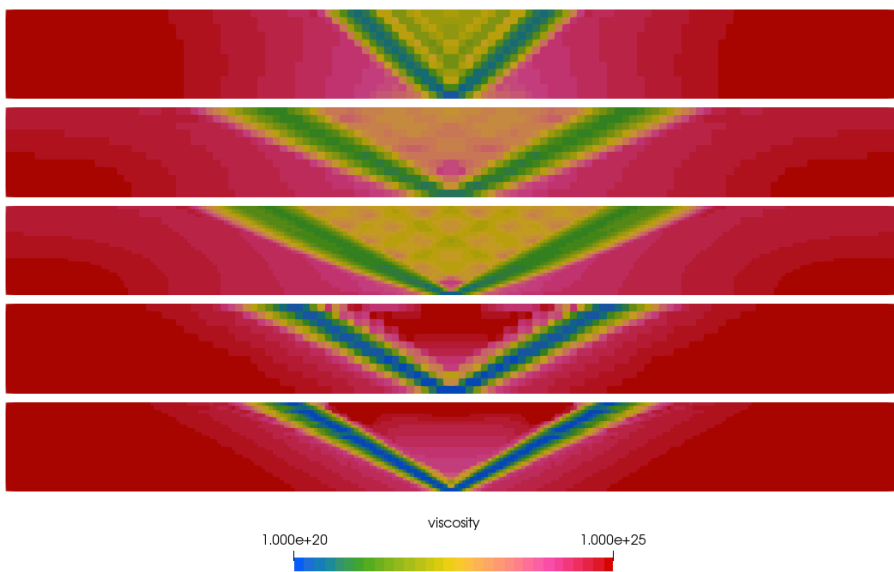
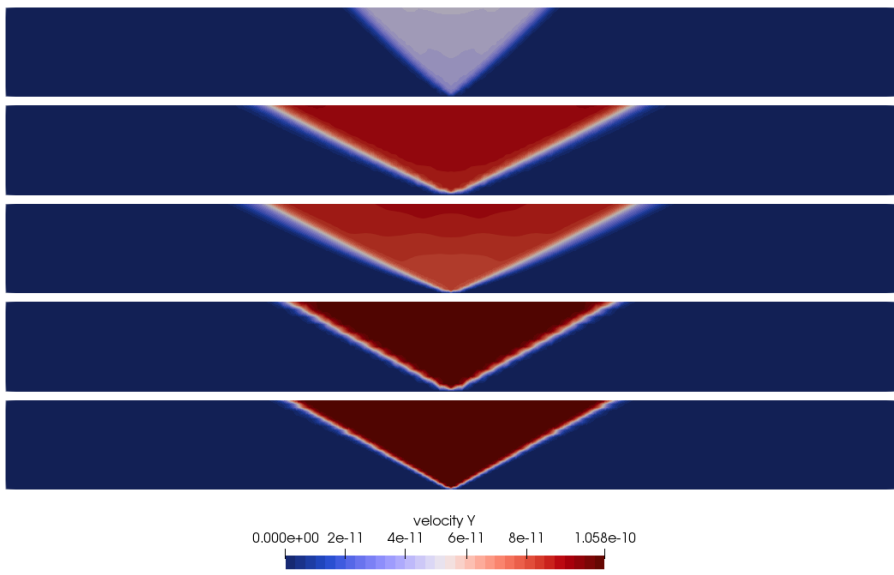


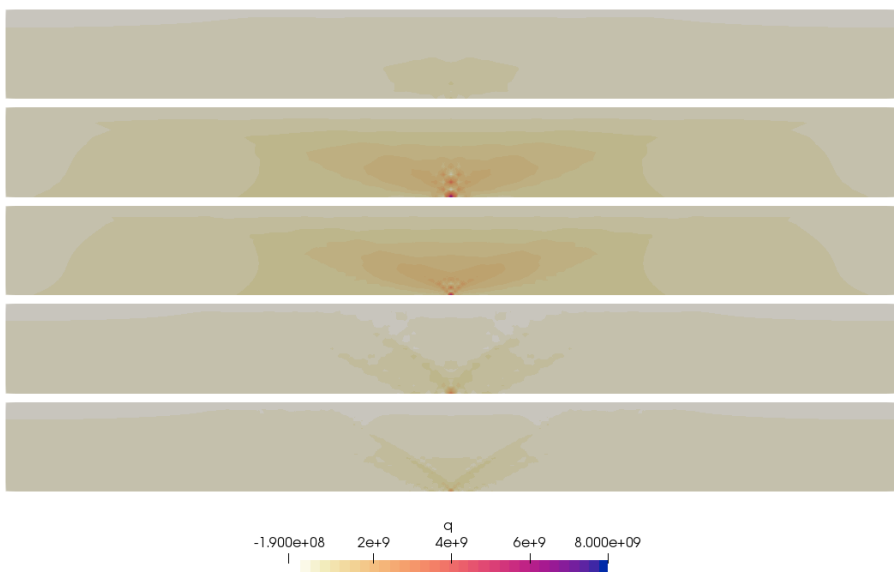
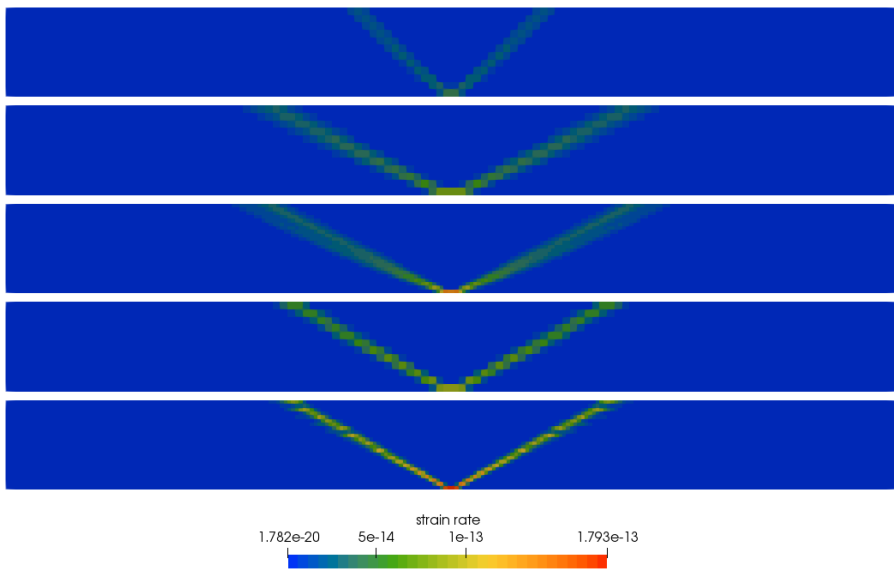




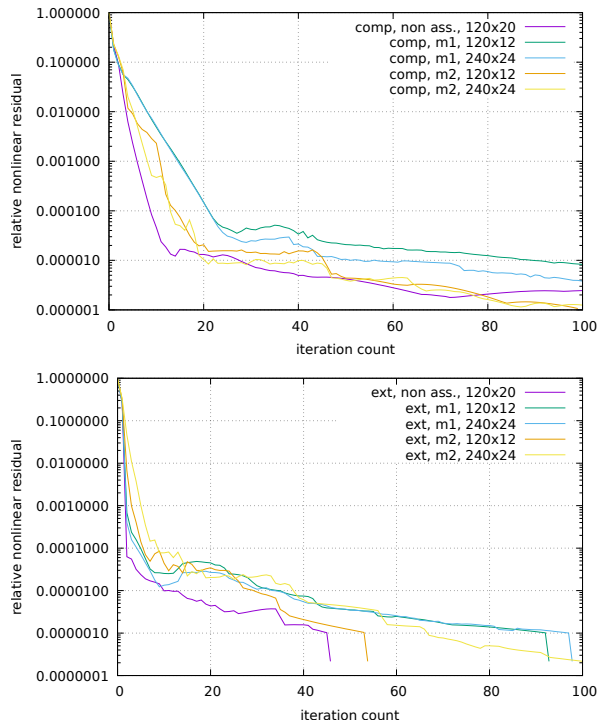
Extension. 1st row: Non-associative plasticity; 2nd and 3rd row: associative plasticity ( $\psi = \phi$ ) with method 1 for two resolutions 120x12 and 240; 4th and 5th row: associative plasticity ( $\psi = \phi$ ) with method 2 for two resolutions 120x12 and 240



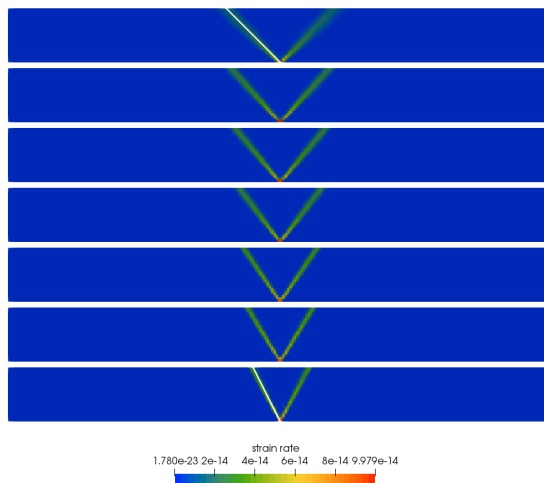


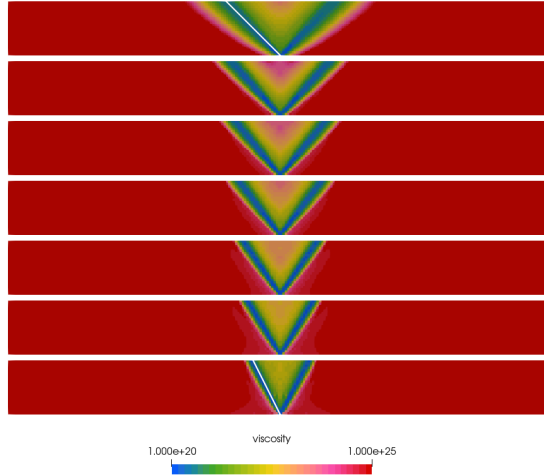


Compression. 1st row: Non-associative plasticity; 2nd and 3rd row: associative plasticity ( $\psi = \phi$ ) with method 1 for two resolutions 120x12 and 240; 4th and 5th row: associative plasticity ( $\psi = \phi$ ) with method 2 for two resolutions 120x12 and 240



One can also run the extension model for  $\phi = \psi = 0, 5, 10, 15, 20, 25, 30^\circ$





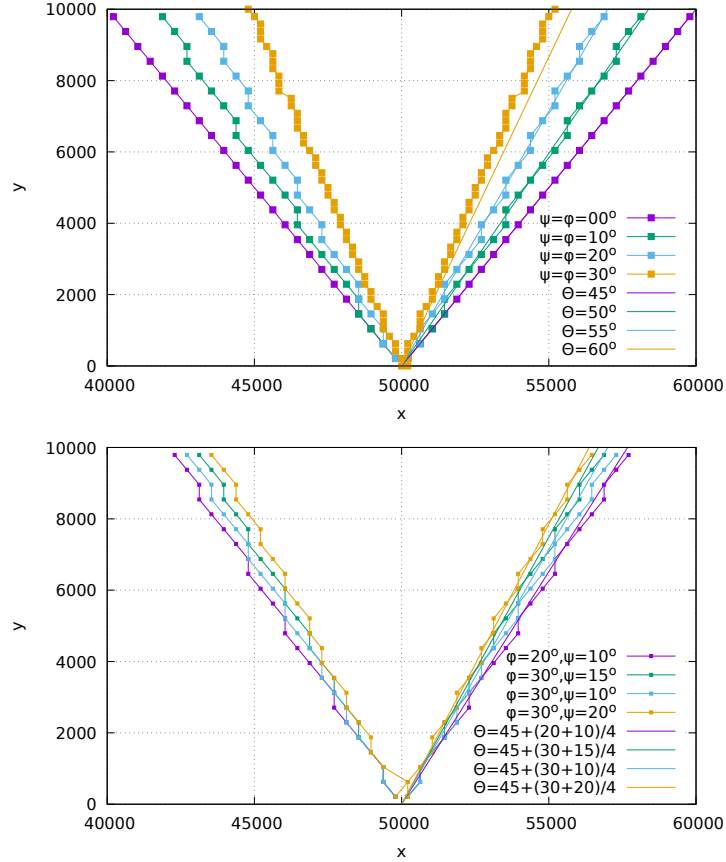
Three angles are mechanically stable (e.g. [1396]):

$$\theta = \frac{\pi}{4} \pm \frac{\psi}{2} \quad \text{Roscoe angle}$$

$$\theta = \frac{\pi}{4} \pm \frac{\phi}{2} \quad \text{Coulomb angle}$$

$$\theta = \frac{\pi}{4} \pm \frac{\phi + \psi}{4} \quad \text{Arthur angle}$$

In the case of associative plasticity,  $\phi = \psi$ , so that all three angles are the same. Per row of elements, and per half of the domain (left and right) we find the element with the highest strain-rate and record their center coordinates on the figure hereunder. These elements are shown for  $\phi = \psi = \{0, 10, 20, 30\}^\circ$  alongside a line corresponding to the expected analytical shear band angle value.



Results obtained on a 240x24 grid, max 50 nl iterations.

Note that benchmarking this is not easy. One solution Timo and I found was to add a velocity field  $\vec{v} = (x, y, z)$  (with  $\nabla \cdot \vec{v} = 3$ ) to an existing analytical problem, e.g. the Burstedde benchamrk.

### The 2016 brick

The setup is similar to the one in [2396]. It is a 2D Cartesian domain filled with an isoviscous layer at the bottom and a visco-plastic material on top, as shown here:

In what follows the nonlinear tolerance is set to  $10^{-6}$ . Due to a lack of resolution, I do not implement the rounded edges of the seed.  $U_0$  is set to 25mm/yr and the background viscosity of the brittle layer is set to  $\eta_0 = 10^{24}$ Pa.s. Note that the effective viscosity of the brittle layer is computed as follows:

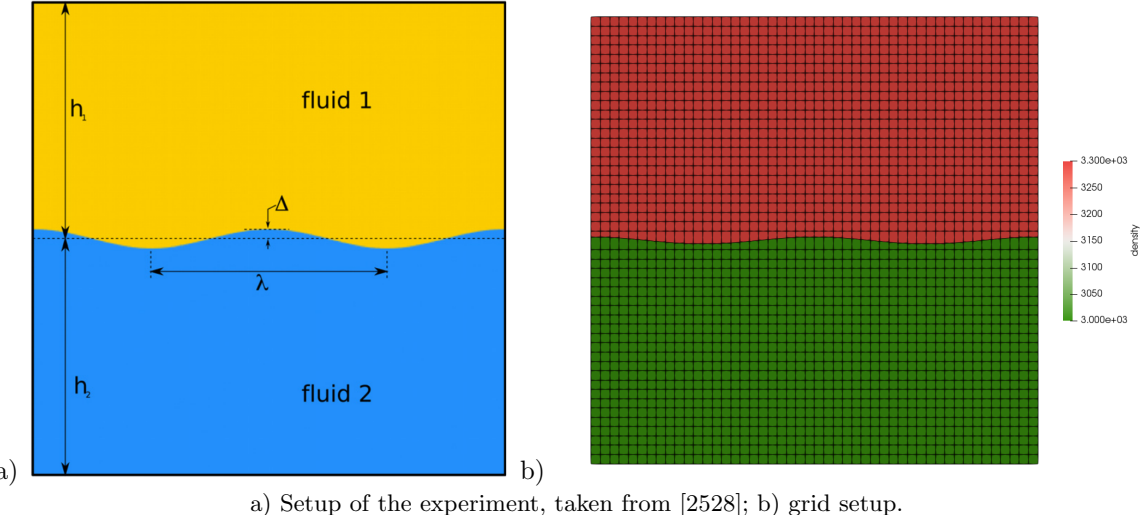
$$\eta_{eff} = \left( \frac{1}{\eta_0} + \frac{1}{\eta_p} \right)^{-1} = \left( \frac{1}{\eta_0} + \frac{2\dot{\epsilon}_{ii}}{Y} \right)^{-1}$$

with  $Y = p \sin \phi + c \cos \phi$ . Note that the pressure colour bars in Fig(6) of [2396] are most likely not correct at all, and in order for my results to look like theirs I had to change it for VM, DDM and DP.

## Stone 40: Rayleigh-Taylor instability

This benchmark is carried out in [688, 953, 2528] and is based on the analytical solution by Ramberg (1968). It consists of a two-layer system driven by gravity. Free slip are imposed on the sides while no-slip boundary conditions are imposed on the top and the bottom of the box.

Fluid 1 ( $\rho_1, \eta_1$ ) of thickness  $h_1$  overlays fluid 2 ( $\rho_2, \eta_2$ ) of thickness  $h_2$  (with  $h_1 + h_2 = L_y$ ). An initial sinusoidal disturbance of the interface between these layers is introduced and is characterised by an amplitude  $\Delta$  and a wavelength  $\lambda = L_x/2$  as shown in Figure ??.



a) Setup of the experiment, taken from [2528]; b) grid setup.

Under this condition, the velocity of the diapiric growth  $v_y$  is given by the relation

$$\frac{v_y}{\Delta} = -K \frac{\rho_1 - \rho_2}{2\eta_2} h_2 g$$

with the dimensionless growth factor  $K$  being

$$K = \frac{-d_{12}}{c_{11}j_{22} - d_{12}i_{21}}$$

and

$$c_{11} = \frac{\eta_1 2\phi_1^2}{\eta_2(\cosh 2\phi_1 - 1 - 2\phi_1^2)} - \frac{2\phi_2^2}{\cosh 2\phi_2 - 1 - 2\phi_2^2} \quad (1049)$$

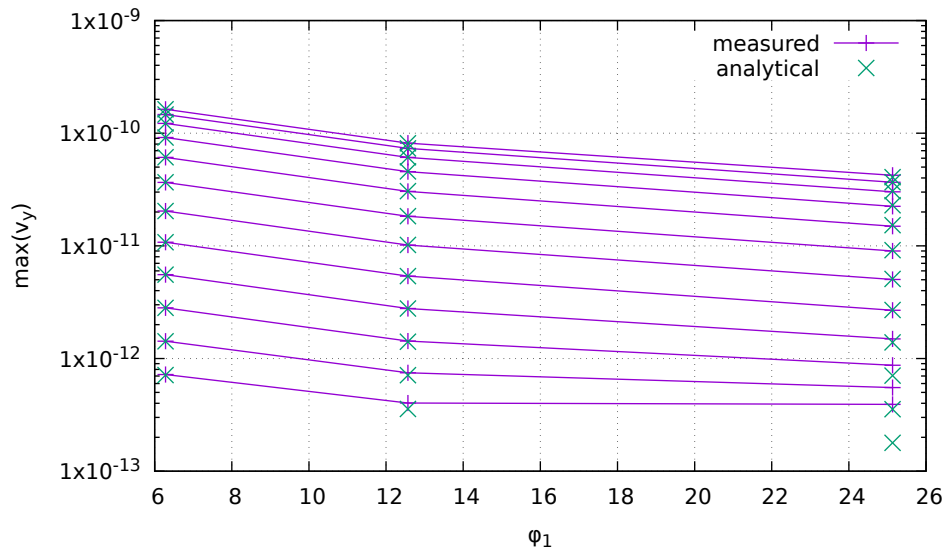
$$d_{12} = \frac{\eta_1(\sinh 2\phi_1 - 2\phi_1)}{\eta_2(\cosh 2\phi_1 - 1 - 2\phi_1^2)} + \frac{\sinh 2\phi_2 - 2\phi_2}{\cosh 2\phi_2 - 1 - 2\phi_2^2} \quad (1050)$$

$$i_{21} = \frac{\eta_1 \phi_2 (\sinh 2\phi_1 + 2\phi_1)}{\eta_2(\cosh 2\phi_1 - 1 - 2\phi_1^2)} + \frac{\phi_2 (\sinh 2\phi_2 + 2\phi_2)}{\cosh 2\phi_2 - 1 - 2\phi_2^2} \quad (1051)$$

$$j_{22} = \frac{\eta_1 2\phi_1^2 \phi_2}{\eta_2(\cosh 2\phi_1 - 1 - 2\phi_1^2)} - \frac{2\phi_2^3}{\cosh 2\phi_2 - 1 - 2\phi_2^2} \quad (1052)$$

$$\phi_1 = \frac{2\pi h_1}{\lambda} \quad (1053)$$

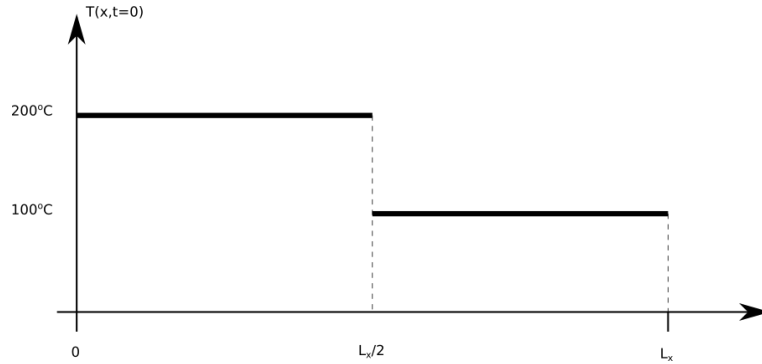
$$\phi_2 = \frac{2\pi h_2}{\lambda} \quad (1054)$$



Note that in [2528] I fixed  $\lambda = L_x/2$  and varied  $L_x$ . Here I keep  $L_x$  fixed and vary  $\lambda = L_x/2, L_x, 4, L_x/8$ . Each line corresponds to a different value of the viscosity  $\eta_2$ .

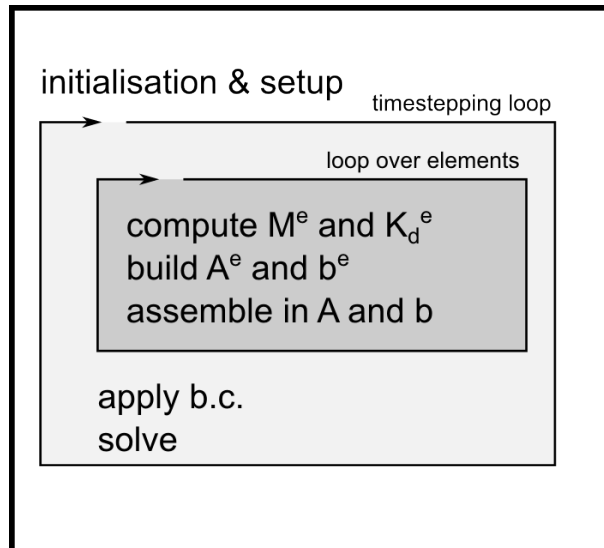
## Stone 42: 1D diffusion

This is the simplest case for a FE code: a 1D (temperature) diffusion problem. It puts into practice what is presented in section 5.1. The initial temperature profile is as follows:



$$T(x, t = 0) = 200 \quad x < L_x/2 \quad T(x, t = 0) = 100 \quad x \geq L_x/2$$

The properties of the material are as follows:  $\rho = 3000$ ,  $k = 3$ ,  $C_p = 1000$  and the domain size is  $L_x = 100\text{km}$ . Boundary conditions are  $T(t, x = 0) = 200^\circ\text{C}$  and  $T(t, x = L_x) = 100^\circ\text{C}$ . There are `nelt` elements and `nnx` nodes. All elements are `hx` long. The code will carry out `nstep` timesteps of length `dt` or will stop before that when steady state is reached. The code structure is summarised hereunder:



## Stone 43: the rotating cone

This benchmark originates in [711]. It is also carried out in [181]. It considers the advection of a product-cosine hill in a prescribed velocity field. The initial temperature is:

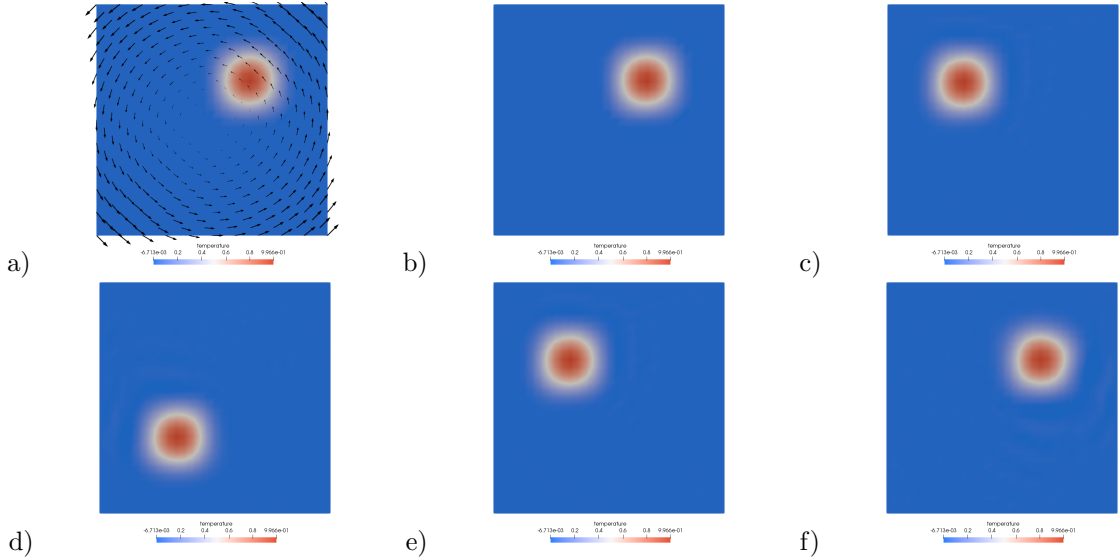
$$T_0(x, y) = \begin{cases} \frac{1}{4} \left(1 + \cos \pi \frac{x-x_c}{\sigma}\right) \left(1 + \cos \pi \frac{y-y_c}{\sigma}\right) & \text{if } (x - x_c)^2 + (y - y_c)^2 \leq \sigma^2 \\ 0 & \text{otherwise} \end{cases} \quad (1055)$$

The boundary conditions are  $T(x, y) = 0$  on all four sides of the unit square domain. In what follows we set  $x_c = y_c = 1/6$  and  $\sigma = 0.2$ . The velocity field is analytically prescribed:  $\vec{v} = (-(y - y_c), +(x - x_c))$ .

In what follows we test the time integration scheme by setting  $\alpha_T = 1$  (fully implicit formulation),  $\alpha = 0$  (fully explicit formulation) and  $\alpha_T = 1/2$  (Crank-Nicolson). The timestep is set to  $\delta t = 2\pi/200$ . The density and heat capacity values are set to 1. We monitor the minimum and maximum value of the temperature field, as well as the total thermal energy  $E_T$  in the system during the 200 time steps ( $2\pi$  rotation of the cone):

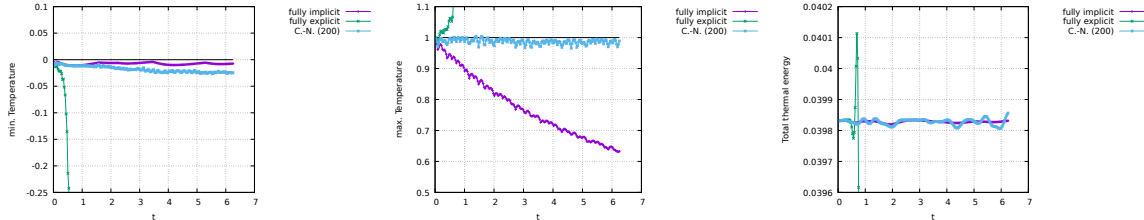
$$E_T = \int_{\Omega} \rho_0 C_p T dV = \int_{\Omega} T dV = |\Omega| \langle T \rangle \quad \text{where} \quad \langle T \rangle = \frac{1}{|\Omega|} \int_{\Omega} T dV$$

The time evolution of the temperature with the Crank-Nicolson algorithm is shown hereunder:



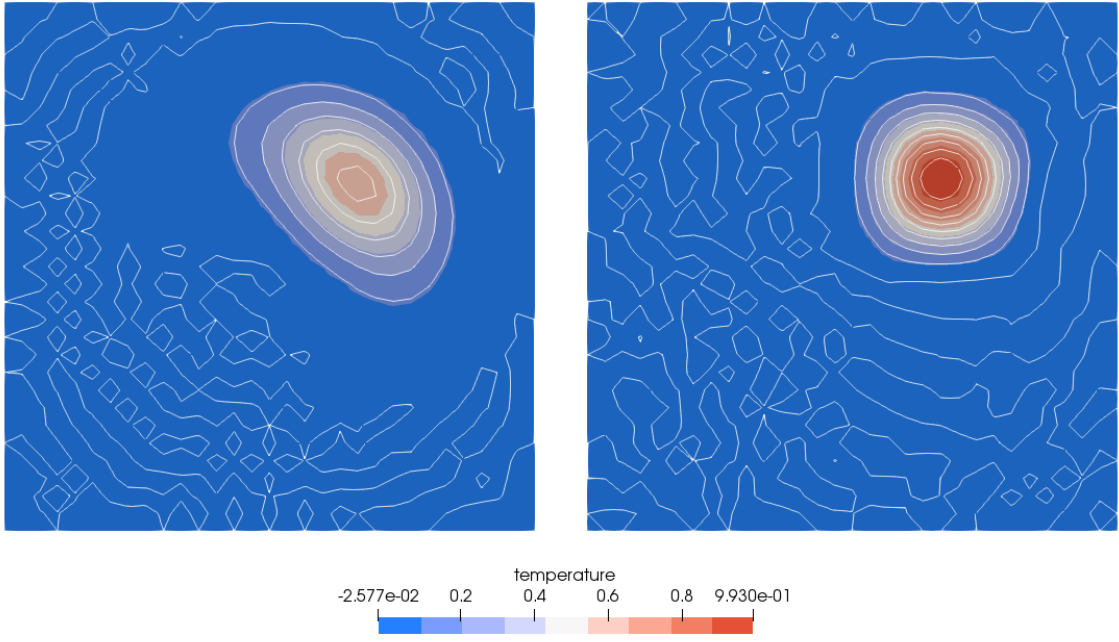
a) Velocity field and initial temperature; b,c,d,e,f) Temperature field at timesteps 0,50,100,150,199.

Turning now to the statistics, we plot  $\min(T)$ ,  $\max(T)$  and  $E_T$  as a function of time:



Time evolution of the min and max temperature and the total energy

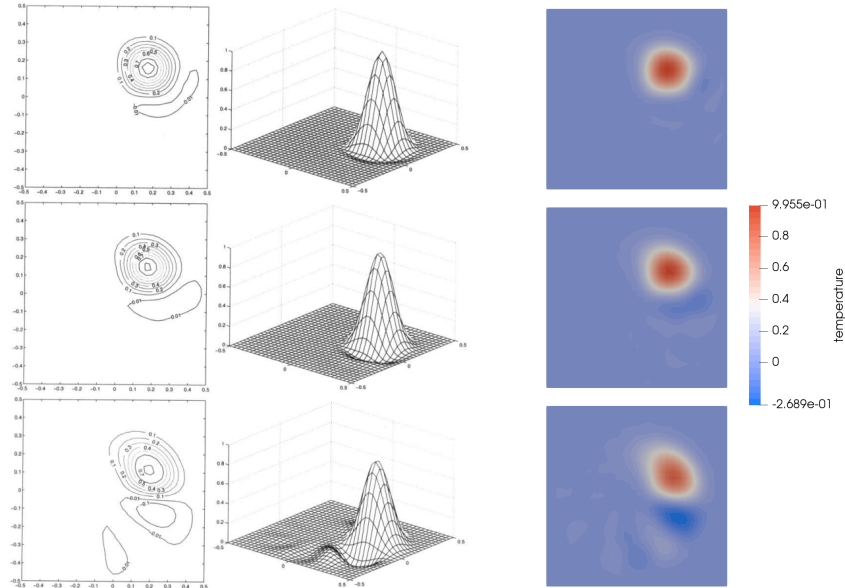
The conclusions are clear: the explicit method diverges quickly and is unusable. The fully implicit and Crank-Nicolson method yield similar energy conservation but the fully-implicit showcases a clear loss in maximum temperature as shown in the following figure:



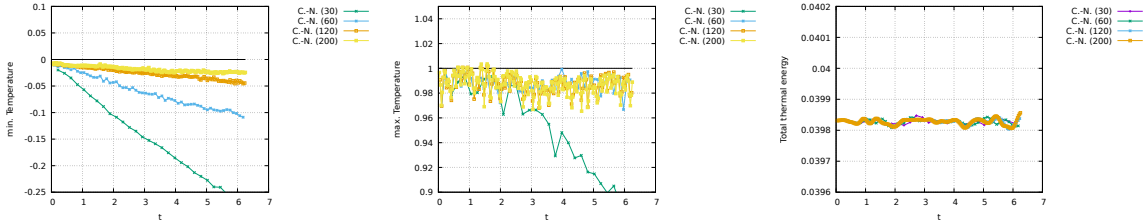
Temperature field after a full rotation with isocontours every 0.1 value.

Left: Fully-implicit; Right: Crank-Nicolson

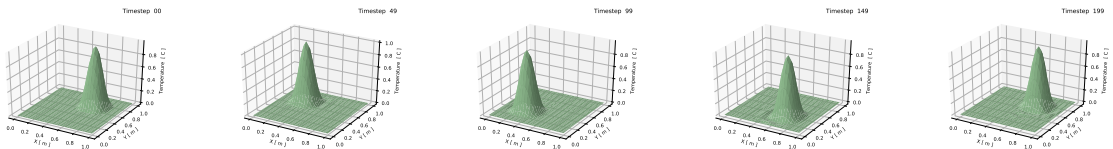
Finally we can run the experiment (still a  $2\pi$  rotation) with three different time steps ( $\delta t = 2\pi/30, 2\pi/60, 2\pi/120$ ) and we recover very similar results to those presented in [711]:



From top to bottom:  $\delta t = 2\pi/120, 2\pi/60, 2\pi/30$  with Crank-Nicolson. Left panel is taken from donea & Huerta [711]



Time evolution of the min and max temperature and the total energy obtained with the Crank-Nicolson algorithm for 4 values of the timestep as indicated by the number between parenthesis.

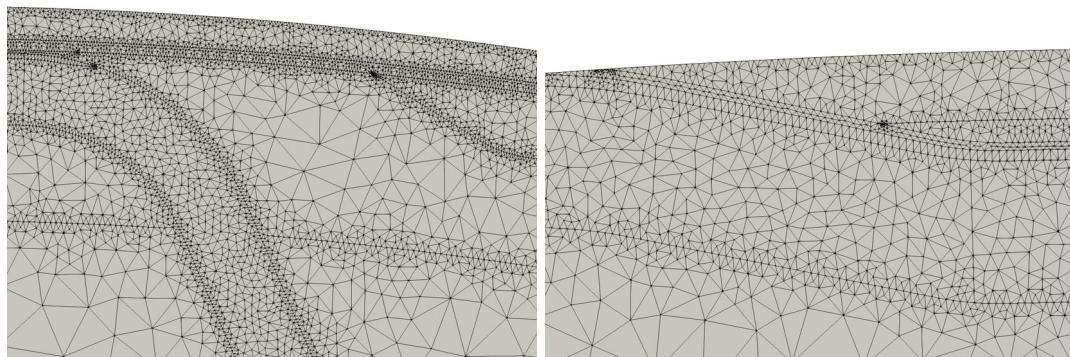
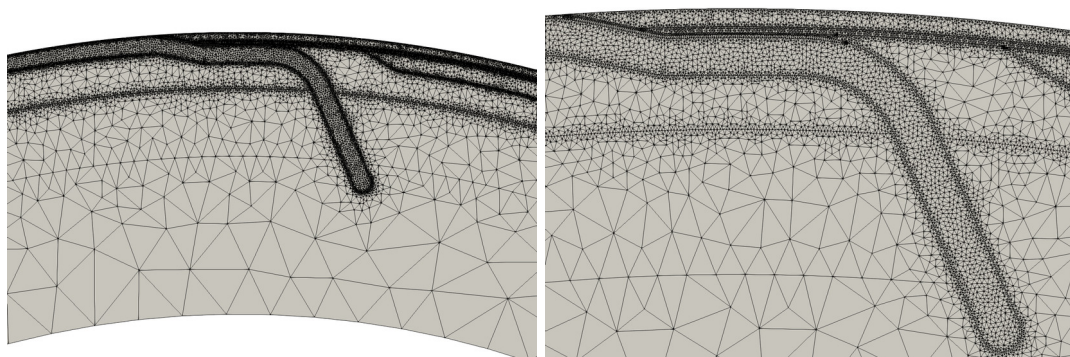
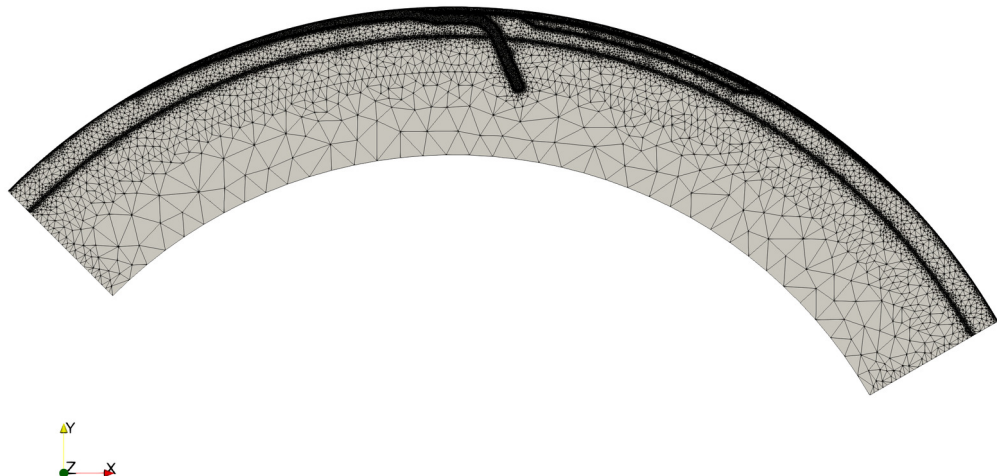


Time evolution of the temperature field for  $\delta t = 2\pi/200$  with Crank-Nicolson.

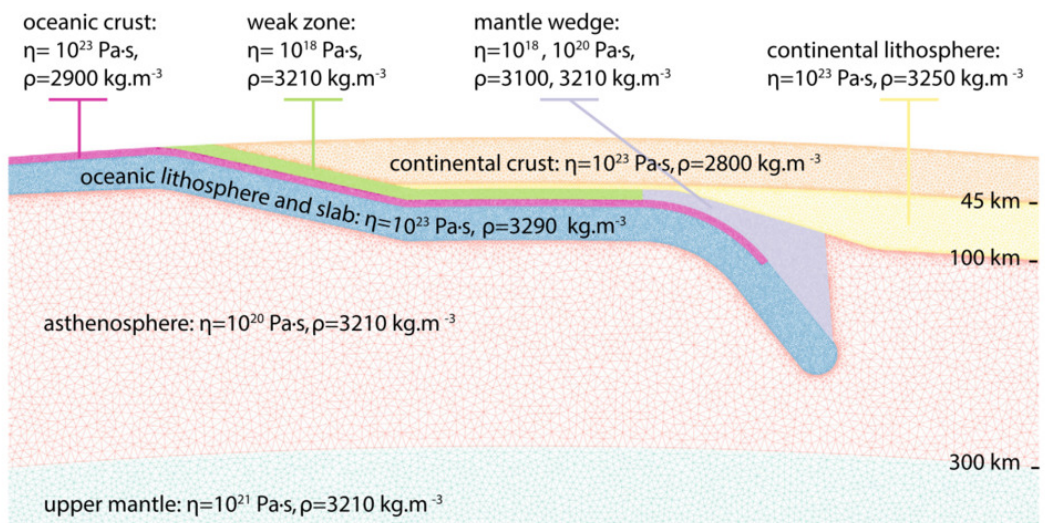
## Stone 44: the flat slab

WORK in PROGRESS

I need a list of nodes on the boundary I need a GCOORD.txt file with more decimals I need an even lower resolution grid I need the scaling factors for rho,eta, ...



371km, 300km depth, 660km depth, 1500km.

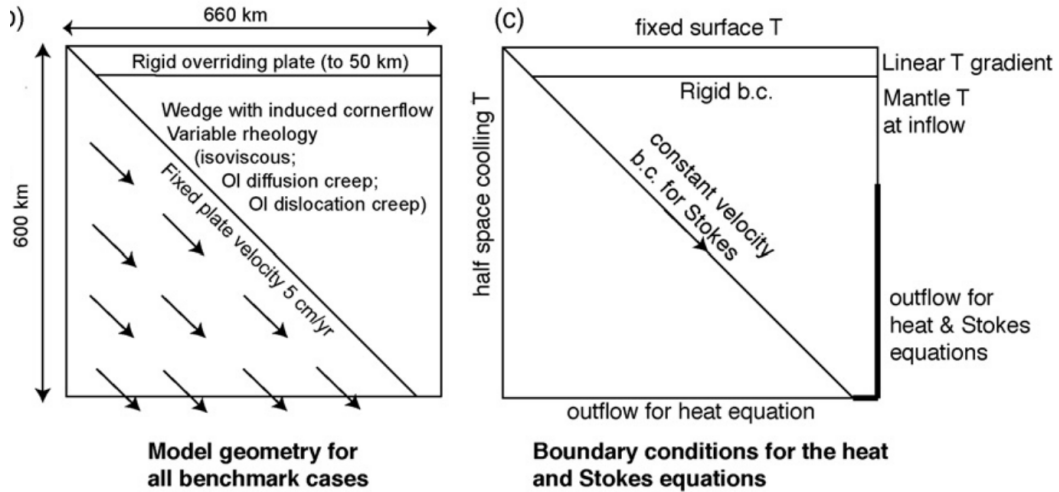


Taken from [2352]

## Stone 45: the corner flow

This experiment is based on the benchmark paper by van Keken et al, 2008 [2655]. It shares similarities with the time dehydration processes in subduction zones work by Magni et al., 2014 [1686] and the 3D corner flow study of Plunder et al, 2018[2043]. See also Cerpa et al, 2017 [432] for a study of fluid migration in the mantle wedge.

The domain is 660km × 600km. Note that in the original paper the origin of the coordinate system is at the top left while it is at the lower left corner in our code.



As shown in the figure above, the inflow boundaries (at both wedge and trench sides) and top of the model have prescribed temperature. The wedge is assumed to be an incompressible fluid that is driven only by the kinematic forcing of the slab. The wedge is confined by the top of the slab and the base of the rigid overriding plate (located at a depth of 50km). The boundary conditions for the wedge are no-slip below the overriding plate and constant velocity along the top of the slab. The velocity boundary conditions for the boundaries of the wedge are either provided by the Batchelor cornerflow solution (cases 1a and 1b) or based on free inflow/outflow boundaries. The velocity field is discontinuous between the slab and the overriding plate. The velocity in the slab is constant (5cm/yr) and it dips at a 45° angle. There is no radiogenic shear heating.

The flow is assumed to be incompressible and buoyancy effects are neglected. All the experiments shown in the paper are at steady state, i.e. the temperature field satisfies:

$$\rho C_p \vec{v} \cdot \vec{\nabla} T = \vec{\nabla} \cdot (k \vec{\nabla} T) \quad (1056)$$

In the paper a simplified diffusion creep formulation is adopted and the effective diffusion creep viscosity is computed as follows:

$$\eta_{\text{diff}} = A_{\text{diff}} \exp \frac{Q_{\text{diff}}}{RT}$$

The dislocation creep effective viscosity is given by

$$\eta_{\text{disl}} = A_{\text{disl}} \dot{\varepsilon}^{(1-n)/n} \exp \frac{Q_{\text{disl}}}{nRT}$$

Note that in both the activation volume has been set to zero, which decouples pressure from the effective viscosities. Both effective viscosities are limited with a maximum viscosity as follows:

$$\eta_{\text{diff}}^* = \left( \frac{1}{\eta_{\text{diff}}} + \frac{1}{\eta_{\text{max}}} \right)^{-1} \quad \eta_{\text{disl}}^* = \left( \frac{1}{\eta_{\text{disl}}} + \frac{1}{\eta_{\text{max}}} \right)^{-1}$$

The top boundary condition is  $T_{\text{top}} = T(y = L_y) = 273K$ . At the inflow boundary of the wedge (i.e. where  $u < 0$ )<sup>87</sup> temperature is fixed at  $T_0 = 1573K$  and a linear geotherm is used at the left hand

<sup>87</sup>Think about it: it makes little sense to prescribe a temperature where the fluid is leaving the domain

boundary of the overriding plate from 0 to 50 km depth. The temperature at the slab inflow boundary is described by an error-function solution for half-space cooling for 50 Myr:

$$T(x = 0, y) = T_{top} + (T_0 - T_{top}) \operatorname{erf} \frac{L_y - y}{2\sqrt{\kappa t_{50}}}$$

where  $t_{50}$  is the age of the slab.

At the slab and wedge outflow boundaries we prescribe the natural boundary condition (zero curvature) for the heat equation.

the original paper considers multiple cases:

- Case 1a: analytical cornerflow model. The wedge flow is prescribed by the analytical expression for cornerflow [99], so that we do not need to solve for the Stokes equations, only the energy equation.
- Case 1b: dynamical flow in isoviscous wedge I This case is the same as 1a, except that the solution for the wedge flow is determined by solving the Stokes equations while the Batchelor solution is imposed on the inflow and outflow boundaries. This case tests the ability of the numerical method to accurately reproduce the corner flow solution.
- Case 1c: dynamical flow in isoviscous wedge II. Same as case 1b, but with stress-free boundary conditions on the mantle wedge.
- Case 2a: dynamical flow with diffusion creep
- Case 2b: dynamical flow with dislocation creep

The temperature field as discreted values  $T_{ij}$  on an equidistant grid with 6km spacing, which is a  $111 \times 101$  matrix stored row-wise starting in the top left corner. From this grid the following measurements are extracted for direct comparison:

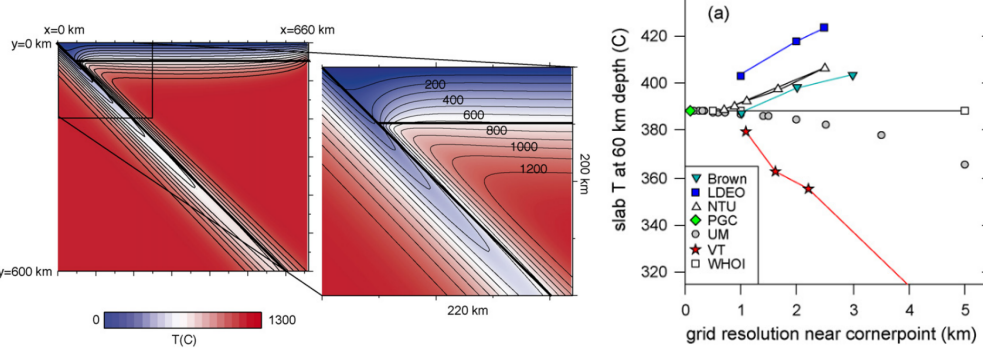
1. the temperature  $T_{11,11}$  which is at coordinates (60, 60km) and just down-stream from the corner point. This provides therefore one of the most critical tests of accuracy of the numerical codes;
2. the L2 norm of the slab-wedge interface temperature between 0 and 210 km depth defined by

$$T_{\text{slab}} = \sqrt{\frac{1}{36} \sum_{i=1}^{36} T_{ii}^2}$$

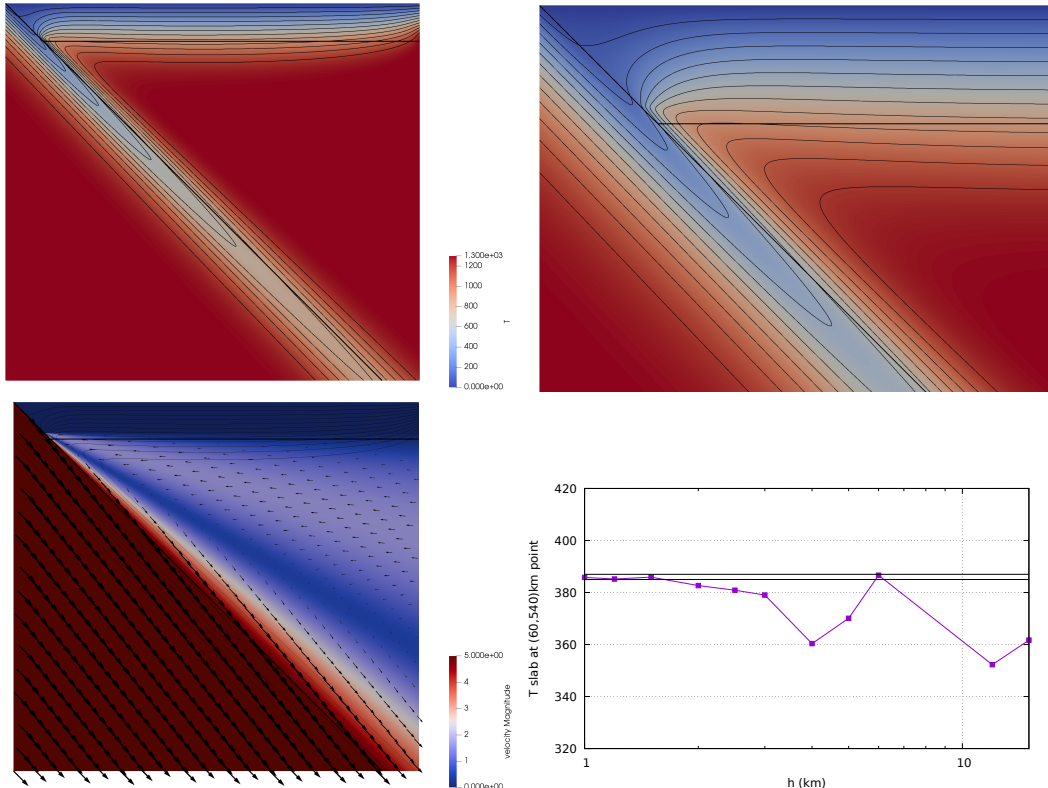
3. the L2 norm of the temperature in the triangular part of the tip of the wedge, between 54 and 120 km depth:

$$T_{\text{wedge}} = \sqrt{\frac{1}{78} \sum_{i=10}^{21} \sum_{j=10}^i T_{ij}^2}$$

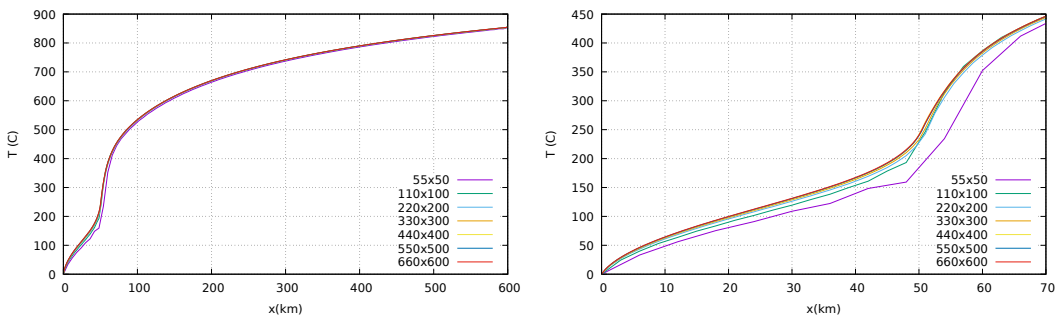
## Results for case 1a



(a) Temperature prediction for case 1a. The bold lines indicate the top of the slab and base of the overriding plate. (b) Close up of the top left part of the model. Figures taken from [2655].



Results obtained on mesh 660x600(x2) elements. Black lines on lower right figure correspond to a visible range of values as shown in Fig.3a of [2655].

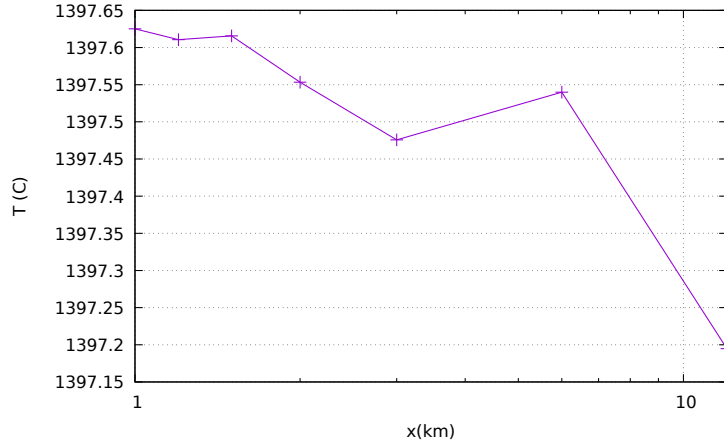


Temperature values on the slab top surface ( $y = L_y - x$ ) plotted as a function of the  $x$  coordinate. Left is entire slab, right is zoom on the first 70km

The average temperature

$$\langle T \rangle = \frac{1}{|\Omega|} \int_{\Omega} T \, dV$$

is plotted in the following figure:



Average temperature in the domain.

We see that this measurement is not appropriate to assert whether the resolution is sufficient so that results converge to a single value, as opposed to the point wise temperature measurement presented above. The average temperature changes by about 0.4 for an average value of about 1397, which is not much for a factor 12 increase in resolution (from 55x50 to 660x600).

carry out other two measurements (need interpolation onto other grid for this

### Results for case 1b

TODO

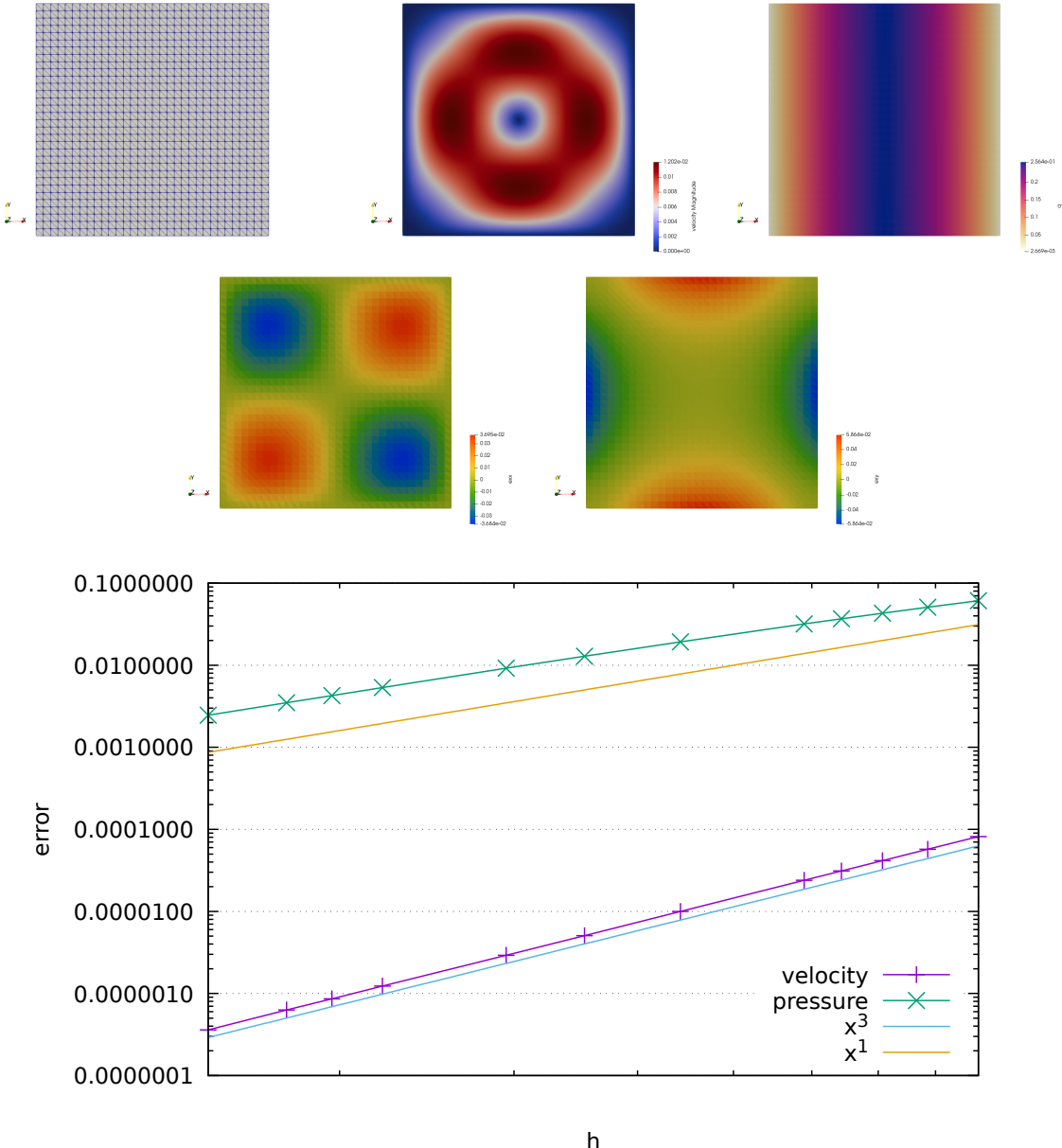
### Results for case 1c

TODO

## Stone 46: MMS1 with Crouzeix-Raviart ( $P_2^+ \times P_{-1}$ ) elements

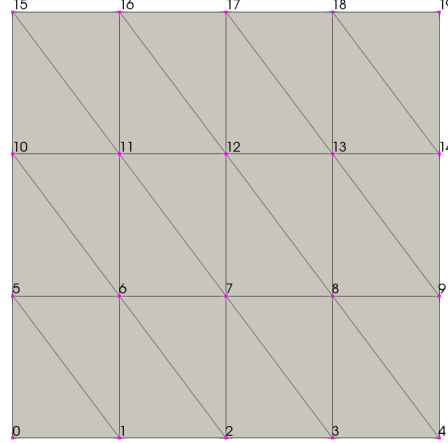
This stone showcases the Crouzeix-Raviart element (see Section 6.2.10) used to solve the analytical problem "Donea & Huerta" (see Section 8.6.1).

Out of convenience the pressure is set to zero at location  $(x, y) = (1, 1)$ , so that the analytical solution is now  $p(x, y) = x(1 - x)$ .



## Stone 47: MMS1 with MINI ( $P_1^+ \times P_1$ ) elements

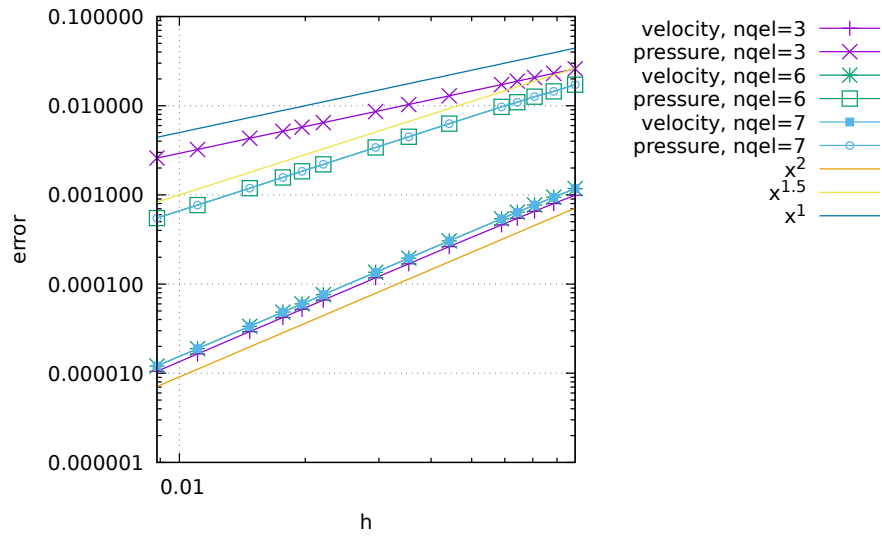
The grid is composed of triangles but for simplicity these are obtained by splitting rectangles in two, as shown hereunder:



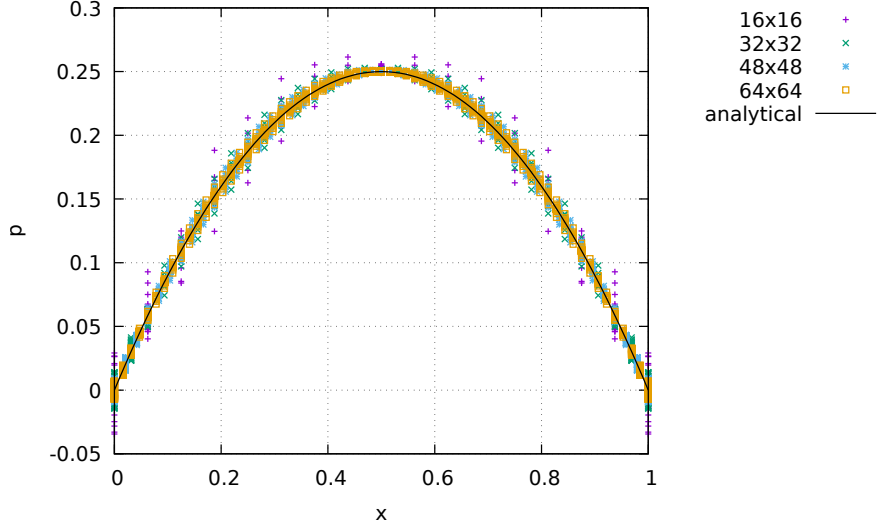
Not shown are the nodes for the bubbles in the middle of each triangle.

This stone showcases the MINI element (see Section 6.2.8) used to solve the analytical problem "Donea & Huerta" (see Section 8.6.1). Out of convenience the pressure is set to zero at location  $(x, y) = (1, 1)$ , so that the analytical solution is now  $p(x, y) = x(1 - x)$ .

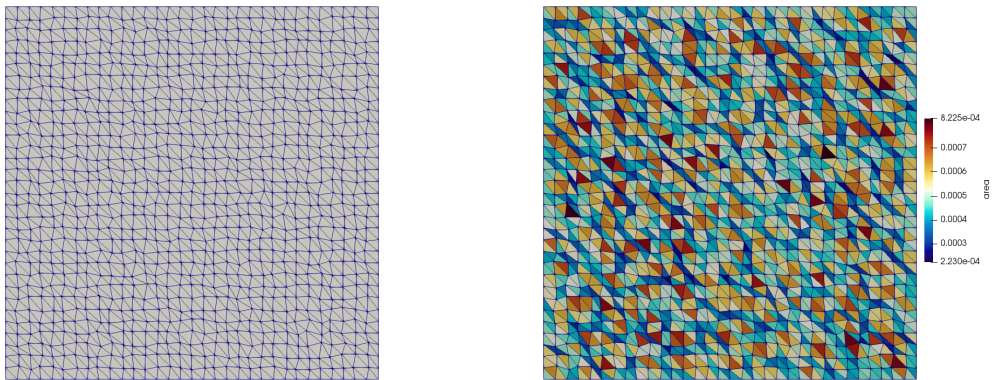
As an experiment I have run convergence tests for two cases: using  $nqel=3$  quadrature points and using  $nqel=6$  quadrature points. We find that the velocity and pressure errors converge depend on this crucial parameter. For  $nqel=3$  the velocity and pressure errors converge quadratically and linearly respectively but for  $nqel=6$  they converge as  $h^2$  and  $h^{1.5}$  respectively:



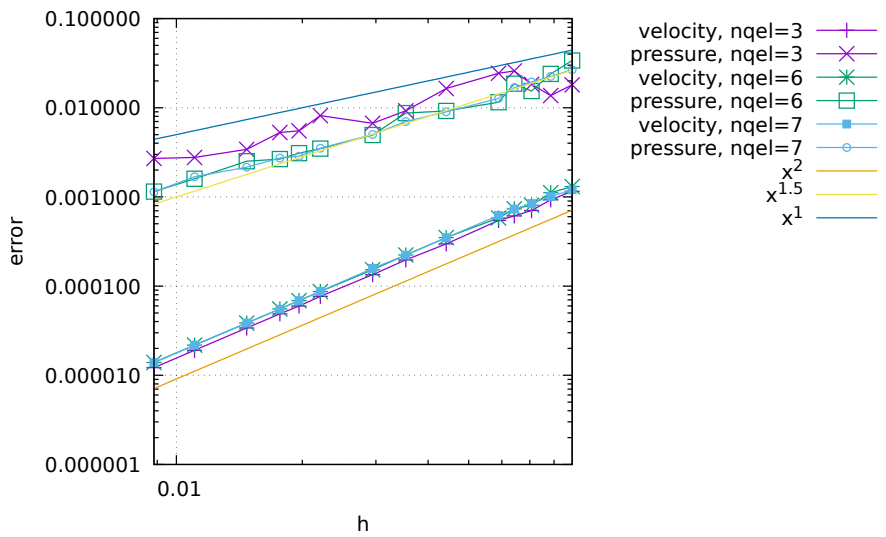
It is worth noticing that although the element is stable, and the error converges at a respectable rate, the pressure solution is not 'clean': as shown on the following figure, there is still some under/overshoot with respect to the analytical solution.



Let us now explore the case where the nodes inside the domain are randomly perturbed, i.e. a random value  $(\delta_x, \delta_y) \in [-h_x/5, h_x/5] \times [-h_y/5, h_y/5]$  is added to their position (while preserving the position of the bubble as the barycenter of each triangle), as shown hereunder:



Looking again at the convergence rates of the errors, we see that the velocity errors are virtually unchanged but we observe that the pressure errors no more align on a single line and that the rates are only maintained on average.



## Stone 48: D&H with $Q_1 \times P_0$ , $Q_2 \times Q_1$ , $Q_3 \times Q_2$ and $Q_4 \times Q_3$ elements

In this experiment we consider 4 different finite elements. The idea behind this stone is to build a code which code(the FEM build and assembly) is common to all. The setup is the Donea & HUerta benchmark (Section 8.6.1), which has been modified so that the pressure is zero at the top right corner.

Q4xQ3	Q3xQ2	Q2xQ1	Q1Q0
20====21====22====23====24	12====13====14====15	06=====07=====08	02=====03
20====21====22====23====24			
	08====09====10====11		
20====21====22====23====24			
	03=====04=====05		
	04=====05=====06=====07		
20====21====22====23====24			
	00=====01=====02=====03		
20====21====22====23====24	00=====01=====02=====03	00=====01=====02	00=====01
12====13====14====15	06=====07=====08	02=====03	.
08====09====10====11			
	03=====04=====05		00
	04=====05=====06=====07		
00=====01=====02=====03	00=====01=====02	00=====01	.
mV=25, mP=16	mV=16, mP=9	mV=9, mP=4	mV=4, mP=1

In the code the 'order' parameter can take values 1,2,3 and 4 which correspond to the polynomial order of the velocity approximation ( $Q_1$ ,  $Q_2$ ,  $Q_3$  and  $Q_4$ ).

When both nelx and nely values have been chosen, the total number of element for a regular 2D grid is simply:

```
nel=nelx*nely
```

The number of nodes in each direction is then easily computed:

```
nmx=order*nelx+1
nny=order*nely+1
```

and so is then the total number of velocity nodes:

```
NV=nmx*nny
```

The total number of pressure nodes is as follows:

```

if order==1:
    NP=nelx*nely
if order==2:
    NP=(nelx+1)*(nely+1)
if order==3:
    NP=(2*nelx+1)*(2*nely+1)
if order==4:
    NP=(3*nelx+1)*(3*nely+1)

```

Each velocity node has 2 dofs (ndofV=2) while pressure nodes have one dof (ndofP=1) so that the size of the blocks and the assembled FE matrix are given by:

```

NfemV=NV*ndofV
NfemP=NP*ndofP
Nfem=NfemV+NfemP

```

For the linear element, 2 quadrature points per dimension are enough (nqperdim=2), while 3 are necessary for the quadratic element (nqperdim=3) and 4 are used for the cubic element (nqperdim=4), and 5 for the quartic element, which can be conveniently implemented as follows:

```
nqperdim=order+1
```

The quadrature points location and weight is document in Section 4.1.

Because we wish to use a regular grid, the layout of the points for all three elements can be implemented easily:

```

counter=0
for j in range(0,nny):
    for i in range(0,nnx):
        xV[counter]=i*hx/order
        yV[counter]=j*hy/order
        counter+=1

```

The position of the pressure nodes follows a similar logic.

When it comes to the connectivity array, I first started by building it for each element as follows:

```

if order==1:
    counter=0
    for j in range(0,nely):
        for i in range(0,nelx):
            iconV[0,counter]=(i)*1+0+(j)*1*nnx+nnx*0
            iconV[1,counter]=(i)*1+1+(j)*1*nnx+nnx*0
            iconV[2,counter]=(i)*1+0+(j)*1*nnx+nnx*1
            iconV[3,counter]=(i)*1+1+(j)*1*nnx+nnx*1
            counter += 1

if order==2:
    counter = 0
    for j in range(0,nely):
        for i in range(0,nelx):
            iconV[0,counter]=(i)*2+0+(j)*2*nnx+nnx*0
            iconV[1,counter]=(i)*2+1+(j)*2*nnx+nnx*0
            iconV[2,counter]=(i)*2+2+(j)*2*nnx+nnx*0
            iconV[3,counter]=(i)*2+0+(j)*2*nnx+nnx*1
            iconV[4,counter]=(i)*2+1+(j)*2*nnx+nnx*1
            iconV[5,counter]=(i)*2+2+(j)*2*nnx+nnx*1
            iconV[6,counter]=(i)*2+0+(j)*2*nnx+nnx*2
            iconV[7,counter]=(i)*2+1+(j)*2*nnx+nnx*2
            iconV[8,counter]=(i)*2+2+(j)*2*nnx+nnx*2
            counter += 1

if order==3:
    counter = 0
    for j in range(0,nely):
        for i in range(0,nelx):
            iconV[0,counter]=(i)*3+0+(j)*3*nnx+0*nnx
            iconV[1,counter]=(i)*3+1+(j)*3*nnx+0*nnx
            iconV[2,counter]=(i)*3+2+(j)*3*nnx+0*nnx

```

```

...
iconV[13, counter]=(i)*3+1+(j)*3*nnx+3*nnx
iconV[14, counter]=(i)*3+2+(j)*3*nnx+3*nnx
iconV[15, counter]=(i)*3+3+(j)*3*nnx+3*nnx
counter += 1

```

Having done so, it becomes quickly apparent that the connectivity array can be computed for all elements as follows:

```

counter=0
for j in range(0, nely):
    for i in range(0, nelx):
        counter2=0
        for k in range(0, order+1):
            for l in range(0, order+1):
                iconV[counter2, counter]=i*order+l+j*order*nnx+nnx*k
                counter2+=1
        counter += 1

```

The same approach is taken to build the pressure connectivity array, although the  $Q_1 \times P_0$  element requires special attention since the pressure is elemental and attributed to a single node inside the element.

For the other elements I started from:

```

if order==2:
    counter=0
    for j in range(0, nely):
        for i in range(0, nelx):
            iconP[0, counter]=(i)*1+0+(j)*1*(nelx+1)+(nelx+1)*0
            iconP[1, counter]=(i)*1+1+(j)*1*(nelx+1)+(nelx+1)*0
            iconP[2, counter]=(i)*1+0+(j)*1*(nelx+1)+(nelx+1)*1
            iconP[3, counter]=(i)*1+1+(j)*1*(nelx+1)+(nelx+1)*1
            counter += 1

if order==3:
    counter=0
    for j in range(0, nely):
        for i in range(0, nelx):
            iconP[0, counter]=(i)*2+0+(j)*2*(2*nelx+1)+(2*nelx+1)*0
            iconP[1, counter]=(i)*2+1+(j)*2*(2*nelx+1)+(2*nelx+1)*0
            iconP[2, counter]=(i)*2+2+(j)*2*(2*nelx+1)+(2*nelx+1)*0
            iconP[3, counter]=(i)*2+0+(j)*2*(2*nelx+1)+(2*nelx+1)*1
            iconP[4, counter]=(i)*2+1+(j)*2*(2*nelx+1)+(2*nelx+1)*1
            iconP[5, counter]=(i)*2+2+(j)*2*(2*nelx+1)+(2*nelx+1)*1
            iconP[6, counter]=(i)*2+0+(j)*2*(2*nelx+1)+(2*nelx+1)*2
            iconP[7, counter]=(i)*2+1+(j)*2*(2*nelx+1)+(2*nelx+1)*2
            iconP[8, counter]=(i)*2+2+(j)*2*(2*nelx+1)+(2*nelx+1)*2
            counter += 1

if order==4:
    etc ...

```

and quickly arrived at the following compact form:

```

if order >1:
    om1=order-1
    counter=0
    for j in range(0, nely):
        for i in range(0, nelx):
            counter2=0
            for k in range(0, order):
                for l in range(0, order):
                    iconP[counter2, counter]=i*om1+l+j*om1*(om1*nelx+1)+(om1*nelx+1)*k
                    counter2+=1
            counter += 1

```

The core of the code is rather similar if not identical to other stones (i.e. the loop over elements, the calculation of the elemental matrices, their assembly, and the solve).

What is here somewhat elegant is the projection of the pressure field onto the velocity grid nodes (mostly for plotting purposes). For each element I loop over each velocity node, and evaluate the pressure

shape function at this location, compute the pressure with it and add it in the array q while keeping count of how many contributions there are in total per velocity node.

```

for iel in range(0,nel):
    for i in range(0,mV):
        NNNP[0:mP]=NNP(rVnodes[i],sVnodes[i],order)
        q[iconV[i,iel]]+=np.dot(p[iconP[0:mP,iel]],NNNP[0:mP])
        c[iconV[i,iel]]+=1.

q=q/c

```

Finally, since the vtu format does not support higher order elements, I here chose to only extract the corner values for each element, which translates as follows:

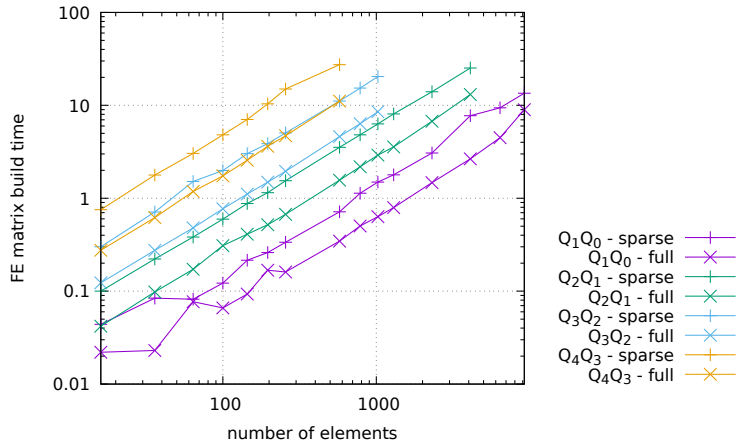
```

vtufile.write("<DataArray _type='Int32' _Name='connectivity' _Format='ascii'>\n")
if order==1:
    for iel in range(0,nel):
        vtufile.write("%d%d%d%d\n" %(iconV[0,iel],iconV[1,iel],iconV[3,iel],iconV[2,iel]))
if order==2:
    for iel in range(0,nel):
        vtufile.write("%d%d%d%d\n" %(iconV[0,iel],iconV[2,iel],iconV[8,iel],iconV[6,iel]))
if order==3:
    for iel in range(0,nel):
        vtufile.write("%d%d%d%d\n" %(iconV[0,iel],iconV[3,iel],iconV[15,iel],iconV[12,iel]))
if order==4:
    for iel in range(0,nel):
        vtufile.write("%d%d%d%d\n" %(iconV[0,iel],iconV[4,iel],iconV[24,iel],iconV[20,iel]))
vtufile.write("</DataArray>\n")

```

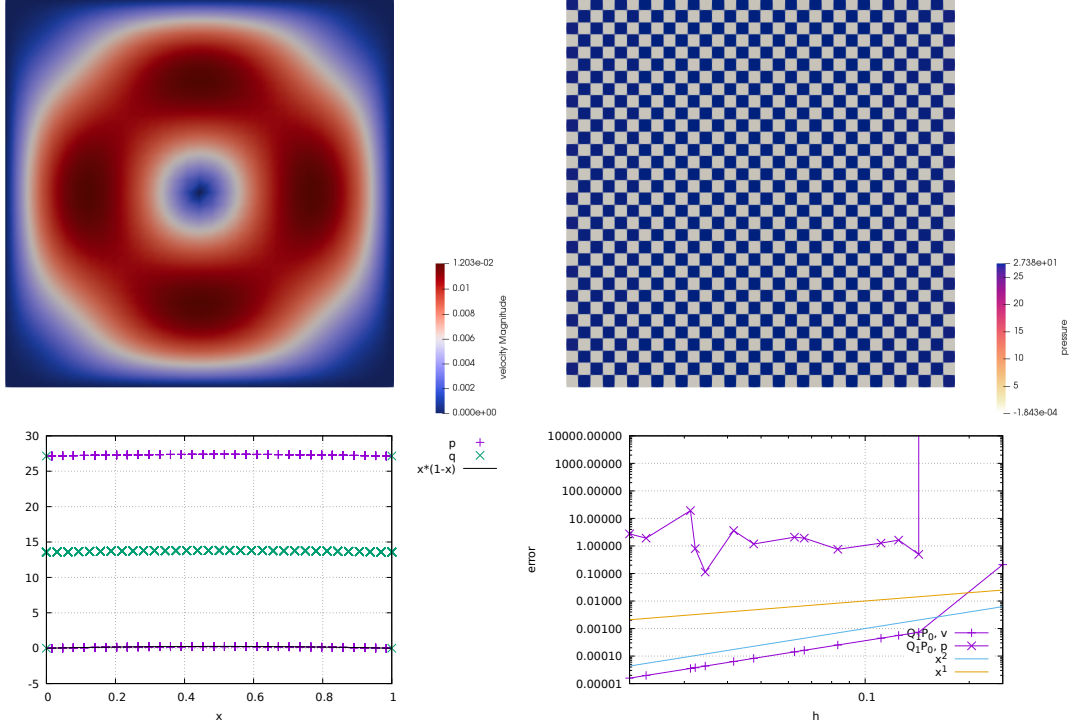
The following results are obtained by running one of the four scripts *script\_errorsX* where X=1,2,3,4. The gnuplot script is to be found in the *images* folder.

The stone implements two ways of building the FE matrix. When the flag *sparse* is false, the  $\mathbb{K}$  and  $\mathbb{G}$  matrices are built as full arrays, later assembled in a larger full array, and then only converted to Compressed Sparse Row if it is passed to the solver. When the flag is true, the global FE matrix is defined as a *lil\_matrix* (a List of Lists) and it grows in size/memory every time a new term is added to it. As shown on the following plot, it is about twice as slow compared to the first option, but it uses only a fraction of the memory that the first one does.



Also not very surprising: the cost of building the FE matrix increases with the order of the used elements. A matrix corresponding to  $100 Q_1 \times P_0$  elements can be built in about 1s, while it will take 7s when  $Q_4 \times Q_3$  elements are used.

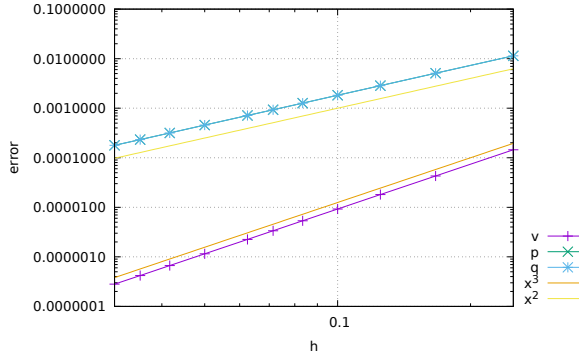
## Results with $Q_1 \times P_0$ element



We see that we recover a second order convergence rate for velocity (as expected) but because of the checkerboard pattern the pressure convergence is simply random. The smoothed pressure  $q$  shows virtually no checkerboard pattern, except on the boundaries. This is a perfect example for the use of more accurate/clever smoothing procedure, see Section 8.12.

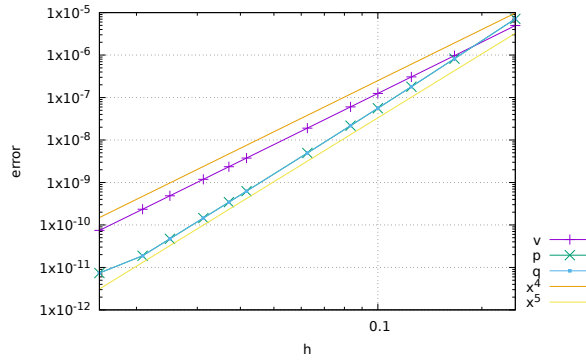
## Results with $Q_2 \times Q_1$ element

We recover the cubic convergence for the velocity error and the quadratic convergence for the pressure:



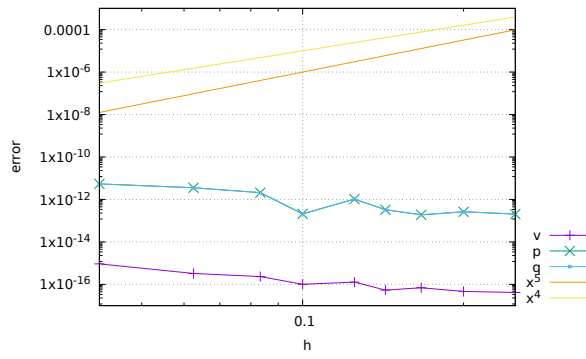
## Results with $Q_3 \times Q_2$ element

The analytical solution is a second order polynomial, which means that the pressure shape functions can adequately represent the solution. We recover a fourth-order convergence for the velocity error and a superconvergent (fifth order) pressure error (but why is it 5th order ?).



## Results with $Q_4 \times Q_3$ element

Rather interestingly, now both velocity and pressure analytical solutions can be represented exactly by their respective polynomial spaces, so that the errors are at machine precision.

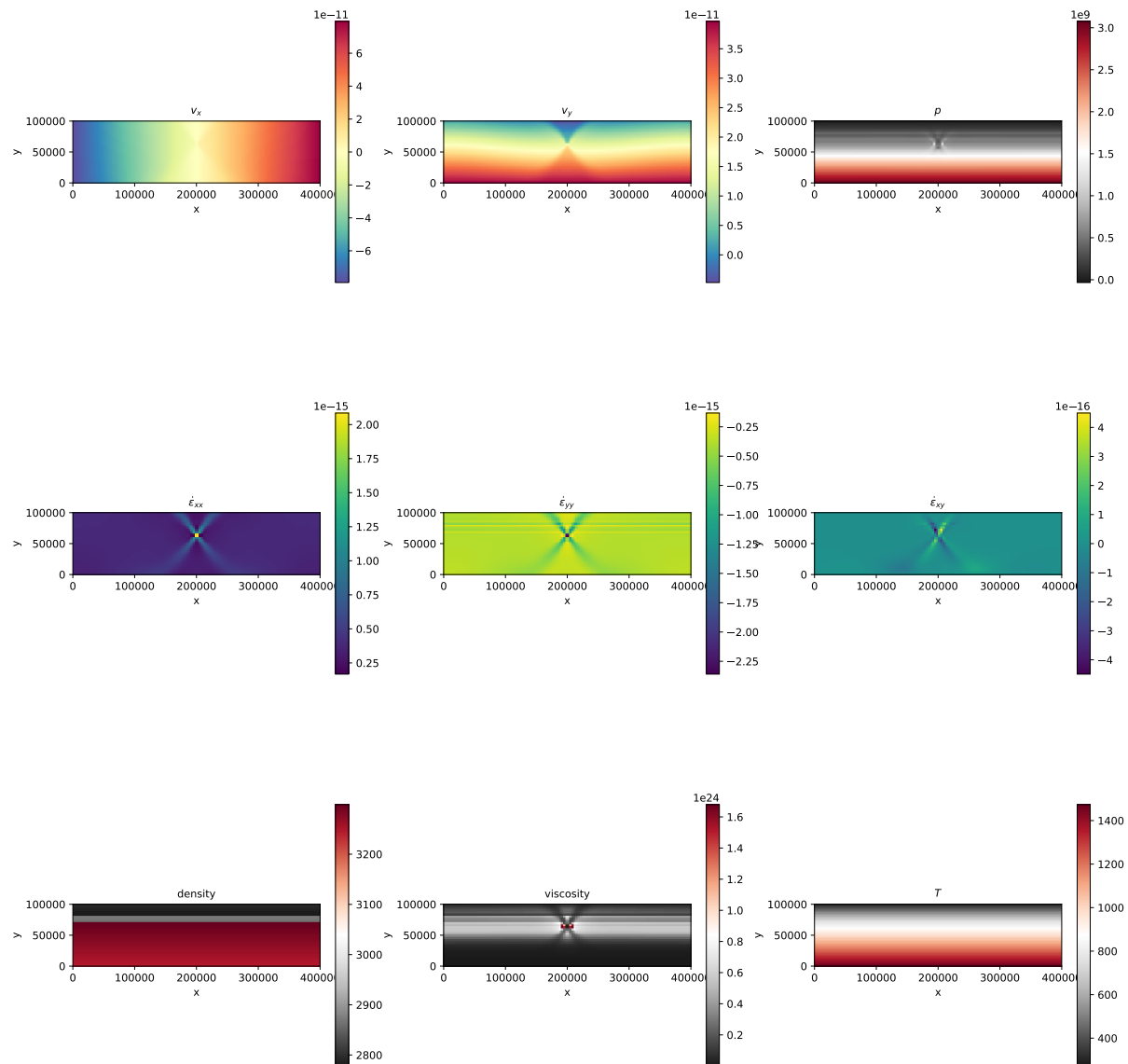


**Stone 49: Consistent Boundary Flux method on D&H benchmark with 4 elements**

Looking at the four different elements

Looking at the influence of the mas matrix lumping

## Stone 50: Lithosphere extension



## Stone 51: Triangular domain benchmark with MINI element

This fieldstone was developed in collaboration with L. van de Wiel.

The following problem is studied in [1353]. The equations that they solve are the thermo-mechanically coupled steady state equations:

$$-\vec{\nabla}p + \Delta\vec{v} + RaTe_y = 0 \quad (1057)$$

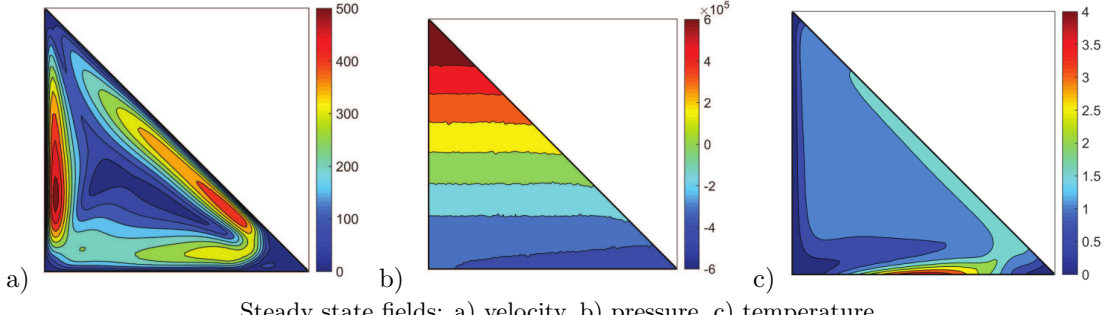
$$\vec{\nabla} \cdot \vec{v} = 0 \quad (1058)$$

$$-\Delta T + \vec{v} \cdot \nabla T = 0 \quad (1059)$$

In our case the code is based on the MINI element (a.k.a.  $P_1^+ \times P_1$ ), see Section 6.2.8 and we set  $Ra = 10^6$ .

The domain is chosen to be the right triangle with vertices  $(0, 0)$ ,  $(1, 0)$ , and  $(0, 1)$ . The boundary is considered to be solid walls (no-slip). For the temperature, a sinusoidal heat source is enforced on the bottom boundary with a Dirichlet condition ( $T(x) = 2(1 - \cos(2\pi x))$ ), the left wall is set to a constant temperature of zero, and the hypotenuse wall is perfectly insulated so that a Neumann boundary condition is appropriate.

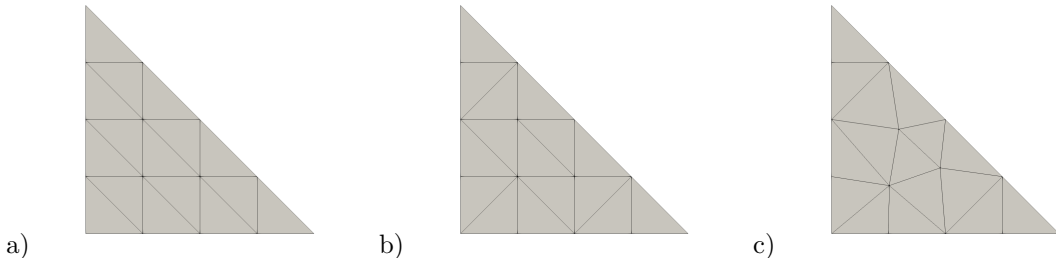
The steady state velocity pressure and temperature fields as shown in [1353] are as follows:



Steady state fields: a) velocity, b) pressure, c) temperature.

Although it is not mentioned in the original article it appears that the pressure field has been normalised so that  $\langle p \rangle = \int_{\Omega} pdV = 0$ .

As opposed to the mesh presented in [1353] I build a regular mesh. An example of such a mesh is shown hereunder (a) for  $n = 5$  (the number of nodes per side of the triangular domain). In order to generate a mesh which is more isotropic some edges between triangles can be flipped (b). Note that this mesh can also be modified in such a way that the position of nodes inside the domain is perturbed by a small random value (c). In what follows I denote by  $h$  the distance between nodes on the horizontal (or vertical) boundaries, i.e.  $h = L_x/(n - 1) = L_y/(n - 1)$ .



a) regular mesh for  $n=5$ . b) flipped edges mesh. c) randomized+flipped edges mesh.

Since I am solving for the steady-state solution I set the mass matrix in the heat transport part of the code to zero. However, since I am solving the Stokes equations and the heat transport equation alternatively until convergence is reached, it is well known that this approach does not converge fast (if at all). I then implement a simple relaxation scheme [2716]. After I have solved for velocity (using the most recent temperature field in the rhs), I do:

$$\vec{v}^k = \gamma \vec{v}^k + (1 - \gamma) \vec{v}^{k-1}$$

and after having solved for temperature having used the most recent velocity field, I do the same for temperature:

$$T^k = \gamma T^k + (1 - \gamma) T^{k-1}$$

where the relaxation parameter  $\gamma$  is between 0 and 1.

Additionally I measure:

- the Nusselt number defined by

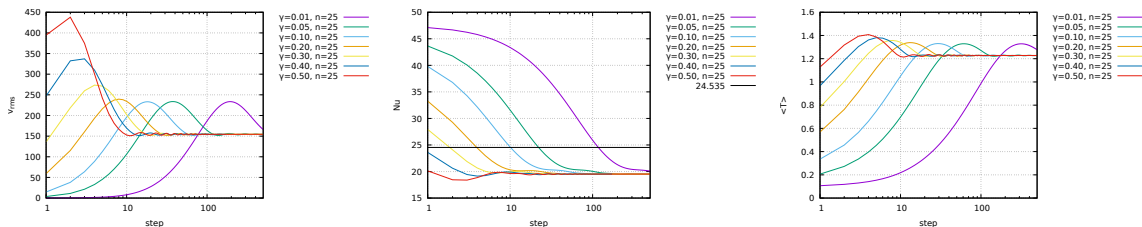
$$Nu = \int_{y=0} \vec{\nabla} T \cdot \vec{n} dS = - \int_{x=0}^{x=1} \frac{\partial T}{\partial y} dx$$

It is reported to be 24.535 in [1353].

- the temperature on the hypotenuse.
- the root mean square velocity
- the mean temperature  $\langle T \rangle = |\Omega|^{-1} \int_{\Omega} T dV$

### On the importance of the relaxation parameter $\gamma$

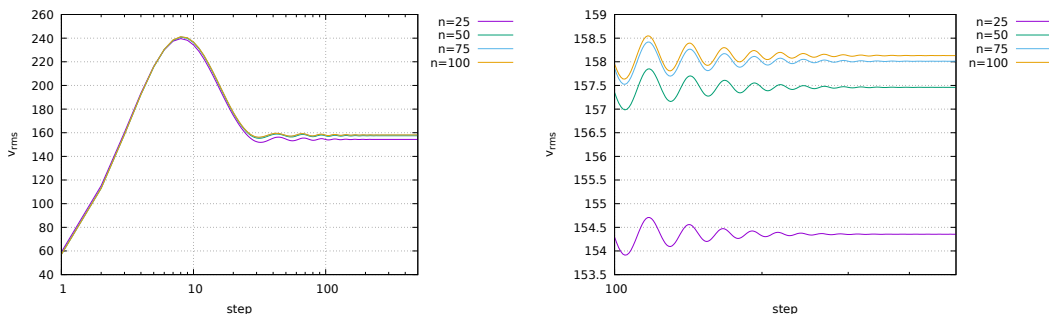
In what follows the internal node coordinate randomness is switched off. I have run the model for various values of  $\gamma$  for  $n = 25$ , and results are shown on the following figures. We see that all simulations seem to converge to the same steady state, which is very reassuring. However, it looks like too small a value of  $\gamma$  delays greatly the convergence and too large a value also seems detrimental. In light of this, I have chosen  $\gamma = 0.2$  for all what follows.

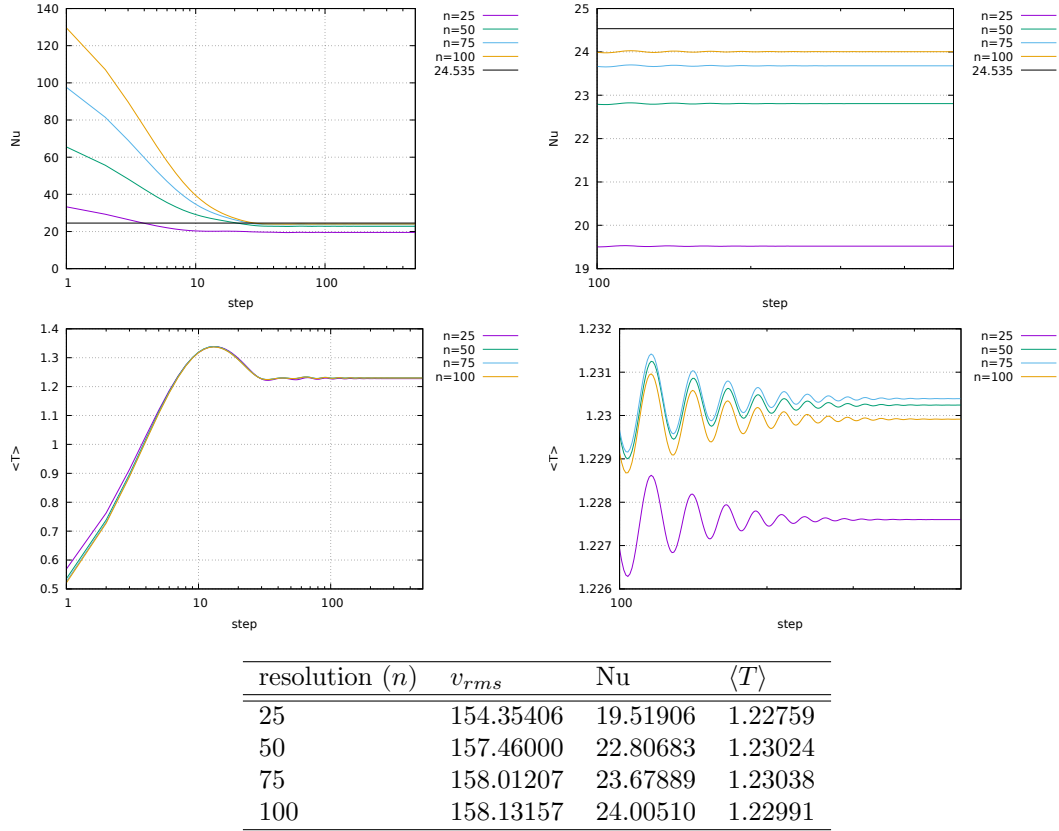


Left to right: Root mean square velocity, Nusselt number and average temperature as a function of the iteration counter.

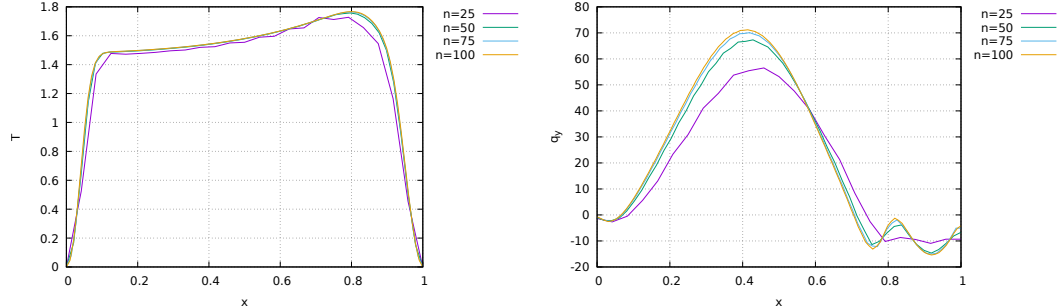
### On the influence of mesh resolution

I now explore the influence of the mesh resolution on the results and run steady state calculations for  $n = 25, 50, 75, 100$ .

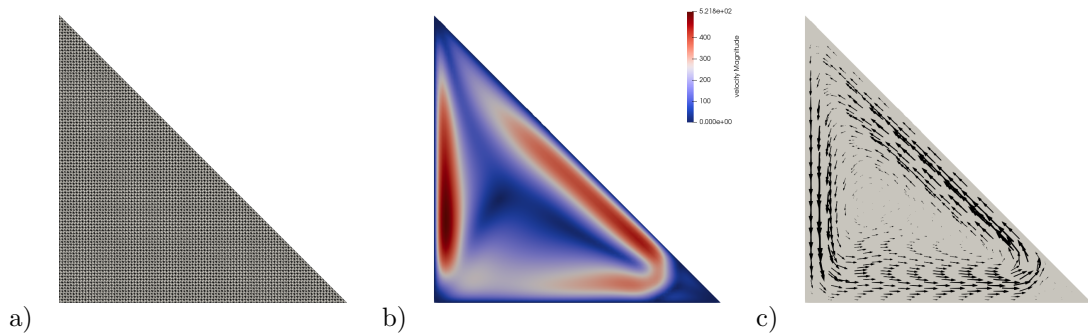


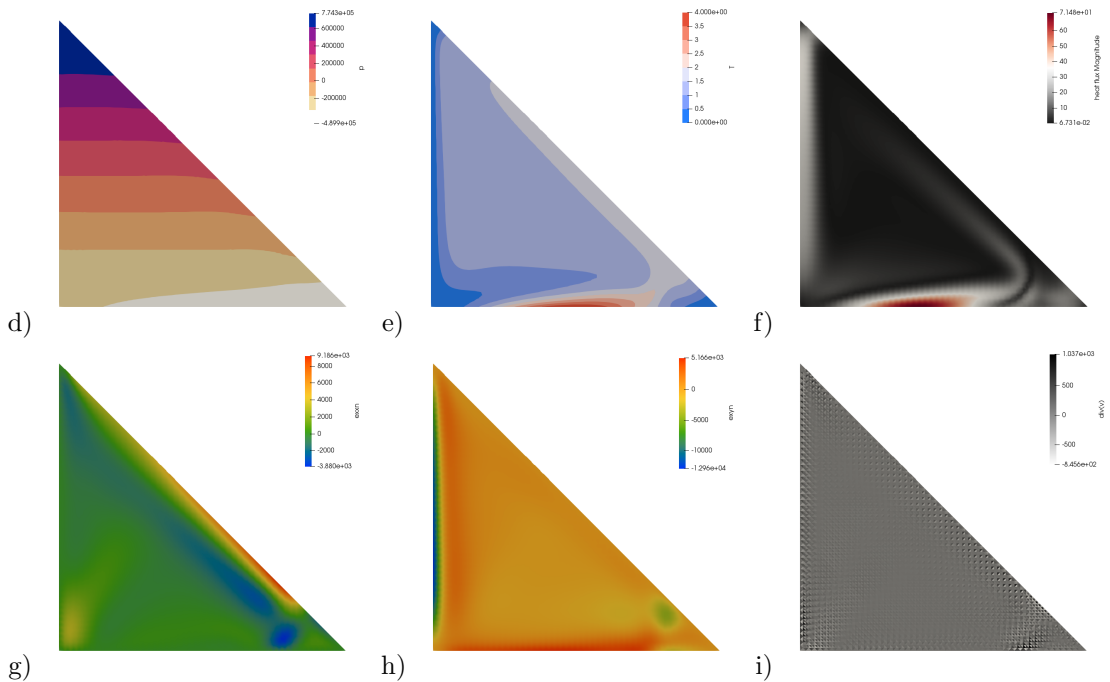


The following two plots show the temperature along the hypotenuse (as a function of  $x$  for simplicity) at steady-state and the heat flux measured at the bottom.



Finally, here are the fields for  $n = 100$  at steady state:





Steady state fields: a) grid ( $n=100$ ), b,c) velocity, d) pressure, e) temperature, f) heat flux, g)  $\dot{\varepsilon}_{xx}$ , h)  $\dot{\varepsilon}_{xy}$ , i) velocity divergence measured in the middle of the element.

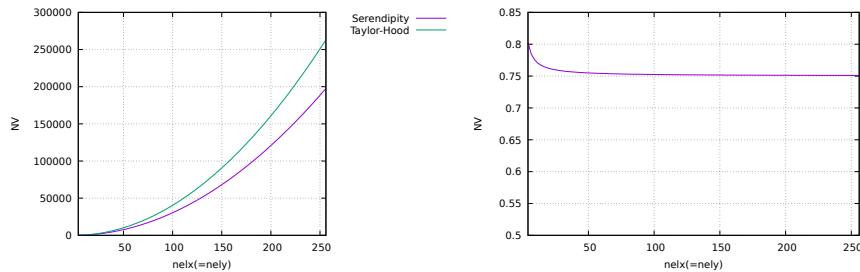
## Stone 52: Serendipity element in 2D

In order to test the grid point and connectivity algorithms, we use this simple  $4 \times 3$  element mesh:

Q_2 X Q1 (serendipity)	Q_2 X Q1 (regular)
15--47--16--48--17--49--18--50--19	54--55--56--57--58--59--60--61--62
	:   :   :   :
42 43 44 45 46	45..46..47..48..49..50..51..52..53
	:   :   :   :
10--38--11--39--12--40--13--41--14	36--37--38--39--40--41--42--43--44
	:   :   :   :
33 34 35 36 37	27..28..29..30..31..32..33..34..35
	:   :   :   :
05--29--06--30--07--31--08--32--09	18--19--20--21--22--23--24--25--26
	:   :   :   :
24 25 26 27 28	09..10..11..12..13..14..15..16..17
	:   :   :   :
00--20--01--21--02--22--03--23--04	00--01--02--03--04--05--06--07--08
iel= 0:	iel= 0
node 0 : 0 at pos. 0.0 0.0	node 0 : 0 at pos. 0.0 0.0
node 1 : 1 at pos. 1.0 0.0	node 1 : 2 at pos. 1.0 0.0
node 2 : 6 at pos. 1.0 1.0	node 2 : 20 at pos. 1.0 1.0
node 3 : 5 at pos. 0.0 1.0	node 3 : 18 at pos. 0.0 1.0
node 4 : 20 at pos. 0.5 0.0	node 4 : 1 at pos. 0.5 0.0
node 5 : 25 at pos. 1.0 0.5	node 5 : 11 at pos. 1.0 0.5
node 6 : 29 at pos. 0.5 1.0	node 6 : 19 at pos. 0.5 1.0
node 7 : 24 at pos. 0.0 0.5	node 7 : 9 at pos. 0.0 0.5
	node 8 : 10 at pos. 0.5 0.5

We see that the serendipity element-based mesh counts only 51 nodes, as opposed to 63 for its counterpart.

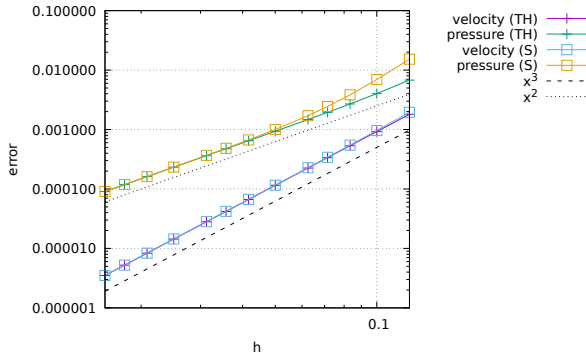
Setting  $nelx = nely$ , we can look at the number of velocity nodes for each as a function of  $nelx$ , as shown hereunder:



Looking at the ratio between both, we see that ultimately at high resolution, a mesh composed of serendipity elements will count 25% less nodes than a mesh with Taylor-Hood elements. Since there is not free lunch, what is the price paid in terms of accuracy when using the cheaper serendipity?

The shape functions and their derivatives are in Section 4.5.3.

Although the vtk format does not understand the  $Q_2$  element in 2D or 3D, it surprisingly does understand the serendipity element in 2D (type=23) and 3D (type=25).

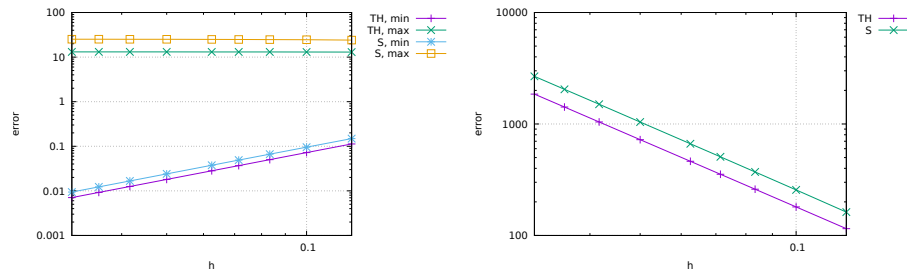


It looks like the serendipity element yields the same errors and error convergence rates as its Taylor-Hood counterpart. Since it is cheaper in terms of dofs, one could think that it should be preferred. However, most modern codes use an iterative solver approach to solve the discretised Stokes problem, and often the  $\mathbb{K}$  matrix (which is SPD) is 'solved' with a conjugate gradient solver. The convergence of this type of solver depends on the condition number of the matrix itself, i.e. the ratio of the largest and smallest eigenvalues. Note that this is rather trivial with Python:

```
print('condition_number:', nel, linalg.cond(K_mat))
```

However, since I was also curious about the values of the eigenvalues, I implemented it as follows:

```
eigvals, eigvecs = linalg.eig(K_mat)
print('eigenvalues:', nel, eigvals.min(), eigvals.max())
```



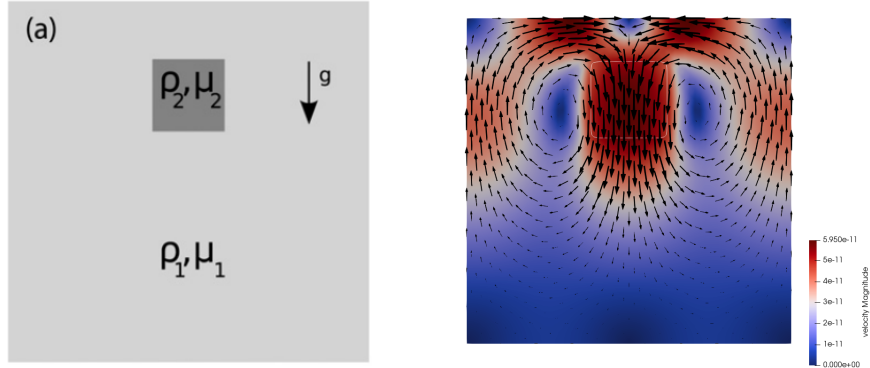
Left: min and max eigenvalues for both types of elements as a function of  $h$ ; Right: condition number

As it turns out, the condition number is twice as high for the serendipity element, which means that the CG would have to iterate more to arrive at the solution, thereby offsetting the benefit of less dofs.

## Stone 53: the sinking block benchmark

[https://github.com/cedrict/fieldstone/tree/master/python\\_codes/fieldstone\\_53](https://github.com/cedrict/fieldstone/tree/master/python_codes/fieldstone_53)

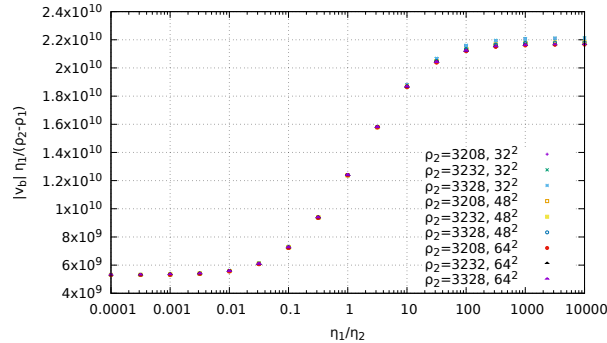
This simple benchmark provides challenging numerical experiments dealing with large viscosity variations within the simulation domain. It appears in [953] and consists of a bulk of fluid 1 ( $\rho_1, \eta_1$ ) in which a block of fluid 2 ( $\rho_2, \eta_2$ ) falls under its own weight. The domain is a square of size  $L_x = L_y = 512\text{km}$  and the block is initially centred at point ( $x = 256\text{ km}, y = 384\text{ km}$ ) with size  $128 \times 128\text{ km}$ :



Left: setup. Right: velocity field for  $\rho_2 = 3208$ ,  $\eta_1 = 10^{21}$  and  $\eta_2 = 10^{22}$ .

The simulation is carried out on  $32 \times 32$ ,  $48 \times 48$  and  $64 \times 64$  grids. Free slip boundary conditions are imposed on all sides of the domain. In all experiments the density of the surrounding fluid is  $\rho_1 = 3200\text{kg/m}^3$ . The velocity  $v_b$  of the falling block is measured in its centre (note that due to symmetry the horizontal component should be zero).

As explained in [2528], following physical intuition, one expects the velocity  $v_b$  of the block to (a) decrease when the viscosity of the surrounding medium  $\eta_1$  increases; (b) increase with the density contrast  $\rho_2 - \rho_1$ . The quantity  $v_b \eta_1 / (\rho_2 - \rho_1)$  is therefore monitored and shown hereunder as a function of the viscosity ratio.



Series of experiments have been conducted with  $\rho_2 = 3208, 3232, 3328$ ,  $\log_{10}(\eta_1) = 20, 21, 22$  and  $\log_{10}(\eta_2) = 18, 18.5, 19, \dots, 22.5, 23, 23.5, 24$ , all with 3 mesh resolutions.

All experimental points line up on a single curve which further indicates that the code can deal with gravity driven simulations in the presence of large viscosity contrasts. These results have been successfully compared with those obtained with ASPECT with the same setup.

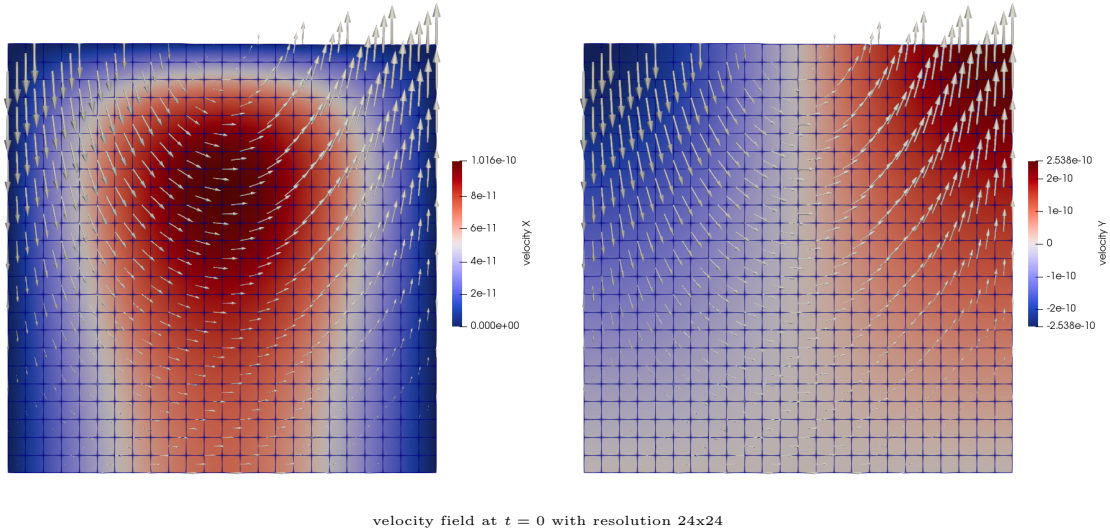
## Stone 54: ALEs

[https://github.com/cedrikt/fieldstone/tree/master/python\\_codes/fieldstone\\_54](https://github.com/cedrikt/fieldstone/tree/master/python_codes/fieldstone_54)

This stone implements three different free surface/mesh deformation algorithms. The first one has all the nodes move with the computed velocity (Lagrangian method) and is coined 'method 1'. The second one ('method 2') only has the top row of nodes moving with the computed velocity, while all the nodes underneath are static (this is obviously not a viable method for large deformations). The third one ('method 3') is the method used in ASPECT and described in Rose et al (2017) [2197]. Its implementation is described in Section 8.1.

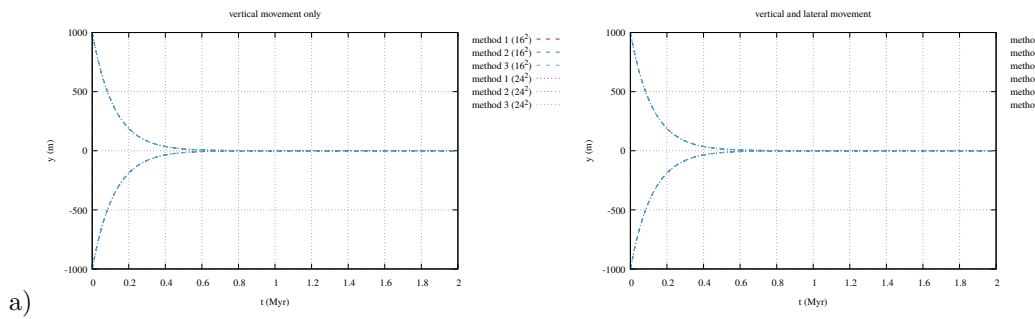
### Experiment 1 - relaxation of topography

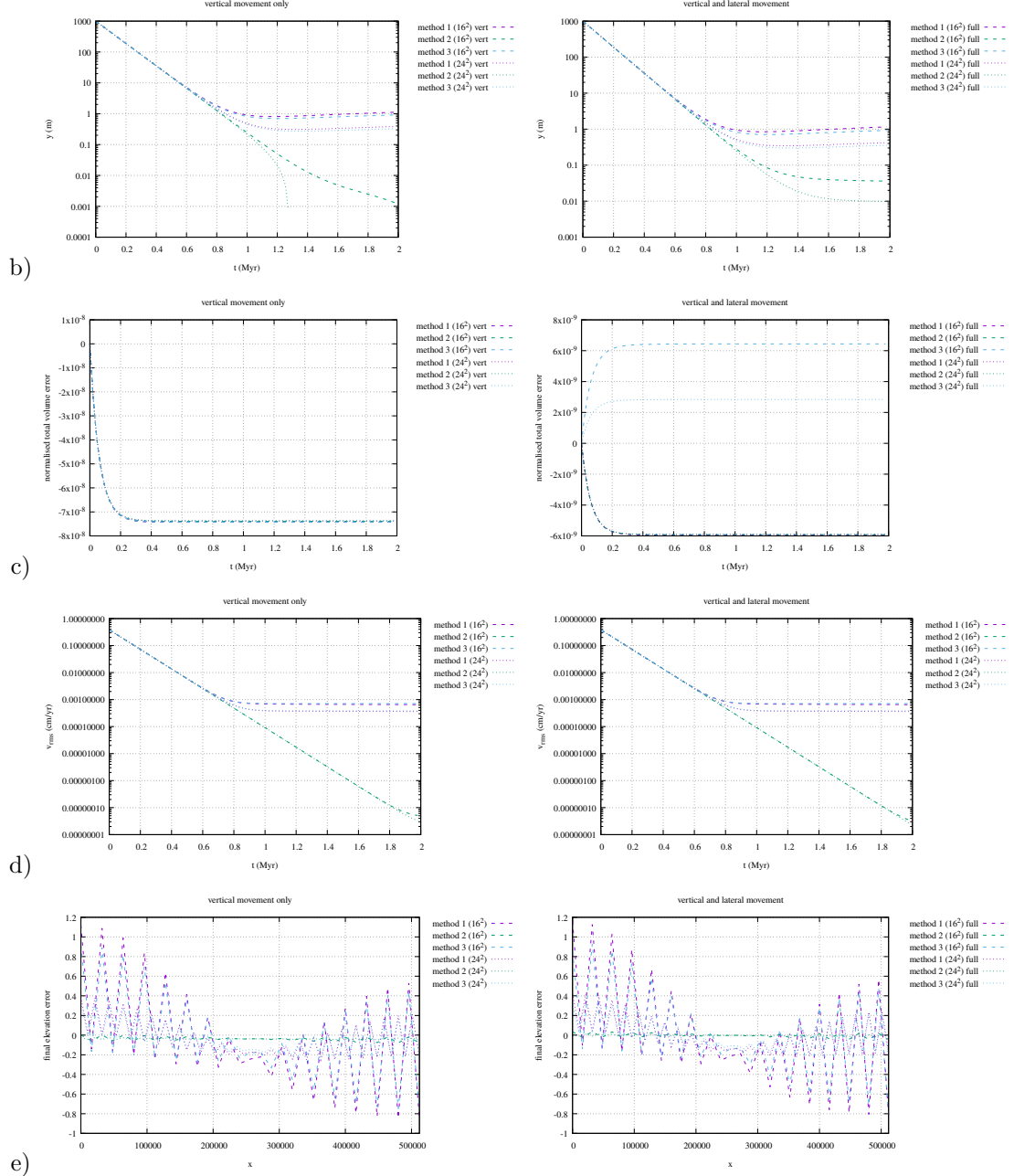
The domain is a 2D Cartesian box of size  $512 \times 512$  km, with free slip on left, bottom and right sides, free surface at the top. Mantle material characterised by  $\rho_m = 3200$  and  $\eta_m = 10^{22}$ . Gravity is vertical and Earth like. The surface is perturbed at startup by  $\delta y = A \cos(\pi x / L_x)$  with  $A=1$  km. 200 time steps with  $\delta t = 10$  kyr are carried out. The root mean square velocity, the total volume of the domain, the min/max elevation values of the surface are recorded over time.



velocity field at  $t = 0$  with resolution  $24 \times 24$

The results hereunder are obtained for all three methods at two different resolutions ( $16 \times 16$  and  $24 \times 24$  elements). The plots on the left column are obtained with the movement of the top nodes being constrained in the vertical direction, while the plots on the right column are obtained with nodes being allowed to move in both  $x$  and  $y$  directions (note that for method 3 the normals are not -yet- computed with the method of Eq. 49 in [2197] but instead by a simple geometric rule).

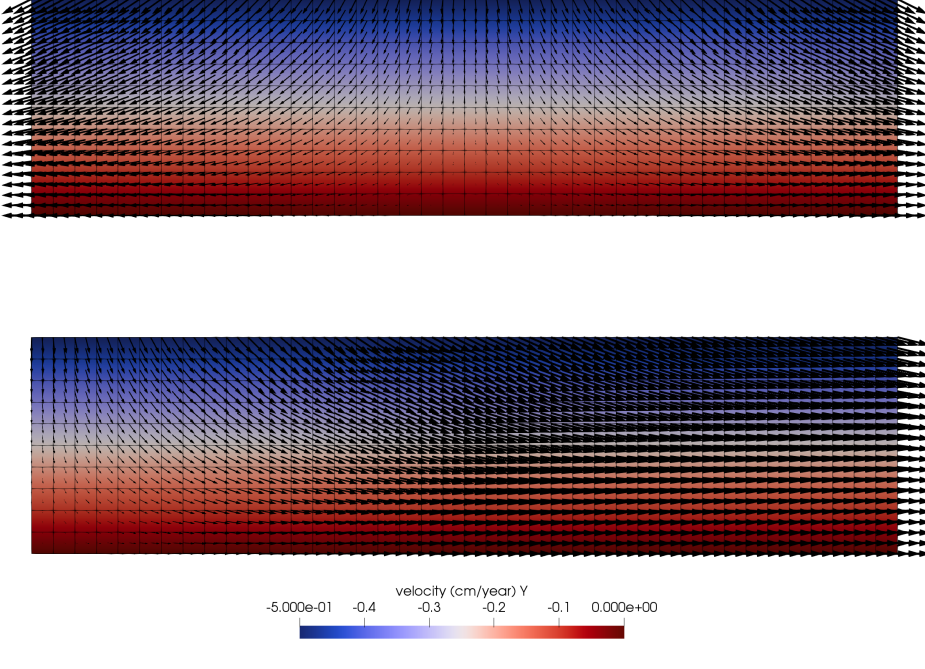




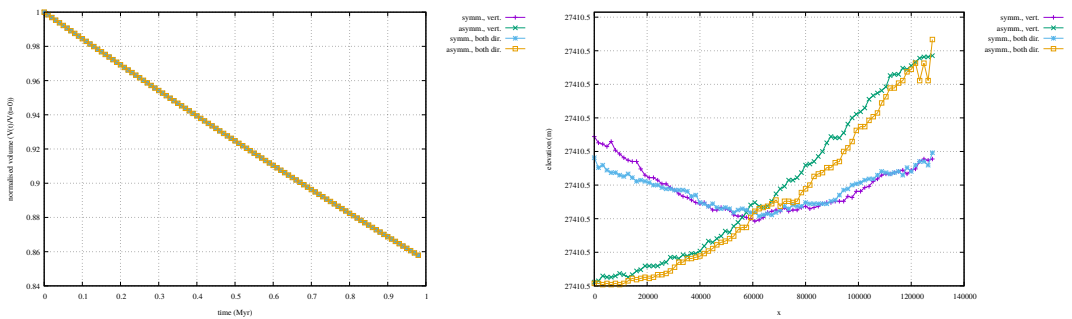
a) min/max of free surface topo as a function of time; b) free surface topo maximum (in log scale) as a function of time; c) measured volume of the domain with numerical quadrature normalised by the expected volume  $L_x L_y$ ; d) root mean square velocity as a function of time; e) final elevation at the 200th time step.

## Experiment 2,3 - extension

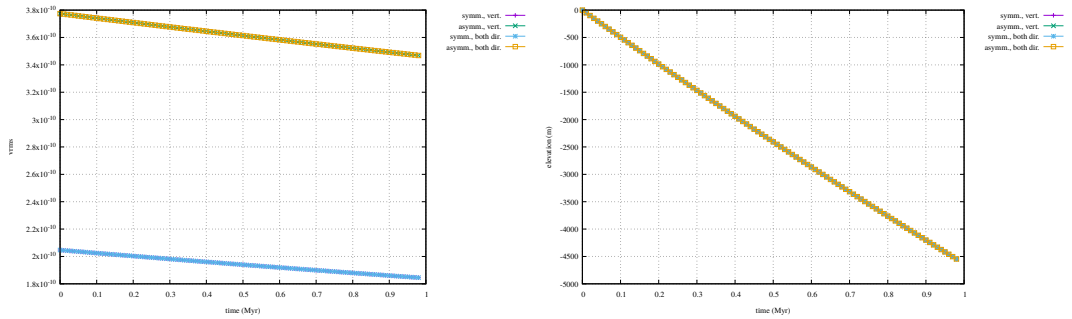
We now consider a rectangular domain (crust sized) of  $128 \times 32\text{km}$ , discretised by means of  $40 \times 10$  elements. The fluid is identical to the one above and so is gravity. Extensional boundary conditions are applied. In the first case, a  $1\text{cm/yr}$  horizontal velocity is applied on both sides, while in the second case a  $2\text{cm/yr}$  velocity is applied on the right while  $0$  is prescribed to the left. Free slip conditions are otherwise prescribed on the sides and bottom. 100 time steps are carried out with  $\delta t = 10^4\text{yr}$ . Only method 3 is used here.



Despite the asymmetry in the boundary conditions, we expect the same evolution of the domain geometry. This is indeed what we recover with surprising accuracy. 'vert' stands for only vertical movement allowed (i.e.  $n_x = 0$ ,  $n_y = 1$ ) while 'both dir' stands for the use of dynamically computed normal vectors (based on geometrical consideration).



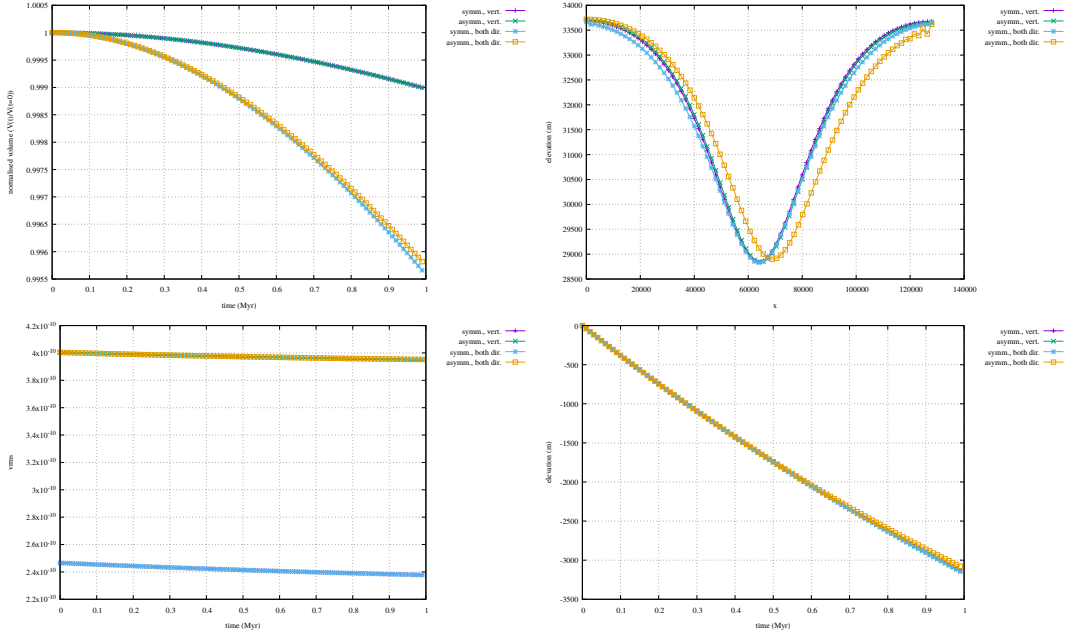
Left: time evolution of the normalised volume for both boundary condition types; Right: surface at the end of the simulation.



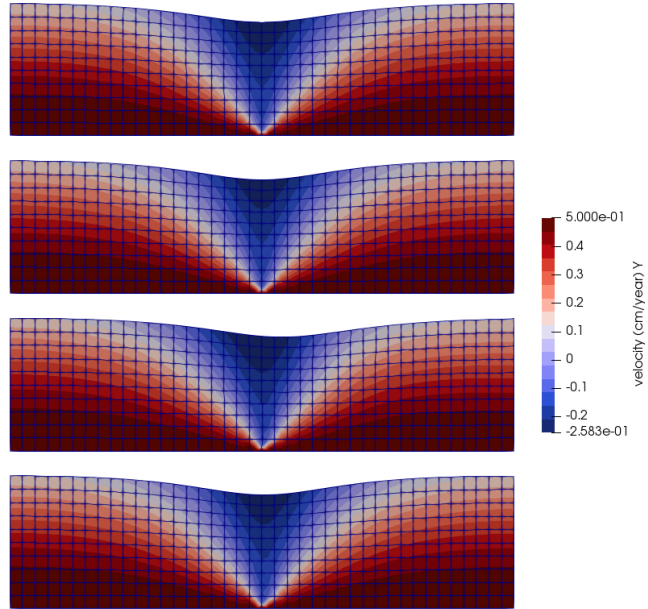
Left: Root mean square velocity as a function of time; Right: time evolution of the elevation (min and max virtually indistinguishable).

### Experiment 4,5 - extension with bottom inflow

This is the same setup as above, but we now impose an influx boundary condition at the bottom:  $v = 0.5\text{cm}$  (this balances the outflux exactly) and the horizontal component at the bottom is set to the left value (-1 or 0 cm/yr) for  $x \leq L_x/2$  and to the right value +1 or +2 cm/yr for  $x \geq L_x/2$ .

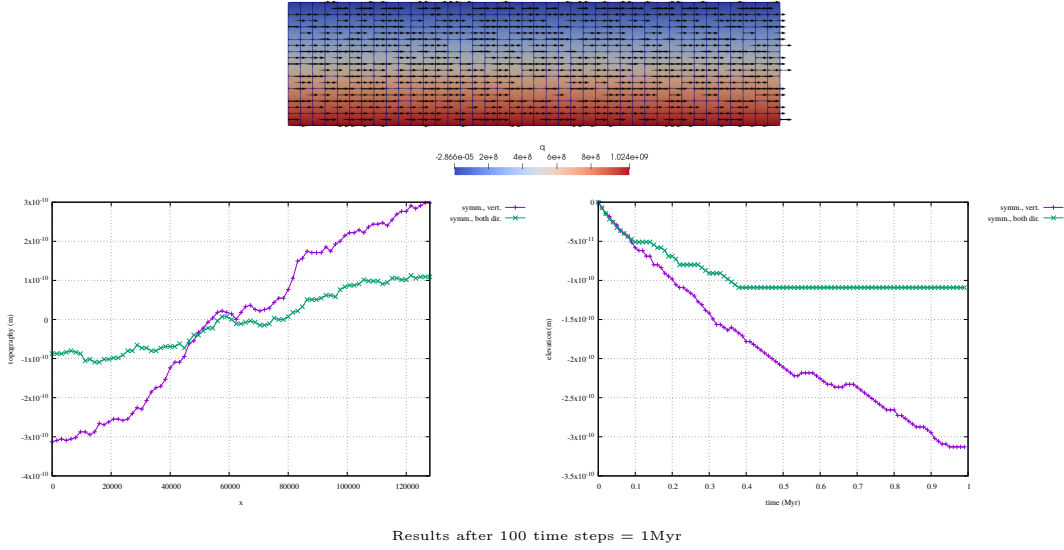


We can conclude that the 'vertical movement only' conserves volume/mass better and the free surface remains symmetrical unless the full normal is used which is simply explained by having  $\vec{v} \cdot \vec{n}$  as a boundary condition: in the asymmetric extension case, the velocity is always to the right while the normal has an  $x$  component which is negative and positive, therefore introducing an asymmetry in the surface boundary conditions.



Top to bottom: symmetric extension, full normal vector; symmetric extension, vertical normal vector; asymmetric extension, full normal vector; asymmetric extension, vertical normal vector

## Experiment 6 - pure advection test



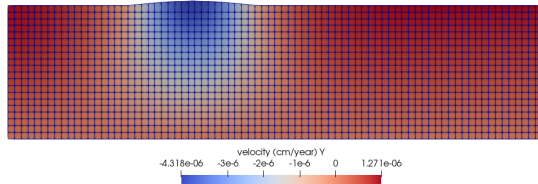
## Experiment 7 - pure advection test of a cosine bump

The initial topography bump is given by

$$y(x) = A \left[ 1 + \cos \left( \frac{x - x_0}{w} \pi \right) \right]$$

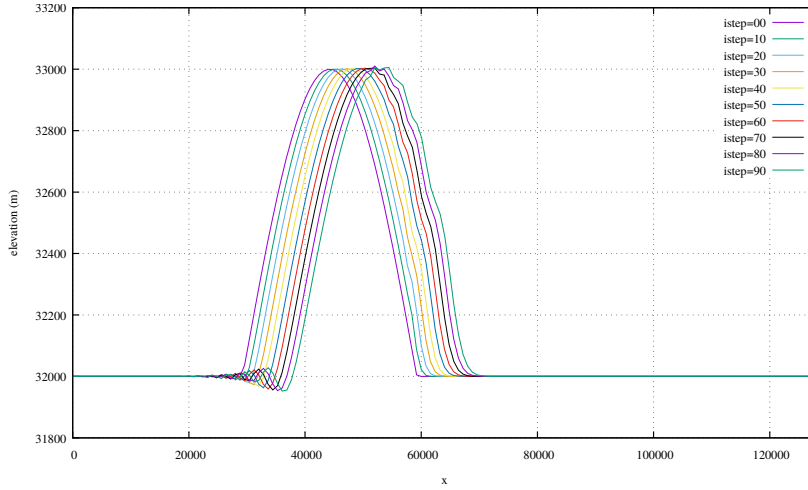
with  $A = 1000\text{m}$ ,  $x_0 = 0.345678L_x$  and  $w = 15\text{km}$ . This is a somewhat ideal case since the transition from flat to bump is very smooth.

The viscosity is set to  $10^{26}\text{Pa}\cdot\text{s}$  so that the velocity of the viscous relaxation of the topography is negligible with regards to the advection velocity (+1cm/yr on left and right boundaries). I also choose a resolution of 80x20 elements.

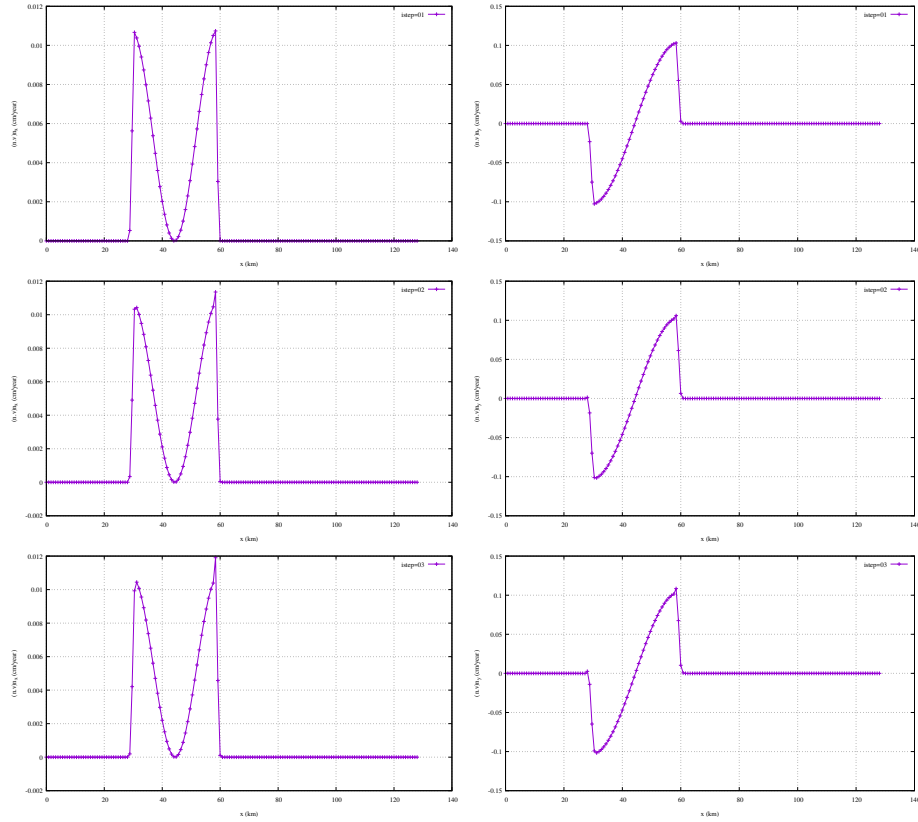


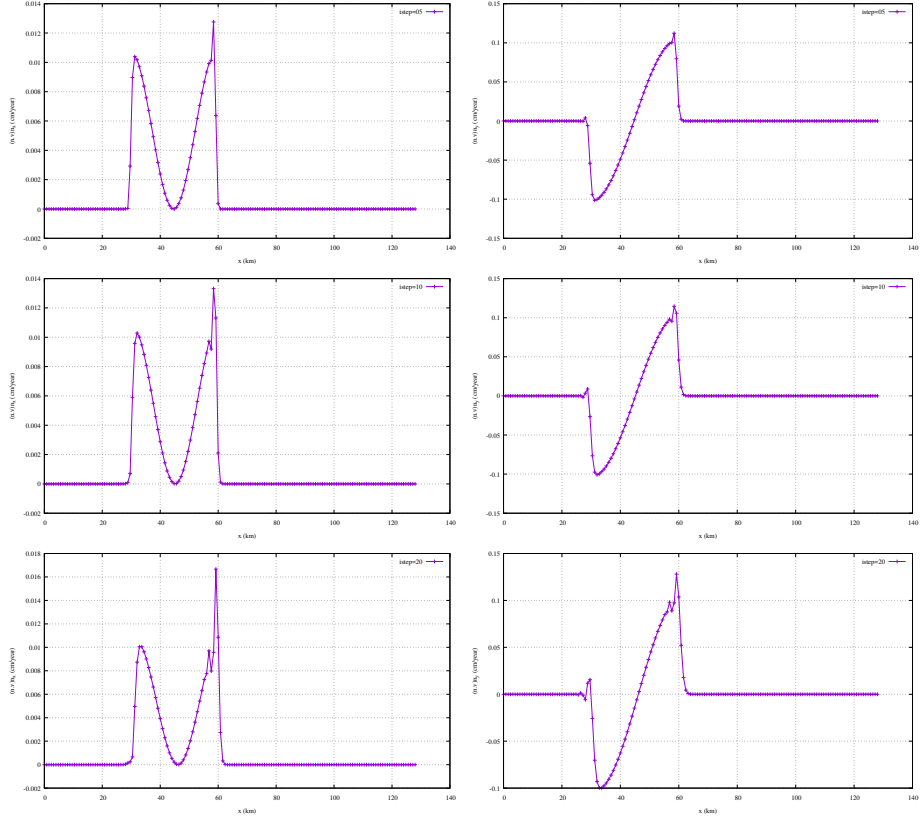
If only the vertical normal is used then *nothing* moves since the velocity is always perpendicular to the normal.

What follows is obtained when the full normal is used. After 20 timesteps the topography has been advected and we already observe some visible asymmetry (and oscillations) on the surface:



On the following plots the left column shows  $(\vec{v} \cdot \vec{n})n_x$  as a function of the  $x$ -coordinate and the right column shows  $(\vec{v} \cdot \vec{n})n_y$ , both for timesteps 1,2,3,5,10,20. Both quantities form the boundary conditions for the mesh deformation. Since I have chosen  $x_0$  such that it does not fall on a node, the initial topography is *not* symmetric and therefore the normal vectors at the nodes on the left and right of the peak are not identical. From the second timestep (the first one for which the free surface algo uses a non zero Stokes velocity as boundary condition) we see that both components  $(\vec{v} \cdot \vec{n})n_x$  and  $(\vec{v} \cdot \vec{n})n_y$  are asymmetric!

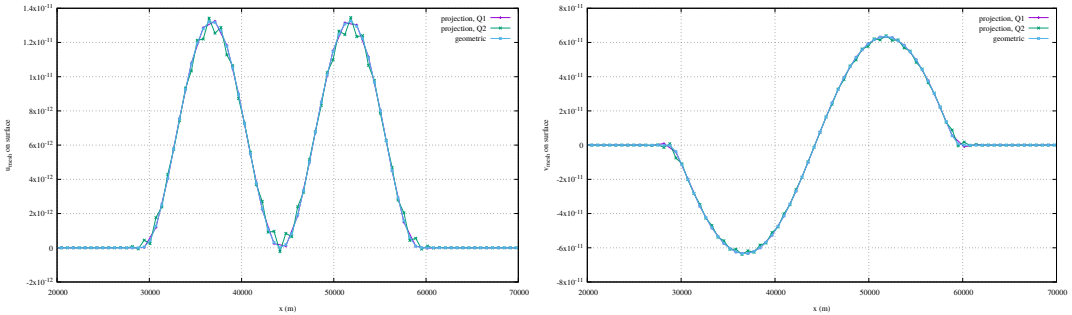


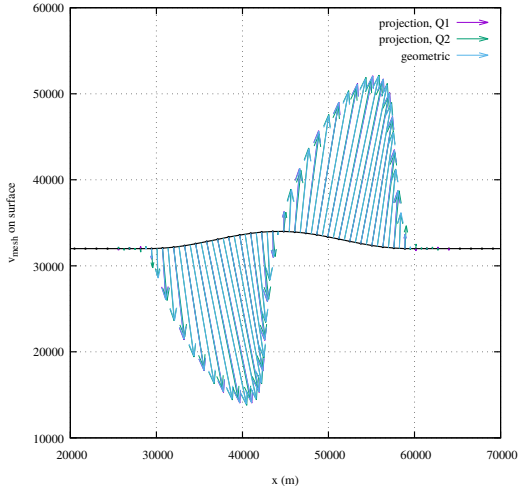


The inescapable conclusion is that the algorithm (as it is now implemented with the normal vector) is incapable of advecting a bump.

In what follows, the Stokes system is solved once, and the obtained velocity is used to compute the mesh velocity boundary condition for the Laplace system. The resolution is set to 100x25. I have implemented the  $L_2$  projection approach of [2197] for both Q1 and Q2 elements. For such a smooth topography the Q1 and geometrical approach (i.e. using geometrically computed normal vectors) are very similar although Q1 produces tiny undershoots. Q2 however generates oscillations which makes the computed velocity not suited as a boundary condition to move surface nodes.

From left to right: horizontal component, vertical component, and vector form of the computed mesh velocity bc.

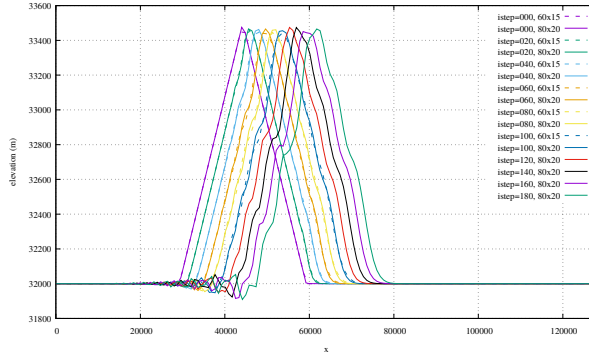
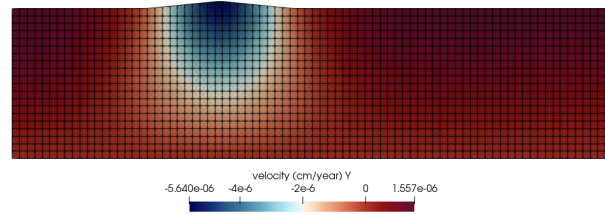


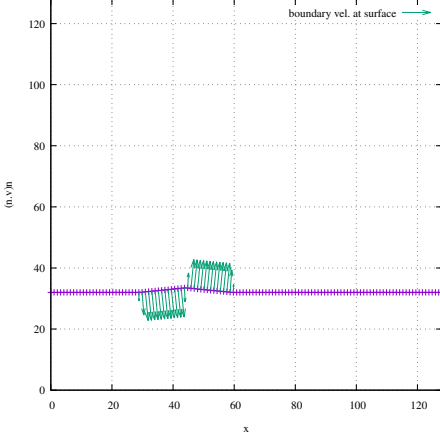


I haven't used any of the projections to carry out timestepping.

### Experiment 8 - pure advection test of a pyramidal bump

This is a nearly identical experiment as the previous one, but now the bump is composed of two straight lines, of slopes  $\pm 0.1$ . Pyramid centered at  $x = 0.345678L_x$ , of half width 15km.  $\rho = 3000$ ,  $\eta = 10^{26}$ . Resolution 60x15. +1cm/yr prescribed on left and right.  $dt=10\text{kyr}$ .

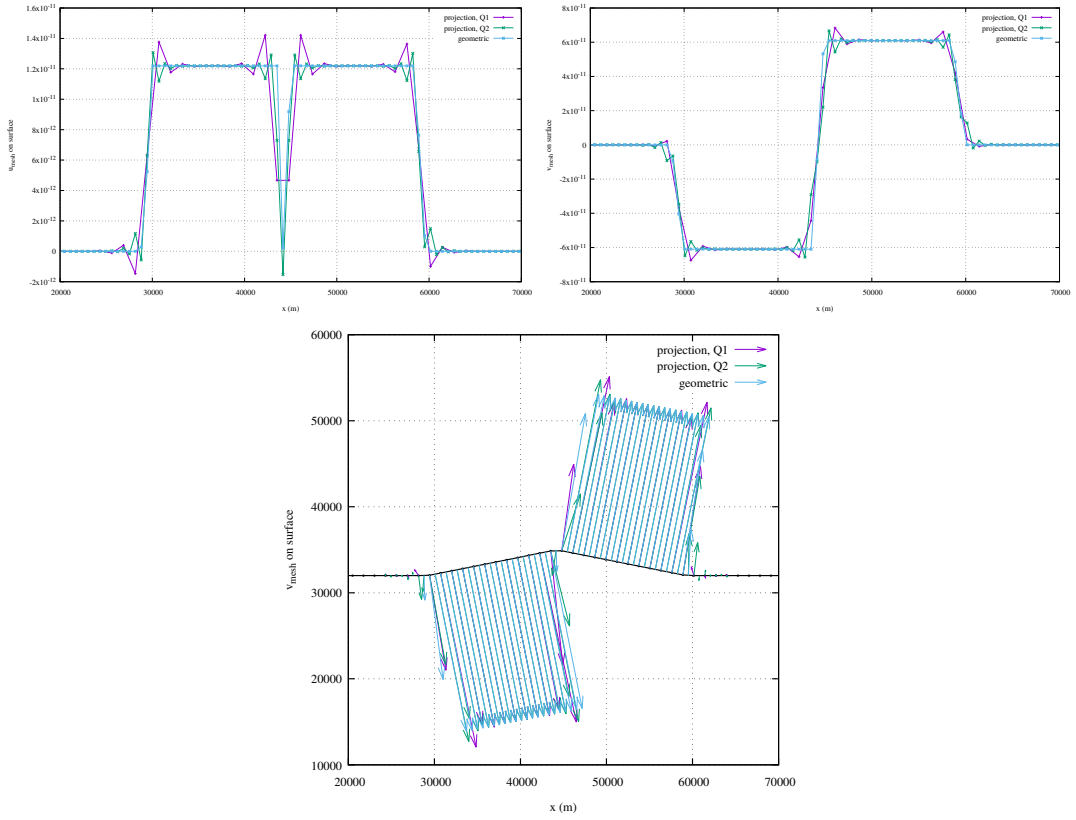




Results are not crazy bad, but we should be able to do better ... the pyramid becomes more and more deformed after only 20km of advection (but surprisingly retains its height).

In what follows, the Stokes system is solved once, and the obtained velocity is used to compute the mesh velocity boundary condition for the Laplace system. The resolution is set to 100x25. I have implemented the  $L_2$  projection approach of [2197] for both Q1 and Q2 elements. For such a broken line topography the geometrical approach (i.e. using geometrically computed normal vectors) is better. Q1 and Q2 both produce under/overshoots/oscillations with no clear winner.

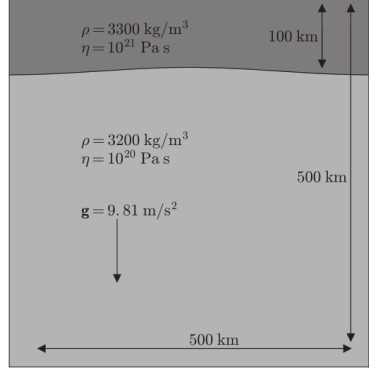
From left to right: horizontal component, vertical component, and vector form of the computed mesh velocity bc.



I haven't used any of the projections to carry out timestepping.

### Experiment 9 - Rayleigh-Taylor instability

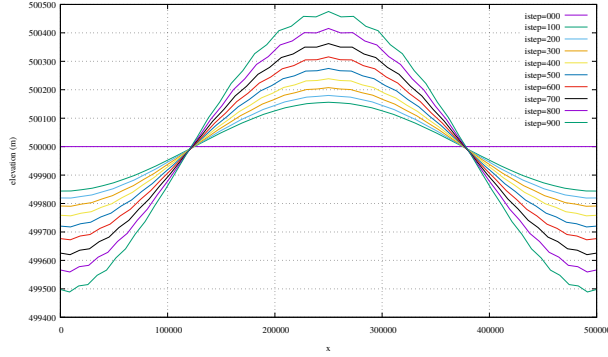
The setup is as follows:



The sinusoidal perturbation is given by

$$y(x) = 400e3 - 500 \cos(2\pi x/L_x)$$

Because I do not have compositional fields or markers implemented in this code I have to align the mesh with the initial sinusoidal perturbation and run the model in Lagrangian mode. Also, as shown in [1398], this experiment is prone to drunken sailor instabilities and I have therefore fixed  $dt=1000\text{yr}$ . As a consequence, the model will run until elements become too distorted.



## Stone 55: Subduction as a thin-sheet problem

This stone was partially contributed by E. van der Wiel.

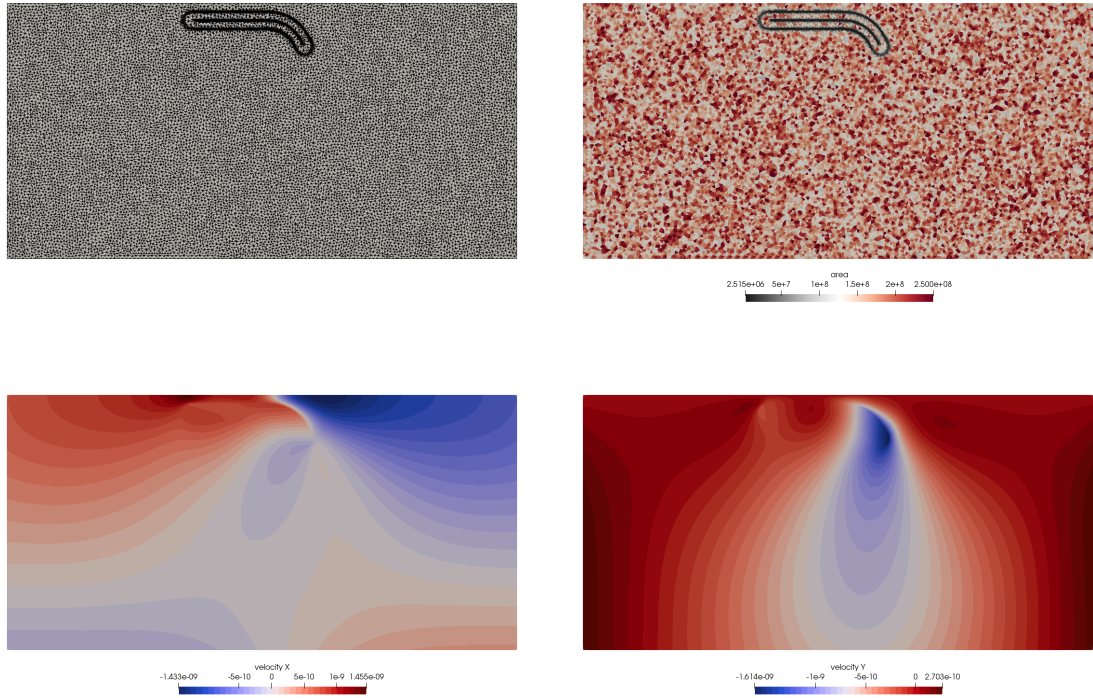
[https://github.com/cedrict/fieldstone/tree/master/python\\_codes/fieldstone\\_55](https://github.com/cedrict/fieldstone/tree/master/python_codes/fieldstone_55)

Parameters for the setup are defined in *parameters.py*. This file is used in *generate\_nodes.py* which produces the *subd.node* file which contains the coordinates of all key points on the boundary of the domain and along the material interfaces. This file is then further processed by the triangle program<sup>88</sup> as follows:

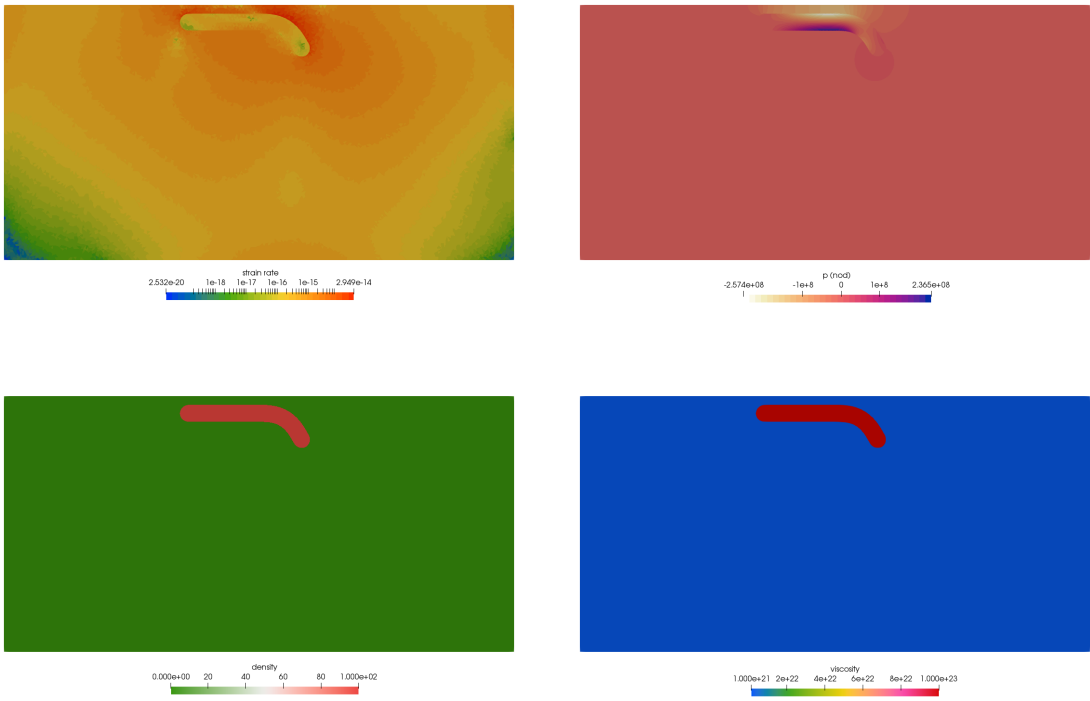
```
./triangle -q -a200000000 -o2 subd.node
```

The '*-q*' option adds vertices to the mesh to ensure that all angles are between 20 and 140 degrees. The '*-a*' makes sure that no triangle has an area larger than the supplied number. The '*-o2*' generates a mesh composed of second order triangles (six nodes per element, rather than three) and the three extra nodes of an element fall at the midpoints of the three edges. This generates two files: '*subd.1.ele*' which contains the connectivity of all generated triangles and '*subd.1.node*' which contains the coordinates of all nodal points. These two files are then read in *fieldstone.py* and stored in the *xV*, *yV* and *iconV* arrays.

Gravity is vertical and Earth-like. Free-slip boundary conditions are imposed on the top while the other boundaries are free (in/outflow determined freely based on the internal dynamics). In order to remove the horizontal null space the average horizontal velocity is set to zero. Crouzeix-Raviart elements are used, see Section 6.2.10. The density of the mantle is set to zero while the subducting plate has a density  $\delta\rho$ .

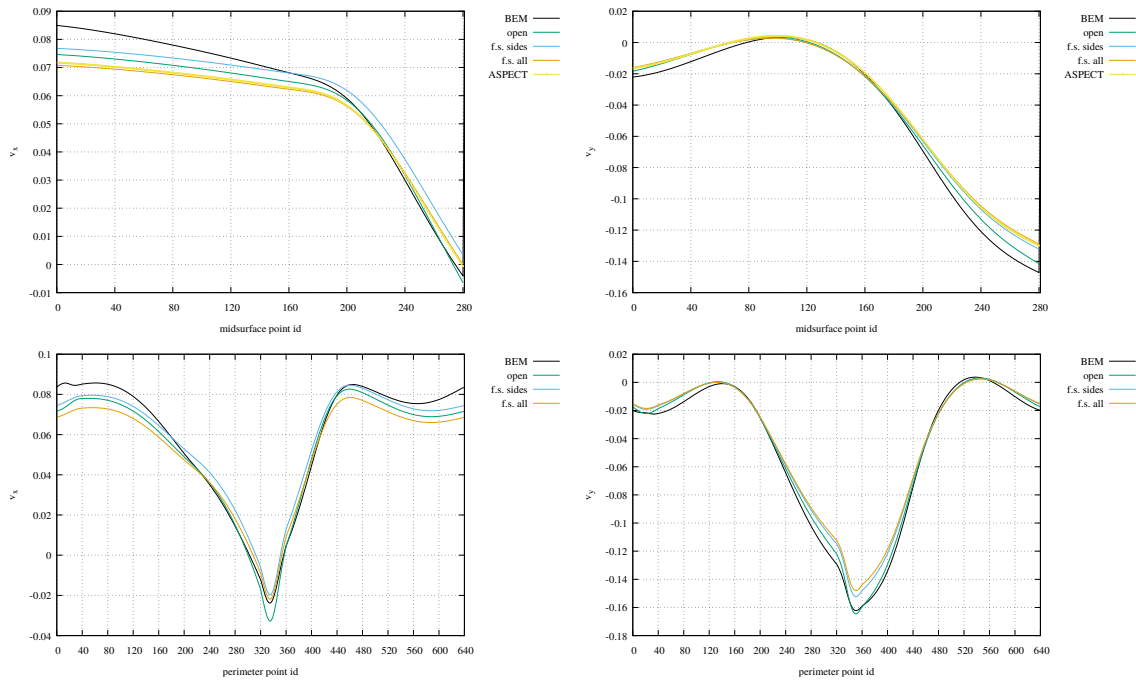


<sup>88</sup><https://www.cs.cmu.edu/~quake/triangle.html>



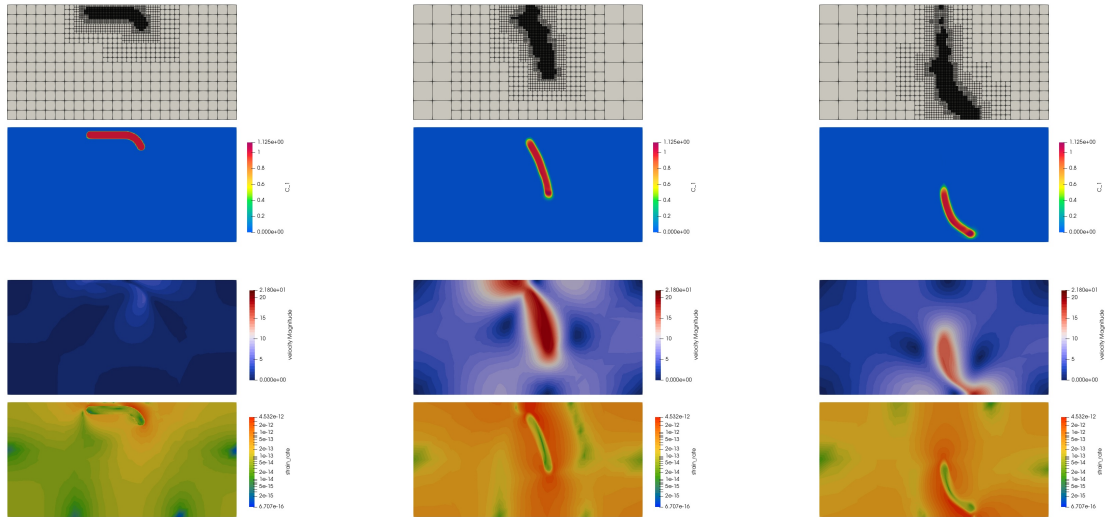
Mesh composed of 31,765 triangles. Other parameters:  $\theta_0 = 60^\circ$ ,  $\eta_1 = 10^{21}$ ,  $\gamma = 100$ ,  $L_x = 3000\text{km}$ ,  $L_y = 1500\text{km}$ ,  $\delta\rho = 100$ ,  $L = 400\text{km}$ ,  $h = 100\text{km}$ ,  $d = 50\text{km}$ . Note that the bottom boundary is open.

We have also run this model with ASPECT for the case where free slip boundary conditions are prescribed on all sides. Velocities on the midsurface are reported hereunder alongside those obtained with fieldstone and the BEM method.

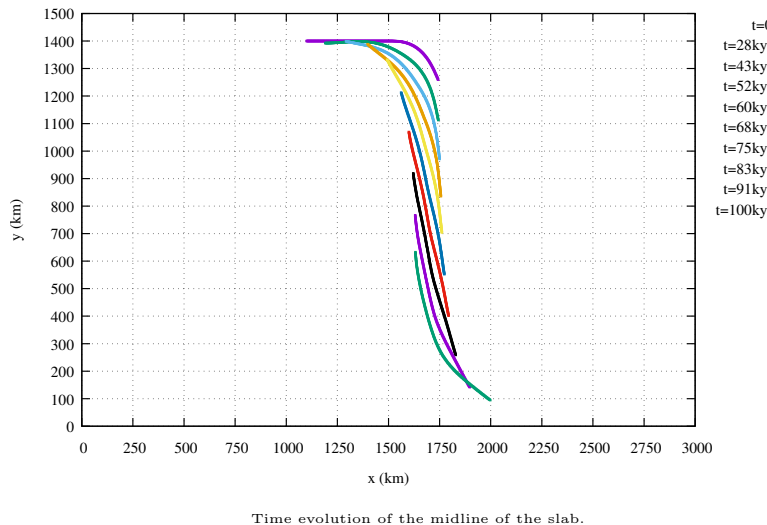


Top row: midsurface velocity measurements. Bottom row: slab/plate perimeter velocity measurements. 'open' means no b.c. on sides and bottom; 'f.s. sides' means free slip b.c. on left and right sides, open at the bottom; 'f.s. all' means free slip b.c. on sides and bottom.

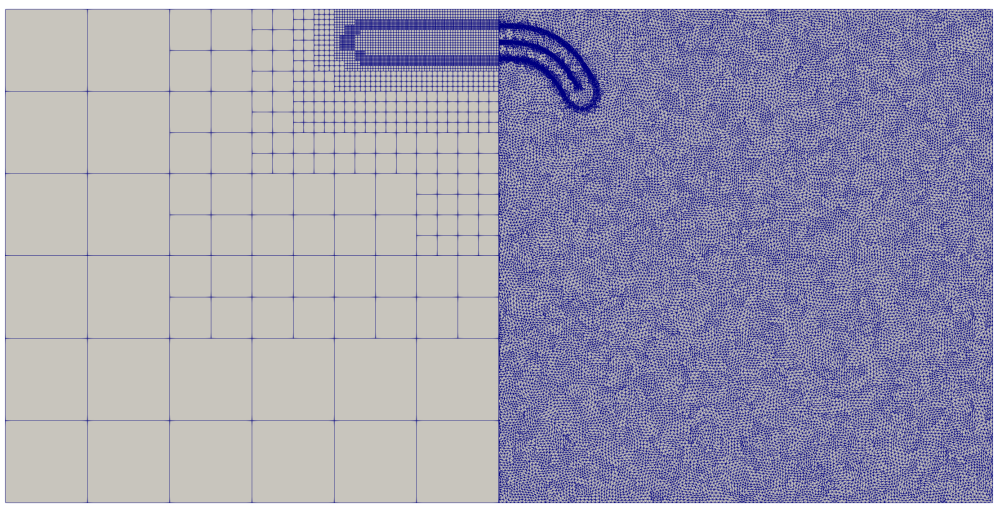
Finally, we have run this experiment over time with ASPECT (unfortunately viscosities were 100 times too small so that the times should be multiplied by 100):



Left:  $t=0$ , middle  $t=64\text{kyr}$ , right:  $t=100\text{kyr}$ .



Time evolution of the midline of the slab.



Literature: [859]

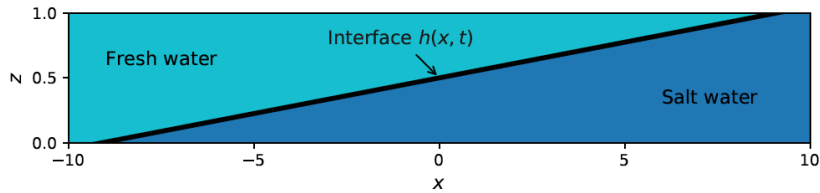
## Stone 56: Dynamics of the Salt Water - Fresh Water Interface

Saltwater intrusion in coastal aquifers is a world wide observable phenomena. The mixing of salt and fresh water reduces groundwater quality. It potentially threatens the usability as drinking water. Extensive pumping causing a decrease of groundwater levels amplifies this effect.

Gravity drives salty sea water land inward due to its higher density if an aquifer's water table is lower than sea level. An interface develops between salt and fresh water, which is stable due to the density difference. Along the interface slight mixing occurs due to diffusion. As for most processes in nature, coupled partial differential equations describe the movement of the interface between salt and fresh water.

The target of this exercise is to model a simplified form of the process. Basic assumption hereby are: (i) groundwater flow is mostly horizontal (called *Deput assumption*); (ii) the salt and fresh water interface is sharp, meaning we neglect mixing due to dispersion and diffusion.

We investigate a portion of an aquifer of length  $L$  and depth  $H$ . Within the aquifer, an interface separates salt water and fresh water as illustrated here under:



The interface  $h(x, t)$  is a function of the horizontal location  $x$  and time  $t$ . For simplicity, we assume an aquifer thickness of  $H = 1$ . Thus, the values for the position of the interface as a function in the  $z$  direction range between zero and one:  $h(x, t) \in [0, 1]$ .

The differential equation describing the movement of the interface  $h(x, t)$  is given by

$$\frac{\partial h(x, t)}{\partial t} = \Gamma \frac{\partial}{\partial x} \left( \frac{h(1-h)\partial h/\partial x}{1 + (\partial h/\partial x)^2} \right) \quad (1060)$$

The constant  $\Gamma = \frac{\kappa}{\mu g(\rho_{\text{salt}} - \rho_{\text{fresh}})}$  summarizes the physical properties: of the aquifer (permeability  $\kappa$ ), of the fluids (viscosity  $\mu$ , density of salt water  $\rho_{\text{salt}}$  and density of fresh water  $\rho_{\text{fresh}}$ ) and the gravity constant  $g$ .

The differential equation has the character of a non-linear diffusion equation with a non-constant diffusion coefficient  $D(h)$ :

$$\frac{\partial h}{\partial t} = \Gamma \frac{\partial}{\partial x} \left( D(h) \frac{\partial h}{\partial x} \right) \quad D(h(x, t)) = \frac{h(1-h)}{1 + (\partial h/\partial x)^2} \quad (1061)$$

According to the value range of  $h \in [0, 1]$ ,  $D$  has the property of  $D(0) = D(1) = 0$  (this differential equation is therefore called *degenerate*).

Despite the complexity of the initial differential equation, an analytical solution can be postulated in the form of:

$$h(x, t) = a(t) \cdot x + 0.5 \quad (1062)$$

The interface  $h$  is a linear function in  $x$  with a time-dependent slope  $a(t)$ . It rotates with time around the fix point  $(0; 0.5)$ . The slope  $a(t)$  can be determined by the ordinary differential equation (REF??):

$$\frac{da(t)}{dt} = - \frac{2a^3}{1 + a^2} \quad (1063)$$

The value range of  $a$  is limited to  $0 < a(t) < 1$  corresponding to a maximal slope angle of  $45^\circ$ . The differential equation in  $a(t)$  has an implicit solution:

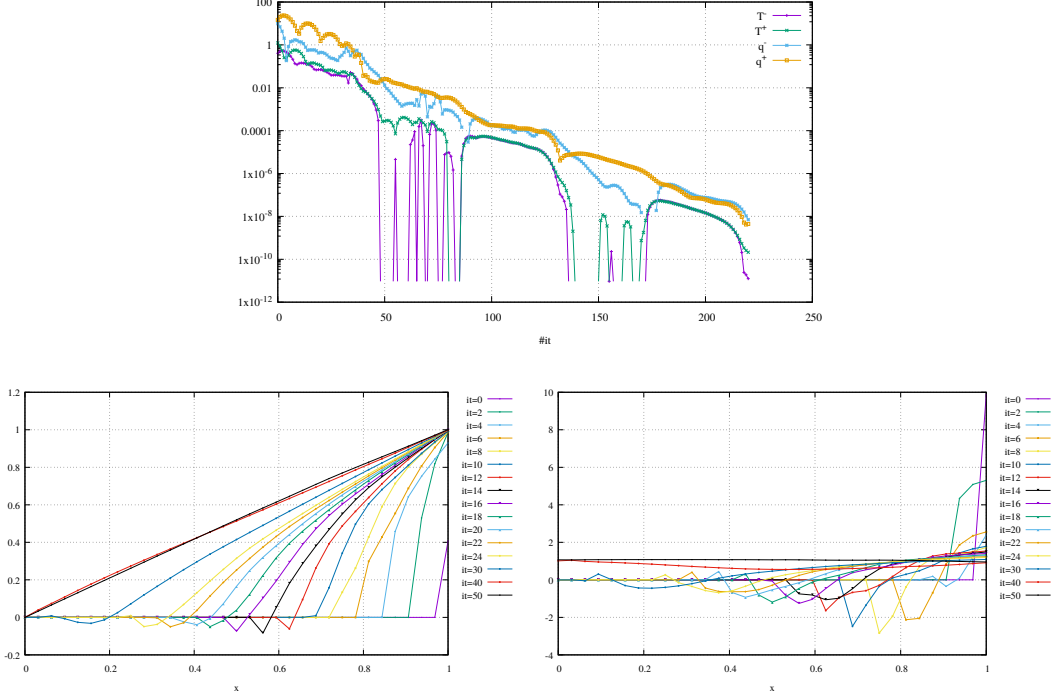
$$t = \frac{1}{2} \ln \left( \frac{a(0)}{a(t)} \right) + \frac{1}{4} \left( \frac{1}{a(t)^2} - \frac{1}{a(0)^2} \right) \quad (1064)$$

We aim to implement a numerical solution of the differential equation 1 which allows us to calculate the location of the interface  $h(x, t)$  at specified locations  $x$  and times  $t$ .

To Do in 2D only

## Stone 57: 1D steady state diffusion with DG-FEM

We follow the discretisation presented in Section 7.2 and use the successive substitution to arrive at the solution. Let us start by fixing  $\mathcal{E} = 4$  and  $\mathcal{C} = 0$  and setting the absolute convergence tolerance to  $10^{-8}$ .



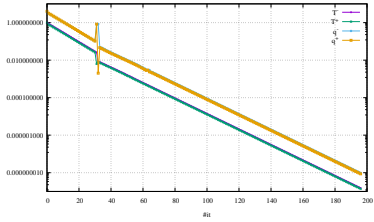
**Effect of resolution** Keeping the same parameters we see that the number of required iterations to convergence increases linearly with the number of elements.

nelx	# iterations
08	60
16	116
32	220
64	436
128	857

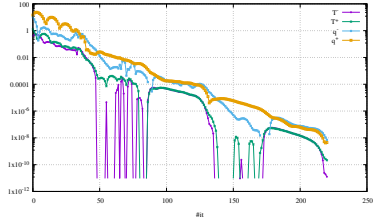
**Effect of  $\mathcal{E}$  &  $\mathcal{C}$  values** We now keep nelx=32 and explore the effect of these parameters on the required number of iterations:

$\mathcal{E}$	$\mathcal{C}$	# iterations
1	0	772
2	0	414
3	-0.5	<b>104</b>
3	0	284
3	0.5	129
4	-1/2	196
4	0	220
4	+1/2	196
5	-1/2	256
5	0	195
5	+1/2	256
6	0	246
10	0	486

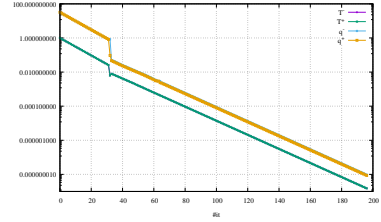
$\mathcal{E} = 4 \text{ & } \mathcal{C} = -1/2$



$\mathcal{E} = 4 \text{ & } \mathcal{C} = 0$

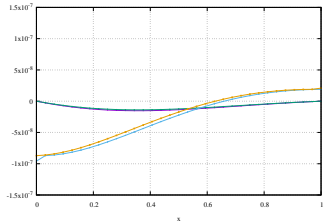


$\mathcal{E} = 4 \text{ & } \mathcal{C} = +1/2$

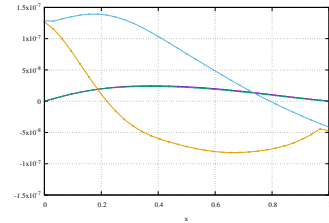


Using  $\mathcal{C} \neq 0$  yields a very linear convergence.

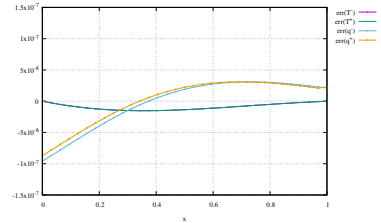
$\mathcal{E} = 4 \text{ & } \mathcal{C} = -1/2$



$\mathcal{E} = 4 \text{ & } \mathcal{C} = 0$

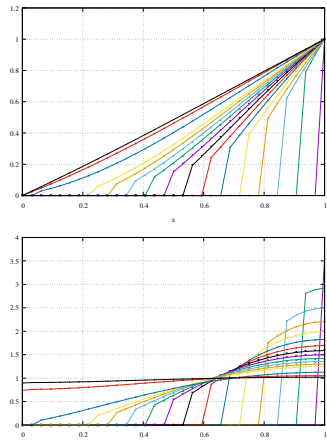


$\mathcal{E} = 4 \text{ & } \mathcal{C} = +1/2$

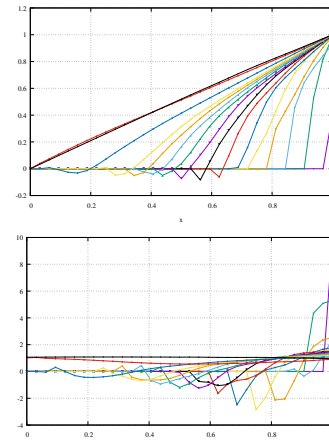


Error between computed and analytical solution as a function of  $x$

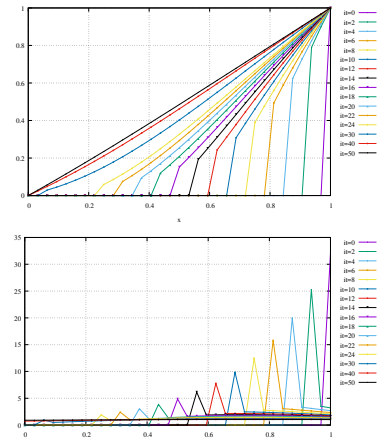
$\mathcal{E} = 4 \text{ & } \mathcal{C} = -1/2$



$\mathcal{E} = 4 \text{ & } \mathcal{C} = 0$



$\mathcal{E} = 4 \text{ & } \mathcal{C} = +1/2$



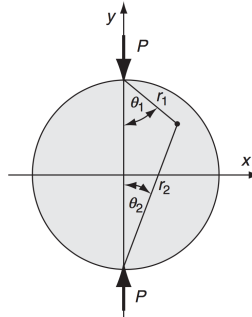
The path to a converged solution is quite different for the three values of  $\mathcal{C}$  tested.

## Stone 58: Elastic disk under compression

 Relevant Literature[309],[310],[311],[1198],[312],[2736] [2808][2876]

### Experiment 1

This benchmark is well document in [2217]. Let us investigate the solution to the plane problem shown hereunder of a circular disk loaded by equal but opposite concentrated forces along a given diameter. This particular problem is of special interest since this geometry is used in standard testing of bituminous and other brittle materials such as concrete, asphalt, rock, and ceramics. Normally referred to as the Brazilian or indirect tension test, the sample and loading geometry create a tension zone along the loaded diameter, thus allowing determination of the tensile strength of the specimen material. Standard direct tension testing on such brittle materials has led to difficulty in establishing a failure region in the samples central interior away from the gripping locations.

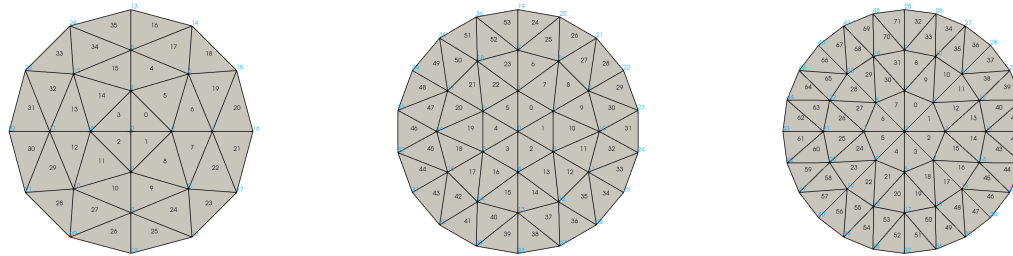


Disk under diametrical compression.

Setup of the experiment.

The mesh is regular and made of concentric layers of triangles. The original algorithm which was used in ELEFANT was written by L. van Wiel. Given the nature of the boundary conditions we wish to apply we make sure that two faces are present at the top and bottom locations of the disc, which is why the mesh is rotated 90° after it is generated.

The mesh is composed of `nsection` sections (must be an even number) as shown hereunder (for `nLayers=3`).



Mesh composed of 4 sections (left), 6 sections (middle) and 8 sections (right).

The pressure  $P$  prescribed at  $y = \pm R$  is actually given by  $P\delta(\mathbf{r}_\pm)$ . From [2217] (example 8.10, p209), the stress solution is given by:

$$\sigma_{xx}(x, y) = -\frac{2P}{\pi} \left[ \frac{(R-y)x^2}{r_1^4} + \frac{(R+y)x^2}{r_2^4} - \frac{1}{D} \right] \quad (1065)$$

$$\sigma_{yy}(x, y) = -\frac{2P}{\pi} \left[ \frac{(R-y)^3}{r_1^4} + \frac{(R+y)^3}{r_2^4} - \frac{1}{D} \right] \quad (1066)$$

$$\sigma_{xy}(x, y) = \frac{2P}{\pi} \left[ \frac{(R-y)^2 x}{r_1^4} - \frac{(R+y)^2 x}{r_2^4} \right] \quad (1067)$$

where

$$r_1 = \sqrt{x^2 + (R - y)^2} \quad r_2 = \sqrt{x^2 + (R + y)^2}$$

The pressure is given by:

$$p(x, y) = -\frac{1}{2}(\sigma_{xx} + \sigma_{yy}) \quad (1068)$$

$$= \frac{P}{\pi} \left[ \frac{(R - y)x^2}{r_1^4} + \frac{(R + y)x^2}{r_2^4} - \frac{1}{D} \right] + \frac{P}{\pi} \left[ \frac{(R - y)^3}{r_1^4} + \frac{(R + y)^3}{r_2^4} - \frac{1}{D} \right] \quad (1069)$$

On the  $x$ -axis ( $y = 0$ ) these results simplify to give

$$\sigma_{xx}(x, 0) = \frac{2P}{\pi D} \left( \frac{D^2 - 4x^2}{D^2 + 4x^2} \right)^2 \quad (1070)$$

$$\sigma_{yy}(x, 0) = -\frac{2P}{\pi D} \left( \frac{4D^4}{(D^2 + 4x^2)^2} - 1 \right) \quad (1071)$$

$$\sigma_{xy}(x, 0) = 0 \quad (1072)$$

$$p(x, 0) = \frac{P}{\pi} \left[ \frac{(R - y)x^2 + (R - y)^3}{r_1^4} + \frac{(R + y)x^2 + (R + y)^3}{r_2^4} - \frac{2}{D} \right] \quad (1073)$$

$$= \frac{P}{\pi} \left[ \frac{Rx^2 + R^3}{(x^2 + R^2)^2} + \frac{Rx^2 + R^3}{(x^2 + R^2)^2} - \frac{2}{D} \right] \quad (1074)$$

$$= \frac{2P}{\pi} \left[ \frac{R(x^2 + R^2)}{(x^2 + R^2)^2} - \frac{1}{D} \right] \quad (1075)$$

$$= \frac{2P}{\pi} \left[ \frac{R}{x^2 + R^2} - \frac{1}{D} \right] \quad (1076)$$

$$(1077)$$

On the  $y$ -axis ( $x = 0$ ) the stresses are

$$\sigma_{xx}(0, y) = \frac{2P}{\pi D} \quad (1078)$$

$$\sigma_{yy}(0, y) = -\frac{2P}{\pi} \left( \frac{2}{D - 2y} + \frac{2}{D + 2y} - \frac{1}{D} \right) \quad (1079)$$

$$= -\frac{2P}{\pi} \left( \frac{1}{R - y} + \frac{1}{R + y} - \frac{1}{D} \right) \quad (1080)$$

$$\sigma_{xy}(0, y) = 0 \quad (1081)$$

$$p(0, y) = \frac{P}{\pi} \left[ \frac{(R - y)^3}{(R - y)^4} + \frac{(R + y)^3}{(R + y)^4} - \frac{2}{D} \right] \quad (1082)$$

$$= \frac{P}{\pi} \left[ \frac{1}{R - y} + \frac{1}{R + y} - \frac{2}{D} \right] \quad (1083)$$

$$(1084)$$

In the code the pressure is retrieved after the displacements are computed. In 2D, we have (using Eq. 73 for the stress tensor):

$$p = -\frac{1}{2}(\sigma_{xx} + \sigma_{yy}) \quad (1085)$$

$$= -\frac{1}{2} [\lambda(\varepsilon_{xx} + \varepsilon_{yy}) + 2\mu\varepsilon_{xx} + \lambda(\varepsilon_{xx} + \varepsilon_{yy}) + 2\mu\varepsilon_{yy}] \quad (1085)$$

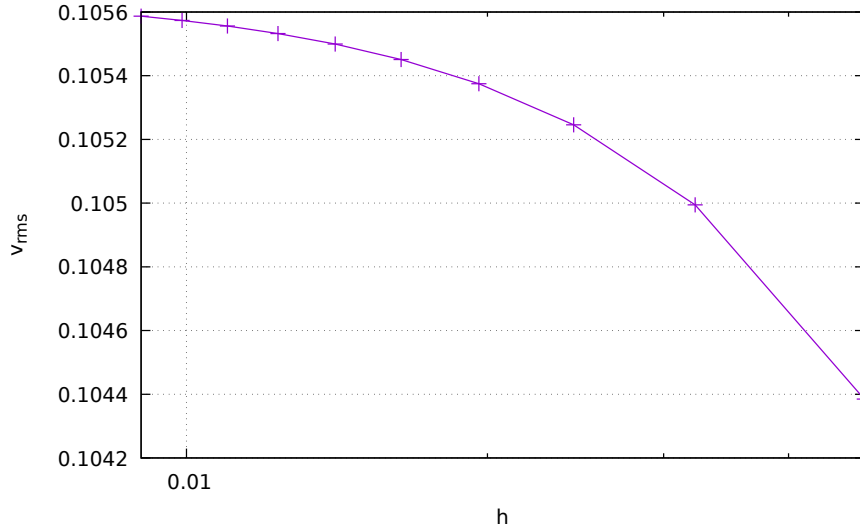
$$= -\frac{1}{2} [2\lambda(\varepsilon_{xx} + \varepsilon_{yy}) + 2\mu(\varepsilon_{xx} + \varepsilon_{yy})] \quad (1086)$$

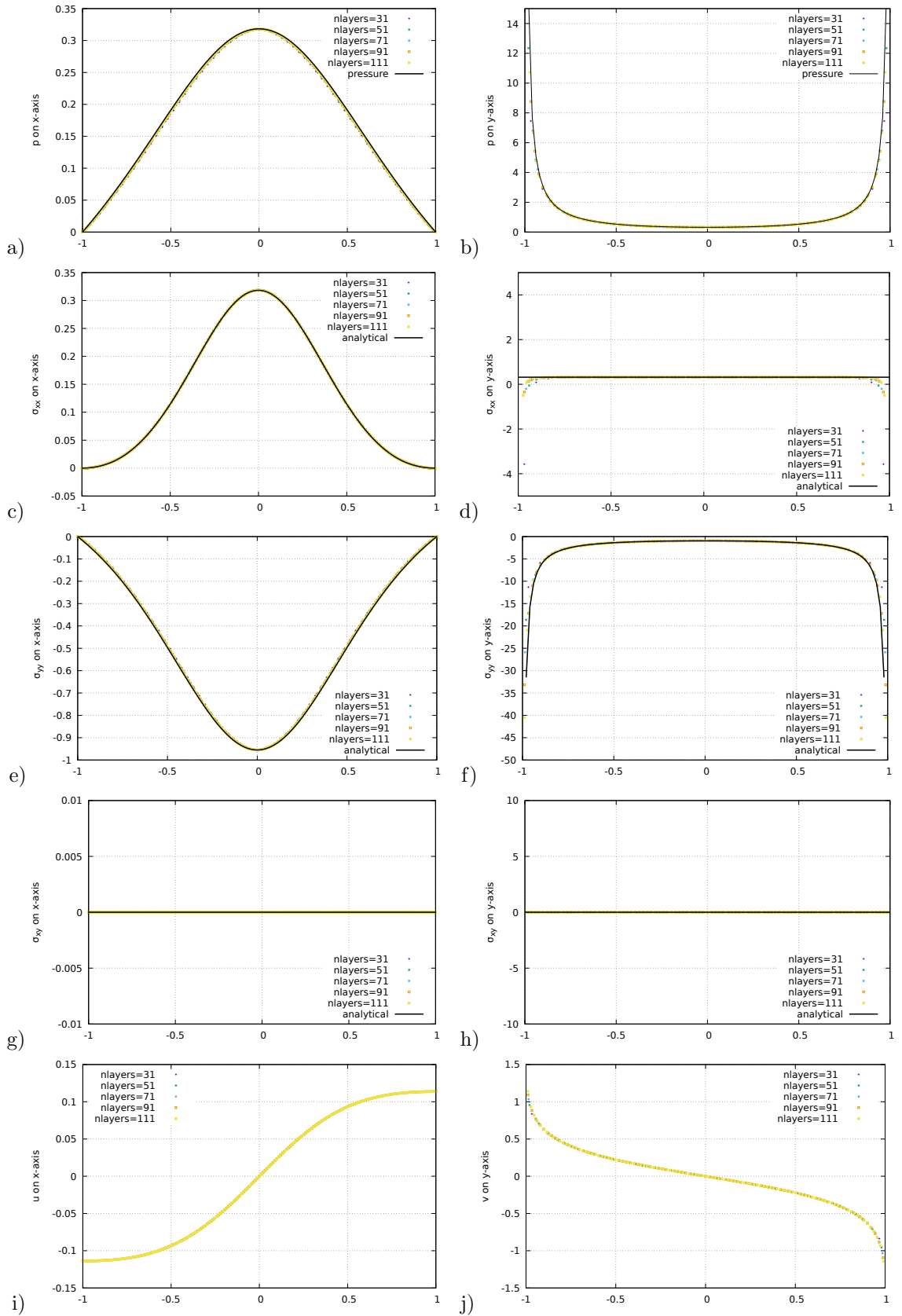
$$= -(\lambda + \mu)(\varepsilon_{xx} + \varepsilon_{yy}) \quad (1086)$$

The radius is set to  $R = 1$ , and the disc is centered on the origin. The disc is discretised by means of  $n_{\text{layers}}$  concentric layers of  $P_1$  triangles. I set  $\mu = 1$  and  $\nu = 0.25$ .

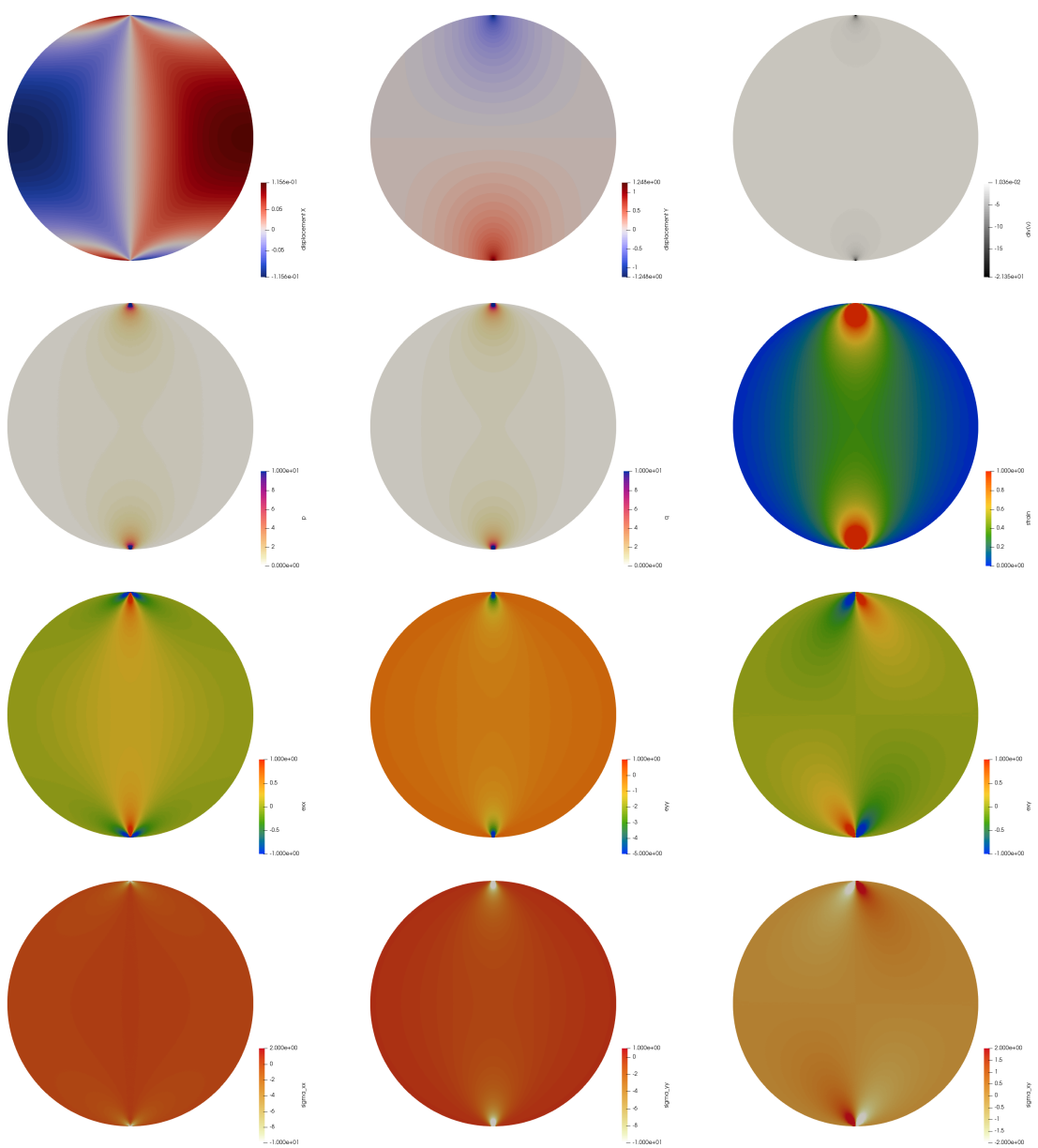
The boundary conditions are as follows: on the two vertical edges at  $y = R$  and  $y = -R$  the pressure is applied. Furthermore because of the symmetry of the problem, and in order to remove the expected nullspaces in the displacement field, we fix  $u = 0$  on the vertical axis and  $v = 0$  on the horizontal axis. In the coming plots the number of layers (which needs to be odd) is varied, from 31 to 111. Note that the displacement is not analytically known but the computed displacement nicely converge to a single smooth curve.

<b>nlayers</b>	<b>NV</b>	<b>nel</b>	<b>Nfem</b>	<b><math>v_{rms}</math></b>
21	1387	2646	2774	1.043847e-01
31	2977	5766	5954	1.049944e-01
41	5167	10086	10334	1.052457e-01
51	7957	15606	15914	1.053750e-01
61	11347	22326	22694	1.054509e-01
71	15337	30246	30674	1.054994e-01
81	19927	39366	39854	1.055324e-01
91	25117	49686	50234	1.055560e-01
101	30907	61206	61814	1.055735e-01
111	37297	73926	74594	1.055868e-01

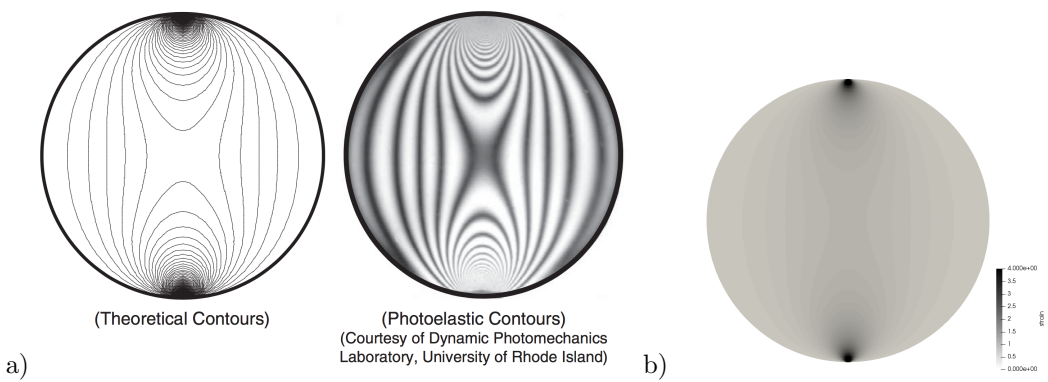




a,b) pressure along the  $x$ -axis; c,d)  $\sigma_{xx}$  along the  $x$ - and  $y$ -axis; e,f)  $\sigma_{yy}$  along the  $x$ - and  $y$ -axis; g,h)  $\sigma_{xy}$  along the  $x$ - and  $y$ -axis; i) horizontal displacement along the  $x$ -axis; j) vertical displacement along the  $y$ -axis



Results for  $n\text{Layers}=11$



a) Maximum shear stress contours and corresponding photoelastic isochromatic for a disk under diametrical compression [2217]; b) computed second invariant of the strain tensor.

CHECK AGAINST MY NOTES! We can also look at the principal stresses. The principal direction angle  $\theta_p$  defines the principal directions where the only stresses are normal stresses, and is given by the relationship:

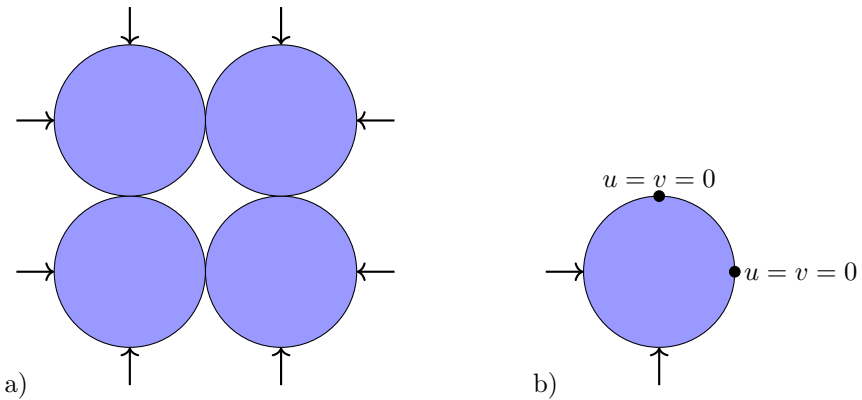
$$\tan(2\theta_p) = \frac{2\sigma_{xy}}{\sigma_{xx} - \sigma_{yy}}$$

The principal stresses are found from the original stresses via

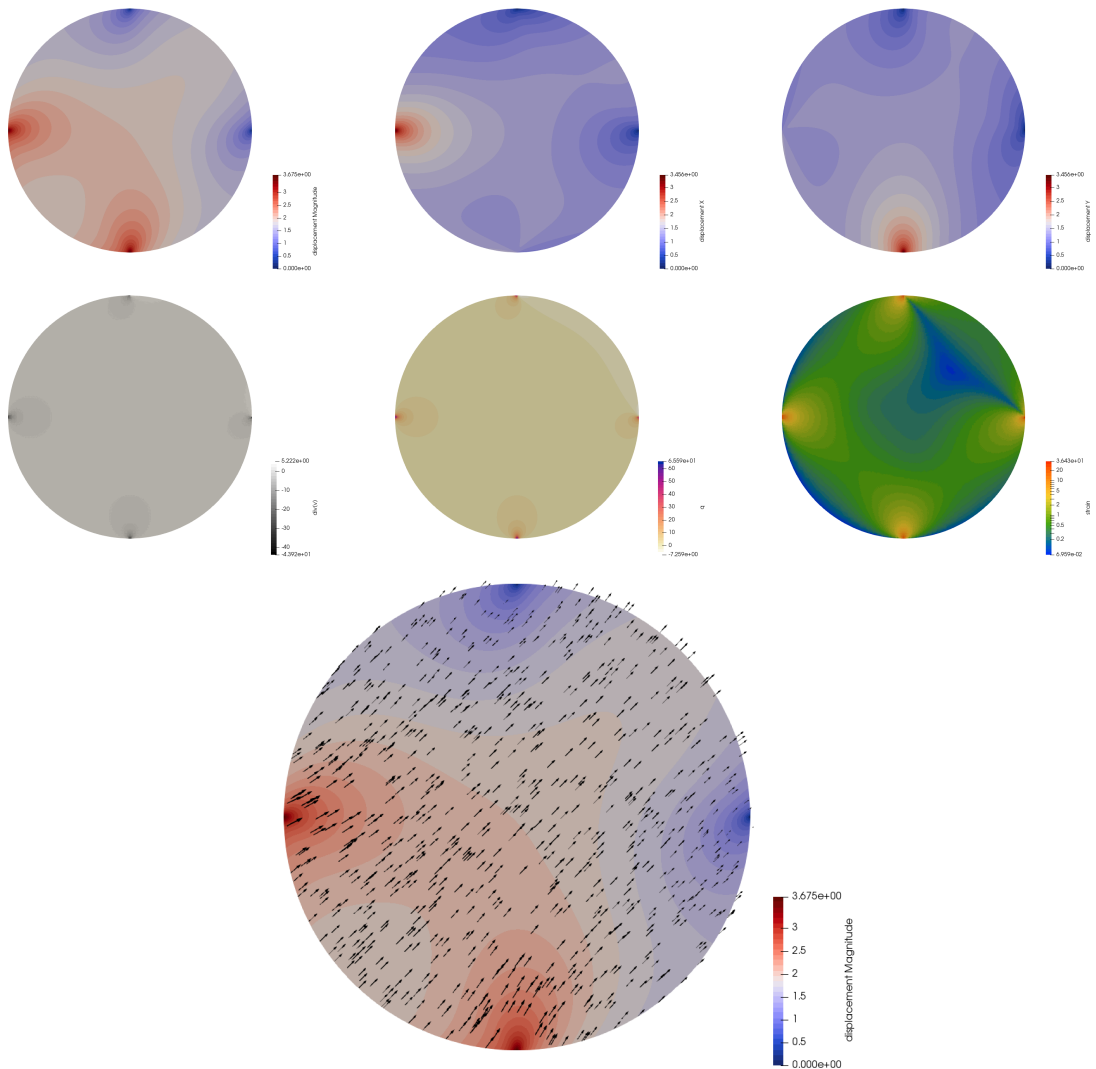
$$\sigma_{1,2} = \frac{\sigma_{xx} + \sigma_{yy}}{2} \pm \sqrt{\left(\frac{\sigma_{xx} - \sigma_{yy}}{2}\right)^2 + \sigma_{xy}^2}$$

## Experiment 2

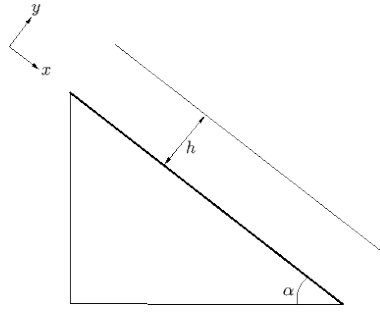
This experiment was designed in collaboration with T. Shinohara . Unlike the previous one it does not have an analytical solution.



a) assembly of four circular grains and the pressure boundary conditions; b) simplified setup of a single grain.



## Stone 59: Flow Down an Inclined Plane



REDO with tikz

**Linear viscous fluid** We start from the Stokes equation for isoviscous fluids:

$$\eta \Delta \vec{v} - \vec{\nabla} p + \rho \vec{g} = \vec{0}$$

Assuming that the fluid is incompressible and that the incline is infinite, then  $\vec{v} = (u(y), 0)$ . The  $x$ -component of the equation then writes:

$$\begin{aligned} \eta \left( \frac{\partial^2 u}{\partial x^2} + \frac{\partial^2 u}{\partial y^2} \right) - \frac{\partial p}{\partial x} + \rho g_x &= 0 \\ \Rightarrow \quad \eta \frac{\partial^2 u}{\partial y^2} + \rho g \sin \alpha &= 0 \end{aligned}$$

since  $\partial_x \rightarrow 0$ . This 2nd order ODE can be integrated twice. The two integration constants are determined by setting  $u(y = 0) = 0$  (no slip) and the shear stress to be zero at the (free) surface. The velocity profile is given by:

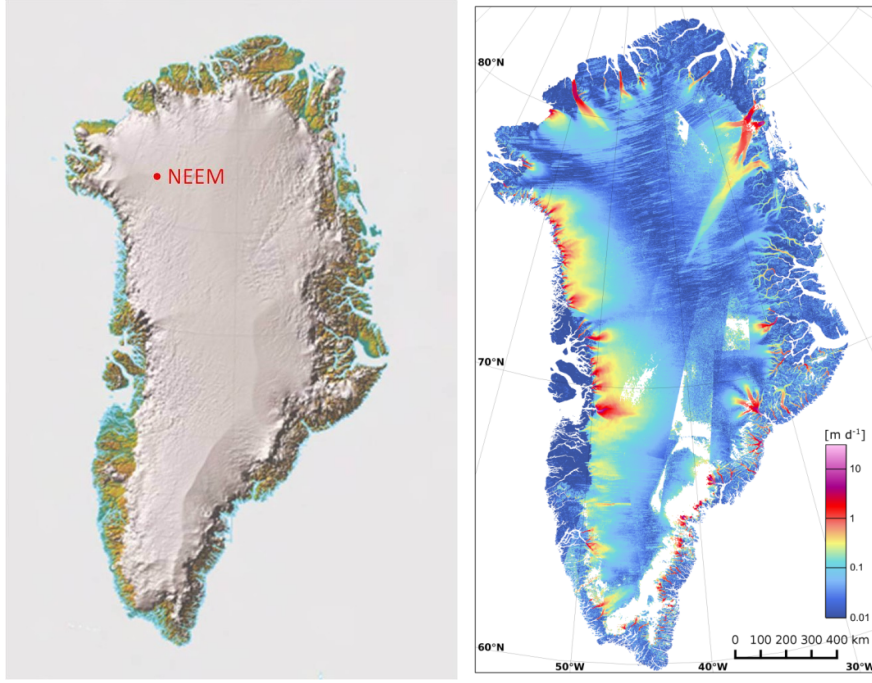
$$u(y) = \frac{\rho g \sin \alpha}{2\eta} (2h - y)y$$

We can now compute the components of the strain rate tensor:

$$\dot{\epsilon}_{xx} = 0 \quad \dot{\epsilon}_{yy} = 0 \quad \dot{\epsilon}_{xy} = \frac{1}{2} \left( \frac{\partial u}{\partial y} + \frac{\partial v}{\partial x} \right) = \frac{1}{2} \frac{\partial u}{\partial y} = \frac{\rho g \sin \alpha}{2\eta} (h - y)$$

We now make the assumption that this problem is a very simplified ice sheet flow problem. The angle  $\alpha$  is typically small and for  $\alpha \sim 0.5 - 1^\circ$ , then  $\sin \alpha \sim 0.01$ . We also have  $\rho \sim 1000$ ,  $g \sim 10$ ,  $h \sim 2500$  and we postulate the ice viscosity to be  $\eta \sim 10^m$ . The velocity is maximum at the surface and is given by

$$u(y = h) = \frac{\rho g \sin \alpha}{2\eta} h^2 \sim \frac{1000 \cdot 10 \cdot 0.01}{2 \cdot 10^m} 2500^2 \sim 3 \cdot 10^{8-m} \quad (1087)$$



Ice velocity map (magnitude, in logarithmic scale) of the Greenland Ice Sheet derived from SAR data of the Sentinel-1A satellite, acquired in Interferometric Wide Swath Mode (IW) between January and March 2015. Taken from [1893].

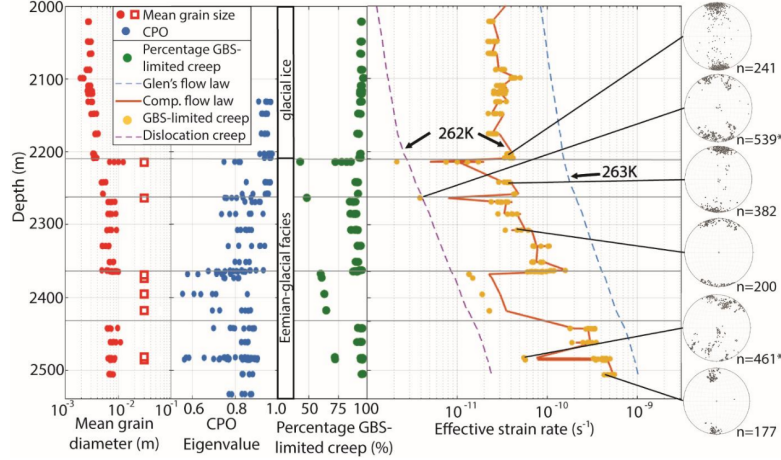
As shown on the figures above the typical ice sheet velocity values around the NEEM ice core is  $\sim 0.03\text{m/day} \simeq 3 \cdot 10^{-7}\text{m/s}$ . Then, in order for the top of the ice sheet to flow at this speed it requires  $m = 15$ .

Having obtained the (effective linear) viscosity of the ice, i.e.  $\eta \simeq 10^{15}\text{Pa.s}$ , we can compute the strain rate at the bottom and in the middle:

$$\dot{\varepsilon}_{xy}(y=0) = \frac{\rho g \sin \alpha}{2\eta} h \sim \frac{1000 \cdot 10 \cdot 0.01}{2 \cdot 10^{15}} 2500 \sim 10^{-10}\text{s}^{-1}$$

$$\dot{\varepsilon}_{xy}(y=h/2) = \frac{\rho g \sin \alpha}{2\eta} \frac{h}{2} \sim \frac{1000 \cdot 10 \cdot 0.01}{2 \cdot 10^{15}} \frac{2500}{2} \sim 5 \cdot 10^{-11}\text{s}^{-1}$$

which are reasonable values as confirmed by the following figure (see yellow line):



Taken from Kuiper et al [1511].

The conclusion from this exercise is that if ice could be described by a linear viscous fluid flowing on an infinite incline, a viscosity of  $\eta \simeq 10^{15}\text{Pa.s}$  would yield observations that match recorded velocities and strain rates.

**Nonlinear power-law viscosity** However, the picture is way more complex, as it was observed very early on by Glen in 1955 [1001] and many others later (see Section 3.22.2). It was then found that

$$\dot{\varepsilon} = A\tau^n,$$

i.e. the ice behaves as a power-law fluid (see Section 3.22.2), with  $n = 3$  and  $A \simeq 2.4 \cdot 10^{-24}$  at  $0^\circ$ (REF?).

More recently Kuiper et al. [1512, 1511] derived a composite flow law to model deformation in the NEEM deep ice core. They start from the flow law proposed by Goldsby & Kohlstedt [1023]:

$$\dot{\varepsilon}_T = \dot{\varepsilon}_{disl} + \left( \frac{1}{\dot{\varepsilon}_{basal}} + \frac{1}{\dot{\varepsilon}_{GBS}} \right)^{-1} + \dot{\varepsilon}_{diff}$$

where  $\dot{\varepsilon}_T$  is the total strain rate, composed of strain rates for basal slip accommodated by non-basal slip or dislocation creep,  $\dot{\varepsilon}_{disl}$ , grain boundary sliding (GBS) accommodated by basal slip,  $\dot{\varepsilon}_{basal}$ , and basal slip accommodated by GBS,  $\dot{\varepsilon}_{GBS}$ , and diffusion creep,  $\dot{\varepsilon}_{diff}$ . Each of these creep mechanisms can be described by a power law relation of the form:

$$\dot{\varepsilon} = A\tau^n d^{-p} \exp\left(-\frac{Q+pV}{RT}\right)$$

where  $A$  is a material parameter,  $\tau$  is the differential stress (MPa),  $n$  is the stress exponent,  $d$  is the grain size diameter (m),  $p$  is the grain size exponent,  $Q$  is the activation energy for the creep mechanism at stake ( $J \cdot mol^{-1}$ ),  $p$  is the hydrostatic pressure (MPa),  $V$  the activation volume ( $m^3 \cdot mol^{-1}$ ),  $R$  is the gas constant ( $J \cdot K^{-1} \cdot mol^{-1}$ ), and  $T$  the absolute temperature (K). The effect of  $pV$  is assumed to be very small [746] and is ignored for the remainder of this work.

As explained in [1512] the composite flow law can actually be simplified to:

$$\dot{\varepsilon}_T = \dot{\varepsilon}_{disl} + \dot{\varepsilon}_{GBS}$$

The material parameters for these deformation mechanisms are available in [1511]:

Creep regime	A	n	p	Q ( $J \cdot mol^{-1}$ )
Glen's flow law ( $T < 263K$ )	$3.61 \cdot 10^5 \text{ MPa}^{-3.0} \text{ s}^{-1}$	3.0	0	60
Glen's flow law ( $T > 263K$ )	$1.73 \cdot 10^{21} \text{ MPa}^{-3.0} \text{ s}^{-1}$	3.0	0	139
Dislocation creep ( $T < 262K$ )	$5.0 \cdot 10^5 \text{ MPa}^{-4.0} \text{ s}^{-1}$	4.0	0	64
Dislocation creep ( $T > 262K$ )	$6.96 \cdot 10^{23} \text{ MPa}^{-4.0} \text{ s}^{-1}$	4.0	0	155
GBS-limited creep ( $T < 262K$ )	$1.1 \cdot 10^2 \text{ MPa}^{-1.8} \text{ m}^{1.4} \text{ s}^{-1}$	1.8	1.4	70
GBS-limited creep ( $T > 262K$ )	$8.5 \cdot 10^{37} \text{ MPa}^{-1.8} \text{ m}^{1.4} \text{ s}^{-1}$	1.8	1.4	250

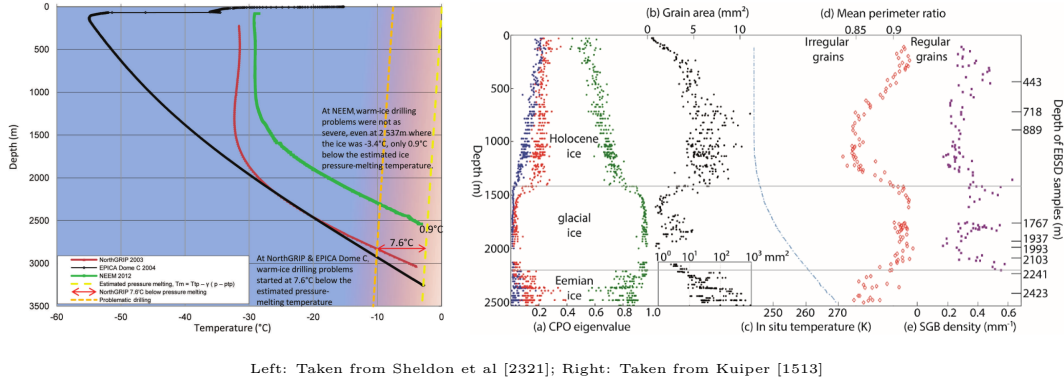
The associated effective viscosity is then given by

$$\eta = \frac{1}{2} A^{-\frac{1}{n}} \dot{\varepsilon}^{\frac{1}{n}-1} d^{\frac{p}{n}} \exp\left(\frac{Q+pV}{nRT}\right)$$

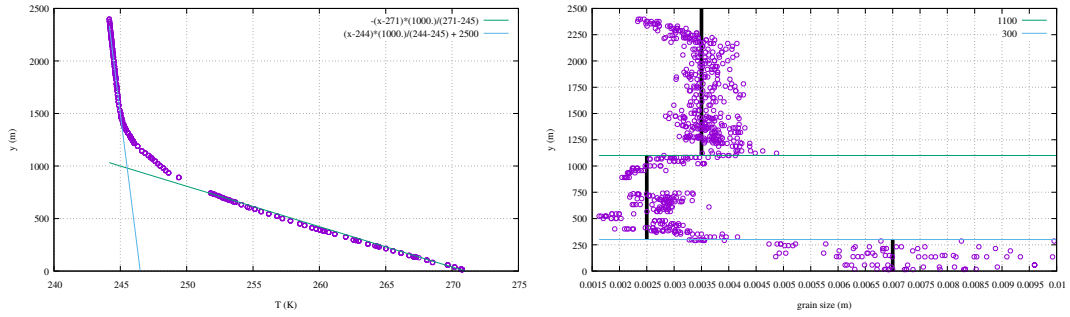
Note that the  $A$  parameter is given in MPa and not Pa so that when computing the associated effective viscosities these have to be multiplied by  $10^6$ . Because the strain rates are added together we know that the two deformation mechanisms are in series and their effective viscosity is then the harmonic average of both viscosities:

$$\eta_{eff} = \left( \frac{1}{\eta_{disl}} + \frac{1}{\eta_{GBS}} \right)^{-1}$$

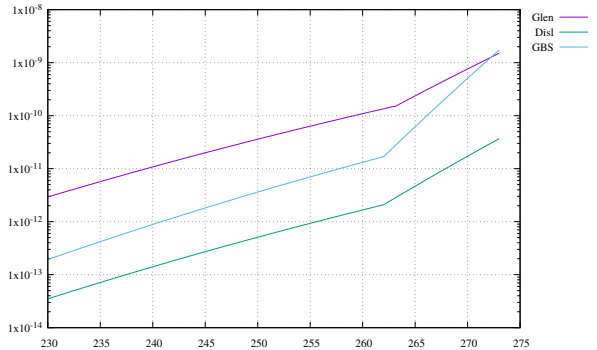
**Numerical setup** The geometry is a 2D cartesian domain of size  $L_x \times L_y$ . Instead of tilting it by an angle  $\alpha$  I choose to instead 'tilt' the gravity vector so that it becomes  $\vec{g} = (\rho g \sin \alpha, -\rho g \cos \alpha)$ . The boundary conditions are as follows: no slip at the bottom, free surface at the top, free slip on the left (we assume that this corresponds to a ridge - zero horizontal velocity) and we need to be careful about the right boundary which is where the ice exits the domain: if we leave the boundary open ice will rush out, generate high strain rates and the nonlinear rheologies will respond by generating low viscosities which in turn will promote a fast exit. Instead we opt to prescribe the analytical solution of Eq. (1087) with  $\eta = 10^{15}$ . We neglect any kind of phase change and precipitation and only carry out a single time step. The domain is discretised with nel=nelx×nely  $Q_2 Q_1$  elements (see Section 6.2.5). We set  $L_x = 125\text{km}$  and  $L_y = 2500\text{m}$ ,  $\rho = 917\text{kg}\cdot\text{m}^{-3}$ ,  $\alpha = 0.1^\circ$ .



I have obtained the raw data (courtesy from E.N. Kuiper) and it is plotted hereunder:



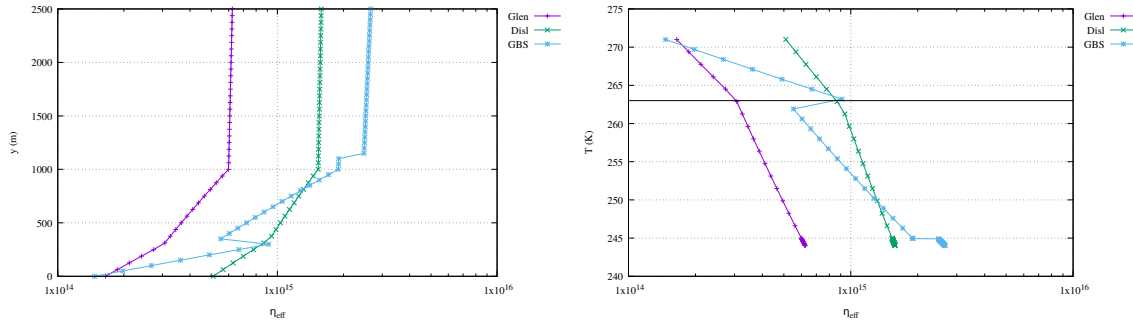
In order to verify that the values reported in the table above are the ones used in [1511] I have reproduced the figure 3 of that paper (code and gnuplot script in ./data folder):



Log strain rate versus temperature for Glens flow law and the two mechanisms (dislocation creep and GBS-limited creep) that form the end members of the modified composite flow law, using the flow law parameters from the table above. A stress of 0.07MPa and a mean grain diameter of 5mm were used to calculate the strain rate.

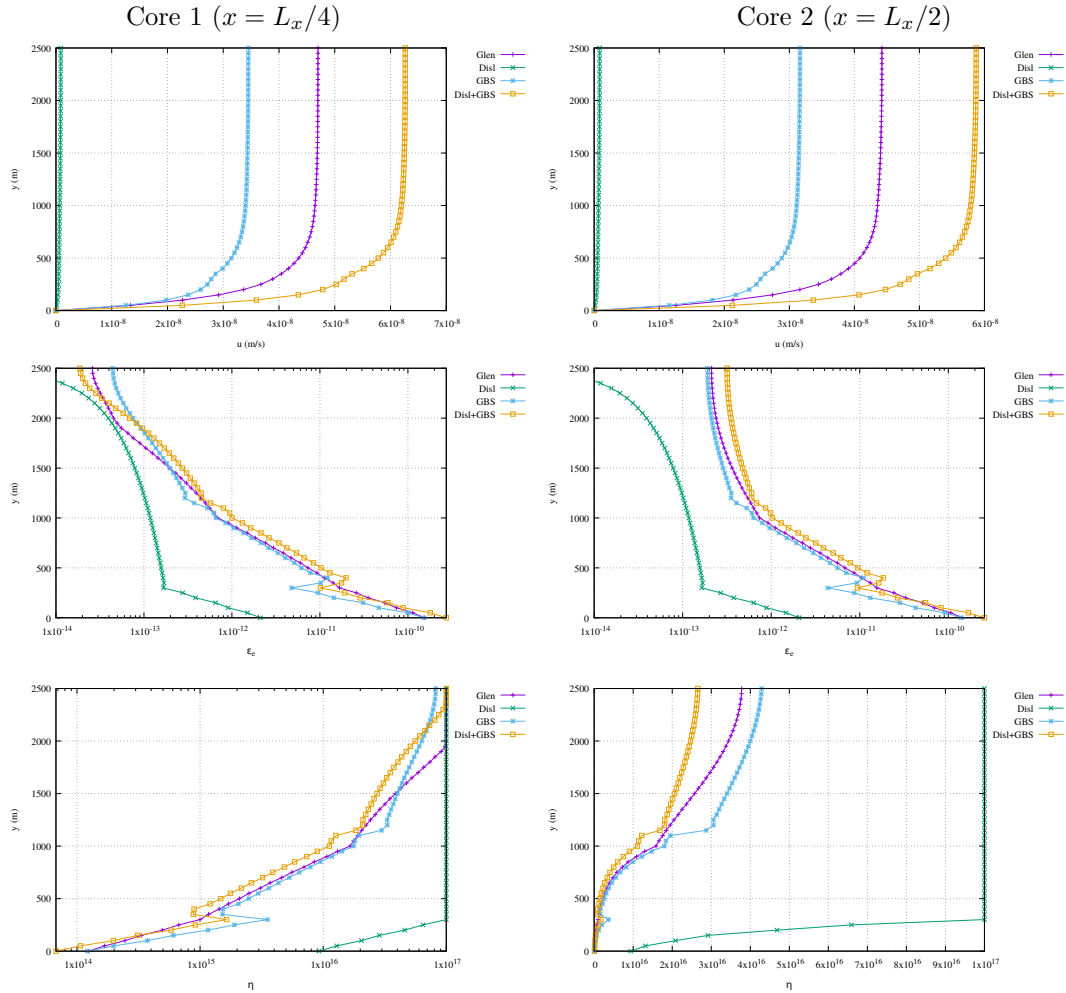
In our models, the temperature profile is simplified as shown on the plots above. Concerning the grain size distribution the ice sheet has been divided in three layers and an average grain size is used for each.

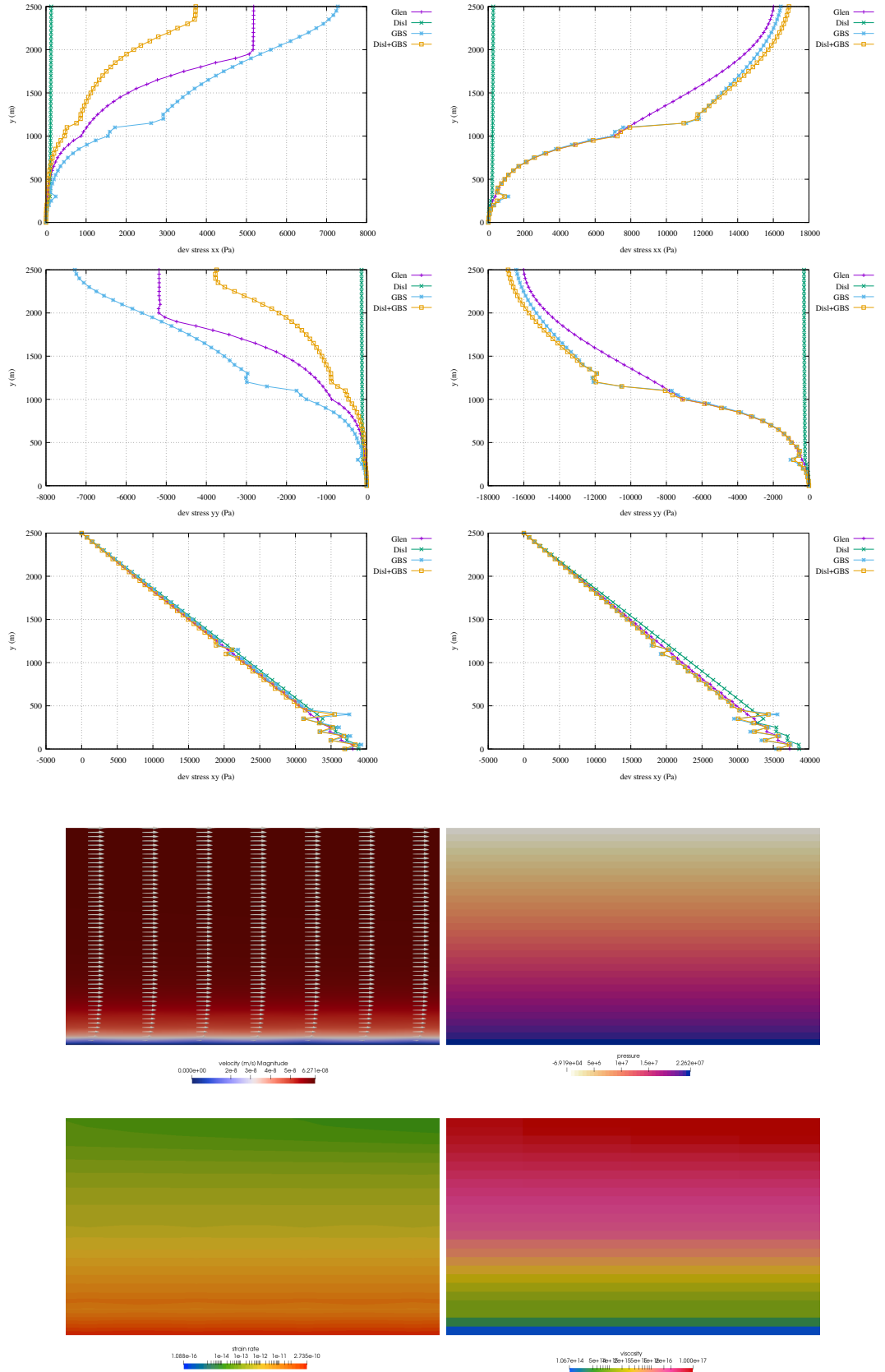
We have computed the effective viscosity for all four rheologies with the implemented temperature and grain size profiles for  $\dot{\varepsilon}_e = 10^{-10} \text{ s}^{-1}$ :



Note that smaller strain rates shift the curves to the right (higher viscosities).

Because the rheologies are non linear we need to carry out nonlinear iterations (see Section 8.31.1). In what follows we run models for Glen's flow law (rheology=1), dislocation creep (rheology=2), GBS (rheology=3) and dislocation+GBS (rheology=4). Note that in the case of rheology=4, the partitioning of the strain rates between both mechanisms is not done (YET) so that the results are not really consistent with the rest!





Velocity, pressure, strain rate and viscosity in the middle of the ice sheet for rheology=4

Check: ELMER/ice <http://elmerice.elmerfem.org/capabilities>

Improvements: better density profile? more realistic geometry ? partitioning of strain rates. Better temperature profile. Better grain size description. Influence of tilt angle?



Relevant Literature[318][1287][1008][2875][2834][2954][1170] [1587]

## Stone 60: 1D advection with DG-FEM

We consider the following advection problem taken from [1596, ex 5.2]:

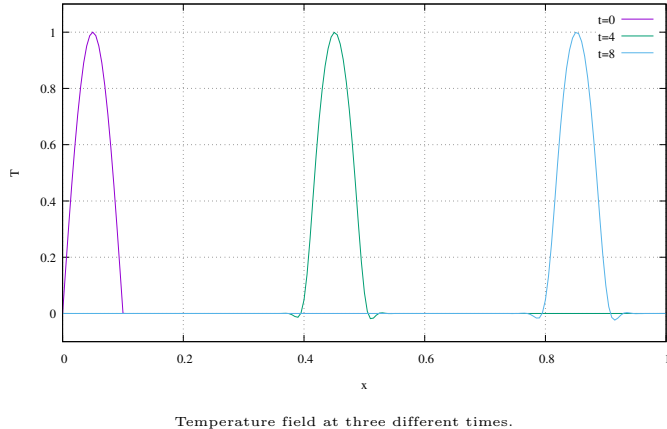
$$\frac{\partial T}{\partial t} + u \frac{\partial T}{\partial x} = 0$$

for  $x \in [0, 1]$  and with the initial conditions:

$$T(x, 0) = \begin{cases} \sin(10\pi x) & \text{for } x \leq 0.1 \\ 0 & \text{for } x \geq 0.1 \end{cases}$$

The velocity is set to  $u = 0.1$ . We use 200 elements and a time step of  $\delta t = 10^{-4}$ . We run the model to time  $t = 8$  so we need 80,000 time steps. Note that the CFL-number is then very small:

$$C = \frac{\delta t \cdot u}{h} = \frac{10^{-4} \cdot 0.1}{1/200} = 0.002$$



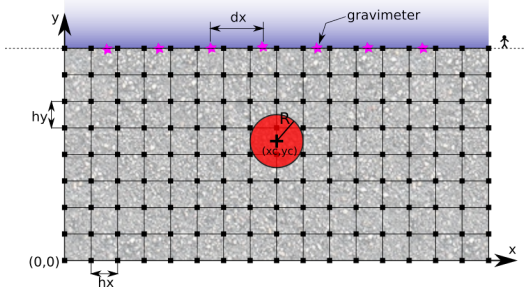
## 10 fieldstone: Gravity: buried sphere

Before you proceed further, please read :

[http://en.wikipedia.org/wiki/Gravity\\_anomaly](http://en.wikipedia.org/wiki/Gravity_anomaly)

<http://en.wikipedia.org/wiki/Gravimeter>

Let us consider a vertical domain  $Lx \times Ly$  where  $L_x = 1000\text{km}$  and  $L_y = 500\text{km}$ . This domain is discretised by means of a grid which counts  $nnp = nnx \times nny$  nodes. This grid then counts  $nel = nelx \times nely = (nnx - 1) \times (nny - 1)$  cells. The horizontal spacing between nodes is  $hx$  and the vertical spacing is  $hy$ .



Assume that this domain is filled with a rock type which mass density is given by  $\rho_{medium} = 3000\text{kg/m}^3$ , and that there is a circular inclusion of another rock type ( $\rho_{sphere} = 3200\text{kg/m}^3$ ) at location  $(xsphere, ysphere)$  of radius  $rsphere$ . The density in the system is then given by

$$\rho(x, y) = \begin{cases} \rho_{sphere} & \text{inside the circle} \\ \rho_{medium} & \text{outside the circle} \end{cases}$$

Let us now assume that we place  $nsurf$  gravimeters at the surface of the model. These are placed equidistantly between coordinates  $x = 0$  and coordinates  $x = Lx$ . We will use the arrays  $xsurf$  and  $ysurf$  to store the coordinates of these locations. The spacing between the gravimeters is  $\delta_x = Lx/(nsurf - 1)$ .

At any given point  $(x_i, y_i)$  in a 2D space, one can show that the gravity anomaly due to the presence of a circular inclusion can be computed as follows:

$$g(x_i, y_i) = 2\pi G(\rho_{sphere} - \rho_0)R^2 \frac{y_i - ysphere}{(x_i - xsphere)^2 + (y_i - ysphere)^2} \quad (1088)$$

where  $r_{sphere}$  is the radius of the inclusion,  $(xsphere, ysphere)$  are the coordinates of the center of the inclusion, and  $\rho_0$  is a reference density.

However, the general formula to compute the gravity anomaly at a given point  $(x_i, y_i)$  in space due to a density anomaly of any shape is given by:

$$g(x_i, y_i) = 2G \int \int_{\Omega} \frac{\Delta\rho(x, y)(y - y_i)}{(x - x_i)^2 + (y - y_i)^2} dxdy \quad (1089)$$

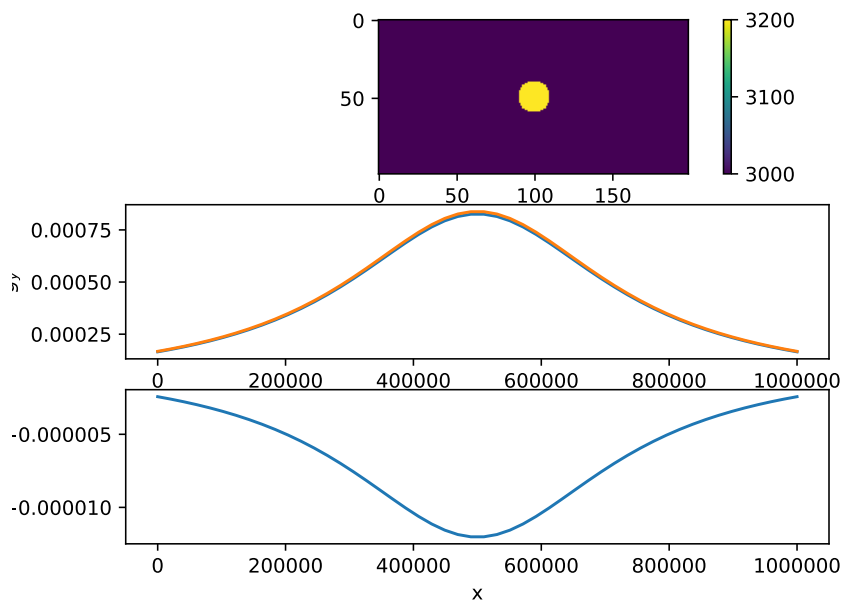
where  $\Omega$  is the area of the domain on which the integration is to be carried out. Furthermore the density anomaly can be written :  $\Delta\rho(x, y) = \rho(x, y) - \rho_0$ . We can then carry out the integration for each cell and sum their contributions:

$$g(x_i, y_i) = 2G \sum_{ic=1}^{nel} \int \int_{\Omega_e} \frac{(\rho(x, y) - \rho_0)(y - y_i)}{(x - x_i)^2 + (y - y_i)^2} dxdy \quad (1090)$$

where  $\Omega_e$  is now the area of a single cell. Finally, one can assume the density to be constant within each cell so that  $\rho(x, y) \rightarrow \rho(ic)$  and  $\int \int_{\Omega_e} dxdy \rightarrow hx \times hy$  and then

$$g(x_i, y_i) = 2G \sum_{ic=1}^{nel} \frac{(\rho(ic) - \rho_0)(y(ic) - y_i)}{(x(ic) - x_i)^2 + (y(ic) - y_i)^2} s_x s_y \quad (1091)$$

We will then use the array  $gsurf$  to store the value of the gravity anomaly measured at each gravimeter at the surface.



### To go further

- explore the effect of the size of the inclusion on the gravity profile.
- explore the effect of the  $\rho_0$  value.
- explore the effect of the grid resolution.
- measure the time that is required to compute the gravity. How does this time vary with nsurf ? how does it vary when the grid resolution is doubled ?
- Assume now that  $\rho_2 < \rho_1$ . What does the gravity profile look like ?
- what happens when the gravimeters are no more at the surface of the Earth but in a satellite ?
- if you feel brave, redo the whole exercise in 3D...

## 11 Problems, to do list and projects for students

- Bsc thesis
  - Darcy flow. redo WAFLE (see <http://cedrichieulot.net/wafle.html>)
  - chunk grid
- MSc guided research/thesis
  - surface tension see [2118] p28-29 - see ibuprofem
  - elasticity with markers
  - navier-stokes ? (LUKAS) use dohu matlab code
  - pure shear deformation of inclusions [2564]
  - redo Buck and Sokoutis benchmark for continental convergence [315]
  - redo topo and geoid calculations a la [1441]
  - redo Travis study [2563] which is close to Blankenbach [209]. Note that [1690] looks at kinetic energy for [2563]
  - propagator matrix ? what is it ? [2149] (**MSc Thesis**)  Relevant Literature [1114, 1115, 2155, 2912, 562, 1815, 2908, 1582, 1592, 1870, 1795, 850, 1652, 320]
  - redo early compressional orogen study by Beaumont [129]
  - redo erosion solutions by [606] (**MSc Thesis**)
  - redo extension 3D Allken papers + [2052, 1393]
  - redo convection at high Ra 2D [2294]
  - redo very early FE paper 1971 [2431]
  - redo early 3D subd [2911]
  - redo improved method of Nusselt number calculation [1207]
- Miscellaneous /to do
  - write about impose bc on el matrix
  - free-slip bc on annulus and sphere . See for example p540 Gresho and Sani book. find book [679]. also check [780] !!
  - constraints [3]
  - formatting of code style
  - Finish nonlinear cavity case5.
  - write about stream functions
  - create stone for layeredflow (see folder one up)
  - in the context of mesh generation on sphere cite [1854]
  - illustrate early boundary fitted static meshes with [2522]
  - [181] spell out the derivation of Jaumann derivative in appendix
  - look at strain-rate softening in [140]
  - write section in features about thermo mechanical simulations and how/why we solve vp, then T.
  - Material point method [2452, 2454, 2453]
  - redo/explore dyn topo bench of [218]
- carry out critical Rayleigh experiments for various geometries/aspect ratios. Use Arie's notes.
- Indentor/punch with stress b.c. ?

- read in crust 1.0 in 2D on chunk
- compute gravity based on tetrahedra
- NS a la [http://ww2.lacan.upc.edu/huerta/exercises/Incompressible/Incompressible\\_Ex2.htm](http://ww2.lacan.upc.edu/huerta/exercises/Incompressible/Incompressible_Ex2.htm)
- write Scott about matching compressible2 setup with his paper
- including phase changes (w. R. Myhill)
- GEO1442 indenter setup in plane ?
- redo puth17 2 layer experiment
- SIMPLE a la p667 [1351]
- implement/monitor div v
- shape fct, trial fct, basis fct vs test fct doc
- write/draw the whole FEM process for a 4x3 grid for compgeo
- lukas' 2D and 3D benchmark
- ROTATING disc
- cylindrical footing on (elasto)-viscous medium - analytical solution, Haskell, etc ...
- check the BASIL code by Houseman et al <http://homepages.see.leeds.ac.uk/~eargah/basil/> on which the ELLE code is based <http://elle.ws/>
- try Anderson acceleration for Uzawa [1206] with m=1
- $Q_1^+ \times P_0$  Look at fort81 , rota87b and vadv03
- check [383] for RT0 element use
- deformation around rigid particles [1283]
- write about flexural isostasy [1690], bottom Sopale
- mesh containing both quadrilaterals and triangles [37]
- redo/adapt bsc thesis with inversion on stokes sphere
- implementation of fault in FEM codes [2910, 2900]
- [https://en.wikipedia.org/wiki/Bernstein\\_polynomial](https://en.wikipedia.org/wiki/Bernstein_polynomial)
- cvi [2064],[1761]
- van keken instantane MINI elt
- check  $Q_2 \times Q_{-1}$  element, [1065] p 697. pressure basis function based at the four 2x2 gauss points.
- look at condition number of  $\mathbb{K}$  block for Q1P0 and Q2Q1 as a function of resolution. Insert results in section about why q1p0 should not be used.
- write about splines as shape functions [478]. second or third order shape functions , using extra nodes instead of using more nodes per element. Smaller matrix than Q2 or Q3 but: spline coeffs on nodes are no more unknowns. Plus bc are complicated. Does it work well with visc contrasts ?
- write about vorticity-velocity method: [927, 1087, 676, 792]

`|Cells|, |DataArray type=Int32 Name=connectivity ...|, |DataArray type=Int32 Name=offsets ...|, |DataArray type=UInt8 Name=types ...|, |/Cells|`

open questions: what does it mean to have a negative pressure ? should we threshold it when computing yield strength ?

velocity-based

geometry: element type: mixed or penalty: number of dimensions: physics: solver: matrix storage: compressible (Y/N): analytical benchmark (Y/N): numerical benchmark (Y/N): error convergence (Y/N): thermo-mechanically coupled (Y/N): time-stepping (Y/N): non-linear (Y/N) mesher (Y/N)

displacement-based stones

stream function stones

other stones

## A Three-dimensional applications

In the following table I list many papers which showcase high-resolution models of geodynamical processes (subduction, rifting, mantle flow, plume transport, ...). Given the yearly output of our community and the long list of journal in which research can be disseminated, this list can not be exhaustive.

Ref.	topic	resolution
[226]	Effect of margin curvature on plate deformation in a 3D subduction zones	
[83]	Small-scale sublithospheric convection in the Pacific	$448 \times 56 \times 64$
[2408]	Migration and morphology of subducted slabs in the upper mantle	$50 \times 50 \times 25$
[2074]	Subduction scissor across the South Island of New Zealand	$17 \times 9 \times 9$
[1731]	Influence of a buoyant oceanic plateau on subduction zones	$80 \times 40 \times 80$
[410]	Subduction dynamics, origin of Andean orogeny and the Bolivian orocline	$96 \times 96 \times 64$
[773]	Feedback between rifting and diapirism, ultrahigh-pressure rocks exhumation	$100 \times 64 \times 20$
[25]	Numerical modeling of upper crustal extensional systems	$160 \times 160 \times 12$
[26]	Rift interaction in brittle-ductile coupled systems	$160 \times 160 \times 23$
[1541]	Kinematic interpretation of the 3D shapes of metamorphic core complexes	$67 \times 67 \times 33$
[1313]	Role of rheology and slab shape on rapid mantle flow: the Alaska slab edge	$960 \times 648 \times 160$
[409]	Complex mantle flow around heterogeneous subducting oceanic plates	$96 \times 96 \times 64$
[300]	Oblique rifting and continental break-up	$150 \times 50 \times 30$
[179]	Influence of mantle plume head on dynamics of a retreating subduction zone	$80 \times 40 \times 80$
[299]	Rift to break-up evolution of the Gulf of Aden	$83 \times 83 \times 40$
[301]	Thermo-mechanical impact of plume arrival on continental break-up	$100 \times 70 \times 20$
[415]	Subduction and slab breakoff controls on Asian indentation tectonics	$96 \times 96 \times 64$
[802]	Modeling of upper mantle deformation and SKS splitting calculations	$96 \times 64 \times 96$
[2252]	Backarc extension/shortening, slab induced toroidal/poloidal mantle flow	$352 \times 80 \times 64$
[1693]	Sediment transports in the context of oblique subduction modelling	$500 \times 164 \times 100$
[2921]	Crustal growth at active continental margins	$404 \times 164 \times 100$
[1545]	Dynamics of India-Asia collision	$257 \times 257 \times 33$
[2776]	Strain-partitioning in the Himalaya	$256 \times 256 \times 40$
[1609]	Collision of continental corner from 3-D numerical modeling	$500 \times 340 \times 164$
[2067]	Dependence of mid-ocean ridge morphology on spreading rate	$196 \times 196 \times 100$
[801]	Mid mantle seismic anisotropy around subduction zones	$197 \times 197 \times 53$
[1168]	Oblique rifting of the Equatorial Atlantic	$120 \times 80 \times 20$
[1840]	Dynamics of continental accretion	$256 \times 96 \times 96$
[2206]	Thrust wedges: infl. of decollement strength on transfer zones	$309 \times 85 \times 149$
[369]	Asymmetric three-dimensional topography over mantle plumes	$500 \times 500 \times 217$
[2534]	modelled crustal systems undergoing orogeny and subjected to surface processes	$96 \times 32 \times 14$
[1618]	Thermo-mechanical modeling of continental rifting and seafloor spreading	$197 \times 197 \times 197$
[178]	Geodynamics of oceanic plateau and plume head accretion	$256 \times 96 \times 96$

## B Codes in geodynamics

In what follows I make a quick inventory of the main codes of computational geodynamics, for crust, lithosphere and/or mantle modelling.

in order to find all CIG-codes citations go to: <https://geodynamics.org/cig/news/publications-refbase/>

- **ABAQUS**

[260] [942] [903] [1127] [411] [1515] [1706] [412] [1919] [2014] [1892] [1891]

- **ANSYS**

[1928]

- **ADELI**

1997: [1158]

2001: [463]

2004: [1006]

2006: [2693][1007]

2008: [225][226]

2012: [941][991]

2013: [2728]

2014: [431]

2015: [429]

2018: [430][943]

- **ASPECT**

This code is hosted by CIG at <https://geodynamics.org/cig/software/aspect/>. It is an open source community code based on the finite element library deal.II [89, 51]. It is massively parallel, relies on the p4est library for adaptive mesh refinement, uses the Trilinos solver library [1184], and can deal with 2D and 3D geometries.

2012: [1507]

2015: [62][2556]

2016: [620][924][2885]

2017: [1164][618][1169][2197][2198][61] [2530][282][1968][2495][2877]

2018: [619][1970][1002][1183][925][2013] [2062][281]

2019: [111][2419][575][1650][926][622] [1951][2311]

- **BASIL/ELLE** <http://elle.ws/>

[230] [1656]

- **BEM**

[599] [1393] [1861] [1862] [1865] [2084][397] [2083] [937]

- **CHIC**

[1952]

- **CitcomS and CitComCU**

These codes are hosted by CIG at <https://geodynamics.org/cig/software/citcomcu/> and <https://geodynamics.org/cig/software/citcoms/>.

1995: [1850][1856]

1996: [2378][1843][2911]

1997: [1849][356][2379]

1998: [1847][2904][1103][2121]

1999: [1853][357][2652][1573][2122]

2000: [2909][1095][1572][1102][2372]

2001: [193][1577][2913]

2002: [2500][2380]  
2003: [2648][564][194][1579][1570][190][2696]  
2004: [2375][877][1580][568][1763]  
2005: [195][1765][1764][1578]  
2006: [136][2032][2498][139][565][878][569] [2895][1408][2174][2878]  
2007: [196][2907][1702][84][2164][1870][563] [2081][1238][2175]  
2008: [998][921][2905][1213][1576][1644][447] [134][137][2358][1582][1440][1641][1783] [2173][2394][695][2678]  
2009: [1616][50][2882][43][847][361][132] [85][1583][247][2896][558][567][1409] [1703][1918][2172][2393]  
2010: [340][2680][83][362][2881][187][556] [1312][2924][234][1216][1148][809][700] [808][984][1531][1762][2324][2391,  
2392] [2399]  
2011: [138][1571][2641][1585][1643][81][248] [2571][1958][184][2886][699][1978][1734] [2502][2101][2241][2636][2668][2879]  
2012: [56][1313][197][240][1271][2914][2376] [1197][1316][1705][2376][2570][580][1132] [1215][1270][1642][1792][2669][1924][2170]  
[2171][2323][2400][2767][2880][2867][1687]  
2013: [79][250][251][1314][2085][1963] [57][566][363][842][555][985][1239] [1428][2670][1688]  
2014: [841][339][1368][58][2722][2307] [12][1686][2925]  
2015: [80][249][241][2312][621][2642][2080] [2731][2720][2719][1156][2509][1586][2509] [82][1869][1653][2769][2793][2733]  
2016: [2771][2768][1310][888][2183][212][1740] [1076][1430][1760][2721][2732][2768][2835] [2838][1311]  
2017: [11][1685][876][1163][1678][990][2505] [2836]  
2018: [1192][1449][1369][2723][1236][1601][497] [2572][2770][2839][1709][192]  
2019: [1739][891][1684][1676][1710][211][1574] [2257][28][2113]

- **COMSOL**

[2181]

- **ConMan** This code is hosted by CIG at <https://geodynamics.org/cig/software/conman/>

1990: [1454][1448][1093][1267][1442]  
1991: [1416][1566]  
1992: [2398][2897]  
1993: [1418][1429][1561][1567][2902][2898]  
1994: [1296][818][913][1096][1443][1562][1563] [2899]  
1995: [1451][1564][1568][2065][2066][2901]  
1996: [1530][1565][1848][2903]  
1997: [2659][1419][1417][1849]  
1998: [1452][1297][2655][1452][1559][1826]  
1999: [133][1573][559][545][1128][2199][2338]  
2000: [1569][554][766][1569]  
2001: [557][1268]  
2002: [768]  
2003: [821][2492][2229][2492]  
2004: [767][2333]  
2005: [1471][542][1801][2334][2501]  
2006: [1914]  
2007: [1915][633][544][765][1665][1915][2119]  
2008: [1129]  
2009: [817][1165][1441][1547][2750]  
2010: [1439][560][1130][1548]  
2011: [1131][1549]  
2014: [1433][1550]  
2015: [1453][1432][1622]

- **CONVRS**

[2851] [2849]

- **DOUAR**

[269][2533] [2828] [271][1663] [1888][2776] [1932] [1492]

- Nameless code of Trompert and Hansen  
[2565] [2567][2566] [1009] [1659] [1658] [2409] [2413] [2411] [2414]
- MC3D  
[2410]
- DYNEARTHSOL  
[470] [1332] [1661]
- ELMER Elmer is an open source multiphysical simulation software mainly developed by CSC - IT Center for Science (CSC). Elmer development was started 1995 in collaboration with Finnish Universities, research institutes and industry. Elmer includes physical models of fluid dynamics, structural mechanics, electromagnetics, heat transfer and acoustics, for example. These are described by partial differential equations which Elmer solves by the Finite Element Method (FEM).  
<https://www.csc.fi/web/elmer>  
[1691]
- LaCoDe  
[664]
- M-DOODS, Duretz code  
[2830] [2827] [2832] [456][744][2018]
- FENICS  
[20]
- GAIA  
[2557] [1275] [1934]
- GALE  
This code is hosted by CIG at <https://geodynamics.org/cig/software/gale/>  
[826] [1045] [182] [604] [1541][1608] [57]
- (G)TECTON  
1980: [1773]  
1981: [1772]  
1993: [1039]  
1995: [1040]  
1996: [1101][997]  
1999: [1041][905]  
2001: [327][1044]  
2002: [328]  
2005: [1042][2679][2681][1042]  
2006: [865][1655][2271]  
2007: [2682]  
2008: [662][661]  
2009: [1519][2039]  
2010: [2596][2038]  
2011: [71][72]  
2013: [2040][2741]  
2014: [2597]  
2015: [1715][1942]  
2016: [934][1716]  
2017: [1984]  
2018: [1043][1943][1174]

- ELEFANT  
[2556] [1683] [332] [1535] [2530] [2043] [2803] [871]
- ELLIPSIS Section 3 of [2081] presents the evolutionary path which lead to this code.  
2003: [1842][2782][1875][2763][1987]  
2005: [2781][1974][1975]  
2006: [1969]  
2007: [1846][978][749][1973]  
2008: [1971]  
2009: [1972]  
2010: [2074]  
2011: [1585]  
2012: [1581]  
2014: [2145]
- FANTOM  
[2528][25] [26] [27] [791][2534] [789] [2220] [790][2523]
- FDCON  
[788] [585] [893] [892]
- FLUIDITY  
[637] [1503] [918][2706] [29]
- I2(3)E(L)VIS  
2003: [974][975][973]  
2004: [976][977][971][960]  
2005: [353][1714][2443]  
2006: [323][951][1027][966]  
2007: [952][1026][964][1029][1031]  
2008: [2272][965][2586][803][2920][354] [426][1800][1945][970]  
2009: [967][352][1624][805][1615]  
2010: [949][1944][105][1610][2354]  
2011: [737][739][1611][950][969][208] [1946][1021][1625][2008][2923][961]  
2012: [585][736][2866][804][1030][2587][2256] [2353][2710]  
2013: [1609][1916][1693][2631][2630][2921][750] [968][1722][445][446][735][427][1620] [2708][962][958][1791][2206][2298]  
2014: [738][2067][2707][76][1619][2436][1704] [369][1028][2632][1723][77][1020][954] [963][995][2355]  
2015: [2588][2207][972][2207][1490][1186]  
2016: [1489][1694][840][1707][734][1776]  
2017: [1708][1491][2711][2331]  
2018: [2918][1692][957][1185]  
2019: [1488][1613][2356][1775][1088]
- I3MG  
[801]
- LaMEM  
[2272] [1398] [1544] [1742] [1545][540][107][831][830] [2063][832][539] [1402][541] [2] [761]
- LAPEX2D,LAPEX3D (LAgrangian Particle EXplicit, based on the prototype code PAROVOZ)  
[2364][68][2363] [323][69] [2021][2020] [67] [2272] [2365]
- LITMOD3D  
[7] [6] [898] [899]

- MARC

[1927] [1926]

- MILAMIN, MILAMIN\_VEP

MILAMIN is a finite element method implementation in native MATLAB that is capable of doing one million degrees of freedom per minute on a modern desktop computer. This includes pre-processing, solving, and post-processing. The MILAMIN strategies and package are applicable to a broad class of problems in Earth science. <http://milamin.org/>

2008: [614][2278]

2009: [1019]

2010: [1509][1396][689]

2011: [2831]

2012: [938][2209][2524]

2013: [2261]

2014: [1354]

2015: [1672][939][2525][1886]

2016: [1334][1725][406]

2018: [743][1335][1333][579][1348][2102][455]

2019: [42][2352][111][2385]

- PARAVOZ/FLAMAR/FLAC

1989: [608][1209]

1993: [2045][2890]

1994: [2796]

1996: [1147][2891]

1998: [945]

2000: [1537]

2001: [371][364]

2002: [70][510]

2003: [1122][944][2592]

2004: [1094][946][2560][2544][513][2561]

2005: [370]

2006: [375][1542]

2007: [2823][372][440]

2008: [2825][2545][373]

2009: [947][2828][379][2548][2829]

2012: [45][941][1086][940]

2013: [2749][867][2546]

2014: [866][915][367][368]

2015: [2817][933][697]

2016: [1729]

2018: [948]

2019: [1330]

- PINK3D

[2714]

- PLASTI

[900]

- pTatin3D: A nice succinct description of the code is given in Appendix B of [1543].

2013: [2024]

2014: [1746]

2015: [1743]

2017: [1543][1711]

2018: [1361]  
2019: [1360]

- PyLith There are tons of papers with PyLith.

[1]

- RHEA

[380] [2402] [19] [382]

- SAMOVAR

[764]

- SEPRAN

SEPRAN [2305] is a Fortran-based multi-purpose Finite Element package developed by SEPRA engineering company in cooperation with the department of applied mathematics of Delft Technical University starting in the early 1980s. The package has been used for 25 yr in the education and research program at Utrecht University and many students have used the package in their work dealing with numerical modelling in geodynamics. SEPRAN is available for a range of platforms including Linux/Unix and Microsoft Windows. It contains a mesh generator with a flexible scripting interface for general 2-D and 3-D mesh configurations.

The package provides tools for a range of applications in science and engineering, including second order elliptic, parabolic and hyperbolic equations, suitable for mechanical problems dealing with linear elasticity and for flow problems for both incompressible and compressible viscous media.

1993: [2601][2618]

1994: [2705][2667]

1995: [2620][2607]

1996: [2619]

1997: [2608][2653]

1998: [667]

1999: [668]

2000: [665][2643]

2001: [723][2644]

2002: [496][2646][2665][2645][2611]

2003: [2673][2664]

2004: [2674][2675][2676][2614][2647]

2005: [2677][2305][2604]

2006: [1629][1630]

2007: [2672][503][259][258][1462]

2008: [2037][257][1464][2649]

2009: [2687][2671]

2010: [2603][2458][671][2602][2612]

2011: [2657][1306][2613]

2012: [2605][155][457]

2013: [44][498]

2014: [458][1859][460]

2015: [2606][499]

2017: [495][2756]

2018: [2388][459]

2019: [2894][2616][408][2666]

- SISTER

[1962]

- SLIM3D

[2054] [2090] [300] [301] [299] [298] [1168] [1487] [509] [303] [73][2585][2584]

- **SLOMO**  
[1395] [1403]
- **SNAC** SNAC (StGermaiN Analysis of Continua) is an updated Lagrangian explicit finite difference code for modeling a finitely deforming elasto-visco-plastic solid in 3D. The code is hosted at <https://geodynamics.org/cig/software/snac/>.  
[472] [471] [2079] [473]
- **SPECFEM3D** SPECFEM3D Cartesian simulates acoustic (fluid), elastic (solid), coupled acoustic/elastic, poroelastic or seismic wave propagation in any type of conforming mesh of hexahedra (structured or not.) It can, for instance, model seismic waves propagating in sedimentary basins or any other regional geological model following earthquakes. It can also be used for non-destructive testing or for ocean acoustics.  
It is an open source code hosted by the CIG at <https://geodynamics.org/cig/software/specfem3d/>  
[1476]
- **MICROFEM/SOPALE** For an explanation of nested version of the numerical model, see appendix A of [2773].
  - 1993: [2784]
  - 1994: [2789][119][129]
  - 1995: [901][772]
  - 1996: [124][116][2748]
  - 1998: [770][1321][2747]
  - 1999: [2787][2785][771][769][117][2009]
  - 2000: [2071][126][2022]
  - 2001: [122]
  - 2002: [1262][2072]
  - 2003: [1257][2684][2791][2076][330][2800]
  - 2004: [123][2073][2070][775][932][1323]
  - 2005: [931][1265]
  - 2006: [2069][2309][1991][1325][127][607][602]
  - 2007: [1263][610][1839][2310][337][1324][2320]
  - 2008: [2308][2744][2745][1016][329][1264][612]
  - 2009: [1425][121][331][1049][2347]
  - 2010: [18][17][1057][2075][16][1327][1286] [1285]
  - 2011: [609][395][1256][1318]
  - 2012: [1058][1059][1478][1047][1328][21][1050] [1034][120]
  - 2013: [392][454][836][837][1033][1060] [1463][1948][1510]
  - 2014: [1015][1329][1258][393]
  - 2015: [22][394][1182][611]
  - 2016: [1649][23][1422]
  - 2017: [391][1048]
  - 2018: [2773][2772]
- **STAG3D/STAGYY**  
1994: [2485]  
1995: [2292]  
1996: [2486][2469]  
1998: [1833][2540]  
2000: [2488][2470][2472][2471]  
2001: [2473]  
2002: [820][2474][2483]  
2003: [2494]  
2004: [2820][2819][1895][1897][1896][2296]  
2005: [1070][819][1898][1899][1894]

2006: [1808]  
 2007: [1072][1071][1176][2479]  
 2008: [683][1178][1177][2230][1901][2490][2634]  
 2009: [684][1907][1415]  
 2010: [685][1902][1858][2231][1908]  
 2011: [2188][1021][1903]  
 2012: [2187][588][550][687][680][49][1909] [2590]  
 2013: [2205][2475][1905][1835]  
 2014: [2844][586][2189][546][143][1607][2202] [1906]  
 2015: [144][682]  
 2016: [2342][587]  
 2017: [543][2017]  
 2018: [551][214][548][54][590][592][1524]  
 2019: [1080][55][681][1996][547][591][2591]  
 2020: [1525]

- **SUBMAR**

[1719] [1718] [2179]

- **SULEC**

<http://www.geodynamics.no/buiter/sulec.html>

SULEC is a 2D/3D arbitrary Lagrangian Eulerian finite-element code developed by Susanne Buiter and Susan Ellis. It solves the equation for conservation of momentum for an incompressible fluid combined with the heat equation. Pressure is calculated as mean stress following an Uzawa iterative penalty formulation (Pelletier et al. (1989) [2000]). Materials are tracked with tracers which are advected with a 2nd-order Runge-Kutta scheme. A true free surface is obtained by a slight vertical stretch of the Eulerian mesh to accommodate surface displacements and the effects of surface processes (Fullsack 1995 [901]). SULEC includes a stabilization term that suppresses numerical overshoot of isostatic restoring forces at interfaces with strong density contrasts (Kaus et al. (2010) [1398]; Quinquis et al. (2011) [2087]). The mechanical and thermal equations are solved using the direct sparse solver PARDISO (Schenk and Gaertner (2004) [2255]).

2011: [2087][773]  
 2012: [325][2513][585][1073]  
 2013: [979]  
 2014: [980][2088]  
 2015: [1913]  
 2016: [2951]  
 2017: [1917]  
 2018: [2515]  
 2019: [774]

- **TERRA** The computational grid is based on a projection of the regular icosahedron onto a sphere and successive dyadic refinements [110]. Concentric copies of such spherical layers of nodes build the domain in radial direction.

[108] [349] [999] [2481] [2482] [347] [346][2842] [344] [2477] [343] [645] [2026][2806][1035] [2833] [2805][1279] [634][2325] [635] [2633] [2807] [981]

- **TERRA-NEO**

[2766]

- **TerraFERMA** TerraFERMA is the Transparent Finite Element Rapid Model Assembler, a software system for the rapid and reproducible construction and exploration of coupled multi-physics models.

TerraFERMA leverages three advanced open-source libraries for scientific computation that provide high level problem description (FEniCS), composable solvers for coupled multi-physics problems (PETSc) and a science neutral options handling system (SPuD) that allows the hierarchical management of all model options.

TerraFERMA inherits most of its functionality from the underlying libraries but adds a layer of control and guidance for building reusable and reproducible applications.

<http://terraferma.github.io/>

[2798] [2797] [2396] [432] [433]

- **YACC** This stands for 'Yet Another Convection Code'.

[2233] [2558] [2556] [2554]

- **UNDERWORLD 1&2** Section 3 of [2081] presents the evolutionary path which lead to this code.

2006: [2407][1844]

2007: [1846][2251][2081]

2008: [1556][1985][1045][2405][2254]

2010: [416][1731][2408][2406][823][417]

2011: [1781][410]

2012: [409]

2013: [179][2252][802][415][572]

2014: [822][2317]

2015: [2080][178][2253][2318]

2016: [2319][1986][1455]

2017: [114][1456][2242][2735]

2018: [1779][2841][115][1823]

2019: [2234][2837][414][418][2235][218]

- **VEMAN**

[181]

## C Matrix properties

### C.1 Symmetric matrices

Any symmetric matrix has only real eigenvalues, is always diagonalizable, and has orthogonal eigenvectors. A symmetric  $N \times N$  real matrix  $\mathbf{M}$  is said to be

- **positive definite** if  $\vec{x} \cdot \mathbf{M} \cdot \vec{x} > 0$  for every non-zero vector  $\vec{x}$  of  $n$  real numbers. All the eigenvalues of a Symmetric Positive Definite (SPD) matrix are positive. If  $A$  and  $B$  are positive definite, then so is  $A+B$ . The matrix inverse of a positive definite matrix is also positive definite. An SPD matrix has a unique Cholesky decomposition. In other words the matrix  $\mathbf{M}$  is positive definite if and only if there exists a unique lower triangular matrix  $\mathbf{L}$ , with real and strictly positive diagonal elements, such that  $\mathbf{M} = \mathbf{LL}^T$  (the product of a lower triangular matrix and its conjugate transpose). This factorization is called the Cholesky decomposition of  $\mathbf{M}$ .
- **positive semi-definite** if  $\vec{x} \cdot \mathbf{M} \cdot \vec{x} \geq 0$
- **negative definite** if  $\vec{x} \cdot \mathbf{M} \cdot \vec{x} < 0$
- **negative semi-definite** if  $\vec{x} \cdot \mathbf{M} \cdot \vec{x} \leq 0$

The Stokes linear system

$$\begin{pmatrix} \mathbb{K} & \mathbb{G} \\ \mathbb{G}^T & 0 \end{pmatrix} \cdot \begin{pmatrix} \mathbf{v} \\ \mathbf{p} \end{pmatrix} = \begin{pmatrix} \mathbf{f} \\ \mathbf{g} \end{pmatrix}$$

is **indefinite** (i.e. it has positive as well as negative eigenvalues).

A square matrix that is not invertible is called **singular** or degenerate. A square matrix is singular if and only if its determinant is 0. Singular matrices are rare in the sense that if you pick a random square matrix, it will almost surely not be singular.

### C.2 Eigenvalues of positive definite matrix

Suppose our matrix  $\mathbf{M}$  has eigenvalue  $\lambda$ .

If  $\lambda = 0$ , then there is some eigenvector  $\vec{x}$  so that  $\mathbf{M} \cdot \vec{x} = \lambda \vec{x} = \vec{0}$ . But then  $\vec{x}^T \cdot \mathbf{M} \cdot \vec{x} = 0$ , and so  $\mathbf{M}$  is not positive definite.

If  $\lambda < 0$ , then there is some eigenvector  $\vec{x}$  so that  $\mathbf{M} \cdot \vec{x} = \lambda \vec{x}$ . But then  $\vec{x}^T \cdot \mathbf{M} \cdot \vec{x} = \lambda |\vec{x}|^2$ , which is negative since  $|\vec{x}|^2 > 0$  and  $\lambda < 0$ . Thus  $\mathbf{M}$  is not positive definite.

And so if  $\mathbf{M}$  is positive definite, it only has positive eigenvalues.

### C.3 Schur complement

From wiki. In linear algebra and the theory of matrices, the Schur complement of a matrix block (i.e., a submatrix within a larger matrix) is defined as follows. Suppose  $\mathbf{A}, \mathbf{B}, \mathbf{C}, \mathbf{D}$  are respectively  $p \times p$ ,  $p \times q$ ,  $q \times p$  and  $q \times q$  matrices, and  $\mathbf{D}$  is invertible. Let

$$\mathbf{M} = \begin{pmatrix} \mathbf{A} & \mathbf{B} \\ \mathbf{C} & \mathbf{D} \end{pmatrix}$$

so that  $\mathbf{M}$  is a  $(p+q) \times (p+q)$  matrix. Then the Schur complement of the block  $\mathbf{D}$  of the matrix  $\mathbf{M}$  is the  $p \times p$  matrix

$$\mathbf{S} = \mathbf{A} - \mathbf{B} \cdot \mathbf{D}^{-1} \cdot \mathbf{C}$$

Application to solving linear equations: The Schur complement arises naturally in solving a system of linear equations such as

$$\begin{aligned} \mathbf{A} \cdot \vec{x} + \mathbf{B} \cdot \vec{y} &= \vec{f} \\ \mathbf{C} \cdot \vec{x} + \mathbf{D} \cdot \vec{y} &= \vec{g} \end{aligned}$$

where  $\vec{x}, \vec{f}$  are  $p$ -dimensional vectors,  $\vec{y}, \vec{g}$  are  $q$ -dimensional vectors, and  $\mathbf{A}, \mathbf{B}, \mathbf{C}, \mathbf{D}$  are as above. Multiplying the bottom equation by  $\mathbf{B} \cdot \mathbf{D}^{-1}$  and then subtracting from the top equation one obtains

$$(\mathbf{A} - \mathbf{B} \cdot \mathbf{D}^{-1} \cdot \mathbf{C}) \cdot \vec{x} = \vec{f} - \mathbf{B} \cdot \mathbf{D}^{-1} \cdot \vec{g}$$

Thus if one can invert  $\mathbf{D}$  as well as the Schur complement of  $\mathbf{D}$ , one can solve for  $\vec{x}$ , and then by using the equation  $\mathbf{C} \cdot \vec{x} + \mathbf{D} \cdot \vec{y} = \vec{g}$  one can solve for  $y$ . This reduces the problem of inverting a  $(p+q) \times (p+q)$  matrix to that of inverting a  $p \times p$  matrix and a  $q \times q$  matrix. In practice one needs  $\mathbf{D}$  to be well-conditioned in order for this algorithm to be numerically accurate.

Considering now the Stokes system:

$$\begin{pmatrix} \mathbb{K} & \mathbb{G} \\ \mathbb{G}^T & -\mathbb{C} \end{pmatrix} \cdot \begin{pmatrix} \vec{v} \\ \vec{p} \end{pmatrix} = \begin{pmatrix} \vec{f} \\ \vec{g} \end{pmatrix}$$

Factorising for  $\vec{p}$  we end up with a **velocity-Schur complement**. Solving for  $\vec{p}$  in the second equation and inserting the expression for  $\vec{p}$  into the first equation we have

$$\mathbb{S}_v \cdot \vec{v} = \vec{f} \quad \text{with} \quad \mathbb{S}_v = \mathbb{K} + \mathbb{G} \cdot \mathbb{C}^{-1} \cdot \mathbb{G}^T$$

Factorising for  $\vec{v}$  we get a **pressure-Schur complement**.

$$\mathbb{S}_p \cdot \vec{p} = \mathbb{G}^T \cdot \mathbb{K}^{-1} \cdot \vec{f} \quad \text{with} \quad \mathbb{S}_p = \mathbb{G}^T \cdot \mathbb{K}^{-1} \cdot \mathbb{G} + \mathbb{C}$$

## D Dont be a hero - unless you have to

What follows was published online on July 17th, 2017 at <https://blogs.egu.eu/divisions/gd/2017/07/19/dont-be-a-hero-unless-you-have-to/> It was written by me and edited by Iris van Zelst, at the time PhD student at ETH Zürich.

In December 2013, I was invited to give a talk about the ASPECT code [1] at the American Geological Union conference in San Francisco. Right after my talk, Prof. Louis Moresi took the stage and gave a talk entitled: *Underworld: What we set out to do, How far did we get, What did we Learn?*

The abstract went as follows:

"Underworld was conceived as a tool for modelling 3D lithospheric deformation coupled with the underlying / surrounding mantle flow. The challenges involved were to find a method capable of representing the complicated, non-linear, history dependent rheology of the near surface as well as being able to model mantle convection, and, simultaneously, to be able to solve the numerical system efficiently. [] The elegance of the method is that it can be completely described in a couple of sentences. However, there are some limitations: it is not obvious how to retain this elegance for unstructured or adaptive meshes, arbitrary element types are not sufficiently well integrated by the simple quadrature approach, and swarms of particles representing volumes are usually an inefficient representation of surfaces."

Aside from the standard numerical modelling jargon, Louis used a term during his talk which I thought at the time had a nice ring to it: hero codes. In short, I believe he meant the codes written essentially by one or two people who at some point in time spent great effort into writing a code (usually choosing a range of applications, a geometry, a number of dimensions, a particular numerical method to solve the relevant PDEs(1), and a tracking method for the various fields of interest).

In the long list of Hero codes, one could cite (in alphabetical order) CITCOM [1], DOUAR [8], FANTOM [2], IELVIS [5], LaMEM [3], pTatin [4], SLIM3D [10], SOPALE [7], StaggYY [6], SULEC [11], Underworld [9], and I apologise to all other heroes out there whom I may have overlooked. And who does not want to be a hero? The Spiderman of geodynamics, the Superwoman of modelling?

Louis' talk echoed my thoughts on two key choices we (computational geodynamicists) are facing: Hero or not, and if yes, what type?

### Hero or not?

Speaking from experience, it is an intense source of satisfaction when peer-reviewed published results are obtained with the very code one has painstakingly put together over months, if not years. But is it worth it?

On the one hand, writing one owns code is a source of deep learning, a way to ensure that one understands the tool and knows its limitations, and a way to ensure that the code has the appropriate combination of features which are necessary to answer the research question at hand. On the other hand, it is akin to a journey; a rather long term commitment; a sometimes frustrating endeavour, with no guarantee of success. Let us not deny it many a student has started with one code only to switch to plan B sooner or later. Ultimately, this yields a satisfactory tool with often little to no perennial survival over the 5 year mark, a scarce if at all existent documentation, and almost always not compliant with the growing trend of long term repeatability. Furthermore, the resulting code will probably bear the marks of its not-all-knowing creator in its DNA and is likely not to be optimal nor efficient by modern computational standards.

This brings me to the second choice: elegance & modularity or taylored code & raw performance? Should one develop a code in a very broad framework using as much external libraries as possible or is there still space for true heroism?

It is my opinion that the answer to this question is: both. The current form of heroism no more lies in writing ones own FEM(2)/FDM(3) packages, meshers, or solvers from scratch, but in cleverly taking advantage of state-of-the-art packages such as for example p4est [15] for Adaptive Mesh Refinement, PetSc [13] or Trilinos [14] for solvers, Saint Germain [17] for particle tracking, deal.ii [12] or Fenics [16] for FEM, and sharing their codes through platforms such as svn, bitbucket or github.

In reality, the many different ways of approaching the development or usage of a (new) code is linked to the diversity of individual projects, but ultimately anyone who dares to touch a code (let alone write one) is a hero in his/her own right: although (super-)heroes can be awesome on their own, they often

complete each other, team up and join forces for maximum efficiency. Let us all be heroes, then, and join efforts to serve Science to the best of our abilities.

#### Abbreviations

- (1) PDE: Partial Differential Equation
- (2) FEM: Finite Element Method
- (3) FDM: Finite Difference Method

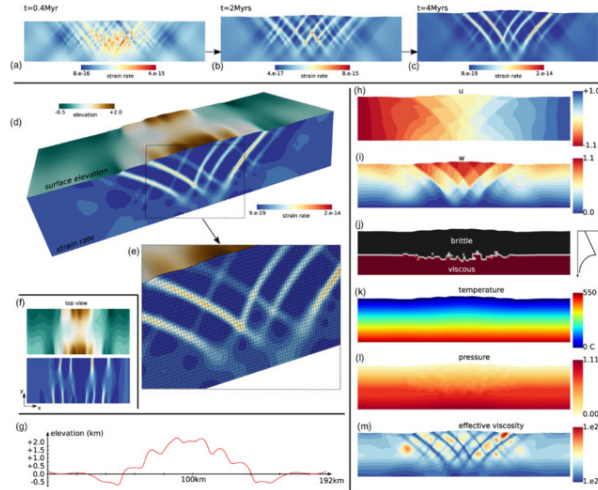
#### References

- [1] Zhong et al., JGR 105, 2000;
- [2] Thieulot, PEPI 188, 2011;
- [3] Kaus et al., NIC Symposium proceedings, 2016;
- [4] May et al, CMAME 290, 2015
- [5] Gerya and Yuen, PEPI 163, 2007
- [6] Tackley, PEPI 171, 2008
- [7] Fullsack, GJI 120, 1995
- [8] Braun et al., PEPI 171, 2008
- [9] <http://www.underworldcode.org/>
- [10] Popov and Sobolev, PEPI 171, 2008
- [11] <http://www.geodynamics.no/buiter/sulec.html>
- [12] Bangerth et al., J. Numer. Math., 2016; <http://www.dealii.org/>
- [13] <http://www.mcs.anl.gov/petsc/>
- [14] <https://trilinos.org/>
- [15] Burstedde et al., SIAM journal on Scientific Computing, 2011; <http://www.p4est.org/>
- [16] <https://fenicsproject.org/>
- [17] Quenette et al., Proceedings 19th IEEE, 2007

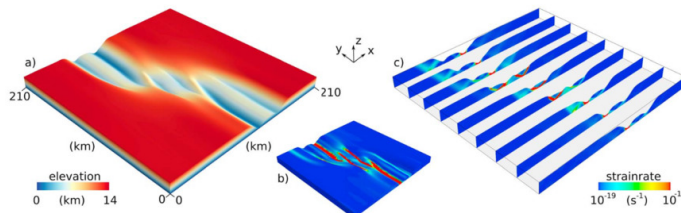
## E A FANTOM, an ELEFANT and a GHOST

While a post-doctoral researcher at Bergen University I developed the FANTOM code. Here is what other people and I have published with it:

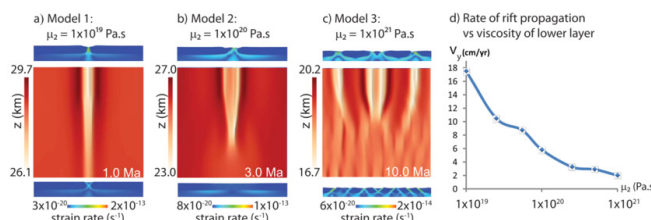
- *FANTOM : two- and three-dimensional numerical modelling of creeping flows for the solution of geological problems*, C. Thieulot, Physics of the Earth and Planetary Interiors, 188, 2011.



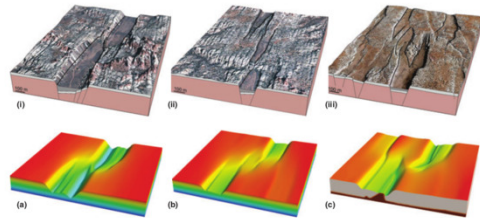
- *Three-dimensional numerical modeling of upper crustal extensional systems*, V. Allken, R.S. Huismans and C. Thieulot, JGR 116, 2011. <https://doi.org/10.1029/2011JB008319>



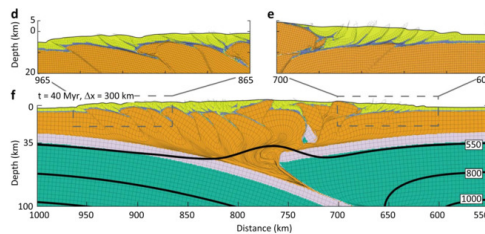
- *Factors controlling the mode of rift interaction in brittle-ductile coupled systems: A 3D numerical study*, V. Allken, R.S. Huismans and C. Thieulot, Geochem. Geophys. Geosyst. 13(5), 2012. <https://doi.org/10.1029/2012GC004077>



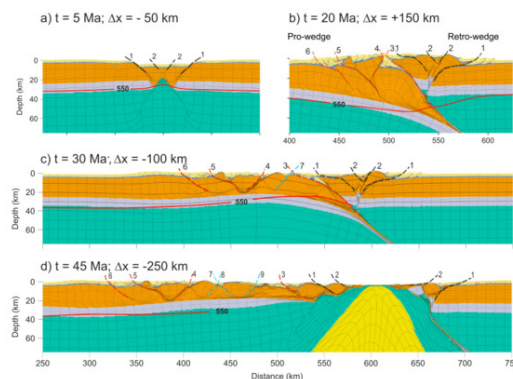
- *3D numerical modelling of graben interaction and linkage: a case study of the Canyonlands grabens, Utah*, V. Allken, R.S. Huismans, Haakon Fossen and C. Thieulot, Basin Research, 25, 1-14, 2013. <https://doi.org/10.1111/bre.12010>



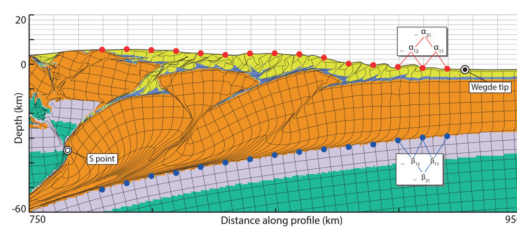
- Three-dimensional numerical simulations of crustal systems undergoing orogeny and subjected to surface processes, C. Thieulot, P. Steer and R.S. Huismans, *Geochem. Geophys. Geosyst.*, 15, 2014. doi:10.1002/2014GC005490
- Extensional inheritance and surface processes as controlling factors of mountain belt structure, Z. Erdős, R.S. Huismans, P. van der Beek, and C. Thieulot, *J. Geophys. Res. Solid Earth*, 119, 2014. doi:10.1002/2014JB011408



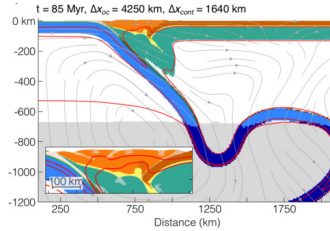
- First-order control of syntectonic sedimentation on crustal-scale structure of mountain belts, Z. Erdős, R.S. Huismans, P. van der Beek, *J. Geophys. Res. Solid Earth*, 120, 5362-5377, 2015. doi:10.1002/2014JB011785
- The Wilson Cycle and Effects of Tectonic Structural Inheritance on Rifted Passive Margin Formation, C.A. Salazar-Mora, R.S. Huismans, H. Fossen and M. Egydio-Silva, *Tectonics*, 37, 3085-3101, 2017. doi:10.1029/2018TC004962



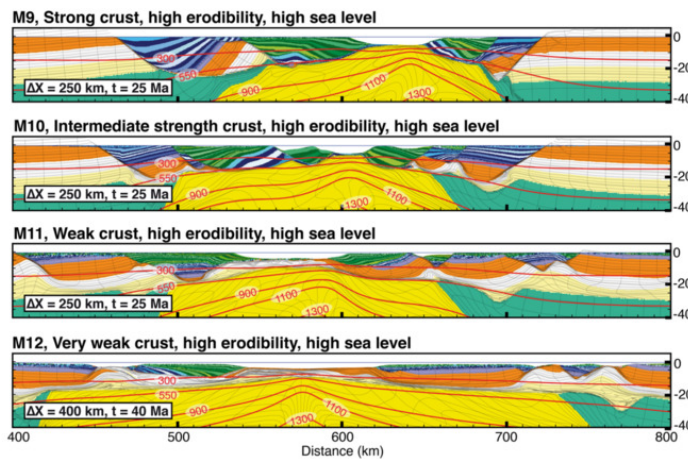
- Control of increased sedimentation on orogenic fold-and-thrust belt structure - insights into the evolution of the Western Alps, Z. Erdős, R.S. Huismans and P. van der Beek, *Solid Earth*, 10, 391-404, 2019. <https://doi.org/10.5194/se-10-391-2019>



- Mountain building or backarc extension in ocean-continent subduction systems - a function of backarc lithospheric strength and absolute plate velocities, S.G. Wolf and R.S. Huismans, JGR, 2019. <https://doi.org/10.1029/2018JB017171> [2803]

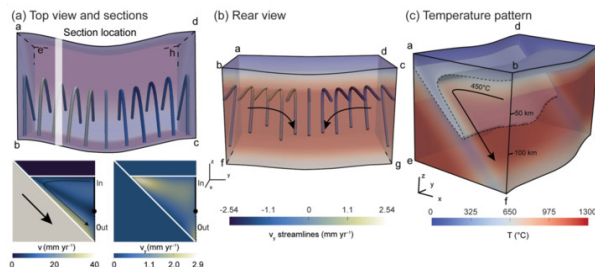


- LongTerm Coupling and Feedback Between Tectonics and Surface Processes During NonVolcanic Rifted Margin Formation, Th. Theunissen and R.S. Huismans, JGR Solid Earth, 124, 2019. [2523]

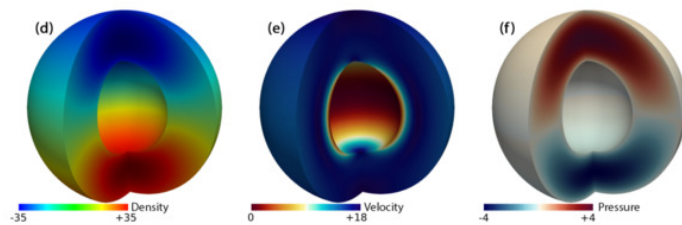


Upon my arrival at Utrecht University in 2012 I started working on a more flexible code, called ELEFANT, which has since very much diverged from FANTOM.

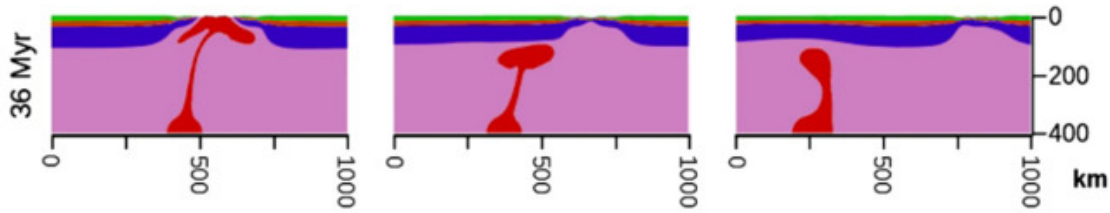
- The effect of obliquity on temperature in subduction zones: insights from 3-D numerical modeling, A. Plunder, C. Thieulot and D.J.J. van Hinsbergen, Solid Earth 9, 759-776, 2018. <https://doi.org/10.5194/se-9-759-2018>



- Analytical solution for viscous incompressible Stokes flow in a spherical shell, C. Thieulot, Solid Earth 8, 1181-1191, 2017. <https://doi.org/10.5194/se-8-1181-2017>



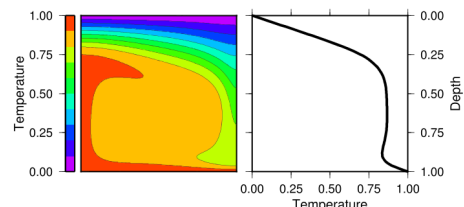
- *Lithosphere erosion and continental breakup: interaction of extension, plume upwelling and melting*, A. Lavecchia, C. Thieulot, F. Beekman, S. Cloetingh and S. Clark, E.P.S.L. 467, p89-98, 2017.



- *Benchmarking numerical models of brittle thrust wedges*, Susanne J.H. Buiter, Guido Schreurs, Markus Albertz, Taras V. Gerya, Boris Kaus, Walter Landry, Laetitia le Pourhiet, Yury Mishin, David L. Egholm, Michele Cooke, Bertrand Maillot, Cedric Thieulot, Tony Crook, Dave May, Pauline Souloumiac, Christopher Beaumont Journal of Structural Geology 92, p140-177, 2016. <https://doi:10.1016/j.jsg.2016.03.003>



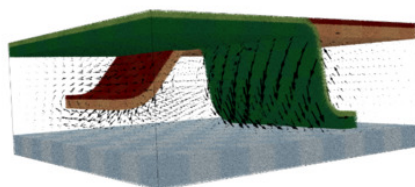
- *A community benchmark for viscoplastic thermal convection in a 2-D square box*, N. Tosi, C. Stein, L. Noack, C. Huettig, P. Maierova, H. Samuel, D.R. Davies, C.R. Wilson, S.C. Kramer, C. Thieulot, A. Glerum, M. Fraters, W. Spakman, A. Rozel, P.J. Tackley, Geochem. Geophys. Geosyst. 16, doi:10.1002/2015GC005807, 2015.



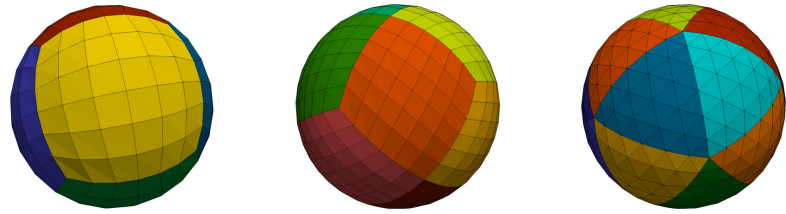
- *Dynamics of intraoceanic subduction initiation: 1. Oceanic detachment fault inversion and the formation of supra-subduction zone ophiolites*, M. Maffione, C. Thieulot, D.J.J. van Hinsbergen, A. Morris, O. Pluempfer and W. Spakman, Geochem. Geophys. Geosyst. 16, p1753-1770, 2015.



- *The Geodynamic World Builder: a solution for complex initial conditions in numerical modelling*, M. Fraters, C. Thieulot, A. van den Berg and W. Spakman, Solid Earth, <https://doi.org/10.5194/se-2019-24>, 2019.



- *GHOST: Geoscientific Hollow Sphere Tessellation*, C. Thieulot, Solid Earth, 9, 11691177, 2018.  
<https://doi.org/10.5194/se-9-1169-2018>



title=Long-term coupling and feedback between tectonics and surface processes during non-volcanic rifted margin formation, author=Theunissen, Thomas and Huismans, Ritske S, journal=Journal of Geophysical Research: Solid Earth,

## F Some useful Python commands

### F.1 Sparse matrices

So far, the best way I have found to deal with sparse matrices is to declare the matrix as a 'lil\_matrix' (linked list).

```
from scipy.sparse import csr_matrix, lil_matrix  
A_mat = lil_matrix((Nfem,Nfem), dtype=np.float64)
```

One then adds terms to it as if it was a full/dense matrix. Once the assembly is done, the conversion to CSR format is trivial:

```
A_mat=A_mat.tocsr()
```

Finally the solver can be called:

```
sol=sps.linalg.spsolve(A_mat,rhs)
```

### F.2 condition number

if the matrix has been declared as lil\_matrix, first convert it to a dense matrix:

```
A_mat=A_mat.dense()
```

The condition number of the matrix is simply obtained as follows:

```
from numpy import linalg as LA  
print(LA.cond(A_mat))
```

## G Some useful maths

### G.1 Inverse of a 3x3 matrix

Let us assume we wish to solve the system  $\mathbf{A} \cdot \vec{X} = \vec{b}$ , with  $\vec{X} = (x, y)$ . Then the solution is given by  
The solution is given by

$$x = \frac{1}{\det(\mathbf{A})} \begin{vmatrix} b_1 & a_{21} \\ b_2 & a_{22} \end{vmatrix} \quad y = \frac{1}{\det(\mathbf{A})} \begin{vmatrix} a_{11} & b_1 \\ a_{21} & b_2 \end{vmatrix}$$

### G.2 Inverse of a 3x3 matrix

Let us consider the 3x3 matrix  $\mathbf{M}$

$$\mathbf{M} = \begin{pmatrix} M_{xx} & M_{xy} & M_{xz} \\ M_{yx} & M_{yy} & M_{yz} \\ M_{zx} & M_{zy} & M_{zz} \end{pmatrix}$$

1. Find  $\det(\mathbf{M})$ , the determinant of the Matrix  $\mathbf{M}$ . The determinant will usually show up in the denominator of the inverse. If the determinant is zero, the matrix won't have an inverse.
2. Find  $\mathbf{M}^T$ , the transpose of the matrix. Transposing means reflecting the matrix about the main diagonal.

$$\mathbf{M}^T = \begin{pmatrix} M_{xx} & M_{yx} & M_{zx} \\ M_{xy} & M_{yy} & M_{zy} \\ M_{xz} & M_{yz} & M_{zz} \end{pmatrix}$$

3. Find the determinant of each of the 2x2 minor matrices. For instance  $\tilde{M}_{xx} = M_{yy}M_{zz} - M_{yz}M_{zy}$ , or  $\tilde{M}_{xz} = M_{xy}M_{yz} - M_{xz}M_{yy}$ .
4. assemble the  $\tilde{\mathbf{M}}$  matrix:

$$\tilde{\mathbf{M}} = \begin{pmatrix} +\tilde{M}_{xx} & -\tilde{M}_{xy} & +\tilde{M}_{xz} \\ -\tilde{M}_{yx} & +\tilde{M}_{yy} & -\tilde{M}_{yz} \\ +\tilde{M}_{zx} & -\tilde{M}_{zy} & +\tilde{M}_{zz} \end{pmatrix}$$

5. the inverse of  $\mathbf{M}$  is then given by

$$\mathbf{M}^{-1} = \frac{1}{\det(\mathbf{M})} \tilde{\mathbf{M}}$$

Another approach which of course is equivalent to the above is Cramer's rule. Let us assume we wish to solve the system  $\mathbf{A} \cdot \vec{X} = \vec{b}$ , with  $\vec{X} = (x, y, z)$ . Then the solution is given by

$$x = \frac{1}{\det(\mathbf{M})} \begin{vmatrix} b_1 & a_{12} & a_{13} \\ b_2 & a_{22} & a_{23} \\ b_3 & a_{32} & a_{33} \end{vmatrix} \quad y = \frac{1}{\det(\mathbf{M})} \begin{vmatrix} a_{11} & b_1 & a_{13} \\ a_{21} & b_2 & a_{23} \\ a_{31} & b_3 & a_{33} \end{vmatrix} \quad z = \frac{1}{\det(\mathbf{M})} \begin{vmatrix} a_{11} & a_{12} & b_1 \\ a_{21} & a_{22} & b_2 \\ a_{31} & a_{32} & b_3 \end{vmatrix}$$

## H Topics in (computational) geodynamics literature

This is a *very* rough attempt at classifying my somewhat extensive bibliography per theme/topic. It goes without saying that this cannot be extensive and that since I started computational geodynamics myself around 2006 these lists are biased towards the last 2 decades or so. In retrospect, the categories I have chosen could have been subdivided into narrower fields. I understand that having 100+ references for 'subduction' or 'mantle convection' is not particularly useful, but it means that all these papers show up in the bibliography section of this book, and the titles of said papers are then searchable per keyword.

### H.1 Big review papers - very good for students

- Subduction

- 1982 Controls of subduction geometry, location of magmatic arcs, and tectonics of (back-)arc regions [598]
- 1995 From the trench to the core-mantle boundary [1436]
- 2001 Stagnant slabs in the upper and lower mantle transition region [895]
- 2001 A Review of the Role of Subduction Dynamics for Regional and Global Plate Motions [132]
- 2002 Subduction zones [2432]
- 2008 Modeling the subduction dynamics [188]
- 2009 Exhumation of oceanic blueschists and eclogites in subduction zones [8]
- 2010 Slab dynamics in the transition zone [187]
- 2011 Future directions in subduction modeling [950]
- 2013 Introduction to the special issue on Subduction Zones of Solid Earth [326]
- 2014 Rheological and geodynamic controls on the mechanisms of subduction and HP/UHP exhumation of crustal rocks during continental collision [367, 368]
- 2017 Subduction-transition zone interaction: A review [1011]
- 2018 Slab breakoff: A critical appraisal of a geological theory as applied in space and time [923]

- Orogeny:

- 1970 Mountain Belts and the New Global Tectonics (1970) [692]
- 2013 the origin of orogens [1320]
- 2012 Experimental modelling of orogenic wedges: A review [1056]

- Mantle convection

- 2005 Numerical and laboratory studies of mantle convection [2484]
- 2012 Dynamics and evolution of the deep mantle [2491]

- Mantle & plates:

- 2009 Supercontinentsuperplume coupling, true polar wander and plume mobility [1616]
- 2011 Mantle convection models featuring plate tectonic behavior [1669]
- 2012 Interior dynamics and long term evolution of habitable planets [2476]
- 2014 Review of Wilson Cycle plate margins [338]
- 2014 Mantle dynamics in the Mediterranean [811]
- 2017 A mantle convection perspective on global tectonics [543]

- Mantle structure

- Thermo-chemical structure of the lower mantle [686]
- Mantle mixing: the generation, preservation, and destruction of chemical heterogeneities [2658]

- Geophysics of Chemical Heterogeneity in the Mantle [2442]
  - Heterogeneity of the lowermost mantle [920]
  - 5 page review of Earth's mantle structure [1171]
- Computational geodynamics
  - 1997 Quantification of uncertainty in computational fluid dynamics [2168]
  - 2000 Modelling plate tectonics and convection in the mantle [1852]
  - 2001 Overview of numerical methods for Earth simulations [1855]
  - 2002 Uncertainty Quantification for Multiscale Simulations [690]
  - 2005 Numerical solution of saddle point problems [159]
  - 2008 Recent advances in computational geodynamics: Theory, numerics and applications [1405]
  - 2013 Overview of adaptive finite element analysis in computational geodynamics [1745]
  - 2013 What makes computational open source software libraries successful? [90]
  - 2014 Advances and challenges in geotectonic modelling [376]
  - 2015 Attributes of a community computer code [571]
  - 2015 Attributes of a community lithospheric modeling computer code [571]
  - 2015 Moving lithospheric modeling forward: Attributes of a community computer code [571]
  - 2017 Software and the Scientist: Coding and Citation Practices in Geodynamics [1277]
  - 2019 Impact of Outreach through Software Citation for Community Software [1278]
- Extensional systems
  - Fault linkage and relay structures in extensional settings [856]
  - Rifted Margins: State of the Art and Future Challenges [2012]
  - Rifted margin architecture and crustal rheology: Reviewing Iberia-Newfoundland, Central South Atlantic, and South China Sea [305]
- Rheology
  - 1983 Rheology of the lithosphere [1460]
  - 1987 Rheology of the Lithosphere [1459]
  - 1999 The yield stress - a review [93]
  - 2002 The Origins of Rheology: A Short Historical Excursion [712]
  - 2003 Modeling shear zones: solid- and fluid-thermalmechanical approaches [2127]
  - 2008 Rheology of the Lower Crust and Upper Mantle [358]
  - 2008 Tectonic pressure: Theoretical concepts and modelled examples [1700]
  - 2010 Rheology of deep upper mantle [1385]
  - 2011 Rheology and strength of the lithosphere [377]
  - 2012 Serpentine in active subduction zones [2147]
  - 2015 Tectonic significance of serpentinites [1085]
- Miscellaneous
  - The solid Earth's influence on sea level [555]
  - Vening Meinesz [2704]
  - The geoscience of coupled deep Earth-surface processes in Europe [515]
- The lithosphere

- Lithosphere tectonics and thermo-mechanical properties: An integrated modelling approach for Enhanced Geothermal Systems exploration in Europe [514]
- The behavior of the lithosphere on seismic to geologic timescales [2752]
- Evolution of the continental lithosphere [2359]
- The structural evolution of the deep continental lithosphere [570]
- Analogue modelling: historical outline [1501]; Approaches, scaling, materials and quantification, with an application to subduction experiments [2243]
- Exhumation of (ultra-)high-pressure terranes: concepts and mechanisms [2743]
- Paradigms, new and old, for ultra-high-pressure tectonism [1112]
- The role of solid-solid phase transitions in mantle convection [806]
- Verification, validation and confirmation of numerical models [1976]
- Experimental modelling of orogenic wedges [1056]
- Structure and dynamics of the mantle wedge [2663]
- Mountain building, observations and models of dynamic topography [842, 812]
- Reconciling laboratory and observational models of mantle rheology in geodynamic modelling [1445]
- Controlling parameters, surface expressions and the future directions in delamination modeling [1018]
- Salt tectonics at passive margins: Geology versus models [297]
- Structural dynamics of salt systems [1302]
- Crustal versus mantle core complexes [296]
- Precambrian geodynamics: concepts and models [954]
- A review of brittle compressional wedge models [325]
- accreted terranes: a compilation of island arcs, oceanic plateaus, submarine ridges, seamounts, and continental fragments [2514]
- Hotspot swells [1450]
- Theory of scale models as applied to the study of geologic structures [1240]

## H.2 Analogue modelling

1975: [704]  
 1982: [2506]  
 1988: [2006][603]  
 1990: [1750][1355]  
 1991: [651]  
 1992: [2222]  
 1993: [1920][2322]  
 1997: [2653]  
 1998: [351]  
 1999: [630][133][813][1922]  
 2000: [2246][2367][439]  
 2001: [1125][441]  
 2002: [631]  
 2003: [2361][1882][1921]

2004: [2248][2247]  
2005: [1364][2249][2368]  
2006: [2287][2547][602][1542][1991][1735]  
2007: [2369]  
2008: [516][902][797]  
2009: [2029][227]  
2011: [632][1017][1055]  
2012: [1056]  
2013: [1674][2656][1083][1789][1784][725][1426]  
2015: [405][2196][1457][451]  
2016: [2288][452]  
2017: [404]  
2018: [2035]  
2019: [1813][2250][1887][2953]

### H.3 Archean tectonics, early Earth

[236] [2705] [1375] [665] [2675] [2674] [2146] [2649] [1057] [1677] [1986] [840] [414][955]

### H.4 Anisotropy, Lattice/Crystal preferred orientation, SKS splitting

[2890] [1874] [1875] [1876][1376] [139] [563][2164] [134][137] [556][1315] [1958][2241] [1792] [802] [801] [752] [1678] [2013]

### H.5 Benchmark, analytical solutions, code comparisons, methodology, num. methods, theory

1974: [1201]  
1975: [2717][2718]  
1984: [2865]  
1989: [209]  
1990: [2563]  
1993: [1561]  
1994: [277]  
1995: [278][1850][901]  
1996: [2912][1848]  
1997: [2162]  
1999: [1632][203]  
2001: [1851][2650]  
2002: [1874]  
2003: [2492][1842][974][975][2494][2279]  
2004: [1401][1367][1373][1876]  
2005: [1881]  
2006: [1400][1863][1969][1880][2498]  
2007: [2555][467][1397][1392][1846][952][633] [2946]  
2008: [2905][688][2573][1508][1744][945] [2655][1177][269][614][447][2490][1276]  
2009: [1441][930][2689][2089]  
2010: [1396][1398][764][1439]  
2011: [739][2589][1190][1879][637][1558]  
2012: [585][457][1503][1742][940][60]  
2013: [470][1413][968][1275]  
2014: [2526][1746][1657][2412]  
2015: [1555][2204][469][1743]  
2016: [745][210]  
2017: [2197][2797][1697]  
2018: [1779][590]  
2019: [508][1650][664][926][871][2858]

## H.6 Core dynamics, core formation, CMB temperature/heat flux

[1146][219] [2609] [1896] [1538][1022][2230] [1438] [1902][1531][2231] [2879] [580][2577] [1905] [1524] [2847]

## H.7 Computational Structural geology

1971: [2431]  
1995: [839]  
2000: [4][2564]  
2001: [1701]  
2008: [1700][2264]  
2011: [882]  
2013: [2386][1540]  
2015: [2014][1332]  
2017: [1892][2266]  
2018: [1891]  
2019: [1656][2826][2385]

## H.8 Channel flow model

[1323] [1325][1767][127] [1324] [1318]

## Continental collision

[1822] [1230] [770][351] [769][2785] [2367] [2123] [2368] [2268] [1544] [1687] [2261] [1545] [2063] [1692][948]

## H.9 Core complexes

[978] [2545] [2548] [1541][2256] [2015] [296]

## H.10 Dataset (gravity, goce, grace, tomography, gps, heat flow) and/or their calculations/use

1977: [2192]  
1981: [751]  
1990: [1627]  
1991: [2390]  
1993: [1380]  
1998: [186]  
2001: [343]  
2003: [1505][2384][2034][2384]  
2006: [1719]  
2007: [1788][1671][2164]  
2008: [2917][2917][2191]  
2010: [642][2344]  
2011: [2163]  
2012: [1162][2135][1162][833][2346]  
2013: [2136][754][644]  
2014: [1994][753][1504][1617]  
2015: [242][291]  
2016: [1470][1871][2195][727, 2874]  
2017: [2194]  
2018: [1990][1161]  
2019: [2370][2336]

## H.11 Discontinuous Galerkin (DG)

1973: [2120]  
1997: [97]  
1998: [533]  
1999: [2167]  
2000: [530][287][424]  
2002: [425][529][53][1084]  
2003: [534]  
2004: [525]  
2005: [421][526][520][521][522]  
2007: [527][829]  
2008: [1377][1831][708][2007]  
2009: [528][523][524][1936][2335][66][537]  
2010: [1937][532][1832][1378][536]  
2011: [936][1938]  
2012: [1394][1935][1662, chapt. 31]  
2013: [2716][2148]  
2015: [1555][1365]  
2016: [535][1726]  
2017: [828][1282][1164][453][2289][2291] [2290][2889]  
2018: [2062][2804][800][1872]

## H.12 Dynamo

### H.13 (role of) Elasticity in geodynamics modelling

1984:[2865]  
1995:[378]  
1996:[1147]  
1998:[552]  
2001:[2686]  
2002:[1877][1841]  
2003:[1242][2751]  
2005:[1881]  
2006:[1400][1880]  
2007:[1397]  
2008:[67][907]  
2009:[2089]  
2010:[181]  
2012:[940][1370]  
2013:[2728]  
2014:[822][859]  
2015:[2525]  
2016:[78][1334][1962][78]  
2018:[743]  
2019:[1996]

### H.14 (Geodynamics+) surface processes, erosion, sedimentation, topography evolution

1953: [1588]  
1960: [606]  
1990: [1820][785]  
1992: [118][437]  
1993: [2050][2784]  
1994: [1233][1483][1480][994]

1995: [434][1484]  
1996: [64][124][1481]  
1997: [268][916][102]  
1998: [677][2598]  
1999: [2787][350][103][2551]  
2001: [2873][2580][279][364][581][593][1819]  
2002: [2790][1830][917][2778]  
2003: [262]  
2004: [838][1006][2348][2357]  
2005: [1533][2792][1520]  
2006: [2185][263][228][2350][2447][1007]  
2007: [372][2310][2550][2446]  
2008: [24][2186]  
2009: [2777][1515][1706][2029][652][227]  
2010: [2788][2578][274][274][271][604]  
2011: [2184][1055]  
2012: [1458][280]  
2013: [2694][270][836][837][267][445][2579] [423]  
2014: [594][540][791][789][2404]  
2015: [2588][861][539]  
2016: [541]  
2018: [1361]  
2019: [42][2221]

## H.15 Geotechnics

[2437] [1037] [2919] [1036] [1038] [376]

## H.16 Glacier dynamics, ice sheets, ice flow, ice rheology

[2796] [1066] [877] [59][878] [2453][2954] [2875] [2051] [1587] [1287][883] [1502] [1661] [1170]

## H.17 (use of) Inverse methods, inversion, adjoint methods, assimilation

1998: [401]  
1999: [2223][2224]  
2001: [233][1399]  
2002: [2315]  
2003: [348]  
2004: [1292]  
2007: [1289]  
2008: [2394][1641]  
2009: [2725][2393][2345]  
2012: [1924]  
2014: [2813][1224][1617]  
2015: [2730]  
2016: [982][213][2838][106]  
2017: [1597]  
2018: [214][981]

## H.18 Large scale mantle-plate interaction, whole Earth models

[2862] [1670] [565] [2742][1010][2402][556] [19][2187][588] [985][2827] [1698] [1236][2584]

## **H.19 Crust/Lithosphere modelling, plate motion, plate stress**

1977: [600]  
1981: [289]  
1984: [1516][2151]  
1986: [2445]  
1988: [650][649]  
1989: [1319]  
1990: [448]  
1991: [462][651]  
1992: [1814][374][1446]  
1993: [1933][272][1053]  
1994: [315][119]  
1995: [152][276][1451][378][772][2901]  
1996: [124][169][1322]  
1997: [2538][102][365][1849]  
1998: [200][1590][1452][1717][1730][1103] [170][1730]  
1999: [2785][203][511][905][1853][1573]  
2000: [1137][1537][1572][1102][1569][2019] [2286]  
2001: [1231][135][1399]  
2002: [1536][561][70][942][1447]  
2003: [2791][2751][973][2592][2684][330][1579] [1987]  
2004: [2544][946][568][2070]  
2005: [1123][2781][1755]  
2006: [324][69][1404][900][569][1991][602] [2236]  
2007: [7][1493][978][1324]  
2008: [6][2545][1154][355][516][472] [1403][826][471][335][1971]  
2009: [331][2039][2165][352][567]  
2010: [1159][823][1057][2596][2038][2391][2075] [1327]  
2011: [2142][473]  
2012: [2740][2669][325][1478][1030][2570]  
2013: [2752][1510][867][2741][732][2206] [2298]  
2014: [1368][741][2722][2776][2260] [1691][1082][911][1888]  
2015: [2720][2525][1715][733][742]  
2016: [2732]  
2017: [2208][1984][2711][2505][1298]  
2018: [2723][1943][115][1932]  
2019: [1492][1461][591][2018][1712][461]

## **H.20 Delamination, edge driven convection, gravitational instability, mantle unrooting**

[1451] [1227] [1452][2284][1717] [1448][2285] [1838] [765] [1016][2678] [2680] [1593] [1510][2435] [92][1368] [2733] [114] [2013]

## **H.21 Detachment faults**

[2764] [1331] [2142] [1683] [1088]

## **H.22 Dynamic topography**

1985: [1117]  
1987: [2143]  
1992: [1431]  
1993: [1099][1098]  
1999: [357]  
2003: [564]  
2009: [558]

2010: [234][274][2409][2324]  
2011: [2101]  
2012: [2323][2880]  
2013: [267][842]  
2015: [62][1457][646]  
2016: [1212][1109][2838][2424]  
2017: [2840][61]  
2018: [2585]  
2019: [681][636][218]

## H.23 Lithospheric stress, intraplate stress

1975: [848]  
1976: [2156]  
1977: [436]  
1979: [2158]  
1989: [239]  
1991: [2810]  
1992: [2157][2818][2948][517]  
2001: [2422]  
2004: [1635]  
2005: [2543]  
2008: [204][987]  
2009: [989][1918]  
2010: [181]  
2012: [1919][988]  
2013: [986][2741]  
2014: [2597]  
2018: [2585]

## H.24 Passive margins

[518] [1633] [931] [516] [1403] [823] [1944] [2101] [1946] [297] [1722] [2827] [1723] [933] [1942] [2220] [1884] [2515] [2915]

## H.25 Folding, buckling

1970: [2099]  
1971: [2100]  
1991: [845]  
1993: [2890]  
1995: [846]  
1996: [2891]  
1999: [1922]  
2001: [2269]  
2002: [1877]  
2003: [1921]  
2006: [884]  
2008: [2265][1700][2278]  
2009: [2351]  
2010: [2116]  
2011: [880]  
2012: [2114][1054][2263]  
2013: [2115]  
2014: [879][881]  
2016: [885]

## H.26 Geoid

1984: [638][1116][2151][2155]

1985: [1117]

1986: [639]

1988: [167][849]

1992: [2897][1431]

1993: [2884][2152]

1994: [1443]

1995: [1444][1856]

1996: [1843]

1998: [401][442]

2001: [2913]

2008: [1783]

2009: [1441]

2010: [984][2392]

2012: [1197]

2013: [2313]

2015: [1653]

2017: [1046]

2018: [1449]

## H.27 Geothermal Energy

[2080] [2137]

## H.28 Grain size (evolution) & influence on geodynamics

[1384] [266] [659][2374] [2377] [1124][2127] [2381] [2203] [172] [166] [2527][2583][2014][1004] [432][618][1883][2266] [161][142][1884] [1885]

## H.29 LLSVP, ULVZ, CMB layer, thermo-chemical piles, D" layer

1986: [640]

1988: [1144]

1989: [1145]

1996: [219]

1997: [1417]

1998: [2478]

2001: [2366]

2002: [2380][2500] 2004: [1763][1895]

2005: [1765][1898][1899]

2006: [1900]

2007: [1176][1825][2003][1199][2863]

2008: [921][1901][2421]

2010: [2423][1762][1902][2602]

2011: [248][2502][2613]

2012: [2428][634][680]

2013: [1602][250][251]

2014: [339][1607][2553]

2015: [1886][1156][682][2793]

2016: [716][2552]

2017: [1200]

2018: [619][1601][1192]

2019: [1180][2113]

## **H.30 Magma ocean**

[768] [671] [2590] [2042] [1677]

## **H.31 Magma transport / melting / two phase flow/ (intra-plate) volcanism / lava flow/ continental flood basalt**

1984: [2301][1753]

1986: [2302]

1988: [2300]

1993: [2397][2493]

1994: [1349]

1995: [206]

1996: [1530]

1998: [2092]

1999: [668]

2000: [766]

2001: [173]

2002: [2362]

2003: [171]

2005: [1974]

2006: [1969]

2007: [2401][1839][765][544]

2008: [1178][1175]

2009: [85]

2010: [83][1150][560][689]

2011: [81][2922][2923][184][1828]

2012: [2830][1371][2590]

2013: [1413][1811][1835]

2014: [1372]

2015: [2583][1869][2132][2160][2144][2832]

2016: [1414][2633][1776]

2017: [701]

2018: [1668]

2019: [622][2276]

## **H.32 Mantle convection/dynamics, whole Earth models, plate interaction**

1972: [2001]

1974: [2856]

1975: [1191][386]

1976: [1757]

1978: [1727][1234][1114]

1979: [1675][387][2316]

1980: [1964][1339][2297][2872]

1981: [388][1309][1115]

1982: [1340][1229][390]

1983: [1232][1228][480][1756][479][2871]

1984: [1965][1341][1139][1152][638][236][481] [1867][843]

1985: [1342][109][485][605][2294]

1986: [639][1100][2078]

1987: [2864]

1988: [1142][999]

1989: [165][2274][2416]

1990: [2563][1093][1420][2371]

1991: [482][1681][910][2617]

1992: [164][1695][2651][478]  
1993: [2884][1343][2467][389][402][2618][2481] [2898][1728][2870][2662]  
1994: [1143][487][2482][1296][1562]  
1995: [2900][2620][347][2110][168][2065][2066] [2373][2607][1680]  
1996: [2888][1219][2212][2213][2486][2574] [205][345][1375][1101][2619][2112][2111] [1565][1299][349]  
1997: [1220][1300][346][1849][2379][2109][500] [2608][1528]  
1998: [38][1301][667][2487][2478][2566] [2567][344][1826][1559][2609][2755]  
1999: [728][2652][630][2477][559][501]  
2000: [15][1141][665][2488][2470][2472][2471] [2909][1560][554][2372]  
2001: [2650][2154][1577][2615][1824][2913]  
2002: [2464][1841][2474][2611][2610][2483]  
2003: [1124][1570][1875][821][101][2343]  
2004: [2675][2820][2819][1897][2614][285]  
2005: [2484][396][1070][1578][1471][1764][2604] [1898][1894][466]  
2006: [136][1914][1659][2430][2853]  
2007: [1915][1737][259][258][1072][1071][1238] [2479][2499][1338]  
2008: [2490][2489][465][257][683][2037][1213] [2634][1013]  
2009: [2806][847][1035][684][1972][2750][2671] [283]  
2010: [340][685][2833][1902][1216][2881][2612] [284]  
2011: [1669][2188][2805][1571][138]  
2012: [185][549][687][2376][2767]  
2013: [1214][635][2558][250][382][1809] [812][550][572][566][2411][2042]  
2014: [58][1181][586][841][2189][546][143] [1906][2414][2412]  
2015: [2525][2766][144]  
2016: [888][2342][212][2768][2771][2633][468]  
2017: [990][495]  
2018: [548][54][551][2770]  
2019: [1080][1710][547][1574][2591][211][891]  
2020: [1525]

### H.33 Mantle rheology, phase transitions, stratification, (temperature) profile

1923: [2795]  
1952: [199]  
1982: [2861][483]  
1985: [488]  
1992: [2893]  
1993: [2481][174][1429][2418]  
1994: [2667][2899][2417]  
1995: [2887][484][2292][2468]  
1996: [2002][1802][2469]  
1997: [1803][2004]  
1998: [401][1424]  
1999: [2338][1421][2621]  
2005: [1179][1899][1894][2439][2438]  
2006: [1307][2420]  
2007: [1997][1870][2479][2440][1634][1308]  
2009: [1907]  
2010: [1391]  
2011: [1306][824][1903][2613][2441]  
2012: [2491][2233][1909][2442]  
2013: [816][2475][1303]  
2015: [82][1004]  
2016: [2549][154]  
2017: [2622][1304]  
2018: [1709]

2019: [1305]

### **H.34 Mantle wedge**

1978: [2562]  
1992: [641]  
2001: [193][1125]  
2003: [2663]  
2006: [1027][966]  
2007: [1026][1462][1665]  
2008: [1464][426]  
2009: [1547][1165]  
2010: [2179][1222]  
2011: [2923]  
2014: [2706][1686]  
2018: [2043]

### **H.35 Mixing, stirring, degassing**

[1965] [1420] [2002] [545] [1268] [2658] [821][2664] [542] [1026][1915][2654] [1571][2227] [1970]

### **H.36 Obduction, ophiolites**

[1110] [1111] [1836] [9] [734] [2190]

### **H.37 Plate motion and mantle, plate tectonic reconstruction**

1973: [1759]  
1974: [2382]  
1990: [673]  
1992: [2930]  
1994: [1096]  
1998: [2904]  
2002: [2426]  
2003: [799][2141]  
2007: [2907]  
2009: [1616][2623]  
2010: [2423][674]  
2012: [1273][1104][2084][1215][715][2325]  
2013: [1864][566]  
2015: [2852]  
2017: [2448]  
2019: [2512]

### **H.38 Plume dynamics**

1991: [1416]  
1993: [1418]  
1994: [1911][818][1563][1140]  
1997: [2653][1419][1528]  
1998: [2540][2425]  
1999: [1529]  
2002: [820][631][1939][2500]  
2003: [2229]  
2004: [1009][2296]  
2005: [2501]

2006: [1293][1629][1630][2895][1808][1953][2082] [1408]  
2009: [2687][247][817]  
2011: [2557][2502][360][1781][632][2571]  
2013: [628][1733][39][2656]  
2015: [621][1156]  
2016: [1430]  
2017: [2877][1837]  
2018: [627][2572]  
2019: [55]

## H.39 Plume-Lithosphere interaction, LIP, hotspots

1994: [2150][818]  
1995: [2779]  
1996: [2903]  
1998: [186][1833]  
1999: [1834][2327]  
2001: [2686]  
2002: [858]  
2003: [2648]  
2005: [370][819]  
2006: [645]  
2007: [2429]  
2008: [2586][2358]  
2009: [379][2920][83][2510][1703]  
2010: [809]  
2011: [2365][2636]  
2012: [1270][1086][760]  
2013: [179][301]  
2014: [369][963][338][334][1550]  
2015: [178][972][1490][1782][1622][1780][886]  
2016: [840][924][1489]  
2017: [95][282][95][156][1491]  
2018: [619][868]  
2019: [1488][2419]

## H.40 Porous media

[2302] [2300] [2397] [2281] [750]

## H.41 Preconditioner business

[158] [160] [2593]

## H.42 Reservoir modeling

[1977]

## H.43 Regenauer-Lieb

2000: [2126]  
2003: [2127]  
2004: [2134]  
2006: [2129][2125]  
2009: [2131]  
2013: [2124]

## H.44 Rheology, material parameters, rock mechanics

1951: [719][1113]  
1952: [720]  
1968: [399]  
1969: [1133]  
1972: [420]  
1974: [1475]  
1979: [1014][798]  
1980: [253]  
1981: [675]  
1984: [2107][475][2692]  
1986: [1386]  
1987: [1459]  
1990: [2783]  
1992: [74][474][1382][1472]  
1993: [1383]  
1994: [870]  
1995: [1474][1000]  
1996: [2726][1203]  
1997: [795, 794] 1998: [552][1682]  
1999: [1374]  
2000: [2210][2105][1769, 1770]  
2001: [1660]  
2002: [1205]  
2003: [1204][1381][1829]  
2005: [702][722]  
2006: [2211][375][1844][1600]  
2007: [1194][1473][825]  
2008: [1556][358][1494][996]  
2009: [1390][1407]  
2011: [1546][1411]  
2012: [2147]  
2013: [1539][1790][1827]  
2015: [469]  
2017: [221]  
2019: [2113][1138]

## H.45 Rifting, seafloor spreading, mid-ocean ridges, pull-apart basins, extension

1972: [1518]  
1973: [890]  
1978: [2415][1752]  
1980: [288]  
1982: [125]  
1983: [784]  
1984: [2052]  
1985: [237]  
1986: [1226][2950][2949][1857][1754][313]  
1988: [314]  
1989: [1774][275][1295][2383][265][264] 1990: [814][1626][1750][448][449]  
1991: [2568][316]  
1992: [2929][757]  
1993: [1039]  
1994: [2576][1349]

1995: [1040][1393]  
1996: [731][153][1738]  
1998: [2093]  
1999: [295][317][1041]  
2000: [2282]  
2001: [1261][1260][873][875][874]  
2002: [1262][1135][626][2683][140][1266] [1259][2683][1536]  
2003: [1257][1136][578][2782]  
2004: [1193][2303]  
2005: [1265][584][2679][2681]  
2006: [2547][577][595][2021][1542][1735]  
2007: [1247][1724][2682][749][1263][372][2369] [2764]  
2008: [576][1081][329][1264][2020][2133][582]  
2009: [10][1427][2347]  
2010: [63][953][857][949]  
2011: [25][773][1256]  
2012: [26][300][120]  
2013: [27][299][454][1463][1426][1797][2749] [958][1620][962][756]  
2014: [1168][1619][298][1487][755][2067][1618] [1258][1015][755]  
2015: [1913][509][1272][2318][697][2817]  
2016: [1962][1346][2951]  
2017: [1543][303][156][1917]  
2018: [455][306][302][2515][1347][2220][2016] [1823][2773][2772][957]  
2019: [1598][2952][42][744][1813][456][2523] [1330][2953]

## H.46 Salt tectonics, Shale tectonics

1978: [2801]  
1991: [2496]  
1992: [2869]  
1993: [1920][2660][2757][2759]  
1996: [1747]  
1998: [993]  
2004: [1290][932][1749]  
2007: [1243][1732]  
2009: [1049]  
2010: [17][16][1286][1285][18]  
2011: [297]  
2012: [835][1608][1047][21][1050][1034][2209]  
2013: [1033][1948]  
2014: [107][831][830][980][1947]i[1999]  
2015: [832][539]  
2016: [1716][23]  
2017: [1048][1167]

## H.47 Sea Level evolution

[2005] [1997] [558] [555]

## H.48 Segregated methods to solve the Stokes system

[2095] [1151] [1595] [724] [2738] [2739] [2594]

## H.49 Seismo-tectonics, subduction earthquakes

[224] [2724] [2631, 2630][1791][1890] [2632] [1186] [1043][1174][1185]

## H.50 Subduction

This category should be subdivided into continental collision, subduction 2D & 3D...

- 1978: [1114]  
1980: [1773]  
1982: [598]  
1985: [2522]  
1986: [1336][1805]  
1989: [239][1804]  
1990: [1235][1442]  
1992: [2897][2780][1097]  
1993: [1357][748][2784][2322]  
1994: [2910][2789][2753][2754][129][913]  
1995: [1720]  
1996: [486][997][2748][2911]  
1997: [1158][1437][1960][1927]  
1998: [1297][333][308][1321][2747]  
1999: [1128][133][357][2199][771][2277][769] [117][1926]  
2000: [2516][261][126][439]  
2001: [371][327][441][557]  
2002: [496][510][959][2432][1326]  
2003: [2123][903][944][190]  
2004: [2560][245][123][2561][2248][2247][787] [977]  
2005: [1337][1521][1042][788][46][1042] [1714][2443][2249][1521]  
2006: [865][2201][1719][951][904][2032][2407] [1655][1127]  
2007: [47][2823][610][503][1718][411][2244] [1029][1031][1702][1861][1973][1665][2946] [196]  
2008: [2825][1985][998][2744][2745][226] [1800][225][67][803][965][902][373] [662][661][970][1945][2308][612][2816] [695]  
2009: [2828][189][807][121][1425][947][967] [805][1615][1862][1664][132][8][2829] [1269]  
2010: [1121][1663][1731][412][416][1610][2406] [1865][2924][2090][1858][1548][2354][2408] [2458]  
2011: [1611][1643][395][72][410][969][2087] [208][961][1549][2254][1017][1012]  
2012: [45][1328][1313][1316][2866][1058][1059] [2181][2513][2524][240][502][413][409] [938][1614][155][2587][197][2353][2710] [397][2851][991]  
2013: [1916][1112][44][1910][2849][2921][1609] [1314][1288][1674][725][2546][392][2252] [896][1693][1889][1789][1060][2631][2630] [427][2708][2085][363][1890][2245]  
2014: [2180][1221][2182][1840][822][859][866] [918][2709][2707][1612][245][76][2436] [77][2632][1433][1329][367][368][460] [458][2355][2317][1859]  
2015: [178][241][249][429][1453][2642][646] [1721][2207][451][726][2855][499]  
2016: [2554][1105][2183][1740][1694][1729][1776] [1310][1311][1628][452]  
2017: [1456][2242][2017][2711][1678][2824][2331]  
2018: [2841][592][2388][459][2839][1709][2] [1692][192]  
2019: [1684][1739][2257][418][2234][2356][1775] [2666][231]  
2020: [29]

## H.51 Subduction - slab detachment, break-off

- 1985: [894]  
1992: [2811]  
1995: [2854][2712][643]  
1997: [2809]  
1998: [654][419]  
2000: [2812]  
2002: [328]  
2004: [976]  
2006: [810]  
2008: [2947]  
2009: [43][361]  
2010: [362][105]  
2011: [737][2641][2258]

2012: [736][740]  
2013: [415][1688][979][735]  
2014: [738][166][2715]  
2015: [2714][861]  
2017: [876][1685]  
2018: [923][142]  
2019: [162]

## H.52 Subduction + water (fluids)

[2665] [2179] [969][2657] [804] [2088][1686][1704][2798] [241] [432][2756] [433][1775][1613]

## H.53 Subduction/plate tectonics initiation

1978: [202]  
1982: [518]  
1984: [422]  
1989: [512]  
1991: [1873]  
1996: [1423]  
1998: [2559]  
1999: [813]  
2000: [2071]  
2001: [706][2128][260]  
2004: [2433][1094][2375]  
2003: [1122]  
2005: [195]  
2007: [1493]  
2008: [2586]  
2010: [1944][366]  
2011: [71][1946][1585]  
2012: [2434][2524][1581][2326]  
2013: [750][1722][1496][1789]  
2014: [2145][1723]  
2015: [1683][2015][2640][1586]  
2016: [587][1725]  
2017: [1711]  
2018: [2918][73]  
2019: [130][1088][2591]  
2020: [48]

## H.54 Subduction - flat/low angle/horizontal subduction

2000: [2643]  
2001: [2644]  
2002: [2646][2645]  
2004: [2647]  
2008: [2010][797]  
2011: [609]  
2012: [1705][2181]  
2015: [939][2509][752]  
2016: [464]  
2019: [2352][2235][1676]

## H.55 Teaching

[1052] [1412] [180]

## **H.56 Tectonics, small deformation, rock mechanics**

REMOVE CATEGORY!! [1283] [1187]

## **H.57 Wilson cycle, supercontinent cycles**

[2575] [799] [2907][544] [2882][1972] [1571][360] [338][1181][2189] [2807] [130][2799]

## **H.58 Meshless methods (SPH, RKPM, DEM, FPM, ...)**

[1673] [147] [1866] [2927] [151][1604] [1281] [1606][1645][1605] [1646][1741] [2729][1245] [834][1648][2535][2536][2537] [1647][2822] [321] [322][1551] [625] [2058][1514][1387][2461][1217] [2460] [1477][2702] [624][1557] [1950] [1506] [1777][1778]

## **H.59 Element Free Galerkin Method**

[145] [149] [150] [146][573] [148] [2053][2926] [1134][1388] [1246] [2848][1654]

## **H.60 Planetary accretion, exoplanets, planet formation, segregation**

[1576] [1624][1019] [2612] [1625][2668] [2670] [1020][2844] [1934][2616]

## **H.61 Accretionary wedges, nappes, thrust wedges, orogenic wedge, fold-thrust belt**

[2444][647] [615][617] [616] [1483] [2800][2361][1882][2684] [2350][2822] [2209] [2206] [1707] [1708][2208] [774][1777][1778]

## **H.62 Thrust-wrench fault**

[2196]

## **H.63 Transpressional systems**

[2541] [2538] [1485][2592] [1554] [1892][2208] [1891]

## **H.64 Urey ratio**

[1495] [1904]

## **H.65 Intrusions, diapirism, Rayleigh-Taylor instability**

1968: [2098]

1972: [177]

1975: [704]

1981: [289]

1988: [2275]

1992: [2651][2869][2758][2762][2690]

1993: [2661][1920][2044][2050][2660][2045] [2049][2759][2662]

1994: [2765]

1995: [2760][206][2760]

1997: [2761]

1999: [721]

2001: [1399][723]

2003: [973][2673]

2004: [971][1290][960]

2007: [964]

2008: [354][2947][1815]

2011: [773][2008]

2013: [893]  
2014: [830]  
2015: [832][892]  
2016: [406]  
2018: [948]

## H.66 Visualization, rendering

[815] [447][2405][191] [1742] [590]

## H.67 Solving Stokes Saddle Point problem

[1526] [2176] [862] [778] [438][777] [256] [1651] [709][1925] [1206]

## H.68 Celestial bodies

- Europa [2333, 2334, 1801, 1129][1130][1131, 1372, 28]

- Moon [768][767][671][670] [2894]

- Venus 1990: [2295]

1991: [1566]  
1992: [1431, 2398]  
1993: [1429, 1567]  
1995: [1568, 1856]  
1996: [2378]  
1998: [1682][2121][1847][2027]  
1999: [2122]  
2003: [2696]  
2005: [2677]  
2010: [2409]  
2011: [1978]  
2012: [49]  
2013: [1239]  
2014: [995][963]  
2017: [589][629]  
2018: [1449]

- Mars

1990: [2295]  
1996: [1147]  
1998: [2121]  
2001: [1949]  
2004: [1580][2676]  
2005: [2677][1974]  
2006: [1659, 2174, 1408]  
2007: [2175]  
2008: [1658]  
2009: [1415, 2896, 2172, 1409]  
2010: [2399]  
2011: [1021]  
2012: [2400][2170]  
2013: [2205]  
2014: [2307]  
2016: [2885, 1430]  
2018: [497]

- Mercury [2119, 1440, 2171]

- Pluto [1760]
- Super-Earths & exoplanets [2410][2635][2413][2769]
- Icy satellites [1371]
- Enceladus [2173, 141, 1132, 2202]
- Io [2480] [2473]

## H.69 Locations

- South America, Andes, Andean orogeny [2754] [1107] [2645] [68][2363] [69][1768] [797] [1425][947] [1271][2323] [611][752] [2183][1729][464] [2242] [2837]
- North America [2240] [1267] [356] [139] [2394] [2393] [985][2339] [2160]
- Apennines [333] [2320] [2642]
- Alps [116] [2130] [654] [2022] [371] [2023] [2034] [353] [1718] [2697] [1674][112] [392] [393] [2259][861]
- Mediterranean region [2033][1927] [1926] [2812] [2034] [234][808] [460][458][2638] [1776] [2388]
- New Zealand [1482] [276] [124] [2747] [103] [942][2072] [944][1485][2592] [1655] [2074][2391] [1073] [2435]
- Zagros [2693] [1159] [2831] [1948] [866] [980] [541] [2208]
- Himalayan region, Tibetan plateau, India collision
  - 1975: [1822]
  - 1977: [1816]
  - 1978: [202]
  - 1982: [2506][2698][782]
  - 1984: [2699]
  - 1986: [2700][1817][783]
  - 1988: [2006]
  - 1989: [1818]
  - 1990: [1355]
  - 1993: [1821]
  - 1994: [2789]
  - 1995: [434][1564]
  - 1997: [2200]
  - 1999: [2629]
  - 2000: [450][505][1218]
  - 2001: [122][1534][2873][2508]
  - 2002: [1486]
  - 2003: [2141]
  - 2004: [123][1323][2883][2140]
  - 2005: [504][2177][2178]
  - 2006: [506][1325][1007]
  - 2007: [1766]
  - 2008: [355][2449]
  - 2010: [1159][1358]
  - 2011: [138][2886][2636][1318][1279]
  - 2012: [2867][2637]
  - 2013: [415][445][446]
  - 2014: [2776][1888][2436][1545]
  - 2015: [2063][1317][2852]
  - 2016: [1422]
  - 2017: [391]
  - 2018: [2035][2][844]
  - 2019: [2250][2257][2734][2267]

- Pyrenees [477] [2086] [993] [126] [1749][2337] [1331] [2703] [837] [1329] [744][1360]
- Caribbean [2596] [2595] [235][2597][1929] [1210][1930]
- East mediterranean - Aegean region, Turkey [928] [417] [779] [1356] [1984] [2190]
- Ethiopian and Afar rift [1788] [576] [1427] [182] [2025][2239] [303] [304] [575]
- Alaskan region [1315] [1313] [1314] [1163] [1794]
- Farallon plate [1644] [1643] [1642] [1649]
- Japan, Izu-Bonin [1665] [1889] [1435][1550][1859][1221] [1432] [2836] [2837]
- Tonga-Kermadec subduction zone, Fiji [190][194] [2878]
- Western United States [139]
- Australian plate [1196][2763][2076] [1975] [1148][700] [1734][699] [1028] [2253]
- Barents sea [337] [912] [911]
- Carpathians [513] [1291] [1928] [2311]
- African continent [994] [2639] [336] [915] [2735] [428]
- Hawaii [2648] [2510] [2906]
- Hellenic zone/ Greece [2389] [1083]
- Gibraltar zone [1106] [899] [1793] [1780] [408]
- Norway [2386] [394]
- Canyonlands [2576] [2299] [1074]
- Dead Sea [2364]
- Canada [294] [2009]
- Basin and Range [264] [2775]
- China [2924] [2731]
- Arabian plate [2132]
- Scotia plate [1931]
- Cantabria & North-Iberian margin [510] [1998]
- South East Asia [2140] [2855][1126][1782]
- Colorado plateau [2680] [1593]
- Antarctica [1247]
- Greenland [2427][1182][2419]
- Atlas, Morroco [1368]
- Taiwan [441][1628]

# I Elemental mass matrices for simple geometries

In what follows I compute the mass matrix for a variety of reference elements. If you wish to use these in a code, do not forget to take the jacobian of the transformation/mapping into account.

## I.1 1D segments

### I.1.1 Linear basis functions

Let us start with the mass matrix (which we encountered in Section 5.1 – although we leave the  $\rho C_p$  term out):

$$\mathbf{M}_e = \int_{\Omega_e} \vec{N}^T \vec{N} dV = \int_{-1}^{+1} \vec{N}^T \vec{N} dr \quad (1092)$$

on the reference element, with

$$\vec{N}^T = \begin{pmatrix} N_1(r) \\ N_2(r) \end{pmatrix} = \frac{1}{2} \begin{pmatrix} 1-r \\ 1+r \end{pmatrix}$$

We have

$$\int_{-1}^{+1} N_1(r) N_1(r) dr = 2/3 \quad (1093)$$

$$\int_{-1}^{+1} N_1(r) N_2(r) dr = 1/3 \quad (1094)$$

$$\int_{-1}^{+1} N_2(r) N_2(r) dr = 2/3 \quad (1095)$$

Following the procedure in Section 5.1 we arrive at

$$\mathbf{M}^e = \frac{1}{3} \begin{pmatrix} 2 & 1 \\ 1 & 2 \end{pmatrix}$$

The lumped mass matrix is then

$$\bar{\mathbf{M}}^e = \frac{1}{3} \begin{pmatrix} 2+1 & 0 \\ 0 & 1+2 \end{pmatrix} = \begin{pmatrix} 1 & 0 \\ 0 & 1 \end{pmatrix} \quad (1096)$$

**Remark.** The sum of all the terms in the mass matrix must be equal to 2. Indeed:

$$\begin{aligned} \sum_{ij} M_{ij} &= \sum_{ij} \int_{-1}^{+1} N_i N_j dr \\ &= \int_{-1}^{+1} (N_1 N_1 + N_1 N_2 + N_2 N_1 + N_2 N_2) dr \\ &= \int_{-1}^{+1} [N_1(N_1 + N_2) + N_2(N_1 + N_2)] dr \\ &= \int_{-1}^{+1} (N_1 + N_2) dr \\ &= 2 \end{aligned}$$

### I.1.2 Quadratic basis functions

There are now three nodes in the segment so that the mass matrix is now a  $3 \times 3$  matrix. We have (see Section 4.4.1)

$$\vec{N}^T(r) = \begin{pmatrix} N_1(r) \\ N_2(r) \\ N_3(r) \end{pmatrix} = \begin{pmatrix} \frac{1}{2}r(r-1) \\ 1-r^2 \\ \frac{1}{2}r(r+1) \end{pmatrix} \quad (1097)$$

We then have to compute

$$\begin{aligned}
\int_{-1}^{+1} N_1(r)N_1(r)dr &= \frac{8}{30} = 0.26666 \\
\int_{-1}^{+1} N_1(r)N_2(r)dr &= \frac{4}{30} = 0.13333 \\
\int_{-1}^{+1} N_1(r)N_3(r)dr &= -\frac{2}{30} = -0.06666... \\
\int_{-1}^{+1} N_2(r)N_2(r)dr &= \frac{16}{15} = 1.06666 \\
\int_{-1}^{+1} N_2(r)N_3(r)dr &= \frac{4}{30} = 0.13333 \\
\int_{-1}^{+1} N_3(r)N_3(r)dr &= \frac{8}{30} = 0.26666
\end{aligned}$$

and finally

$$\boldsymbol{M}^e = \frac{1}{30} \begin{pmatrix} 8 & 4 & -2 \\ 4 & 32 & 4 \\ -2 & 4 & 8 \end{pmatrix} \quad (1098)$$

The lumped mass matrix is then

$$\begin{aligned}
\bar{\boldsymbol{M}}^e &= \frac{1}{30} \begin{pmatrix} 8+4-2 & 0 & 0 \\ 0 & 4+32+4 & -2+4+8 \\ 0 & 0 & -2+4+8 \end{pmatrix} \\
&= \frac{1}{30} \begin{pmatrix} 10 & 0 & 0 \\ 0 & 40 & 0 \\ 0 & 0 & 10 \end{pmatrix} \\
&= \frac{1}{3} \begin{pmatrix} 1 & 0 & 0 \\ 0 & 4 & 0 \\ 0 & 0 & 1 \end{pmatrix}
\end{aligned} \quad (1099)$$

We can easily verify that

$$\sum_{ij} M_{ij} = 2 \quad \sum_{ij} \bar{M}_{ij} = 2$$

### I.1.3 Cubic basis functions

There are now four nodes in the segment so that the mass matrix is now a  $4 \times 4$  matrix. We have (see Section 4.4.3)

$$\vec{N}^T(r) = \begin{pmatrix} N_1(r) \\ N_2(r) \\ N_3(r) \\ N_4(r) \end{pmatrix} = \frac{1}{16} \begin{pmatrix} -1+r+9r^2-9r^3 \\ 9-27r-9r^2+27r^3 \\ 9+27r-9r^2-27r^3 \\ -1-r+9r^2+9r^3 \end{pmatrix} \quad (1100)$$

$$\begin{aligned}
\int_{-1}^{+1} N_1(r)N_1(r)dr &= \frac{1}{256} \frac{4096}{105} \\
\int_{-1}^{+1} N_1(r)N_2(r)dr &= \frac{1}{256} \frac{1056}{35} \\
\int_{-1}^{+1} N_1(r)N_3(r)dr &= -\frac{1}{256} \frac{384}{35} \\
\int_{-1}^{+1} N_1(r)N_4(r)dr &= \frac{1}{256} \frac{608}{105} \\
\int_{-1}^{+1} N_2(r)N_2(r)dr &= \frac{1}{256} \frac{6912}{35} \\
\int_{-1}^{+1} N_2(r)N_3(r)dr &= -\frac{1}{256} \frac{864}{35} \\
\int_{-1}^{+1} N_2(r)N_4(r)dr &= -\frac{1}{256} \frac{384}{35} \\
\int_{-1}^{+1} N_3(r)N_3(r)dr &= \frac{1}{256} \frac{6912}{35} \\
\int_{-1}^{+1} N_3(r)N_4(r)dr &= \frac{1}{256} \frac{1056}{35} \\
\int_{-1}^{+1} N_4(r)N_4(r)dr &= \frac{1}{256} \frac{4096}{105}
\end{aligned}$$

and finally

$$\mathbf{M}^e = \frac{1}{16} \frac{1}{105} \begin{pmatrix} 256 & 198 & -72 & 38 \\ 198 & 1296 & -162 & -72 \\ -72 & -162 & 1296 & 198 \\ 38 & -72 & 198 & 256 \end{pmatrix} \quad (1101)$$

The lumped mass matrix is then

$$\begin{aligned}
\bar{\mathbf{M}}^e &= \frac{1}{16} \frac{1}{105} \begin{pmatrix} 256 + 198 - 72 + 38 & 0 & 0 & 0 \\ 0 & 198 + 1296 - 162 - 72 & 0 & 0 \\ 0 & 0 & -72 - 162 + 1296 + 198 & 0 \\ 0 & 0 & 0 & 38 - 72 + 198 + 256 \end{pmatrix} \\
&= \frac{1}{16} \frac{1}{105} \begin{pmatrix} 420 & 0 & 0 & 0 \\ 0 & 1260 & 0 & 0 \\ 0 & 0 & 1260 & 0 \\ 0 & 0 & 0 & 420 \end{pmatrix} \\
&= \frac{1}{4} \begin{pmatrix} 1 & 0 & 0 & 0 \\ 0 & 3 & 0 & 0 \\ 0 & 0 & 3 & 0 \\ 0 & 0 & 0 & 1 \end{pmatrix}
\end{aligned}$$

We can easily verify that

$$\sum_{ij} M_{ij} = 2 \quad \sum_{ij} \bar{M}_{ij} = 2$$

#### I.1.4 Quartic basis functions

There are now five nodes in the segment so that the mass matrix is now a  $5 \times 5$  matrix. We have (see Section 4.4.4)

$$\vec{N}^T(r) = \begin{pmatrix} N_1(r) \\ N_2(r) \\ N_3(r) \\ N_4(r) \\ N_5(r) \end{pmatrix} = \frac{1}{6} \begin{pmatrix} r - r^2 - 4r^3 + 4r^4 \\ -8r + 16r^2 + 8r^3 - 16r^4 \\ 6 - 30r^2 + 24r^4 \\ 8r + 16r^2 - 8r^3 - 16r^4 \\ -r - r^2 + 4r^3 + 4r^4 \end{pmatrix} \quad (1102)$$

$$\begin{aligned} \int_{-1}^{+1} N_1(r)N_1(r)dr &= \frac{1}{36} \frac{1168}{315} \\ \int_{-1}^{+1} N_1(r)N_2(r)dr &= \frac{1}{36} \frac{1184}{315} \\ \int_{-1}^{+1} N_1(r)N_3(r)dr &= -\frac{1}{36} \frac{232}{105} \\ \int_{-1}^{+1} N_1(r)N_4(r)dr &= \frac{1}{36} \frac{32}{45} \\ \int_{-1}^{+1} N_1(r)N_5(r)dr &= -\frac{1}{36} \frac{116}{315} \\ \int_{-1}^{+1} N_2(r)N_2(r)dr &= \frac{1}{36} \frac{1024}{45} \\ \int_{-1}^{+1} N_2(r)N_3(r)dr &= -\frac{1}{36} \frac{512}{105} \\ \int_{-1}^{+1} N_2(r)N_4(r)dr &= \frac{1}{36} \frac{1024}{315} \\ \int_{-1}^{+1} N_2(r)N_5(r)dr &= \frac{1}{36} \frac{32}{45} \\ \int_{-1}^{+1} N_3(r)N_3(r)dr &= \frac{1}{36} \frac{832}{35} \\ \int_{-1}^{+1} N_3(r)N_4(r)dr &= -\frac{1}{36} \frac{512}{105} \\ \int_{-1}^{+1} N_3(r)N_5(r)dr &= -\frac{1}{36} \frac{232}{105} \\ \int_{-1}^{+1} N_4(r)N_4(r)dr &= \frac{1}{36} \frac{1024}{45} \\ \int_{-1}^{+1} N_4(r)N_5(r)dr &= \frac{1}{36} \frac{1184}{315} \\ \int_{-1}^{+1} N_5(r)N_5(r)dr &= \frac{1}{36} \frac{1168}{315} \end{aligned} \quad (1103)$$

$$M^e = \frac{1}{36} \frac{1}{315} \begin{pmatrix} 1168 & 1184 & -696 & 224 & -116 \\ 1184 & 7168 & -1536 & 1024 & 224 \\ -696 & -1536 & 7488 & -1536 & -696 \\ 224 & 1024 & -1536 & 7168 & 1184 \\ -116 & 224 & -696 & 1184 & 1168 \end{pmatrix} \quad (1104)$$

The lumped mass matrix is then

$$\bar{\mathbf{M}}^e = \frac{1}{36} \frac{1}{315} \begin{pmatrix} 1764 & 0 & 0 & 0 & 0 \\ 0 & 8064 & 0 & 0 & 0 \\ 0 & 0 & 3024 & 0 & 0 \\ 0 & 0 & 0 & 8064 & 0 \\ 0 & 0 & 0 & 0 & 1764 \end{pmatrix} = \frac{1}{45} \begin{pmatrix} 7 & 0 & 0 & 0 & 0 \\ 0 & 32 & 0 & 0 & 0 \\ 0 & 0 & 12 & 0 & 0 \\ 0 & 0 & 0 & 32 & 0 \\ 0 & 0 & 0 & 0 & 7 \end{pmatrix} \quad (1105)$$

We can once again easily verify that

$$\sum_{ij} M_{ij} = 2 \quad \sum_{ij} \bar{M}_{ij} = 2$$

Note that all the integrals above were done very conveniently with the WolframAlpha software/web-site<sup>89</sup>. Example:

The screenshot shows the WolframAlpha interface. At the top, there is a search bar with the query "int\_{-1}^{+1} (r - r^2 - 4r^3 + 4r^4)(r - r^2 - 4r^3 + 4r^4) dr". Below the search bar are several icons: a star, a square, a grid, and a camera. To the right of the search bar are buttons for "Browse Examples" and "Surprise Me". In the center, there is a box labeled "Definite integral:" containing the integral expression and its result:  $\int_{-1}^{+1} (r - r^2 - 4r^3 + 4r^4)(r - r^2 - 4r^3 + 4r^4) dr = \frac{1168}{315} \approx 3.7079$ . To the right of this box are buttons for "More digits" and "Step-by-step solution" (which is checked). At the bottom right of the central box is a link "Open code" with a small icon.

## I.2 Quadrilaterals: rectangular elements

We here assume that each element is a rectangle of size  $h_x \times h_y$ .

## I.3 Hexahedra: cuboid elements

We here assume that each element is a cuboid<sup>90</sup> of size  $h_x \times h_y \times h_z$ .

<sup>89</sup><https://www.wolframalpha.com/>

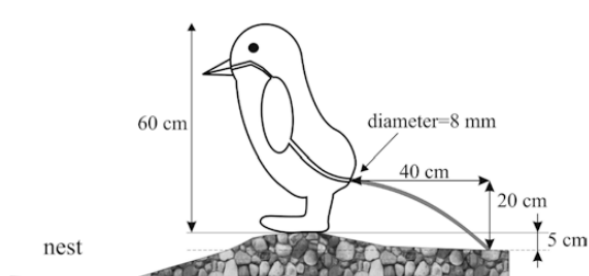
<sup>90</sup><https://en.wikipedia.org/wiki/Cuboid>

## J Finite element terminology in various languages

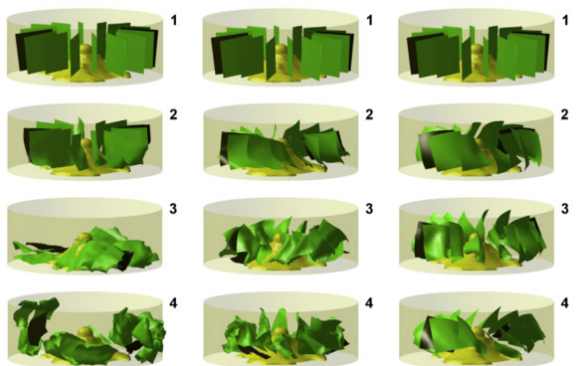
English	French	Dutch
Finite Element Method	Méthode des éléments finis	Eindige-elementenmethode
Finite Difference Method	Méthode des différences finies	Eindige-differentiemethode
Finite Volume Method	Méthode des volumes finis	
Matrix	Matrice	
Heat transport eq.	Equation de transport de la chaleur	Warmtetransport vergelijking
Momentum conservation eq.	équation de conservation du moment	Wet van behoud van impuls
Mass conservation / continuity eq.		Continuïteitsvergelijking
Iterative solver	solveur itératif	
Elemental matrix		
Boundary conditions	conditions aux limites	randvoorwaarden
(In)compressible	(in)compressible	
Surface processes	processus de surface	
an element	un élément	
Computational geodynamics	géodynamique numérique	
Assembly	assemblage	
Strong form		
Weak form	formulation variationnelle / formulation faible	
Basis function		
Shape function		
Partial differential eq. (PDE)	équation aux dérivées partielles (EDP)	partiële differentiaalvergelijking
Node	noeud	knooppunt
Grid, mesh	(la) maille / (le) maillage	rooster
Stiffness matrix	matrice de raideur	stijfheidsmatrix
Displacement vector	vecteur déplacement	verplaatsingsvector
Tessellation	pavage	Betegeling
Mass matrix	matrice de masse	
Classical mechanics	mécanique Newtonienne	(de) klassieke mechanica
Momentum	(le) moment	(de) impuls

## K Fun modelling

Because sometimes numerical modelling is fun ...



Pressures produced when penguins pooh - calculations on avian defaecation [1785]



Clothes washing simulations [13]

*Computers and Fluids* Vol. 9, pp. 223-231  
Pergamon Press Ltd., 1981. Printed in Great Britain

0045-7990(81)0001-022\$02.00/0

INTERNATIONAL JOURNAL FOR NUMERICAL METHODS IN FLUIDS, VOL. 9, 99-112 (1989)

DON'T SUPPRESS THE WIGGLES—THEY'RE TELLING YOU SOMETHING!†

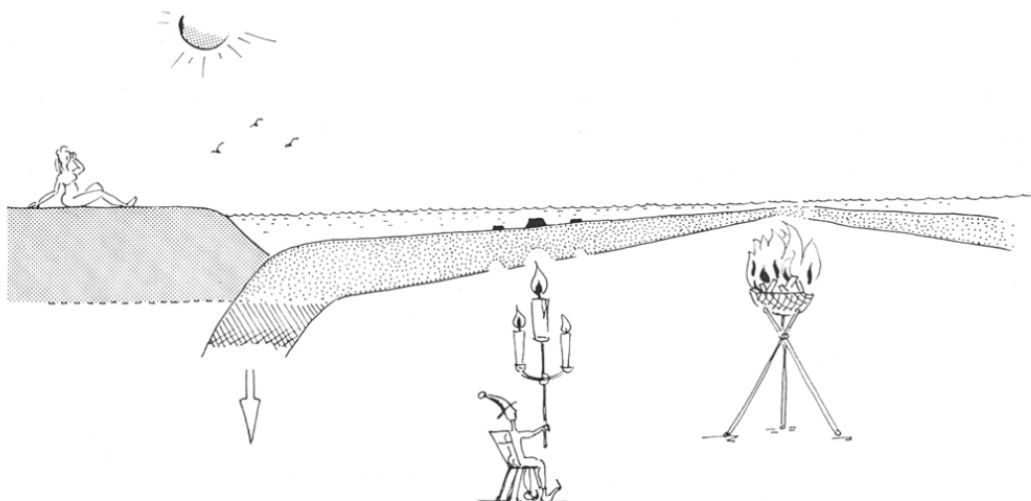
PHILIP M. GRESHO AND ROBERT L. LEE

[1062]

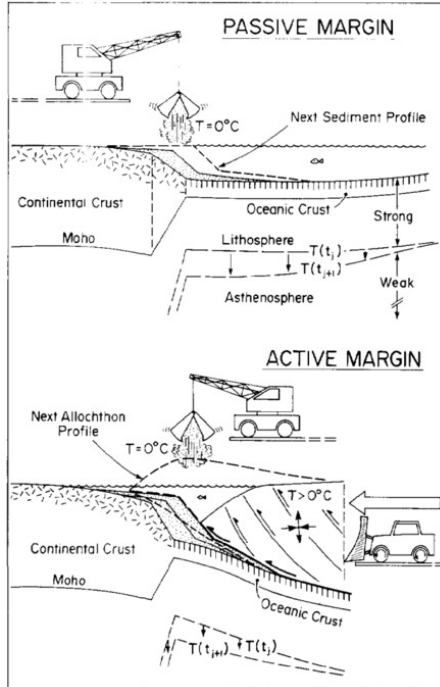
ARE FEM SOLUTIONS OF INCOMPRESSIBLE FLOWS REALLY INCOMPRESSIBLE? (OR HOW SIMPLE FLOWS CAN CAUSE HEADACHES!)

DOMINIQUE PELLETIER, ANDRE FORTIN AND RICARDO CAMARERO

[2000]



Lithospheric thickness anomaly near the trench and possible driving force of subduction [894]



Convergent margin tectonics [2445]

INTERNATIONAL JOURNAL FOR NUMERICAL METHODS IN ENGINEERING, VOL. 32, 1189–1203 (1991)

## INCOMPRESSIBILITY WITHOUT TEARS—HOW TO AVOID RESTRICTIONS OF MIXED FORMULATION

O. C. ZIENKIEWICZ AND J. WU

*Institute of Numerical Methods in Engineering, University College of Swansea, Swansea, U.K.*

[2944]

### Collective Motion of Humans in Mosh and Circle Pits at Heavy Metal Concerts

Jesse L. Silverberg,\* Matthew Bierbaum, James P. Sethna, and Itai Cohen

*Department of Physics and Laboratory of Atomic and Solid State Physics, Cornell University, Ithaca, New York 14853, USA*

(Received 13 February 2013; published 29 May 2013)

Human collective behavior can vary from calm to panicked depending on social context. Using videos publicly available online, we study the highly energized collective motion of attendees at heavy metal concerts. We find these extreme social gatherings generate similarly extreme behaviors: a disordered gaslike state called a *mosh pit* and an ordered vortexlike state called a *circle pit*. Both phenomena are reproduced in flocking simulations demonstrating that human collective behavior is consistent with the predictions of simplified models.

[2340]

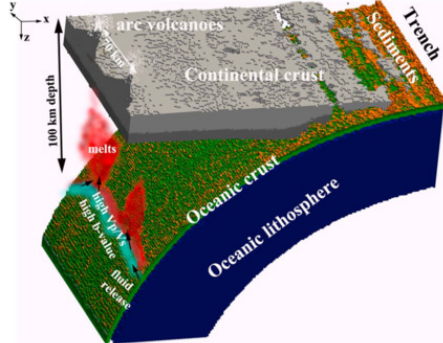
## Toasting the jelly sandwich: The effect of shear heating on lithospheric geotherms and strength

Ebbe H. Hartz Physics of Geological Processes, University of Oslo, 0316 Oslo, Norway, and Aker Exploration,  
Haakon VII's gt. 9, P.O. Box 580, Sentrum, NO, 4003 Stavanger, Norway

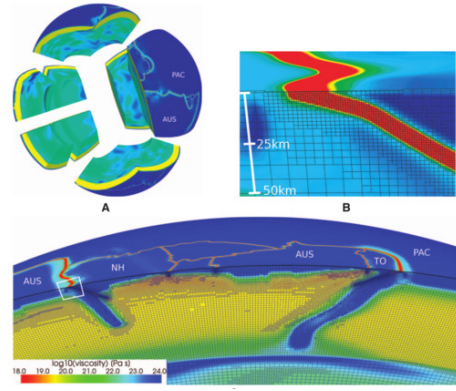
Yuri Y. Podladchikov Physics of Geological Processes, University of Oslo, 0316 Oslo, Norway

[1154]

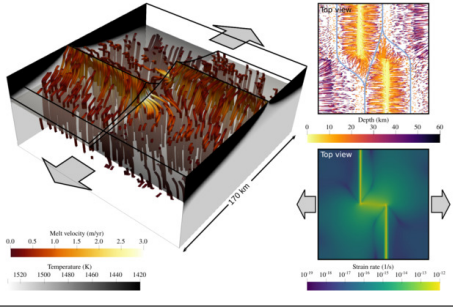
## L Beautiful/interesting images from computational geodynamics



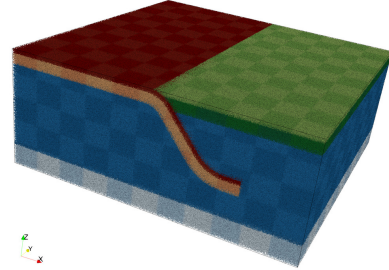
[2921]



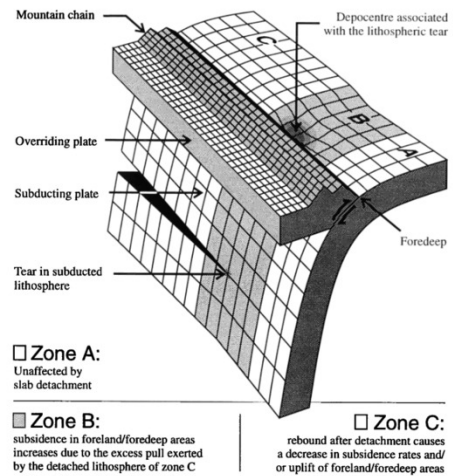
[2402]



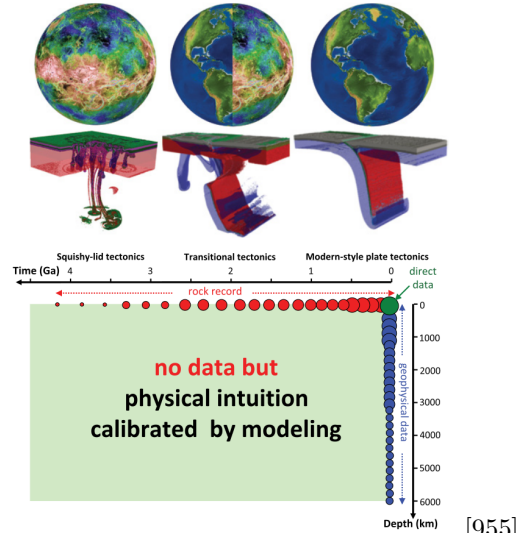
[622]



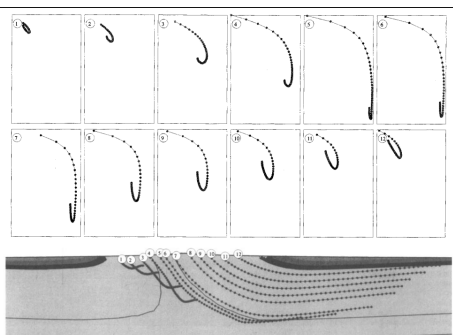
[871]



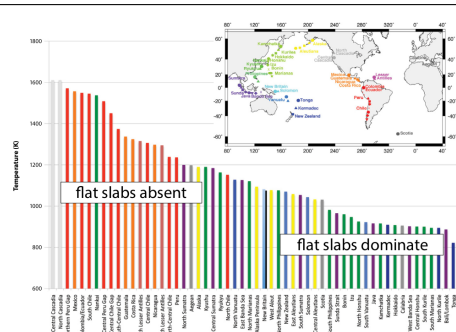
[2624]



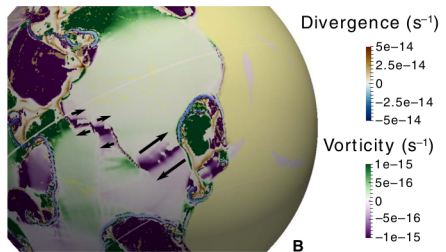
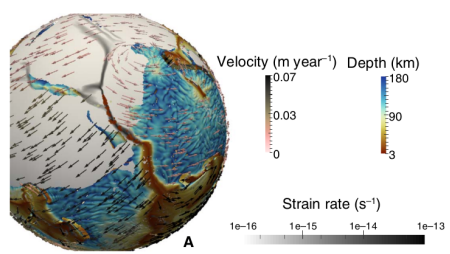
[955]



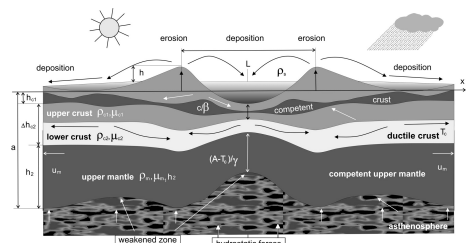
[102]



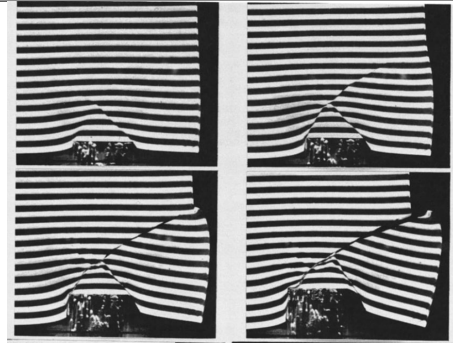
[1453]



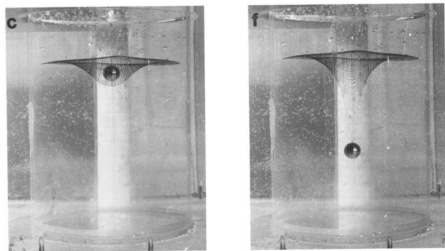
[547]



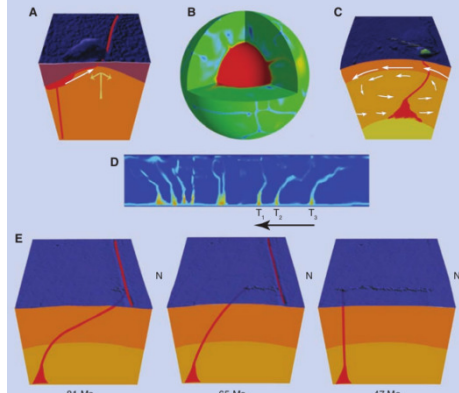
[365]



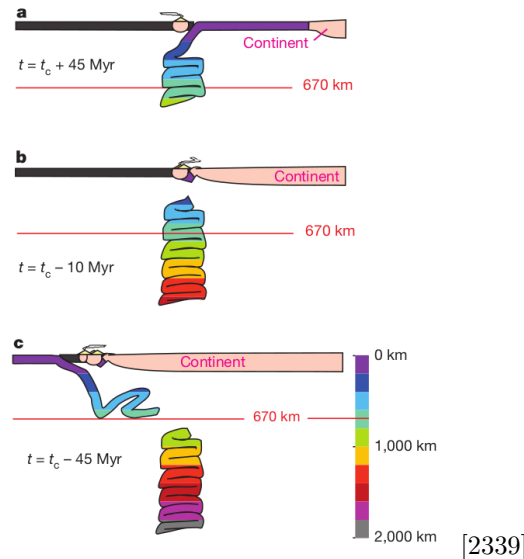
[2006]



[603]



[2510]



[2339]

## M People

This is relevant to me only. Bibliography work.

- Thorsten Becker
- Sascha Brune
- Susanne Buiter. done
- Fabio Cramer
- Fabio Capitanio
- Anne Davaille
- J. Dannberg
- Huw Davies
- Taras Gerya. done
- R. Gassmöller
- Gregor Golabek
- Mike Gurnis
- Ulrich Hansen. done
- Laurent Husson
- Boris Kaus
- Julian Lowman
- Louis Moresi. done
- Anne Replumaz
- Neil Ribe
- Tobias Rolf
- V. Solomatov
- Paul Tackley. done
- Arie van den Berg. done
- Peter van Keken
- Ylona van Dinther
- Jeroen van Hunen
- Iris van Zelst
- Philippe Yamato. done
- HP Bunger - done

## N Working with Git

This appendix was contributed by E. van der Wiel.

1. make sure that you have an account on GitHub (say, <https://github.com/myusername>) and carry out a proper setup on your local computer as follows:

```
$ git config --global user.name "firstname lastname"  
$ git config --global user.email your@email
```

2. On github.com, fork the official fieldstone repository to your repository:  
go to <https://github.com/cedrikt/fieldstone> and click on the 'fork' button on the upper right corner of the screen.

3. On your machine, in a terminal, clone your repository with

```
$ git clone git@github.com:myusername/fieldstone.git
```

. This is now your master branch.

4. On your machine, find your security key <sup>91</sup> with `$ less ~/.ssh/id_dsa.pub` and copy this into github.com so you can push to your repository. See <https://help.github.com/en/articles/connecting-to-github-with-ssh> on how to configure github with ssh support (no more login/-password to type – if you have cloned the repository wish ssh, not html). Please also check the instructions at <https://help.github.com/en/articles/connecting-to-github-with-ssh>.

5. create a remote of your (online) repository

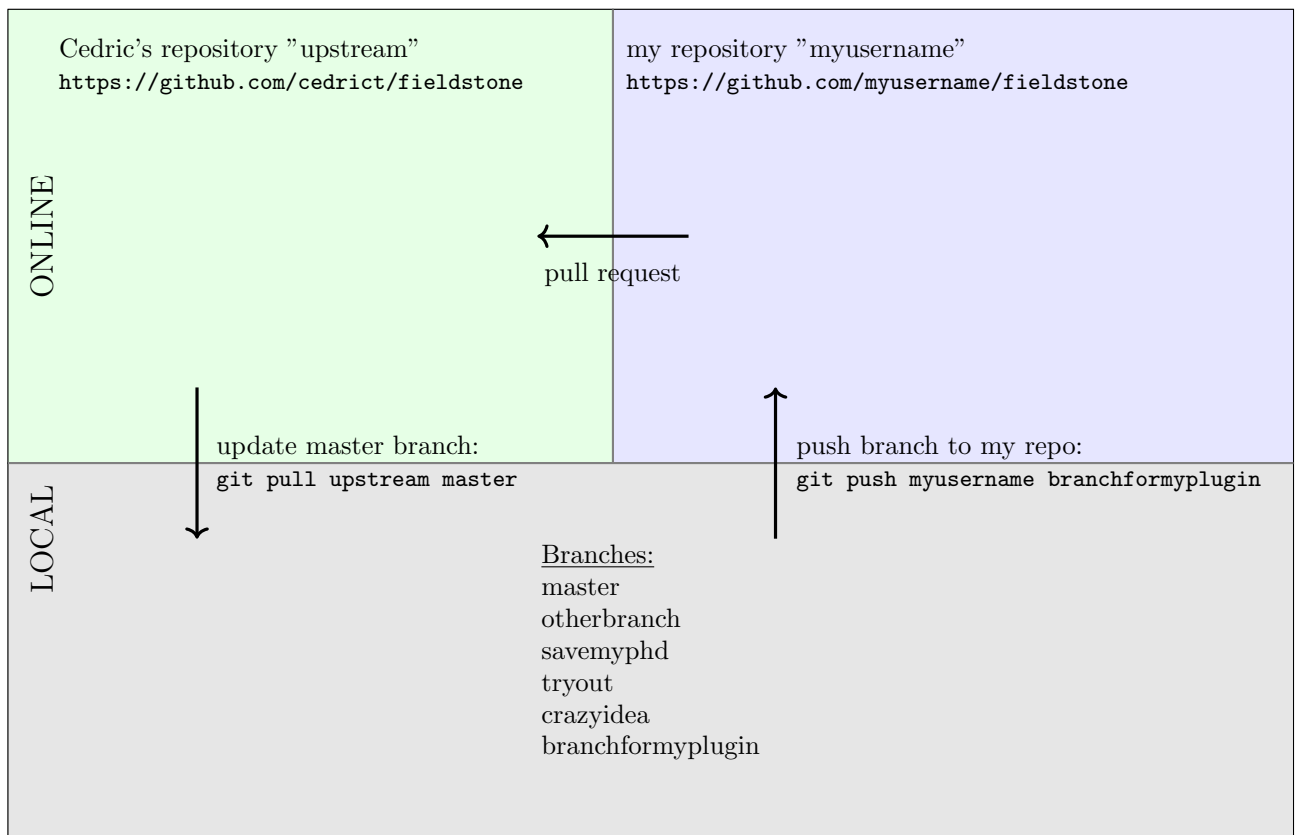
```
git remote add origin git@github.com:myusername/fieldstone.git
```

 and in order to avoid potential confusion later on, we shall rename our github repo as follows:

```
$ git remote rename origin myusername
```

6. Also create a remote of the official version with

```
$ git remote add upstream https://github.com/cedrikt/fieldstone
```



<sup>91</sup> Note that you can create a public key as follows: <https://help.github.com/articles/generating-ssh-keys/>

**Very concretely, if you wish to contribute:** Let us assume that you have found a typo in the file "physics.tex" and you wish to report the problem to me. The easiest way is to write me an email with the nature of the problem and the proposed fix. Although I will be grateful for your contribution, this approach can be improved upon by using git's "pull request" command.

1. If this is the very first time you use git, the following instruction is not needed. If not, make sure that your terminal points at your master branch: `$ git checkout master`
2. Then, make sure you update your local version: `$ git pull upstream master` and also update your own repo online: `$ git push`
3. Create a new branch with a self explanatory name: `$ git branch fix_typo` Then do `$ git branch` to see all your branches. The one that is coloured is the active branch. In order to switch to this new branch, do `$ git checkout fix_typo`. Redo `$ git branch` to verify that the branch 'fix\_typo' is highlighted.
4. Edit the file and correct the typo, save and exit. Do `$ git status` and you should see the filename highlighted next to 'modified'.
5. If this is the only modification you wish to communicate, you then need to add and commit it as follows:

```
git add physics.tex
```

If you do git status again, the file should have changed colour (?). Then do

```
git commit -m "message"
```

where 'message' is a very short description of the modification (e.g. 'I fixed a typo').

6. We now need to bring this modification online

```
git push myusername fix_typo
```

7. You are nearly done. The last step takes place on github.com: when you log onto your own github fieldstone page, you should see a large green rectangle "Compare and pull request". Click on this button.
8. a new page opens, entitled "Open a pull request". If necessary, add a detailed description of the pull request (this makes sense when you contribute a piece of code, or a whole new section, etc ...). You can review the requested changes at the bottom. In the end, simply click "Create pull request".
9. Once you have done so, I will receive an email which notifies me of the pull request. I will then review it. If I have no comment, I will accept the PR and your modification will then be incorporated in the master repo. If I have comments, you will be notified via github and a back-and-forth discussion will ensue until I accept the PR.
10. After the PR has been accepted, the branch is no longer needed. Switch back to your local master branch: `$ git checkout master` . Update your local master and online repo (see step # 2) and then delete the no-longer-needed branch as follows:

```
git branch -d fix_typo
```

```

(base) UU062931:fieldstone vanderWiel$ git branch
  master
* my_work
(base) UU062931:fieldstone vanderWiel$ git checkout master
Switched to branch 'master'
Your branch is up to date with 'origin/master'.
(base) UU062931:fieldstone vanderWiel$ git pull upstream master
From https://github.com/cedrict/fieldstone
 * branch           master      -> FETCH_HEAD
 Already up to date.
(base) UU062931:fieldstone vanderWiel$ git push
Everything up-to-date
(base) UU062931:fieldstone vanderWiel$ █

(base) UU062931:fieldstone vanderWiel$ git branch fix_typos
(base) UU062931:fieldstone vanderWiel$ git branch
fix_typos
* master
my_work
(base) UU062931:fieldstone vanderWiel$ git checkout fix_typos
Switched to branch 'fix_typos'
(base) UU062931:fieldstone vanderWiel$ git branch
* fix_typos
master
my_work
(base) UU062931:fieldstone vanderWiel$ █

(base) UU062931:fieldstone vanderWiel$ vi physics.tex
(base) UU062931:fieldstone vanderWiel$ git status
On branch fix_typos
Changes not staged for commit:
  (use "git add <file>..." to update what will be committed)
    (use "git restore <file>..." to discard changes in working directory)
       modified:   physics.tex

no changes added to commit (use "git add" and/or "git commit -a")
(base) UU062931:fieldstone vanderWiel$ git add physics.tex
(base) UU062931:fieldstone vanderWiel$ git status
On branch fix_typos
Changes to be committed:
  (use "git restore --staged <file>..." to unstage)
       modified:   physics.tex

(base) UU062931:fieldstone vanderWiel$ git commit -m "I fixed a typo"
[fix_typos 85beb3e] I fixed a typo
  1 file changed, 1 insertion(+), 1 deletion(-)
(base) UU062931:fieldstone vanderWiel$ git push origin fix_typos
Enumerating objects: 5, done.
Counting objects: 100% (5/5), done.
Delta compression using up to 4 threads
Compressing objects: 100% (3/3), done.
Writing objects: 100% (3/3), 294 bytes | 294.00 KiB/s, done.
Total 3 (delta 2), reused 0 (delta 0)
remote: Resolving deltas: 100% (2/2), completed with 2 local objects.
remote:
remote: Create a pull request for 'fix_typos' on GitHub by visiting:
remote:   https://github.com/e-wiel/fieldstone/pull/new/fix_typos
remote:
To https://github.com/e-wiel/fieldstone.git
 * [new branch]      fix_typos -> fix_typos
(base) UU062931:fieldstone vanderWiel$ █



```

Screen captures of the procedure described above as carried out by E. van der Wiel on his Apple laptop.

In what follows we summarize the most important commands one should and remember while working with github. After creating an account one can 'fork' a repository (repo) in the online environment. This repository is a copy from the master directory of the developer and should not be used to adapt or change, as changes from the developer (updates) should be obtained in this 'fork', or as it could also be called; your master branch.

In order to be able to work within a repository, for instance, to run and compile different programs, you should have your own branch of the repository in which YOU CAN make changes. The following commands should be used to make, copy and publish your own version of the repo to your local device and the online github environment.

<b>command</b>	<b>what it does</b>
git branch	shows all branches of your repository and highlights the one you're in.
git checkout -b <my_own_branch>	This makes your own branch called "my_own_branch".
git push origin <my_own_branch>	This pushes your own, local, branch to as a second branch in the online repo of github.
git checkout <name>	changing the branch you're working in (e.g. master or my_own_branch). Or replace the name with a hyphen to switch to the last branch.
git branch -d <my_own_branch>	Delete your local branch.

The following commands should be used in order to update your own local branches from updates made by somewhere else (upstream/master is the main repository). One should do this for the local master branch and, where possible as well for the different local branches you have committed changes to already.

<b>command</b>	<b>what it does</b>
git checkout master	To make sure you are in the right branch
git fetch upstream	to fetch updates from upstream repositories to your own local branch (e.g. to update your master branch).
git merge upstream/master	Command to update the branch with the fetched repo from 'upstream'.
git push origin master	To level your own online repository again with the one on your local drive (and thus the one upstream).
git checkout <my_own_branch>	To switch to your own adapted branch of the repo.
git merge master	Used from another branch working directory to combine the new released version of the master repo with the one where all your own changes are put. -> Then git finds all conflicts in different files which you need to resolve.
git add .	This adds the resolved issues in your own local branch (not master). After which you are able to commit and push your changes back to the online repository.

While you are working in your own branch you can change, add or delete files in any amount you want. However, always check whether your changes do not inflict the outcome of for instance your code. And when uploading from your terminal: if you commit and then push from master branch your changes will automatically be inserted in the online version of your master branch, when done from another branch it will be shown as a pull request towards your master branch. This request can then, for instance be forwarded to the main repo.

<b>command</b>	<b>what it does</b>
git commit -a	This will send your changes/updates from your branch as a commit to your own local branch.
git push origin <changes>	To update the remote repository (on Github) from you local repository (in this case the 'changes' branch). (Actually upload the new version). Online one can then judge what to do with it. !! this is a pull request towards your own fork/local_branch
git status	Showing the status of your current branch; it shows which files are different between the master file and your adapted branch.
git diff <changes>	This shows the exact differences between the different branches; one can simply ask for the difference between two branches when pwd in one branch ask for the other branch.
git merge <my_own_branch>	When used from the master branch (or any other???) this accepts the changes made in your branch and puts them in your local(!) master branch.
git pull origin master	if the main repository changes, one can pull the newest version towards it's own master file. While keeping your own branches alive with you own changes and vica versa: by running this command the origin/master (remote file) will be cloned and updated to the working branch you are in.
git stash (apply)	?? While updating your local branch, sometimes git wants to overrule your own changes, with this command you can 'stash' them to look at the differences later. ??

## References

- [1] B.T. Aagaard, M.G. Knepley, and C.A. Williams. A domain decomposition approach to implementing fault slip in finite-element models of quasi-static and dynamic crustal deformation. *J. Geophys. Res.*, 118:3059–3079, 2013.
- [2] A.E. Pusok and B.J.P. Kaus and A.A. Popov. The effect of rheological approximations in 3-D numerical simulations of subduction and collision. *Tectonophysics*, 746:296–311, 2018.
- [3] John F Abel and Mark S Shephard. An algorithm for multipoint constraints in finite element analysis. *International Journal for Numerical Methods in Engineering*, 14(3):464–467, 1979.
- [4] V. Acocella, A. Gudmundsson, and R. Funiciello. Interaction and linkage of extension fractures and normal faults: examples from the rift zone of Iceland. *Journal of Structural Geology*, 22(9):1233–1246, 2000.
- [5] F.J Adewale, A.P. Lucky, A.P. Oluwabunmi, and E.F. Boluwaji. Selecting the most appropriate model for rheological characterization of synthetic based drilling mud. *International Journal of Applied Engineering Research*, 12(18):7614–7649, 2017.
- [6] J. C. Afonso, M. Fernandez, G. Ranalli, W.L. Griffin, and J.A.D. Connolly. Integrated geophysical-petrological modeling of the lithosphere and sublithospheric upper mantle: Methodology and applications. *Geochem. Geophys. Geosyst.*, 9(5):doi:10.1029/2007GC001834, 2008.
- [7] J.C. Afonso, G. Ranalli, and M. Fernandez. Density structure and buoyancy of the oceanic lithosphere revisited. *Geophys. Res. Lett.*, 34(L10302), 2007.
- [8] P. Agard, P. Yamato, L. Jolivet, and E. Burov. Exhumation of oceanic blueschists and eclogites in subduction zones: Timing and mechanisms. *Earth-Science Reviews*, 92(1-2):53–79, 2009.
- [9] Ph. Agard, X. Zuo, N. Bellahsen, C. Faccenna, and D. Savva. Obduction: Why, how and where. Clues from analog models. *Earth Planet. Sci. Lett.*, 393:132–145, 2014.
- [10] Andrea Agostini, Giacomo Corti, Antonio Zeoli, and Genene Mulugeta. Evolution, pattern, and partitioning of deformation during oblique continental rifting: Inferences from lithospheric-scale centrifuge models. *Geochem. Geophys. Geosyst.*, 10(11):Q11015, 2009.
- [11] R. Agrusta, S. Goes, and J. van Hunen. Subducting-slab transition-zone interaction: Stagnation, penetration and mode switches. *Earth and Planetary Science Letters*, 464:10–23, 2017.
- [12] R. Agrusta, J. van Hunen, and S. Goes. The effect of metastable pyroxene on the slab dynamics. *Geophys. Res. Lett.*, 41:8800–8808, 2014.
- [13] Deniz Tolga Akcabay, David R Dowling, and William W Schultz. Clothes washing simulations. *Computers & Fluids*, 100:79–94, 2014.
- [14] Francis Albarède and Rob D van der Hilst. Zoned mantle convection. *Philosophical Transactions of the Royal Society of London. Series A: Mathematical, Physical and Engineering Sciences*, 360(1800):2569–2592, 2002.
- [15] M. Albers. A local mesh refinement multigrid method for 3D convection problems with strongly variable viscosity. *J. Comp. Phys.*, 160:126–150, 2000.
- [16] M. Alberts, C. Beaumont, and S.J. Ings. Geodynamic modeling of sedimentation-induced overpressure, gravitational spreading, and deformation of passive margin mobile shale basins. *AAPG Memoir*, 93:29–62, 2010.
- [17] M. Albertz and C. Beaumont. An investigation of salt tectonic structural styles in the Scotian Basin, offshore Atlantic Canada: 2. Comparison of observations with geometrically complex numerical models. *Tectonics*, 29(TC4018), 2010.
- [18] M. Albertz, C. Beaumont, J.W. Shimeld, S.J. Ingsand, and S. Gradmann. An investigation of salt tectonic structural styles in the Scotian Basin, offshore Atlantic Canada: Part 1, comparison of observations with geometrically simple numerical models. *Tectonics*, 29, 2010.
- [19] L. Alisic, M. Gurnis, G. Stadler, C. Burstedde, and O. Ghattas. Multi-scale dynamics and rheology of mantle flow with plates. *J. Geophys. Res.*, 117, 2012.
- [20] L. Alisic, J.F. Rudge, R.F. Katz, G.N. Wells, and S. Rhebergen. Compaction around a rigid, circular inclusion in partially molten rock. *J. Geophys. Res.*, 119:5903–5920, 2014.
- [21] J. Allen and C. Beaumont. Impact of inconsistent density scaling on physical analogue models of continental margin scale salt tectonics. *Journal of Geophysical Research: Solid Earth*, 117(8), 2012.
- [22] J. Allen and C. Beaumont. Continental Margin Syn-Rift Salt Tectonics at Intermediate Width Margins. *Basin Research*, page doi: 10.1111/bre.12123, 2014.

- [23] J. Allen and C. Beaumont. Continental margin syn-rift salt tectonics at intermediate width margins. *Basin Research*, 28(5):598–633, 2016.
- [24] P.A. Allen. From landscapes into geological history. *Nature*, 451:274–276, 2008.
- [25] V. Allken, R. Huismans, and C. Thieulot. Three dimensional numerical modelling of upper crustal extensional systems. *J. Geophys. Res.*, 116:B10409, 2011.
- [26] V. Allken, R. Huismans, and C. Thieulot. Factors controlling the mode of rift interaction in brittle-ductile coupled systems: a 3d numerical study. *Geochem. Geophys. Geosyst.*, 13(5):Q05010, 2012.
- [27] V. Allken, R.S. Huismans, H. Fossen, and C. Thieulot. 3D numerical modelling of graben interaction and linkage: a case study of the Canyonlands grabens, Utah. *Basin Research*, 25:1–14, 2013.
- [28] D. Allu Peddinti and A. K. McNamara. Dynamical investigation of a thickening ice-shell: Implications for the icy moon europa. *Icarus*, 2019.
- [29] Manar Alsaif, Fanny Garel, Frédéric Gueydan, and D Rhodri Davies. Upper plate deformation and trench retreat modulated by subduction-driven shallow asthenospheric flows. *Earth and Planetary Science Letters*, 532:116013, 2020.
- [30] P.R. Amestoy and I.S. Duff. Vectorization of a multiprocessor multifrontal code. *International Journal of Supercomputer Applications*, 3:41–59, 1989.
- [31] P.R. Amestoy, I.S. Duff, J.Koster, and J.-Y. LExcellent. A fully asynchronous multifrontal solver using distributed dynamic scheduling. *SIAM Journal of Matrix Analysis and Applications*, 23(1):15–41, 2001.
- [32] P.R. Amestoy, I.S. Duff, and J.-Y. L'Excellent. Multifrontal parallel distributed symmetric and unsymmetric solvers. *Computer Methods in Applied Mechanics and Engineering*, 184:501–520, 2000.
- [33] P.R. Amestoy, A. Guermouche, J.-Y. LExcellent, and S. Pralet. Hybrid scheduling for the parallel solution of linear systems. *Parallel Computing*, 32(2):136–156, 2006.
- [34] Christophe Ancey and Steve Cochard. The dam-break problem for herschel–bulkley viscoplastic fluids down steep flumes. *Journal of Non-Newtonian Fluid Mechanics*, 158(1-3):18–35, 2009.
- [35] Edward Anders and Nicolas Grevesse. Abundances of the elements: Meteoritic and solar. *Geochimica et Cosmochimica acta*, 53(1):197–214, 1989.
- [36] Bret D Anderson, Steven E Benzley, and Steven J Owen. *Automatic all quadrilateral mesh adaption through refinement and coarsening*, pages 557–574. Springer, 2009.
- [37] C.A. Anderson and R.J. Bridwell. A finite element method for studying the transient non-linear thermal creep of geological structures. *International Journal for Numerical and Analytical Methods in Geomechanics*, 4:255–276, 1980.
- [38] D.L. Anderson. The scales of mantle convection. *Tectonophysics*, 284(1-2):1–17, 1998.
- [39] DL Anderson. The persistent mantle plume myth. *Australian Journal of Earth Sciences*, 60(6-7):657–673, 2013.
- [40] J.D. Anderson. *Computational Fluid Dynamics*. McGraw-Hill, 1995.
- [41] Miguel Andrés-Martínez, Jason P Morgan, Marta Pérez-Gussinyé, and Lars Rüpke. A new free-surface stabilization algorithm for geodynamical modelling: Theory and numerical tests. *Physics of the Earth and Planetary Interiors*, 246:41–51, 2015.
- [42] Miguel Andrés-Martínez, Marta Pérez-Gussinyé, John Armitage, and Jason P Morgan. Thermomechanical implications of sediment transport for the architecture and evolution of continental rifts and margins. *Tectonics*, 38(2):641–665, 2019.
- [43] E.R. Andrews and M.I. Billen. Rheologic controls on the dynamics of slab detachment. *Tectonophysics*, 464:60–69, 2009.
- [44] A. Androvicova, H. Čížková, and A. van den Berg. The effects of rheological decoupling on slab deformation in the Earth's upper mantle. *Stud. Geophys. Geod.*, 57:460–481, 2013.
- [45] S. Angiboust, S. Wolf, E. Burov, P. Agard, and P. Yamato. Effect of fluid circulation on subduction interface tectonic processes: Insights from thermo-mechanical numerical modelling. *Earth Planet. Sci. Lett.*, 357–358:238–248, 2012.
- [46] D. Arcay, E. Tric, and M.-P. Doin. Numerical simulations of subduction zones. effect of slab dehydration on the mantle wedge dynamics. *Phys. Earth. Planet. Inter.*, 149:133–153, 2005.
- [47] D. Arcay, E. Tric, and M.-P. Doin. Slab surface temperature in subduction zones: influence of the interplate decoupling depth and upper plate thinning processes. *Earth Planet. Sci. Lett.*, 255:324–338, 2007.

- [48] Diane Arcay, Serge Lallemand, Sarah Abecassis, and Fanny Garel. Can subduction initiation at a transform fault be spontaneous? *Solid Earth*, 11:37–62, 2020.
- [49] M. Armann and P.J. Tackley. Simulating the thermochemical magmatic and tectonic evolution of Venus' mantle and lithosphere: Two-dimensional models. *J. Geophys. Res.*, 117(E12003), 2012.
- [50] J.J. Armitage, T.J. Henstock, T.A. Minshull, and J.R. Hopper. Lithospheric controls on melt production during continental breakup at slow rates of extension: Application to the North Atlantic. *Geochem. Geophys. Geosyst.*, 10(6), 2009.
- [51] D. Arndt, W. Bangerth, T. C. Clevenger, D. Davydov, M. Fehling, D. Garcia-Sanchez, G. Harper, T. Heister, L. Heltai, M. Kronbichler, R. M. Kynch, M. Maier, J.-P. Pelteret, B. Turcksin, and D. Wells. The **deal.II** library, version 9.1. *Journal of Numerical Mathematics*, 2019. accepted.
- [52] D.N. Arnold, F. Brezzi, and M. Fortin. A stable finite element for the Stokes equation. *Calcolo*, XXI(IV):337–344, 1984.
- [53] Douglas N Arnold, Franco Brezzi, Bernardo Cockburn, and L Donatella Marini. Unified analysis of discontinuous galerkin methods for elliptic problems. *SIAM journal on numerical analysis*, 39(5):1749–1779, 2002.
- [54] M Arnould, Nicolas Coltice, Nicolas Flament, V Seigneur, and RD Müller. On the scales of dynamic topography in whole-mantle convection models. *Geochemistry, Geophysics, Geosystems*, 19(9):3140–3163, 2018.
- [55] Maëlis Arnould, Jérôme Ganne, Nicolas Coltice, and Xiaojun Feng. Northward drift of the azores plume in the earths mantle. *Nature communications*, 10(1):3235, 2019.
- [56] K. M. Arredondo and M. I. Billen. Rapid weakening of subducting plates from trench-parallel estimates of flexural rigidity. *Physics of the Earth and Planetary Interiors*, 196–197:1–13, 2012.
- [57] P.-A. Arrial and M.I. Billen. Influence of geometry and eclogitization on oceanic plateau subduction . *Earth Planet. Sci. Lett.*, 363:34–43, 2013.
- [58] P.A. Arrial, N. Flyer, G.B. Wright, and L.H. Kellogg. On the sensitivity of 3-D thermal convection codes to numerical discretization: a model intercomparison. *Geosci. Model Dev.*, 7:2065–2076, 2014.
- [59] A. Aschwanden and H. Blatter. Numerical modeling of glacier flow. *COMSOL Users Conference*, 2006.
- [60] Alireza Asgari and LN Moresi. Multiscale particle-in-cell method: from fluid to solid mechanics. *Advanced Methods for Practical Applications in Fluid Mechanics. InTech, Croatia*, pages 185–208, 2012.
- [61] J. Austermann, J. X. Mitrovica, P. Huybers, and A. Rovere. Detection of a dynamic topography signal in last interglacial sea-level records. *Science Advances*, 3(7):1700457, 2017.
- [62] J. Austermann, D. Pollard, J. X. Mitrovica, R. Moucha, A. M. Forte, R. M. DeConto, D. B. Rowley, and M. E. Raymo. The impact of dynamic topography change on antarctic ice sheet stability during the mid-pliocene warm period. *Geology*, 43(10):927–930, 2015.
- [63] J. Autin, N. Bellahsen, L. Husson, M.O. Beslier, S. Leroy, and E. d'Acremont. Analog models of oblique rifting in a cold lithosphere. *Tectonics*, 29(6):TC6016, 2010.
- [64] JP Avouac and EB Burov. Erosion as a driving mechanism of intracontinental mountain growth. *J. Geophys. Res.*, 101(B8):17747, 1996.
- [65] EH Ayachour. A fast implementation for gmres method. *Journal of Computational and Applied Mathematics*, 159(2):269–283, 2003.
- [66] J. Guzmán B. Cockburn, B. Dong. A superconvergent LDG-hybridizable Galerkin method for second-order elliptic problems. *Mathematics of Computation*, 77(264):1887–1916, 2008.
- [67] A. Babeyko and S. Sobolev. High-resolution numerical modeling of stress distribution in visco-elasto-plastic subducting slabs. *Lithos*, 103:205–216, 2008.
- [68] Andrey Y Babeyko and Stephan V Sobolev. Quantifying different modes of the late cenozoic shortening in the central andes. *Geology*, 33(8):621–624, 2005.
- [69] Andrey Y Babeyko, Stephan V Sobolev, Tim Vietor, Onno Oncken, and Robert B Trumbull. Numerical study of weakening processes in the central andean back-arc. In *The Andes*, pages 495–512. Springer, 2006.
- [70] A.Yu. Babeyko, S.V. Sobolev, R.B. Trumbull, O. Oncken, and L.L. Lavie. Numerical models of crustal scale convection and partial melting beneath the Altiplano-Puna plateau. *Earth Planet. Sci. Lett.*, 199:373–388, 2002.
- [71] M. Baes, R. Govers, and R. Wortel. Subduction initiation along the inherited weakness zone at the edge of a slab: Insights from numerical models. *Geophys. J. Int.*, 184:991–1008, 2011.

- [72] M. Baes, R. Govers, and R. Wortel. Switching between alternative responses of the lithosphere to continental collision. *Geophys. J. Int.*, 2011.
- [73] Marzieh Baes, Stephan V Sobolev, and Javier Quinteros. Subduction initiation in mid-ocean induced by mantle suction flow. *Geophysical Journal International*, 215(3):1515–1522, 2018.
- [74] Quan Bai and DL Kohlstedt. High-temperature creep of olivine single crystals, 2. dislocation structures. *Tectonophysics*, 206(1-2):1–29, 1992.
- [75] W. Bai. The quadrilateral Mini finite element for the Stokes problem. *Computer Methods in Applied Mechanics and Engineering*, 143:41–47, 1997.
- [76] B. Baitsch-Ghirardello, Taras V. Gerya, and J.-P. Burg. Geodynamic regimes of intra-oceanic subduction: Implications for arc extension vs. shortening processes. *Gondwana Research*, 25:546–560, 2014.
- [77] Bettina Baitsch-Ghirardello, Andreas Stracke, James AD Connolly, Ksenia M Nikolaeva, and Taras V Gerya. Lead transport in intra-oceanic subduction zones: 2d geochemical–thermo-mechanical modeling of isotopic signatures. *Lithos*, 208:265–280, 2014.
- [78] R.R. Bakker, M. Frehner, and M. Lupi. How temperature-dependent elasticity alters host rock/magmatic reservoir models: A case study on the effects of ice-cap unloading on shallow volcanic systems. *epsl*, 456:16–25, 2016.
- [79] M. D. Ballmer, C. P. Conrad, E. I. Smith, and N. Harmon. Non-hotspot volcano chains produced by migration of shear-driven upwelling toward the east pacific rise. *Geology*, 41(4):479–482, 2013.
- [80] M. D. Ballmer, C. P. Conrad, E. I. Smith, and R. Johnsen. Intraplate volcanism at the edges of the colorado plateau sustained by a combination of triggered edge-driven convection and shear-driven upwelling. *Geochemistry, Geophysics, Geosystems*, 16(2):366–379, 2015.
- [81] Maxim D Ballmer, Garrett Ito, Jeroen van Hunen, and Paul J Tackley. Spatial and temporal variability in hawaiian hotspot volcanism induced by small-scale convection. *Nature Geoscience*, 4(7):457, 2011.
- [82] Maxim D Ballmer, Nicholas C Schmerr, Takashi Nakagawa, and Jeroen Ritsema. Compositional mantle layering revealed by slab stagnation at~ 1000-km depth. *Science advances*, 1(11):e1500815, 2015.
- [83] M.D. Ballmer, G. Ito, J. van Hunen, and P.J. Tackley. Small-scale sublithospheric convection reconciles geochemistry and geochronology of 'Superplume' volcanism in th western and south pacific. *Earth Planet. Sci. Lett.*, 290:224–232, 2010.
- [84] M.D. Ballmer, J. van Hunen, G. Ito, P.J. Tackley, and T.A. Bianco. Non-hotspot volcano chains originating from small-scale sublithospheric convection. *Geophys. Res. Lett.*, 34(L23310):doi:10.1029/2007GL031636, 2007.
- [85] MD v Ballmer, J van Hunen, G Ito, TA Bianco, and PJ Tackley. Intraplate volcanism with complex age-distance patterns: A case for small-scale sublithospheric convection. *Geochemistry, Geophysics, Geosystems*, 10(6), 2009.
- [86] NJ Balmforth, RV Craster, P Perona, AC Rust, and R Sassi. Viscoplastic dam breaks and the bostwick consistometer. *Journal of non-newtonian fluid mechanics*, 142(1-3):63–78, 2007.
- [87] N.J. Balmforth, Y. Forterre, and O. Pouliquen. The viscoplastic stokes layer. *Journal of Non-Newtonian Fluid Mechanics*, 158:46–53, 2009.
- [88] N.J. Balmforth and A.C. Rust. Weakly nonlinear viscoplastic convection. *Journal of Non-Newtonian Fluid Mechanics*, 158:36–45, 2009.
- [89] W. Bangerth, R. Hartmann, and G. Kanschat. deal.II - a general purpose object oriented finite element library. *ACM Transaction on mathematical software*, 33(4), 2007.
- [90] W. Bangerth and T. Heister. What makes computational open source software libraries successful? *Computational Science & Discovery*, 6, 2013.
- [91] W. Bangerth, T. Heister, et al. ASPECT: *Advanced Solver for Problems in Earths Convection*. Computational Infrastructure for Geodynamics, 2019.
- [92] Xuewei Bao, David W Eaton, and Bernard Guest. Plateau uplift in western canada caused by lithospheric delamination along a craton edge. *Nature Geoscience*, 7(11):830, 2014.
- [93] H.A. Barnes. The yield stress - everything flows? *J. Non-Newtonian Fluid Mech.*, 81:133–178, 1999.
- [94] HA Barnes and K Walters. The yield stress myth? *Rheologica acta*, 24(4):323–326, 1985.
- [95] N. Barnett-Moore, R. Hassan, N. Flament, and D. Müller. The deep Earth origin of the Iceland plume and its effects on regional surface uplift and subsidence. *Solid Earth*, 8:235–254, 2017.

- [96] R. Barrett, M. Berry, T.F. Chan, J. Demmel, J.M. Donato, J. Dongarra, V. Eijkhout, R. Pozo, C. Romine, and H. van der Vorst. *Templates for the solution of linear systems: building blocks for iterative methods*. SIAM, 1994.
- [97] Francesco Bassi and Stefano Rebay. High-order accurate discontinuous finite element solution of the 2d euler equations. *Journal of computational physics*, 138(2):251–285, 1997.
- [98] Francesco Bassi, Stefano Rebay, G Mariotti, Savini Pedinotti, and M Savini. A high-order accurate discontinuous finite element method for inviscid and viscous turbomachinery flows. In *Proceedings of the 2nd European Conference on Turbomachinery Fluid Dynamics and Thermodynamics*, pages 99–109. Technologisch Instituut, Antwerpen, Belgium, 1997.
- [99] G.K. Batchelor. *An introduction to fluid dynamics*. Cambridge University Press, 1967.
- [100] K.-J. Bathe. *Finite Element Procedures in Engineering Analysis*. Prentice-Hall, 1982.
- [101] K.J. Bathe, editor. *Three-dimensional spherical shell convection at infinite Prandtl number using the cubed sphere method*, Proceedings Second MIT Conference on Computational Fluid and Solid Mechanics June 1720, 2003. Elsevier, 2003.
- [102] GE Batt and J Braun. On the thermomechanical evolution of compressional orogens. *Geophysical Journal International*, 128(2):364–382, 1997.
- [103] Geoffrey E Batt and Jean Braun. The tectonic evolution of the southern alps, new zealand: insights from fully thermally coupled dynamical modelling. *Geophysical Journal International*, 136(2):403–420, 1999.
- [104] L. Battaglia, M.A. Storti, and J. D’Elia. An interface capturing finite element approach for free surface flows using unstructured grids. *Mecanica Computational*, XXVII:33–48, 2008.
- [105] Cyrill Baumann, Taras V Gerya, and James AD Connolly. Numerical modelling of spontaneous slab breakoff dynamics during continental collision. *Geological Society, London, Special Publications*, 332(1):99–114, 2010.
- [106] TS Baumann. Appraisal of geodynamic inversion results: a data mining approach. *Geophysical Supplements to the Monthly Notices of the Royal Astronomical Society*, 207(2):667–679, 2016.
- [107] T.S. Baumann, B.J.P. Kaus, and A.A. Popov. Constraining effective rheology through parallel joint geodynamic inversion. *Tectonophysics*, 631:197–211, 2014.
- [108] JR Baumgardner. *A Three-Dimensional Finite Element Model for Mantle Convection*. PhD thesis, UCLA, 1983.
- [109] J.R. Baumgardner. Three-Dimensional treatment of convective flow in the Earth’s mantle. *Journal of Statistical Physics*, 39(5/6):501–511, 1985.
- [110] J.R. Baumgardner and P.O. Frederickson. Isocahedral discretisation of the two-sphere. *SIAM J. Numer Anal.*, 22(6):1107–1115, 1985.
- [111] A. Bauville and T. S. Baumann. geomio: an open-source matlab toolbox to create the initial configuration of 2d/3d thermo-mechanical simulations from 2d vector drawings. *Geochemistry, Geophysics, Geosystems*, 2019.
- [112] Arthur Bauville, Jean-Luc Epard, and Stefan M Schmalholz. A simple thermo-mechanical shear model applied to the morels fold nappe (western alps). *Tectonophysics*, 583:76–87, 2013.
- [113] Zdeněk P Bažant and Milan Jirásek. Nonlocal integral formulations of plasticity and damage: survey of progress. *Journal of Engineering Mechanics*, 128(11):1119–1149, 2002.
- [114] Adam P Beall, Louis Moresi, and Tim Stern. Dripping or delamination? a range of mechanisms for removing the lower crust or lithosphere. *Geophysical Journal International*, 210(2):671–692, 2017.
- [115] AP Beall, Louis Moresi, and Catherine M Cooper. Formation of cratonic lithosphere during the initiation of plate tectonics. *Geology*, 46(6):487–490, 2018.
- [116] C. Beaumont, S. Ellis, J. Hamilton, and P. Fullsack. Mechanical model for subduction-collision tectonics of alpine-type compressional orogens. *Geology*, 24(8):675–678, 1996.
- [117] C. Beaumont, S. Ellis, and A. Pfiffner. Dynamics of sediment subduction-accretion at convergent margins: Short-term modes, long-term deformation, and tectonic implications. *Journal of Geophysical Research: Solid Earth*, 104(B8):17573–17601, 1999.
- [118] C. Beaumont, P. Fullsack, and J. Hamilton. Erosional control of active compressional orogens. *Thrust Tectonics*, 99:1–18, 1992.
- [119] C. Beaumont, P. Fullsack, and J. Hamilton. Styles of crustal deformation in compressional orogens caused by subduction of the underlying lithosphere. *Tectonophysics*, 232:119–132, 1994.

- [120] C. Beaumont and S.J. Ings. Effect of depleted continental lithosphere counterflow and inherited crustal weakness on rifting of the continental lithosphere: General results. *Journal of Geophysical Research: Solid Earth*, 117(8), 2012.
- [121] C. Beaumont, R.A. Jamieson, J.P. Butler, and C.J. Warren. Crustal structure: A key constraint on the mechanism of ultra-high-pressure rock exhumation. *Earth Planet. Sci. Lett.*, 287:116–129, 2009.
- [122] C. Beaumont, R.A. Jamieson, M.H. Nguyen, and B. Lee. Himalayan tectonics explained by extrusion of a low-viscosity crustal channel coupled to focused surface denudation. *Nature*, 414:738–742, 2001.
- [123] C. Beaumont, R.A. Jamieson, M.H. Nguyen, and S. Medvedev. Crustal channel flows: 1. Numerical models with applications to the tectonics of the Himalayan-Tibetan orogen. *J. Geophys. Res.*, 109(B06406), 2004.
- [124] C. Beaumont, P.J. Kamp, J. Hamilton, and P. Fullsack. The continental collision zone, south island, new zealand: comparison of geodynamical models and observations. *J. Geophys. Res.*, 101:3333–3359, 1996.
- [125] C. Beaumont, C.E. Keen, and R. Boutilier. On the evolution of rifted continental margins: comparison of models and observations for the nova scotian margin. *Geophysical Journal of the Royal Astronomical Society*, 70(3):667–715, 1982.
- [126] C. Beaumont, J.A. Munoz, J. Hamilton, and P. Fullsack. Factors controlling the alpine evolution of the central pyrenees inferred from a comparison of observations and geodynamical models. *J. Geophys. Res.*, 105:8121–8145, 2000.
- [127] C. Beaumont, M.H. Nguyen, R.A. Jamieson, and S. Ellis. Crustal flow modes in large hot orogens. *Geological Society Special Publication*, 268:91–145, 2006.
- [128] Christopher Beaumont and Anthony Lambert. Crustal structure from surface load tilts, using a finite element model. *Geophysical Journal International*, 29(2):203–226, 1972.
- [129] Christopher Beaumont and Garry Quinlan. A geodynamic framework for interpreting crustal-scale seismic-reflectivity patterns in compressional orogens. *Geophysical Journal International*, 116(3):754–783, 1994.
- [130] Stéphane J Beaussier, Taras V Gerya, and Jean-Pierre Burg. Near-ridge initiation of intraoceanic subduction: Effects of inheritance in 3d numerical models of the wilson cycle. *Tectonophysics*, 763:1–13, 2019.
- [131] J.M. Becker and M. Bevis. Love’s problem. *Geophy. J. Int.*, 156:171–178, 2004.
- [132] T. W. Becker and C. Faccenna. *Subduction Zone Geodynamics*, chapter A Review of the Role of Subduction Dynamics for Regional and Global Plate Motions, pages 3–34. Springer Berlin Heidelberg, 2009.
- [133] T. W. Becker, C. Faccenna, R. J. O’Connell, and D. Giardini. The development of slabs in the upper mantle: Insights from numerical and laboratory experiments. *Journal of Geophysical Research: Solid Earth*, 104(B7):15207–15226, 1999.
- [134] Thorsten W Becker, Bogdan Kustowski, and Göran Ekström. Radial seismic anisotropy as a constraint for upper mantle rheology. *Earth and Planetary Science Letters*, 267(1-2):213–227, 2008.
- [135] Thorsten W Becker and Richard J O’Connell. Predicting plate velocities with mantle circulation models. *Geochemistry, Geophysics, Geosystems*, 2(12), 2001.
- [136] T.W. Becker. On the effect of temperature and strain-rate dependent viscosity on global mantle flow, net rotation, and plate-driving forces. *Geophy. J. Int.*, 167:943–957, 2006.
- [137] TW Becker. Azimuthal seismic anisotropy constrains net rotation of the lithosphere. *Geophysical Research Letters*, 35(5), 2008.
- [138] T.W. Becker and C. Faccenna. Mantle conveyor beneath the Tethyan collisional belt. *Earth Planet. Sci. Lett.*, 310:453–461, 2011.
- [139] T.W. Becker, V. Schulte-Pelkum, D.K. Blackman, J.B. Kellogg, and R.J. O’Connell. Mantle flow under the western United States from shear wave splitting. *Earth Planet. Sci. Lett.*, 247:235–251, 2006.
- [140] M.D. Behn, J. Lin, and M.T. Zuber. A continuum mechanics model for normal faulting using a strain-rate softening rheology: implications for thermal and rheological controls on continental and oceanic rifting. *Earth Planet. Sci. Lett.*, 202:725–740, 2002.
- [141] Marie Běhouková, Gabriel Tobie, Gaël Choblet, and Ondřej Čadek. Coupling mantle convection and tidal dissipation: Applications to enceladus and earth-like planets. *Journal of Geophysical Research: Planets*, 115(E9), 2010.
- [142] A. Bellas, Sh. Zhong, D. Bercovici, and E. Mulyukova. Dynamic weakening with grain-damage and implications for slab detachment. *Phys. Earth. Planet. Inter.*, 285:76–90, 2018.
- [143] Léa Bello, Nicolas Coltice, Tobias Rolf, and Paul J Tackley. On the predictability limit of convection models of the earth’s mantle. *Geochemistry, Geophysics, Geosystems*, 15(6):2319–2328, 2014.

- [144] Léa Bello, Nicolas Coltice, Paul J Tackley, R Dietmar Müller, and John Cannon. Assessing the role of slab rheology in coupled plate-mantle convection models. *Earth and Planetary Science Letters*, 430:191–201, 2015.
- [145] T. Belytschko, L. Gu, and Y.Y. Lu. Fracture and crack growth by element free galerkin method. *Modelling Simul. Mater. Sci. Eng.*, 2:519–534, 1994.
- [146] T. Belytschko, Y. Krongauz, M. Fleming, D. Organ, and W.K.S. Liu. Smoothing and accelerated computations in the element free galerkin method. *Journal of Computational and Applied Mathematics*, 74:111–126, 1996.
- [147] T. Belytschko, Y. Krongauz, D. Organ, M. Fleming, and P. Krysl. Meshless methods: an overview and recent developments. *Comput. Methods Appl. Mech. Engrg.*, 139:3–47, 1996.
- [148] T. Belytschko, P. Krysl, and Y. Krongauz. A three-dimensional explicit element-free galerkin method. *International journal for numerical methods in fluids*, 24:1253–1270, 1997.
- [149] T. Belytschko, Y.Y. Lu, and L. Gu. Crack propagation by element-free galerkin methods. *Engineering Fracture Mechanics*, 51:295–315, 1995.
- [150] T. Belytschko, Y.Y. Lu, and M. Tabbara. Element-free galerkin methods for static and dynamic fracture. *International Journal of Solids and Structures*, 32:2547–2570, 1995.
- [151] Ted Belytschko, Yong Guo, Wing Kam Liu, and Shao Ping Xiao. A unified stability analysis of meshless particle methods. *International Journal for Numerical Methods in Engineering*, 48(9):1359–1400, 2000.
- [152] Z Ben-Avraham, V Lyakhovsky, and M Grasso. Simulation of collision zone segmentation in the central mediterranean. *Tectonophysics*, 243(1-2):57–68, 1995.
- [153] Vladimir Benes and Philippe Davy. Modes of continental lithospheric extension: experimental verification of strain localization processes. *Tectonophysics*, 254(1-2):69–87, 1996.
- [154] Nina Benesova and Hana Ciskova. Effect of post-perovskite rheology on the thermal evolution of the Earth. *Phys. Earth. Planet. Inter.*, 251:1–10, 2016.
- [155] A.K. Bengtson and P.E. van Keeken. Three-dimensional thermal structure of subduction zones: effects of obliquity and curvature. *Solid Earth*, 3:365–373, 2012.
- [156] A Beniest, A Koptev, and Evgenii Burov. Numerical models for continental break-up: Implications for the south atlantic. *Earth and Planetary Science Letters*, 461:176–189, 2017.
- [157] David J Benson. An efficient, accurate, simple ale method for nonlinear finite element programs. *Computer methods in applied mechanics and engineering*, 72(3):305–350, 1989.
- [158] M. Benzi. Preconditioning Techniques for Large Linear Systems: A Survey. *J. Comp. Phys.*, 182:418–477, 2002.
- [159] M. Benzi, G.H. Golub, and J. Liesen. Numerical solution of saddle point problems. *Acta Numerica*, 14:1–137, 2005.
- [160] M. Benzi and A.J. Wathen. In W.H.A. Schilders, H.A. van der Vorst, and Joost Rommes, editors, *Model Order Reduction: Theory, Research Aspects and Applications*, pages 195–211. Springer, 2008.
- [161] D. Bercovici and E. Mulyukova. A continuum theory for phase mixing and grain-damage relevant to tectonic plate boundary evolution. *Phys. Earth. Planet. Inter.*, 285:23–44, 2018.
- [162] D. Bercovici, E. Mulyukova, and M.D. Long. A simple toy model for coupled retreat and detachment of subducting slabs. *Journal of Geodynamics*, 129:275–289, 2019.
- [163] D. Bercovici and G. Schubert. *Treatise on geophysics: Mantle dynamics. Vol. 7*. Elsevier, 2009.
- [164] D. Bercovici, G. Schubert, and G.A. Glatzmaier. Three-dimensional convection of an infinite Prandtl-number compressible fluid in a basally heated spherical shell. *J. Fluid Mech.*, 239:683–719, 1992.
- [165] D. Bercovici, G. Schubert, G.A. Glatzmaier, and A. Zebib. Three-dimensional thermal convection in a spherical shell. *J. Fluid Mech.*, 206:75–104, 1989.
- [166] D. Bercovici, G. Schubert, and Yanick Ricard. Abrupt tectonics and rapid slab detachment with grain damage. *Proceedings of the National Academy of Sciences*, 2014.
- [167] D. Bercovici, G. Schubert, and A. Zebib. Geoid and topography for infinite Prandtl number convection in a shell. *J. Geophys. Res.*, 93(B6):6430–6436, 1988.
- [168] David Bercovici. A source-sink model of the generation of plate tectonics from non-newtonian mantle flow. *Journal of Geophysical Research: Solid Earth*, 100(B2):2013–2030, 1995.
- [169] David Bercovici. Plate generation in a simple model of lithosphere-mantle flow with dynamic self-lubrication. *Earth and Planetary Science Letters*, 144(1-2):41–51, 1996.

- [170] David Bercovici. Generation of plate tectonics from lithosphere–mantle flow and void–volatile self-lubrication. *Earth and Planetary Science Letters*, 154(1-4):139–151, 1998.
- [171] David Bercovici and Yanick Ricard. Energetics of a two-phase model of lithospheric damage, shear localization and plate-boundary formation. *Geophysical Journal International*, 152(3):581–596, 2003.
- [172] David Bercovici and Yanick Ricard. Generation of plate tectonics with two-phase grain-damage and pinning: Source–sink model and toroidal flow. *Earth and Planetary Science Letters*, 365:275–288, 2013.
- [173] David Bercovici, Yanick Ricard, and Gerald Schubert. A two-phase model for compaction and damage: 1. general theory. *Journal of Geophysical Research: Solid Earth*, 106(B5):8887–8906, 2001.
- [174] David Bercovici, Gerald Schubert, and Paul J Tackley. On the penetration of the 660 km phase change by mantle downflows. *Geophysical research letters*, 20(23):2599–2602, 1993.
- [175] M. Bercovier and M. Engelman. A finite-element for the numerical solution of viscous incompressible flows. *J. Comp. Phys.*, 30:181–201, 1979.
- [176] M. Bercovier and M. Engelman. A finite-element method for incompressible Non-Newtonian flows. *J. Comp. Phys.*, 36:313–326, 1980.
- [177] H Berner, Hans Ramberg, and Ove Stephansson. Diapirism theory and experiment. *Tectonophysics*, 15(3):197–218, 1972.
- [178] Peter G Betts, Louis Moresi, Meghan S Miller, and David Willis. Geodynamics of oceanic plateau and plume head accretion and their role in phanerozoic orogenic systems of china. *Geoscience Frontiers*, 6(1):49–59, 2015.
- [179] P.G. Betts, W.G. Mason, and L. Moresi. The influence of a mantle plume head on the dynamics of a retreating subduction zone. *Geology*, 40(8):739–742, 2012.
- [180] Romain Beucher, Louis Moresi, Julian Giordani, John Mansour, Dan Sandiford, Rebecca Farrington, Luke Mondy, Claire Mallard, Patrice Rey, Guillaume Duclaux, et al. Uwgeodynamics: A teaching and research tool for numerical geodynamic modelling. *Journal of Open Source Software*, 4(36):1136, 2019.
- [181] M.J. Beuchert and Y.Y. Podladchikov. Viscoelastic mantle convection and lithospheric stresses. *GJI*, 183:35–63, 2010.
- [182] E. Beutel, J. van Wijk, C. Ebinger, D. Keir, and A. Agostini. Formation and stability of magmatic segments in the Main Ethiopian and Afar rifts. *Earth Planet. Sci. Lett.*, 293:225–235, 2010.
- [183] L Beuth, Z Wieckowski, and PA Vermeer. Solution of quasi-static large-strain problems by the material point method. *International Journal for Numerical and Analytical Methods in Geomechanics*, 35(13):1451–1465, 2011.
- [184] T. A. Bianco, C. P. Conrad, and E. I. Smith. Time dependence of intraplate volcanism caused by shear-driven upwelling of low-viscosity regions within the asthenosphere. *Journal of Geophysical Research: Solid Earth*, 116(B11), 2011.
- [185] Andrew J Biggin, Bernard Steinberger, Julien Aubert, Neil Suttie, Richard Holme, Trond Helge Torsvik, Douwe G van der Meer, and DJJ van Hinsbergen. Possible links between long-term geomagnetic variations and whole-mantle convection processes. *Nature Geoscience*, 5(8):526, 2012.
- [186] Harmen Bijwaard and Wim Spakman. Tomographic evidence for a narrow whole mantle plume below iceland. *Earth and Planetary Science Letters*, 166(3-4):121–126, 1999.
- [187] M. I. Billen. Slab dynamics in the transition zone. *Physics of the Earth and Planetary Interiors*, 183(1-2):296–308, 2010.
- [188] Magali I Billen. Modeling the dynamics of subducting slabs. *Annu. Rev. Earth Planet. Sci.*, 36:325–356, 2008.
- [189] Magali I Billen. Tectonics: Soaking slabs. *Nature Geoscience*, 2(11):744, 2009.
- [190] Magali I Billen, Michael Gurnis, and Mark Simons. Multiscale dynamics of the tongakermadec subduction zone. *Geophysical Journal International*, 153(2):359–388, 2003.
- [191] Magali I Billen, Oliver Kreylos, Bernd Hamann, Margarete A Jadamec, Louise H Kellogg, Oliver Staadt, and Dawn Y Sumner. A geoscience perspective on immersive 3d gridded data visualization. *Computers & Geosciences*, 34(9):1056–1072, 2008.
- [192] M.I. Billen and K.M. Arredondo. Decoupling of plate-asthenosphere motion caused by non-linear viscosity during slab folding in the transition zone. *Phys. Earth. Planet. Inter.*, 281:17–30, 2018.
- [193] M.I. Billen and M. Gurnis. A low wedge in subduction zones. *Earth Planet. Sci. Lett.*, 193:227–236, 2001.

- [194] M.I. Billen and M. Gurnis. Comparison of dynamic flow models for the Central Aleutian and Tonga-Kermadec subduction zones. *Geochem. Geophys. Geosyst.*, 4(4), 2003.
- [195] M.I. Billen and G. Hirth. Newtonian versus non-Newtonian upper mantle viscosity: Implications for subduction initiation. *Geophys. Res. Lett.*, 32(L19304):doi:10.1029/2005GL023457, 2005.
- [196] M.I. Billen and G. Hirth. Rheologic controls on slab dynamics. *Geochem. Geophys. Geosyst.*, 8(8):doi:10.1029/2007GC001597, 2007.
- [197] M.I. Billen and M. Jadamec. Origin of localized fast mantle flow velocity in numerical models of subduction. *Geochem. Geophys. Geosyst.*, 13(1), 2012.
- [198] E.C. Bingham. *Fluidity and Plasticity*. McGraw-Hill, New York, 1922.
- [199] Francis Birch. Elasticity and constitution of the earth's interior. *Journal of Geophysical Research*, 57(2):227–286, 1952.
- [200] P. Bird. Testing hypotheses on plate-driving mechanisms with global lithosphere models including topography, thermal structure, and faults. *J. Geophys. Res.*, 103(B5):10,115–10,129, 1998.
- [201] Peter Bird. Finite element modeling of lithosphere deformation: the Zagros collision orogeny. *Tectonophysics*, 50(2-3):307–336, 1978.
- [202] Peter Bird. Initiation of intracontinental subduction in the Himalaya. *Journal of Geophysical Research: Solid Earth*, 83(B10):4975–4987, 1978.
- [203] Peter Bird. Thin-plate and thin-shell finite-element programs for forward dynamic modeling of plate deformation and faulting. *Computers & Geosciences*, 25(4):383–394, 1999.
- [204] Peter Bird, Zhen Liu, and William Kurt Rucker. Stresses that drive the plates from below: Definitions, computational path, model optimization, and error analysis. *Journal of Geophysical Research: Solid Earth*, 113(B11), 2008.
- [205] BI Birger. Rheological model of the earth's and the terrestrial planets' mantles. *Computational Seismology and Geodynamics*, 3:1–7, 1996.
- [206] D. Bittner and H. Schmeling. Numerical modelling of melting processes and induced diapirism in the lower crust. *Geophy. J. Int.*, 123:59–70, 1995.
- [207] J Blackery and E Mitsoulis. Creeping motion of a sphere in tubes filled with a Bingham plastic material. *Journal of non-newtonian fluid mechanics*, 70(1-2):59–77, 1997.
- [208] I.F. Blanco-Quintero, T.V. Gerya, A. Garcia-Casco, and A. Castro. Subduction of young oceanic plates: A numerical study with application to aborted thermalchemical plumes. *Geochem. Geophys. Geosyst.*, 12(10), 2011.
- [209] B. Blankenbach, F. Busse, U. Christensen, L. Cserepes, D. Gunkel, U. Hansen, H. Harder, G. Jarvis, M. Koch, G. Marquart, D. Moore, P. Olson, H. Schmeling, and T. Schnaubelt. A benchmark comparison for mantle convection codes. *Geophys. J. Int.*, 98:23–38, 1989.
- [210] Irina Blinova, Ilya Makeev, and Igor Popov. Benchmark solutions for Stokes flows in cylindrical and spherical geometry. *Bulletin of the Transilvania University of Brasov. Mathematics, Informatics, Physics. Series III*, 9(1):11, 2016.
- [211] AM Bobrov and AA Baranov. Thermochemical mantle convection with drifting deformable continents: Main features of supercontinent cycle. *Pure and Applied Geophysics*, pages 1–21, 2019.
- [212] AM Bobrova and AA Baranov. The mantle convection model with non-newtonian rheology and phase transitions: The flow structure and stress fields. *Izvestiya, Physics of the Solid Earth*, 52(1):129–143, 2016.
- [213] M Bocher, Nicolas Coltice, Alexandre Fournier, and Paul J Tackley. A sequential data assimilation approach for the joint reconstruction of mantle convection and surface tectonics. *Geophysical Journal International*, 204(1):200–214, 2016.
- [214] Marie Bocher, Alexandre Fournier, and Nicolas Coltice. Ensemble Kalman filter for the reconstruction of the earth's mantle circulation. *Nonlinear Processes in Geophysics*, 25(1):99–123, 2018.
- [215] P. B. Bochev, C. R. Dohrmann, and M. D. Gunzburger. Stabilization of low-order mixed finite elements for the Stokes equations. *SIAM Journal on Numerical Analysis*, 44(1):82–101, 2006.
- [216] Pavel B Bochev and Clark R Dohrmann. A computational study of stabilized, low-order C0 finite element approximations of Darcy equations. *Computational Mechanics*, 38(4-5):323–333, 2006.
- [217] Pavel B Bochev, Max D Gunzburger, and Richard B Lehoucq. On stabilized finite element methods for the Stokes problem in the small time step limit. *International Journal for Numerical Methods in Fluids*, 53(4):573–597, 2007.

- [218] Ömer F Bodur and Patrice F Rey. The impact of rheological uncertainty on dynamic topography predictions. *Solid Earth*, 10(6):2167–2178, 2019.
- [219] Reinhard Boehler. Melting temperature of the earth’s mantle and core: Earth’s thermal structure. *Annual Review of Earth and Planetary Sciences*, 24(1):15–40, 1996.
- [220] D. Boffi and L. Gastaldi. On the quadrilateral Q2-P1 element for the Stokes problem. *Int. J. Num. Meth. Fluids*, 39:1001–1011, 2002.
- [221] Francesca Boioli, Philippe Carrez, Patrick Cordier, Benoit Devincre, Karine Gouriet, Pierre Hirel, Antoine Kraych, and Sebastian Ritterbex. Pure climb creep mechanism drives flow in earths lower mantle. *Science advances*, 3(3):e1601958, 2017.
- [222] Peter Charles Bollada and Timothy Nigel Phillips. On the mathematical modelling of a compressible viscoelastic fluid. *Archive for Rational Mechanics and Analysis*, 205(1):1–26, 2012.
- [223] Alessandro Bonaccorso and Paul M Davis. Models of ground deformation from vertical volcanic conduits with application to eruptions of mount st. helens and mount etna. *Journal of Geophysical Research: Solid Earth*, 104(B5):10531–10542, 1999.
- [224] Marco Bonini, Giacomo Corti, Dimitrios Sokoutis, Gianfranco Vannucci, Paolo Gasperini, and Sierd Cloetingh. Insights from scaled analogue modelling into the seismotectonics of the iranian region. *Tectonophysics*, 376(3-4):137–149, 2003.
- [225] M.-A. Bonnardot, R. Hassani, and E. Tric. Numerical modelling of lithosphereasthenosphere interaction in a subduction zone. *Earth Planet. Sci. Lett.*, 272:698–708, 2008.
- [226] M.-A. Bonnardot, R. Hassani, E. Tric, E. Ruellan, and M. Regnier. Effect of margin curvature on plate deformation in a 3-D numerical model of subduction zones. *Geophys. J. Int.*, 173:1084–1094, 2008.
- [227] S. Bonnet. Shrinking and splitting of drainage basins in orogenic landscapes from the migration of the main drainage divide. *Nature Geoscience*, 2:766–771, 2009.
- [228] Stephane Bonnet and Alain Crave. Macroscale dynamics of experimental landscapes. *Geological Society, London, Special Publications*, 253(1):327–339, 2006.
- [229] Alain Bonneville and Patrick Capolsini. Thermic: a 2-d finite-element tool to solve conductive and advective heat transfer problems in earth sciences. *Computers & Geosciences*, 25(10):1137–1148, 1999.
- [230] P.D. Bons, D. Koehn, and M.W. Jessell, editors. *Microdynamics Simulation*. Lecture Notes in Earth Sciences. Springer, 2008.
- [231] K Boonma, Ajay Kumar, Daniel García-Castellanos, Ivone Jiménez-Munt, and Manel Fernández. Lithospheric mantle buoyancy: the role of tectonic convergence and mantle composition. *Scientific Reports*, 9(1):1–8, 2019.
- [232] René de Borst. Some recent issues in computational failure mechanics. *International Journal for Numerical Methods in Engineering*, 52(1-2):63–95, 2001.
- [233] F Boschetti and Louis Moresi. Interactive inversion in geosciences. *Geophysics*, 66(4):1226–1234, 2001.
- [234] Lapo Boschi, Claudio Faccenna, and TW Becker. Mantle structure and dynamic topography in the mediterranean basin. *Geophysical Research Letters*, 37(20), 2010.
- [235] L.M. Boschman, D.J.J. van Hinsbergen, T.H. Torsvik, W. Spakman, and J.L. Pindell. Kinematic reconstruction of the caribbean region since the early jurassic. *Earth-Science Reviews*, 138:102–136, 2014.
- [236] AP Boss, CL Angevine, and IS Sacks. Finite-amplitude models of convection in the early mantle. *Physics of the earth and planetary interiors*, 36(3-4):328–336, 1984.
- [237] William Bosworth. Geometry of propagating continental rifts. *Nature*, 316(6029):625, 1985.
- [238] O. Botella and R. Peyret. Benchmark spectral results on the lid-driven cavity flow. *Computers and Fluids*, 27(4):421–433, 1998.
- [239] MHP Bott, GD Waghorn, and A Whittaker. Plate boundary forces at subduction zones and trench-arc compression. *Tectonophysics*, 170(1-2):1–15, 1989.
- [240] A.D. Bottrill, J. van Hunen, and M.B. Allen. Insight into collision zone dynamics from topography: numerical modelling results and observations. *Solid Earth*, 3:387–399, 2012.
- [241] P. Bouilhol, V. Magni, J. van Hunen, and L. Kaislaniemi. A numerical approach to melting in warm subduction zones. *Earth Planet. Sci. Lett.*, 411:37–44, 2015.
- [242] Johannes Bouman, Jörg Ebbing, Sjef Meekes, Rader Abdul Fattah, Martin Fuchs, Sofie Gradmann, Roger Haagmans, Verena Lieb, Michael Schmidt, Denise Dettmering, et al. Goce gravity gradient data for lithospheric modeling. *International Journal of Applied Earth Observation and Geoinformation*, 35:16–30, 2015.

- [243] L. Bourgouin, H.-B. Mühlhaus, A.J. Hale, and A. Arsac. Towards realistic simulations of lava dome growth using the level set method. *Acta Geotechnica*, 1:225–236, 2006.
- [244] L. Bourgouin, H.-B. Mühlhaus, A.J. Hale, and A. Arsac. Studying the influence of a solid shell on lava dome growth and evolution using the level set method. *Geophys. J. Int.*, 170:1431–1438, 2007.
- [245] D. Boutelier, A. Chemenda, and C. Jorand. Continental subduction and exhumation of high-pressure rocks: insights from thermo-mechanical laboratory modelling. *Earth Planet. Sci. Lett.*, 222:209–216, 2004.
- [246] Allan F Bower. *Applied mechanics of solids*. CRC press, 2009.
- [247] Dan J Bower, Michael Gurnis, Jennifer M Jackson, and Wolfgang Sturhahn. Enhanced convection and fast plumes in the lower mantle induced by the spin transition in ferropericlase. *Geophysical Research Letters*, 36(10), 2009.
- [248] Dan J Bower, June K Wicks, Michael Gurnis, and Jennifer M Jackson. A geodynamic and mineral physics model of a solid-state ultralow-velocity zone. *Earth and Planetary Science Letters*, 303(3-4):193–202, 2011.
- [249] D.J. Bower, M. Gurnis, and N. Flament. Assimilating lithosphere and slab history in 4-D Earth models. *Phys. Earth. Planet. Inter.*, 238:8–22, 2015.
- [250] D.J. Bower, M. Gurnis, and M. Seton. Lower mantle structure from paleogeographically constrained dynamic Earth models. *Geochem. Geophys. Geosyst.*, 14(1):44–63, 2012.
- [251] D.J. Bower, M. Gurnis, and D. Sun. Dynamic origins of seismic wavespeed variation in D''. *Phys. Earth. Planet. Inter.*, 214:74–86, 2013.
- [252] Malte Braack and Gert Lube. Finite elements with local projection stabilization for incompressible flow problems. *Journal of Computational Mathematics*, pages 116–147, 2009.
- [253] W.F. Brace and D.L. Kohlstedt. Limits on lithospheric stress imposed by laboratory experiments. *J. Geophys. Res.*, 85:6248–6252, 1980.
- [254] D. Braess. *Finite Elements*. Cambridge, 2007.
- [255] Henning Braess and Peter Wriggers. Arbitrary lagrangian eulerian finite element analysis of free surface flow. *Computer Methods in Applied Mechanics and Engineering*, 190(1-2):95–109, 2000.
- [256] J.H. Bramble, J.E. Pasciak, and A.T. Vassilev. Analysis of the inexact Uzawa algorithm for saddle point problems. *SIAM J. Numer. Anal.*, 34:1072–1092, 1997.
- [257] J.P. Brandenburg, E.H. Hauri, P.E. van Keken, and C.J. Ballentine. A multiple-system study of the geochemical evolution of the mantle with force-balanced plates and thermochemical effects. *Earth Planet. Sci. Lett.*, 276:1–13, 2008.
- [258] J.P. Brandenburg and P.E. van Keken. Deep storage of oceanic crust in a vigorously convecting mantle. *J. Geophys. Res.*, 112(B06403), 2007.
- [259] J.P. Brandenburg and P.E. van Keken. Methods for thermochemical convection in Earth's mantle with force-balanced plates. *Geochem. Geophys. Geosyst.*, 8(11), 2007.
- [260] J.M. Branolund, K. Regenauer-Lieb, and D.A. Yuen. Weak zone formation for initiating subduction from thermo-mechanical feedback of low-temperature plasticity. *Earth Planet. Sci. Lett.*, 190:237–250, 2001.
- [261] Joy M Branolund, Masanori C Kameyama, David A Yuen, and Yoshiyuki Kaneda. Effects of temperature-dependent thermal diffusivity on shear instability in a viscoelastic zone: implications for faster ductile faulting and earthquakes in the spinel stability field. *Earth and Planetary Science Letters*, 182(2):171–185, 2000.
- [262] J. Braun. Pecube: a new finite-element code to solve the 3D heat transport equation including the effects of a time-varying, finite amplitude surface topography. *Computers and Geosciences*, 29:787–794, 2003.
- [263] J. Braun. Recent advances and current problems in modelling surface processes and their interaction with crustal deformation. *Analogue and Numerical Modelling of Crustal-Scale Processes. Geological Society, London. Special Publications*, 253:307–325, 2006.
- [264] J. Braun and C. Beaumont. *Contrasting styles of lithospheric extension: implications for differences between the Basin and Range Province and rifted continental margins*. 1989.
- [265] J. Braun and C. Beaumont. Dynamical models of the role of crustal shear zones in asymmetric continental extension. *Earth and Planetary Science Letters*, 93(3-4):405–423, 1989.
- [266] J. Braun, J. Chéry, A. Poliakov, D. Mainprice, A. Vauchez, A. Tomassi, and M. Daignières. A simple parameterization of strain localization in the ductile regime due to grain-size reduction: a case study for olivine. *J. Geophys. Res.*, 104:25,167–25,181, 1999.

- [267] J Braun, Xavier Robert, and T Simon-Labré. Eroding dynamic topography. *Geophysical Research Letters*, 40(8):1494–1499, 2013.
- [268] J. Braun and M. Sambridge. Modelling landscape evolution on geological time scales: a new method based on irregular spatial discretisation. *Basin Research*, 9:27–52, 1997.
- [269] J. Braun, C. Thieulot, P. Fullsack, M. DeKool, and R.S. Huismans. DOUAR: a new three-dimensional creeping flow model for the solution of geological problems. *Phys. Earth. Planet. Inter.*, 171:76–91, 2008.
- [270] J. Braun and S.D. Willett. A very efficient O( $n$ ), implicit and parallel method to solve the stream power equation governing fluvial incision and landscape evolution. *Geomorphology*, 180–181:170–179, 2013.
- [271] J. Braun and P. Yamato. Structural evolution of a three-dimensional, finite-width crustal wedge. *Tectonophysics*, 484:181–192, 2010.
- [272] Jean Braun. Three-dimensional numerical modeling of compressional orogenies: Thrust geometry and oblique convergence. *Geology*, 21(2):153–156, 1993.
- [273] Jean Braun. Three-dimensional numerical simulations of crustal-scale wrenching using a non-linear failure criterion. *Journal of Structural Geology*, 16(8):1173–1186, 1994.
- [274] Jean Braun. The many surface expressions of mantle dynamics. *Nature Geoscience*, 3(12):825, 2010.
- [275] Jean Braun and Christopher Beaumont. A physical explanation of the relation between flank uplifts and the breakup unconformity at rifted continental margins. *Geology*, 17(8):760–764, 1989.
- [276] Jean Braun and Christopher Beaumont. Three-dimensional numerical experiments of strain partitioning at oblique plate boundaries: Implications for contrasting tectonic styles in the southern Coast Ranges, California, and central South Island, New Zealand. *J. Geophys. Res.*, 100(B9):18,059–18,074, 1995.
- [277] Jean Braun and Malcolm Sambridge. Dynamical lagrangian remeshing (dlr): a new algorithm for solving large strain deformation problems and its application to fault-propagation folding. *Earth and Planetary Science Letters*, 124(1-4):211–220, 1994.
- [278] Jean Braun and Malcolm Sambridge. A numerical method for solving partial differential equations on highly irregular evolving grids. *Nature*, 376(6542):655, 1995.
- [279] Jean Braun and Russell Shaw. A thin-plate model of palaeozoic deformation of the australian lithosphere: implications for understanding the dynamics of intracratonic deformation. *Geological Society, London, Special Publications*, 184(1):165–193, 2001.
- [280] Jean Braun, Peter Van Der Beek, Pierre Valla, Xavier Robert, Frédéric Herman, Christoph Glotzbach, Vivi Pedersen, Claire Perry, Thibaud Simon-Labré, and Cecile Prigent. Quantifying rates of landscape evolution and tectonic processes by thermochronology and numerical modeling of crustal heat transport using pecube. *Tectonophysics*, 524:1–28, 2012.
- [281] E. Bredow and B. Steinberger. Variable melt production rate of the kerguelen hotspot due to long-term plume-ridge interaction. *Geophysical Research Letters*, 45(1):126–136, 2018.
- [282] E. Bredow, B. Steinberger, R. Gassmöller, and J. Dannberg. How plume-ridge interaction shapes the crustal thickness pattern of the réunion hotspot track. *Geochemistry, Geophysics, Geosystems*, 2017.
- [283] M Breuer and U Hansen. Turbulent convection in the zero reynolds number limit. *EPL (Europhysics Letters)*, 86(2):24004, 2009.
- [284] M Breuer, A Manglik, J Wicht, T Trümper, H Harder, and U Hansen. Thermochemically driven convection in a rotating spherical shell. *Geophysical Journal International*, 183(1):150–162, 2010.
- [285] M Breuer, S Wessling, J Schmalzl, and U Hansen. Effect of inertia in rayleigh-bénard convection. *Physical Review E*, 69(2):026302, 2004.
- [286] Franco Brezzi, Marie-Odile Bristeau, Leopoldo P Franca, Michel Mallet, and Gilbert Rogé. A relationship between stabilized finite element methods and the galerkin method with bubble functions. *Computer Methods in Applied Mechanics and Engineering*, 96(1):117–129, 1992.
- [287] Franco Brezzi, Gianmarco Manzini, Donatella Marini, Paola Pietra, and Alessandro Russo. Discontinuous galerkin approximations for elliptic problems. *Numerical Methods for Partial Differential Equations: An International Journal*, 16(4):365–378, 2000.
- [288] RJ Bridwell and CA Anderson. Thermomechanical models of the rio grande rift. Technical report, Los Alamos Scientific Lab., NM (USA), 1980.
- [289] RJ Bridwell and C Potzick. Thermal regimes, mantle diapirs and crustal stresses of continental rifts. *Tectonophysics*, 73(1-3):15–32, 1981.
- [290] William L Briggs, Steve F McCormick, et al. *A multigrid tutorial*, volume 72. Siam, 2000.

- [291] Taco Broerse, Riccardo Riva, Wim Simons, Rob Govers, and Bert Vermeersen. Postseismic GRACE and GPS observations indicate a rheology contrast above and below the Sumatra slab. *Journal Of Geophysical Research*, 120:5343–5361, 2015.
- [292] A.N. Brooks and T.J.R. Hughes. Streamline Upwind/Petrov-Galerkin formulations for convection dominated flows with particular emphasis on the incompressible Navier-Stokes equations. *Computer Methods in Applied Mechanics and Engineering*, 32:199–259, 1982.
- [293] Geoffrey C Brown and Alan E Mussett. *The Inaccessible Earth: An Integrated View of its Structure and Composition*, 276 pp. Chapman and Hall, London, 1993.
- [294] R.L. Brown, C. Beaumont, and S.D. Willett. Comparison of the selkirk fan structure with mechanical models: implications for interpretation of the southern canadian cordillera. *Geology*, 21(11):1015–1018, 1993.
- [295] J.-P. Brun. Narrow rifts versus wide rifts: inferences for the mechanics of rifting from laboratory experiments. *Philosophical Transactions of the Royal Society A*, 357:695–712, 1999.
- [296] J.-P. Brun, D. Sokoutis, C. Tirel, F. Gueydan, J. van Den Driessche, and M.-O. Beslier. Crustal versus mantle core complexes. *Tectonophysics*, 746:22–45, 2018.
- [297] Jean-Pierre Brun and Xavier Fort. Salt tectonics at passive margins: Geology versus models. *Marine and Petroleum Geology*, 28(6):1123–1145, 2011.
- [298] S. Brune. Evolution of stress and fault patterns in oblique rift systems: 3-D numerical lithospheric-scale experiments from rift to breakup. *Geochem. Geophys. Geosyst.*, 15:3392–3415, 2014.
- [299] S. Brune and J. Autin. The rift to break-up evolution of the Gulf of Aden: Insights from 3D numerical lithospheric-scale modelling. *Tectonophysics*, 607:65–79, 2013.
- [300] S. Brune, A.A. Popov, and S. Sobolev. Modeling suggests that oblique extension facilitates rifting and continental break-up. *J. Geophys. Res.*, 117(B08402), 2012.
- [301] S. Brune, A.A. Popov, and S. Sobolev. Quantifying the thermo-mechanical impact of plume arrival on continental break-up. *Tectonophysics*, 604:51–59, 2013.
- [302] Sascha Brune. Modelling continental rift dynamics, 2018.
- [303] Sascha Brune, Giacomo Corti, and Giorgio Ranalli. Controls of inherited lithospheric heterogeneity on rift linkage: Numerical and analog models of interaction between the kenyan and ethiopian rifts across the turkana depression. *Tectonics*, 36(9):1767–1786, 2017.
- [304] Sascha Brune, Giacomo Corti, and Giorgio Ranalli. Controls of inherited lithospheric heterogeneity on rift linkage: Numerical and analog models of interaction between the kenyan and ethiopian rifts across the turkana depression. *Tectonics*, 36(9):1767–1786, 2017.
- [305] Sascha Brune, Christian Heine, Peter D Clift, and Marta Pérez-Gussinyé. Rifted margin architecture and crustal rheology: reviewing iberia-newfoundland, central south atlantic, and south china sea. *Marine and Petroleum Geology*, 79:257–281, 2017.
- [306] Sascha Brune, Simon E Williams, and R Dietmar Müller. Oblique rifting: the rule, not the exception. *Solid Earth*, 9(5):1187–1206, 2018.
- [307] C.-H. Bruneau and M. Saad. The 2D lid-driven cavity problem revisited. *Computers & Fluids*, 35:326–348, 2006.
- [308] David Brunet, Philippe Machetel, and David A Yuen. Slab weakening by the exothermic olivine-spinel phase change. *Geophysical research letters*, 25(17):3231–3234, 1998.
- [309] RH Brzesowsky, SJT Hangx, N Brantut, and CJ Spiers. Compaction creep of sands due to time-dependent grain failure: Effects of chemical environment, applied stress, and grain size. *Journal of Geophysical Research: Solid Earth*, 119(10):7521–7541, 2014.
- [310] RH Brzesowsky, CJ Spiers, CJ Peach, and SJT Hangx. Failure behavior of single sand grains: theory versus experiment. *Journal of Geophysical Research: Solid Earth*, 116(B6), 2011.
- [311] RH Brzesowsky, CJ Spiers, CJ Peach, and SJT Hangx. Time-independent compaction behavior of quartz sands. *Journal of Geophysical Research: Solid Earth*, 119(2):936–956, 2014.
- [312] Rudolf Heinrich Brzesowsky. *Micromechanics of sand grain failure and sand compaction*. PhD thesis, Faculteit Aardwetenschappen, Utrecht University, 1995.
- [313] W Roger Buck. Small-scale convection induced by passive rifting: the cause for uplift of rift shoulders. *Earth and Planetary Science Letters*, 77(3-4):362–372, 1986.
- [314] W Roger Buck, Fernando Martinez, Michael S Steckler, and James R Cochran. Thermal consequences of lithospheric extension: pure and simple. *Tectonics*, 7(2):213–234, 1988.

- [315] W Roger Buck and Dimitrios Sokoutis. Analogue model of gravitational collapse and surface extension during continental convergence. *Nature*, 369(6483):737, 1994.
- [316] W.R. Buck. Modes of Continental Lithospheric Extension. *J. Geophys. Res.*, 96(B2):20,161–20,178, 1991.
- [317] W.R. Buck, L.L. Lavier, and A.N.B. Poliakov. How to make a rift wide. *Phil. Trans. R. Soc. Lond. A*, 357:671–693, 1999.
- [318] WF Budd and TH Jacka. A review of ice rheology for ice sheet modelling. *Cold Regions Science and Technology*, 16(2):107–144, 1989.
- [319] Richard Gordon Budynas. *Advanced strength and applied stress analysis*. McGraw-Hill, 1999.
- [320] B.A. Buffet, C.W. Gable, and R.J. R.J. OConnell. Linear stability of a layered fluid with mobile surface plates. *J. Geophys. Res.*, 99(B10):19,885–19,900, 1994.
- [321] Ha H Bui, K Sako, and R Fukagawa. Numerical simulation of soil–water interaction using smoothed particle hydrodynamics (spf) method. *Journal of Terramechanics*, 44(5):339–346, 2007.
- [322] H.H. Bui, R. Fukugawa, K. Sako, and S. Ohno. Lagrangian meshfree particles method (SPH) for large deformation and failure flows of geomaterial using elasticplastic soil constitutive model. *Int. J. Numer. Anal. Geomech.*, 32(12):1537–1570, 2008.
- [323] S. Buitter, A.Y. Babeyko, S. Ellis, T.V. Gerya, B.J.P. Kaus, A. Kellner, G. Schreurs, and Y. Yamada. The numerical sandbox: comparison of model results for a shortening and an extension experiment. *Analogue and Numerical Modelling of Crustal-Scale Processes. Geological Society, London. Special Publications*, 253:29–64, 2006.
- [324] S. Buitter, A.Y. Babeyko, S. Ellis, T.V. Gerya, B.J.P. Kaus, A. Kellner, G. Schreurs, and Y. Yamada. The numerical sandbox: comparison of model results for a shortening and an extension experiment. *Analogue and Numerical Modelling of Crustal-Scale Processes. Geological Society, London. Special Publications*, 253:29–64, 2006.
- [325] S.J.H. Buitter. A review of brittle compressional wedge models. *Tectonophysics*, 530:1–17, 2012.
- [326] SJH Buitter, F Funiciello, and J van Hunen. Introduction to the special issue on “subduction zones”. *Solid Earth*, 4(1):129, 2013.
- [327] S.J.H. Buitter, R. Govers, and M.J.R. Wortel. A modelling study of vertical surface displacements at convergent plate margins. *Geophys. J. Int.*, 147:415–427, 2001.
- [328] S.J.H. Buitter, R. Govers, and M.J.R. Wortel. Two-dimensional simulations of surface deformation caused by slab detachment. *Tectonophysics*, 354:195–210, 2002.
- [329] S.J.H. Buitter, R.S. Huismans, and C. Beaumont. Dissipation analysis as a guide to mode selection during crustal extension and implications for the styles of sedimentary basins. *J. Geophys. Res.*, 113(B06406):B06406, 2008.
- [330] S.J.H. Buitter and O.A. Pfiffner. Numerical models of the inversion of half-graben basins. *Tectonics*, 22, 2003.
- [331] S.J.H. Buitter, O.A. Pfiffner, and C. Beaumont. Inversion of extensional sedimentary basins: A numerical evaluation of the localisation of shortening. *Earth Planet. Sci. Lett.*, 288:492–504, 2009.
- [332] S.J.H. Buitter, G. Schreurs, M. Albertz, T.V. Gerya, B. Kaus, W. Landry, L. le Pourhiet, Y. Mishin, D.L. Egholm, M. Cooke, B. Maillot, C. Thieulot, T. Crook, D. May, P. Souloumiac, and C. Beaumont. Benchmarking numerical models of brittle thrust wedges. *Journal of Structural Geology*, 92:140–177, 2016.
- [333] SJH Buitter, MJR Wortel, and R Govers. The role of subduction in the evolution of the apennines foreland basin. *Tectonophysics*, 296(3-4):249–268, 1998.
- [334] Susanne Buitter. Geodynamics: how plumes help to break plates. *Nature*, 513(7516):36, 2014.
- [335] Susanne JH Buitter. Rheology in numerical models of lithosphere deformation. *Bollettino della Società geologica italiana*, 127(2):193–198, 2008.
- [336] Susanne JH Buitter, Bernhard Steinberger, Sergei Medvedev, and Joya L Tetreault. Could the mantle have caused subsidence of the congo basin? *Tectonophysics*, 514:62–80, 2012.
- [337] Susanne JH Buitter and Trond H Torsvik. Horizontal movements in the eastern barents sea constrained by numerical models and plate reconstructions. *Geophysical Journal International*, 171(3):1376–1389, 2007.
- [338] Susanne JH Buitter and Trond H Torsvik. A review of wilson cycle plate margins: A role for mantle plumes in continental break-up along sutures? *Gondwana Research*, 26(2):627–653, 2014.
- [339] A.L. Bull, M. Domeier, and T.H. Torsvik. The effect of plate motion history on the longevity of deep mantle heterogeneities. *Earth Planet. Sci. Lett.*, 401:172–182, 2014.

- [340] A.L. Bull, A.K. McNamara, T.W. Becker, and J. Ritsema. Global scale models of the mantle flow field predicted by synthetic tomography models. *Phys. Earth. Planet. Inter.*, 182:129–138, 2010.
- [341] Keith Edward Bullen. *The Earth's density*. Springer Science & Business Media, 1975.
- [342] P.S. Bullen. *Handbook of Means and Their Inequalities*. Springer; 2nd edition, 2003.
- [343] H.-P. Bunge and J.H. Davies. Tomographic images of a mantle circulation model. *Geophysical Research Letters*, 28(1):77–80, 2001.
- [344] H.-P. Bunge, M. Richards, C. Lithgow-Bertelloni, J.R. Baumgardner, S.P. Grand, and B. Romanowicz. Time scales and heterogeneous structure in geodynamic Earth models. *Science*, 280:91–95, 1998.
- [345] H.-P. Bunge, M.A. Richards, and J.R. Baumgardner. Effect of depth-dependent viscosity on the planform of mantle convection. *Nature*, 379:436–438, 1996.
- [346] H.-P. Bunge, M.A. Richards, and J.R. Baumgardner. A sensitivity study of three-dimensional spherical mantle convection at  $10^8$  Rayleigh number: Effects of depth-dependent viscosity, heating mode, and endothermic phase change. *J. Geophys. Res.*, 102(B6):11,991–12,007, 1997.
- [347] Hans-Peter Bunge and John R Baumgardner. Mantle convection modeling on parallel virtual machines. *Computers in physics*, 9(2):207–215, 1995.
- [348] Hans-Peter Bunge, CR Hagelberg, and BJ Travis. Mantle circulation models with variational data assimilation: inferring past mantle flow and structure from plate motion histories and seismic tomography. *Geophysical Journal International*, 152(2):280–301, 2003.
- [349] Hans-Peter Bunge and Mark A Richards. The origin of large scale structure in mantle convection: effects of plate motions and viscosity stratification. *Geophysical Research Letters*, 23(21):2987–2990, 1996.
- [350] DW Burbank and N Pinter. Landscape evolution: the interactions of tectonics and surface processes. *Basin Research*, 11(1):1–6, 1999.
- [351] D.R. Burbridge and J. Braun. Analogue models of obliquely convergent continental plate boundaries. *J. Geophys. Res.*, 103(B7):15,221–15,237, 1998.
- [352] J.-P. Burg, J.-L. Bodinier, T. Gerya, R.-M. Bedini, F. Boudier, J.-M. Dautria, V. Prikhodko, A. Efimov, E. Pupier, and J.-L. Balanec. Translithospheric mantle diapirism: Geological evidence and numerical modelling of the kondyor zoned ultramafic complex (russian far-east). *Journal of Petrology*, 50(2), 2009.
- [353] J.-P. Burg and T.V. Gerya. The role of viscous heating in Barrovian metamorphism of collisional orogens: thermomechanical models and application to the Lepontine Dome in the Central Alps. *J. Metamorphic Geology*, 23:75–95, 2005.
- [354] J.-P. Burg and T.V. Gerya. Modelling intrusion of mafic and ultramafic magma into the continental crust: numerical methodology and results . *Boll. Soc. Geol. It.*, 127(2), 2008.
- [355] J.-P. Burg and S.M. Schmalholz. Viscous heating allows thrusting to overcome crustal-scale buckling: Numerical investigation with application to the Himalayan syntaxes. *Earth Planet. Sci. Lett.*, 274:189–203, 2008.
- [356] Peter M Burgess, Michael Gurnis, and Louis Moresi. Formation of sequences in the cratonic interior of north america by interaction between mantle, eustatic, and stratigraphic processes. *Geological Society of America Bulletin*, 109(12):1515–1535, 1997.
- [357] PM Burgess and LN Moresi. Modelling rates and distribution of subsidence due to dynamic topography over subducting slabs: is it possible to identify dynamic topography from ancient strata? *Basin Research*, 11(4):305–314, 1999.
- [358] Roland Bürgmann and Georg Dresen. Rheology of the lower crust and upper mantle: Evidence from rock mechanics, geodesy, and field observations. *Annu. Rev. Earth Planet. Sci.*, 36:531–567, 2008.
- [359] Gilmer R Burgos, Andreas N Alexandrou, and Vladimir Entov. On the determination of yield surfaces in herschel–bulkley fluids. *Journal of Rheology*, 43(3):463–483, 1999.
- [360] Kevin Burke. Plate tectonics, the wilson cycle, and mantle plumes: geodynamics from the top. *Annual Review of Earth and Planetary Sciences*, 39:1–29, 2011.
- [361] E.R. Burkett and M.I. Billen. Dynamics and implications of slab detachment due to ridge-trench collision. *J. Geophys. Res.*, 114(B12402), 2009.
- [362] E.R. Burkett and M.I. Billen. Three-dimensionality of slab detachment due to ridge-trench collision: Laterally simultaneous boudinage versus tear propagation. *Geochem. Geophys. Geosyst.*, 11(11), 2010.
- [363] Erin Burkett and Michael Gurnis. Stalled slab dynamics. *Lithosphere*, 5(1):92–97, 2013.

- [364] E. Burov and A. Poliakov. Erosion and rheology controls on synrift and postrift evolution: Verifying old and new ideas using a fully coupled numerical model. *J. Geophys. Res.*, 106(B8):16,461–16,481, 2001.
- [365] E. Burov and S. Cloetingh. Erosion and rift dynamics: new thermomechanical aspects of post-rift evolution of extensional basins. *Earth Planet. Sci. Lett.*, 150:7–26, 1997.
- [366] E. Burov and S. Cloetingh. Plume-like upper mantle instabilities drive subduction initiation. *Geophys. Res. Letters*, 37(L03309), 2010.
- [367] E. Burov, T. Francois, P. Agard, L. Le Pourhiet, B. Meyer, C. Tirel, S. Lebedev, P. Yamato, and J.-P. Brun. Rheological and geodynamic controls on the mechanisms of subduction and HP/UHP exhumation of crustal rocks during continental collision: Insights from numerical models. *Tectonophysics*, 25(2):464–493, 2014.
- [368] E. Burov, T. Francois, P. Yamato, and S. Wolf. Mechanisms of continental subduction and exhumation of hp and uhp rocks. *Gondwana Research*, 25(2):464–493, 2014.
- [369] E. Burov and T. Gerya. Asymmetric three-dimensional topography over mantle plumes. *Nature*, 513:doi:10.1038/nature13703, 2014.
- [370] E. Burov and L. Guillou-Frottier. The plume head-continental lithosphere interaction using a tectonically realistic formulation for the lithosphere. *Geophys. J. Int.*, 161:469–490, 2005.
- [371] E. Burov, L. Jolivet, L. Le Pourhiet, and A. Poliakov. A thermomechanical model of exhumation of high pressure (HP) and ultra-high pressure (UHP) metamorphic rocks in Alpine-type collision belts. *Tectonophysics*, 342:113–136, 2001.
- [372] E. Burov and G. Toussaint. Surface processes and tectonics: Forcing of continental subduction and deep processes. *Global and Planetary Change*, 58:141–164, 2007.
- [373] E. Burov and P. Yamato. Continental plate collision, p-t-t-z conditions and unstable vs. stable plate dynamics: Insights from thermo-mechanical modelling. *Lithos*, 103(1-2):178–204, 2008.
- [374] EB Burov and Michel Diament. Flexure of the continental lithosphere with multilayered rheology. *Geophysical Journal International*, 109(2):449–468, 1992.
- [375] EB Burov, AB Watts, et al. The long-term strength of continental lithosphere:” jelly sandwich” or” crème brûlée”? *GSA today*, 16(1):4, 2006.
- [376] Evgene Burov, Thomas François, Philippe Yamato, and Sylvie Wolf. Advances and challenges in geotectonic modelling. *Bulletin de la Société Géologique de France*, 185(3):147–168, 2014.
- [377] Evgene Burov. Rheology and strength of the lithosphere. *Marine and Petroleum Geology*, 28(8):1402–1443, 2011.
- [378] Evgene Burov and Michel Diament. The effective elastic thickness ( $t_e$ ) of continental lithosphere: what does it really mean? *Journal of Geophysical Research: Solid Earth*, 100(B3):3905–3927, 1995.
- [379] Evgueni Burov and Sierd Cloetingh. Controls of mantle plumes and lithospheric folding on modes of intraplate continental tectonics: differences and similarities. *Geophysical Journal International*, 178(3):1691–1722, 2009.
- [380] C. Burstedde, O. Ghattas, M. Gurnis, G. Stadler, E. Tan, T. Tu, L.C. Wilcox, and S. Zhong. Scalable Adaptive Mantle Convection Simulation on Petascale Supercomputers. *ACM/IEEE SC Conference Series, 2008*, 2008.
- [381] C. Burstedde, O. Ghattas, G. Stadler, T. Tu, and L.C. Wilcox. Parallel scalable adjoint-based adaptive solution of variable-viscosity Stokes flow problems. *Computer Methods in Applied Mechanics and Engineering*, 198:1691–1700, 2009.
- [382] C. Burstedde, G. Stadler, L. Alisic, L.C. Wilcox, E. Tan, M. Gurnis, and O. Ghattas. Large-scale adaptive mantle convection simulation. *Geophys. J. Int.*, 192:889–906, 2013.
- [383] Carsten Burstedde, Jose A Fonseca, and Bram Metsch. An amg saddle point preconditioner with application to mixed poisson problems on adaptive quad/cube meshes. *arXiv preprint arXiv:1901.05830*, 2019.
- [384] Carsten Burstedde, Omar Ghattas, Michael Gurnis, Tobin Isaac, Georg Stadler, Tim Warburton, and Lucas Wilcox. Extreme-scale amr. In *Proceedings of the 2010 ACM/IEEE International Conference for High Performance Computing, Networking, Storage and Analysis*, pages 1–12. IEEE Computer Society, 2010.
- [385] Carsten Burstedde, Lucas C. Wilcox, and Omar Ghattas. **p4est**: Scalable algorithms for parallel adaptive mesh refinement on forests of octrees. *SIAM Journal on Scientific Computing*, 33(3):1103–1133, 2011.

- [386] F.H. Busse. Patterns of convection in spherical shells. *J. Fluid Mech.*, 72(1):67–85, 1975.
- [387] FH Busse. High prandtl number convection. *Physics of the Earth and Planetary Interiors*, 19(2):149–157, 1979.
- [388] FH Busse. On the aspect ratios of two-layer mantle convection. *Physics of the Earth and Planetary Interiors*, 24(4):320–324, 1981.
- [389] F.H. Busse, U. Christensen, R. Clever, L. Cserepes, C. Gable, E. Giannandrea, L. Guillou, G. Houseman, H.-C. Nataf, M. Ogawa, M. Parmentier, C. Sotin, and B. Travis. 3D convection at infinite Prandtl number in Cartesian geometry - a benchmark comparison. *Geophys. Astrophys. Fluid Dynamics*, 75:39–59, 1993.
- [390] F.H. Busse and N. Riahi. Patterns of convection in spherical shells. Part 2. *J. Fluid Mech.*, 123:283–301, 1982.
- [391] J.P. Butler and C. Beaumont. Subduction zone decoupling/retreat modeling explains south Tibet (Xigaze) and other supra-subduction zone ophiolites and their UHP mineral phases. *Earth Planet. Sci. Lett.*, 463:101–117, 2017.
- [392] J.P. Butler, C. Beaumont, and R.A. Jamieson. The Alps 1: A working geodynamic model for burial and exhumation of (ultra)high-pressure rocks in Alpine-type orogens. *Earth Planet. Sci. Lett.*, 337–378:114–131, 2013.
- [393] J.P. Butler, C. Beaumont, and R.A. Jamieson. The alps 2: Controls on crustal subduction and (ultra)high-pressure rock exhumation in alpine-type orogens. *Journal of Geophysical Research: Solid Earth*, 119(7):5987–6022, 2014.
- [394] J.P. Butler, C. Beaumont, and R.A. Jamieson. Paradigm lost: Buoyancy thwarted by the strength of the Western Gneiss Region (ultra)high-pressure terrane, Norway. *Lithosphere*, page doi:10.1130/L426.1, 2015.
- [395] J.P. Butler, C. Beaumont, and R.A. Jamieson. Crustal emplacement of exhuming (ultra)high-pressure rocks: Will that be pro- or retro-side? *Geology*, 39:635–638, 2011.
- [396] SL Butler, WR Peltier, and SO Costin. Numerical models of the earth's thermal history: Effects of inner-core solidification and core potassium. *Physics of the Earth and Planetary Interiors*, 152(1-2):22–42, 2005.
- [397] NP Butterworth, L Quevedo, G Morra, and RD Müller. Influence of overriding plate geometry and rheology on subduction. *Geochemistry, Geophysics, Geosystems*, 13(6), 2012.
- [398] James Byerlee. Friction of rocks. In *Rock friction and earthquake prediction*, pages 615–626. Springer, 1978.
- [399] James D Byerlee. Brittle-ductile transition in rocks. *Journal of Geophysical Research*, 73(14):4741–4750, 1968.
- [400] Mauro Cacace and Antoine B Jacquay. Flexible parallel implicit modelling of coupled thermal–hydraulic–mechanical processes in fractured rocks. *Solid Earth*, 8(5):921–941, 2017.
- [401] O Čadek and AP van den Berg. Radial profiles of temperature and viscosity in the earth's mantle inferred from the geoid and lateral seismic structure. *Earth and Planetary Science Letters*, 164(3-4):607–615, 1998.
- [402] Ondřej Čadek, Yanick Ricard, Zdeněk Martinec, and Ctirad Matyska. Comparison between newtonian and non-newtonian flow driven by internal loads. *Geophysical Journal International*, 112(1):103–114, 1993.
- [403] J. Cahouet and J.-P. Chabard. Some fast 3D finite element solvers for the generalized Stokes problem. *Int. J. Num. Meth. Fluids*, 8:869–895, 1988.
- [404] Elisa Calignano, Dimitrios Sokoutis, E Willingshofer, J-P Brun, Frédéric Gueydan, and S Cloetingh. Oblique contractional reactivation of inherited heterogeneities: Cause for arcuate orogens. *Tectonics*, 36(3):542–558, 2017.
- [405] Elisa Calignano, Dimitrios Sokoutis, Ernst Willingshofer, Frédéric Gueydan, and Sierd Cloetingh. Strain localization at the margins of strong lithospheric domains: Insights from analog models. *Tectonics*, 34(3):396–412, 2015.
- [406] Wenrong Cao, Boris JP Kaus, and Scott Paterson. Intrusion of granitic magma into the continental crust facilitated by magma pulsing and dike-diapir interactions: Numerical simulations. *Tectonics*, 35(6):1575–1594, 2016.
- [407] Z.-H. Cao. Fast Uzawa algorithm for generalized saddle point problems . *Applied Numerical Mathematics*, 46:157–171, 2003.
- [408] W. Capella, W. Spakman, D.J.J. van Hinsbergen, M.V. Chertova, and W. Krijgsman. Mantle resistance against gibraltar slab dragging as a key cause of the messinian salinity crisis. *Terra Nova*, 2019.
- [409] F.A. Capitanio and M. Faccenda. Complex mantle flow around heterogeneous subducting oceanic plates. *Earth Planet. Sci. Lett.*, 353–354:29–37, 2012.

- [410] F.A. Capitanio, C. Faccenna, S. Zlotnik, and D.R. Stegman. Subduction dynamics and the origin of Andean orogeny and the Bolivian orocline. *Nature*, 480:doi:10.1038/nature10596, 2011.
- [411] FA Capitanio, G Morra, and S Goes. Dynamic models of downgoing plate-buoyancy driven subduction: Subduction motions and energy dissipation. *Earth and Planetary Science Letters*, 262(1-2):284–297, 2007.
- [412] FA Capitanio, G Morra, S Goes, RF Weinberg, and L Moresi. India–asia convergence driven by the subduction of the greater indian continent. *Nature Geoscience*, 3(2):136, 2010.
- [413] FA Capitanio and Gabriele Morra. The bending mechanics in a dynamic subduction system: Constraints from numerical modelling and global compilation analysis. *Tectonophysics*, 522:224–234, 2012.
- [414] FA Capitanio, O Nebel, PA Cawood, RF Weinberg, and F Clos. Lithosphere differentiation in the early earth controls archean tectonics. *Earth and Planetary Science Letters*, 525:115755, 2019.
- [415] F.A. Capitanio and A. Replumaz. Subduction and slab breakoff controls on Asian indentation tectonics and Himalayan western syntaxis formation . *Geochem. Geophys. Geosyst.*, 14(9):doi:10.1002/ggge.20171, 2013.
- [416] F.A. Capitanio, D.R. Stegman, L.N. Moresi, and W. Sharples. Upper plate controls on deep subduction, trench migrations and deformations at convergent margins. *Tectonophysics*, 483:80–92, 2010.
- [417] F.A. Capitanio, S. Zlotnik, and C. Faccenna. Controls on subduction reorganization in the Hellenic margin, eastern Mediterranean. *Geophys. Res. Lett.*, 37(L14309), 2010.
- [418] R Carluccio, B Kaus, FA Capitanio, and LN Moresi. The impact of a very weak and thin upper asthenosphere on subduction motions. *Geophysical Research Letters*, 46:11,893–11,905, 2019.
- [419] E. Carminati, M.J.R. Wortel, W. Spakman, and R. Sabadini. The role of slab detachment processes in the opening of the westerncentral Mediterranean basins: some geological and geophysical evidence. *Earth Planet. Sci. Lett.*, 160:651–665, 1998.
- [420] P.J. Carreau. Rheological Equations from Molecular Network Theories. *Transactions of the Society of rheology*, 16(1):99–127, 1972.
- [421] J. Carrero, B. Cockburn, and D. Schötzau. Hybridized globally divergence-free LDG methods. Part I: The Stokes problem. *Mathematics of Computation*, 75(254):533–563, 2005.
- [422] JF Casey and JF Dewey. Initiation of subduction zones along transform and accreting plate boundaries, triple-junction evolution, and forearc spreading centresimplications for ophiolitic geology and obduction. *Geological Society, London, Special Publications*, 13(1):269–290, 1984.
- [423] S. Castelltort and P. Yamato. The influence of surface slope on the shape of river basins: Comparison between nature and numerical landscape simulations. *Geomorphology*, 192:71–79, 2013.
- [424] P. Castillo, B. Cockburn, I. Perugia, and D. Schötzau. An a priori error analysis of the local discontinuous Galerkin method for elliptic problems. *SIAM J. Numer. Anal.*, 38:1676–1706, 2000.
- [425] P. Castillo, B. Cockburn, I. Perugia, and D. Schötzau. Local discontinuous Galerkin methods for elliptic problems. *Commun. Numer. Meth. Engng*, 18:69–75, 2002.
- [426] A. Castro and T.V. Gerya. Magmatic implications of mantle wedge plumes: Experimental study. *Lithos*, 103:138–148, 2008.
- [427] Antonio Castro, Katharina Vogt, and Taras Gerya. Generation of new continental crust by sublithospheric silicic-magma relamination in arcs: a test of taylor’s andesite model. *Gondwana Research*, 23(4):1554–1566, 2013.
- [428] Nicolas Luca Celli, Sergei Lebedev, Andrew J Schaeffer, and Carmen Gaina. African cratonic lithosphere carved by mantle plumes. *Nature Communications*, 11(1):1–10, 2020.
- [429] N.G. Cerpa, R. Araya, M. Gerbault, and R. Hassani. Relationship between slab dip and topography segmentation in an oblique subduction zone: Insights from numerical modeling. *Geophys. Res. Lett.*, 41:10.1002/2015GL064047, 2015.
- [430] N.G. Cerpa, B. Guillaume, and J.Martinod. The interplay between overriding plate kinematics, slab dip and tectonics. *Geophy. J. Int.*, 215:1789–1802, 2018.
- [431] N.G. Cerpa, R. Hassani, M. Gerbault, and J.-H. Prévost. A fictitious domain method for lithosphere-asthenosphere interaction: Application to periodic slab folding in the upper mantle. *Geochem. Geophys. Geosyst.*, 15, 2014.
- [432] N.G. Cerpa, I. Wada, and C.R. Wilson. Fluid migration in the mantle wedge: Influence of mineral grain size and mantle compaction. *J. Geophys. Res.*, 122:6247–6268, 2017.
- [433] N.G. Cerpa, I. Wada, and C.R. Wilson. Effects of fluid influx, fluid viscosity, and fluid density on fluid migration in the mantle wedge and their implications for hydrous melting. *Geosphere*, 15(1):1–23, 2019.

- [434] Edouard Chalalon, Jean Louis Mugnier, and Georges Mascle. Control on thrust tectonics in the himalayan foothills: a view from a numerical model. *Tectonophysics*, 248(1-2):139–163, 1995.
- [435] D.S. Chapman. Thermal gradients in the continental crust. *Geological Society, London, Special Publications*, 24:63–70, 1986.
- [436] William M Chapple and Terry E Tullis. Evaluation of the forces that drive the plates. *Journal of geophysical research*, 82(14):1967–1984, 1977.
- [437] Clement G Chase. Fluvial landsculpting and the fractal dimension of topography. *Geomorphology*, 5(1-2):39–57, 1992.
- [438] J.-P. Chebab. Solution of generalized Stokes problems using hierarchical methods and Incremental Unknowns. *Applied Numerical Mathematics*, 21:9–42, 1996.
- [439] A Chemenda, S Lallemand, and A Bokun. Strain partitioning and interplate friction in oblique subduction zones: Constraints provided by experimental modeling. *Journal of Geophysical Research: Solid Earth*, 105(B3):5567–5581, 2000.
- [440] A.I. Chemenda. The formation of shear-band/fracture networks from a constitutive instability: Theory and numerical experiment. *J. Geophys. Res.*, 112(B11404), 2007.
- [441] AI Chemenda, R-K Yang, J-F Stephan, EA Konstantinovskaya, and GM Ivanov. New results from physical modelling of arc–continent collision in taiwan: evolutionary model. *Tectonophysics*, 333(1-2):159–178, 2001.
- [442] J. Chen and S. D. King. The influence of temperature and depth dependent viscosity on geoid and topography profiles from models of mantle convection. *Physics of the Earth and Planetary Interiors*, 106(1-2):75–92, 1998.
- [443] J.S. Chen, C. Pan, and T.Y.P. Chang. On the control of pressure oscillation in bilinear-displacement constant-pressure element. *Comput. Methods Appl. Mech. Engrg.*, 128:137–152, 1995.
- [444] L Chen, H Nguyen-Xuan, T Nguyen-Thoi, KY Zeng, and SC Wu. Assessment of smoothed point interpolation methods for elastic mechanics. *International Journal for Numerical Methods in Biomedical Engineering*, 26(12):1635–1655, 2010.
- [445] Lin Chen, Taras Gerya, Zhongjie Zhang, Guizhi Zhu, Thibault Duretz, and Wolfgang R Jacoby. Numerical modeling of eastern tibetan-type margin: influences of surface processes, lithospheric structure and crustal rheology. *Gondwana Research*, 24(3-4):1091–1107, 2013.
- [446] Lin Chen, Taras V Gerya, Zhong-Jie Zhang, Alan Aitken, Zhong-Hai Li, and Xiao-Feng Liang. Formation mechanism of steep convergent intracontinental margins: Insights from numerical modeling. *Geophysical Research Letters*, 40(10):2000–2005, 2013.
- [447] Shi Chen, Huai Zhang, David A Yuen, Shuxia Zhang, Jian Zhang, and Yaolin Shi. Volume rendering visualization of 3d spherical mantle convection with an unstructured mesh. *Visual Geosciences*, 13(1):97–104, 2008.
- [448] Yongshun Chen and W Jason Morgan. A nonlinear rheology model for mid-ocean ridge axis topography. *Journal of Geophysical Research: Solid Earth*, 95(B11):17583–17604, 1990.
- [449] Yongshun Chen and W Jason Morgan. Rift valley/no rift valley transition at mid-ocean ridges. *Journal of Geophysical Research: Solid Earth*, 95(B11):17571–17581, 1990.
- [450] Z. Chen, B.C. Burchfiel, Y. Liu, R.W. King, L.H. Royden, W. Tang, E. Wang, J. Zhao, and X. Zhang. Global positioning system measurements from eastern tibet and their implications for india/eurasia intercontinental deformation. *J. Geophys. Res.*, 105:16,215–16,227, 2000.
- [451] Zhihao Chen, Wouter P Schellart, and João C Duarte. Quantifying the energy dissipation of overriding plate deformation in three-dimensional subduction models. *Journal of Geophysical Research: Solid Earth*, 120(1):519–536, 2015.
- [452] Zhihao Chen, Wouter P Schellart, Vincent Strak, and João C Duarte. Does subduction-induced mantle flow drive backarc extension? *Earth and Planetary Science Letters*, 441:200–210, 2016.
- [453] Jian Cheng, Xiaodong Liu, Tiegang Liu, and Hong Luo. A parallel, high-order direct discontinuous galerkin method for the navier-stokes equations on 3d hybrid grids. *Communications in Computational Physics*, 21(5):1231–1257, 2017.
- [454] P. Chenin and C. Beaumont. Influence of offset weak zones on the development of rift basins: Activation and abandonment during continental extension and breakup. *J. Geophys. Res.*, 118:1–23, 2013.
- [455] P. Chenin, S.M. Schmalholz, G. Manatschal, and G.D. Karner. Necking of the lithosphere: A reappraisal of basic concepts with thermo-mechanical numerical modeling. *Journal of Geophysical Research: Solid Earth*, 123(6):5279–5299, 2018.

- [456] Pauline Chenin, Gianreto Manatschal, Alessandro Decarlis, Stefan M Schmalholz, Thibault Duretz, and Marco Beltrando. Emersion of distal domains in advanced stages of continental rifting explained by asynchronous crust and mantle necking. *Geochemistry, Geophysics, Geosystems*, 2019.
- [457] M.V. Chertova, T. Geenen, A. van den Berg, and W. Spakman. Using open sidewalls for modelling self-consistent lithosphere subduction dynamics . *Solid Earth*, 3:313–326, 2012.
- [458] M.V. Chertova, W. Spakman, T. Geenen, A.P. van den Berg, and D.J.J. van Hinsbergen. Underpinning tectonic reconstructions of the western Mediterranean region with dynamic slab evolution from 3-D numerical modeling. *J. Geophys. Res.*, 119:10.1002/ 2014JB011150, 2014.
- [459] M.V. Chertova, W. Spakman, and B. Steinberger. Mantle flow influence on subduction evolution. *Earth and Planetary Science Letters*, 489:258–266, 2018.
- [460] MV Chertova, W Spakman, AP van den Berg, and DJJ van Hinsbergen. Absolute plate motions and regional subduction evolution. *Geochemistry, Geophysics, Geosystems*, 15(10):3780–3792, 2014.
- [461] VV Chervov and GG Chernykh. Numerical modeling of convection in the zone of spreading and subduction. *Journal of Engineering Thermophysics*, 28(1):14–25, 2019.
- [462] Jean Chéry, Alain Bonneville, Jean Pierre Vilotte, and Dave Yuen. Numerical modelling of caldera dynamical behaviour. *Geophysical Journal International*, 105(2):365–379, 1991.
- [463] Jean Chéry, Mark D Zoback, and Riad Hassani. An integrated mechanical model of the san andreas fault in central and northern california. *Journal of Geophysical Research: Solid Earth*, 106(B10):22051–22066, 2001.
- [464] Claudio Chiarabba, Pasquale De Gori, Claudio Faccenna, Fabio Speranza, Danilo Seccia, Viviana Dionicio, and Germán A Prieto. Subduction system and flat slab beneath the e astern c ordillera of c olombia. *Geochemistry, Geophysics, Geosystems*, 17(1):16–27, 2016.
- [465] S. Chiw-Webster, E.J. Hinch, and J.R. Lister. Very viscous horizontal convection. *J. Fluid Mech.*, 611:395–426, 2008.
- [466] G. Choblet. Modelling thermal convection with large viscosity gradients in one block of the ‘cubed sphere’. *J. Comp. Phys.*, 205:269–291, 2005.
- [467] G. Choblet, O. Čadek, F. Couturier, and C. Dumoulin. OEDIPUS: a new tool to study the dynamics of planetary interiors. *Geophy. J. Int.*, 170:9–30, 2007.
- [468] Gael Choblet, H Amit, and L Husson. Constraining mantle convection models with palaeomagnetic reversals record and numerical dynamos. *Geophysical Supplements to the Monthly Notices of the Royal Astronomical Society*, 207(2):1165–1184, 2016.
- [469] E. Choi and K.D. Petersen. Making Coulomb angle-oriented shear bands in numerical tectonic models. *Tectonophysics*, 657:94–101, 2015.
- [470] E. Choi, E. Tan, L.L. Lavier, and V.M. Calo. DynEarthSol2D: An efficient unstructured finite element method to study long-term tectonic deformation. *J. Geophys. Res.*, 118:1–16, 2013.
- [471] Eun-seo Choi and Michael Gurnis. Thermally induced brittle deformation in oceanic lithosphere and the spacing of fracture zones. *Earth and Planetary Science Letters*, 269(1-2):259–270, 2008.
- [472] Eunseo Choi, Luc Lavier, and Michael Gurnis. Thermomechanics of mid-ocean ridge segmentation. *Phys. Earth Planet. Interiors*, 171:374–386, 2008.
- [473] Eunseo Choi, Leonardo Seeber, Michael S Steckler, and Roger Buck. One-sided transform basins and inverted curtains: Implications for releasing bends along strike-slip faults. *Tectonics*, 30(6), 2011.
- [474] A Chopelas and R Boehler. Thermal expansivity in the lower mantle. *Geophysical Research Letters*, 19(19):1983–1986, 1992.
- [475] PN Chopra and MS Paterson. The role of water in the deformation of dunite. *Journal of Geophysical Research: Solid Earth*, 89(B9):7861–7876, 1984.
- [476] A.J. Chorin. A numerical method for solving incompressible viscous flow problems. *J. Comp. Phys.*, 2:12–26, 1967.
- [477] Pierre Choukroune. Tectonic evolution of the pyrenees. *Annual Review of Earth and Planetary Sciences*, 20(1):143–158, 1992.
- [478] R.R. Christensen. An Eulerian technique for thermomechanical modeling of lithospheric extension. *J. Geophys. Res.*, 97(B2):2015–2036, 1992.
- [479] U Christensen. Convection in a variable-viscosity fluid: Newtonian versus power-law rheology. *Earth and Planetary Science Letters*, 64(1):153–162, 1983.

- [480] U Christensen. Convection in a variable-viscosity fluid: Newtonian versus power-law rheology. *Earth and Planetary Science Letters*, 64(1):153–162, 1983.
- [481] U Christensen. Convection with pressure-and temperature-dependent non-newtonian rheology. *Geophysical Journal International*, 77(2):343–384, 1984.
- [482] U. Christensen and H. Harder. 3-D convection with variable viscosity. *Geophys. J. Int.*, 104:213–226, 1991.
- [483] Ulrich Christensen. Phase boundaries in finite amplitude mantle convection. *Geophysical Journal International*, 68(2):487–497, 1982.
- [484] Ulrich Christensen. Effects of phase transitions on mantle convection. *Annual Review of Earth and Planetary Sciences*, 23(1):65–87, 1995.
- [485] Ulrich R Christensen. Thermal evolution models for the earth. *Journal of Geophysical Research: Solid Earth*, 90(B4):2995–3007, 1985.
- [486] Ulrich R Christensen. The influence of trench migration on slab penetration into the lower mantle. *Earth and Planetary Science Letters*, 140(1-4):27–39, 1996.
- [487] Ulrich R Christensen and Albrecht W Hofmann. Segregation of subducted oceanic crust in the convecting mantle. *Journal of Geophysical Research: Solid Earth*, 99(B10):19867–19884, 1994.
- [488] Ulrich R Christensen and David A Yuen. Layered convection induced by phase transitions. *Journal of Geophysical Research: Solid Earth*, 90(B12):10291–10300, 1985.
- [489] U.R. Christensen and D.A. Yuen. The interaction of a subducting lithospheric slab with a chemical or phase boundary. *J. Geophys. Res.*, 89(B6):4389–4402, 1984.
- [490] Edmund Christiansen and Knud D. Andersen. Computation of collapse states with von mises type yield condition. *International Journal for Numerical Methods in Engineering*, 46:1185–1202, 1999.
- [491] Edmund Christiansen and Ole S. Pedersen. Automatic mesh refinement in limit analysis. *International Journal for Numerical Methods in Engineering*, 50:1331–1346, 2001.
- [492] M.A. Christon. Dealing with pressure: FEM solution strategies for the pressure in the time-dependent NavierStokes equations . *Int. J. Num. Meth. Fluids*, 38:1177–1198, 2002.
- [493] M.A. Christon and G.O. Cook. *LS-DYNA’s Incompressible Flow Solver User’s Manual*. Livermore Software Technology Corporation.
- [494] M.A. Christon, P.M. Gresho, and S.B. Sutton. Computational predictability of time-dependent natural convection flows in enclosures (including a benchmark solution). *Int. J. Num. Meth. Fluids*, 40:953–980, 2002.
- [495] H. Ciskova, A. van den Berg, and M. Jacobs. Impact of compressibility on heat transport characteristics of large terrestrial planets. *Phys. Earth. Planet. Inter.*, 268:65–77, 2017.
- [496] H. Ciskova, J. van Hunen, A.P. van den Berg, and N.J. Vlaar. The influence of rheological weakening and yield stress on the interaction of slabs with the 670 km discontinuity. *Earth Planet. Sci. Lett.*, 199:447–457, 2002.
- [497] R. I. Citron, M. Manga, and E. Tan. A hybrid origin of the martian crustal dichotomy: Degree-1 convection antipodal to a giant impact. *Earth and Planetary Science Letters*, 491:58–66, 2018.
- [498] H. Čížková and C.R. Bina. Effects of mantle and subduction-interface rheologies on slab stagnation and trench rollback. *Earth Planet. Sci. Lett.*, 379:95–103, 2013.
- [499] H. Čížková and C.R. Bina. Geodynamics of trench advance: Insights from a Philippine-Sea-style geometry. *Earth Planet. Sci. Lett.*, 430:408–415, 2015.
- [500] H. Čížková, O. Čadek, and A.P. Van Den Berg. Influence of the load wavelength on the permeability of a viscosity interface in the mantle. *Studia Geophysica et Geodaetica*, 41(1):64–72, 1997.
- [501] H. Čížková, O. Čadek, A.P. Van Den Berg, and N.J. Vlaar. Can lower mantle slab-like seismic anomalies be explained by thermal coupling between the upper and lower mantles? *Geophysical Research Letters*, 26(10):1501–1504, 1999.
- [502] H. Čížková, A.P. van den Berg, W. Spakman, and Ctirad Matyska. The viscosity of the earth’s lower mantle inferred from sinking speed of subducted lithosphere. *Phys. Earth. Planet. Inter.*, 200–201:56–62, 2012.
- [503] Hana Čížková, Jeroen van Hunen, and Arie van den Berg. Stress distribution within subducting slabs and their deformation in the transition zone. *Physics of the Earth and Planetary Interiors*, 161(3-4):202–214, 2007.

- [504] Marin K Clark, John WM Bush, and Leigh H Royden. Dynamic topography produced by lower crustal flow against rheological strength heterogeneities bordering the tibetan plateau. *Geophysical Journal International*, 162(2):575–590, 2005.
- [505] Marin Kristen Clark and Leigh Handy Royden. Topographic ooze: Building the eastern margin of tibet by lower crustal flow. *Geology*, 28(8):703–706, 2000.
- [506] M.K. Clark, LH Royden, KX Whipple, BC Burchfiel, X Zhang, and W Tang. Use of a regional, relict landscape to measure vertical deformation of the eastern tibetan plateau. *Journal of Geophysical Research: Earth Surface*, 111(F3), 2006.
- [507] T.C. Clevenger, T. Heister, G. Kanschat, and M. Kronbichler. A flexible, parallel, adaptive geometric multigrid method for fem. *XXX*, page XXX, 2009.
- [508] Thomas C Clevenger and Timo Heister. Comparison between algebraic and matrix-free geometric multigrid for a stokes problem on adaptive meshes with variable viscosity. *arXiv preprint arXiv:1907.06696*, 2019.
- [509] P.D. Clift, S. Brune, and J. Quinteros. Climate changes control offshore crustal structure at South China Sea continental margin. *Earth Planet. Sci. Lett.*, 420:66–72, 2015.
- [510] S. Cloetingh, E. Burov, F. Beekman, B. Andeweg, P.A.M. Andriessen, D. Garcia-Castellanos, G. de Vicente, and R. Vegas. Lithospheric folding in Iberia. *Tectonics*, 21(5):10.1029/2001TC901031, 2002.
- [511] S. Cloetingh, E. Burov, and A. Poliakov. Lithosphere folding: Primary response to compression? (from central asia to paris basin). *Tectonics*, 18:1064–1083, 1999.
- [512] S. Cloetingh, R. Wortel, and N.J. Vlaar. On the Initiation of Subduction Zones. *Pure and Applied Geophysics*, 129(1/2):7–25, 1989.
- [513] S.A.P.L. Cloetingh, E. Burov, L. Matenco, G. Toussaint, G. Bertotti, P.A.M. Andriessen, M.J.R. Wortel, and W. Spakman. thermo-mechanical controls on the mode of continental collision in the se carpathians (romania). *Earth Planet. Sci. Lett.*, 218:57–76, 2004.
- [514] SAPL Cloetingh, Jan Diederik van Wees, PA Ziegler, L Lenkey, F Beekman, M Tesauro, A Förster, B Norden, M Kaban, N Hardebol, et al. Lithosphere tectonics and thermo-mechanical properties: An integrated modelling approach for Enhanced Geothermal Systems exploration in Europe. *Earth-Science Reviews*, 102:159, 2010.
- [515] S.A.P.L. Cloetingh, P.A. Ziegler, P.J.F. Bogaard, P.A.M. Andriessen, I.M. Artemieva, G. Bada, R.T. van Balen, F. Beekman, Z. Ben-Avraham, J.-P. Brun, H.P. Bunge, E.B. Burov, R. Carbonell, C. Facenna, A. Friedrich, J. Gallart, A.G. Green, O. Heidbach, A.G. Jones, L. Matenco, J. Mosar, O. Oncken, C. Pascal, G. Peters, S. Sliaupa, A. Soesoo, W. Spakman, R.A. Stephenson, H. Thybo, T. Torsvik, G. de Vicente, F. Wenzel, and M.J.R. Wortel. Topo-europe: The geoscience of coupled deep earth-surface processes. *Global and Planetary Change*, 58(1-4):1–118, 2007.
- [516] Sierd Cloetingh, Fred Beekman, Peter A Ziegler, Jan-Diederik van Wees, and Dimitrios Sokoutis. Post-rift compressional reactivation potential of passive margins and extensional basins. *Geological Society, London, Special Publications*, 306(1):27–70, 2008.
- [517] Sierd Cloetingh and Henk Kooi. Intraplate stresses and dynamical aspects of rifted basins. *Tectonophysics*, 215(1-2):167–185, 1992.
- [518] Sierd Auke Pieter Leonard Cloetingh, MJR Wortel, and NJ Vlaar. Evolution of passive continental margins and initiation of subduction zones. *Nature*, 297(5862):139, 1982.
- [519] S Cochard and C Ancey. Experimental investigation of the spreading of viscoplastic fluids on inclined planes. *Journal of Non-Newtonian Fluid Mechanics*, 158(1-3):73–84, 2009.
- [520] B. Cockburn and J. Gopalakrishnan. Incompressible Finite elements via Hybridization. Part I: The Stokes System in Two Space Dimensions. *SIAM J. Numer. Anal.*, 43(4):1627–1650, 2005.
- [521] B. Cockburn and J. Gopalakrishnan. Incompressible Finite elements via Hybridization. Part II: The Stokes System in Three Space Dimensions. *SIAM J. Numer. Anal.*, 43(4):1651–1672, 2005.
- [522] B. Cockburn and J. Gopalakrishnan. New hybridization techniques. *GAMM-Mitt*, 28(2):154–182, 2005.
- [523] B. Cockburn and J. Gopalakrishnan. The derivation of hybridizable discontinuous Galerkin methods for Stokes flow. *SIAM J. Numer. Anal.*, 47(2):1092–1125, 2009.
- [524] B. Cockburn, J. Gopalakrishnan, and R. Lazarov. Unified Hybridization of Discontinuous Galerkin, Mixed, and Continuous Galerkin Methods for Second Order Elliptic Problems. *Mathematics and Statistics Faculty Publications and Presentations*, 2009.
- [525] B. Cockburn, G. Kanschat, and D. Schötzau. A locally conservative LDG method for the incompressible Navier-Stokes equations. *Mathematics of Computation*, 74(251):1067–1095, 2004.

- [526] B. Cockburn, G. Kanschat, and D. Schötzau. The local discontinuous Galerkin method for linearized incompressible fluid flow: a review. *Computers and Fluids*, 34:491–506, 2005.
- [527] B. Cockburn, G. Kanschat, and D. Schötzau. A Note on Discontinuous Galerkin Divergence-free Solutions of the NavierStokes Equations. *J. Sci. Comput.*, 31(112):61–73, 2007.
- [528] B. Cockburn, G. Kanschat, and D. Schötzau. An Equal-Order DG Method for the Incompressible Navier-Stokes Equations. *J. Sci. Comput.*, 40:188–210, 2009.
- [529] B. Cockburn, G. Kanschat, D. Schoetzau, and C. Schwab. Local discontinuous Galerkin methods for the Stokes system. *SIAM J. Numer. Anal.*, 40(1):319–343, 2002.
- [530] B. Cockburn, G.E. Karniadakis, and C.W. Shu. The Development of Discontinuous Galerkin Methods. *Discontinuous Galerkin Methods. Lecture Notes in Computational Science and Engineering*, 11, 2000.
- [531] B. Cockburn, G.E. Karniadakis, and C.-W. Shu. *Discontinuous Galerkin Methods. Theory, Computation and Applications*. Springer, 2000.
- [532] B. Cockburn, N.C. Nguyen, and J. Peraire. A Comparison of HDG Methods for Stokes Flow. *J. Sci. Comput.*, 45:215–237, 2010.
- [533] B. Cockburn and C.-W. Shu. The Local Discontinuous Galerkin Method for Time-Dependent Convection-Diffusion Systems. *SIAM J. Numer. Anal.*, 35(6):2440–2463, 1998.
- [534] Bernardo Cockburn. Discontinuous galerkin methods. *ZAMM-Journal of Applied Mathematics and Mechanics*, 83(11):731–754, 2003.
- [535] Bernardo Cockburn. Static condensation, hybridization, and the devising of the hdg methods. In *Building bridges: connections and challenges in modern approaches to numerical partial differential equations*, pages 129–177. Springer, 2016.
- [536] Bernardo Cockburn, Jayadeep Gopalakrishnan, and Francisco-Javier Sayas. A projection-based error analysis of hdg methods. *Mathematics of Computation*, 79(271):1351–1367, 2010.
- [537] Bernardo Cockburn, Johnny Guzmán, and Haiying Wang. Superconvergent discontinuous galerkin methods for second-order elliptic problems. *Mathematics of Computation*, 78(265):1–24, 2009.
- [538] Bernardo Cockburn, Guido Kanschat, and Dominik Schötzau. The local discontinuous galerkin method for the oseen equations. *Mathematics of Computation*, 73(246):569–593, 2004.
- [539] M. Collignon, N. Fernandez, and B.J.P. Kaus. Influence of surface processes and initial topography on lateral fold growth and fold linkage mode. *Tectonics*, 34:1622–1645, 2015.
- [540] M. Collignon, B.J.P. Kaus, D.A. May, and N. fernandez. Influences of surface processes on fold growth during 3-D detachment folding. *Geochem. Geophys. Geosyst.*, 15:doi:10.1002/2014GC005450, 2014.
- [541] M. Collignon, P. Yamato, S. Castelltort, and B.J.P. Kaus. Modeling of wind gap formation and development of sedimentary basins during fold growth: application to the zagros fold belt, iran. *Earth Surface Processes and Landforms*, 41(11):1521–1535, 2016.
- [542] N. Coltice. The role of convective mixing in degassing the earth’s mantle. *Earth and Planetary Science Letters*, 234(1-2):15–25, 2005.
- [543] N. Coltice, M. Gerault, and M. Ulvrova. A mantle convection perspective on global tectonics. *Earth-Science Reviews*, 165:120–150, 2017.
- [544] N. Coltice, B. R. Phillips, H. Bertrand, Y. Ricard, and P. Rey. Global warming of the mantle at the origin of flood basalts over supercontinents. *Geology*, 35(5):391, 2007.
- [545] N. Coltice and Y. Ricard. Geochemical observations and one layer mantle convection. *Earth and Planetary Science Letters*, 174(1-2):125–137, 1999.
- [546] N. Coltice, T. Rolf, and P.J. Tackley. Seafloor spreading evolution in response to continental growth. *Geology*, 42(3):235–238, 2014.
- [547] Nicolas Coltice, Laurent Husson, Claudio Faccenna, and Maëlis Arnould. What drives tectonic plates? *Science Advances*, 5(10), 2019.
- [548] Nicolas Coltice, Gaspard Larrouтуrou, Eric Debayle, and Edward J Garnero. Interactions of scales of convection in the earth’s mantle. *Tectonophysics*, 746:669–677, 2018.
- [549] Nicolas Coltice, Tobias Rolf, Paul J Tackley, and Stéphane Labrosse. Dynamic causes of the relation between area and age of the ocean floor. *Science*, 336(6079):335–338, 2012.
- [550] Nicolas Coltice, Maria Seton, Tobias Rolf, RD Müller, and Paul J Tackley. Convergence of tectonic reconstructions and mantle convection models for significant fluctuations in seafloor spreading. *Earth and Planetary Science Letters*, 383:92–100, 2013.

- [551] Nicolas Coltice and Grace E Shephard. Tectonic predictions with mantle convection models. *Geophysical Journal International*, 213(1):16–29, 2018.
- [552] JAD Connolly and Yu Yu Podladchikov. Compaction-driven fluid flow in viscoelastic rock. *Geodinamica Acta*, 11(2-3):55–84, 1998.
- [553] James AD Connolly and Yury Y Podladchikov. An analytical solution for solitary porosity waves: dynamic permeability and fluidization of nonlinear viscous and viscoplastic rock. *Geofluids*, 15(1-2):269–292, 2015.
- [554] C. P. Conrad. Convective instability of thickening mantle lithosphere. *Geophysical Journal International*, 143(1):52–70, 2000.
- [555] C. P. Conrad. The solid earth’s influence on sea level. *Geological Society of America Bulletin*, 125(7-8):1027–1052, 2013.
- [556] C. P. Conrad and M. D. Behn. Constraints on lithosphere net rotation and asthenospheric viscosity from global mantle flow models and seismic anisotropy. *Geochemistry, Geophysics, Geosystems*, 11(5), 2010.
- [557] C. P. Conrad and B. H. Hager. Mantle convection with strong subduction zones. *Geophysical Journal International*, 144(2):271–288, 2001.
- [558] C. P. Conrad and L. Husson. Influence of dynamic topography on sea level and its rate of change. *Lithosphere*, 1(2):110–120, 2009.
- [559] C. P. Conrad and P. Molnar. Convective instability of a boundary layer with temperature-and strain-rate-dependent viscosity in terms of ‘available buoyancy’. *Geophysical Journal International*, 139(1):51–68, 1999.
- [560] C. P. Conrad, B. Wu, E. I. Smith, T. A. Bianco, and A. Tibbetts. Shear-driven upwelling induced by lateral viscosity variations and asthenospheric shear: A mechanism for intraplate volcanism. *Physics of the Earth and Planetary Interiors*, 178(3-4):162–175, 2010.
- [561] Clinton P Conrad and Carolina Lithgow-Bertelloni. How mantle slabs drive plate tectonics. *Science*, 298(5591):207–209, 2002.
- [562] Clinton P Conrad and Peter Molnar. The growth of rayleightaylor-type instabilities in the lithosphere for various rheological and density structures. *Geophysical Journal International*, 129(1):95–112, 1997.
- [563] C.P. Conrad, M.D. Behn, and P.G. Silver. Global mantle flow and the development of seismic anisotropy: Differences between the oceanic and continental upper mantle. *J. Geophys. Res.*, 112(B07317), 2007.
- [564] C.P. Conrad and M. Gurnis. Seismic tomography, surface uplift, and the breakup of Gondwanaland: Integrating mantle convection backwards in time. *Geochem. Geophys. Geosyst.*, 4(3), 2003.
- [565] C.P. Conrad and C. Lithgow-Bertelloni. Influence of continental roots and asthenosphere on plate-mantle coupling. *Geophys. Res. Lett.*, 33(L05312), 2006.
- [566] C.P. Conrad, B. Steinberger, and T.H. Torsvik. Stability of active mantle upwelling revealed by net characteristics of plate tectonics. *Nature*, 498:479, 2013.
- [567] C. M. Cooper and C. P. Conrad. Does the mantle control the maximum thickness of cratons? *Lithosphere*, 1(2):67–72, 2009.
- [568] Catherine M Cooper, Adrian Lenardic, and L Moresi. The thermal structure of stable continental lithosphere within a dynamic mantle. *Earth and Planetary Science Letters*, 222(3-4):807–817, 2004.
- [569] Catherine M Cooper, Adrian Lenardic, and L Moresi. Effects of continental insulation and the partitioning of heat producing elements on the earth’s heat loss. *Geophysical Research Letters*, 33(13), 2006.
- [570] CM Cooper, Meghan S Miller, and Louis Moresi. The structural evolution of the deep continental lithosphere. *Tectonophysics*, 695:100–121, 2017.
- [571] CM Cooper, Eric Mittelstaedt, Claire A Currie, Jolante van Wijk, Louise H Kellogg, Lorraine Hwang, and Ramon Arrowsmith. Moving lithospheric modeling forward: Attributes of a community computer code. *GSA Today*, 25(6):42–43, 2015.
- [572] C.M. Cooper, L.-N. Moresi, and A. Lenardic. Effects of continental configuration on mantle heat loss. *Geophys. Res. Lett.*, 40:2647–2651, 2013.
- [573] LW Cordes and B Moran. Treatment of material discontinuity in the element-free galerkin method. *Computer Methods in Applied Mechanics and Engineering*, 139(1-4):75–89, 1996.
- [574] I. Cormeau. Numerical stability in quasi-static elasto-visco-plasticity. *Int. J. Num. Meth. Eng.*, 9:109–127, 1975.
- [575] G. Corti, R. Cioni, Z. Franceschini, F. Sani, Stéphane Scailet, P. Molin, I. Isola, F. Mazzarini, S. Brune, D. Keir, A. Erbello, A. Muluneh, F. Illsley-Kemp, and A. Glerum. Aborted propagation of the ethiopian rift caused by linkage with the kenyan rift. *Nature Communications*, 10, 2019.

- [576] Giacomo Corti. Control of rift obliquity on the evolution and segmentation of the main ethiopian rift. *Nature Geoscience*, 1(4):258, 2008.
- [577] Giacomo Corti and Piero Manetti. Asymmetric rifts due to asymmetric mohos: An experimental approach. *Earth and Planetary Science Letters*, 245(1-2):315–329, 2006.
- [578] Giacomo Corti, Jolante van Wijk, Marco Bonini, Dimitrios Sokoutis, Sierd Cloetingh, Fabrizio Innocenti, and Piero Manetti. Transition from continental break-up to punctiform seafloor spreading: How fast, symmetric and magmatic. *Geophysical Research Letters*, 30(12), 2003.
- [579] N.J. Cosentino, J.P. Morgan, and T.E. Jordan. Modeling trench sediment-controlled flow in subduction channels: Implications for the topographic evolution of the central andean fore arc. *Journal of Geophysical Research: Solid Earth*, 123(10):9121–9135, 2018.
- [580] S. Cottaar and B. Buffett. Convection in the earth’s inner core. *Physics of the Earth and Planetary Interiors*, 198–199:67–78, 2012.
- [581] T.J. Coulthard. Landscape evolution models: a software review. *Hydrological processes*, 15:165–173, 2001.
- [582] D Coumou, T Driesner, and Christoph A Heinrich. The structure and dynamics of mid-ocean ridge hydrothermal systems. *Science*, 321(5897):1825–1828, 2008.
- [583] P. Coussot. Yield stress fluid flows: A review of experimental data. *Journal of Non-Newtonian Fluid Mechanics*, 211:31–49, 2014.
- [584] Patience A Cowie, John R Underhill, Mark D Behn, Jian Lin, and Caroline E Gill. Spatio-temporal evolution of strain accumulation derived from multi-scale observations of late jurassic rifting in the northern north sea: A critical test of models for lithospheric extension. *Earth and Planetary Science Letters*, 234(3–4):401–419, 2005.
- [585] F. Crameri, H. Schmeling, G.J. Golabek, T. Duretz, R. Orendt, S.J.H. Buiter, D.A. May, B.J.P. Kaus, T.V. Gerya, and P.J. Tackley. A comparison of numerical surface topography calculations in geodynamic modelling: an evaluation of the ‘sticky air’ method. *Geophys. J. Int.*, 189:38–54, 2012.
- [586] F. Crameri and P.J. Tackley. Spontaneous development of arcuate single-sided subduction in global 3-D mantle convection models with a free surface. *J. Geophys. Res.*, 119:doi:10.1002/2014JB010939, 2014.
- [587] F. Crameri and P.J. Tackley. Subduction initiation from a stagnant lid and global overturn: new insights from numerical models with a free surface. *Progress in Earth and Planetary Science*, 3, 2016.
- [588] F. Crameri, P.J. Tackley, I. Meilick, T.V. Gerya, and B.J.P. Kaus. A free plate surface and weak oceanic crust produce single-sided subduction on earth. *Geophys. Res. Lett.*, 39, 2012.
- [589] Fabio Crameri. Sinking plates on venus. *Nature Geoscience*, 2017.
- [590] Fabio Crameri. Geodynamic diagnostics, scientific visualisation and staglab 3.0. *Geoscientific Model Development*, 11(6):2541–2562, 2018.
- [591] Fabio Crameri, Clinton P Conrad, Laurent Montési, and Carolina R Lithgow-Bertelloni. The dynamic life of an oceanic plate. *Tectonophysics*, 760:107–135, 2019.
- [592] Fabio Crameri and Carolina Lithgow-Bertelloni. Abrupt upper-plate tilting during slab-transition-zone collision. *Tectonophysics*, 746:199–211, 2018.
- [593] A Crave and Ph Davy. A stochastic precipiton model for simulating erosion/sedimentation dynamics. *Computers & Geosciences*, 27(7):815–827, 2001.
- [594] T. Croissant and J. Braun. Constraining the stream power law: a novel approach combining a landscape evolution model and an inversion method. *Earth Surf. Dynam.*, 2:155–166, 2014.
- [595] AJL Crook, SM Willson, JG Yu, and DRJ Owen. Predictive modelling of structure evolution in sandbox experiments. *Journal of Structural Geology*, 28(5):729–744, 2006.
- [596] AG Crosby, D McKenzie, and JG Sclater. The relationship between depth, age and gravity in the oceans. *Geophysical Journal International*, 166(2):553–573, 2006.
- [597] M.M. Cross. Rheology of non-Newtonian fluids: a new flow equation for pseudoplastic systems. *Journal of Colloid Science*, 20:417–437, 1965.
- [598] Timothy A Cross and Rex H Pilger Jr. Controls of subduction geometry, location of magmatic arcs, and tectonics of arc and back-arc regions. *Geological Society of America Bulletin*, 93(6):545–562, 1982.
- [599] Steven L Crouch, Antony M Starfield, and FJ Rizzo. Boundary element methods in solid mechanics. *Journal of Applied Mechanics*, 50:704, 1983.
- [600] S Thomas Crough. Approximate solutions for the formation of the lithosphere. *Physics of the Earth and Planetary Interiors*, 14(4):365–377, 1977.

- [601] M. Crouzeix and P.-A. Raviart. Conforming and nonconforming finite element methods for solving the stationary Stokes equations I. *R.A.I.R.O.*, 7(3):33–75, 1973.
- [602] Alexander R Cruden, Mohammad HB Nasseri, and Russell Pysklywec. Surface topography and internal strain variation in wide hot orogens from three-dimensional analogue and two-dimensional numerical vice models. *Geological Society, London, Special Publications*, 253(1):79–104, 2006.
- [603] AR Cruden. Deformation around a rising diapir modeled by creeping flow past a sphere. *Tectonics*, 7(5):1091–1101, 1988.
- [604] L. Cruz, J. Malinski, A. Wilson, W.A. Take, and G. Hilley. Erosional control of kinematics and geometry of fold-and-thrust belts imaged in a physical and numerical sandbox. *J. Geophys. Res.*, 115(B09404):doi:10.1029/2010JB007472, 2010.
- [605] L Cserepes and M Rabinowicz. Gravity and convection in a two-layer mantle. *Earth and Planetary Science Letters*, 76(1-2):193–207, 1985.
- [606] WEH Culling. Analytical theory of erosion. *The Journal of Geology*, 68(3):336–344, 1960.
- [607] N.G. Culshaw, C. Beaumont, and R.A. Jamieson. The orogenic superstructure-infrastructure concept: Revisited, quantified, and revived. *Geology*, 34(9):733–736, 2006.
- [608] Peter A Cundall. Numerical experiments on localization in frictional materials. *Ingenieur-archiv*, 59(2):148–159, 1989.
- [609] C.A. Currie and C. Beaumont. Are diamond-bearing Cretaceous kimberlites related to low-angle subduction beneath western North America. *Earth Planet. Sci. Lett.*, 303:59–70, 2011.
- [610] C.A. Currie, C. Beaumont, and R.S. Huismans. The fate of subducted sediments: a case for backarc intrusion and underplating. *Geology*, 35(12):1111–1114, 2007.
- [611] C.A. Currie, M.N. Ducea, P.G. DeCelles, and C. Beaumont. Geodynamic models of cordilleran orogens: Gravitational instability of magmatic arc roots. *Memoir of the Geological Society of America*, 212:1–22, 2015.
- [612] Claire A Currie, Ritske S Huismans, and Christopher Beaumont. Thinning of continental backarc lithosphere by flow-induced gravitational instability. *Earth and Planetary Science Letters*, 269(3-4):436–447, 2008.
- [613] C. Cuvelier, A. Segal, and A.A. van Steenhoven. *Finite Element Methods and Navier-Stokes Equations*. D. Reidel Publishing Company, 1986.
- [614] M. Dabrowski, M. Krotkiewski, and D.W. Schmid. Milamin: Matlab based finite element solver for large problems. *Geochem. Geophys. Geosyst.*, 9(4):Q04030, 2008.
- [615] FA Dahlen. Noncohesive critical coulomb wedges: An exact solution. *Journal of Geophysical Research: Solid Earth*, 89(B12):10125–10133, 1984.
- [616] FA Dahlen. Critical taper model of fold-and-thrust belts and accretionary wedges. *Annual Review of Earth and Planetary Sciences*, 18(1):55–99, 1990.
- [617] FA Dahlen, John Suppe, and Dan Davis. Mechanics of fold-and-thrust belts and accretionary wedges: Cohesive coulomb theory. *Journal of Geophysical Research: Solid Earth*, 89(B12):10087–10101, 1984.
- [618] J. Dannberg, Z. Eilon, U. Faul, R. Gassmöller, P. Moulik, and R. Myhill. The importance of grain size to mantle dynamics and seismological observations. *Geochem. Geophys. Geosyst.*, 18:3034–3061, 2017.
- [619] J. Dannberg and R. Gassmöller. Chemical trends in ocean islands explained by plume-slab interaction. *PNAS*, 115(17):4351–4356, 2018.
- [620] J. Dannberg and T. Heister. Compressible magma/mantle dynamics: 3-D, adaptive simulations in ASPECT. *Geophy. J. Int.*, 207:1343–1366, 2016.
- [621] J. Dannberg and S.V. Sobolev. Low-buoyancy thermochemical plumes resolve controversy of classical mantle plume concept. *Nature Communications*, 6(6960):doi:10.1038/ncomms7960, 2015.
- [622] Julianne Dannberg, Rene Gassmöller, Ryan Grove, and Timo Heister. A new formulation for coupled magma/mantle dynamics. *Geophysical Journal International*, 219(1):94–107, 2019.
- [623] KD Danov, TD Gurkov, H Raszillier, and F Durst. Stokes flow caused by the motion of a rigid sphere close to a viscous interface. *Chemical Engineering Science*, 53(19):3413–3434, 1998.
- [624] R Das, Y Zhang, P Schaubs, and PW Cleary. Modelling rock fracturing caused by magma intrusion using the smoothed particle hydrodynamics method. *Computational Geosciences*, 18(6):927–947, 2014.
- [625] Rajarshi Das and PW Cleary. Effect of rock shapes on brittle fracture using smoothed particle hydrodynamics. *Theoretical and Applied Fracture Mechanics*, 53(1):47–60, 2010.

- [626] O Dauteuil, O Bourgeois, and T Mauduit. Lithosphere strength controls oceanic transform zone structure: insights from analogue models. *Geophysical Journal International*, 150(3):706–714, 2002.
- [627] A. Davaille, Ph. Carrez, and P. Cordier. Fat plumes may reflect the complex rheology of the lower mantle. *Geophys. Res. Lett.*, 45, 2018.
- [628] A. Davaille, B. Guesclin, A. Massmeyer, and E. Di Giuseppe. Thermal instabilities in a yield stress fluid: Existence and morphology. *Journal of Non-Newtonian Rheology*, 193:144–153, 2013.
- [629] A Davaille, SE Smrekar, and S Tomlinson. Experimental and observational evidence for plume-induced subduction on venus. *Nature Geoscience*, 10(5):349, 2017.
- [630] Anne Davaille. Simultaneous generation of hotspots and superswells by convection in a heterogeneous planetary mantle. *Nature*, 402(6763):756, 1999.
- [631] Anne Davaille, Fabien Girard, and Michael Le Bars. How to anchor hotspots in a convecting mantle? *Earth and Planetary Science Letters*, 203(2):621–634, 2002.
- [632] Anne Davaille, Angela Limare, Floriane Touitou, Ichiro Kumagai, and Judith Vatteville. Anatomy of a laminar starting thermal plume at high prandtl number. *Experiments in Fluids*, 50(2):285–300, 2011.
- [633] D. R. Davies, J. H. Davies, O. Hassan, K. Morgan, and P. Nithiarasu. Investigations into the applicability of adaptive finite element methods to two-dimensional infinite prandtl number thermal and thermochemical convection. *Geochemistry, Geophysics, Geosystems*, 8(5), 2007.
- [634] D Rhodri Davies, Saskia Goes, JH Davies, BSA Schubert, H-P Bunge, and J Ritsema. Reconciling dynamic and seismic models of earth’s lower mantle: The dominant role of thermal heterogeneity. *Earth and Planetary Science Letters*, 353:253–269, 2012.
- [635] D.R. Davies, J.H. Davies, P.C. Bollada, O. Hassan, K. Morgan, and P. Nithiarasu. A hierarchical mesh refinement technique for global 3-D spherical mantle convection modelling. *Geosci. Model Dev.*, 6:1095–1107, 2013.
- [636] DR Davies, AP Valentine, SC Kramer, N Rawlinson, MJ Hoggard, CM Eakin, and CR Wilson. Earths multi-scale topographic response to global mantle flow. *Nature Geoscience*, 12(10):845–850, 2019.
- [637] D.R. Davies, C.R. Wilson, and S.C. Kramer. Fluidity: A fully unstructured anisotropic adaptive mesh computational modeling framework for geodynamics. *Geochem. Geophys. Geosyst.*, 12(6), 2011.
- [638] Geoffrey F Davies. Lagging mantle convection, the geoid and mantle structure. *Earth and planetary science letters*, 69(1):187–194, 1984.
- [639] Geoffrey F Davies. Mantle convection under simulated plates: effects of heating modes and ridge and trench migration, and implications for the core-mantle boundary, bathymetry, the geoid and benioff zones. *Geophys. J. R. astr. Soc.*, 84(1):153–183, 1986.
- [640] Geoffrey F Davies and Michael Gurnis. Interaction of mantle dregs with convection: Lateral heterogeneity at the core-mantle boundary. *Geophysical Research Letters*, 13(13):1517–1520, 1986.
- [641] J. H. Davies and D. J. Stevenson. Physical model of source region of subduction zone volcanics. *Journal of Geophysical Research: Solid Earth*, 97(B2):2037–2070, 1992.
- [642] J Huw Davies and D Rhodri Davies. Earth’s surface heat flux. *Solid Earth*, 1(1):5–24, 2010.
- [643] J Huw Davies and Friedhelm von Blanckenburg. Slab breakoff: a model of lithosphere detachment and its test in the magmatism and deformation of collisional orogens. *Earth and Planetary Science Letters*, 129(1-4):85–102, 1995.
- [644] J.H. Davies. Global map of solid Earth surface heat flow. *Geochem. Geophys. Geosyst.*, 14(10), 2013.
- [645] J.H. Davies and H.-P. Bunge. Are splash plumes the origin of minor hotspots? *Geology*, 34(5):349–352, 2006.
- [646] Federico M Dávila and Carolina Lithgow-Bertelloni. Dynamic uplift during slab flattening. *Earth and Planetary Science Letters*, 425:34–43, 2015.
- [647] Dan Davis, John Suppe, and FA Dahlen. Mechanics of fold-and-thrust belts and accretionary wedges. *Journal of Geophysical Research: Solid Earth*, 88(B2):1153–1172, 1983.
- [648] R.O. Davis and A.P.S. Selvadurai. *Elasticity and Geomechanics*. Cambridge University Press, 1996.
- [649] P. Davy and P. Cobbold. Indentation tectonics in nature and experiment. 1. central asia. *Bulletin of the Geological Institutions of Uppsala*, 14:143–162, 1988.
- [650] P. Davy and P. Cobbold. Indentation tectonics in nature and experiment. 1. experiments scaled for gravity. *Bulletin of the Geological Institutions of Uppsala*, 14:129–141, 1988.

- [651] Ph. Davy and P. Cobbold. Experiments on shortening of a 4-layer model of the continental lithosphere. *Tectonophysics*, 188:1–25, 1991.
- [652] Philippe Davy and Dimitri Lague. Fluvial erosion/transport equation of landscape evolution models revisited. *Journal of Geophysical Research: Earth Surface*, 114(F3), 2009.
- [653] B. Deglo de Besses, A. Magnin, and P. Jay. Sphere drag in a viscoplastic fluid. *AIChE Journal*, 50(10):2627–2629, 2004.
- [654] H. de Boorder, W. Spakman, S.H. White, and M.J.R. Wortel. Late Cenozoic mineralization, orogenic collapse and slab detachment in the European Alpine Belt. *Earth Planet. Sci. Lett.*, 164:569–575, 1998.
- [655] R. de Borst. Bifurcations in Finite Element models with a non-associated flow law. *Int. J. Num. Meth. Eng.*, 12:99–116, 1988.
- [656] R De Borst, Lambertus J Sluys, H-B Muhlhaus, and Jerzy Pamin. Fundamental issues in finite element analyses of localization of deformation. *Engineering computations*, 10(2):99–121, 1993.
- [657] Rene De Borst. Simulation of strain localization: a reappraisal of the cosserat continuum. *Engineering computations*, 8(4):317–332, 1991.
- [658] René De Borst and Hans-Bernd Mühlhaus. Gradient-dependent plasticity: formulation and algorithmic aspects. *International Journal for Numerical Methods in Engineering*, 35(3):521–539, 1992.
- [659] J De Bresser, J Ter Heege, and C Spiers. Grain size reduction by dynamic recrystallization: can it result in major rheological weakening? *International Journal of Earth Sciences*, 90(1):28–45, 2001.
- [660] Arne De Coninck, Bernard De Baets, Drosos Kourounis, Fabio Verbosio, Olaf Schenk, Steven Maenhout, and Jan Fostier. Needles: Toward large-scale genomic prediction with marker-by-environment interaction. 203(1):543–555, 2016.
- [661] R De Franco, Rob Govers, and R Wortel. Nature of the plate contact and subduction zones diversity. *Earth And Planetary Science Letters*, 271(1-4):245–253, 2008.
- [662] Roberta De Franco, Rob Govers, and Rinus Wortel. Dynamics of continental collision: influence of the plate contact. *Geophysical Journal International*, 174(3):1101–1120, 2008.
- [663] J. de Frutos, V. John, and J. Novo. Projection methods for incompressible ow problems with WENO nite difference schemes. *J. Comp. Phys.*, 309:368–386, 2016.
- [664] Albert de Montserrat, Jason P Morgan, and Jörg Hasenclever. Lacode: a lagrangian two-dimensional thermo-mechanical code for large-strain compressible visco-elastic geodynamical modeling. *Tectonophysics*, page 228173, 2019.
- [665] J De Smet, AP van den Berg, and NJ Vlaar. Early formation and long-term stability of continents resulting from decompression melting in a convecting mantle. *Tectonophysics*, 322(1-2):19–33, 2000.
- [666] Jeroen H De Smet, Arie P van Den Berg, Nico J Vlaar, and David A Yuen. A characteristics-based method for solving the transport equation and its application to the process of mantle differentiation and continental root growth. *Geophysical Journal International*, 140(3):651–659, 2000.
- [667] JH De Smet, AP van den Berg, and NJ Vlaar. Stability and growth of continental shields in mantle convection models including recurrent melt production. *Tectonophysics*, 296(1-2):15–29, 1998.
- [668] J.H. de Smet, A.P. van den Berg, and N.J. Vlaar. The evolution of continental roots in numerical thermo-chemical mantle convection models including differentiation by partial melting. *Lithos*, 24:153–170, 1999.
- [669] G de Vahl Davis and IP Jones. Natural convection in a square cavity: a comparison exercise. *International Journal for numerical methods in fluids*, 3(3):227–248, 1983.
- [670] J. de Vries, M.H.G. Jacobs, A.P. van den Berg, M. Wehber, C. Lathe, C.A. McCammon, and W. van Westrenen. Thermal equation of state of synthetic orthofersilite at lunar pressures and temperatures. *Physics and Chemistry of Minerals*, 40(9):691–703, 2013.
- [671] J. de Vries, A. van den Berg, and W. van Westrenen. Formation and evolution of a lunar core from ilmenite-rich magma ocean cumulates. *Earth Planet. Sci. Lett.*, 292:139–147, 2010.
- [672] A. Deb, J.H. Prevost, and B. Loret. Adaptive meshing for dynamic strain localisation. *Comput. Methods Appl. Mech. Engrg.*, 137:285–306, 1996.
- [673] Charles DeMets, R Go Gordon, DF Argus, and Seth Stein. Current plate motions. *Geophysical journal international*, 101(2):425–478, 1990.
- [674] Charles DeMets, Richard G Gordon, and Donald F Argus. Geologically current plate motions. *Geophysical Journal International*, 181(1):1–80, 2010.

- [675] Carlos A Dengo and John M Logan. Implications of the mechanical and frictional behavior of serpentinite to seismogenic faulting. *Journal of Geophysical Research: Solid Earth*, 86(B11):10771–10782, 1981.
- [676] SCR Dennis and JD Hudson. Methods of solution of the velocity-vorticity formulation of the navier-stokes equations. *Journal of Computational Physics*, 122(2):300–306, 1995.
- [677] Alexander L Densmore, Michael A Ellis, and Robert S Anderson. Landsliding and the evolution of normal-fault-bounded mountains. *Journal of geophysical research: solid earth*, 103(B7):15203–15219, 1998.
- [678] S Dequand, JFH Willems, M Leroux, R Vullings, M van Weert, C Thieulot, and Abraham Hirschberg. Simplified models of flue instruments: Influence of mouth geometry on the sound source. *The Journal of the Acoustical Society of America*, 113(3):1724–1735, 2003.
- [679] C.S. Desai and J.F. Abel. *Introduction to the Finite Element Method: A Numerical Method for Engineering Analysis*. Van Nostrand Reinhold, 1972.
- [680] Frédéric Deschamps, Laura Cobden, and Paul J Tackley. The primitive nature of large low shear-wave velocity provinces. *Earth and Planetary Science Letters*, 349:198–208, 2012.
- [681] Frédéric Deschamps and Yang Li. Core-mantle boundary dynamic topography: influence of post-perovskite viscosity. *Journal of Geophysical Research: Solid Earth*, 2019.
- [682] Frédéric Deschamps, Yang Li, and Paul J Tackley. Large-scale thermo-chemical structure of the deep mantle: observations and models. In *The Earth's Heterogeneous Mantle*, pages 479–515. 2015.
- [683] Frédéric Deschamps and Paul J Tackley. Searching for models of thermo-chemical convection that explain probabilistic tomography: I. principles and influence of rheological parameters. *Physics of the Earth and Planetary Interiors*, 171(1-4):357–373, 2008.
- [684] Frédéric Deschamps and Paul J Tackley. Searching for models of thermo-chemical convection that explain probabilistic tomography. iiinfluence of physical and compositional parameters. *Physics of the Earth and Planetary Interiors*, 176(1-2):1–18, 2009.
- [685] Frédéric Deschamps, Paul J Tackley, and Takashi Nakagawa. Temperature and heat flux scalings for isoviscous thermal convection in spherical geometry. *Geophysical Journal International*, 182(1):137–154, 2010.
- [686] Frédéric Deschamps, Jeannot Trampert, and Paul J Tackley. Thermo-chemical structure of the lower mantle: seismological evidence and consequences for geodynamics. In *Superplumes: beyond plate tectonics*, pages 293–320. Springer, 2007.
- [687] Frédéric Deschamps, Chloé Yao, Paul J Tackley, and C Sanchez-Valle. High rayleigh number thermal convection in volumetrically heated spherical shells. *Journal of Geophysical Research: Planets*, 117(E9), 2012.
- [688] Y. Deubelbeiss and B.J.P. Kaus. Comparison of Eulerian and Lagrangian numerical techniques for the Stokes equations in the presence of strongly varying viscosity. *Phys. Earth Planet. Interiors*, 171:92–111, 2008.
- [689] Y Deubelbeiss, BJP Kaus, and JAD Connolly. Direct numerical simulation of two-phase flow: Effective rheology and flow patterns of particle suspensions. *Earth and Planetary Science Letters*, 290(1-2):1–12, 2010.
- [690] B DeVolder, J Glimm, JW Grove, Y Kang, Y Lee, K Pao, DH Sharp, and K Ye. Uncertainty quantification for multiscale simulations. *Journal of Fluids Engineering*, 124(1):29–41, 2002.
- [691] Byron DeVries, Joe Iannelli, Christian Trefftz, Kurt A O'Hearn, and Greg Wolffe. Parallel implementations of fgmres for solving large, sparse non-symmetric linear systems. *Procedia Computer Science*, 18:491–500, 2013.
- [692] J.F. dewey and J.M. Bird. Montain belts and the new global tectonics. *J. Geophys. Res.*, 75:2625–2647, 1970.
- [693] G. Dhatt and G. Hubert. A study of penalty elements for incompressible laminar flows. *Int. J. Num. Meth. Fluids*, 6:1–19, 1986.
- [694] E Di Giuseppe, F Corbi, F Funiciello, A Massmeyer, TN Santimano, M Rosenau, and A Davaille. Characterization of carbopol® hydrogel rheology for experimental tectonics and geodynamics. *Tectonophysics*, 642:29–45, 2015.
- [695] E Di Giuseppe, J Van Hunen, F Funiciello, C Faccenna, and D Giardini. Slab stiffness control of trench motion: Insights from numerical models. *Geochemistry, Geophysics, Geosystems*, 9(2), 2008.
- [696] D.A. di Pietro and A. Ern. *Mathematical Aspects of Discontinuous Galerkin Methods*. Springer, 2012.

- [697] A.E. Svartman Dias, L.L. Lavier, and N.W. Hayman. Conjugate rifted margins width and asymmetry: The interplay between lithospheric strength and thermomechanical processes. *J. Geophys. Res.*, 120:8672–8700, 2015.
- [698] V Dias da Silva. A simple model for viscous regularization of elasto-plastic constitutive laws with softening. *Communications in Numerical Methods in Engineering*, 20(7):547–568, 2004.
- [699] L. DiCaprio, M. Gurnis, R. D. Muller, and E. Tan. Mantle dynamics of continentwide cenozoic subsidence and tilting of australia. *Lithosphere*, 3(5):311–316, 2011.
- [700] L. DiCaprio, R. D. Muller, and M. Gurnis. A dynamic process for drowning carbonate reefs on the northeastern australian margin. *Geology*, 38(1):11–14, 2010.
- [701] Hannah R Dietterich, Einat Lev, Jiangzhi Chen, Jacob A Richardson, and Katharine V Cashman. Benchmarking computational fluid dynamics models of lava flow simulation for hazard assessment, forecasting, and risk management. *Journal of Applied Volcanology*, 6(1):9, 2017.
- [702] Alexandre Dimanov and Georg Dresen. Rheology of synthetic anorthite-diopside aggregates: Implications for ductile shear zones. *Journal of Geophysical Research: Solid Earth*, 110(B7), 2005.
- [703] I. Dione, C. Tibirna, and J. Urquiza. Stokes equations with penalised slip boundary conditions. *International Journal of Computational Fluid Dynamics*, 27(6-7):283–296, 2013.
- [704] John M Dixon. Finite strain and progressive deformation in models of diapiric structures. *Tectonophysics*, 28(1-2):89–124, 1975.
- [705] C.R. Dohrmann and P.B. Bochev. A stabilized finite element method for the Stokes problem based on polynomial pressure projections. *Int. J. Num. Meth. Fluids*, 46:183–201, 2004.
- [706] Marie-Pierre Doin and Pierre Henry. Subduction initiation and continental crust recycling: the roles of rheology and eclogitization. *Tectonophysics*, 342(1-2):163–191, 2001.
- [707] V. Dolejsí and M. Feistauer. *Discontinuous Galerkin Methods. Analysis and Applications to Compressible Flow*. Springer, 2015.
- [708] Vít Dolejší. Analysis and application of the iipg method to quasilinear nonstationary convection–diffusion problems. *Journal of Computational and Applied Mathematics*, 222(2):251–273, 2008.
- [709] H.S. Dollar, N.I.M. Gould, W.H.A. Schilders, and A.J. Wathen. Implicit-factorisation preconditioning and iterative solvers for regularised saddle-point systems. *SIAM J. Matrix Anal. Appl.*, 28(1):170–189, 2006.
- [710] J Donea, Antonio Huerta, J-Ph Ponthot, and A Rodriguez-Ferran. Arbitrary lagrangian-eulerian methods, volume 1 of encyclopedia of computational mechanics, chapter 14. *John Wiley & Sons Ltd*, 3:1–25, 2004.
- [711] Jean Donea and Antonio Huerta. *Finite Element Methods for Flow Problems*. John Wiley & Sons, 2003.
- [712] Deepak Doraiswamy. The origins of rheology: a short historical excursion. *Rheology Bulletin*, 71(1):1–9, 2002.
- [713] J.R. Dormand and P.J. Prince. A family of embedded runge-kutta formulae. *Journal of Computational and Applied Mathematics*, 6(1):19–26, 1980.
- [714] J.R. Dormand and P.J. Prince. A reconsideration of some embedded runge-kutta formulae. *Journal of Computational and Applied Mathematics*, 15:203–211, 1986.
- [715] Pavel V Doubrovine, Bernhard Steinberger, and Trond H Torsvik. Absolute plate motions in a reference frame defined by moving hot spots in the pacific, atlantic, and indian oceans. *Journal of Geophysical Research: Solid Earth*, 117(B9), 2012.
- [716] Pavel V Doubrovine, Bernhard Steinberger, and Trond H Torsvik. A failure to reject: Testing the correlation between large igneous provinces and deep mantle structures with edf statistics. *Geochemistry, Geophysics, Geosystems*, 17(3):1130–1163, 2016.
- [717] J. Douglas and T. Dupont. Interior penalty procedures for elliptic and parabolic Galerkin methods. *Computing methods in applied sciences (Second Internat. Sympos., Versailles, 1975)*, 58:207–216, 1976.
- [718] M van Driel, Lion Krischer, Simon C Stähler, Kambod Hosseini, and Tarje Nissen-Meyer. Instaseis: Instant global seismograms based on a broadband waveform database. *Solid Earth*, 6(2):701–717, 2015.
- [719] Daniel Charles Drucker. A more fundamental approach to plastic stress-strain relations. In *Proc. of 1st US National Congress of Applied Mechanics, 1951*, pages 487–491, 1951.
- [720] D.C. Drucker and W. Prager. Soil mechanics and plastic analysis or limit design. *Quarterly of Applied Mathematics*, 10(2):157–165, 1952.
- [721] M. Drury, J. de Smet, H. van Roermund, A. van den Berg, and N. Vlaar. Emplacement of deep mantle rocks into cratonic lithosphere by convection and diapiric upwelling. *Ophioliti*, 24(1 A):93–94, 1999.

- [722] Martyn R Drury. Dynamic recrystallization and strain softening of olivine aggregates in the laboratory and the lithosphere. *Geological Society, London, Special Publications*, 243(1):143–158, 2005.
- [723] M.R. Drury, H.L.M. Van Roermund, D.A. Carswell, J.H. De Smet, A.P. Van Den Berg, and N.J. Vlaar. Emplacement of deep upper-mantle rocks into cratonic lithosphere by convection and diapiric upwelling. *Journal of Petrology*, 42(1):131–140, 2001.
- [724] C.G. du Toit. Finite element solution of the Navier-Stokes equations for incompressible flow using a segregated algorithm. *Computer Methods in Applied Mechanics and Engineering*, 151:131–141, 1998.
- [725] J.C. Duarte, W.P. Schellart, and A.R. Cruden. Three-dimensions dynamic laboratory models of subduction with an overriding plate and variable interplate rheology . *Geophys. J. Int.*, 2013.
- [726] João C Duarte, Wouter P Schellart, and Alexander R Cruden. How weak is the subduction zone interface? *Geophysical Research Letters*, 42(8):2664–2673, 2015.
- [727] CP Dubey and VM Tiwari. Computation of the gravity field and its gradient: Some applications. *Computers & geosciences*, 88:83–96, 2016.
- [728] F Dubuffet, DA Yuen, and M Rabinowicz. Effects of a realistic mantle thermal conductivity on the patterns of 3-d convection. *Earth and Planetary Science Letters*, 171(3):401–409, 1999.
- [729] J.K. Dukowicz. Efficient Volume Computation for Three- Dimensional Hexahedral Cells. *J. Comp. Phys.*, 74:493–496, 1988.
- [730] D.A. Dunavant. High-degree efficient symmetrical Gaussian quadrature rules for the triangle. *Int. J. Num. Meth. Eng.*, 21:1129–1148, 1985.
- [731] J.A. Dunbar and D.S. Sawyer. Three-dimensional dynamical model of continental rift propagation and margin plateau formation. *J. Geophys. Res.*, 101(B12):27,845–27,863, 1996.
- [732] S. Duprat-Oualid, P. Yamato, and P. Pitra. Major role of shear heating in intracontinental inverted metamorphism: Inference from a thermo-kinematic parametric study. *Tectonophysics*, 608:812–831, 2013.
- [733] S. Duprat-Oualid, P. Yamato, and S.M. Schmalholz. A dimensional analysis to quantify the thermal budget around lithospheric-scale shear zones. *Terra Nova*, 27(3):163–168, 2015.
- [734] T. Duretz, Ph. Agard, Ph. Yamato, C. Ducassou, E.B. Burov, and T.V. Gerya. Thermo-mechanical modeling of the obduction process based on the oman ophiolite case. *Gondwana Research*, 32:1–10, 2016.
- [735] T. Duretz and T.V. Gerya. Slab detachment during continental collision: Influence of crustal rheology and interaction with lithospheric delamination. *Tectonophysics*, 602:124–140, 2013.
- [736] T. Duretz, T.V. Gerya, B.J.P. Kaus, and T.B. Andersen. Thermomechanical modeling of slab eduction. *J. Geophys. Res.*, 117(B08411), 2012.
- [737] T. Duretz, T.V. Gerya, and D.A. May. Numerical modelling of spontaneous slab breakoff and subsequent topographic response. *Tectonophysics*, 502:244–256, 2011.
- [738] T. Duretz, T.V. Gerya, and W. Spakman. Slab detachment in laterally varying subduction zones: 3-D numerical modeling. *Geophys. Res. Lett.*, 41:1951–1956, 2014.
- [739] T. Duretz, D.A. May, T.V. Gerya, and P.J. Tackley. Discretization errors and free surface stabilisation in the finite difference and marker-in-cell method for applied geodynamics: A numerical study. *Geochem. Geophys. Geosyst.*, 12(Q07004), 2011.
- [740] T. Duretz, S.M. Schmalholz, and T.V. Gerya. Dynamics of slab detachment. *Geochem. Geophys. Geosyst.*, 13(3):doi:10.1029/2011GC004024, 2012.
- [741] T. Duretz, S.M. Schmalholz, and Y.Y. Podladchikov. Physics-controlled thickness of shear zones caused by viscous heating: Implications for crustal shear localization. *Geophys. Res. Lett.*, page doi: 10.1002/2014GL060438, 2014.
- [742] T. Duretz, S.M. Schmalholz, and Y.Y. Podladchikov. Shear heating-induced strain localization across the scales. *Philosophical Magazine*, 2015.
- [743] T. Duretz, A. Souche, R. de Borst, and L. Le Pourhiet. The Benefits of Using a Consistent Tangent Operator for Viscoelastoplastic Computations in Geodynamics. *Geochem. Geophys. Geosyst.*, 19, 2018.
- [744] Thibault Duretz, Riccardo Asti, Yves Lagabrielle, Jean-Pierre Brun, Anthony Jourdon, Camille Clerc, and Benjamin Corre. Numerical modelling of cretaceous pyrenean rifting: The interaction between mantle exhumation and syn-rift salt tectonics. *Basin Research*, 2019.
- [745] Thibault Duretz, Dave A May, and Philippe Yamato. A free surface capturing discretization for the staggered grid finite difference scheme. *Geophysical Journal International*, 204(3):1518–1530, 2016.

- [746] WB Durham and LA Stern. Rheological properties of water iceapplications to satellites of the outer planets. *Annual Review of Earth and Planetary Sciences*, 29(1):295–330, 2001.
- [747] A. Düster and E. Rank. The p-version of the nite element method compared to an adaptive h-version for the deformation theory of plasticity. *Computer Methods in Applied Mechanics and Engineering*, 190:1925–1935, 2011.
- [748] Jack Dvorkin, Amos Nur, Gary Mavko, and Zvi Ben-Avraham. Narrow subducting slabs and the origin of backarc basins. *Tectonophysics*, 227(1-4):63–79, 1993.
- [749] S. Dyksterhuis, P. Rey, R.D. Mueller, and L. Moresi. Effects of initial weakness on rift architecture. *Geological Society, London, Special Publications*, 282:443–455, 2007.
- [750] D Dymkova and T Gerya. Porous fluid flow enables oceanic subduction initiation on earth. *Geophysical Research Letters*, 40(21):5671–5676, 2013.
- [751] A.M. Dziewonski and D.L. Anderson. Preliminary reference Earth model. *Phys. Earth. Planet. Inter.*, 25:297–356, 1981.
- [752] Caroline M Eakin, Maureen D Long, Lara S Wagner, Susan L Beck, and Hernando Tavera. Upper mantle anisotropy beneath peru from sks splitting: Constraints on flat slab dynamics and interaction with the nazca ridge. *Earth and Planetary Science Letters*, 412:152–162, 2015.
- [753] J Ebbing, J Bouman, M Fuchs, S Gradmann, and R Haagmans. Sensitivity of goce gravity gradients to crustal thickness and density variations: Case study for the northeast atlantic region. In *Gravity, Geoid and Height Systems*, pages 291–298. Springer, 2014.
- [754] Jörg Ebbing, Johannes Bouman, Martin Fuchs, Verena Lieb, Roger Haagmans, JAC Meekes, and Rader Abdul Fattah. Advancements in satellite gravity gradient data for crustal studies. *The Leading Edge*, 32(8):900–906, 2013.
- [755] C. Ebinger and J. van Wijk. Roadmap to continental rupture: Is obliquity the route to success? *Geology*, 42(3):271–272, 2014.
- [756] Cynthia J Ebinger, Jolante van Wijk, and Derek Keir. The time scales of continental rifting: Implications for global processes. *Geol. Soc. Am. Spec. Pap*, 500:371–396, 2013.
- [757] SS Egan. The flexural isostatic response of the lithosphere to extensional tectonics. *Tectonophysics*, 202(2-4):291–308, 1992.
- [758] David L. Egholm. A new strategy for discrete element numerical models: 1. Theory. *J. Geophys. Res.*, 112:B05203, doi:10.1029/2006JB004557, 2007.
- [759] David L. Egholm, Mike Sandiford, Ole R. Clausen, and Søren B. Nielsen. A new strategy for discrete element numerical models: 2. Sandbox applications. *J. Geophys. Res.*, 112:B05204, doi:10.1029/2006JB004558, 2007.
- [760] Takao EGUCHI, Mizuho ISHIDA, Kiyoshi MATSUBARA, Takumi MURAKOSHI, and Yasuyuki IWASE. Basic numerical simulation of large-scale plume activity due to the circum-pacific lithosphere subduction and implications for the elementary process associated with the static-layered terrestrial mantle. 2017.
- [761] Philipp Eichheimer, Marcel Thielmann, Anton Popov, Gregor J Golabek, Wakana Fujita, Maximilian O Kottwitz, and Boris JP Kaus. Pore-scale permeability prediction for newtonian and non-newtonian fluids. *Solid Earth*, 10(5):1717–1731, 2019.
- [762] R. Eid. Higher order isoparametric finite element solution of Stokes flow . *Applied Mathematics and Computation*, 162:1083–1101, 2005.
- [763] V. Eijkhout. *Introduction to High Performance Scientific Computing*. Creative Commons, 2013.
- [764] Y. Elesin, T. Gerya, I.M. Artemieva, and H. Thybo. Samovar: a thermomechanical code for modeling of geodynamic processes in the lithospshere – application to basin evolution. *Arabian Journal of Geosciences*, 3:477–497, 2010.
- [765] L. T. Elkins-Tanton. Continental magmatism, volatile recycling, and a heterogeneous mantle caused by lithospheric gravitational instabilities. *Journal of Geophysical Research*, 112(B3), 2007.
- [766] L. T. Elkins-Tanton and B. H. Hager. Melt intrusion as a trigger for lithospheric foundering and the eruption of the siberian flood basalts. *Geophysical Research Letters*, 27(23):3937–3940, 2000.
- [767] L. T. Elkins-Tanton, B. H. Hager, and T. L. Grove. Magmatic effects of the lunar late heavy bombardment. *Earth and Planetary Science Letters*, 222(1):17–27, 2004.
- [768] L. T. Elkins-Tanton, J. A. van Orman, B. H. Hager, and T. L. Grove. Re-examination of the lunar magma ocean cumulate overturn hypothesis: melting or mixing is required. *Earth and Planetary Science Letters*, 196(3-4):239–249, 2002.

- [769] S. Ellis and C. Beaumont. Models of convergent boundary tectonics: Implications for the interpretation of lithoprobe data. *Canadian Journal of Earth Sciences*, 36(10):1711–1741, 1999.
- [770] S. Ellis, C. Beaumont, R.A. Jamieson, and G. Quinlan. Continental collision including a weak zone: The vise model and its application to the newfoundland appalachians. *Canadian Journal of Earth Sciences*, 35(11):1323–1346, 1998.
- [771] S. Ellis, C. Beaumont, and O.A. Pfiffner. Geodynamic models of crustal-scale episodic tectonic accretion and underplating in subduction zones. *Journal of Geophysical Research: Solid Earth*, 104(B7):15169–15190, 1999.
- [772] S. Ellis, P. Fullsack, and C. Beaumont. Oblique convergence of the crust driven by basal forcing: implications for length-scales of deformation and strain partitioning in orogens. *Geophys. J. Int.*, 120:24–44, 1995.
- [773] S.M. Ellis, T.A. Little, L.M. Wallace, B.R. Hacker, and S.J.H. Buiter. Feedback between rifting and diapirism can exhume ultrahigh-pressure rocks. *Earth Planet. Sci. Lett.*, 311:427–438, 2011.
- [774] Susan Ellis, Francesca Ghisetti, Philip M Barnes, Carolyn Boulton, Åke Fagereng, and Susanne Buiter. The contemporary force balance in a wide accretionary wedge: numerical models of the southcentral hikurangi margin of new zealand. *Geophysical Journal International*, 219(2):776–795, 2019.
- [775] Susan Ellis, Guido Schreurs, and Marion Panien. Comparisons between analogue and numerical models of thrust wedge development. *Journal of Structural Geology*, 26(9):1659–1675, 2004.
- [776] H. Elman, D. Silvester, and A. Wathen. *Finite Elements and Fast Iterative Solvers*. Oxford Science Publications, 2014.
- [777] H.C. Elman. Multigrid and Krylov subspace methods for the discrete Stokes equations. *Int. J. Num. Meth. Fluids*, 22:755–770, 1996.
- [778] H.C. Elman and G.H. Golub. Inexact and preconditioned Uzawa algorithms for saddle point problems. *SIAM J. Numer. Anal.*, 31(6):1645–1661, 1994.
- [779] Brigitte Endrun, Sergei Lebedev, Thomas Meier, Céline Tirel, and Wolfgang Friederich. Complex layered deformation within the aegean crust and mantle revealed by seismic anisotropy. *Nature geoscience*, 4(3):203, 2011.
- [780] M.S. Engelman, R.L. Sani, and P.M. Gresho. The implementation of normal and/or tangential boundary conditions in finite element codes for incompressible fluid flow. *Int. J. Num. Meth. Fluids*, 2:225–238, 1982.
- [781] MS Engelman, Gilbert Strang, and K-J Bathe. The application of quasi-newton methods in fluid mechanics. *International Journal for Numerical Methods in Engineering*, 17(5):707–718, 1981.
- [782] P. England. Some numerical investigations of large scale continental deformation. In *Mountain Building Processes*, pages 129–189. Academic Press, 1982.
- [783] P. England and G. Houseman. A dynamical model of lithosphere extension and sedimentary basin formation. *J. Geophys. Res.*, 91(B3):3664–3676, 1986.
- [784] Philip England. Constraints on extension of continental lithosphere. *Journal of Geophysical Research: Solid Earth*, 88(B2):1145–1152, 1983.
- [785] Philip England and Peter Molnar. Surface uplift, uplift of rocks, and exhumation of rocks. *Geology*, 18:1173–117, December 1990.
- [786] Philip England and Peter Molnar. Active deformation of asia: From kinematics to dynamics. *Science*, 278(5338):647–650, 1997.
- [787] Philip England and Catherine Wilkins. A simple analytical approximation to the temperature structure in subduction zones. *Geophysical Journal International*, 159(3):1138–1154, 2004.
- [788] A. Enns, T.W. Becker, and H. Schmeling. The dynamics of subduction and trench migration for viscosity stratification. *Geophys. J. Int.*, 160:761–775, 2005.
- [789] Z. Erdos, R.S. huismans, and P. van der Beek. First-order control of syntectonic sedimentation on crustal-scale structure of mountain belts . *J. Geophys. Res.*, 120:doi:10.1002/2014JB011785, 2015.
- [790] Z. Erdos, R.S. Huismans, and P. van der Beek. Control of increased sedimentation on orogenic fold-and-thrust belt structure - insights into the evolution of the Western Alps. *Solid Earth*, 10:391–404, 2019.
- [791] Z. Erdos, R.S. huismans, P. van der Beek, and C. Thieulot. Extensional inheritance and surface processes as controlling factors of mountain belt structure. *J. Geophys. Res.*, 119:doi:10.1002/2014JB011408, 2014.
- [792] A Ern, J-L Guermond, and L Quartapelle. Vorticity-velocity formulations of the stokes problem in 3d. *Mathematical methods in the applied sciences*, 22(6):531–546, 1999.

- [793] E. Erturk. Discussions on Driven Cavity Flow. *Int. J. Num. Meth. Fluids*, 60:275–294, 2009.
- [794] J. Escartin, G. Hirth, and B. Evans. Effects of serpentization on the lithospheric strength and the style of normal faulting at slow-spreading ridges . *Earth Planet. Sci. Lett.*, 151:181–189, 1997.
- [795] J. Escartin, G. Hirth, and B. Evans. Nondilatant brittle deformation of serpentinites: Implications for Mohr-Coulomb theory and the strength of faults. *J. Geophys. Res.*, 102(B2):2897–2913, 1997.
- [796] Pep Espanol and Cedric Thieulot. Microscopic derivation of hydrodynamic equations for phase-separating fluid mixtures. *The Journal of chemical physics*, 118(20):9109–9127, 2003.
- [797] Nicolas Espurt, Francesca Funiciello, Joseph Martinod, Benjamin Guillaume, Vincent Regard, Claudio Faccenna, and Stéphane Brusset. Flat subduction dynamics and deformation of the south american plate: Insights from analog modeling. *Tectonics*, 27(3), 2008.
- [798] Brian Evans and Christopher Goetze. The temperature variation of hardness of olivine and its implication for polycrystalline yield stress. *Journal of Geophysical Research: Solid Earth*, 84(B10):5505–5524, 1979.
- [799] D.A.D. Evans. True polar wander and supercontinents. *Tectonophysics*, 362:303–320, 2003.
- [800] Maurice S Fabien, Matthew G Knepley, and Béatrice M Rivière. A hybridizable discontinuous galerkin method for two-phase flow in heterogeneous porous media. *International Journal for Numerical Methods in Engineering*, 116(3):161–177, 2018.
- [801] M. Faccenda. Mid mantle seismic anisotropy around subduction zones. *Phys. Earth. Planet. Inter.*, 227:1–19, 2014.
- [802] M. Faccenda and F.A. Capitanio. Seismic anisotropy around subduction zones: Insights from three-dimensional modeling of upper mantle deformation and SKS splitting calculations . *Geochem. Geophys. Geosyst.*, 14(1):doi:10.1029/2012GC004451, 2013.
- [803] M. Faccenda, T.V. Gerya, and S. Chakraborty. Styles of post-subduction collisional orogeny: Influence of convergence velocity, crustal rheology and radiogenic heat production. *Lithos*, 103:257–287, 2008.
- [804] M. Faccenda, T.V. Gerya, N.S. Mancktelow, and L. Moresi. Fluid flow during slab unbending and dehydration: Implications for intermediate-depth seismicity, slab weakening and deep water recycling. *Geochem. Geophys. Geosyst.*, 13(1):doi:10.1029/2011GC003860, 2012.
- [805] M Faccenda, G Minelli, and TV Gerya. Coupled and decoupled regimes of continental collision: numerical modeling. *Earth and Planetary Science Letters*, 278(3-4):337–349, 2009.
- [806] Manuele Faccenda and Luca Dal Zilio. The role of solid–solid phase transitions in mantle convection. *Lithos*, 268:198–224, 2017.
- [807] Manuele Faccenda, Taras V Gerya, and Luigi Burlini. Deep slab hydration induced by bending-related variations in tectonic pressure. *Nature Geoscience*, 2(11):790, 2009.
- [808] C. Faccenna and T. W. Becker. Shaping mobile belts by small-scale convection. *Nature*, 465(7298):602–605, 2010.
- [809] C. Faccenna, T. W. Becker, S. Lallemand, Y. Lagabrielle, F. Funiciello, and C. Piromallo. Subduction-triggered magmatic pulses: A new class of plumes? *Earth and Planetary Science Letters*, 299(1-2):54–68, 2010.
- [810] C. Faccenna, O. Bellier, J. Martinod, C. Piromallo, and V. Regard. Slab detachment beneath eastern Anatolia: A possible cause for the formation of the North Anatolian fault. *Earth Planet. Sci. Lett.*, 242:85–97, 2006.
- [811] Claudio Faccenna, Thorsten W Becker, Ludwig Auer, Andrea Billi, Lapo Boschi, Jean Pierre Brun, Fabio A Capitanio, Francesca Funiciello, Ferenc Horváth, Laurent Jolivet, Claudia Piromallo, Leigh Royden, Federico Rossetti, and Enrico Serpelloni. Mantle dynamics in the mediterranean. *Reviews of Geophysics*, 52(3):283–332, 2014.
- [812] Claudio Faccenna, Thorsten W Becker, Clinton P Conrad, and Laurent Husson. Mountain building and mantle dynamics. *Tectonics*, 32(1):80–93, 2013.
- [813] Claudio Faccenna, Domenico Giardini, Philippe Davy, and Alessio Argentieri. Initiation of subduction at atlantic-type margins: Insights from laboratory experiments. *Journal of Geophysical Research: Solid Earth*, 104(B2):2749–2766, 1999.
- [814] K Fadaie and Giorgio Ranalli. Rheology of the lithosphere in the east african rift system. *Geophysical Journal International*, 102(2):445–453, 1990.
- [815] G. Farin and D. Hansford. *Mathematical principles for scientific computing and visualisation*. A.K. Peters, Ltd., 2008.

- [816] Robert JM Farla, Shun-ichiro Karato, and Zhengyu Cai. Role of orthopyroxene in rheological weakening of the lithosphere via dynamic recrystallization. *Proceedings of the National Academy of Sciences*, 110(41):16355–16360, 2013.
- [817] C. G. Farnetani and A. W. Hofmann. Dynamics and internal structure of a lower mantle plume conduit. *Earth and Planetary Science Letters*, 282(1-4):314–322, 2009.
- [818] C. G. Farnetani and M. A. Richards. Numerical investigations of the mantle plume initiation model for flood basalt events. *Journal of Geophysical Research: Solid Earth*, 99(B7):13813–13833, 1994.
- [819] CG Farnetani and H Samuel. Beyond the thermal plume paradigm. *Geophysical Research Letters*, 32(7), 2005.
- [820] Cinzia G Farnetani, Bernard Legras, and Paul J Tackley. Mixing and deformations in mantle plumes. *Earth and Planetary Science Letters*, 196(1-2):1–15, 2002.
- [821] Cinzia G Farnetani and Henri Samuel. Lagrangian structures and stirring in the earths mantle. *Earth and Planetary Science Letters*, 206(3-4):335–348, 2003.
- [822] R.J. Farrington, L.-N. Moresi, and F.A. Capitanio. The role of viscoelasticity in subducting plates. *Geochem. Geophys. Geosyst.*, 15:4291–4304, 2014.
- [823] R.J. Farrington, D.R. Stegman, L.N. Moresi, M. Sandiford, and D.A. May. Interactions of 3D mantle flow and continental lithosphere near passive margins. *Tectonophysics*, 483:20–28, 2010.
- [824] U.H. Faul, J.D. Fitz Gerald, R. J.M. Farlai, R. Ahlefeldt, and I. Jackson. Dislocation creep of finegrained olivine. *J. Geophys. Res.*, 116(B01203,):doi:10.1029/2009JB007174, 2011.
- [825] Ulrich H Faul and Ian Jackson. Diffusion creep of dry, melt-free olivine. *Journal of Geophysical Research: Solid Earth*, 112(B4), 2007.
- [826] N.P. Fay, R.A. Bennett, J.C. Spinler, and E.D. Humphreys. Small-scale upper mantle convection and crustal dynamics in southern California. *Geochem. Geophys. Geosyst.*, 9(8), 2008.
- [827] E. Fehlberg. Some old and new Runge-Kutta formulas with stepsize control and their error coefficients. *Computing*, 34:265–270, 1985.
- [828] N. Fehn, W.A. Wall, and M. Kronbichler. On the stability of projection methods for the incompressible NavierStokes equations based on high-order discontinuous Galerkin discretizations. *J. Comp. Phys.*, 351:392–421, 2017.
- [829] Miloslav Feistauer and V Kučera. On a robust discontinuous galerkin technique for the solution of compressible flow. *Journal of Computational Physics*, 224(1):208–221, 2007.
- [830] N. Fernandez and B. Kaus. Influence of pre-existing salt diapirs on 3D folding patterns . *Tectonophysics*, 637:354–369, 2014.
- [831] N. Fernandez and B. Kaus. Fold interaction and wavelength selection in 3D models of multilayer detachment folding. *Tectonophysics*, 632:199–217, 2014.
- [832] N. Fernandez and B. Kaus. Pattern formation in 3-D numerical models of down-built diapirs initiated by a RayleighTaylor instability. *Geophy. J. Int.*, 202:1253–1270, 2015.
- [833] Javier Fernández-Lozano, Dimitrios Sokoutis, Ernst Willingshofer, Endre Dombrádi, Alfonso M Martín, Gerardo De Vicente, and Sierd Cloetingh. Integrated gravity and topography analysis in analog models: Intraplate deformation in iberia. *Tectonics*, 31(6), 2012.
- [834] Sonia Fernández-Méndez, Javier Bonet, and Antonio Huerta. Continuous blending of sph with finite elements. *Computers & structures*, 83(17-18):1448–1458, 2005.
- [835] O. Ferrer, M.P.A. Jackson, E. Roca, and M. Rubinat. Evolution of salt structures during extension and inversion of the Offshore Parentis Basin (Eastern Bay of Biscay) . *Salt Tectonics, Sediments and Prospectivity. Geological Society, London, Special Publications*, 363:361–379, 2012.
- [836] C. Fillon, R.S. Huismans, and P. van der Beek. Syntectonic sedimentation effects on the growth of fold-and-thrust belts . *Geology*, 41(1):83–86, 2013.
- [837] C. Fillon, R.S. Huismans, P. van der Beek, and J.A. Mu noz. Syntectonic sedimentation controls on the evolution of the southern Pyrenean fold-and-thrust belt: Inferences from coupled tectonic-surface processes models. *J. Geophys. Res.*, 118:5665–5680, 2013.
- [838] KD Fischer, T Jahr, and G Jentzsch. Evolution of the variscan foreland-basin: modelling the interactions between tectonics and surface processes. *Physics and Chemistry of the Earth, Parts A/B/C*, 29(10):665–671, 2004.

- [839] Mark P Fischer, Michael R Gross, Terry Engelder, and Roy J Greenfield. Finite-element analysis of the stress distribution around a pressurized crack in a layered elastic medium: implications for the spacing of fluid-driven joints in bedded sedimentary rock. *Tectonophysics*, 247(1-4):49–64, 1995.
- [840] R. Fischer and T. Gerya. Early Earth plume-lid tectonics: A high-resolution 3D numerical modelling approach. *Journal of Geodynamics*, 100:198–214, 2016.
- [841] N. Flament, M. Gurnis, S. Williams, M. Seton, J. Skogseid, C. Heine, and D. Müller. Topographic asymmetry of the South Atlantic from global models of mantle flow and lithospheric stretching. *Earth Planet. Sci. Lett.*, 387:107–119, 2014.
- [842] Nicolas Flament, Michael Gurnis, and R Dietmar Müller. A review of observations and models of dynamic topography. *Lithosphere*, 5(2):189–210, 2013.
- [843] Luce Fleitout and David A Yuen. Secondary convection and the growth of the oceanic lithosphere. *Physics of the earth and planetary interiors*, 36(3-4):181–212, 1984.
- [844] L Flesch, R Bendick, and S Bischoff. Limitations on inferring 3d architecture and dynamics from surface velocities in the india-eurasia collision zone. *Geophysical Research Letters*, 45(3):1379–1386, 2018.
- [845] Raymond C Fletcher. Three-dimensional folding of an embedded viscous layer in pure shear. *Journal of Structural Geology*, 13(1):87–96, 1991.
- [846] Raymond C Fletcher. Three-dimensional folding and necking of a power-law layer: are folds cylindrical, and, if so, do we understand why? *Tectonophysics*, 247(1-4):65–83, 1995.
- [847] B.J. Foley and T.W. Becker. Generation of plate-like behavior and mantle heterogeneity from a spherical, viscoplastic convection model. *Geochem. Geophys. Geosyst.*, 10(8):doi:10.1029/2009GC002378, 2009.
- [848] Donald Forsyth and Seiya Uyeda. On the relative importance of the driving forces of plate motion. *Geophysical Journal International*, 43(1):163–200, 1975.
- [849] AM Forte and WR Peltier. Lateral heterogeneity and the geoid: the importance of the surface kinematic constraints. In *Mathematical Geophysics*, pages 291–323. 1988.
- [850] A.M. Forte and W.R. Peltier. Viscous flow models of global geophysical observables. 1. forward problems. *J. Geophys. Res.*, 96:20,131–20,159, 1991.
- [851] A. Fortin, M. Jardak, J.J. Gervais, and R. Pierre. Old and new results on the two-dimensional poiseuille flow. *J. Comp. Phys.*, 115(2):455–469, 1994.
- [852] M. Fortin. Old and new finite elements for incompressible flows. *Int. J. Num. Meth. Fluids*, 1:347–364, 1981.
- [853] M. fortin and S. Boivin. Iterative stabilisation of the bilinear velocity-constant pressure element. *Int. J. Num. Meth. Fluids*, 10:125–140, 1990.
- [854] M. Fortin and A. Fortin. Experiments with several elements for viscous incompressible flows. *Int. J. Num. Meth. Fluids*, 5:911–928, 1985.
- [855] Michel Fortin and F Thomasset. Mixed finite-element methods for incompressible flow problems. *Journal of Computational Physics*, 31(1):113–145, 1979.
- [856] Haakon Fossen and Atle Rotevatn. Fault linkage and relay structures in extensional settingsa review. *Earth-Science Reviews*, 154:14–28, 2016.
- [857] Haakon Fossen, Richard A Schultz, Egil Rundhovde, Atle Rotevatn, and Simon J Buckley. Fault linkage and graben stepovers in the canyonlands (utah) and the north sea viking graben, with implications for hydrocarbon migration and accumulation. *AAPG bulletin*, 94(5):597–613, 2010.
- [858] GR Foulger. Plumes, or plate tectonic processes? *Astronomy & Geophysics*, 43(6):6–19, 2002.
- [859] L. Fourel, S. Goes, and G. Morra. The role of elasticity in slab bending. *Geochem. Geophys. Geosyst.*, 15:4507–4525, 2014.
- [860] Marc Fournier, Laurent Jolivet, Philippe Davy, and Jean-Charles Thomas. Backarc extension and collision: an experimental approach to the tectonics of asia. *Geophysical Journal International*, 157(2):871–889, 2004.
- [861] Matthew Fox, Frédéric Herman, Edi Kissling, and Sean D Willett. Rapid exhumation in the western alps driven by slab detachment and glacial erosion. *Geology*, 43(5):379–382, 2015.
- [862] L.P. Franca and T.J.R. Hughes. Convergence analyses of Galerkin least-squares methods for symmetric advective-diffusive forms of the Stokes and incompressible Navier-Stokes equations. *Computer Methods in Applied Mechanics and Engineering*, 105:285–298, 1993.
- [863] L.P. Franca and S.P. Oliveira. Pressure bubbles stabilization features in the Stokes problem. *Computer Methods in Applied Mechanics and Engineering*, 192:1929–1937, 2003.

- [864] L.P. Franca, S.P. Oliveira, and M. Sarkis. Continuous q1q1 stokes elements stabilised with non-conforming null edge average velocity functions. *Mathematical Models and Methods in Applied Sciences*, 17:439–459, 2007.
- [865] R. De Franco, R. Govers, and R. Wortel. Numerical comparison of different convergent plate contacts: subduction channel and subduction fault. *Geophys. J. Int.*, pages 10.1111/j.1365–246X.2006.03498.x, 2006.
- [866] T. Francois, E. Burov, P. Agard, and B. Meyer. Buildup of a dynamically supported orogenic plateau: Numerical modeling of the Zagros/Central Iran case study. *Geochem. Geophys. Geosyst.*, 15:doi:10.1002/2013GC005223, 2014.
- [867] Thomas François, Evgueni Burov, Bertrand Meyer, and Philippe Agard. Surface topography as key constraint on thermo-rheological structure of stable cratons. *Tectonophysics*, 602:106–123, 2013.
- [868] Thomas François, Alexander Koptev, Sierd Cloetingh, Evgueni Burov, and Taras Gerya. Plume-lithosphere interactions in rifted margin tectonic settings: Inferences from thermo-mechanical modelling. *Tectonophysics*, 746:138–154, 2018.
- [869] DA Frank-Kamenetskii. *Diffusion and heat transfer in chemical kinetics*. New York: Plenum Press, 1969.
- [870] Raymond CMW Franssen. The rheology of synthetic rocksalt in uniaxial compression. *Tectonophysics*, 233(1-2):1–40, 1994.
- [871] M. Fraters, C. Thieulot, A. van den Berg, and W. Spakman. The geodynamic world builder: a solution for complex initial conditions in numerical modelling. *Solid Earth*, 2019.
- [872] M.R.T. Fraters, W. Bangerth, C. Thieulot, A.C. Glerum, and W. Spakman. Efficient and Practical Newton Solvers for Nonlinear Stokes Systems in Geodynamic Problems. *Geophys. J. Int.*, 2019.
- [873] S. Frederiksen and J. Braun. Numerical modelling of strain localisation during extension of the continental lithosphere. *Earth Planet. Sci. Lett.*, 188:241–251, 2001.
- [874] Susanne Frederiksen, Søren Bom Nielsen, and Niels Balling. A numerical dynamic model for the norwegian–danish basin. *Tectonophysics*, 343(3-4):165–183, 2001.
- [875] Susanne Frederiksen, Søren Bom Nielsen, and Niels Balling. Post-permian evolution of the central north sea: a numerical model. *Tectonophysics*, 343(3-4):185–203, 2001.
- [876] R. Freeburn, P. Bouilhol, B. Mauder, V. Magni, and J. van Hunen. Numerical models of the magmatic processes induced by slab breakoff. *Earth Planet. Sci. Lett.*, 478:203–213, 2017.
- [877] J. Freeman, L. Moresi, and D.A. May. Evolution into the stagnant lid convection regime with a non-newtonian water ice rheology. *Geophys. Res. Lett.*, 31, 2004.
- [878] J Freeman, L Moresi, and DA May. Thermal convection with a water ice i rheology: Implications for icy satellite evolution. *Icarus*, 180(1):251–264, 2006.
- [879] M. Frehner. 3D fold growth rates. *Terra Nova*, 26:417–424, 2014.
- [880] Marcel Frehner. The neutral lines in buckle folds. *Journal of Structural Geology*, 33(10):1501–1508, 2011.
- [881] Marcel Frehner and Ulrike Exner. Strain and foliation refraction patterns around buckle folds. *Geological Society, London, Special Publications*, 394(1):21–37, 2014.
- [882] Marcel Frehner, Ulrike Exner, Neil S Mancktelow, and Djordje Grujic. The not-so-simple effects of boundary conditions on models of simple shear. *Geology*, 39(8):719–722, 2011.
- [883] Marcel Frehner, Anna Hui Mee Ling, and Isabelle Gärtner-Roer. Furrow-and-ridge morphology on rock-glaciers explained by gravity-driven buckle folding: A case study from the murtèl rockglacier (switzerland). *Permafrost and Periglacial Processes*, 26(1):57–66, 2015.
- [884] Marcel Frehner and Stefan M Schmalholz. Numerical simulations of parasitic folding in multilayers. *Journal of Structural Geology*, 28(9):1647–1657, 2006.
- [885] Marcel Frehner and Timothy Schmid. Parasitic folds with wrong vergence: How pre-existing geometrical asymmetries can be inherited during multilayer buckle folding. *Journal of Structural Geology*, 87:19–29, 2016.
- [886] Scott W French and Barbara Romanowicz. Broad plumes rooted at the base of the earth’s mantle beneath major hotspots. *Nature*, 525(7567):95, 2015.
- [887] P.J. Frey and P.-L. George. *Mesh generation*. Hermes Science, 2000.
- [888] EH Fritzell, AL Bull, and GE Shephard. Closure of the mongol–okhotsk ocean: Insights from seismic tomography and numerical modelling. *Earth and Planetary Science Letters*, 445:1–12, 2016.

- [889] Jörg Frohne, Timo Heister, and Wolfgang Bangerth. Efficient numerical methods for the large-scale, parallel solution of elastoplastic contact problems. *International Journal for Numerical Methods in Engineering*, 105(6):416–439, 2016.
- [890] C. Froidevaux. Energy dissipation and geometric structure at spreading plate boundaries. *Earth Planet. Sci. Lett.*, 20:419–424, 1973.
- [891] L. Fuchs and Th.W. Becker. Role of strain-dependent weakening memory on the style of mantle convection and plate boundary stability. *Geophys. J. Int.*, 218:601–618, 2019.
- [892] L. Fuchs, H. Koyi, and H. Schmeling. Numerical modeling of the effect of composite rheology on internal deformation in down-built diapirs. *Tectonophysics*, 646:79–95, 2015.
- [893] L. Fuchs and H. Schmeling. A new numerical method to calculate inhomogeneous and time-dependent large deformation of two-dimensional geodynamic flows with application to diapirism. *Geophys. J. Int.*, 194(2):623–639, 2013.
- [894] Hiromi Fujimoto and Yoshibumi Tomoda. Lithospheric thickness anomaly near the trench and possible driving force of subduction. *Tectonophysics*, 112(1-4):103–110, 1985.
- [895] Y. Fukao, S. Widjiantoro, and M. Obayashi. Stagnant slabs in the upper and lower mantle transition region. *Reviews of Geophysics*, 39:291–323, 2001.
- [896] Yoshio Fukao and Masayuki Obayashi. Subducted slabs stagnant above, penetrating through, and trapped below the 660 km discontinuity. *Journal of Geophysical Research: Solid Earth*, 118(11):5920–5938, 2013.
- [897] T. Fukuchi. Numerical calculation of fully-developed laminar flows in arbitrary cross-sections using finite difference method. *AIP Advances*, 1:042109, 2011.
- [898] J. Fullea, J.C. Afonso, J.A.D. Connolly, M. Fernandez, D. Garcia-Castellanos, and H. Zeyen. Lit-Mod3D: An interactive 3-D software to model the thermal, compositional, density, seismological, and rheological structure of the lithosphere and sublithospheric upper mantle. *Geochem. Geophys. Geosyst.*, 10(8):doi:10.1029/2009GC002391, 2009.
- [899] J. Fullea, M. Fernandez, J.C. Afonso, J. Verges, and H. Zeyen. The structure and evolution of the lithosphereasthenosphere boundary beneath the AtlanticMediterranean Transition Region. *Lithos*, 120(1–2):74–95, 2010.
- [900] Ch.W. Fuller, S.D. Willett, and M.T. Brandon. Formation of forearc basins and their influence on subduction zone earthquakes. *Geology*, 34(2):65–68, 2006.
- [901] P. Fullsack. An arbitrary Lagrangian-Eulerian formulation for creeping flows and its application in tectonic models. *Geophys. J. Int.*, 120:1–23, 1995.
- [902] F. Funiciello, C Faccenna, Arnauld Heuret, Serge Lallemand, Erika Di Giuseppe, and TW Becker. Trench migration, net rotation and slab–mantle coupling. *Earth and Planetary Science Letters*, 271(1-4):233–240, 2008.
- [903] F. Funiciello, K. Regenauer-Lieb G. Morra, and D. Giardini. Dynamics of retreating slabs: 1. Insights from two-dimensional numerical experiments. *J. Geophys. Res.*, 108(B4):2206, 2003.
- [904] F. Funiciello, M. Moroni, C. Piromallo, C. Faccenna, A. Cenedese, and H.A. Bui. Mapping mantle flow during retreating subduction: Laboratory models analyzed by feature tracking. *J. Geophys. Res.*, 111(B03402), 2006.
- [905] KP Furlong and Rob Govers. Ephemeral crustal thickening at a triple junction: The Mendocino crustal conveyor. *GEOLOGY*, 27(2):127, 1999.
- [906] Mikito Furuichi. Numerical modeling of three dimensional self-gravitating stokes flow problem with free surface. *Procedia Computer Science*, 4:1506–1515, 2011.
- [907] M. Furuichi, M. Kameyama, and A. Kageyama. Three-dimensional Eulerian method for large deformation of viscoelastic fluid: Toward plate-mantle simulation. *J. Comp. Phys.*, 227:4977–4997, 2008.
- [908] M. Furuichi and D. Nishiura. Robust coupled fluid-particle simulation scheme in Stokes-flow regime: Toward the geodynamic simulation including granular media. *Geochem. Geophys. Geosyst.*, 15:2865–2882, 2014.
- [909] Mikito Furuichi, Dave A May, and Paul J Tackley. Development of a stokes flow solver robust to large viscosity jumps using a schur complement approach with mixed precision arithmetic. *Journal of Computational Physics*, 230(24):8835–8851, 2011.
- [910] Carl W Gable, Richard J O'connell, and Bryan J Travis. Convection in three dimensions with surface plates: Generation of toroidal flow. *Journal of Geophysical Research: Solid Earth*, 96(B5):8391–8405, 1991.

- [911] Sébastien Gac, Ritske S Huismans, Nina SC Simon, Jan Inge Faleide, and Yuri Y Podladchikov. Effects of lithosphere buckling on subsidence and hydrocarbon maturation: a case-study from the ultra-deep east barents sea basin. *Earth and Planetary Science Letters*, 407:123–133, 2014.
- [912] Sébastien Gac, Ritske S Huismans, Nina SC Simon, Yuri Y Podladchikov, and Jan Inge Faleide. Formation of intracratonic basins by lithospheric shortening and phase changes: a case study from the ultra-deep east barents sea basin. *Terra Nova*, 25(6):459–464, 2013.
- [913] J. B. Gaherty and B. H. Hager. Compositional vs. thermal buoyancy and the evolution of subducted lithosphere. *Geophysical Research Letters*, 21(2):141–144, 1994.
- [914] Sashikumaar Ganesan, Gunar Matthies, and Lutz Tobiska. Local projection stabilization of equal order interpolation applied to the stokes problem. *Mathematics of Computation*, 77(264):2039–2060, 2008.
- [915] J. Ganne, M. Gerbault, and S. Block. Thermo-mechanical modeling of lower crust exhumation – Constraints from the metamorphic record of the Palaeoproterozoic Eburnean orogeny, West African Craton. *Precambrian Research*, 243:88–109, 2014.
- [916] D Garcia-Castellanos, M Fernández, and M Torne. Numerical modeling of foreland basin formation: a program relating thrusting, flexure, sediment geometry and lithosphere rheology. *Computers & Geosciences*, 23(9):993–1003, 1997.
- [917] Daniel Garcia-Castellanos. Interplay between lithospheric flexure and river transport in foreland basins. *Basin Research*, 14(2):89–104, 2002.
- [918] F. Garel, S. Goes, D.R. Davies, J.H. Davies, S.C. Kramer, and C.R. Wilson. Interaction of subducted slabs with the mantle transition-zone: A regime diagram from 2-D thermo-mechanical models with a mobile trench and an overriding plate. *Geochem. Geophys. Geosyst.*, 15(1739–1765):doi:10.1002/2014GC005257, 2014.
- [919] Rao Garimella. Conformal refinement of unstructured quadrilateral meshes. pages 31–44, 2009.
- [920] Edward J Garnero. Heterogeneity of the lowermost mantle. *Annual Review of Earth and Planetary Sciences*, 28(1):509–537, 2000.
- [921] E.J. Garnero and A.K. McNamara. Structure and Dynamics of Earths Lower Mantle. *Science*, 320:626–628, 2008.
- [922] D.K. Gartling. Nachos - a finite element computer program for incompressible flow problems. Technical Report Sand77-1333, Sandia Laboratories, 1978.
- [923] E. Garzanti, G. Radeff, and M.G. Malus. Slab breakoff: A critical appraisal of a geological theory as applied in space and time. *Earth-Science Reviews*, 177:303–319, 2018.
- [924] R. Gassmöller, J. Dannberg, E. Bredow, B. Steinberger, and T. H. Torsvik. Major influence of plume-ridge interaction, lithosphere thickness variations, and global mantle flow on hotspot volcanism-the example of tristan. *Geochem. Geophys. Geosyst.*, 17(4):1454–1479, 2016.
- [925] R. Gassmöller, H. Lokavarapu, E. M. Heien, E. G. Puckett, and W. Bangerth. Flexible and scalable particle-in-cell methods with adaptive mesh refinement for geodynamic computations. *Geochem. Geophys. Geosyst.*, 19(9):3596–3604, 2018.
- [926] Rene Gassmöller, Harsha Lokavarapu, Wolfgang Bangerth, and Gerry Puckett. Evaluating the accuracy of hybrid finite element/particle-in-cell methods for modelling incompressible stokes flow. *Geophy. J. Int.*, 2019.
- [927] Thomas B Gatski. Review of incompressible fluid flow computations using the vorticity-velocity formulation. *Applied Numerical Mathematics*, 7(3):227–239, 1991.
- [928] Pierre Gautier, Jean-Pierre Brun, Richard Moriceau, Dimitrios Sokoutis, Joseph Martinod, and Laurent Jolivet. Timing, kinematics and cause of aegean extension: a scenario based on a comparison with simple analogue experiments. *Tectonophysics*, 315(1-4):31–72, 1999.
- [929] Andrey A Gavrilov, Konstantin A Finnikov, and Evgeny V Podryabinkin. Modeling of steady herschel–bulkley fluid flow over a sphere. *Journal of Engineering Thermophysics*, 26(2):197–215, 2017.
- [930] T. Geenen, M. ur Rehman, S.P. MacLahlan, G. Segal, C. Vuik, A.P. van den Berg, and W. Spakman. Scalable robust solvers for unstructured FE geodynamic modeling applications: Solving the Stokes equation for models with large localized viscosity contrasts. *Geochem. Geophys. Geosyst.*, 10(9), 2009.
- [931] L. Gemmer, C. Beaumont, and S. Ings. Dynamic modelling of passive margin salt tectonics: effects of water loading, sediment properties and sedimentation patterns. *Basin Research*, 17:383–402, 2005.
- [932] L. Gemmer, S.J. Ings, S. Medvedev, and C. Beaumont. Salt tectonics driven by differential sediment loading: stability analysis and finite-element experiments. *Basin Research*, 16:199–218, 2004.

- [933] L. Geoffroy, E.B. Burov, and P. Werner. Volcanic passive margins: another way to break up continents. *Scientific Reports*, 5:DOI:10.1038/srep14828, 2015.
- [934] O A George, R Malservisi, Rob Govers, C B Connor, and L J Connor. Is uplift of volcano clusters in the Tohoku Volcanic Arc, Japan, driven by magma accumulation in hot zones? A geodynamic modeling study. *Journal Of Geophysical Research*, 121:4780–4796, 2016.
- [935] P.-L. George and H. Borouchaki. *Delaunay Triangulation and Meshing*. Hermès, 1998.
- [936] E.H. Georgoulis. Discontinuous Galerkin Methods for Linear Problems: An Introduction. In E.H. Georgoulis, A. Iske, and J. Levesley, editors, *Approximation algorithms for Complex Systems*, pages 91–126. Springer-Verlag, Berlin Heidelberg, 2011.
- [937] Gianluca Gerardi, Neil M Ribe, and Paul J Tackley. Plate bending, energetics of subduction and modeling of mantle convection: A boundary element approach. *Earth and Planetary Science Letters*, 515:47–57, 2019.
- [938] M. Gerault, T.W. Becker, B.J.P. Kaus, C. Faccenna, L. Moresi, and L. Husson. The role of slabs and oceanic plate geometry in the net rotation of the lithosphere, trench motions, and slab return flow. *Geochem. Geophys. Geosyst.*, 13(4):Q04001, doi:10.1029/2011GC003934, 2012.
- [939] M. Gérald, L. Husson, M.S. Miller, and E.D. Humphreys. Flat-slab subduction, topography, and mantle dynamics in southwestern Mexico. *Tectonics*, 34:10.1002/2015TC003908, 2015.
- [940] M. Gerbault. Pressure conditions for shear and tensile failure around a circular magma chamber; insight from elasto-plastic modelling. *Geological Society, London, Special Publications*, 367:111–130, 2012.
- [941] M. Gerbault, F. Cappa, and R. Hassani. Elasto-plastic and hydromechanical models of failure around an infinitely long magma chamber. *Geochem. Geophys. Geosyst.*, 13(3):doi:10.1029/2011GC003917, 2012.
- [942] M. Gerbault, F. Davey, and S. Henrys. Three-dimensional lateral crustal thickening in continental oblique collision: an example from the Southern Alps, New Zealand. *Geophy. J. Int.*, 150:770–779, 2002.
- [943] M. Gerbault, R. Hassani, C. Novoa Lizama, and A. Souche. Three-Dimensional Failure Patterns Around an Inflating Magmatic Chamber. *Geochem. Geophys. Geosyst.*, 19:749–771, 2018.
- [944] M. Gerbault, S. Henrys, and F. Davey. Numerical models of lithospheric deformation forming the Southern Alps of New Zealand. *J. Geophys. Res.*, 108(B7), 2003.
- [945] M. Gerbault, A.N.B. Poliakov, and M. Daignieres. Prediction of faulting from the theories of elasticity and plasticity: what are the limits? *Journal of Structural Geology*, 20:301–320, 1998.
- [946] M. Gerbault and W. Willingshofer. Lower crust indentation or horizontal ductile flow during continental collision? *Tectonophysics*, 387:169–187, 2004.
- [947] Muriel Gerbault, José Cembrano, C Mpodozis, M Farias, and M Pardo. Continental margin deformation along the andean subduction zone: Thermo-mechanical models. *Physics of the Earth and Planetary Interiors*, 177(3-4):180–205, 2009.
- [948] Muriel Gerbault, Julie Schneider, A Reverso-Peila, and Michel Corsini. Crustal exhumation during ongoing compression in the variscan maures-tanneron massif, france-geological and thermo-mechanical aspects. *Tectonophysics*, 746:439–458, 2018.
- [949] T. Gerya. Dynamical instability produces transform faults at mid-ocean ridges. *Science*, 329:1047–1050, 2010.
- [950] T. Gerya. Future directions in subduction modeling. *Journal of Geodynamics*, 52:344–378, 2011.
- [951] T. Gerya and B. Stöckhert. Two-dimensional numerical modeling of tectonic and metamorphic histories at active continental margins. *Int J Earth Sci (Geol Rundsch)*, 95:250–274, 2006.
- [952] T. Gerya and D.A. Yuen. Robust characteristics method for modelling multiphase visco-elasto-plastic thermo-mechanical problems. *Phys. Earth. Planet. Inter.*, 163:83–105, 2007.
- [953] Taras Gerya. *Numerical Geodynamic Modelling*. Cambridge University Press, 2010.
- [954] Taras Gerya. Precambrian geodynamics: concepts and models. *Gondwana Research*, 25(2):442–463, 2014.
- [955] Taras Gerya. Geodynamics of the early earth: Quest for the missing paradigm. *Geology*, 47(10):1006–1007, 2019.
- [956] Taras Gerya. *Numerical Geodynamic Modelling - 2nd edition*. Cambridge University Press, 2019.
- [957] Taras Gerya and Evgueni Burov. Nucleation and evolution of ridge-ridge-ridge triple junctions: Thermo-mechanical model and geometrical theory. *Tectonophysics*, 746:83–105, 2018.
- [958] Taras V Gerya. Three-dimensional thermomechanical modeling of oceanic spreading initiation and evolution. *Physics of the Earth and Planetary Interiors*, 214:35–52, 2013.

- [959] Taras V Gerya, Bernhard Stöckhert, and Alexey L Perchuk. Exhumation of high-pressure metamorphic rocks in a subduction channel: A numerical simulation. *Tectonics*, 21(6):6–1, 2002.
- [960] Taras V Gerya, Ronald Uken, Juergen Reinhardt, Michael K Watkeys, Walter V Maresch, and Brendan M Clarke. "cold" diapirs triggered by intrusion of the bushveld complex: Insight from two-dimensional numerical modeling. *Special Papres – Geological Society of America*, pages 117–128, 2004.
- [961] TV Gerya. Intra-oceanic subduction zones. In *Arc-continent collision*, pages 23–51. Springer, 2011.
- [962] TV Gerya. Initiation of transform faults at rifted continental margins: 3d petrological-thermomechanical modeling and comparison to the woodlark basin. *Petrology*, 21(6):550–560, 2013.
- [963] TV Gerya. Plume-induced crustal convection: 3d thermomechanical model and implications for the origin of novae and coronae on venus. *Earth and Planetary Science Letters*, 391:183–192, 2014.
- [964] T.V. Gerya and J.-P. Burg. Intrusion of ultramafic magmatic bodies into the continental crust: Numerical simulation. *Phys. Earth. Planet. Inter.*, 160:124–142, 2007.
- [965] T.V. Gerya, J.A.D. Connolly, and D.A. Yuen. Why is terrestrial subduction one-sided ? *Geology*, 36(1):43–46, 2008.
- [966] T.V. Gerya, J.A.D. Connolly, D.A. Yuen, W. Gorczyk, and A.M. Capel. Seismic implications of mantle wedge plumes. *Phys. Earth. Planet. Inter.*, 156:59–74, 2006.
- [967] T.V. Gerya, D. Fossati, C. Cantieni, and D. Seward. Dynamic effects of aseismic ridge subduction: numerical modelling. *Eur. J. Mineral*, 21:649–661, 2009.
- [968] T.V. Gerya, D.A. May, and T. Duretz. An adaptive staggered grid finite difference method for modeling geodynamic Stokes flows with strongly variable viscosity. *Geochem. Geophys. Geosyst.*, 14(4), 2013.
- [969] T.V. Gerya and F.I. Meilick. Geodynamic regimes of subduction under an active margin: effects of rheological weakening by fluids and melts. *Journal of Metamorphic Geology*, 29:7–31, 2011.
- [970] TV Gerya, LL Perchuk, and J-P Burg. Transient hot channels: perpetrating and regurgitating ultrahigh-pressure, high-temperature crust–mantle associations in collision belts. *Lithos*, 103(1-2):236–256, 2008.
- [971] T.V. Gerya, L.L. Perchuk, W.V. Maresch, and A.P. Willner. Inherent gravitational instability of hot continental crust: Implications for doming and diapirism in granulite facies terrains. *Geological Society of America*, 380:97–115, 2004.
- [972] T.V. Gerya, R.J. Stern, M.Baes, S.V. Sobolev, and S.A. Whattam. Plate tectonics on the Earth triggered by plume-induced subduction initiation. *Nature*, 527, 2015.
- [973] T.V. Gerya, R. Uken, J. Reinhardt, M. Watkeys, W.V. Maresch, and B.M. Clarke. Cold fingers in a hot magma: Numerical modeling of country-rock diapirs in the Bushveld Complex, South Africa. *Geology*, 31(9):753–756, 2003.
- [974] T.V. Gerya and D.A. Yuen. Characteristics-based marker-in-cell method with conservative finite-differences schemes for modeling geological flows with strongly variable transport properties. *Phys. Earth. Planet. Inter.*, 140:293–318, 2003.
- [975] T.V. Gerya and D.A. Yuen. Rayleigh-Taylor instabilities from hydration and melting propel 'cold plumes' at subduction zones. *Earth Planet. Sci. Lett.*, 212:47–62, 2003.
- [976] T.V. Gerya, D.A. Yuen, and W.V. Maresch. Thermomechanical modelling of slab detachment. *Earth Planet. Sci. Lett.*, 226:101–116, 2004.
- [977] T.V. Gerya, D.A. Yuen, and E.O.D. Sevre. Dynamical causes for incipient magma chambers above slabs. *Geology*, 32(1):89–92, 2004.
- [978] Klaus Gessner, Chris Wijns, and Louis Moresi. Significance of strain localization in the lower crust for structural evolution and thermal history of metamorphic core complexes. *Tectonics*, 26(2), 2007.
- [979] R.K. Ghazian and S.J.H. Buiter. A numerical investigation of continental collision styles. *GJI*, 2013.
- [980] R.K. Ghazian and S.J.H. Buiter. Numerical modelling of the role of salt in continental collision: An application to the southeast Zagros fold-and-thrust belt. *Tectonophysics*, 632:96–110, 2014.
- [981] S. Ghelichkhan and H.-P. Bunge. The adjoint equations for thermochemical compressible mantle convection: Derivation and verification by twin experiments. *Proceedings of the Royal Society A: Mathematical, Physical and Engineering Sciences*, 474(2220), 2018.
- [982] Siavash Ghelichkhan and Hans-Peter Bunge. The compressible adjoint equations in geodynamics: derivation and numerical assessment. *GEM-International Journal on Geomathematics*, 7(1):1–30, 2016.
- [983] U. Ghia, K.N. Ghia, and C.T. Shin. High-Re Solutions for incompressible flow using the Navier-Stokes equations and a multigrid method. *J. Comp. Phys.*, 48:387–411, 1982.

- [984] A. Ghosh, T. W. Becker, and S. J. Zhong. Effects of lateral viscosity variations on the geoid: Lvv geoid. *Geophysical Research Letters*, 37(1), 2010.
- [985] A. Ghosh, TW Becker, and ED Humphreys. Dynamics of the north american continent. *Geophysical Journal International*, 194(2):651–669, 2013.
- [986] A. Ghosh, WE Holt, and L. Wen. Predicting the lithospheric stress field and plate motions by joint modeling of lithosphere and mantle dynamics. *Journal of Geophysical Research: Solid Earth*, 118(1):346–368, 2013.
- [987] A. Ghosh, WE Holt, L. Wen, AJ Haines, and LM Flesch. Joint modeling of lithosphere and mantle dynamics elucidating lithosphere-mantle coupling. *Geophysical Research Letters*, 35(16), 2008.
- [988] Attreyee Ghosh and William E Holt. Plate motions and stresses from global dynamic models. *Science*, 335(6070):838–843, 2012.
- [989] Attreyee Ghosh, William E Holt, and Lucy M Flesch. Contribution of gravitational potential energy differences to the global stress field. *Geophysical Journal International*, 179(2):787–812, 2009.
- [990] Attreyee Ghosh, G Thyagarajulu, and Bernhard Steinberger. The importance of upper mantle heterogeneity in generating the indian ocean geoid low. *Geophysical Research Letters*, 44(19):9707–9715, 2017.
- [991] G. Gibert, M. Gerbault, R. Hassani, and E. Tric. Dependency of slab geometry on absolute velocities and conditions for cyclicity: insights from numerical modelling. *Geophy. J. Int.*, 189:747–760, 2012.
- [992] Frederic Gibou, Ronald Fedkiw, and Stanley Osher. A review of level-set methods and some recent applications. *Journal of Computational Physics*, 353:82–109, 2018.
- [993] JA Gil and Maria José Jurado. Geological interpretation and numerical modelling of salt movement in the barbastro–balaguer anticline, southern pyrenees. *Tectonophysics*, 293(3-4):141–155, 1998.
- [994] A.R. Gilchrist, H. Kooi, and C. Beaumont. Post-gondwana geomorphic evolution of southwestern africa: implications for the controls on landscape development from observations and numerical experiments. *Journal of Geophysical Research*, 99(B6):12,211–12,228, 1994.
- [995] Cedric Gillmann and Paul Tackley. Atmosphere/mantle coupling and feedbacks on venus. *Journal of Geophysical Research: Planets*, 119(6):1189–1217, 2014.
- [996] Daniele Giordano, James K Russell, and Donald B Dingwell. Viscosity of magmatic liquids: a model. *Earth and Planetary Science Letters*, 271(1-4):123–134, 2008.
- [997] Carlo Giunchi, Roberto Sabadini, Enzo Boschi, and Paolo Gasperini. Dynamic models of subduction: geophysical and geological evidence in the tyrrhenian sea. *Geophysical Journal International*, 126(2):555–578, 1996.
- [998] E. Di Giuseppe, J. van Hunen, F. Funiciello, C. Faccenna, and D. Giardini. Slab stiffness control of trench motion: Insights from numerical models. *Geochem. Geophys. Geosyst.*, 9(2), 2008.
- [999] G.A. Glatzmaier. Numerical simulations of mantle convection: Time-dependent, three-dimensional, compressible, spherical shell. *Geophys. Astrophys. Fluid Dyn.*, 43:223–264, 1988.
- [1000] G.C. Gleason and J. Tullis. A flow law for dislocation creep of quartz aggregates determined with the molten salt cell. *Tectonophysics*, 247:1–23, 1995.
- [1001] John W Glen. The creep of polycrystalline ice. *Proceedings of the Royal Society of London. Series A. Mathematical and Physical Sciences*, 228(1175):519–538, 1955.
- [1002] A. Glerum, C. Thieulot, M. Fraters, C. Blom, and W. Spakman. Nonlinear viscoplasticity in ASPECT: benchmarking and applications to subduction. *Solid Earth*, 9(2):267–294, 2018.
- [1003] P Glišović, AM Forte, and Robert Moucha. Time-dependent convection models of mantle thermal structure constrained by seismic tomography and geodynamics: implications for mantle plume dynamics and cmb heat flux. *Geophysical Journal International*, 190(2):785–815, 2012.
- [1004] Petar Glišović, Alessandro M Forte, and Michael W Ammann. Variations in grain size and viscosity based on vacancy diffusion in minerals, seismic tomography, and geodynamically inferred mantle rheology. *Geophysical Research Letters*, 42(15):6278–6286, 2015.
- [1005] R. Glowinski. *Handbook of Numerical Analysis, vol IX: Numerical methods for fluids*. North-Holland, 2003.
- [1006] Vincent Godard, R Cattin, and J Lavé. Numerical modeling of mountain building: Interplay between erosion law and crustal rheology. *Geophysical Research Letters*, 31(23), 2004.
- [1007] Vincent Godard, Jérôme Lavé, and Rodolphe Cattin. Numerical modelling of erosion processes in the himalayas of nepal: Effects of spatial variations of rock strength and precipitation. *Geological Society, London, Special Publications*, 253(1):341–358, 2006.

- [1008] Heiko Goelzer, Alexander Robinson, Helene Seroussi, and Roderik Sw Van De Wal. Recent progress in greenland ice sheet modelling. *Current climate change reports*, 3(4):291–302, 2017.
- [1009] S. Goes, F. Cammarano, and U. Hansen. Synthetic seismic signature of thermal mantle plumes. *Earth and Planetary Science Letters*, 218(3-4):403–419, 2004.
- [1010] S Goes, JJP Loohuis, MJR Wortel, and Rob Govers. The effect of plate stresses and shallow mantle temperatures on tectonics of northwestern Europe. *Global and Planetary Change*, 27(1-4):23–38, 2000.
- [1011] Saskia Goes, Roberto Agrusta, Jeroen Van Hunen, and Fanny Garel. Subduction-transition zone interaction: A review. *Geosphere*, 13(3):644–664, 2017.
- [1012] Saskia Goes, FA Capitanio, Gabriele Morra, M Seton, and D Giardini. Signatures of downgoing plate-buoyancy driven subduction in cenozoic plate motions. *Physics of the Earth and Planetary Interiors*, 184(1-2):1–13, 2011.
- [1013] Saskia Goes, Fabio A Capitanio, and Gabriele Morra. Evidence of lower-mantle slab penetration phases in plate motions. *Nature*, 451(7181):981, 2008.
- [1014] C. Goetze and B. Evans. Stress and temperature in the bending lithosphere as constrained by experimental rock mechanics. *GJI*, 59(3):463–478, 1979.
- [1015] Oguz H. Gogus. Rifting and subsidence following lithospheric removal in continental back arcs. *Geology*, page doi:10.1130/G36305.1, 2014.
- [1016] Oğuz H Göğüş and Russell N Pysklywec. Mantle lithosphere delamination driving plateau uplift and synconvergent extension in eastern anatolia. *Geology*, 36(9):723–726, 2008.
- [1017] Oğuz H Göğüş, Russell N Pysklywec, Fabio Corbi, and Claudio Faccenna. The surface tectonics of mantle lithosphere delamination following ocean lithosphere subduction: Insights from physical-scaled analogue experiments. *Geochemistry, Geophysics, Geosystems*, 12(5), 2011.
- [1018] Oğuz H Göğüş and Kosuke Ueda. Peeling back the lithosphere: Controlling parameters, surface expressions and the future directions in delamination modeling. *Journal of Geodynamics*, 117:21–40, 2018.
- [1019] GJ Golabek, TV Gerya, BJP Kaus, R Ziethe, and PJ Tackley. Rheological controls on the terrestrial core formation mechanism. *Geochemistry, Geophysics, Geosystems*, 10(11), 2009.
- [1020] Gregor J Golabek, Bernard Bourdon, and Taras V Gerya. Numerical models of the thermomechanical evolution of planetesimals: Application to the acapulcoite-lodranite parent body. *Meteoritics & Planetary Science*, 49(6):1083–1099, 2014.
- [1021] Gregor J Golabek, Tobias Keller, Taras V Gerya, Guizhi Zhu, Paul J Tackley, and James AD Connolly. Origin of the martian dichotomy and tharsis from a giant impact causing massive magmatism. *Icarus*, 215(1):346–357, 2011.
- [1022] Gregor J Golabek, Harro Schmeling, and Paul J Tackley. Earth’s core formation aided by flow channelling instabilities induced by iron diapirs. *Earth and Planetary Science Letters*, 271(1-4):24–33, 2008.
- [1023] DL Goldsby and DL Kohlstedt. Superplastic deformation of ice: Experimental observations. *Journal of Geophysical Research: Solid Earth*, 106(B6):11017–11030, 2001.
- [1024] G. Goltz and M. Böse. Configurational entropy of critical earthquake populations. *Geophys. Res. Lett.*, 29(20), 2002.
- [1025] G.H. Golub and C.F. van Loan. *Matrix Computations, 4th edition*. John Hopkins University Press, 2013.
- [1026] W. Gorczyk, T.V. Gerya, J.A.D. Connolly, and D.A. Yuen. Growth and mixing dynamics of mantle wedge plumes. *Geology*, 35(7):587–590, 2007.
- [1027] W. Gorczyk, T.V. Gerya, J.A.D. Connolly, D.A. Yuen, and M. Rudolph. Large-scale rigid-body rotation in the mantle wedge and its implications for seismic tomography . *Geochem. Geophys. Geosyst.*, 7(5):10.1029/2005GC001075, 2006.
- [1028] W. Gorczyk, H. Smithies, F. Korhonen, H. Howard, and R. Quentin De Gromard. Ultra-hot Mesoproterozoic evolution of intracontinental central Australia. *Geoscience Frontiers*, 6(1):23–37, 2014.
- [1029] Weronika Gorczyk, Stéphane Guillot, Taras V Gerya, and Kéiko Hattori. Asthenospheric upwelling, oceanic slab retreat, and exhumation of uhp mantle rocks: Insights from greater antilles. *Geophysical Research Letters*, 34(21), 2007.
- [1030] Weronika Gorczyk, Bruce Hobbs, and Taras Gerya. Initiation of rayleigh–taylor instabilities in intra-cratonic settings. *Tectonophysics*, 514:146–155, 2012.
- [1031] Weronika Gorczyk, Arne P Willner, Taras V Gerya, James AD Connolly, and Jean-Pierre Burg. Physical controls of magmatic productivity at pacific-type convergent margins: Numerical modelling. *Physics of the Earth and Planetary Interiors*, 163(1-4):209–232, 2007.

- [1032] H Gossman. Slope modelling with changing boundary conditions-effects of climate and lithology. *Z. Geomorph. NF*, 25:72–88, 1976.
- [1033] R. Goteti, C. Beaumont, and S.J. Ings. Factors controlling early stage salt tectonics at rifted continental margins and their thermal consequences. *J. Geophys. Res.*, 117:1–31, 2013.
- [1034] R. Goteti, S.J. Ings, and C. Beaumont. Development of salt minibasins initiated by sedimentary topographic relief. *Earth and Planetary Science Letters*, 339–340:103–116, 2012.
- [1035] Klaus-D Gottschaldt, Uwe Walzer, Dave R Stegman, John R Baumgardner, and Hans B Mühlhaus. Mantle dynamics—a case study. In *Advances in Geocomputing*, pages 139–181. Springer, 2009.
- [1036] S. Gourvenec. Bearing capacity under combined loading. In *9th Australia New Zealand Conference on Geomechanics, Auckland, New Zealand, 8-11 february 2004.*, 2004.
- [1037] S. Gourvenec and M. Randolph. Effect of strength non-homogeneity on the shape of failure envelopes for combined loading of strip and circular foundations on clay. *Géotechnique*, 53:575–586, 2003.
- [1038] S. Gourvenec, M. Randolph, and O. Kingsnorth. Undrained bearing capacity of square and rectangular footings. *International Journal of Geomechanics*, 6:147–157, 2006.
- [1039] R Govers and MJR Wortel. Initiation of asymmetric extension in continental lithosphere. *Tectonophysics*, 223(1-2):75–96, 1993.
- [1040] R. Govers and M.J.R. Wortel. Extension of stable continental lithosphere and the initiation of lithospheric scale faults. *Tectonics*, 14(4):1041–1055, 1995.
- [1041] R. Govers and M.J.R. Wortel. Some remarks on the relation between vertical motions of the lithosphere during extension and the necking depth parameter inferred from kinematic modeling studies. *J. Geophys. Res.*, 104:23,245–23,253, 1999.
- [1042] R. Govers and M.J.R. Wortel. Lithosphere tearing at STEP faults: Response to edges of subduction zones. *Earth Planet. Sci. Lett.*, 236:505–523, 2005.
- [1043] Rob Govers, K P Furlong, L van de Wiel, M W Herman, and T Broerse. The Geodetic Signature of the Earthquake Cycle at Subduction Zones: Model Constraints on the Deep Processes. *Reviews Of Geophysics*, 56:6–49, 2018.
- [1044] Rob Govers and PT Meijer. On the dynamics of the Juan de Fuca plate. *Earth And Planetary Science Letters*, 189(3-4):115–131, 2001.
- [1045] Shea Goyette, Masa Takatsuka, Stuart Clark, R Dietmar Müller, Patrice Rey, and Dave R Stegman. Increasing the usability and accessibility of geodynamic modelling tools to the geoscience community: Underworldgui. *Visual Geosciences*, 13(1):25–36, 2008.
- [1046] Alexia Grabkowiak. *Analyse du gode et sparation des sources pour la comprhension de l'organisation verticale des anomalies de masse dans le manteau*. PhD thesis, Institut de Physique du Globe de Paris, 2017.
- [1047] S. Gradmann and C. Beaumont. Coupled fluid flow and sediment deformation in margin-scale salt-tectonic systems: 2. Layered sediment models and application to the northwestern Gulf of Mexico. *Tectonics*, 31(TC4011), 2012.
- [1048] S. Gradmann and C. Beaumont. Numerical modelling study of mechanisms of mid-basin salt canopy evolution and their potential applications to the northwestern gulf of mexico. *Basin Research*, 29(4):490–520, 2017.
- [1049] S. Gradmann, C. Beaumont, and M. Albertz. Factors controlling the evolution of the Perdido Fold Belt, northwestern Gulf of Mexico, determined from numerical models. *Tectonics*, 28(TC2002), 2009.
- [1050] S. Gradmann, C. Beaumont, and S.J. Ings. Coupled fluid flow and sediment deformation in margin-scale salt-tectonic systems: 1. development and application of simple, single-lithology models. *Tectonics*, 31(4), 2012.
- [1051] J. Grandy. Efficient computation of volume of hexahedral cells. Technical Report UCRL-ID-128886, Lawrence Livermore National Laboratory, 1997.
- [1052] Ronni Grapenthin. Computer programing for geosciences: Teach your students how to make tools. *Eos, Transactions American Geophysical Union*, 92(50):469–470, 2011.
- [1053] Bernhard Grasemann and Neil S Mancktelow. Two-dimensional thermal modelling of normal faulting: the simplon fault zone, central alps, switzerland. *Tectonophysics*, 225(3):155–165, 1993.
- [1054] Bernhard Grasemann and Stefan M Schmalholz. Lateral fold growth and fold linkage. *Geology*, 40(11):1039–1042, 2012.

- [1055] Fabien Graveleau, J-E Hurtrez, Stéphane Dominguez, and Jacques Malavieille. A new experimental material for modeling relief dynamics and interactions between tectonics and surface processes. *Tectonophysics*, 513(1-4):68–87, 2011.
- [1056] Fabien Graveleau, Jacques Malavieille, and Stéphane Dominguez. Experimental modelling of orogenic wedges: A review. *Tectonophysics*, 538:1–66, 2012.
- [1057] R. Gray and R.N. Pysklywec. Geodynamic models of Archean continental collision and the formation of mantle lithosphere keels. *Geophys. Res. Lett.*, 37(L19301), 2010.
- [1058] R. Gray and R.N. Pysklywec. Geodynamic models of mature continental collision: Evolution of an orogen from lithospheric subduction to continental retreat/delamination. *J. Geophys. Res.*, 117(B03408), 2012.
- [1059] R. Gray and R.N. Pysklywec. Influence of sediment deposition on deep lithospheric tectonics. *Geophys. Res. Lett.*, 39(L11312), 2012.
- [1060] R. Gray and R.N. Pysklywec. Influence of viscosity pressure dependence on deep lithospheric tectonics during continental collision. *J. Geophys. Res.*, 118, 2013.
- [1061] P.M. Gresho, S.T. Chan, M.A. Christon, and A.C. Hindmarsh. A little more on stabilised  $Q_1 Q_1$  for transient viscous incompressible flow. *Int. J. Num. Meth. Fluids*, 21:837–856, 1995.
- [1062] P.M. Gresho and R.L. Lee. Don't suppress the wiggles - They're telling you something! *Computers and Fluids*, 9:223–253, 1981.
- [1063] PM Gresho and RL Lee. Partial vindication of the bilinear velocity, piecewise constant pressure element. *Journal of Computational Physics*, 60(1):161–164, 1985.
- [1064] P.M. Gresho, R.L. Lee, R.L. Sani, M.K. Maslanik, and B.E. Eaton. The consistent Galerkin FEM for computing derived boundary quantities in thermal and/or fluid problems. *Int. J. Num. Meth. Fluids*, 7:371–394, 1987.
- [1065] P.M. Gresho and R.L. Sani. *Incompressible flow and the Finite Element Method, vol II*. John Wiley and Sons, Ltd, 2000.
- [1066] Ralf Greve. Application of a polythermal three-dimensional ice sheet model to the greenland ice sheet: response to steady-state and transient climate scenarios. *Journal of Climate*, 10(5):901–918, 1997.
- [1067] Ralf Greve and Heinz Blatter. *Dynamics of ice sheets and glaciers*. Springer Science & Business Media, 2009.
- [1068] M. Griebel, T. Dornseifer, and T. Neunhoeffer. *Numerical simulation in Fluid Dynamics*. SIAM, 1997.
- [1069] D. Griffiths and D. Silvester. Unstable modes of the q1-p0 element. Technical Report 257, University of MAnchester/UMIST, 1994.
- [1070] Cécile Grigné, Stéphane Labrosse, and Paul J Tackley. Convective heat transfer as a function of wavelength: Implications for the cooling of the earth. *Journal of Geophysical Research: Solid Earth*, 110(B3), 2005.
- [1071] Cécile Grigné, Stéphane Labrosse, and PJ Tackley. Convection under a lid of finite conductivity: Heat flux scaling and application to continents. *Journal of Geophysical Research: Solid Earth*, 112(B8), 2007.
- [1072] Cécile Grigné, Stéphane Labrosse, and PJ Tackley. Convection under a lid of finite conductivity in wide aspect ratio models: Effect of continents on the wavelength of mantle flow. *Journal of Geophysical Research: Solid Earth*, 112(B8), 2007.
- [1073] S.G. Grigull, S.M. Ellis, T.A. Little, M.P. Hill, and S.J.H. Buiter. Rheological constraints on quartz derived from scaling relationships and numerical models of sheared brittle-ductile quartz veins, central Southern alps, New Zealand. *Journal of Structural Geology*, 37:200–222, 2012.
- [1074] EB Grosfils, RA Schultz, and G Kroeger. Geophysical exploration within northern devils lane graben, canyonlands national park, utah: implications for sediment thickness and tectonic evolution. *Journal of Structural Geology*, 25(3):455–467, 2003.
- [1075] L. Gross, L. Bourgouin, A. Hale, and H.-B. Mühlhaus. Interface modeling in incompressible media using level sets in Escript. *Phys. Earth. Planet. Inter.*, 163:23–34, 2007.
- [1076] T. Gu, M. Li, C. McCammon, and K. K. M. Lee. Redox-induced lower mantle density contrast and effect on mantle structure and primitive oxygen. *Nature Geoscience*, 2016.
- [1077] J.-L. Guermond, R. Pasquetti, and Bojan Popov. Entropy viscosity method for nonlinear conservation laws. *J. Comp. Phys.*, page doi:10.1016/j.jcp.2010.11.043, 2011.
- [1078] Jean-Luc Guermond and Richard Pasquetti. Entropy viscosity method for high-order approximations of conservation laws. In *Spectral and high order methods for partial differential equations*, pages 411–418. Springer, 2011.

- [1079] Jean Luc Guermond, Richard Pasquetti, and Bojan Popov. Entropy viscosity for conservation equations. In *V European Conference on Computational Fluid Dynamics (Eccomas CFD 2010)*, 2010.
- [1080] JM Guerrero, Julian P Lowman, and Paul J Tackley. Spurious transitions in convective regime due to viscosity clipping: ramifications for modeling planetary secular cooling. *Geochemistry, Geophysics, Geosystems*, 20(7):3450–3468, 2019.
- [1081] F. Gueydan, C. Morency, and J.-P. Brun. Continental rifting as a function of lithosphere mantle strength. *Tectonophysics*, 460:83–93, 2008.
- [1082] Frédéric Gueydan, Jacques Précigout, and Laurent GJ Montesi. Strain weakening enables continental plate tectonics. *Tectonophysics*, 631:189–196, 2014.
- [1083] Benjamin Guillaume, Laurent Husson, Francesca Funiciello, and Claudio Faccenna. The dynamics of laterally variable subductions: laboratory models applied to the hellenides. *Solid Earth*, 4:179–200, 2013.
- [1084] M.J. Guillot, B. Rivière, and M.F. Wheeler. Discontinuous Galerkin methods for mass conservation equations for environmental modelling. In Gray W.G. Hassanzadeh S.M., Schotting R.J. and Pinder G.F., editors, *Computational Methods in Water Resources, Developments in Water Science*, pages 939–946. 2002.
- [1085] Stéphane Guillot, Stéphane Schwartz, Bruno Reynard, Philippe Agard, and Cécile Prigent. Tectonic significance of serpentinites. *Tectonophysics*, 646:1–19, 2015.
- [1086] L. Guillou-Frottier, E. Burov, S. Cloetingh, E. Le Goff, Y. Deschamps, B. Huet, and V. Bouchot. Plume-induced dynamic instabilities near cratonic blocks: Implications for PT paths and metallogeny. *Global and Planetary Change*, 90-91:37–50, 2012.
- [1087] G Guj and F Stella. A vorticity-velocity method for the numerical solution of 3d incompressible flows. *Journal of Computational Physics*, 106(2):286–298, 1993.
- [1088] A.J.P. Gürler, S.J. Beaussier, and T.V. Gerya. On the formation of oceanic detachment faults and their influence on intra-oceanic subduction initiation: 3D thermomechanical modeling. *Earth Planet. Sci. Lett.*, 506:195–208, 2019.
- [1089] M. Gunzburger. *Finite Element Methods for Viscous Incompressible Flows: A Guide to Theory, Practice and Algorithms*. Academic, Boston, 1989.
- [1090] Anshul Gupta, George Karypis, and Vipin Kumar. Highly scalable parallel algorithms for sparse matrix factorization. *IEEE Transactions on Parallel and Distributed Systems*, 8(5):502–520, May 1997.
- [1091] Anshul Gupta, Seid Koric, and Thomas George. Sparse matrix factorization on massively parallel computers. In *SC09 (International Conference for High Performance Computing, Networking, Storage and Analysis)*, 2009.
- [1092] PS Gupta and AS Gupta. Squeezing flow between parallel plates. *Wear*, 45(2):177–185, 1977.
- [1093] M. Gurnis. Plate-mantle coupling and continental flooding. *Geophysical Research Letters*, 17(5):623–626, 1990.
- [1094] M. Gurnis, C. Hall, and L. Lavier. Evolving force balance during incipient subduction. *Geochem. Geophys. Geosyst.*, 5(7), 2004.
- [1095] M. Gurnis, J.X. Mitrovica, J. Ritsema, and H.-J. van Heijst. Constraining mantle density structure using geological evidence of surface uplift rates: The case of the African superplume. *Geochem. Geophys. Geosyst.*, 1, 2000.
- [1096] M. Gurnis and T. H. Torsvik. Rapid drift of large continents during the late precambrian and paleozoic: Paleomagnetic constraints and dynamic models. *Geology*, 22(11):1023, 1994.
- [1097] Michael Gurnis. Rapid continental subsidence following the initiation and evolution of subduction. *Science*, 255(5051):1556–1558, 1992.
- [1098] Michael Gurnis. Depressed continental hypsometry behind oceanic trenches: A clue to subduction controls on sea-level change. *Geology*, 21(1):29–32, 1993.
- [1099] Michael Gurnis. Phanerozoic marine inundation of continents driven by dynamic topography above subducting slabs. *Nature*, 364(6438):589, 1993.
- [1100] Michael Gurnis and Geoffrey F Davies. Numerical study of high rayleigh number convection in a medium with depth-dependent viscosity. *Geophysical Journal International*, 85(3):523–541, 1986.
- [1101] Michael Gurnis, Christophe Eloy, and Shijie Zhong. Free-surface formulation of mantle convectionii. implication for subduction-zone observables. *Geophysical Journal International*, 127(3):719–727, 1996.

- [1102] Michael Gurnis, Louis Moresi, and R Dietmar Müller. Models of mantle convection incorporating plate tectonics: The australian region since the cretaceous. *The history and dynamics of global plate motion, Geophysical monograph*, 121, 2000.
- [1103] Michael Gurnis, R Dietmar Müller, and Louis Moresi. Cretaceous vertical motion of australia and the australianantarctic discordance. *Science*, 279(5356):1499–1504, 1998.
- [1104] Michael Gurnis, Mark Turner, Sabin Zahirovic, Lydia DiCaprio, Sonja Spasojevic, R Dietmar Müller, James Boyden, Maria Seton, Vlad Constantin Manea, and Dan J Bower. Plate tectonic reconstructions with continuously closing plates. *Computers & Geosciences*, 38(1):35–42, 2012.
- [1105] M-A Gutscher, F Klingelhoefer, T Theunissen, W Spakman, Théo Berthet, TK Wang, and C-S Lee. Thermal modeling of the sw ryukyu forearc (taiwan): Implications for the seismogenic zone and the age of the subducting philippine sea plate (huatung basin). *Tectonophysics*, 692:131–142, 2016.
- [1106] M.-A. Gutscher, J. Malod, J.-P. Rehault, I. Contrucci, F. Klingelhoefer, L. Mendes-Victor, and W. Spakman. Evidence for active subduction beneath gibraltar. *Geology*, 30(12):1071–1074, 2002.
- [1107] M.-A. Gutscher, W. Spakman, H. Bijwaard, and E.R. Engdahl. Geodynamics of flat subduction: Seismicity and tomographic constraints from the andean margin. *Tectonics*, 19(5):814–833, 2000.
- [1108] Pierre Guyot and John E Dorn. A critical review of the peierls mechanism. *Canadian Journal of Physics*, 45(2):983–1016, 1967.
- [1109] Zohar Gvirtzman, Claudio Faccenna, and Thorsten W Becker. Isostasy, flexure, and dynamic topography. *Tectonophysics*, 683:255–271, 2016.
- [1110] B.R. Hacker. Simulation of the metamorphic and deformational history of the metamorphic sole of the Oman ophiolite. *J. Geophys. Res.*, 95(B4):4895–4907, 1990.
- [1111] B.R. Hacker. The role of deformation in the formation of metamorphic gradients: ridge subduction beneath the Oman ophiolite. *Tectonics*, 10(2):455–473, 1991.
- [1112] B.R. Hackley and T.V. Gerya. Paradigms, new and old for ultrahigh-pressure tectonism. *Tectonophysics*, 603:79–88, 2013.
- [1113] W. Hafner. Stress distributions and faulting. *Bulletin of the Geological Society of America*, 62:373–398, 1951.
- [1114] B.H. Hager and R.J. O'Connell. Subduction zone dip angles and flow driven by plate motion. *Tectonophysics*, 50:111–133, 1978.
- [1115] B.H. Hager and R.J. O'Connell. A simple global model of plate dynamics and mantle convection. *J. Geophys. Res.*, 86(B6):4843–4867, 1981.
- [1116] Bradford H Hager. Subducted slabs and the geoid: Constraints on mantle rheology and flow. *Journal of Geophysical Research: Solid Earth*, 89(B7):6003–6015, 1984.
- [1117] Bradford H Hager, Robert W Clayton, Mark A Richards, Robert P Comer, and Adam M Dziewonski. Lower mantle heterogeneity, dynamic topography and the geoid. *Nature*, 313(6003):541, 1985.
- [1118] E. Hairer, S.P. Nørsett, and G. Wanner. *Solving Ordinary Differential Equations I*. Springer, 1993.
- [1119] E. Hairer and G. Wanner. *Solving Ordinary Differential Equations II. Stiff and Differential-Algebraic Problems*. Springer-Verlag, Berlin, 1991.
- [1120] A.J. Hale, L. Bourgouin, and H.B. Muehlhaus. Using the level set method to model endogenous lava dome growth . *J. Geophys. Res.*, 112(B03213), 2007.
- [1121] A.J. Hale, K.-D. Gottschaldt, G. Rosenbaum, L. Bourgouin, M. Bauchy, and Hans Mühlhaus. Dynamics of slab tear faults: Insights from numerical modelling. *Tectonophysics*, 483:58–70, 2010.
- [1122] C.E. Hall, M. Gurnis, M. Sdrolias, L.L. Lavie, and R.D. Mueller. Catastrophic initiation of subduction following forced convergence across fracture zones. *Earth Planet. Sci. Lett.*, 212:15–30, 2003.
- [1123] Chad E Hall and Michael Gurnis. Strength of fracture zones from their bathymetric and gravitational evolution. *Journal of Geophysical Research: Solid Earth*, 110(B1), 2005.
- [1124] Chad E Hall and EM Parmentier. Influence of grain size evolution on convective instability. *Geochemistry, Geophysics, Geosystems*, 4(3), 2003.
- [1125] Paul S Hall and Chris Kincaid. Diapiric flow at subduction zones: A recipe for rapid transport. *Science*, 292(5526):2472–2475, 2001.
- [1126] R. Hall and W. Spakman. Mantle structure and tectonic history of SE Asia. *Tectonophysics*, 658:14–45, 2015.

- [1127] Andrea Hampel and Adrian Pfiffner. Relative importance of trenchward upper plate motion and friction along the plate interface for the topographic evolution of subduction-related mountain belts. *Geological Society, London, Special Publications*, 253(1):105–115, 2006.
- [1128] L. Han and M. Gurnis. How valid are dynamic models of subduction and convection when plate motions are prescribed? *Physics of the Earth and Planetary Interiors*, 110(3-4):235–246, 1999.
- [1129] L. Han and A. P. Showman. Implications of shear heating and fracture zones for ridge formation on europa. *Geophysical Research Letters*, 35(3), 2008.
- [1130] L. Han and A. P. Showman. Coupled convection and tidal dissipation in europa’s ice shell. *Icarus*, 207(2):834–844, 2010.
- [1131] L. Han and A. P. Showman. Coupled convection and tidal dissipation in europa’s ice shell using non-newtonian grain-size-sensitive (gss) creep rheology. *Icarus*, 212(1):262–267, 2011.
- [1132] L. Han, G. Tobie, and A. P. Showman. The impact of a weak south pole on thermal convection in enceladus’ ice shell. *Icarus*, 218(1):320–330, 2012.
- [1133] J. Handin. On the Coulomb-Mohr failure criterion. *J. Geophys. Res.*, 74(22):5343, 1969.
- [1134] D.L. Hansen. A meshless formulation for geodynamic modeling. *J. Geophys. Res.*, 108:doi:10.1029/2003JB002460, 2003.
- [1135] D.L. Hansen and S.B. Nielsen. Does thermal weakening explain basin inversion? Stochastic modelling of the thermal structure beneath sedimentary basins. *Earth Planet. Sci. Lett.*, 198:113–127, 2002.
- [1136] D.L. Hansen and S.B. Nielsen. Why rifts invert in compression. *Tectonophysics*, 373:5–24, 2003.
- [1137] D.L. Hansen, S.B. Nielsen, and H. Lykke-Andersen. The post-Triassic evolution of the SorgenfreiTornquist Zone - results from thermo-mechanical modelling. *Tectonophysics*, 328:245–267, 2000.
- [1138] Lars N Hansen, Kathryn M Kumamoto, Christopher A Thom, David Wallis, William B Durham, David L Goldsby, Thomas Breithaupt, Cameron D Meyers, and David L Kohlstedt. Low-temperature plasticity in olivine: Grain size, strain hardening, and the strength of the lithosphere. *Journal of Geophysical Research: Solid Earth*, 2019.
- [1139] U Hansen and A Ebel. Experiments with a numerical model related to mantle convection: boundary layer behaviour of small-and large scale flows. *Physics of the earth and planetary interiors*, 36(3-4):374–390, 1984.
- [1140] U. Hansen and D.A. Yuen. Effects of depth-dependent thermal expansivity on the interaction of thermal-chemical plumes with a compositional boundary. *Physics of the Earth and Planetary Interiors*, 86(1-3):205–221, 1994.
- [1141] U Hansen and DA Yuen. Extended-boussinesq thermal–chemical convection with moving heat sources and variable viscosity. *Earth and Planetary Science Letters*, 176(3-4):401–411, 2000.
- [1142] Ulrich Hansen and Adolf Ebel. Time-dependent thermal convection-a possible explanation for a multiscale flow in the earth’s mantle. *Geophysical Journal International*, 94(2):181–191, 1988.
- [1143] Ulrich Hansen and Adolf Ebel. Time-dependent thermal convection-a possible explanation for a multiscale flow in the earth’s mantle. *Geophysical Journal International*, 94(2):181–191, 1988.
- [1144] Ulrich Hansen and David A Yuen. Numerical simulations of thermal-chemical instabilities at the core–mantle boundary. *Nature*, 334(6179):237, 1988.
- [1145] Ulrich Hansen and David A Yuen. Dynamical influences from thermal-chemical instabilities at the core–mantle boundary. *Geophysical Research Letters*, 16(7):629–632, 1989.
- [1146] Ulrich Hansen and David A Yuen. Potential role played by viscous heating in thermal-chemical convection in the outer core. *Geochimica et cosmochimica acta*, 60(7):1113–1123, 1996.
- [1147] H. Harder and U.R. Christensen. A one-plume model of martian mantle convection. *Nature*, 380:507–509, 1996.
- [1148] C. Harig, S. Zhong, and F. J. Simons. Constraints on upper mantle viscosity from the flow-induced pressure gradient across the australian continental keel: Continental keel motion and the geoid. *Geochemistry, Geophysics, Geosystems*, 11(6), 2010.
- [1149] F.H. Harlow and J.E. Welch. Numerical calculation of time-dependent viscous incompressible flow of fluid with free surface. *The physics of fluids*, 8(12):2182, 1965.
- [1150] Nicholas Harmon and Donna K Blackman. Effects of plate boundary geometry and kinematics on mantle melting beneath the back-arc spreading centers along the lau basin. *Earth and Planetary Science Letters*, 298(3-4):334–346, 2010.

- [1151] V. Haroutunian, M.S. Engelman, and I. Hasbani. Segregated Finite Element algorithms for the numerical solution of large-scale incompressible flow problems. *Int. J. Num. Meth. Fluids*, 17:323–348, 1993.
- [1152] JF Harper. Mantle flow due to internal vertical forces. *Physics of the Earth and Planetary Interiors*, 36(3-4):285–290, 1984.
- [1153] Nathan J Harris, Steven E Benzley, and Steven J Owen. Conformal refinement of all-hexahedral element meshes based on multiple twist plane insertion. pages 157–168, 2004.
- [1154] E.H. Hartz and Y.Y. Podlachikov. Toasting the jelly sandwich: The effect of shear heating on lithospheric geotherms and strength. *Geology*, 36(4):331–334, 2008.
- [1155] N.A. Haskell. The Motion of a Viscous Fluid Under a Surface Load. *Physics*, 6:265–269, 1935.
- [1156] R. Hassan, N. Flament, M. Gurnis, D.J. Bower, and D. Müller. Provenance of plumes in global convection models. *Geochem. Geophys. Geosyst.*, 16:1465–1489, 2015.
- [1157] R. Hassani and J Chéry. Anelasticity explains topography associated with basin and range normal faulting. *Geology*, 24(12):1095–1098, 1996.
- [1158] R. Hassani, D. Jongmans, and Jean Chéry. Study of plate deformation and stress in subduction processes using two-dimensional numerical models. *J. Geophys. Res.*, 102(B8):17,951–17,96, 1997.
- [1159] Denis Hatzfeld and Peter Molnar. Comparisons of the kinematics and deep structures of the zagros and himalaya and of the iranian and tibetan plateaus and geodynamic implications. *Reviews of Geophysics*, 48(2), 2010.
- [1160] Hiroshi Hayashi and Akira Kageyama. Yin–yang–zhong grid: An overset grid system for a sphere. *Journal of Computational Physics*, 305:895–905, 2016.
- [1161] G.P. Hayes, G.L. Moore, D.E. Portner, M. Hearne, H. Flamme, M. Furtney, and G.M. Smoczyk. Slab2, a comprehensive subduction zone geometry model. *Science*, 2018.
- [1162] G.P. Hayes, D.J. Wald, and R.L. Johnson. Slab1.0: A threedimensional model of global subduction zone geometries. *J. Geophys. Res.*, 117(B01302), 2012.
- [1163] K.L. Haynie and M.A. Jadamec. Tectonic drivers of the Wrangell block: Insights on fore-arc sliver processes from 3-D geodynamic models of Alaska. *Tectonics*, 36, 2017.
- [1164] Y. He, E.G. Puckett, and M.I. Billen. A discontinuous Galerkin method with a bound preserving limiter for the advection of non-diffusive fields in solid Earth geodynamics. *Phys. Earth. Planet. Inter.*, 263:23–37, 2017.
- [1165] L. B. Hebert, P. Antoshechkina, P. Asimow, and M. Gurnis. Emergence of a low-viscosity channel in subduction zones through the coupling of mantle flow and thermodynamics. *Earth and Planetary Science Letters*, 278(3-4):243–256, 2009.
- [1166] Otto M Heeres, Akke SJ Suiker, and René de Borst. A comparison between the perzyna viscoplastic model and the consistency viscoplastic model. *European Journal of Mechanics-A/Solids*, 21(1):1–12, 2002.
- [1167] Mahdi Heidari, Maria A Nikolinakou, Peter B Flemings, and Michael R Hudec. A simplified stress analysis of rising salt domes. *Basin Research*, 29(3):363–376, 2017.
- [1168] C. Heine and S. Brune. Oblique rifting of the Equatorial Atlantic: Why there is no Saharan Atlantic Ocean. *Geology*, 42(3):211–214, 2014.
- [1169] T. Heister, J. Dannberg, R. Gassmöller, and W. Bangerth. High Accuracy Mantle Convection Simulation through Modern Numerical Methods. II: Realistic Models and Problems. *Geophy. J. Int.*, 210(2):833–851, 2017.
- [1170] Christian Helanow and Josefina Ahlkrona. Stabilized equal low-order finite elements in ice sheet modeling—accuracy and robustness. *Computational Geosciences*, 22(4):951–974, 2018.
- [1171] George R Helffrich and Bernard J Wood. The earth’s mantle. *Nature*, 412(6846):501, 2001.
- [1172] Heinrich Hencky. Zur theorie plastischer deformationen und der hierdurch im material hervorgerufenen nachspannungen. *ZAMM-Journal of Applied Mathematics and Mechanics/Zeitschrift für Angewandte Mathematik und Mechanik*, 4(4):323–334, 1924.
- [1173] P. Hénon, P. Ramet, and J. Roman. PaStiX: A High-Performance Parallel Direct Solver for Sparse Symmetric Definite Systems. *Parallel Computing*, 28(2):301–321, 2002.
- [1174] Matthew W Herman, Kevin P Furlong, and Rob Govers. The Accumulation of Slip Deficit in Subduction Zones in the Absence of Mechanical Coupling: Implications for the Behavior of Megathrust Earthquakes. *Journal Of Geophysical Research*, 123(9):8260–8278, 2018.

- [1175] John W Hernlund, David J Stevenson, and Paul J Tackley. Buoyant melting instabilities beneath extending lithosphere: 2. linear analysis. *Journal of Geophysical Research: Solid Earth*, 113(B4), 2008.
- [1176] John W Hernlund and Paul J Tackley. Some dynamical consequences of partial melting in earths deep mantle. *Physics of the Earth and Planetary Interiors*, 162(1-2):149–163, 2007.
- [1177] John W Hernlund and Paul J Tackley. Modeling mantle convection in the spherical annulus. *Physics of the Earth and Planetary Interiors*, 171(1-4):48–54, 2008.
- [1178] John W Hernlund, Paul J Tackley, and David J Stevenson. Buoyant melting instabilities beneath extending lithosphere: 1. numerical models. *Journal of Geophysical Research: Solid Earth*, 113(B4), 2008.
- [1179] John W Hernlund, Christine Thomas, and Paul J Tackley. A doubling of the post-perovskite phase boundary and structure of the earth’s lowermost mantle. *Nature*, 434(7035):882, 2005.
- [1180] John William Hernlund and Irene Bonati. Modeling ultralow velocity zones as a thin chemically distinct dense layer at the core-mantle boundary. *Journal of Geophysical Research: Solid Earth*, 2019.
- [1181] Philip J Heron and Julian P Lowman. The impact of rayleigh number on assessing the significance of supercontinent insulation. *Journal of Geophysical Research: Solid Earth*, 119(1):711–733, 2014.
- [1182] P.J. Heron, R.N. Pysklywec, and R. Stephenson. Intraplate orogenesis within accreted and scarred lithosphere: Example of the Eurekan Orogeny, Ellesmere Island. *Tectonophysics*, 2015.
- [1183] P.J. Heron, R.N. Pysklywec, R. Stephenson, and J. van Hunen. Deformation driven by deep and distant structures: Influence of a mantle lithosphere suture in the ouachita orogeny, southeastern united states. *Geology*, 2018.
- [1184] M.A. Heroux and J.M. Willenbring. A new overview of the Trilinos project. *Scientific Programming*, 20:83–88, 2012.
- [1185] Robert Herrendörfer, Taras Gerya, and Ylona van Dinther. An invariant rate-and state-dependent friction formulation for viscoeastoplastic earthquake cycle simulations. *Journal of Geophysical Research: Solid Earth*, 123(6):5018–5051, 2018.
- [1186] Robert Herrendörfer, Ylona van Dinther, Taras Gerya, and Luis Angel Dalguer. Earthquake supercycle in subduction zones controlled by the width of the seismogenic zone. *Nature Geoscience*, 8(6):471, 2015.
- [1187] H.J. Herrmann, A.N.B. Poliakov, and F. Tzschichholz. Examples of fractals in rock mechanics. *Size-Scale Effects in the Failure Mechanisms of Materials and Structures*, page 58, 1996.
- [1188] M.R. Hestenes and E. Stiefel. Methods of Conjugate Gradients for Solving Linear Systems. *Journal of Research of the National Bureau of Standards*, 49(6):409–436, 1952.
- [1189] J.S. Hesthaven and T. Warbuton. Nodal Discontinuous Galerkin Methods. Algorithms, Analysis, and Applications. In J.E. Marsden, L. Sirovich, and S.S. Antman, editors, *Texts in Applied Mathematics*. Springer, 2008.
- [1190] G. Hetényi, V. Godard, R. Cattin, and J.A.D. Connolly. Incorporating metamorphism in geodynamic models: the mass conservation problem. *Geophys. J. Int.*, 186:6–10, 2011.
- [1191] J.M. Hewitt, D.P. McKenzie, and N.O. Weiss. Dissipative heating in convective flows. *J. Fluid Mech.*, 68(4):721–738, 1975.
- [1192] B.H. Heyn, C.P. Conrad, and R.G. Tronnes. Stabilizing Effect of Compositional Viscosity Contrasts on Thermochemical Piles. *Geophys. Res. Lett.*, 45:7523–7532, 2018.
- [1193] Christoph F Hieronymus. Control on seafloor spreading geometries by stress-and strain-induced lithospheric weakening. *Earth and Planetary Science Letters*, 222(1):177–189, 2004.
- [1194] N. Hilairat, B. Reynard, Y. Wang, I. Daniel, S. Merkel, N. Nishiyama, and S. Petitgirard. High-Pressure creep of Serpentine, interseismic deformation, and initiation of subduction. *Science*, 318:1910–1913, 2007.
- [1195] B. Hillebrand, C. Thieulot, T. Geenen, A. P. van den Berg, and W. Spakman. Using the level set method in geodynamical modeling of multi-material flows and earth’s free surface. *Solid Earth*, 5(2):1087–1098, 2014.
- [1196] Richard R Hillis and R Dietmar Mueller. *Evolution and dynamics of the Australian Plate*, volume 372. Geological Society of America, 2003.
- [1197] J.M. Hines and M.I. Billen. Sensitivity of the short- to intermediate-wavelength geoid to rheologic structure in subduction zones. *J. Geophys. Res.*, 117(B05410), 2012.
- [1198] Yoshio Hiramatsu and Yukitoshi Oka. Determination of the tensile strength of rock by a compression test of an irregular test piece. In *International Journal of Rock Mechanics and Mining Sciences & Geomechanics Abstracts*, volume 3, pages 89–90, 1966.

- [1199] Kei Hirose, John Brodholt, Thorne Lay, David A Yuen, et al. An introduction to post-perovskite: The last mantle phase transition. *GEOPHYSICAL MONOGRAPH-AMERICAN GEOPHYSICAL UNION*, 174:1, 2007.
- [1200] Kei Hirose, Ryosuke Sinmyo, and John Hernlund. Perovskite in earths deep interior. *Science*, 358(6364):734–738, 2017.
- [1201] C.W. Hirt, A. Amsden, and J.L. Cook. An Arbitrary Lagrangian-Eulerian computing method for all flow speeds. *J. Comp. Phys.*, 14:227–253, 1974.
- [1202] C.W. Hirt and B.D. Nichols. Volume of Fluid (VOF) Method for the dynamics of Free Boundaries. *J. Comp. Phys.*, 39:201–225, 1981.
- [1203] G. Hirth and D. L. Kohlstedt. Water in the oceanic upper mantle: Implications for rheology, melt extraction and the evolution of the lithosphere. *Earth Planet. Sci. Lett.*, 144:93–108, 1996.
- [1204] G. Hirth and D.L. Kohlstedt. Rheology of the upper mantle and the mantle wedge: A view from the experimentalists. *in Inside the Subduction Factory*, ed. J. Eiler, *Geophysical Monograph American Geophysical Union, Washington, D.C.*, 138:83–105, 2003.
- [1205] Greg Hirth. Laboratory constraints on the rheology of the upper mantle. *Reviews in Mineralogy and Geochemistry*, 51(1):97–120, 2002.
- [1206] N. Ho, S.D. Olson, and H.F. Walker. Accelerating the Uzawa algorithm. *SIAM J. Sci. Comput.*, 39(5):S461–S476, 2017.
- [1207] P. Ho-Liu, B.H. Hager, and A. Raefsky. An improved method of Nusselt number calculation. *Geophys. J. R. astr. Soc.*, 88:205–215, 1987.
- [1208] BE Hobbs, H-B Mühlhaus, and A Ord. Instability, softening and localization of deformation. *Geological Society, London, Special Publications*, 54(1):143–165, 1990.
- [1209] BE Hobbs and A Ord. Numerical simulation of shear band formation in a frictional-dilatational material. *Ingenieur-Archiv*, 59(3):209–220, 1989.
- [1210] Michael Hodges and Meghan S Miller. Mantle flow at the highly arcuate northeast corner of the lesser antilles subduction zone: Constraints from shear-wave splitting analyses. *Lithosphere*, 7(5):579–587, 2015.
- [1211] AJ Hogg and GP Matson. Slumps of viscoplastic fluids on slopes. *Journal of Non-Newtonian Fluid Mechanics*, 158(1-3):101–112, 2009.
- [1212] Mark James Hoggard, N White, and David Al-Attar. Global dynamic topography observations reveal limited influence of large-scale mantle flow. *Nature Geoscience*, 9(6):456, 2016.
- [1213] T. Höink and A. Lenardic. Three-dimensional mantle convection simulations with a low-viscosity asthenosphere and the relationship between heat flow and the horizontal length scale of convection. *Geophys. Res. Lett.*, 35(L10304), 2008.
- [1214] T. Höink, A. Lenardic, and A.M. Jellinek. Earth’s thermal evolution with multiple convection modes: A Monte-Carlo approach. *Phys. Earth. Planet. Inter.*, 221:22–26, 2013.
- [1215] T. Höink, A. Lenardic, and M. Richards. Depth-dependent viscosity and mantle stress amplification: implications for the role of the asthenosphere in maintaining plate tectonics: Asthenosphere and mantle stress amplification. *Geophysical Journal International*, 191(1):30–41, 2012.
- [1216] Tobias Höink and Adrian Lenardic. Long wavelength convection, poiseuille-couette flow in the low-viscosity asthenosphere and the strength of plate margins. *Geophysical Journal International*, 180(1):23–33, 2010.
- [1217] David W Holmes, John R Williams, and Peter Tilke. A framework for parallel computational physics algorithms on multi-core: Sph in parallel. *Advances in Engineering Software*, 42(11):999–1008, 2011.
- [1218] WE Holt. Correlated crust and mantle strain fields in tibet. *Geology*, 28(1):67–70, 2000.
- [1219] S Honda. Local rayleigh and nusselt numbers for cartesian convection with temperature-dependent viscosity. *Geophysical research letters*, 23(18):2445–2448, 1996.
- [1220] S Honda. A possible role of weak zone at plate margin on secular mantle cooling. *Geophysical research letters*, 24(22):2861–2864, 1997.
- [1221] S. Honda. Strength of slab inferred from the seismic tomography and geologic history around the Japanese Islands. *Geochem. Geophys. Geosyst.*, 15:1333–1347, 2014.
- [1222] Satoru Honda, Taras Gerya, and Guizhi Zhu. A simple three-dimensional model of thermo-chemical convection in the mantle wedge. *Earth and Planetary Science Letters*, 290(3-4):311–318, 2010.
- [1223] P. Hood and C. Taylor. NavierStokes equations using mixed interpolation. In J.T. Oden, R.H. Gallagher, O.C. Zienkiewicz, and C. Taylor, editors, *Finite element methods in flow problems*. Huntsville Press, University of Alabama, 1974.

- [1224] André Horbach, Hans-Peter Bunge, and Jens Oeser. The adjoint method in geodynamics: derivation from a general operator formulation and application to the initial condition problem in a high resolution mantle circulation model. *GEM-International Journal on Geomathematics*, 5(2):163–194, 2014.
- [1225] C.O. Horgan. Korn’s inequalities and their applications in continuum mechanics. *SIAM Review*, 37(4):491–511, 1995.
- [1226] G. Houseman and P. England. A dynamical model of lithosphere extension and sedimentary basin formation. *J. Geophys. Res.*, 91(B1):719–729, 1986.
- [1227] G.A. Houseman and P. Molnar. Gravitational (Rayleigh-Taylor) instability of a layer with non-linear viscosity and convective thinning of continental lithosphere. *Geophys. J. Int.*, 128:125–150, 1997.
- [1228] Greg Houseman. Large aspect ratio convection cells in the upper mantle. *Geophysical Journal International*, 75(2):309–334, 1983.
- [1229] Greg Houseman and Dan P McKenzie. Numerical experiments on the onset of convective instability in the earth’s mantle. *Geophysical Journal International*, 68(1):133–164, 1982.
- [1230] Gregory Houseman and Philip England. Finite strain calculations of continental deformation: 1. method and general results for convergent zones. *Journal of Geophysical Research: Solid Earth*, 91(B3):3651–3663, 1986.
- [1231] Gregory Houseman and Peter Molnar. Mechanisms of lithospheric rejuvenation associated with continental orogeny. *Geological Society, London, Special Publications*, 184(1):13–38, 2001.
- [1232] Gregory A Houseman. The deep structure of ocean ridges in a convecting mantle. *Earth and Planetary Science Letters*, 64(2):283–294, 1983.
- [1233] Alan D Howard. A detachment-limited model of drainage basin evolution. *Water resources research*, 30(7):2261–2285, 1994.
- [1234] Albert T Hsui. Numerical simulation of finite-amplitude thermal convection with large viscosity variation in axisymmetric spherical geometry: effect of mechanical boundary conditions. *Tectonophysics*, 50(2-3):147–162, 1978.
- [1235] Albert T Hsui, Tang Xiao-Ming, and M Nafi Toksöz. On the dip angle of subducting plates. *Tectonophysics*, 179(3-4):163–175, 1990.
- [1236] JiaShun Hu, LiJun Liu, and Quan Zhou. Reproducing past subduction and mantle flow using high-resolution global convection models. *Earth and Planetary Physics*, 2(3):189–207, 2018.
- [1237] Chongyu Hua. An inverse transformation for quadrilateral isoparametric elements: analysis and application. *Finite elements in analysis and design*, 7(2):159–166, 1990.
- [1238] J. Huang and G. F. Davies. Geochemical processing in a three-dimensional regional spherical shell model of mantle convection. *Geochemistry, Geophysics, Geosystems*, 8(11), 2007.
- [1239] J. Huang, A. Yang, and S. Zhong. Constraints of the topography, gravity and volcanism on venusian mantle dynamics and generation of plate tectonics. *Earth and Planetary Science Letters*, 362:207–214, 2013.
- [1240] M King Hubbert. Theory of scale models as applied to the study of geologic structures. *Bulletin of the Geological Society of America*, 48(10):1459–1520, 1937.
- [1241] Ch. Huber, A. Parmigiani, B. Chopard, M. Manga, and O. Bachmann. Lattice Boltzmann model for melting with natural convection. *International Journal of Heat and Fluid Flow*, 29:1469–1480, 200.
- [1242] Aurélia Hubert-Ferrari, Geoffrey King, Isabelle Manighetti, Rolando Armijo, Bertrand Meyer, and Paul Tappognier. Long-term elasticity in the continental lithosphere; modelling the aden ridge propagation and the anatolian extrusion process. *Geophysical Journal International*, 153(1):111–132, 2003.
- [1243] M.R. Hudec and M.P.A. Jackson. Terra infirma: Understanding salt tectonics. *Earth-Science Reviews*, 82:1–28, 2007.
- [1244] A. Huerta and W.K. Liu. Viscous flow with large free surface motion. *Computer Methods in Applied Mechanics and Engineering*, 69:277–324, 1988.
- [1245] Antonio Huerta, Sonia Fernández-Méndez, and Wing Kam Liu. A comparison of two formulations to blend finite elements and mesh-free methods. *Computer methods in applied mechanics and engineering*, 193(12-14):1105–1117, 2004.
- [1246] Antonio Huerta, Yolanda Vidal, and Pierre Villon. Pseudo-divergence-free element free galerkin method for incompressible fluid flow. *Computer Methods in Applied Mechanics and Engineering*, 193(12-14):1119–1136, 2004.

- [1247] Audrey D Huerta and Dennis L Harry. The transition from diffuse to focused extension: Modeled evolution of the west antarctic rift system. *Earth and Planetary Science Letters*, 255(1-2):133–147, 2007.
- [1248] Thomas JR Hughes, Wing Kam Liu, and Thomas K Zimmermann. Lagrangian-eulerian finite element formulation for incompressible viscous flows. *Computer methods in applied mechanics and engineering*, 29(3):329–349, 1981.
- [1249] Thomas JR Hughes, Michel Mallet, and Akira Mizukami. A new finite element formulation for computational fluid dynamics: II. beyond supg. *Computer methods in applied mechanics and engineering*, 54(3):341–355, 1986.
- [1250] T.J.R. Hughes. Numerical implementation of constitutive models: rate-independent deviatoric plasticity. 1983.
- [1251] T.J.R. Hughes. *The Finite Element Method. Linear Static and Dynamic Finite Element Analysis*. Dover Publications, Inc., 2000.
- [1252] T.J.R. Hughes and A. Brooks. A theoretical framework for petrov-galerkin methods with discontinuous weighting functions: application to the streamline-upwind procedure. *Finite Elements in Fluids*, 4:47–65, 1982.
- [1253] T.J.R. Hughes, L.P. Franca, and M. Balestra. A new finite element formulation for computational fluid dynamics: V. Circumventing the Babuška-Brezzi condition: A stable Petrov-Galerkin formulation of the Stokes problem accommodating equal-order interpolations. *Computer Methods in Applied Mechanics and Engineering*, 59(1):85–99, 1986.
- [1254] T.J.R. Hughes, W.K. Liu, and A. Brooks. Finite element analysis of Incompressible viscous flows by the penalty function formulation. *J. Comp. Phys.*, 30:1–60, 1979.
- [1255] Hoon Huh, Choong Ho Lee, and Wei H. Yang. A general algorithm for plastic flow simulation by finite element limit analysis. *International Journal of Solids and Structures*, 36:1193–1207, 1999.
- [1256] R. Huismans and C. Beaumont. Depth-dependent extension, two-stage breakup and cratonic underplating at rifted margins. *Nature*, 473:74–79, 2011.
- [1257] R. S. Huismans and C. Beaumont. Symmetric and asymmetric lithospheric extension: Relative effects of frictional-plastic and viscous strain softening. *J. Geophys. Res.*, 108 (B10)(2496), 2003.
- [1258] Ritske S Huismans and Christopher Beaumont. Rifted continental margins: The case for depth-dependent extension. *Earth and Planetary Science Letters*, 407:148–162, 2014.
- [1259] Ritske S Huismans and Giovanni Bertotti. The transylvanian basin, transfer zone between coeval extending and contracting regions: Inferences on the relative importance of slab pull and rift push in arc–back arc systems. *Tectonics*, 21(2):2–1, 2002.
- [1260] Ritske S Huismans, Yuri Y Podladchikov, and Sierd Cloetingh. Dynamic modeling of the transition from passive to active rifting, application to the pannonian basin. *Tectonics*, 20(6):1021–1039, 2001.
- [1261] Ritske S Huismans, Yuri Y Podladchikov, and Sierd Cloetingh. Transition from passive to active rifting: Relative importance of asthenospheric doming and passive extension of the lithosphere. *Journal of Geophysical Research: Solid Earth*, 106(B6):11271–11291, 2001.
- [1262] R.S. Huismans and C. Beaumont. Complex rifted continental margins explained by dynamical models of depth-dependent lithospheric extension. *Geology*, 30(3):211–214, 2002.
- [1263] R.S. Huismans and C. Beaumont. Roles of lithospheric strain softening and heterogeneity in determining the geometry of rifts and continental margins. In *Imaging, Mapping and Modelling Continental Lithosphere Extension and Breakup*, volume 282, pages 111–138. Geological Society, London, Special Publications, 2007.
- [1264] R.S. Huismans and C. Beaumont. Complex rifted continental margins explained by dynamical models of depth-dependent lithospheric extension. *Geology*, 36(2):163–166, 2008.
- [1265] R.S. Huismans, S.J.H. Buitter, and C. Beaumont. Effect of plastic-viscous layering and strain softening on mode selection during lithospheric extension. *J. Geophys. Res.*, 110:B02406, 2005.
- [1266] RS Huismans, YY Podladchikov, and SAPL Cloetingh. The pannonian basin: dynamic modelling of the transition from passive to active rifting. *EGU Stephan Mueller Special Publication Series*, 3:41–63, 2002.
- [1267] E. D. Humphreys and B. H. Hager. A kinematic model for the late cenozoic development of southern California crust and upper mantle. *Journal of Geophysical Research*, 95(B12):19747, 1990.
- [1268] D. L. Hunt and L. H. Kellogg. Quantifying mixing and age variations of heterogeneities in models of mantle convection: Role of depth-dependent viscosity. *Journal of Geophysical Research: Solid Earth*, 106(B4):6747–6759, 2001.

- [1269] L. Husson, J.-P. Brun, P. Yamato, and C. Faccenna. Episodic slab rollback fosters exhumation of hp-uhp rocks. *Geophysical Journal International*, 179(3):1292–1300, 2009.
- [1270] L. Husson and C. P. Conrad. On the location of hotspots in the framework of mantle convection. *Geophysical Research Letters*, 39(17), 2012.
- [1271] L. Husson, C.P. Conrad, and C. Faccenna. Plate motions, Andean orogeny, and volcanism above the South Atlantic convection cell. *Earth Planet. Sci. Lett.*, 317-318:126–135, 2012.
- [1272] L. Husson, P. Yamato, and A. Bzoz. Ultraslow, slow, or fast spreading ridges: Arm wrestling between mantle convection and far-field tectonics. *Earth and Planetary Science Letters*, 429:205–215, 2015.
- [1273] Laurent Husson. Trench migration and upper plate strain over a convecting mantle. *Physics of the Earth and Planetary Interiors*, 212:32–43, 2012.
- [1274] C. Hüttig and K. Stemmer. The spiral grid: A new approach to discretize the sphere and its application to mantle convection. *Geochem. Geophys. Geosyst.*, 9(2), 2008.
- [1275] C. Hüttig, N. Tosi, and W.B. Moore. An improved formulation of the incompressible NavierStokes equations with variable viscosity. *Phys. Earth. Planet. Inter.*, 220:11–18, 2013.
- [1276] Christian Hüttig and Kai Stemmer. Finite volume discretization for dynamic viscosities on voronoi grids. *Physics of the Earth and Planetary Interiors*, 171(1-4):137–146, 2008.
- [1277] Lorraine Hwang, Allison Fish, Laura Soito, MacKenzie Smith, and Louise H Kellogg. Software and the scientist: Coding and citation practices in geodynamics. *Earth and Space Science*, 4(11):670–680, 2017.
- [1278] Lorraine J Hwang, Richard A Pauloo, and Jane Carlen. Assessing impact of outreach through software citation for community software in geodynamics. *Computing in Science & Engineering*, 2019.
- [1279] Giampiero Iaffaldano, Laurent Husson, and Hans-Peter Bunge. Monsoon speeds up indian plate motion. *Earth and Planetary Science Letters*, 304(3-4):503–510, 2011.
- [1280] S. Idelsohn, M. Storti, and N. Nigro. Stability analysis of mixed finite element formulations with special mention of equal-order interpolations. *Int. J. Num. Meth. Fluids*, 20:1003–1022, 1995.
- [1281] Sergio Rodolfo Idelsohn, Mario Alberto Storti, and Eugenio Oñate. Lagrangian formulations to solve free surface incompressible inviscid fluid flows. *Computer methods in applied mechanics and engineering*, 191(6-7):583–593, 2001.
- [1282] I. Igreja and A.F.D. Loula. Stabilized velocity and pressure mixed hybrid DGFEM for the stokes problem. *Int. J. Num. Meth. Eng.*, 112:603–628, 2017.
- [1283] Benoit Ildefonse and Neil S Mancktelow. Deformation around rigid particles: the influence of slip at the particle/matrix interface. *Tectonophysics*, 221(3-4):345–359, 1993.
- [1284] F. Ilinca and D. Pelletier. Computation of accurate nodal derivatives of finite element solutions: The finite node displacement method. *Int. J. Num. Meth. Eng.*, 71:1181–1207, 2007.
- [1285] S.J. Ings and C. Beaumont. Continental margin shale tectonics: Preliminary results from coupled fluid-mechanical models of large-scale delta instability. *Journal of the Geological Society*, 167(3):571–582, 2010.
- [1286] Steven J Ings and Christopher Beaumont. Shortening viscous pressure ridges, a solution to the enigma of initiating salt ‘withdrawal’ minibasins. *Geology*, 38(4):339–342, 2010.
- [1287] Tobin Isaac, Georg Stadler, and Omar Ghattas. Solution of nonlinear stokes equations discretized by high-order finite elements on nonconforming and anisotropic meshes, with application to ice sheet dynamics. *SIAM Journal on Scientific Computing*, 37(6):B804–B833, 2015.
- [1288] A. Ismail-Zadeh, S. Honda, and I. Tsepelev. Linking mantle upwelling with the lithosphere descent and the Japan Sea evolution: a hypothesis. *Scientific Reports*, 3(1137):doi://10.1038/srep01137, 2013.
- [1289] A Ismail-Zadeh, A Korotkii, G Schubert, and I Tsepelev. Quasi-reversibility method for data assimilation in models of mantle dynamics. *Geophysical Journal International*, 170(3):1381–1398, 2007.
- [1290] A. Ismail-Zadeh, I. Sepelev, C. Talbot, and A. Korotkii. Three-dimensional forward and backward modelling of diapirism: numerical approach and its applicability to the evolution of salt structures in the Priscaspian basin. *Tectonophysics*, 387:81–103, 2004.
- [1291] Alik Ismail-Zadeh, Birgit Mueller, and Gerald Schubert. Three-dimensional numerical modeling of contemporary mantle flow and tectonic stress beneath the earthquake-prone southeastern carpathians based on integrated analysis of seismic, heat flow, and gravity data. *Physics of the Earth and Planetary Interiors*, 149(1-2):81–98, 2005.
- [1292] Alik Ismail-Zadeh, Gerald Schubert, Igor Tsepelev, and Alexander Korotkii. Inverse problem of thermal convection: numerical approach and application to mantle plume restoration. *Physics of the Earth and Planetary Interiors*, 145(1-4):99–114, 2004.

- [1293] Alik Ismail-Zadeh, Gerald Schubert, Igor Tsepelev, and Alexander Korotkii. Three-dimensional forward and backward numerical modeling of mantle plume evolution: Effects of thermal diffusion. *Journal of Geophysical Research: Solid Earth*, 111(B6), 2006.
- [1294] Alik Ismail-Zadeh and Paul Tackley. *Computational Methods for Geodynamics*. Cambridge University Press, 2010.
- [1295] D. Issler, H. McQueen, and C. Beaumont. Thermal and isostatic consequences of simple shear extension of the continental lithosphere. *Earth and Planetary Science Letters*, 91(3-4):341–358, 1989.
- [1296] J. Ita and S.D. King. Sensitivity of convection with an endothermic phase change to the form of governing equations, initial conditions, boundary conditions, and equation of state. *J. Geophys. Res.*, 99(B8):15,919–15,938, 1994.
- [1297] J. Ita and S.D. King. The influence of thermodynamic formulation on simulations of subduction zone geometry and history. *Geophys. Res. Lett.*, 25(9):1463–1466, 1998.
- [1298] Pablo Cristián Iturrieta, Daniel E Hurtado, José Cembrano, and Ashley Stanton-Yonge. States of stress and slip partitioning in a continental scale strike-slip duplex: Tectonic and magmatic implications by means of finite element modeling. *Earth Planet. Sci. Lett.*, 473:71–82, 2017.
- [1299] Y. Iwase. Three-dimensional infinite Prandtl number convection in a spherical shell with temperature-dependent viscosity. *J. Geomag. Geoelectr.*, 48:1499–1514, 1996.
- [1300] Yasuyuki Iwase and Satoru Honda. An interpretation of the nusselt-rayleigh number relationship for convection in a spherical shell. *Geophysical journal international*, 130(3):801–804, 1997.
- [1301] Yasuyuki Iwase and Satoru Honda. Effects of geometry on the convection with core-cooling. *Earth, planets and space*, 50(5):387–395, 1998.
- [1302] M.P.A. Jackson, B.C. Vendeville, and D.D. Schultz-Ela. Structural Dynamics of Salt Systems. *Annu. Rev. Earth Planet. Sci.*, 22:93–117, 1994.
- [1303] M.H.G. Jacobs, R. Schmid-Fetzer, and A.P. van den Berg. An alternative use of kieffer's lattice dynamics model using vibrational density of states for constructing thermodynamic databases. *Physics and Chemistry of Minerals*, 40(3):207–227, 2013.
- [1304] M.H.G. Jacobs, R. Schmid-Fetzer, and A.P. van den Berg. Phase diagrams, thermodynamic properties and sound velocities derived from a multiple einstein method using vibrational densities of states: an application to mgosio2. *Physics and Chemistry of Minerals*, 44(1):43–62, 2017.
- [1305] M.H.G. Jacobs, R. Schmid-Fetzer, and A.P. van den Berg. Thermophysical properties and phase diagrams in the system mgosio2feo at upper mantle and transition zone conditions derived from a multiple-einstein method. *Physics and Chemistry of Minerals*, 46(5):513–534, 2019.
- [1306] M.H.G. Jacobs and A.P. van den Berg. Complex phase distribution and seismic velocity structure of the transition zone: Convection model predictions for a magnesium-endmember olivinepyroxene mantle. *Phys. Earth. Planet. Inter.*, 186:36–48, 2011.
- [1307] M.H.G. Jacobs, A.P. van den Berg, and B.H.W.S. de Jong. The derivation of thermo-physical properties and phase equilibria of silicate materials from lattice vibrations: Application to convection in the earth's mantle. *Calphad: Computer Coupling of Phase Diagrams and Thermochemistry*, 30(2):131–146, 2006.
- [1308] Michel HG Jacobs and Bernard HWS de Jong. Placing constraints on phase equilibria and thermophysical properties in the system mgo–sio<sub>2</sub> by a thermodynamically consistent vibrational method. *Geochimica et Cosmochimica Acta*, 71(14):3630–3655, 2007.
- [1309] Wolfgang R Jacoby and Harro Schmelting. Convection experiments and the driving mechanism. *Geologische Rundschau*, 70(1):207–230, 1981.
- [1310] M. A. Jadamec. Insights on slab-driven mantle flow from advances in three-dimensional modelling. *Journal of Geodynamics*, 2016.
- [1311] MA Jadamec. Slab-driven mantle weakening and rapid mantle flow. *Subduction Dynamics: From Mantle Flow to Mega Disasters, Geophys. Monogr. Ser.*, pages 135–155, 2016.
- [1312] M.A. Jadamec and M.I. Billen. Reconciling surface plate motions with rapid three-dimensional mantle flow around a slab edge. *Nature*, 465:338–341, 2010.
- [1313] M.A. Jadamec and M.I. Billen. The role of rheology and slab shape on rapid mantle flow: Three-dimensional numerical models of the Alaska slab edge. *J. Geophys. Res.*, 117(B02304), 2012.
- [1314] M.A. Jadamec, M.I. Billen, and S.M. Roeske. Three-dimensional numerical models of flat slab subduction and the Denali fault driving deformation in south-central Alaska. *Earth Planet. Sci. Lett.*, 376:29–42, 2013.

- [1315] Margarete A Jadamec and Magali I Billen. Reconciling surface plate motions with rapid three-dimensional mantle flow around a slab edge. *Nature*, 465(7296):338, 2010.
- [1316] Margarete A Jadamec, Magali I Billen, and Oliver Kreylos. Three-dimensional simulations of geometrically complex subduction with large viscosity variations. In *Proceedings of the 1st Conference of the Extreme Science and Engineering Discovery Environment: Bridging from the eXtreme to the campus and beyond*, page 31. ACM, 2012.
- [1317] Oliver Jagoutz, Leigh Royden, Adam F Holt, and Thorsten W Becker. Anomalously fast convergence of india and eurasia caused by double subduction. *Nature Geoscience*, 8(6):475, 2015.
- [1318] R. A. Jamieson and C. Beaumont. Coeval thrusting and extension during lower crustal ductile flow - implications for exhumation of high-grade metamorphic rocks. *Journal of Metamorphic Geology*, 29(1):33–51, 2011.
- [1319] R.A. Jamieson and C. Beaumont. Deformation and metamorphism in convergent orogens: A model for uplift and exhumation of metamorphic terrains. *Geological Society Special Publication*, 43:117–129, 1989.
- [1320] R.A. Jamieson and C. Beaumont. On the origin of orogens. *Bulletin of the Geological Society of America*, 125(11-12):1671–1702, 2013.
- [1321] R.A. Jamieson, C. Beaumont, P. Fullsack, and B. Lee. Barrovian regional metamorphism: where's the heat? *Geological Society Special Publication*, 138:23–51, 1998.
- [1322] R.A. Jamieson, C. Beaumont, J. Hamilton, and P. Fullsack. Tectonic assembly of inverted metamorphic sequences. *Geology*, 24(9):839–842, 1996.
- [1323] R.A. Jamieson, C. Beaumont, S. Medvedev, and M.H. Nguyen. Crustal channel flows: 2. numerical models with implications for metamorphism in the himalayan-tibetan orogen. *Journal of Geophysical Research: Solid Earth*, 109(6):B06407 1–24, 2004.
- [1324] R.A. Jamieson, C. Beaumont, M.H. Nguyen, and N.G. Culshaw. Synconvergent ductile flow in variable-strength continental crust: Numerical models with application to the western grenville orogen. *Tectonics*, 26(5), 2007.
- [1325] R.A. Jamieson, C. Beaumont, M.H. Nguyen, and D. Grujic. Provenance of the greater himalayan sequence and associated rocks: Predictions of channel flow models. *Geological Society Special Publication*, 268:165–182, 2006.
- [1326] R.A. Jamieson, C. Beaumont, M.H. Nguyen, and B. Lee. Interaction of metamorphism, deformation and exhumation in large convergent orogens. *Journal of Metamorphic Geology*, 20(1):9–24, 2002.
- [1327] R.A. Jamieson, C. Beaumont, C.J. Warren, and M.H. Nguyen. The grenville orogen explained? applications and limitations of integrating numerical models with geological and geophysical data. *Canadian Journal of Earth Sciences*, 47(4):517–539, 2010.
- [1328] S. Jammes and R.S. Huismans. Structural styles of mountain building: Controls of lithospheric rheologic stratification and extensional inheritance. *J. Geophys. Res.*, 117, 2012.
- [1329] S. Jammes, R.S. Huismans, and J.A. Muñoz. Lateral variation in structural style of mountain building: controls of rheological and rift inheritance. *Terra Nova*, 26:201–207, 2014.
- [1330] S. Jammes and L.L. Lavier. Effect of contrasting strength from inherited crustal fabrics on the development of rifting margins. *Geosphere*, 15(2):407–422, 2019.
- [1331] S. Jammes, G. Manatschal, and L. Lavier. Interaction between prerift salt and detachment faulting in hyperextended rift systems: The example of the Parentis and Mauléon basins (Bay of Biscay and western Pyrenees). *AAPG Bulletin*, 94(7):957–975, 2010.
- [1332] Suzon Jammes, Luc L Lavier, and Jacqueline E Reber. Localization and delocalization of deformation in a bimineralic material. *Journal of Geophysical Research: Solid Earth*, 120(5):3649–3663, 2015.
- [1333] Y. Jaquet, T. Duretz, D. Grujic, H. Masson, and S.M. Schmalholz. Formation of orogenic wedges and crustal shear zones by thermal softening, associated topographic evolution and application to natural orogens. *Tectonophysics*, 746:512–529, 2018.
- [1334] Y. Jaquet, Th. Duretz, and S.M. Schmalholz. Dramatic effect of elasticity on thermal softening and strain localization during lithospheric shortening. *Geophy. J. Int.*, 204:780–784, 2016.
- [1335] Y. Jaquet and S.M. Schmalholz. Spontaneous ductile crustal shear zone formation by thermal softening and related stress, temperature and strain rate evolution. *Tectonophysics*, 746:384–397, 2018.
- [1336] Richard D Jarrard. Relations among subduction parameters. *Reviews of Geophysics*, 24(2):217–284, 1986.
- [1337] Gary T Jarvis and Julian P Lowman. Sinking slabs below fossil subduction zones. *Physics of the Earth and Planetary Interiors*, 152(1-2):103–115, 2005.

- [1338] Gary T Jarvis and Julian P Lowman. Survival times of subducted slab remnants in numerical models of mantle flow. *Earth and Planetary Science Letters*, 260(1-2):23–36, 2007.
- [1339] Gary T. Jarvis and Dan P. McKenzie. Convection in a compressible fluid with infinite prandtl number. *Journal of Fluid Mechanics*, 96(3):515–583, 1980.
- [1340] Gary T Jarvis and WR Peltier. Mantle convection as a boundary layer phenomenon. *Geophysical Journal International*, 68(2):389–427, 1982.
- [1341] GT Jarvis. Time-dependent convection in the earth’s mantle. *Physics of the earth and planetary interiors*, 36(3-4):305–327, 1984.
- [1342] GT Jarvis. The long wavelength component of mantle convection. *Physics of the earth and planetary interiors*, 40(1):24–42, 1985.
- [1343] G.T. Jarvis. Effects of curvature on two-dimensional models of mantle convection: cylindrical polar coordinates. *J. Geophys. Res.*, 98(B3):4477–4485, 1993.
- [1344] C. Jaupart and J.-C. Mareschal. *Heat Generation and Transport in the Earth*. Cambridge, 2011.
- [1345] P. Jay, A. Magnin, and J.-M. Piau. Viscoplastic Fluid Flow Through a Sudden Axisymmetric Expansion. *AIChE Journal*, 47(10):2155–2166, 2001.
- [1346] L. Jeanniot, N. Kusznir, G. Mohn, G. Manatschal, and L. Cowie. Constraining lithosphere deformation modes during continental breakup for the IberiaNewfoundland conjugate rifted margins. *Tectonophysics*, 680:28–49, 2016.
- [1347] Ludovic Jeanniot and Susanne JH Buitter. A quantitative analysis of transtensional margin width. *Earth and Planetary Science Letters*, 491:95–108, 2018.
- [1348] K.E. Jensen. Topology optimization of stokes flow on dynamic meshes using simple optimizers. *Computers and Fluids*, 174:66–77, 2018.
- [1349] Kopal Jha, EM Parmentier, and Jason Phipps Morgan. The role of mantle-depletion and melt-retention buoyancy in spreading-center segmentation. *Earth and Planetary Science Letters*, 125(1-4):221–234, 1994.
- [1350] V. John. A posteriori L2-error estimates for the nonconforming P1/P0-finite element discretization of the Stokes equations. *Journal of Computational and Applied Mathematics*, 96:99–116, 1998.
- [1351] V. John. *Finite Element Methods for Incompressible Flow Problems* . Springer, 2016.
- [1352] Volker John. Higher order finite element methods and multigrid solvers in a benchmark problem for the 3d navier–stokes equations. *International Journal for Numerical Methods in Fluids*, 40(6):775–798, 2002.
- [1353] Volker John, Alexander Linke, Christian Merdon, Michael Neilan, and Leo G Rebholz. On the divergence constraint in mixed finite element methods for incompressible flows. *SIAM review*, 59(3):492–544, 2017.
- [1354] T.E. Johnson, M. Brown, B.J.P. Kaus, and J.A. VanTongeren. Delamination and recycling of Archaean crust caused by gravitational instabilities. *Nature Geoscience*, 7:47–52, 2014.
- [1355] L. Jolivet, P. Davy, and P. Cobbold. Right-lateral shear along the Northwest Pacific margin and the India-Eurasia collision. *Tectonics*, 9(6):1409–1419, 1990.
- [1356] Laurent Jolivet, Claudio Faccenna, Benjamin Huet, Loic Labrousse, Laetitia Le Pourhiet, Olivier Lacombe, Emmanuel Lecomte, Evguenii Burov, Yoann Denèle, Jean-Pierre Brun, et al. Aegean tectonics: Strain localisation, slab tearing and trench retreat. *Tectonophysics*, 597:1–33, 2013.
- [1357] FW Jones, F Pascal, and ME Ertman. The thermal regime of a three-dimensional subducting lithospheric slab and its electromagnetic response: a numerical model. *Tectonophysics*, 225(1-2):35–48, 1993.
- [1358] Ganesh Raj Joshi and Daigoro Hayashi. Finite element modelling of the pull-apart formation: implication for tectonics of bengo co pull-apart basin, southern tibet. *Natural Science*, 2(06):654, 2010.
- [1359] MS Joun and MC Lee. Quadrilateral finite-element generation and mesh quality control for metal forming simulation. *International Journal for Numerical Methods in Engineering*, 40(21):4059–4075, 1997.
- [1360] A. Jourdon, L. Le Pourhiet, Mouthereau F, and E. Masini. Role of rift maturity on the architecture and shortening distribution in mountain belts. *Earth Planet. Sci. Lett.*, 512:89–99, 2019.
- [1361] A. Jourdon, L. Le Pourhiet, C. Petit, and Y. Rolland. Impact of range-parallel sediment transport on 2D thermo-mechanical models of mountain belts: Application to the Kyrgyz Tien Shan. *Terra Nova*, 30:279–288, 2018.
- [1362] M Jull and D McKenzie. The effect of deglaciation on mantle melting beneath iceland. *Journal of Geophysical Research: Solid Earth*, 101(B10):21815–21828, 1996.
- [1363] S. Jun and S. Im. Multiple-scale meshfree adaptivity for the simulation of adiabatic shear band formation. *Computational Mechanics*, 15:257, 2000.

- [1364] D Jurine, C Jaupart, G Brandeis, and PJ Tackley. Penetration of mantle plumes through depleted lithosphere. *Journal of Geophysical Research: Solid Earth*, 110(B10), 2005.
- [1365] H. Kabaria, A.J. Lew, and B. Cockburn. A hybridizable discontinuous Galerkin formulation for non-linear elasticity. *Computer Methods in Applied Mechanics and Engineering*, 283:303–329, 2015.
- [1366] L.M. Kachanov. *Fundamentals of the Theory of Plasticity*. Dover Publications, Inc., 2004.
- [1367] A. Kageyama and T. Sato. Yin-Yang grid: An overset grid in spherical geometry. *Geochem. Geophys. Geosyst.*, 5(9):DOI:10.1029/2004GC000734, 2004.
- [1368] L. Kaislaniemi and J. van Hunen. Dynamics of lithospheric thinning and mantle melting by edge-driven convection: Application to Moroccan Atlas mountains. *Geochem. Geophys. Geosyst.*, 15:3175–3189, 2014.
- [1369] L. Kaislaniemi, J. van Hunen, and P. Bouilhol. Lithosphere destabilization by melt weakening and crust-mantle interactionsâimplications for generation of granite-migmatite belts. *Tectonics*, 2018.
- [1370] K Kalousová, O Souček, and O Čadek. Deformation of an elastic shell with variable thickness: a comparison of different methods. *Geophysical Journal International*, 190(2):726–744, 2012.
- [1371] K Kalousová, O Souček, and O Čadek. Two-phase convection in icy satellites. *Acta Universitatis Carolinae. Mathematica et Physica*, 53(1):61–71, 2012.
- [1372] Klára Kalousová, Ondřej Souček, Gabriel Tobie, Gaël Choblet, and Ondřej Čadek. Ice melting and downward transport of meltwater by two-phase flow in europa’s ice shell. *Journal of Geophysical Research: Planets*, 119(3):532–549, 2014.
- [1373] M. Kameyama, A. Kageyamab, and T. Sato. Multigrid-based simulation code for mantle convection in spherical shell using YinYang grid. *Phys. Earth. Planet. Inter.*, 171:19–32, 2008.
- [1374] M. Kameyama, D.A. Yuen, and S.-I. Karato. Thermal-mechanical effects of low-temperature plasticity (the Peierls mechanism) on the deformation of a viscoelastic shear zone. *Earth Planet. Sci. Lett.*, 168:159–172, 1999.
- [1375] Masanori Kameyama, Hiromi Fujimoto, and Masaki Ogawa. A thermo-chemical regime in the upper mantle in the early earth inferred from a numerical model of magma-migration in a convecting upper mantle. *Physics of the earth and planetary interiors*, 94(3-4):187–215, 1996.
- [1376] Edouard Kaminski, Neil M Ribe, and Jules T Browaeys. D-rex, a program for calculation of seismic anisotropy due to crystal lattice preferred orientation in the convective upper mantle. *Geophysical Journal International*, 158(2):744–752, 2004.
- [1377] G. Kanschat. Divergence-free discontinuous Galerkin schemes for the Stokes equations and the MAC scheme. *Int. J. Num. Meth. Fluids*, 56:941–950, 2008.
- [1378] G. Kanschat and B. Rivière. A strongly conservative finite element method for the coupling of Stokes and Darcy flow. *J. Comp. Phys.*, 229:5933–5943, 2010.
- [1379] S. Karato, M.R. Riedel, and D.A. Yuen. Rheological structure and deformation of subducted slabs in the mantle transition zone: implications for mantle circulation and deep earthquakes. *Phys. Earth. Planet. Inter.*, 127:83–108, 2001.
- [1380] S.-I. Karato. Importance of anelasticity in the interpretation of seismic tomography. *Geophys. Res. Lett.*, 20(15):1623–1626, 1993.
- [1381] S.-I. Karato and H. Jung. Effects of pressure on high-temperature dislocation creep in olivine. *Philosophical Magazine*, 83(3):401–414, 2003.
- [1382] S.-I. Karato and P. Li. Diffusion Creep in Perovskite: Implications for the Rheology of the Lower Mantle. *Science*, 255(5049):1238, 1992.
- [1383] S.-I. Karato and P. Wu. Rheology of the Upper Mantle: A synthesis. *Science*, 260:771–778, 1993.
- [1384] Shun-Ichiro Karato. Grain-size distribution and rheology of the upper mantle. *Tectonophysics*, 104(1-2):155–176, 1984.
- [1385] Shun-ichiro Karato. Rheology of the deep upper mantle and its implications for the preservation of the continental roots: A review. *Tectonophysics*, 481(1-4):82–98, 2010.
- [1386] Shun-Ichiro Karato, Mervyn S Paterson, and John D FitzGerald. Rheology of synthetic olivine aggregates: influence of grain size and water. *Journal of Geophysical Research: Solid Earth*, 91(B8):8151–8176, 1986.
- [1387] Shivakumar Karekal, Raj Das, Luke Mosse, and Paul W Cleary. Application of a mesh-free continuum method for simulation of rock caving processes. *International Journal of Rock Mechanics and Mining Sciences*, 48(5):703–711, 2011.

- [1388] MH Kargarnovin, HE Toussi, and SJ Fariborz. Elasto-plastic element-free galerkin method. *Computational Mechanics*, 33(3):206–214, 2004.
- [1389] I. Katayama and S. Karato. Low-temperature, high-stress deformation of olivine under water-saturated conditions. *Phys. Earth. Planet. Inter.*, 168(3-4):125–133, 2008.
- [1390] Tomoo Katsura, Sho Yokoshi, Kazuaki Kawabe, Anton Shatskiy, MA Geeth M Manthilake, Shuangmeng Zhai, Hiroshi Fukui, HA Chamathnhi I Hegoda, Takashi Yoshino, Daisuke Yamazaki, et al. P-v-t relations of mgsio<sub>3</sub> perovskite determined by in situ x-ray diffraction using a large-volume high-pressure apparatus. *Geophysical Research Letters*, 36(1), 2009.
- [1391] Tomoo Katsura, Akira Yoneda, Daisuke Yamazaki, Takashi Yoshino, and Eiji Ito. Adiabatic temperature profile in the mantle. *Physics of the Earth and Planetary Interiors*, 183(1-2):212–218, 2010.
- [1392] Richard F Katz, Matthew G Knepley, Barry Smith, Marc Spiegelman, and Ethan T Coon. Numerical simulation of geodynamic processes with the portable extensible toolkit for scientific computation. *Physics of the Earth and Planetary Interiors*, 163(1-4):52–68, 2007.
- [1393] Rafael Katzman, Uri S ten Brink, and Jian Lin. Three-dimensional modeling of pull-apart basins: Implications for the tectonics of the dead sea basin. *Journal of Geophysical Research: Solid Earth*, 100(B4):6295–6312, 1995.
- [1394] Peter Kaufmann. *Discontinuous Galerkin FEM in Computer Graphics*. PhD thesis, ETH Zurich, 2012.
- [1395] B. Kaus. *Modelling approaches to geodynamic processes*. PhD thesis, ETH Zurich, 2005.
- [1396] B.J.P. Kaus. Factors that control the angle of shear bands in geodynamic numerical models of brittle deformation. *Tectonophysics*, 484:36–47, 2010.
- [1397] B.J.P. Kaus and T.W. Becker. Effects of elasticity on the RayleighTaylor instability: implications for large-scale geodynamics. *Geophys. J. Int.*, 168(843–862), 2007.
- [1398] B.J.P. Kaus, H. Mühlhaus, and D.A. May. A stabilization algorithm for geodynamic numerical simulations with a free surface. *Phys. Earth. Planet. Inter.*, 181:12–20, 2010.
- [1399] B.J.P. Kaus and Y.Y. Podlachikov. Forward and Reverse Modeling of the Three-Dimensional Viscous Rayleigh-Taylor Instability. *Geophys. Res. Lett.*, 28(6):1095–1098, 2001.
- [1400] B.J.P. Kaus and Y.Y. Podlachikov. Initiation of localized shear zones in viscoelastoplastic rocks. *J. Geophys. Res.*, 111(B04412), 2006.
- [1401] B.J.P. Kaus, Y.Yu. Podladchikov, and D.W. Schmid. Eulerian Spectral/Finite Difference Method for Large Deformation Modelling of Visco-Elasto-Plastic Geomaterials. *Bulletino di Geofisica*, 45:346–349, 2004.
- [1402] B.J.P. Kaus, A.A. Popov, T.S. Baumann, A.E. Pusok, A. Bauville, N. Fernandez, and M. Collignon. Forward and Inverse Modelling of Lithospheric Deformation on Geological Timescales. *NIC Symposium 2016*, pages 299–307, 2016.
- [1403] B.J.P. Kaus, C. Steedman, and T.W. Becker. From passive continental margin to mountain belt: insights from analytical and numerical models and application to Taiwan. *Phys. Earth. Planet. Inter.*, 171:235–251, 2008.
- [1404] Boris J. P. Kaus and Stefan M. Schmalholz. 3d finite amplitude folding: Implications for stress evolution during crustal and lithospheric deformation. *Geophys. Res. Lett.*, 33, 2006.
- [1405] Boris JP Kaus, Taras V Gerya, and Daniel W Schmid. Recent advances in computational geodynamics: Theory, numerics and applications. *Physics of the earth and planetary interiors*, 1(171):2–6, 2008.
- [1406] M. Kawaguti. Numerical solution of the Navier-Stokes equations for the flow in a two-dimensional cavity. *Journal of the Physical Society of Japan*, 16(12):2307–2315, 1961.
- [1407] Takaaki Kawazoe, Shun-ichiro Karato, Kazuhiko Otsuka, Zhicheng Jing, and Mainak Mookherjee. Shear deformation of dry polycrystalline olivine under deep upper mantle conditions using a rotational drickamer apparatus (rda). *Physics of the Earth and Planetary Interiors*, 174(1-4):128–137, 2009.
- [1408] Y. Ke and V. S. Solomatov. Early transient superplumes and the origin of the martian crustal dichotomy. *Journal of Geophysical Research*, 111(E10), 2006.
- [1409] Y. Ke and V. S. Solomatov. Coupled core-mantle thermal evolution of early mars. *Journal of Geophysical Research*, 114(E7), 2009.
- [1410] N. Kechkar and D. Silvester. Analysis of locally stabilised mixed finite element methods for the Stokes problem. *Mathematics of Computation*, 58(197):1–10, 1992.
- [1411] JW Keefner, SJ Mackwell, DL Kohlstedt, and F Heidelbach. Dependence of dislocation creep of dunite on oxygen fugacity: implications for viscosity variations in earth's mantle. *Journal of Geophysical Research: Solid Earth*, 116(B5), 2011.

- [1412] Henk Keers, Stéphane Rondenay, Yaël Harlap, and Ivar Nordmo. Resources for computational geophysics courses. *Eos, Transactions American Geophysical Union*, 95(37):335–336, 2014.
- [1413] T. Keller, D.A. May, and B.J.P. Kaus. Numerical modelling of magma dynamics coupled to tectonic deformation of lithosphere and crust. *Geophys. J. Int.*, page doi:10.1093/gji/ggt306, 2013.
- [1414] Tobias Keller and Richard F Katz. The role of volatiles in reactive melt transport in the asthenosphere. *Journal of Petrology*, 57(6):1073–1108, 2016.
- [1415] Tobias Keller and Paul J Tackley. Towards self-consistent modeling of the martian dichotomy: The influence of one-ridge convection on crustal thickness distribution. *Icarus*, 202(2):429–443, 2009.
- [1416] L. H. Kellogg. Interaction of plumes with a compositional boundary at 670 km. *Geophysical Research Letters*, 18(5):865–868, 1991.
- [1417] L. H. Kellogg. Growing the earth’s d“ layer: Effect of density variations at the core-mantle boundary. *Geophysical Research Letters*, 24(22):2749–2752, 1997.
- [1418] L. H. Kellogg and S. D. King. Effect of mantle plumes on the growth of d” by reaction between the core and mantle. *Geophysical Research Letters*, 20(5):379–382, 1993.
- [1419] L. H. Kellogg and S. D. King. The effect of temperature dependent viscosity on the structure of new plumes in the mantle: Results of a finite element model in a spherical, axisymmetric shell. *Earth and Planetary Science Letters*, 148(1-2):13–26, 1997.
- [1420] LH Kellogg and DL Turcotte. Mixing and the distribution of heterogeneities in a chaotically convecting mantle. *Journal of Geophysical Research: Solid Earth*, 95(B1):421–432, 1990.
- [1421] Louise H Kellogg, Bradford H Hager, and Rob D Van Der Hilst. Compositional stratification in the deep mantle. *Science*, 283(5409):1881–1884, 1999.
- [1422] S. Kelly, J.P. Butler, and C. Beaumont. Continental collision with a sandwiched accreted terrane: Insights into himalayan-tibetan lithospheric mantle tectonics? *Earth and Planetary Science Letters*, 455:176–195, 2016.
- [1423] David V Kemp and David J Stevenson. A tensile, flexural model for the initiation of subduction. *Geophysical Journal International*, 125(1):73–93, 1996.
- [1424] BLN Kennett. On the density distribution within the earth. *Geophysical Journal International*, 132(2):374–382, 1998.
- [1425] D.F. Keppie, C.A. Currie, and C. Warren. Subduction erosion modes: comparing finite element numerical models with the geological record. *Earth Planet. Sci. Lett.*, 287:241–254, 2009.
- [1426] R Keppler, FM Rosas, and TJ Nagel. Thin viscous middle-crust and evolving fault distribution during continental rifting: Insights from analog modeling experiments. *Tectonophysics*, 608:161–175, 2013.
- [1427] Katie M Keranen, Simon L Klemperer, Jordi Julia, Jesse F Lawrence, and Andy A Nyblade. Low lower crustal velocity across ethiopia: Is the main ethiopian rift a narrow rift in a hot craton? *Geochemistry, Geophysics, Geosystems*, 10(5), 2009.
- [1428] K. Key, S. Constable, L. Liu, and A. Pommier. Electrical image of passive mantle upwelling beneath the northern east pacific rise. *Nature*, 495(7442):499–502, 2013.
- [1429] W. S. Kiefer. Mantle viscosity stratification and flow geometry: Implications for surface motions on earth and venus. *Geophysical Research Letters*, 20(4):265–268, 1993.
- [1430] W. S. Kiefer and Q. Li. Water undersaturated mantle plume volcanism on present-day mars. *Meteoritics & Planetary Science*, 2016.
- [1431] W.S. Kiefer and B. Hager. Geoid anomalies and dynamic topography from convection in cylindrical geometry: applications to mantle plumes on Earth and Venus. *Geophys. J. Int.*, 108:198–214, 1992.
- [1432] Y. H. Kim, C. Lee, and S-S Kim. Tectonics and volcanism in east asia: Insights from geophysical observations. *Journal of Asian Earth Sciences*, 113:842–856, 2015.
- [1433] Y-M Kim and C. Lee. Effect of time-evolving age and convergence rate of the subducting plate on the cenozoic adakites and boninites. *Journal of Asian Earth Sciences*, 95:300–312, 2014.
- [1434] Madlen Kimmritz and Malte Braack. Equal-order finite elements for the hydrostatic stokes problem. *Computational Methods in Applied Mathematics Comput. Methods Appl. Math.*, 12(3):306–329, 2012.
- [1435] Jun-Ichi Kimura, James B Gill, Tomoyuki Kunikiyo, Isaku Osaka, Yusuke Shimoshioiri, Maiko Katakuse, Susumu Kakubuchi, Takashi Nagao, Katsuhiro Furuyama, Atsushi Kamei, et al. Diverse magmatic effects of subducting a hot slab in sw japan: Results from forward modeling. *Geochemistry, Geophysics, Geosystems*, 15(3):691–739, 2014.

- [1436] Chris Kincaid. Subduction dynamics: From the trench to the core-mantle boundary. *Reviews of Geophysics*, 33(S1):401–412, 1995.
- [1437] Chris Kincaid and I Selwyn Sacks. Thermal and dynamical evolution of the upper mantle in subduction zones. *Journal of Geophysical Research: Solid Earth*, 102(B6):12295–12315, 1997.
- [1438] E.M. King, S. Stellmach, J. Noir, U. Hansen, and J.M. Aurnou. Boundary layer control of rotating convection systems. *Nature*, 457(7227):301–304, 2009.
- [1439] S. King, C. Lee, P. van Keken, W. Leng, S. Zhong, E. Tan, N. Tosi, and M. Kameyama. A community benchmark for 2D Cartesian compressible convection in the Earths mantle. *Geophys. J. Int.*, 180:7387, 2010.
- [1440] S. D. King. Pattern of lobate scarps on mercury’s surface reproduced by a model of mantle convection. *Nature Geoscience*, 1(4):229–232, 2008.
- [1441] S. D. King. On topography and geoid from 2-d stagnant lid convection calculations. *Geochemistry, Geophysics, Geosystems*, 10(3):n/a–n/a, 2009.
- [1442] S. D. King and B. H. Hager. The relationship between plate velocity and trench viscosity in newtonian and power-law subduction calculations. *Geophysical Research Letters*, 17(13):2409–2412, 1990.
- [1443] S. D. King and B. H. Hager. Subducted slabs and the geoid: 1. numerical experiments with temperature-dependent viscosity. *Journal of Geophysical Research: Solid Earth*, 99(B10):19843–19852, 1994.
- [1444] Scott D King. Radial models of mantle viscosity: results from a genetic algorithm. *Geophysical Journal International*, 122(3):725–734, 1995.
- [1445] Scott D King. Reconciling laboratory and observational models of mantle rheology in geodynamic modelling. *Journal of Geodynamics*, 100:33–50, 2016.
- [1446] Scott D King, Carl W Gable, and Stuart A Weinstein. Models of convection-driven tectonic plates: a comparison of methods and results. *Geophysical Journal International*, 109(3):481–487, 1992.
- [1447] Scott D King, Julian P Lowman, and Carl W Gable. Episodic tectonic plate reorganizations driven by mantle convection. *Earth and Planetary Science Letters*, 203(1):83–91, 2002.
- [1448] Scott D King and Jeroen Ritsema. African hot spot volcanism: small-scale convection in the upper mantle beneath cratons. *Science*, 290(5494):1137–1140, 2000.
- [1449] S.D. King. Venus Resurfacing Constrained by Geoid and Topography. *JGR: Planets*, 123:1041–1060, 2018.
- [1450] S.D. King and C. Adam. Hotspot swells revisited. *Phys. Earth. Planet. Inter.*, 235:66–83, 2014.
- [1451] S.D. King and D.L. Anderson. An alternative mechanism of flood basalt formation. *Earth Planet. Sci. Lett.*, 136:269–279, 1995.
- [1452] S.D. King and D.L. Anderson. Edge-driven convection. *Earth Planet. Sci. Lett.*, 160:289–296, 1998.
- [1453] S.D. King, D.J. Frost, and D.C. Rubie. Why cold slabs stagnate in the transition zone. *Geology*, page doi:10.1130/G36320.1, 2015.
- [1454] S.D. King, A. Raefsky, and B.H. Hager. ConMan: Vectorizing a finite element code for incompressible two-dimensional convection in the Earths mantle. *Phys. Earth. Planet. Inter.*, 59:195–208, 1990.
- [1455] A. Kiraly, F.A. Capitanio, F. Funiciello, and C. Faccenna. Subduction zone interaction: Controls on arcuate belts. *Geology*, 2016.
- [1456] A. Király, F.A. Capitanio, F. Funiciello, and C. Faccenna. Subduction induced mantle flow: Length-scales and orientation of the toroidal cell. *Earth Planet. Sci. Lett.*, 479:284–297, 2017.
- [1457] A. Kiraly, C. Faccenna, F. Funiciello, and A. Sembroni. Coupling surface and mantle dynamics: A novel experimental approach. *Geophys. Res. Lett.*, 42, 2015.
- [1458] Eric Kirby and Kelin X Whipple. Expression of active tectonics in erosional landscapes. *Journal of Structural Geology*, 44:54–75, 2012.
- [1459] S.H. Kirby and A.K. Kronenberg. Rheology of the lithosphere: Selected topics. *Reviews of Geophysics*, 25(6), 1987.
- [1460] Stephen H Kirby. Rheology of the lithosphere. *Reviews of Geophysics*, 21(6):1458–1487, 1983.
- [1461] Dániel Kiss, Yuri Podladchikov, Thibault Duretz, and Stefan M Schmalholz. Spontaneous generation of ductile shear zones by thermal softening: Localization criterion, 1d to 3d modelling and application to the lithosphere. *Earth and Planetary Science Letters*, 519:284–296, 2019.
- [1462] EA Kneller, PE van Keken, I Katayama, and S-i Karato. Stress, strain, and b-type olivine fabric in the fore-arc mantle: Sensitivity tests using high-resolution steady-state subduction zone models. *Journal of Geophysical Research: Solid Earth*, 112(B4), 2007.

- [1463] Erik A. Kneller, Markus Albertz, Garry D. Karner, , and Christopher A. Johnson. Testing inverse kinematic models of paleocrustal thickness in extensional systems with high-resolution forward thermo-mechanical models. *Geochem. Geophys. Geosyst.*, 2013.
- [1464] Erik A Kneller and Peter E van Keken. Effect of three-dimensional slab geometry on deformation in the mantle wedge: Implications for shear wave anisotropy. *Geochemistry, Geophysics, Geosystems*, 9(1), 2008.
- [1465] Matthew G. Knepley. *Computational Science I*. Rice University - Department of Computational and Applied Mathematics, 2017.
- [1466] P. Knobloch. On Korn's inequality for nonconforming Finite Elements. *Technische Mechanik*, 20(3):205–214, 2000.
- [1467] P. Knobloch and L. Tobiska. Stabilisation methods of bubble type for the  $Q_1/Q_1$  element applied to the incompressible Navier-Stokes equations. *Mathematical Modelling and Numerical Analysis*, 34(1):85–107, 2000.
- [1468] Dana A Knoll and David E Keyes. Jacobian-free newton–krylov methods: a survey of approaches and applications. *Journal of Computational Physics*, 193(2):357–397, 2004.
- [1469] G.M. Kobelkov and M.A. Olshanskii. Effective preconditioning of Uzawa type schemes for a generalized Stokes problem. *Numer. Math.*, 86:443–470, 2000.
- [1470] P. Koelemeijer, J. Ritsema, A. Deuss, and H.-J. van Heijst. SP12RTS: a degree-12 model of shear- and compressional-wave velocity for Earth's mantle. *Geophy. J. Int.*, 204:1024–1039, 2016.
- [1471] D. E. Koglin Jr., S. R. Ghias, S. D. King, G. T. Jarvis, and J. P. Lowman. Mantle convection with reversing mobile plates: A benchmark study. *Geochemistry, Geophysics, Geosystems*, 6(9), 2005.
- [1472] David L Kohlstedt. Role of water and melts on upper mantle viscosity and strength. *Mantle Flow and Melt Generation at Mid-Ocean Ridges. Am. Geophys. Union, Washington DC*, pages 103–121, 1992.
- [1473] David L Kohlstedt. Properties of rocks and minerals-constitutive equations, rheological behavior, and viscosity of rocks. In *Treatise on Geophysics*, pages 389–417. Elsevier, 2007.
- [1474] D.L. Kohlstedt, B. Evans, and S.J. Mackwell. Strength of the lithosphere: Constraints imposed by laboratory experiments. *J. Geophys. Res.*, 100:17587–17602, 1995.
- [1475] D.L. Kohlstedt and C. Goetze. Low-StressHigh-Temperature Creep in Olivine Single Crystals. *J. Geophys. Res.*, 79(14):2045, 1974.
- [1476] Dimitri Komatitsch, Seiji Tsuboi, Jeroen Tromp, A Levander, and G Nolet. The spectral-element method in seismology. *GEOPHYSICAL MONOGRAPH-AMERICAN GEOPHYSICAL UNION*, 157:205, 2005.
- [1477] Andrea Komoróczki, Steffen Abe, and Janos L Urai. Meshless numerical modeling of brittle–viscous deformation: first results on boudinage and hydrofracturing using a coupling of discrete element method (dem) and smoothed particle hydrodynamics (sph). *Computational Geosciences*, 17(2):373–390, 2013.
- [1478] T. Komut, R. Gray, R. Pysklywec, and O. Gogus. Mantle flow uplift of western Anatolia and the Aegean: Interpretation from geophysical analyses and geodynamic modeling. *J. Geophys. Res.*, 117(B11412), 2012.
- [1479] L. Komzsik and P. Poschmann. Iterative solution techniques for finite element applications. *Finite Elements in Analysis and Design*, 14:373–379, 1993.
- [1480] Henk Kooi and Christopher Beaumont. Escarpment evolution on high-elevation rifted margins: Insights derived from a surface processes model that combines diffusion, advection, and reaction. *Journal of Geophysical Research: Solid Earth*, 99(B6):12191–12209, 1994.
- [1481] Henk Kooi and Christopher Beaumont. Large-scale geomorphology: Classical concepts reconciled and integrated with contemporary ideas via a surface processes model. *Journal of Geophysical Research: Solid Earth*, 101(B2):3361–3386, 1996.
- [1482] P.O. Koons. Two-sided orogen: Collision and erosion from the sandbox to the Southern Alps, New Zealand. *Geology*, 18:679–682, 1990.
- [1483] P.O. Koons. Three-dimensional critical wedges: Tectonics and topography in oblique collisional orogen. *J. Geophys. Res.*, 99(B6):12,301–12,315, 1994.
- [1484] P.O. Koons. Modeling the topographic evolution of collisional belts. *Annu. Rev. Earth Planet. Sci.*, 23:375–408, 1995.
- [1485] P.O. Koons, R.J. Norris, D. Craw, and A.F. Cooper. Influence of exhumation on the structural evolution of transpressional plate boundaries: An example from the Southern Alps, New Zealand. *Geology*, 31(1):3–6, 2003.
- [1486] P.O. Koons, P.K. Zeitler, C.P. Chamberlain, D. Craw, and A.S. Meltzer. Mechanical links between erosion and metamorphism in Nanga Parbat, Pakistan Himalaya. *American Journal of Science*, 302:749–733, 2002.

- [1487] H. Koopmann, S. Brune, D. Franke, and S. Breuer. Linking rift propagation barriers to excess magmatism at volcanic rifted margins. *Geology*, page doi:10.1130/G36085.1, 2014.
- [1488] A. Koptev, A. Beniest, L. Jolivet, and S. Leroy. PlumeInduced Breakup of a Subducting Plate: Micro-continent Formation Without Cessation of the Subduction Process. *Geophys. Res. Lett.*, 46:3663–3675, 2019.
- [1489] A. Koptev, E. Burov, E. Calais, S. Leroy, T. Gerya, L. Guillou-Frottier, and S. Cloetingh. Contrasted continental rifting via plume-craton interaction: Applications to Central East African Rift. *Geoscience Frontiers*, 7:221–236, 2016.
- [1490] A. Koptev, E. Calais, E. Burov, S. Leroy, and T. Gerya. Dual continental rift systems generated by plume-lithosphere interaction. *Nature Geoscience*, page DOI: 10.1038/NGEO2401, 2015.
- [1491] A. Koptev, S. Cloetingh, E. Burov, T. Francois, and T. Gerya. Long-distance impact of Iceland plume on Norway's rifted margin. *Scientific Reports*, 7(10408), 2017.
- [1492] Alexander Koptev, Todd A Ehlers, Matthias Nettesheim, and David Whipp. Response of a rheologically stratified lithosphere to subduction of an indenter-shaped plate: Insights into localized exhumation at orogen syntaxes. *Tectonics*, 2019.
- [1493] J. Korenaga. Thermal cracking and the deep hydration of oceanic lithosphere: A key to the generation of plate tectonics? *J. Geophys. Res.*, 112(B05408), 2007.
- [1494] J. Korenaga and S.-I. Karato. A new analysis of experimental data on olivine rheology. *J. Geophys. Res.*, 113(B02403), 2008.
- [1495] Jun Korenaga. Urey ratio and the structure and evolution of earth's mantle. *Reviews of Geophysics*, 46(2), 2008.
- [1496] Jun Korenaga. Initiation and evolution of plate tectonics on earth: theories and observations. *Annual review of earth and planetary sciences*, 41:117–151, 2013.
- [1497] J.R. Koseff and R.L. Street. The Lid-Driven Cavity Flow: A Synthesis of Qualitative and Quantitative Observations. *J. Fluids Eng.*, 106:390–398, 1984.
- [1498] D. Kourounis, A. Fuchs, and O. Schenk. Towards the next generation of multiperiod optimal power flow solvers. *IEEE Transactions on Power Systems*, PP(99):1–10, 2018.
- [1499] L.I.G. Kovasznay. Laminar flow behind a two-dimensional grid. *Mathematical Proceedings of the Cambridge Philosophical Society*, 44(1):58–62, 1948.
- [1500] Peter Kovesi. Good colour maps: How to design them. *CoRR*, abs/1509.03700, 2015.
- [1501] Hemin Koyi. Analogue modelling: from a qualitative to a quantitative techniquea historical outline. *Journal of Petroleum Geology*, 20(2):223–238, 1997.
- [1502] M. Krabbendam. Sliding of temperate basal ice on a rough, hard bed: creep mechanisms, pressure melting, and implications for ice streaming. *The Cryosphere*, 10:1915–1932, 2016.
- [1503] Stephan C Kramer, Cian R Wilson, and D Rhodri Davies. An implicit free surface algorithm for geodynamical simulations. *Physics of the Earth and Planetary Interiors*, 194:25–37, 2012.
- [1504] Corné Kreemer, Geoffrey Blewitt, and Elliot C Klein. A geodetic plate motion and global strain rate model. *Geochemistry, Geophysics, Geosystems*, 15(10):3849–3889, 2014.
- [1505] Corné Kreemer, William E Holt, and A John Haines. An integrated global model of present-day plate motions and plate boundary deformation. *Geophysical Journal International*, 154(1):8–34, 2003.
- [1506] Abdelkader Krimi, Mehdi Rezoug, Sofiane Khelladi, Xesús Nogueira, Michael Deligant, and Luis Ramírez. Smoothed particle hydrodynamics: a consistent model for interfacial multiphase fluid flow simulations. *Journal of Computational Physics*, 358:53–87, 2018.
- [1507] M. Kronbichler, T. Heister, and W. Bangerth. High accuracy mantle convection simulation through modern numerical methods . *Geophys. J. Int.*, 191:12–29, 2012.
- [1508] M Krotkiewski, M Dabrowski, and YY Podladchikov. Fractional steps methods for transient problems on commodity computer architectures. *Physics of the Earth and Planetary Interiors*, 171(1-4):122–136, 2008.
- [1509] Marcin Krotkiewski and Marcin Dabrowski. Parallel symmetric sparse matrix–vector product on scalar multi-core cpus. *Parallel Computing*, 36(4):181–198, 2010.
- [1510] Neil J Krystopowicz and Claire A Currie. Crustal eclogitization and lithosphere delamination in orogens. *Earth and Planetary Science Letters*, 361:195–207, 2013.

- [1511] E.-J. N. Kuiper, J. H. P. de Bresser, M. R. Drury, J. Eichler, G. M. Pennock, and I. Weikusat. Using a composite flow law to model deformation in the neem deep ice core, greenland: Part 2 the role of grain size and premelting on ice deformation at high homologous temperature. *The Cryosphere Discussions*, 2019:1–30, 2019.
- [1512] E.-J. N. Kuiper, I. Weikusat, J. H. P. de Bresser, D. Jansen, G. M. Pennock, and M. R. Drury. Using a composite flow law to model deformation in the neem deep ice core, greenland: Part 1 the role of grain size and grain size distribution on the deformation of holocene and glacial ice. *The Cryosphere Discussions*, 2019:1–32, 2019.
- [1513] E.N. Kuiper. *Flow in naturally deformed ice: a cryogenic electron microscopy and modelling study of the NEEM ice core*. PhD thesis, Utrecht University, 2019.
- [1514] S Kulasegaram, Bhushan Lal Karihaloo, and A Ghanbari. Modelling the flow of self-compacting concrete. *International Journal for Numerical and Analytical Methods in Geomechanics*, 35(6):713–723, 2011.
- [1515] D. Kurfess and O. Heidbach. CASQUS: A new simulation tool for coupled 3D finite element modeling of tectonic and surface processes based on ABAQUS and CASCADE. *Computers and Geosciences*, 35:1959–1967, 2009.
- [1516] NJ Kusznir and RG Park. The strength of intraplate lithosphere. *Physics of the Earth and Planetary Interiors*, 36(3-4):224–235, 1984.
- [1517] Oh-In Kwon and C. Park. A new quadrilateral MINI element for Stokes equations. *ESAIM: Mathematical Modelling and Numerical Analysis*, 48:955–968, 2014.
- [1518] A.H. Lachenbruch and G.A. Thompson. Oceanic ridges and transform faults: their intersection angles and resistance to plate motion. *Earth Planet. Sci. Lett.*, 15:116–122, 1972.
- [1519] Peter Lafemina, Timothy H Dixon, Rob Govers, Edmundo Norabuena, Henry Turner, Armando Saballos, Glen Mattioli, Marino Protti, and Wilfried Strauch. Fore-arc motion and Cocos Ridge collision in Central America. *Geochemistry Geophysics Geosystems*, 10(5), 2009.
- [1520] Dimitri Lague, Niels Hovius, and Philippe Davy. Discharge, discharge variability, and the bedrock channel profile. *Journal of Geophysical Research: Earth Surface*, 110(F4), 2005.
- [1521] Serge Lallemand, Arnauld Heuret, and David Boutelier. On the relationships between slab dip, back-arc stress, upper plate absolute motion, and crustal nature in subduction zones. *Geochemistry, Geophysics, Geosystems*, 6(9), 2005.
- [1522] B.P. Lamichhane. A quadrilateral mini finite element for the Stokes problem using a single bubble function. 2015.
- [1523] W. Landry, L. Hodkinson, and S. Kientz. Gale user manual. Technical report, CIG, VPAC, 2011.
- [1524] Sean M Langemeyer, Julian P Lowman, and Paul J Tackley. The sensitivity of core heat flux to the modeling of plate-like surface motion. *Geochemistry, Geophysics, Geosystems*, 19(4):1282–1308, 2018.
- [1525] Sean M Langemeyer, Julian P Lowman, and Paul J Tackley. The dynamics and impact of compositionally originating provinces in a mantle convection model featuring rheologically obtained plates. *Geophysical Journal International*, 220(3):1700–1716, 2020.
- [1526] U. Langer and W. Queck. On the convergence factor of Uzawa’s algorithm. *Journal of Computational and Applied Mathematics*, 15:191–202, 1986.
- [1527] BE Larock and LR Herrmann. Improved flux prediction using low order finite elements. In *International Conference on Finite Elements in Water Resources, Part II*, 1976.
- [1528] Tine B Larsen, David A Yuen, Jiří Moser, and Bengt Fornberg. A high-order finite-difference method applied to large rayleigh number mantle convection. *Geophysical & Astrophysical Fluid Dynamics*, 84(1-2):53–83, 1997.
- [1529] Tine B Larsen, David A Yuen, and Michael Storey. Ultrafast mantle plumes and implications for flood basalt volcanism in the northern atlantic region. *Tectonophysics*, 311(1-4):31–43, 1999.
- [1530] R. L. Larson and C. Kincaid. Onset of mid-cretaceous volcanism by elevation of the 670 km thermal boundary layer. *Geology*, 24(6):551, 1996.
- [1531] T. M. Lassak, A. K. McNamara, E. J. Garnero, and S. Zhong. Core-mantle boundary topography as a possible constraint on lower mantle chemistry and dynamics. *Earth and Planetary Science Letters*, 289(1-2):232–241, 2010.
- [1532] Gautier Laurent, Guillaume Caumon, and Mark Jessell. Interactive editing of 3d geological structures and tectonic history sketching via a rigid element method. *Computers & geosciences*, 74:71–86, 2015.

- [1533] J Lavé. Analytic solution of the mean elevation of a watershed dominated by fluvial incision and hillslope landslides. *Geophysical research letters*, 32(11), 2005.
- [1534] J. Lavé and JP Avouac. Fluvial incision and tectonic uplift across the Himalayas of central Nepal. *J. Geophys. Res.*, 106(B11):26561, 2001.
- [1535] A. Lavecchia, C. Thieulot, F. Beekman, S. Cloetingh, and S. Clark. Lithosphere erosion and continental breakup: Interaction of extension, plume upwelling and melting. *Earth Planet. Sci. Lett.*, 467:89–98, 2017.
- [1536] Luc L Lavier and W Roger Buck. Half graben versus large-offset low-angle normal fault: Importance of keeping cool during normal faulting. *Journal of Geophysical Research: Solid Earth*, 107(B6):ETG–8, 2002.
- [1537] Luc L Lavier, W Roger Buck, and Alexei NB Poliakov. Factors controlling normal fault offset in an ideal brittle layer. *Journal of Geophysical Research: Solid Earth*, 105(B10):23431–23442, 2000.
- [1538] Thorne Lay, John Hernlund, and Bruce A Buffett. Core–mantle boundary heat flow. *Nature geoscience*, 1(1):25, 2008.
- [1539] L. Le Pourhiet. Strain Localization Due to Structural Softening During Pressure Sensitive Rate Independent Yielding. *Bull. Soc. Geol. France*, 184:357–371, 2013.
- [1540] L. Le Pourhiet, B. Huet, L. Labrousse, K. Yao, P. Agard, and L. Jolivet. Strain localisation in mechanically layered rocks beneath detachment zones: insights from numerical modelling. *Solide Earth*, 4:135–152, 2013.
- [1541] L. Le Pourhiet, B. Huet, D.A. May, L. Labrousse, and L. Jolivet. Kinematic interpretation of the 3D shapes of metamorphic core complexes. *Geochem. Geophys. Geosyst.*, 13(Q09002), 2012.
- [1542] Laetitia Le Pourhiet, L Mattioni, and I Moretti. 3d modelling of rifting through a pre-existing stack of nappes in the gulf of corinth (greece): a mixed analogue/numerical approach. *Geological Society, London, Special Publications*, 253(1):233–252, 2006.
- [1543] Laetitia Le Pourhiet, Dave A May, Lucas Huille, Louise Watremez, and Sylvie Leroy. A genetic link between transform and hyper-extended margins. *Earth and Planetary Science Letters*, 465:184–192, 2017.
- [1544] S.M. Lechmann, D.A. May, B.J.P. Kaus, and S.M. Schmalholz. Comparing thin-sheet models with 3-D multilayer models for continental collision. *Geophy. J. Int.*, 187:10–33, 2011.
- [1545] SM Lechmann, SM Schmalholz, G Hetényi, DA May, and BJP Kaus. Quantifying the impact of mechanical layering and underthrusting on the dynamics of the modern india-asia collisional system with 3-d numerical models. *Journal of Geophysical Research: Solid Earth*, 119(1):616–644, 2014.
- [1546] E. Lecomte, L. Le Pourhiet, O. Lacombe, and L. Jolivet. A continuum mechanics approach to quantify brittle strain on weak faults: application to the extensional reactivation of shallow dipping discontinuities. *Geophy. J. Int.*, 184:1–11, 2011.
- [1547] C. Lee and S. D. King. Effect of mantle compressibility on the thermal and flow structures of the subduction zones. *Geochemistry, Geophysics, Geosystems*, 10(1):n/a–n/a, 2009.
- [1548] C. Lee and S. D. King. Why are high-mg# andesites widespread in the western aleutians? a numerical model approach. *Geology*, 38(7):583–586, 2010.
- [1549] C. Lee and S. D. King. Dynamic buckling of subducting slabs reconciles geological and geophysical observations. *Earth and Planetary Science Letters*, 312(3-4):360–370, 2011.
- [1550] C. Lee and C. Lim. Short-term and localized plume-slab interaction explains the genesis of abukuma adakite in northeastern japan. *Earth and Planetary Science Letters*, 396:116–124, 2014.
- [1551] E-S Lee, Charles Moulinec, Rui Xu, Damien Violeau, Dominique Laurence, and Peter Stansby. Comparisons of weakly compressible and truly incompressible algorithms for the sph mesh free particle method. *Journal of computational Physics*, 227(18):8417–8436, 2008.
- [1552] Junhwan Lee, Rodrigo Salgado, and Sooil Kim. Bearing capacity of circular footings under surcharge using state-dependent finite element analysis. *Computers and Geotechnics*, 32:445–457, 2005.
- [1553] R. Lee, P. Gresho, and R. Sani. Smooting techniques for certain primitive variable solutions of the Navier-Stokes equations. . *Int. J. Num. Meth. Eng.*, 14:1785–1804, 1979.
- [1554] K.A. Leever, R.H. Gabrielsen, D. Sokoutis, and E. Willingshofer. The effect of convergence angle on the kinematic evolution of strain partitioning in transpressional brittle wedges: Insight from analog modeling and high-resolution digital image analysis. *Tectonics*, 30(TC2013):10.1029/2010TC002823, 2011.
- [1555] R.S. Lehmann, M. Lukacova-Medvidova, B.J.P. Kaus, and A.A. Popov. Comparison of continuous and discontinuous Galerkin approaches for variable-viscosity Stokes flow. *Z. Angew. Math. Mech.*, pages 1–14, 2015.
- [1556] V. Lemiale, H.-B. Mühlhaus, L. Moresi, and J. Stafford. Shear banding analysis of plastic models formulated for incompressible viscous flows. *Phys. Earth. Planet. Inter.*, 171:177–186, 2008.

- [1557] Vincent Lemiale, Laura Karantgis, and Philip Broadbridge. Smoothed particle hydrodynamics applied to the modelling of landslides. In *Applied Mechanics and Materials*, volume 553, pages 519–524, 2014.
- [1558] Vincent Lemiale, H-B Mühlhaus, Catherine Meriaux, L Moresi, and L Hodkinson. Rate effects in dense granular materials: Linear stability analysis and the fall of granular columns. *International Journal for Numerical and Analytical Methods in Geomechanics*, 35(2):293–308, 2011.
- [1559] A. Lenardic. On the partitioning of mantle heat loss below oceans and continents over time and its relationship to the archaean paradox: Mantle heat partitioning and the archaean paradox. *Geophysical Journal International*, 134(3):706–720, 1998.
- [1560] A. Lenardic, Laurent Guillou-Frottier, JC Mareschal, C Jaupart, LN Moresi, and WM Kaula. What the mantle sees: the effects of continents on mantle heat flow. *GEOPHYSICAL MONOGRAPH-AMERICAN GEOPHYSICAL UNION*, 121:95–112, 2000.
- [1561] A. Lenardic and W. M. Kaula. A numerical treatment of geodynamic viscous flow problems involving the advection of material interfaces. *Journal of Geophysical Research: Solid Earth*, 98(B5):8243–8260, 1993.
- [1562] A. Lenardic and W. M. Kaula. Self-lubricated mantle convection: Two-dimensional models. *Geophysical Research Letters*, 21(16):1707–1710, 1994.
- [1563] A. Lenardic and W. M. Kaula. Tectonic plates, d” thermal structure, and the nature of mantle plumes. *Journal of Geophysical Research*, 99(B8):15697, 1994.
- [1564] A. Lenardic and W. M. Kaula. More thoughts on convergent crustal plateau formation and mantle dynamics with regard to tibet. *Journal of Geophysical Research: Solid Earth*, 100(B8):15193–15203, 1995.
- [1565] A. Lenardic and W. M. Kaula. Near-surface thermal/chemical boundary layer convection at infinite prandtl number: two-dimensional numerical experiments. *Geophysical Journal International*, 126(3):689–711, 1996.
- [1566] A. Lenardic, W. M. Kaula, and D. L. Bindschadler. The tectonic evolution of western ishtar terra, venus. *Geophysical Research Letters*, 18(12):2209–2212, 1991.
- [1567] A. Lenardic, W. M. Kaula, and D. L. Bindschadler. A mechanism for crustal recycling on venus. *Journal of Geophysical Research*, 98(E10):18697, 1993.
- [1568] A. Lenardic, W. M. Kaula, and D. L. Bindschadler. Some effects of a dry crustal flow law on numerical simulations of coupled crustal deformation and mantle convection on venus. *Journal of Geophysical Research*, 100(E8):16949, 1995.
- [1569] A. Lenardic and L. Moresi. A new class of equilibrium geotherms in the deep thermal lithosphere of continents. *Earth and Planetary Science Letters*, 176(3-4):331–338, 2000.
- [1570] A. Lenardic and L Moresi. Thermal convection below a conducting lid of variable extent: heat flow scalings and two-dimensional, infinite prandtl number numerical simulations. *Physics of Fluids*, 15(2):455–466, 2003.
- [1571] A. Lenardic, L. Moresi, A.M. Jellinek, C.J. O'Neill, C.M. Cooper, and C.T. Lee. Continents, supercontinents, mantle thermal mixing, and mantle thermal isolation: Theory, numerical simulations, and laboratory experiments. *Geochem. Geophys. Geosyst.*, 12(10), 2011.
- [1572] A. Lenardic, L Moresi, and H Mühlhaus. The role of mobile belts for the longevity of deep cratonic lithosphere: the crumple zone model. *Geophysical Research Letters*, 27(8):1235–1238, 2000.
- [1573] A. Lenardic and L-N Moresi. Some thoughts on the stability of cratonic lithosphere: Effects of buoyancy and viscosity. *Journal of Geophysical Research: Solid Earth*, 104(B6):12747–12758, 1999.
- [1574] A. Lenardic, M. Weller, T. Höink, and J. Seales. Toward a boot strap hypothesis of plate tectonics: Feedbacks between plates, the asthenosphere, and the wavelength of mantle convection. *Physics of the Earth and Planetary Interiors*, 296:106299, 2019.
- [1575] Adrian Lenardic, CM Cooper, and L Moresi. A note on continents and the earths urey ratio. *Physics of the Earth and Planetary Interiors*, 188(1-2):127–130, 2011.
- [1576] Adrian Lenardic, AM Jellinek, and L-N Moresi. A climate induced transition in the tectonic style of a terrestrial planet. *Earth and Planetary Science Letters*, 271(1-4):34–42, 2008.
- [1577] Adrian Lenardic and L Moresi. Heat flow scaling for mantle convection below a conducting lid: Resolving seemingly inconsistent modeling results regarding continental heat flow. *Geophysical research letters*, 28(7):1311–1314, 2001.
- [1578] Adrian Lenardic, L-N Moresi, AM Jellinek, and M Manga. Continental insulation, mantle cooling, and the surface area of oceans and continents. *Earth and Planetary Science Letters*, 234(3-4):317–333, 2005.

- [1579] Adrian Lenardic, L-N Moresi, and H Mühlhaus. Longevity and stability of cratonic lithosphere: insights from numerical simulations of coupled mantle convection and continental tectonics. *Journal of Geophysical Research: Solid Earth*, 108(B6), 2003.
- [1580] Adrian Lenardic, Francis Nimmo, and L Moresi. Growth of the hemispheric dichotomy and the cessation of plate tectonics on mars. *Journal of Geophysical Research: Planets*, 109(E2), 2004.
- [1581] W. Leng, M. Gurnis, and P. Asimov. From basalts to boninites: The geodynamics of volcanic expression during induced subduction initiation. *Initiation and Termination of Subduction: Rock Record, Geodynamic Models, Modern Plate Boundaries*, 2012.
- [1582] W. Leng and S. Zhong. Viscous heating, adiabatic heating and energetic consistency in compressible mantle convection. *Geophy. J. Int.*, 173:693–702, 2008.
- [1583] W. Leng and S. Zhong. More constraints on internal heating rate of the earth’s mantle from plume observations. *Geophysical Research Letters*, 36(2):n/a–n/a, 2009.
- [1584] W. Leng and S. Zhong. Implementation and application of adaptive mesh refinement for thermochemical mantle convection studies. *Geochem. Geophys. Geosyst.*, 12(4), 2011.
- [1585] Wei Leng and Michael Gurnis. Dynamics of subduction initiation with different evolutionary pathways. *Geochem. Geophys. Geosyst.*, 12(12):Q12018, doi:10.1029/2011GC003877, 2011.
- [1586] Wei Leng and Michael Gurnis. Subduction initiation at relic arcs. *Geophys. Res. Lett.*, 42:7014–7021, 2015.
- [1587] Wei Leng, Lili Ju, Yan Xie, Tao Cui, and Max Gunzburger. Finite element three-dimensional stokes ice sheet dynamics model with enhanced local mass conservation. *Journal of Computational Physics*, 274:299–311, 2014.
- [1588] Luna Bergere Leopold and Thomas Maddock. *The hydraulic geometry of stream channels and some physiographic implications*, volume 252. US Government Printing Office, 1953.
- [1589] Y Leroy and M Ortiz. Finite element analysis of strain localization in frictional materials. *International Journal for Numerical and Analytical Methods in Geomechanics*, 13(1):53–74, 1989.
- [1590] O Lesne, E Calais, and J Deverchere. Finite element modelling of crustal deformation in the baikal rift zone: new insights into the active–passive rifting debate. *Tectonophysics*, 289(4):327–340, 1998.
- [1591] P. LeTallec and V. Ruas. On the convergence of the bilinear-velocity constant-pressure finite element method in viscous flow. *Computer Methods in Applied Mechanics and Engineering*, 54:235–243, 1986.
- [1592] Einat Lev and Bradford H Hager. Rayleigh–taylor instabilities with anisotropic lithospheric viscosity. *Geophysical Journal International*, 173(3):806–814, 2008.
- [1593] A Levander, B Schmandt, MS Miller, K Liu, KE Karlstrom, RS Crow, C-TA Lee, and ED Humphreys. Continuing colorado plateau uplift by delamination-style convective lithospheric downwelling. *Nature*, 472(7344):461, 2011.
- [1594] R.J. Leveque. High-resolution conservative algorithms for advection in incompressible flow. *SIAM J. Numer. Anal.*, 33(2):627–665, 1996.
- [1595] R.W. Lewis, K. Ravindran, and A.S. Usmani. Finite Element Solution of Incompressible Flows Using an Explicit Segregated Approach. *Archives of Computational Methods in Engineering*, 2(4):69–93, 1995.
- [1596] Ben Q Li. *Discontinuous finite elements in fluid dynamics and heat transfer*. Springer Science & Business Media, 2006.
- [1597] D. Li, M. Gurnis, and G. Stadler. Towards adjoint-based inversion of time-dependent mantle convection with nonlinear viscosity. *Geophy. J. Int.*, 209:86–105, 2017.
- [1598] Fucheng Li, Zhen Sun, Xiong Pang, Jie Liao, Hongfeng Yang, Hui Xie, Haiteng Zhuo, and Zhongxian Zhao. Low-viscosity crustal layer controls the crustal architecture and thermal distribution at hyper-extended margins: Modeling insight and application to the northern south china sea margin. *Geochemistry, Geophysics, Geosystems*, 2019.
- [1599] J. Li, Y. He, and Z. Chen. Performance of several stabilized finite element methods for the Stokes equations based on the lowest equal-order pairs. *Computing*, 86:37–51, 2009.
- [1600] L. Li, D. Weidner, P. Ratteron, J. Chen, M. Vaughan, S. Mei, and B. Duham. Deformation of olivine at mantle pressure using the D-DIA. *Eur. J. Mineral.*, 18:7–19, 2006.
- [1601] M. Li, S. Zhong, and P. Olson. Linking lowermost mantle structure, core-mantle boundary heat flux and mantle plume formation. *Physics of the Earth and Planetary Interiors*, 2018.
- [1602] Mingming Li and Allen K McNamara. The difficulty for subducted oceanic crust to accumulate at the earth’s core-mantle boundary. *Journal of Geophysical Research: Solid Earth*, 118(4):1807–1816, 2013.

- [1603] S. Li and W.K. Liu. *Meshfree Particle Methods*. Springer, 2004.
- [1604] Shaofan Li, Wei Hao, and Wing Kam Liu. Mesh-free simulations of shear banding in large deformation. *International Journal of solids and structures*, 37(48-50):7185–7206, 2000.
- [1605] Shaofan Li and Wing Kam Liu. Meshfree and particle methods and their applications. *Applied Mechanics Reviews*, 55(1):1–34, 2002.
- [1606] Shaofan Li, Wing Kam Liu, Ares J Rosakis, Ted Belytschko, and Wei Hao. Mesh-free galerkin simulations of dynamic shear band propagation and failure mode transition. *International Journal of solids and structures*, 39(5):1213–1240, 2002.
- [1607] Yang Li, Frédéric Deschamps, and Paul J Tackley. The stability and structure of primordial reservoirs in the lower mantle: insights from models of thermochemical convection in three-dimensional spherical geometry. *Geophysical Journal International*, 199(2):914–930, 2014.
- [1608] Yanyou Li and Jiafu Qi. Salt-related contractional structure and its main controlling factors of kelasu structural zone in kuqa depression: insights from physical and numerical experiments. *Procedia Engineering*, 31:863–867, 2012.
- [1609] Z.-H. Li, Z. Xu, T. Gerya, and J.-P. Burg. Collision of continental corner from 3-D numerical modeling. *Earth Planet. Sci. Lett.*, 380:98–111, 2013.
- [1610] ZH Li, TV Gerya, and J-P Burg. Influence of tectonic overpressure on p-t paths of hp-uhp rocks in continental collision zones: thermomechanical modelling. *Journal of Metamorphic Geology*, 28(3):227–247, 2010.
- [1611] Z.H. Li, Z.Q. Xu, and T.V. Gerya. Flat versus steep subduction: Contrasting modes for the formation and exhumation of high- to ultrahigh-pressure rocks in continental collision zones. *Earth Planet. Sci. Lett.*, 301:65–77, 2011.
- [1612] Zhong-Hai Li, Jeanette F Di Leo, and Neil M Ribe. Subduction-induced mantle flow, finite strain, and seismic anisotropy: Numerical modeling. *Journal of Geophysical Research: Solid Earth*, 119(6):5052–5076, 2014.
- [1613] Zhong-Hai Li, Taras Gerya, and James AD Connolly. Variability of subducting slab morphologies in the mantle transition zone: Insight from petrological-thermomechanical modeling. *Earth-Science Reviews*, 2019.
- [1614] Zhong-Hai Li and Neil M Ribe. Dynamics of free subduction from 3-d boundary element modeling. *Journal of Geophysical Research: Solid Earth*, 117(B6), 2012.
- [1615] Zhonghai Li and Taras V Gerya. Polyphase formation and exhumation of high-to ultrahigh-pressure rocks in continental subduction zone: Numerical modeling and application to the sulu ultrahigh-pressure terrane in eastern china. *Journal of Geophysical Research: Solid Earth*, 114(B9), 2009.
- [1616] Z.-X. Lia and S. Zhong. Supercontinentsuperplume coupling, true polar wander and plume mobility: Plate dominance in whole-mantle tectonics. *Phys. Earth. Planet. Inter.*, 176:143–156, 2009.
- [1617] Qing Liang, Chao Chen, and Yaoguo Li. 3-d inversion of gravity data in spherical coordinates with application to the grail data. *Journal of Geophysical Research: Planets*, 119(6):1359–1373, 2014.
- [1618] J. Liao and T. Gerya. From continental rifting to seafloor spreading: Insight from 3D thermo-mechanical modeling. *Gondwana Research*, 2014.
- [1619] J. Liao and T. Gerya. Influence of lithospheric mantle stratification on craton extension: Insight from two-dimensional thermo-mechanical modeling. *Tectonophysics*, 2014.
- [1620] J Liao, T Gerya, and Q Wang. Layered structure of the lithospheric mantle changes dynamics of craton extension. *Geophysical Research Letters*, 40(22):5861–5866, 2013.
- [1621] Q. Liao and D. Sylvester. Robust stabilized Stokes approximation methods for highly stretched grids. *IMA Journal of Numerical Analysis*, page doi:10.1093/imanum/drs012, 2012.
- [1622] C. Lim and C. Lee. Effects of temporal plume-slab interaction on the partial melting of the subducted oceanic crust. *Journal of Asian Earth Sciences*, 113:857–865, 2015.
- [1623] A. Limache, S. Idelsohn, R. Rossi, and E. Oñate. The violation of objectivity in Laplace formulations of the NavierStokes equations. *Int. J. Num. Meth. Fluids*, 54:639–664, 2007.
- [1624] Ja-Ren Lin, Taras V Gerya, Paul J Tackley, David A Yuen, and Gregor J Golabek. Numerical modeling of protocore destabilization during planetary accretion: Methodology and results. *Icarus*, 204(2):732–748, 2009.

- [1625] Ja-Ren Lin, Taras V Gerya, Paul J Tackley, David A Yuen, and Gregor J Golabek. Protocore destabilization in planetary embryos formed by cold accretion: Feedbacks from non-newtonian rheology and energy dissipation. *Icarus*, 213(1):24–42, 2011.
- [1626] Jian Lin and EM Parmentier. A finite amplitude necking model of rifting in brittle lithosphere. *Journal of Geophysical Research: Solid Earth*, 95(B4):4909–4923, 1990.
- [1627] John Lin, GM Purdy, H Schouten, J-C Sempere, and C Zervas. Evidence from gravity data for focused magmatic accretion along the mid-atlantic ridge. *Nature*, 344(6267):627, 1990.
- [1628] S.-C. Lin and B.-Y. Kuo. Dynamics of the opposite-verging subduction zones in the Taiwan region: Insights from numerical models. *J. Geophys. Res.*, 121:2174–2192, 2016.
- [1629] S.-C. Lin and P.E. van Keken. Dynamics of thermochemical plumes: 1. Plume formation and entrainment of a dense layer. *Geochem. Geophys. Geosyst.*, 7(2), 2006.
- [1630] S.-C. Lin and P.E. van Keken. Dynamics of thermochemical plumes: 2. Complexity of plume structures and its implications for mapping mantle plumes . *Geochem. Geophys. Geosyst.*, 7(3), 2006.
- [1631] Johannes Linden, Guy Lonsdale, Barbara Steckel, and Klaus Stueben. Multigrid for the steady-state incompressible navier-stokes equations: A survey. In *11th International Conference on Numerical Methods in Fluid Dynamics*, pages 57–68. Springer, 1989.
- [1632] E. Rune Lindgren. The motion of a sphere in an incompressible viscous fluid at Reynolds numbers considerably less than one. *Physica Scripta*, 60:97–110, 1999.
- [1633] G.S. Lister, M.A. Etheridge, and P.A. Symonds. Detachment faulting and the evolution of passive continental margins. *Geology*, 14:246–250, 1986.
- [1634] Konstantin D Litasov and Eiji Ohtani. Effect of water on the phase relations in earth’s mantle and deep water cycle. *Special Papers-Geological Society of America*, 421:115, 2007.
- [1635] C. Lithgow-Bertelloni and J.H. Guynn. Origin of the lithospheric stress field. *J. Geophys. Res.*, 109(B01408), 2004.
- [1636] Benjamin T Liu, Susan J Muller, and Morton M Denn. Convergence of a regularization method for creeping flow of a bingham material about a rigid sphere. *Journal of non-newtonian fluid mechanics*, 102(2):179–191, 2002.
- [1637] G.R. Liu. *Mesh Free Methods*. CRC press, 2003.
- [1638] G.R. Liu and Y.T. Gu. *An introduction to meshfree methods and their programming*. Springer, 2005.
- [1639] G.R. Liu and M.B. Liu. *Smoothed Particle Hydrodynamics*. World Scientific, 2003.
- [1640] GR Liu and ZH Tu. An adaptive procedure based on background cells for meshless methods. *Computer Methods in Applied Mechanics and Engineering*, 191(17-18):1923–1943, 2002.
- [1641] L. Liu and M. Gurnis. Simultaneous inversion of mantle properties and initial conditions using an adjoint of mantle convection. *Journal of Geophysical Research*, 113(B8), 2008.
- [1642] L. Liu and D. R. Stegman. Origin of columbia river flood basalt controlled by propagating rupture of the farallon slab. *Nature*, 482(7385):386–389, 2012.
- [1643] L. Liu and D.R. Stegman. Segmentation of the Farallon slab. *Earth Planet. Sci. Lett.*, 311:1–10, 2011.
- [1644] Lijun Liu, Sonja Spasojević, and Michael Gurnis. Reconstructing farallon plate subduction beneath north america back to the late cretaceous. *Science*, 322(5903):934–938, 2008.
- [1645] MB Liu, GR Liu, and KY Lam. Investigations into water mitigation using a meshless particle method. *Shock waves*, 12(3):181–195, 2002.
- [1646] MB Liu, GR Liu, and KY Lam. Constructing smoothing functions in smoothed particle hydrodynamics with applications. *Journal of Computational and applied Mathematics*, 155(2):263–284, 2003.
- [1647] MB Liu and Gui-Rong Liu. Restoring particle consistency in smoothed particle hydrodynamics. *Applied numerical mathematics*, 56(1):19–36, 2006.
- [1648] Mou B Liu, WP Xie, and GR Liu. Modeling incompressible flows using a finite particle method. *Applied mathematical modelling*, 29(12):1252–1270, 2005.
- [1649] S. Liu and C.A. Currie. Farallon plate dynamics prior to the Laramide orogeny: Numerical models of flat subduction. *Tectonophysics*, 666:33–47, 2016.
- [1650] S. Liu and S.D. King. A benchmark study of incompressible Stokes flow in a 3-D spherical shell using ASPECT. *Geophys. J. Int.*, 217:650–667, 2019.
- [1651] W. Liu and S. Xu. A new improved Uzawa method for finite element solution of Stokes problem. *Computational Mechanics*, 27:305–310, 2001.

- [1652] X. Liu and S. Zhong. Analyses of marginal stability, heat transfer and boundary layer properties for thermal convection in a compressible fluid with infinite Prandtl number. *Geophys. J. Int.*, 194:125–144, 2013.
- [1653] X. Liu and S. Zhong. The long-wavelength geoid from three-dimensional spherical models of thermal and thermochemical mantle convection. *Journal of Geophysical Research: Solid Earth*, 120(6):4572–4596, 2015.
- [1654] Yan Liu and Ted Belytschko. A new support integration scheme for the weakform in mesh-free methods. *International journal for numerical methods in engineering*, 82(6):699–715, 2010.
- [1655] Z. Liu and P. Bird. Two-dimensional and three-dimensional finite element modelling of mantle processes beneath central South Island, New Zealand. *Geophys. J. Int.*, 165:1003–1028, 2006.
- [1656] M.-G. Llorens. Stress and strain evolution during single-layer folding under pure and simple shear. *Journal of Structural Geology*, 126:245–257, 2019.
- [1657] IS Lobanov, I Yu Popov, AI Popov, and TV Gerya. Numerical approach to the stokes problem with high contrasts in viscosity. *Applied Mathematics and Computation*, 235:17–25, 2014.
- [1658] A. Loddoch and U. Hansen. Temporally transitional mantle convection: Implications for mars. *Journal of Geophysical Research*, 113(E9), 2008.
- [1659] A. Loddoch, C. Stein, and U. Hansen. Temporal variations in the convective style of planetary mantles. *Earth and Planetary Science Letters*, 251(1-2):79–89, 2006.
- [1660] J. Lof and A.H. van den Boogaard. Adaptive return mapping algorithms for  $J_2$  elasto-viscoplastic flow. *Int. J. Num. Meth. Eng.*, 51:1283–1298, 2001.
- [1661] Liz C Logan, Luc L Lavier, Eunseo Choi, Eh Tan, and Ginny A Catania. Semi-brittle rheology and ice dynamics in dyneearthsol3d. *The Cryosphere*, 11(1):117–132, 2017.
- [1662] Anders Logg, Kent-Andre Mardal, and Garth Wells. *Automated solution of differential equations by the finite element method: The FEniCS book*, volume 84. Springer Science & Business Media, 2012.
- [1663] C. Loiselet, J. Braun, L. Husson, C. Le Carlier de Veslud, C. Thieulot, P. Yamato, and D. Grujic. Subducting slabs: Jellyfishes in the Earth’s mantle. *Geochem. Geophys. Geosyst.*, 11(8):doi:10.1029/2010GC003172, 2010.
- [1664] Christelle Loiselet, Laurent Husson, and Jean Braun. From longitudinal slab curvature to slab rheology. *Geology*, 37(8):747–750, 2009.
- [1665] M. D. Long, B. H. Hager, M. V. de Hoop, and R. D. van der Hilst. Two-dimensional modelling of subduction zone anisotropy with application to southwestern japan. *Geophysical Journal International*, 170(2):839–856, 2007.
- [1666] Benjamin Loret and Jean H Prevost. Dynamic strain localization in elasto-(visco-) plastic solids, part 1. general formulation and one-dimensional examples. *Computer Methods in Applied Mechanics and Engineering*, 83(3):247–273, 1990.
- [1667] Frank Losasso, Ronald Fedkiw, and Stanley Osher. Spatially adaptive techniques for level set methods and incompressible flow. *Computers & Fluids*, 35(10):995–1010, 2006.
- [1668] Diogo L Lourenço, Antoine B Rozel, Taras Gerya, and Paul J Tackley. Efficient cooling of rocky planets by intrusive magmatism. *Nature Geoscience*, 11(5):322, 2018.
- [1669] Julian P Lowman. Mantle convection models featuring plate tectonic behavior: An overview of methods and progress. *Tectonophysics*, 510(1-2):1–16, 2011.
- [1670] Julian P Lowman and Gary T Jarvis. Mantle convection models of continental collision and breakup incorporating finite thickness plates. *Physics of the Earth and Planetary Interiors*, 88(1):53–68, 1995.
- [1671] SJ Loyd, TW Becker, CP Conrad, C Lithgow-Bertelloni, and FA Corsetti. Time variability in cenozoic reconstructions of mantle heat flow: plate tectonic cycles and implications for earth’s thermal evolution. *Proceedings of the National Academy of Sciences*, 104(36):14266–14271, 2007.
- [1672] G. Lu, B.J.P. Kaus, L. Zhao, and T. Zheng. Self-consistent subduction initiation induced by mantle flow. *Terra Nova*, page doi: 10.1111/ter.12140, 2015.
- [1673] Leon B Lucy. A numerical approach to the testing of the fission hypothesis. *The astronomical journal*, 82:1013–1024, 1977.
- [1674] Stefan Luth, Ernst Willingshofer, Dimitrios Sokoutis, and Sierd Cloetingh. Does subduction polarity changes below the alps? inferences from analogue modelling. *Tectonophysics*, 582:140–161, 2013.
- [1675] Richard A Lux, Geoffrey F Davies, and John H Thomas. Moving lithospheric plates and mantle convection. *Geophysical Journal International*, 58(1):209–228, 1979.

- [1676] P. Ma, S. Liu, M. Gurnis, and B. Zhang. Slab Horizontal Subduction and Slab Tearing Beneath East Asia. *Geophys. Res. Lett.*, 46:5161–5169, 2019.
- [1677] C. Maas and U. Hansen. Effects of earth's rotation on the early differentiation of a terrestrial magma ocean. *Journal of Geophysical Research: Solid Earth*, 120(11):7508–7525, 2015.
- [1678] Julia G MacDougall, Margarete A Jadamec, and Karen M Fischer. The zone of influence of the subducting slab in the asthenospheric mantle. *Journal of Geophysical Research: Solid Earth*, 122(8):6599–6624, 2017.
- [1679] F. Machado, F. Zinani, and S. Frey. Herschel-Bulkley Fluid Flows Through a Sudden Axisymmetric Expansion via Galerkin Least-Squares Methodology.
- [1680] Philippe Machetel, Catherine Thoraval, and David Brunet. Spectral and geophysical consequences of 3-d spherical mantle convection with an endothermic phase change at the 670 km discontinuity. *Physics of the Earth and Planetary Interiors*, 88(1):43–51, 1995.
- [1681] Philippe Machetel and Patrice Weber. Intermittent layered convection in a model mantle with an endothermic phase change at 670 km. *Nature*, 350(6313):55, 1991.
- [1682] S.J. Mackwell, M. E. Zimmerman, and D. L. Kohlstedt. High-temperature deformation of dry diabase with application to tectonics on Venus. *J. Geophys. Res.*, 103:975–984, 1998.
- [1683] M. Maffione, C. Thieulot, D.J.J. van Hinsbergen, A. Morris, O. Plimper, and W. Spakman. Dynamics of intraoceanic subduction initiation: 1. Oceanic detachment fault inversion and the formation of supra-subduction zone ophiolites. *Geochem. Geophys. Geosyst.*, 16:1753–1770, 2015.
- [1684] V. Magni. The effects of back-arc spreading on arc magmatism. *Earth Planet. Sci. Lett.*, 519:141–151, 2019.
- [1685] V. Magni, M.B. Allen, J. van Hunen, and P. Bouilhol. Continental underplating after slab break-off. *Earth Planet. Sci. Lett.*, 474:59–67, 2017.
- [1686] V. Magni, P. Bouilhol, and J. van Hunen. Deep water recycling through time. *Geochem. Geophys. Geosyst.*, 15:4203–4216, 2014.
- [1687] V Magni, J van Hunen, F Funiciello, and C Faccenna. Numerical models of slab migration in continental collision zones. *Solid earth.*, 3(2):293–306, 2012.
- [1688] Valentina Magni, Claudio Faccenna, Jeroen van Hunen, and Francesca Funiciello. Delamination vs. break-off: the fate of continental collision. *Geophysical Research Letters*, 40(2):285–289, 2013.
- [1689] R. Mahmood, N. Kousar, M. Yaqub, and K. Jabeen. Numerical Simulations of the Square Lid Driven Cavity Flow of Bingham Fluids Using Nonconforming Finite Elements Coupled with a Direct Solver. *Advances in Mathematical Physics*, 2017.
- [1690] P. Maierová. *Evolution of the Bohemian Massif: Insights from numerical modeling*. PhD thesis, Charles University in Prague, 2012.
- [1691] P. Maierová, O. Lexa, K. Schulmann, and P. Stipska. Contrasting tectono-metamorphic evolution of orogenic lower crust in the Bohemian Massif: A numerical model. *Gondwana Research*, 25:509–521, 2014.
- [1692] Petra Maierová, Karel Schulmann, and Taras Gerya. Relamination styles in collisional orogens. *Tectonics*, 37(1):224–250, 2018.
- [1693] C. Malatesta, T. Gerya, L. Crispini, L. Federico, and G. Capponi. Oblique subduction modelling indicates along-trench tectonic transport of sediments. *Nature Communications*, 4, 2013.
- [1694] C. Malatesta, T. Gerya, L. Crispini, L. Federico, and G. Capponi. Interplate deformation at early-stage oblique subduction: 3-D thermomechanical numerical modeling. *Tectonics*, 35:1610–1625, 2016.
- [1695] Andrei V Malevsky, David A Yuen, and LM Weyer. Viscosity and thermal fields associated with strongly chaotic non-newtonian thermal convection. *Geophysical research letters*, 19(2):127–130, 1992.
- [1696] D.S. Malkus and T.J.R. Hughes. Mixed finite element methods - reduced and selective integration techniques: a unification of concepts. *Comput. Meth. Appl. Mech. Eng.*, 15:63–81, 1978.
- [1697] C Mallard, B Jacquet, and N Coltice. Adopt: A tool for automatic detection of tectonic plates at the surface of convection models. *Geochemistry, Geophysics, Geosystems*, 18(8):3197–3208, 2017.
- [1698] Claire Mallard, Nicolas Coltice, Maria Seton, R Dietmar Müller, and Paul J Tackley. Subduction controls the distribution and fragmentation of earths tectonic plates. *Nature*, 535(7610):140, 2016.
- [1699] L.E. Malvern. *Introduction to the mechanics of a continuous medium*. Prentice-Hall, Inc., 1969.
- [1700] N.S. Mancktelow. Tectonic pressure: Theoretical concepts and modelled examples. *Lithos*, 103:149–177, 2008.

- [1701] N Mandal, Susanta Kumar Samanta, and Chandan Chakraborty. Numerical modeling of heterogeneous flow fields around rigid objects with special reference to particle paths, strain shadows and foliation drag. *Tectonophysics*, 330(3-4):177–194, 2001.
- [1702] V. Manea and M. Gurnis. Subduction zone evolution and low viscosity wedges and channels. *Earth Planet. Sci. Lett.*, 264:22–45, 2007.
- [1703] V. C. Manea, M. Manea, W. P. Leeman, and D. L. Schutt. The influence of plume head-lithosphere interaction on magmatism associated with the yellowstone hotspot track. *Journal of Volcanology and Geothermal Research*, 188(1-3):68–85, 2009.
- [1704] V.C. Manea, W.P. Leeman, T. Gerya, M. Manea, and G. Zhu. Subduction of fracture zones controls mantle melting and geochemical signature above slabs. *Nature Communications*, page doi:10.1038/ncomms6095, 2014.
- [1705] Vlad C Manea, Marta Pérez-Gussinyé, and Marina Manea. Chilean flat slab subduction controlled by overriding plate thickness and trench rollback. *Geology*, 40(1):35–38, 2012.
- [1706] G. Maniatis, D. Kurfess, A. Hampel, and O. Heidbach. Slip acceleration on normal faults due to erosion and sedimentation Results from a new three-dimensional numerical model coupling tectonics and landscape evolution. *Earth Planet. Sci. Lett.*, 284:570–582, 2009.
- [1707] Utsav Mannu, Kosuke Ueda, Sean D Willett, Taras V Gerya, and Michael Strasser. Impact of sedimentation on evolution of accretionary wedges: Insights from high-resolution thermomechanical modeling. *Tectonics*, 35(12):2828–2846, 2016.
- [1708] Utsav Mannu, Kosuke Ueda, Sean D Willett, Taras V Gerya, and Michael Strasser. Stratigraphic signatures of forearc basin formation mechanisms. *Geochemistry, Geophysics, Geosystems*, 18(6):2388–2410, 2017.
- [1709] Wei Mao and Shijie Zhong. Slab stagnation due to a reduced viscosity layer beneath the mantle transition zone. *Nature Geoscience*, 11(11):876, 2018.
- [1710] Wei Mao and Shijie Zhong. Controls on global mantle convective structures and their comparison with seismic models. *Journal of Geophysical Research: Solid Earth*, 2019.
- [1711] X. Mao, M. Gurnis, and D.A. May. Subduction Initiation With Vertical Lithospheric Heterogeneities and New Fault Formation. *Geophys. Res. Lett.*, 44:10.1002/2017GL075389, 2017.
- [1712] Yadan Mao, Jin-Qiang Zhong, and Jun Zhang. The dynamics of an insulating plate over a thermally convecting fluid and its implication for continent movement over convective mantle. *Journal of Fluid Mechanics*, 868:286–315, 2019.
- [1713] J.-P. Marcotte. *Méthodes itératives pour la résolution, par éléments finis, du problème de Stokes non linéaire*. PhD thesis, Ecole Polytechnique de Montréal, 2000.
- [1714] Walter V Maresch and Taras V Gerya. Blueschists and blue amphiboles: How much subduction do they need? *International Geology Review*, 47(7):688–702, 2005.
- [1715] G. Marketos, R. Govers, and C.J. Spiers. Ground motions induced by a producing hydrocarbon reservoir that is overlain by a viscoelastic rocksalt layer: a numerical model. *Geophys. J. Int.*, 203:228–242, 2015.
- [1716] G Marketos, C J Spiers, and Rob Govers. Impact of rock salt creep law choice on subsidence calculations for hydrocarbon reservoirs overlain by evaporite caprocks. *Journal Of Geophysical Research*, 121(6):4249–4267, 2016.
- [1717] AM Marotta, M Fernandez, and R Sabadini. Mantle unrooting in collisional settings. *Tectonophysics*, 296(1-2):31–46, 1998.
- [1718] A.M. Marotta and M.I. Spalla. Permian-Triassic high thermal regime in the Alps: Result of late Variscan collapse or continental rifting? Validation by numerical modeling. *Tectonics*, 26(TC4016):oi:10.1029/2006TC002047, 2007.
- [1719] A.M. Marotta, E. Spelta, and C. Rizzetto. Gravity signature of crustal subduction inferred from numerical modelling. *Geophys. J. Int.*, 166:923–938, 2006.
- [1720] Anna Maria Marotta and Roberto Sabadini. The style of the tyrrhenian subduction. *Geophysical research letters*, 22(7):747–750, 1995.
- [1721] Hauke Marquardt and Lowell Miyagi. Slab stagnation in the shallow lower mantle linked to an increase in mantle viscosity. *Nature Geoscience*, 8(4):311, 2015.
- [1722] Fernando O Marques, Ksenia Nikolaeva, Marcelo Assumpção, Taras V Gerya, Francisco HR Bezerra, Aderson F do Nascimento, and Joaquim M Ferreira. Testing the influence of far-field topographic forcing on subduction initiation at a passive margin. *Tectonophysics*, 608:517–524, 2013.

- [1723] F.O. Marques, F.R. Cabral, T.V. Gerya, G. Zhu, and D.A. May. Subduction initiates at straight passive margins. *geology*, 2014.
- [1724] FO Marques, PR Cobbold, and N Lourenço. Physical models of rifting and transform faulting, due to ridge push in a wedge-shaped oceanic lithosphere. *Tectonophysics*, 443(1-2):37–52, 2007.
- [1725] F.O. Marques and B.J.P. Kaus. Speculations on the impact of catastrophic subduction initiation on the Earth System. *Journal of Geodynamics*, 93:1–16, 2016.
- [1726] Simone Marras, Michal A Kopera, Emil M Constantinescu, Jenny Suckale, and Francis X Giraldo. A continuous/discontinuous galerkin solution of the shallow water equations with dynamic viscosity, high-order wetting and drying, and implicit time integration. *arXiv preprint arXiv:1607.04547*, 2016.
- [1727] Robert S Marshall, Juan C Heinrich, and OC Zienkiewicz. Natural convection in a square enclosure by a finite-element, penalty function method using primitive fluid variables. *Numerical Heat Transfer, Part B: Fundamentals*, 1(3):315–330, 1978.
- [1728] Zdeněk Martinec, Ctirad Matyska, Ondřej Čadek, and Pavel Hrdina. The stokes problem with 3d newtonian rheology in a spherical shell. *Computer physics communications*, 76(1):63–79, 1993.
- [1729] J. Martinod, V. Regard, Y. Letourmy, H. Henry, R. Hassani, S. Baratchart, and S. Carretier. How do subduction processes contribute to forearc Andean uplift? Insights from numerical models. *Journal of Geodynamics*, 96:6–18, 2016.
- [1730] J.G. Masek and C. Duncan. Minimum-work mountain building. *J. Geophys. Res.*, 103(B1):907–917, 1998.
- [1731] W.G. Mason, L. Moresi, P.G. Betts, and M.S. Miller. Three-dimensional numerical models of the influence of a buoyant oceanic plateau on subduction zones. *Tectonophysics*, 483:71–79, 2010.
- [1732] P. Massimi, A. Quarteroni, F. Saleri, and G. Scrofani. Modeling of salt tectonics. *Comput. Methods Appl. Mech. Engrg.*, 197:281–293, 2007.
- [1733] A. Massmeyer, E. Di Giuseppe, A. Davaille, T. Rolf, and P.J. Tackley. Numerical simulation of thermal plumes in a Herschel-Bulkley fluid. *Journal of Non-Newtonian Rheology*, 195:32–45, 2013.
- [1734] K. J. Matthews, A. J. Hale, M. Gurnis, R. D. Müller, and L. DiCaprio. Dynamic subsidence of eastern australia during the cretaceous. *Gondwana Research*, 19(2):372–383, 2011.
- [1735] L Mattioni, Laetitia Le Pourhiet, and I Moretti. Rifting through a heterogeneous crust: insights from analogue models and application to the gulf of corinth. *Geological Society, London, Special Publications*, 253(1):213–231, 2006.
- [1736] Ctirad Matyska and David A Yuen. Profiles of the bullen parameter from mantle convection modelling. *Earth and Planetary Science Letters*, 178(1-2):39–46, 2000.
- [1737] Ctirad Matyska and David A Yuen. Lower-mantle material properties and convection models of multiscale plumes. *Special Papers – Geological Society of America*, 430:137, 2007.
- [1738] T. Mauduit and O. Dauteuil. Small-scale models of oceanic transform zones. *J. Geophys. Res.*, 101(B9):20,195–20,209, 1996.
- [1739] B. Maunder, J. van Hunen, P. Bouilhol, and V. Magni. Modeling Slab Temperature: A Reevaluation of the Thermal Parameter. *Geochem. Geophys. Geosyst.*, 2019.
- [1740] B. Maunder, J. van Hunen, V. Magni, and P. Bouilhol. Relamination of mafic subducting crust throughout earth’s history. *Earth and Planetary Science Letters*, 449:206–216, 2016.
- [1741] D. A. May and J. J. Monaghan. Can a single bubble sink a ship? *American Journal of Physics*, 71(9):842–849, 2003.
- [1742] D.A. May. Volume reconstruction of point cloud data sets derived from computational geodynamic simulations. *Geochem. Geophys. Geosyst.*, 13(5):Q05019, 2012.
- [1743] D.A. May, J. Brown, and L. Le Pourhiet. A scalable, matrix-free multigrid preconditioner for finite element discretizations of heterogeneous Stokes flow. *Computer Methods in Applied Mechanics and Engineering*, 290:496–523, 2015.
- [1744] D.A. May and L. Moresi. Preconditioned iterative methods for Stokes flow problems arising in computational geodynamics. *Phys. Earth. Planet. Inter.*, 171:33–47, 2008.
- [1745] D.A. May, W.P. Schellart, and L. Moresi. Overview of adaptive finite element analysis in computational geodynamics. *Journal of Geodynamics*, 70:1–20, 2013.
- [1746] Dave A May, Jed Brown, and Laetitia Le Pourhiet. ptatin3d: High-performance methods for long-term lithospheric dynamics. In *Proceedings of the international conference for high performance computing, networking, storage and analysis*, pages 274–284. IEEE Press, 2014.

- [1747] RA Mazariegos, MJ Andrews, and JE Russell. Modeling the evolution of salt structures using nonlinear rocksalt flow laws. *Tectonophysics*, 256(1-4):129–143, 1996.
- [1748] Neil McBride and Iain Gilmour. *The Solar System: Part 2*. Open University, 2003.
- [1749] K. McClay, J.-A. Muñoz, and J. García-Senz. Extensional salt tectonics in a contractional orogen: A newly identified tectonic event in the Spanish Pyrenees . *Geology*, 32:373–740, 2004.
- [1750] KR McClay. Extensional fault systems in sedimentary basins: a review of analogue model studies. *Marine and petroleum Geology*, 7(3):206–233, 1990.
- [1751] S. McKee, M.F. Tome, V.G. Ferreira, J.A. Cuminato, A. Castelo, F.S. Sousa, and N. Mangiavacchi. The MAC method. *Computers and Fluids*, 37:907–930, 2008.
- [1752] D. McKenzie. Some remarks on the development of sedimentary basins. *Earth Planet. Sci. Lett.*, 40:25–32, 1978.
- [1753] Dan McKenzie. The generation and compaction of partially molten rock. *Journal of Petrology*, 25:713–765, 1984.
- [1754] Dan McKenzie. The geometry of propagating rifts. *Earth and planetary science letters*, 77(2):176–186, 1986.
- [1755] Dan McKenzie, James Jackson, and Keith Priestley. Thermal structure of oceanic and continental lithosphere. *Earth and Planetary Science Letters*, 233(3-4):337–349, 2005.
- [1756] Dan P McKenzie. The earth's mantle. *Scientific American*, 249(3):66–81, 1983.
- [1757] Di P McKenzie and Frank Richter. Convection currents in the earth's mantle. *Scientific American*, 235(5):72–89, 1976.
- [1758] D.P. McKenzie. Speculations on the consequences and causes of plate motions. *Geophys. J. R. astr. Soc.*, 18:1–32, 1969.
- [1759] DP McKenzie and JG Selater. The evolution of the indian ocean. *Scientific American*, 228(5):62–74, 1973.
- [1760] W. B. McKinnon, F. Nimmo, T. Wong, P. M. Schenk, O. L. White, J. H. Roberts, J. M. Moore, J. R. Spencer, A. D. Howard, O. M. Umurhan, S. A. Stern, H. A. Weaver, C. B. Olkin, L. A. Young, K. E. Smith, R. Beyer, M. Buie, B. Buratti, A. Cheng, D. Cruikshank, C. Dalle Ore, R. Gladstone, W. Grundy, T. Lauer, I. Linscott, C. Olkin, J. Parker, S. Porter, H. Reitsema, D. Reuter, S. Robbins, M. Showalter, K. Singer, D. Strobel, M. Summers, L. Tyler, H. Weaver, M. Banks, O. Barnouin, V. Bray, B. Carcich, A. Chaikin, C. Chavez, C. Conrad, D. Hamilton, C. Howett, J. Hofgartner, J. Kammer, C. Lisse, A. Marquette, A. Parker, K. Rutherford, M. Saina, K. Runyon, E. Schindhelm, J. Stansberry, A. Steffl, T. Stryk, H. Throop, C. Tsang, A. Verbiscer, H. Winters, and A. Zangari. Convection in a volatile nitrogen-ice-rich layer drives pluto's geological vigour. *Nature*, 534(7605):82–85, 2016.
- [1761] Colin P McNally. Divergence-free interpolation of vector fields from point values exact  $\nabla \cdot b = 0$  in numerical simulations. *Monthly Notices of the Royal Astronomical Society: Letters*, 413(1):L76–L80, 2011.
- [1762] A. K. McNamara, E. J. Garnero, and S. Rost. Tracking deep mantle reservoirs with ultra-low velocity zones. *Earth and Planetary Science Letters*, 299(1-2):1–9, 2010.
- [1763] A. K. McNamara and S. Zhong. Thermochemical structures within a spherical mantle: Superplumes or piles? *Journal of Geophysical Research: Solid Earth*, 109(B7), 2004.
- [1764] A.K. McNamara and S. Zhong. Degree-one mantle convection: Dependence on internal heating and temperature-dependent rheology. *Geophys. Res. Lett.*, 32(L01301), 2005.
- [1765] A.K. McNamara and S. Zhong. Thermochemical structures beneath Africa and the Pacific Ocean. *Nature*, 437:1136, 2005.
- [1766] Brendan J Meade. Present-day kinematics at the india-asia collision zone. *Geology*, 35(1):81–84, 2007.
- [1767] S. Medvedev and C. Beaumont. Growth of continental plateaus by channel injection: Models designed to address constraints and thermomechanical consistency. *Geological Society Special Publication*, 268:147–164, 2006.
- [1768] Sergei Medvedev, Yuri Podladchikov, Mark R Handy, and Ekkehard Scheuber. Controls on the deformation of the central and southern andes ( $10\text{--}35^\circ$ ): insight from thin-sheet numerical modeling. In *The Andes*, pages 475–494. 2006.
- [1769] S. Mei and D.L. Kohlstedt. Influence of water on plastic deformation of olivine aggregates 1. Diffusion creep regime. *J. Geophys. Res.*, 105(B9):21,457–21,469, 2000.
- [1770] S. Mei and D.L. Kohlstedt. Influence of water on plastic deformation of olivine aggregates 2. Dislocation creep regime. *J. Geophys. Res.*, 105(B9):21,471–21,481, 2000.

- [1771] S. Mei, A.M. Suzuki, D.L. Kohlstedt, N.A. Dixon, and W.B. Durham. Experimental constraints on the strength of the lithospheric mantle. *J. Geophys. Res.*, 115(B08204), 2010.
- [1772] HJ Melosh and A Raefsky. A simple and efficient method for introducing faults into finite element computations. *Bulletin of the Seismological Society of America*, 71(5):1391–1400, 1981.
- [1773] HJ Melosh and Arthur Raefsky. The dynamical origin of subduction zone topography. *Geophysical Journal International*, 60(3):333–354, 1980.
- [1774] HJ Melosh and CA Williams Jr. Mechanics of graben formation in crustal rocks: A finite element analysis. *Journal of Geophysical Research: Solid Earth*, 94(B10):13961–13973, 1989.
- [1775] Armel Menant, Samuel Angiboust, and Taras Gerya. Stress-driven fluid flow controls long-term megathrust strength and deep accretionary dynamics. *Scientific reports*, 9(1):1–11, 2019.
- [1776] Armel Menant, Pietro Sternai, Laurent Jolivet, Laurent Guillou-Frottier, and Taras Gerya. 3d numerical modeling of mantle flow, crustal dynamics and magma genesis associated with slab roll-back and tearing: The eastern mediterranean case. *Earth and Planetary Science Letters*, 442:93–107, 2016.
- [1777] Qingfeng Meng and David Hodgetts. Combined control of décollement layer thickness and cover rock cohesion on structural styles and evolution of fold belts: A discrete element modelling study. *Tectonophysics*, 757:58–67, 2019.
- [1778] Qingfeng Meng and David Hodgetts. Structural styles and decoupling in stratigraphic sequences with double décollements during thin-skinned contractional tectonics: Insights from numerical modelling. *Journal of Structural Geology*, 127:103862, 2019.
- [1779] C.A. Mériaux, A. May D, J. Mansour, Z. Chen, and O. Kaluza. Benchmark of three-dimensional numerical models of subduction against a laboratory experiment. *Phys. Earth. Planet. Inter.*, 283:110–121, 2018.
- [1780] CA Mériaux, João C Duarte, SS Duarte, Wouter Pieter Schellart, Zhihao Chen, F Rosas, Joao Mata, and Pedro Terrinha. Capture of the canary mantle plume material by the gibraltar arc mantle wedge during slab rollback. *Geophysical Journal International*, 201(3):1717–1721, 2015.
- [1781] CA Mériaux, JA Mansour, Louis N Moresi, RC Kerr, and David Alexander May. On the rise of strongly tilted mantle plume tails. *Physics of the Earth and Planetary Interiors*, 184(1-2):63–79, 2011.
- [1782] Catherine A Mériaux, João C Duarte, Wouter P Schellart, and Anne-Sophie Mériaux. A two-way interaction between the hainan plume and the manila subduction zone. *Geophysical Research Letters*, 42(14):5796–5802, 2015.
- [1783] L. Métivier and C. P. Conrad. Body tides of a convecting, laterally heterogeneous, and aspherical earth. *Journal of Geophysical Research*, 113(B11), 2008.
- [1784] Clio Meyer and Wouter Pieter Schellart. Three-dimensional dynamic models of subducting plate-overriding plate-upper mantle interaction. *Journal of Geophysical Research: Solid Earth*, 118(2):775–790, 2013.
- [1785] Victor Benno Meyer-Rochow and Jozsef Gal. Pressures produced when penguins poohcalculations on avian defaecation. *Polar Biology*, 27(1):56–58, 2003.
- [1786] R. L. Michalowski. Upper-bound load estimates on square and rectangular footings. *Géotechnique*, 51(9):787–798, 2001.
- [1787] K. Michibayashi and D. Mainprice. The role of pre-existing mechanical anisotropy on shear zone development within oceanic mantle lithosphere: an example from the oman ophiolite. *J. Petrol.*, 45(2):405–414, 2004.
- [1788] K Mickus, Ketsela Tadesse, GR Keller, and Befekadu Oluma. Gravity analysis of the main ethiopian rift. *Journal of African Earth Sciences*, 48(2-3):59–69, 2007.
- [1789] Ivar Midtkandal, Jean-Pierre Brun, Roy H Gabrielsen, and Ritske S Huismans. Control of lithosphere rheology on subduction polarity at initiation: Insights from 3d analogue modelling. *Earth and Planetary Science Letters*, 361:219–228, 2013.
- [1790] C. Miehe, F. Aldakheel, and S. Mauthe. Mixed variational principles and robust finite element implementations of gradient plasticity at small strains. *Int. J. Num. Meth. Eng.*, 94:1037–1074, 2013.
- [1791] V Mikhailov, V Lyakhovsky, I v Panet, Y van Dinther, M Diament, T d Gerya, O deViron, and E Timoshkina. Numerical modelling of post-seismic rupture propagation after the sumatra 26.12.2004 earthquake constrained by grace gravity data. *Geophysical Journal International*, 194(2):640–650, 2013.
- [1792] M. S. Miller and T. W. Becker. Mantle flow deflected by interactions between subducted slabs and cratonic keels. *Nature Geoscience*, 5(10):726–730, 2012.

- [1793] Meghan S Miller, Amir A Allam, Thorsten W Becker, Jeanette F Di Leo, and James Wookey. Constraints on the tectonic evolution of the westernmost mediterranean and northwestern africa from shear wave splitting analysis. *Earth and Planetary Science Letters*, 375:234–243, 2013.
- [1794] Meghan S Miller and Louis Moresi. Mapping the alaskan moho. *Seismological Research Letters*, 89(6):2430–2436, 2018.
- [1795] K. Milner, T.W. Becker, L. Boschi, J. Sain, D. Schorlemmer, and H. Waterhouse. New software framework to share research tools. *Eos Trans. AGU*, 90(12):104–104, 2009.
- [1796] Chohong Min and Frédéric Gibou. A second order accurate level set method on non-graded adaptive cartesian grids. *Journal of Computational Physics*, 225(1):300–321, 2007.
- [1797] A.N. Minakov, Y.Y. Podlachikov, J.I. Faleide, and R.S. Huismans. Rifting assisted by shear heating and formation of the Lomonosov ridge. *Earth Planet. Sci. Lett.*, 373:31–40, 2013.
- [1798] Y. Mishin. *Adaptive multiresolution methods for problems of computational geodynamics*. PhD thesis, ETH Zurich, 2011.
- [1799] Y. Mishin. *Adaptive multiresolution methods for problems of computational geodynamics*. PhD thesis, ETH Zurich, 2011.
- [1800] Y.A. Mishin, T.V. Gerya, J.-P. Burg, and J.A.D. Connolly. Dynamics of double subduction: Numerical modeling. *Phys. Earth. Planet. Inter.*, 171:280–295, 2008.
- [1801] G. Mitri and A. P. Showman. Convective-conductive transitions and sensitivity of a convecting ice shell to perturbations in heat flux and tidal-heating rate: Implications for europa. *Icarus*, 177(2):447–460, 2005.
- [1802] Jerry X Mitrovica. Haskell [1935] revisited. *Journal of Geophysical Research: Solid Earth*, 101(B1):555–569, 1996.
- [1803] Jerry X Mitrovica and Alessandro M Forte. Radial profile of mantle viscosity: results from the joint inversion of convection and postglacial rebound observables. *Journal of Geophysical Research: Solid Earth*, 102(B2):2751–2769, 1997.
- [1804] J.X. Mitrovica, C. Beaumont, and G.T. Jarvis. Tilting of continental interiors by the dynamical effects of subduction. *Tectonics*, 8(5):1079–1094, 1989.
- [1805] J.X. Mitrovica, R.N. Pysklywec, C. Beaumont, and A. Rutty. The devonian to permian sedimentation of the russian platform: An example of subduction-controlled long-wavelength tilting of continents. *Journal of Geodynamics*, 22(1-2):79–96, 1996.
- [1806] E. Mitsoulis and S. Galazoulas. Simulation of viscoplastic flow past cylinders in tubes. *Journal of Non-Newtonian Fluid Mechanics*, 158:132–141, 2009.
- [1807] E. Mitsoulis and Th. Zisis. Flow of Bingham plastics in a lid-driven square cavity. *Journal of Non-Newtonian Fluid Mechanics*, 101:173–180, 2001.
- [1808] Eric Mittelstaedt and Paul J Tackley. Plume heat flow is much lower than cmb heat flow. *Earth and Planetary Science Letters*, 241(1-2):202–210, 2006.
- [1809] Arata Miyauchi and Masanori Kameyama. Influences of the depth-dependence of thermal conductivity and expansivity on thermal convection with temperature-dependent viscosity. *Physics of the Earth and Planetary Interiors*, 223:86–95, 2013.
- [1810] A. Mizukami. A mixed Finite Element method for boundary flux computation. *Computer Methods in Applied Mechanics and Engineering*, 57:239–243, 1986.
- [1811] Arash Mohajeri, Yaron Finzi, Hans Muhlhaus, and Gideon Rosenbaum. Melt and shear interactions in the lithosphere: Theory and numerical analysis of pure shear extension. *Journal of Geophysical Research: Solid Earth*, 118(5):2488–2499, 2013.
- [1812] P.K. Mohapatra, V. Eswaran, and S. Murty Bhallamudi. Two-dimensional analysis of dam-break flow in vertical plane. *Journal of Hydraulic Engineering*, 125(2):183–192, 1999.
- [1813] Nicolas E Molnar, Alexander R Cruden, and Peter G Betts. Interactions between propagating rifts and linear weaknesses in the lower crust. *Geosphere*, 2019.
- [1814] P. Molnar. *Brace-Goetze strength profiles, the partitioning of strike-slip and thrust faulting at zones of oblique convergence, and the stress-heat flow paradox of the San Andreas Fault*. Academic Press Ltd, 1992.
- [1815] P. Molnar, G.A. Houseman, and C.P. Conrad. RayleighTaylor instability and convective thinning of mechanically thickened lithosphere: effects of non-linear viscosity decreasing exponentially with depth and of horizontal shortening of the layer. *Geophys. J. Int.*, 133:568–584, 1998.
- [1816] P. Molnar and P. Tapponnier. Relation of the tectonics of eastern China to the India-Eurasia collision: Application of the slip-line field theory to large-scale continental tectonics. *Geology*, 5:212–216, 1977.

- [1817] Peter Molnar. The structure of mountain ranges. *Scientific American*, 255(1):70–79, 1986.
- [1818] Peter Molnar. The geologic evolution of the tibetan plateau. *American Scientist*, 77:350–360, 1989.
- [1819] Peter Molnar. Climate change, flooding in arid environments, and erosion rates. *Geology*, 29(12):1071–1074, 2001.
- [1820] Peter Molnar and Philip England. Late cenozoic uplift of mountain ranges and global climate change: chicken or egg? *Nature*, 346, july 1990.
- [1821] Peter Molnar, Philip England, and Joseph Martinod. Mantle dynamics, uplift of the tibetan plateau, and the indian monsoon. *Reviews of Geophysics*, 31(4):357–396, November 1993.
- [1822] Peter Molnar and Paul Tapponnier. Cenozoic tectonics of asia: Effects of a continental collision. *Science*, 189:419–426, 1975.
- [1823] Luke S Mondy, Patrice F Rey, Guillaume Duclaux, and Louis Moresi. The role of asthenospheric flow during rift propagation and breakup. *Geology*, 46(2):103–106, 2017.
- [1824] Marc Monnereau and Sandrine Quéré. Spherical shell models of mantle convection with tectonic plates. *Earth and Planetary Science Letters*, 184(3-4):575–587, 2001.
- [1825] Marc Monnereau and David A Yuen. Topology of the postperovskite phase transition and mantle dynamics. *Proceedings of the National Academy of Sciences*, 104(22):9156–9161, 2007.
- [1826] N. L. Montague, L. H. Kellogg, and M. Manga. High rayleigh number thermo-chemical models of a dense boundary layer in d". *Geophysical Research Letters*, 25(13):2345–2348, 1998.
- [1827] Laurent GJ Montési. Fabric development as the key for forming ductile shear zones and enabling plate tectonics. *Journal of Structural Geology*, 50:254–266, 2013.
- [1828] Laurent GJ Montési, Mark D Behn, Laura B Hebert, Jian Lin, and Jennifer L Barry. Controls on melt migration and extraction at the ultraslow southwest indian ridge 10–16 e. *Journal of Geophysical Research: Solid Earth*, 116(B10), 2011.
- [1829] Laurent GJ Montési and Greg Hirth. Grain size evolution and the rheology of ductile shear zones: from laboratory experiments to postseismic creep. *Earth and Planetary Science Letters*, 211(1-2):97–110, 2003.
- [1830] D.R. Montgomery and M.T. Brandon. Topographic controls on erosion rates in tectonically active mountain ranges. *Earth Planet. Sci. Lett.*, 201:481–489, 2002.
- [1831] A. Montlaur, S. Fernandez-Mendez, and A. Huerta. Discontinuous Galerkin methods for the Stokes equations using divergence-free approximations. *Int. J. Num. Meth. Fluids*, 57(08):1071–1092, 2008.
- [1832] A. Montlaur, S. Fernandez-Mendez, J. Peraire, and A. Huerta. Discontinuous Galerkin methods for the NavierStokes equations using solenoidal approximations. *Int. J. Num. Meth. Fluids*, 64:549–564, 2010.
- [1833] William B Moore, Gerald Schubert, and Paul Tackley. Three-dimensional simulations of plume-lithosphere interaction at the hawaiian swell. *Science*, 279(5353):1008–1011, 1998.
- [1834] William B Moore, Gerald Schubert, and Paul J Tackley. The role of rheology in lithospheric thinning by mantle plumes. *Geophysical Research Letters*, 26(8):1073–1076, 1999.
- [1835] William B Moore and A Alexander G Webb. Heat-pipe earth. *Nature*, 501(7468):501, 2013.
- [1836] Eldridge M Moores, Louise H Kellogg, and Yildirim Dilek. Tethyan ophiolites, mantle convection, and tectonic” historical contingency”: A resolution of the” ophiolite conundrum”. *SPECIAL PAPERS-GEOLOGICAL SOCIETY OF AMERICA*, 349:3–12, 2000.
- [1837] Peter Mora and David A Yuen. Simulation of plume dynamics by the lattice boltzmann method. *Geophysical Journal International*, 210(3):1932–1937, 2017.
- [1838] C. Morency and M.-P. Doin. Numerical simulations of the mantle lithosphere delamination. *J. Geophys. Res.*, 109(B03410), 2004.
- [1839] C. Morency, R.S. Huismans, C. Beaumont, and P. Fullsack. A numerical model for coupled fluid flow and matrix deformation with applications to disequilibrium compaction and delta stability. *J. Geophys. Res.*, 112(B10407), 2007.
- [1840] L. Moresi, P.G. Betts, M.S. Miller, and R.A. Cayley. Dynamics of continental accretion. *Nature*, 2014.
- [1841] L. Moresi, F. Dufour, and H.B. Mühlhaus. Mantle Convection Modeling with Viscoelastic/Brittle Lithosphere: Numerical Methodology and Plate Tectonic Modeling. *Pure and Applied Geophysics*, 159:159, 2002.
- [1842] L. Moresi, F. Dufour, and H.B. Mühlhaus. A Lagrangian integration point finite element method for large deformation modeling of visco-elastic geomaterials. *J. Comp. Phys.*, 184(2):476–497, 2003.

- [1843] L. Moresi and M. Gurnis. Constraints on the lateral strength of slabs from three-dimensional dynamic flow models. *Earth and Planetary Science Letters*, 138(1):15–28, 1996.
- [1844] L Moresi and H-B Mühlhaus. Anisotropic viscous models of large-deformation mohr–coulomb failure. *Philosophical Magazine*, 86(21-22):3287–3305, 2006.
- [1845] L Moresi, H-B Mühlhaus, Vincent Lemiale, and D May. Incompressible viscous formulations for deformation and yielding of the lithosphere. *Geological Society, London, Special Publications*, 282(1):457–472, 2007.
- [1846] L. Moresi, S. Quenette, V. Lemiale, C. Mériaux, B. Appelbe, and H.-B. Mühlhaus. Computational approaches to studying non-linear dynamics of the crust and mantle. *Phys. Earth. Planet. Inter.*, 163:69–82, 2007.
- [1847] L. Moresi and V. Solomatov. Mantle convection with a brittle lithosphere: thoughts on the global tectonics styles of the earth and venus. *Geophys. J. Int.*, 133:669–682, 1998.
- [1848] L. Moresi, S. Zhong, and M. Gurnis. The accuracy of finite element solutions of stokes' flow with strongly varying viscosity. *Physics of the Earth and Planetary Interiors*, 97(1-4):83–94, 1996.
- [1849] L-N Moresi and A. Lenardic. Three-dimensional numerical simulations of crustal deformation and subcontinental mantle convection. *Earth and Planetary Science Letters*, 150(3-4):233–243, 1997.
- [1850] L.-N. Moresi and V.S. Solomatov. Numerical investigation of 2D convection with extremely large viscosity variations. *Physics of Fluids*, 7(9):2154–2162, 1995.
- [1851] Louis Moresi, Francois Dufour, and HB Mühlhaus. Viscoelastic formulation for modeling of plate tectonics. *Bifurcation and localization in soils and rocks*, pages 337–344, 2001.
- [1852] Louis Moresi, Michael Gurnis, and Shijie Zhong. Plate tectonics and convection in the earths mantle: Toward a numerical simulation. *Computing in Science & Engineering*, 2(3):22, 2000.
- [1853] Louis Moresi and Adrian Lenardic. Three-dimensional mantle convection with continental crust: first-generation numerical simulations. *Earth Interactions*, 3(2):1–14, 1999.
- [1854] Louis Moresi and Ben Mather. Stripy: A python module for (constrained) triangulation in cartesian coordinates and on a sphere. *Journal of Open Source Software*, 2019.
- [1855] Louis Moresi, Hans Mühlhaus, and Frédéric Dufour. An overview of numerical methods for earth simulations. In *Exploration Geodynamics Chapman Conference, Dunsborough, Australia*, 2001.
- [1856] Louis Moresi and Barry Parsons. Interpreting gravity, geoid, and topography for convection with temperature dependent viscosity: Application to surface features on venus. *Journal of Geophysical Research: Planets*, 100(E10):21155–21171, 1995.
- [1857] Isabelle Moretti and Claude Froidevaux. Thermomechanical models of active rifting. *Tectonics*, 5(4):501–511, 1986.
- [1858] M Morishige, S Honda, and Paul J Tackley. Construction of semi-dynamic model of subduction zone with given plate kinematics in 3d sphere. *Earth, planets and space*, 62(9):665–673, 2010.
- [1859] M. Morishige and P.E. van Keken. Along-arc variation in the 3-D thermal structure around the junction between the Japan and Kurile arcs. *Geochem. Geophys. Geosyst.*, 15:2225–2240, 2014.
- [1860] Gabriele Morra. Pythonic geodynamics. *Lecture Notes in Earth System Sciences*, 2018.
- [1861] Gabriele Morra, Philippe Chatelain, Paul Tackley, and Petros Koumoutsakos. Large scale three-dimensional boundary element simulation of subduction. In *International Conference on Computational Science*, pages 1122–1129. Springer, 2007.
- [1862] Gabriele Morra, Philippe Chatelain, Paul Tackley, and Petros Koumoutsakos. Earth curvature effects on subduction morphology: Modeling subduction in a spherical setting. *Acta Geotechnica*, 4(2):95–105, 2009.
- [1863] Gabriele Morra and K Regenauer-Lieb. A coupled solid–fluid method for modelling subduction. *Philosophical magazine*, 86(21-22):3307–3323, 2006.
- [1864] Gabriele Morra, Maria Seton, Leonardo Quevedo, and R Dietmar Müller. Organization of the tectonic plates in the last 200 myr. *Earth and Planetary Science Letters*, 373:93–101, 2013.
- [1865] Gabriele Morra, David A Yuen, L Boschi, P Chatelain, P Koumoutsakos, and PJ Tackley. The fate of the slabs interacting with a density/viscosity hill in the mid-mantle. *Physics of the Earth and Planetary Interiors*, 180(3-4):271–282, 2010.
- [1866] J.P. Morris, P.J. Fox, and Y. Zhu. Modeling Low Reynolds Number Incompressible Flows Using SPH. *J. Comp. Phys.*, 136:214–226, 1997.

- [1867] S Morris and D Canright. A boundary-layer analysis of benard convection in a fluid of strongly temperature-dependent viscosity. *Physics of the Earth and planetary interiors*, 36(3-4):355–373, 1984.
- [1868] K.W. Morton and D.F. Mayers. *Numerical Solution of Partial Differential Equations: An Introduction*. Cambridge, 2005.
- [1869] M. H. Motoki and M. D. Ballmer. Intraplate volcanism due to convective instability of stagnant slabs in the mantle transition zone. *Geochemistry, Geophysics, Geosystems*, 16(2):538–551, 2015.
- [1870] R. Moucha, A.M. Forte, J.X. Mitrovica, and A. Daradich. Lateral variations in mantle rheology: implications for convection related surface observables and inferred viscosity models. *Geophys. J. Int.*, 169:113–135, 2007.
- [1871] P. Moulik and G. Ekström. The relationships between large-scale variations in shear velocity, density, and compressional velocity in the Earth’s mantle. *J. Geophys. Res.*, 121:doi:10.1002/2015JB012679, 2016.
- [1872] L. Mu, J. Wang, X. Ye, and S. Zhang. A discrete divergence free weak Galerkin finite element method for the Stokes equations. *Applied Numerical Mathematics*, 125:172–182, 2018.
- [1873] S. Mueller and R.J. Phillips. On the initiation of subduction. *J. Geophys. Res.*, 96(B1):651–665, 1991.
- [1874] H-B Mühlhaus, Frédéric Dufour, Louis Moresi, and Bruce Hobbs. A director theory for visco-elastic folding instabilities in multilayered rock. *International Journal of Solids and Structures*, 39(13-14):3675–3691, 2002.
- [1875] H-B Mühlhaus, L Moresi, and M Čada. Anisotropy model for mantle convection. In *Computational Fluid and Solid Mechanics 2003*, pages 1044–1046. Elsevier, 2003.
- [1876] H-B Mühlhaus, L Moresi, and Miroslav Cada. Emergent anisotropy and flow alignment in viscous rock. *pure and applied geophysics*, 161(11-12):2451–2463, 2004.
- [1877] H.-B. Mühlhaus, L. Moresi, B. Hobbs, and F. Dufour. Large amplitude folding in finely layered viscoelastic rock structures. *Pure appl. Geophys.*, 159:2311–2333, 2002.
- [1878] Hans Muhlhaus, Louis Moresi, Lutz Gross, and Joseph Grotowski. The influence of non-coaxiality on shear banding in viscous-plastic materials. *Granular Matter*, 12(3):229–238, 2010.
- [1879] Hans B Mühlhaus, Jingyu Shi, Louise Olsen-Kettle, and Louis Moresi. Effects of a non-coaxial flow rule on shear bands in viscous-plastic materials. *Granular Matter*, 13(3):205–210, 2011.
- [1880] Hans-Bernd Mühlhaus, Matt Davies, and Louis Moresi. Elasticity, yielding and episodicity in simple models of mantle convection. In *Computational Earthquake Physics: Simulations, Analysis and Infrastructure, Part I*, pages 2031–2047. Springer, 2006.
- [1881] H.B. Muhlhaus and K. Regenauer-Lieb. Towards a self-consistent plate mantle model that includes elasticity: simple benchmarks and application to basic modes of convection. *Geophys. J. Int.*, 163:788–800, 2005.
- [1882] G Mulugeta and D Sokoutis. Hanging wall accommodation styles in ramp-flat thrust models. *Geological Society, London, Special Publications*, 212(1):197–207, 2003.
- [1883] E. Mulyukova and D. Bercovici. Formation of lithospheric shear zones: Effect of temperature on two-phase grain damage. *Phys. Earth. Planet. Inter.*, 270:195–212, 2017.
- [1884] E. Mulyukova and D. Bercovici. Collapse of passive margins by lithospheric damage and plunging grain size. *Earth Planet. Sci. Lett.*, 484:341–352, 2018.
- [1885] E. Mulyukova and D. Bercovici. A theoretical model for the evolution of microstructure in lithospheric shear zones. *Geophys. J. Int.*, 216:803–819, 2019.
- [1886] E. Mulyukova, B. Steinberger, M. Dabrowski, and S.V. Sobolev. Survival of LLSVPs for billions of years in a vigorously convecting mantle: Replenishment and destruction of chemical anomaly. *J. Geophys. Res.*, 120:3824–3847, 2015.
- [1887] Ioan Munteanu, E Willingshofer, L Matenco, D Sokoutis, C Dinu, and SAPL Cloetingh. Far-field strain transmission and contractional step-overs. *Tectonophysics*, 766:194–204, 2019.
- [1888] M.A. Murphy, M.H. Taylor, J. Gosse, C.R.P. Silver, D.M. Whipp, and C. Beaumont. Limit of strain partitioning in the Himalaya marked by large earthquakes in western Nepal. *Nature Geoscience*, 7(1):38–42, 2014.
- [1889] Jun Muto, Bunichiro Shibasaki, Yoshihiro Ito, Takeshi Iinuma, Mako Ohzono, Takumi Matsumoto, and Tomomi Okada. Two-dimensional viscosity structure of the northeastern japan islands arc-trench system. *Geophysical Research Letters*, 40(17):4604–4608, 2013.
- [1890] R Myhill. Slab buckling and its effect on the distributions and focal mechanisms of deep-focus earthquakes. *Geophysical Journal International*, 192(2):837–853, 2012.

- [1891] Seyed Tohid Nabavi, Seyed Ahmad Alavi, Soheil Mohammadi, and Mohammad Reza Ghassemi. Mechanical evolution of transpression zones affected by fault interactions: insights from 3d elasto-plastic finite element models. *Journal of Structural Geology*, 106:19–40, 2018.
- [1892] Seyed Tohid Nabavi, Seyed Ahmad Alavi, Soheil Mohammadi, Mohammad Reza Ghassemi, and Marcel Frehner. Analysis of transpression within contractional fault steps using finite-element method. *Journal of Structural Geology*, 96:1–20, 2017.
- [1893] Thomas Nagler, Helmut Rott, Markus Hetzenecker, Jan Wuite, and Pierre Potin. The sentinel-1 mission: New opportunities for ice sheet observations. *Remote Sensing*, 7(7):9371–9389, 2015.
- [1894] T. Nakagawa and B.A. Buffett. Mass transport mechanism between the upper and lower mantle in numerical simulations of thermochemical mantle convection with multicomponent phase changes. *Earth Planet. Sci. Lett.*, 230:11–27, 2005.
- [1895] Takashi Nakagawa and Paul J Tackley. Effects of a perovskite-post perovskite phase change near core-mantle boundary in compressible mantle convection. *Geophysical Research Letters*, 31(16), 2004.
- [1896] Takashi Nakagawa and Paul J Tackley. Effects of thermo-chemical mantle convection on the thermal evolution of the earth's core. *Earth and Planetary Science Letters*, 220(1-2):107–119, 2004.
- [1897] Takashi Nakagawa and Paul J Tackley. Thermo-chemical structure in the mantle arising from a three-component convective system and implications for geochemistry. *Physics of the Earth and Planetary Interiors*, 146(1-2):125–138, 2004.
- [1898] Takashi Nakagawa and Paul J Tackley. Deep mantle heat flow and thermal evolution of the earth's core in thermochemical multiphase models of mantle convection. *Geochemistry, Geophysics, Geosystems*, 6(8), 2005.
- [1899] Takashi Nakagawa and Paul J Tackley. The interaction between the post-perovskite phase change and a thermo-chemical boundary layer near the core–mantle boundary. *Earth and Planetary Science Letters*, 238(1-2):204–216, 2005.
- [1900] Takashi Nakagawa and Paul J Tackley. Three-dimensional structures and dynamics in the deep mantle: Effects of post-perovskite phase change and deep mantle layering. *Geophysical research letters*, 33(12), 2006.
- [1901] Takashi Nakagawa and Paul J Tackley. Lateral variations in cmb heat flux and deep mantle seismic velocity caused by a thermal-chemical-phase boundary layer in 3d spherical convection. *Earth and Planetary Science Letters*, 271(1-4):348–358, 2008.
- [1902] Takashi Nakagawa and Paul J Tackley. Influence of initial cmb temperature and other parameters on the thermal evolution of earth's core resulting from thermochemical spherical mantle convection. *Geochemistry, Geophysics, Geosystems*, 11(6), 2010.
- [1903] Takashi Nakagawa and Paul J Tackley. Effects of low-viscosity post-perovskite on thermo-chemical mantle convection in a 3-d spherical shell. *Geophysical research letters*, 38(4), 2011.
- [1904] Takashi Nakagawa and Paul J Tackley. Influence of magmatism on mantle cooling, surface heat flow and urey ratio. *Earth and Planetary Science Letters*, 329:1–10, 2012.
- [1905] Takashi Nakagawa and Paul J Tackley. Implications of high core thermal conductivity on earth's coupled mantle and core evolution. *Geophysical Research Letters*, 40(11):2652–2656, 2013.
- [1906] Takashi Nakagawa and Paul J Tackley. Influence of combined primordial layering and recycled morb on the coupled thermal evolution of earth's mantle and core. *Geochemistry, Geophysics, Geosystems*, 15(3):619–633, 2014.
- [1907] Takashi Nakagawa, Paul J Tackley, Frederic Deschamps, and James AD Connolly. Incorporating self-consistently calculated mineral physics into thermochemical mantle convection simulations in a 3-d spherical shell and its influence on seismic anomalies in earth's mantle. *Geochemistry, Geophysics, Geosystems*, 10(3), 2009.
- [1908] Takashi Nakagawa, Paul J Tackley, Frederic Deschamps, and James AD Connolly. The influence of morb and harzburgite composition on thermo-chemical mantle convection in a 3-d spherical shell with self-consistently calculated mineral physics. *Earth and Planetary Science Letters*, 296(3-4):403–412, 2010.
- [1909] Takashi Nakagawa, Paul J Tackley, Frédéric Deschamps, and James AD Connolly. Radial 1-d seismic structures in the deep mantle in mantle convection simulations with self-consistently calculated mineralogy. *Geochemistry, Geophysics, Geosystems*, 13(11), 2012.
- [1910] Tomoeki Nakakuki and Erika Mura. Dynamics of slab rollback and induced back-arc basin formation. *Earth Planet. Sci. Lett.*, 361:287–297, 2013.

- [1911] Tomoeki Nakakuki, Hiroki Sato, and Hiromi Fujimoto. Interaction of the upwelling plume with the phase and chemical boundary at the 670 km discontinuity: Effects of temperature-dependent viscosity. *Earth Planet. Sci. Lett.*, 121(3–4):369–384, 1994.
- [1912] SM Nakiboglu and Kurt Lambeck. A study of the earth's response to surface loading with application to lake bonneville. *Geophysical Journal International*, 70(3):577–620, 1982.
- [1913] J. Naliboff and S.J.H. Buiter. Rift reactivation and migration during multiphase extension. *Earth Planet. Sci. Lett.*, 421:58–67, 2015.
- [1914] J. B. Naliboff and L. H. Kellogg. Dynamic effects of a step-wise increase in thermal conductivity and viscosity in the lowermost mantle. *Geophysical Research Letters*, 33(12), 2006.
- [1915] J. B. Naliboff and L. H. Kellogg. Can large increases in viscosity and thermal conductivity preserve large-scale heterogeneity in the mantle? *Physics of the Earth and Planetary Interiors*, 161(1–2):86–102, 2007.
- [1916] J.B. Naliboff, M.I. Billen, T. Gerya, and J. saunders. Dynamics of outer-rise faulting in oceanic-continental subduction systems. *Geochem. Geophys. Geosyst.*, 14(7):10.1002/ggge.20155, 2013.
- [1917] J.B. Naliboff, S.J.H. Buiter, G. Péron-Pinvidic, P.T. Osmundsen, and J. Tetraeault. Complex fault interaction controls continental rifting. *Nature Communications*, 8:1179, 2017.
- [1918] J.B. Naliboff, C.P. Conrad, and C. Lithgow-Bertelloni. Modification of the lithospheric stress field by lateral variations in plate-mantle coupling. *Geophys. Res. Lett.*, 36(L22307), 2009.
- [1919] J.B. Naliboff, C. Lithgow-Bertelloni, L.J. Ruff, and N. de Koker. The effects of lithospheric thickness and density structure on Earths stress field. *Geophy. J. Int.*, 188:1–17, 2012.
- [1920] T Nalpas and J-P Brun. Salt flow and diapirism related to extension at crustal scale. *Tectonophysics*, 228(3–4):349–362, 1993.
- [1921] T Nalpas, D Gapais, J Verges, L Barrier, V Gestain, G Leroux, D Rouby, and J-J Kermarrec. Effects of rate and nature of synkinematic sedimentation on the growth of compressive structures constrained by analogue models and field examples. *Geological Society, London, Special Publications*, 208(1):307–319, 2003.
- [1922] Thierry Nalpas, Istvan Gyorfi, Francois Guillocheau, Francois Lafont, and Peter Homewood. Influence de la charge sedimentaire sur le développement d'anticlinaux synsedimentaires; modélisation analogique et exemple de terrain (bordure sud du bassin de jaca). *Bulletin de la Société Géologique de France*, 170(5):733–740, 1999.
- [1923] A. Napov and Y. Notay. An algebraic multigrid method with guaranteed convergence rate. *SIAM J. Sci. Comput.*, 34:A1079–A1109, 2012.
- [1924] S. I. Natarov and C. P. Conrad. The role of poiseuille flow in creating depth-variation of asthenospheric shear: Poiseuille flow and asthenospheric shear. *Geophysical Journal International*, 190(3):1297–1310, 2012.
- [1925] Y. Lina nd Y. Cao. A new nonlinear Uzawa algorithm for generalised saddle point problems. *Applied Mathematics and Computation*, 175:1432–1454, 2006.
- [1926] A.M. Negredo, R. Sabadini, G. Bianco, and M. Fernandez. Three-dimensional modelling of crustal motions caused by subduction and continental convergence in the central Mediterranean. *Geophy. J. Int.*, 136:261–274, 1999.
- [1927] A.M. Negredo, R. Sabadini, and C. Giunchi. Interplay between subduction and continental convergence:a three- dimensional dynamic model for the Central Mediterranean. *Geophy. J. Int.*, 131:F9–F13, 1997.
- [1928] Michal Nemčok and Andreas Henk. Oil reservoirs in foreland basins charged by thrustbelt source rocks: insights from numerical stress modelling and geometric balancing in the west carpathians. *Geological Society, London, Special Publications*, 253(1):415–428, 2006.
- [1929] R. Nerlich, S.R. Clark, and H.-P. Bunge. Reconstructing the link between the galapagos hotspot and the caribbean plateau. *GeoResJ*, 1–2:1–7, 2014.
- [1930] R. Nerlich, S.R. Clark, and H.-P. Bunge. An outlet for pacific mantle: The caribbean sea? *GeoResJ*, 7:59–65, 2015.
- [1931] Rainer Nerlich, Stuart R Clark, and Hans-Peter Bunge. The scotia sea gateway: no outlet for pacific mantle. *Tectonophysics*, 604:41–50, 2013.
- [1932] M. Nettesheim, T.A. Ehlers, D.M. Whipp, and A. Koptev. The influence of upper-plate advance and erosion on overriding plate deformation in orogen syntaxes. *Solid Earth*, 9:1207–1224, 2018.

- [1933] Gregory A Neumann and Donald W Forsyth. The paradox of the axial profile: Isostatic compensation along the axis of the mid-atlantic ridge? *Journal of Geophysical Research: Solid Earth*, 98(B10):17891–17910, 1993.
- [1934] Wladimir Neumann. Towards 3d modelling of convection in planetesimals and meteorite parent bodies. *Monthly Notices of the Royal Astronomical Society: Letters*, 490(1):L47–L51, 2019.
- [1935] N.C. Nguyen and J. Peraire. Hybridizable discontinuous Galerkin methods for partial differential equations in continuum mechanics. *J. Comp. Phys.*, 231:5955–5988, 2012.
- [1936] N.C. Nguyen, J. Peraire, and B. Cockburn. An implicit high-order hybridizable discontinuous Galerkin method for linear convectiondiffusion equations . *J. Comp. Phys.*, 228:3232–3254, 2009.
- [1937] N.C. Nguyen, J. Peraire, and B. Cockburn. A hybridizable discontinuous Galerkin method for Stokes flow. *Comput. Methods Appl. Mech. Engrg.*, 199:582–597, 2010.
- [1938] N.C. Nguyen, J. Peraire, and B. Cockburn. An implicit high-order hybridizable discontinuous Galerkin method for the incompressible NavierStokes equations. *J. Comp. Phys.*, 230:1147–1170, 2011.
- [1939] Sida Ni, Eh Tan, Michael Gurnis, and Don Helmberger. Sharp sides to the african superplume. *science*, 296(5574):1850–1852, 2002.
- [1940] G. Nicolas and T. Fouquet. Adaptive mesh refinement for conformal hexahedral meshes. *Finite Elements in Analysis and Design*, 67:1–12, 2013.
- [1941] G. Nicolas and T. Fouquet. Conformal hexahedral meshes and adaptive mesh refinement. *VI International Conference on Adaptive Modeling and Simulation*, 2013.
- [1942] Nicolai Nijholt and Rob Govers. The role of passive margins on the evolution of Subduction-Transform Edge Propagators (STEPS). *Journal Of Geophysical Research*, 120(10):7203–7230, 2015.
- [1943] Nicolai Nijholt, Rob Govers, and Rinus Wortel. On the forces that drive and resist deformation of the south-central Mediterranean: a mechanical model study. *Geophys. J. Int.*, 214(2):876–894, 2018.
- [1944] K. Nikolaeva, T.V. Gerya, and F.O. Marques. Subduction initiation at passive margins: numerical modeling. *J. Geophys. Res.*, 115(B03406), 2010.
- [1945] Ksenia Nikolaeva, Taras V Gerya, and James AD Connolly. Numerical modelling of crustal growth in intraoceanic volcanic arcs. *Physics of the Earth and Planetary Interiors*, 171(1-4):336–356, 2008.
- [1946] Ksenia Nikolaeva, Taras V Gerya, and Fernando O Marques. Numerical analysis of subduction initiation risk along the atlantic american passive margins. *Geology*, 39(5):463–466, 2011.
- [1947] Maria A Nikolinakou, Peter B Flemings, and Michael R Hudec. Modeling stress evolution around a rising salt diapir. *Marine and Petroleum Geology*, 51:230–238, 2014.
- [1948] F. Nilfouroushan, R. Pysklywec, A. Cruden, and H. Koyi. Thermal-mechanical modeling of salt-based mountain belts with pre-existing basement faults: Application to the Zagros fold and thrust belt, southwest Iran. *Tectonics*, 32:1212–1226, 2013.
- [1949] F Nimmo and DJ Stevenson. Estimates of martian crustal thickness from viscous relaxation of topography. *Journal of Geophysical Research: Planets*, 106(E3):5085–5098, 2001.
- [1950] Daisuke Nishiura, Mikito Furuichi, and Hide Sakaguchi. Computational performance of a smoothed particle hydrodynamics simulation for shared-memory parallel computing. *Computer Physics Communications*, 194:18–32, 2015.
- [1951] Emmanuel A. Njinju, Estella A. Atekwana, D. Sarah Stamps, Mohamed G. Abdelsalam, Eliot A. Atekwana, Kevin L. Mickus, Stewart Fishwick, Folarin Kolawole, Tahiry A. Rajaonarison, and Victor N. Nyulugwe. Lithospheric structure of the malawi rift: Implications for magma-poor rifting processes. *Tectonics*, 2019.
- [1952] L. Noack, A. Rivoldini, and T. van Hoolst. CHIC Coupling Habitability, Interior and Crust. *INFOCOMP 2015 : The Fifth International Conference on Advanced Communications and Computation*, 2015.
- [1953] Guust Nolet, Shun-Ichiro Karato, and Raffaella Montelli. Plume fluxes from seismic tomography. *Earth and Planetary Science Letters*, 248(3-4):685–699, 2006.
- [1954] S. Norburn and D. Silvester. Stabilised vs. stable mixed methods for incompressible flow. *Computer Methods in Applied Mechanics and Engineering*, 166:131–141, 1998.
- [1955] S. Norburn and D. Silvester. Fourier analysis of stabilized Q1-Q1 mixed finite element approximation. *SIAM J. Numer. Anal.*, 39:817–833, 2001.
- [1956] Y. Notay. Aggregation-based algebraic multigrid for convection-diffusion equations. *SIAM J. Sci. Comput.*, 34:A2288–A2316, 2012.

- [1957] JL Nowinski. On the three-dimensional cerruti problem for an elastic nonlocal half-space. *ZAMM-Journal of Applied Mathematics and Mechanics/Zeitschrift für Angewandte Mathematik und Mechanik*, 72(7):243–249, 1992.
- [1958] H. Obermaier, M. I. Billen, H. Hagen, M. Hering-Bertram, and B. Hamann. Visualizing strain anisotropy in mantle flow fields. *Computer Graphics Forum*, 30(8):2301–2313, 2011.
- [1959] J Tinsley Oden, Noboru Kikuchi, and Young Joon Song. Penalty-finite element methods for the analysis of stokesian flows. *Computer Methods in Applied Mechanics and Engineering*, 31(3):297–329, 1982.
- [1960] D. Olbertz, M.J.R. Wortel, and U. Hansen. Trench migration and subduction zone geometry. *Geophysical Research Letters*, 24(3):221–224, 1997.
- [1961] D. Oldham, J.H. Davies, and T.N. Phillips. Generic polyhedron grid generation for solving partial differential equations on spherical surfaces. *Computers and Geosciences*, 39:11–17, 2012.
- [1962] J.-A. Olive, M.D. Behn, E. Mittelstaedt, G. Ito, and B.Z. Klein. The role of elasticity in simulating long-term tectonic extension. *Geophy. J. Int.*, 205:728–743, 2016.
- [1963] P. Olson, R. Deguen, L.A. Hinov, and S. Zhong. Controls on geomagnetic reversals and core evolution by mantle convection in the Phanerozoic. *Phys. Earth. Planet. Inter.*, 214:87–103, 214.
- [1964] Peter Olson and GM Corcos. A boundary layer model for mantle convection with surface plates. *Geophysical Journal International*, 62(1):195–219, 1980.
- [1965] Peter Olson, David A. Yuen, and Derick Balsiger. Convective mixing and the fine structure of mantle heterogeneity. *Phys. Earth. Planet. Inter.*, 36(3–4):291–304, 1984.
- [1966] E. Olsson and G. Kreiss. A conservative level set method for two phase flow. *J. Comp. Phys.*, 210:225–246, 2005.
- [1967] E. Olsson, G. Kreiss, and S. Zahedi. A conservative level set method for two phase flow ii. *J. Comp. Phys.*, 225:785–807, 2007.
- [1968] C. O'Neill, S. Marchi, S. Zhang, and W. Bottke. Impact-driven subduction on the hadean earth. *Nature Geoscience*, 10(10):793, 2017.
- [1969] C. O'Neill, L. Moresi, D. Müller, R. Albert, and F. Dufour. Ellipsis 3D: a particle-in-cell finite element hybrid code for modelling mantle convection and lithospheric deformation. *Computers and Geosciences*, 32:1769–1779, 2006.
- [1970] C. J. O'Neill and S. Zhang. Lateral mixing processes in the hadean. *Journal of geophysical research.*, 123:7074–7089, 2018.
- [1971] C.J. O'Neill, A. Lenardic, W.L. Griffin, and S.Y. O'Reilly. Dynamics of cratons in an evolving mantle. *Lithos*, 102:12–24, 2008.
- [1972] Craig O'Neill, Adrian Lenardic, AM Jellinek, and Louis Moresi. Influence of supercontinents on deep mantle flow. *Gondwana Research*, 15(3-4):276–287, 2009.
- [1973] Craig O'Neill, Adrian Lenardic, L Moresi, Trond Helge Torsvik, and C-TA Lee. Episodic precambrian subduction. *Earth and Planetary Science Letters*, 262(3-4):552–562, 2007.
- [1974] Craig O'Neill, L Moresi, and Adrian Lenardic. Insulation and depletion due to thickened crust: effects on melt production on mars and earth. *Geophysical research letters*, 32(14), 2005.
- [1975] Craig J O'Neill, Louis Moresi, and AL Jaques. Geodynamic controls on diamond deposits: implications for australian occurrences. *Tectonophysics*, 404(3-4):217–236, 2005.
- [1976] Naomi Oreskes, Kristin Shrader-Frechette, and Kenneth Belitz. Verification, validation, and confirmation of numerical models in the earth sciences. *Science*, 263(5147):641–646, 1994.
- [1977] B Orlic and BBT Wassing. A study of stress change and fault slip in producing gas reservoirs overlain by elastic and viscoelastic caprocks. *Rock Mechanics and Rock Engineering*, 46(3):421–435, 2013.
- [1978] C. P. Orth and V. S. Solomatov. The isostatic stagnant lid approximation and global variations in the venusian lithospheric thickness. *Geochemistry, Geophysics, Geosystems*, 12(7), 2011.
- [1979] S. Osher and R. Fedkiw. Level set methods: an overview and some recent results. *J. Comp. Phys.*, 169:463–502, 2001.
- [1980] S. Osher and C.-W. Shu. High-order essentially non-oscillatory schemes for HamiltonJacobi equations. *SIAM J. Numer. Anal.*, 28:907–922, 1991.
- [1981] Tim A Osswald and Natalie Rudolph. *Polymer rheology: fundamentals and applications*. Carl Hanser Verlag GmbH Co KG, 2014.

- [1982] J.M. Ottino. *The kinematics of mixing: stretching, chaos, and transport*, volume 3. Cambridge university press, 1989.
- [1983] D.R.J. Owen and E. Hinton. *Finite Elements in Plasticity*. Pineridge press, 1980.
- [1984] Ali Değer Özbakır, Rob Govers, and Rinus Wortel. Active faults in the anatolian-aegean plate boundary region with nubia. *Turkish Journal Of Earth Sciences*, pages 30–56, 2017.
- [1985] M. OzBench, K. Regenauer-Lieb, D.R. Stegman, G. Morra, R. Farrington, A. Hale, D.A. May, J. Freeman, L. Bourgoin, H.-B. Mühlhaus, and L. Moresi. A model comparison study of large-scale mantle-lithosphere dynamics driven by subduction. *Phys. Earth. Planet. Inter.*, 171:224–234, 2008.
- [1986] C. O'Neill, A. Lenardic, M. Weller, L. Moresi, S. Quenette, and S. Zhang. A window for plate tectonics in terrestrial planet evolution? *Phys. Earth. Planet. Inter.*, 255(80–92), 2016.
- [1987] Craig J O'Neill and Louis Moresi. How long can diamonds remain stable in the continental lithosphere? *Earth and Planetary Science Letters*, 213(1-2):43–52, 2003.
- [1988] C.C. Paige and M.A. Saunders. Solution of sparse indefinite systems of linear equations. *SIAM J. Numer. Anal.*, 12(4):617–629, 1975.
- [1989] F. Pan and A. Acrivos. Steady flows in rectangular cavities. *J. Fluid Mech.*, 28(4):643–655, 1967.
- [1990] Isabelle Panet, Sylvain Bonvalot, Clément Narteau, Dominique Remy, and Jean-Michel Lemoine. Migrating pattern of deformation prior to the tohoku-oki earthquake revealed by grace data. *Nature Geoscience*, 11(5):367, 2018.
- [1991] Marion Panien, SJH Buiter, Guido Schreurs, and Othmar-Adrian Pfiffner. Inversion of a symmetric basin: insights from a comparison between analogue and numerical experiments. *Geological Society, London, Special Publications*, 253(1):253–270, 2006.
- [1992] Tasos C Papanastasiou. Flows of materials with yield. *Journal of Rheology*, 31(5):385–404, 1987.
- [1993] Barry Parsons and Stephen Daly. The relationship between surface topography, gravity anomalies, and temperature structure of convection. *Journal of Geophysical Research: Solid Earth*, 88(B2):1129–1144, 1983.
- [1994] M.E. Pasyanos, T.G. Masters, G. Laske, and Z. Ma. Litho1.0: An updated crust and lithospheric model of the earth. *J. Geophys. Res.*, 119:2153–2173, 03 2014.
- [1995] WSB Paterson and WF Budd. Flow parameters for ice sheet modeling. *Cold Regions Science and Technology*, 6(2):175–177, 1982.
- [1996] V Patočka, H Čížková, and PJ Tackley. Do elasticity and a free surface affect lithospheric stresses caused by upper-mantle convection? *Geophysical Journal International*, 216(3):1740–1760, 2019.
- [1997] Archie Paulson, Shijie Zhong, and John Wahr. Inference of mantle viscosity from grace and relative sea level data. *Geophysical Journal International*, 171(2):497–508, 2007.
- [1998] David Pedreira, Juan Carlos Afonso, Javier A Pulgar, Jorge Gallastegui, Alberto Carballo, Manel Fernández, Daniel García-Castellanos, Ivone Jiménez-Munt, Julia Semprich, and Olga García-Moreno. Geophysical-petrological modeling of the lithosphere beneath the cantabrian mountains and the north-iberian margin: geodynamic implications. *Lithos*, 230:46–68, 2015.
- [1999] F.J. Peel. How do salt withdrawal minibasins form? Insights from forward modelling, and implications for hydrocarbon migration. *Tectonophysics*, 630:222–235, 2014.
- [2000] D. Pelletier, A. Fortin, and R. Camarero. Are fem solutions of incompressible flows really incompressible? (or how simple flows can cause headaches!). *International journal for numerical methods in fluids*, 9:99–112, 1989.
- [2001] WR Peltier. Penetrative convection in the planetary mantle. *Geophysical Fluid Dynamics*, 5(1):47–88, 1972.
- [2002] WR Peltier. Phase-transition modulated mixing in the mantle of the earth. *Philosophical Transactions of the Royal Society of London. Series A: Mathematical, Physical and Engineering Sciences*, 354(1711):1425–1447, 1996.
- [2003] WR Peltier. Mantle dynamics and the d'' layer: Impacts of the post perovskite phase. *GEOPHYSICAL MONOGRAPH-AMERICAN GEOPHYSICAL UNION*, 174:217, 2007.
- [2004] WR Peltier, S Butler, and LP Solheim. The influence of phase transformations on mantle mixing and plate tectonics. *Earths Deep Interior. Gordon & Breach, Amsterdam*, pages 405–430, 1997.
- [2005] WR Peltier, WE Farrell, and JA Clark. Glacial isostasy and relative sea level: a global finite element model. *Tectonophysics*, 50(2-3):81–110, 1978.

- [2006] G. Peltzer and P. Tapponnier. Formation and evolution of strike-slip faults, rifts, and basins during the india-asia collision: an experimental approach. *J. Geophys. Res.*, 93(B12):15085–15177, 1988.
- [2007] J. Peraire and P.-O. Persson. The compact discontinuous Galerkin method for elliptic problems. *SIAM J. Sci. Comput.*, 30(4):1806–1824, 2008.
- [2008] Leonid L Perchuk and Taras V Gerya. Formation and evolution of precambrian granulite terranes: a gravitational redistribution model. *Geological Society of America Memoirs*, 207:289–310, 2011.
- [2009] J.A. Percival, S.B. Lucas, A.G. Jones, C. Beaumont, D. Eaton, and T. Rivers. How will lithoprobe's final chapter be written? *Geoscience Canada*, 26(1):17–26, 1999.
- [2010] Xyoli Pérez-Campos, YoungHee Kim, Allen Husker, Paul M Davis, Robert W Clayton, Arturo Iglesias, Javier F Pacheco, Shri K Singh, Vlad Constantin Manea, and Michael Gurnis. Horizontal subduction and truncation of the cocos plate beneath central mexico. *Geophysical Research Letters*, 35(18), 2008.
- [2011] D. Perić and C. Huang. Analytical solutions for the three-invariant cam clay model: drained and undrained loading. *16th ASCE Engineering Mechanics Conference*, 2003.
- [2012] Gwenn Peron-Pinvidic, Gianreto Manatschal, et al. Rifted margins: state of the art and future challenges. *Frontiers in Earth Science*, 7:218, 2019.
- [2013] J. Perry-Houts and L. Karlstrom. Anisotropic viscosity and time-evolving lithospheric instabilities due to aligned igneous intrusions. *Geophysical Journal International*, 216(2):794–802, 2018.
- [2014] M. Peters, M. Veveakis, T. Poulet, A. Karrech, M. Herwegh, and K. Regenauer-Lieb. Boudinage as a material instability of elasto-visco-plastic rocks. *Journal of Structural Geology*, 78:86–102, 2015.
- [2015] Kenni Dinesen Petersen and W Roger Buck. Eduction, extension, and exhumation of ultrahigh-pressure rocks in metamorphic core complexes due to subduction initiation. *Geochemistry, Geophysics, Geosystems*, 16(8):2564–2581, 2015.
- [2016] Kenni Dinesen Petersen, Christian Schiffer, and Thorsten Nagel. Lip formation and protracted lower mantle upwelling induced by rifting and delamination. *Scientific reports*, 8(1):16578, 2018.
- [2017] Robert I Petersen, Dave R Stegman, and Paul J Tackley. The subduction dichotomy of strong plates and weak slabs. *Solid Earth*, 8(2):339–350, 2017.
- [2018] Benoît Petri, Thibault Duretz, Geoffroy Mohn, Stefan M Schmalholz, Garry D Karner, and Othmar Müntener. Thinning mechanisms of heterogeneous continental lithosphere. *Earth and Planetary Science Letters*, 512:147–162, 2019.
- [2019] K Petrini and YY Podladchikov. Lithospheric pressure-depth relationship in compressive regions of thickened crust. *Journal of Metamorphic Geology*, 18:67–77, 2000.
- [2020] A.G. Petrunin and S.V. Sobolev. Three-dimensional numerical models of the evolution of pull-apart basins. *Phys. Earth. Planet. Inter.*, 171:387–399, 2008.
- [2021] Alexey Petrunin and Stephan V Sobolev. What controls thickness of sediments and lithospheric deformation at a pull-apart basin? *Geology*, 34(5):389–392, 2006.
- [2022] O.A. Pfiffner, S. Ellis, and C. Beaumont. Collision tectonics in the swiss alps: Insight fro geodynamic modeling. *Tectonics*, 19(6):1065–1094, 2000.
- [2023] Othmar-Adrian Pfiffner, Fritz Schlunegger, and SJH Buiter. The swiss alps and their peripheral foreland basin: Stratigraphic response to deep crustal processes. *Tectonics*, 21(2):3–1, 2002.
- [2024] Thomas Philippe. *Single viscous layer fold interplay and linkage*. PhD thesis, ETH Zurich, 2013.
- [2025] M. Philippon, G. Corti, F. Sani, M. Bonini, M.-L. Balestrieri, P. Molin, E. Willingshofer, D. Sokoutis, and S. Cloetingh. Evolution, distribution, and characteristics of rifting in southern Ethiopia. *Tectonics*, 33, 2014.
- [2026] B.R. Phillips, H.-P. Bunge, and K. Schaber. True polar wander in mantle convection models with multiple, mobile continents. *Gondwana Research*, 15:288–296, 2009.
- [2027] Roger J Phillips and Vicki L Hansen. Geological evolution of venus: Rises, plains, plumes, and plateaus. *Science*, 279(5356):1492–1497, 1998.
- [2028] E. Pichelin and T. Coupez. Finite element solution of the 3D mold filling problem for viscous incompressible fluid. *Computer Methods in Applied Mechanics and Engineering*, 163:359–371, 1998.
- [2029] Thibaud Pichot and Thierry Nalpas. Influence of synkinematic sedimentation in a thrust system with two decollement levels; analogue modelling. *Tectonophysics*, 473(3-4):466–475, 2009.
- [2030] D.A. Di Pietro, S. Lo Forte, and N. Parolini. Mass preserving finite element implementations of the level set method. *Applied Numerical Mathematics*, 56:1179–1195, 2006.

- [2031] A. Pinelli and A. Vacca. Chebyshev collocation method and multidomain decomposition for the incompressible Navier-Stokes equations. *International Journal for numerical methods in fluids*, 18:781–799, 1994.
- [2032] C. Piromallo, T.W. Becker, F. Funiciello, and C. Faccenna. Three-dimensional instantaneous mantle flow induced by subduction. *Geophys. Res. Lett.*, 33(L08304), 2006.
- [2033] Claudia Piromallo and Andrea Morelli. Imaging the mediterranean upper mantle by p-wave travel time tomography. *Annals of Geophysics*, 40(4), 1997.
- [2034] Claudia Piromallo and Andrea Morelli. P wave tomography of the mantle under the alpine-mediterranean area. *Journal of Geophysical Research: Solid Earth*, 108(B2), 2003.
- [2035] Paul Pitard, Anne Replumaz, Francesca Funiciello, Laurent Husson, and Claudio Faccenna. Mantle kinematics driving collisional subduction: Insights from analogue modeling. *Earth and Planetary Science Letters*, 502:96–103, 2018.
- [2036] J. Pitkäranta and T. Saarinen. A Multigrid Version of a Simple Finite Element Method for the Stokes Problem. *Mathematics of Computation*, 45(171):1–14, 1985.
- [2037] T. Plank and P.E. van Keken. The ups and downs of sediments. *Nature Geoscience*, 1:17, 2008.
- [2038] C Plattner, R Malservisi, K P Furlong, and Rob Govers. Development of the Eastern California Shear Zone — Walker Lane belt: The effects of microplate motion and pre-existing weakness in the Basin and Range. *Tectonophysics*, 485(1-4):78–84, 2010.
- [2039] C Plattner, R Malservisi, and Rob Govers. On the plate boundary forces that drive and resist Baja California motion. *GEOLOGY*, 37(4):359–362, 2009.
- [2040] Christina Plattner, Falk Amelung, Scott Baker, Rob Govers, and Michael Patrick Poland. The role of viscous magma mush spreading in volcanic flank motion at Kīlauea Volcano, Hawai’i. *Journal of Geophysical Research*, 118(5):2474–2487, 2013.
- [2041] A.-C. Plesa. Mantle Convection in a 2D Spherical Shell. *NFOCOMP 2011 : The First International Conference on Advanced Communications and Computation*, 2011.
- [2042] Ana-Catalina Plesa, Nicola Tosi, and Christian Hüttig. Thermo-chemical convection in planetary mantles: advection methods and magma ocean overturn simulations. In *Integrated Information and Computing Systems for Natural, Spatial, and Social Sciences*, pages 302–323. 2013.
- [2043] A. Plunder, C. Thieulot, and D.J.J. van Hinsbergen. The effect of obliquity on temperature in subduction zones: insights from 3D numerical modeling. *Solid Earth*, 9:759–776, 2018.
- [2044] Yu. Podlachikov, C. Talbot, and A.N.B. Poliakov. Numerical models of complex diapirs. *Tectonophysics*, 228:189–198, 1993.
- [2045] A. Poliakov, P. Cundall, P. Podlachikov, and V. Lyakhovsky. An explicit inertial method for the simulation of viscoelastic flow: an evaluation of elastic effects on diapiric flow in two- and three-layers models. In *Flow and creep in the solar system: Observations, Modeling and theory*, pages 175–195. Kluwer Academic Publishers, 1993.
- [2046] A. Poliakov and Y. Podlachikov. Diapirism and topography. *Geophy. J. Int.*, 109:553–564, 1992.
- [2047] A.N.B. Poliakov and H.J. Herrmann. Self-organized criticality of plastic shear bands in rocks. *Geophys. Res. Lett.*, 21(19):2143–2146, 1994.
- [2048] A.N.B. Poliakov, H.J. Herrmann, and Y.Yu. Podladchikov. Fractal plastic shear bands. *Fractals*, 2(4):567–581, 1994.
- [2049] A.N.B. Poliakov, Yu. Podlachikov, and C. talbot. Initiation of salt diapirs with frictional overburdens: numerical experiments. *Tectonophysics*, 228:199–210, 1993.
- [2050] A.N.B. Poliakov, R. van Balen, Yu. Podladchikov, B. Daudre, S. Cloetingh, and C. Talbot. Numerical analysis of how sedimentation and redistribution of surficial sediments affects salt diapirism. *Tectonophysics*, 226:199–216, 1993.
- [2051] D. Pollard and R.M. DeConto. Description of a hybrid ice sheet-shelf model, and application to Antarctica. *Geosci. Model Dev.*, 5:1273–1295, 2012.
- [2052] David D Pollard and Atilla Aydin. Propagation and linkage of oceanic ridge segments. *Journal of Geophysical Research: Solid Earth*, 89(B12):10017–10028, 1984.
- [2053] J-P Ponthot and Ted Belytschko. Arbitrary lagrangian-eulerian formulation for element-free galerkin method. *Computer methods in applied mechanics and engineering*, 152(1-2):19–46, 1998.
- [2054] A.A. Popov and S.V. Sobolev. SLIM3D: a tool for three-dimensional thermomechanical modelling of lithospheric deformation with elasto-visco-plastic rheology. *Phys. Earth. Planet. Inter.*, 171(1):55–75, 2008.

- [2055] AI Popov, IS Lobanov, I Yu Popov, and TV Gerya. Benchmark solutions for nanoflows. : , , , 5(3), 2014.
- [2056] Igor Yu Popov and Ilya V Makeev. A benchmark solution for 2d stokes flow over cavity. *Zeitschrift für angewandte Mathematik und Physik*, 65(2):339–348, 2014.
- [2057] I.Yu. Popov, I.S. Lobanov, S.I. Popov, A.I. Popov, and T. Gerya. Practical analytical solutions for benchmarking of 2D and 3D geodynamic Stokes problems with variable viscosity. *Solid Earth*, 5:461–476, 2014.
- [2058] Mahesh Prakash and Paul W Cleary. Three dimensional modelling of lava flow using smoothed particle hydrodynamics. *Applied Mathematical Modelling*, 35(6):3021–3035, 2011.
- [2059] Jean H Prevost and Benjamin Loret. Dynamic strain localization in elasto-(visco-) plastic solids, part 2. plane strain examples. *Computer Methods in Applied Mechanics and Engineering*, 83(3):275–294, 1990.
- [2060] P.J. Prince and J.R. Dormand. High order embedded runge-kutta formulae. *Journal of Computational and Applied Mathematics*, 7(1):67–75, 1981.
- [2061] A. Prosperetti. Motion of two superposed viscous fluids. *Phys. Fluids*, 24(7):1217–1223, 1981.
- [2062] E.G. Puckett, D.L. Turcotte, Y. He, H. Lokavarapu, J.M. Robey, and L.H. Kellogg. New numerical approaches for modeling thermochemical convection in a compositionally stratified fluid. *Phys. Earth. Planet. Inter.*, 276:10–35, 2018.
- [2063] A.E. Pusok and B.J.P. Kaus. Development of topography in 3D continental collision models. *Geochem. Geophys. Geosyst.*, page doi:10.1002/2015GC005732, 2015.
- [2064] A.E. Pusok, B.J.P. Kaus, and A.A. Popov. On the Quality of Velocity Interpolation Schemes for Marker-in-Cell Method and Staggered Grids. *Pure and Applied Geophysics*, pages doi:10.1007/s00024–016–1431–8, 2016.
- [2065] P. Puster, B. H. Hager, and T. H. Jordan. Mantle convection experiments with evolving plates. *Geophysical Research Letters*, 22(16):2223–2226, 1995.
- [2066] P. Puster, T. H. Jordan, and B. H. Hager. Characterization of mantle convection experiments using two-point correlation functions. *Journal of Geophysical Research: Solid Earth*, 100(B4):6351–6365, 1995.
- [2067] C. Pütthe and T. Gerya. Dependence of mid-ocean ridge morphology on spreading rate in numerical 3-D models. *Gondwana Research*, 25:270–283, 2014.
- [2068] W.M. Putman and S.-J. Lin. Finite-Volume transport on various cubed-sphere grids. *J. Comp. Phys.*, 227:55–78, 2007.
- [2069] R.N. Pysklywec. Surface erosion control on the evolution of the deep lithosphere. *Geology*, 34:225–228, 2006.
- [2070] R.N. Pysklywec and C. Beaumont. Intraplate tectonics: feedback between radioactive thermal weakening and crustal deformation driven by mantle lithosphere instabilities. *Earth Planet. Sci. Lett.*, 221:275–292, 2004.
- [2071] R.N. Pysklywec, C. Beaumont, and P. Fullsack. Modeling the behavior of continental mantle lithosphere during plate convergence. *Geology*, 28(7):655–658, 2000.
- [2072] R.N. Pysklywec, C. Beaumont, and P. Fullsack. Lithospheric deformation during the early stages of continental collision: Numerical experiments and comparison with South Island, New Zealand. *J. Geophys. Res.*, 107(B72133), 2002.
- [2073] R.N. Pysklywec and A.R. Cruden. Coupled crust-mantle dynamics and intraplate tectonics: Two-dimensional numerical and three-dimensional analogue modeling. *Geochem. Geophys. Geosyst.*, 5(10), 2004.
- [2074] R.N. Pysklywec, S.M. Ellis, and A.R. Gorman. Three-dimensional mantle lithosphere deformation at collisional plate boundaries: A subduction scissor across the South Island of New Zealand. *Earth Planet. Sci. Lett.*, 289:334–346, 2010.
- [2075] R.N. Pysklywec, O. Gogus, J. Percival, A.R. Cruden, and C. Beaumont. Insights from geodynamical modeling on possible fates of continental mantle lithosphere: collision, removal, and overturn. *Can. J. Earth Sci.*, 47:541–563, 2010.
- [2076] R.N. Pysklywec, J.X. Mitrovica, and M. Ishii. Mantle avalanche as a driving force for tectonic reorganization in the southwest Pacific. *Earth Planet. Sci. Lett.*, 209:29–38, 2003.
- [2077] J. Qin and S. Zhang. On the selective local stabilization of the mixed Q1-P0 element. *Int. J. Num. Meth. Eng.*, 55(12):1121–1141, 2007.
- [2078] Francesca Quarenici, David A Yuen, and Marc R Saari. Adiabaticity and viscosity in deep mantle convection. *Geophysical Research Letters*, 13(1):38–41, 1986.

- [2079] S. Quenette and L. Lavier. Snac v1.2.0 [software], 2010.
- [2080] S. Quenette, Y. Xi, J. Mansour, L. Moresi, and D. Abramson. Underworld-GT Applied to Guangdong, a Tool to Explore the Geothermal Potential of the Crust. *Journal of Earth Sciences*, 26(1):78–88, 2015.
- [2081] Steve Quenette, Louis Moresi, PD Sunter, and Bill F Appelbe. Explaining stgermain: An aspect oriented environment for building extensible computational mechanics modeling software. In *2007 IEEE International Parallel and Distributed Processing Symposium*, pages 1–8. IEEE, 2007.
- [2082] Sandrine Quere and Alessandro M Forte. Influence of past and present-day plate motions on spherical models of mantle convection: implications for mantle plumes and hotspots. *Geophysical Journal International*, 165(3):1041–1057, 2006.
- [2083] L Quevedo, B Hansra, G Morra, N Butterworth, and RD Müller. Oblique mid ocean ridge subduction modelling with the parallel fast multipole boundary element method. *Computational Mechanics*, 51(4):455–463, 2013.
- [2084] L Quevedo, G Morra, and RD Müller. Global paleo-lithospheric models for geodynamical analysis of plate reconstructions. *Physics of the Earth and Planetary Interiors*, 212:106–113, 2012.
- [2085] S. Quere, J.P. Lowman, J. Arkani-Hamed, J.H. Roberts, and R. Moucha. Subcontinental sinking slab remnants in a spherical geometry mantle model. *J. Geophys. Res.*, 118:1760–1777, 2013.
- [2086] G. Quinlan, C. Beaumont, and J. Hall. Tectonic model for crustal seismic reflectivity patterns in compressional orogens. *Geology*, 21(7):663–666, 1993.
- [2087] Matthieu E.T. Quinquis, Suzanne J.H. Buiter, and Susan Ellis. The role of boundary conditions in numerical models of subduction zone dynamics. *Tectonophysics*, 497:57–70, 2011.
- [2088] M.E.T. Quinquis and S.J.H. Buiter. Testing the effects of basic numerical implementations of water migration on models of subduction dynamics. *Solid Earth*, 5:537–555, 2014.
- [2089] J. Quinteros, V.A. Ramos, and P.M. Jacobkis. An elasto-visco-plastic model using the finite element method for crustal and lithospheric deformation. *Journal of Geodynamics*, 48:83–94, 2009.
- [2090] J. Quinteros, S.V. Sobolev, and A.A. Popov. Viscosity in transition zone and lower mantle: Implications for slab penetration . *Geophys. Res. Lett.*, 37(L09307,), 2010.
- [2091] T. Rabczuk, P.M.A. Areias, and T. Belytschko. A simplified mesh-free method for shear bands with cohesive surfaces . *Int. J. Num. Meth. Eng.*, 69:993–1021, 2007.
- [2092] M Rabinowicz, J Boulegue, and P Genton. Two-and three-dimensional modeling of hydrothermal convection in the sedimented middle valley segment, juan de fuca ridge. *Journal of Geophysical Research: Solid Earth*, 103(B10):24045–24065, 1998.
- [2093] Bret Rahe, David A Ferrill, and Alan P Morris. Physical analog modeling of pull-apart basin evolution. *Tectonophysics*, 285(1-2):21–40, 1998.
- [2094] A. Ramachandran. Parallel adaptive finite element simulation using distributed quad-tree/octree forest. Master’s thesis, Institute for Structural Mechanics, Ruhr University Bochum, 2016.
- [2095] B. Ramaswamy and T.C. Jue. A segregated finite element formulation of Navier-Stokes equations under laminar conditions. *Finite Elements in Analysis and Design*, 9:257–270, 1991.
- [2096] Balasubramaniam Ramaswamy. Numerical simulation of unsteady viscous free surface flow. *Journal of Computational Physics*, 90(2):396–430, 1990.
- [2097] Balasubramaniam Ramaswamy and Mutsuto Kawahara. Arbitrary lagrangian–eulerian finite element method for unsteady, convective, incompressible viscous free surface fluid flow. *International Journal for Numerical Methods in Fluids*, 7(10):1053–1075, 1987.
- [2098] Hans Ramberg. Instability of layered systems in the field of gravity. *Phys. Earth. Planet. Inter.*, 1:427–447, 1968.
- [2099] Hans Ramberg. Folding of laterally compressed multilayers in the field of gravity, i. *Physics of the Earth and Planetary Interiors*, 2(4):203–232, 1970.
- [2100] Hans Ramberg. Folding of laterally compressed multilayers in the field of gravity, ii numerical examples. *Physics of the Earth and Planetary Interiors*, 4(2):83–120, 1971.
- [2101] T. Ramsay and R. Pysklywec. Anomalous bathymetry, 3d edge driven convection, and dynamic topography at the western atlantic passive margin. *Journal of Geodynamics*, 52(1):45–56, 2011.
- [2102] H. Ran, P.D. Bons, G. Wang, F. Steinbach, M.A. Finch, A. Griera, E. Gomez-Rivas, M.-G. Llorens, S. Ran, X. Liang, and J. Zhou. High-strain deformation of conglomerates: Numerical modelling, strain analysis, and an example from the wutai mountains, north china craton. *Journal of Structural Geology*, 114:222–234, 2018.

- [2103] G. Ranalli. *Rheology of the Earth*. Springer, 1995.
- [2104] G. Ranalli. Rheology of the lithosphere in space and time. *Geological Society Special Publications*, 121:19–37, 1997.
- [2105] G. Ranalli. Rheology of the crust and its role in tectonic reactivation. *Journal of Geodynamics*, 30:3–15, 2000.
- [2106] Giorgio Ranalli. Rheology and deep tectonics. *Annals of Geophysics*, 40(3), 1997.
- [2107] Giorgio Ranalli and B Fischer. Diffusion creep, dislocation creep, and mantle rheology. *Physics of the earth and planetary interiors*, 34(1-2):77–84, 1984.
- [2108] R. Rannacher and S. Turek. Simple Nonconforming Quadrilateral Stokes Element. *Numerical Methods for Partial Differential Equations*, 8:97–111, 1992.
- [2109] James Todd Ratcliff, Paul J Tackley, Gerald Schubert, and Abdelfattah Zebib. Transitions in thermal convection with strongly variable viscosity. *Physics of the earth and planetary interiors*, 102(3-4):201–212, 1997.
- [2110] J.T. Ratcliff, G. Schubert, and A. Zebib. Three-dimension variable viscosity convection of an infinite Prandtl number Boussinesq fluid in a spherical shell. *Geophys. Res. Lett.*, 22(16):2227–2230, 1995.
- [2111] J.T. Ratcliff, G. Schubert, and A. Zebib. Effects of temperature-dependent viscosity on thermal convection in a spherical shell. *Physica D*, 97:242–252, 1996.
- [2112] J.T. Ratcliff, G. Schubert, and A. Zebib. Steady tetrahedral and cubic patterns of spherical shell convection with temperature-dependent viscosity. *J. Geophys. Res.*, 101(B11):25,473–25,484, 1996.
- [2113] R. Reali, J. M. Jackson, J. van Orman, D. J. Bower, P. Carrez, and P. Cordier. Modeling viscosity of (mg,fe)o at lowermost mantle conditions. *Physics of the Earth and Planetary Interiors*, 287:65–75, 2019.
- [2114] J.E. Reber, M. Dabrowski, and D.W. Schmid. Sheath fold formation around slip surfaces. *Terra Nova*, pages doi:10.1111/j.1365-3121.2012.01081.x, 2012.
- [2115] J.E. Reber, O. Galland, P.R. Cobbold, and C. Le Carlier de Veslud. Experimental study of sheath fold development around a weak inclusion in a mechanically layered matrix. *Tectonophysics*, 586:130–144, 2013.
- [2116] JE Reber, Stefan M Schmalholz, and J-P Burg. Stress orientation and fracturing during three-dimensional buckling: Numerical simulation and application to chocolate-tablet structures in folded turbidites, sw portugal. *Tectonophysics*, 493(1-2):187–195, 2010.
- [2117] J.N. Reddy. On penalty function methods in the finite element analysis of flow problems. *Int. J. Num. Meth. Fluids*, 2:151–171, 1982.
- [2118] J.N. Reddy and D.K. Gartling. *The Finite Element Method in Heat Transfer and Fluid Dynamics*. CRC Press, 2010.
- [2119] H. L. Redmond and S. D. King. Does mantle convection currently exist on mercury? *Physics of the Earth and Planetary Interiors*, 164(3-4):221–231, 2007.
- [2120] William H Reed and TR Hill. Triangular mesh methods for the neutron transport equation. Technical report, Los Alamos Scientific Lab., N. Mex.(USA), 1973.
- [2121] CC Reese, VS Solomatov, and L-N Moresi. Heat transport efficiency for stagnant lid convection with dislocation viscosity: Application to mars and venus. *Journal of Geophysical Research: Planets*, 103(E6):13643–13657, 1998.
- [2122] CC Reese, VS Solomatov, and L-N Moresi. Non-newtonian stagnant lid convection and magmatic resurfacing on venus. *Icarus*, 139(1):67–80, 1999.
- [2123] V. Regard, C. Faccenna, J. Martinod, O. Bellier, and J.-C. Thomas. From subduction to collision: Control of deep processes on the evolution of convergent plate boundary. *J. Geophys. Res.*, 108(B4):doi:10.1029/2002JB001943, 2003.
- [2124] K. Regenauer-Lieb, M. Veveakis, T. Poulet, F. Wellmann, A. Karrech, J. Liu, J. Hauser, C. Schrank, O. Gaede, and M. Trefry. Multiscale coupling and multiphysics approaches in earth sciences: Theory. *J. Coupled Syst. Multiscale Dyn.*, 1(1):doi:10.1166/jcsmd.2013.1012, 2013.
- [2125] K. Regenauer-Lieb, R.F. Weinberg, and G. Rosenbaum. The effect of energy feedbacks on continental strength. *Nature*, 442:67–70, 2006.
- [2126] K Regenauer-Lieb and DA Yuen. Fast mechanisms for the formation of new plate boundaries. *Tectonophysics*, 322(1-2):53–67, 2000.
- [2127] K. Regenauer-Lieb and D.A. Yuen. Modeling shear zones in geological and planetary sciences: solid- and fluid-thermalmechanical approaches. *Earth-Science Reviews*, 63:295–349, 2003.

- [2128] K. Regenauer-Lieb, D.A. Yuen, and J. Branylund. The initiation of subduction: Criticality by addition of water ? *Science*, 294:578–580, 2001.
- [2129] Klaus Regenauer-Lieb, Bruce Hobbs, David A Yuen, Alison Ord, Yanhua Zhang, Hans B Mulhaus, and Gabriele Morra. From point defects to plate tectonic faults. *Philosophical Magazine*, 86(21-22):3373–3392, 2006.
- [2130] Klaus Regenauer-Lieb and Jean-Pierre Petit. Cutting of the european continental lithosphere: Plasticity theory applied to the present alpine collision. *J. Geophys. Res.*, 102:7731–7746, april 1997.
- [2131] Klaus Regenauer-Lieb, Thomas Poulet, Delphine Siret, Florian Fusseis, Jie Liu, Klaus Gessner, Oliver Gaede, Gabriele Morra, Bruce Hobbs, Alison Ord, et al. First steps towards modeling a multi-scale earth system. In *Advances in Geocomputing*, pages 1–25. Springer, 2009.
- [2132] Klaus Regenauer-Lieb, Gideon Rosenbaum, Vladimir Lyakhovsky, Jie Liu, Roberto Weinberg, Amit Segev, and Yishai Weinstein. Melt instabilities in an intraplate lithosphere and implications for volcanism in the harrat ash-shaam volcanic field (nw arabia). *Journal of Geophysical Research: Solid Earth*, 120(3):1543–1558, 2015.
- [2133] Klaus Regenauer-Lieb, Gideon Rosenbaum, and Roberto F Weinberg. Strain localisation and weakening of the lithosphere during extension. *Tectonophysics*, 458(1-4):96–104, 2008.
- [2134] Klaus Regenauer-Lieb and Dave Yuen. Positive feedback of interacting ductile faults from coupling of equation of state, rheology and thermal-mechanics. *Physics of the Earth and Planetary Interiors*, 142(1-2):113–135, 2004.
- [2135] Mirko Reguzzoni and Daniele Sampietro. Moho estimation using goce data: a numerical simulation. In *Geodesy for Planet Earth*, pages 205–214. Springer, 2012.
- [2136] Mirko Reguzzoni, Daniele Sampietro, and Fernando Sansò. Global moho from the combination of the crust2. 0 model and goce data. *Geophysical Journal International*, 195(1):222–237, 2013.
- [2137] Theo Renaud, Patrick Verdin, and Gioia Falcone. Numerical simulation of a deep borehole heat exchanger in the krafla geothermal system. *International Journal of Heat and Mass Transfer*, 143:118496, 2019.
- [2138] Robert J Renka. Algorithm 751: Tripack: a constrained two-dimensional delaunay triangulation package. *ACM Transactions on Mathematical Software (TOMS)*, 22(1):1–8, 1996.
- [2139] Robert J Renka. Algorithm 772: Stripack: Delaunay triangulation and voronoi diagram on the surface of a sphere. *ACM Transactions on Mathematical Software (TOMS)*, 23(3):416–434, 1997.
- [2140] Anne Replumaz, Hrafnkell Kárason, Rob D van der Hilst, Jean Besse, and Paul Tapponnier. 4-d evolution of se asias mantle from geological reconstructions and seismic tomography. *Earth and Planetary Science Letters*, 221(1-4):103–115, 2004.
- [2141] Anne Replumaz and P Tapponnier. Reconstruction of the deformed collision zone between india and asia by backward motion of lithospheric blocks. *Journal of Geophysical Research: Solid Earth*, 108(B6), 2003.
- [2142] TJ Reston and César R Ranero. The 3-d geometry of detachment faulting at mid-ocean ridges. *Geochemistry, Geophysics, Geosystems*, 12(7), 2011.
- [2143] J. Revenaugh and B. Parsons. Dynamic topography and gravity anomalies for fluid layers whose viscosity varies exponentially with depth. *Geophysical Journal of the Royal Astronomical Society*, 90(2):349–368, 1987.
- [2144] Patrice F Rey. Research focus: The geodynamics of mantle melting. *Geology*, 43(4):367–368, 2015.
- [2145] Patrice F Rey, Nicolas Coltice, and Nicolas Flament. Spreading continents kick-started plate tectonics. *Nature*, 513(7518):405, 2014.
- [2146] Patrice F Rey and Gregory Houseman. Lithospheric scale gravitational flow: the impact of body forces on orogenic processes from archaean to phanerozoic. *Geological Society, London, Special Publications*, 253(1):153–167, 2006.
- [2147] B. Reynard. Serpentine in active subduction zones . *Lithos*, 2012.
- [2148] S. Rhebergen, B. Cockburn, and J.J.W. van der Vegt. A spacetime discontinuous Galerkin method for the incompressible NavierStokes equations. *J. Comp. Phys.*, 233:339–358, 2013.
- [2149] Neil M Ribe. *Theoretical Mantle Dynamics*. Cambridge University Press, 2018.
- [2150] NM Ribe and UR Christensen. Three-dimensional modeling of plume-lithosphere interaction. *Journal of Geophysical Research: Solid Earth*, 99(B1):669–682, 1994.
- [2151] Y. Ricard, L. Fleitout, and C. Froidevaux. Geoid heights and lithospheric stresses for a dynamic Earth. *Annales Geophysicae*, 2(3):267–286, 1984.

- [2152] Y. Ricard, M. Richards, C. Lithgow-Bertelloni, and Y. Le Stunff. A geodynamic model of mantle density heterogeneity. *J. Geophys. Res.*, 98:21,895–21,909, 1993.
- [2153] J.G. Rice and R.J. Schmidke. An equal-order velocity-pressure formulation that does not exhibit spurious pressure modes. *Computer Methods in Applied Mechanics and Engineering*, 58:135–149, 1986.
- [2154] M.A. Richards, W.-S. Yang, J.R. Baumgardner, and H.-P. Bunge. Role of a low-viscosity zone in stabilizing plate tectonics: Implications for comparative terrestrial planetology. *Geochem. Geophys. Geosyst.*, 2, 2001.
- [2155] Mark A. Richards and Bradford H. Hager. Geoid anomalies in a dynamic earth. *Journal of Geophysical Research: Solid Earth*, 89(B7):5987–6002, 1984.
- [2156] Randall M. Richardson, Sean C. Solomon, and Norman H. Sleep. Intraplate stress as an indicator of plate tectonic driving forces. *Journal of Geophysical Research*, 81(11):1847–1856, 1976.
- [2157] R.M. Richardson. Ridge Forces, Absolute Plate Motions, and the Intraplate Stress Field. *J. Geophys. Res.*, 97(B8):11,739–11,748, 1992.
- [2158] R.M. Richardson and S.C. Solomon. Tectonic stress in the plates. *Reviews of Geophysics and Space Physics*, 17(5):981, 1979.
- [2159] F.M. Richter and S.F. Daly. Convection models having a multiplicity of large horizontal scales. *J. Geophys. Res.*, 83:4951–4956, 1978.
- [2160] A. Rigo, C. Adam, M. Grégoire, Muriel Gerbault, R. Meyer, M. Rabinowicz, F. Fontaine, and Sylvain Bonvalot. Insights for the melt migration, the volcanic activity and the ultrafast lithosphere delamination related to the yellowstone plume (western usa). *Geophysical Journal International*, 203(2):1274–1301, 2015.
- [2161] A. E. Ringwood. *Composition and Petrology of the Earth's Mantle*. McGraw-Hill, New York, 1975.
- [2162] G.H. Ristow. Wall correction for sinking cylinders in fluids. *Physical Review E*, 55(3):2808–2813, 1997.
- [2163] J. Ritsema, A. Deuss, H.J. van Heijst, and J.H. Woodhouse. S40rts: a degree-40 shear-velocity model for the mantle from new rayleigh wave dispersion, teleseismic traveltimes and normal-mode splitting function measurements. *Geophys. J. Int.*, 184:1223–1236, 2011.
- [2164] J. Ritsema, A.K. McNamara, and A.L. Bull. Tomographic filtering of geodynamic models: Implications for model interpretation and large-scale mantle structure. *J. Geophys. Res.*, 112(B01303), 2007.
- [2165] Riccardo E. M. Riva and Rob Govers. Relating viscosities from postseismic relaxation to a realistic viscosity structure for the lithosphere. *Geophys. J. Int.*, 176(2):614–624, 2009.
- [2166] B. Rivière. *Discontinuous Galerkin Methods for Solving Elliptic and Parabolic Equations*. SIAM, 2008.
- [2167] Béatrice Rivière, Mary F. Wheeler, and Vivette Girault. Improved energy estimates for interior penalty, constrained and discontinuous galerkin methods for elliptic problems. part i. *Computational Geosciences*, 3(3-4):337–360, 1999.
- [2168] Patrick J. Roache. Quantification of uncertainty in computational fluid dynamics. *Annual review of fluid Mechanics*, 29(1):123–160, 1997.
- [2169] GP Roberts, HA Barnes, and P Carew. Modelling the flow behaviour of very shear-thinning liquids. *Chemical Engineering Science*, 56(19):5617–5623, 2001.
- [2170] J. H. Roberts and J. Arkani-Hamed. Impact-induced mantle dynamics on mars. *Icarus*, 218(1):278–289, 2012.
- [2171] J. H. Roberts and O. S. Barnouin. The effect of the caloris impact on the mantle dynamics and volcanism of mercury. *Journal of Geophysical Research: Planets*, 117(E2), 2012.
- [2172] J. H. Roberts, R. J. Lillis, and M. Manga. Giant impacts on early mars and the cessation of the martian dynamo. *Journal of Geophysical Research*, 114(E4), 2009.
- [2173] J. H. Roberts and F. Nimmo. Tidal heating and the long-term stability of a subsurface ocean on enceladus. *Icarus*, 194(2):675–689, 2008.
- [2174] J. H. Roberts and S. Zhong. Degree-1 convection in the martian mantle and the origin of the hemispheric dichotomy. *Journal of Geophysical Research*, 111(E6), 2006.
- [2175] J. H. Roberts and S. Zhong. The cause for the north-south orientation of the crustal dichotomy and the equatorial location of tharsis on mars. *Icarus*, 190(1):24–31, 2007.
- [2176] M.P. Robichaud, P.A. Tanguy, and M. Fortin. An iterative implementation of the uzawa algorithm for 3D fluid flow problems. *Int. J. Num. Meth. Fluids*, 10:429–442, 1990.
- [2177] Jörg Robl and Kurt Stüwe. Continental collision with finite indenter strength: 1. concept and model formulation. *Tectonics*, 24(4), 2005.

- [2178] Jörg Robl and Kurt Stüwe. Continental collision with finite indenter strength: 2. european eastern alps. *Tectonics*, 24(4), 2005.
- [2179] M. Roda, A.M. Marotta, and M.I. Spalla. Numerical simulations of an oceancontinent convergent system: Influence of subduction geometry and mantle wedge hydration on crustal recycling. *Geochem. Geophys. Geosyst.*, 11(5):10.1029/2009GC003015, 2010.
- [2180] J. Rodriguez-González, M.I. Billen, and A.M. Negredo. Non-steady-state subduction and trench-parallel flow induced by overriding plate structure . *Earth Planet. Sci. Lett.*, 401:227–235, 2014.
- [2181] J. Rodriguez-González, A.M. Negredo, and M.I. Billen. The role of the overriding plate thermal state on slab dip variability and on the occurrence of flat subduction. *Geochem. Geophys. Geosyst.*, 13(1):10.1029/2011GC003859, 2012.
- [2182] J. Rodriguez-Gonzalez, A.M. Negredo, and E. Carminati. Slab-mantle flow interaction: influence on subduction dynamics and duration. *Terra Nova*, 0:1–8, 2014.
- [2183] Juan Rodríguez-González, Magali I Billen, Ana M Negredo, and Laurent GJ Montesi. Along-strike variation in subducting plate velocity induced by along-strike variation in overriding plate structure: Insights from 3d numerical models. *Journal of Geodynamics*, 100:175–183, 2016.
- [2184] Gerard H Roe and Mark T Brandon. Critical form and feedbacks in mountain-belt dynamics: Role of rheology as a tectonic governor. *Journal of Geophysical Research: Solid Earth*, 116(B2), 2011.
- [2185] Gerard H Roe, Drew B Stolar, and Sean D Willett. Response of a steady-state critical wedge orogen to changes in climate and tectonic forcing. *SPECIAL PAPERS-GEOLOGICAL SOCIETY OF AMERICA*, 398:227, 2006.
- [2186] Gerard H Roe, Kelin X Whipple, and Jennifer K Fletcher. Feedbacks among climate, erosion, and tectonics in a critical wedge orogen. *American Journal of Science*, 308(7):815–842, 2008.
- [2187] T Rolf, Nicolas Coltice, and P.J Tackley. Linking continental drift, plate tectonics and the thermal state of the earth's mantle. *Earth and Planetary Science Letters*, 351:134–146, 2012.
- [2188] T. Rolf and P.J. Tackley. Focussing of stress by continents in 3D spherical mantle convection with selfconsistent plate tectonics. *Geophys. Res. Lett.*, 38(L18301):10.1029/2011GL048677, 2011.
- [2189] Tobias Rolf, Nicolas Coltice, and Paul J Tackley. Statistical cyclicity of the supercontinent cycle. *Geophysical Research Letters*, 41(7):2351–2358, 2014.
- [2190] Y Rolland, M Hässig, D Bosch, O Bruguier, R Melis, G Galoyan, G Topuz, L Sahakyan, A Avagyan, and M Sosson. The east anatolia-lesser caucasus ophiolite: An exceptional case of large-scale obduction, synthesis of data and numerical modelling. *Geoscience Frontiers*, 11:83–108, 2020.
- [2191] Barbara Romanowicz. Using seismic waves to image earth's internal structure. *Nature*, 451(7176):266, 2008.
- [2192] Barbara Romanowicz and Kurt Lambeck. The mass and moment of inertia of the earth. *Physics of the Earth and Planetary Interiors*, 15(1):P1–P4, 1977.
- [2193] C. Ronchi, R. Iacono, and P.S. Paolucci. The "Cubed Sphere": A New Method for the Solution of Partial Differential Equations in Spherical Geometry. *J. Comp. Phys.*, 124:93–114, 1996.
- [2194] B.C. Root, J. Ebbing, W. van der Wal, R.W. England, and L.L.A. Vermeersen. Comparing gravity-based to seismic-derived lithosphere densities: a case study of the British Isles and surrounding areas. *Geophys. J. Int.*, 208:1796–1810, 2017.
- [2195] B.C. Root, P. Novak, D. Dirkx, M. Kaban, W. van der Wal, and L.L.A. Vermeersen. On a spectral method for forward gravity field modelling. *Journal of Geodynamics*, 97:22–30, 2016.
- [2196] Filipe M Rosas, João C Duarte, Wouter Pieter Schellart, Ricardo Tomas, Vili Grigorova, and Pedro Terrinha. Analogue modelling of different angle thrust-wrench fault interference in a brittle medium. *Journal of Structural Geology*, 74:81–104, 2015.
- [2197] I. Rose, B. Buffet, and T. Heister. Stability and accuracy of free surface time integration in viscous flows. *Phys. Earth. Planet. Inter.*, 262:90–100, 2017.
- [2198] I. Rose and B. Buffett. Scaling rates of true polar wander in convecting planets and moons. *Physics of the Earth and Planetary Interiors*, 2017.
- [2199] A. Rowland and J. H. Davies. Buoyancy rather than rheology controls the thickness of the overriding mechanical lithosphere at subduction zones. *Geophysical Research Letters*, 26(19):3037–3040, 1999.
- [2200] Leigh H Royden, B Clark Burchfiel, Robert W King, Erchie Wang, Zhiliang Chen, Feng Shen, and Yuping Liu. Surface deformation and lower crustal flow in eastern tibet. *science*, 276(5313):788–790, 1997.

- [2201] Leigh H Royden and Laurent Husson. Trench motion, slab geometry and viscous stresses in subduction systems. *Geophysical Journal International*, 167(2):881–905, 2006.
- [2202] A Rozel, J Besserer, GJ Golabek, M Kaplan, and PJ Tackley. Self-consistent generation of single-plume state for enceladus using non-newtonian rheology. *Journal of Geophysical Research: Planets*, 119(3):416–439, 2014.
- [2203] Antoine Rozel, Yanick Ricard, and David Bercovici. A thermodynamically self-consistent damage equation for grain size evolution during dynamic recrystallization. *Geophysical Journal International*, 184(2):719–728, 2011.
- [2204] Johann Rudi, A Cristiano I Malossi, Tobin Isaac, Georg Stadler, Michael Gurnis, Peter WJ Staar, Yves Ineichen, Costas Bekas, Alessandro Curioni, and Omar Ghattas. An extreme-scale implicit solver for complex pdes: highly heterogeneous flow in earth’s mantle. In *Proceedings of the international conference for high performance computing, networking, storage and analysis*, page 5. ACM, 2015.
- [2205] Thomas Ruedas, Paul J. Tackley, and Sean C. Solomon. Thermal and compositional evolution of the martian mantle: Effects of phase transitions and melting. *Phys. Earth. Planet. Inter.*, 216:32–58, 2013.
- [2206] J.B. Ruh, T. Gerya, and J.-P. Burg. High-resolution 3D numerical modeling of thrust wedges: Influence of décollement strength on transfer zones. *Geochem. Geophys. Geosyst.*, 14(4):1131–1155, 2013.
- [2207] J.B. Ruh, L. Le Pourhiet, Ph. Agard, E. Burov, and T. Gerya. Tectonic slicing of subducting oceanic crust along plate interfaces: Numerical modeling. *Geochem. Geophys. Geosyst.*, 16:10.1002/2015GC005998, 2015.
- [2208] Jonas B Ruh, Taras Gerya, and Jean-Pierre Burg. Toward 4d modeling of orogenic belts: Example from the transpressive zagros fold belt. *Tectonophysics*, 702:82–89, 2017.
- [2209] Jonas B Ruh, Boris JP Kaus, and Jean-Pierre Burg. Numerical investigation of deformation mechanics in fold-and-thrust belts: Influence of rheology of single and multiple décollements. *Tectonics*, 31(3), 2012.
- [2210] E Rybacki and G Dresen. Dislocation and diffusion creep of synthetic anorthite aggregates. *Journal of Geophysical Research: Solid Earth*, 105(B11):26017–26036, 2000.
- [2211] E Rybacki, M Gottschalk, R Wirth, and G Dresen. Influence of water fugacity and activation volume on the flow properties of fine-grained anorthite aggregates. *Journal of Geophysical Research: Solid Earth*, 111(B3), 2006.
- [2212] VV Rykov and VP Trubitsyn. 3-d model of mantle convection incorporating moving continents. *Computational Seismology and Geodynamics*, 3:23–32, 1996.
- [2213] VV Rykov and VP Trubitsyn. Numerical technique for calculation of three-dimensional mantle convection and tectonics of continental plates. *Computational Seismology and Geodynamics*, 3:17–22, 1996.
- [2214] Y. Saad. A flexible inner-outer preconditioned GMRES algorithm. *SIAM J. Sci. Comput.*, 14(2):461–469, 1993.
- [2215] Y. Saad. *Iterative methods for sparse linear systems*. SIAM, 2003.
- [2216] Y. Saad and M.H. Schultz. GMRES: A Generalized Minimal Residual Algorithm for Solving Nonsymmetric Linear Systems. *SIAM Journal on Scientific and Statistical Computing*, 7(3):856–869, 1986.
- [2217] M.H. Sadd. *Elasticity. Theory, applications and numerics (Third edition)*. Elsevier, 2014.
- [2218] R. Sadourny. Conservative Finite-Difference Approximations of the Primitive Equations on Quasi-Uniform Spherical Grids. *Monthly Weather Review*, 100(2):136–144, 1972.
- [2219] M. Saito and Y. Abe. Consequences of anisotropic viscosity in the earths mantle (in japanese, with english abstract). *Zisin*, 37:237–245, 1984.
- [2220] C.A. Salazar-Mora, R. Huismans, H. Fossen, and M. Egydio-Silva. The Wilson Cycle and Effects of Tectonic Structural Inheritance on Rifted Passive Margin Formation. *Tectonics*, 37, 2018.
- [2221] T. Salles. escape: Regional to global scale landscape evolution model v2.0. *Geoscientific Model Development*, 12(9):4165–4184, 2019.
- [2222] Sarah D Saltzer. Boundary conditions in sandbox models of crustal extension: an analysis using distinct elements. *Tectonophysics*, 215(3-4):349–362, 1992.
- [2223] M. Sambridge. Geophysical inversion with a neighbourhood algorithm -i. searching a parameter space. *Geophys. J. Int.*, 138:479–494, 1999.
- [2224] M. Sambridge. Geophysical inversion with a neighbourhood algorithm -ii. appraising the ensemble. *Geophys. J. Int.*, 138:727–746, 1999.

- [2225] M. Sambridge, J. Braun, and H. McQueen. Geophysical parametrization and interpolation of irregular data using natural neighbours. *Geophys. J. Int.*, 122:837–857, 1995.
- [2226] M. Sambridge, J. Braun, and H. McQueen. Computational methods for natural neighbour interpolation in two and three dimensions. In R. L. May and A. K. Easton (eds), editors, *Computational Techniques and Applications*, pages 685–692. World Scientific, 1996.
- [2227] H Samuel, V Aleksandrov, and B Deo. The effect of continents on mantle convective stirring. *Geophysical Research Letters*, 38(4), 2011.
- [2228] H. Samuel and M. Evonuk. Modeling advection in geophysical flows with particle level sets. *Geochem. Geophys. Geosyst.*, 11(8):doi:10.1029/2010GC003081, 2010.
- [2229] H. Samuel and C. G. Farnetani. Thermochemical convection and helium concentrations in mantle plumes. *Earth and Planetary Science Letters*, 207(1-4):39–56, 2003.
- [2230] H Samuel and PJ Tackley. Dynamics of core formation and equilibration by negative diapirism. *Geochemistry, Geophysics, Geosystems*, 9(6), 2008.
- [2231] H Samuel, PJ Tackley, and M Evonuk. Heat partitioning in terrestrial planets during core formation by negative diapirism. *Earth and Planetary Science Letters*, 290(1-2):13–19, 2010.
- [2232] Henri Samuel. A deformable particle-in-cell method for advective transport in geodynamic modelling. *Geophysical Journal International*, 214(3):1744–1773, 2018.
- [2233] Henri Samuel and Nicola Tosi. The influence of post-perovskite strength on the earth’s mantle thermal and chemical evolution. *Earth and Planetary Science Letters*, 323:50–59, 2012.
- [2234] D. Sandiford and L. Moresi. Improving subduction interface implementation in dynamic numerical models. *Solid Earth*, 10:969–985, 2019.
- [2235] Dan Sandiford, Louis Moresi, Mike Sandiford, and Ting Yang. Geometric controls on flat slab seismicity. *Earth and Planetary Science Letters*, 527:115787, 2019.
- [2236] Mike Sandiford, David L Hansen, and Sandra N McLaren. Lower crustal rheological expression in inverted basins. *Geological Society, London, Special Publications*, 253(1):271–283, 2006.
- [2237] R.L. Sani, P.M. Gresho, R.L. Lee, and D.F. Griffiths. The cause and cure (?) of the spurious pressures generated by certain FEM solutions of the incompressible Navier-Stokes equations: part 1. *Int. J. Num. Meth. Fluids*, 1:17–43, 1981.
- [2238] R.L. Sani, P.M. Gresho, R.L. Lee, D.F. Griffiths, and M. Engelman. The cause and cure (?) of the spurious pressures generated by certain fem solutions of the incompressible navier-stokes equations: part 2. *Int. J. Num. Meth. Fluids*, 1:171–204, 1981.
- [2239] E Saria, E Calais, DS Stamps, D Delvaux, and CJH Hartnady. Present-day kinematics of the east african rift. *Journal of Geophysical Research: Solid Earth*, 119(4):3584–3600, 2014.
- [2240] J.C. Savage and R.O. Burford. Geodetic Determination of Relative Plate Motion in Central California. *J. Geophys. Res.*, 78(5):832–845, 1973.
- [2241] J. F. Schaefer, L. Boschi, T. W. Becker, and E. Kissling. Radial anisotropy in the european mantle: Tomographic studies explored in terms of mantle flow. *Geophysical Research Letters*, 38(23), 2011.
- [2242] W. P. Schellart. Andean mountain building and magmatic arc migration driven by subduction-induced whole mantle flow. *Nature Communications*, 8, 2010.
- [2243] Wouter P Schellart and Vincent Strak. A review of analogue modelling of geodynamic processes: Approaches, scaling, materials and quantification, with an application to subduction experiments. *Journal of Geodynamics*, 100:7–32, 2016.
- [2244] Wouter Pieter Schellart, Justin Freeman, David Robert Stegman, L Moresi, and David May. Evolution and diversity of subduction zones controlled by slab width. *Nature*, 446(7133):308–311, 2007.
- [2245] Wouter Pieter Schellart and Nick Rawlinson. Global correlations between maximum magnitudes of subduction zone interface thrust earthquakes and physical parameters of subduction zones. *Physics of the Earth and Planetary Interiors*, 225:41–67, 2013.
- [2246] WP Schellart. Shear test results for cohesion and friction coefficients for different granular materials: scaling implications for their usage in analogue modelling. *Tectonophysics*, 324(1-2):1–16, 2000.
- [2247] WP Schellart. Kinematics of subduction and subduction-induced flow in the upper mantle. *Journal of Geophysical Research: Solid Earth*, 109(B7), 2004.
- [2248] WP Schellart. Quantifying the net slab pull force as a driving mechanism for plate tectonics. *Geophysical research letters*, 31(7), 2004.

- [2249] W.P. Schellart. Influence of the subducting plate velocity on the geometry of the slab and migration of the subduction hinge. *Earth Planet. Sci. Lett.*, 231:197–219, 2005.
- [2250] W.P. Schellart, Z. Chen, V. Strak, J.C. Duarte, and F.M. Rosas. Pacific subduction control on asian continental deformation including tibetan extension and eastward extrusion tectonics. *Nature Communications*, 10, 2019.
- [2251] W.P. Schellart, J. Freeman, D.R. Stegman, L. Moresi, and D. May. Evolution and diversity of subduction zones controlled by slab width. *Nature*, 446:308–311, 2007.
- [2252] W.P. Schellart and L. Moresi. A new driving mechanism for backarc extension and backarc shortening through slab sinking induced toroidal and poloidal mantle flow: Results from dynamic subduction models with an overriding plate. *J. Geophys. Res.*, 118:1–28, 2013.
- [2253] W.P. Schellart and W. Spakman. Australian plate motion and topography linked to fossil New Guinea slab below Lake Eyre. *Earth Planet. Sci. Lett.*, 421:107–116, 2015.
- [2254] WP Schellart, DR Stegman, RJ Farrington, and L Moresi. Influence of lateral slab edge distance on plate velocity, trench velocity, and subduction partitioning. *Journal of Geophysical Research: Solid Earth*, 116(B10), 2011.
- [2255] O. Schenk and K. Gaertner. Solving unsymmetric sparse systems of linear equations with pardiso. *Future Gener. Comput. Syst.*, 20:475–487, 2004.
- [2256] Filippo L Schenker, Taras Gerya, and J-P Burg. Bimodal behavior of extended continental lithosphere: Modeling insight and application to thermal history of migmatitic core complexes. *Tectonophysics*, 579:88–103, 2012.
- [2257] Nicholas Schliffke, Jeroen van Hunen, Valentina Magni, and Mark B. Allen. The role of crustal buoyancy in the generation and emplacement of magmatism during continental collision. *Geochem. Geophys. Geosyst.*, 2019.
- [2258] S.M. Schmalholz. A simple analytical solution for slab detachment. *Earth Planet. Sci. Lett.*, 304:45–54, 2011.
- [2259] S.M. Schmalholz and T. Duretz. Shear zone and nappe formation by thermal softening, related stress and temperature evolution, and application to the Alps. *J. Metamorphic Geol.*, 33:887–908, 2015.
- [2260] S.M. Schmalholz, S. Medvedev, S.M. Lechmann, and Y. Podladchikov1. Relationship between tectonic overpressure, deviatoric stress, driving force, isostasy and gravitational potential energy. *Geophy. J. Int.*, 2014.
- [2261] S.M. Schmalholz and Y.Y. Podlachikov. Tectonic overpressure in weak crustal-scale shear zones and implications for the exhumation of high-pressure rocks. *Geophys. Res. Lett.*, 40(1-5), 2013.
- [2262] S.M. Schmalholz, Y.Yu. Podladchikov, and D.W. Schmid. A spectral/finite difference method for simulating large deformations of heterogeneous, viscoelastic materials. *Geophy. J. Int.*, 145:199–208, 2001.
- [2263] S.M. Schmalholz and D.W. Schmid. Folding in power-law viscous multi-layers. *Phil. Trans. R. Soc. A*, 370:1798–1826, 2012.
- [2264] S.M. Schmalholz, D.W. Schmid, and R.C. Fletcher. Evolution of pinch-and-swell structures in a power-law layer. *Journal of Structural Geology*, 30(30):649–663, 2008.
- [2265] Stefan M Schmalholz. 3d numerical modeling of forward folding and reverse unfolding of a viscous single-layer: Implications for the formation of folds and fold patterns. *Tectonophysics*, 446(1-4):31–41, 2008.
- [2266] Stefan M Schmalholz and Thibault Duretz. Impact of grain size evolution on necking in calcite layers deforming by combined diffusion and dislocation creep. *Journal of Structural Geology*, 103:37–56, 2017.
- [2267] Stefan M Schmalholz, Thibault Duretz, György Hetényi, and Sergei Medvedev. Distribution and magnitude of stress due to lateral variation of gravitational potential energy between indian lowland and tibetan plateau. *Geophysical Journal International*, 216(2):1313–1333, 2018.
- [2268] Stefan M Schmalholz, Boris JP Kaus, and Jean-Pierre Burg. Stress-strength relationship in the lithosphere during continental collision. *Geology*, 37(9):775–778, 2009.
- [2269] Stefan M Schmalholz and Yuri Yu Podladchikov. Strain and competence contrast estimation from fold shape. *Tectonophysics*, 340(3-4):195–213, 2001.
- [2270] Jörg Schmalzl and Alexander Loddoch. Using subdivision surfaces and adaptive surface simplification algorithms for modeling chemical heterogeneities in geophysical flows. *Geochemistry, Geophysics, Geosystems*, 4(9), 2003.

- [2271] G Schmalzle, T Dixon, R Malservisi, and Rob Govers. Strain accumulation across the Carrizo segment of the San Andreas Fault, California: Impact of laterally varying crustal properties. *Journal Of Geophysical Research*, 111, 2006.
- [2272] H. Schmeling, A.Y. Babeyko, A. Enns, C. Faccenna, F. Funiciello, T. Gerya, G.J. Golabek, S. Grigull, B.J.P. Kaus, G. Morra, S.M. Schmalholz, and J. van Hunen. A benchmark comparison of spontaneous subduction models - Towards a free surface. *Phys. Earth. Planet. Inter.*, 171:198–223, 2008.
- [2273] H. Schmeling and W.R. Jacoby. On modelling the lithosphere in mantle convection with non-linear rheology. *Journal of Geophysics*, 50:89–100, 1981.
- [2274] Harro Schmeling. Compressible convection with constant and variable viscosity: The effect on slab formation, geoid, and topography. *Journal of Geophysical Research: Solid Earth*, 94(B9):12463–12481, 1989.
- [2275] Harro Schmeling, Alexander R Cruden, and Gabriele Marquart. Finite deformation in and around a fluid sphere moving through a viscous medium: implications for diapiric ascent. *Tectonophysics*, 149(1-2):17–34, 1988.
- [2276] Harro Schmeling, Gabriele Marquart, Roberto Weinberg, and Herbert Wallner. Modelling melting and melt segregation by two-phase flow: new insights into the dynamics of magmatic systems in the continental crust. *Geophysical Journal International*, 217(1):422–450, 2019.
- [2277] Harro Schmeling, Ralf Monz, and David C Rubie. The influence of olivine metastability on the dynamics of subduction. *Earth and Planetary Science Letters*, 165(1):55–66, 1999.
- [2278] D.W. Schmid, M. Dabrowski, and M. Krotkiewski. Evolution of large amplitude 3D fold patterns: A FEM study. *Phys. Earth. Planet. Inter.*, 171:400–408, 2008.
- [2279] D.W. Schmid and Y.Y. Podlachikov. Analytical solutions for deformable elliptical inclusions in general shear. *Geophys. J. Int.*, 155:269–288, 2003.
- [2280] G.E. Schneider, G.D. Raithby, and M.M. Yovanovich. Finite-element solution procedures for solving the incompressible Navier-Stokes equations using equal order variable interpolation. *Numerical Heat Transfer*, 1:433–451, 1978.
- [2281] Stan Schoofs, Ron A Trompert, and Ulrich Hansen. The formation and evolution of layered structures in porous media: effects of porosity and mechanical dispersion. *Physics of the Earth and Planetary Interiors*, 118(3-4):205–225, 2000.
- [2282] Stan Schoofs, Ron A Trompert, and Ulrich Hansen. Thermochemical convection in and beneath intracrustal basins: Onset and effects. *Journal of Geophysical Research: Solid Earth*, 105(B11):25567–25585, 2000.
- [2283] Martin PJ Schöpfer, Conrad Childs, and Tom Manzocchi. Three-dimensional failure envelopes and the brittle-ductile transition. *Journal of Geophysical Research: Solid Earth*, 118(4):1378–1392, 2013.
- [2284] B Schott and H Schmeling. Delamination and detachment of a lithospheric root. *Tectonophysics*, 296(3-4):225–247, 1998.
- [2285] B. Schott, D.A. Yuen, and H. Schmeling. The significance of shear heating in continental delamination. *Phys. Earth. Planet. Inter.*, 118:273–290, 2000.
- [2286] Bertram Schott, David A Yuen, and Harro Schmeling. The diversity of tectonics from fluid-dynamical modeling of the lithosphere–mantle system. *Tectonophysics*, 322(1-2):35–51, 2000.
- [2287] Guido Schreurs, Susanne JH Buiter, David Boutelier, Giacomo Corti, Elisabetta Costa, Alexander R Cruden, J Daniel, Silvan Hoth, Hemin A Koyi, Nina Kukowski, et al. Analogue benchmarks of shortening and extension experiments. *Special Publication-Geological Society of London*, 253:1, 2006.
- [2288] Guido Schreurs, Susanne JH Buiter, Jennifer Boutelier, Caroline Burberry, Jean-Paul Callot, Cristian Cavigazzi, Mariano Cerca, Jian-Hong Chen, Ernesto Cristallini, Alexander R Cruden, et al. Benchmarking analogue models of brittle thrust wedges. *Journal of structural geology*, 92:116–139, 2016.
- [2289] P. Schroeder and G. Lube. Stabilised dG-FEM for incompressible natural convection flows with boundary and moving interior layers on non-adapted meshes. *J. Comp. Phys.*, 335:760–779, 2017.
- [2290] P.W. Schroeder and G. Lube. Divergence-Free H(div)-FEM for Time-Dependent Incompressible Flows with Applications to High Reynolds Number Vortex Dynamics. *J. Sci. Comput.*, 2007.
- [2291] P.W. Schroeder and G. Lube. Pressure-robust analysis of divergence-free and conforming FEM for evolutionary incompressible NavierStokes flows. *Journal of Numerical Mathematics*, 25(4):249–276, 2017.
- [2292] G Schubert and PJ Tackley. Mantle dynamics: The strong control of the spinel-perovskite transition at a depth of 660 km. *Journal of geodynamics*, 20(4):417–428, 1995.

- [2293] G. Schubert, D.L. Turcotte, and P. Olson. *Mantle Convection in the Earth and Planets*. Cambridge University Press, 2001.
- [2294] Gerald Schubert and Charles A Anderson. Finite element calculations of very high rayleigh number thermal convection. *Geophysical Journal International*, 80(3):575–601, 1985.
- [2295] Gerald Schubert, D Bercovici, and GA Glatzmaier. Mantle dynamics in mars and venus: Influence of an immobile lithosphere on three-dimensional mantle convection. *Journal of Geophysical Research: Solid Earth*, 95(B9):14105–14129, 1990.
- [2296] Gerald Schubert, G Masters, P Olson, and P Tackley. Superplumes or plume clusters? *Physics of the Earth and Planetary Interiors*, 146(1-2):147–162, 2004.
- [2297] Gerald Schubert, David Stevenson, and Patrick Cassen. Whole planet cooling and the radiogenic heat source contents of the earth and moon. *Journal of Geophysical Research: Solid Earth*, 85(B5):2531–2538, 1980.
- [2298] M Schubert, T Driesner, TV Gerya, and P Ulmer. Mafic injection as a trigger for felsic magmatism: A numerical study. *Geochemistry, Geophysics, Geosystems*, 14(6):1910–1928, 2013.
- [2299] D.D. Schultz-Ela and P. Walsh. Modeling of grabens extending above evaporites in Canyonlands National Park, Utah. *Journal of Structural Geology*, 24(2):247–275, 2002.
- [2300] David R Scott. The competition between percolation and circulation in a deformable porous medium. *Journal of Geophysical Research: Solid Earth*, 93(B6):6451–6462, 1988.
- [2301] David R Scott and David J Stevenson. Magma solitons. *Geophysical Research Letters*, 11(11):1161–1164, 1984.
- [2302] David R Scott and David J Stevenson. Magma ascent by porous flow. *Journal of Geophysical Research: Solid Earth*, 91(B9):9283–9296, 1986.
- [2303] R.C. Searle and J. Escartin. The rheology and morphology of Oceanic Lithosphere and Mid-Ocean Ridges. *Mid-Ocean Ridges: Hydrothermal interactions between the lithosphere and oceans: AGU Monograph 148*, edited by C. German, J. Lin, and L.M. Parson, pages 63–94, 2004.
- [2304] A. Segal. *Finite element methods for the incompressible Navier-Stokes equations*. Delft University of Technology, 2012.
- [2305] A. Segal and N.P. Praagman. The sepran fem package. Technical report, Technical Report, Ingenieursbureau Sepra, The Netherlands. <http://ta.twi.tudelft.nl/sepran/sepran.html>, 2005.
- [2306] A. Segal, M. ur Rehman, and C. Vuik. Preconditioners for Incompressible Navier-Stokes Solvers. *Numer. Math. Theor. Meth. Appl.*, 3(3):245–275, 2010.
- [2307] P. Sekhar and S.D. King. 3D spherical models of Martian mantle convection constrained by melting history. *Earth Planet. Sci. Lett.*, 388:27–37, 2014.
- [2308] C. Selzer, S.J.H. Buiter, and O.A. Pfiffner. Numerical modeling of frontal and basal accretion at collisional margins. *Tectonics*, 27(TC3001):doi:10.1029/2007TC002169, 2008.
- [2309] Cornelia Selzer. *Tectonic accretion styles at convergent margins: A numerical modelling study*. PhD thesis, University of Bern, 2006.
- [2310] Cornelia Selzer, Susanne JH Buiter, and O Adrian Pfiffner. Sensitivity of shear zones in orogenic wedges to surface processes and strain softening. *Tectonophysics*, 437(1-4):51–70, 2007.
- [2311] E Şengül Uluçak, RN Pysklywec, OH Göğüş, and EU Ulugergerli. Multi-dimensional geodynamic modeling in the southeast carpathians: Upper mantle flow induced surface topography anomalies. *Geochemistry, Geophysics, Geosystems*, 2019.
- [2312] Maria Seton, Nicolas Flament, Joanne Whittaker, R Dietmar Müller, Michael Gurnis, and Dan J Bower. Ridge subduction sparked reorganization of the pacific plate-mantle system 60–50 million years ago. *Geophysical Research Letters*, 42(6):1732–1740, 2015.
- [2313] M. Shahraki and H. Schmeling. Geoid and topography of Earth-like planets: A comparison between compressible and incompressible models for different rheologies. *Phys. Earth. Planet. Inter.*, 216:74–90, 2013.
- [2314] P.N. Shankar and M.D. Deshpande. Fluid mechanics in the driven cavity. *Annu. Rev. Fluid Mech.*, 32:93–136, 2000.
- [2315] NM Shapiro and MH Ritzwoller. Monte-carlo inversion for a global shear-velocity model of the crust and upper mantle. *Geophysical Journal International*, 151(1):88–105, 2002.
- [2316] Howard N Sharpe and WR Peltier. A thermal history model for the earth with parameterized convection. *Geophysical Journal International*, 59(1):171–203, 1979.

- [2317] W. Sharples, M.A. Jadamec, L.N. Moresi, and F.A. Capitanio. Overriding plate controls on subduction evolution. *J. Geophys. Res.*, 119:6684–6704, 2014.
- [2318] W. Sharples, L.-N. Moresi, and M. A. Jadamec and J. Revote. Styles of rifting and fault spacing in numerical models of crustal extension. *J. Geophys. Res.*, 120:4379–4404, 2015.
- [2319] W. Sharples, L.N. Moresi, M. Velic, M.A. Jadamec, and D.A. May. Simulating faults and plate boundaries with a transversely isotropic plasticity model. *Phys. Earth. Planet. Inter.*, 252:77–90, 2016.
- [2320] M. Shaw and R. Pysklywec. Anomalous uplift of the Apennines and subsidence of the Adriatic: The result of active mantle flow? *Geophys. Res. Lett.*, 34(L04311):doi:10.1029/2006GL028337, 2007.
- [2321] Simon G Sheldon, Jørgen P Steffensen, Steffen B Hansen, Trevor J Popp, and Sigríður J Johnsen. The investigation and experience of using estisol 240 and coasol for ice-core drilling. *Annals of Glaciology*, 55(68):219–232, 2014.
- [2322] Alexander I Shemenda. Subduction of the lithosphere and back arc dynamics: Insights from physical modeling. *Journal of Geophysical Research: Solid Earth*, 98(B9):16167–16185, 1993.
- [2323] G. E. Shephard, L. Liu, R. D. Müller, and M. Gurnis. Dynamic topography and anomalously negative residual depth of the argentine basin. *Gondwana Research*, 22(2):658–663, 2012.
- [2324] G. E. Shephard, R. D. Müller, L. Liu, and M. Gurnis. Miocene drainage reversal of the amazon river driven by plate-mantle interaction. *Nature Geoscience*, 3(12):870–875, 2010.
- [2325] Grace E Shephard, H-P Bunge, Bernhard SA Schubert, RD Müller, AS Talsma, C Moder, and TCW Landgrebe. Testing absolute plate reference frames and the implications for the generation of geodynamic mantle heterogeneity structure. *Earth and Planetary Science Letters*, 317:204–217, 2012.
- [2326] John W Shervais and Sung Hi Choi. Subduction initiation along transform faults: The proto-franciscan subduction zone. *Lithosphere*, 4(6):484–496, 2012.
- [2327] HC Sheth. Flood basalts and large igneous provinces from deep mantle plumes: fact, fiction, and fallacy. *Tectonophysics*, 311(1-4):1–29, 1999.
- [2328] Jonathan Richard Shewchuk. Delaunay refinement algorithms for triangular mesh generation. *Computational geometry*, 22(1-3):21–74, 2002.
- [2329] Jonathan Richard Shewchuk. Reprint of: Delaunay refinement algorithms for triangular mesh generation. *Computational Geometry*, 47(7):741–778, 2014.
- [2330] J.R. Shewchuk. Triangle: Engineering a 2D Quality Mesh Generator and Delaunay Triangulator. In Ming C. Lin and Dinesh Manocha, editors, *Applied Computational Geometry: Towards Geometric Engineering*, volume 1148 of *Lecture Notes in Computer Science*, pages 203–222. Springer-Verlag, May 1996. From the First ACM Workshop on Applied Computational Geometry.
- [2331] Yanan Shi, Dongping Wei, Zhong-Hai Li, Ming-Qi Liu, and Mengxue Liu. Subduction mode selection during slab and mantle transition zone interaction: Numerical modeling. *Pure Appl. Geophys.*, pages 5–24, 2017.
- [2332] J. S. Shiau, A.V. Lyamin, and S. W. Sloan. Bearing capacity of a sand layer on clay by finite element limit analysis. *Can. Geotech. J.*, 40:900–915, 2003.
- [2333] A. P. Showman and L. Han. Numerical simulations of convection in europa’s ice shell: Implications for surface features. *Journal of Geophysical Research*, 109(E1), 2004.
- [2334] A. P. Showman and L. Han. Effects of plasticity on convection in an ice shell: Implications for europa. *Icarus*, 177(2):425–437, 2005.
- [2335] Chi-Wang Shu. Discontinuous galerkin methods: general approach and stability. *Numerical solutions of partial differential equations*, 201, 2009.
- [2336] Alexey Shulgin and Irina Artemieva. Thermo-chemical heterogeneity and density of continental and oceanic upper mantle in the european-north atlantic region. *Journal of Geophysical Research: Solid Earth*, 124:9280–9312, 2019.
- [2337] Jean-Claude Sibuet, Shiri P Srivastava, and Wim Spakman. Pyrenean orogeny and plate kinematics. *Journal of Geophysical Research: Solid Earth*, 109(B8), 2004.
- [2338] I. Sidorin, M. Gurnis, and D. V. Helmberger. Dynamics of a phase change at the base of the mantle consistent with seismological observations. *Journal of Geophysical Research: Solid Earth*, 104(B7):15005–15023, 1999.
- [2339] Karin Sigloch and Mitchell G Mihalynuk. Intra-oceanic subduction shaped the assembly of cordilleran north america. *Nature*, 496(7443):50, 2013.

- [2340] Jesse L Silverberg, Matthew Bierbaum, James P Sethna, and Itai Cohen. Collective motion of humans in mosh and circle pits at heavy metal concerts. *Physical review letters*, 110(22):228701, 2013.
- [2341] D.J. Silvester and N. Kechkar. Stabilised bilinear-constant velocity-pressure finite elements for the conjugate gradient solution of the stokes problem. *Computer Methods in Applied Mechanics and Engineering*, 79(1):71–86, 1990.
- [2342] Shi J Sim, Dave R Stegman, and Nicolas Coltice. Influence of continental growth on mid-ocean ridge depth. *Geochemistry, Geophysics, Geosystems*, 17(11):4425–4437, 2016.
- [2343] R Simitev and FH Busse. Patterns of convection in rotating spherical shells. *New Journal of Physics*, 5(1):97, 2003.
- [2344] N.A. Simmons, A.M. Forte, L. Boschi, and S.P. Grand. GyPSuM: A joint tomographic model of mantle density and seismic wave speeds. *J. Geophys. Res.*, 115(B12310), 2010.
- [2345] N.A. Simmons, A.M. Forte, and S.P. Grand. Joint seismic, geodynamic and mineral physical constraints on three-dimensional mantle heterogeneity: Implications for the relative importance of thermal versus compositional heterogeneity. *Geophys. J. Int.*, 177:1284–1304, 2009.
- [2346] N.A. Simmons, S.C. Myers, G. Johannesson, and E. Matzel. LLNL-G3Dv3: Global P wave tomography model for improved regional and teleseismic travel time prediction. *J. Geophys. Res.*, 117(B10302), 2012.
- [2347] K. Simon, R.S. Huismans, and C. Beaumont. Dynamical modelling of lithospheric extension and small-scale convection: implications for magmatism during the formation of volcanic rifted margins. *Geophys. J. Int.*, 176:327–350, 2009.
- [2348] Guy Simpson. A dynamic model to investigate coupling between erosion, deposition, and three-dimensional (thin-plate) deformation. *Journal of Geophysical Research: Earth Surface*, 109(F2), 2004.
- [2349] Guy Simpson. *Practical Finite Element Modelin in Earth Science Using Matlab*. Wiley-Blackwell, 2017.
- [2350] Guy DH Simpson. Modelling interactions between fold-thrust belt deformation, foreland flexure and surface mass transport. *Basin Research*, 18(2):125–143, 2006.
- [2351] Guy DH Simpson. Mechanical modelling of folding versus faulting in brittle–ductile wedges. *Journal of Structural Geology*, 31(4):369–381, 2009.
- [2352] Gaia Siravo, Claudio Faccenna, Mélanie Gérault, Thorsten W Becker, Maria Giuditta Fellin, Frédéric Herman, and Paola Molin. Slab flattening and the rise of the eastern cordillera, colombia. *Earth and Planetary Science Letters*, 512:100–110, 2019.
- [2353] E Sizova, T Gerya, and M Brown. Exhumation mechanisms of melt-bearing ultrahigh pressure crustal rocks during collision of spontaneously moving plates. *Journal of Metamorphic Geology*, 30(9):927–955, 2012.
- [2354] E Sizova, T Gerya, M Brown, and LL Perchuk. Subduction styles in the precambrian: Insight from numerical experiments. *Lithos*, 116(3-4):209–229, 2010.
- [2355] E Sizova, Taras Gerya, and M Brown. Contrasting styles of phanerozoic and precambrian continental collision. *Gondwana Research*, 25(2):522–545, 2014.
- [2356] Elena Sizova, Christoph Hauzenberger, Harald Fritz, Shah Wali Faryad, and Taras Gerya. Late orogenic heating of (ultra) high pressure rocks: Slab rollback vs. slab breakoff. *Geosciences*, 9(12):499, 2019.
- [2357] L.S. Sklar and W.E. Dietrich. A mechanistic model for river incision into bedrock by saltating bed load. *Water Resources Research*, 40(6):W06301, 2004.
- [2358] N. H. Sleep. Channeling at the base of the lithosphere during the lateral flow of plume material beneath flow line hot spots: Channeling during lateral flow of plume material. *Geochemistry, Geophysics, Geosystems*, 9(8), 2008.
- [2359] Norman H Sleep. Evolution of the continental lithosphere. *Annu. Rev. Earth Planet. Sci.*, 33:369–393, 2005.
- [2360] L.J. Sluys and R. de Borst. Wave propagation and localisation in a rate-dependent cracked medium - model formulation and one-dimensional examples. *Int. J. Solids Structures*, 29(23):2945–2958, 1992.
- [2361] JHW Smit, JP Brun, and D Sokoutis. Deformation of brittle-ductile thrust wedges in experiments and nature. *Journal of Geophysical Research: Solid Earth*, 108(B10), 2003.
- [2362] Alexander V Sobolev. Hunting for earths primary melts. *Humboldt Kosmos*, 79:19–20, 2002.
- [2363] Stephan V Sobolev and A Yu Babeyko. What drives orogeny in the andes? *Geology*, 33(8):617–620, 2005.
- [2364] S.V. Sobolev, A. Petrunin, Z. Garfunkel, and A.Y. Babeyko. Thermo-mechanical model of the Dead Sea Transform. *Earth Planet. Sci. Lett.*, 238:78–95, 2005.

- [2365] S.V. Sobolev, A.V. Sobolev, D.V. Kuzmin, N.A. Krivolutskaya, A.G. Petrunin, N.T. Arndt, V.A. Radko, and Y.R. Vasiliev. Linking mantle plumes, large igneous provinces and environmental catastrophes. *Nature*, 477:312, 2011.
- [2366] F. Soboutia, A. Ghodsib, and J. Arkani-Hamed. On the advection of sharp material interfaces in geodynamic problems: entrainment of the D'' layer. *Journal of Geodynamics*, 31:459–479, 2001.
- [2367] Dimitrios Sokoutis, Marco Bonini, Sergei Medvedev, Mario Boccaletti, Christopher J Talbot, and Hemin Koyi. Indentation of a continent with a built-in thickness change: experiment and nature. *Tectonophysics*, 320(3-4):243–270, 2000.
- [2368] Dimitrios Sokoutis, Jean-Pierre Burg, Marco Bonini, Giacomo Corti, and Sierd Cloetingh. Lithospheric-scale structures from the perspective of analogue continental collision. *Tectonophysics*, 406(1-2):1–15, 2005.
- [2369] Dimitrios Sokoutis, Giacomo Corti, Marco Bonini, Jean Pierre Brun, Sierd Cloetingh, Thomas Mauduit, and Piero Manetti. Modelling the extension of heterogeneous hot lithosphere. *Tectonophysics*, 444(1-4):63–79, 2007.
- [2370] Santiago R Soler, Agustina Pesce, Mario E Gimenez, and Leonardo Uieda. Gravitational field calculation in spherical coordinates using variable densities in depth. *Geophysical Journal International*, 218(3):2150–2164, 2019.
- [2371] LP Solheim and WR Peltier. Heat transfer and the onset of chaos in a spherical, axisymmetric, anelastic model of whole mantle convection. *Geophysical & Astrophysical Fluid Dynamics*, 53(4):205–255, 1990.
- [2372] Viatcheslav S Solomatov and L-N Moresi. Scaling of time-dependent stagnant lid convection: Application to small-scale convection on earth and other terrestrial planets. *Journal of Geophysical Research: Solid Earth*, 105(B9):21795–21817, 2000.
- [2373] VS Solomatov. Scaling of temperature-and stress-dependent viscosity convection. *Physics of Fluids*, 7(2):266–274, 1995.
- [2374] VS Solomatov. Grain size-dependent viscosity convection and the thermal evolution of the earth. *Earth and Planetary Science Letters*, 191(3-4):203–212, 2001.
- [2375] V.S. Solomatov. Initiation of subduction by small-scale convection. *J. Geophys. Res.*, 109(B01412), 2004.
- [2376] V.S. Solomatov. Localized subcritical convective cells in temperature-dependent viscosity fluids. *Phys. Earth. Planet. Inter.*, 200-201:63–71, 2012.
- [2377] VS Solomatov, R El-Khozondar, and V Tikare. Grain size in the lower mantle: constraints from numerical modeling of grain growth in two-phase systems. *Physics of the Earth and planetary interiors*, 129(3-4):265–282, 2002.
- [2378] V.S. Solomatov and L.-N. Moresi. Stagnant lid convection on Venus. *J. Geophys. Res.*, 101(E2):4737–4753, 1996.
- [2379] VS Solomatov and L-N Moresi. Three regimes of mantle convection with non-newtonian viscosity and stagnant lid convection on the terrestrial planets. *Geophysical Research Letters*, 24(15):1907–1910, 1997.
- [2380] VS Solomatov and L-N Moresi. Small-scale convection in the d layer. *Journal of Geophysical Research: Solid Earth*, 107(B1):ETG-3, 2002.
- [2381] VS Solomatov and CC Reese. Grain size variations in the earth's mantle and the evolution of primordial chemical heterogeneities. *Journal of Geophysical Research: Solid Earth*, 113(B7), 2008.
- [2382] Sean C Solomon and Norman H Sleep. Some simple physical models for absolute plate motions. *Journal of Geophysical Research*, 79(17):2557–2567, 1974.
- [2383] L.J. Sonder and Ph.C. england. Effects of a temperaturedependent rheology on largescale continental extension. *JGR*, 94(B6), 1989.
- [2384] Teh-Ru Alex Song and Mark Simons. Large trench-parallel gravity variations predict seismogenic behavior in subduction zones. *Science*, 301(5633):630–633, 2003.
- [2385] A. Souche, O. Galland, O. Haug, and M. Dabrowski. Impact of host rock heterogeneity on failure around pressurized conduits: Implications for finger-shaped magmatic intrusions. *Tectonophysics*, 765:52–63, 2019.
- [2386] A. Souche, S. Medvedev, T.B. Andersen, and M. Dabrowski. Shear heating in extensional detachments: implications for the thermal history of the Devonian basins of W Norway. *Tectonophysics*, 608:1073–1085, 2013.
- [2387] M. Souli and J.P. Zolesio. Arbitrary Lagrangian-Eulerian and free surface methods in fluid mechanics. *Comput. Methods Appl. Mech. Engrg.*, 191:451–466, 2001.

- [2388] W. Spakman, M.V. Chertova, A. van den Berg, and D.J.J. van Hinsbergen. Puzzling features of western Mediterranean tectonics explained by slab dragging. *Nature Geoscience*, 11:211–216, 2018.
- [2389] W. Spakman, M.J.R. Wortel, and N.J. Vlaar. The hellenic subduction zone: A tomographic image and its geodynamic implications. *Geophysical Research Letters*, 15(1):60–63, 1988.
- [2390] Wim Spakman. Delay-time tomography of the upper mantle below europe, the mediterranean, and asia minor. *Geophysical Journal International*, 107(2):309–332, 1991.
- [2391] S. Spasojevic, M. Gurnis, and R. Sutherland. Inferring mantle properties with an evolving dynamic model of the antarctica-new zealand region from the late cretaceous. *Journal of Geophysical Research*, 115(B5), 2010.
- [2392] S. Spasojevic, M. Gurnis, and R. Sutherland. Mantle upwellings above slab graveyards linked to the global geoid lows. *Nature Geoscience*, 3(6):435–438, 2010.
- [2393] S. Spasojevic, L. Liu, and M. Gurnis. Adjoint models of mantle convection with seismic, plate motion, and stratigraphic constraints: North america since the late cretaceous. *Geochemistry, Geophysics, Geosystems*, 10(5), 2009.
- [2394] S. Spasojevic, L. Liu, M. Gurnis, and R. D. Müller. The case for dynamic subsidence of the u.s. east coast since the eocene. *Geophysical Research Letters*, 35(8), 2008.
- [2395] Edward A Spiegel and G Veronis. On the boussinesq approximation for a compressible fluid. *The Astrophysical Journal*, 131:442, 1960.
- [2396] M. Spiegelman, D.A. May, and C. Wilson. On the solvability of incompressible Stokes with viscoplastic rheologies in geodynamics. *Geochem. Geophys. Geosyst.*, 17:2213–2238, 2016.
- [2397] Marc Spiegelman. Flow in deformable porous media. part 2 numerical analysis—the relationship between shock waves and solitary waves. *Journal of Fluid Mechanics*, 247:39–63, 1993.
- [2398] S. W. Squyres, D. G. Jankowski, M. Simons, S. C. Solomon, B. H. Hager, and G. E. McGill. Plains tectonism on venus: The deformation belts of lavinia planitia. *Journal of Geophysical Research*, 97(E8):13579, 1992.
- [2399] O. Srámk and S. Zhong. Long-wavelength stagnant lid convection with hemispheric variation in lithospheric thickness: Link between martian crustal dichotomy and tharsis? *Journal of Geophysical Research*, 115(E9), 2010.
- [2400] O. Srámk and S. Zhong. Martian crustal dichotomy and tharsis formation by partial melting coupled to early plume migration. *Journal of Geophysical Research: Planets*, 117(E1), 2012.
- [2401] Ondřej Šrámk, Yanick Ricard, and David Bercovici. Simultaneous melting and compaction in deformable two-phase media. *Geophysical Journal International*, 168(3):964–982, 2007.
- [2402] G. Stadler, M. Gurnis, C. Burstedde, L.C. Wilcox, L. Alisic, and O. Ghattas. The dynamics of plate tectonics and mantle flow: from local to global scales. *Science*, 329:1033–1038, 2010.
- [2403] Ph. Steer, R. Cattin, J. Lavé, and V. Godard. Surface Lagrangian Remeshing: A new tool for studying long term evolution of continental lithosphere from 2D numerical modelling. *Computers and Geosciences*, 37(8):1067–1074, 2010.
- [2404] Ph. Steer, M. Simoes, R. Cattin3, and J.B.H. Shyu. Erosion influences the seismicity of active thrust faults. *Nature Communications*, 5:5564, 2014.
- [2405] Dave R Stegman, Louis Moresi, Robert Turnbull, Julian Giordani, Patrick Sunter, Alan Lo, and Steve Quenette. glucifer: next generation visualization framework for high-performance computational geodynamics. *Visual Geosciences*, 13(1):71–84, 2008.
- [2406] D.R. Stegman, R. Farrington, F.A. Capitanio, and W.P. Schellart. A regime diagram for subduction styles from 3-D numerical models of free subduction. *Tectonophysics*, 483:29–45, 2010.
- [2407] D.R. Stegman, J. Freeman, W.P. Schellart, L. Moresi, and D. May. Influence of trench width on subduction hinge retreat rates in 3-D models of slab rollback. *Geochem. Geophys. Geosyst.*, 7(3):doi:10.1029/2005GC001056, 2006.
- [2408] D.R. Stegman, W.P. Schellart, and J. Freeman. Competing influences of plate width and far-field boundary conditions on trench migration and morphology of subducted slabs in the upper mantle. *Tectonophysics*, 483:46–57, 2010.
- [2409] C. Stein, A. Fahl, and U. Hansen. Resurfacing events on venus: Implications on plume dynamics and surface topography. *Geophysical Research Letters*, 37(1), 2010.

- [2410] C. Stein, A. Finnenkutter, J.P. Lowman, and U. Hansen. The pressure-weakening effect in super-earths: Consequences of a decrease in lower mantle viscosity on surface dynamics. *Geophysical Research Letters*, 38(21), 2011.
- [2411] C. Stein and U. Hansen. Arrhenius rheology versus frank-kamenetskii rheology implications for mantle dynamics. *Geochemistry, Geophysics, Geosystems*, 14(8):2757–2770, 2013.
- [2412] C. Stein, J. Lowman, and U. Hansen. A comparison of mantle convection models featuring plates. *Geochem. Geophys. Geosyst.*, 15:2689–2698, 2014.
- [2413] C. Stein, J.P. Lowman, and U. Hansen. The influence of mantle internal heating on lithospheric mobility: Implications for super-earths. *Earth and Planetary Science Letters*, 361:448–459, 2013.
- [2414] Claudia Stein and Ulrich Hansen. Numerical investigation of a layered temperature-dependent viscosity convection in comparison to convection with a full temperature dependence. *Physics of the Earth and Planetary Interiors*, 226:1–13, 2014.
- [2415] S. Stein. A model for the relation between spreading rate and oblique spreading. *Earth Planet. Sci. Lett.*, 39:313–318, 1978.
- [2416] Volker Steinbach, Ulrich Hansen, and Adolf Ebel. Compressible convection in the earth’s mantle: a comparison of different approaches. *Geophysical Research Letters*, 16(7):633–636, 1989.
- [2417] Volker Steinbach and David A Yuen. Effects of depth-dependent properties on the thermal anomalies produced in flush instabilities from phase transitions. *Physics of the Earth and Planetary Interiors*, 86(1–3):165–183, 1994.
- [2418] Volker Steinbach, David A Yuen, and Wuling Zhao. Instabilities from phase transitions and the timescales of mantle thermal evolution. *Geophysical research letters*, 20(12):1119–1122, 1993.
- [2419] B. Steinberger, E. Bredow, S. Lebedev, A. Schaeffer, and T. H. Torsvik. Widespread volcanism in the greenland-north atlantic region explained by the iceland plume. *Nature Geoscience*, 12(1):61, 2019.
- [2420] B. Steinberger and A.R. Calderwood. Models of large-scale viscous flow in the Earth’s mantle with constraints from mineral physics and surface observations. *Geophys. J. Int.*, 167:1461–1481, 2006.
- [2421] B. Steinberger and R. Holme. Mantle flow models with core-mantle boundary constraints and chemical heterogeneities in the lowermost mantle. *Journal of Geophysical Research: Solid Earth*, 113(B5), 2008.
- [2422] B. Steinberger, H. Schmeling, and G. Marquart. Large-scale lithospheric stress field and topography induced by global mantle circulation. *Earth Planet. Sci. Lett.*, 186:75–91, 2001.
- [2423] Bernard Steinberger and Trond H Torsvik. Toward an explanation for the present and past locations of the poles. *Geochemistry, Geophysics, Geosystems*, 11(6), 2010.
- [2424] Bernhard Steinberger. Topography caused by mantle density variations: observation-based estimates and models derived from tomography and lithosphere thickness. *Geophysical Supplements to the Monthly Notices of the Royal Astronomical Society*, 205(1):604–621, 2016.
- [2425] Bernhard Steinberger and Richard J O’Connell. Advection of plumes in mantle flow: implications for hotspot motion, mantle viscosity and plume distribution. *Geophysical Journal International*, 132(2):412–434, 1998.
- [2426] Bernhard Steinberger and Richard J O’Connell. The convective mantle flow signal in rates of true polar wander. *Ice Sheets, Sea Level and the Dynamic Earth, Geodyn. Ser.*, 29:233–256, 2002.
- [2427] Bernhard Steinberger, Wim Spakman, Peter Japsen, and Trond H Torsvik. The key role of global solid-earth processes in preconditioning greenland’s glaciation since the pliocene. *Terra Nova*, 27(1):1–8, 2015.
- [2428] Bernhard Steinberger and Trond H Torsvik. A geodynamic model of plumes from the margins of large low shear velocity provinces. *Geochemistry, Geophysics, Geosystems*, 13(1), 2012.
- [2429] Stephen A Steiner and Clinton P Conrad. Does active mantle upwelling help drive plate motions? *Physics of the Earth and Planetary Interiors*, 161(1-2):103–114, 2007.
- [2430] K. Stemmer, H. Harder, and U. Hansen. A new method to simulate convection with strongly temperature- and pressure-dependent viscosity in a spherical shell: Applications to the Earth’s mantle. *Phys. Earth. Planet. Inter.*, 157:223–249, 2006.
- [2431] Ove Stephansson and Harald Berner. The finite element method in tectonic processes. *Physics of the Earth and Planetary Interiors*, 4(4):301–321, 1971.
- [2432] R.J. Stern. Subduction zones. *Reviews of Geophysics*, 40(4):doi:10.1029/2001RG000108, 2002.
- [2433] R.J. Stern. Subduction initiation: spontaneous and induced. *Earth Planet. Sci. Lett.*, 226:275–292, 2004.

- [2434] Robert J Stern, M Reagan, O Ishizuka, Y Ohara, and S Whattam. To understand subduction initiation, study forearc crust: To understand forearc crust, study ophiolites. *Lithosphere*, 4(6):469–483, 2012.
- [2435] Tim Stern, Gregory Houseman, Michelle Salmon, and Lynn Evans. Instability of a lithospheric step beneath western north island, new zealand. *Geology*, 41(4):423–426, 2013.
- [2436] P. Sternai, L. Jolivet, A. Menant, and T. Gerya. Driving the upper plate surface deformation by slab rollback and mantle flow. *Earth Planet. Sci. Lett.*, 405:110–118, 2014.
- [2437] D. Sterpi. An analysis of geotechnical problems involving strain softening effects. *International Journal fro Numerical and Analytical Methods in Geomechanics*, 23:1427–1454, 1999.
- [2438] Lars Stixrude and Carolina Lithgow-Bertelloni. Mineralogy and elasticity of the oceanic upper mantle: Origin of the low-velocity zone. *Journal of Geophysical Research: Solid Earth*, 110(B3), 2005.
- [2439] Lars Stixrude and Carolina Lithgow-Bertelloni. Thermodynamics of mantle minerals i. physical properties. *Geophysical Journal International*, 162(2):610–632, 2005.
- [2440] Lars Stixrude and Carolina Lithgow-Bertelloni. Influence of phase transformations on lateral heterogeneity and dynamics in earth’s mantle. *Earth and Planetary Science Letters*, 263(1-2):45–55, 2007.
- [2441] Lars Stixrude and Carolina Lithgow-Bertelloni. Thermodynamics of mantle minerals-ii. phase equilibria. *Geophysical Journal International*, 184(3):1180–1213, 2011.
- [2442] Lars Stixrude and Carolina Lithgow-Bertelloni. Geophysics of chemical heterogeneity in the mantle. *Annual Review of Earth and Planetary Sciences*, 40:569–595, 2012.
- [2443] Bernhard Stöckhert and Taras V Gerya. Pre-collisional high pressure metamorphism and nappe tectonics at active continental margins: A numerical simulation. *Terra Nova*, 17(2):102–110, 2005.
- [2444] Glen S Stockmal. Modeling of large-scale accretionary wedge deformation. *Journal of Geophysical Research: Solid Earth*, 88(B10):8271–8287, 1983.
- [2445] Glen S Stockmal, Christopher Beaumont, and Ross Boutilier. Geodynamic models of convergent margin tectonics: transition from rifted margin to overthrust belt and consequences for foreland-basin development. *AAPG Bulletin*, 70(2):181–190, 1986.
- [2446] Drew Stolar, Gerard Roe, and Sean Willett. Controls on the patterns of topography and erosion rate in a critical orogen. *Journal of Geophysical Research: Earth Surface*, 112(F4), 2007.
- [2447] Drew B Stolar, Sean D Willett, and Gerard H Roe. Climatic and tectonic forcing of a critical orogen. *SPECIAL PAPERS-GEOLOGICAL SOCIETY OF AMERICA*, 398:241, 2006.
- [2448] Ingo Leonardo Stotz, Giampiero Iaffaldano, and DR Davies. Late miocene pacific plate kinematic change explained with coupled global models of mantle and lithosphere dynamics. *Geophysical Research Letters*, 44(14):7177–7186, 2017.
- [2449] Kurt Stüwe, Jörg Robl, Stefan Hergarten, and Lynn Evans. Modeling the influence of horizontal advection, deformation, and late uplift on the drainage development in the india-asia collision zone. *Tectonics*, 27(6), 2008.
- [2450] J. Suckale, B.H. Hager, L.T. ElkinsTanton, and J.Ch. Nave. It takes three to tango: 2. Bubble dynamics in basaltic volcanoes and ramifications for modeling normal Strombolian activity. *J. Geophys. Res.*, 115(B7), 2010.
- [2451] J. Suckale, J.-C. Nave, and B.H. Hager. It takes three to tango: 1. Simulating buoyancy-driven flow in the presence of large viscosity contrasts. *J. Geophys. Res.*, 115(B07409), 2010.
- [2452] Deborah Sulsky, Zhen Chen, and Howard L Schreyer. A particle method for history-dependent materials. *Computer methods in applied mechanics and engineering*, 118(1-2):179–196, 1994.
- [2453] Deborah Sulsky, Howard Schreyer, Kara Peterson, Ron Kwok, and Max Coon. Using the material-point method to model sea ice dynamics. *Journal of Geophysical Research: Oceans*, 112(C2), 2007.
- [2454] Deborah Sulsky and Howard L Schreyer. Axisymmetric form of the material point method with applications to upsetting and taylor impact problems. *Computer Methods in Applied Mechanics and Engineering*, 139(1-4):409–429, 1996.
- [2455] J. Sung, H.G. Choi, and J.Y. Yoo. Time-accurate computation of unsteady free surface flows using an ALE-segregated equal-order FEM. *Computer Methods in Applied Mechanics and Engineering*, 190:1425–1440, 2000.
- [2456] M. Sussman and E.G. Puckett. A Coupled Level Set and Volume-of-Fluid Method for Computing 3D and Axisymmetric Incompressible Two-Phase Flows. *J. Comp. Phys.*, 162:301–337, 2000.

- [2457] K. Sverdrup, N. Nikiforakis, and A. Almgren. Highly parallelisable simulations of time-dependent viscoplastic fluid flow simulations with structured adaptive mesh refinement. *Physics of Fluids*, 30:093102, 2018.
- [2458] E.M. Syracuse, P.E. van Keken, and G.A. Abers. The global range of subduction zone thermal models. *Phys. Earth. Planet. Inter.*, 183:73–90, 2010.
- [2459] A. Syrakos, G.C. Georgiou, and A.N. Alexandrou. Performance of the finite volume method in solving regularised Bingham flows: Inertia effects in the lid-driven cavity flow. *Journal of Non-Newtonian Fluid Mechanics*, 208–209:88–107, 2014.
- [2460] Kamil Szewc, Jacek Pozorski, and J-P Minier. Analysis of the incompressibility constraint in the smoothed particle hydrodynamics method. *International Journal for Numerical Methods in Engineering*, 92(4):343–369, 2012.
- [2461] Kamil Szewc, Jacek Pozorski, and A Taniere. Modeling of natural convection with smoothed particle hydrodynamics: non-boussinesq formulation. *International Journal of Heat and Mass Transfer*, 54(23–24):4807–4816, 2011.
- [2462] M. Tabata and A. Suzuki. A stabilized finite element method for the Rayleigh-Bénard equations with infinite Prandtl number in a spherical shell. *Computer Methods in Applied Mechanics and Engineering*, 190:387–402, 2000.
- [2463] M. Tabata and A. Suzuki. Mathematical modeling and numerical simulation of Earth’s mantle convection. *Mathematical modeling and numerical simulation in continuum mechanics, lecture notes in computational science and engineering*, 19:219–231, 2002.
- [2464] Masahisa Tabata and Atsushi Suzuki. Mathematical modeling and numerical simulation of earths mantle convection. In *Mathematical Modeling and Numerical Simulation in Continuum Mechanics*, pages 219–231. Springer, 2002.
- [2465] M. Tachibana and Y. Iemoto. Steady flow around, and drag on a circular cylinder moving at low speeds in a viscous liquid between two parallel planes. *Fluid Dynamics Research*, 2:125–137, 1987.
- [2466] P. Tackley. *Three-dimensional models of mantle convection: Influence of phase transitions and temperature-dependent viscosity*. PhD thesis, California Institute of Technology, 1994.
- [2467] Paul J Tackley. Effects of strongly temperature-dependent viscosity on time-dependent, three-dimensional models of mantle convection. *Geophysical Research Letters*, 20(20):2187–2190, 1993.
- [2468] Paul J Tackley. On the penetration of an endothermic phase transition by upwellings and downwellings. *Journal of Geophysical Research: Solid Earth*, 100(B8):15477–15488, 1995.
- [2469] Paul J Tackley. On the ability of phase transitions and viscosity layering to induce long wavelength heterogeneity in the mantle. *Geophysical Research Letters*, 23(15):1985–1988, 1996.
- [2470] Paul J Tackley. Mantle convection and plate tectonics: Toward an integrated physical and chemical theory. *Science*, 288(5473):2002–2007, 2000.
- [2471] Paul J Tackley. The quest for self-consistent generation of plate tectonics in mantle convection models. *Geophysical Monograph-American Geophysical Union*, 121:47–72, 2000.
- [2472] Paul J Tackley. Self-consistent generation of tectonic plates in time-dependent, three-dimensional mantle convection simulations 2. strain weakening and asthenosphere. *Geochemistry, Geophysics, Geosystems*, 1(8), 2000.
- [2473] Paul J Tackley. Convection in io’s asthenosphere: Redistribution of nonuniform tidal heating by mean flows. *Journal of Geophysical Research: Planets*, 106(E12):32971–32981, 2001.
- [2474] Paul J Tackley. Strong heterogeneity caused by deep mantle layering. *Geochemistry, Geophysics, Geosystems*, 3(4):1–22, 2002.
- [2475] Paul J Tackley, Michael Ammann, John P Brodholt, David P Dobson, and Diana Valencia. Mantle dynamics in super-earths: Post-perovskite rheology and self-regulation of viscosity. *Icarus*, 225(1):50–61, 2013.
- [2476] Paul J Tackley, Michael M Ammann, John P Brodholt, David P Dobson, and Diana Valencia. Habitable planets: Interior dynamics and long-term evolution. *Proceedings of the International Astronomical Union*, 8(S293):339–349, 2012.
- [2477] Paul J Tackley, John R Baumgardner, Gary A Glatzmaier, Peter Olson, and Tom Clune. Three-dimensional spherical simulations of convection in earths mantle and core using massively-parallel computers. In *Proc. High. Performance Computing Symposium-HPC99*, pages 95–100, 1999.

- [2478] Paul J Tackley et al. Three-dimensional simulations of mantle convection with a thermo-chemical basal boundary layer: D''. *The Core-Mantle Boundary Region, Geodyn. Ser*, 28:231–253, 1998.
- [2479] Paul J Tackley, Takashi Nakagawa, and John W Hernlund. Influence of the post-perovskite transition on thermal and thermo-chemical mantle convection. *GEOPHYSICAL MONOGRAPH-AMERICAN GEOPHYSICAL UNION*, 174:229, 2007.
- [2480] Paul J Tackley, Gerald Schubert, Gary A Glatzmaier, Paul Schenk, J Todd Ratcliff, and Jean-Philippe Matas. Three-dimensional simulations of mantle convection in io. *Icarus*, 149(1):79–93, 2001.
- [2481] Paul J Tackley, David J Stevenson, Gary A Glatzmaier, and Gerald Schubert. Effects of an endothermic phase transition at 670 km depth in a spherical model of convection in the earth's mantle. *Nature*, 361(6414):699, 1993.
- [2482] Paul J Tackley, David J Stevenson, Gary A Glatzmaier, and Gerald Schubert. Effects of multiple phase transitions in a three-dimensional spherical model of convection in earth's mantle. *Journal of Geophysical Research: Solid Earth*, 99(B8):15877–15901, 1994.
- [2483] Paul J Tackley and Shunxing Xie. The thermochemical structure and evolution of earth's mantle: constraints and numerical models. *Philosophical Transactions of the Royal Society of London. Series A: Mathematical, Physical and Engineering Sciences*, 360(1800):2593–2609, 2002.
- [2484] Paul J Tackley, Shunxing Xie, Takashi Nakagawa, and John W Hernlund. Numerical and laboratory studies of mantle convection: Philosophy, accomplishments, and thermochemical structure and evolution. *GEOPHYSICAL MONOGRAPH-AMERICAN GEOPHYSICAL UNION*, 160:83, 2005.
- [2485] P.J. Tackley. *Three-dimensional models of mantle convection: influence of phase transitions and temperature-dependent viscosity*. PhD thesis, California Institute of Technology, 1994.
- [2486] P.J. Tackley. Effects of strongly variable viscosity on three-dimensional compressible convection in planetary mantles. *J. Geophys. Res.*, 101(B2):3311–3332, 1996.
- [2487] P.J. Tackley. Self-consistent generation of tectonic plates in three-dimensional mantle convection. *Earth Planet. Sci. Lett.*, 157:9–22, 1998.
- [2488] P.J. Tackley. Self-consistent generation of tectonic plates in time-dependent, three-dimensional mantle convection simulations 1. Pseudoplastic yielding. *Geochem. Geophys. Geosyst.*, 1(1), 2000.
- [2489] P.J. Tackley. Layer cake or plum pudding? *Nature Geoscience*, 1:157–158, 2008.
- [2490] P.J. Tackley. Modelling compressible mantle convection with large viscosity contrasts in a three-dimensional spherical shell using the yin-yang grid. *Phys. Earth. Planet. Inter.*, 171:7–18, 2008.
- [2491] P.J. Tackley. Dynamics and evolution of the deep mantle resulting from thermal, chemical, phase and melting effects. *Earth-Science Reviews*, 110:1–25, 2012.
- [2492] P.J. Tackley and S.D. King. Testing the tracer ratio method for modeling active compositional fields in mantle convection simulations. *Geochem. Geophys. Geosyst.*, 4(4), 2003.
- [2493] PJ Tackley and DJ Stevenson. A mechanism for spontaneous self-perpetuating volcanism on the terrestrial planets. In *Flow and Creep in the Solar System: Observations, Modeling and Theory*, pages 307–321. 1993.
- [2494] PJ Tackley and S Xie. Stag3d: a code for modeling thermo-chemical multiphase convection in earth's mantle. In *Computational Fluid and Solid Mechanics 2003*, pages 1524–1527. Elsevier, 2003.
- [2495] K. Takeyama, T. R. Saitoh, and J. Makino. Variable inertia method: A novel numerical method for mantle convection simulation. *New Astronomy*, 2017.
- [2496] Christopher J Talbot, Peter Rönnlund, H Schmeling, Hemin Koyi, and MPA Jackson. Diapiric spoke patterns. *Tectonophysics*, 188(1-2):187–201, 1991.
- [2497] E. Taliadorou, G.C. Georgiou, and I. Moultsas. Weakly compressible poiseuille flows of a herschelbulkley fluid. *Journal of Non-Newtonian Fluid Mechanics*, 158:162–169, 2009.
- [2498] E. Tan, E. Choi, P. Thoutireddy, M. Gurnis, and M. Aivazis. GeoFramework: Coupling multiple models of mantle convection within a computational framework. *Geochem. Geophys. Geosyst.*, 7(6):10.1029/2005GC001155, 2006.
- [2499] E. Tan and M. Gurnis. Compressible thermochemical convection and application to lower mantle structures. *J. Geophys. Res.*, 112(B06304), 2007.
- [2500] E. Tan, M. Gurnis, and L. Han. Slabs in the lower mantle and their modulation of plume formation. *Geochem. Geophys. Geosyst.*, 3(11), 2002.
- [2501] E. Tan and Michael Gurnis. Metastable superplumes and mantle compressibility. *Geophysical Research Letters*, 32(20), 2005.

- [2502] Eh Tan, Wei Leng, Shijie Zhong, and Michael Gurnis. On the location of plumes and lateral movement of thermochemical structures with high bulk modulus in the 3-d compressible mantle. *Geochemistry, Geosystems, Geophysics*, 12(7), 2011.
- [2503] A. Tanaka, Y. Sanada, Y. Yamada, T. Matsuoka, and Y. Ashida. disctree element simulations of continental collision in asia. *Exploration Geophysics*, 36(1):1–6, 2005.
- [2504] R.I. Tanner and E. Tanner. Heinrich hencky: a rheological pioneer. *Rheol. Acta*, 42:93–101, 2003.
- [2505] C. A. Taposeeaa, J. J. Armitage, and J. S. Collier. Asthenosphere and lithosphere structure controls on early onset oceanic crust production in the southern south atlantic. *Tectonophysics*, 2017.
- [2506] P. Tapponnier, G. Peltzer, A.Y. Le Dain, R. Armijo, and P. Cobbold. Propagating extrusion tectonics in asia: new insights from simple experiments with plasticine. *Geology*, 10:611–616, 1982.
- [2507] Paul Tapponnier and Peter Molnar. Slip-line field theory and large-scale continental tectonics. *Nature*, 264:319–324, November 1976.
- [2508] Paul Tapponnier, Xu Zhiqin, Françoise Roger, Bertrand Meyer, Nicolas Arnaud, Gerard Wittlinger, and Yang Jingsui. Oblique stepwise rise and growth of the tibet plateau. *Science*, 294:1671–1677, 2001.
- [2509] J.M. Taramon, J. Rodriguez-Gonzalez, A.M. Negredo, and M.I. Billen. Influence of cratonic lithosphere on the formation and evolution of flat slabs: Insights from 3-D time-dependent modeling. *Geochem. Geophys. Geosyst.*, 16:doi:10.1002/2015GC005940, 2015.
- [2510] J. Tarduno, H.P. Bunge, N. Sleep, and U. Hansen. The bent hawaiian-emperor hotspot track: inheriting the mantle wind. *Science*, 324(5923):50–53, 2009.
- [2511] C. Tayloor and P. Hood. A numerical solution of the Navier-Stokes equations using the finite element technique. *Comput. Fluids*, 1:73–100, 1973.
- [2512] Michael G Tetley, Simon E Williams, Michael Gurnis, Nicolas Flament, and R Dietmar Müller. Constraining absolute plate motions since the triassic. *Journal of Geophysical Research: Solid Earth*, 2019.
- [2513] J.L. Tetreault and S.J.H. Buiter. Geodynamic models of terrane accretion: Testing the fate of island arcs, oceanic plateaus, and continental fragments in subduction zones. *J. Geophys. Res.*, 2012.
- [2514] JL Tetreault and SJH Buiter. Future accreted terranes: a compilation of island arcs, oceanic plateaus, submarine ridges, seamounts, and continental fragments. *Solid Earth*, 5(2):1243–1275, 2014.
- [2515] J.L. Tetreault and S.J.H. Buiter. The influence of extension rate and crustal rheology on the evolution of passive margins from rifting to break-up. *Tectonophysics*, 746:155–172, 2018.
- [2516] M Tetzlaff and H Schmeling. The influence of olivine metastability on deep subduction of oceanic lithosphere. *Physics of the Earth and Planetary Interiors*, 120(1-2):29–38, 2000.
- [2517] Jannis Teunissen and Ute Ebert. Afivo: A framework for quadtree/octree amr with shared-memory parallelization and geometric multigrid methods. *Computer Physics Communications*, 233:156–166, 2018.
- [2518] Tayfun E Tezduyar, Mittal Behr, S Mittal, and J Liou. A new strategy for finite element computations involving moving boundaries and interfaces - the deforming-spatial-domain/space-time procedure: II. computation of free-surface flows, two-liquid flows, and flows with drifting cylinders. *Computer methods in applied mechanics and engineering*, 94(3):353–371, 1992.
- [2519] Tayfun E Tezduyar, Sanjay Mittal, SE Ray, and R Shih. Incompressible flow computations with stabilized bilinear and linear equal-order-interpolation velocity-pressure elements. *Computer Methods in Applied Mechanics and Engineering*, 95(2):221–242, 1992.
- [2520] Tayfun E. Tezduyar and Yasuo Osawa. Finite element stabilization parameters computed from element matrices and vectors. *Computer Methods in Applied Mechanics and Engineering*, 190:411–430, 2000.
- [2521] T.E. Tezduyar. Stabilized Finite Element Formulations for Incompressible Flow Computations. *Advances in Applied Mechanics*, 28:1–44, 1992.
- [2522] Thomas M Tharp. Numerical models of subduction and forearc deformation. *Geophysical Journal International*, 80(2):419–437, 1985.
- [2523] Thomas Theunissen and Ritske S Huismans. Long-term coupling and feedback between tectonics and surface processes during non-volcanic rifted margin formation. *Journal of Geophysical Research: Solid Earth*, 124, 2019.
- [2524] M. Thielmann and B.J.P. Kaus. Shear heating induced lithospheric-scale localization: Does it result in subduction? . *Earth Planet. Sci. Lett.*, 359-360:1–13, 2012.
- [2525] M. Thielmann, B.J.P. Kaus, and A.A. Popov. Lithospheric stresses in RayleighBenard convection: effects of a free surface and a viscoelastic Maxwell rheology. *Geophys. J. Int.*, 203:2200–2219, 2015.

- [2526] M. Thielmann, D.A. May, and B.J.P. Kaus. Discretization errors in the Hybrid Finite Element Particle-In-Cell Method. *Pure and Applied Geophysics*, 171(9):2164–2184, 2014.
- [2527] M. Thielmann, A. Rozel, B.J.P. Kaus, and Y. Ricard. Intermediate-depth earthquake generation and shear zone formation caused by grain size reduction and shear heating. *Geology*, page doi:10.1130/G36864.1, 2015.
- [2528] C. Thieulot. FANTOM: two- and three-dimensional numerical modelling of creeping flows for the solution of geological problems. *Phys. Earth. Planet. Inter.*, 188(1):47–68, 2011.
- [2529] C. Thieulot. ELEFANT: a user-friendly multipurpose geodynamics code. *Solid Earth Discussions*, 6:1949–2096, 2014.
- [2530] C. Thieulot. Analytical solution for viscous incompressible stokes flow in a spherical shell. *Solid Earth Discussions*, 2017:1–19, 2017.
- [2531] C. Thieulot. GHOST: Geoscientific Hollow Sphere Tesselation. *Solid Earth*, 9(1–9), 2018.
- [2532] C. Thieulot and W. Bangerth. On the use of equal order elements in geodynamics. *Solid Earth*, 2019.
- [2533] C. Thieulot, P. Fullsack, and J. Braun. Adaptive octree-based finite element analysis of two- and three-dimensional indentation problems. *J. Geophys. Res.*, 113:B12207, 2008.
- [2534] C. Thieulot, P. Steer, and R.S. Huismans. Three-dimensional numerical simulations of crustal systems undergoing orogeny and subjected to surface processes. *Geochem. Geophys. Geosyst.*, 15, 2014.
- [2535] Cedric Thieulot and Pep Español. Non-isothermal diffusion in a binary mixture with smoothed particle hydrodynamics. *Computer physics communications*, 169(1–3):172–176, 2005.
- [2536] Cedric Thieulot, LPBM Janssen, and Pep Español. Smoothed particle hydrodynamics model for phase separating fluid mixtures. i. general equations. *Physical Review E*, 72(1):016713, 2005.
- [2537] Cedric Thieulot, LPBM Janssen, and Pep Español. Smoothed particle hydrodynamics model for phase separating fluid mixtures. ii. diffusion in a binary mixture. *Physical Review E*, 72(1):016714, 2005.
- [2538] Alan Bruce Thompson, Karel Schulmann, and Josef Jezek. Thermal evolution and exhumation in obliquely convergent (transpressive) orogens. *Tectonophysics*, 280(1–2):171–184, 1997.
- [2539] J.F. Thompson, B.K. Soni, and N.P. Weatherill. *Handbook of grid generation*. CRC press, 1998.
- [2540] Paul F Thompson and Paul J Tackley. Generation of mega-plumes from the core-mantle boundary in a compressible mantle with temperature-dependent viscosity. *Geophysical research letters*, 25(11):1999–2002, 1998.
- [2541] B. Tikoff and C. Teyssier. Strain modeling of displacement-field partitioning in transpressional orogens. *Journal of Structural Geology*, 16(11):1575–1588, 1994.
- [2542] F. Tin-Loi and N.S. Ngo. Performance of the p-version finite element method for limit analysis. *International Journal of Mechanical Sciences*, 45:1149–1166, 2003.
- [2543] M. Tingay, B. Mueller, and J. Reinecker. Understanding tectonic stress in the oil patch: The World Stress Map Project. *The leading edge*, page 1276, 2005.
- [2544] C. Tirel, J.-P. Brun, and E. Burov. Thermomechanical modeling of extensional gneiss domes. *Geological Society of America Special Papers*, 380:67–78, 2004.
- [2545] C. Tirel, J.-P. Brun, and E. Burov. Dynamics and structural development of metamorphic core complexes. *J. Geophys. Res.*, 113(B04403), 2008.
- [2546] C. Tirel, J.-P. Brun, E. Burov, M.J.R. Wortel, and S. Lebedev. A plate tectonics oddity: Caterpillar-walk exhumation of subducted continental crust. *Geology*, 41(5):555–558, 2013.
- [2547] C. Tirel, J.-P. Brun, and D. Sokoutis. Extension of thickened and hot lithospheres: Inferences from laboratory modeling. *Tectonics*, 25(1), 2006.
- [2548] Céline Tirel, Pierre Gautier, DJJ van Hinsbergen, and MJR Wortel. Sequential development of interfering metamorphic core complexes: numerical experiments and comparison with the cyclades, greece. *Geological Society, London, Special Publications*, 311(1):257–292, 2009.
- [2549] M. Tirone. On the thermal gradient in the earths deep interior. *Solid Earth*, 7:229–238, 2016.
- [2550] Jonathan H Tomkin. Coupling glacial erosion and tectonics at active orogens: A numerical modeling study. *Journal of Geophysical Research: Earth Surface*, 112(F2), 2007.
- [2551] Jonathan H Tomkin and Jean Braun. Simple models of drainage reorganisation on a tectonically active ridge system. *New Zealand Journal of Geology and Geophysics*, 42(1):1–10, 1999.
- [2552] Trond H Torsvik, Bernhard Steinberger, Lewis D Ashwal, Pavel V Doubrovine, and Reidar G Trønnes. Earth evolution and dynamicsa tribute to kevin burke. *Canadian Journal of Earth Sciences*, 53(11):1073–1087, 2016.

- [2553] Trond H Torsvik, Rob van der Voo, Pavel V Doubrovine, Kevin Burke, Bernhard Steinberger, Lewis D Ashwal, Reidar G Trønnes, Susan J Webb, and Abigail L Bull. Deep mantle structure as a reference frame for movements in and on the earth. *Proceedings of the National Academy of Sciences*, 111(24):8735–8740, 2014.
- [2554] N. Tosi, P. Maierová, and D.A. Yuen. Influence of Variable Thermal Expansivity and Conductivity on Deep Subduction. In *Subduction Dynamics: From Mantle Flow to Mega Disasters, Geophysical Monograph 211*, pages 115–133. John Wiley & Sons, Inc., 2016.
- [2555] N. Tosi and Z. Martinec. Semi-analytical solution for viscous Stokes flow in two eccentrically nested spheres. *Geophys. J. Int.*, 170:1015–1030, 2007.
- [2556] N. Tosi, C. Stein, L. Noack, C. Huettig, P. Maierova, H. Samuel, D.R. Davies, C.R. Wilson, S.C. Kramer, C. Thieulot, A. Glerum, M. Fraters, W. Spakman, A. Rozel, and P.J. Tackley. A community benchmark for viscoplastic thermal convection in a 2-D square box. *Geochem. Geophys. Geosyst.*, 16(7):21752196, 2015.
- [2557] Nicola Tosi and David A Yuen. Bent-shaped plumes and horizontal channel flow beneath the 660 km discontinuity. *Earth and Planetary Science Letters*, 312(3-4):348–359, 2011.
- [2558] Nicola Tosi, David A Yuen, Nico de Koker, and Renata M Wentzcovitch. Mantle dynamics with pressure- and temperature-dependent thermal expansivity and conductivity. *Physics of the Earth and Planetary Interiors*, 217:48–58, 2013.
- [2559] J. Toth and M. Gurnis. Dynamics of subduction initiation at preexisting fault zones. *J. Geophys. Res.*, 103(B8):18,053–18,067, 1998.
- [2560] G. Toussaint, E. Burov, and J.-P. Avouac. Tectonic evolution of a continental collision zone: A thermo-mechanical numerical model. *Tectonics*, 23(TC6003):doi:10.1029/2003TC001604, 2004.
- [2561] G. Toussaint, E. Burov, and L. Jolivet. Continental plate collision: unstable vs. stable slab dynamics. *Geology*, 32:33–36, 2004.
- [2562] Aaron Tovich, Gerald Schubert, and Bruce P Luyendyk. Mantle flow pressure and the angle of subduction: Non-newtonian corner flows. *Journal of Geophysical Research: Solid Earth*, 83(B12):5892–5898, 1978.
- [2563] B.J. Travis, C. Anderson, J. Baumgardner, C.W. Gable, B.H. Hager, R.J. O'Connell, P. Olson, A. Raefsky, and G. Schubert. A benchmark comparison of numerical methods for infinite Prandtl number thermal convection in two-dimensional Cartesian geometry. *Geophysical & Astrophysical Fluid Dynamics*, 55(3-4):137–160, 1990.
- [2564] S.H. Treagus and L. Lan. Pure shear deformation of square objects, and applications to geological strain analysis. *Journal of Structural Geology*, 22:105–122, 2000.
- [2565] R.A. Trompert and U. Hansen. The application of a finite volume multigrid method to three-dimensional flow problems in a highly viscous fluid with a variable viscosity. *Geophysical and Astrophysical Fluid Dynamics*, 83(3-4):261–291, 1996.
- [2566] R.A. Trompert and U. Hansen. Mantle convection simulations with rheologies that generate plate-like behaviour . *Nature*, 395:686–689, 1998.
- [2567] R.A. Trompert and U. Hansen. On the Rayleigh number dependence of convection with a strongly temperature-dependent viscosity. *Physics of Fluids*, 10(2):351–360, 1998.
- [2568] Virginie Tron and Jean-Pierre Brun. Experiments on oblique rifting in brittle-ductile systems. *Tectonophysics*, 188(1-2):71–84, 1991.
- [2569] Ulrich Trottenberg, Cornelius W. Oosterlee, and Anton Schuller. *Multigrid*. 2001.
- [2570] V. P. Trubitsyn. Rheology of the mantle and tectonics of the oceanic lithospheric plates. *Izvestiya, Physics of the Solid Earth*, 48(6):467–485, 2012.
- [2571] V. P. Trubitsyn, A. N. Evseev, M. N. Evseev, and E. V. Kharybin. Mantle plumes in the models of quasi-turbulent thermal convection. *Izvestiya, Physics of the Solid Earth*, 47(12):1027–1033, 2011.
- [2572] V. P. Trubitsyn and M. N. Evseev. Plume mode of thermal convection in the earth's mantle. *Izvestiya, Physics of the Solid Earth*, 54(6):838–848, 2018.
- [2573] VP Trubitsyn. Equations of thermal convection for a viscous compressible mantle of the earth including phase transitions. *Izvestiya, Physics of the Solid Earth*, 44(12):1018–1026, 2008.
- [2574] VP Trubitsyn and AM Bobrov. Thermal and mechanical interaction of continents with the mantle. *Computational Seismology and Geodynamics*, 3:33–41, 1996.
- [2575] VP Trubitsyn and VV Rykov. A 3-d numerical model of the wilson cycle. *Journal of geodynamics*, 20(1):63–75, 1995.

- [2576] B. Trudgill and J. Cartwright. Relay-ramp forms and normal-fault linkages, Canyonlands National Park, Utah. *Geological Society of America Bulletin*, 106(9):1143–1157, 1994.
- [2577] T Trümper, M Breuer, and U Hansen. Numerical study on double-diffusive convection in the earths core. *Physics of the Earth and Planetary Interiors*, 194:55–63, 2012.
- [2578] G.E. Tucker and G.R. Hancock. Modelling landscape evolution. *Earth Surface Processes and Landforms*, 35:28–50, 2010.
- [2579] GE Tucker and P van Der Beek. A model for post-orogenic development of a mountain range and its foreland. *Basin Research*, 25(3):241–259, 2013.
- [2580] Gregory E Tucker, Stephen T Lancaster, Nicole M Gasparini, Rafael L Bras, and Scott M Rybarczyk. An object-oriented framework for distributed hydrologic and geomorphic modeling using triangulated irregular networks. *Computers & Geosciences*, 27(8):959–973, 2001.
- [2581] D.L. Turcotte and G. Schubert. *Geodynamics*, 2nd edition. Cambridge, 2012.
- [2582] S. Turek. *Efficient Solvers for Incompressible Flow Problems*. Springer, 1999.
- [2583] Andrew J Turner, Richard F Katz, and Mark D Behn. Grain-size dynamics beneath mid-ocean ridges: Implications for permeability and melt extraction. *Geochemistry, Geophysics, Geosystems*, 16(3):925–946, 2015.
- [2584] A. Osei Tutu, S.V. Sobolev, B. Steinberger, A.A. Popov, and I. Rogozhina. Evaluating the Influence of Plate Boundary Friction and Mantle Viscosity on Plate Velocities. *Geochem. Geophys. Geosyst.*, 19:642–666, 2018.
- [2585] A. Osei Tutu, B. Steinberger, S.V. Sobolev, I. Rogozhina, and A.A. Popov. Effects of upper mantle heterogeneities on the lithospheric stress field and dynamic topography. *Solid Earth*, 9:649–668, 2018.
- [2586] K. Ueda, T. Gerya, and S.V. Sobolev. Subduction initiation by thermalchemical plumes: Numerical studies. *Phys. Earth. Planet. Inter.*, 171:296–312, 2008.
- [2587] K Ueda, Taras V Gerya, and J-P Burg. Delamination in collisional orogens: Thermomechanical modeling. *Journal of Geophysical Research: Solid Earth*, 117(B8), 2012.
- [2588] K. Ueda, S.D. Willett, T. Gerya, and J. Ruh. Geomorphologicalthermo-mechanical modeling: Application to orogenic wedge dynamics. *Tectonophysics*, 659:12–30, 2015.
- [2589] Leonardo Uieda, Everton P Bomfim, Carla Braatenberg, and Eder Molina. Optimal forward calculation method of the marussi tensor due to a geologic structure at goce height. In *Proceedings of the 4th International GOCE User Workshop*. Munich Germany, 2011.
- [2590] Martina Ulvrová, Stéphane Labrosse, Nicolas Coltice, P Råback, and PJ Tackley. Numerical modelling of convection interacting with a melting and solidification front: Application to the thermal evolution of the basal magma ocean. *Physics of the Earth and Planetary Interiors*, 206:51–66, 2012.
- [2591] Martina M Ulvova, Nicolas Coltice, Simon Williams, and Paul J Tackley. Where does subduction initiate and cease? a global scale perspective. *Earth and Planetary Science Letters*, 528:115836, 2019.
- [2592] Phædra Upton, Peter O Koons, and Donna Eberhart-Phillips. Extension and partitioning in an oblique subduction zone, new zealand: Constraints from three-dimensional numerical modeling. *Tectonics*, 22(6), 2003.
- [2593] M. ur Rehman, C. Vuik, and G. Segal. A comparison of preconditioners for incompressible Navier-Stokes solvers. *Int. J. Num. Meth. Fluids*, 57:1731–1751, 2008.
- [2594] T. Utnes. A segregated implicit pressure projection method for incompressible flows. *J. Comp. Phys.*, 227:2198–2211, 2008.
- [2595] S. Van Benthem, R. Govers, W. Spakman, and R. Wortel. Tectonic evolution and mantle structure of the caribbean. *Journal of Geophysical Research: Solid Earth*, 118(6):3019–3036, 2013.
- [2596] S van Benthem and Rob Govers. The Caribbean plate: Pulled, pushed, or dragged? *Journal Of Geophysical Research*, 115(B10):B10409, 2010.
- [2597] S van Benthem, Rob Govers, and Rinus Wortel. What drives microplate motion and deformation in the northeastern Caribbean plate boundary region? *TECTONICS*, 33, 2014.
- [2598] P van de Beek and Jean Braun. Numerical modelling of landscape evolution on geological time-scales: A parameter analysis and comparison with the south-eastern highlands of australia. *Basin Research*, 10(1):49–68, 1998.
- [2599] FN Van de Vosse, J De Hart, CHGA Van Oijen, D Bessems, TWM Gunther, A Segal, BJBM Wolters, JMA Stijnen, and FPT Baaijens. Finite-element-based computational methods for cardiovascular fluid-structure interaction. *Journal of engineering mathematics*, 47(3-4):335–368, 2003.

- [2600] F.N. van de Vosse, A.A. van Steenhoven, A. Segal, and J.D. Janssen. A finite element analysis of the steady laminar entrance flow in a 90° curved tube. *Int. J. Num. Meth. Fluids*, 9:275–287, 1989.
- [2601] A. van den Berg, P.E. van Keken, and D.A. Yuen. The effects of a composite non-Newtonian and Newtonian rheology on mantle convection. *Geophys. J. Int.*, 115:62–78, 1993.
- [2602] A.P. van den Berg, M.V. De Hoop, D.A. Yuen, A. Duchkov, R.D. van der Hilst, and M.H.G. Jacobs. Geodynamical modeling and multiscale seismic expression of thermo-chemical heterogeneity and phase transitions in the lowermost mantle. *Physics of the Earth and Planetary Interiors*, 180(3-4):244–257, 2010.
- [2603] A.P. van den Berg, M.V. De Hoop, D.A. Yuen, A. Duchkov, R.D. van der Hilst, and M.H.G. Jacobs. Geodynamical modeling and multiscale seismic expression of thermo-chemical heterogeneity and phase transitions in the lowermost mantle. *Phys. Earth. Planet. Inter.*, 180:244–257, 2010.
- [2604] A.P. van den Berg, E.S.G. Rainey, and D.A. Yuen. The combined influences of variable thermal conductivity, temperature- and pressure-dependent viscosity and core-mantle coupling on thermal evolution. *Physics of the Earth and Planetary Interiors*, 149(3-4):259–278, 2005.
- [2605] A.P. van den Berg, G. Segal, and D. Yuen. SEPRAN: A Versatile Finite-Element Package for Realistic Problems in Geosciences. *International Workshop of Deep Geothermal Systems, Wuhan, China, June 29-30*, 2012.
- [2606] A.P. van den Berg, G. Segal, and D.A. Yuen. SEPRAN: A Versatile Finite-Element Package for a Wide Variety of Problems in Geosciences. *Journal of Earth Science*, 26(1):089–095, 2015.
- [2607] A.P. van den Berg and D.A. Yuen. Convectively induced transition in mantle rheological behavior. *Geophysical Research Letters*, 22(12):1549–1552, 1995.
- [2608] A.P. Van Den Berg and D.A. Yuen. The role of shear heating in lubricating mantle flow. *Earth and Planetary Science Letters*, 151(1-2):33–42, 1997.
- [2609] A.P. Van Den Berg and D.A. Yuen. Modelling planetary dynamics by using the temperature at the core-mantle boundary as a control variable: effects of rheological layering on mantle heat transport. *Physics of the Earth and Planetary Interiors*, 108(3):219–234, 1998.
- [2610] A.P. Van den Berg and D.A. Yuen. Delayed cooling of the earth's mantle due to variable thermal conductivity and the formation of a low conductivity zone. *Earth and Planetary Science Letters*, 199(3-4):403–413, 2002.
- [2611] A.P. Van den Berg, D.A. Yuen, and J.R. Allwardt. Non-linear effects from variable thermal conductivity and mantle internal heating: Implications for massive melting and secular cooling of the mantle. *Physics of the Earth and Planetary Interiors*, 129(3-4):359–375, 2002.
- [2612] A.P. van den Berg, D.A. Yuen, G.L. Beebe, and M.D. Christiansen. The dynamical impact of electronic thermal conductivity on deep mantle convection of exosolar planets. *Physics of the Earth and Planetary Interiors*, 178(3-4):136–154, 2010.
- [2613] A.P. van den Berg, D.A. Yuen, M.H.G. Jacobs, and M.V. de Hoop. Small-scale mineralogical heterogeneity from variations in phase assemblages in the transition zone and d" layer predicted by convection modelling. *Journal of Earth Science*, 22(2):160–168, 2011.
- [2614] A.P. van den Berg, D.A. Yuen, and E.S.G. Rainey. The influence of variable viscosity on delayed cooling due to variable thermal conductivity. *Physics of the Earth and Planetary Interiors*, 142(3-4):283–295, 2004.
- [2615] A.P. Van Den Berg, D.A. Yuen, and V. Steinbach. The effects of variable thermal conductivity on mantle heat-transfer. *Geophysical Research Letters*, 28(5):875–878, 2001.
- [2616] A.P. van den Berg, D.A. Yuen, K. Umemoto, M.H.G. Jacobs, and R.M. Wentzcovitch. Mass-dependent dynamics of terrestrial exoplanets using ab initio mineral properties. *Icarus*, 317:412–426, 2019.
- [2617] A.P. van den Berg, D.A. Yuen, and P.E. van Keken. Effects of depthvariations in creep laws on the formation of plates in mantle dynamics. *Geophysical Research Letters*, 18(12):2197–2200, 1991.
- [2618] Arie P van den Berg, Peter E van Keken, and David A Yuen. The effects of a composite non-newtonian and newtonian rheology on mantle convection. *Geophysical Journal International*, 115(1):62–78, 1993.
- [2619] Arie P van den Berg and David A Yuen. Is the lower-mantle rheology newtonian today? *Geophysical research letters*, 23(16):2033–2036, 1996.
- [2620] Arie P van Den Berg, David A Yuen, and Peter E van Keken. Rheological transition in mantle convection with a composite temperature-dependent, non-newtonian and newtonian rheology. *Earth and Planetary Science Letters*, 129(1-4):249–260, 1995.
- [2621] Rob D van der Hilst and Hrafnkell Kárason. Compositional heterogeneity in the bottom 1000 kilometers of earth's mantle: Toward a hybrid convection model. *Science*, 283(5409):1885–1888, 1999.

- [2622] D.G. van der Meer, D.J.J. van Hinsbergen, and Wim Spakman. Atlas of the Underworld: slab remnants in the mantle, their sinking history, and a new outlook on lower mantle viscosity. *Tectonophysics*, 723:309–448, 2017.
- [2623] Douwe G van Der Meer, Wim Spakman, Douwe JJ van Hinsbergen, Maisha L Amaru, and Trond H Torsvik. Towards absolute plate motions constrained by lower-mantle slab remnants. *Nature Geoscience*, 3(1):36, 2010.
- [2624] M.J. van der Meulen, S.J.H. Buiter, J.E. Meulenkamp, and M.J.R. Wortel. An early pliocene uplift of the central apenninic foredeep and its geodynamic significance. *Tectonics*, 19:300–313, 2000.
- [2625] SP Van Der Pijl, A Segal, and C Vuik. Modelling of three-dimensional bubbly flows with a mass-conserving level-set method. In *Proceedings of the 4th European Congress on Computational Methods in Applied Sciences and Engineering, ECCOMAS*, 2004.
- [2626] SP Van der Pijl, A Segal, C Vuik, and P Wesseling. A mass-conserving level-set method for modelling of multi-phase flows. *International journal for numerical methods in fluids*, 47(4):339–361, 2005.
- [2627] SP Van der Pijl, A Segal, C Vuik, and P Wesseling. Computing three-dimensional two-phase flows with a mass-conserving level set method. *Computing and Visualization in Science*, 11(4-6):221–235, 2008.
- [2628] H. van der Veen, C. Vuik, and R. de Borst. An Eigenvalue Analysis of Nonassociated Plasticity. *Computers and Mathematics with Applications*, 38:107–115, 1999.
- [2629] Rob van der Voo, Wim Spakman, and Harmen Bijwaard. Tethyan subducted slabs under india. *Earth and Planetary Science Letters*, 171(1):7–20, 1999.
- [2630] Y. van Dinther, T.V. Gerya, L.A. Dalguer, F. Corbi, F. Funiciello, and P.M. Mai. The seismic cycle at subduction thrusts: 2. Dynamic implications of geodynamic simulations validated with laboratory models. *J. Geophys. Res.*, 118:1502–1525, 2013.
- [2631] Y. van Dinther, T.V. Gerya, L.A. Dalguer, P.M. Mai, G. Morra, and D. Giardini. The seismic cycle at subduction thrusts: Insights from seismo-thermo-mechanical models. *J. Geophys. Res.*, 118:1–20, 2013.
- [2632] Y. van Dinther, P.M. Mai, L.A. Dalguer, and T.V. Gerya. Modeling the seismic cycle in subduction zones: The role and spatiotemporal occurrence of off-megathrust earthquakes. *Geophys. Res. Lett.*, 41:1194–1201, 2014.
- [2633] H.J. van Heck, J.H. Davies, T. Elliott, and D. Porcelli. Global-scale modelling of melting and isotopic evolution of Earths mantle: melting modules for TERRA. *Geosci. Model Dev.*, 9:1399–1411, 2016.
- [2634] HJ Van Heck and PJ Tackley. Planforms of self-consistently generated plates in 3d spherical geometry. *Geophysical Research Letters*, 35(19), 2008.
- [2635] HJ van Heck and PJ Tackley. Plate tectonics on super-earths: equally or more likely than on earth. *Earth and Planetary Science Letters*, 310(3-4):252–261, 2011.
- [2636] D. J. J. van Hinsbergen, B. Steinberger, P. V. Doubrovine, and R. Gassmöller. Acceleration and deceleration of india-asia convergence since the cretaceous: Roles of mantle plumes and continental collision. *Journal of Geophysical Research*, 116(B6), 2011.
- [2637] D.J.J. Van Hinsbergen, P.C. Lippert, G. Dupont-Nivet, N. McQuarrie, P.V. Doubrovine, W. Spakman, and T.H. Torsvik. Greater india basin hypothesis and a two-stage cenozoic collision between india and asia. *Proceedings of the National Academy of Sciences of the United States of America*, 109(20):7659–7664, 2012.
- [2638] D.J.J. Van Hinsbergen, R.L.M. Vissers, and W. Spakman. Origin and consequences of western mediterranean subduction, rollback, and slab segmentation. *Tectonics*, 33(4):393–419, 2014.
- [2639] Douwe JJ Van Hinsbergen, Susanne JH Buiter, Trond H Torsvik, Carmen Gaina, and Susan J Webb. The formation and evolution of africa from the archaean to present: introduction. *Geological Society, London, Special Publications*, 357(1):1–8, 2011.
- [2640] Douwe JJ van Hinsbergen, Kalijn Peters, Marco Maffione, Wim Spakman, Carl Guilmette, Cedric Thieulot, Oliver Plümper, Derya Gürer, Frauke M Brouwer, Ercan Aldanmaz, et al. Dynamics of intraoceanic subduction initiation: 2. suprasubduction zone ophiolite formation and metamorphic sole exhumation in context of absolute plate motions. *Geochemistry, Geophysics, Geosystems*, 16(6):1771–1785, 2015.
- [2641] J. van Hunen and M.B. Allen. Continental collision and slab break-off: A comparison of 3-D numerical models with observations. *Earth Planet. Sci. Lett.*, 302:27–37, 2011.
- [2642] J. van Hunen and M.S. Miller. Collisional processes and links to episodic changes in subduction zones. *Elements*, 11:119–124, 2015.

- [2643] J. Van Hunen, A.P. Van Den Berg, and N.J. Vlaar. A thermo-mechanical model of horizontal subduction below an overriding plate. *Earth and Planetary Science Letters*, 182(2):157–169, 2000.
- [2644] J. Van Hunen, A.P. Van den Berg, and N.J. Vlaar. Latent heat effects of the major mantle phase transitions on low-angle subduction. *Earth and Planetary Science Letters*, 190(3-4):125–135, 2001.
- [2645] J. van Hunen, A.P. van den Berg, and N.J. Vlaar. The impact of the south-american plate motion and the nazca ridge subduction on the flat subduction below south peru. *Geophysical Research Letters*, 29(14):35–1, 2002.
- [2646] J. van Hunen, A.P. van den Berg, and N.J. Vlaar. On the role of subducting oceanic plateaus in the development of shallow flat subduction. *Tectonophysics*, 352(3-4):317–333, 2002.
- [2647] J. van Hunen, A.P. van den Berg, and N.J. Vlaar. Various mechanisms to induce present-day shallow flat subduction and implications for the younger earth: A numerical parameter study. *Physics of the Earth and Planetary Interiors*, 146(1-2):179–194, 2004.
- [2648] J. van Hunen and S. Zhong. New insight in the Hawaiian plume swell dynamics from scaling laws. *Geophys. Res. Lett.*, 30(15):doi:10.1029/2003GL017646,, 2003.
- [2649] Jeroen van Hunen and Arie P van den Berg. Plate tectonics on the early earth: limitations imposed by strength and buoyancy of subducted lithosphere. *Lithos*, 103(1-2):217–235, 2008.
- [2650] P. van Keken. Cylindrical scaling for dynamical cooling models of the Earth. *Phys. Earth. Planet. Inter.*, 124:119–130, 2001.
- [2651] P. van Keken, D.A. Yuen, and A. van den Berg. Pulsating diapiric flows: Consequences of vertical variations in mantle creep laws. *Earth Planet. Sci. Lett.*, 112:179–194, 1992.
- [2652] P. van Keken and S. Zhong. Mixing in a 3D spherical model of present-day mantle convection. *Earth Planet. Sci. Lett.*, 171:533–547, 1999.
- [2653] P.E. van Keken. Evolution of starting mantle plumes: a comparison between numerical and laboratory models. *Earth Planet. Sci. Lett.*, 148:1–11, 1997.
- [2654] P.E. van Keken, C.J. Ballentine, and E.H. Hauri. 2.12 - convective mixing in the earth's mantle. In Heinrich D. Holland and Karl K. Turekian, editors, *Treatise on Geochemistry*, pages 1 – 21. Pergamon, Oxford, 2007.
- [2655] P.E. van Keken, C. Currie, S.D. King, M.D. Behn, Amandine Cagnioncle, J. Hee, R.F. Katz, S.-C. Lin, E.M. Parmentier, M. Spiegelman, and K. Wang. A community benchmark for subduction zone modelling. *Phys. Earth. Planet. Inter.*, 171:187–197, 2008.
- [2656] P.E. van Keken, A. Davaille, and J. Vatteville. Dynamics of a laminar plume in a cavity: The influence of boundaries on the steady state stem structure. *Geochemistry, Geophysics, Geosystems*, 14(1):158–178, 2013.
- [2657] P.E. van Keken, B.R. Hacker, E.M. Syracuse, and G.A. Abers. Subduction factory: 4. Depthdependent flux of H<sub>2</sub>O from subducting slabs worldwide. *J. Geophys. Res.*, 116(B01401), 2011.
- [2658] P.E. van Keken, E.H. Hauri, and C.J. Ballentine. Mantle mixing: the generation, preservation and destruction of chemical heterogeneity. *Annu. Rev. Earth Sci.*, 30:493–525, 2002.
- [2659] P.E. van Keken, S.D. King, H. Schmeling, U.R. Christensen, D. Neumeister, and M.-P. Doin. A comparison of methods for the modeling of thermochemical convection. *J. Geophys. Res.*, 102(B10):22,477–22,495, 1997.
- [2660] P.E. van Keken, C.J. Spiers, A.P. van den Berg, and E.J. Muyzert. The effective viscosity of rocksalt: implementation of steady-state creep laws in numerical models of salt diapirism. *Tectonophysics*, 225:457–476, 1993.
- [2661] P.E. van Keken, C.J. Spiers, A.P. van den Berg, and E.J. Muyzert. The effective viscosity of rocksalt: implementation of steady-state creep laws in numerical models of salt diapirism. *Tectonophysics*, 225:457–476, 1993.
- [2662] P.E. van Keken, D.A. Yuen, and A.P. van den Berg. The effects of shallow rheological boundaries in the upper mantle on inducing shorter time scales of diapiric flows. *Geophysical Research Letters*, 20(18):1927–1930, 1993.
- [2663] Peter E van Keken. The structure and dynamics of the mantle wedge. *Earth and planetary science letters*, 215(3-4):323–338, 2003.
- [2664] Peter E Van Keken, Chris J Ballentine, and Erik H Hauri. Convective mixing in the earths mantle. *Treatise on geochemistry*, 2:1–21, 2003.

- [2665] Peter E Van Keken, Boris Kiefer, and Simon M Peacock. High-resolution models of subduction zones: Implications for mineral dehydration reactions and the transport of water into the deep mantle. *Geochemistry, Geophysics, Geosystems*, 3(10), 2002.
- [2666] Peter E van Keken, Ikuko Wada, Nathan Sime, and Geoffrey A Abers. Thermal structure of the forearc in subduction zones: a comparison of methodologies. *Geochemistry, Geophysics, Geosystems*, 20, 2019.
- [2667] Peter E van Keken, David A Yuen, and Arie P van den Berg. Implications for mantle dynamics from the high melting temperature of perovskite. *Science*, 264(5164):1437–1439, 1994.
- [2668] J. van Summeren, C. P. Conrad, and E. Gaidos. Mantle convection, plate tectonics, and volcanism on hot exoEarths. *The Astrophysical Journal*, 736(1):L15, 2011.
- [2669] J. van Summeren, C.P. Conrad, and C. Lithgow-Bertelloni. The importance of slab pull and a global asthenosphere to plate motions. *Geochem. Geophys. Geosyst.*, 13(1):10.1029/2011GC003873, 2012.
- [2670] J. van Summeren, E. Gaidos, and C. P. Conrad. Magnetodynamo lifetimes for rocky, earth-mass exoplanets with contrasting mantle convection regimes. *Journal of Geophysical Research: Planets*, 118(5):938–951, 2013.
- [2671] J.R.G. van Summerena, A.P. van den Berg, and R.D. van der Hilst. Upwellings from a deep mantle reservoir filtered at the 660 km phase transition in thermo-chemical convection models and implications for intra-plate volcanism. *Phys. Earth. Planet. Inter.*, 172:210–224, 2009.
- [2672] P. van Thienen. Convective vigour and heat flow in chemically differentiated systems. *Geophys. J. Int.*, 169(2):747–766, 2007.
- [2673] P. Van Thienen, A.P. Van Den Berg, J.H. De Smet, J. Van Hunen, and M.R. Drury. Interaction between small-scale mantle diapirs and a continental root. *Geochemistry, Geophysics, Geosystems*, 4(2), 2003.
- [2674] P. van Thienen, A.P. van den Berg, and N.J. Vlaar. On the formation of continental silicic melts in thermochemical mantle convection models: implications for early Earth. *Tectonophysics*, 394(1-2):111–124, 2004.
- [2675] P van Thienen, AP van den Berg, and NJ Vlaar. Production and recycling of oceanic crust in the early earth. *Tectonophysics*, 386(1-2):41–65, 2004.
- [2676] P. van Thienen, N.J. Vlaar, and A.P. van den Berg. Plate tectonics on the terrestrial planets. *Phys. Earth. Planet. Inter.*, 142:61–74, 2004.
- [2677] P. van Thienen, N.J. Vlaar, and A.P. van den Berg. Assessment of the cooling capacity of plate tectonics and flood volcanism in the evolution of Earth, Mars and Venus. *Phys. Earth. Planet. Inter.*, 150:287–315, 2005.
- [2678] J van Wijk, J van Hunen, and S Goes. Small-scale convection during continental rifting: Evidence from the rio grande rift. *Geology*, 36(7):575–578, 2008.
- [2679] J.W. van Wijk. Role of weak zone orientation in continental lithosphere extension. *Geophys. Res. Lett.*, 32(L02303), 2005.
- [2680] J.W. van Wijk, W.S. Baldridge, J. van Hunen, S. Goes, R. Aster, D.D. Coblenz, S.P. Grand, and J. Ni. Small-scale convection at the edge of the Colorado Plateau: Implications for topography, magmatism, and evolution of Proterozoic lithosphere. *Geology*, 38:611–614, 2010.
- [2681] J.W. van Wijk and D.K. Blackman. Dynamics of continental rift propagation: the end-member modes. *Earth Planet. Sci. Lett.*, 229:247–258, 2005.
- [2682] J.W. van Wijk and D.K. Blackman. Development of en echelon magmatic segments along oblique spreading ridges. *Geology*, 35(7):599–602, 2007.
- [2683] J.W. van Wijk and S.A.P.L. Cloetingh. Basin migration caused by slow lithospheric extension. *Earth Planet. Sci. Lett.*, 198:275–288, 2002.
- [2684] O. Vanderhaeghe, S. Medvedev, P. Fullsack, C. Beaumont, and R.A. Jamieson. Evolution of orogenic wedges and continental plateaux: insights from crustal thermal-mechanical overlying subduction mantle lithosphere. *Geophys. J. Int.*, 153:27–51, 2003.
- [2685] R.S. Varga. *Matrix Iterative Analysis*. Prentice-Hall, Inc., 1963.
- [2686] Oleg V. Vasilyev, Yuri Yu. Podladchikov, and David A. Yuen. Modelling of viscoelastic plume-lithosphere interaction using the adaptive multilevel wavelet collocation method. *Geophys. J. Int.*, 147:579–589, 2001.
- [2687] J. Vattreville, P.E. van Keken, A. Limare, and A. Davaille. Starting laminar plumes: Comparison of laboratory and numerical modeling. *Geochem. Geophys. Geosyst.*, 10(12):doi:10.1029/2009GC002739, 2009.
- [2688] A. Vauchez, A. Tomassi, and G. Barroul. Rheological heterogeneity, mechanical anisotropy and deformation of the continental lithosphere. *Tectonophysics*, 296:61–86, 1998.

- [2689] Mirko Velić, Dave May, and Louis Moresi. A fast robust algorithm for computing discrete voronoi diagrams. *Journal of Mathematical Modelling and Algorithms*, 8(3):343–355, 2009.
- [2690] Bruno C Vendeville and Martin PA Jackson. The rise of diapirs during thin-skinned extension. *Marine and Petroleum Geology*, 9(4):331–354, 1992.
- [2691] Fabio Verbosio, Arne De Coninck, Drosos Kourounis, and Olaf Schenk. Enhancing the scalability of selected inversion factorization algorithms in genomic prediction. *Journal of Computational Science*, 22(Supplement C):99 – 108, 2017.
- [2692] Pieter A Vermeer and R De Borst. Non-associated plasticity for soils, concrete and rock. *HERON*, 29(3), 1984.
- [2693] Ph. Vernant and J. Chery. Mechanical modelling of oblique convergence in the Zagros, Iran. *Geophy. J. Int.*, 165:991–1002, 2006.
- [2694] Philippe Vernant, F Hivert, Jean Chery, Philippe Steer, Rodolphe Cattin, and Alexis Rigo. Erosion-induced isostatic rebound triggers extension in low convergent mountain ranges. *Geology*, 41(4):467–470, 2013.
- [2695] A Verruijt. Deformations of an elastic half plane with a circular cavity. *International Journal of Solids and Structures*, 35(21):2795–2804, 1998.
- [2696] Alexei V Vezolainen, Viatcheslav S Solomatov, James W Head, Alexander T Basilevsky, and L-N Moresi. Timing of formation of beta regio and its geodynamical implications. *Journal of Geophysical Research: Planets*, 108(E1), 2003.
- [2697] Gianluca Vignaroli, Claudio Faccenna, Laurent Jolivet, Claudia Piromallo, and Federico Rossetti. Subduction polarity reversal at the junction between the western alps and the northern apennines, italy. *Tectonophysics*, 450(1-4):34–50, 2008.
- [2698] Jean-Pierre Vilotte, M Daignieres, and Raul Madariaga. Numerical modeling of intraplate deformation: Simple mechanical models of continental collision. *Journal of Geophysical Research: Solid Earth*, 87(B13):10709–10728, 1982.
- [2699] Jean-Pierre Vilotte, Marc Daignieres, R Madariaga, and OC Zienkiewicz. The role of a heterogeneous inclusion during continental collision. *Physics of the earth and planetary interiors*, 36(3-4):236–259, 1984.
- [2700] Jean-Pierre Vilotte, Raul Madariaga, Marc Daignieres, and O Zienkiewicz. Numerical study of continental collision: influence of buoyancy forces and an initial stiff inclusion. *Geophysical Journal International*, 84(2):279–310, 1986.
- [2701] C. Vincent and R. Boyer. A preconditioned conjugate gradient Uzawa-type method for the solution of the Stokes problem by mixed Q1-P0 stabilised finite elements. *Int. J. Num. Meth. Fluids*, 14:289–298, 1992.
- [2702] S. Virgo, S. Abe, and J.L. Urai. Extension fracture propagation in rocks with veins: Insight into the crack-seal process using Discrete Element Method modeling. *J. Geophys. Res.*, 118:5236–5251,, 2013.
- [2703] RLM Vissers and P Th Meijer. Mesozoic rotation of iberia: subduction in the pyrenees? *Earth-Science Reviews*, 110(1-4):93–110, 2012.
- [2704] Nicolaas J Vlaar. Vening meinesza student of the earth. *Eos, Transactions American Geophysical Union*, 70(9):129–140, 1989.
- [2705] N.J. Vlaar, P.E. van Keken, and A.P. van den Berg. Cooling of the Earth in the Archean: Consequences of pressure-release melting in a hotter mantle. *Earth Planet. Sci. Lett.*, 121:1–18, 1994.
- [2706] G. Le Voci, D.R. Davies, S. Goes, S.C. Kramer, and C.R. Wilson. A systematic 2-D investigation into the mantle wedges transient flow regime and thermal structure: Complexities arising from a hydrated rheology and thermal buoyancy. *Geochem. Geophys. Geosyst.*, 15(1), 2014.
- [2707] K. Vogt and T. Gerya. Deep plate serpentinization triggers skinning of subducting slabs. *Geology*, page doi:10.1130/G35565.1, 2014.
- [2708] Katharina Vogt, Antonio Castro, and Taras Gerya. Numerical modeling of geochemical variations caused by crustal relamination. *Geochemistry, Geophysics, Geosystems*, 14(2):470–487, 2013.
- [2709] Katharina Vogt and Taras V Gerya. From oceanic plateaus to allochthonous terranes: numerical modelling. *Gondwana Research*, 25(2):494–508, 2014.
- [2710] Katharina Vogt, Taras V Gerya, and Antonio Castro. Crustal growth at active continental margins: numerical modeling. *Physics of the Earth and Planetary Interiors*, 192:1–20, 2012.
- [2711] Katharina Vogt, Liviu Matenco, and Sierd Cloetingh. Crustal mechanics control the geometry of mountain belts. insights from numerical modelling. *Earth and Planetary Science Letters*, 460:12–21, 2017.

- [2712] F. von Blanckenburg and J.H. Davies. Slab breakoff: A model for syncollisional magmatism and tectonics in the Alps. *Tectonics*, 14(1):120–131, 1995.
- [2713] R. von Mises. Mechanik der festen korper im plastisch deformablen zustand. *Nachrichten der Koniglichen Gesellschaft der Wissenschaften*, page 582, 1913.
- [2714] M. von Tscharner and S. M. Schmalholz. A 3-D Lagrangian finite element algorithm with remeshing for simulating large-strain hydrodynamic instabilities in power law viscoelastic fluids. *Geochem. Geophys. Geosyst.*, 16:215–245, 2015.
- [2715] M. von Tscharner, S.M. Schmalholz, and T. Duretz. Three-dimensional necking during viscous slab detachment. *Geophys. Res. Lett.*, 41:10.1002/2014GL060075, 2014.
- [2716] L. Vynnytska, M.E. Rognes, and S.R. Clark. Benchmarking FEniCS for mantle convection simulations. *Computers & Geosciences*, 50:95–105, 2013.
- [2717] Shoichi Wakiya. Application of bipolar coordinates to the two-dimensional creeping motion of a liquid. i. flow over a projection or a depression on a wall. *Journal of the Physical Society of Japan*, 39(4):1113–1120, 1975.
- [2718] Shoichi Wakiya. Application of bipolar coordinates to the two-dimensional creeping motion of a liquid. ii. some problems for two circular cylinders in viscous fluid. *Journal of the Physical Society of Japan*, 39(6):1603–1607, 1975.
- [2719] H. Wang, R. Agrusta, and J. van Hunen. Advantages of a conservative velocity interpolation (CVI) scheme for particle-in-cell methods with application in geodynamic modeling. *Geochem. Geophys. Geosyst.*, 16:doi:10.1002/2015GC005824, 2015.
- [2720] H. Wang, J. van Hunen, , and D.G. Pearson. The thinning of subcontinental lithosphere: The roles of plume impact and metasomatic weakening. *Geochem. Geophys. Geosyst.*, 16:1156–1171, 2015.
- [2721] H. Wang, J. van Hunen, and D. G. Pearson. Making archean cratonic roots by lateral compression: A two-stage thickening and stabilization model. *Tectonophysics*, 2016.
- [2722] H. Wang, J. van Hunen, D.G. Pearson, and M.B. Allen. Craton stability and longevity: The roles of composition-dependent rheology and buoyancy. *Earth Planet. Sci. Lett.*, 391:224–233, 2014.
- [2723] Hongliang Wang, Jeroen van Hunen, and D Graham Pearson. Making archean cratonic roots by lateral compression: a two-stage thickening and stabilization model. *Tectonophysics*, 746:562–571, 2018.
- [2724] Kelin Wang, Yan Hu, and Jiangheng He. Deformation cycles of subduction earthquakes in a viscoelastic earth. *Nature*, 484(7394):327, 2012.
- [2725] Li Wang and Dimitri J Mavriplis. Adjoint-based h–p adaptive discontinuous galerkin methods for the 2d compressible euler equations. *Journal of Computational Physics*, 228(20):7643–7661, 2009.
- [2726] W.M. Wang, L.J. Sluys, and R. de Borst. Interaction between material length scale and imperfection size for localisation phenomena in viscoplastic media. *Eur. J. Mech. A/Solids*, 15(3):447–464, 1996.
- [2727] W.M. Wang, L.J. Sluys, and R. de Borst. Viscoplasticity for instabilities due to strain softening and strain-rate softening. *Int. J. Num. Meth. Eng.*, 40:3839–3864, 1997.
- [2728] X. Wang, J. He, L. Ding, and R. Gao. A possible mechanism for the initiation of the Yinggehai Basin: A visco-elasto-plastic model. *Journal of Asian Earth Sciences*, 74:25–36, 2013.
- [2729] X. Wang and W.K. Liu. Extended immersed boundary method using FEM and RKPM. *Comput. Methods Appl. Mech. Engrg.*, 193:1305–1321, 2004.
- [2730] Xinguo Wang, William E Holt, and Attreyee Ghosh. Joint modeling of lithosphere and mantle dynamics: Evaluation of constraints from global tomography models. *Journal of Geophysical Research: Solid Earth*, 120(12):8633–8655, 2015.
- [2731] Y. Wang, J. Huang, and S. Zhong. Episodic and multistaged gravitational instability of cratonic lithosphere and its implications for reactivation of the North China Craton. *Geochem. Geophys. Geosyst.*, 16:815–833, 2015.
- [2732] Y. Wang, J. Huang, S. Zhong, and J. Chen. Heat flux and topography constraints on thermochemical structure below north china craton regions and implications for evolution of cratonic lithosphere: Heat flux and topography constraints. *Journal of Geophysical Research: Solid Earth*, 2016.
- [2733] Yongming Wang, Jinshui Huang, and Shijie Zhong. Episodic and multistaged gravitational instability of cratonic lithosphere and its implications for reactivation of the north china craton. *Geochemistry, Geophysics, Geosystems*, 16(3):815–833, 2015.
- [2734] Zewei Wang, Dapeng Zhao, Rui Gao, and Yuanyuan Hua. Complex subduction beneath the tibetan plateau: A slab warping model. *Physics of the Earth and Planetary Interiors*, 292:42–54, 2019.

- [2735] Zhensheng Wang, Timothy M Kusky, and Fabio A Capitanio. Ancient continental lithosphere dislocated beneath ocean basins along the mid-lithosphere discontinuity: A hypothesis. *Geophysical Research Letters*, 44(18):9253–9260, 2017.
- [2736] Zhijie Wang and Radoslaw L Michalowski. Contact fatigue in silica sand observations and modeling. *Geomechanics for Energy and the Environment*, 4:88–99, 2015.
- [2737] G.H. Wannier. A contribution to the hydrodynamics of lubrication. *Quarterly of Applied Mathematics*, VIII:1–32, 1950.
- [2738] N. Wansophark and P. Dechaumphai. Enhancement of Segregated Finite Element Method with Adaptive Meshing Technique for Viscous Incompressible Thermal Flow Analysis. *ScienceAsia*, 29:155–162, 2003.
- [2739] N. Wansophark and P. Dechaumphai. Combined adaptive meshing technique and segregated finite element algorithm for analysis of free and forced convection heat transfer. *Finite Elements in Analysis and Design*, 40:645–663, 2004.
- [2740] Karin N Warners-Ruckstuhl, Rob Govers, and Rinus Wortel. Lithosphere–mantle coupling and the dynamics of the eurasian plate. *Geophysical Journal International*, 189(3):1253–1276, 2012.
- [2741] Karin N Warners-Ruckstuhl, Rob Govers, and Rinus Wortel. Tethyan collision forces and the stress field of the Eurasian Plate. *Geophys. J. Int.*, 195(1):1–15, 2013.
- [2742] KN Warners-Ruckstuhl, P Th Meijer, Rob Govers, and MJR Wortel. A lithosphere-dynamics constraint on mantle flow: Analysis of the Eurasian plate. *Geophysical Research Letters*, 37:L18308, 2010.
- [2743] C.J. Warren. Exhumation of (ultra-)high-pressure terranes: concepts and mechanisms . *Solid Earth*, 4:75–92, 2013.
- [2744] C.J. Warren, C. Beaumont, and R.A. Jamieson. Formation and exhumation of ultra-high-pressure rocks during continental collision: Role of detachment in the subduction channel. *Geochem. Geophys. Geosyst.*, 9, 2008.
- [2745] C.J. Warren, C. Beaumont, and R.A. Jamieson. Modelling tectonic styles and ultra-high pressure (UHP) rock exhumation during the transition from oceanic subduction to continental collision. *Earth Planet. Sci. Lett.*, 267:129–145, 2008.
- [2746] Clare J Warren, Christopher Beaumont, and Rebecca A Jamieson. Deep subduction and rapid exhumation: Role of crustal strength and strain weakening in continental subduction and ultrahigh-pressure rock exhumation. *Tectonics*, 27(6), 2008.
- [2747] P. Waschbusch, G. Batt, and C. Beaumont. Subduction zone retreat and recent tectonics of the south island of new zealand. *Tectonics*, 17(2):267–284, 1998.
- [2748] P. Waschbusch and C. Beaumont. Effect of a retreating subduction zone on deformation in simple regions of plate convergence. *Journal of Geophysical Research B: Solid Earth*, 101(12):28133–28148, 1996.
- [2749] Louise Watremez, Evgenii Burov, Elia d’Acremont, Sylvie Leroy, Benjamin Huet, Laetitia Le Pourhiet, and Nicolas Bellahsen. Buoyancy and localizing properties of continental mantle lithosphere: Insights from thermomechanical models of the eastern gulf of aden. *Geochemistry, Geophysics, Geosystems*, 14(8):2800–2817, 2013.
- [2750] W. A. Watters, M. T. Zuber, and B. H. Hager. Thermal perturbations caused by large impacts and consequences for mantle convection. *Journal of Geophysical Research*, 114(E2), 2009.
- [2751] AB Watts and EB Burov. Lithospheric strength and its relationship to the elastic and seismogenic layer thickness. *Earth and Planetary Science Letters*, 213(1-2):113–131, 2003.
- [2752] AB Watts, SJ Zhong, and J Hunter. The behavior of the lithosphere on seismic to geologic timescales. *Annual Review of Earth and Planetary Sciences*, 41:443–468, 2013.
- [2753] Shimon Wdowinski and Yehuda Bock. The evolution of deformation and topography of high elevated plateaus: 1. model, numerical analysis, and general results. *Journal of Geophysical Research: Solid Earth*, 99(B4):7103–7119, 1994.
- [2754] Shimon Wdowinski and Yehuda Bock. The evolution of deformation and topography of high elevated plateaus: 2. application to the central andes. *Journal of Geophysical Research: Solid Earth*, 99(B4):7121–7130, 1994.
- [2755] D. Weeraratne and M. Manga. Transitions in the style of mantle convection at high Rayleigh numbers. *Earth Planet. Sci. Lett.*, 160:563–568, 1998.
- [2756] S Shawn Wei, Douglas A Wiens, Peter E van Keeken, and Chen Cai. Slab temperature controls on the tonga double seismic zone and slab mantle dehydration. *Science advances*, 3(1):e1601755, 2017.

- [2757] R. Weijermars, MPA t Jackson, and B Vendeville. Rheological and tectonic modeling of salt provinces. *Tectonophysics*, 217(1-2):143–174, 1993.
- [2758] R.F. Weinberg. Internal circulation in a buoyant two-fluid Newtonian sphere: implications for composed magmatic diapirs. *Earth Planet. Sci. Lett.*, 110:77–94, 1992.
- [2759] R.F. Weinberg. The upward transport of inclusions in Newtonian and power-law salt diapirs. *Tectonophysics*, 228:141–150, 1993.
- [2760] R.F. Weinberg. The rise of solid-state diapirs. *Journal of Structural Geology*, 17(8):1183–1195, 1995.
- [2761] R.F. Weinberg. Diapir-driven crustal convection: decompression melting, renewal of the magma source and the origin of nested plutons. *Tectonophysics*, 271:217–229, 1997.
- [2762] R.F. Weinberg and H. Schmeling. Polydiapirs: multiwavelength gravity structures. *Journal of Structural Geology*, 14(4):425–436, 1992.
- [2763] Roberto F Weinberg, Louis Moresi, and Peter Van der Borgh. Timing of deformation in the norseman-wiluna belt, yilgarn craton, western australia. *Precambrian Research*, 120(3-4):219–239, 2003.
- [2764] Roberto F Weinberg, Klaus Regenauer-Lieb, and Gideon Rosenbaum. Mantle detachment faults and the breakup of cold continental lithosphere. *Geology*, 35(11):1035–1038, 2007.
- [2765] Roberto Ferrez Weinberg and Yuri Podladchikov. Diapiric ascent of magmas through power law crust and mantle. *Journal of Geophysical Research: Solid Earth*, 99(B5):9543–9559, 1994.
- [2766] Jens Weismüller, Björn Gmeiner, Siavash Ghelichkhan, Markus Huber, Lorenz John, Barbara Wohlmuth, Ulrich Rüde, and Hans-Peter Bunge. Fast asthenosphere motion in high-resolution global mantle flow models. *Geophysical Research Letters*, 42(18):7429–7435, 2015.
- [2767] M. B. Weller and A. Lenardic. Hysteresis in mantle convection: Plate tectonics systems. *Geophysical Research Letters*, 39(10), 2012.
- [2768] M. B. Weller and A. Lenardic. The energetics and convective vigor of mixed-mode heating: Velocity scalings and implications for the tectonics of exoplanets: The energetics of mixed-mode convection. *Geophysical Research Letters*, 43:9469–9474, 2016.
- [2769] M. B. Weller, A. Lenardic, and C. O'Neill. The effects of internal heating and large scale climate variations on tectonic bi-stability in terrestrial planets. *Earth and Planetary Science Letters*, 420:85–94, 2015.
- [2770] Matthew B Weller and Adrian Lenardic. On the evolution of terrestrial planets: Bi-stability, stochastic effects, and the non-uniqueness of tectonic states. *Geoscience Frontiers*, 9(1):91–102, 2018.
- [2771] M.B. Weller, A. Lenardic, and W.B. Moore. Scaling relationships and physics for mixed heating convection in planetary interiors: Isoviscous spherical shells. *J. Geophys. Res.*, 121, 2016.
- [2772] S. Wenker and C. Beaumont. Can metasomatic weakening result in the rifting of cratons? *Tectonophysics*, 746:3–21, 2018.
- [2773] S. Wenker and C. Beaumont. Effects of lateral strength contrasts and inherited heterogeneities on necking and rifting of continents. *Tectonophysics*, 746:46–63, 2018.
- [2774] Pieter Wesseling and Cornelis W Oosterlee. Geometric multigrid with applications to computational fluid dynamics. *Journal of Computational and Applied Mathematics*, 128(1-2):311–334, 2001.
- [2775] John D West, Matthew J Fouch, Jeffrey B Roth, and Linda T Elkins-Tanton. Vertical mantle flow associated with a lithospheric drip beneath the great basin. *Nature Geoscience*, 2(6):439, 2009.
- [2776] D.M. Whipp, C. Beaumont, and J. Braun. Feeding the aneurysm: Orogen-parallel mass transport into Nanga Parbat and the western Himalayan syntaxis. *J. Geophys. Res.*, 119:doi:10.1002/2013JB010929, 2014.
- [2777] Kelin X Whipple. The influence of climate on the tectonic evolution of mountain belts. *Nature geoscience*, 2(2):97, 2009.
- [2778] Kelin X Whipple and Gregory E Tucker. Implications of sediment-flux-dependent river incision models for landscape evolution. *Journal of Geophysical Research: Solid Earth*, 107(B2):ETG–3, 2002.
- [2779] RS White and D McKenzie. Mantle plumes and flood basalts. *Journal of Geophysical Research: Solid Earth*, 100(B9):17543–17585, 1995.
- [2780] A Whittaker, MHP Bott, and GD Waghorn. Stresses and plate boundary forces associated with subduction plate margins. *Journal of Geophysical Research: Solid Earth*, 97(B8):11933–11944, 1992.
- [2781] C. Wijns, R. Weinberg, K. Gessner, and L. Moresi. Mode of crustal extension determined by rheological layering. *Earth Planet. Sci. Lett.*, 236:120–134, 2005.

- [2782] Chris Wijns, Fabio Boschetti, and Louis Moresi. Inverse modelling in geology by interactive evolutionary computation. *Journal of Structural Geology*, 25:1615–1621, 2003.
- [2783] K.R. Wilks and N.L. Carter. Rheology of some continental lower crustal rocks. *Tectonophysics*, 182(1-2):57–77, 1990.
- [2784] S. Willett, C. Beaumont, and P. Fullsack. Mechanical model for the tectonics of doubly vergent compressional orogens. *Geology*, 21:371–374, 1993.
- [2785] S. D. Willett. Rheological dependence of extension in wedge models of convergent orogens. *Tectonophysics*, 305:419–435, 1999.
- [2786] S.D. Willett. Dynamic and kinematic growth and change of a coulomb wedge. In K.R. McClay, editor, *Thrust Tectonics*, pages 19–31. Chapman and Hall, 1992.
- [2787] S.D. Willett. Orogeny and orography: The effects of erosion on the structure of mountain belts. *J. Geophys. Res.*, 104(B12):28957, 1999.
- [2788] S.D. Willett. Erosion on a line. *Tectonophysics*, 484:168–180, 2010.
- [2789] S.D. Willett and C. Beaumont. Subduction of Asian lithosphere mantle beneath Tibet inferred from models of continental collision. *Nature*, 369:642–645, 1994.
- [2790] Sean D Willett and Mark T Brandon. On steady states in mountain belts. *Geology*, 30(2):175–178, 2002.
- [2791] Sean D. Willett and Daniel C. Pope. Thermo-mechanical models of convergent orogenesis: Thermal and rheologic dependence of crustal deformation. In *Rheology and deformation of the lithosphere at continental margins.*, pages 166–222. Columbia University Press, 2003.
- [2792] Garry Willgoose. Mathematical modeling of whole landscape evolution. *Annual Review of Earth and Planetary Sciences*, 33(1):443–459, 2005.
- [2793] C. D. Williams, M. Li, A. K. McNamara, E. J. Garnero, and M. C. van Soest. Episodic entrainment of deep primordial mantle material into ocean island basalts. *Nature Communications*, 6:8937, 2015.
- [2794] S. Williams, L. Oliker, R. Vuduc, J. Shalf, K. Yelick, and J. Demmel. Optimization of Sparse Matrix-Vector Multiplication on Emerging Multicore Platforms. In *SC'07 proceedings of the 2007 ACM/IEEE conference on supercomputing*. ACM NY, 2007.
- [2795] Erskine D Williamson and Leason H Adams. Density distribution in the earth. *Journal of the Washington Academy of Sciences*, 13(19):413–428, 1923.
- [2796] CJL Wilson and Yu Zhang. Comparison between experiment and computer modelling of plane-strain simple-shear ice deformation. *Journal of Glaciology*, 40(134):46–55, 1994.
- [2797] C.R. Wilson, M. Spiegelman, and P.E. van Keken. TerraFERMA: The Transparent Finite Element Rapid Model Assembler for multiphysics problems in Earth sciences. *Geochem. Geophys. Geosyst.*, 18:769–810, 2017.
- [2798] C.R. Wilson, M. Spiegelman, P.E. van Keken, and B.R. Hacker. Fluid flow in subduction zones: The role of solid rheology and compaction pressure. *Earth Planet. Sci. Lett.*, 401:261–274, 2014.
- [2799] RW Wilson, GA Houseman, SJH Buitier, KJW McCaffrey, and AG Doré. Fifty years of the wilson cycle concept in plate tectonics: An overview. *Geological Society, London, Special Publications*, 470, 2019.
- [2800] SB Wissing, S Ellis, and Othmar-Adrian Pfiffner. Numerical models of alpine-type cover nappes. *Tectonophysics*, 367(3-4):145–172, 2003.
- [2801] W.-D. Woidt. Finite element calculations applied to salt dome analysis. *Tectonophysics*, 50:369–386, 1978.
- [2802] Marek Wojciechowski. A note on the differences between drucker-prager and mohr-coulomb shear strength criteria. *Studia Geotechnica et Mechanica*, 2018.
- [2803] Sebastian G Wolf and Ritske S Huismans. Mountain building or backarc extension in ocean-continent subduction systems-a function of backarc lithospheric strength and absolute plate velocities. *Journal of Geophysical Research: Solid Earth*, 2019.
- [2804] Stephanie Wollherr, Alice-Agnes Gabriel, and Carsten Uphoff. Off-fault plasticity in three-dimensional dynamic rupture simulations using a modal Discontinuous Galerkin method on unstructured meshes: Implementation, verification, and application. *Geoph. J. Int.*, 214(3):1556–1584, sep 2018.
- [2805] M. Wolstencroft and J.H. Davies. Influence of the Ringwoodite-Perovskite transition on mantle convection in spherical geometry as a function of Clapeyron slope and Rayleigh number. *Solid Earth*, 2:315–326, 2011.
- [2806] M. Wolstencroft, J.H. Davies, and D.R. Davies. NusseltRayleigh number scaling for spherical shell Earth mantle simulation up to a Rayleigh number of  $10^9$ . *Phys. Earth. Planet. Inter.*, 176:132–141, 2009.

- [2807] Martin Wolstencroft and J Huw Davies. Breaking supercontinents; no need to choose between passive or active. *Solid Earth*, 8(4):817–825, 2017.
- [2808] Teng-Fong Wong and Li-Chun Wu. Tensile stress concentration and compressive failure in cemented granular material. *Geophysical Research Letters*, 22(13):1649–1652, 1995.
- [2809] S.Y.N. Wong-A-Ton and M.J.R. Wortel. Slab detachment in continental collision zones: An analysis of controlling parameters. *Geophys. Res. Lett.*, 24(16):2095–2098, 1997.
- [2810] MJR Wortel, MJN Remkes, R Govers, SAPL Cloetingh, and P Th Meijer. Dynamics of the lithosphere and the intraplate stress field. *Philosophical Transactions of the Royal Society of London. Series A: Physical and Engineering Sciences*, 337(1645):111–126, 1991.
- [2811] MJR Wortel and W Spakman. Structure and dynamics of subducted lithosphere in the mediterranean region. *Proceedings of the Koninklijke Nederlandse Akademie van Wetenschappen*, 95(3):325–347, 1992.
- [2812] M.J.R. Wortel and W. Spakman. Subduction and slab detachment in the Mediterranean-Carpathian region. *Science*, 290(5498):1910–1917, 2000.
- [2813] Jennifer Worthen, Georg Stadler, Noemi Petra, Michael Gurnis, and Omar Ghettas. Towards adjoint-based inversion for rheological parameters in nonlinear viscous mantle flow. *Physics of the Earth and Planetary Interiors*, 234:23–34, 2014.
- [2814] G.B. Wright, N. Flyer, and D.A. Yuen. A hybrid radial basis functionpseudospectral method for thermal convection in a 3D spherical shell. *Geochem. Geophys. Geosyst.*, 11(7), 2010.
- [2815] B. Wu, Z. Xu, and Z. Li. A note on imposing displacement boundary conditions in finite element analysis. *Commun. Numer. Meth. Engng*, 24:777–784, 2008.
- [2816] Benjun Wu, Clinton P Conrad, Arnauld Heuret, Carolina Lithgow-Bertelloni, and Serge Lallemand. Reconciling strong slab pull and weak plate bending: The plate motion constraint on the strength of mantle slabs. *Earth and Planetary Science Letters*, 272(1-2):412–421, 2008.
- [2817] G. Wu, L.L. Lavier, and E. Choi. Modes of continental extension in a crustal wedge. *Earth Planet. Sci. Lett.*, 421:89–97, 2015.
- [2818] B. Wuming, C. Vigny, Y. ricard, and C. Froidevaux. On the origin of deviatoric stresses in the lithosphere. *J. Geophys. Res.*, 97(B8):11,729–11,737, 1992.
- [2819] Shunxing Xie and Paul J Tackley. Evolution of helium and argon isotopes in a convecting mantle. *Physics of the Earth and Planetary Interiors*, 146(3-4):417–439, 2004.
- [2820] Shunxing Xie and Paul J Tackley. Evolution of u-pb and sm-nd systems in numerical models of mantle convection and plate tectonics. *Journal of Geophysical Research: Solid Earth*, 109(B11), 2004.
- [2821] H. Xing, W. Yu, and J. Zhang. 3d mesh generation in geocomputing. In *Advances in Geocomputing, Lecture Notes in Earth Sciences*. Springer-Verlag, Berlin Heidelberg, 2009.
- [2822] Yasuhiro Yamada, Kei Baba, and Toshifumi Matsuoka. Analogue and numerical modelling of accretionary prisms with a decollement in sediments. *Geological Society, London, Special Publications*, 253(1):169–183, 2006.
- [2823] P. Yamato, P. Agard, E. Burov, L. Le Pourhet, L. Jolivet, and C. Tiberi. Burial and exhumation in a subduction wedge: Mutual constraints from thermomechanical modeling and natural P-T-t data (Schistes Lustres, western Alps). *J. Geophys. Res.*, 112(B07410):doi:10.1029/2006JB004441, 2007.
- [2824] P. Yamato and J.P. Brun. Metamorphic record of catastrophic pressure drops in subduction zones. *Nature Geoscience*, 10(1):46–50, 2017.
- [2825] P. Yamato, E. Burov, P. Agard, L. Le Pourhet, and L. Jolivet. HP-UHP exhumation during slow continental subduction: Self-consistent thermodynamically and thermomechanically coupled model with application to the Western Alps. *Earth Planet. Sci. Lett.*, 271:63–74, 2008.
- [2826] P. Yamato, T. Duretz, and S. Angiboust. Brittle/ductile deformation of eclogites: Insights from numerical models. *Geochemistry, Geophysics, Geosystems*, 20(7):3116–3133, 2019.
- [2827] P. Yamato, L. Husson, T.W. Becker, and K. Pedoja. Passive margins getting squeezed in the mantle convection vice. *Tectonics*, 32:1559–1570, 2013.
- [2828] P. Yamato, L. Husson, J. Braun, C. Loiselet, and C. Thieulot. Influence of surrounding plates on 3D subduction dynamics. *Geophys. Res. Lett.*, 36(L07303), 2009.
- [2829] P. Yamato, F. Mouthereau, and E. Burov. Taiwan mountain building: Insights from 2-d thermomechanical modelling of a rheologically stratified lithosphere. *Geophysical Journal International*, 176(1):307–326, 2009.
- [2830] P. Yamato, R. Tartese, T. Duretz, and D.A. May. Numerical modelling of magma transport in dykes . *Tectonophysics*, 526-529:97–109, 2012.

- [2831] Ph. Yamato, B.J.P. Kaus, F. Mouthereau, and S. Castelltort. Dynamic constraints on the crustal-scale rheology of the Zagros fold belt, Iran. *Geology*, 39(9):815–818, 2011.
- [2832] Philippe Yamato, Thibault Duretz, David A May, and Romain Tartese. Quantifying magma segregation in dykes. *Tectonophysics*, 660:132–147, 2015.
- [2833] Takatoshi Yanagisawa, Yasuko Yamagishi, Yozo Hamano, and Dave R Stegman. Mechanism for generating stagnant slabs in 3-d spherical mantle convection models at earth-like conditions. *Physics of the Earth and Planetary Interiors*, 183(1-2):341–352, 2010.
- [2834] S. Yang and Y. Shi. Three-dimensional numerical simulation of glacial trough forming process. *Science China: Earth Sciences*, pages 10.1007/s11430-015-5120-8, 2015.
- [2835] T. Yang, M. Gurnis, and S. Zahirovic. Slab avalanche-induced tectonics in self-consistent dynamic models. *Tectonophysics*, 2016.
- [2836] T. Yang, M. Gurnis, and Z. Zhan. Trench motion-controlled slab morphology and stress variations: Implications for the isolated 2015 bonin islands deep earthquake. *Geophysical Research Letters*, 2017.
- [2837] T. Yang, L. Moresi, M. Gurnis, S. Liu, D. Sandiford, S. Williams, and F.A. Capitanio. Contrasted East Asia and South America tectonics driven by deep mantle flow. *Earth Planet. Sci. Lett.*, 517:106–116, 2019.
- [2838] Ting Yang and Michael Gurnis. Dynamic topography, gravity and the role of lateral viscosity variations from inversion of global mantle flow. *Geophysical Supplements to the Monthly Notices of the Royal Astronomical Society*, 207(2):1186–1202, 2016.
- [2839] Ting Yang, Michael Gurnis, and Sabin Zahirovic. Slab avalanche-induced tectonics in self-consistent dynamic models. *Tectonophysics*, 746:251–265, 2018.
- [2840] Ting Yang, Louis Moresi, R Dietmar Müller, and Michael Gurnis. Oceanic residual topography agrees with mantle flow predictions at long wavelengths. *Geophysical Research Letters*, 44(21):10–896, 2017.
- [2841] Ting Yang, Louis Moresi, Dapeng Zhao, Dan Sandiford, and Joanne Whittaker. Cenozoic lithospheric deformation in northeast asia and the rapidly-aging pacific plate. *Earth Planet. Sci. Lett.*, 492:1–11, 2018.
- [2842] Woo-Sun Yang. *Variable viscosity thermal convection at infinite Prandtl number in a thick spherical shell*. PhD thesis, University of Illinois, 1997.
- [2843] Woo-Sun Yang and John R Baumgardner. A matrix-dependent transfer multigrid method for strongly variable viscosity infinite prandtl number thermal convection. *Geophysical & Astrophysical Fluid Dynamics*, 92(3-4):151–195, 2000.
- [2844] C. Yao, F. Deschamps, J.P. Lowman, C. Sanchez-Valle, and P.J. Tackley. Stagnant lid convection in bottom-heated thin 3-D spherical shells: Influence of curvature and implications for dwarf planets and icy moons. *J. Geophys. Res.*, 119:1895–1913, 2014.
- [2845] Irad Yavneh. Why multigrid methods are so efficient. *Computing in science & engineering*, 8(6):12, 2006.
- [2846] Tao Ye, Rajat Mittal, HS Udaykumar, and Wei Shyy. An accurate cartesian grid method for viscous incompressible flows with complex immersed boundaries. *Journal of computational physics*, 156(2):209–240, 1999.
- [2847] Liang Yin, Chao Yang, Shi-Zhuang Ma, and Ke-Ke Zhang. Parallel and fully implicit simulations of the thermal convection in the earths outer core. *Computers & Fluids*, 193:104278, 2019.
- [2848] He Yiqian and Yang Haitian. Solving inverse couple-stress problems via an element-free galerkin (efg) method and gauss–newton algorithm. *Finite Elements in Analysis and Design*, 46(3):257–264, 2010.
- [2849] M. Yoshida. The role of harzburgite layers in the morphology of subducting plates and the behavior of oceanic crustal layers. *Geophys. Res. Lett.*, 40:5387–5392, 2013.
- [2850] M. Yoshida and A. Kageyama. Application of the Yin-Yang grid to a thermal convection of a Boussinesq fluid with infinite Prandtl number in a three-dimensional spherical shell. *Geophys. Res. Lett.*, 31(L12609), 2004.
- [2851] M. Yoshida, F. Tajima, S. Honda, and M. Morishige. The 3D numerical modeling of subduction dynamics: Plate stagnation and segmentation, and crustal advection in the wet mantle transition zone. *J. Geophys. Res.*, 117(B04104), 2012.
- [2852] Masaki Yoshida and Yozo Hamano. Pangea breakup and northward drift of the indian subcontinent reproduced by a numerical model of mantle convection. *Scientific reports*, 5:8407, 2015.
- [2853] Masaki Yoshida and Akira Kageyama. Low-degree mantle convection with strongly temperature-and depth-dependent viscosity in a three-dimensional spherical shell. *Journal of Geophysical Research: Solid Earth*, 111(B3), 2006.

- [2854] S. Yoshioka and M.J.R. Wortel. Three-dimensional numerical modeling of detachment of subducted lithosphere. *J. Geophys. Res.*, 100(B10):20,223–20,244, 1995.
- [2855] Shoichi Yoshioka, Yoku Torii, and Michael R Riedel. Impact of phase change kinetics on the mariana slab within the framework of 2-d mantle convection. *Physics of the Earth and Planetary Interiors*, 240:70–81, 2015.
- [2856] Richard E Young. Finite-amplitude thermal convection in a spherical shell. *Journal of Fluid Mechanics*, 63(4):695–721, 1974.
- [2857] Warren Clarence Young and Richard Gordon Budynas. *Roark's formulas for stress and strain*, volume 7. McGraw-Hill New York, 2002.
- [2858] Hongzheng Yu and Shimin Wang. Unified linear stability analysis for thermal convections in spherical shells under different boundary conditions and heating modes. *Earth and Space Science*, 2019.
- [2859] X. Yu and F. Tin-Loi. A simple mixed finite element for static limit analysis. *Computers and Structures*, 84:1906–1917, 2006.
- [2860] K.Y. Yuan, Y.S. Huang, H.T. Yang, and T.H.H. Pian. The inverse mapping and distortion measures for 8-node hexahedral isoparametric elements. *Computational Mechanics*, 14:189–199, 1994.
- [2861] DA Yuen, R Sabadini, and E Boschi. Mantle rheology from a geodynamical standpoint. *La Rivista del Nuovo Cimento (1978-1999)*, 5(8):1–35, 1982.
- [2862] David A Yuen and Luce Fleitout. Thinning of the lithosphere by small-scale convective destabilization. *Nature*, 313(5998):125, 1985.
- [2863] David A Yuen, Ctirad Matyska, Ondrej Cadek, and Masanori Kameyama. The dynamical influences from physical properties in the lower mantle and post-perovskite phase transition. *GEOPHYSICAL MONOGRAPH-AMERICAN GEOPHYSICAL UNION*, 174:249, 2007.
- [2864] David A Yuen, Francesca Quarenici, and H-J Hong. Effects from equation of state and rheology in dissipative heating in compressible mantle convection. *Nature*, 326(6108):67, 1987.
- [2865] David A Yuen and Roberto Sabadini. Secular rotational motions and the mechanical structure of a dynamical viscoelastic earth. *Physics of the earth and planetary interiors*, 36(3-4):391–412, 1984.
- [2866] Z. Xu Z. Li and T.V. Gerya. Numerical Geodynamic Modeling of Continental Convergent Margins, Earth Sciences. In Dr. Imran Ahmad Dar, editor, *Earth Sciences*. InTech, 2012.
- [2867] S. Zahirovic, R. D. Müller, M. Seton, N. Flament, M. Gurnis, and J. Whittaker. Insights on the kinematics of the india-eurasia collision from global geodynamic models. *Geochemistry, Geophysics, Geosystems*, 13(4), 2012.
- [2868] S.T. Zalesak. Fully Multidimensional Flux-Corrected Transport Algorithms for Fluids. *J. Comp. Phys.*, 31:335–362, 1979.
- [2869] S. Zaleski and P. Julien. Numerical simulation of Rayleigh-Taylor instability for single and multiple salt diapirs. *Tectonophysics*, 206:55–69, 1992.
- [2870] A. Zebib. Linear and Weakly Nonlinear Variable Viscosity Convection in Spherical Shells. *Theoret. Comput. Fluid Dynamics*, 4:241–253, 1993.
- [2871] Abdelfattah Zebib, Gerald Schubert, James L Dein, and Ramesh C Paliwal. Character and stability of axisymmetric thermal convection in spheres and spherical shells. *Geophysical & Astrophysical Fluid Dynamics*, 23(1):1–42, 1983.
- [2872] Abdelfattah Zebib, Gerald Schubert, and Joe M Straus. Infinite prandtl number thermal convection in a spherical shell. *Journal of Fluid Mechanics*, 97(2):257–277, 1980.
- [2873] Peter K Zeitler, Anne S Meltzer, Peter O Koons, David Craw, Bernard Hallet, C Page Chamberlain, William SF Kidd, Stephen K Park, Leonardo Seeber, Michael Bishop, et al. Erosion, himalayan geodynamics, and the geomorphology of metamorphism. *GSA Today*, 11(1):4–9, 2001.
- [2874] Dailei Zhang and Danian Huang. Comments on; computation of the gravity field and its gradient. *Computers and Geosciences*, 106:217–220, 2017.
- [2875] Huai Zhang, Lili Ju, Max Gunzburger, Todd Ringler, and Stephen Price. Coupled models and parallel simulations for three-dimensional full-stokes ice sheet modeling. *Numerical Mathematics: Theory, Methods and Applications*, 4(3):396–418, 2011.
- [2876] Jiaxiang Zhang, Teng-Fong Wong, and Daniel M Davis. Micromechanics of pressure-induced grain crushing in porous rocks. *Journal of Geophysical Research: Solid Earth*, 95(B1):341–352, 1990.
- [2877] N. Zhang and Z-X Li. Formation of mantle "lone plumes" in the global downwelling zone – A case for subduction-controlled plume generation beneath the South China Sea. *Tectonophysics*, 2017.

- [2878] N. Zhang and R. N. Pysklywec. Role of mantle flow at the north fiji basin: Insights from anomalous topography. *Geochemistry, Geophysics, Geosystems*, 7(12), 2006.
- [2879] N. Zhang and S. Zhong. Heat fluxes at the earth's surface and core-mantle boundary since pangea formation and their implications for the geomagnetic superchrons. *Earth and Planetary Science Letters*, 306(3-4):205–216, 2011.
- [2880] N. Zhang, S. Zhong, and R. M. Flowers. Predicting and testing continental vertical motion histories since the paleozoic. *Earth and Planetary Science Letters*, 317-318:426–435, 2012.
- [2881] N. Zhang, S. Zhong, W. Leng, , and Z.X. Li. A model for the evolution of the Earths mantle structure since the Early Paleozoic. *J. Geophys. Res.*, 115(B06401), 2010.
- [2882] N. Zhang, S. Zhong, and A.K. McNamara. Supercontinent formation from stochastic collision and mantle convection models. *Gondwana Research*, 15:267–275, 2009.
- [2883] Pei-Zhen Zhang, Zhengkang Shen, Min Wang, Weijun Gan, Roland Burgmann, Peter Molnar, Qi Wang, Zhiping Niu, Jianzhong Sun, Jianchun Wu, et al. Continuous deformation of the tibetan plateau from global positioning system data. *Geology*, 32(9):809–812, 2004.
- [2884] S. Zhang and U. Christensen. Some effects of lateral viscosity variations on geoid and surface velocities induced by density anomalies in the mantle. *Geophys. J. Int.*, 114:531–547, 1993.
- [2885] S. Zhang and C. O'Neill. The early geodynamic evolution of mars-type planets. *Icarus*, 265:187–208, 2016.
- [2886] S. Zhang, H. L. Xing, D. A. Yuen, H. Zhang, and Y. Shi. Regional stress fields under tibet from 3d global flow simulation. *Journal of Earth Science*, 22(2):155–159, 2011.
- [2887] S. Zhang and D.A. Yuen. The influences of lower mantle viscosity stratification on 3D spherical-shell mantle convection. *Earth Planet. Sci. Lett.*, 132:157–166, 1995.
- [2888] S. Zhang and DA Yuen. Intense local toroidal motion generated by variable viscosity compressible convection in 3-d spherical-shell. *Geophysical research letters*, 23(22):3135–3138, 1996.
- [2889] X. Zhang. On positivity-preserving high order discontinuous Galerkin schemes for compressible Navier-Stokes equations. *J. Comp. Phys.*, 328:301–343, 2017.
- [2890] Y. Zhang, BE Hobbs, and MW Jessell. Crystallographic preferred orientation development in a buckled single layer: a computer simulation. *Journal of structural geology*, 15(3-5):265–276, 1993.
- [2891] Y. Zhang, BE Hobbs, A. Ord, and HB Mühlhaus. Computer simulation of single-layer buckling. *Journal of Structural Geology*, 18(5):643–655, 1996.
- [2892] L. Zhao, X. Bai, T. Li, and J.J.R. Williams. Improved conservative level set method. *Int. J. Num. Meth. Fluids*, 2014.
- [2893] W. Zhao. Da yuen s. honda. *Multiple phase transitions and the style of mantle convection*, *Phys. Earth Planet. Int.*, 72:185–210, 1992.
- [2894] Y. Zhao, J. de Vries, A.P. van den Berg, M.H.G. Jacobs, and W. van Westrenen. The participation of ilmenite-bearing cumulates in lunar mantle overturn. *Earth Planet. Sci. Lett.*, 511:1–11, 2019.
- [2895] S. Zhong. Constraints on thermochemical convection of the mantle from plume heat flux, plume excess temperature, and upper mantle temperature. *Journal of Geophysical Research*, 111(B4), 2006.
- [2896] S. Zhong. Migration of tharsis volcanism on mars caused by differential rotation of the lithosphere. *Nature Geoscience*, 2(1):19–23, 2009.
- [2897] S. Zhong and M. Gurnis. Viscous flow model of a subduction zone with a faulted lithosphere: Long and short wavelength topography, gravity and geoid. *Geophysical Research Letters*, 19(18):1891–1894, 1992.
- [2898] S. Zhong and M. Gurnis. Dynamic feedback between a continentlike raft and thermal convection. *Journal of Geophysical Research: Solid Earth*, 98(B7):12219–12232, 1993.
- [2899] S. Zhong and M. Gurnis. Role of plates and temperature-dependent viscosity in phase change dynamics. *Journal of Geophysical Research*, 99(B8):15903, 1994.
- [2900] S. Zhong and M. Gurnis. Mantle convection with plates and Mobile, Faulted Plate Margins. *Science*, 267(5199):838–843, 1995.
- [2901] S. Zhong and M. Gurnis. Towards a realistic simulation of plate margins in mantle convection. *Geophysical Research Letters*, 22(8):981–984, 1995.
- [2902] S. Zhong, M. Gurnis, and G. Hulbert. Accurate determination of surface normal stress in viscous flow from a consistent boundary flux method. *Physics of the Earth and Planetary Interiors*, 78(1-2):1–8, 1993.
- [2903] S. Zhong, M. Gurnis, and L. Moresi. Free-surface formulation of mantle convection-i. basic theory and application to plumes. *Geophysical Journal International*, 127(3):708–718, 1996.

- [2904] S. Zhong, M. Gurnis, and L. Moresi. Role of faults, nonlinear rheology, and viscosity structure in generating plates from instantaneous mantle flow models. *J. Geophys. Res.*, 103(B7):15,255–15,268, 1998.
- [2905] S. Zhong, A. McNamara, E. Tan, L. Moresi, and M. Gurnis. A benchmark study on mantle convection in a 3-D spherical shell using CitcomS. *Geochem. Geophys. Geosyst.*, 9(10), 2008.
- [2906] S. Zhong and A.B. Watts. Lithospheric deformation induced by loading of the Hawaiian Islands and its implications for mantle rheology. *J. Geophys. Res.*, 118:6025–6048, 2013.
- [2907] S. Zhong, N. Zhang, Z.-X. Li, and J.H. Roberts. Supercontinent cycles, true polar wander, and very long-wavelength mantle convection. *Earth Planet. Sci. Lett.*, 261:551–564, 2007.
- [2908] S. Zhong and M.T. Zuber. Long-wavelength topographic relaxation for self-gravitating planets and implications for the time-dependent compensation of surface topography. *J. Geophys. Res.*, 105:4153–4164, 2000.
- [2909] S. Zhong, M.T. Zuber, L.N. Moresi, and M. Gurnis. The role of temperature-dependent viscosity and surface plates in spherical shell models of mantle convection. *J. Geophys. Res.*, 105(B5):11,063–11,082, 2000.
- [2910] Sh. Zhong and M. Gurnis. Controls on trench topography from dynamic models of subducted slabs. *J. Geophys. Res.*, 99(B8):15,683–15,695, 1994.
- [2911] Sh. Zhong and M. Gurnis. Interaction of weak faults and non-Newtonian rheology produces plate tectonics in a 3D model of mantle flow. *Nature*, 383:245–247, 1996.
- [2912] Shijie Zhong. Analytic solutions for Stokes flow with lateral variations in viscosity. *Geophys. J. Int.*, 124(1):18–28, 1996.
- [2913] Shijie Zhong. Role of ocean-continent contrast and continental keels on plate motion, net rotation of lithosphere, and the geoid. *Journal of Geophysical Research: Solid Earth*, 106(B1):703–712, 2001.
- [2914] S.J. Zhong, D.A. Yuen, L.N. Moresi, and M.G. Knepley. 7.05 - numerical methods for mantle convection. In Gerald Schubert, editor, *Treatise on Geophysics (Second Edition)*, pages 197 – 222. Elsevier, Oxford, second edition edition, 2015.
- [2915] Xinyi Zhong and Zhong-Hai Li. Forced subduction initiation at passive continental margins: velocity-driven versus stress-driven. *Geophysical Research Letters*, 2019.
- [2916] S-S Zhou and X-L Gao. Solutions of the generalized half-plane and half-space cerruti problems with surface effects. *Zeitschrift für angewandte Mathematik und Physik*, 66(3):1125–1142, 2015.
- [2917] X. Zhou. 2D vector gravity potential and line integrals for the gravity anomaly caused by a 2D mass of depth-dependent density contrast. *Geophysics*, 73(6):143–150, 2008.
- [2918] X. Zhou, Z.-H. Li, T.V. Gerya, R.J. Stern, Z. Xu, and J. Zhang. Subduction initiation dynamics along a transform fault control trench curvature and ophiolite ages. *Geology*, 46(7):607–610, 2018.
- [2919] D.Y. Zhu, C.F. Lee, and K.T. Law. Determination of bearing capacity of shallow foundations without using superposition approximation. *Can. Geotech. J.*, 40:450–459, 2003.
- [2920] G. Zhu, T. Gerya, D.A. Yuen, S. Honda, T. Yoshida, and T. Connolly. Three-dimensional dynamics of hydrous thermal-chemical plumes in oceanic subduction zones. *Geochem. Geophys. Geosyst.*, 10:doi:10.1029/2009GC002625, 2009.
- [2921] G. Zhu, T.V. Gerya, P.J. Tackley, and E. Kissling. Four-dimensional numerical modeling of crustal growth at active continental margins. *J. Geophys. Res.*, 118:4682–4698, 2013.
- [2922] Guizhi Zhu, Taras Gerya, and David A Yuen. Melt evolution above a spontaneously retreating subducting slab in a three-dimensional model. *Journal of Earth Science*, 22(2):137–142, 2011.
- [2923] Guizhi Zhu, Taras V Gerya, Satoru Honda, Paul J Tackley, and David A Yuen. Influences of the buoyancy of partially molten rock on 3-d plume patterns and melt productivity above retreating slabs. *Physics of the Earth and Planetary Interiors*, 185(3-4):112–121, 2011.
- [2924] Guizhi Zhu, Yaolin Shi, and Paul Tackley. Subduction of the western pacific plate underneath northeast china: implications of numerical studies. *Physics of the Earth and Planetary Interiors*, 178(1-2):92–99, 2010.
- [2925] T. Zhu. Tomography-based mantle flow beneath Mongolia-Baikal area. *Phys. Earth. Planet. Inter.*, 237:40–50, 2014.
- [2926] T. Zhu and S.N. Atluri. A modified collocation method and a penalty formulation for enforcing the essential boundary conditions in the element free galerkin method. *Computational Mechanics*, 21:211–222, 1998.
- [2927] Yi Zhu, Patrick J Fox, and Joseph P Morris. A pore-scale numerical model for flow through porous media. *International journal for numerical and analytical methods in geomechanics*, 23(9):881–904, 1999.

- [2928] Yongning Zhu and Robert Bridson. Animating sand as a fluid. *ACM Transactions on Graphics (TOG)*, 24(3):965–972, 2005.
- [2929] Peter A Ziegler. Geodynamics of rifting and implications for hydrocarbon habitat. *Tectonophysics*, 215(1-2):221–253, 1992.
- [2930] Peter A Ziegler. Plate tectonics, plate moving mechanisms and rifting. *Tectonophysics*, 215(1-2):9–34, 1992.
- [2931] O. Zienkiewicz and S. Nakazawa. The penalty function method and its application to the numerical solution of boundary value problems. *The American Society of Mechanical Engineers*, 51, 1982.
- [2932] O.C. Zienkiewicz. Visco-plasticity, plasticity, creep and visco-plastic flow. *Lecture Notes in Mathematics*, 461:297–328, 1975.
- [2933] O.C. Zienkiewicz and I.C. Cormeau. Visco-plasticity and creep in elastic solids - a unified numerical solution approach. *Int. J. Num. Meth. Eng.*, 8:821–845, 1974.
- [2934] O.C. Zienkiewicz and I.C. Cormeau. Visco-plasticity and plasticity. an alternative for finite element solution of material nonlinearities. *Lecture notes in Computer Science*, 10:259–287, 1974.
- [2935] O.C. Zienkiewicz and P.N. Godbole. Flow of plastic and visco-plastic solids with special reference to extrusion and forming processes. *Int. J. Num. Meth. Eng.*, 8:3–16, 1974.
- [2936] O.C. Zienkiewicz and P.N. Godbole. A penalty function approach to problems of plastic flow of metals with large surface deformation. *Journal of Strain analysis*, 10(3):180–183, 1975.
- [2937] O.C. Zienkiewicz, M. Huang, and M. Pastor. Localization problems in plasticity using finite elements with adaptive remeshing. *International Journal for Numerical and Analytical Methods in Geomechanics*, 19:127–148, 1995.
- [2938] O.C. Zienkiewicz, C. Humpheson, and R.W. Lewis. Associated and non-associated visco-plasticity and plasticity in soil mechanics . *Géotechnique*, 25(4):671–689, 1975.
- [2939] O.C. Zienkiewicz, P.C. Jain, and E. Oñate. Flow of solids during forming and extrusion: some aspects of numerical solutions. *Int. J. Solids Structures*, 14:15–38, 1978.
- [2940] O.C. Zienkiewicz, M. Pastor, and Maosong Huang. Softening, localisation and adaptive remeshing. capture of discontinuous solutions. *Computational Mechanics*, 17:98–106, 1995.
- [2941] O.C. Zienkiewicz and R.L. Taylor. *The Finite Element Method. Vol. 2: Solid Mechanics*. Butterworth and Heinemann, 2002.
- [2942] O.C. Zienkiewicz, R.L. Taylor, and D.D. Fox. *The Finite Element Method for solid and structural mechanics*. Elsevier B.H., 2014.
- [2943] O.C. Zienkiewicz, J.P. Villette, and S. Toyoshima. Iterative method for constrained and mixed approximation. An inexpensive improvement of FEM performance. *Computer Methods in Applied Mechanics and Engineering*, 51:3–29, 1985.
- [2944] O.C. Zienkiewicz and J. Wu. Incompressibility without tears - How to avoid restrictions of mixed formulations. *Int. J. Num. Meth. Eng.*, 32:1189–1203, 1991.
- [2945] F. Zinani and S. Frey. Galerkin Least-Squares Solutions for Purely Viscous Flows of Shear- Thinning Fluids and Regularized Yield Stress Fluids. *J. of the Braz. Soc. of Mech. Sci. & Eng.*, XXIX:432–443, 2007.
- [2946] S. Zlotnik, P. Diez, M. Fernandez, and J. Verges. Numerical modelling of tectonic plates subduction using X-FEM. *Comput. Methods Appl. Mech. Engrg*, 196:4283–4293, 2007.
- [2947] S. Zlotnik, M. Fernandez, P. Diez, and J. Verges. Modelling gravitational instabilities: slab break-off and Rayleigh-Taylor diapirism. *Pure appl. geophys.*, 165:1491–1510, 2008.
- [2948] M.L. Zoback. First- and second-order patterns of stress in the lithosphere: the World Stress Map project. *J. Geophys. Res.*, 97(B8):11,703–11,728, 1992.
- [2949] M.T. Zuber and E.M. Parmentier. Lithospheric necking: a dynamic model for rift morphology. *Earth Planet. Sci. Lett.*, 77:373–383, 1986.
- [2950] M.T. Zuber, E.M. Parmentier, and R.C. Fletcher. Extension of Continental Lithosphere: A Model for Two Scales of Basin and Range Deformation. *J. Geophys. Res.*, 91(B5):4826–4838, 1986.
- [2951] F. Zwaan, G. Scheurs, J. Naliboff, and S.J.H. Buiter. Insights into the effects of oblique extension on continental rift interaction from 3D analogue and numerical models. *Tectonophysics*, 2016.
- [2952] F. Zwaan, G. Schreurs, and S.J.H. Buiter. A systematic comparison of experimental set-ups for modelling extensional tectonics. *Solid Earth*, 10:1063–1097, 2019.

- [2953] Frank Zwaan, Guido Schreurs, and Matthias Rosenau. Rift propagation in rotational versus orthogonal extension: Insights from 4d analogue models. *Journal of Structural Geology*, page 103946, 2019.
- [2954] T. Zwinger, R. Greve, O. Gagliardini, T. Shiraiwa, and M. Lylly. A full stokes-flow thermo-mechanical model for firn and ice applied to the gorshkov crater glacier, kamchatka. *Annals of Glaciology*, 45:29–37, 2007.

# General Index

- $H^1$  norm, 282
- $H^1$  semi-norm, 282
- $H^1(\Omega)$  space, 282
- $L_1$  norm, 282
- $L_2$  norm, 282
- $P_1$ , 105, 107, 113, 117
- $P_1 \times P_0$ , 137
- $P_1^+$ , 108, 114
- $P_2$ , 110
- $P_2^+$ , 111, 117
- $P_3$ , 113
- $P_m \times P_n$ , 91
- $P_m \times P_{-n}$ , 91
- $Q_1 \times P_0$ , 134
- $Q_1$ , 92, 99
- $Q_1^+ \times Q_1$ , 137
- $Q_2 \times P_0$ , 137
- $Q_2 \times Q_1$ , 91
- $Q_2$ , 93, 101, 116
- $Q_2^{(20)}$ , 118
- $Q_2^{(8)}$ , 102
- $Q_3$ , 93, 104
- $Q_4$ , 96, 105
- $Q_m \times P_{-n}$ , 91
- $Q_m \times Q_n$ , 91
- $Q_m \times Q_{-n}$ , 91
- ABAQUS code, 553
- Adaptive Mesh Refinement, 239
- ADELI code, 553
- Advection-Diffusion Equation, 126
- ALA, 34
- ALE, 170
- AMR, 239
- Anelastic Liquid Approximation, 34
- Angular Momentum, 301
- Angular Velocity, 301
- ANSYS code, 553
- Arbitrary Lagrangian Eulerian, 170
- Arrhenius law, 76
- ASPECT code, 553
- Associated Legendre polynomials, 350
- Augmented Lagrangian, 259
- Average Operator, 164
- Backward Euler, 129
- Barycentric Coordinates, 108
- basis functions, 99
- BDF-2, 130
- BEM, 553
- Biharmonic Operator, 307, 308
- Bingham model, 59
- Bird-Carreau model, 58
- Bird-Carreau-Yasuda model, 58
- Boundary Element Method, 553
- Boussinesq Approximation, 39
- Bow-tied element, 167
- BSc Thesis, 187, 190, 191, 204, 278
- Bubble Function, 91, 108
- Bulk Modulus, 40
- Bulk Viscosity, 33
- Cam-clay failure criterion, 73
- Capacitance matrix, 122
- Carreau model, 58
- CG, 255
- Chain Rule, 261
- Checkerboard mode, 249
- CHIC code, 553
- CitComS code, 553
- Compositional Field, 294
- Compressed Sparse Column, 230
- Compressed Sparse Row, 230
- COMSOL, 554
- Conforming Element, 92
- Conjugate Gradient, 255
- ConMan code, 554
- Connectivity Array, 234
- Convex Polygon, 234
- Courant-Friedrichs-Lowy Condition, 265
- Crank-Nicolson, 129
- Critical Rayleigh Number, 44
- Crouzeix-Raviart, 111
- CSC, 230
- CSR, 230
- Defect Correction Formulation, 305
- Diffusion creep, 61
- Dirichlet Boundary Condition, 43
- Dislocation creep, 61
- Dissipation Number, 35
- Divergence Theorem, 261
- Divergence-free, 32
- Divergence-free Flow, 133
- Domain Decomposition, 306
- DOUAR code, 554
- Drucker-Prager, 70
- Dynamic Viscosity, 33
- DYNEARTHSOL code, 555
- Elasto-Visco-Plasticity, 78
- ELEFANT code, 556
- ELLIPSIS code, 556
- ELMER code, 555
- ENO, 294
- Essential Boundary Conditions, 288
- Extended Boussinesq Approximation, 39

Extrapolation, 283  
 FANTOM, 556  
 FDCON, 556  
 FENICS code, 555  
 FLAC, 557  
 FLAMAR, 557  
 FLUIDITY, 556  
 Forward Euler, 129  
 Frank-Kamenetskii, 77  
 Free Surface, 167  
 GAIA, 555  
 GALE, 555  
 Gauss-Legendre Quadrature, 86  
 Gauss-Lobatto, 90  
 Generalized Newtonian Fluid, 57  
 Geoid, 317  
 Geometric Multigrid, 312  
 Griffith-Murrell, 73  
 GTECTON, 555  
 Haigh-Westergaard Coordinates, 51  
 Herschel-Bulkley model, 59  
 Heun's emthod, 276  
 hyperbolic PDE, 265  
 I2(3)(EL)VIS code, 556  
 Isoparametric, 266  
 Isotropic, 131  
 Jump Operator, 164  
 Kelvin-Voigt Model, 78  
 LaCoDe code, 555  
 Lamé Parameter, 40  
 LaMEM code, 556  
 LAPEX code, 556  
 Laplace Operator, 36, 37  
 Laplacian, 36, 37  
 Lax-Friedrichs flux, 161  
 LBB, 133  
 Legendre Polynomial, 86  
 Level-set Function, 294  
 Level-set Method, 294  
 Lode Angle, 50, 56  
 Lode Coordinates, 51  
 Lode Parameter, 52  
 LSF, 294  
 LSM, 294  
 Lyapunov Time, 318  
 MAC, 291  
 Marker Chain method, 296  
 Marker-and-Cell, 291  
 Mass matrix, 122  
 Maximum Shear Stress, 46  
 Maxwell Model, 78  
 MC3D code, 555  
 Meshless, 234  
 Method of Manufactured Solutions, 183  
 MICROFEM code, 559  
 Midpoint Method, 276  
 Midpoint Rule, 85  
 MILAMIN, 557  
 MILAMIN\_VEP, 557  
 MINI element, 135  
 Mixed Formulation, 141  
 MMS, 183  
 Mohr-Coulomb, 69  
 Moment Invariant, 52  
 Moment of Inertia, 301  
 MSc Thesis, 60, 82, 131, 209, 210, 305, 549  
 Natural Boundary Conditions, 288  
 Neumann Boundary Condition, 43  
 Newton's method, 280  
 Newton-Cotes, 86  
 Newtonian fluid, 57  
 Non-Conforming Element, 92  
 Nonlinear PDE, 304  
 Normal Stress, 29  
 Nullspace, 252  
 Nusselt Number, 45  
 Optimal Rate, 133  
 optimal rate, 283  
 Orthotropic, 131  
 PARAVOZ, 557  
 Particle-in-Cell, 291  
 Peierls creep, 76  
 Penalty Formulation, 137  
 Periodic Boundary Conditions, 300  
 PIC, 291  
 Picard Iterations, 304  
 Piecewise, 91  
 Plain Strain, 54  
 Plastic Hardening, 179  
 Poiseuille flow, 187  
 Poisson Ratio, 40  
 Power-law model, 58  
 Prandtl Number, 45  
 Prandtl number, 35  
 Preconditioned Conjugate Gradient, 258  
 pressure nullspace, 188  
 pressure scaling, 251  
 Pressure Smoothing, 249  
 Principal Invariants, 49  
 Principal Stress, 46  
 Principal Stress Ratio, 55  
 pTatin3D, 557

PyLith, 558  
 Quadrature, 86  
 Rayleigh Number, 44  
 Rectangle Rule, 85  
 reference element, 266  
 Relaxation, 304  
 RHEA, 558  
 Richardson Iterations, 254  
 RK2, 276  
 RK3, 276  
 RK4, 276  
 RK45, 276  
 Runge-Kutta-Fehlberg method, 276  
 Schur Complement, 254  
 Second Viscosity, 33  
 SEPRAN code, 558  
 Serendipity element, 102, 118  
 Shear Heating, 187  
 Shear Modulus, 40  
 Shear Stress, 29  
 SISTER code, 558  
 SLIM3D code, 558  
 SLOMO code, 559  
 SNAC code, 559  
 Solenoidal Field, 32, 133  
 SOPALE code, 559  
 Sparse Matrix-Vector Multiplication, 233  
 SPD, 254  
 SPECFEM3D code, 559  
 Spin Tensor, 30  
 SpMV, 233  
 STAG3D code, 559  
 STAGYY code, 559  
 Static Condensation, 136, 298  
 Sticky Air, 168  
 Strain Rate, 30  
 Strain Rate Tensor, 44  
 Strain Tensor, 40, 44  
 Stream Function, 307, 308  
 Stress Tensor, 29, 44  
 Stress Vector, 29  
 strong form, 133  
 Structured Grid, 234  
 SUBMAR code, 560  
 Subparametric, 266  
 SULEC code, 560  
 Superparametric, 266  
 Symmetric Positive Definite, 562  
 Taylor-Hood, 133  
 TECTON, 555  
 Tensor Invariant, 52  
 TERRA code, 560  
 TERRA-NEO, 560  
 TerraFERMA code, 560  
 Traction, 29  
 Trapezoidal Rule, 85  
 Tresca, 68  
 Underworld code, 561  
 Unstructured Grid, 234  
 Validation, 84  
 Velocity Gradient, 30  
 Verification, 84  
 Viscoelasticity, 78  
 Viscosity Rescaling Method, 248  
 von Mises, 65  
 VRM, 248  
 Weak Form, 139  
 weak form, 133  
 YACC code, 561  
 Young's Modulus, 40

## **Contributors**

A. van den Berg, 322

E. Hoogen, 383

E. van der Wiel, 525

E.G.P. Puckett, 371

J. Mos, 351

L. van de Wiel, 469, 532

Rens Elbertsen, 435, 456

T. Shinohara, 538

T. Weir, 410, 412

W. Spakman, 28

## Topics in the literature

- (Absolute) Plate Motion, 585  
Accretionary Prism, 591  
Accretionary Wedge, 591  
Adjoint Methods, 579  
Aegean region, 594  
Afar rift, 594  
African Continent, 594  
Alaskan region, 594  
Alps, 593  
Analogue Modelling, 575  
Anatolia, 594  
Andes, 593  
Anisotropy, 576  
Antarctica, 594  
Apennines, 593  
Arabian plate, 594  
Archean tectonics, 576  
Assimilation, 579  
Atlas, Morocco, 594  
Australian plate, 594  
  
Barents sea, 594  
Basin and Range, 594  
Buckling, 581  
  
Canada, 594  
Cantabria & North-Iberian margin, 594  
Canyonlands, 594  
Caribbean region, 594  
Carpathians, 594  
Channel Flow, 577  
China, 594  
CMB, 577  
Colorado plateau, 594  
Continental Collision, 577  
Core Dynamics, 577  
  
D” layer, 582  
Dead Sea, 594  
Delamination, 580  
DEM, 591  
Detachment faults, 580  
DG-FEM, 578  
Diapirism, 591  
Discontinuous Galerkin Method, 578  
Discrete Element Method, 591  
Dynamic Topography, 580  
Dynamo, 578  
  
Early Earth, 576  
Edge Driven Convection, 580  
EFGM, 591  
Elasticity in Geodynamics, 578  
  
Element Free Galerkin Method, 591  
Enceladus, 593  
Erosion, 578  
Europa, 592  
Exo-planets, 591  
Extension, 587  
  
Farallon plate, 594  
Flat/low angle subduction, 590  
Fold-Thrust Belt, 591  
Folding, 581  
  
Geoid, 582  
Geotechnics, 579  
Geothermal Energy, 582  
Gibraltar area, 594  
Glacier Dynamics, 579  
GOCE, 577  
GPS, 577  
GRACE, 577  
Grain Damage, 582  
Grain Size (Evolution), 582  
Gravity, 577  
Greece/Hellenic area, 594  
Greenland, 594  
  
Hawaii, 594  
Heat Flow, 577  
Himalayan region, 593  
Hotspots, 586  
  
Ice flow, 579  
Ice Rheology, 579  
Ice Sheets, 579  
Icy satellites, 593  
Intraplate Stress, 581  
Intrusions, 591  
Inverse Methods, 579  
Io, 593  
Izu-Bonin, 594  
  
Japan, 594  
  
Landscape Evolution, 578  
Large Igneous Provinces, 586  
Lithospheric Stress, 581  
LLSVP, 582  
LPO/CPO, 576  
  
Magma Oceans, 583  
Magma Transport, 583  
Mantle Convection, 583  
Mantle Rheology, 584  
Mantle Stratification, 584

- Mantle Tomography, 577  
Mantle Unrooting, 580  
Mantle Wedge, 585  
Mars, 592  
Mediterranean Region, 593  
Melt Migration, 583  
Melting, 583  
Mercury, 592  
Metamorphic Core Complex, 577  
Mid-Ocean Ridge, 587  
Mixing, 585  
Moon, 592  
New Zealand, 593  
North America, 593  
Norway, 594  
Obduction, 585  
Ophiolites, 585  
Passive Margins, 581  
Phase Diagram, 584  
Phase Transition, 584  
Planet Formation, 591  
Planetary Accretion, 591  
Plate Kinematics, 585  
Plate motion modelling, 580  
Plate Tectonics Reconstruction, 585  
Plume Dynamics, 585  
Plume-Lithosphere Interaction, 586  
Pluto, 593  
Porous Media, 586  
Postperovskite Phase Transition, 582  
Pyrenees, 594  
Rayleigh-Taylor Instability, 591  
Rheology, 574, 587  
Rifting, 587  
Salt Tectonics, 588  
Scotia Plate, 594  
Sea Level, 574, 588  
Seafloor spreading, 587  
Sedimentation, 578  
Seismo-tectonics, 588  
Shale Tectonics, 588  
SKS splitting, 576  
Slab Detachment, 589  
Slab Break-off, 589  
Smoothed Particle Hydrodynamics, 591  
South America, 593  
South East Asia, 594  
SPH, 591  
Stirring, 585  
Structural Geology, 577  
Subduction, 589  
Subduction Initiation, 590  
Subduction+fluids, 590  
Super-Earths, 593  
Supercontinent Cycle, 591  
Supercontinent Formation, 591  
Surface Processes, 578  
Taiwan, 594  
Teaching, 590  
Thermo-chemical pile, 582  
Thrust Wedge, 591  
Thrust-Wrench Fault, 591  
Tibetan plateau, 593  
Tonga-Kermadec subduction, 594  
Topography Evolution, 578  
Transpressional system, 591  
True Polar Wander, 585  
Turkey, 594  
Two Phase Flow, 583  
Urey Ratio, 591  
Uzawa-type algorithms, 592  
Venus, 592  
Visualization, 592  
Wilson cycle, 591  
Zagros, 593

## Notes

VERIFY all this ! . . . . .	36
finish. not happy with definition. Look at literature . . . . .	45
derive formula for Earth size R1 and R2 . . . . .	46
check aspect manual The 2D cylindrical shell benchmarks by Davies et al. 5.4.12 . . . . .	46
What of all this if the flow is compressible? . . . . .	55
look at folder, codes, clean up, change labels new and old . . . . .	65
I need to talk about Byerlee's law. [398] . . . . .	83
insert here figure . . . . .	85
insert here figure . . . . .	85
citation needed . . . . .	101
find reference . . . . .	111
VERIFY that when $\eta_1 = 1 - r - s$ , $\eta_2 = r$ and $\eta_3 = s$ we find the above $r, s$ shape functions . . . . .	113
verify those . . . . .	113
REFS ??? better definition of functions ! . . . . .	117
find/build shape functions! . . . . .	118
NOT happy with this statement!! . . . . .	119
add source term!! . . . . .	129
find literature . . . . .	133
Check Cuvelier book chapter 8 for modified element . . . . .	137
list codes which use this approach . . . . .	138
reduced integration [1254] . . . . .	140
write about 3D to 2D . . . . .	140
insert here link(s) to manual and literature . . . . .	141
surface terms arising from the integration by parts are neglected. EXPLAIN WHY! . . . . .	174
Find analytical expression for pressure. Compute expression for rhs. Make stone . . . . .	191
there are discrepancies between [2094] and [444] . . . . .	210
finish vrms calculation of benchmark . . . . .	215
produce drawing of node numbering . . . . .	235
write about gmesh . . . . .	238
insert here the rederivation 2.1.1 of spmw16 . . . . .	248
produce figure to explain this . . . . .	250
link to proto paper . . . . .	250
link to least square and nodal derivatives . . . . .	250
check this, and report page number . . . . .	255
add biblio . . . . .	256
how to compute $M$ for the Schur complement ? . . . . .	259
finish GMRES algo description. not sure what to do, hard to explain, not easy to code. . . . .	260
why does array contain only T?? . . . . .	263
finish . . . . .	263
re ask Wolfgang about this - correlate with deal.ii . . . . .	273
missing refs for Butcher tableau . . . . .	276
write about case when element is rectangle/cuboid . . . . .	281
to finish . . . . .	285
to finish . . . . .	285
refs! . . . . .	289
tie to fieldstone 12 . . . . .	289
it would be nice to have a Q1 and Q2 drawing of a 1D element and show that indeed negative values arise . . . . .	292
write more about particle averaging and projection . . . . .	293
write about DG approach . . . . .	295
ask Arie to write something . . . . .	296
I still have pics from the old days using DOUAR- include . . . . .	296
check . . . . .	298
implement and report . . . . .	299

missing picture . . . . .	300
explain why our eqs are nonlinear . . . . .	304
write about nonlinear residual . . . . .	304
FIND refs. check new version of Vol7 theoretical geophys . . . . .	308
get these papers . . . . .	310
build S and have python compute its smallest and largest eigenvalues as a function of resolution?	390
finish structure of C matrix for q1q1 . . . . .	408
compare my rates with original paper! . . . . .	409
explain how Medge is arrived at! . . . . .	433
compare with ASPECT ??!	433
pressure average on surface instead of volume ? . . . . .	433
carry out other two measurements (need interpolation onto other grid for this . . . . .	496